The Petrology and Transformation History of Continental Crust in the Tso Morari Complex, Ladakh, Himalaya

By

Anna Bidgood

Thesis submitted to the University of Oxford

for the degree of Doctor of Philosophy

in

Geology and Mineralogy







DOCTORAL TRAINING PARTNERSHIP
ENVIRONMENTAL RESEARCH

Department of Earth Sciences

and

University College

January 2020

Supervised by Prof. Dave Waters, Prof. Mike Searle and Dr Nick Roberts

“I have made this longer than usual because I have not had

time to make it shorter”

Blaise Pascal
Lettres Provinciales
1657

UNIVERSITY OF OXFORD

DATE: January 2020

AUTHOR: Anna Bidgood

TITLE: The petrology and transformation history of continental crust in the Tso Morari complex, Ladakh, Himalaya

DEPARTMENT: Earth Sciences

COLLEGE: University

DEGREE: Doctor of Philosophy

SUPERVISORS: Dave Waters, Mike Searle, Nick Roberts

Declaration

Although the work presented in this thesis has benefitted from discussion with supervisors, publication co-authors and suggested corrections as a result of the peer-review process, it remains solely the result of my own labour. This includes all data acquisition, analysis and interpretation, unless explicitly stated otherwise.

Copyright ©, by Anna Bidgood, 2020.

All rights reserved.

No part of the material protected by this copyright notice may be reproduced or utilised in any form or by any means, electronic or mechanical, including photocopying, recording or by any information storage and retrieval system, without written permission from the copyright owner.

Printed in the United Kingdom.

Abstract

The petrology and transformation history of continental crust in the Tso Morari complex, Ladakh, Himalaya

Anna Bidgood

University College, Oxford

January 2020

Ultrahigh-pressure (UHP) metamorphism has long been associated with deep subduction. UHP minerals, such as coesite and microdiamond, are often found in discrete mafic units, hosted in larger scale continental terranes, such as in the mafic eclogites of the Tso Morari complex, Ladakh, Himalaya. Terranes such as these have commonly been overprinted by amphibolite facies, Barrovian metamorphism, so their early history is difficult to decipher. Samples of mafic eclogite dykes hosted in low-strain metagranite were collected from the centre of the Tso Morari complex in Ladakh, Himalaya, where the granite has been observed to transition into granite gneiss towards the high-strain mafic–felsic lithological boundary. All three of these lithologies are shown to preserve high pressure metamorphism indicating that the entire unit must also have been subducted to high pressure conditions.

Low-strain metagranites provide a window into the early history of the rocks, where feldspar, white mica and pseudomorphs after cordierite preserve evidence of hydrothermal alteration prior to high pressure metamorphism. Kyanite inclusions within garnet also indicate that the high-Al bulk composition of the granite gneiss must have been achieved prior to garnet growth, also indicating that hydrothermal alteration prior to garnet growth may have been significant. Palisade quartz microtextures after coesite in the matrix of a granite indicate that part of the dome transformed at ultrahigh-pressure conditions and preserves the first reported evidence of twinning in coesite recorded in quartz.

Elemental zonation within garnets from mafic eclogite and granite gneiss protoliths show a similar zoning pattern in rocks of different bulk compositions, indicating that both rock types share a similar prograde high-pressure metamorphic evolution, where highest pressure conditions are preserved in the garnet rims. Previous modelling of mafic eclogites has shown that there are two possible isopleth intersections for garnet core growth at ca. 20-23 kbar, 520-550°C and 10-13 kbar, 575-625°C. However, alteration of inclusion assemblages has made it difficult to determine the actual conditions of core growth. Combined modelling of mafic and felsic protoliths, shows that the lower pressure intercept of 10-14 kbar, 410-460°C is common in both bulk compositions in water undersaturated conditions.

A new and precise U-Pb age of zircon crystallisation at 46.9 ± 0.04 Ma is interpreted as the age of eclogite-facies metamorphism. U-Pb ages of xenotime, titanite and rutile are interpreted as ages representing crustal conditions, indicating that the Tso Morari complex was exhumed from ultrahigh-pressure to crustal conditions in <1 Myr before stalling in the lower crust.

Extended Abstract

The petrology and transformation history of continental crust in the Tso Morari complex, Ladakh, Himalaya

Anna Bidgood

University College, Oxford

January 2020

Ultrahigh-pressure continental terranes are areas of continental lithosphere that have experienced pressures greater than that of the transition from quartz to the higher-pressure silica polymorph coesite. Ultrahigh-pressure conditions have now been recorded in most continental collision zones in the Phanerozoic and are achieved by the subduction of continental lithosphere. However, the mechanism by which they are subducted and exhumed is debated and the importance that the process of continental subduction plays in the orogenic cycle is poorly understood. Metamorphic rocks offer the best opportunity to study processes such as continental subduction in detail as growth of new metamorphic phases provides a snapshot of absolute P-T conditions achieved at different pressure and temperature conditions. Age constraints obtained through geochronological data can be combined with petrological data in order to calculate the timing and rates of processes responsible.

There is abundant geological evidence showing that continental subduction occurred during continent-continent collision in many orogens throughout Earth's history. One of the youngest examples of continent-continent collision is the Himalayan orogen which formed as a result of the collision of India with Asia. Two ultrahigh-pressure terranes have been identified in the Himalaya where subducted continental rocks have been exhumed to the surface, providing a natural laboratory for the investigation of plate tectonic processes. One of these forms the case study for this thesis.

Although evidence for continental subduction is increasingly identified in orogens active throughout Earth's history, textures formed during continental subduction are often overprinted by retrograde metamorphism and deformation during continued collision. Detailed microscale analysis is required to unravel the metamorphic history of each rock. Lithologies of varying bulk composition record snapshots from different parts of the P-T history and can be pieced together to decipher a more complete history of subduction and

exhumation. This thesis investigates the metamorphic history of the Tso Morari ultrahigh-pressure complex in Ladakh, Himalaya. Each chapter explores the metamorphic record preserved in different lithologies from within the complex, with a focus on the high-pressure history, including the absolute P-T conditions, timing of metamorphism, timing and temperature of deformation and the extent of transformation.

Previous studies of the Tso Morari complex have focussed on the ultrahigh-pressure metamorphic history preserved in accessible outcrops of mafic eclogites, while other, broader studies have examined the structural evolution of the complex and the surrounding units (e.g. De Sigoyer *et al.,* 2000, Epard and Steck, 2008). Eclogite-facies mineral assemblages have been observed in many locations across the complex. However, detailed petrographic analysis and evidence of UHP metamorphism has only been identified in two outcrops within the complex and evidence that the entire complex underwent a comparable metamorphic history is lacking. This is due in part to the difficult accessibility of many parts of the complex, owing to a single road, the high altitude, steep topography and difficult terrane. Previous studies of the Tso Morari complex also present a paucity of spatial and temporal data, making tectonic synthesis difficult. In chapter 2, I record field observations from different locations across the complex and document the location of samples described in subsequent chapters. This record allows the variations and similarities between samples to be analysed with respect to their spatial distribution and outcrop scale observations.

In chapter 5, I explore the petrographic variation in a range of eclogites from the Tso Morari complex, in order to determine the major variations in bulk composition, peak P-T conditions and the common prograde and retrograde trends. Mafic rocks are the best recorders of UHP metamorphism, forming eclogite-facies mineral assemblages. Zoned garnet, omphacite and quartz are common features of the peak assemblage, whereas talc, phengite, kyanite and dolomite are present in varying abundances. Results of conventional thermobarometric calculations predict peak P–T conditions ranging from 19–30 kbar, 450–650°C and are mostly dependent on the presence of phengite as a peak phase. Multi-equilibrium average thermobarometry (AvePT) estimates are more consistent, 23.5-33.5 kbar, 580–700°C, suggesting that there is no resolvable difference in peak P–T conditions between samples; however, the large pressure uncertainty on these calculations does not allow pressure differences of $< \pm 5$ kbar to be resolved.

There is evidence of initial post–peak hydration of the eclogites in the garnet mineral chemistry, which is linked to the replacement of amphibole inclusions in garnet and the growth of matrix amphibole cores, followed by growth of clinozoisite poikiloblasts. Conditions of prograde metamorphism are therefore difficult to constrain petrographically due to alteration of prograde mineral assemblages. New phase equilibrium models of prograde metamorphism in water undersaturated conditions, constrained by garnet growth mechanisms and 'trustworthy' inclusion assemblages, produce P–T estimates at much lower pressures and temperatures than previous models, defining an isothermal up-pressure trajectory followed by isobaric heating. Predicted P–T conditions of garnet core growth are shown to be very sensitive to bulk composition and water saturation. This study highlights the importance of detailed petrographic study in order to confidently characterise the input parameters for thermodynamic modelling and estimation of P–T conditions. It also highlights the sensitivity of garnet composition isopleths, previously thought to be the most robust indicator of prograde P–T conditions, to water saturation and hydration state in certain bulk compositions.

In chapter 4, I investigate the complex metamorphic history preserved in low-strain granitoids in the Tso Morari complex. Low-strain zones provide a window into metamorphic processes that occurred prior to deformation. The domainal microstructure of these rocks preserves the original igneous textures, which contain white mica compositions and textures indicative of hydrothermal alteration during the late stages of emplacement, including the formation of pseudomorphs after cordierite during the late-stage alteration of the granite. High-pressure assemblages replacing the cordierite pseudomorphs, coronas of garnet and phengite around igneous biotite and prograde zoned garnets, are evidence that the rocks later experienced eclogite facies metamorphism, as recorded by the included mafic bodies.

Later recrystallisation and metamorphism in the amphibolite facies does not completely alter the chemical and textural record preserved in the granite domains, allowing a complex 479 Myr history to be observed within the granites. This chapter provides the first thorough petrographic description of the metagranites of the Tso Morari dome. It also documents the first example of high-pressure metamorphism within metagranitoids in the Himalaya, displaying similarities with known high-pressure terrains around the world, and the first description of high-pressure assemblages in cordierite pseudomorphs.

In chapter 5, I investigate the record of high-pressure metamorphism in the deformed granite gneiss (Puga Gneiss) which forms the most abundant lithology in the Tso Morari complex. The Puga Gneiss is formed from a heterogeneous granitic protolith but can be difficult to distinguish in hand specimen from metasedimentary-derived garnet-mica schists, owing to deformation processes causing recrystallisation of distinctive magmatic phases. Felsic rocks are less easily transformed to ultrahigh-pressure assemblages and more easily overprinted by retrograde processes, making evidence of high-pressure metamorphism rare. Zoned garnet poikiloblasts preserve growth zoning and alteration patterns comparable to garnets in the ultrahigh-pressure mafic eclogites, indicating that these rocks underwent a similar high-pressure history.

Phase equilibrium modelling demonstrates that garnet core growth occurred in water undersaturated conditions in the kyanite stability field and culminated in the growth of the garnet rims in hydrous, high-pressure conditions. Primary igneous plagioclase is no longer present and broke down to form white mica, albite and clinozoisite. The lack of observed clinopyroxene, and the discrepancy between predicted and observed grossular contents in garnet rims, indicates that the breakdown of plagioclase did not occur within the clinopyroxene stability field, and that plagioclase persisted metastably to high pressures. Variations in quartz deformation microstructures and the implied temperature of quartz recrystallisation indicates a temperature gradient existed between structurally deep samples in the middle of the dome, where annealing of quartz took place after the development of the high strain fabric, and structurally higher samples where little annealing has taken place.

In chapter 6, I study a specific metagranite sample which preserves a palisade texture in quartz, indicative of transformation to coesite at ultrahigh-pressure conditions, followed by inversion back to quartz. The dominantly felsic composition of ultrahigh-pressure continental terranes means that petrology-based techniques for determining peak pressures and temperatures are often not possible. In such cases, the detection of ultrahigh-pressure conditions depends on the preservation of coesite. Unfortunately, coesite rapidly transforms to quartz on decompression, making identification difficult. The qualitative identification of palisade quartz microstructures that form during the retrograde transformation of coesite to quartz is often used to determine the existence of UHP terranes. In the sample studied, the shape of quartz domains matches that of igneous single quartz grains observed in neighbouring granite, which have not undergone

transformation to coesite. Electron Backscatter Diffraction (EBSD) and misorientation analysis are used to demonstrate that these domains of palisade quartz are bisected by boundaries separating subdomains with 'single-crystal' crystallographic preferred orientations (CPOs). Within a single subdomain, adjacent palisade quartz grains have a respective misorientation of 60°/[0001], equivalent to the quartz dauphiné twin law.

Adjacent subdomains of palisade quartz grains have respective misorientations of $\mathbf{90}^{\circ}/<\boldsymbol{a}>$ which is consistent with the inheritance of twinning in the former coesite. My observations imply that the coesite-to-quartz transformation is crystallographically controlled and suggest that identification of quartz-after-coesite microstructures in other UHP quartz-bearing rocks may be determined from a crystallographically-defined set of criteria. I believe this is the first reported evidence of twinning in former coesite inherited by daughter grains of quartz and the first quantitative approach to use quartz crystallographic preferred orientations as an indicator of burial to UHP conditions.

In chapter 7, I focus on the age constraints of metamorphism obtained through geochronology. Determination of the U-Pb age of eclogite facies zircon crystallisation in one sample, via chemical abrasion isotope-dilution mass spectrometry, produces a precise estimate on the timing of high-pressure metamorphism. Xenotime, titanite and rutile ages are interpreted to represent the time when then rocks were exhumed to crustal depths. These data were collected using laser-ablation mass spectrometry and provide constraints on a part of the geochronological history of the Tso Morari complex, from 47 to 22 Ma, that currently is lacking in age data but is extensively recorded in retrograde metamorphic microstructures and in amphibole and garnet compositions. Rutile and titanite ages across the complex provide a new dataset which can be used in conjunction with temperature estimates from the Zr content of rutile to further constrain the exhumation style of the Tso Morari nappe.

Finally, in chapter 8, I focus on the synthesis of field, structural, geochemical, thermobarometric and geochronological data from different lithologies of the Tso Morari complex, in order to further understand the subduction and exhumation history. The new and precise age of eclogite-facies metamorphism at 46.9 ± 0.04 Ma is used to calculate the duration of subduction of the Tso Morari complex and is considered with respect to three different models for the India-Asia collision, their shortfalls and their assumptions.

Different stages of P-T-t history of the Tso Morari complex are considered, including the shape of the prograde path, peak pressure conditions achieved, partial transformation in the eclogite facies, detachment of material at depth, isothermal decompression to crustal conditions, temperatures achieved after exhumation to crustal levels and exhumation from the lower crust. Phase equilibrium modelling combined with petrographic analysis, as described in earlier chapters, indicates a prograde P-T path initially dominated by loading and followed by heating. The discrepancy in apparent peak pressures suggests that local overpressure may have been important in transforming only some of the quartz to coesite. Only partial transformation of other phases occurred in the eclogite facies owing to the scarcity of fluids during subduction.

Combining textural observations, trace element analysis and P-T determination with age constraints allows the rates of tectonic processes to be estimated from different samples across the complex and provides insights into the exhumation mechanisms. Age data indicates that samples from the Tso Morari nappe were exhumed quickly from ultrahigh-pressure depths in <1 Myr, before stalling in the lower crust for 10-20 Myr, contributing to the characteristic kinked exhumation path. The mechanism by which the rocks were exhumed to the lower crust, where buoyancy contrast drives exhumation, and from the lower crust, where neutral buoyancy is achieved, must therefore have been different.

Acknowledgements

First of all, I would like to thank my supervisors Dave Waters and Mike Searle for envisioning this project and for their contributions during discussions, particularly over tea in the researcher's common room. I would also like to thank my supervisor Nick Roberts for his guidance and expertise in all things geochronology, as well as Simon Tapster for analysing my samples and taking the time to teach me. I would like to thank the Oxford DTP in environmental science for funding me, as well as the following organisations and grants which supported my fieldwork: Geological Society of London (Mike Coward Fund), Royal Geographical Society (teaching and learning fund), University College Oxford, the Mineralogical Society and Edinburgh Geological Society.

My project required approximately 3 months of fieldwork which would not have been possible without the help of the following people, for which I thank them. Talat Ahmad, Vice Chancellor of Jamie Millia Islamia, New Delhi, for his contacts and in country expertise and arranging transportation of my samples. Nabiley and his family at Sia La Guesthouse for organising the in-country logistics and accommodation. Stanzin Stofail for his 'patient' driving and hammering skills. Tsering Choldan for his incredible cooking, organisation and guiding skills and for putting up with me and my egg-based diet for 3 months of fieldwork. Micah and Laura Jessup for accompanying me in the field despite the fact that I failed to turn up. I'd also like to thank my field assistants Jack Utting, Eloise Chambers, Jo Male and Oscar Boyd, who carried my rocks, labelled the samples, fed me chocolate and entertained me for endless hours. A special shout out goes to Oscar Boyd for re-summitting Stok Kangri with me after I lay down in the snow and to Jo Male for propping me up.

It has been a pleasure to be part of the Hard Rock group. I learnt so much discussing rocks in the pub. I thank Phil Gopon and Jon Wade for their training and expertise on the SEM and electron microprobe. I thank Ed Baker for helping me on the probe and helping me to set up the Oxford Society of Economic Geologists. I thank Rellie Goddard, Andy Parsons and Geoff Lloyd for their training, expertise and discussion relating to EBSD analysis of my granites, an unplanned part of the thesis that ended up as an extra chapter. I thank Tom Lamont for letting me accompany him on his PhD fieldwork to the Cyclades and for asking me about pseudosections first thing on Sunday mornings. I thank the 4th years who really added to Hard Rock group

discussions and scared me into learning more about amphiboles. I thank Tyler Ambrose for keeping me sane and calm. I thank Clare Warren for discussions on modelling and the Himalaya. I thank Brendan Dyck for his advice and discussions on all aspects of geology.

I thank Vicky Elliot, Ronnie Guthrie, Rellie Goddard and Sean Selzer for the great company in office 20.15. I thank Ronnie for providing the snacks and Rellie for eating them. I thank Sean Selzer for pretending to be interested in my work. I thank Jon Wells for making many excellent thin sections and Adrian wood for the training and conversations in the mineral separation lab. I thank Eleni Wood for hosting me on 'work aways', putting up with my incessant talking and being so supportive.

One of the biggest experiences of my time in Oxford was playing rugby for the Blues team and playing four out of six varsity matches at Twickenham stadium. I would like to thank every player and coach who has stood beside me. I cannot imagine my time in Oxford without rugby.

A big thank you goes to my family who have supported me through every decision. I thank my mum and dad for encouraging me to do my best in all aspects of my life and for coming to watch every Twickenham match. I thank my sister for always being able to put a smile on my face and my nephew Kimball for asking "what's in the rocks".

Contents

Declaration……i

Abstract…… .iii

Extended Abstract……..v

Acknowledgements……...xi

Contents……...…xiii

Chapter 1 – Introduction

Introduction to ultrahigh-pressure terranes……...……1

Common features of ultrahigh-pressure terranes……...……...3

Continental subduction geodynamics……...……6

Formation of ultrahigh-pressure terranes……...……7

Detaching a continent……...……...8

Exhuming a continent……...……10

Himalayan High-Pressure rocks……...……..18

The Himalayan Orogen……...……...18

Metamorphic evolution……...……..20

India-Asia collision……...……22

High-Pressure metamorphism in the Himalaya……...…….24

Thesis Objectives……...……30

Thesis Structure ……..……32

Chapter 2 - Field relationships of the Tso Morari complex

The Tso Morari dome ……...…….33

Terminology ……..……...37

Stratigraphy……...37

Origin of the Tso Morari mafic rocks……..……..41

Structural history of the Tso Morari complex…….…….…….42

Metamorphic evolution of Tso Morari complex …….…….46

Published data from the Tso Morari complex……..…….47

Aim of this chapter …….50

Key localities in the Tso Morari dome …….…….....51

The western shore of Tso Morari ……..……60

The Bridge……..…….....62
North shore of Kiagar Tso ……..……..64
Kiagar La ……..……66
Berthelsen Outcrop ……..…….68
Road to Ribil Sumdo ……..……..70
Ribil Valley and the Zildat shear zone ……..……70
Eastern Puga Valley ……..……72
Puga hot springs ……..……..74
Puga school ……..…….75
Puga valley halfway up the pass……..……..76
Polokongka La pass ……..…….....78
Polokongka La ridge ……..……..79
Thukje……..…….80
North of Ponganagu……..…….82
Ridge west of Ponganagu……..……84
Nuruchen……..…….87
Nuruchen to Gyama Barma……..…….91
Tetraogal nappe……..…….....93
Karzok ……..95
Mata nappe……...……...……..95

Chapter 3 - Petrography and thermodynamic modelling of the Tso Morari eclogites

Introduction……...…….....98
The Tso Morari eclogites……..……...……..……100
Petrography and mineral chemistry…….....……..107
Sampling strategy and analytical methods……..108
Kiagar Tso……...…….……..111
Kiagar La……...…….114
Berthelsen outcrop……...……...……...…….120
Puga Valley…….....……123
Polokongka La pass……...…….129
Polokongka La ridge……...……130
Discussion…….....……...…136
Thermobarometry and Phase Equilibrium Modelling…….……155
Discussion……...…….....…183
Summary……...……...……..193

Chapter 4 - Eclogite-facies metamorphism in low–strain metagranites of the Tso Morari complex

Introduction……..…196
Petrography and Mineral Compositions……...198
Geochronology……...……..214
Phase equilibrium modelling……216
Interpretation……...….217
Evolution of the Tso Morari granitoids……..……..224
Summary ……...……..229

Chapter 5 – The transformation of continental crust during eclogite facies metamorphism

Introduction……...……...230
Sampling strategy and analytical methods……..……..…..…….……232
Results……..…….……...234
Whole Rock Geochemistry…… 234
Petrography and Mineral Chemistry.…….……240
Phase equilibrium modelling..……264
Discussion...…….268
Summary…...……...279

Chapter 6 - EBSD analysis of palisade quartz textures: implications for coesite-quartz transformation

Introduction…….……281
Sample description……...…283
Crystallographic preferred orientation and grain boundary misorientation analysis……..….285
Discussion...……292
Summary .....……...……...…. ……..….300

Chapter 7 - Geochronology of the Tso Morari nappe

Introduction ……...……...301
Methods.……..……...…….304
Radioisotopic dating……..…….304
Zirconium in Rutile thermometry…….……..……305
Results……..…….……...309
Discussion…….……..…….321
Summary……...……..……...……332

Chapter 8 – Tectonic synthesis

Summary ……336

The North Indian margin……339

Timing of continental collision……340

Competing models for the India-Asia collision……341

Subduction of continental crust……343

Loading/burial then heating……349

Peak metamorphism……350

Detachment……352

Isothermal decompression……354

Temperatures achieved after exhumation to crustal levels……356

Exhumation from the lower crust……358

Exhumation mechanisms: ……359

The history of the Indian crust in Ladakh……360

Future work……363

Appendix 1 – Sample locations

Appendix 2 - Methods

Appendix 3 – Radioisotopic data

Appendix 4 – XRF data

Appendix 5 – EPMA data

Appendix 6 – Isocon analysis

List of Figures

Chapter 1 – Introduction

Figure 1 Map of known ultrahigh-pressure terranes worldwide 1
Figure 2 General characteristic of ultrahigh-pressure terranes..... 4
Figure 3 Schematic representation of the formation of ultrahigh-pressure terranes 8
Figure 4 Schematic representation of exhumation mechanisms 13
Figure 5 Exhumation model and P-T-t paths compared to data from the Tso Morari dome 17
Figure 6 Geological map and cross section of the Himalaya-Tibet orogenic system 18
Figure 7 Cartoon summary of the evolution of the Himalaya. 23
Figure 8 Summary of P-T results and proposed P-T paths for the Himalayan eclogites 24

Chapter 2 - Field relationships of the Tso Morari complex

Figure 1 Geological map of NW India 35
Figure 2 Geological map of the Himalaya and Tso Morari dome 36
Figure 3 Stratigraphic sections from northern India 40
Figure 4 Structural map of the Tso Morari dome. 45
Figure 5 Map showing the location of published samples. 48
Figure 6 Overview map of localities in the Tso Morari dome 52
Figure 7 Map of locality numbers on eastern side of traverse. 53
Figure 8 Geological map of the northern margin of the dome.. 54
Figure 9 Map of the NW of the Tso Morari complex around Tso Kar.. 55
Figure 10 Structural map of the NW of the Tso Morari complex around Tso Kar.. 56
Figure 11 Map of the SW of the Tso Morari complex around Tso Kar. 57
Figure 12 Structural map of the SW of the Tso Morari complex around Tso Kar. 58
Figure 13 Map of the southern part of the Tso Morari dome. 59
Figure 14 Western shore of Tso Morari lake. 61
Figure 15 Photos of variations within Puga gneiss outcrops. 62
Figure 16 The Bridge locality. 63
Figure 17: Photos from the northern shore of Kiagar Tso.. 65
Figure 18 Kiagar La locality. 67
Figure 19 Berthelsen locality. 69
Figure 20 Ribil Sumdo to Sumdo village. 71
Figure 21 Metasedimentary raft with compositional layering. 73
Figure 22 a. Puga Gneiss 73
Figure 23 Puga hot springs locality 75

Figure 24 Puga school locality. 76
Figure 25 Puga valley halfway up the pass locality. 77
Figure 26 Polokongka La pass locality 78
Figure 27 Polokongka La ridge locality 79
Figure 28 Thukje locality 81
Figure 29 North of Ponganagu locality 83
Figure 30 Ridge west of Ponganagu locality 85
Figure 31 Ridge west of Ponganagu locality. 86
Figure 32 North of Nuruchen Nuruchen. 89
Figure 33 Nuruchen locality. 90
Figure 34 Nuruchen to Gyama Barma. 92
Figure 35 Gyama Barma to Karzok. 94

Chapter 3 - Petrography and thermodynamic modelling of the Tso Morari eclogites

Figure 1 Summary of P-T results and proposed P-T paths for Tso Morari eclogites.. 102
Figure 2 Changes in mineralogy of eclogites from pseudosection modelling along different P-T paths ..
..... 103
Figure 3 Photomicrographs showing peak metamorphic assemblage of Berthelsen outcrop 105
Figure 4 Photomicrographs showing retrograde phases overgrowing peak assemblages 106
Figure 5 Map of eclogite sample locations 109
Figure 6 Element maps of sample a03-16 111
Figure 7 Photomicrographs of sample a03–16 113
Figure 8 Element maps of garnet from sample a03–16. 113
Figure 9 Field photographs of sample 05-04D 114
Figure 10 Element maps of sample 05–04D 116
Figure 11 Photomicrographs of sample 05–04D 117
Figure 12 Element maps of garnet from sample 05–04D. 119
Figure 13 Field photographs of the Berthelsen outcrop 120
Figure 14 Element maps of garnet from sample L08–03B 122
Figure 15 Photomicrographs of sample a03–21 123
Figure 16 Element maps of sample 10–05 125
Figure 17. Photomicrographs of sample 10–05 126
Figure 18 Photomicrographs of sample a04–31. 130
Figure 19 Element maps of sample 11-05 132
Figure 20 Photomicrographs of samples 11-05 to 11-07 133
Figure 21 Element maps of garnet from sample 11-05 134
Figure 22 EPMA amphibole data 139

Figure 23 Photomicrographs of amphiboles. 141
Figure 24 Ternary diagram of garnet compositions 145
Figure 25 Pyroxene classification 148
Figure 26 Bulk rock geochemistry data 153
Figure 27 T-XH2O and P-XH2O phase diagrams for sample 11-05 165
Figure 1 Cartoon detailing the garnet fractionation method described……...167
Figure 29 P-T pseudosection for sample 11-05 showing sensitivity of garnet isopleths to water saturation 168
Figure 30 P-T pseudosection for sample L08-03A showing sensitivity of garnet isopleths to water saturation 168
Figure 31 Pseudosection for sample 11-05 showing sensitivity of garnet isopleths to bulk composition 170
Figure 32 P-T pseudosection for sample 11-05 based on an unfractionated bulk composition in water undersaturated conditions.....170
Figure 33 P-T pseudosection for sample 11-05 based on a fractionated bulk composition in water undersaturated conditions.....172
Figure 34 P-T pseudosection for sample 11-05 based on a fractionated bulk composition in water saturated conditions 175
Figure 35 P-T pseudosection for sample 11-05 for aH2O<1 177
Figure 36 Results of conventional geobarometry.....182
Figure 37 AvePT results.....189
Figure 2 Summary of P-T results from sample 11-05 ……..194

Chapter 4 - Eclogite-facies metamorphism in low–strain metagranites of the Tso Morari complex

Figure 1 Sample 11-01 photomicrographs showing the location of representative domains.....202
Figure 2 Photomicrographs of quartz microstructures 204
Figure 3 Photomicrographs of feldspar microstructure.....206
Figure 4 Photomicrographs of garnet microstructures 208
Figure 5 Photomicrographs of white mica microstructures and mineral chemistry.....211
Figure 6 Photomicrographs of cordierite pseudomorphs. 213
Figure 7 U-Pb monazite data.....215
Figure 8 Phase equilibrium diagram for local bulk composition of domain 5 showing kyanite modal percentage and observed garnet isopleth intersections. ……217
Figure 8 Photomicrographs of skeletal muscovite forming after K-feldspar in metagranitoids 220
Figure 9 Photomicrographs of cordierite pseudomorphs in metagranites.....224

Chapter 5 – The transformation of continental crust during eclogite facies metamorphism

Figure 1 Map of the Tso Morari complex showing locations of Puga Gneiss samples. 231
Figure 2 a. Classifications of whole rock samples using the IUGS-TAS diagram 234
Figure 3 Tectonic discrimination diagrams for felsic rocks using major elements. 236
Figure 4 Tectonic discrimination diagrams for felsic rocks using t major and trace elements. 238
Figure 5 Field photos and photomicrographs showing variations in the Puga Gneiss. 242
Figure 6 Petrographic criteria used for identification of Puga gneiss. 243
Figure 7 Map of Polokongka La pass outcrop relationships 244
Figure 8 Transect from granite to garnet-mica schist 245
Figure 9 Photomicrographs of transect 248
Figure 10 Photomicrographs of sample 10-04. 251
Figure 11 Outcrop relationships in Ribil valley 253
Figure 12 Photomicrographs of samples from Ribil valley. 254
Figure 13 Photomicrograph of transect from Berthelsen outcrop. 257
Figure 14 Photomicrographs of sample 05-05C. 258
Figure 15 Photomicrographs of sample 05-02 260
Figure 16: EPMA data for sample 05-02 261
Figure 17. Element maps of garnet in sample 05-02 262
Figure 18 P-XH2O and T- XH2O pixel maps for sample 05-02 266
Figure 19 P-T pixel maps for sample 05-02 267
Figure 20 Microstructural observation diagram 280

Chapter 6 - EBSD analysis of palisade quartz textures: implications for coesite-quartz transformation

Figure 1- Photomicrographs of sample a05-10 show distinct igneous quartz domains 284
Figure 2 Results of EBSD and misorientation analysis of Area 1. 287
Figure 3. Results of EBSD and misorientation analysis of Area 2.. 288
Figure 4 - Results of EBSD and misorientation analysis of Area 3 289
Figure 5 Results of EBSD and misorientation analysis of Area 4 290
Figure 6 Results of EBSD and misorientation analysis of palisade quartz inclusion 291
Figure 7 Band contrast map showing targeted areas and misorientations 295
Figure 8 Summary of coesite and α-quartz crystallography. 299

Chapter 7 - Geochronology of the Tso Morari nappe

Figure 1 Summary of geochronology results for the Tso Morari complex 303
Figure 2 Map of sample locations for geochronology. 307
Figure 3 Photomicrographs of mafic eclogite sample a03-16. 309
Figure 4 Cathodoluminescence imaging of zircon grains 310
Figure 5. LA-ICP-MS REE and U-Pb zircon data for sample a03-12 311

Figure 6 LA-ICP-MS U-Pb titanite data 312
Figure 7 U, Pb and grain size data for rutile separates 313
Figure 8 LA-ICP-MS U-Pb rutile data 314
Figure 9 LA-ICP-MS U-Pb zircon data for Puga Gneiss sample 05-02 317
Figure 10 Zr in rutile thermometry results. 319
Figure 11 Zr in rutile thermometry results at different pressures 320
Figure 12 Phase equilibrium models of sample 11-05 showing titanite and rutile stability 325
Figure 13 Summary of P-T results and proposed P-T paths for the Tso Morari with Zr in Rutile data and U-Pb ages 329
Figure 14 Age vs distance plot showing geochronological data 333
Figure 15 Summary of geochronology results for the Tso Morari nappe 334

Chapter 8 – Tectonic synthesis

Figure 1 Summary of P-T results and proposed P-T paths for the Tso Morari and Kaghan eclogites 338
Figure 2 Restoration of the Indus Group molasse basin along the Indus Suture Zone 341
Figure 3 Greater India restorations for models of the India-Asia collision 343
Figure 4 Velocity of India over time. 346
Figure 5 Model for the evolution of the western Himalaya 362

List of Tables

Chapter 1 – Introduction

Table 1 Geological characteristic of ultrahigh-pressure terranes 12

Chapter 2 - Field relationships of the Tso Morari complex

Table 1 showing published sample locations 49

Chapter 3 - Petrography and thermodynamic modelling of the Tso Morari eclogites

Table 1 Eclogite sample descriptions 110
Table 2 Representative mineral compositions for sample 10-05 128
Table 3 Sample 11-05. Composition of garnet zones 132
Table 4 Sample 11-05, representative mineral compositions 135
Table 5 Average pyroxene compositions from mafic eclogite 151
Table 6 Calculated bulk composition of sample 11-05 and the bulk compositions randomly generated using the Monte-Carlo method. 163
Table 7 Fractionated bulk compositions for sample 11-05 166
Table 8 Analysis used for Grt–Cpx–Phe–Ky–Qz equilibria 179

Table 9 Results of conventional thermobarometry 179

Table 10 THERMOCALC AvePT results for mafic eclogite peak pressure assemblage 181

Chapter 4 - Eclogite-facies metamorphism in low–strain metagranites of the Tso Morari complex

Table 1 List of granite sample locations, rock type, assemblage and domains present 199

Table 2 Representative data for biotites in the Tso Morari granites. 209

Table 3 Composition of domain 5 214

Table 4 Mineral paragenesis in the Tso Morari granites 224

Chapter 5 – The transformation of continental crust during eclogite facies metamorphism

Table 1 Results of statistical analysis of whole rock major element ratios 237

Table 2 Results of statistical analysis of whole rock major and trace element 239

Table 3 Representative mineral analyses from sample 05-02 263

Chapter 6 - EBSD analysis of palisade quartz textures: implications for coesite-quartz transformation

Chapter 7 - Geochronology of the Tso Morari nappe

Table 1 Analytical conditions used in Zr in rutile analysis 306

Table 2 Summary of LA-ICP-MS U-Pb geochronology results 308

Table 3 LA-ICP-MS data of rutile separates 315

Table 4 Results of Zr in Rutile thermometry 320

Chapter 8 – Tectonic synthesis

Table 1 Calculation of horizontal distance of subducted at different subduction zone dips 347

Table 2 Calculation of horizontal distance subducted based on northward velocity of India 347

Chapter 1 – Introduction

Introduction to ultrahigh-pressure terranes

Ultrahigh-pressure terranes (UHP) are characterised by the preservation of features that indicate pressures within the coesite stability field (26 kbar at 600°C) or even into the diamond stability field (>40 kbar). The discovery of coesite within rocks hosted in continental crust by Chopin (1984) and Smith (1984), led to the deduction that subduction of continental crust was responsible for the formation of the high-pressure

continental crust. The exhumed rocks provide the only direct insights into the long-term dynamics and physical conditions inside continental subduction zones which are not measurable using geophysical techniques. Ultrahigh-pressure conditions have now been recorded in most continental collision zones in the Phanerozoic (Figure 1) (Warren, 2013). However, the mechanism by which they are subducted and exhumed is debated (e.g. Hacker and Gerya, 2013; Warren, 2013) and the importance that the process of continental subduction plays in the orogenic cycle is poorly understood (Capitanio *et al.*, 2010; Afonso *et al.*, 2011).



Figure 1 Map showing the location of known ultrahigh-pressure terranes worldwide. Taken from Warren (2013), modified from Chopin, (2003), Liou et al., (2004) and Tsujimori et al., (2006).

Ultrahigh-pressure terranes vary in size, structural setting and age but are shown to share a number of common features including a lower- to mid-crustal origin, a small volume of mafic rock hosted in a large volume of felsic rock and are often found to be positioned close to the suture zone of the orogen (Liou *et al.*, 2004). There is no common mechanism or rate of exhumation responsible for the exhumation of ultrahigh-pressure terranes; some are thought to form during the early stages of continental collision whereas others are thought to form later. Geological observations such as metamorphic pressure-temperature (*P-T*) estimates, radiometric dating and field relationships, combined with numerical models, led to the suggestion that different tectonic environments exhume high-pressure rocks at different rates and by different mechanisms.

Exhumation of continental ultrahigh-pressure terranes has always been ascribed to positive buoyancy of the abundant quartzofeldspathic rocks. It was originally thought that the preservation of eclogite-facies mineral assemblages and high-pressure minerals such as coesite or diamond was a consequence of the rapid exhumation of the terrane at relatively low temperatures, where minimal melting occurred (Mosenfelder *et al.*, 2005). Since then, it has been shown that there are a variety of ultrahigh-pressure terranes, of varying size, preserving a range of exhumation rates, temperatures and proportions of melt. This variety of terrane type implies that formation and exhumation could have happened by a variety of different geodynamic mechanisms (Hacker and Gerya, 2013).

In order to understand fully the formation and exhumation of ultrahigh-pressure terranes, thorough pressure-temperature-time-deformation-space records need to be established. Often, complete datasets, encompassing structural geology, petrology and geochronology are lacking. These data, in combination with geodynamic and thermodynamic modelling, can be used to build models which can be compared to existing ultrahigh-pressure terranes worldwide. For example, characteristic features of interest include burial rate; the magnitude, distribution, age and duration of peak temperature and pressure; spatial variations during subduction and exhumation; the magnitude, kinematics, age, duration and spatial variations in deformation during subduction and exhumation and the tectonic relationships with respect to surrounding units.

This study focusses on the record of (ultra)high-pressure metamorphism in continental, high-pressure, low-temperature terranes, within a range of lithologies. Mafic rocks in these terranes provide the best record of (ultra)high-pressure metamorphism as they are more likely to form and preserve (ultra)high-pressure mineral

assemblages. Felsic rocks are the most abundant rocks in continental terranes but rarely preserve (ultra)high-pressure metamorphic assemblages (e.g. Young and Kylander-Clark, 2015). Mafic and felsic lithologies show a close association in their field relationships in terms of proximity, distribution and structural features, but preserve different aspects of the collisional history, recorded in their metamorphic minerals. The parallel study of mafic and felsic rocks within the context of their field relationships is therefore an important comparison, as the P-T record of the subducted unit gives insight into the factors influencing the geodynamics and exhumation mechanisms of the continental margin, such as the (non)-transformation of subducted felsic rocks in the eclogite facies (Warren, 2013). A combined approach, considering transformation in different lithologies, is therefore an important approach when trying to understand the process of continental subduction.

Common features of ultrahigh-pressure terranes

There are around 15 examples of continental ultrahigh-pressure metamorphism preserved worldwide. Examples include the Triassic ultrahigh-pressure metamorphism where passive margin sedimentary and volcanic sequences are preserved in Dabie Shan, eastern China (Schmid *et al.*, 2003), Palaeozoic subduction of the Kokchetav massif, Kazakhstan (Dobretsov *et al.*, 1995) and Palaeogene subduction of part of the Eurasian plate during the Alpine orogeny (Chopin, 1984). Continental ultrahigh-pressure terranes can be generally divided into two end members: small terranes (e.g. in Oman, the Alps and Himalayas), where exhumation occurred quickly during the early stages of continental collision, vs large terranes (e.g. in the Western Gneiss Region and Dabie Sulu), where exhumation slowly occurred during the later stages of continental collision (Kylander-Clark *et al.*, 2012).

There are 3 types of crustal material that have been identified from (ultra)high-pressure terranes: accretionary wedge sediments, oceanic crust and continental crust (Guillot *et al.*, 2009). Continental ultrahigh-pressure terranes are often located near to the accretionary wedge, immediately beneath the suture and are often associated with ophiolitic rocks (e.g. Saih Hatat region, Northern Oman, Searle *et al.*, 1994). These terranes are typically made up of mid to upper crustal continental margin sequences and/or gneissic basement and occupy the core of the domed nappe stacks, between 5 and 50km across. The nappe stacks are separated from other nappes of different pressure conditions by thrust-directed ductile shear zones (Beaumont *et al.*, 2009).

Steep, ductile, internal structures related to high-pressure metamorphism are overprinted by later, shallow, pervasive amphibolite facies structures which are in turn overprinted by extensional fabrics related to dome formation in shallow crustal conditions. Key diagnostic minerals, such as coesite, are usually found in mafic enclaves and are rarely found in felsic rocks.

Most continental ultrahigh-pressure terranes record pressures between 2.5 and 4 GPa (Hacker, 2006; Guillot *et al.*, 2009). Much greater pressures (~6 GPa) have been recorded in peridotite bodies within ultrahigh-pressure terranes (e.g. Hacker *et al.*, 2003; Vrijmoed *et al.*, 2008). However, estimates from these bodies are not consistent with *P-T* estimates from adjacent mafic bodies and the timing and mechanism of their incorporation into the crust is debated (e.g. Brueckner *et al.*, 2010). Following the achievement of peak pressure conditions, most ultrahigh-pressure terranes record near-isothermal decompression to crustal depths (~1.0-0.5 GPa) at rates of $cm.a^{-1}$ (e.g. Rubatto and Hermann, 2001; Parrish *et al.*, 2006). This fast, isothermal stage of exhumation is followed by a much slower rate of exhumation, interpreted to occur by a different mechanism (e.g. Parrish *et al.*, 2006; Agard *et al.*, 2009; Kylander-Clark *et al.*, 2012).

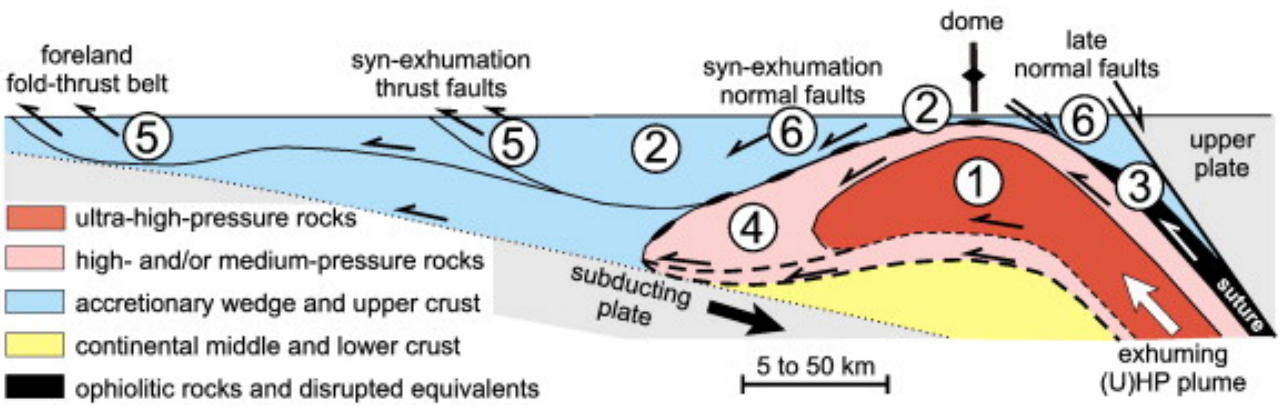


Figure 2 General characteristic of ultrahigh-pressure terranes and the surrounding units taken from Beaumont and Jamieson, 2009. Adapted from (Kaneko et al., 2000; Avigad et al., 2003; Faure et al., 2003; Xu et al., 2006; Epard et al., 2008). 1. Structural dome with ultrahigh-pressure core. 2. Overlying lower grade rocks. 3. Ophiolite in the suture zone. 4. Overlying lower grade nappes. 5. Thrust faults. 6. Normal faults.

Geochronology

The dating of peak metamorphic conditions relies on the crystallisation of major and accessory mineral phases useful as geochronometers. Minerals such as allanite have been shown to form in the eclogite facies, recording near-peak conditions (e.g. Parrish *et al.*, 2006; Smye *et al.*, 2011). Other minerals such as garnet and zircon crystallise more continuously during the prograde to peak history of the rock and, in combination with trace and/or major element chemistry, may provide information as to the timing growth with respect to the coincident metamorphic conditions (e.g. Mattinson *et al.*, 2006; Kylander-Clark *et al.*, 2009).

The combination of multiple geochronometers within a single ultrahigh-pressure terrane provide information as to the timing and rates of processes occurring during continental subduction. The amount of time spent at ultrahigh-pressure conditions has been shown to vary between terranes such as Kaghan and Tso Morari, NW Himalaya, which are predicted to have spent ~ 1 Ma at ultrahigh-pressure conditions (Parrish *et al.*, 2006), compared to Dabie Sulu and Qaidam terranes, China and the Western Gneiss Region in Norway, which are thought to have spent >10-20 Ma at ultrahigh-pressure conditions (Hacker, 2006; Kylander-Clark *et al.*, 2009).

Initial rates of exhumation and cooling rates between these terranes also varies from 3-8 $cm.a^{-1}$ for Dora Maira and Kaghan (Rubatto *et al.*, 2001; Parrish *et al.*, 2006), compared to <1 $cm.a^{-1}$ for the Western Gneiss Region (Kylander-Clark *et al.*, 2008). Rates of exhumation from peak pressure to crustal depths is constrained by the combination of geochronometers recording near-peak conditions with geochronometers which record later parts of the exhumation history such as U-Pb titanite and rutile or Ar-Ar of muscovite or biotite. However, the interpretation of data from geochronometers can be uncertain due to a lack of understanding as to the timing of formation of minerals such as rutile or titanite, which can record the timing of crystallisation of phases or the time the mineral passed below the isotopic closure temperature of the particular mineral. Other uncertainties include uncertainties in diffusion parameters, incorporation of common Pb of the same isotopic mass as radiogenic Pb (e.g. Cherniak, 2000) and the incorporation of excess Ar in to the grain (e.g. Warren *et al.*, 2012), causing the 'apparent age' of the mineral to older than the time when it passed through the nominal closure temperature. Many of these factors increase the apparent age of ultrahigh-pressure

terranes, allowing us to interpret the ages as maximum estimates and should be considered with caution when estimating exhumation rates which can also be overestimated (Warren *et al.,* 2012).

Continental subduction geodynamics

Continental ultrahigh-pressure terranes are only found in continental collision zones, particularly of Phanerozoic age. The possibility of subduction of continental material is supported by the discovery of coesite in continental terranes (Chopin, 1984; Smith, 1984), experimental data at high pressures (e.g. Wu *et al.*, 2009) and seismic imaging of continental fragments (e.g. Roecker, 1982). Exhumation has been shown to occur in continental collision zones during a single short-lived event, over a single protracted event or even as multiple events (e.g. Kylander-Clark *et al.*, 2012; Warren, 2013). It is becoming increasingly clear that there is no single exhumation model that dominates in a particular tectonic environment and the exhumation mechanism can very within a single subduction zone (Warren, 2013).

It is thought that global tectonic forces transmitted by plate motions are responsible for the subduction of ultrahigh-pressure rocks, whereas external tectonic forces and the body forces derived from the buoyancy of subducted continental rocks are a major factor contributing to their exhumation (Molnar and Gray, 1979; Gerya *et al.*, 2011). The style and force balance within a subduction zone respond to changes in the width, subduction velocity, composition of material subducted and steepness of subduction zones (Gerya et al., 2011). Continental crust is buoyant and so in order to subduct buoyant material, it must be attached to a stronger and denser substrate (Molnar and Gray, 1979). Buoyancy is affected by pressure, temperature, composition and phase transformations (Gerya et al., 2011). At temperatures of 800-900°C, continental crust is positively buoyant with respect to the mantle at pressures of up to 40 kbar (Massonne *et al.*, 2007). This is true whether or not metamorphic transformation at high pressure occurs (Walsh *et al.*, 2004; Peterman *et al.*, 2009) and within continental terrane of 50:50 felsic:mafic composition. Beyond 40 kbar, continental crust that transforms can be negatively buoyant (e.g. Palin *et al.*, 2017). At higher temperatures, melting increases the buoyancy of the subducted material. However, if melt proportions are high enough for melt migration to occur, the residue may be insufficiently buoyant to rise out of the mantle (Hacker, 2006). This may explain why very few ultrahigh-pressure terranes record temperatures exceeding 800°C. Surface traction, pressure

gradients and rheology can also play a role during exhumation of ultrahigh-pressure terranes (Scholz *et al.*, 1995; Chemenda *et al.*, 1996; Heuret *et al.*, 2005).

Formation of ultrahigh-pressure terranes

In order to achieve ultrahigh pressures within continental rocks, subduction of the continental material must have occurred to transport the continental material into the mantle. The discovery of ultrahigh-pressure rocks in continental terranes goes some way towards explaining how ultrahigh-pressure rocks exhume but say nothing about how they form. There are approximately six tectonic mechanisms by which continental material can reach mantle depths as discussed in Hacker and Gerya (2013): 1) continental margin subduction, 2) microcontinent subduction, 3) sediment subduction, 4) Intracontinental subduction, 5) subduction erosion and 6) foundering of a crustal root.

Continental subduction can be observed today in Indo-Australia, where the Australian continent is being subducted beneath the Banda Arc (Hamilton, 1979; Harris, 2003) and in New Guinea (Ufford *et al.*, 2005). In both of these examples, continental subduction occurs beneath an oceanic upper plate. Intracontinental subduction is also thought to be ongoing beneath the Pamir (Burtman *et al.*, 1993; Sippl *et al.*, 2013) where seismic imaging has identified portions of continental lithosphere sinking into the mantle (Burtman and Molnar, 1993). Sediment subduction and subduction erosion is occurring in arcs around the world (von Huene *et al.*, 1991; Scholl *et al.*, 2007) and has been recognised to contribute to arc lava composition from volcanoes on the overlying plates (Plank *et al.*, 1993).

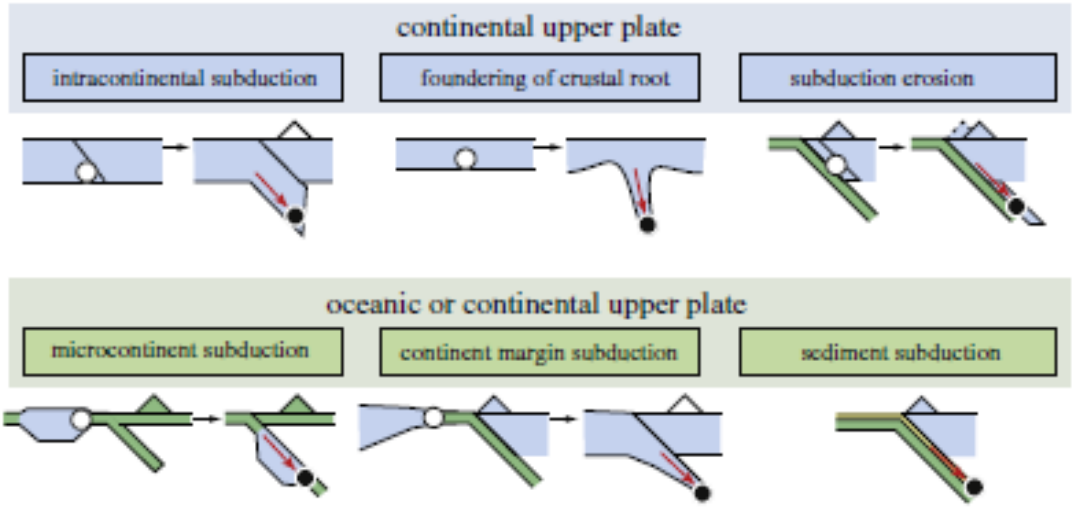


Figure 3 Formation of ultrahigh-pressure terranes from Hacker and Gerya, 2013

Detaching a continent

Exhumation may involve the whole scale detachment of the ultrahigh-pressure terrane from the subducting slab, perhaps with continuing subduction, or could involve the reversal of the entire plate motion (eduction) due to the removal of the negatively buoyant root of the subducting slab (see Warren, 2013). Buoyancy contributes to exhumation (England *et al.*, 1979) but cannot explain detachment in the channel and upper crustal geology (Beaumont *et al.*, 2009). Duretz *et al.* (2012; 2013) demonstrated that delamination of subducted crust from underlying mantle is more likely to occur during slow subduction (1-2 $cm.yr^{-1}$) or if the subducted continental margin is thin. If the subducted plate is strong then it will undergo little internal deformation.

Exposed ultrahigh-pressure terranes show that they can form a continuum between internally, pervasively deformed terranes (Terry *et al.*, 2004) to terranes consisting of low-strain blocks separated by ductile shear zones which formed during exhumation, rather than at ultrahigh-pressure conditions (Labrousse *et al.*, 2004; Jolivet *et al.*, 2005). Many terranes show examples of well-preserved, low-strain features such as granites (Biino *et al.*, 1992; Wallis *et al.*, 1997), gabbros (Zhang *et al.*, 1997; Krabbendam *et al.*, 2000) and pillow basalts (Bearth, 1959; Puga *et al.*, 1995). Ultrahigh-pressure shear zones have been recorded in the Sulu orogenic belt in China (Zhao *et al.*, 2003), however high-pressure shear zones are more common (Pognante, 1985; Austrheim, 1986), possibly due to the overprinting of previous features by metamorphism and/or

deformation (Stöckhert, 2002). Development of these weak shear zones could potentially act as a detachment zone as these zones of weakness, once formed, could remain weak (Holyoke *et al.*, 2006).

Weakening mechanisms resulting in the detachment of subducted material from the down-going slab could include strain weakening, increases in temperature, hydration, melting, grain size reduction, the development of a foliation and metamorphic reactions (Warren *et al.*, 2008a). These mechanisms decrease the effective viscosity of the rock and may involve the development of local shear zones, forming a detachment zone, or they may act on a zone of material allowing it to flow. Factors which affect the buoyancy and overall strength of the crust include metamorphic reactions, metastability and the composition of the subducted crust (Warren *et al.*, 2008a).

The effect of strain weakening has been studied using experimental data from monomineralic starting materials (e.g. Bystricky *et al.*, 2000; Barnhoorn *et al.*, 2004). The rheological behaviour of most rocks is defined by several minerals. However, weak mineral phases within a rock may control the rheology, and strength vs composition relationships are nonlinear (Jordan, 1988; Handy, 1990). Application of experimentally defined physical constraints to natural systems could therefore result in inaccurate rheological predictions due to the differing behaviour of polymineralic compared to monomineralic assemblages. Recrystallisation of minerals in shear zones can also change the strength of material and could result in weak and strong zones developing in different parts of a terrane at different times.

Strain weakening, in addition to its dependence on stress, pressure and temperature, has also been used as a general term covering more specific mechanisms such as grain size reduction, hydration and metamorphic reactions (Babeyko *et al.*, 2005; Warren *et al.*, 2008a). In these models, deformation localises into discrete shear zones and the bulk crust weakens (Warren *et al.,* 2008a). Grain size reduction can also decrease the effective viscosity of a rock by changing the deformation mechanism from dislocation creep (grain size insensitive) to diffusion creep (grain size sensitive) and can be triggered by processes such as metamorphic reactions, dynamic recrystallisation (De Bresser *et al.*, 2001) or by processes that inhibit grain growth such as pinning (Bercovici *et al.*, 2012).

Eclogitisation of the crust increases the density of crustal material and can also decrease the effective lithospheric strength by 25-30% of the original strength (Babeyko and Sobolev, 2005). Transformation on a prograde subduction path can be assisted by fluids, where the crystallisation of weak, foliation-forming minerals such as phengite, helps to localise deformation in high-strain zones and aids the preservation of low-strain (ultra)high-pressure zones (Guillot *et al.*, 2009). Addition of fluids along shear zones or channelised networks is responsible for triggering eclogite-facies reactions in the high-pressure Bergen Arcs of Norway, implying that hydration weakening could occur under eclogite-facies conditions and could play a role in the initial weakening and development of weak zones in crustal material (Austrheim *et al.*, 1985). Once triggered, these weak eclogite-facies zones cause deformation to become localised. Partial transformation during prograde metamorphism of drier crustal material therefore has implications for the strength and buoyancy of subducted material. Transformation weakening associated with phase transformations (White *et al.*, 1978) may also be important to the formation and exhumation of ultrahigh-pressure terranes (Warren, 2013) due to the densification at ultrahigh pressure (>20 kbar) (Semprich *et al.*, 2010) forming a zone of weakened material where a detachment surface could nucleate.

Exhuming a continent

The final depth and style of exhumation of subducted continental material depends on the convergence rate and rheology of the crust and mantle (Gerya *et al.*, 2006; Warren *et al.*, 2008b; Yamato *et al.*, 2008; Beaumont *et al.*, 2009; Li *et al.*, 2010). Bulk rheological differences and their subsequent mechanical behaviour during subduction strongly influences the dynamics of collision. Felsic crust can be strong and therefore will behave coherently during subduction and exhumation, increasing the effective buoyancy during subduction (Ranalli, 2000). On the other hand, weak felsic crust can delaminate, reducing its contribution towards the effective buoyancy of the subducted slab (Ranalli et al., 2000).

There are a number of different exhumation mechanism proposed for ultrahigh-pressure terranes based on numerical models which are summarised in the text below and in Table 1. Some of these models are related to the mode of formation of ultrahigh-pressure terranes whereas other are independent of this. The main styles of exhumation predicted by numerical models are pulse-like buoyant exhumation, syn-collisional exhumation and continuous circulation within the wedge of an accretionary prism, the first two of which are able to

reproduce *P-T* paths compatible with observations in ultrahigh-pressure terranes (Beaumont *et al.*, 2009; Li and Gerya, 2009). In all these models, buoyancy of subducted continental material is the main force driving exhumation.

Buoyancy alone is thought to be insufficient to exhume ultrahigh-pressure rocks all the way to the Earth's surface. Continental crust is positively buoyant in the mantle but may reach a point of neutral buoyancy at the base of the crust, requiring a different mechanism to bring it back to the surface. This may suggest that some exhumed ultrahigh-pressure material may not make it back to the surface but could underplate the overlying material by relamination (Hacker *et al.*, 2013).

	Structural	Petrological	Chronological	Length scale	Example
Eduction ("Andersen model")	Relatively weakly deformed, no thrust fault at base	Monotonic down-dip gradient in peak P & T	Up to 10 Myr subduction & exhumation in models, monotonic down-dip gradient in ages	Thickness of educting lithospheric section	Western Gneiss Region
Microplate rotation	Rotation of lineaments in space and time, possible thrust fault a base with increasing offset from rotation axis	P & T gradient with respect to rotation axis	Not yet modelled, age gradient with respect to rotation axis	Thickness of rotation lithospheric section, unless diminished by basal thrust	Dabie Shan
Crustal stacking ("Chemenda model")	Relatively coherent slab, thrust fault at base above another crustal section	Monotonic down-dip gradient in P & T	Up to 20 Myr in models, monotonic down-dip gradient in ages	Crust	Dora Maria (?)
Slab rollback	Microcontinent, thrust fault at base	Associated back-arc spreading	15 Myr in Mediterranean, monotonic down-dip gradient in ages	Microcontinent crust	Not yet (?) demonstrated for UHP rocks
Channel flow	Nappes or strong mixing	Mixing of domains of different pressures, possible pressure cycling of individual domains	A few Myr to tens of Myr in models, mixing of domains with different ages	Metres to kilometres	Unknown
Trans-mantle diapir	Radially symmetric structures, dome within upper plate, no basal fault	Significant local melting, mixing of domains of different pressures, concurrent magmatism	Rapid (<1 Myr) ascents of diapirs over a period of tens of Myr	10-20 km diapir radius	North Qaidam

Table 1 Geological characteristic of ultrahigh-pressure terranes exhumed by different mechanisms taken from Hacker and Gerya, 2013, table 1

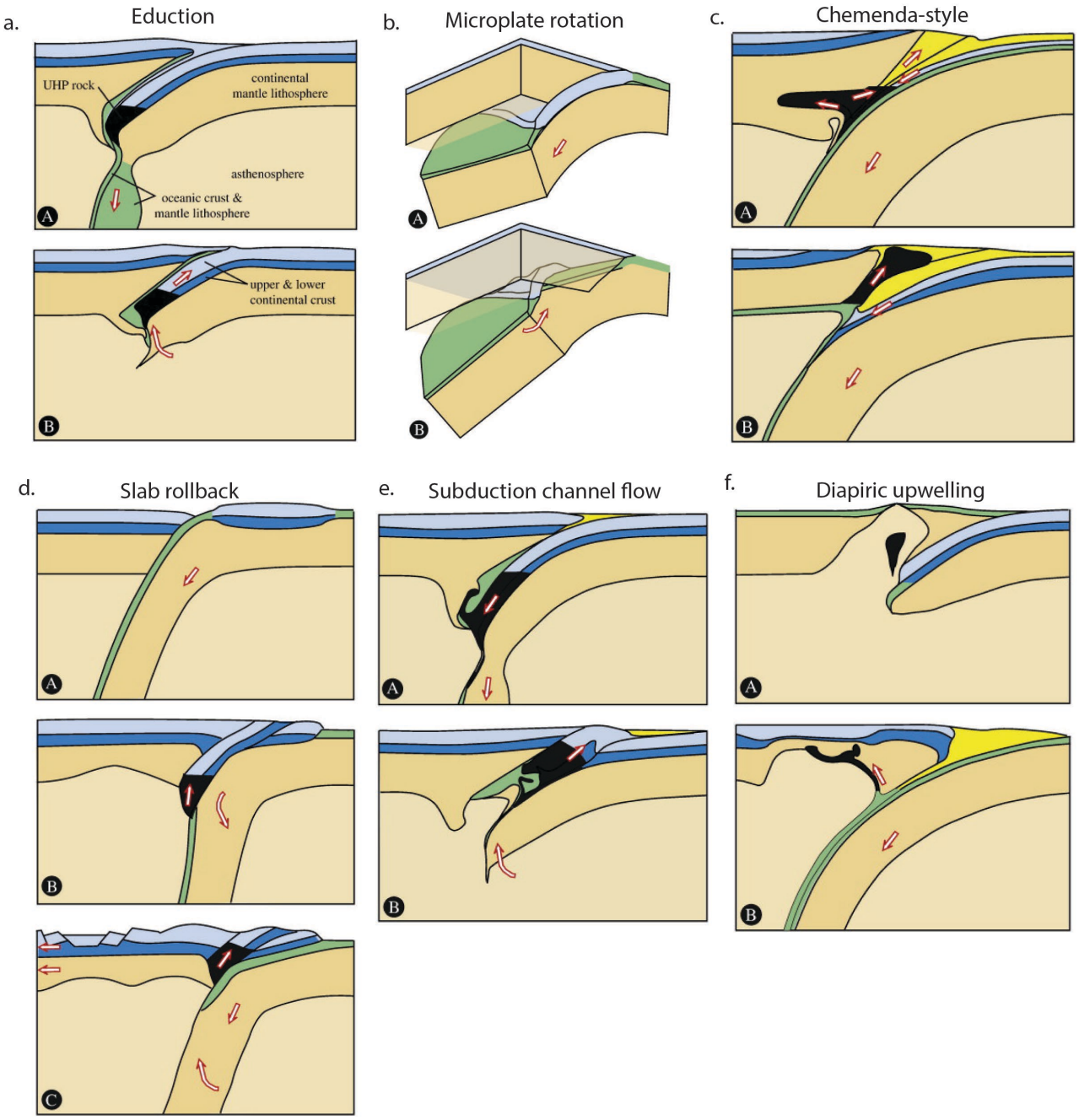


Figure 4 Schematic representation of exhumation mechanisms taken from Hacker and Gerya (2013), figures 2-7. a. Eduction (Andersen et al., 1991; Duretz et al., 2012). b. Microplate rotation (Hacker et al., 2000). c. Chemenda-style delamination and stacking (Duretz and Gerya, 2013). d. Slab rollback (Brun and Faccenna, 2008). e. Subduction channel flow (Li and Gerya, 2009). f. Diapiric upwelling (Gerya and Meilick, 2011; Little et al., 2011)

Exhumation models

'Eduction' refers to wholescale reversals of plate motions, leading to exhumation of the subducted plate with little internal strain (Andersen *et al.*, 1991)(*Figure 4*a). Eduction is thought to be favoured in terranes where subduction of cold oceanic lithosphere is relatively fast and subducted continental crust and underlying mantle is strongly coupled (Duretz *et al.*, 2012). Strong subducted continental lithosphere would therefore undergo little internal deformation during subduction and exhumation. The duration of subduction of continental lithosphere could be as long as 15 Myr and exhumation from ultrahigh-pressure depths to the lower crust could be as long as 7 Myr (Gerya, 2013; Duretz et al., 2012). Subduction of continental material in this model is driven by negative buoyancy of the attached oceanic lithosphere. Detachment occurs due to the downwards pull exceeding the strength of the slab causing necking (Hunen *et al.*, 2011). Exhumation is driven by buoyancy of the continental material at a rate driven by plate motions and rheology of subducted material (Duretz *et al.,* 2012).

This mechanism has been applied to the Western Gneiss Region of Norway where the presence of foreland thrust faults beneath the ultrahigh-pressure rocks is debated (Robinson *et al.*, 2014b; Young, 2018), suggesting that the overlying Laurentia was drawn off the top of subducted Baltica (Andersen *et al.*, 2008). Strain concurrent with eclogite-facies metamorphism also seems to be minor, and pressure and temperature gradients show gradual increases towards the core of the orogen, suggesting exhumation of a relatively coherent slab (Hacker *et al.*, 2010). However, timescales for continental subduction recorded in the Western Gneiss Region (Kylander-Clark et al., 2009) are much shorter than predicted by eduction models (Hacker and Gerya, 2013).

During subduction of continental material, detachment could occur beneath a positively buoyant unit. This unit may then exhume upwards as a semi-coherent sheet (*Figure 4*c). This exhumation mechanism was originally proposed to explain the Dora Maira massif (Chopin, 1987) and the Dabie Shan (Okay *et al.*, 1992) and demonstrated with analogue experiments by Chemenda *et al.*, (1995). Sizova *et al.*, (2012) improved on this idea by numerical models using spontaneously moving plates and a large dense slab which allowed subduction of continental crust with a narrow passive margin. In the models, detachment occurs at depth, causing crustal stacking to occur over the down-going plate followed by exhumation from ultrahigh-pressure

depths, driven by buoyancy (Sizova *et al.,* 2012). For this style of exhumation, expected surface features would include units of semi-coherent rock, underlain by a detachment and separated by shear zones, with juxtaposed *P-T-t* paths following ultrahigh-pressure metamorphism. Subduction durations of 10 Myr and exhumation durations of up to 7 Myr are thought to be possible for this style of exhumation (Duretz et al. 2013).

Removal of buoyant material by subduction erosion or within a confined channel can lead to exhumation of ultrahigh-pressure rocks within a channel where there is an interplay between basal traction and buoyancy forces (England and Holland, 1979; Cloos and Shreve, 1988; Raimbourg *et al.*, 2007) (*Figure 4*e). Continuous subduction of continental material pushes old material upwards and exhumation is driven by buoyancy forces in the middle to upper parts of the channel (Gerya *et al.*, 2008; Warren *et al.*, 2008b). Subduction channel flow can be complex and produce a 'washing machine' effect, with semi-coherent blocks within a melange (Burov *et al.*, 2001; Gerya *et al.*, 2008; Warren *et al.*, 2008b; Yamato *et al.*, 2008; Beaumont *et al.*, 2009). The position of the exhumed material once it reaches the surface varies between numerical models depending on the strength of the upper plate, the presence of a continental indenter or the location of the subduction channel (Gerya *et al.*, 2008; Li *et al.*, 2009; Butler *et al.*, 2011). It is worth noting that subduction channel flow is a prescribed outcome of models with plate convergence and is not common in models with randomly moving plates (e.g. Beaumont *et al.,* 2009; Warren *et al.,* 2008b; Sizova *et al.,* 2012). The Massif Central (Lardeaux *et al.*, 2001) and the Tso Morari complex (Beaumont et al., 2009) were proposed to have been deformed and exhumed within a channel. Neither of these examples record extensive mixing of rock masses recording different metamorphic conditions.

Changing boundary conditions or body forces can cause a plate to rotate, assisting in the eduction of material that has been subducted, leading to exhumation of ultrahigh-pressure rocks (Bottrill *et al.*, 2014) (*Figure 4*b). However, there are no numerical models that simulate this mechanism. Microplate rotation is thought to occur in small terranes that are relatively coherent, with displacement accommodated along a basal thrust fault where offset and metamorphic pressures increase away from the rotation axis and stretching lineations measured in the field would be compatible with the rotation around a pole (Hacker and Gerya, 2013). The most compatible ultrahigh-pressure terrane with this model is the Dabie terrane in Eastern China, where

stretching lineations and gradients in metamorphic pressure indicate rotation during exhumation (Hacker *et al.*, 2000). Rotation of the Woodlark microplate has also been proposed as a suggested mechanism for the exhumation of the Papua New Guinea ultrahigh-pressure terrane (Webb *et al.*, 2008).

Changing boundary conditions could also cause rollback and steepening of the subducted slab, causing the buoyant portion of the lithosphere to detach and exhume (Brun *et al.*, 2008) (*Figure 4*d). This model could be used to explain repeated cycles of subduction and exhumation of high-pressure rocks e.g. in the numerical models of the Aegean and Calabria-Apennine orogens (Faccenda *et al.*, 2009) and micro-continent accretion (Tirel *et al.*, 2013; Vogt *et al.*, 2014).

A final suggested exhumation model is the formation of trans-mantle diapirs, where buoyant ultrahigh-pressure material rises in plumes beneath the over-riding plate forming a sheet of melange (*Figure 4*f). This model was suggested due to the small size of the Alpine ultrahigh-pressure terranes and their formation prior to continent collision (Stöckhert *et al.*, 2005; Gerya *et al.*, 2006). This model was also suggested for the North Qaidam ultrahigh-pressure terrane in Tibet to explain the long duration of ultrahigh-pressure metamorphism (Yin *et al.*, 2007) and the Papua New Guinea ultrahigh-pressure terrane (Little, Hacker, Gordon, *et al.*, 2011). Exhumed material would show a significant amount of mixing of sediment and crystalline material from the subducted plate and the upper plate, with no basal fault, concurrent magmatism in the upper plate (Yin et al., 2007) and significant local melting (Gordon *et al.*, 2012).

A range of formation and exhumation models for ultrahigh-pressure terranes have been presented here, with some links made to existing ultrahigh-pressure terranes. The structural, petrological and geochronological record within these terranes will provide a clue as to which mechanism or combination of mechanisms may be operating. Table 1 lists the geological characteristics which would be observed for each mechanism including structural characteristics, such as if the terrane is planar or domal, the presence or absence of a basal thrust fault, the degree of internal deformation, the relative orientation of lineation across the dome. Petrological characteristics include the variation in pressure across the dome, the degree of melting and the timing of magmatism. Geochronological characteristics include the *P-T-t* history of rocks across the dome whereas the dimensions of ultrahigh-pressure terranes affect the timescale for thermal diffusion. The variation in observations within ultrahigh-pressure terranes suggests that there are different mechanisms of formation

and exhumation. However, the scarcity of geologic data within each ultrahigh-pressure terrane makes it difficult to predict their evolution.

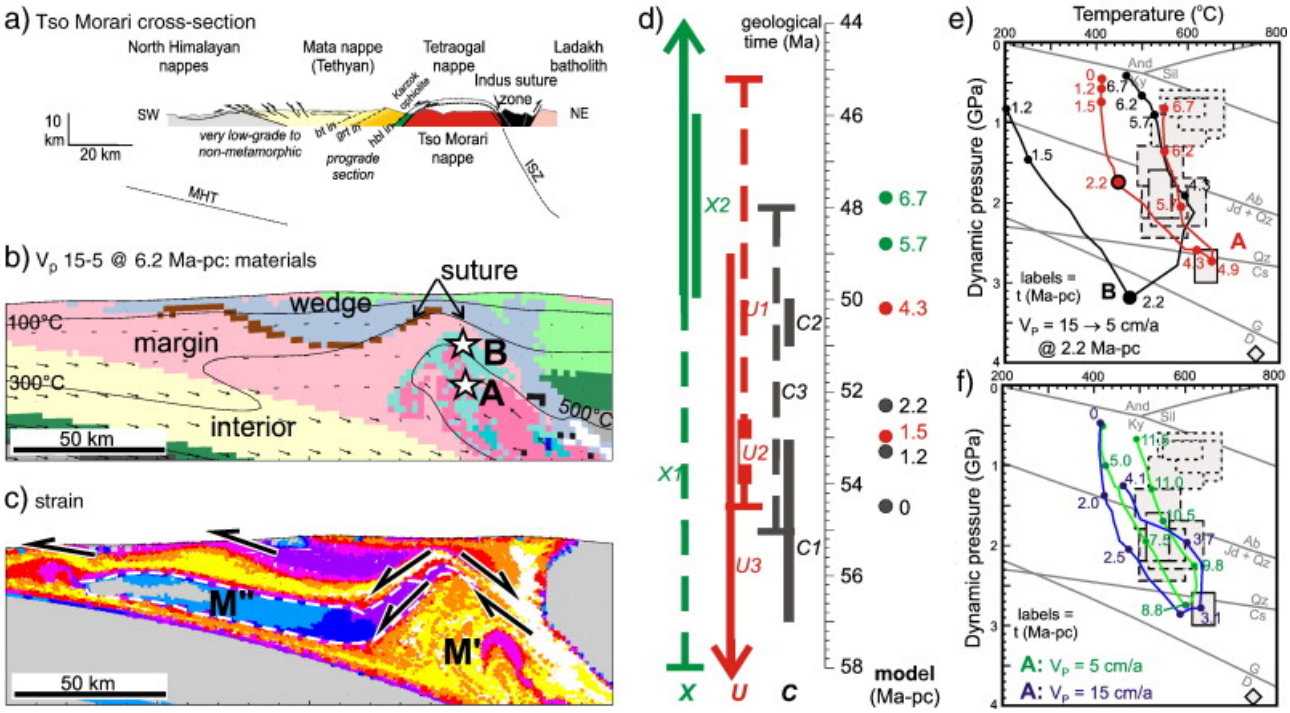


Figure 5 Exhumation model and P-T-t paths compared to data from the Tso Morari dome, taken from Beaumont et al., 2009. a) Simplified cross section of Tso Morari after Epard and Steck, 2008. Main Himalayan thrust (MHT), Indus suture zone (ISZ). b) Material distribution from the model on same scale as cross section. Stars show tracking points A and B (panel e). c) Strain and faults map of model. d) Observation vs models. Exhumation (X, green): X1 = whole-rock-mineral isochrons from amphibolites (de Sigoyer et al., 2000); X2 = Ar-Ar phengite (de Sigoyer et al., 2000). (U)HP metamorphism (U, red): U1 = U-Pb zircon (Leech et al., 2007); U2 = cited time for peak UHP metamorphism (Leech et al., 2005); U3 = whole-rock-mineral isochrons from eclogites (de Sigoyer et al., 2000). Collision (C, black): C1 = onset of collision from syn-orogenic sediments (Clift et al., 2002; Guillot et al., 2003; DeCelles et al., 2004); C2 = Last marine sediments (Guillot et al., 2003; Najman et al., 2005; Zhu et al., 2005; Green et al., 2008); C3 = time range for velocity decrease (Guillot et al., 2003; Zhu et al., 2005). Solids circles and corresponding colour represent equivalent events in model (Ma). e) Representative P-T-t paths from model, compared to Tso Morari (De Sigoyer et al., 1997; Guillot et al., 1997; de Sigoyer et al., 2004; Sachan et al., 2004; Mukherjee et al., 2004). Time in Ma. f) P-T-t paths for point A in model. Ma-pc = million years post collision

Himalayan High-Pressure rocks

The Himalayan Orogen

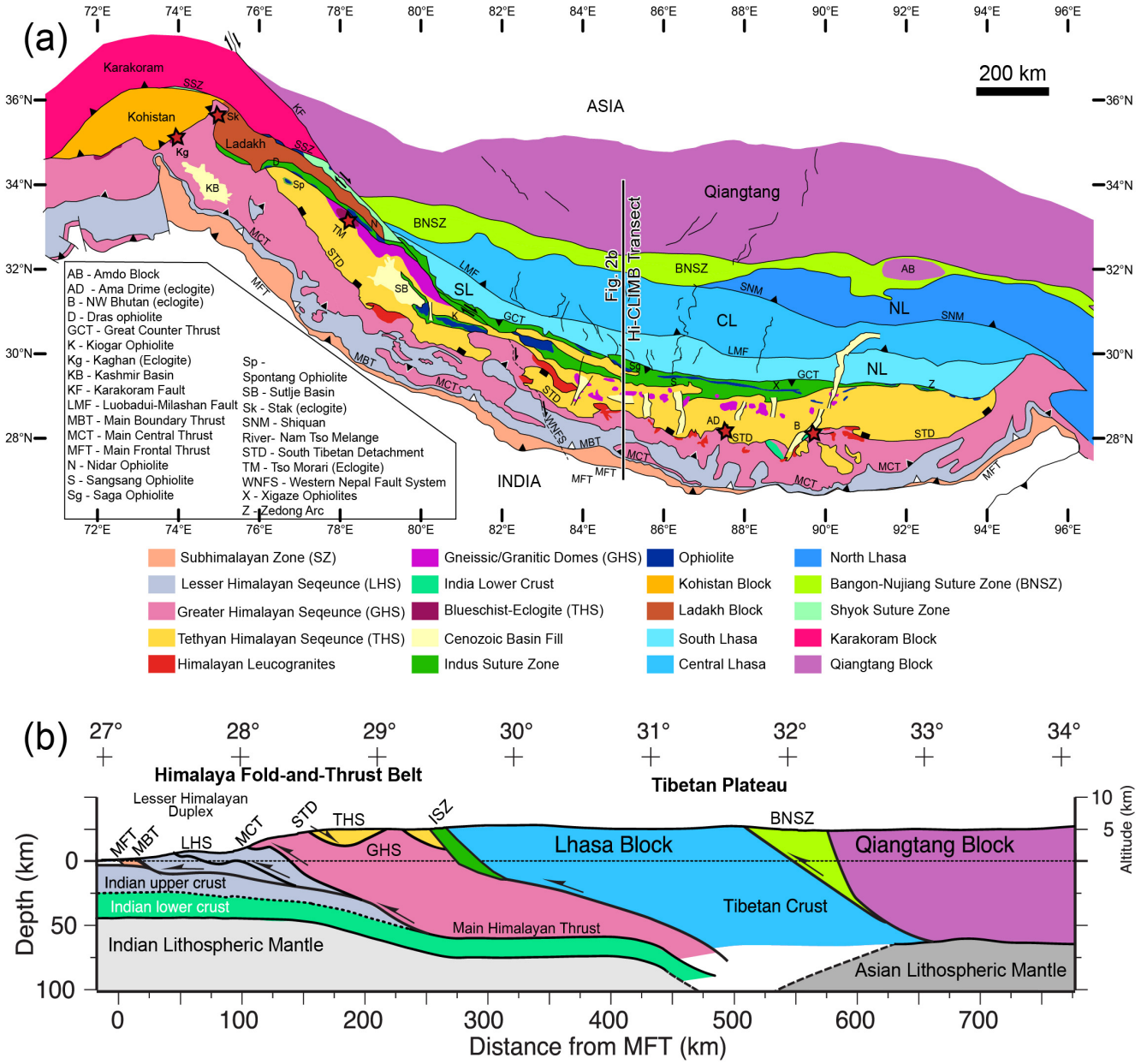


Figure 6 Geological map and cross section of the Himalaya-Tibet orogenic system From Parsons et al., (2019), figure 2. Geological map based on Yin and Harrison, (2000), Searle et al. (2011), Parsons et al. (2016), Martin (2017), Goscombe et al. (2018), Li et al. (2018), Kapp and DeCelles (2019). Lithospheric sketch cross section after Godin and Harris (2014), based on the Hi-CLIMB receiver function profile of Nábělek et al. (2009).

The Himalayan mountain range formed from the collision between the Indian and Asian continents, after the closure of the Neo-Tethys Ocean (Hodges, 2000; Yin *et al.*, 2000; Najman *et al.*, 2010). The Himalayan collision resulted in up to 70 km of crustal thickening, over 750 km of crustal shortening and the formation of a mountain range approximately 2500 km long, which stretches from the Afghanistan-Pakistan border to the South China-Myanmar border (Corfield and Searle, 2000; Hodges, 2000; Guillot *et al.*, 2003; Yin, 2006; Nábělek *et al.*, 2009). It forms part of the larger Himalaya-Alpine orogenic system which stretches from the Mediterranean Sea to Indonesia. Due to its young age and ongoing tectonic activity, the Himalaya presents an ideal example in which to study the evolution on the continental crust during orogenesis. However, contrary to ancient and eroded orogens, exposures of deep crustal rocks are rare and enigmatic.

The Himalayan orogen can be broadly subdivided into four continuous tectonostratigraphic units which extend from west to east, along the length of the orogen (Figure 5). These units comprise the Sub-Himalayan zone (SHZ) in the south, the Lesser Himalayan Sequence (LHS) further north, the Greater Himalayan Sequence (GHS) and the most northerly Tethyan Himalayan Sequence (THS) (Martin, 2017). These units are separated by high-strain zones that run parallel to the orogen.

The SHZ is comprised of the Siwaliks group, unmetamorphosed synorogenic sediments deposited in a basin, underlain by the Main Frontal Thrust (MFT) (DeCelles *et al.*, 1998). The LHS lies structurally above the SHZ, separated by the Main Boundary Thrust (MBT) and emplaced towards the south. It comprises Palaeoproterozoic to Pleistocene rocks with sedimentary and volcanic units, Cambro–Ordovician granites and gneisses, Palaeoproterozoic igneous intrusions interpreted as being part of the Indian passive margin and Neoproterozoic weakly metamorphosed metasediments (Haimanta or Cheka group) (Martin, 2017; Goscombe *et al.*, 2018). Separating the LHS and the structurally overlying GHS is the Main Central Thrust Zone (MCTZ), emplaced towards the south (Searle *et al.*, 2008). The MCTZ is a pervasive km-thick shear zone and forms the roof thrust to the duplexed LHS (D. M. Robinson *et al.*, 2014; Larson *et al.*, 2015).

The GHS forms the highest-grade metamorphic rocks in the Himalaya and is comprised of metapelites, orthogneisses, migmatites and leucogranites derived from the Indian continental margin. Metasediments of the GHS were deposited in the Proterozoic to early Palaeozoic and were intruded by different types and ages of granitic intrusions (Martin, 2017; Goscombe *et al.*, 2018; Spencer *et al.*, 2019). There are three main

intrusive granitic phases preserved within the Indian passive margin sediments; Neoproterozoic (800 Ma) granites, Cambrian–Ordovician (550 to 470 Ma) S– and I–type granitic intrusions and Eocene–Miocene (25 to 9 Ma) S-type leucogranitic intrusions derived from melting during the Himalayan orogeny (Le Fort *et al.*, 1987; Harris *et al.*, 1995; Parrish *et al.*, 1996; Carosi *et al.*, 2012).

The THS lies structurally above the GHS and is separated by the South Tibetan Detachment System (STDS) showing top-down-N brittle-ductile structures (Carosi *et al.*, 1998; Searle *et al.*, 2003; Kellett *et al.*, 2019). The THS is made up of Cambrian to Eocene sediments with Permian, Triassic and early Cretaceous igneous intrusions and is thought to also form part of the Indian passive margin but represents more distal facies than the structurally lower units. The northern extent of the THS is marked by the Indus-Tsangpo Suture Zone (ITSZ), an ~50 km wide, extensively deformed and folded zone containing sedimentary rocks of Indian and Asian affinity and is separated from the underlying GHS by the Zanskar shear zone (ZSZ). Ophiolites emplaced into the Indian margin in a supra-subduction zone setting can be found along the length of the Himalaya. Examples such as the Nidar ophiolite are located within the ITSZ, have an intra-oceanic arc geochemical signature and formed ~150-110 Ma (Hébert *et al.*, 2012; Chan *et al.*, 2015; Kapp *et al.*, 2019), whereas the Spontang ophiolite, located within the THS, is an older Jurassic ophiolite with island–arc affinity (Corfield *et al.*, 1999, 2001).

Metamorphic evolution

Geochronological and thermobarometric studies of the GHS have produced a 3-stage model of formation of the Himalaya which is largely consistent along strike. This model includes initial ultrahigh-pressure metamorphism of the northern–western margin of the Indian continent, burial and accretion followed by decompression-related exhumation. Initial metamorphism is recorded in the coesite-bearing eclogite of the Kaghan Valley, Pakistan, at 46.4 ± 0.1 Ma (U-Pb zircon and allanite), >27.5 kbar, 720-7700°C (Parrish *et al.*, 2006) and the Tso Morari complex, NW India, at 56-43 Ma, >27 kbar, >600°C (Leech *et al.*, 2005; Donaldson *et al.*, 2013). These terranes record similar *P-T-t* histories and are located over 450 km apart, within the THS. These metamorphic domes indicate that the leading edge of the Indian continental margin underwent subduction to depths of >100 km around the time of the India-Asia collision. However, there is

strong disagreement about the timing and peak conditions of subduction and exhumation of the Tso Morari mafic eclogites. Further discussion is given in chapters 5, 6 and 7.

The initial burial and accretion of rocks within the GHS beneath the THS occurred along a thrust zone equivalent to the STDS at 56-54 Ma (Kellett *et al.,* 2019). This early burial and accretion is recorded in the Himalayan gneiss domes (Smit *et al.*, 2014; Ding *et al.*, 2016) and between the MCTZ and STDS at 51-30 Ma (Catlos *et al.*, 2001; Carosi *et al.*, 2010; Wang *et al.*, 2013; Ambrose *et al.*, 2015; Iaccarino *et al.*, 2015; Larson *et al.*, 2015; Parsons *et al.*, 2016; Braden *et al.*, 2017; Goscombe *et al.*, 2018). Further accretion and crustal thickening of the GHS took place along internal thrust sense shear zones (Godin *et al.*, 2001; Ambrose *et al.*, 2015; Carosi *et al.*, 2016; Goscombe *et al.*, 2018; Waters, 2019). Burial and metamorphism in the structurally lowest unit of the GHS, part of the Indian lower crust, is recorded at 38 Ma (Kellett *et al.*, 2014). Kyanite grade metamorphism is recorded at 37-30 Ma by U-Pb monazite and Sm-Nd garnet ages (Vance *et al.*, 1999; Walker *et al.*, 2001), with peak *P-T* estimates are in the range of 9-12 kbar and 550-680°C (Vannay *et al.*, 2003).

Crustal thickening resulting in sillimanite-grade metamorphism is recorded at 24-15 Ma, using U-Pb of monazite with peak *P-T* estimates in the arrange of 620-770°C, 4.5-7 kbar, and is followed by decompression and heating (Noble *et al.*, 1995; Searle *et al.*, 1997, 2003; Murphy *et al.*, 1999; Searle, 1999; Vance *et al.*, 1999; Simpson *et al.*, 2000; Walker *et al.*, 2001; Cottle *et al.*, 2009). Muscovite and biotite dehydration melting within the sillimanite stability field initiated a period of anatexis and leucogranite formation from ca. 25 to 9 Ma (Searle *et al.*, 2009).

The metamorphic record within the LHS, GHS and THS records near-continuous burial, underplating and accretion of material. The eastern and western syntaxis of the Himalaya provide exception to the metamorphic and structural evolution of the Himalaya along strike. These regions underwent distinct episodes of metamorphism and deformation, producing Pliocene migmatites (e.g. Crowley *et al.*, 2009), separating them from the main GHS.

India-Asia collision

The India-Asia collision zone is one of the most widely studied orogens in Earth history. However, the manner in which India collided with Asia is highly debated. Models used to describe the collision, based on a combination of geological and/or geophysical data, include the single subduction model, where India collided directly with Asia following subduction of the Tethys ocean (e.g. Hu *et al.*, 2016; Ingalls *et al.*, 2016). Other models invoke collision of India with an intra-oceanic arc prior to the collision with Asia (e.g. (Aitchison *et al.*, 2007; Burg *et al.*, 2018; Searle, 2018) or collision of an Indian microcontinent with Asia, prior to the collision of Greater India (e.g. Hinsbergen *et al.*, 2019). The main distinction between these end-member models would be the number and timing of collision-related events such as continental subduction. The transition from oceanic subduction to continental collision is recorded in the rocks of the accretionary prism incorporated into the ITSZ in NW India and Pakistan (Honegger *et al.*, 1982, 1989). Key minerals indicating high pressure low temperature subduction of the Tethys ocean during the Cretaceous include carpholite, kyanite and cordierite (O'Brien, 2018a), lawsonite-bearing blueschists (Groppo *et al.*, 2016) and carpholite-bearing metasediments (Oberhänsli, 2013). Ophiolite obduction, contemporaneous to the formation of Cretaceous high-pressure rocks, is preserved in multiple locations within the ITSZ (Bédard *et al.*, 2009).

The timing of the India-Asia collision can be constrained in a number of ways, for example, the first arrival of allochthonous sediments, the timing of ultrahigh-pressure metamorphism, reduction of plate velocity, cessation of arc magmatism and the final marine sediments in the suture zone. The earliest arrival of Indian continental lithosphere to the subduction zone has been determined at 59 ± 1 Ma based on the identification of Asian-derived zircons with deep marine Palaeocene sedimentary rocks on the Greater Indian continental rise (DeCelles *et al.*, 2014; Wu *et al.*, 2014; Hu *et al.*, 2015; Metcalf *et al.*, 2017). This is consistent with the development of an erosional unconformity at 57-56 Ma, the deposition of shallow marine Asian sediments (56-54 Ma) and clastic sediments (53-50 Ma) on the Greater Indian continental shelf and the end of marine sedimentation along the Greater Indian margin by 50 Ma (Green *et al.*, 2008; Najman *et al.*, 2010; Hu *et al.*, 2015, 2016; Searle, 2018). Ultrahigh-pressure metamorphism of subducted continental crust is recorded between ~56-43 Ma (Leech *et al.*, 2005; Parrish *et al.*, 2006; Donaldson *et al.*, 2013) and the earliest prograde metamorphism of the GHS gneiss domes at 56-54 Ma (Smit *et al.*, 2014; Ding *et al.*, 2016).

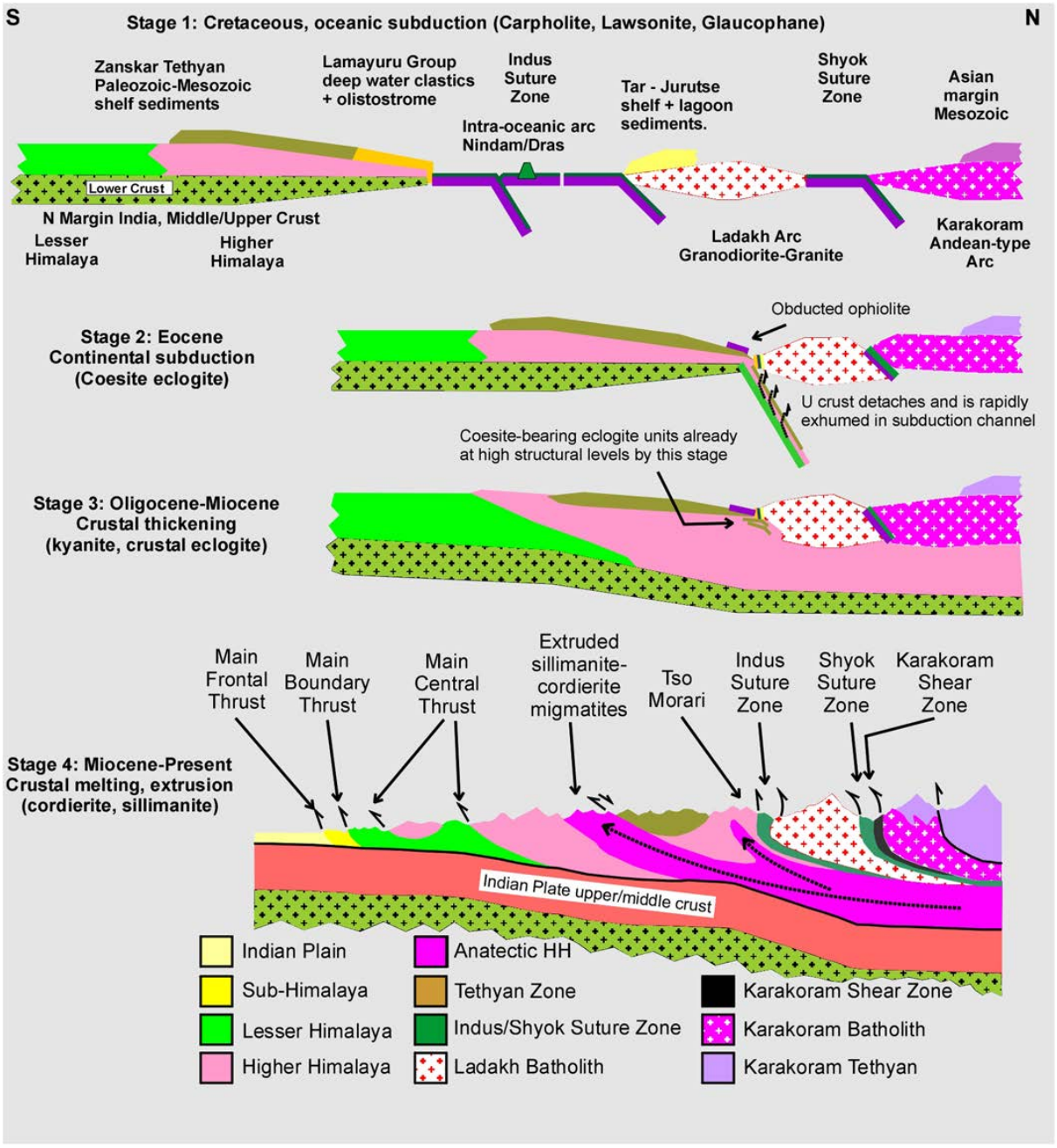


Figure 7 Cartoon summary of the evolution of the Himalaya (not to scale), taken from O'Brien (2018). The timing of blueschist, coesite eclogite, kyanite and cordierite-sillimanite formation is indicated, based on Jain et al. (2012).

High-Pressure metamorphism in the Himalaya

There are two major types of eclogite occurrences in the Himalaya characterised by their contrasting *P-T-t* paths and tectonic histories. One type, known as granulitised eclogites, are known to occur in Northwest Bhutan in the upper GHS (Grujic *et al.*, 2011; Warren *et al.*, 2011; Tobgay *et al.*, 2012), Sikkim in the upper GHS (Rolfo *et al.*, 2008; Kellett *et al.*, 2013), the Arun valley, Nepal in the mid GHS (Lombardo *et al.*, 2000b; Corrie *et al.*, 2010), Dinggye, China in the upper GHS (Wang *et al.*, 2017) and Ama Drime, Southern Tibet, within a dome at the top of the Main Central Thrust Zone (MCTZ) (Groppo *et al.*, 2007; J. Cottle *et al.*, 2009). In contrast, the high pressure - low temperature (HP-LT) eclogite types occur in three localities in Pakistan and north-west India, close to the suture zone between the Indian and Asian continents. These are Kaghan (Parrish *et al.*, 2006), Stak (Fort *et al.*, 1997) and Tso Morari (Sachan *et al.*, 2004).

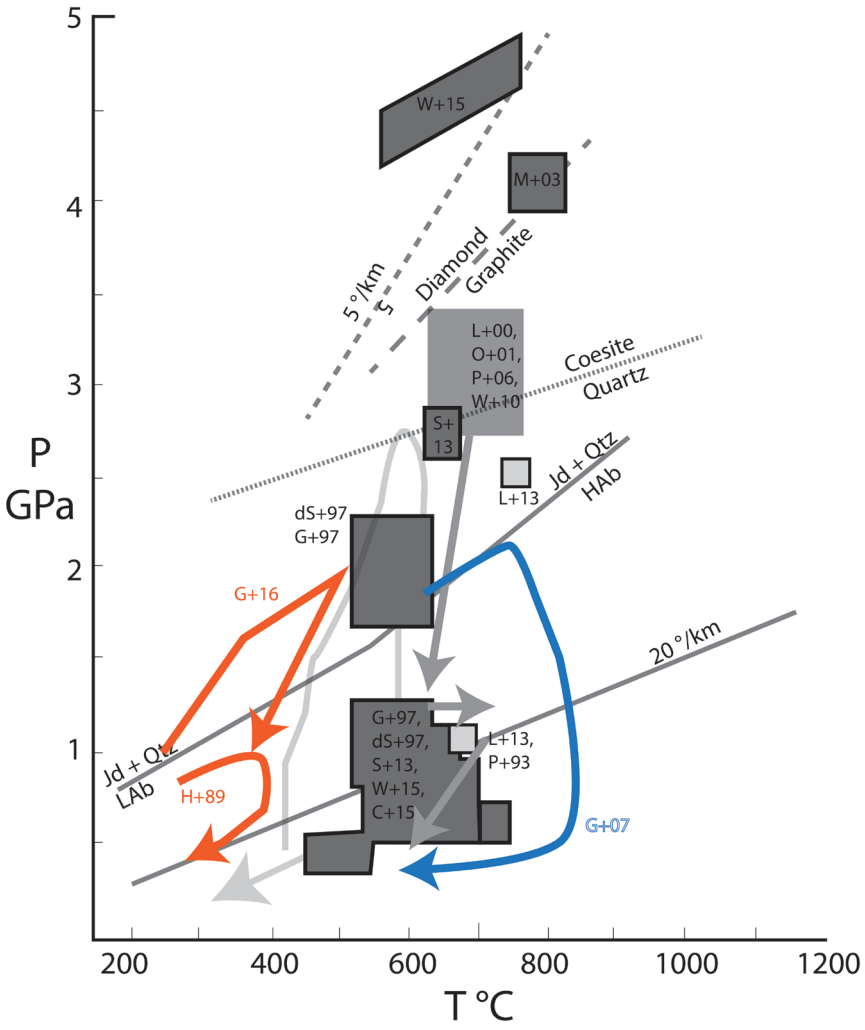


Figure 8 . Summary of P-T results and proposed P-T paths for the Himalayan eclogites after O'Brien (2018a). Dark grey with black box for Tso Morari eclogites, medium grey for Kaghan, light grey for Stak eclogites. Black arrow shows summary P-T loop for Tso Morari, grey arrow for Kaghan, light grey arrow with black outline for Stak, blue arrow for Ame Drime, Orange arrows for ITSZ blueschists. Coesite to quartz (Bohlen and Boettcher, 1982), Albite to jadeite + quartz (Holland (1980), diamond to graphite (Bundy, 1980). P-T estimates: G + 97 (Guillot et al., 1997), dS + 97 (de Sigoyer et al., 1997), M + 03 (Mukherjee et al., 2003), S + 13 (St-Onge et al., 2013), CJ15 (Chatterjee and Jagoutz, 2015), W + 15 (Wilke et al., 2015), L+00 (Lombardo et al., 2000), O+01 (O'Brien et al., 2001), P+06, W+10 (Wilke et al., 2010), L+13 (Lanari et al., 2013), P+93 (Pognante et al., 1993), G+07 (Groppo et al., 2007), H+89 (Honegger et al., 1989), G+16 (Groppo et al., 2016)

Granulitised eclogites

Granulitised eclogite-types occur within mafic boudins hosted in deformed and metamorphosed felsic rocks. Evidence for eclogite facies metamorphism is predominantly recorded in the textural relicts after a high-pressure phase, such as clinopyroxene-plagioclase intergrowths after omphacite (e.g. Kellett *et al.*, 2014). Trace element geochemistry shows that zircons present in these rocks grew in plagioclase absent, garnet present conditions marked by the lack of an Eu anomaly and flat heavy rare earth element profiles (Grujic *et al.*, 2011; Wang *et al.*, 2017). Peak pressures and associated temperatures recorded in the eclogites ranges from >15 kbar, 600°C (Corrie *et al.*, 2010) to 21-22 kbar, 720-760°C (Wang *et al.,* 2017) with a granulite facies overprint recording temperatures of around 750°C (Wang et al., 2017) to 800°C (Warren et al., 2011). The timing of high-pressure metamorphism ranges from 15.3 Ma in NW Bhutan (Grujic et al., 2011), 20.7 ± 0.4 Ma in the Arun Valley (Corrie *et al.,* 2010), 14.9-13.9 Ma in Dinggye (Wang *et al.,* 2017) and ~38 Ma in Ama Drime (Kellet *et al.,* 2014). These ages are much younger than the ages of ultrahigh-pressure metamorphism described in the HP-LT eclogites below.

Subduction-related eclogites

The HP-LT eclogites of Pakistan and north-west India differ from the granulitised eclogites by preserving eclogite facies peak assemblages in the mafic boudins, such as garnet, omphacite, phengite, talc, kyanite, coesite, clinozoisite. The *P-T-t* paths are much steeper, with peak pressures reaching 26-42 kbar (e.g. St-Onge *et al.*, 2013; Wilke *et al.*, 2015) and exhumation rates on the order of 11mm.yr^{-1} (Parrish *et al.*, 2006).

Stak

In the Stak Area of Northern Pakistan, located between the Kaghan and Tso Morari massifs, eclogite and high-pressure granulite have been described in contact with the Kohistan arc (Le Fort *et al.*, 1997). Felsic gneisses within the Palaeozoic and Mesozoic metasedimentary cover are host to boudins of mafic eclogites,

with garnet and omphacite zoning comparable to the Kaghan eclogites (Lanari *et al.*, 2013; Kouketsu *et al.*, 2016) but without retrograde glaucophane and/or barroisite, with additional high temperature brown hornblende (O'Brien, 2018a). The mafic rocks are geochemically similar to the Panjal trap basalts (Kouketsu *et al.*, 2017).

A retrogressed eclogite was first reported by Le Fort (1997) who suggested peak metamorphic conditions of >1.3 GPa and >610°C. Further estimates using pseudosection modelling by Lanari *et al* (2013), estimated prograde conditions increasing from 650°C and 2.4 GPa to peak conditions at 2.5 GPa and 750°C, followed by retrogression to 700-650°C and 1.6-0.9 GPa under high-pressure granulite and amphibolite facies conditions.

Zircons show a range in U-Pb ages from 80 to 48.1 Ma, with peaks around 60.4 and 51 Ma (Riel *et al.*, 2008). The youngest age, preserved as rims on metamorphic zircons are thought to represent the age of high-pressure metamorphism at 51 Ma (Riel et al, 2008). Younger zircons from the eclogites, with clustered trace element chemistry, record an age of 32 Ma which correlates to the Ar-Ar of hornblende ages of the adjacent Nanga Parbat Himalayan Massif (NPHM) (Guillot *et al.*, 2008) and the youngest age of the Kohistan intrusives (Zeitler *et al.*, 1989). The small zircon size, many of these ages may represent a mixed age and the relationship between the 32 Ma age and the eclogite-facies stage is not clear. It has been suggested that the Stak eclogites resided at lower crustal depths following high pressure at metamorphism, where they underwent heating coincident with the NPHM at 31 Ma (Kouketsu et al., 2015).

Kaghan

The upper Kaghan and Neelum valleys consist of Proterozoic basement containing pelitic and psammitic metasediments and granitic orthogneiss, overlain by Palaeozoic clastic metasediments and Palaeozoic-Mesozoic carbonate-rich metasediments. This area contains isoclinally folded thrust sheets, refolded into east-west trending structures (Greco *et al.*, 1993; Kaneko *et al.*, 2003; Wilke, O'Brien, Gerdes, *et al.*, 2010). The units host metabasic and felsic intrusive rocks (Chaudry *et al.*, 1987; Greco *et al.*, 1993) which preserve eclogite and amphibolitised eclogite assemblages in the mafic protoliths (Pognante *et al.*, 1991), and a geochemical signature comparable to the Panjal trap sub-alkaline tholeiitic basalts (Rehman *et al.*, 2016). Most eclogites occur in the uppermost thrust sheet, with coronitic dolerites preserved in the lowermost nappe

unit (Fontan *et al.*, 2000; Wilke, O'Brien, Gerdes, *et al.*, 2010). The eclogite-facies mineral assemblages contain coesite inclusions ± glaucophane ± magnesite/dolomite (Wilke *et al.*, 2010a; Wilke *et al.*, 2010b), with secondary sodic-calcic amphibole with glaucophane cores (Lombardo *et al.*, 2000a; Wilke *et al.*, 2010a). Amphibolitisation of the eclogites corresponds to the grade of the host metapelites and marbles, with extensional N-directed shearing and a greenschist facies overprint evident in the albite poikiloblasts.

The formation conditions of Kaghan valley eclogites are estimated at 25-32 kbar, 700 ± 70°C based on garnet + omphacite + phengite +coesite/quartz + rutile phase equilibria (Lombardo *et al.*, 2000a; O'Brien *et al.*, 2001; Parrish *et al.*, 2006; Wilke *et al.*, 2010b) at 46.4 ± 0.1 Ma based on U-Pb of zircon (Parrish *et al.,* 2006). Peak pressure was initially followed by cooling to 580-620°C at 10-17kbar as deduced from the growth of glaucophane (Wilke *et al.*, 2010a). Amphibolite-facies overprinting is marked by the development of clinopyroxene-plagioclase ± amphibole symplectites after omphacite, growth of sodic-calcic amphibole, and replacement/rimming of rutile by ilmenite ± titanite, indicating heating to 650-700°C at 10-12 kbar (Lombardo *et al.,* 2000; Kaneko *et al.,* 2003; Parrish *et al.,* 2006; Wilke *et al.*, 2010a). Ar-Ar of amphibole records ages of 39-42Ma (Chamberlain *et al.*, 1991; Smith *et al.*, 1994; Hubbard *et al.*, 1995) and Ar-Ar of mica and apatite fission-track records ages of 24.5 ± 3.7 Ma (Wilke *et al.*, 2010b; Wilke *et al.*, 2012).

Tso Morari

Multiple studies have been conducted on the eclogites of the Tso Morari nappe. De Sigoyer et al., (1997; 2004) and Guillot *et al.* (1997) took samples from a wide area, whereas later studies focussed on the outcrop first discovered by Berthelsen (1953) (e.g. St-Onge *et al.*, 2013; Palin *et al.*, 2014; Chatterjee and Jagoutz, 2015) (summarised in Chapter 5). Recent *P-T* estimates have predicted conditions, recorded in garnet and omphacite compositions, at 25.5-27.5 kbar, 630-635°C (St-Onge *et al.*, 2013) and 22-23 kbar, 400-425°C (Chatterjee and Jagoutz, 2015). Studies looking at the carbonate mineral assemblages suggest that peak estimates for the Tso Morari eclogites lie within the diamond stability field but are not recorded in the garnet and omphacite compositions (Wilke *et al.*, 2015; O'Brien, 2018b) (discussed further in Chapter 8). Ultrahigh-pressure metamorphism occurred at around 47-43 Ma based on U-Pb of zircon (Donaldson *et al.*, 2013; St-Onge *et al.*, 2013) (discussed in Chapter 7), before being exhumed to 12.5 ± 0.5 kbar, 690 ± 25°C followed by a higher temperature overprint at 7-84 kbar, 705-755°C at 45.3 ±1.1 Ma, based on U-Pb of monazite (St-

Onge et al., 2013) (discussed in Chapter 8). Exhumation to temperatures <300°C, based on Ar-Ar of muscovite is predicted to have occurred by ~30 Ma (Schlup *et al.*, 2003), whilst the rocks of the GHS were undergoing peak, kyanite-grade metamorphism.

Tectonic settings/ P-T-t paths and timing

The *P-T-t* paths of the HP-LT eclogites are thought to be characteristic of those that formed within a subduction setting, where rapid exhumation rates were controlled by the positive buoyancy of the felsic material that hosts the mafic rocks and exhumation is confined to the slab interface which accommodated structural translation. These rocks are often found along the suture zone of the orogen. Peak pressure estimates from the Kaghan and Tso Morari eclogites both lie just within the coesite stability field, based on garnet and omphacite chemistry, whereas the Stak eclogites are estimated to have formed at much lower pressures of 24 kbar. Temperature estimates at peak pressure are ca. 100°C higher in the Kaghan and Stak compared to the Tso Morari eclogites. However, peak temperatures recorded in the amphibolite-overprint is comparable across all these units at ca. 750°C, and the shape of the exhumation-related *P-T* paths at low pressures suggest that these three units were brought to the surface by a similar mechanism.

The timing of eclogite-facies metamorphism has been well constrained in the Kaghan eclogites using ID-TIMS and linked to high pressure metamorphism using rare earth element patterns in zircon and allanite textures (Parrish *et al.,* 2006). This estimate falls in the same region as the less precise estimates from the Tso Morari complex, constrained using a variety of different methods, the most precise of which, U-Pb of zircon, has an error of ± 1 Myr and has been linked to high pressure metamorphism using rare earth element patterns in zircon.

The Stak eclogite records an additional phase of distinct zircon growth with a younger age of 32 Ma, correlating to the age of the youngest Kohistan intrusives, suggesting that the Stak eclogites resided at lower crustal depths following high pressure at metamorphism ~51 Ma, where they underwent heating coincident with the Nanga Parbat Himalayan Massif at 31 Ma (Kouketsu *et al.*, 2016). In contrast Ar-Ar ages of muscovite from metapelites in the Tso Morari complex (Schlup *et al.,* 2003) suggest that these rocks were cooler than 300°C by ~30 Ma. Ar-Ar ages of amphibole in Kaghan eclogites at 39-42 Ma suggest that

continental subduction was over soon after the peak at ~47 Ma, but didn't cool below 300°C until around 24.5 Ma (O'Brien, 2018a).

Thesis Objectives

1. Did continental crust transform under eclogite facies conditions?

Previous work on the Tso Morari dome has focussed on (1) the structural evolution of the dome, which is dominated by the later, amphibolite facies deformation (Epard and Steck, 2008), and (2) the metamorphic history of the eclogites, particularly from the Berthelsen outcrop. Mafic eclogites within the Tso Morari complex are the best recorders of (ultra)high-pressure metamorphism but constitute <1% of the rocks. The majority of the Tso Morari complex is made up of granite, granite gneiss and metasediments which, due to their close association with the mafic rocks, were presumed to have been subducted to equivalent depths to the enclosed mafic rocks. So far, little evidence exists to show whether the felsic gneiss and metagranites of the Tso Morari complex experienced eclogite facies metamorphism and to what extent they transformed.

Numerical models of continental subduction highlight the possible mechanisms for the detachment and exhumation of continental material, for example the potential importance of processes such as transformation weakening in causing localised detachment of slithers of continental material (Warren *et al.*, 2008b). Even in the absence of metamorphic transformation at eclogite facies, subduction to ultrahigh-pressure depths could trigger phase transformation of quartz to coesite, which reverts to alpha-quartz on decompression. This reverse transformation also has the potential to reduce grain size and therefore influence grain size-sensitive deformation mechanisms and therefore crustal rheology during exhumation. The transformation history of the felsic rocks of the Tso Morari complex could therefore provide an important study when considering the mechanism of continental subduction and exhumation.

Quantitative and textural analysis of low– and high–strain granitoids, in terms of their mineral chemistry and quartz microstructures, is undertaken in order to better constrain the transformation history of the Tso Morari complex. Low–strain regions are overprinted less by exhumation–related deformation, suggesting that these zones may better preserve transformation at ultrahigh-pressure conditions.

2. What is the P-T-t history of the Tso Morari nappe?

There is considerable discrepancy in the peak pressure and temperature estimates of the mafic eclogites of the Tso Morari complex and the prograde evolution is poorly constrained (O'Brien, 2018b, Waters and

Utting, 2015). Previous *P-T* estimates using thermodynamic models have assumed water–saturated conditions and have achieved contrasting *P-T* paths based on the interpretation of and variation in amphibole inclusion assemblages (O'Brien, 2018). In this study, thermodynamic modelling is undertaken on the mafic eclogites of the Tso Morari complex, in order to better understand the prograde history of the mafic units and the factors which influence the *P-T* estimates, including bulk composition uncertainty, water saturation, water activity and garnet fractionation.

The timing of ultrahigh-pressure metamorphism has been constrained using in situ techniques to analyse the U-Pb isotopic content of zircon, considered to have formed during eclogite facies metamorphism (Leech *et al.,* 2007; St-Onge *et al.,* 2013; Donaldson *et al.,* 2013). These estimates typically have uncertainties of ±1 Myr. The rate of exhumation from coesite stability field depths to the base of the crust is estimated at ~11mm.yr^{-1}, indicating that the time taken for these rocks to be exhumed from the base of the crust is in the order of <2 Myr (St-Onge et al., 2013). In this study, high precision geochronology has been undertaken using ID-TIMS to better constrain the timing of subduction and exhumation of the Tso Morari complex. The U-Pb age of zircon crystallisation and the U-Pb age of rutile and titanite provide a more complete history of the entire cycle of continental subduction, from peak conditions to exhumation through the lower crust, allowing an insight into the style, timing and mechanisms of exhumation.

Thesis Structure

This thesis sets out to answer the first question in chapters 4, 5 and 6 and the second question in chapters 3, 5 and 7:

- **Chapter 2** introduces the structural and lithological field relationships required in order to interpret the petrological interpretations, P-T modelling and age relationships in subsequent chapters.
- **Chapter 3** presents the results of petrographic analysis, conventional thermobarometry and thermodynamic modelling of a mafic eclogite from the Tso Morari nappe, in order to determine its prograde and peak history. The record in the mafic eclogites is compared to the record of high-pressure metamorphism in the granite gneiss of the Tso Morari nappe
- **Chapter 4** presents the results of petrographic and mineral analysis of low strain metagranites from across the Tso Morari complex and their metamorphic transformation history.
- **Chapter 5** compares the metamorphic record and bulk geochemistry in the granite gneiss with the granites of chapter 3 and 4 in order to determine their transformation history
- **Chapter 6** describes a new quantitative technique for the analysis of quartz microtextures after coesite, based on the analysis of a metagranite from the Polokongka La region
- **Chapter 7** presents geochronological data and conventional thermometry of mafic eclogite samples and their host rocks, in order to better constrain the timing of eclogite facies metamorphism and the exhumation path
- **Chapter 8** contains the overall synthesis, tectonic interpretations and conclusions

Chapter 2

Field relationships of the Tso Morari complex

The Tso Morari dome

The Tso Morari dome takes its name from a lake located in a high–altitude desert region of Ladakh, NW India. It is situated on the north–western margin of the Indian plate and is separated from the Ladakh batholith of the Asian plate by the suture zone sediments and the Nidar ophiolite (Fuchs and Linner, 1996) (Figures 1 and 2). The Tso Morari dome is composed of a set of stacked nappes, forming a doubly plunging northwest–southeast elongate dome, with the stratigraphically lowest units outcropping in the centre of the dome (Steck *et al.*, 1998). The lowermost nappe is known as the Tso Morari complex (Figure 2) and contains Ordovician granite basement of the Indian plate, intruded into Cambrian sediments. This nappe has been overprinted by regional amphibolite facies Barrovian metamorphism and is host to mafic rocks preserving eclogite facies mineralogy and ultrahigh–pressure minerals (de Sigoyer *et al.*, 1997; Guillot *et al.*, 1997; Sachan *et al.*, 2004). The overlying nappes, Tetraogal (TN) and Mata (MNTN) respectively (figure 2), are lithostratigraphically higher, consisting of marine carbonates and schists from amphibolite facies to unmetamorphosed sediments. The structural history of the North Himalayan nappes in the Zanskar range (Figure 1) were first described by Bassoulet *et al.* (1978), Baud *et al.* (1982), Mascle (1985) and by Steck *et al.* (1998) in the Tso Morari region. The nappes formed during the northward convergence of India with the Eurasian margin (Norton and Sclater, 1979). Dome structures are known from the central and eastern Himalaya, between the Indus-Tsangpo Suture Zone and South Tibetan Detachment (Figure 2) (Le Fort *et al.*, 1997; Lee *et al.*, 2004; Jessup *et al.*, 2009). Immediately to the north of the Tso Morari dome are the units that make up the Indus suture zone and the Ladakh, calc–alkaline intrusive rocks (Figure 2), dated at 103–47 Ma (Honegger *et al.*, 1982; Schärer *et al.*, 1984; St-Onge *et al.*, 2010). The Indus suture zone is composed of marine, continental (Figure 2, Indus Molasse group, yellow unit) and ophiolitic sediments, including the Nidar ophiolite (Thakur and Virdi, 1979; Thakur and Misra, 1984), the Drakkarpo unit and the Zildat unit which make up the 'ophiolite & ophiolitic mélange' in figure 2 (dark blue). The Nidar ophiolite is composed of serpentinites, peridotites, gabbros and

pillow basalts, originally forming an intra–oceanic arc with an subduction-related mantle source (Thakur *et al.*, 1983; de Sigoyer, 1998; Mahéo *et al.*, 2000).

Adjacent to the Nidar ophiolite is the Drakkarpo unit, consisting of conglomerates, schists, tuff, basalts, serpentinites, quartzites and radiolarites forming a melange. The geochemical affinity of volcanic rocks within the melange suggest an island arc affinity. (Fuchs and Linner, 1996; De Sigoyer, 1998). The Zildat unit forms the unit directly adjacent to the Tso Morari complex in the hanging wall of the extensional Zildat shear zone (Figure 2) and is composed of the Zildat ophiolitic melange and the Sumdo complex, with slates, marbles and basalts, similar to the Lamayuru Complex (Colchen *et al.*, 1994) and is even documented to contain fragments of Permo–Carboniferous brachiopods (Fuchs and Linner, 1996). East of the Puga valley, overlying the Nidar and Drakkarpo unit is the Shergol conglomerate, thought to be Oligocene age (e.g. Haver, 1984; Fuchs *et al.*, 1996). The marine sediments of the Indus-Tsangpo Suture Zone were deposited along the distal parts of the Indian plate margin shelf in the NeoTethys ocean. Following the India-Asia collision, continental molasse sediments were deposited in a rapidly deepening basin along the suture zone (Indus group) (Mascle, 1986; Garzanti and Van Haver 1988; Fuchs and Linner, 1996).

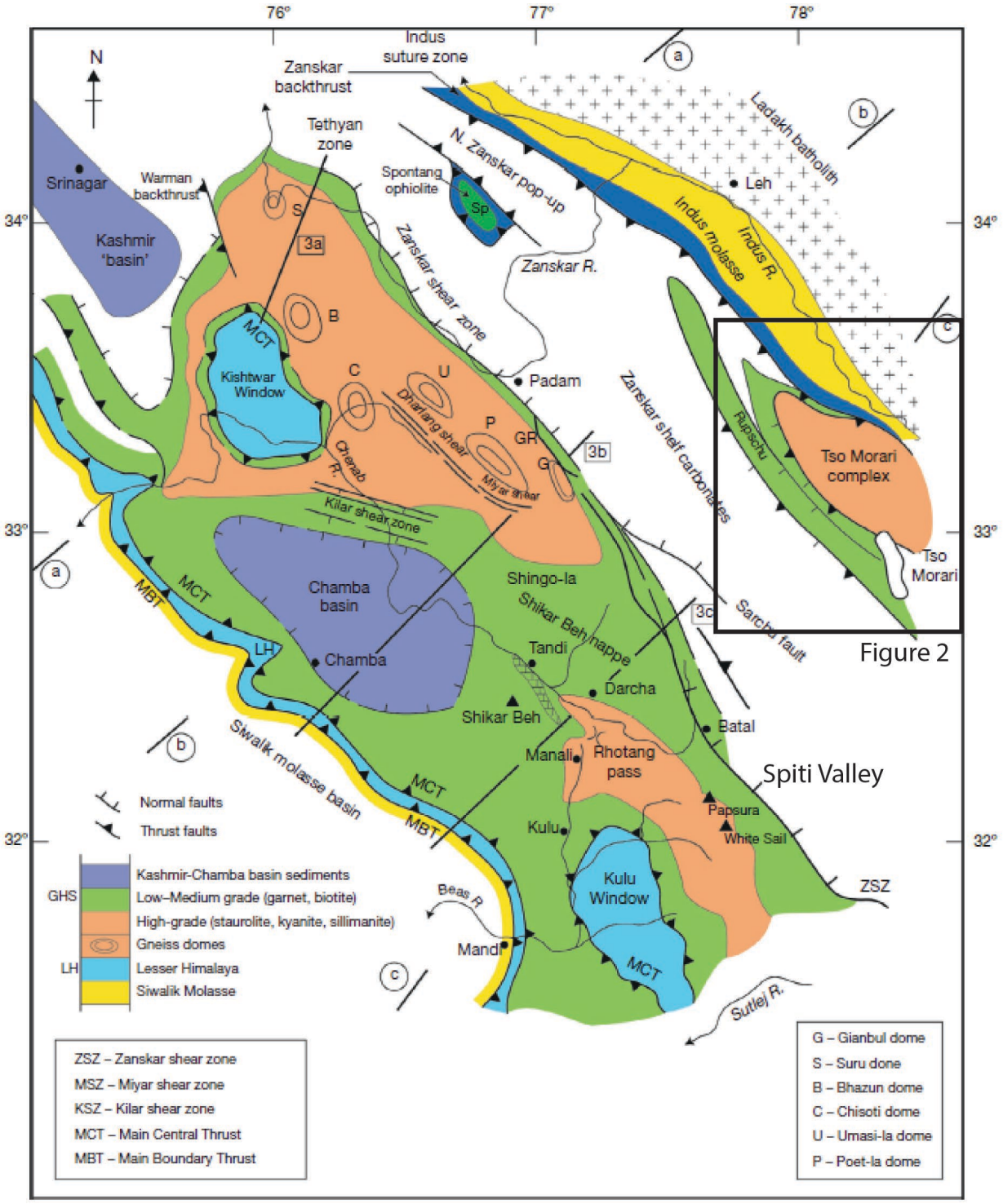


Figure 1 Geological map of NW India taken from Searle (2015) after (Searle et al., 1992, 1999). Tso Morari dome is adjacent to the Indus suture zone, surrounded by Tethyan sediments. High grade metamorphic rocks of the Greater Himalayan Series are found south of the Zanskar shear zone. Metamorphic rocks are shaded brown for amphibolite facies and individually labelled for sillimanite-grade gneiss domes. Greenschist-facies rocks are coloured green and low-grade metasedimentary rocks dark blue. Transects refer to Searle (2015), figure 12. Insert shows the location in figure 2.

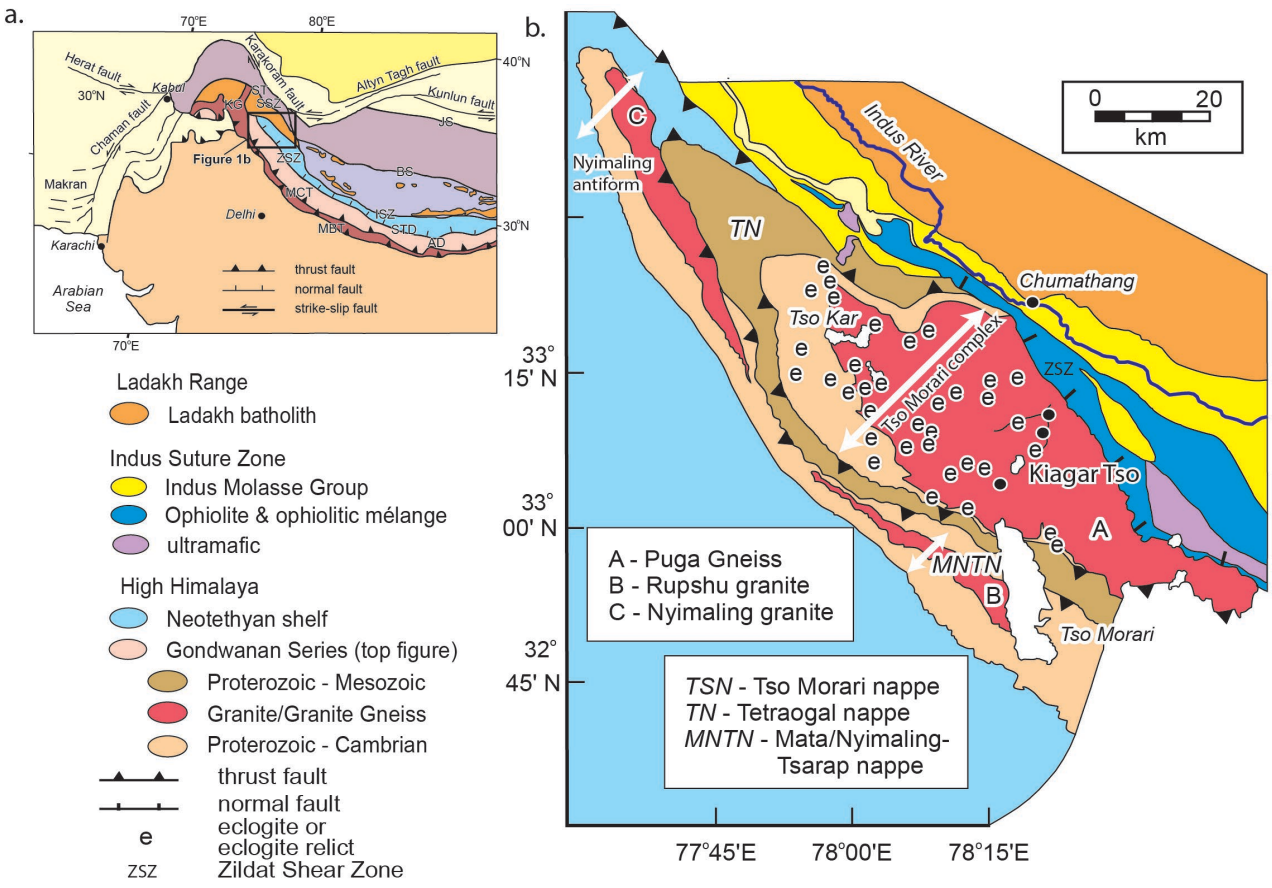


Figure 2 a. map showing the major faults in the Himalaya. b. Generalised geological map of the Tso Morari dome and Mesozoic cover of the Tethyan Himalaya in Ladakh, from Epard and Steck (2008) and references therein, adapted by St–Onge et al., (2013). HFB: Himalayan Frontal Boundary. MBT: Main Boundary Thrust. MCT: Main Central Thrust.

Terminology

There are a range of names in the literature referring to the structural and stratigraphic units surrounding Tso Morari. Epard and Steck (2008) refer to individual structural units as 'nappes', composed of the structurally lowest Tso Morari nappe, Tetraogal nappe and structurally highest Mata nappe. These units combine to form the Tso Morari dome, a term relating to the current structural configuration of units. This thesis focuses on the metamorphic and structural evolution of the Tso Morari dome and concerns constituent units prior to their formation as nappe and dome structures. As such, in this thesis, the naming convention of authors such as Sachan *et al.*, (1999), Leech *et al.*, (2005), Rajkumar (2015) and Jonnalagadda *et al.*, (2017) will be utilised, referring to the lowermost structural unit, host to eclogite facies mafic rocks, as the 'Tso Morari [crystalline] complex'. The Tso Morari complex is equivalent to the Tso Morari nappe of Epard and Steck (2008) when used in a structural context. The term 'Tso Morari dome' will be used as in Epard and Steck (2008) to refer to the geological entity composed of all three nappes, equivalent to the 'Tso Morari massif' of Palin *et al.*, (2014) (Figure 6).

Stratigraphy

Tso Morari was originally regarded as the northern extension of the Greater Himalayan Sequence crystalline slab (Hayden, 1904b; Berthelsen, 1953; Gansser, 1964). The later discovery of Permian conodont fossils in the upper north west limb (Virdi *et al.*, 1978) indicates that the stratigraphy of the Tso Morari dome is not equivalent to the Precambrian rocks of Zanskar but has been correlated with the rocks in the Nyimaling antiform to the northwest (Figure 2) (Stutz *et al.*, 1986; Colchen *et al.*, 1994) and may also be correlated with the stratigraphy of the Kaghan valley in Pakistan (Chapter 1, Figure 6) (Greco *et al.*, 1993). Successive nappes in the Tso Morari dome are very similar and are thought to be derived from adjacent parts of the Indian crust, with the overlying nappes representing younger and more distal facies.

The region surrounding the Tso Morari dome was first described by Stoliczka (1865) in a geological transect from the Spiti valley to the south to the Indus valley to the north (Figure 1). This account described the Silurian to Cretaceous formations including two bodies of Ordovician granitic gneiss known as the Rupshu and the Puga gneiss (Girard and Bussy, 1999). A more detailed account of the Palaeozoic and Mesozoic metasediments of the Spiti valley and their constituent fossils was presented by Hayden (1904), Gansser

(1964), Baud *et al.* (1982), Brookfield *et al. (*1984), Gaetani *et al.* (1985, 1986, 1990, 1991), Bhargava (1987), Vannay (1993), Brookfield (1993), Garzanti *et al. (*1995), Steck (2003), along with geological maps of the Tso Morari dome (Thakur, 1983; Thakur, 1983) and stratigraphic observations from the north west part of the dome (Fuchs and Linner, 1996).

The similarity in the stratigraphic sequences of the juxtaposed nappes in the Tso Morari dome suggests that these nappes were derived from adjacent parts of the crust with shallower shelf sediments becoming more abundant in the uppermost nappes (Epard and Steck, 2008). All three nappes contain Palaeozoic to Cambrian basal sediments, whereas Palaeozoic to Cretaceous sediments are found in the upper Tetraogal and Mata nappes (Steck, 1998). The sediments on the western part of the Tso Morari complex are composed of the Neoproterozoic Haimanta Group and Karsha Formation whereas the Mata nappe contains metasediments that are thought to be the eastern equivalent of the Nyimaling–Tsarap nappe (Figure 2) (Steck *et al.*, 1993, 1998; Steck, 2003).

The metasediments of the Tso Morari complex are composed of greywackes, slates and sandstone, thought to be part of the Upper Haimanta Group (or Phe Formation) of Neoproterozoic to early Cambrian age (Draganits *et al.*, 1998) and Karsha Formation of mid to late Cambrian age (Nanda *et al.*, 1977). The Karsha Formation is identified by the appearance of metre–scale yellow dolomite or limestone layers. The Tso Morari and Tetraogal nappes are intruded by mafic dykes which locally form folds and boudins within the granite gneiss. Geochemical fingerprinting of the major and trace element chemistry of the mafic rocks suggests that the mafic dykes are Permian in age and related to the Panjal trap basalts (Jonnalagadda *et al.*, 2017). The majority of the Tso Morari complex is composed of granite gneiss and regions of macroscopically undeformed granite. The western part of the complex preserves the contact between the granite gneiss and the Haimanta Group and Karsha Formations, characterised by apophyses of granite (Epard and Steck, 2008). The roof of the intrusion can be observed at the top of 6000 m high summits where large sheets of metasediments are visible (Epard and Steck, 2008).

The metasediments of the Tetraogal nappe are composed of greywackes, slates, quartzites, calc–schist, dolomites and limestones, intruded by mafic dykes, sills and layer parallel tuffs (Steck *et al.*, 1998) belonging to the Permian Panjal traps (Fuchs and Linner, 1996; de Sigoyer, 1998). These rocks have an amphibolite facies overprint, with no evidence of eclogite–facies metamorphism. South of Gyama Barma, carbonate–free

slates intercalated with calc–schist and limestone, are interpreted as a transition between slope deposits and a more distal basin environment, similar to the Late Cretaceous sediments of the Nyimaling and Upper Markha valley area (Stutz, 1988). The carbonate–free detrital sediments could be turbidites formed on the northern slope of the Indian shelf, however, no sedimentary structures confirming this have been documented and a lack of microfossils, although supporting this theory, prevents precise dating of the sedimentary series. The Taglang La region, interpreted as the North–west extension of the Tetraogal nappe, contains Permian conodonts (Virdi *et al.*, 1978), allowing the overall interpretation that the Tetraogal nappe consists of mainly Permian and younger sediments, possibly forming a lateral equivalent to the Permian–Mesozoic Lamayuru unit (Fuchs and Linner, 1996).

The Mata nappe forms the uppermost nappe of the Tso Morari dome and is correlated with the Nyimaling–Tsarap nappe to the northwest (Steck *et al.*, 1998; Epard *et al.*, 2004). It contains over 4000 m of later Proterozoic to Cambrian Haimanta Group greywackes, Karsha greywackes and dolomites, overlain by >3000 m of upper Palaeozoic to Cretaceous carbonate sediments of the North Indian shelf (Epard and Steck, 2008). The Mata also contains the Rupshu granite, an I–type granite with a U-Pb zircon age of 482 ± 1 Ma (Girard and Busy, 1999) and the Nyimaling granite, an S–type granite with a U-Pb zircon age of 460 ± 8 Ma (Stutz and Thoni, 1987) which cross–cut metasediments.

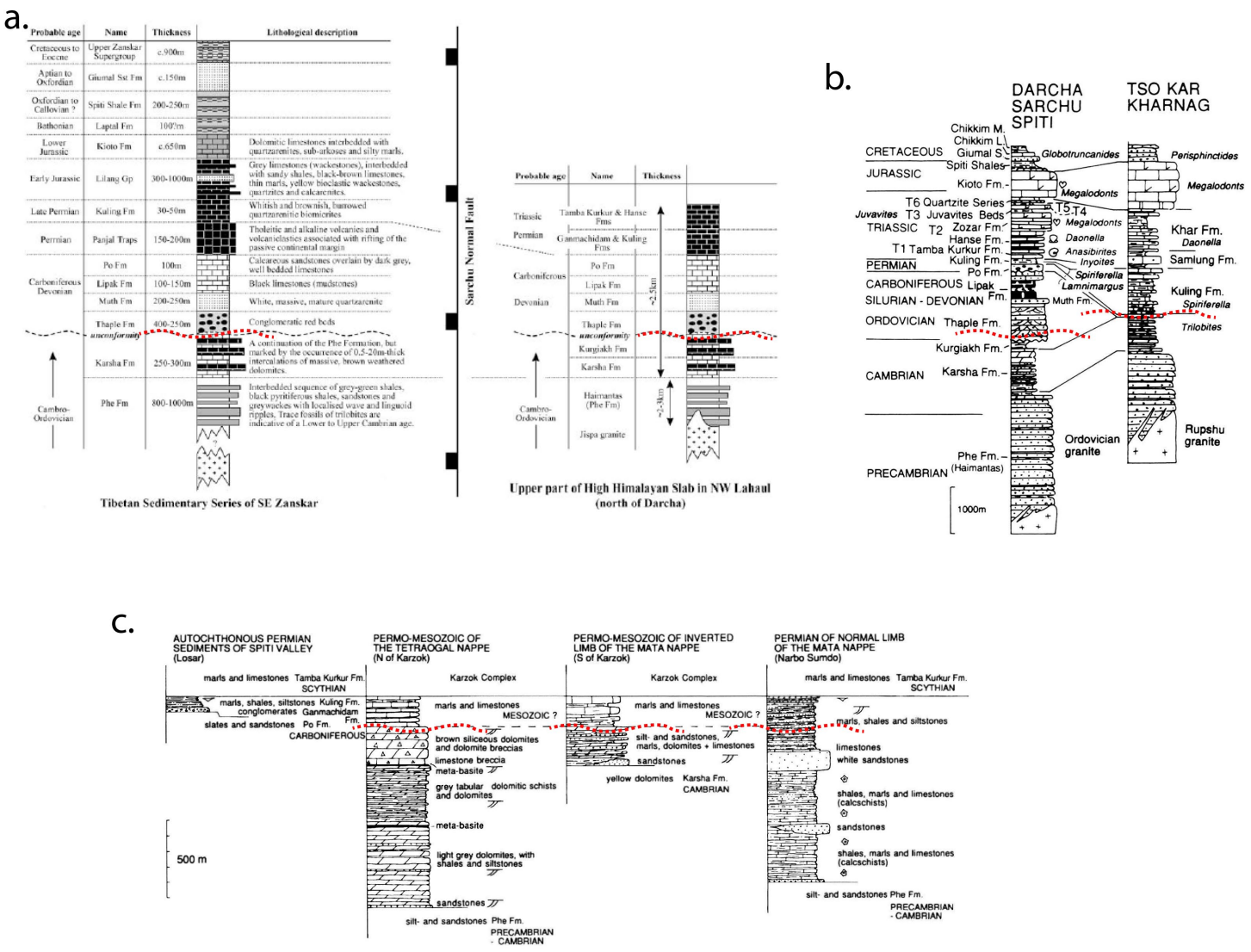


Figure 3 Stratigraphic sections of the Tethyan Himalayan zone and northern zone of the Greater Himalayan Sequence on the North Indian margin. a. Stratigraphic units from either side of the Sarcha normal fault with the Tethyan sediments of SE Zanskar (left) and the upper part of the GHS in Lahoul. Taken from Searle et al., (2007) and references therein. b. Stratigraphic sections from the Tethyan Himalayan zone, towards the Tso Morari complex taken from Steck et al., (1998). c. Stratigraphic sections from the Spiti valley and regions within the Tso Morari complex taken from Steck et al. (1998). Red dashed line marks the approximate location of the Palaeozoic–Mesozoic unconformity above the Karsha formation

Origin of the Tso Morari mafic rocks

The mafic rocks of the Tso Morari dome were intruded into Ordovician granites of the Indian basement and a sedimentary sequence forming the passive margin of the Indian continent. The linearly arranged boudin–shaped outcrops led to the interpretation that the mafic rocks were intruded as basaltic dykes into the Indian passive margin sequence, and subsequently deformed during Himalayan deformation (de Sigoyer *et al.*, 1997). The age of intrusion has not been directly determined, owing to a lack of suitable geochronometers, but correlations with other Himalayan mafic rocks have been made using geochemical fingerprinting (see below). Epard and Steck (2008) suggested that undeformed granite in the core of a folded eclogite boudin could be explained by cogenetic parts of a bimodal magmatism. Wyss *et al.*, (1999) suggested that the magma generation may be related to magmatic underplating in a large zone of extension along the North Indian border. These hypotheses were supported by the fact that the North Indian margin, during the Palaeozoic, was affected by extensional structures (Spring *et al.*, 1993; Steck *et al.*, 1993; Steck, 2003), suggesting that the origin of the mafic dykes could not be related to compressional tectonics as suggested by Girard and Bussy (1999).

Major and trace element analysis of the Tso Morari eclogites show that these rocks plot as sub–alkaline basalts and span the within–plate basalt (WPB) and enriched midocean–ridge basalt (MORB) field (Jonnalagadda *et al.*, 2017). They are thought to be derived from the partial melting of a garnet–free mantle source within the spinel–peridotite field and to have undergone limited fractional crystallisation with moderate crustal contamination (Jonnalagadda *et al.*, 2017). Zr, Th, LREE and Nb patterns are consistent with the proposed origin of continental flood basalts and show similar patterns to the Permian Panjal traps (c.f. Spencer *et al.*, 1995; Guillot *et al.*, 1997; de Sigoyer *et al.*, 2004; Ahmad *et al.*, 2006), particularly the group 1 Panjal trap basalts from the Zanskar and Spiti area (Chauvet *et al.*, 2008; Jonnalagadda *et al.*, 2017). The Panjal traps of north India are the volcanic remnants of continental rifting during the formation of the NeoTethys ocean, where massive basaltic flows were emplaced on the Indian margin rifted platform as observed in Kashmir (Nakazawa *et al.*, 1973; Shellnutt *et al.*, 2014) and as feeder dykes cross–cutting crystalline basement and lower Paleoproterozoic cover (Spencer *et al.*, 1995). Mafic eclogites from the Kaghan Valley, on the northern margin of Greater India, contain zircon cores with a U-Th-Pb age of 267.6 ± 2.4 Ma, consistent with a Panjal trap origin, overprinted by Himalayan ultrahigh-pressure metamorphism

(Rehman *et al.*, 2013). The mafic rocks of Tso Morari dome are thought to be intrusive rocks related to the Panjal trap continental flood basalts, based on geochemical fingerprinting which shows similarities when compared to the Permian Panjal trap basalts of the Kaghan Valley, Zanskar and Spiti valley (Jonnalagadda *et al.*, 2017).

Structural history of the Tso Morari dome

Deformation in the Tso Morari complex has been characterised into four structurally distinct events by Epard and Steck (2008) and summarised here. The earliest phase of deformation (D1) formed a stretching lineation (L1), which is parallel to the top–E shear criteria, and mylonitic structures, related to the extrusion of the Tso Morari complex. Relicts of undeformed granite are present throughout the complex, as well as stages from granite to granite gneiss to mylonites. Isoclinal folding is observed within the gneiss with at least two generations of folding and three generations of schistosity. Ductile deformation within K feldspars indicates temperatures of >500°C during D1 deformation. Rare relicts of orientated omphacite–garnet fabrics within mafic eclogites, correlated with L1, suggest that some deformation began in the eclogite facies.

The dominant fabric within the Tso Morari complex belongs to the mineral assemblages consistent with Barrovian regional metamorphism, postdating the ultrahigh pressure metamorphism and also overprints the rocks of the Tetraogal and Mata nappes. Within the metasediments of the Tso Morari complex, minerals such as staurolite, kyanite and sillimanite indicate a high temperature overprint where secondary fibrolite grew after biotite, parallel to the L1 stretching lineation in top–E shear zones, , indicating westward extrusion of the Tso Morari complex during the decrease in pressure (Epard and Steck, 2008). Sillimanite growth after biotite and kyanite, and muscovite after kyanite indicate metamorphic decompression, as proposed by De Sigoyer et al., (2000). The direction of extrusion is oblique (~40°) to the strike of the NE–dipping Indus suture zone sediments and predates the formation of the dome structure. Top–E structures are restricted to the Tso Morari complex and are particularly prevalent away from major shear zones such as the Zildat shear zone and the shear zones separating the Tso Morari, Tetraogal and Mata nappes (Figure 2).

The structures on the north side of the complex are related to the development of the Zildat shear zone to the north. The Zildat extensional shear zone dips steeply to the NE with NE–plunging stretching lineations and top–NE extensional shear sense (Steck *et al.,* 1998). Metamorphism in the Tso Morari complex in the NE part of the dome, in contact with the colder rocks of the Indus suture zone, record upper greenschist–facies

metamorphism, overprinting earlier eclogite–facies metamorphism (Steck *et al.*, 1998), consistent with metamorphism of the deformed greenschist–facies rocks of the hanging wall.

Deformation events D2–D4 postdate the strong D1 fabrics in the central Tso Morari complex but increase in strength towards the bounding shear zones. Folding of the pre–existing L1 lineation during D2 deformation is observed along with the formation of a second north– or south– plunging lineation (L2), with top–S criteria and conjugate shear zones, indicating a component of pure shear. The L2 stretching is also associated with amphibolite–facies mineral assemblages. Within the Tetraogal and lower part of the Mata nappe, S–directed stretching lineations are interpreted to be part of the same deformation event. It has been suggested that the development of the L2–stretching lineation is related to the north–directed under thrusting of the Tso Morari complex beneath the Tetraogal and Mata nappes.

A later NE–SW stretching lineation (L3) has a top–S shear sense and overprints earlier structures within the Tso Morari complex. This deformation fabric (D3) is present at the southern margin of the Tso Morari complex, as well as extensively within the overlying nappes and is coeval with regional Barrovian metamorphism (Steck *et al.*, 1993). Studies of metasediments within the Tso Morari complex suggest that syn-deformational mineral growth took place at ~30 km depth, whereas metapelites from the Mata and Nyimaling–Tsarap nappe deformed at depths of less than 2 km (Girard, 2001; Schlup *et al.*, 2003).

The development of the dome–like shape of the Tso Morari dome (D4) postdates the NE–directed movement of the Tso Morari complex (D3). The timing of this is constrained by the uplift of the complex below 300°C, as reported by zircon and apatite fission–track data and Ar/Ar on phengite and biotite, to 40 Ma in the Kiagar Tso region (Schlup, 2003; Schlup *et al.,* 2003). Further towards the western part of the complex, in the Nuruchen region, cooling below 300°C occurred by 30 Ma (De Sigoyer *et al.*, 2000), indicating that doming and uplift of the Tso Morari complex started in the east and progressed towards the west. Hundred–metre scale NE–verging back–folds are also observed on the northern side of the Tso Morari dome and within the Mata nappe and thought to have formed between 47 and 30 Ma. Peak metamorphism related to Barrovian metamorphism and SW–directed thrusting in the Himalaya has been dated at 23–20 Ma (Cottle *et al.*, 2009). The formation and exhumation of the Tso Morari complex therefore predates or occurs coevally with the development of the North Himalayan nappe stack. Later erosion has removed tens of km of overburden from the Tso Morari dome since 40–30 Ma at ~ 0.25 $mm.yr^{-1}$ and 7.5 $°C.Ma^{-1}$ (Schlup *et al.,* 2003).

The Tetraogal nappe lies structurally above the Tso Morari complex and outcrops in the southern to north western parts of the dome, with way up structure indicating a normal position (Epard and Steck, 2008). The Mata nappe has been folded into a recumbent fold with Late Palaeozoic to Triassic sediments in both limbs, with the Rupshu granite in the core (Steck *et al.*, 1998). The Tetraogal and Mata nappes are separated by a lens of ophiolite known as the Karzok ophiolite (Berthelsen, 1953), thought to form a distinct structural unit which also contains chromite, radiolarite, marbles, conglomerates, breccia and agglomeratic slates (Buchs *et al.*, 2019). This unit is known as the Karzok-Ribil nappe and has been correlated with the volcano-sedimentary rocks of the Sumdo region (Figure 8).

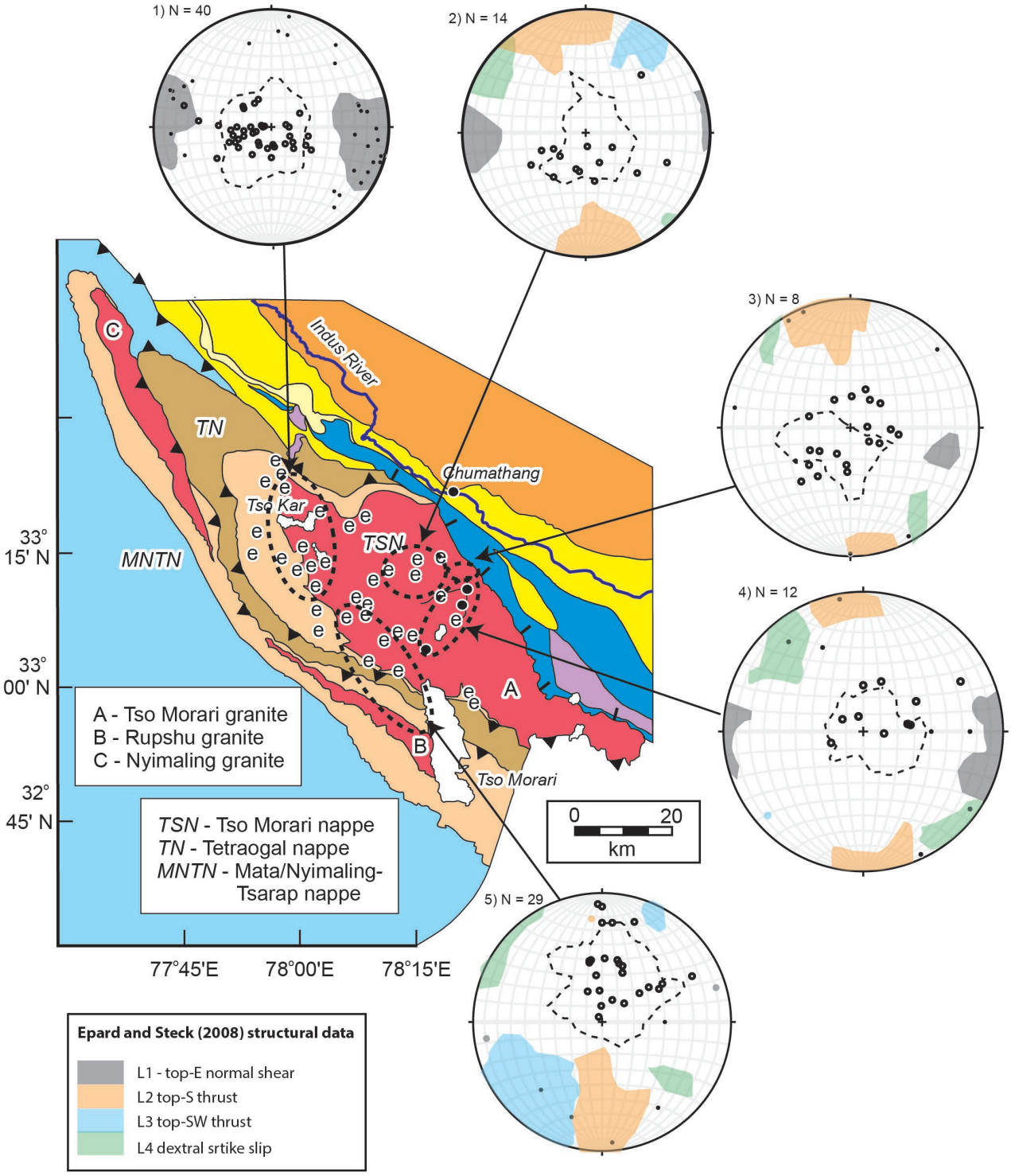


Figure 4 Map of the Tso Morari dome taken from St–Onge et al. (2013). Structural data from this study is plotted on stereonets with open circles for poles to foliation planes and filled circles as lineations. Structural data from Epard and Steck (2008) is summarised as data clouds, dotted lines denoting the poles to foliation cloud and lineations split into L1–L4.

Metamorphic evolution of Tso Morari complex

Five stages of metamorphism have been identified within a combination of lithologies within the Tso Morari complex (Guillot et al., 1997, 2000; de Sigoyer et al., 1997, 2008, 2004; Girard, 2001., Sachan et al., 2004, Mukherjee et al., 2005; St–Onge et al., 2013). The early metamorphic history, related to subduction of the Indian continental margin, is best preserved in mafic lithologies whereas the amphibolite facies overprint is extensively recorded in the felsic rocks of the Tso Morari complex. These stages include subduction–related prograde metamorphism (M1) leading up to peak ultrahigh–pressure eclogite–facies metamorphism (M2), followed by exhumation to the base of the crust (M3). Further metamorphism is defined by an amphibolite facies overprint recorded in the mafic and felsic rocks (M4) and greenschist facies metamorphism in the final stages of exhumation (M5) (St–Onge et al, 2013).

M1 to M2 stages are recorded in the growth zoning profiles of the garnets in the mafic eclogites. M2 represents peak pressure conditions within the eclogite facies and within the coesite stability field for samples of mafic eclogite from the Berthelsen outcrop (e.g. St–Onge et al., 2013). Glaucophane–bearing metasediments from within the Tso Morari complex are rare but indicate that high pressure conditions occurred in other lithologies within the nappe. Evidence of approximately isothermal decompression (M3) is recorded in the zoned amphibole and clinozoisite of the mafic eclogites and is thought to record rapid exhumation to the base of the crust (St–Onge et al., 2013; Palin et al., 2014). Metamorphic stages M1-M3 are thought to be related to D1 deformation and a top-to-east lineation (Epard and Steck, 2008). More detailed discussion on the prograde, peak and initial exhumation–related *P–T* conditions in the mafic eclogites are discussed in Chapter 5.

Later overprinting in the amphibolite facies (M4) and greenschist facies (M5) is recorded in hydrous phases such as the rims of zoned amphibole in mafic eclogite. M4 and M5 metamorphism are also extensively recorded in the granite gneiss and metasediments of the Tso Morari complex in the form of white mica, biotite, garnet, albite and occasionally staurolite, cordierite and sillimanite–bearing assemblages. Syndeformational M4 metamorphism is related to NE-SW lineations (L3) close to the shear zones between the nappes (Epard and Steck, 2008). D4 deformation, relating to formation of the dome structure postdates M5 metamorphism (Schlup et al., 2003). There is little evidence of early (M1 to M3) metamorphism currently

recorded in the Puga gneiss or Tso Morari granite. However, further evidence is early high–pressure metamorphism and where to look for it is discussed in Chapters 3, 4 and 6.

Published data from the Tso Morari complex

The discovery of coesite in a single outcrop in the Tso Morari complex (Sachan *et al.*, 2001) lead to subsequent publications interpreting the entirety of the Tso Morari complex as ultrahigh–pressure, despite very few observations of coesite being documented. Variations in field and petrological observations, as well as *P–T* estimates across the complex may be important when it comes to unravelling the key observations, similarities and differences across the Tso Morari complex. In order to compile and interpret the published data, attempts have been made to determine the location of samples studied. However, due to the lack of clarity and detail concerning sample locations, how many samples were studied, which samples contain the specific features described, etc. this has proved problematic. In many cases, lat/long coordinates are absent or incorrect, locality maps are inaccurate in terms of drainage patterns or generalized geological boundaries or are simply at too small a scale. This study has attempted to determine the locations of samples, observations and data from published studies. These have been compiled on Figure 5. However, due to uncertainty in the exact location, samples are displayed using large symbols.

De Sigoyer *et al.*, (1997) studied 3 eclogite samples, located based on the eclogite locations from Guillot *et al.*, (1997) (Fig. 1). Ts34 is assumed to be the Berthelsen locality, Ts 45 assumed to be the bridge locality and Ts 51 to the north–west of Tso Morari lake in the footwall of the shear zone north of Karzok. Guillot *et al.*, (1997) studied high pressure metasediments from the valley traverse along the road from Sumdo to Kiagar La. These include Ts25, 26, 30, 31 and 39. Sample Ts30 contains minor jadeitic clinopyroxene.

Sachan *et al.*, (2004) shows the location of a coesite–bearing eclogite on a map, with no indication of the location with respect to valleys or roads. The location is implied as the Berthelsen outcrop, however the coordinate at the bottom of the map is wrongly given as 32°40’N rather than 32°54’N. The text refers to the petrography of “coesite–bearing eclogites”, but there is no indication that more than one eclogite body has been studied, more than one sample analysed, or more than one garnet found to contain coesite inclusions. It’s not clear if Fig. 2c (“Diagrammatic sketch of distribution of silica inclusions in garnet”) of Sachan et al., (2004) is a drawing of an actual garnet or is a schematic composite diagram.

Mukherjee and Sachan (2003) describe 11 eclogite samples and present the sample locations on a simplified map with few features. No coordinates are presented. It is possible that sample Ts/01–67 is the Berthelsen locality. Samples Ts/00–22, Ts/01–28, Ts/01–69 and Ts/01–78 contain coesite. Mukherjee *et al.*, (2009) contains a more detailed locality map showing the location of Puga Gneiss samples for fluid inclusion study where it is easier to relate sample locations to topography and other geographical features. Its scale is incorrect: the 8 km bar is actually about 5 km; the lat/long grid does not quite match the geology and valleys when 'correctly' oriented. Ts367 is the Berthelsen locality, on this map.

Jonnalagadda *et al.*, (2017) shows the location of two eclogites containing atoll garnets localities in the general area of the Berthelsen locality and one further south up the valley towards Kiagar La. However, the lat/long given for S7, the sample studied in detail, plots in the middle of the Puga hot springs, 5 km NW of the Berthelsen locality, and is unlikely to be correct. Jonnalagadda et al., (2019) contains more petrography and mineral analyses, but none of these images or data specify the sample numbers concerned.

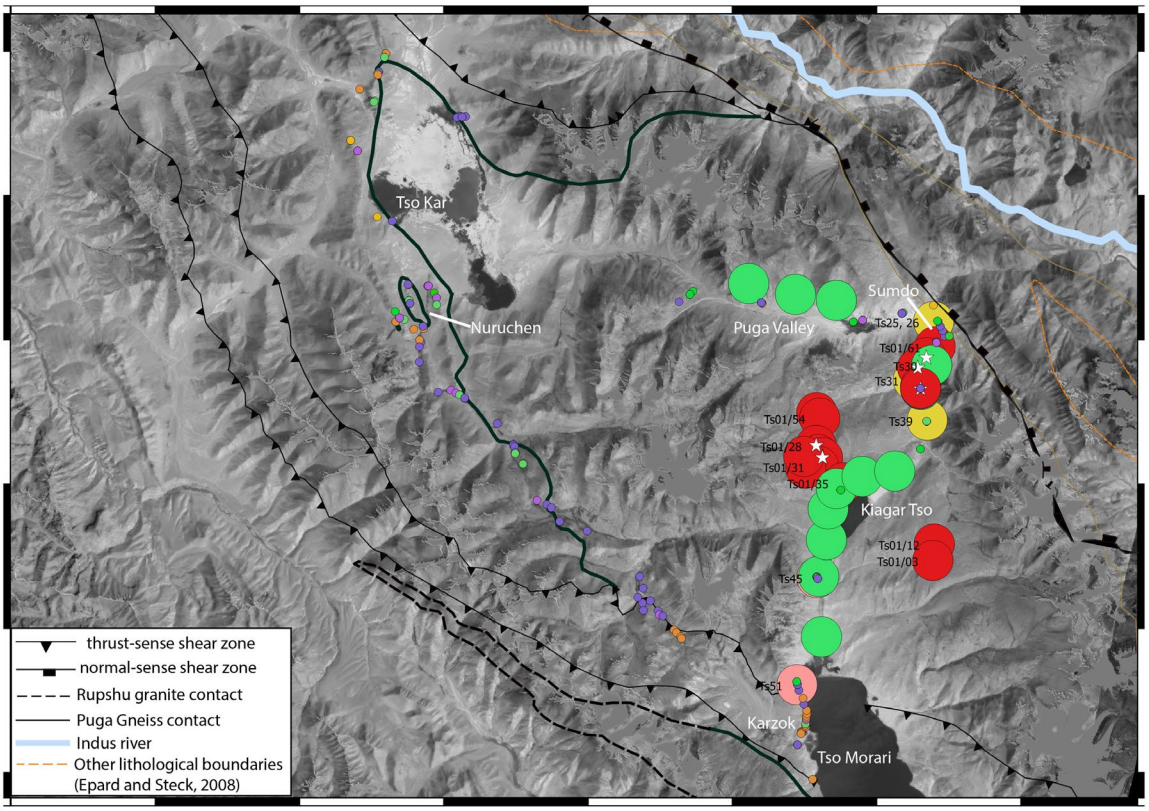


Figure 5 showing the location of published samples. Large symbols related to the uncertainty of locations based on inaccurate maps. Stars indicate coesite–bearing localities. Small dots indicate samples from this study. Included studies: De Sigoyer et al (1997) (pink), Guillot et al., (1997) (yellow), Mukherjee et al., (2003 and Mukherjee et al., (2009) (purple), Sachan et al., (2004) (blue), Jonallagadda et al., (2017) (green). Background USGS landsat data downloaded from https://earthexplorer.usgs.gov/. RGB colouring corresponds to bands 321 respectively.

X	*Y*	*Rock type*	*Source*	*Coordinate*	*Sample*
78.35724	33.18346	eclogite	De Sigoyer et al 1997	estimated using Guillot et al 1997, Fig.1	Ts34
78.27605	33.06726	Eclogite	De Sigoyer et al 1997	Estimated using Guillot et al 1997. fig1	Ts45
78.2588	33.0008	Eclogite	De Sigoyer et al 1997	Estimated from Guillot et al 1997. fig1	Ts51
78.36148	33.16339	Metasediment	Guillot et al 1997	From map	Ts39
78.35215	33.18871	Metasediment	Guillot et al., 1997	From map	Ts31
78.3661	33.19761	Metasediment	Guillot et al., 1997	From map	Ts30
78.36862	33.22478	Metasediment	Guillot et al 1997	From map	Ts25, 26
78.27969	33.17022	eclogite	Mukherjee et al 2003	From map	Ts01/52
78.28177	33.16676	eclogite	Mukherjee et al 2003	From map	Ts01/54
78.36912	33.20906	eclogite	Mukherjee et al 2003	From map	Ts01/61
78.36233	33.20236	coesite eclogite	Mukherjee et al 2003	From map	Ts01/69
78.35565	33.19619	coesite eclogite	Mukherjee et al 2003	From map	Ts01/78
78.2785	33.14976	coesite eclogite	Mukherjee et al 2003	From map	Ts01/28
78.2799	33.144	eclogite	Mukherjee et al 2003	From map	Ts00/27
78.28291	33.14201	coesite eclogite	Mukherjee et al 2003	From map	Ts00/22
78.27995	33.13664	eclogite	Mukherjee et al 2003	From map	Ts01/31
78.29754	33.12595	eclogite	Mukherjee et al 2003	From map	Ts01/35
78.2702	33.1358	eclogite	Mukherjee et al 2003	From map	Ts01/20
78.26902	33.1432	eclogite	Mukherjee et al 2003	From map	Ts01/33
78.36372	33.08588	eclogite	Mukherjee et al 2003	From map	Ts01/12
78.36236	33.07569	eclogite	Mukherjee et al 2003	From map	Ts01/03
78.35735	33.18439	eclogite	Mukherjee et al 2009	From map	Ts367
78.27798	33.0302	eclogite atoll	Jonallagadda et al., 2017	From map	
78.35766	33.18257	eclogite atoll	Jonallagadda et al., 2017	From map	
78.36613	33.19746	eclogite atoll	Jonallagadda et al., 2017	From map	
78.27735	33.06798	eclogite atoll	Jonallagadda et al., 2017	From map	
78.2839	33.0907	eclogite atoll	Jonallagadda et al., 2017	From map	
78.28596	33.10987	eclogite atoll	Jonallagadda et al., 2017	From map	
78.29247	33.12242	eclogite atoll	Jonallagadda et al., 2017	From map	
78.31188	33.12953	eclogite atoll	Jonallagadda et al., 2017	From map	
78.33617	33.13228	eclogite atoll	Jonallagadda et al., 2017	From map	
78.35734	33.183	coesite eclogite	Sachan et al 2004	From map	
78.35736	33.18343	Eclogite	Mukherjee et al 2003	From map	Ts01/67

Table 1 showing estimated sample locations based on published maps with labelled sample numbers where relevant. Note the uncertainty involved when pinpointing localities using simplified small maps.

Aim of this chapter

The following section aims to document key localities across the Tso Morari dome, with a focus on identifying lithologies and recording structural measurements, particularly from within the Tso Morari complex. The compiled published data from the Tso Morari complex highlights the lack of clarity and detail concerning sample locations, how many samples were studied, which samples contain the specific features described. The scarcity of data hindered attempts to compile and evaluate pre-existing data from the Tso Morari complex and in some case required a detailed knowledge of the area, built up over months of fieldwork, in order to determine the actual sample locations. As such, this chapter records a detailed account of sample locations from this study and their corresponding observations and measurements, providing a useful repository of field data, observations and descriptions. This record also provides a necessary synthesis which accompanies the extensive collection of samples catalogued in the Oxford University collections.

Key outcrops are described along route beginning at Karzok, on the shore of lake Tso Morari, following the road towards the northern boundary of the dome before heading west along the road to the shores of Tso Kar. The described route provides a detailed transect of observations and samples across and along the axis of the elongate dome (north-south and east-west respectively) and was planned based on the structural map of Epard and Steck (2008) so that major units were samples close to and away from major structural contacts. From Tso Kar, a route to the south was followed, away from the road, towards Tso Morari, detouring up ridges which were accessible on foot from the trekking route. The described route crosses the boundaries of the nappe units (Tso Morari, Tetraogal and Mata nappe).

Structural measurements were taken in situ and used to verify the detailed structural interpretation of Epard and Steck (2008), as well as to provide context to samples taken for further petrographic study in subsequent chapters of this thesis. All samples collected were oriented, provided they contain a pervasive fabric e.g. gneisses and metasediments.

Key localities in the Tso Morari dome

The following section is organised by locality, describing key features, variation and samples from outcrops across the Tso Morari complex. The first number is either 16 or 17, referring to the year the locality was first visited, this is followed by a locality number. In 2016, the locality number refers to the day followed by the stop number of the day, whereas in 2017 the locality number refers to the cumulative stop number from that field season. This numbering scheme was kept unchanged so that it matches the record in the field notebooks. The corresponding petrological samples, geochronological samples, waypoints and coordinates from each locality are recorded in Appendix 1. Waypoints recorded in this study refer to specific coordinates as determined by GPS. There can be multiple waypoints taken at a single locality. Sample numbers refer to the day followed by the stop number (e.g. 05–02 is day 5 stop 2), the presence of the prefix 'a' before the sample number denotes a sample taken in 2017. Due to separate samples being taken from the same outcrops in 2016 and 2017 field seasons and petrological and geochronological samples being collected separately, a reference table has been compiled in Appendix 1.

In 2016, the route was planned based on the presence of the road from Karzok to Sumdo (~N-S) and Sumdo to Tso Kar (~E-W). Exposure along the river between Tso Morari and Kiagar Tso is accessible from the road but often forms cliffs ~20m high. The road section from Kiagar Tso to Sumdo is much higher in altitude and flanked by hillsides ranging up to >6000m from a base level of ~4500m. The river is incised along this route with 10m high quaternary deposits making access difficult. The river is also known to swell towards the end of the day. The Puga valley is a broader valley, flanked by 100m cliffs, accessible at the base. Towards the Polokongka La pass (5000m) the adjacent ridges are accessible by foot from the road but the altitude and boulder-ridden terrane make access slow.

The area around Tso Kar is steep but accessible on foot and the flat dry plain is crossable by car and is close to the Leh-Manali road, providing a route back to Leh. The popular trekking route passes along the western side of Tso Kar to Nuruchen, all the way to Karzok. This route was followed during the 2017 field season and took 3 days of trekking from Nuruchen to Karzok. Transport of baggage was aided by pack horses and a local Tibetan nomad hired locally. Only one pass was crossed per day due to the high altitude, however detours around the trekking route are possible on route. Ridges adjacent to the trekking route are ~500-600m high and covered in loose scree. The ridges themselves have limited exposure at the top which outcrops

parallel to the strike of the metasediments. The topography, unstable slopes, high altitude and thunderstorms (from mid afternoon) made it difficult to cover large distances each day and often only one ridge (3-4 outcrops along strike) were visited per day.

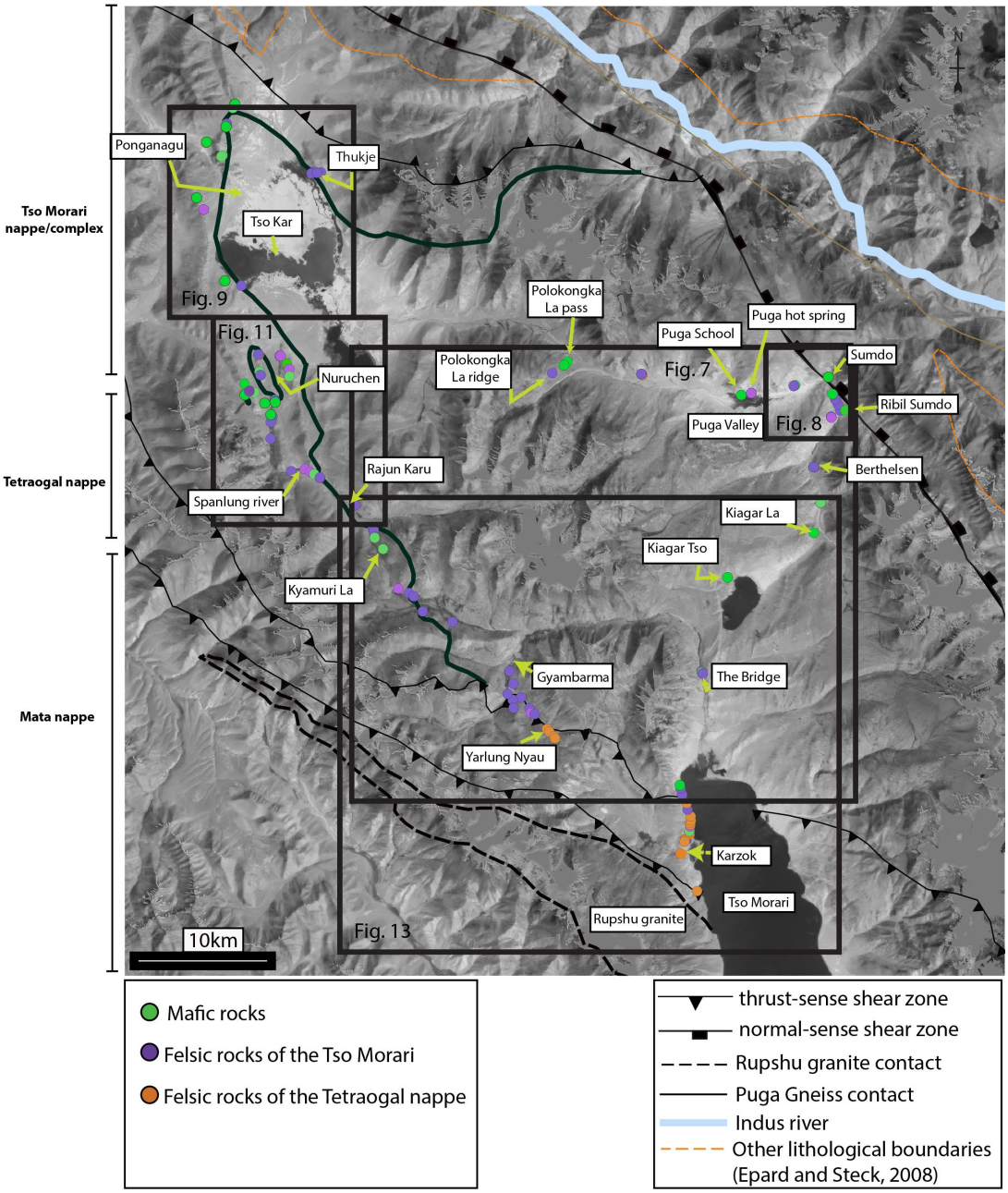


Figure 6 Overview map of localities in the Tso Morari dome discussed in this chapter. See reference table in Appendix 1 and maps below for locality numbers. Background USGS landsat data downloaded from https://earthexplorer.usgs.gov/. RGB colouring corresponds to bands 321 respectively.

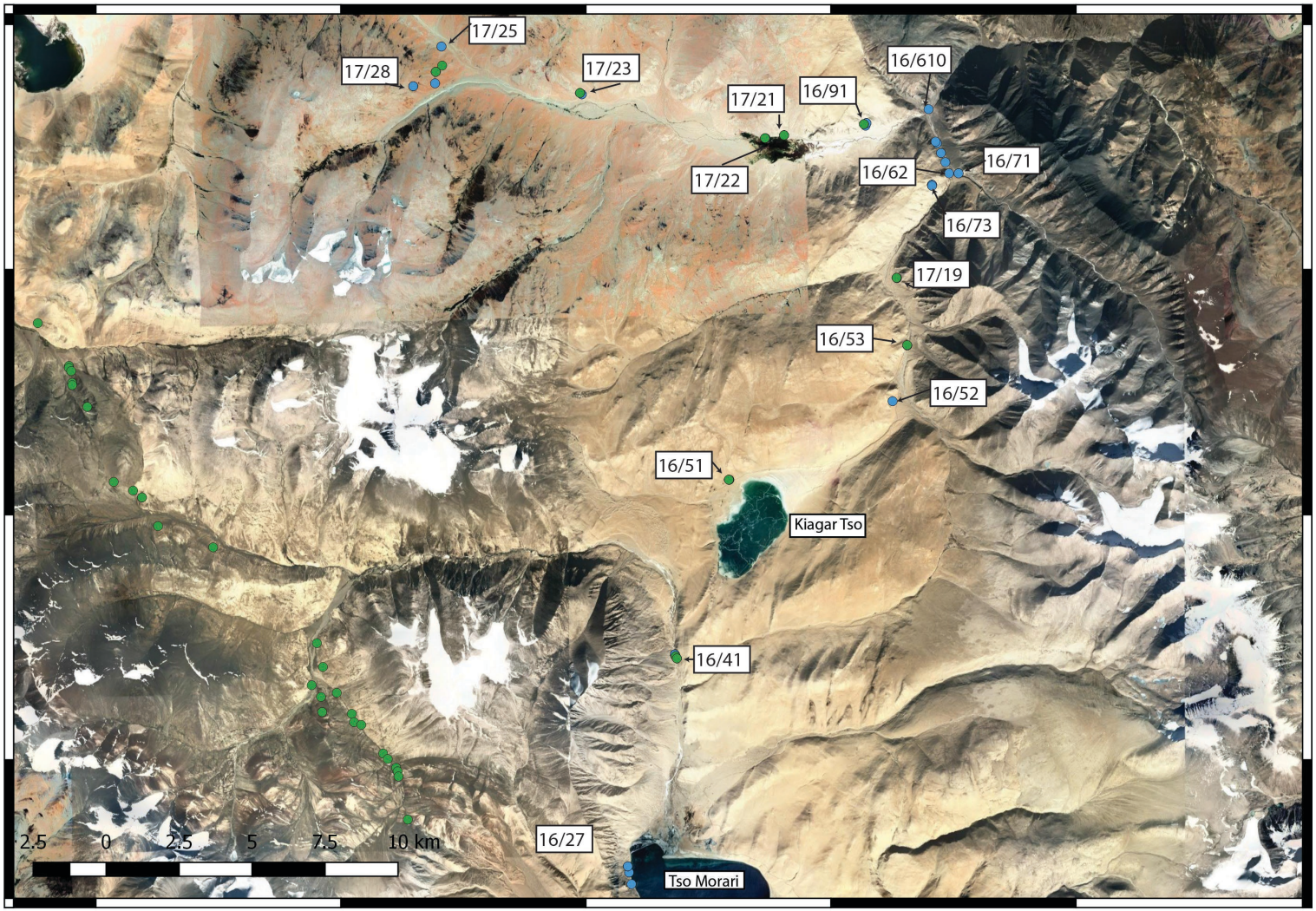


Figure 7 Map of locality numbers on eastern side of traverse. See Table 1 for details.

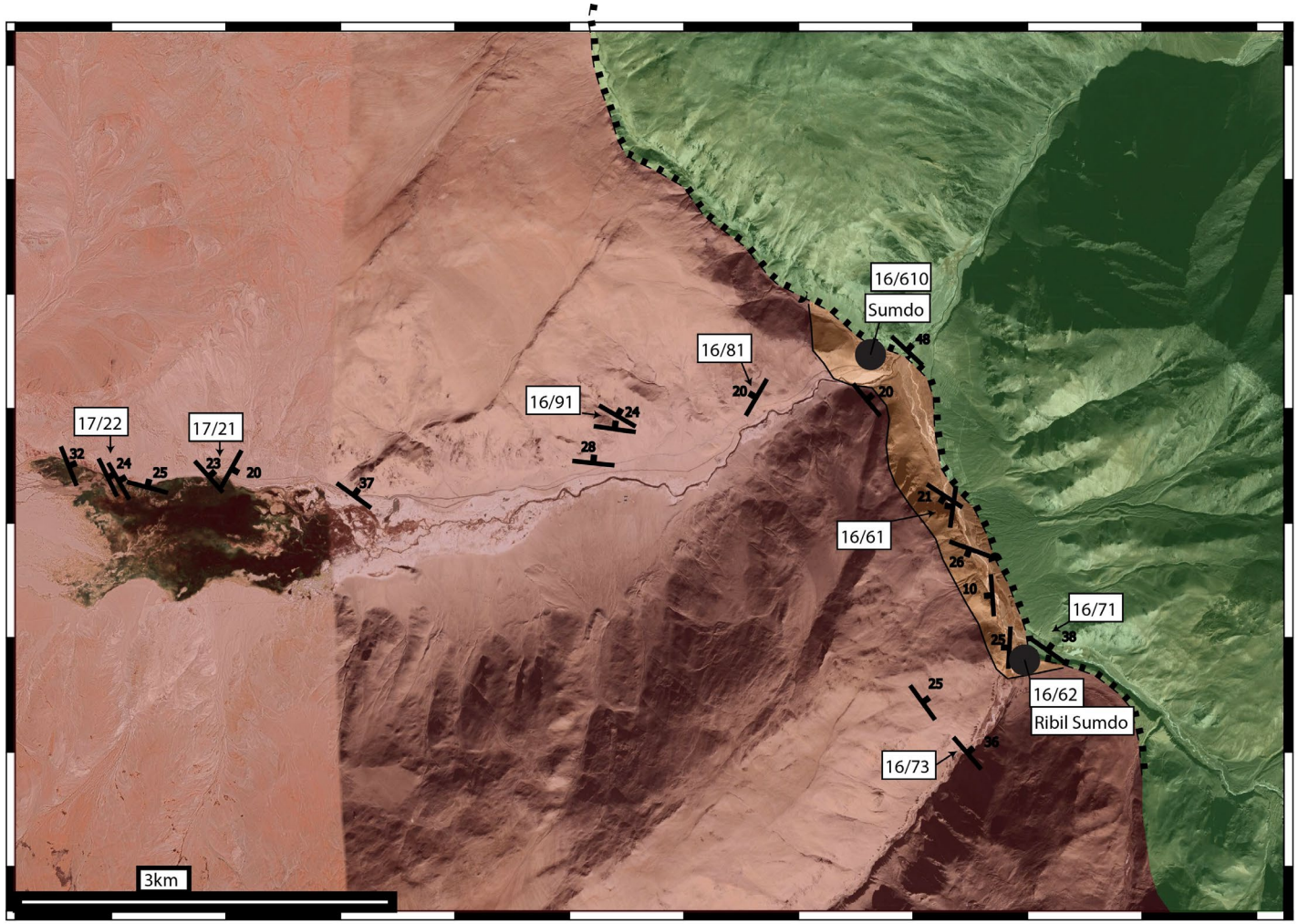


Figure 8 Simple geological map of the northern margin of the dome. Zildat shear zone is marked using box symbols separating the ophiolitic metasediments (green) dipping steeply NE from the Puga gneiss (red). A slither of metasediments (orange) is located close to the shear zone showing a SW dipping foliation. Background shows the outcrop extent via QuickMapServices GNU general public license.

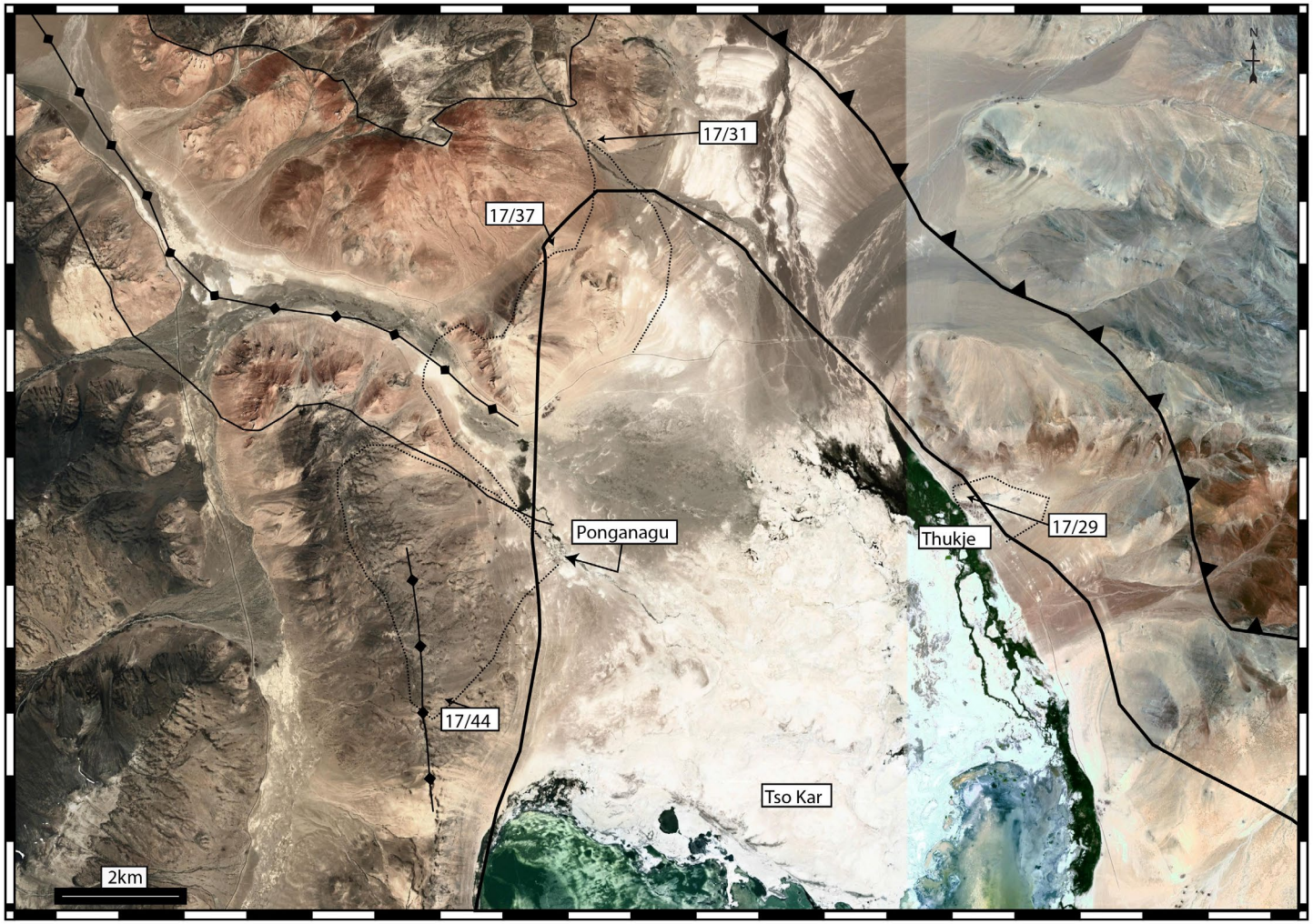


Figure 9 Map of the NW of the Tso Morari complex around Tso Kar. Locality numbers marked. Dotted lines show routes travelled. See Table 1 for details.

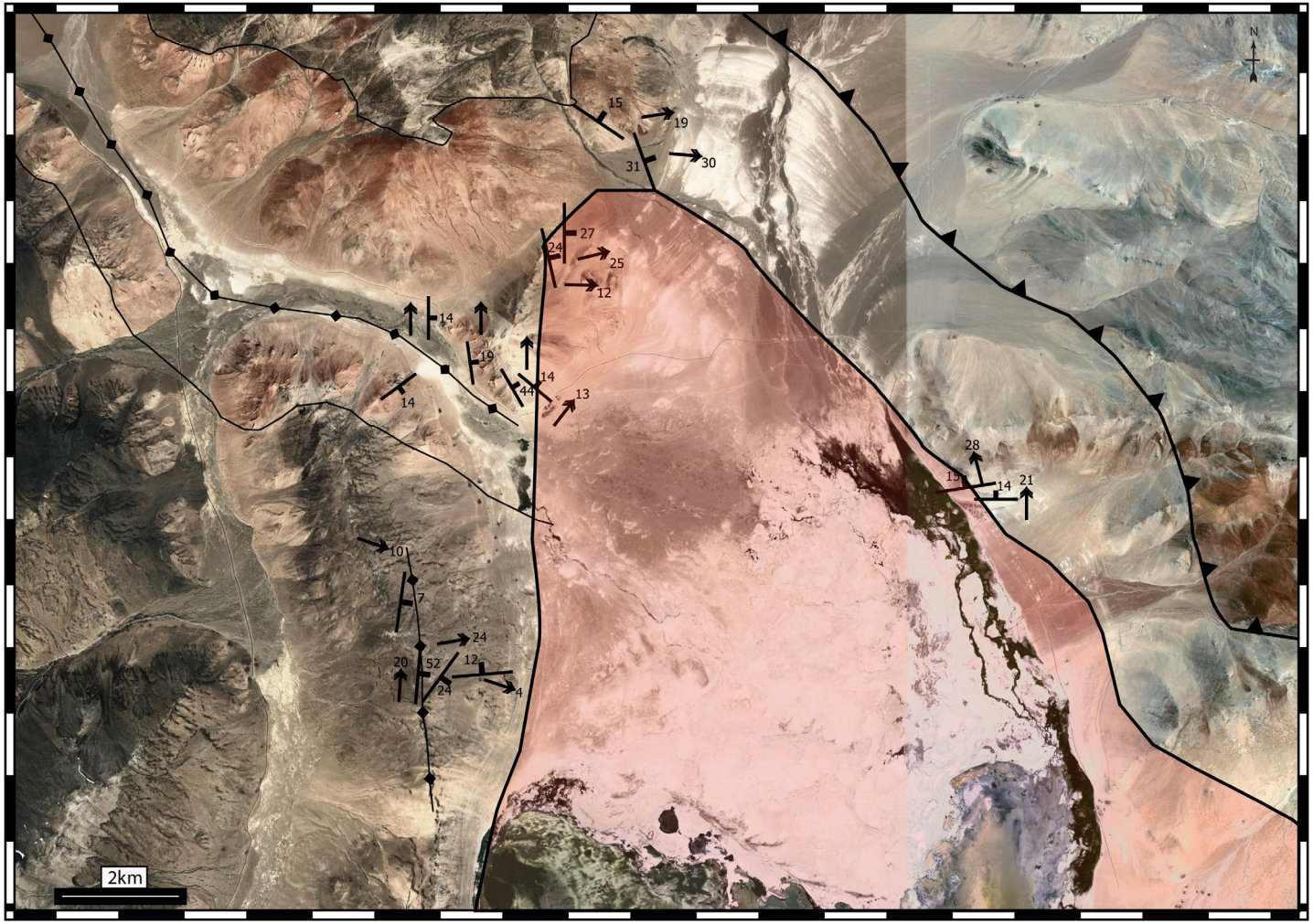


Figure 10 Structural map of the NW of the Tso Morari complex around Tso Kar. Solid black lines = lithological boundaries. triangles = thrust, diamonds = antiform. Strikes and dips = foliations, lineations = mineral stretching. Red = granite, non-red = metasediments. NE of thrust = Tetraogal nappe.



Figure 11 Map of the SW of the Tso Morari complex around Tso Kar. Locality numbers marked. Dotted lines show routes travelled. See Table 1 for details.

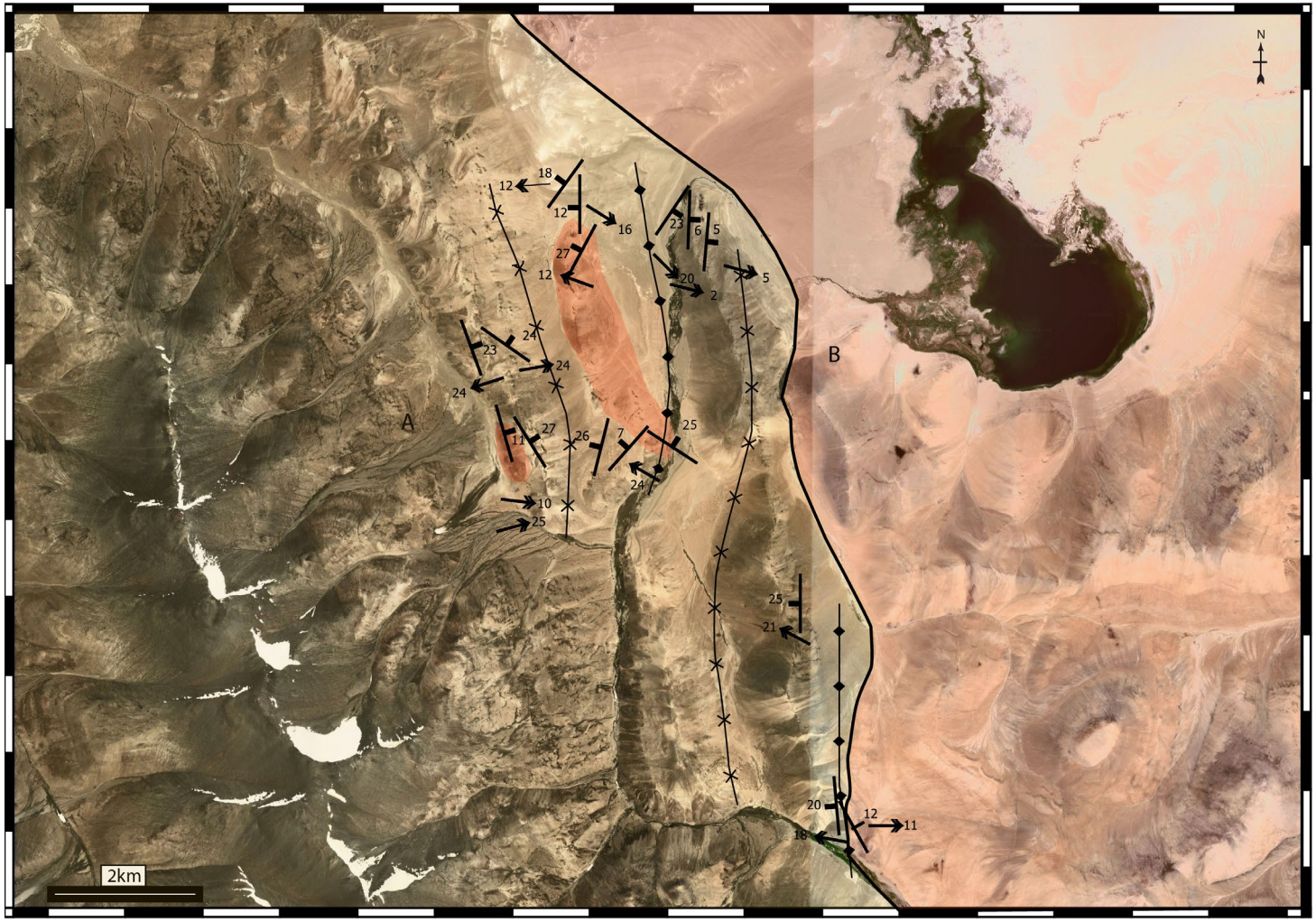


Figure 12 Structural map of the SW of the Tso Morari complex around Tso Kar. Solid black lines = lithological boundaries. triangles = thrust, diamonds = antiform, crosses = synform. Strikes and dips = foliations, lineations = mineral stretching. Red = granite, non-red = metasediments. A and B mark the location of the cross section in Figure 33

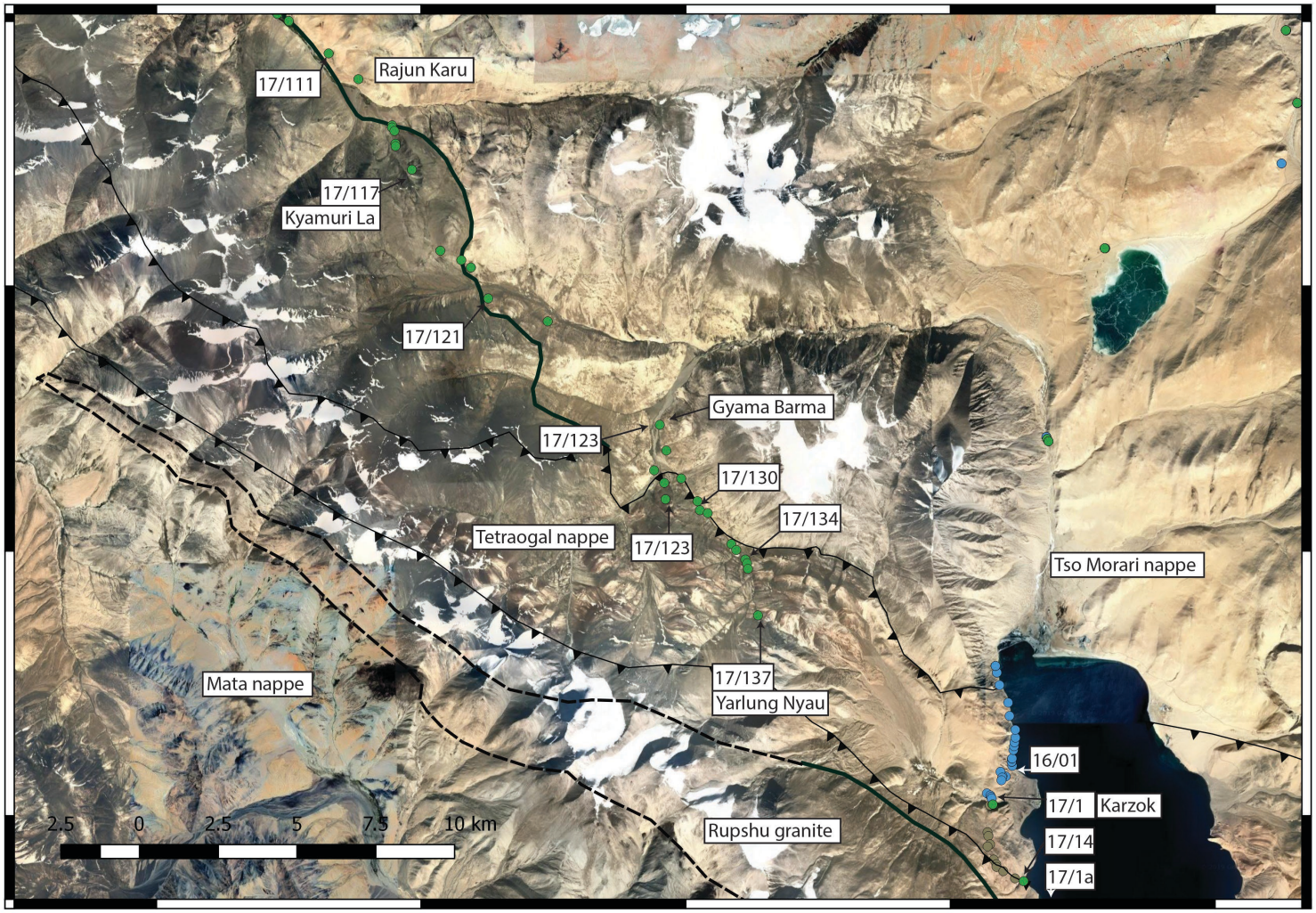


Figure 13 Map of the southern part of the Tso Morari dome. Locality numbers marked. Location of Tso Morari, Tetraogal and Mata nappes marked and divided by thrust sense shear zones (overturned). See Table 1 for details.

The western shore of Tso Morari (Figure 13)

North of Karzok village (locality 16/3 to 16/27), on the western shore of Tso Morari lake, pelites, psammites, carbonates and amphibolites overlie the Puga Gneiss of the Tso Morari dome. The foliation dips at ~150/70° to the south west and contains foliation–parallel isoclinal folds and a mineral stretching lineation defined by amphibole needles oriented at ~090/50°. Discontinuous boudins of mafic amphibolite are observed parallel to the foliation. A north–east dipping crenulation overprints the schistosity, recording a top-to-the-SW shear sense. The stratigraphically highest unit is a purple dolomite, interbedded with calcareous schists (Figure 14c) and intruded by boudinaged quartz veins. The calcareous metasedimentary sequence directly north of Karzok is thought to be part of the Tetraogal nappe (Steck *et al.*, 1998).

The metasediments towards the northern end of Tso Morari lake stratigraphically underlie the metasedimentary rocks immediately north of Karzok and have been interpreted to form part of the Haimanta Group (Steck *et al.*, 1998). These rocks are dominated by pelitic metasediments (Figure 14b), directly adjacent to the Puga gneiss, dipping towards the south west. The adjacent Puga Gneiss extends along the ridge towards the north, forming the 6000 m high peak (Figure 14d). Variations in the composition of Puga Gneiss are evident in the scree slopes and boulders along the lake shore, including variations in grain size, K feldspar modal abundance, biotite modal abundance and the presence of tourmaline parallel to the foliation (Figure 15). The mineralogical and bulk compositional variations observed in the gneisses are discussed in Chapter 6. Mafic boulders of eclogite facies rocks are also present in the scree.

It is worth noting that the presence of K feldspar augens provides a useful indicator, verified by thin section analysis, of a granitic protolith in the rocks of the Tso Morari complex. High strain granitic gneisses lacking large K feldspar porphyroclasts contain a high proportion of white mica and biotite, ± garnet. Similarly, garnet and mica-bearing metasedimentary rafts have also been identified within the orthogneiss, making protolith determination of compositionally similar lithologies difficult. Field relationships are therefore important when trying to determine the potential protolith of a mica–rich rock. Garnet mica schist at the margin of mafic sills, grading into the surrounding augen gneiss, is a useful field relationship indicating a granitic protolith in the Tso Morari complex.



Figure 14 Western shore of Tso Morari lake. a. sheared vertical quartz vein and boudinaged horizontal quartz vein in metasediment. b. Pelitic sequence north of Karzok, dipping towards the SW. c. View looking N from ridge top. Calcareous metasediments and carbonates abundant on the top of the ridge. Peaks in the distance composed of granite gneiss. d. Side view of the peaks of granite gneiss in c. showing foliation dipping towards the SW at more of a shallow angle that in the metasediments in b.

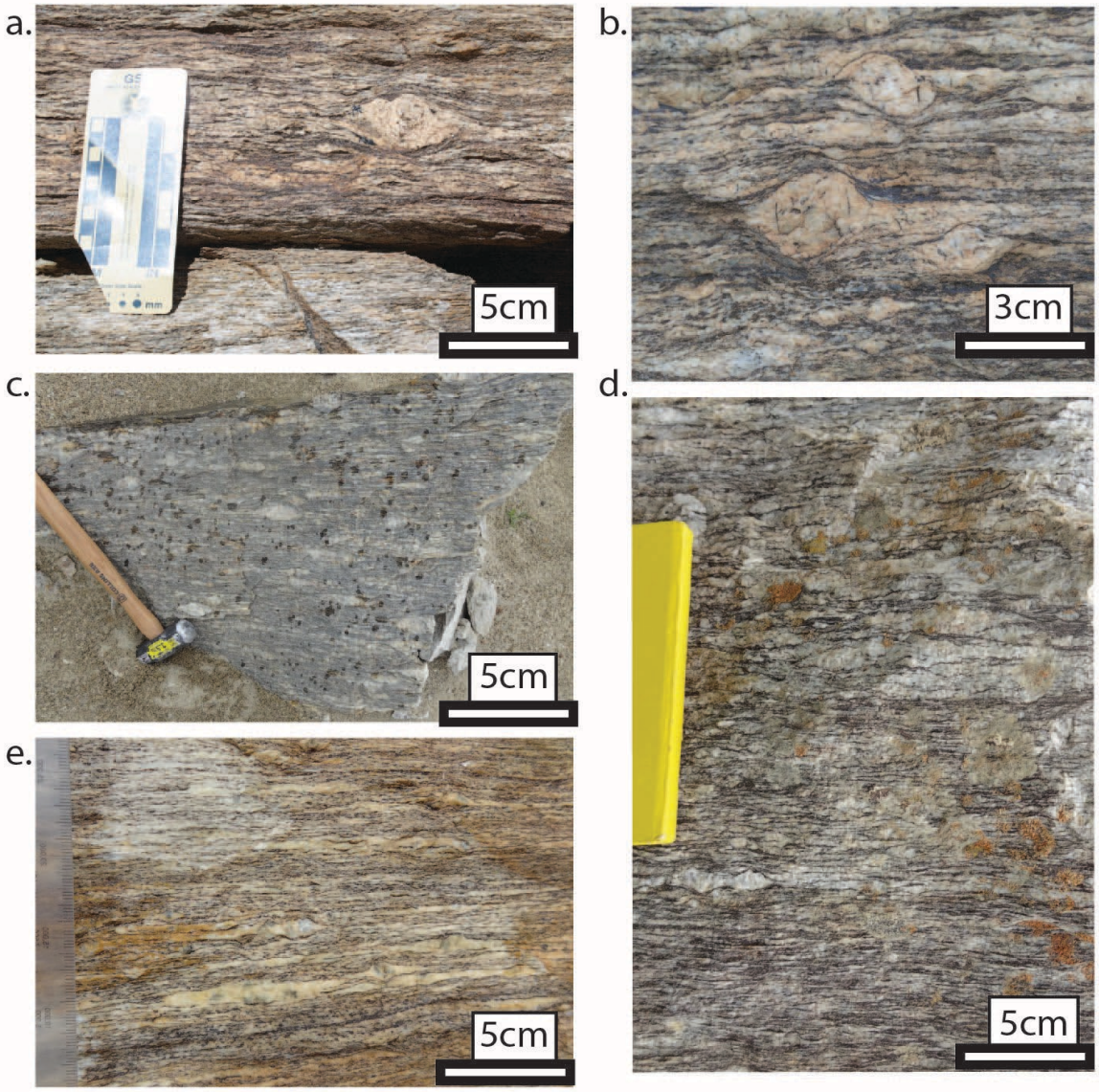


Figure 15 Photos of variations within Puga gneiss outcrops. a. and b. Augen gneiss with coarse feldspar porphyroclasts. c. d. and e. more deformed Puga Gneiss outcrops with elongate porphyroclasts and variations in biotite content.

The Bridge (Figure 7)

North of Tso Morari lake, on the east side of the river, is a cliff section composed of Puga Gneiss (locality 16/41, equivalent to stop D2/6 in the Tso Morari (2008) field guide (Caldwell, 2008)). The foliation in the Puga Gneiss is oriented at 072/10°S and wraps around linearly arranged mafic boudins, 0.5-5 m long (Figure 16). Lineations in the gneiss are defined by elongate tourmaline needles, oriented at 126/07°SE. Foliation-parallel isoclinal folds can be observed in the compositional layering with a hinge line oriented at 085/08° (Figure 16d).

The mafic boudins are wrapped by mica–rich, fine grained schist with few feldspar porphyroclasts and contain eclogite facies assemblages which are heavily retrogressed to garnet amphibolites. Dark coloured biotite– + plagioclase–rich boudinaged layers are present throughout the outcrop, interbanded with quartz– and feldspar–rich gneiss (Figure 16e). Boudinaged quartz veins follow sharp compositional changes, indicating that deformation occurred after the quartz veins were intruded.

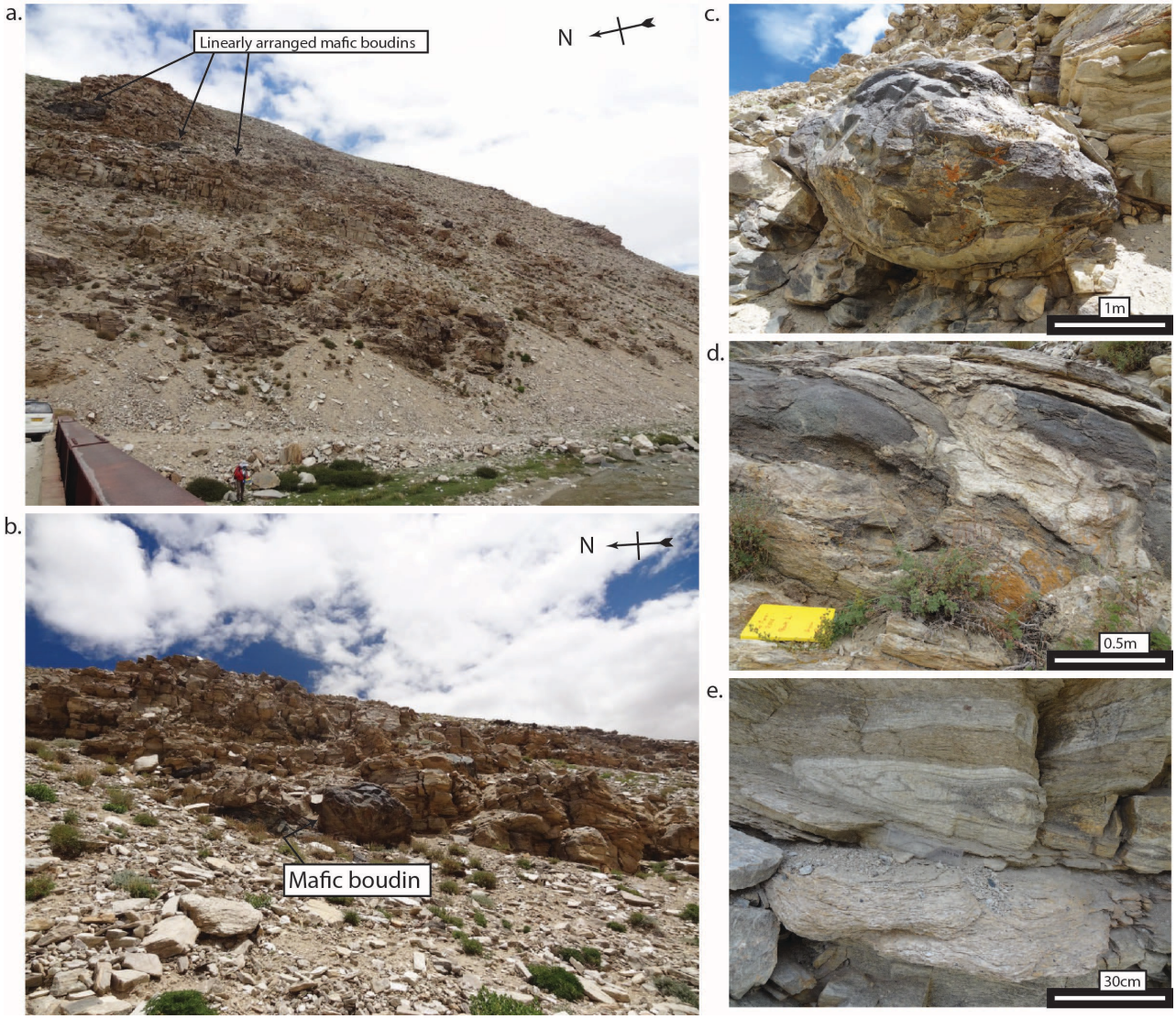


Figure 16 The Bridge. a. View of the outcrop with the bridge in the bottom left with a car for scale. b. Prominent mafic boudin at the bottom of the cliff ~200m to the south of the bridge. c. Mafic boudin from b. d. elongate mafic boudins wrapped by fine grained, mica–rich felsic rocks. E. Isoclinal folding in felsic gneiss.

North shore of Kiagar Tso (Figure 7)

The road from the Bridge (locality 16/41), follows the incised river towards the north, where outcrops of approximately horizontal Puga Gneiss forms cliffs on the eastern bank of the river. Occasional small mafic boudins can be seen in the cliff face, however the river and the vertical cliff make sampling difficult. The high ridge towards the west consists of pale orange–coloured, horizontally foliated Puga Gneiss (Figure 17a). Mafic boudins outcrop at the base of a slope (locality 16/51), ~ 1.5 km east of sample CM71710-4 (Donaldson *et al.,* 2013), surrounded by a step-like outcrop of Puga Gneiss containing quartz, feldspar, biotite and white mica (Figure 17). K feldspar augens, ~ 3-4 mm long, are sparse and elongate, forming leucocratic lenses with a matrix of ~1–2 mm grains. Compositional layers, ~ 2 cm wide, are interspersed with deformed quartz veins and show a slight variation in the proportion of mafic minerals, such as biotite and garnet, giving the rock a darker colour (Figure 17c and d). Porphyroblasts of garnet of <2 mm are visible, with strain shadows parallel to the foliation, indicating that the matrix fabric formed after garnet growth. A quartz vein, ~10 cm wide, occurs at the contact between the prominent mafic boudin and the surrounding gneiss and preserves a stretching lineation, composed of biotite crystals, on the outer surface which wraps around the boudin.

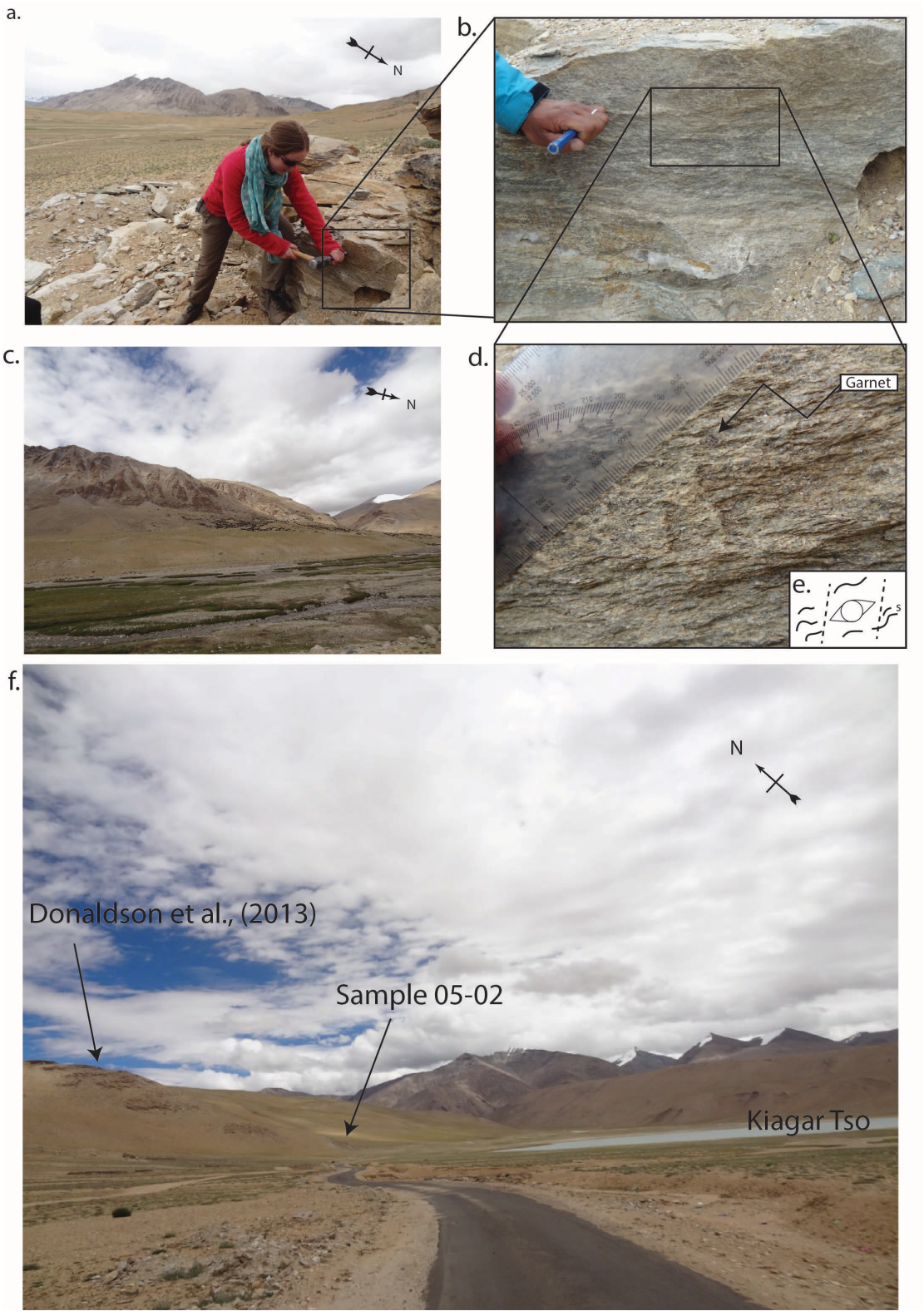


Figure 17: Photos from the northern shore of Kiagar Tso. a. Outcrop of gneiss forming a step in the landscape b. Close up of outcrop from a. with compositional layering evident from the darker layer in the middle of the outcrop and a deformed quartz vein towards the base. c. View towards the west of Kiagar Tso showing cliffs of Puga Gneiss d. Close up of the lighter unit at the top of b. showing feldspar augens and spherical garnet porphyroclasts with strain shadows extending parallel to the foliation (see schematic in e.) f. View from the road looking north towards the location of sample 05–02 and the Donaldson et al., (2013) outcrop on top of the hill.

Kiagar La (Figure 7)

The road over Kiagar La, the pass to the NE of the lake Kiagar Tso, crosses the northern end of Kiagar La lake, ascending to an elevation of about 4839 m, before descending towards a cliff of Puga Gneiss on the western side of the road (locality 16/52). The cliff contains sigma shaped augens of K feldspar, ~1–2 cm long, showing a top-to-the-S sense of shear, a coarse crystalline matrix of 3 mm with a foliation of 172/28°W. The top portion of the cliff contains linearly arranged boudins of mafic rock, parallel to foliation (Figure 18a).

On the opposite side of the valley, east of the road, cliffs of gneiss extend up to the tops of the high peaks, showing variation in colour within the gneiss. Pale orange coloured, folded lenses of gneiss are wrapped by darker, more strongly foliated gneiss (Figure 18b). Small lenses of leucocratic gneiss form asymmetrical sigma shapes indicating a potential top to the south direction of shear.

The road crosses to the eastern bank of the river, 1.5 km to the north, which subsequently begins to form an incised channel immediately to the north of the crossing. At the base of the riverbed (locality 16/53), a 3 m high eclogite boudin stands proud, hosted in an augen gneiss (Figure 18c). The eclogite has a vertical fabric defined by pale green and dark green bands ~ 4–5 cm wide (Figure 18d). These compositional bands contain garnets, which are more retrogressed in the darker band, and are hosted in a dark green matrix. The dark band is interpreted to be a more retrogressed form of the paler unit and forms anastamosing channelised structures, indicating the involvement of fluids (see Chapter 5 for a more detailed discussion).

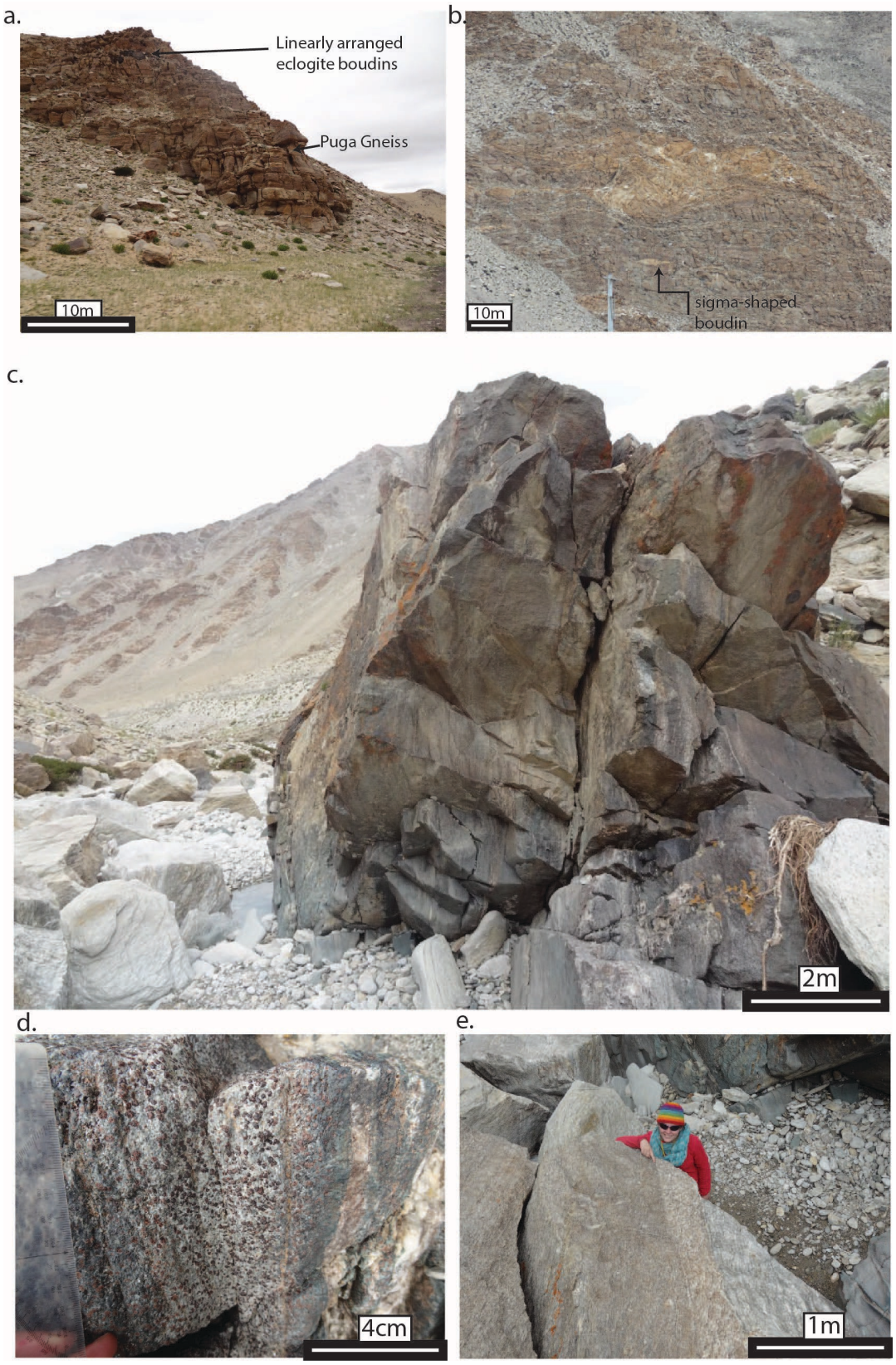


Figure 18 Kiagar La a. Locality 16/52 near Kiagar La showing linearly arranged eclogite boudins. b. View looking east showing leucocratic lenses in a gneiss cliff. c. Outcrop at base of stream bed in Kiagar La, locality 16/53. Mafic eclogite outcrop when stream was low (note: water can be 2–3m higher). Surrounding Puga gneiss has been eroded preferentially. d. Stripy retrogressed eclogite. Pale band consists of fresh garnets and omphacite in the matrix. Dark band contains retrogressed garnets and symplectite after omphacite. e. Surrounding Puga gneiss at base of stream bed. Foliation parallel to compositional banding, marked by variation in biotite content.

Berthelsen Outcrop (Figure 7)

The Berthelsen outcrop lies 1.5 km north of locality 16/53 (Kiagar La), where the road descends via hairpin bends to a river confluence. The outcrop forms a prominent cliff of felsic gneiss (Figure 19a), containing mafic boudins, just east of the road. Easy accessibility, the clean vertical section and the number and size of eclogite boudins make this an ideal location to study structural and petrological relationships. Nevertheless, the predominant focus of published studies on this locality has been on the mafic rocks.

Examination of thin sections in this study shows that typical material is an orthogneiss with a granitic protolith, representative of the Puga gneiss. Compositional variations in outcrop include c. 30 cm thick lenses of biotite-rich gneiss, deformed quartz veins, and tourmaline-quartz pegmatite (Figure 19c-f). Coarse–grained gneiss contains densely packed elongate augen of feldspar, which locally preserve sigma–porphyroclast microstructures indicating top-to-E shear. The gneiss is strongly foliated, but heterogeneities occur where lenses of weakly deformed gneiss are wrapped by a more intense fabric (Figure 19b). Lithological banding in the gneiss, including stretched layers of mafic material, is locally isoclinally folded, with foliation–parallel axial surfaces (Figure 19c and d). The dominant foliation wraps tightly around the larger mafic boudins, with fine–grained mica–rich gneiss filling boudin necks (Figure 19f). Greater compositional variation can be found in the locally–derived scree. Although much resembles the Puga gneiss with feldspar porphyroclasts, there is also a mica–rich variety, which commonly shows a well–developed S-C′ shear-band fabric. St-Onge et al. (2013) described samples of felsic rock from this locality that contained high–temperature aluminous assemblages containing garnet, cordierite and sillimanite, but nothing equivalent to these was found in the present study.

The larger mafic boudins show mineralogical variation from an eclogite–facies core to a retrogressed, amphibolite–facies rim. The amount of garnet decreases towards the rim, while the amount of amphibole increases, and biotite appears as an abundant phase. This pattern is consistent with increasing interaction between the mafic rock and external fluid derived from the surrounding gneiss (cf. Palin et al., 2014).

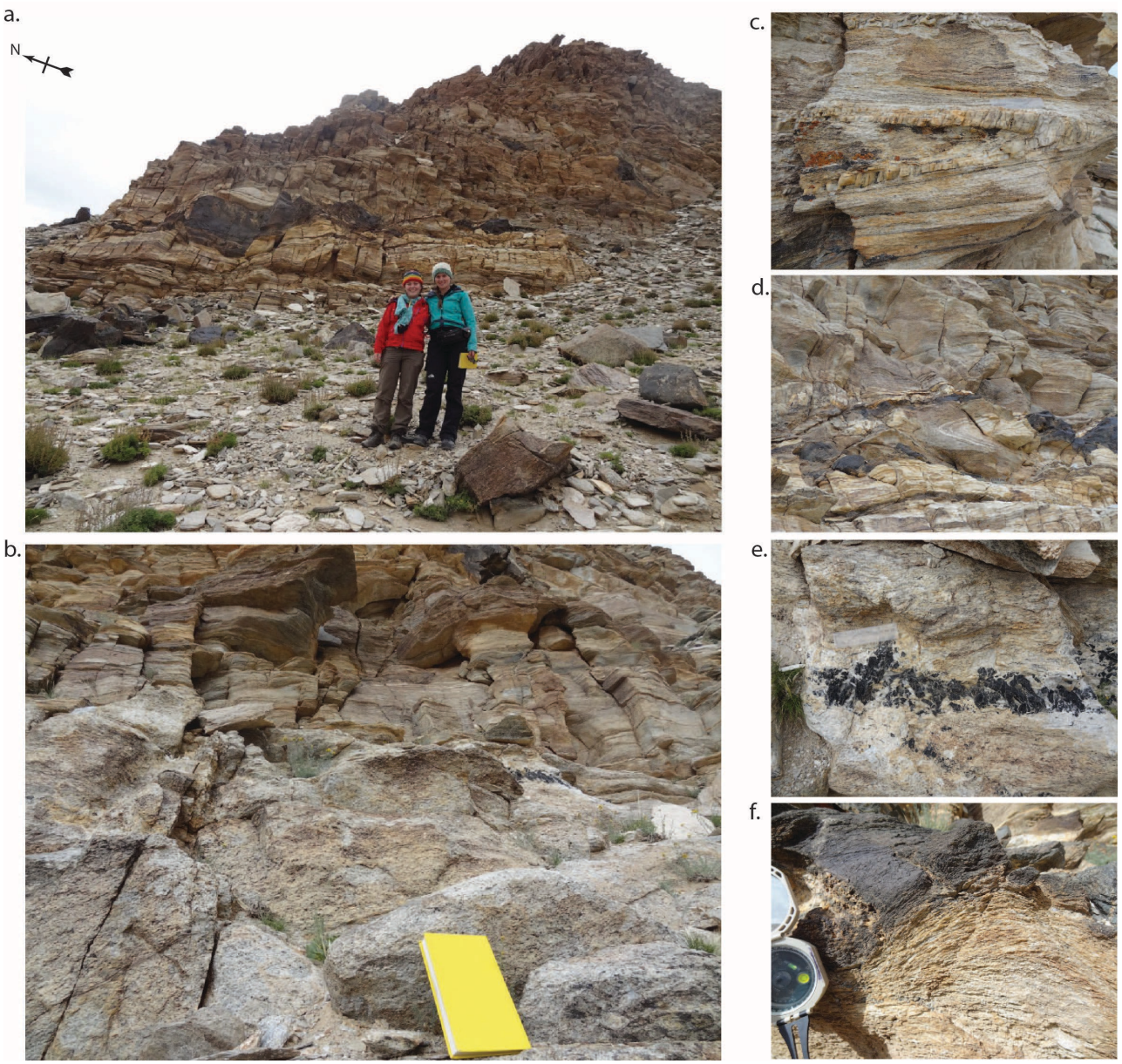


Figure 19 Berthelsen outcrop, locality 16/53. a. View of the cliff outcrop with a distinct dark mafic boudin hosted in the Puga Gneiss. Blocks of mafic eclogite litter the base of the cliff. b. Variation in the Puga Gneiss can be seen throughout the cliff. At bottom of this photo shows relatively undeformed granite. The top of the photo shows foliated Puga Gneiss. c. Isoclinal folding in the Puga Gneiss. d. Isoclinal folding in the Puga Gneiss, interbanded with boudinaged mafic eclogite. e. Tourmaline–quartz pegmatite vein in Puga Gneiss. f. Finely foliated, mica–rich gneiss with a hat shaped geometry. In contact with the neck of a mafic boudin.

Road to Ribil Sumdo (Figure 7 and 8)

South of the river confluence at the village of Ribil Sumdo, an outcrop of gneiss on the western side of the river (locality 16/73) shows compositional variations within the Puga Gneiss. The metamorphic foliation in the lower and upper parts of the cliff, oriented at ~312/28°NE, extends across the compositional boundary. The protolith of the Puga Gneiss at this outcrop is granitic, with a variation in the proportion of mafic minerals such as biotite and tourmaline. Further description of this unit is presented in Chapter 6.

Ribil Valley and the Zildat shear zone (Figure 7 and 8)

Between the Ladakhi village of Ribil Sumdo (locality 16/62) and the Tibetan village of Sumdo (locality 16/81), is a stretch of road which follows the Zildat shear zone. Ophiolitic metasediments outcrop on the north east side of the valley (locality 16/71), separated from the hills of Puga Gneiss to the south west by the normal sense Zildat shear zone. A lens of strongly deformed mica schist outcrop at the base of the Puga Gneiss. Garnets are abundant within compositional layers on a scale of cms to tens of cms and there is no evidence of feldspar porphyroclasts, suggesting a metasedimentary origin. Discontinuous boudins of amphibolite with occasional retrogressed garnets are present throughout the cliff with a chlorite overprint (Figure 20d).

The foliation in the schist is approximately 180/20°SW and contains boudinaged quartz veins parallel to the schistosity and north verging folds with an axial plane of ~110/23°SW and a hinge line measuring 280/10°N. The schistosity is overprinted by an extensional S-C' fabric steeply dipping towards the NE (Figure 20b). Towards the north western end of the valley, close to Sumdo village, a thin (~1 m) band of serpentinite can be followed parallel to foliation. The serpentinite is hosted in mica schist and contains blocks of rotated garnet–mica schist, potentially forming a shear zone separating the metasedimentary rocks at the base of the cliff from the Puga Gneiss at the top of the cliff. The grain size in the garnet–mica schist decreases towards the Zildat shear zone, quartz veins become more sheared and the dip of the foliation changes from south west to north east. The foliation seen in the schist is undulating with a wavelength of ~ 20 m and an ~E-W hinge line (Figure 20a). Cross cutting the foliation are deformed pegmatite dykes consisting of quartz and feldspar. These dykes are crosscut by small, steeply dipping normal faults/shear zones with ~30 cm displacement (Figure 20e).

On the north–east side of the valley (locality 16/71) the dominant lithology is a fine–grained mafic schist dominated by a chlorite–talc–serpentine–rich assemblage (Figure 20f). The schistosity is dipping steeply to the NE at 313/48°NE, showing top to the NE sense of shear and SW verging folds, indicating a normal sense of motion. On the surface of the foliation, mineral stretching lineations are present measuring 239°/49°NE.



Figure 20 Ribil Sumdo to Sumdo village. a. Cliffs on the west side of the river showing gently folded metasediments dipping towards the SW. b. Mica schist from the metasediments west of the road showing a north east dipping S–C fabric. c. Garnet mica schist west of the road. d. Retrogressed eclogite boudin just north of Sumdo village, wrapped by host mica schist. e. Pegmatite with intrusive contact offset but normal sense faults. f. Steeply dipping metavolcanic rocks on NE side of the Zildat shear zone

Eastern Puga Valley (Figure 7 and 8)

Towards the eastern end of the Puga valley, close to Sumdo village, is a cliff section of a slightly darker colour than the surrounding Puga Gneiss (Figure 21). Access to the outcrop is limited due to unstable scree slopes, however a good overview of the lithologies can be gained from variations in the loose scree. The lower part of the cliff can be divided into three distinct coloured units; interbedded metapelite and calcschist with rusty orange marble boudins (Figure 22c and f). The dark brown pelitic metasediment has a high proportion of mica and garnet. The schistosity wraps around more competent, browny-orange, calcareous metapelites, containing a high proportion of carbonate.

The metamorphic foliation is parallel to the compositional layering at 220/14°NW and contains foliation–parallel isoclinal folds, verging towards the south and a well–developed crenulation cleavage. The compositional layering is crosscut by a paler yellowy-orange unit of 'typical' Puga Gneiss, containing quartz, K feldspar and plagioclase with coarse tourmaline crystals. The metamorphic foliation continues across this compositional truncation. Within the loose samples of Puga Gneiss, coarse porphyroclasts of feldspar are relatively euhedral and contain simple 90° twins indicating that these samples are low strain. However, a spaced S-C fabric is present within the coarse– grained gneiss (Figure 22a).

Crosscutting veins of tourmaline and quartz occur obliquely to the metamorphic foliation and show acicular tourmaline crystals oriented perpendicular to the vein walls (Figure 22b). These veins are crosscut by thicker quartz–rich pegmatites (Figure 22e). The calcareous metasediments of this outcrop are discontinuous and make up a large, metasedimentary raft hosted in granite gneiss which preserves an intrusive contact with the metasediments. The development of a foliation postdates the igneous contact as it continues pervasively throughout the surrounding Puga Gneiss.

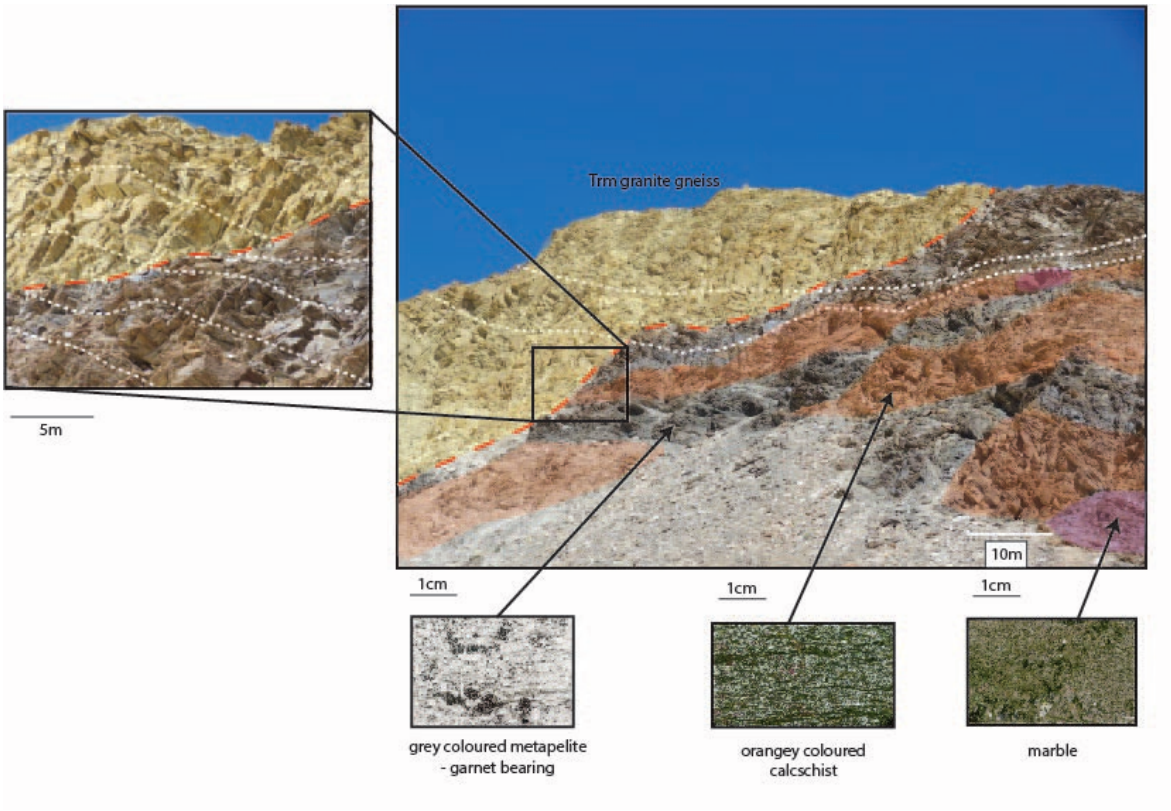


Figure 21 Metasedimentary raft with compositional layering. Intrusive contact with the Puga Gneiss (red dashed line) and a foliation that is continuous across this boundary (white dashed line). Metasediments are composed of metapelites, calc–schists and marbles.



Figure 22 a. Puga Gneiss showing K feldspar porphyroclast wrapped by an extensional S–C fabric. b. Quartz + tourmaline vein in the Puga Gneiss. c. discontinuous meta–marble within a metasedimentary package. d. Puga gneiss with quartz and feldspar augens, a well-developed schistosity and a weakly developed c–fabric. e. Crosscutting pegmatite within metasediments. f. boudin of meta–marble in a calcschist with white calcite veins.

Puga hot springs (Figure 7 and 8)

Within the Puga valley, there are many small retrogressed mafic eclogite boudins, which occur in linearly arranged clusters, suggesting that they were once part of a linear body. These boudins stand proud from the surrounding Puga Gneiss, exposing a smooth amphibolitised rim, making sampling difficult. The boudins are hosted in Puga Gneiss with large feldspar augens indicating a granitic protolith. Towards the strongly sheared margins of the boudin (e.g. locality 17/21), augen gneiss transitions into mica schist, forming a zone approximately 4 m wide with thin, elongate feldspars with discontinuous variations in the proportion of biotite and garnet on a scale of ~0.5 m. Surrounding the rim of the boudins is a friable zone of fine-grained mica schists, ~ 50 cm wide, containing garnet and sparse, elongate feldspars. The foliation within the gneiss is 294/20°NE with a top-to-the-NE shear sense.

Along the Puga valley, boudins of mafic rock can be seen outcropping at the top of the cliffs within an orange coloured augen gneiss, which can be traced to locality 16/91 at the eastern end of the Puga Valley. The orange gneiss strikes parallel to foliation and has been gently folded so that the thickness changes along strike. The base of the cliff is darker in colour, containing 30% biotite and asymmetrical feldspar augen with top to E–NE shear sense. Both units show characteristics of a granitic protolith, highlighting the presence of compositional variations within the Puga Gneiss.

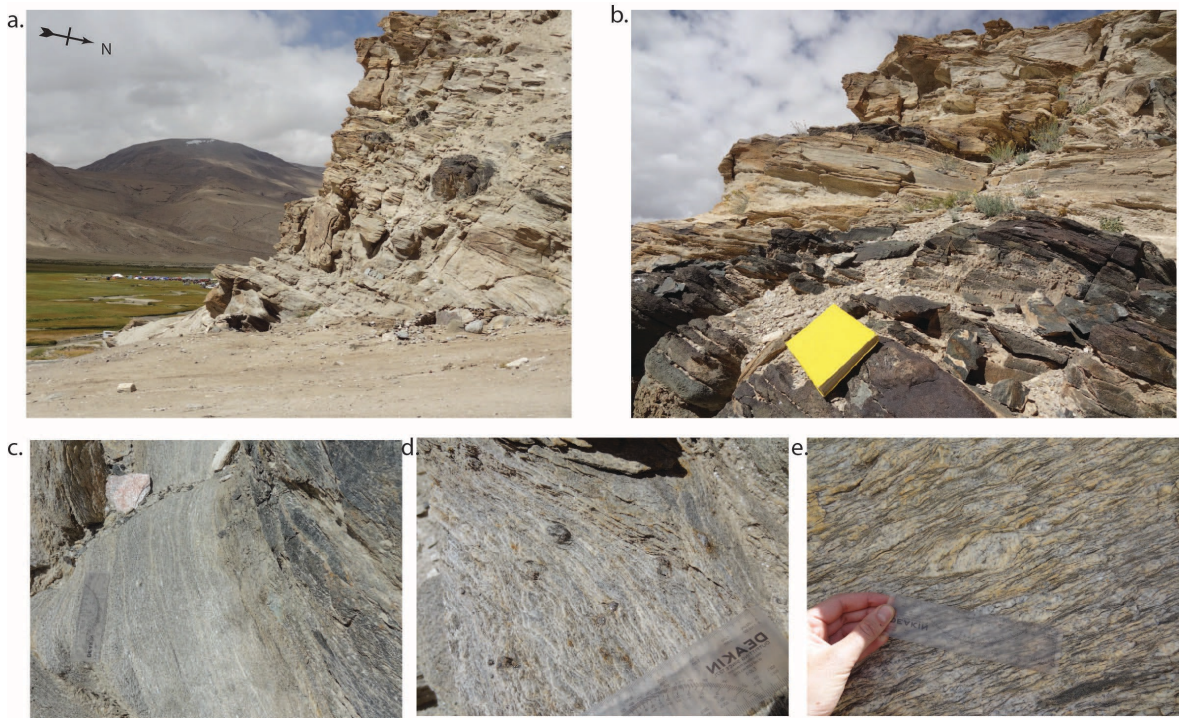


Figure 23 Puga hot springs (locality 17/21). a. View of cliff face looking west down the Puga valley. Mafic eclogite boudins can be seen in the gneiss cliff. b. The top of a mafic boudin showing compositional variations in the gneiss and mafic layers. c. Close up of the contact at the bottom of the mafic boudin in b. showing fine grained mica–rich schist. d. Cloe up of the fine–grained schist containing garnets. e. Augen gneiss from the base of the cliff.

Puga school (Figure 7 and 8)

Two outcrops of amphibolitised eclogite stand prominently within a sand dune close to the road (locality 17/23), wrapped by a mica–rich schist containing elongate augens of quartz and K feldspar. The host gneiss has a grain size of <1 mm, 5% biotite, needles of tourmaline and has a foliation of 338/32°NE. Away from the boudin, the grain size in the Puga Gneiss becomes coarser, preserving equant quartz augens, small 1 mm garnets and mica fish. Tourmaline is not very abundant and is often located within the augens and their strain shadows.

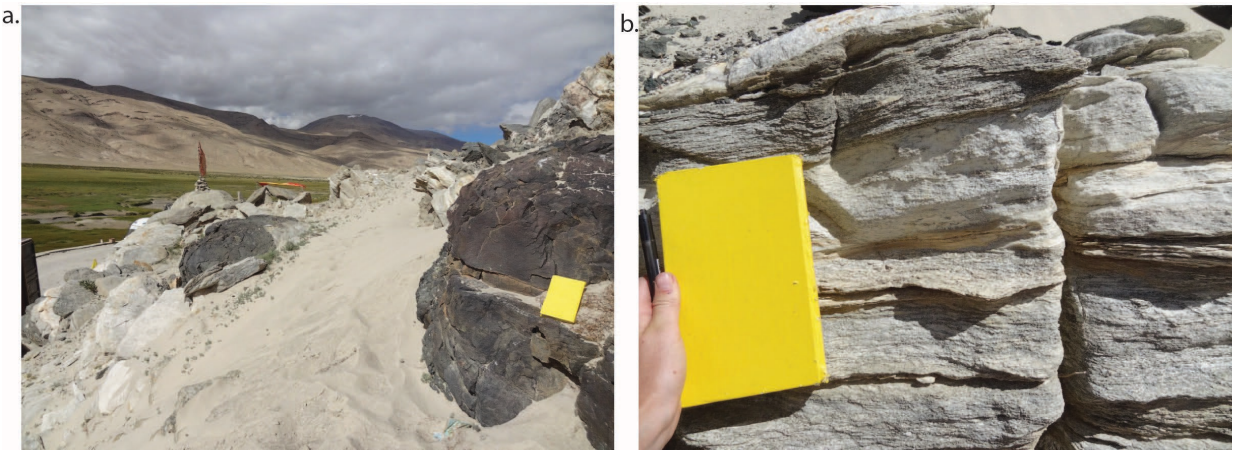


Figure 24 Outcrop close to Puga school showing two prominent eclogite boudins within a sand dune. b. fine grained gneiss from close to the contact with the eclogite boudin.

Puga valley halfway up the pass (Figure 7)

The cliffs on the northern side of the Puga valley are made up of Puga Gneiss. At locality 17/23, partially boudinaged layers of metagranites outcrop on a cliff face, showing variations in composition and in deformation state (Figure 25a). The metagranite at the base of the cliff has a weak foliation of 260/33°N and is composed of 15% biotite, feldspar augens and quartz. Mafic boudins can be seen throughout this layer. The cores of the granite boudins are relatively undeformed and preserves a coarse crystalline igneous texture (Figure 25d and e). Wrapping these low strain units is a fine–grained gneiss with augens of quartz, in a foliated mica–rich matrix (Figure 25b and c), which weathers an orangey-brown colour and resembles a coarse–grained metasandstone. However, when analysed in thin section the rock exhibits characteristics of a metagranite (see chapter 6) and contains zircons of a single population dated at 479 Ma, comparable to the Polokongka La granite.

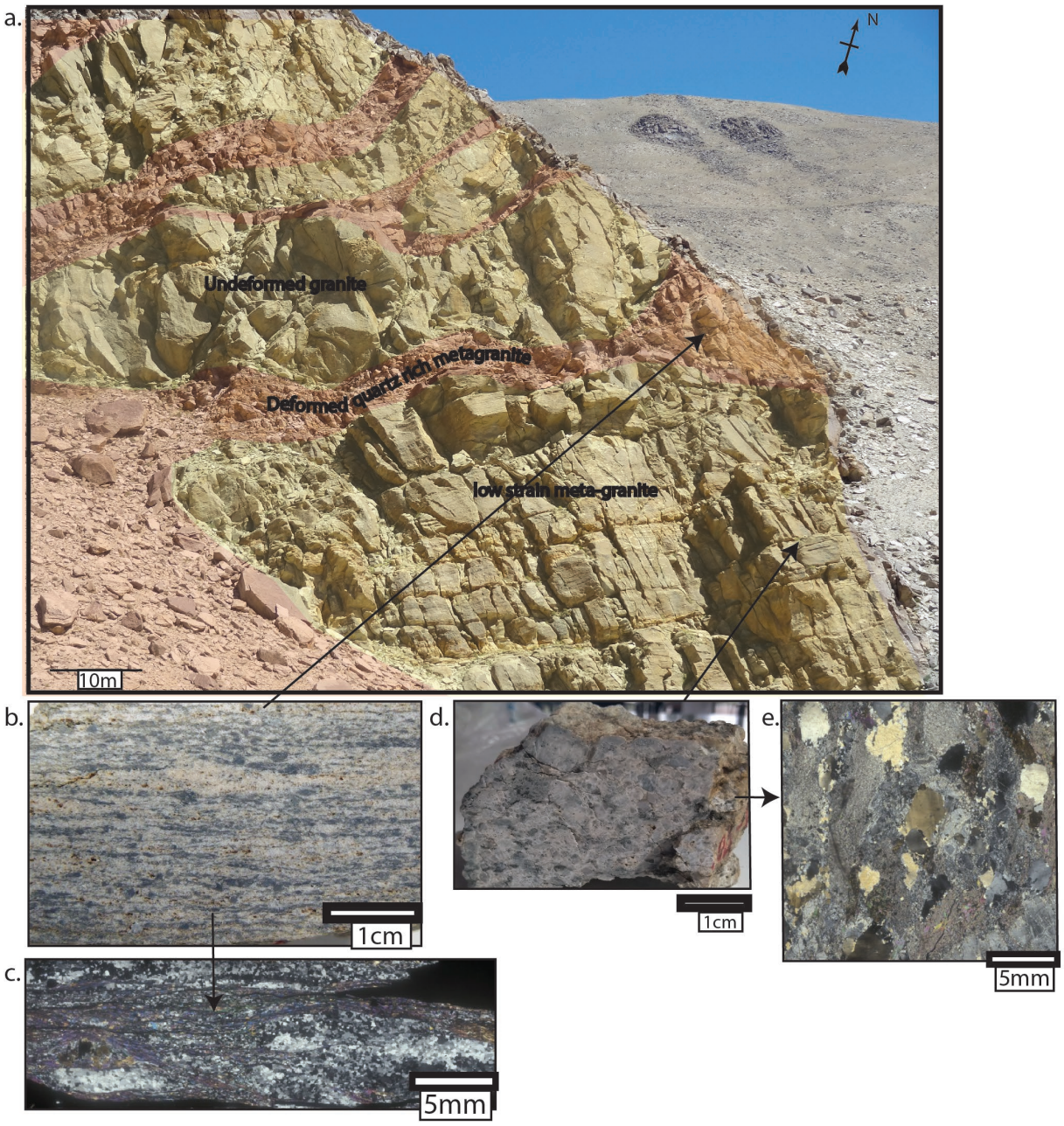


Figure 25 locality 16/114. Puga gneiss outcrop in the Puga Valley showing a. undeformed granite boudins wrapped by quartz–rich augen gneiss. b. sheared mica–rich unit hand specimen. c. Photomicrograph of b. showing elongate domains of recrystallised quartz. d. Undeformed granite hand specimen. e. Photomicrograph of undeformed granite showing igneous domains of deformed and partially recrystallised quartz, altered feldspar domains and microcline porphyroclasts.

Polokongka La pass (Figure 7)

Near to the highest point of the Polokongka La pass (locality 17/25), mafic dykes crosscut the foliation within the Puga Gneiss. The mafic rocks contain an eclogite facies assemblage and occasionally preserve white, rectangular pseudomorphs after plagioclase (see Chapter 5). The margins of the sills are mica–rich and strongly sheared, forming a foliation parallel to the margins of the dyke (Figure 26a). Further from the mafic dykes, sparse outcrops of augen gneiss and abundant scree contains coarse feldspar porphyroclasts. Within 20 m of the dyke, the outcrops consist of relatively undeformed granite (see Chapter 6). At the base of the cliff, a strongly deformed mafic boudin is wrapped by the fabric in the gneiss and contains a core of fine–grained garnet-mica schist ((Figure 26c). Garnet–bearing mica schist is consistently seen along the margin (~1 m) of the mafic bodies throughout the Tso Morari complex (Figure 26d).

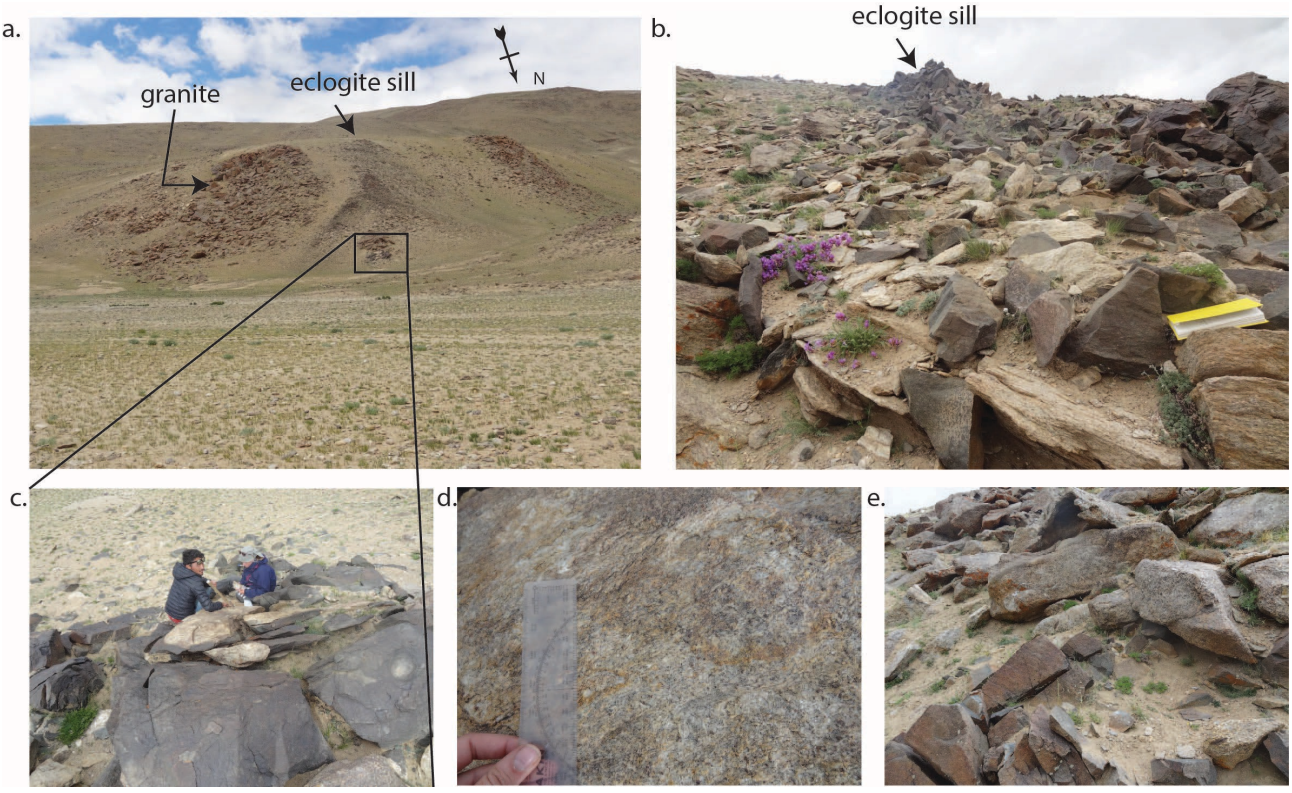


Figure 26 Polokongka La pass, locality 17/25. a. Photo showing the hillside with mafic eclogite (dark scree and granite. b. Fractured hillside with a prominent ridge of mafic eclogite sill. c. Mafic outcrop at the base of the slope with garnet–bearing mica schist at the contact. d. Photo of garnet–mica–schist at the contact of the mafic sill. e. Large blocks of granite fractured in situ with dark coloured, fine grained, porphyritic mafic rock outcropping in the bottom left of the photo.

Polokongka La ridge (Figure 7)

South west of the road, an eclogite sill (30 m wide) outcrops at the top of the ridge at locality 17/28 (Figure 27a and b). The margin of the sill is strongly deformed and amphibolitised, surrounded by ~5 m of finely foliated garnet-mica schist, oriented parallel to the margin of the dyke at 218/44° NW (Figure 27c). Occasional feldspar augens can be found within the mica schist, wrapped by the foliation.



Figure 27 Polokongka La ridge, locality 17/28. a. View of the mafic sill on top of the ridge. b. Frost shattered mafic sill extending along the ridge. c. Contact between the mafic sill and the Puga Gneiss. d. Photo of a sample of fresh mafic eclogite

Thukje (Figure 9)

The cliffs to the north east of Tso Kar are composed of Puga Gneiss. Adjacent to Thukje village, Puga Gneiss outcrops at the base of a road cutting, preserving rare asymmetrical, top-to-the-east, sigma–shaped feldspar augens. The gneiss at locality 17/29 is mica–rich, containing quartz veins of ~0.5 mm, with a strong foliation and crenulation cleavage and boudinaged quartz veins. The Puga gneiss is cut by brittle normal faults with fault breccia and small <1 m displacement. Overlying the gneiss, forming the steep hillside above Thukje is a metasedimentary unit cut by deformed quartz-feldspar pegmatites and containing strongly deformed quartz veins (Figure 28b-e). The metasedimentary rocks contain garnet, mica and abundant quartz with a grain size of 1mm and beds of ~1 m thick.

The hillside north of Thukje is made up of red layered rocks composed of meta–rhyolite alternating with marble and metabasites (Figure 28a) (Steck *et al.*, 1998). These metasediments are thought to be Permian in age and part of the Tetraogal nappe as in the south, due to the association of calc-schists and tholeiitic mafic rock.

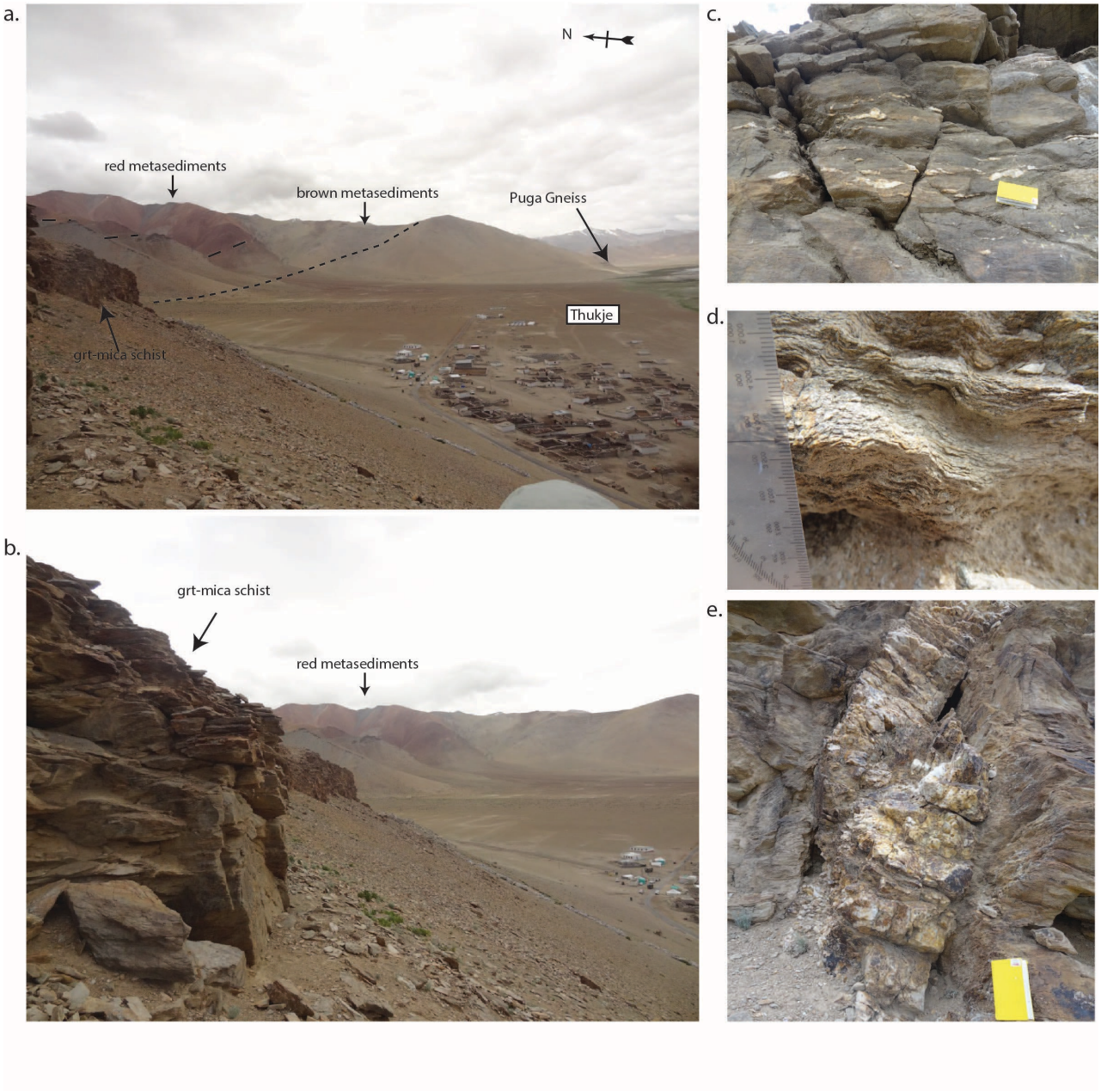


Figure 28 Hill above Thukje village, locality 17/29. a. View looking east with red metasediments at the top of the hill to the north, overlying brown units thought to correlate with the metasedimentary garnet–mica schist above Thukje. The base of the slope near Tso Kar has outcrops of Puga Gneiss. b. Garnet–mica schist outcrop at the top of a scree slope above Thukje. c. Boudinaged quartz vein in semipelite. d. Crenulation of semipelite. d. Cross cutting pegmatite

North of Ponganagu (Figure 9)

West of Tso Kar, the outcrop often occurs at the top of steep scree slopes along a ridge, with small fractured outcrops oriented parallel to strike. North of Ponganagu (locality 17/31), competent outcrops of orange, calcareous quartzite are interbedded with micaceous sandstone with a grain size of ~2 mm (Figure 29a-c). Tourmaline is found as bifurcating needles oriented at 045/25° along foliation planes oriented 014/65°E. Boudinaged quartz veins are present parallel to foliation. The scree contains dark coloured blocks of amphibolite with a chlorite overprint, contrasting to the pale orange felsic rocks which dominate the scree.

Amphibolite can be found in situ near the base of the ridge (locality 17/37), hosted in Puga Gneiss with elongate feldspar augens (Figure 29d and e). The mafic outcrop has a strong metamorphic foliation, parallel to the foliation in the gneiss at 000/24°E with a mineral stretching lineation recorded in the gneiss at 101/18°SE. At the top of the ridge to the south, outcrop of mica schist is interbedded with metasandstone contained aligned tourmaline needles, capped by a thick unit of orange quartzite (Figure 29f-h). The quartzite is also cut by an amphibolite dyke consisting of black amphibole and plagioclase. The orange quartzite makes up the tops of the hills to the west and can be traced using satellite imagery, along the valley towards the west and the Leh–Manali road, for ~10 km. The foliation within the metasediments dips towards the NE on the north side of the valley and towards the SE on the south side of the valley (locality 17/41), marking out an antiform plunging towards the east associated with a late stage of deformation (Figure 29i).



Figure 29 North of Ponganagu. a. Locality 17/31, valley looking N at N end of transect. b. orange quartzite in valley shown in a. c. Mica schist in valley shown in a. d. Amphibolite dyke in ridge towards the south, locality 17/37. e. Puga gneiss hosting amphibolite at locality 17/37. f. View looking towards the south identifying ridge walked in this transect. g. Amphibolite dyke at the top of the ridge hosted in orange quartzite. h. Steep side of ridge composed of orange quartzite. i. Valley and road to the west, linking to the Leh–Manali road. Orange quartzite outcrops on both side of the valley in the foreground. Sediment dipping to NE on N side of the valley and SE on S side of the valley.

Ridge west of Ponganagu (Figure 9)

The lower slopes of the ridge to the west of Ponganagu are composed of Puga Gneiss, with sparse garnet porphyroblasts, elongate feldspar augens and acicular tourmaline needles aligned along the foliation planes (Figure 30e). An S-C fabric is present with a schistosity at 265/12°W and a horizontal mineral stretching lineation of 108°. The top of the ridge is composed of crenulated mica–rich pelites interbedded with rusty orange coloured calc-schists, with a foliation oriented at 036/24°SE, parallel to the ridge line (Figure 30a and d). The metasediments on the eastern margin of the ridge (locality 17/44) show a sharp change in orientation of the foliation over ~5 m, from approximately horizontal to >50°E. This asymmetrical fold verges towards the east and can be observed as parasitic folds within the metasediments with an axial plane measuring 184°/62°W (Figure 30b and f). The north end of ridge, stratigraphically above the pelitic rocks is the orange quartzite (Figure 30b) which forms the SE–dipping limb of an antiform (locality 17/41).

The ridge extends towards the south, along the western shore of Tso Kar. The rocks in the scree slopes adjacent to the lake provide a huge variety in lithologies which have been eroded from the overlying cliff. Slopes like these provide a valuable insight into the lithological variation within the metasediments of this region, as the cliffs themselves are relatively inaccessible (Figure 31). Psammite, garnet-mica schist, and amphibolite are abundant in the scree. Boulders preserve compositional layering of calcareous metasediments with marble and pelites (Figure 31c). Amphibole, tourmaline, garnet and mica are abundant, with coarse idioblastic staurolite identifiable in suitable lithologies (Figure 31d-e).

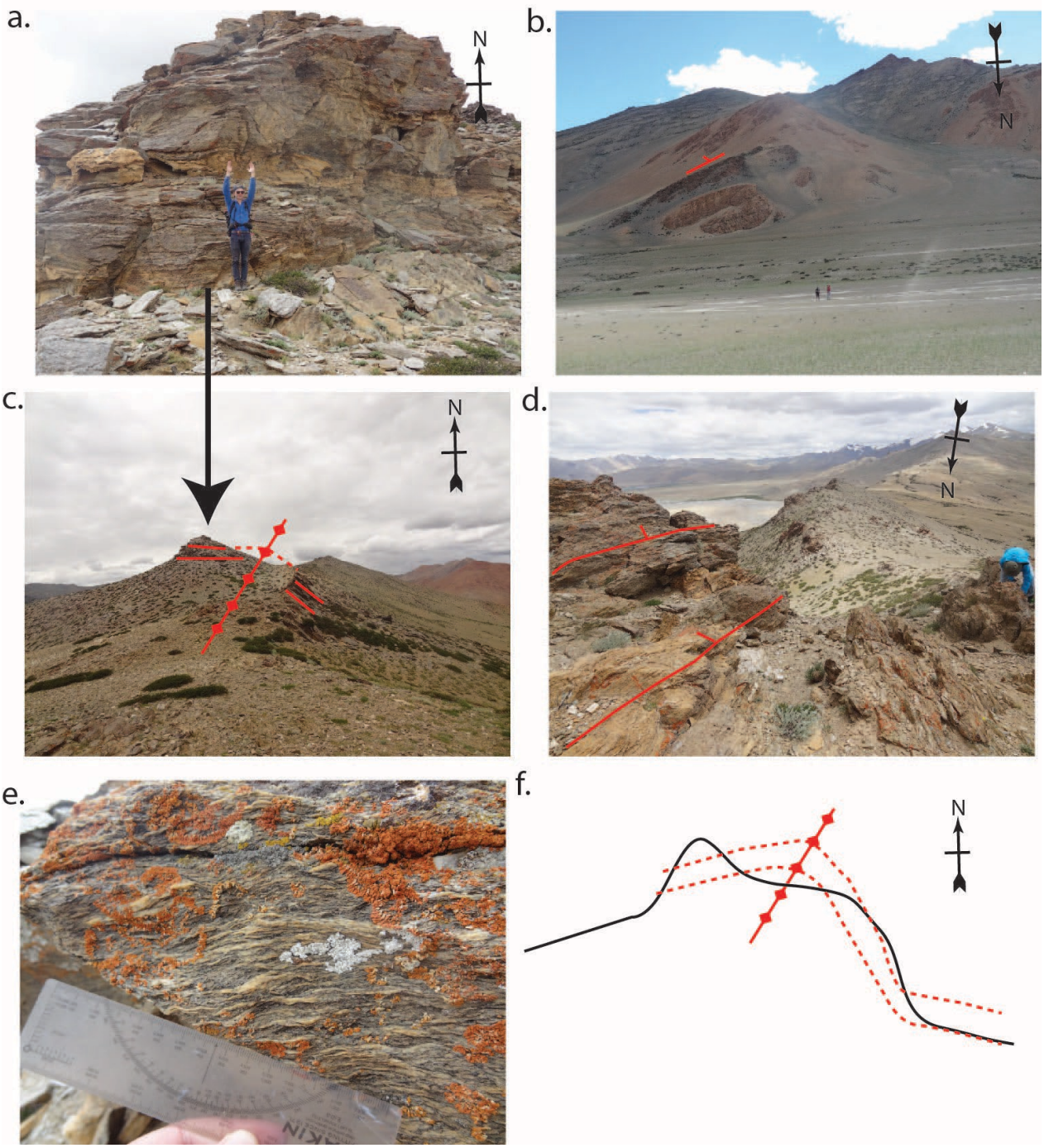


Figure 30 Ridge west of Ponganagu, locality 17/44. a. Outcrop of mica schist interbedded with calcschist on the hilltop. Foliation is dipping gently to the west. b. View of the north end of the ridge looking south. Orange unit composed of quartz–rich metasediments interbedded with dark grey pelites. Units dipping SE. c. View looking north along the top of the ridge. outcrop in a. shown by black arrow. Foliation on the east side of the ridge dipping steeply E. d. View looking south from location of black arrow showing metasediments dipping steeply towards the E. e. Puga Gneiss outcropping on the east side of the ridge, lower down the slope at an approximately horizontal dip. f. Sketch cross section showing relationship between the ridge and the change in dip of the foliation

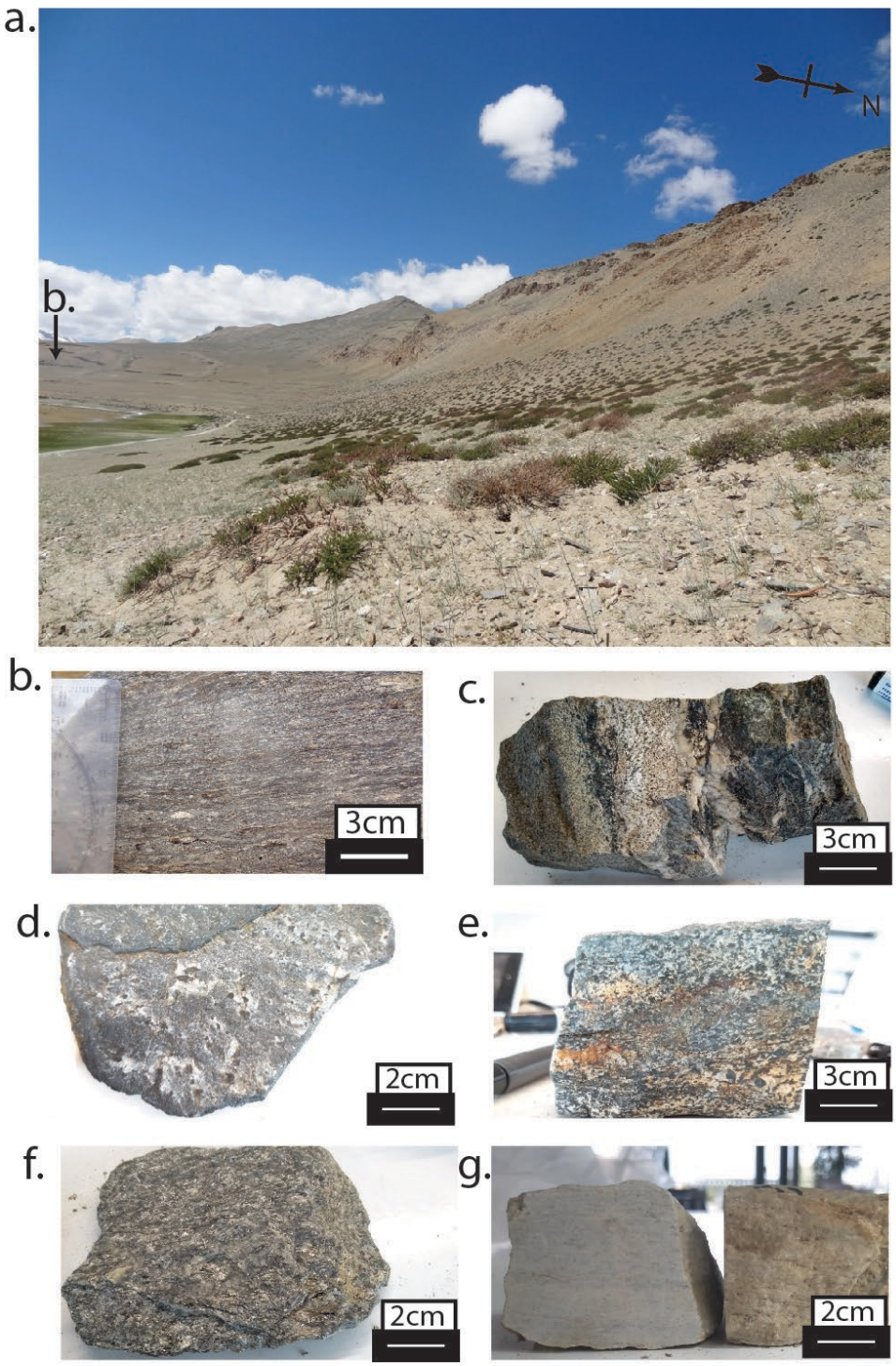


Figure 31 West of Tso Kar. a. View looking SW along ridge. Edge of Tso Kar to the left. Colour variations in the cliffs indicate compositional variations within the metasediments. b. Sample from outcrop on the low-lying shelves just south of Tso Kar. c–g. Samples from the scree at the base of the ridge shown in a. c. Sample a12–04, boulder showing variations in grain size, composition and mineralogy. d. Sample a14–03, mica schists with quartz–rich regions containing coarse staurolite crystals. e. Sample 09–06, compositional banding visible in hand specimen scale. Garnet, biotite, white mica, staurolite, quartz, feldspar. f. Sample a09–04, Mica schist with black, fractured tourmaline needles g. sample a09–01, quartz–rich sandstone + whit mica. Orange coloured weathering.

Nuruchen (Figure 11)

South of Tso Kar a small oasis of green vegetation surrounding a river (Nuruchen), a stark contrast to the pale–coloured hills. A small N-S trending hill to the west has dark brown cliffs on the eastern side composed of Puga Gneiss and contains tourmaline pegmatite vein (Figure 32a-d). The foliation is oriented at 180/12°W, with a lineation of tourmaline needles at 266/16° and porphyroclasts of feldspar showing a top-to-the-east shear sense. The grain size and mica content within this Puga Gneiss is variable, with finer grained, Bt–rich, sheared gneiss increasing in abundance towards the top of the ridge. Retrogressed mafic eclogite boudins containing retrogressed garnets and amphibole are present at the top of the ridge.

The top of the ridge consists of shattered outcrop, with regions of macroscopically undeformed granite containing plagioclase, K feldspar phenocrysts (~1 cm), biotite, quartz and occasionally cordierite (locality 17/63) (Figure 32g and h). Quartz in these samples is euhedral, often forming single crystals. Outcrops of augen gneiss with a strong crenulation cleavage also occur (Figure 32e). Close to Nuruchen (locality 17/87) a cliff of granite contains large, 1m long enclaves of fine–grained quartz + biotite + white mica + garnet (Figure 32f), similar to the pseudomorphs described in Chapter 3. The enclaves are round, with sharp edges showing a sudden change in grain size. They are randomly distributed and more prevalent than in the Polokongka La region.

Surrounding the granite and Puga Gneiss outcrops in the Nuruchen region are pelitic metasediments which form the ridges to the west, south and east. The ridge directly east of Nuruchen provides a good viewpoint to the north (Figure 33a and b) where you can clearly see the orange unit north of Ponganagu and the red unit north of Thukje, thought to be part of the Tetraogal nappe (Epard and Steck, 2008). The rocks outcropping on this ridge (locality 17/67 to 17/76) are mica–rich psammitic schists with tourmaline needles oriented along the foliation planes, occasionally interbedded with more quartz–rich units which weather orange in colour (Figure 33g). The foliation is oriented ~005/5°E, in contrast to the ridges to the west and to the south east of Nuruchen which are dipping towards the west. Amphibolite boulders can be found scattered in the scree on the sides of the ridge.

West of Nuruchen and the Puga gneiss (locality 17/58 to 17/63), a higher ridge, also trending SE-NW, consists of metasediments (locality 17/77 to 17/83). These metasediments are micaceous, containing elongate clusters of biotite visible on the top surface. The foliation is 194/26°W with the elongate axis of the lineation defined by biotite clusters oriented at 300/24°. On the top of the ridge is a 20 m wide, pale coloured rock which cross cuts the compositional layering and foliation within the metasediments (Figure 33c and d). It is extremely hard and dense with no internal foliation. This unit weathers pale orangey brown with a fresh surface which is crystalline and pale with patches of pale red and pale green (Figure 33f). In thin section, this rock is rich in carbonate and clinozoisite with occasional amphibole poikiloblasts, relict garnets and intergrowths of plagioclase and pyroxene (Figure 33e). Analysis of the numerous zircons in this sample show a detrital signature with ages ranging from Archaean to Neoproterozoic.

An isolated outcrop of Puga Gneiss occurs at locality 17/86, containing feldspar augens in a 1–2 mm foliation oriented at 328/27° NE and a lineation defined by elongate biotite clusters at 075/25° NE. A cross section from the east dipping Puga gneiss at locality 17/86 to the east dipping mica schist of locality 17/76 crossing an antiformal structure with low strain metagranite in the core.

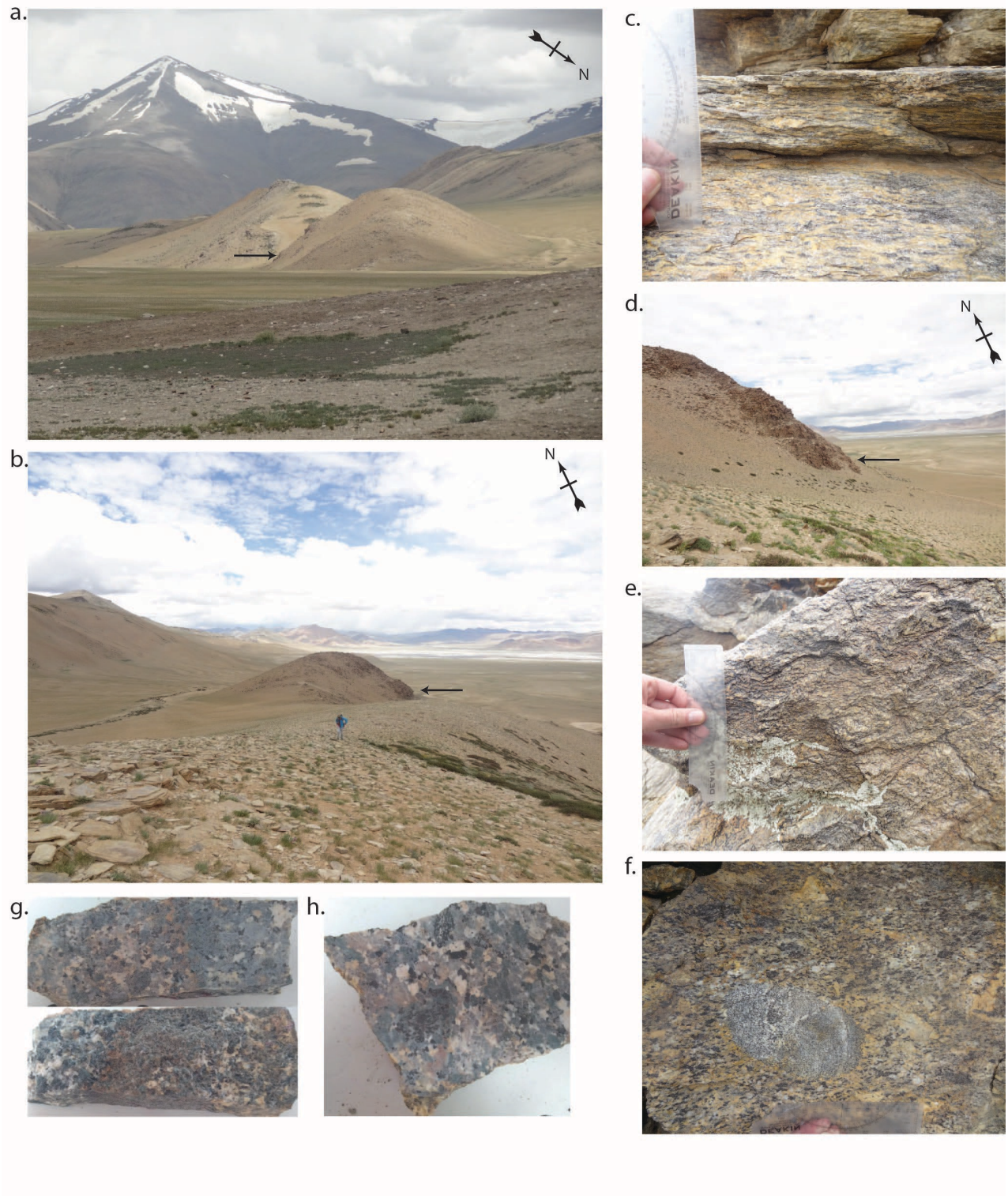


Figure 32 Nuruchen. a. View towards Nuruchen looking south. Double humped hill in is an outcrop of Puga Gneiss, surrounding hills and hill to the east of the photo are metasediments. b. View from the top of double humped hill looking north towards Tso Kar. c. Outcrop photo of augen gneiss from outcrop in d. d. Cliff of Puga Gneiss at base of hill. e. Crenulated Puga Gneiss from south end of ridge. f. Undeformed granite by the river at Nuruchen with a mafic enclave, plagioclase, K feldspar and skeletal biotite phenocrysts. g. Rough and cut surface of sample a10–06 showing an igneous texture in a porphyritic granite on the left and right. The centre shows a mafic small mafic enclave of finer grain size and a higher proportion of mafic minerals. h. Cut section of granite with large skeletal biotite crystals.

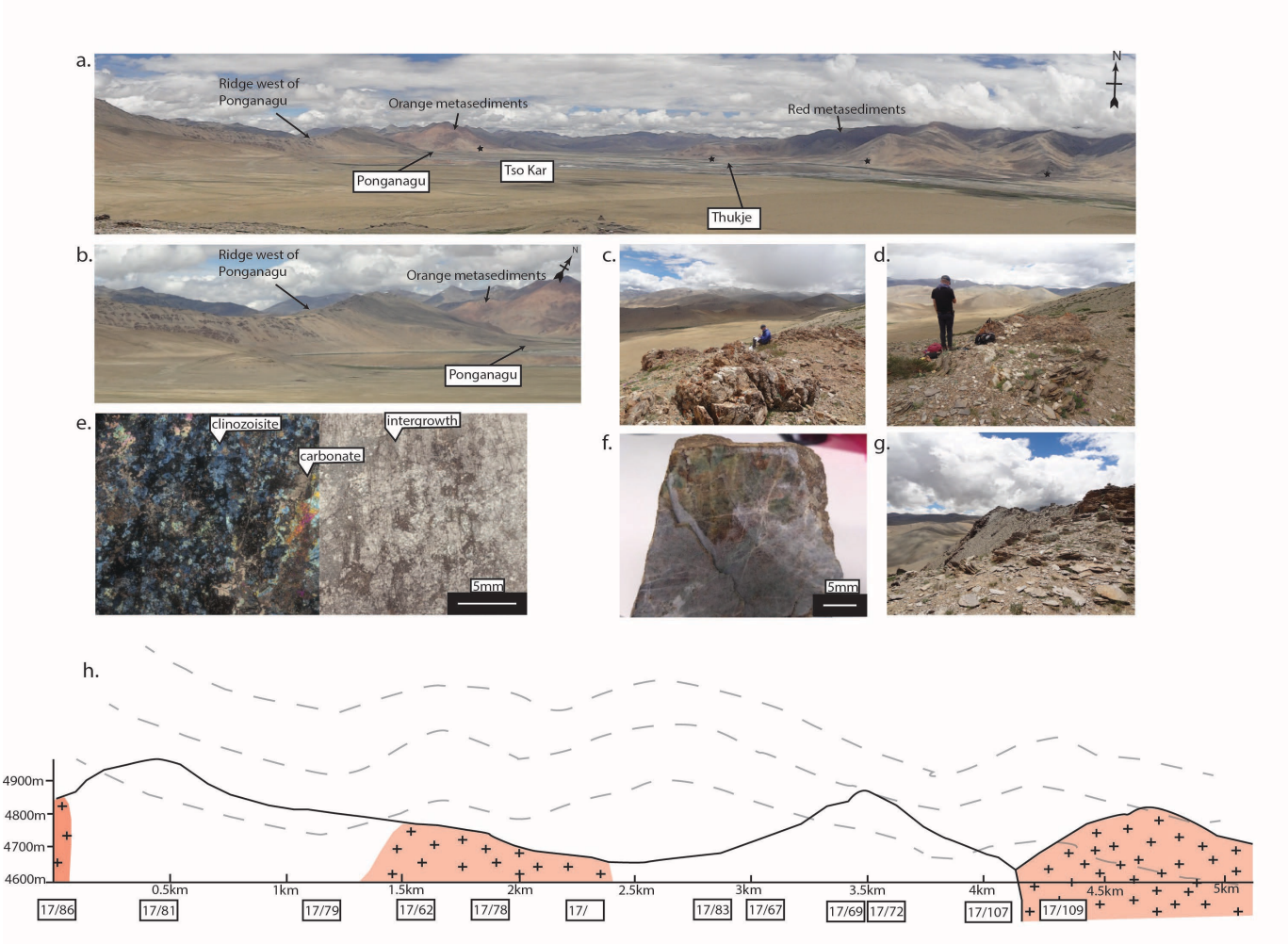


Figure 33 Nuruchen. a. Panoramic view from the ridge east of Nuruchen (locality 17/67) looking north over Tso Kar. Orange metasediments of locality 17/41 can be seen to the north of the ridge above Ponganagu (locality 17/44). Red metasediments north of Thukje are visible further east. b. Photo of the ridge above Ponganagu and the orange metasediments to the north. c. Locality 17/81 showing outcrop of intrusive sample a12–08 which weathers an orangey–brown colour. d. cross–cutting relationship between orangey brown unit and foliated pelitic metasediments. e. Photomicrograph of sample a12–04 in XPL and PPL. f. Hand specimen of sample a12–08. A freshly cut and wetted surface showing red and green patches. g. Outcrop from the ridge east of Nuruchen (locality 17/72) looking north. h. cross section from locality 17/86, perpendicular to the ridges and into the Puga Gneiss on the right. Localities perpendicular to this section were projected along strike to coincide with the line of section.

Nuruchen to Gyama Barma (Figure 11)

South of Nuruchen, below the west dipping metasediments of Horlam Kongka (4930 m), the valley is dominated by scree slopes of Puga gneiss. On the north shore of the Spanlung river, micaceous metasediments are interbedded with metasandstone, dipping towards the west at 184/27°W (locality 17/107) and contain a 1x2 m boudin of amphibolite with 2-3 mm retrogressed garnets. Isoclinal folding is present with a shallow east–dipping attitude of the hinge line and compressional shear fabrics (Figure 34a and d). 300 m to the east, an outcrop of mica schist is adjacent to the Puga Gneiss, dipping at 320/18°E (Figure 34e).

The river section (locality 17/109 to 17/117) follows the contact between the Puga Gneiss to the NE and metasediments to the SW. The boulders at the base of the Puga Gneiss slopes on the north side of the river (locality 17/111) show variations in grain size and mica content. The metasediments forming the boulders on the south side of the river are darker in colour and more mica rich. The valley of Kyamuri La is composed of scree showing changes from Puga Gneiss at the bottom of the slope, to dark coloured pelitic metasediments. A fractured amphibolite dyke outcrops towards the top of Kyamuri La (locality 17/117) with small (1 mm) retrogressed garnets (Figure 34b).

To the south of Kyamuri La, a transition from pelitic metasediments to Puga Gneiss is evident at the base of the scree slopes where the dominant lithology in the scree changes abruptly from west to east (Figure 34f). The cliffs further to the east are composed of pale coloured Puga Gneiss (Figure 34c) which is the dominant lithology in the scree towards Gyama Barma (locality 17/126). The red metasediments of the Tetraogal nappe can be seen towards the south (Figure 34g)

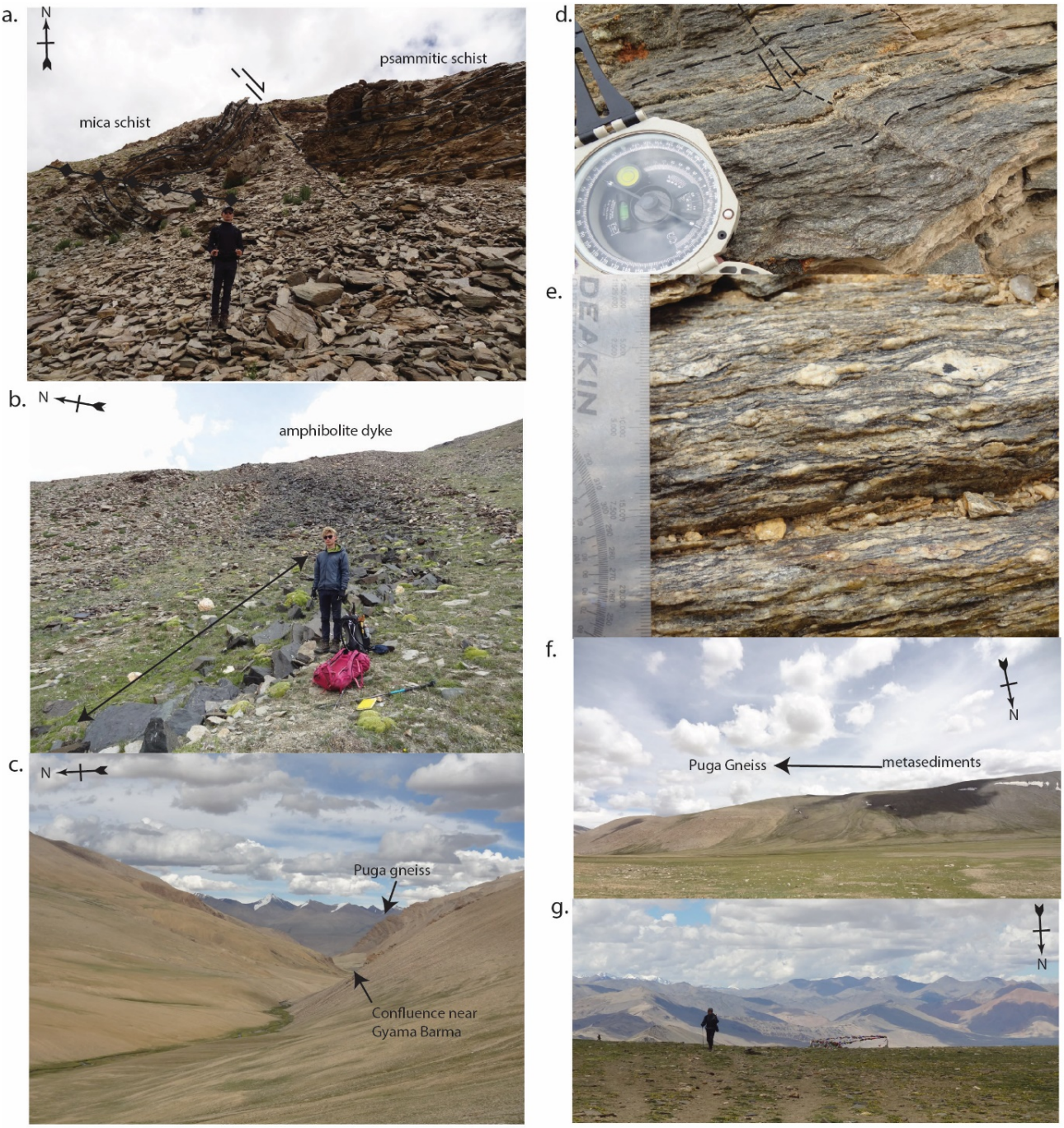


Figure 34 Nuruchen to Gyama Barma. a. Folded metasediments at locality 17/108 cut by normal fault. b. Amphibolite dyke with retrogressed garnets near Kyamuri La. c. Gyamsharma valley looking SE towards the cliffs of Puga Gneiss at the river confluence near Gyama Barma. d. Compressional shear plane within metasediments. e. Puga gneiss from locality 17/111. f. South of Kyamuri La. Coloured scree slopes show change from metasediments to Puga gneiss in the east. g. View from the top of Kyamuri looking south towards the red metasediments of the Tetraogal nappe.

Tetraogal nappe (Figure 13)

The metasediments of the Tetraogal nappe are composed of greywackes, slates, quartzites, calc–schists, dolomites and limestones (Steck *et al.*, 1998). Mafic amphibolites are interbedded with the metasediments as sills and tuffs. The stratigraphic association tholeiitic mafic rocks with calc–schists suggests that these rocks belong to the Permian Panjal traps (Fuchs *et al.*, 1996; Sigoyer, 1998).

South of Gyama Barma camp (locality 17/127), a dramatic colour change marks the transition from pale Puga Gneiss to a hillside of dark, green and red stripy metasediments of the Tetraogal nappe (Figure 35a-c). The boundary between these units occurs in a valley trending NW-SE, where Puga Gneiss with a foliation of 052/47°S lies beneath interbedded metasediments with the same foliation (Figure 35b). The Tetraogal nappe consists of carbonate–free pelitic metasediments, dark in colour and containing mica and small 1 mm dark garnets and randomly oriented black needles of tourmaline. The pelitic unit is interbedded with calc–schist which has a coarse grain size and orange weathering and limestone (Figure 35d-g). Quartz veins are strongly sheared and often show asymmetrical, top to the south, sigma shapes. The foliation in the red stripy Tetraogal nappe is dipping steeply towards the south and can be traced over the pass Yarlung Nyau La (5430 m) (locality 17/137) and to the north of Karzok village.

North of Karzok Phu, a stratigraphic sequence of metasediments can be observed along the shore of Tso Morari, dipping steeply towards the south. The sedimentary structures within the metasedimentary rocks of the Tetraogal nappe indicate a right way up position. Interbedded pelites and calcareous metasediments are interpreted as a lateral transition between slope deposits, still influenced by carbonate detrital input, with a more distal environment (Epard and Steck, 2008). The stratigraphically highest units are rich in dolomite and limestone and have been mapped as a lateral equivalent of the Permian–Mesozoic Lamayuru unit (Fuchs and Linner, 1996). This stratigraphic sequence has been correlated with the Permian to Late Cretaceous sediments from the Nyimaling area (Stutz, 1988) which have been documented to contain coral fossils in life position (Epard and Steck, 2008).

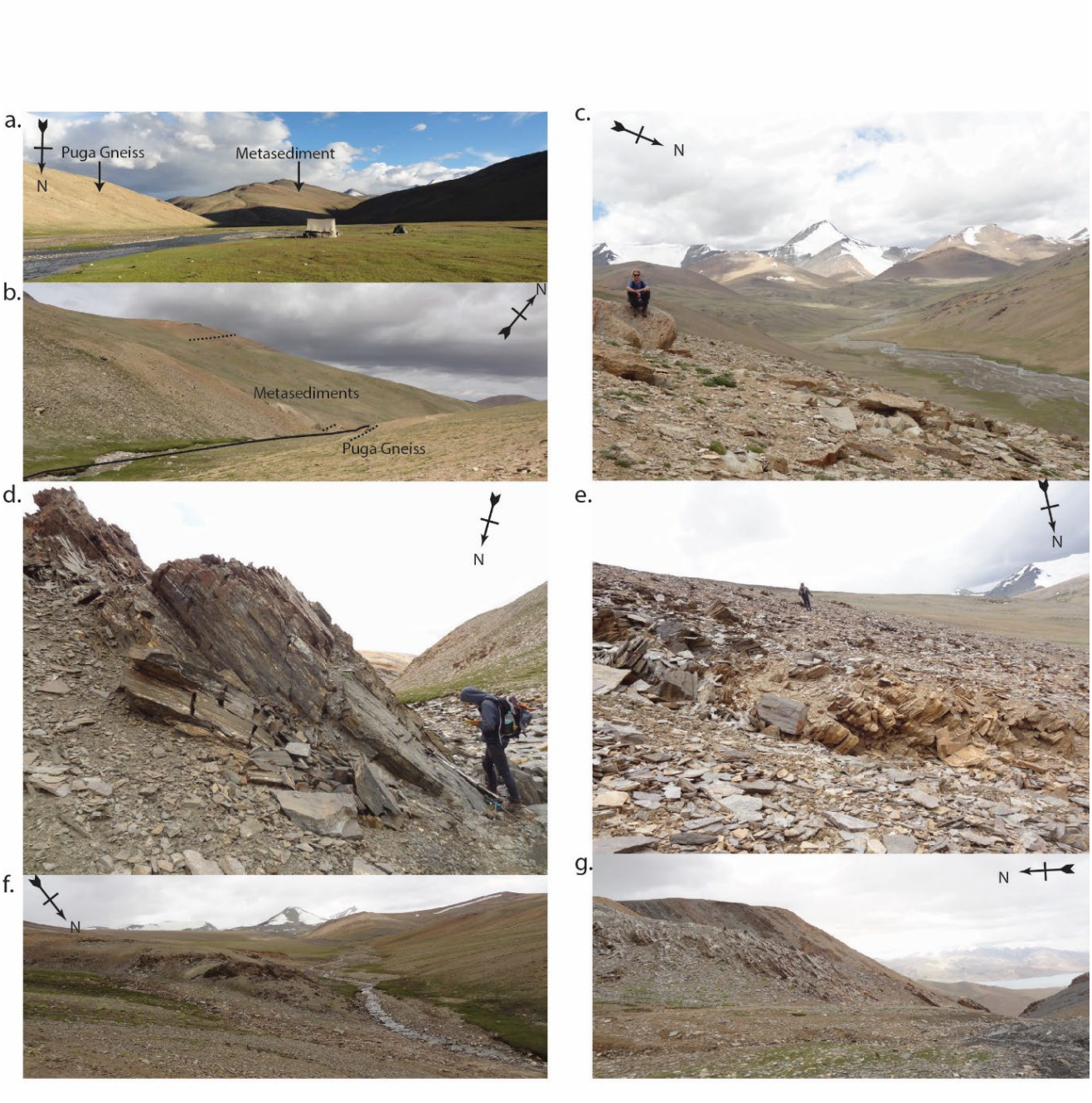


Figure 35 Gyama Barma to Karzok. a. View looking south from Gyama Barma camp (locality 17/123). Pale coloured hill in the foreground composed of Puga Gneiss. Red and green stripy hill in the distance made up of metasediments of the Tetraogal nappe. b. Valley heading south east from Gyama Barma showing the Puga gneiss underneath the red and green metasediments of the Tetraogal nappe, showing a concordant foliation to the nappe boundary. c. View from the hill just south of Gyama Barma looking south over the red–green stripy metasediments of the Tetraogal nappe. d. Steeply dipping metasediments of the Tetraogal nappe between Gyama Barma and Yarlung Nyau. e. Hill just south of Gyama Barma. Pelitic and calcareous metasediments of the Tetraogal nappe interbedded and dipping steeply SE. f. Metasediments as in e. located closer to Yarlung Nyau, dipping towards the SE. g. View from Yarlung Nyau towards Karzok in the E with steeply S–dipping metasediments of the Tetraogal nappe that can be traced all the way to Tso Morari in the distance.

Karzok (Figure 13)

In the valley of Karzok Phu (locality 16/01) is a lens of serpentine–rich ultramafic rock forming part of the Karzok ophiolite ~200x200 m, composed of chromitite, serpentinite, metagabbro and metabasites (Berthelsen, 1953). This outcrop is thought to mark the boundary between the Tetraogal and Mata nappe (Steck et al., 1998), although it was originally thought to be in direct contact with the metasediments of the Tso Morari complex (Guillot *et al.*, 2000; Sigoyer *et al.*, 2004). This zone continues towards the east of Tso Morari and is marked by the presence of lenses of metagabbro and serpentinite. Whole rock geochemistry of the Karzok foliated metagabbro show a subduction-related mantle source, similar to the ophiolites of the Indus suture and is considered to be evidence of an immature Tethyan island arc (Mahéo *et al.*, 2000).

Mata nappe (Figure 13)

The Mata nappe has been correlated with the Nyimaling–Tsarap nappe to the NW and represents the highest tectonic unit in the Tso Morari dome (Steck et al., 1998; Epard and Steck, 2004). It is composed of a 4000 m thick package of metasediments of late Proterozoic to Cambrian age greywackes. The Karsha greywackes and dolomites are thought to make up the base, with >3000 m of upper Palaeozoic to Cretaceous carbonate shelf sediments (Epard and Steck, 2008).

South of Karzok is a 150 m cliff of mica schist interbedded with quartz–rich sandstone dipping ~090/50°S and weathered an orange colour, suggesting a high carbonate content. Metabasalts occur within this sequence and occasional horizons of serpentinite outcrop throughout the hillside, subparallel to foliation. Quartzite and calc–schist become more abundant towards the south. The rocks of this unit show a greenschist facies chlorite-epidote mineral assemblage. Intense folding can be seen within competent sandy units with NE verging folds, with an axial plane oriented at 098/53°S.

South of Karzok, in the Mata range, is the mountain of Mentok. The northern flank is composed of the Rupshu granite, a low strain, I–type, biotite–granite which forms the core of a syncline forming the Mata nappe (Steck et al., 1998). The Rupshu granite has been dated at 482 ± 1 Ma (U–Pb zircon age) (Girard and Bussy, 1999). Close to the western shore of Tso Morari (locality 17/1a), leucocratic granitic bodies crosscut darker granite, indicating that multiple generations of granitic intrusive is present.

However, a weak foliation is present throughout all granite generations. Mafic dykes intrude the Rupshu granite and surrounding metasediments indicating an intrusive relationship and a younger age of formation of the mafic rocks. The margins of the mafic dykes are strongly foliated and contain abundant epidote, becoming less deformed, with a lower proportion of biotite, away from the mafic dyke.

Summary

The Tso Morari dome is comprised of three structurally distinct units, separated by thrust sense shear zones, referred to as the Tso Morari, Tetraogal and Mata nappes from lowest to highest structural level respectively. The structural nappes can be distinguished based on their lithologies and metamorphic mineral assemblages. The Tso Morari nappe is predominantly composed of granitic orthogneiss. Rafts of amphibolite facies metasediments can be found within the gneiss and stratigraphically above the granite with an intrusive contact, similar to that documented by Epard and Steck (2008) who observed large apophyses of granite within the metasediments in the Nuruchen region. The distinguishing feature of the Tso Morari nappe is the presence of retrogressed mafic eclogite boudins or sills.

The Tetraogal nappe is more heterogeneous and contains interbedded carbonate, pelite and basalts metamorphosed in the amphibolite facies. Mafic rocks are amphibolites with no evidence of retrogression from an eclogite facies assemblage. The Mata nappe is compositionally similar to the Tetraogal nappe but contains a larger proportion of carbonate rocks and is host to the Rupshu granite. The Mata nappe is separated from the Tetraogal nappe by the Karzok ophiolite which is observed in the valley of Karzok Phu. The metamorphic grade varies from amphibolite facies close to the Karzok ophiolite, to greenschist facies in the Rupshu granite, south of Karzok village. The stratigraphy of the Tso Morari, Tetraogal and Mata nappes is comparable to the stratigraphic log in the study by Steck et al. (2003) (Figure 3).

The current structural configuration of these units is an elongate dome, such that on the southern limb, the thrust-sense shear zones have been overturned during late stage doming and display a top-to-the-south sense of shear on a south-dipping shear zone. In the core of the Tso Morari complex, top-to-the-east shear sense is commonly recorded in the asymmetrical augen of the Puga Gneiss and corresponds

to the D1 event of Epard and Steck (2008), interpreted to relate to the early exhumation of the rocks to crustal levels.

The southern margin of the dome preserves a strong top-to-the-south shear sense, commonly observed as mineral stretching lineations in tourmaline and biotite, within a ductile fabric which overprints the earlier D1 fabric and is observed in all three nappes. This pervasive ductile fabric increases in strength towards the bounding shear zones. The south-directed fabric corresponds to the D2 fabric of Epard and Steck (2008) which is been interpreted to relate to the north–directed under thrusting of the Tso Morari complex beneath the Tetraogal and Mata nappes. Also prevalent adjacent to the southern margin of the Tso Morari complex is a NE-SW oriented lineation, equivalent to the D3 event of Epard and Steck (2008), coeval with regional Barrovian metamorphism.

The orthogneiss at the northern margin of the complex is overprinted by a steeply dipping top-to-NE normal-sense fabric corresponding to the Zildat shear zone. Figure 4, stereonet 3 shows few E-W oriented lineations based on porphyroclast asymmetry and S-C’ fabrics oriented NE-SW. This ductile fabric occurs within 200-300m of the Zildat shear zone and is associated with an upper greenschist-facies overprint, evident in the mafic rocks and comparable to that described by Steck et al. (1998).

Chapter 3 - Petrography and thermodynamic modelling of the Tso Morari eclogites

This chapter was written by A.K.Bidgood. Fieldwork and sample collection was conducted by A.K. Bidgood and J. Utting in 2016-17. Sample L08-03 was collected by M.P. Searle in 2008. SEM garnet maps of sample L08-03B were collected by J. Utting and D.J. Waters.

Introduction

In continental (ultra)high–pressure terrains worldwide, eclogite–facies metamorphism is commonly preserved in mafic rocks, hosted within continental material. Many occurrences of mafic rocks consist of small, boudinaged bodies, of which some preserve an eclogite–facies peak assemblage including garnet and omphacite (Heinrich, 1982). The slow reaction kinetics and requirement for water to progress the retrograde reactions, causes incomplete reactions to be 'frozen in'. This allows us to determine the conditions during different stages of the *P-T* history of the unit. The host material often preserves amphibolite–facies conditions and rarely preserves evidence of high–pressure metamorphism. Consequently, the mafic eclogites provide us with the most complete record in which to understand the metamorphic history of these rocks. Conventional thermobarometry and pseudosection modelling allows us to determine precise conditions of metamorphism, which in conjunction with the textural observations, allow us to determine the *P-T* history of the rocks.

Following structural mapping of the Tso Morari dome by Epard and Steck (2008), numerous eclogite bodies were identified throughout this 100 x 50 km dome. However, a surprising number of studies have focussed on a single exposure (Sachan *et al.*, 1999, 2004; O'Brien *et al.*, 2000; Mukherjee *et al.*, 2003; Konrad–Schmolke, O'Brien, *et al.*, 2008; St-Onge *et al.*, 2013; Palin *et al.*, 2014; Chatterjee *et al.*, 2015; Wilke *et al.*, 2015), first discovered by Berthelsen in 1953. These previous studies of the Tso Morari eclogite have also failed to produce a consensus on the *P-T–t* history, with debate continuing today (O'Brien, 2018b).

Petrographic analyses of Tso Morari eclogites in published studies are thought to be representative of the mafic eclogite boudins within the Tso Morari complex. However, significant variation in mineral composition and modal abundances are present within a single exposure as shown by extensive studies of the Berthelsen

exposure. For example, inclusions in garnet cores, particularly amphiboles, are often assumed to represent part of the prograde assemblage and variations in garnet compositional zoning from within one outcrop raises questions regarding the role of retrogression in producing observed differences, the limited metamorphic reactions predicted in the coesite and diamond stability fields and the short timescales involved in subduction and exhumation. Previously reported peak pressure estimates range from between ~20 kbar and >39 kbar (de Sigoyer *et al.*, 1997; Konrad-Schmolke *et al.*, 2008; St-Onge *et al.*, 2013; Wilke *et al.*, 2015) and the shape of the *P-T* paths varies based on interpretations of observations and of geodynamic models.

This chapter attempts to summarise the major petrographic variations between samples and determine 1) which observations are a feature of the degree of fluid content and retrogression of a mafic eclogite, 2) the variation in bulk composition between neighbouring mafic boudins resulting from protolith chemistry and 3) the variation in mineral assemblage and composition resulting from pressure and temperature gradients across the dome.

The Tso Morari eclogites

The Tso Morari dome consists of three stacked nappes made up of metamorphosed sediments from the Indian continental margin. The lowermost nappe also contains metamorphosed Ordovician granite and granite gneiss, intruded into the overlying sediments. This nappe, known as the Tso Morari complex, is host to small (metre to tens of metre) mafic eclogite boudins which preserve evidence of ultrahigh–pressure metamorphism (Epard and Steck, 2008). Eclogite facies mafic rocks are located across the dome in all lithologies. The least retrogressed examples are hosted within the Puga gneiss or undeformed granite, making up the majority of the dome. Figure 5 shows the location of mafic eclogite samples considered in this study, as well as the locations of samples used in published petrographic and geochronological studies.

Mafic eclogites undergo retrogression in the presence of an externally derived fluid. This can be observed at outcrop scale owing to the preservation of eclogite facies mineral assemblages in the core of a mafic boudin, with increasing modal abundance of hydrous minerals (e.g. amphibole) towards the rim of the boudin (see chapter 2 for field relationships). This zonation on the scale of an individual boudin, assumed originally to be of homogeneous composition, allows the variation in mineral assemblage and composition to be related to the degree of retrogression. In turn, the petrographic study of other eclogite boudins can be used to investigate the variation in peak assemblage across the terrane prior to the retrograde overprint. Variation may result from diversity in pre–metamorphic bulk composition, or regional trends in peak pressure and temperature. In either case, phase equilibrium modelling can then be applied to investigate the pressure–temperature evolution and the effects of bulk rock composition.

The first indication of metamorphism from the Tso Morari dome was the discovery of garnets in basaltic dykes, towards the south of Tso Morari lake (Hayden, 1904). The first reliably documented discovery of eclogites from the Tso Morari complex didn't take place until Berthelsen (1953) published a petrographic description of the eclogites and suggested their origin as Panjal trap basalts. Modern day analytical techniques were not employed until the discovery of eclogite in the Kaghan valley (Pognante and Spencer, 1991), prompted the parallel studies of Guillot et al. (1997) and de Sigoyer et al. (1997) which looked at the pelitic and mafic lithologies of the Tso Morari complex respectively. Guillot et al., (1997) recorded high pressure

assemblages in the pelitic rocks of 20 ± 2 kbar at 550 ± 50°C with a blueschist facies overprint of 18-13 kbar at the same temperature. Heating in the amphibolite facies at crustal depths, followed by a greenschist facies overprint at 5 kbar and 500°C were also recorded. The parallel study by de Sigoyer et al. (1997) focussed on a mafic eclogite boudin with a peak assemblage of garnet + omphacite ± phengite + rutile + quartz recording pressure of >20 ± 3 kbar at 550 ± 50°C. Zoned garnets and glaucophane after omphacite on the retrograde path were also observed, recording isothermal exhumation with a high temperature overprint at 10 kbar and a lower temperature greenschists facies retrograde overprint (de Sigoyer et al., 1997). Using the garnet, omphacite and phengite data of de Sigoyer et al. (1997) combined with the garnet–omphacite–phengite geobarometer of Waters and Martin (1993), O'Brien (2001) predicted that this assemblage equilibrated in the coesite stability field. This was corroborated by the discovery of coesite as inclusions in garnet in mafic eclogite (Mukherjee and Sachan, 2001; Sachan et al., 2004). Prograde metamorphic *P-T* estimates of 21.5 ± 1.5 kbar and 535 ± 15°C (St-Onge et al., 2013) were made using compositional analysis of zoned garnets in combination with thermodynamic modelling. However, attempts at calculating core conditions based on inclusion assemblages and conventional thermobarometry of included minerals did not lead to tangible results.

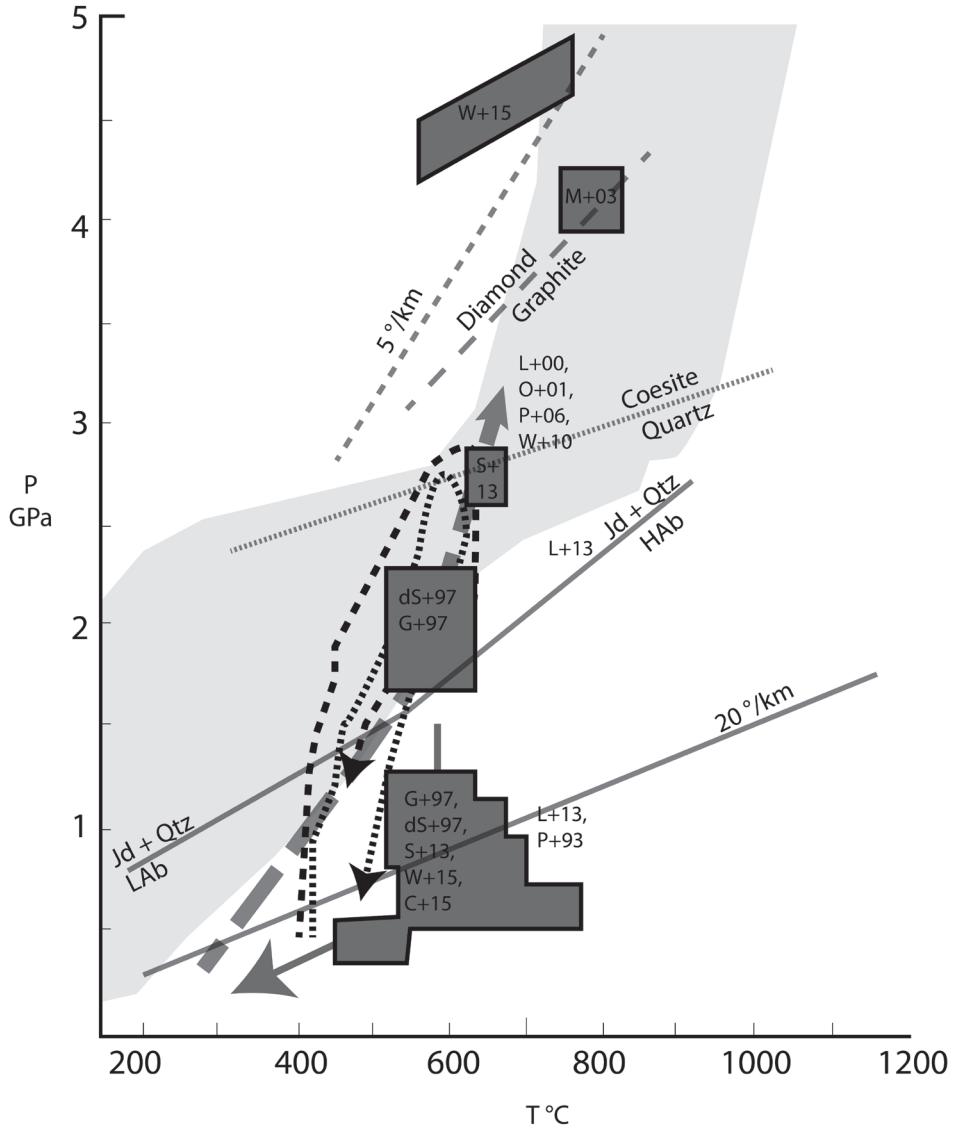


Figure 1 after O'Brien (2018), figure 5. Summary of P-T results and proposed P-T paths for Tso Morari eclogites. Data from Guillot et al. (1997) (G + 97); de Sigoyer et al. (1997) (dS + 97); Mukherjee et al. (2003) (M + 03); St-Onge et al. 2013 (S + 13); Chatterjee & Jagoutz (2015) (CJ15); Wilke et al. (2015) (W + 15) and Palin et al. (2017). Shaded area denotes the range of global slab surface paths from Syracuse et al. (2010); bold arrow is prograde path of Konrad-Schmolke *et al. (2008); grey decompression arrow is from de Sigoyer et al. (1997); stippled paths are from modelling of Warren et al. (2008) (W + 08) and Beaumont et al. (2009) (B + 09). Coe = Qz: Bohlen & Boettcher (1982); Ab = Jd + Qz: Holland (1980); diamond = graphite: Bundy (1980); alpha–quartz = beta–quartz: Swarmy and Saxena (1994). Depth is calculated for a density of 2850 kg m−3.*

To date, approximately 13 studies have focussed on the mafic eclogite boudin initially discovered by Berthelsen (1953) (Sachan et al., 1999; O'Brien and Sachan, 2000; Mukherjee and Sachan, 2001; Mukherjee et al., 2003; Sachan et al., 2004; Konrad-Schmolke et al., 2008; Singh et al., 2013; St-Onge et al., 2013; Palin et al., 2014; 2017; Chatterjee and Jagoutz, 2015; Wilke et al., 2015; Jonallagadda et al., 2017a) owing to its accessibility and proximity to the road. A summary of *P-T* paths for the Tso Morari nappe is shown in Figure

1, with additional data from numerical modelling of *P-T* paths from slab tops of subducted oceanic slabs (Syraceuse et al., 2010) and constraints from numerical modelling of continental subduction (Warren et al., 2008; Beaumont et al., 2009). Some of the peak estimates lie in the coesite stability field, with two predictions which lie in the diamond stability field (Mukherjee et al., 2003; Wilke et al., 2015).

Published *P-T* paths of the Tso Morari nappe can be split into two distinct paths; cold paths (Figure 2a and b) which are concave with respect to the temperature axis (St-Onge et al., 2013; Palin et al., 2014; 2017; Chatterjee and Jagoutz, 2015) and hotter paths (Figure 2c) convex with respect to the temperature axis (Konrad-Schmolke et al., 2008). The colder *P-T* paths follow paths from slab surfaces, modelled by Syraceuse (2010) for oceanic slabs, and are dominated by prograde, lawsonite–bearing assemblages where epidote is consumed and glaucophane is the dominant amphibole. The hotter *P-T* paths follow the model of Warren et al (2008) and Beaumont et al (2009) which model subducted continental margins and pass outside of the lawsonite–bearing assemblage fields, where chlorite, epidote and Na-Ca amphibole are consumed during garnet growth.

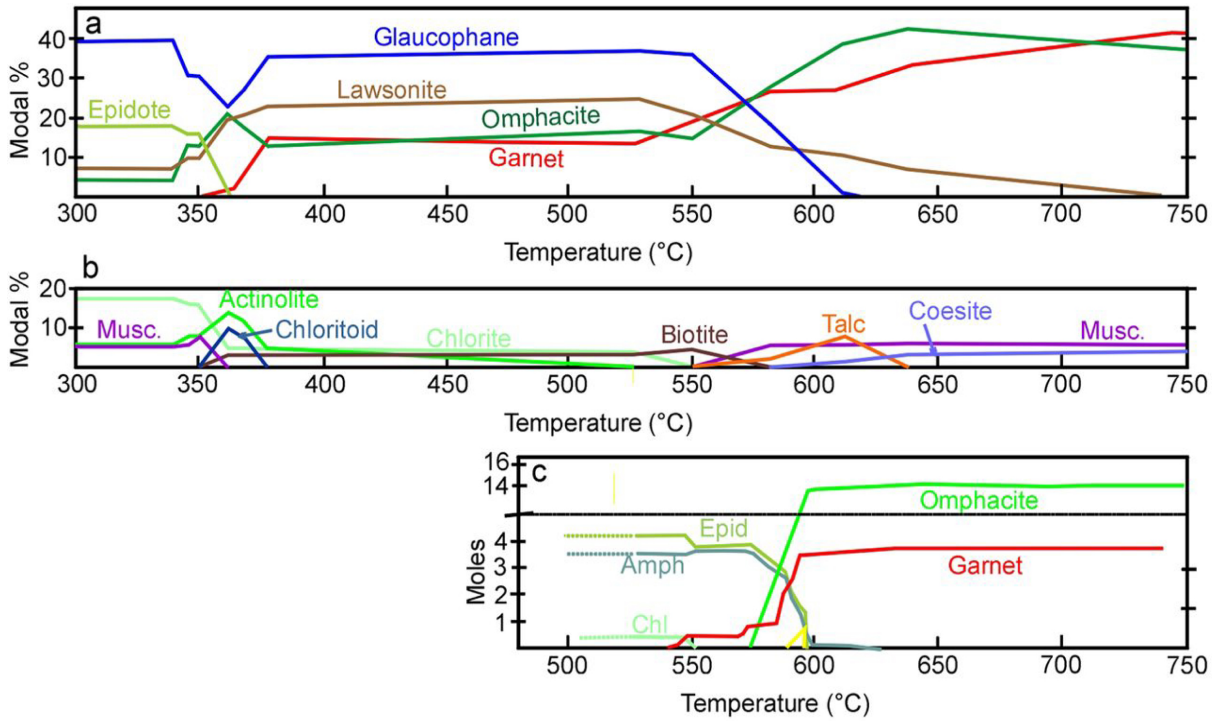


Figure 2 Taken from O'Brien (2018) showing changes in mineralogy of eclogites from pseudosection modelling along different P-T paths. A. and B. show modal proportion along a concave path (Palin et al., 2017). C. Modal proportions along a convex path (Konrad-Schmolke et al., 2008)

The petrographic description below is based on the Berthelsen eclogite which forms the focus of the studies mentioned above. Further petrographic descriptions of other eclogite bodies from across the dome are found in the petrography section of this chapter. In outcrop, the eclogite can be recognised by the distinct colour difference between the mafic boudin and the host gneiss or metasediments. Mafic boudins are dark in colour owing to the abundance of amphibole which increases from core to rim, representing the degree of retrogression due to fluid infiltration on the retrograde path (De Sigoyer & Guillot, 1997). Biotite is present at the rims of the eclogite, close to the contact with the Na– and K– rich Puga gneiss. Clusters of white mica and orange carbonate are also observable in hand specimen (O'Brien, 2018b).

Peak metamorphic conditions (M2) are recorded in mafic eclogite boudins as mineral assemblages containing 1–2 mm idiomorphic garnets, green omphacite, phengite (3.56 Si pfu), blue–green zoned amphibole, zoisite, quartz and rutile (de Sigoyer et al., 1997), with rarer paragonite (Gouzu et al., 2006; Epard and Steck, 2008), carbonates (Gouzu et al., 2006; Wilke et al., 2015), talc and kyanite (Mukherjee et al., 2003). Talc and lawsonite are interpreted to have been present during peak (M2) metamorphism (Palin et al., 2014) but are not present in the matrix assemblage of samples from the Berthelsen outcrop. Chemical zoning in garnets preserves prograde metamorphism (M1) up to peak pressure conditions (M2), from a darker, inclusion–rich core, towards the inclusion–poor, pale–coloured rim with increasing pyrope content. Inclusion assemblages in garnet are often used in combination with garnet isopleths as a record of *P*-*T* conditions during garnet growth.

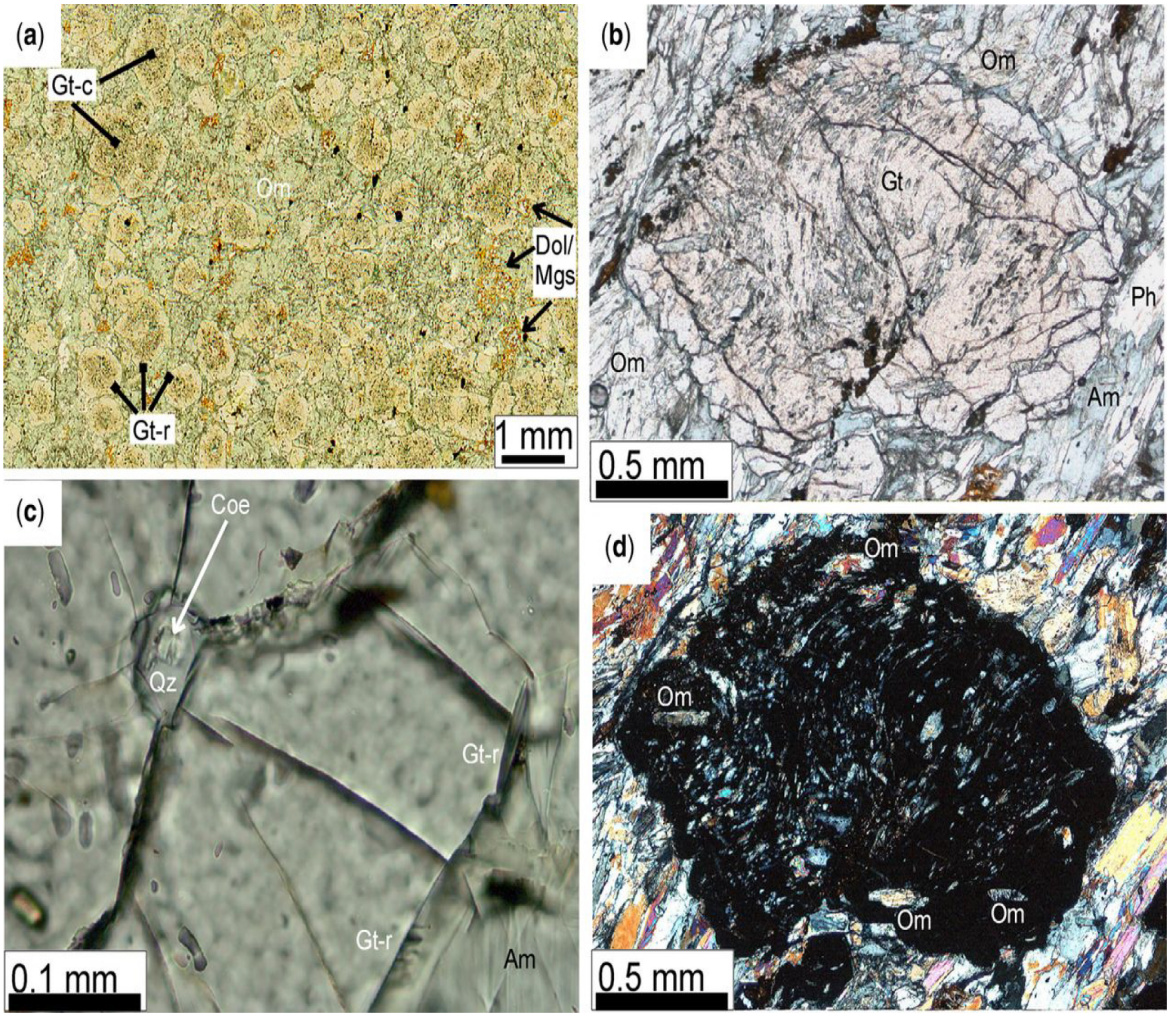


Figure 3 Photomicrographs showing peak metamorphic assemblage of Berthelsen outcrop taken from O'Brien 2018. a. Garnet with inclusion–rich cores (Gt–c) and inclusion–poor rims (Gt–r), omphacite (Om) and dolomite/magnesite (Dolo/Mgs). b. Garnet with a matrix of omphacite, phengite (Ph) and Na–Ca amphibole (Am). c. Coesite inclusion in garnet surrounded by quartz (Qz) at the core-rim boundary. d. Garnet from b. in cross polar

The exhumation history of the Tso Morari complex can be divided into two stages involving an initial steep decompression (M3) followed by an amphibolite facies overprint in the mid crust (M4 to M5) (Figure 1). The cores of mafic boudins preserve peak mineral assemblages but have experienced partial retrogression, documented by partial replacement of peak garnet and omphacite and the formation of zoned sodic-calcic amphiboles (De Sigoyer *et al.,* 1997; Wilke *et al.,* 2015), and clinozoisite porphyroblasts overgrowing the peak assemblage (de Sigoyer *et al.,* 1997; O'Brien *et al.,* 2001; Palin *et al.,* 2014). Following the retrograde growth of the Na-Ca amphibole and clinozoisite, symplectites of Na–rich plagioclase and jadeite–poor clinopyroxene begin to replace omphacite, recording incomplete metamorphic reactions at lower–pressure conditions (O'Brien, 2018b).

Influx of fluid during the later stages of exhumation marks the second stage of the *P-T* path where abundant fluid was available, forming amphibolite–facies assemblages. In mafic protoliths, assemblages are observed containing magnesiohornblende rims on the zoned amphiboles, biotite, chlorite, titanite rims on rutile and cracks or rims of dolomite within magnesite, later altered to calcite, ferroan dolomite and siderite (Wilke *et al.,* 2015). The amphibolite facies overprint is also extensively recorded in the host felsic rocks. Biotite and kyanite/sillimanite textures replacing staurolite, phengite and chlorite were observed in metapelite and metagreywacke units, recording a temperature increase of up to 610 ± 30°C at 9 ± 3 kbar (De Sigoyer *et al.,* 1997), 650 ± 50°C at 9 ± 1 kbar (Girard, 2001) and 630°C ± 30°C at 9 ± 2 kbar (Guillot *et al.,* 1997). Thin cordierite coronas around garnet formed at 7.1 ± 1 kbar and 725 ± 50°C (St-Onge *et al.,* 2013). The latest phase of deformation reportedly occurred in greenschist facies conditions of 5-7 kbar and 500 ± 50°C (Guillot *et al.,* 1997), recorded in extensional shear bands of chlorite, biotite and muscovite (3–3.1 Si pfu) in metagreywackes, and calcite and chloritoid in calc–schists and metapelites (Epard and Steck, 2008).

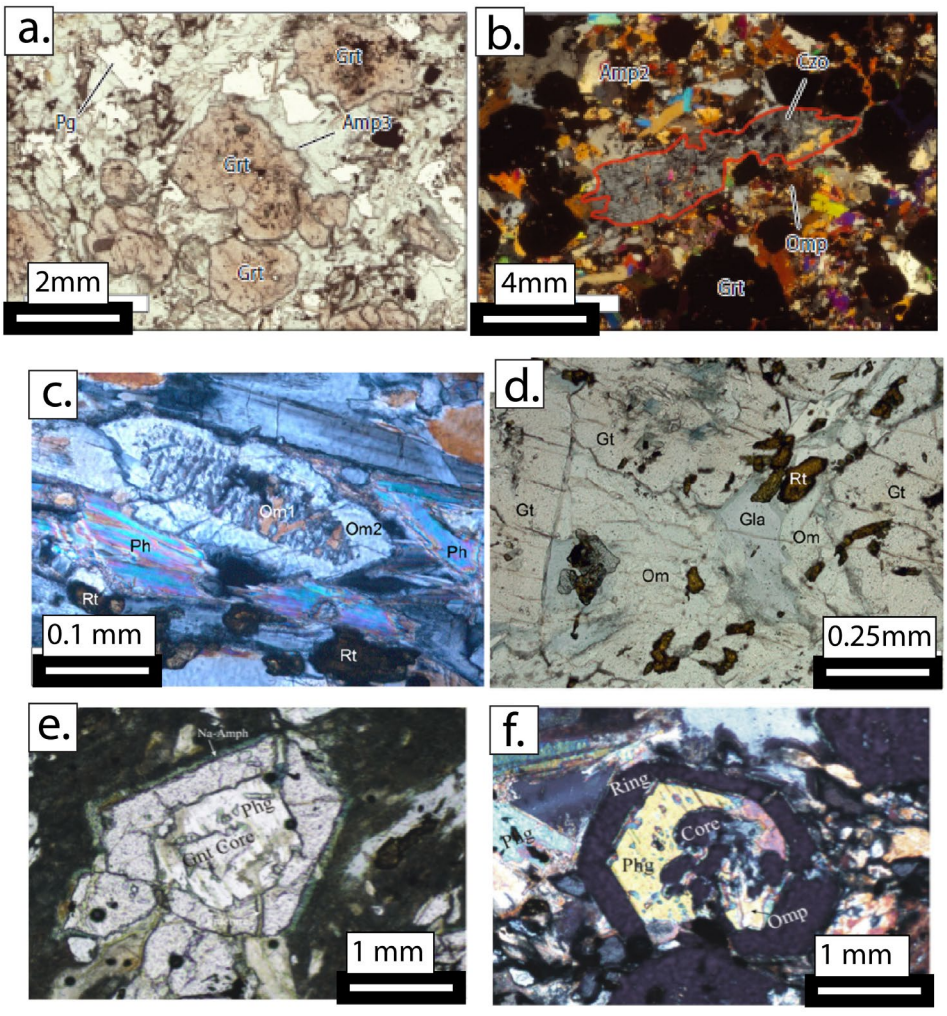


Figure 4 Photomicrographs showing retrograde phases overgrowing peak assemblages a . Photomicrograph (PPL) of sample L08-03A from Palin et al. (2014) showing retrograde amphibole mantling garnet outer rims. b. Large clinozoisite poikiloblasts from sample L08-03A (Palin et al., 2014) trapping various matrix minerals. c. Photomicrograph taken from O'Brien (2018) showing skeletal relict of aegerine–rich omphacite (Om1) and an aegerine–poor rim (Om2) with phengite and rutile. d. Photomicrograph from O'Brien (2018) showing glaucophane core of matrix amphibole replacing omphacite. e. Photomicrograph from Jonnalagadda et al. (2017), figure 7 showing atoll garnets from a mafic eclogite f. Photomicrograph from Jonnalagadda et al. (2017), figure 7 showing atoll garnets from a mafic eclogite

The numerous zoned garnets, within eclogites of the Tso Morari complex, show similar features to garnets from high–pressure and ultrahigh–pressure eclogites worldwide, providing a complex record of the prograde history from an inclusion–rich core up to a high–pressure inclusion–poor rim, where coesite has been identified as inclusions (Sachan, 2004). The main features of garnet growth, as demonstrated in St-Onge *et al.* (2013) and Wilke *et al.* (2015) include a plateaued core profile (*c*. $Alm_{0.65}Grs_{0.17}Prp_{0.17}Sps_{0.02}$) with a bell–shaped spessartine profile indicating prograde garnet growth. The core region has a low pyrope and high grossular and spessartine contents compared to the other garnet zones and abundant inclusions. The cores of the garnet often preserve relict planar or s–shaped inclusion trails indicating post or syn–deformational garnet growth (St-Onge *et al.,* 2013; Wilke *et al.,* 2015). These are truncated by a paler–coloured, inclusion–poor rim. Inclusions in the garnet cores are made up of sodic-calcic amphibole (barroisite), quartz, clinozoisite, albite, aegirine–rich omphacite (garnet core), dolomite, calcite, ilmenite, rutile, apatite and zircon. Amphibole inclusions are visibly zoned and occur almost exclusively in the core, commonly associated with quartz and albite. Towards the garnet rim, there is a marked drop in spessartine and grossular and an increase in pyrope and almandine, with the maximum pyrope content at the rim ($Alm_{0.45}Grs_{0.195}Prp_{0.35}Sps_{0.01}$), where a 20 mol% pyrope increase occurs over 5 μm (O'Brien, 2018). This Mg–rich overgrowth forms an irregular zone around the garnet, is often razor sharp and contains few inclusions.

Petrography and mineral chemistry

This section provides a summary of mineral associations, textures and petrological trends relating to prograde, peak and retrograde metamorphism of the Tso Morari eclogites. Major retrograde textural and compositional trends, as described in this, are common to mafic samples from across the dome. However, variations between eclogites from different locations within the Puga Gneiss, when compared to the Berthelsen outcrop, indicate complexities previously undescribed, which form the basis of this chapter. Based on the previous descriptions of retrograde metamorphism in the Berthelsen eclogite, we can begin to unravel the complex metamorphic

history and establish whether there are variations in the mafic protolith, mineral growth history and/or deformation history, in distinct outcrops of mafic rocks from across the dome. For this reason, the following petrographic descriptions are presented by locality, in order to preserve features that are distinct to specific outcrops and to unravel the major differences between eclogites across the Tso Morari nappe.

Sampling strategy and analytical methods

Polished thin sections were made from the least retrograded samples from twelve eclogite boudins across the Tso Morari complex. Of the thin sections produced, four were selected for more detailed petrological analyses. Major element compositions of minerals that exhibit solid solutions were measured using a Cameca SX-5 field emission electron microprobe with a 15 KeV acceleration potential, 20 nA beam current, 30 second count time per major element and 60 second count time on Ti. The following standards were used: synthetic TiO2 (Ti), sanidine (K), albite (Na, Si, Al), fayalite (Fe), Mn metal (Mn), wollastonite (Ca), periclase (Mg). Fe^{3+} was calculated based on stoichiometric calculation using the methods of Droop (1987).

Full slide maps were collected using a 400 nA beam current, 20 ms dwell time, 10 µm beam and a 30 µm step size. Mg, Ca, Zr, Al and Fe were analysed using WDS spectrometers, whilst C, Na, Si, P, K and Mn were analysed using an EDS detector. High resolution garnet maps were collected using an 18 nA current, 130 ms dwell time, 1 µm beam and a 3 µm step size.

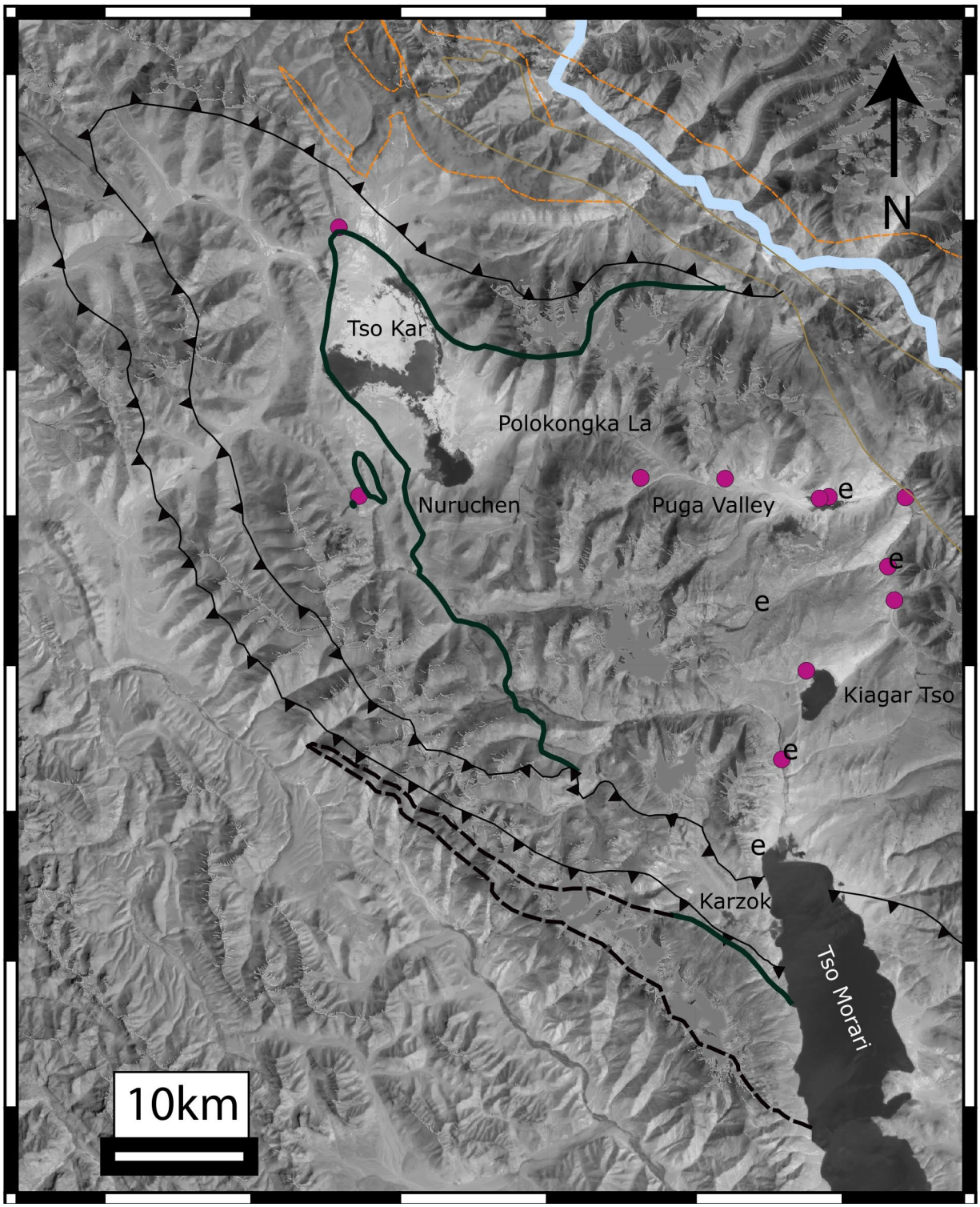


Figure 5 Map of eclogite sample locations and their names (circles). e symbols show the location of mafic eclogites from published petrographic studies. Solid black line marks boundary between Puga gneiss and metasediments.

Location	Sample Number	Corresponding Geochron Sample	Lat/ long	Assemblage
Kiagar Tso	a03–16/ a03–18	a03–19	33.12141/78.29586	Grt, Omp, Amp, Phe, Pl, Tlc, Czo, Qz, Rt, Zrn,
Kiagar La	05–04C/05–04D	a03–20	33.16265/78.36108	Grt, Omp, Amp, Dol, Mag, Cal, Czo, Qz, Pl, Phe, Bt, Tlc, Pg, Rt, Ky, Zrn,
Berthelsen outcrop	JU13/JU13a/ JU12/JU11/L08-03	a03–22	33.18336/78.35717	Grt, Amp, Omp, Czo, Phe, Pl, Rt, Qz, Dol, Mag, Cal, Bt, Tlc, Pg, Zrn
Puga Valley	10–05/10–02/ a04–13	a04–20	33.22615/78.30916	Grt, Omp, Amp, Phe, Pl, Dol, Cal, Tlc, Czo, Bt, Rt, Spn, Di, Czo, Pg, Chl, Qz
Polokongka La pass	a04–30/a04–31	a04–28	33.240002/78.24111	Grt, Amp, Pl, Wm, Czo, Dol, Bt, Qz, Rt,
Polokongka La ridge	11-05/11–06/11–07	a05–15	33.25426/78.19031	Grt, Amp, Phe, Pl, Omp, Qz, Czo, Bt, Pg, Di, Ky, Rt, Zrn, Qz,

Table 1 Eclogite sample descriptions, name, lat/long, peak assemblage, textures

Kiagar Tso

North west of Kiagar Tso, in the central part of the complex, many small boudins of mafic eclogite occur on a scale of 30 cm to 3 m in length. Mafic boudins are wrapped by Puga Gneiss which consists of quartz, phengite and albite. The gneiss surrounding the boudins is strongly foliated and often contains garnets, wrapped by the fabric in the gneiss.

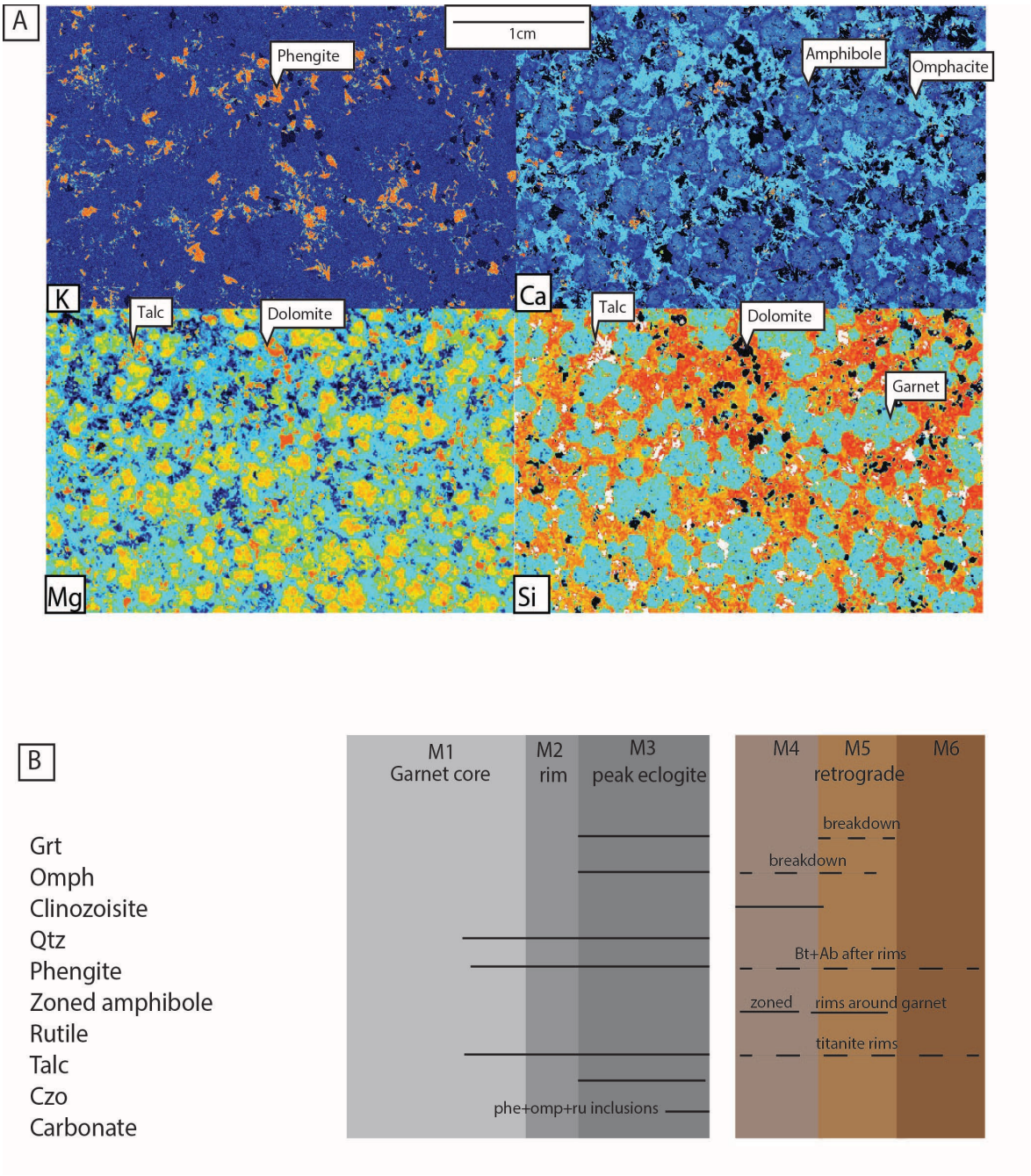


Figure 6 Sample a03-16 A. K-map showing the distribution of phengite (orange). B. Ca-map showing the zoned garnets (pale blue core, dark blue rim), amphibole (medium blue) and omphacite (pale blue). C. Paragenetic history diagram summarising relative timing of mineral growth.

Sample a03-16 is a medium– to coarse– grained eclogite with a granoblastic texture with a major mineral assemblage of garnet (40%), omphacite (23%), phengite (10%), quartz (1%), and talc (2%), with minor amounts of clinozoisite (1%), amphibole (15%), carbonate, rutile. Strongly zoned garnet and omphacite (Jd17-79%) are in textural equilibrium with coarse grained homogeneous phengite (Si 3.54-3.55 pfu) and talc, forming the peak pressure (M2) mineral assemblage. Matrix phengite and talc have a similar grain size and form straight edge contacts with each other and with garnet. Garnet occurs as subhedral porphyroblasts that are 3-4 mm in diameter. The core region has a composition of Alm_{48-42} Grs_{24-29} Pyr_{20-30} Sps_{6-1}, with decreasing almandine and increasing pyrope from core to rim. At the core-rim boundary, a manganese annulus, followed by a calcium trough is evident (See Figure 8) with an increase in calcium towards the rim. The concentric zoning pattern described is interrupted by zones of high pyrope and almandine, extending from the outside edge of the crystal towards to core, often forming channelized features. This later replacement feature is particularly evident on Fe and Mg element maps of garnet.

There are a range of different amphibole inclusions in garnet cores. These are mostly blue-green with the bluest amphibole forming in the cores and the greenest amphibole forming the rims. Thin rims of pale green amphibole surround garnet and coarse, zoned, blue-green amphiboles, similar in colour to amphiboles in garnet cores, are present in the matrix. Other inclusions include rutile and quartz.

Matrix quartz and omphacite contain clusters of zircon inclusions whilst garnet, omphacite, quartz, phengite, and talc contain rutile inclusions. Rutile inclusions in garnet often form coarse rectangular clusters interpreted to be after an original igneous Fe-Ti oxide. Exhumation from peak M2 conditions resulted in the formation of thin rims of titanite surrounding matrix rutile grains, the breakdown of the coarse grained phengite laths to fine–grained white mica aggregates, the formation of symplectite after omphacite and the formation of Na (blue) to Na-Ca (blue-green) amphiboles, similar to the amphiboles described in Palin *et al.* (2014). Omphacite grains have dark symplectite rims of amphibole + plagioclase, with occasional diopside. Dolomite is present in the matrix as large poikiloblasts containing inclusions of phengite, omphacite and rutile.

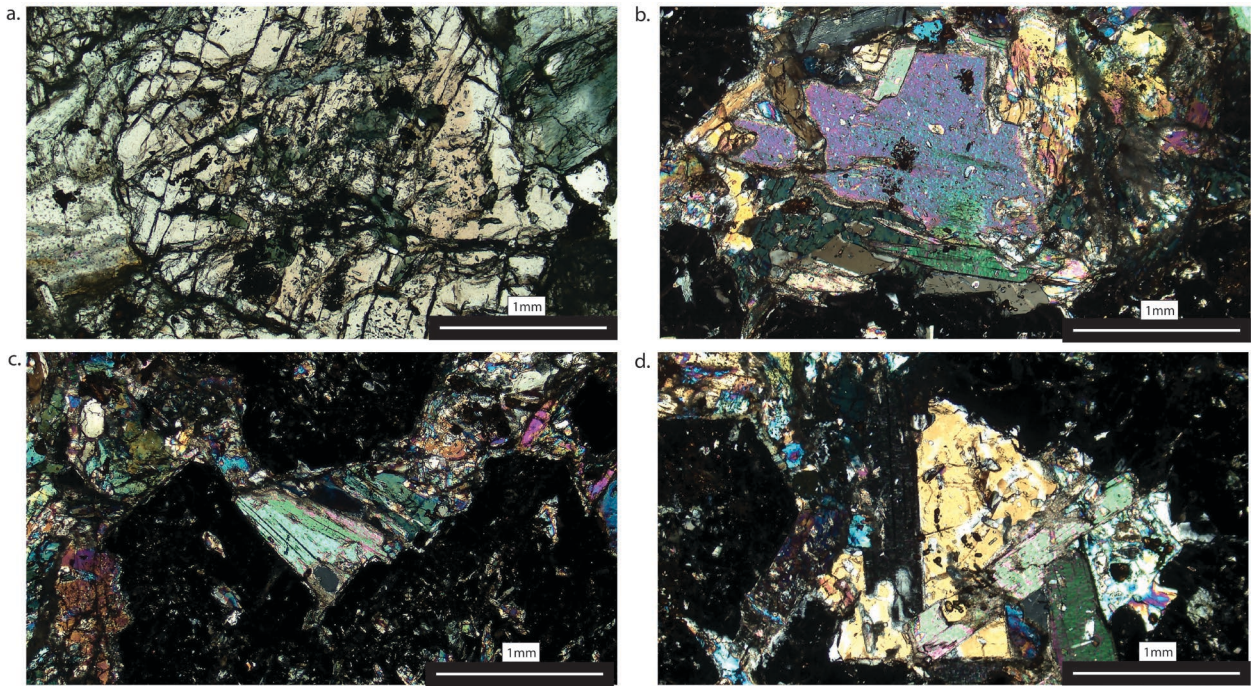


Figure 7 Photomicrographs of sample a03–16. a. PPL x10. Colour zoning in garnet with amphibole inclusions ranging in colour from blue to green. b. XPL x4. Talc, phengite, omphacite and quartz in contact in matrix of eclogite. c. XPL x10. Idioblastic phengite in contact with idioblastic garnet face. d. XPL x10. Omphacite, phengite, garnet with rutile inclusions

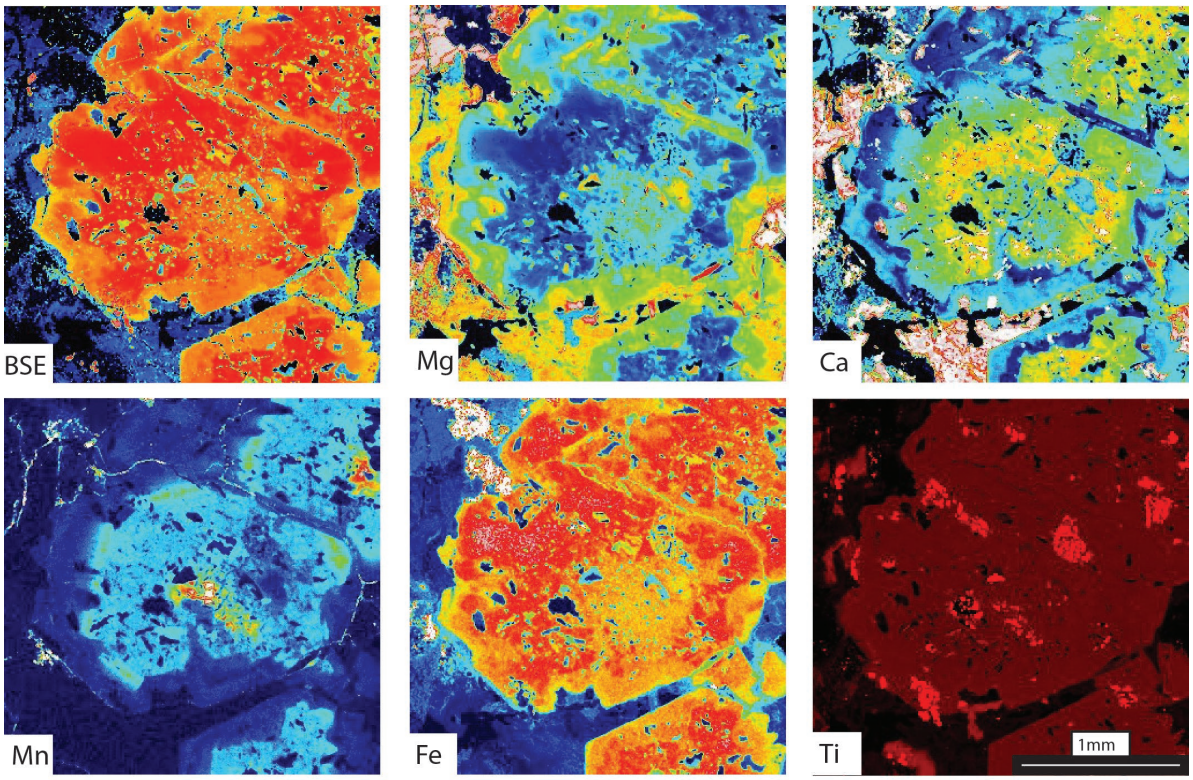


Figure 8 False–colour BSE map and element maps of garnet from sample a03–16. High–Mg embayments extend into and replace garnet core. Faceted Ca-trough surrounds high Ca core. Mn high in garnet core with Mn spike coincident with inner zone of Ca trough. Fe–rich rim and replacement of garnet core region. Bright rutile clusters pseudomorphing igneous titanium oxides

Kiagar La

The Kiagar La occurrence is located to the north east of Kiagar Tso, in a stream bed close to the road. It contains a 5 m high, bulbous eclogite boudin which stands proud at the edge of the stream bed. The surrounding gneiss is an augen gneiss with 5 cm long feldspar augens and variations in biotite minerals abundance on a scale of ~1 m. The outcrop itself contains vertical bands of pale and dark green, variably retrogressed eclogite ~ 3–4 cm wide, forming a network of anastamosing, interconnected channels, often associated with white veinlets, suggesting that their formation is related to the infiltration of a fluid phase.

The pale coloured stripes (sample 05-04B) consist of 1-2 mm idioblastic red garnets in a pale green matrix where fresh omphacite is occasionally visible with low Na (Jd 38-44%), $X_{Mg} > 0.8$ and $Fe^{3+} < 0.1$ (Figure 9). The darker bands (05-04C) have sharp, orange coloured contacts containing a high proportion of carbonates and contain weathered garnets of similar size and shape to the paler bands. Amphibole is present in the matrix and as rims around garnets, however the proportion of amphibole does not significantly increase in the darker colour channels. Symplectites after omphacite and poikiloblastic carbonate are abundant in the darker channels, giving it a dark green colour with rusty orange weathering.

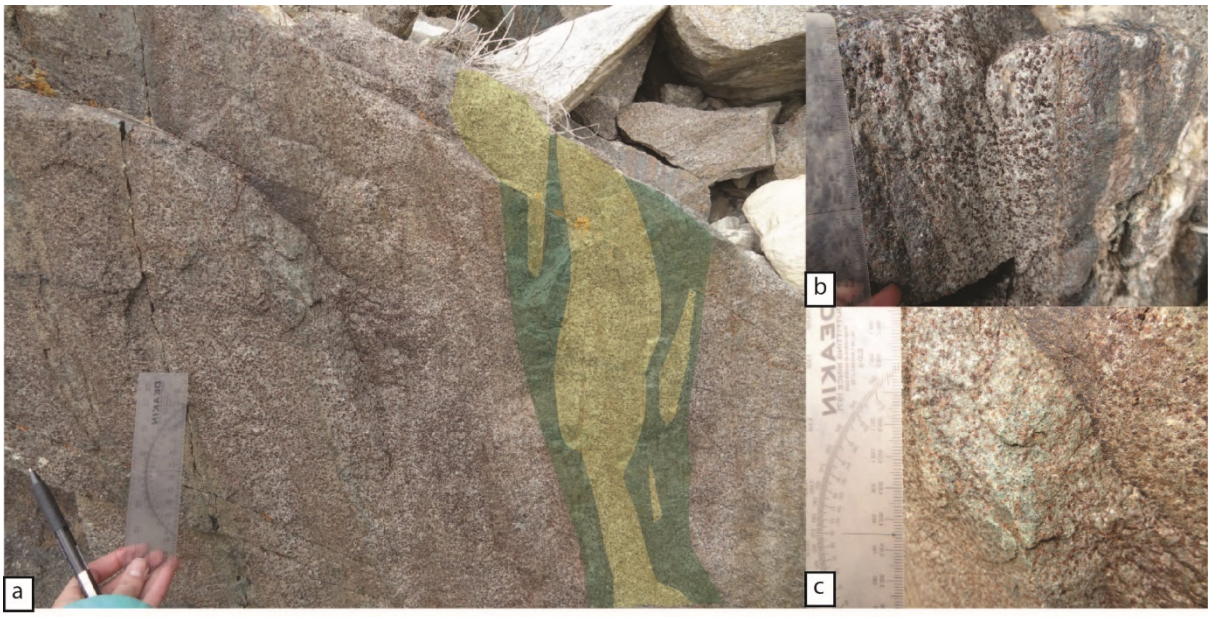


Figure 9 Outcrop relationships of sample 05-04D, equivalent to locality D2/8 in 2008 field guide (Caldwell, 2008). a) Stripy eclogite with green zones emphasising altered (green) domains and yellow emphasising fresher (paler) domains. b) Photo showing altered (dark green) verses fresher domains (white). Fresher domains contain garnet and omphacite, altered domain contain altered garnets and dark green amphibole. c) Fresh looking outcrop with garnet + omphacite

Sample 05-04D, is taken from the freshest part of the outcrop where garnets are glassy and unaltered. Compositional bands are visible on a 3 mm scale containing garnet–rich domains and omphacite–rich domains. There is no obvious foliation preserved in the rock. The major minerals are garnet (36.5%), omphacite (17%), talc (1%), phengite (4%), quartz (5%), dolomite (9.5%), magnesite, clinozoisite (6%), kyanite (<1%) and rutile (<1%). Garnet forms 1-2 mm idioblastic single grains and grain clusters with inclusion–rich cores and inclusion–poor rims. 0.5 mm omphacite grains are present in the matrix and as finer inclusions in garnet cores. They are surrounded by a thin (10-20 μm) symplectite rim consisting of amphibole (16.5% of total), Na-plagioclase (4% of total) and minor diopside, a phase common to symplectites in this sample but not often observed in other eclogite samples. Surrounding the garnets is a rim of blue–green amphibole that partially replaces garnet. Coarse talc and phengite are present in the matrix although not abundant, with a similar grain size to the matrix omphacite. Patches of phengite and talc are often associated with relict kyanite grains which started to break down, suggesting that kyanite is a peak phase, predating the hydrous sheet silicates in the matrix. Patches of quartz are often associated with talc and carbonate with inclusions of zircon and rutile. The single grains often span domains between garnets or are pinned by finer clinozoisite grains.

Carbonate is abundant in the matrix and as inclusions in garnet but has a heterogeneous distribution throughout the slide, with more carbonate in the garnet–rich domains. It is magnesite in composition, with areas partially altered to dolomite and with dark brown, Fe–stained, calcite rims. The edges of the carbonate grains form a flat edge with faceted garnet grains and a grain size similar to the omphacite, talc and quartz in the matrix. The grains themselves are not in contact owing to the presence of the brown calcite rims, a later feature forming from the alteration of dolomite. However, carbonate grains are never seen to encroach on surrounding grains. The grain size and shape of the magnesite indicates that it was likely a peak phase in equilibrium with garnet, omphacite and quartz. Inclusions in matrix carbonate include white mica, rutile, zoisite and quartz. White mica is present in the matrix although not abundant.

Garnets preserved prograde Mn–rich cores with relatively homogenous compositions in the inner core of $Alm_{63}Grs_{27–23}Py_{6–9}Sps_{3.5–1.6}$. The outer core shows a sharp stepped change in grossular and pyrope, often associated with a Mn–annulus which occurs at the outer core-inner rim divide. The inner rim shows a decrease

in grossular (25-17%) and a steep increase in pyrope (8.6-21%). A second Mn–annulus is observable within the inner rim in the high–resolution garnet maps and garnet transects, which corresponds to a slight change in slope in the pyrope increase and grossular decrease. The outer rim consists of a very thin zone where pyrope increases more rapidly to 30% and grossular remains approximately constant. The Mg–rich outer rim is not present on both garnet transects but can be picked out on the full slide garnet maps. Inclusions in the garnet cores include ilmenite, rutile, amphibole, zoisite, dolomite, carbonate and quartz, with amphibole, quartz, carbonate and zoisite in the rims. Coarse grained zoisite inclusions associated with paragonite often span the core-rim divide. Radial fractures around quartz are observed in the garnet rim zone.

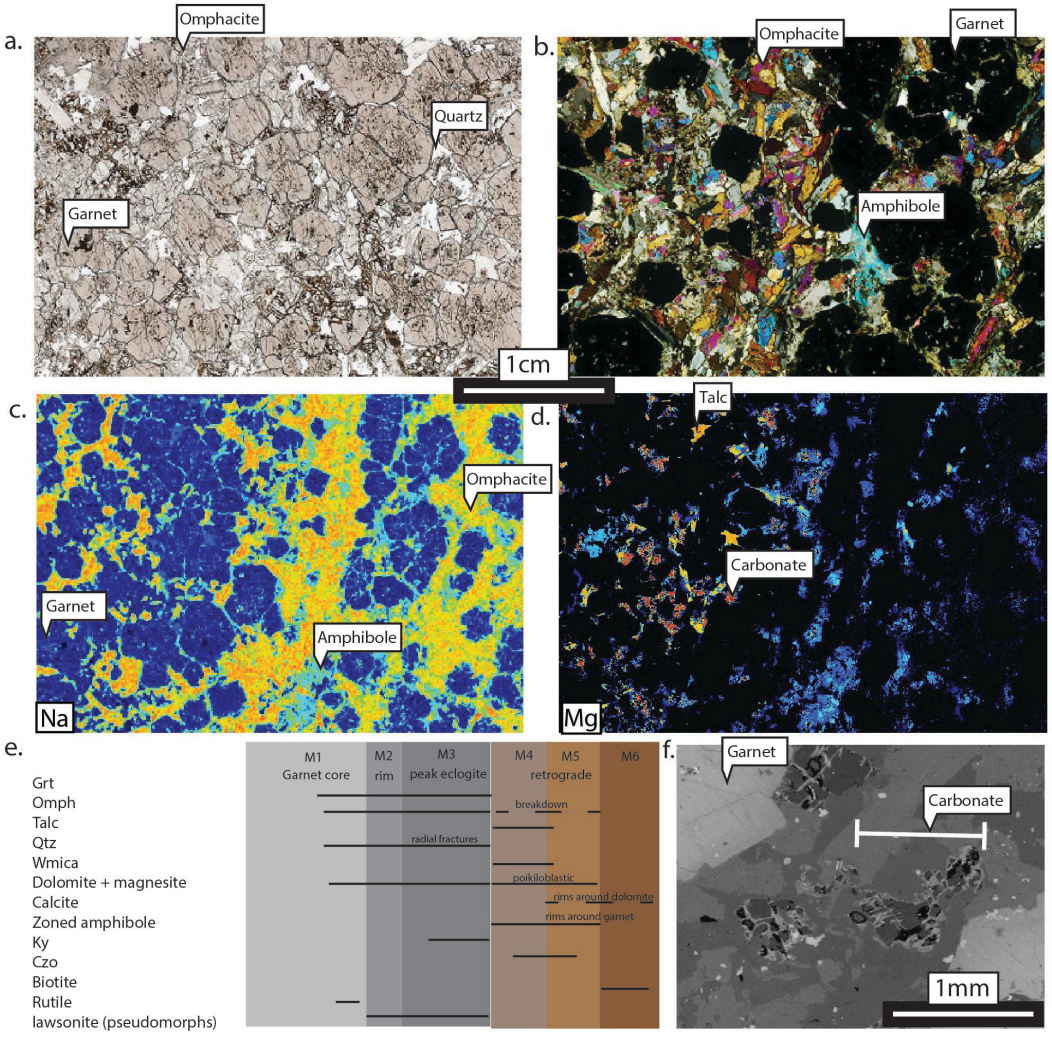
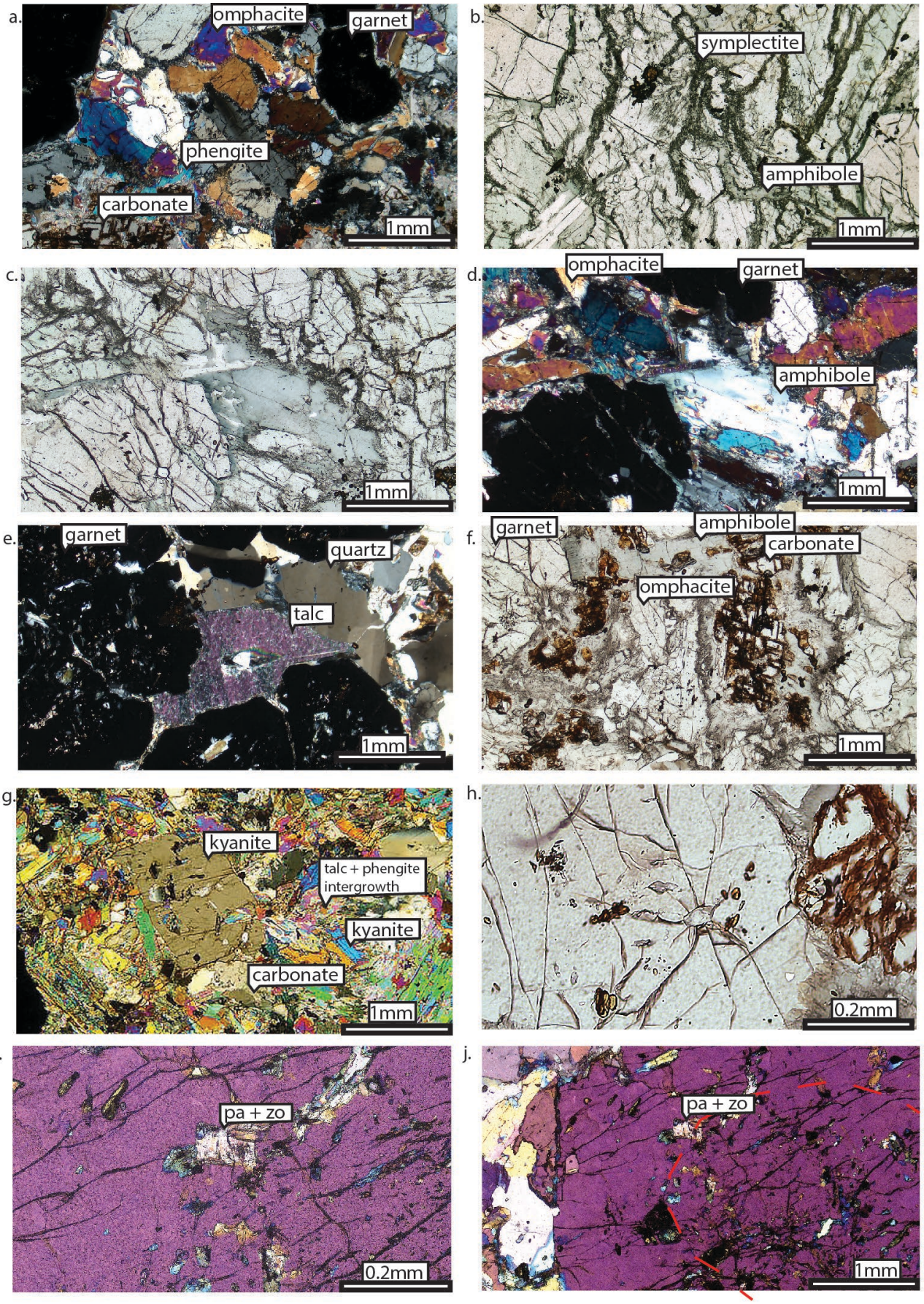


Figure 10 Sample 05–04D, Photomicrographs in a. PPL and b. XPL showing major mineral phases. c. Na-map distinguishing omphacite (red/yellow) and amphibole (blue/green). d. Mg-map showing dolomite (red) and talc (orange). e. Microstructural history diagram summarising relative timing of mineral growth. f. BSE image of carbonate phases. Black = magnesite, dark grey = dolomite, light grey rim = calcite


a.
omphacite
garnet
phengite
carbonate
1mm
b.
symplectite
amphibole
1mm
c.
1mm
d.
omphacite
garnet
amphibole
1mm
e.
garnet
quartz
talc
1mm
f.
garnet
amphibole
carbonate
omphacite
1mm
g.
kyanite
talc + phengite
intergrowth
kyanite
carbonate
1mm
h.
0.2mm
i.
pa + zo
0.2mm
j.
pa + zo
1mm

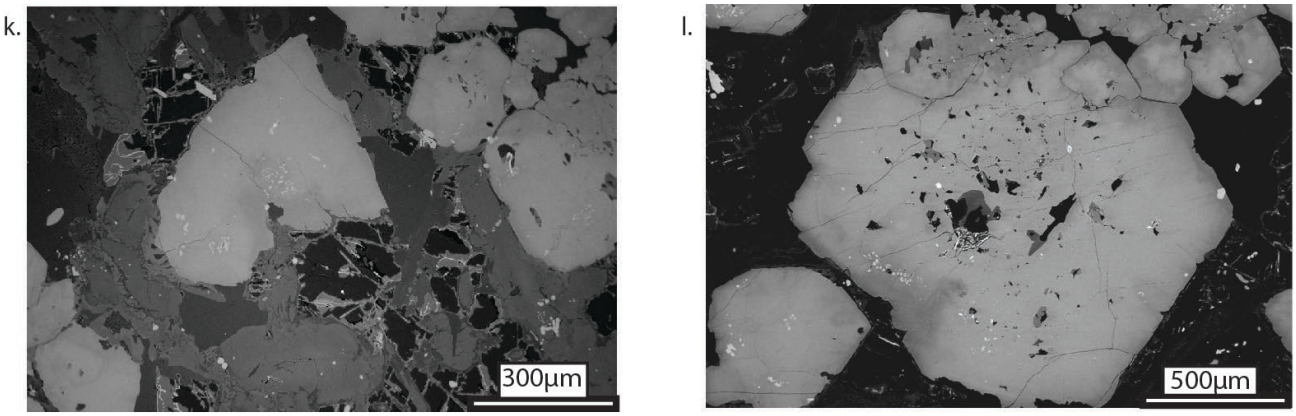
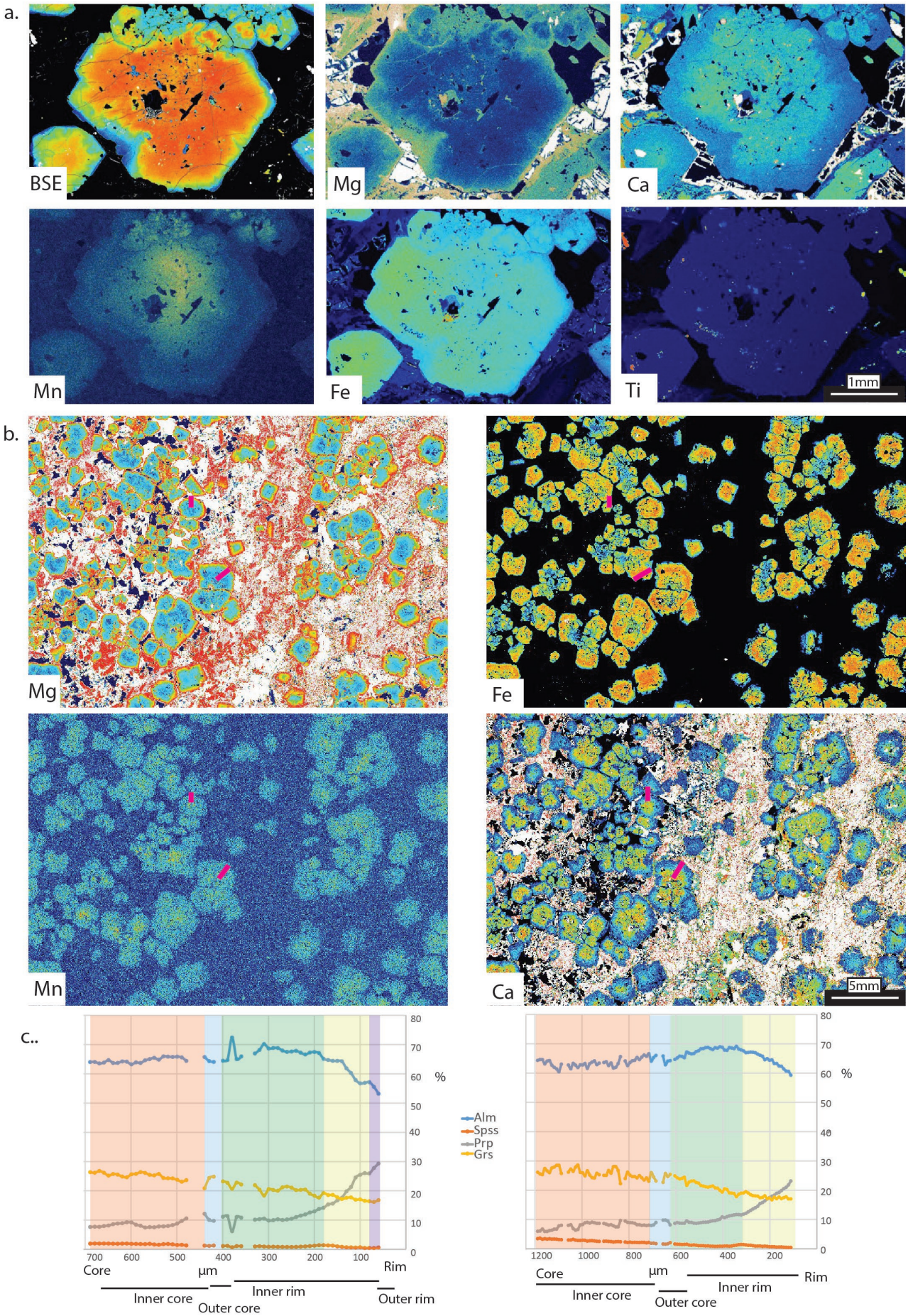


Figure 11 Sample 05–04D a. and b. XPL and PPL photomicrographs of matrix omphacite grains with symplectite and blue–green amphibole along the grain boundaries. c. and d. Zoned blue–green amphibole in matrix, between garnet and omphacite grains. Top of amphibole is encroached by symplectites after omphacite. e. Coarse talc grain in contact with garnet facets and quartz. Quartz exhibits elongate subgrains. f. carbonate with brown calcite rim between omphacite grains with zoned amphibole and symplectites after omphacite between grains. g. Relict kyanite in patch of talc and phengite. Fine relict grains in optical continuity with larger grain. Twinned kyanite grain surrounded by talc and phengite. Carbonate grains visible on left. h. quartz inclusion in garnet with radial fractures i. rectangular intergrowth of paragonite + zoisite after lawsonite. j. rectangular intergrowth of paragonite + zoisite after lawsonite and location of boundary between inclusion–rich core and inclusion–poor rim. k. BSE image of zoned garnet with rutile inclusions. Dark grey magnesite, altered to pale grey dolomite, is visible next to garnet. Bright rims of calcite around dolomite. l. BSE image of zoned garnet with inclusion rich poor. Darker rim defined by low calcium zone. Multiple garnet grains have nucleated and grown on top side of coarse garnet.

Figure 12 (below) Sample 05–04D. a. EDS element maps of garnet showing prograde Mn–rich core, Mn annulus, Ca trough at the rime, high Mg rim. b. full slide probe maps showing variations in garnet zoning across the slide. Location of garnet transects are shown as pink lines. c. Two transects from core to rim of garnet.


a.
BSE
Mg
Ca
Mn
Fe
Ti
1mm
b.
Mg
Fe
Mn
Ca
5mm
c..
%
Alm
Spss
Prp
Grs
Core
Rim
μm
Inner core
Outer core
Inner rim
Outer rim

Berthelsen outcrop

The Berthelsen outcrop is located closer to the Zildat shear zone on the northern edge of the dome. Within the cliff section, multiple mafic boudins are arranged linearly within the foliation of the Puga Gneiss, which wraps the boudin. The largest boudin is approximately 2 m high and 10 m long and is the location of samples JU11, JU12 and JU13, which form a transect form rim to core of the boudin respectively. There are many 5-15 m large angular blocks at the base of the cliff which have fallen from the cliff and contain some of the freshest eclogite samples (JU13a).

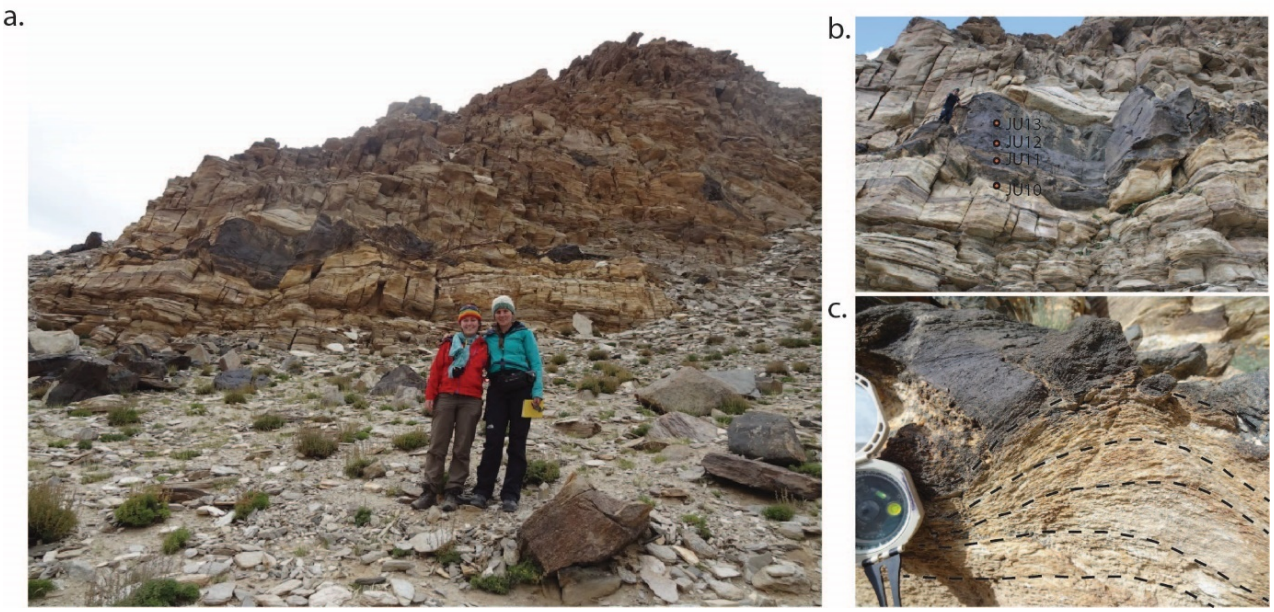


Figure 13 Field photographs of the Berthelsen outcrop. a. Photograph showing linearly arranged mafic boudins hosted in Puga Gneiss. b. Main boudin with the location of sampled transect. c. Foliation in the gneiss and amphibolite at the margin of the boudin.

Samples from this outcrop are coarse grained eclogites with a granoblastic texture and contain strongly colour zoned garnets (1.8 mm diameter) with a darker, inclusion–rich core and inclusion–poor rim. Major minerals include garnet (36%), omphacite (13.5%), zoned amphibole (24%), quartz (1.3%), rutile (<1%), carbonate (1%), clinozoisite (15%), white mica (4.7%) including paragonite, phengite. Talc occurs in this sample as inclusions in garnet and in the matrix, particularly at omphacite triple junctions in sample L08-03B, suggesting that it was in equilibrium with omphacite, perhaps resulting from the breakdown of glaucophane. Symplectites forming after omphacite look dark in thin section and are composed of amphibole (magnesiohornblende and actinolite compositions), plagioclase (An_{2-14}) and occasionally diopside (St-Onge

et al., 2013), with more amphibole present in the more hydrated samples. Phengite (Si = 6.89-7.02 pfu) and paragonite occur in the matrix and as inclusions within omphacite (St-Onge et al., 2013).

Zoned garnets make up a large proportion of the rock, the core of which are marked by a sharp drop from 4% to 1.5% spessartine. The core region contains abundant and varied mineral inclusions and shows patchy composition variation at low grossular content. The core region is followed by a sharp drop in spessartine and grossular and an increase in pyrope and almandine. The Ca-trough outlines faceted garnets with numerous inflection points perhaps indicating multiple nucleation around a single nucleated garnet core. Towards the garnet rim, there is a marked drop in spessartine and grossular and an increase in pyrope and almandine, with the maximum pyrope content at the rim ($Alm_{0.45}Grs_{0.195}Prp_{0.35}Sps_{0.01}$). The garnet rim has few inclusions in its euhedral outline is often corroded except in the freshest samples and locally replaced by high–Al-Fe amphibole.

High resolution EDS and BSE maps (Figure 14) were obtained by the master's student Jack Utting, supervised by Dave Waters. The results of this study are currently unpublished and are summarised in the following paragraph and in Figure 14: High resolution maps highlight textural and compositional domains within the core of the garnets. The garnet cores show a faceted nature around the inclusion–rich garnet core, with a distinctive "netted" texture. Angular patches with sharp boundaries, rounded patches with diffuse boundaries and networks of veins or channels can all be observed. Mg-Ca patches form polygonal domains with elevated Mg surrounded by zones of maximum Ca with sharp boundaries in between. The composition of these domains follows the overall zoning trend but lie towards more evolved compositions. The netted texture is due to variation in the pyrope component of garnet, with higher–Mg (and low Fe) garnet appearing as darker areas on BSE images. These channels have been observed to extend from embayments of high–Mg garnet that originate at the edge of the garnet porphyroblasts and cross–cut any facets that are visible in the external edge of the garnet core.

Matrix amphiboles show a range of mineral chemistry (Figure 22), with occasional glaucophane–rich cores, barroisite/winchite cores and magnesiohornblende rims. The garnet core region contains a range in amphibole compositions from glaucophane–rich cores to pargasite–rich magnesiohornblende rims, forming a continuous array of increasing edenite and tschermakite, decreasing glaucophane and X_{Mg} from winchite through

barroisite, taramite and pargasite. Rectangular clinozoisite/paragonite intergrowths occur at the core/rim boundary. Omphacite is present in garnet rims (Na = 043-047 pfu), clinozoisite poikiloblasts (Na = 0.44-0.49) and in the matrix (Na = 0.44-0.50 pfu) (St-Onge *et al.,* 2013).

Samples JU12 and JU11 are taken from progressively closer to the margin of the boudin. Sample JU11 contains abundant amphibole with bands of biotite, often forming along the hinge of an open crenulation cleavage. Clinozoisite is present and aligned with the schistosity and carbonate is present as poikiloblasts within lenses, wrapped by the biotite rich bands. Garnet is absent from the matrix of sample JU11 but is present as inclusions in coarse matrix amphiboles. Garnet has been observed in varying states of hydration from this outcrop, from pristine and sharply zoned, to atoll garnets (O'Brien & Sachan 2000; St-Onge *et al.* 2013; Jonnalagadda *et al.* 2017). All of these garnets are observed to have the full suite of amphibole compositions.

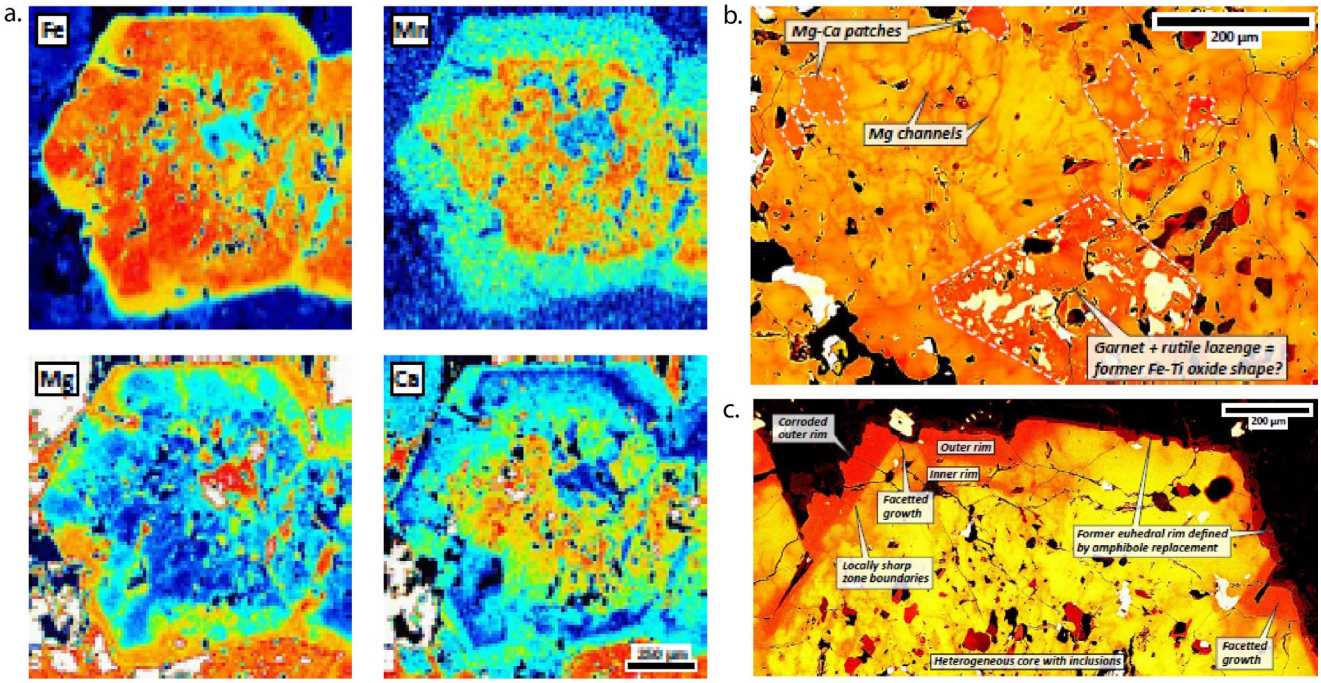


Figure 14 Sample L08–03B a. Fe, Mn, Mg and Ca maps showing garnet zonation, faceted Ca troughs and Mg–embayments b. False colour BSE image showing features of heterogeneous core domain in garnet. c. false colour BSE image showing typical zoning features in garnet including faceted growth.

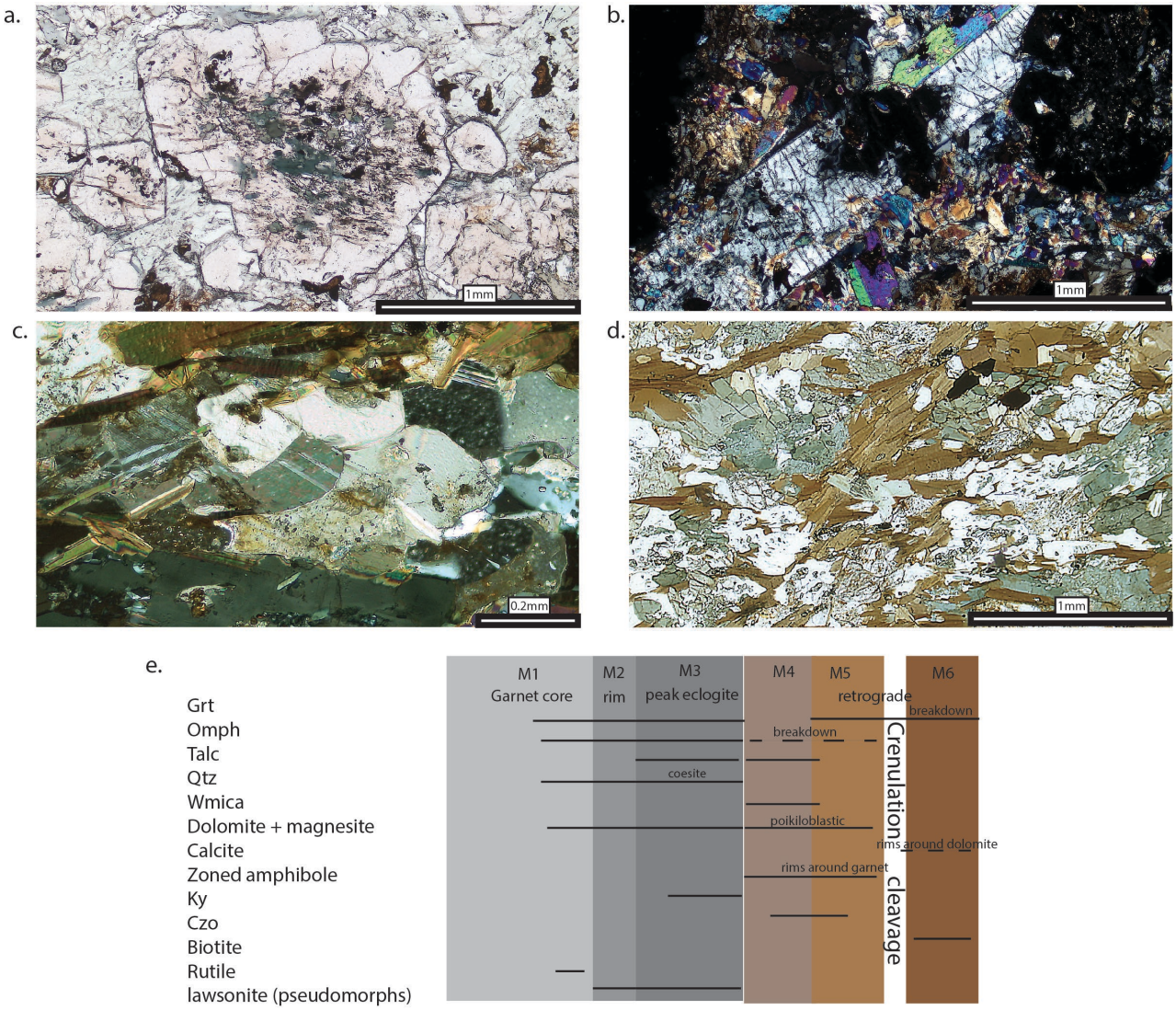


Figure 15 a. Sample a03–21 from core of eclogite boudin. Variation in colour of amphibole inclusions and around garnet visible. b. Sample a03–21 from core of eclogite boudin. Coarse clinozoisite grain in matrix. c. Sample JU11 from rim of boudin. Carbonate lens wrapped by biotite. d. JU11 from rim of boudin. Blue/green amphibole and biotite in matrix with carbonate, albite and quartz. High relief epidote associated with biotite bands. e. Microstructural history diagram

Puga Valley

Within the Puga valley, there are many small retrogressed mafic eclogite boudins, which occur in linearly arranged clusters. Sample 10-05 is fine grained eclogite, taken from an outcrop approximately 10 m above the base of the cliff, containing 0.5 mm garnet poikiloblasts with green amphibole rims and an irregular outline. Major minerals include garnet (21%), omphacite (21%), amphibole (27.5%), carbonate (10%), plagioclase (6.5%), clinozoisite (4%), phengite (3%), talc (4.5%), quartz (2%).

The matrix omphacite has a shape preferred orientation and a patchy texture when viewed in cross polarised light, suggesting abundant recrystallisation has occurred (Figure 17). In BSE images, the omphacite has a patchy texture and an inclusion–rich core region which is brighter using back scattered electron imaging, preserving a jadeite content of 41–55%, an X_{Mg} content of <0.8 and a calculated Fe^{3+} content of 0.06 to 013 cations pfu. The inclusion–poor, darker rims have a jadeite content of 37–54%, an X_{Mg} content of >0.8 and a calculated Fe^{3+} content of 0 to 0.06 (Figure 25). The darker rim regions also form channelised structures which cut cross the core region of the pyroxene. Pyroxene grains have later been altered to intergrowths of amphibole and plagioclase ± diopside, which show a gradient from fine to coarse grain size. A gradient in symplectisation of omphacite can be seen across the slide, whereas green amphibole is abundant throughout.

Matrix amphibole is present as coarse grains with undulose extinction and occasional stripy twins which crosscut the cleavage. Matrix amphibole compositions are plotted in Figure 23 and show a decreasing glaucophane composition from core to rim, with increasing edenite and tschermakite. The compositional trends show a pargasite vs $FeMg^{-1}$ exchange vector with a kinked shape with increasing pargasite. Matrix carbonate is present as irregular relict grains, heterogeneously distributed, often associated with white mica.

Sample 10-02, taken from ~200 m away from sample 10-05 in the Puga valley, is more retrogressed and is SiO_2 saturated. Blue-green amphibole needles in the matrix are partially replaced by biotite. Garnet is more irregular and forms relicts within 1 mm hexagonal domains which are sometimes completely replaced by amphibole, biotite and epidote and pseudomorph an earlier coarse–grained texture.

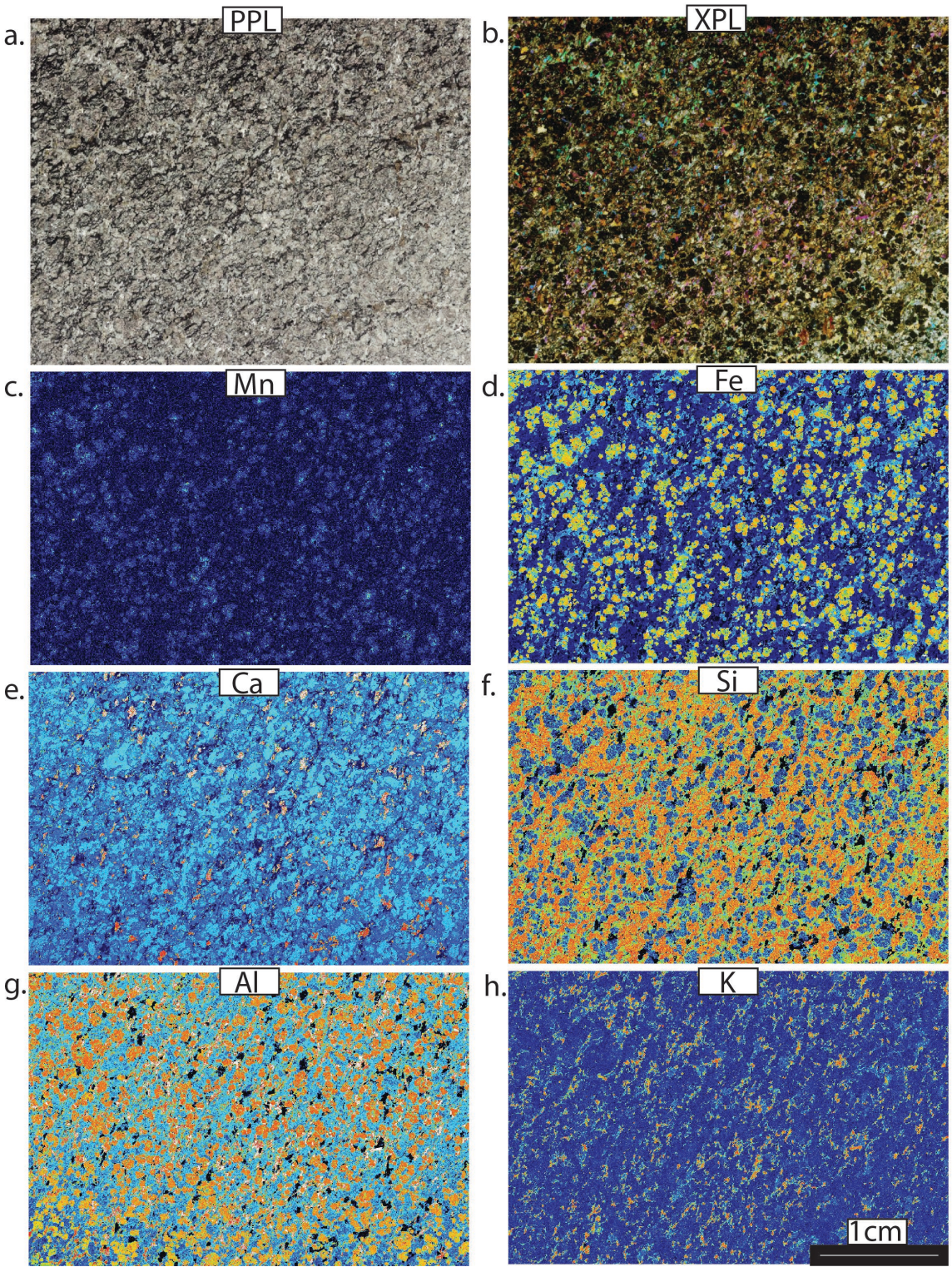
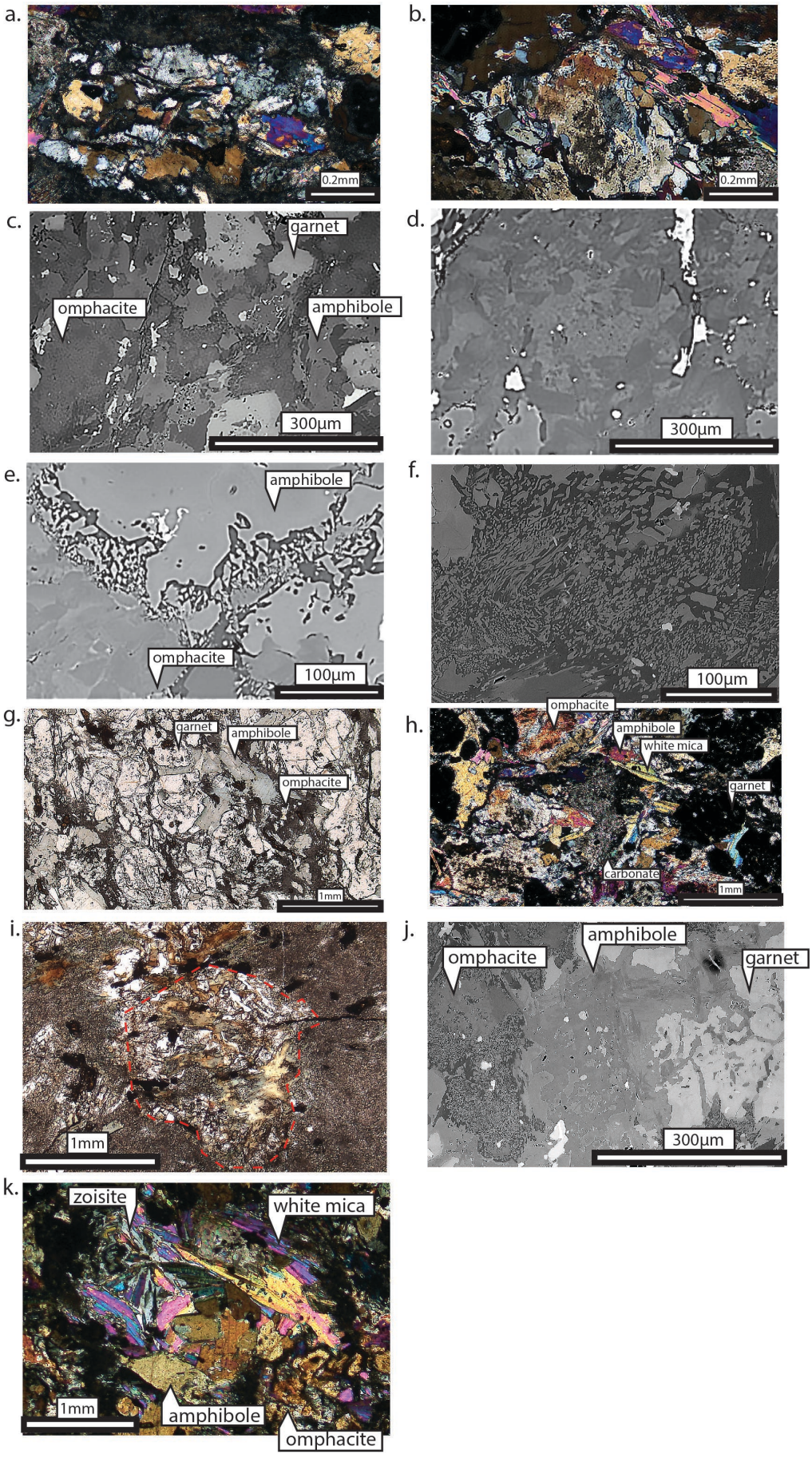


Figure 16 Whole slide scans (a. and b.) of sample 10–05 from the Puga Valley showing fine grained nature of sample are dark symplectites. Element maps (c. to h.) of sample 10–05. c. Mn map shows prograde garnet zoning. d. Fe map allows differentiation between garnet (yellow/orange), amphibole around garnet (light blue) and matrix omphacite (dark blue). e. Ca map shows f. Si map allows differentiation between garnet (dark blue), amphibole around garnet (pale green) and matrix omphacite (orange). g. Al map shows orange garnets with bright Al–rich phengite in the matrix. Note gradient across the slide from beam drift. h. K map shows location of phengite (orange)


a.
0.2mm
b.
0.2mm
c.
garnet
omphacite
amphibole
300µm
d.
300µm
e.
amphibole
omphacite
100µm
f.
100µm
g.
garnet
amphibole
omphacite
1mm
h.
omphacite
amphibole
white mica
garnet
carbonate
1mm
i.
1mm
j.
amphibole
omphacite
garnet
300µm
k.
zoisite
white mica
1mm
amphibole
omphacite

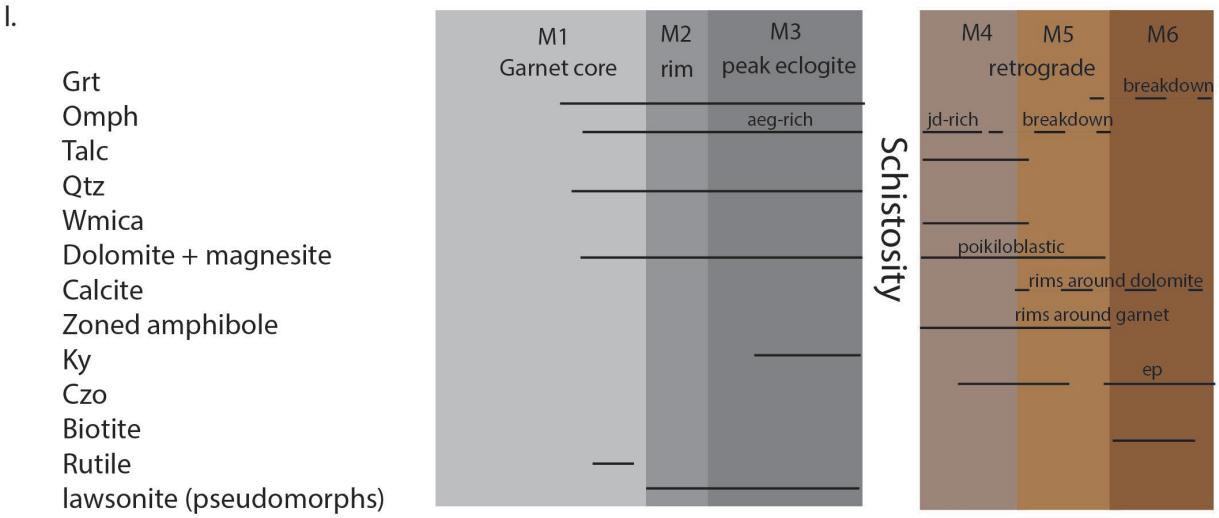


Figure 17. Sample 10–05 a. oriented omphacite grains with dark symplectite rims. b. Omphacite grain in XPL showing patchy texture. c. BSE image of patchy omphacite surrounded by symplectite, coarse zoned amphibole and inclusion–rich garnets. d. BSE image of omphacite grain with patchy texture. Brighter regions have higher Fe content. e. Coarse amphibole and patchy pyroxene with symplectite intergrowth along grain boundary. F. BSE image of symplectite of amphibole + plagioclase after omphacite showing a gradient in grain size which coarsens towards the amphibole and is finest surrounding relict pyroxene. Core of the symplectite forms elongate amphibole texture. g. Sample 10–05. garnet and omphacite with interstitial green amphibole and dark symplectite. h. Sample 10–05. relict carbonate grain surrounded by white mica and amphibole. Omphacite with dark symplectite and garnet also visible. i. Sample 10–02. hexagonal pseudomorph after garnet with green amphibole, partially replaced by brown biotite and high relief, colourless epidote. j. Sample 10–05. irregular garnet with amphibole rim, coarse zoned amphibole, relict omphacite replaced by symplectite. k. Sample 10–05. relict carbonate in a patch surrounded by white mica, radial zoisite and idioblastic amphibole. l. Microstructural history diagram

Mineral	*Location*	*SiO_2*	*TiO_2*	*Al_2O_3*	*FeO*	*MnO*	*MgO*	*CaO*	*Na_2O*	*K_2O*	*Total*	*Si*	*Ti*	*Al*	*Fe^{3+}*	*Fe^{2+}*	*Mn*	*Mg*	*Ca*	*Na*	*K*	*Sum*	*Ox*	*X_{Mg}*
Px	Matrix, core	55.67	0.05	9.58	5.63	0.01	8.24	13.83	7.09	0.01	100.1	1.97	0.00	0.40	0.13	0.04	0.00	0.44	0.53	0.49	0.00	4	6	0.72
Px	Matrix, rim	56.31	0.04	11.25	2.64	0.01	8.98	14.11	7.12	0.00	100.46	1.97	0.00	0.47	0.07	0.01	0.00	0.47	0.53	0.48	0.00	4	6	0.86
Grt	Average spherical Grt											2.93	0	2	0	1.88	0.01	0.23	0.86	0.00	0.00	8	12	
Grt	Core	36.49	0.17	20.51	28.48	0.63	0.22	11.72	0.023	0.01	99.25	2.95	0.01	1.96	0.00	1.93	0.04	0.15	1.02	0.00	0.00	8.06	12	
Grt	Outer rim	38.22	0.04	21.09	28.24	0.30	5.19	6.19	0.00	0.01	99.28	3.02	0.00	1.96	0.00	0.86	0.02	0.61	0.52	0.00	0.00	8.00	12	
Amph	Symplectite after Omph	47.88	0.21	11.81	12.33	0.11	11.27	9.15	3.35	0.33	96.44	7.01	0.023	2.04	0.00	0.51	0.013	2.46	1.43	0.96	0.06	15.51	23	
Pl	Symplectite after Omph	64.74	0.003	21.55	0.20	0.018	0.18	2.74	9.53	0.07	100.03	2.75	0.00	1.06	0.00	0.01	0.00	0.01	0.13	0.77	0.00	4.72	8	
Bt	Rim on Grt	36.10	0.10	20.07	15.40	0.10	12.57	0.02	0.14	9.53	94.03	2.97	0.006	1.95	0.12	0.94	0.01	1.54	0.002	0.02	1.00	8.56	12	
Phe	matrix	51.86	0.28	28.97	1.51	0.002	4.43	0.04	0.33	8.41	95.83	6.75	0.02	4.45	0.00	0.16	0.00	0.86	0.006	0.08	1.40	13.74	22	
Czo	matrix	38.80	0.16	28.04	5.41	0.045	0.00	24	85	0.03	0.06	1.69	0.005	1.44	0.00	0.19	0.00	0.00	1.16	0.003	0.004	4.49	7	

Table 2 Representative mineral compositions for sample 10-05

Polokongka La pass

Near the top of the Polokongka La pass, mafic sills are hosted within an undeformed granite with a foliated garnet–bearing margin in the felsic rock and a foliated amphibolite margin on the dykes. The mafic dyke contains sparse, white rectangular pseudomorphs after phenocrysts of up to 0.5 mm long, in a finer grained matrix. The pseudomorphs contain coarse white mica with evidence of kink banding, 0.5 mm poikiloblastic carbonate with an idioblastic rhombohedral shape and high relief, patchy grey diamond shaped zoisite grains and form pseudomorphs after igneous plagioclase. Carbonate forms straight contacts with coarse–grained white mica which has simple twins (paragonite). Quartz is also present in the rectangular pseudomorphs with undulose extinction and inclusions of zircon and rutile.

In samples a04-31 and a04-30, garnets (45%) form 1-2 mm idioblastic poikiloblasts in the matrix with white mica (12%), clinozoisite (10%), carbonate (7%) and green amphibole (10%). The inclusion rich cores contain abundant rutile clustered into diamond–shaped regions, zoisite needles and quartz. Relict omphacite grains are outlined by dark symplectites (13.5%) which partially replaces the omphacite, giving it a granular appearance. Sample a04-30 has blue-green amphibole (10%) and biotite (2.5%) coronas around idioblastic garnet with a slightly irregular outline. The matrix is predominantly composed of fine–grained symplectite, garnet poikiloblasts and coarse–grained zoned amphibole. Coarse, 0.6 mm, rectangular regions of opaque oxide are present throughout the matrix.

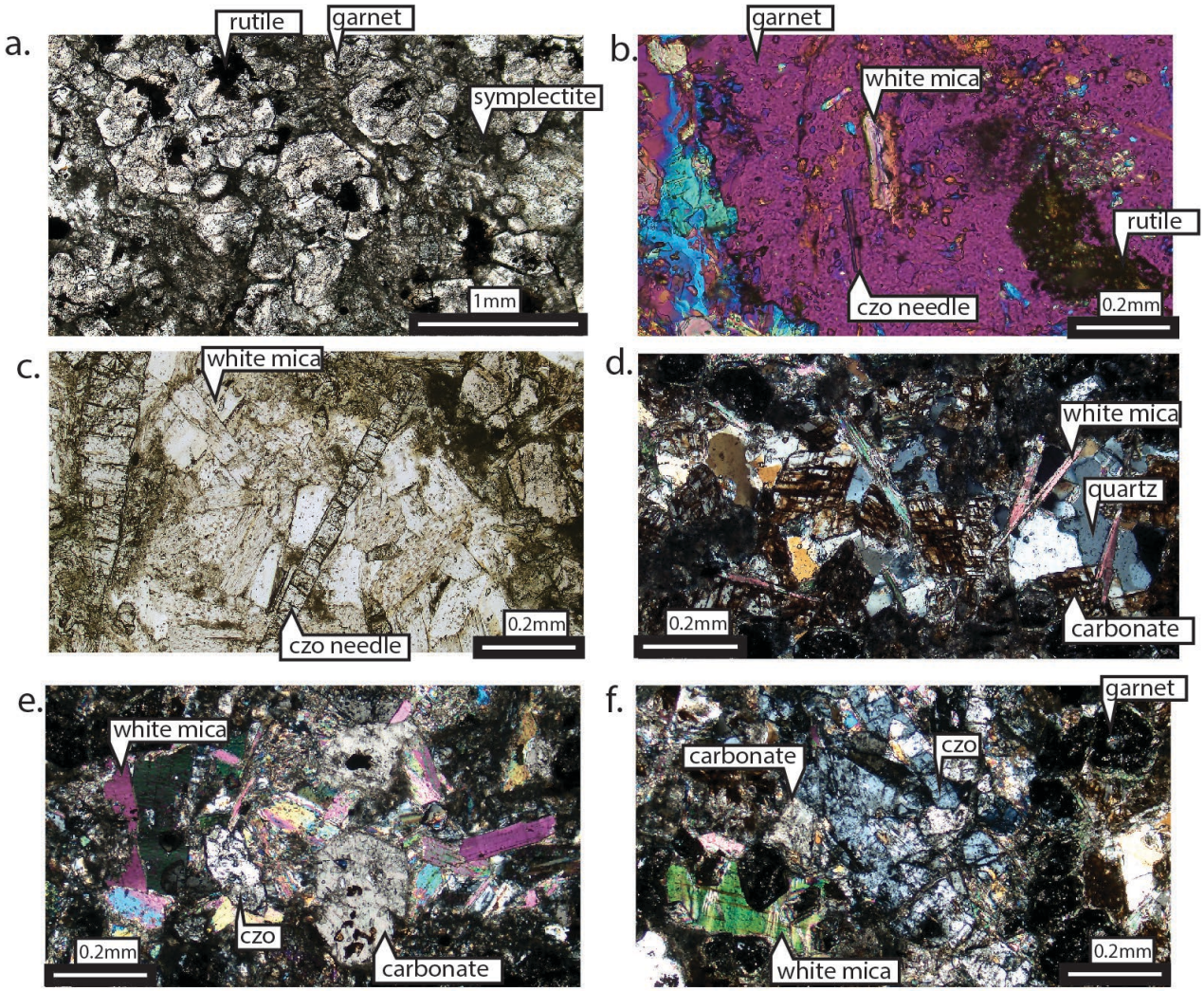


Figure 18 Sample a04–31. a. PPL. garnets in a matrix of fine–grained symplectite with coarse grained rutile clusters. b. XPL + gypsum plate. needles of clinozoisite in the core of a garnet with a coarse rutile pseudomorph. c. rectangular pseudomorph of white mica with clinozoisite needles. d. dolomite grains with brown calcite rims, white mica and quartz with undulose extinction. e. rectangular pseudomorph containing carbonate with rutile inclusions, white mica and high relief clinozoisite. f. rectangular pseudomorph containing clinozoisite needles, kinked white mica, quartz, carbonate, rutile and garnet

Polokongka La ridge

Samples 11-05, -06 and -07 are taken from the mafic sill within the Polokongka La granite and form a transect from core to rim of the 30 m wide sill respectively. The margins of the sill and adjacent granite are strongly sheared and weather as proud outcrops in a boulder strewn landscape. Further away from the contact, the frost–shattered landscape is composed predominantly of macroscopically undeformed granite.

Sample 11-05 is a coarse–grained mafic eclogite with a bimodal texture of coarse clustered garnet (24%), omphacite (10%), talc (1%), phengite (16%), quartz (8%) and clinozoisite (8%) with interstitial sodic-calcic

amphibole (17%) and plagioclase (14%), and minor amounts of kyanite, rutile, apatite, biotite and paragonite. Compositional heterogeneity is present throughout the rock on a centimetre scale where domains of omphacite, white mica and talc and domains of garnet and quartz are dominant. Within the omphacite domains, alignment of omphacite and white mica is evident and wraps around garnet poikiloblasts. Subgrains are present within omphacite grains which are crosscut by poikiloblasts of zoisite which also crosscut the aligned micas, indicating that deformation took place in the eclogite facies. Omphacite has a jadeite content of >50%, X_{Mg} < 0.8 and Fe^{3+} 0.11-0.13 (Figure 25). Phengite and talc occur in clusters, often arranged radially, with relict kyanite grains in the core (Figure 20g). Zoisite has a dark grey core and lighter grey rims, whereas clinozoisite has an anomalous blue colour indication it has an Fe rich composition.

Garnet occurs as euhedral porphyroblasts, ~1-2 mm diameter, with faceted edges in textural equilibrium with the quartz domains. The garnet poikiloblasts show textural and compositional zoning with inclusion–rich cores and inclusion–poor rims. The garnet core inclusions form a fabric with s–shaped microstructures which are truncated at the core-rim boundary. Inclusions in garnet are composed of sodic-calcic amphiboles, rutile, clinozoisite, quartz and biotite. The inclusion–poor rims of the garnets contain quartz, rutile and coarse clinozoisite + paragonite composite inclusions which occur at the core-rim boundary.

Inclusion–rich cores of the zoned garnets have a roughly constant composition with low pyrope and high grossular ($Py_{7–10}Grs_{30}Sps_3Alm_{24}$). Compositional zoning in the garnets allow subdivision into an inner core, outer core, inner rim and outer rim as shown on the zoning profile and in the table below showing increasing pyrope and almandine and decreasing grossular contents towards the rim ($Py_{30}Grs_{15}Sps_1Alm_{18}$). The outer core zone shows a sharp change in composition from the plateaued inner core region to an inner rim with a steeper gradient in composition. This sharp change in composition also marks a sharp textural break in the garnet from an inclusion–rich core to an inclusion–poor rim. The inner rim zone shows a sharp increase in almandine with a slight increase in pyrope and a sharp decrease in grossular. The outer rim zone is narrow and resorbed in many examples but is thickest when in contact with matrix quartz. It shows a sudden decrease in grossular and a steep increase in pyrope. This is reflected in the almandine content which increases as grossular decreases and then decreases as pyrope approaches its maximum at the outermost part of the rim. Spessartine content shows a steady decrease from core to rim.

Samples 11-06 and 11-07 are taken from the same mafic dyke, closer to the sheared margin and show features related to extensive hydration of an eclogite. Coarse, zoned blue-green amphibole occurs in the matrix and around garnet with a range of compositions from winchite, with increasing tschermakite and edenite contents towards a pargasitic rim. Biotite is also observed to be replacing garnet and occurs in interconnected channelised zones on the thin section scale, ~ 3-4mm width. Omphacite has been completely replaced by fine grained intergrowths of plagioclase and amphibole.

	Inner core	***Outer core***	***Inner rim***	***Outer rim***
Almandine	61%	62–55%	55–62%	62–65–59%
Grossular	30–28%	28–35%	35–30–26%	25–17–15%
Pyrope	7–10%	10–8%	8–12%	13–17–25%
Spessartine	3–1%	1%	1%	<1%

Table 3 Sample 11-05. Composition of garnet zones

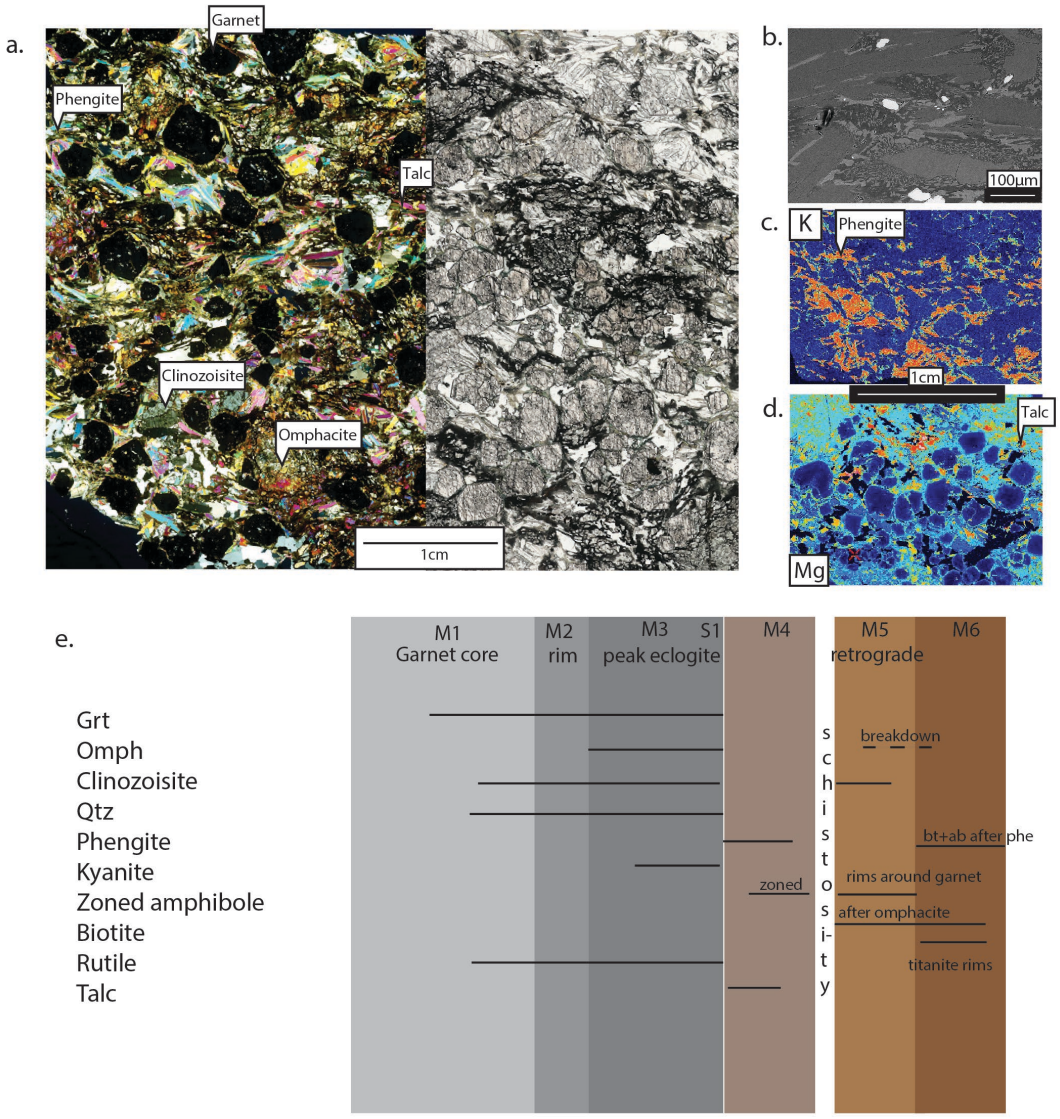


Figure 19 Photomicrographs and phase maps sample 11-05 from the Polokongka La ridge. A. Sample 11-05 Photomicrographs in PPL and XPL. B. BSE image showing symplectite breakdown around omphacite C. K–map showing the distribution of white mica (orange). D. Mg–map showing the distribution of talc (red). E. Microstructural history diagram summarising relative timing of mineral growth and fabric development

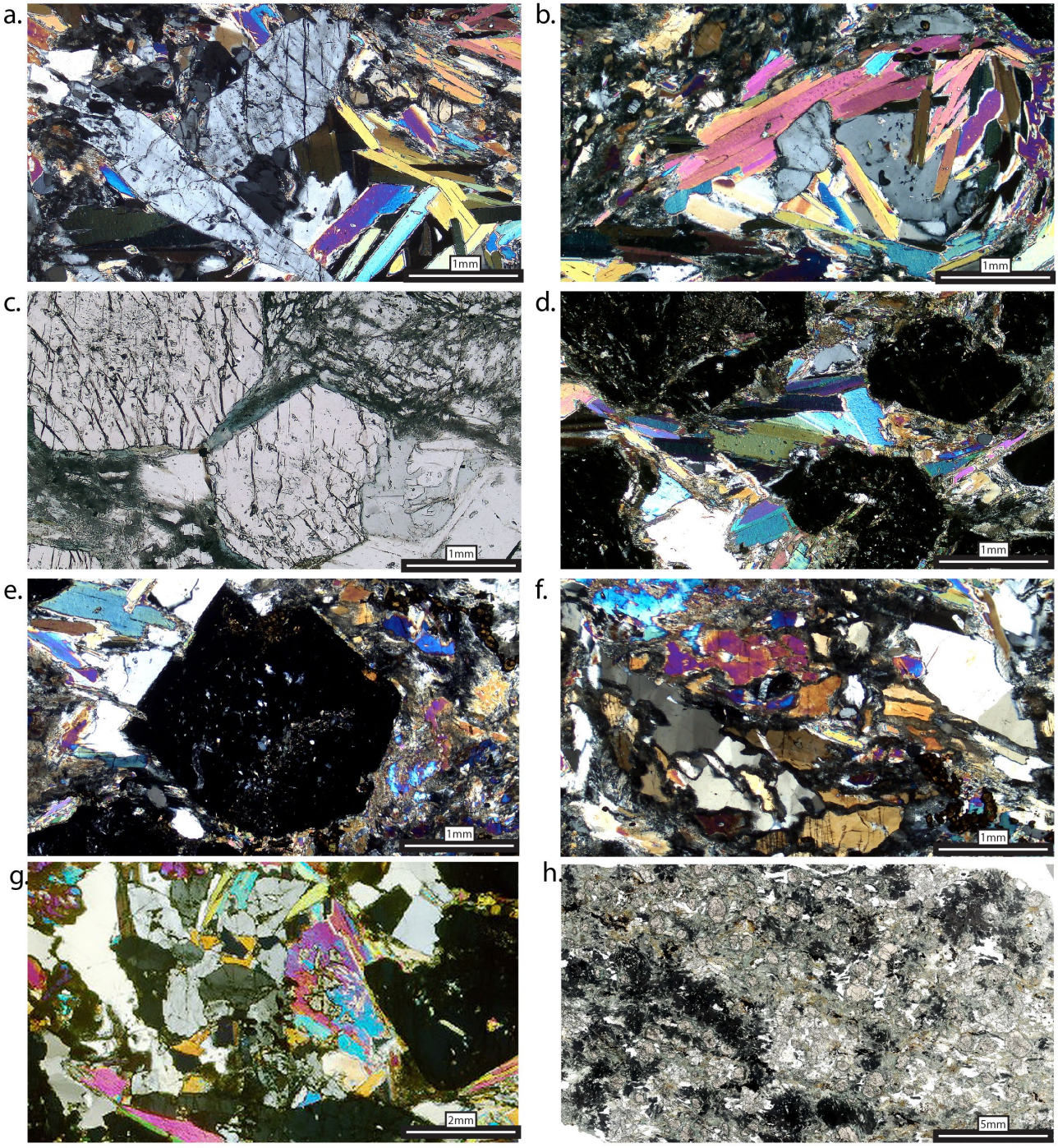


Figure 20 Sample 11-05. a. Coarse zoned clinozoisite grains overgrowing matrix white mica. b. Phengite + talc cluster overgrown by clinozoisite porphyroblast. c. Blue–green amphibole rim around slightly corroded garnet d. coarse grained phengite with fine grained white mica around the rim. e. Euhedral garnet with inclusion–rich core. Quartz + phengite + rutile + omphacite with symplectites in the matrix. f. Matrix omphacite grains with dark symplectite along grain boundaries. g. Relic kyanite surrounded by phengite coarse clinozoisite. h. Sample 11–06 XPL, retrogressed eclogite with relict garnet poikiloblasts with green amphibole and brown biotite rims. Symplectites after omphacite are present as dark patches, forming distinct domains throughout the thin section. Colourless quartz and white mica are present in the matrix

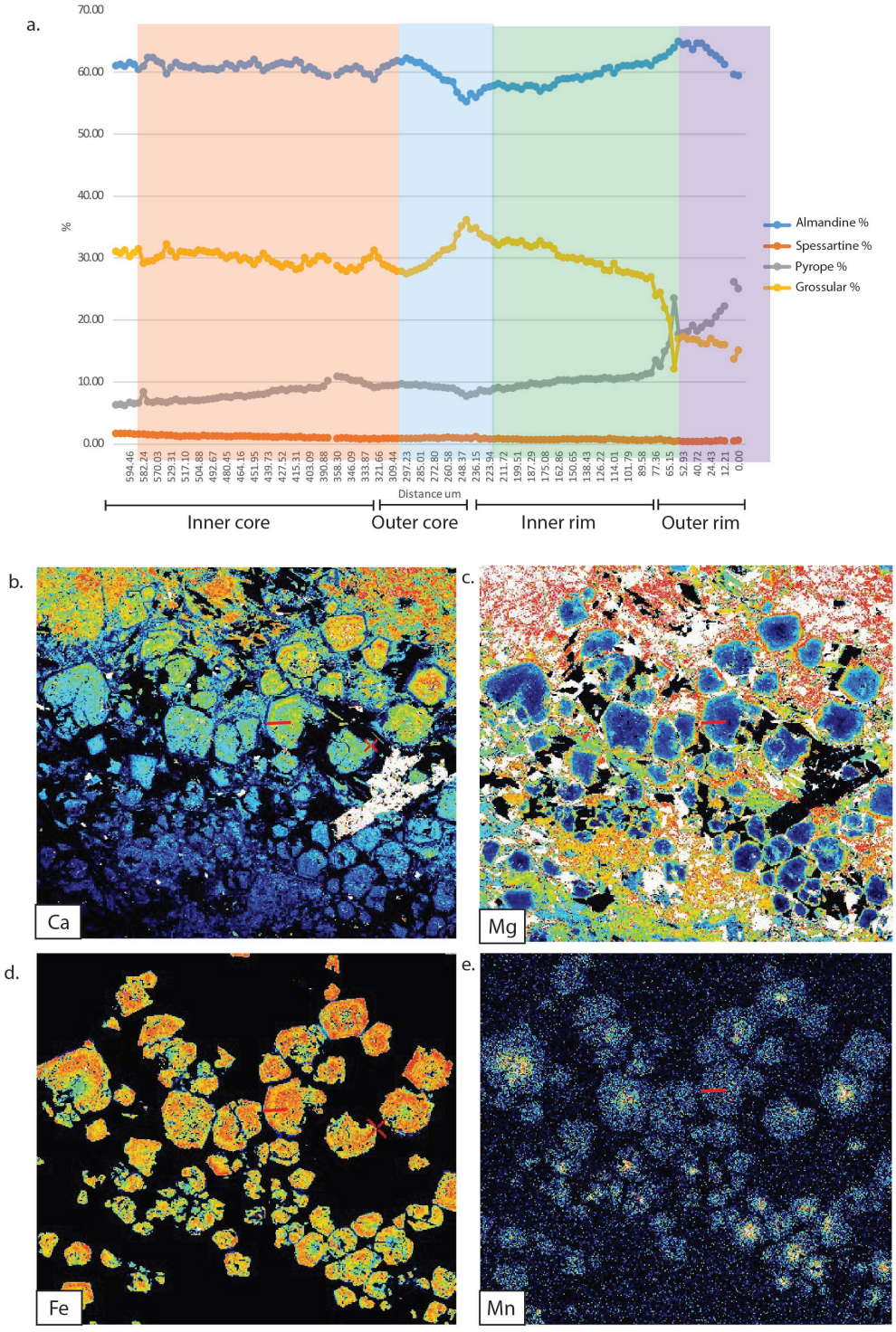


Figure 21 Sample 11-05 a. Garnet profile showing changing Almandine, grossular, Pyrope and Spessartine content from core to rim. Distinct garnet zones are divided based on sharp changes in garnet chemistry, inclusion density and composition. Location of transect marked by red line in maps below. b–e. Whole slide probe maps of sample 11-05 showing variations in garnet zoning in adjacent garnet grains.. Similar zoning can be seen in all garnets. Core region high in Ca and Mn, low in Mg and Fe. Low Fe, High Ca band visible between core and rim. Fe and Mg high at rim with low Ca. Thickness of Fe and Mg rim varies, with thicker rims present at garnet–quartz contact. Variation in thickness of Mg rim due to irregular boundary protruding back into garnet, outlining Mg–embayments discussed in text.

Min	*Location*	*SiO_2*	*TiO_2*	*Al_2O_3*	*FeO*	*MnO*	*MgO*	*CaO*	*Na_2O*	*K_2O*	*Total*	*Si*	*Ti*	*Al*	*Fe^{3+}*	*Fe^{2+}*	*Mn*	*Mg*	*Ca*	*Na*	*K*	*Sum*	*Ox*	*XMg*	*$\%Fe^{3+}$*	*Jd*
Px	matrix	56.27	0.05	10.71	4.70	0.01	7.65	12.53	7.99	0.00	99.91	1.99	0.00	0.45	0.12	0.02	0.00	0.40	0.47	0.55	0.00	4.00	6	0.96	87.53	0.54
Grt	Average spherical Grt											3.00	0	1.17	0	1.81	0.04	0.24	0.91	0	0	8	12	–	–	–
Grt	Core	37.76	0.13	20.91	28.79	0.53	1.81	11.41	0.04	0.01	101.38	2.98	0.01	1.94	0.00	1.90	0.04	0.21	0.96	0.01	0.00	8.05	12	–	–	–
Grt	Outer rim	38.09	0.02	21.55	28.83	0.24	6.82	5.71	0.01	0.04	101.33	2.95	0.00	1.97	0.00	1.87	0.02	0.79	0.47	0.00	0.00	8.07	12	–	–	–
Amph	Symplectite after Omph	51.87	0.20	6.98	7.42	0.01	17.36	11.74	2.02	0.13	97.73	7.33	0.00	1.17	0.00	0.87	0.00	3.64	1.78	0.56	0.00	15.35	23			
Amph	Zoned in matrix	46.23	0.04	11.68	15.28	0.17	12.38	9.46	2.27	0.25	97.77	6.69	0.00	2.02	0.60	1.26	0.00	2.64	1.47	0.64	0.00	15.32	23			
Pl	Symplectite after Omph	66.25	0.13	18.26	1.17	0.00	2.97	2.82	9.43	0.04	101.07	1.06	0.00	0.94	0.00	0.00	0.00	0.00	0.06	0.94	0.00	5.00	8			
Bt	Rim on Grt	37.26	0.03	20.50	15.05	0.059	9.72	7.13	0.66	5.92	96.32	5.46	0.00	3.53	1.86	0.01	2.16	1.08	0.18	1.14	15.43	5.46	22			
Bt	Rim on Phe	36.11	0.77	18.00	16.24	0.093	13.11	0.34	0.14	9.39	94.19	5.48	0.09	3.22	2.06	0.01	2.97	0.056	0.04	1.82	15.75	5.48	22			
Phe	matrix	52.75	0.24	27.59	1.26	0.01	4.71	0.01	0.34	9.39	96.29	3.43	0.02	2.12	0.00	0.06	0.00	0.39	0.00	0.05	0.95	7	22			

Table 4 Sample 11-05, representative mineral compositions

Discussion

The Puga Gneiss is host to boudinaged mafic dykes which preserve eclogite–facies mineral assemblages, including poikiloblasts such as garnet and omphacite. Petrographic study of the eclogites of the Tso Morari complex reveals the preservation of multiple different equilibrium assemblages in these samples. Chemical zoning in garnet is present in samples of slightly different bulk compositions but preserves similar characteristics between samples. Key features recorded in the prograde garnet zoning include bell shaped manganese and yttrium profiles, with relatively constant almandine, pyrope and grossular concentrations. A manganese (and yttrium) annulus marks the core-rim boundary. Faceted, low Ca, garnet growth from multiple nucleation points defines the inner rim, followed by growth of a high-Mg rim with elevated Ca. The high-Mg rim is also the location of primary coesite inclusions (c.f. Sachan *et al.*, 2004), polycrystalline quartz after coesite and pseudomorphs after lawsonite, indicating that these garnets record prograde metamorphism to high–pressure.

Abundant hydrous phases in the matrix and reaction textures preserve clues as to the exhumation history following peak metamorphism. Post peak alteration of garnet is dependent on the location and hydration state of the sample. For example, samples taken from the rims of boudins are more hydrated and have a high proportion of matrix amphibole. These samples also preserve atoll garnet structures, where the garnet cores have broken down as a result of fluid infiltration along fractures in garnet and re-equilibration at lower pressures (e.g. Jonnalagadda et al. 2017). In contrast, samples taken from the core of a large mafic boudin exhibit sharp concentric zoning and lack the Mg-embayments which replace garnet from the outside towards the core (e.g. O'Brien & Sachan 2000). It is these samples, with low degrees of post peak alteration, that are mostly likely to preserve coesite inclusions in the thin Mg-rich rims (e.g. Sachan *et al.*, 2004; Wilke *et al.*, 2015). Samples such as L08-03A (St-Onge et al. 2013; Palin et al. 2014) and L08-03B represent an intermediate hydration state, where the zonation in garnet is slightly less sharp and fluid-mediated alteration of the garnet cores is more significant.

Reaction textures and compositional zoning trends in these samples provide clues as to the metamorphic evolution of the rocks and show broad similarities in peak and retrograde mineral assemblages, with slight

differences in bulk composition and abundance of Ca- and Al-bearing phases. By unravelling the common retrograde petrological features within the eclogites, it is possible to understand and decipher the earlier features overprinted by retrogression.

Retrograde

Zoned blue-green amphibole is observed in all mafic eclogite samples as "inclusions" in garnet and as coarse matrix amphibole. The presence of zoned amphibole and clinozoisite is common in mafic rocks in ultrahigh–pressure terrains around the world (e.g. Palin et al., 2014; Wain, 1997; Amato et al. 1999). The timing of formation of this mineral assemblage is debated, with some studies interpreting this as a peak metamorphic assemblage (e.g. De Sigoyer *et al.,* 1997) and others providing evidence that it formed as a later retrogressive phase during the hydration of a fluid–absent peak assemblage (Massonne, 2012). Fluid–driven retrograde metamorphic reactions provide insight into the behaviour and source of metamorphic fluid during exhumation, where discrete hydrous episodes are thought to have occurred. Palin *et al.,* (2014) constrained the *P-T* conditions of amphibole growth using pseudosection modelling, showing that growth was fluid–mediated and occurred on the retrograde path during exhumation of the Berthelsen eclogite and can be summarised as follows: The destabilisation of talc at ~23 kbar is predicted to have led to a hydration event which resulted in the growth of the zoned amphibole cores and minor clinozoisite at the expense of peak garnet and omphacite. Additional fluid input from external sources at ~19 kbar resulted in further barroisite-winchite amphibole growth along with clinozoisite poikiloblasts. No additional hydration events are recorded until the later retrograde stages of exhumation (M4) in the middle crust, where dehydration of the surrounding orthogneiss may have been responsible for the growth of magnesiohornblende rims on barroisite-winchite cores. Compositional clusters in amphibole inclusion chemistry were also documented by Palin *et al.,* (2014).

Results from this study from matrix amphibole EPMA data (Figure 22a and b) in samples 10-05 and 05-04D and from amphibole inclusion chemistry in sample L08-03B (Figure 22c), show a range of amphibole chemistry from glaucophane–rich cores to pargasite–rich magnesiohornblende rims, forming a continuous array of increasing edenite and tschermakite, decreasing glaucophane and X_{Mg} from winchite through barroisite, taramite and pargasite. The final ferropargasite is comparable to the narrow external rims on garnet, interpreted as forming from the alteration of garnet with the additional components of H_2O and Na.

Occasionally, deep blue amphibole has been observed in the cores of amphibole inclusions in garnet in sample a03-16, one of the freshest and least hydrated eclogite samples collected. These are similar in colour to the rare glaucophane cores recorded in matrix amphibole by De Sigoyer *et al.* (1997) or as inclusions in carbonates (Wilke *et al.,* 2015). Glaucophane is not predicted to be a peak eclogite–facies mineral phase based on the *P-T* estimates for the Berthelsen outcrop (e.g. St-Onge *et al.,* 2013; Wilke *et al.,* 2015). However, the presence of glaucophane as a stable phase during the metamorphic history of these eclogites suggests that glaucophane must have grown just after the amphibole free peak assemblage on a relatively cool trajectory and is indeed seen to be replacing omphacite (O'Brien, 2018).

Matrix amphibole compositions obtained in this study are comparable to the range in amphibole compositions observed as 'inclusions' in garnet in sample L08-03B (Figure 22c), suggesting that the amphibole inclusions in garnet are not primary inclusions but have been altered and belong to the same generations of retrograde amphibole growth as the matrix amphibole. This is consistent with the observation in St-Onge *et al.,* (2013) where no amphibole inclusions were reported to have compositions consistent with growth and entrapment on the prograde path. All amphibole inclusions with $X_{Mg}<0.5$ (almost all of those in direct contact with garnet) are too Fe–rich to be in Fe-Mg exchange equilibrium with enclosing garnet at a reasonable temperature. Some of the inclusion cores match a post–peak matrix generation which formed due to the addition of fluid during exhumation around 20 kbar (c.f. Palin *et al.,* 2014). In other samples, the range in colours observed in matrix amphibole can also be observed in the amphibole inclusions, allowing qualitative chemical comparisons to be drawn in samples in the absence compositional data.

The results of this study indicate that many or most of amphibole inclusions in garnet in the Tso Morari eclogites are not primary but have experienced post-entrapment modification and cannot be used to determine the P-T conditions of prograde garnet growth. These results have implications for studies such as St-Onge et al. (2013) where amphibole chemistry was used to distinguish between two contrasting garnet isopleth intersections.

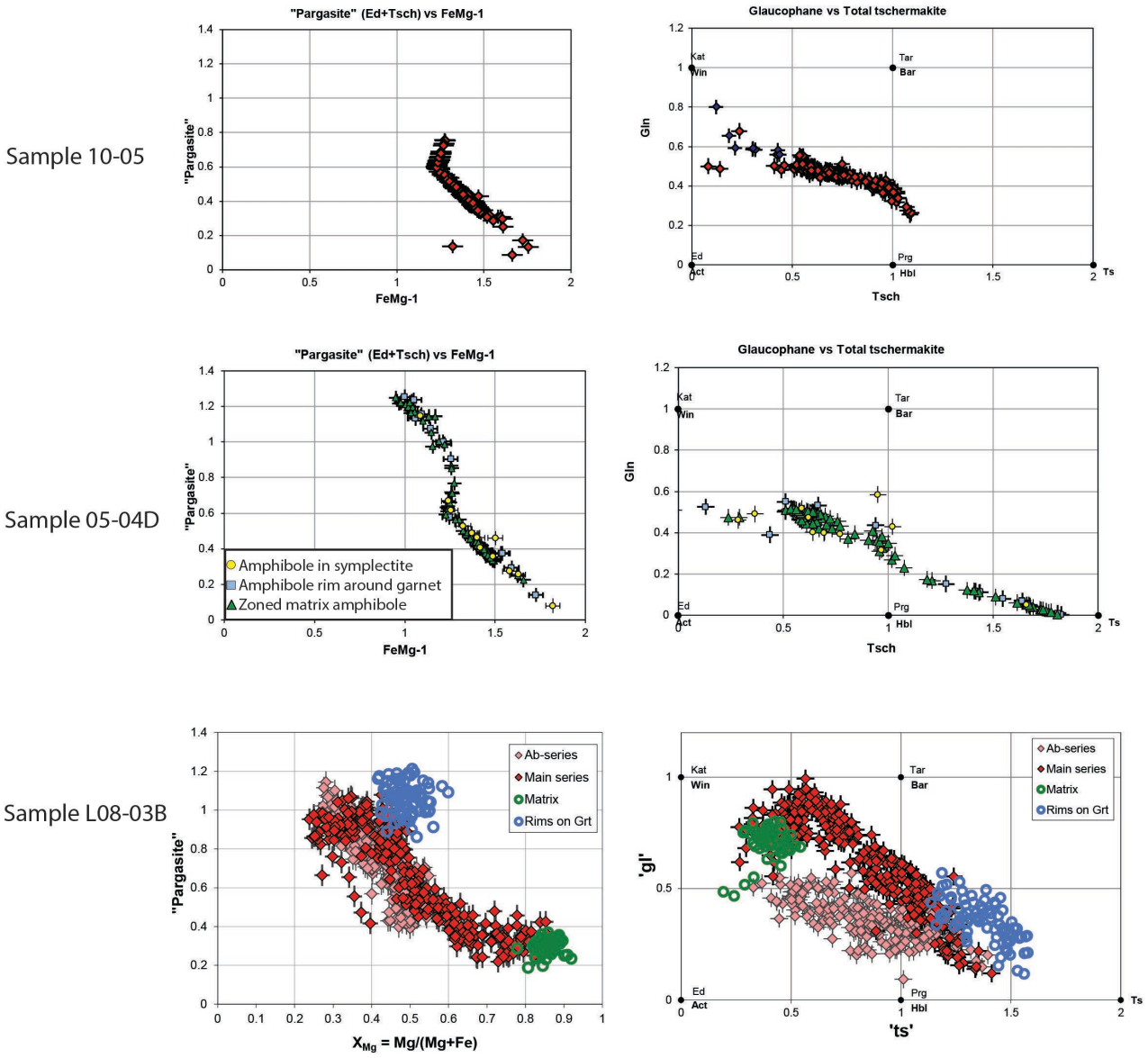


Figure 22 Sample 10-05 (top), 05-04D (middle) matrix amphibole chemistry data showing a continuous progression of increasing edenite and tschermakite with decreasing glaucophane from winchite through barroisite, taramite and pargasite. Sample 05-04D shows texturally distinct amphibole generations. Sample L08-03B (bottom) amphibole "inclusion" chemistry

Sample L08-03A (St-Onge *et al.,* 2013) has a granoblastic texture, whereas Mukherjee *et al.* (2003) and Wilke *et al.* (2015) record clusters of garnet wrapped by domains of elongate omphacite showing a shape preserved orientation, with phengite, carbonate and rutile clusters and occasionally kyanite. In sample 11-05 (this study), a foliation is present, defined by matrix omphacite, talc and phengite grains, as well as garnet– and omphacite–rich domains. These minerals wrap around garnet poikiloblasts but are cut by coarse–grained, elongate, zoned clinozoisite, indicating that deformation occurred in the eclogite facies, before the growth of

clinozoisite. Clinozoisite poikiloblasts are also observed to overgrow phengite and talc clusters in the matrix and often contain inclusions of barroisitic amphibole, omphacite, dolomite, talc, quartz and rutile. Most eclogite samples contain randomly oriented omphacite grains with no shape preferred orientation but with comparable, coarse–grained clinozoisite poikiloblasts, interpreted as forming from a similar post peak hydration event.

Symplectites after omphacite vary in abundance depending on the hydration state of the eclogite and progress along grain boundaries, completely replacing omphacite grains in more hydrated samples. These original omphacite domains can be identified optically by their common extinction angle. They are mostly composed of amphibole and plagioclase. Amphibole in symplectites after omphacite is glaucophane–rich barroisite, similar in composition to the cores of the matrix amphibole, suggesting that the breakdown of matrix omphacite is related to the formation of an early Na-Ca amphibole generation and predates the breakdown of garnet at lower pressures.

Diopside is occasionally present in symplectites after omphacite as well as in coronas surrounding quartz. Sample 05-04 contains the most abundant diopside within symplectites and has no fabric and abundant omphacite. In other samples, diopside is rarely present in symplectites that contain abundant amphibole, suggesting that the pyroxene within the symplectites was later replaced by amphibole. The presence of channelized features, ~3-40 mm wide, such as in sample 05-04, containing abundant poikiloblastic carbonate and symplectites after omphacite, indicate that carbon–bearing fluid was present. The timing of fluid infiltration is thought to have occurred simultaneously to the formation of symplectites after omphacite, as indicated by the abundant symplectites in sample 05-04C in the Kiagar La outcrop, where amphibole abundance does not increase significantly. A later hydration event in the lower crust described by Palin et al. (2014) is responsible for the formation of magnesiohornblende rims around garnet, contributing to most of the fluid input into these rocks.

The suite of samples from core to rim of the Berthelsen outcrop and observations from other hydrated eclogite samples (e.g. 10-02, 10-05, a04-30, a04-31, 11-06, 11-07), also indicates that a later, lower temperature overprint resulted in the replacement of amphibole by biotite and epidote and formation of a crenulation cleavage. This overprint is most notable towards the rims of the boudins in contact with the felsic gneiss,

where deformation fabrics allow externally derived fluids to flow more easily and hydrate the boudins from the outside in, exchanging mobile species such as potassium which is present in very low abundance in the core of the boudin, resulting in retrograde biotite growth.

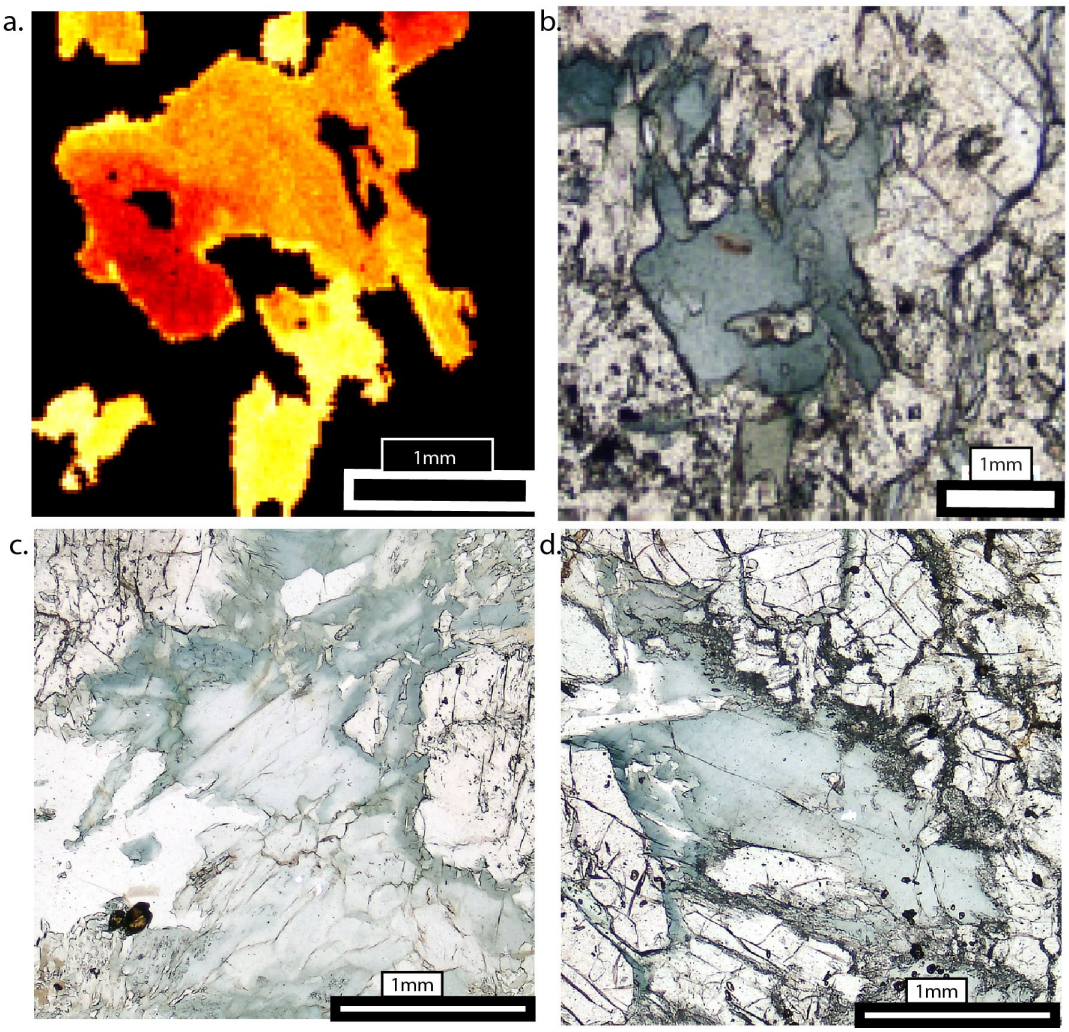


Figure 23 Amphibole inclusions a. false colour X-ray map showing variation of amphibole Al content in inclusions: dark red = low–Al winchite, pale yellow = ferropargasite. Compositions cover the whole range of the 'main series' (red symbols) in b, c and d. b. Thin section view of the same area as in a. showing composite amphibole inclusions. Pale winchite, blue-green barroisite, green ferropargasite. c. Sample 11-05 Zoned matrix amphibole with pale green cores and dark green rims around garnet d. Sample 05-04D. Zoned matrix amphibole.

Prograde metamorphic history

Garnets in (ultra)high–pressure rocks worldwide preserve complex major and trace element zoning profiles, as well as variations in the inclusion assemblage (Vance and O'Nions, 1990; Compagnoni and Hirajima, 2001; Carswell *et al.*, 2003; Davis and Whitney, 2006). The boundaries between these zones, commonly marked by a change in inclusion assemblage, may also be identified by a sharp change in major and trace

element compositions that indicate interrupted garnet growth. Such changes allow a quantitative assessment of the *P-T* conditions of growth and of diffusion effects following growth. Broad similarities have been identified in compositional trends and zoning patterns within garnets from rocks of different high–pressure and ultrahigh–pressure terrains (Konrad-Schmolke *et al.,* 2008). These patterns include increasing pyrope content, with decreasing almandine and spessartine content from core to rim. Grossular is seen to gradually increase towards the inner rim boundary before either sharply decreasing or increasing further towards the rim (e.g. Western Gneiss Region, Konrad-Schmolke *et al.,* 2008).

The prograde metamorphic history of eclogites from the Tso Morari complex is preserved in the chemical zoning of garnet and is similar to the zoning observed in the Berthelsen outcrop. The low pyrope content of the garnet cores and maximum grossular and spessartine content suggest that the initial prograde growth of garnet took place at the lowest temperature conditions. The outer part of the core region is marked in sample 11-05 by an increase in grossular at constant pyrope composition. This zone is present in other samples but can be small in magnitude and very thin. The presence of a Mn and Y annulus surrounding the core zone marks the breakdown of a Mn– and Y– rich phase and could be explained by resorption of garnet. The Mn annulus is not present is every sample, however a textural break occurs in all samples separating an inclusion–rich core from an inclusion–poor rim. The similarity between the core to rim zoning profiles across all samples (Figure 24) but the occasional absence of a Mn annulus could be explained by slight variations in bulk composition, changing the shape of the garnet mode contours in *P-T* space, limiting the degree of resorption that took place at this boundary, or indeed could be due to the fact that the garnets were not cut directly through their centre .

High resolution EPMA maps of sample L08-03B (Figure 14) highlights compositional and textural features related to garnet core growth. Angular patches with elevated Mg content exhibit sharp boundaries with zones of maximum Ca. The composition of these high-Mg domains follows the overall zoning trend but lie towards more evolved compositions, suggesting that these formed later than the garnet core, at a composition equivalent to the garnet outer core. The surrounding garnet of maximum Ca likely represents the earliest generation of garnet grown, where Ca partition into the first garnet grown at low temperatures. The textural distribution of this phase of garnet growth around later Mg garnet suggests that this initial garnet growth was

skeletal and occurred along grain boundaries in water undersaturated conditions. The later replacement of inclusions in garnet by garnet of a more evolved composition is further supported by the sharp compositional boundary surrounding the Mg-Ca patch, the elevated Mg content of the angular patch suggesting garnet growth at higher temperature conditions and a composition comparable to garnet outer rim growth. Resorption of garnet, followed by replacement of its own inclusions, a shift from skeletal to faceted garnet growth and the appearance of composite inclusions of clinozoisite and paragonite at the core-rim boundary, interpreted as pseudomorphs after lawsonite (c.f. Deer et al., 1992), is consistent with a change from water–undersaturated from water–saturated conditions.

Sharply bounded rim zones have few inclusions: an inner rim has low grossular with increasing pyrope; the outer rim shows maximum pyrope with intermediate grossular. The inner rim zone is marked by a decrease in grossular to 27%, followed by faceted garnet growth at low grossular, with pyrope and almandine increasing to 12% and 62% respectively across this zone. The faceted garnet growth is more distinct in samples with a thicker outer rim zone framing the Ca–trough such as in samples L08-03A and a03-16. The decrease in grossular occurs gradually in sample 11-05 with a sharper decrease in grossular towards the outer rim. Sample 05-04D has virtually no outer rim; the low grossular rim of this sample is equivalent to the low–grossular inner rim in other samples, postdating the growth of the inclusion–rich inner core.

At the core-rim boundary, consistent with the decrease in grossular content of garnet, sample 05-04D and L08-03 record the rare appearance of clinozoisite-paragonite pseudomorphs after lawsonite. This zone also coincides with a decrease in heavy rare earth elements (HREEs) and an increase in middle rare earth elements (MREEs) in the garnet outer rim (c.f. REE data from Wilke *et al.,* 2015) in a sample showing comparable zoning patterns, where light rare earth elements (LREEs) are shown to have been depleted early in the core but also show a noticeable decrease at the inner rim followed by an increase towards the outer rim. The decrease in HREEs from core to rim is interpreted as a fractionation feature related to prograde garnet growth. The most MREE–enriched zone of the garnet, also showing an increase in LREEs, corresponds to the most pyrope–rich zone and the location of the coesite inclusions and is interpreted to relate to the breakdown of plagioclase (Wilke *et al.,* 2015). A slightly lower–pyrope and high–grossular rim is recorded by Wilke *et al.*

(2015) showing a significant increase in HREE and a decrease in MREEs, corresponding to the zone of post peak alteration described above.

Thin, concentric, Mg–rich rim zones preserve peak prograde garnet growth. This is confirmed by the discovery of coesite in the highest–Mg rim zones of garnet within the least hydrated samples, where a greater proportion of omphacite and a lower proportion of amphibole is observed (Sachan *et al.*, 2004). All samples record a high–pyrope outer rim, however the thickness and peak pyrope content of this rim varies, preserving a value of ~30% pyrope at its highest. For example, in sample 05-04, the high–Mg rim is thickest in contact with quartz. Samples such as 11-05 preserve a garnet rims analysis with ~26% pyrope in the transect where only a very narrow rim was analysed. The trend in grossular content in the outer rim zone is more variable between samples. In sample 11-05, grossular decreases abruptly as pyrope increases, whereas in sample a03-16 and L08-03, grossular increases towards the rim, and in sample 05-04D there is no sharp change in grossular observed. Additionally, the almandine content in the garnet rim zones changes to accommodate the grossular and pyrope content but trends towards an almandine–rich rim in sample 11-05, this is different to the low almandine rims in sample L08-03A and a03-16. The differences in the garnet rim zoning are obscured by the thin width of the high pyrope garnet rims.

Superimposed on this zonation, traversing the inner rim and core zones, are narrow linear or network–forming features marked by increase in Mg at the expense of Fe. These link inclusions, merge with the outer rim composition, and are interpreted as marking healed fractures that allowed fluid access to garnet interiors. The composition of garnet forming these Mg–embayments and channels is relatively high–Mg and high–Ca compared to the zoning trend recorded from core to rim of the garnets, suggesting that this alteration did not take place during prograde garnet growth but represents alteration during retrograde fluid infiltration. This is evident in the garnet transect from sample a03-16 which extends from the high–spessartine core region, across one of these Mg–embayments, to a composition that is more grossular rich than the rim zones of other garnets (Figure 24). Element maps of this garnet also show remobilisation of the Mn from the garnet core into the recrystallised Mg–embayments (Figure 8). Atoll garnets have been described from a number of locations worldwide and are found at other Tso Morari localities (e.g. Jonallagadda *et al.,* 2017). Atoll garnets are thought to have formed when the fracture of garnet allowed fluid to access the interior of the garnet which is

strongly out of equilibrium with the rim, causing the core to be selectively replaced. The replacement of the core is usually by hydrous minerals also found in the matrix.

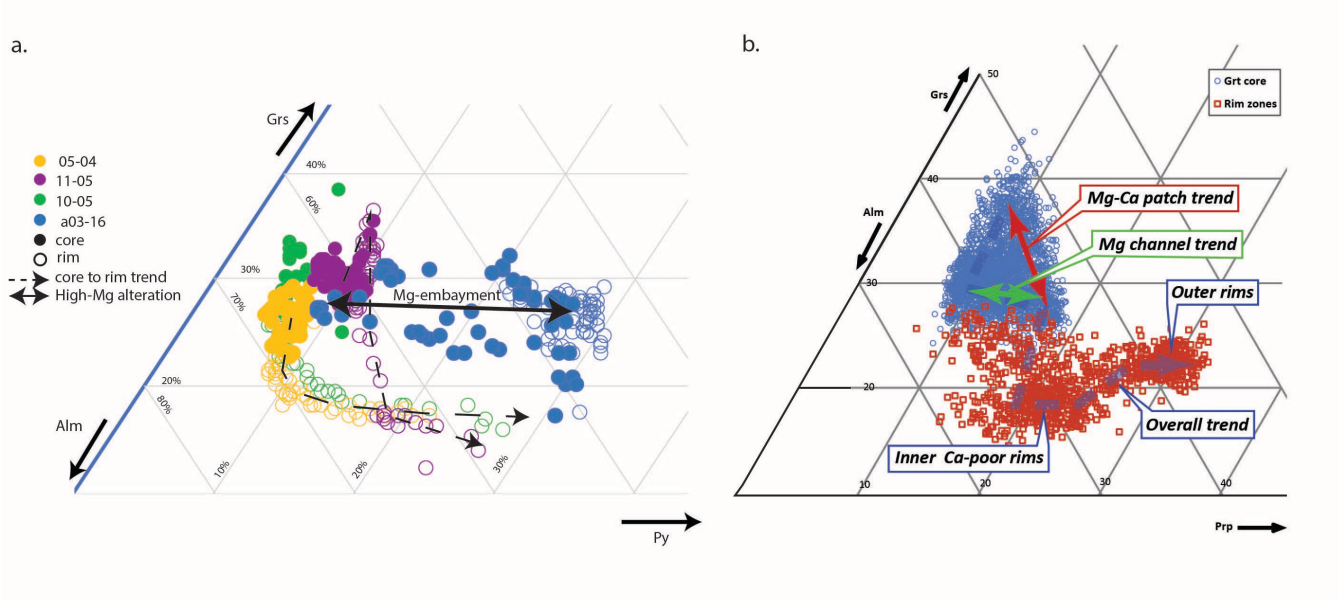


Figure 24 a. Ternary diagram of garnet compositions showing 4 eclogite samples. Samples 05-04D and 10-05 show similar compositions. Sample 11-05 shows a similar trend from core to rim but with steeper increase in pyrope in the inner rim zone. Sample a03-16 transect was taken across an Mg–embayment which has altered the rim zone and parts of the core. The trend shows a rim composition with similar high pyrope and higher grossular than the rim zone of the less altered garnet in other samples. b. Ternary diagram of garnet compositions taken from an EDS map of a single garnet in sample L08-03B (Waters et al., 2020) where alteration textures could be easily distinguished in the core and rim zones

Garnet inclusion assemblages are commonly used to determine the *P-T* conditions of garnet growth in phase equilibria modelling. The Mg–channel network described also connects inclusions to the external matrix. This allows fluid–mediated chemical communication at various stages along the exhumation path. Prograde amphibole inclusions have not survived and therefore amphibole inclusions found in the cores of the garnets are not suitable when trying to establish the prograde *P-T* conditions of garnet formation. Other Fe-Mg bearing hydrous minerals may also have been affected by retrograde alteration such as phengite–paragonite intergrowths, which are often associated with Mg–embayments in the rims of the garnets. These intergrowths are often next to phengite–paragonite intergrowths in the matrix of the rock. Chatterjee and Jagoutz (2015) used Si in phengite thermobarometry on phengite inclusions in garnet cores to interpret the prograde *P-T* path of the garnet, which, considering the results presented above, should be interpreted with caution. The features of later replacement of inclusions and modification of garnet core compositions are prevalent in many garnets

without atoll garnet formation being prevalent. This highlights the need for caution in the interpretation of inclusion suites.

The garnet rim inclusion suite is marked by the presence of jadeite–rich omphacite, quartz, talc and coarse paragonite–zoisite or paragonite–albite rhombohedral inclusions interpreted as pseudomorphs after lawsonite (Palin *et al.,* 2014). Characterisation of the post peak alteration of garnet and amphibole inclusions allows us to determine which inclusions are primary and which have been affected by fluid–mediated Fe-Mg exchange. Omphacite occurs in two textural settings; as inclusions in the garnet rim zones and as central inclusions within Mg–embayments originating from the external edge of the crystal, suggesting that omphacite inclusion chemistry may not be representative of prograde garnet growth. The decrease in abundance of rutile inclusions from core to rim of garnet is considered a primary feature due to the low mobility of titanium. The appearance of pseudomorphs after lawsonite cannot be explained by Fe-Mg alone and therefore its presence/absence can be considered a primary feature. Similarly, talc is observed as composite inclusions with omphacite and amphibole in garnet rims in sample L08-03B but is not observed in the matrix, suggesting that the appearance of talc during prograde garnet growth is a primary feature and that talc and lawsonite were stable at near–peak *P-T* conditions. The coexistence of these composite inclusions with omphacite implies that lawsonite and omphacite were in a stable assemblage at the same time. Carbonate inclusions are rarely found as inclusions in garnet but are occasionally found in the high-Mg rim zone.

Compositional isopleths of garnet core compositions provide a more reliable alternative when considering prograde garnet growth. However, if the textural distribution of elements in garnet are not analysed and interpreted, garnet compositions could produce inaccurate *P-T* results, relating to retrograde garnet alteration rather than prograde garnet growth. Garnet compositional maps present a valuable tool when identifying prograde garnet growth features. When interpreting prograde growth features in these samples, maximum grossular content in the garnet cores, should be considered representative of initial skeletal garnet growth. Mg–channels should be considered when analysing garnet core compositions due to their irregular distribution and narrow width, and can be avoided when deciding on the location of transects across garnet representative of prograde garnet growth (e.g. Figure 24, sample a03-16). Grossular zonation can also be

interpreted with respect to the later Fe-Mg alteration which does not involve a Ca exchange, preserving the Ca compositions at the garnet rims.

The similarities in the prograde garnet zoning pattern in all samples studied suggests that they shared a similar prograde history. The absence of pseudomorphs after lawsonite in garnet rims could be attributed to variations in bulk composition or a low modal abundance and preservation potential of lawsonite during garnet rim growth. The garnet outer rim shows the most variation between samples.

Peak metamorphic conditions

The peak mineral assemblage common to all samples includes garnet and omphacite, often with matrix quartz which preserves inclusions of rutile and zircon. These minerals often form garnet + quartz– and omphacite–rich domains, relating to original igneous heterogeneity.

Bimodal distribution of jadeite and aegirine–rich endmembers is recorded by O'Brien (2018b), with more aegirine rich members ($jd_{30–40}$ $aeg_{15–20}$) forming the cores of the more jadeite rich grains ($jd_{42–52}$ aeg_5). This is consistent with the high–Mg, jadeite–rich end member forming as inclusions in and in equilibrium with the Mg-rich garnet outer rim (O'Brien, 2018b). Sample 10-05 (this study) preserves a range of pyroxene composition of $Jd_{36–56}$ with two different compositions of X_{Mg} <0.8, Fe^{3+} > 0.08 (jd_{41-54} $aeg_{1.6-11}$) cations pfu in the core and X_{Mg} > 0.8, Fe^{3+} <0.08 (jd_{35-55} aeg_{0-12}) cations pfu in the rim (Figure 25). A comparable omphacite population with an X_{Mg} >0.8 and low Fe^{3+} content is also present in samples 05-04D and a03-16 (this study). The omphacite population with X_{Mg}>0.8 and a high Fe^{3+} is also present in sample 11-05 and samples from the Berthelsen outcrop (e.g. L08–03 of St-Onge et *al.,* (2013) and Palin *et al.,* (2014), De Sigoyer *et al.*, (1997), Chatterjee *et al.*, (2015); Rajkumar, (2015), and Jonnalagadda *et al.*, (2017)), with analyses from Konrad-Schmolke *et al.*, (2008) and Wilke *et al.,* (2015) lying in between the two clusters (Figure 25). Inclusions of omphacite in garnet have X_{Mg} <0.8 (de Sigoyer *et al.*, 1997; Konrad-Schmolke *et al.*, 2008; Jonnalagadda *et al.*, 2017), consistent with the interpretation that the early generation of omphacite had a lower X_{Mg} than the later generation.

The occurrence of omphacite with X_{Mg}>0.8 and a higher total Fe and Fe^{3+} content in their cores, is consistent with fractionation of Fe^{3+}, inherited from a protolith phase, into omphacite during prograde pyroxene growth.

The later omphacite growth is subsequently depleted in total Fe, suggesting that an Fe–bearing mineral, such as garnet, grew before the growth of this omphacite generation, reducing the Fe in the effective bulk composition. The later omphacite generation forms rims around Fe–rich cores, forming a channelised and patchy structure, indicating the involvement of fluids. This alteration took place after garnet growth as it is only observed in matrix omphacites. Aegerine–poor rims are also observed in pyroxenes from the Qinglongshan epidote eclogites of the Su Lu province where clinopyroxenes from the zoisite–rich eclogites are aegirine–poor (Zhang *et al.*, 1995) This later generation of omphacite is particularly prevalent in samples from locations other than those from the Berthelsen outcrop.

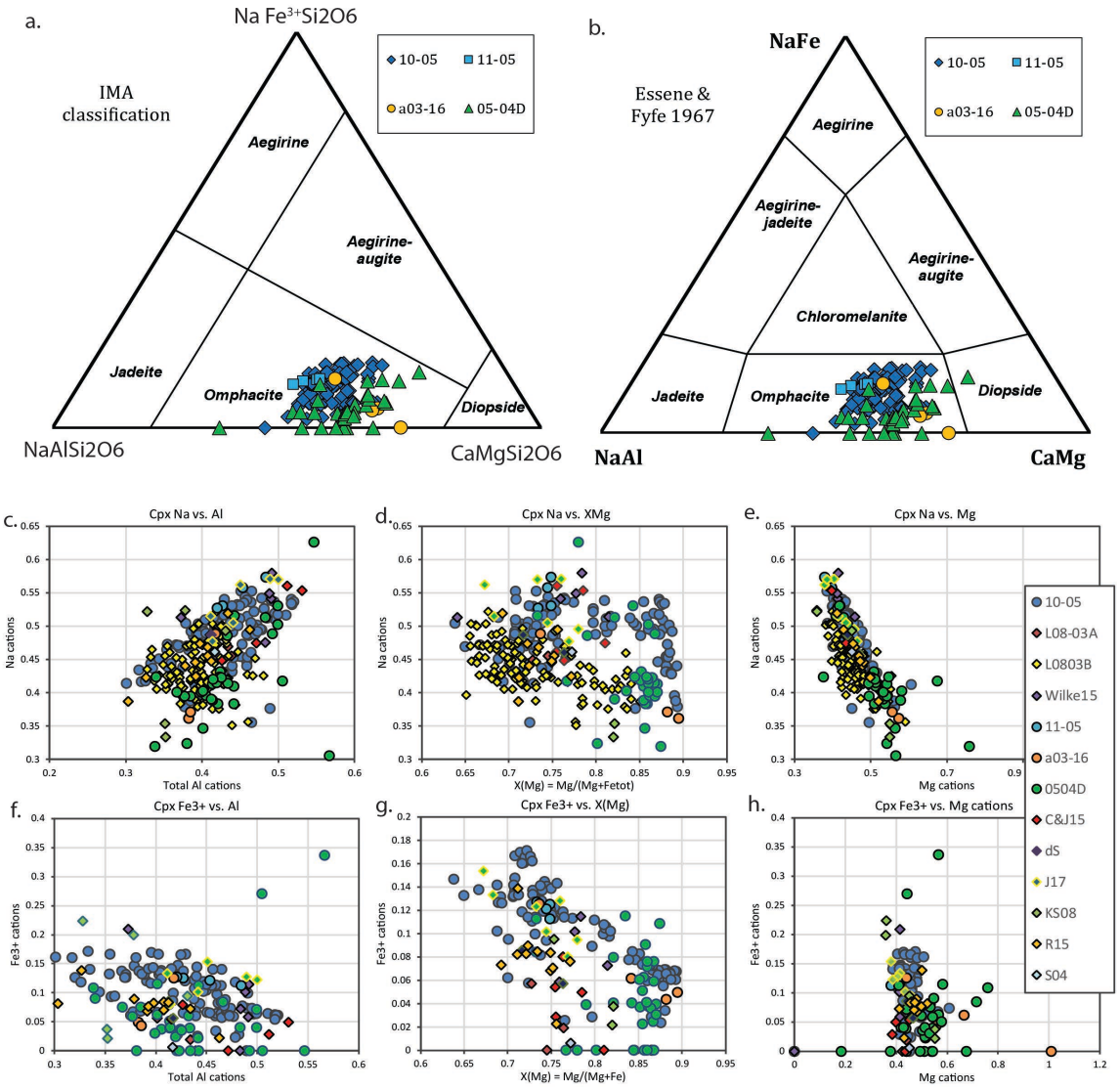


*Figure 25 a. IMA pyroxene classification (Morimoto, 1988). b.Essene and Fyfe (1967) pyroxene classification c. - h. Pyroxene analysis, Samples 10-05, 11-05, a03-16 and 05-04D from this study (circles). Published data from L08-03A (Palin et al., 2014), L08-03B (Waters et al., 2020), Wilke15 (Wilke et al., 2015), C&J15 (Chatterjee and Jagoutz, 2015), dS (de Sigoyer et al., 1997), J17 (Jonallagadda et al., 2017), KS08 (*Konrad-Schmolke *et al., 2008), R15 (Rajkumar, 2015), S04 (Sachan, 2004). X_{Mg} = Mg/(Mg+Fe^{2+}).*

In some samples, the omphacite domains are often associated with abundant talc and less abundant phengite. Coarse–grained idioblastic phengite and talc laths can be observed as isolated grains in contact with garnet and omphacite (e.g. sample a03-16) and relict talc is observed at omphacite triple junctions (e.g. sample L08-03B) suggesting that these phases were part of the peak assemblage in some cases. However, talc and phengite more commonly form closely associated radial clusters with relict kyanite grains in the core of these clusters, indicating that the kyanite was a peak phase that predated the phengite + talc.

The abundance of carbonate can vary significantly throughout a single thin section as well as an outcrop. Sample 05-04 contains carbonate in the most garnet–rich domains, with little carbonate present in the omphacite–rich domains. In the Berthelsen outcrop, fresh samples are observed containing little carbonate in at all, whereas other samples are observed to contain abundant carbonate. Carbonate is observed as relict grains within clusters of white mica (phengite and paragonite), similar to the description by Wilke *et al.* (2015), suggesting that carbonate formed as a peak phase. Towards the amphibolitised rim of the Berthelsen boudin, carbonate is also present as inclusion–rich porphyroclasts, wrapped by a fabric of amphibole and biotite, suggesting that the poikiloblastic carbonate pre dates deformation of the amphibolitised margin, but is a later generation than the relict grains seen in the matrix of the fresh eclogite core.

Relict carbonate in the fresh eclogites is mostly dolomitic, but in samples where magnesite is present, dolomite is observed to extensively replace magnesite. Calcite rims are present around dolomite. These observations are consistent with the observations of Wilke *et al.,* (2015) who verified, by raman spectroscopy, magnesite cores crosscut by fractures containing dolomite, calcite and Fe–oxide which predate the overgrowth of dolomite rims. Later fractures in the dolomite rims are filled with calcite but no Fe–oxide. Wilke *et al.,* (2015) interpreted the observed textures as the breakdown of unstable magnesite to dolomite (X_{Fe} = 0.13) + aragonite at conditions of ca. 37 kbar at 550°C (e.g. Tao *et al.*, 2014). Although aragonite is not observed surrounding magnesite, the coexistence of calcite and goethite suggests that water was a crucial component in the breakdown reaction, accelerating the transformation of aragonite to calcite, as well as inhibiting the formation of aragonite (Brown *et al.*, 1962).

Carbonate in mafic eclogites could have been introduced in a number of ways: 1. Near surface hydrothermal alteration of basalt followed by metamorphism at high pressure. 2. Carbon–rich fluids present during peak metamorphism producing carbonate as part of the peak assemblage. 3. Carbon–rich fluids introducing carbonate as a retrograde phase. The presence of relict carbonate, predating hydrous retrograde minerals, suggests that carbonate was a part of the eclogite facies mineral assemblage and carbon was already present in the bulk composition or introduced during subduction. The later poikiloblastic carbonate shows that carbon was also mobilised in the crust during later metamorphism. The Puga Gneiss which hosts the mafic eclogites, is currently surrounded by and juxtaposed next to a thick carbonate–bearing continental shelf sequence, which, during dehydration and prograde metamorphism, could have been a source of carbon–rich fluids.

Hydrothermally altered basalt often transforms plagioclase into white mica, carbonate and chlorite when subject to seawater–derived solutions (e.g. Humphris *et al.*, 1978; Staudigel *et al.*, 1981; Schaef *et al.*, 2008). Hydrothermal alteration of the basaltic protolith to the mafic eclogites could have introduced carbon into the bulk composition prior to subduction. In order for the crust to have been hydrothermally altered during its history, it must have been exposed to near–surface depths prior to subduction, after emplacement of the mafic dykes in the Permian. Determination of the timing and source of the fluid could be established by the analysis of fluid inclusions in a peak, refractory phase such as quartz. The analysis of fluid inclusions in quartz would determine the composition of the fluid during eclogite–facies metamorphism and whether carbon could have been introduced at this time.

To summarise the petrographic observations, there are variations in the bulk composition and peak metamorphic assemblage in the mafic eclogites of the Tso Morari complex. Talc, phengite, kyanite and dolomite all form parts of the peak assemblage in varying abundance whereas zoned garnet and omphacite are common features. Hydrous mineral such as talc, phengite and lawsonite were not preserved following peak metamorphism; lawsonite, if present, became unstable and broke down, whereas talc and phengite have grown at the expense of kyanite during retrograde metamorphism, overprinting evidence of their presence at peak conditions apart from relict grains at triple junctions.

	11-05	***a03-16***	***05-04D***	***05-04D***	***10-05***	***10-05***
	Omphacite	Omphacite	Omphacite	Diopside	Omphacite X_{Mg} <0.8	Omphacite X_{Mg} >0.8
SiO_2	56.27	55.39	55.99	54.65	55.67	56.32
TiO_2	0.05	0.05	0.05	0.04	0.05	0.04
Al_2O_3	10.71	8.09	10.06	4.56	9.58	11.25
FeO	4.70	3.91	3.03	4.47	5.63	2.64
MnO	0.01	0.01	0.02	0.07	0.01	0.01
MgO	7.65	12.26	9.81	12.76	8.24	8.98
CaO	12.52	16.19	15.31	21.43	13.83	14.11
Na_2O	7.99	4.57	6.08	3.02	7.09	7.12
K_2O	0.00	0.06	0.01	0.00	0.01	0.004
Total	99.91	100.54	100.35	101.00	100.10	100.46
Si	1.99	1.96	1.98	1.96	1.98	1.97
Ti	0.001	0.001	0.001	0.001	0.001	0.001
Al	0.48	0.34	0.42	0.19	0.40	0.47
Fe^{3+}	0.12	0.048	0.041	0.1	0.13	0.07
Fe^{2+}	0.0.15	0.068	0.049	0.034	0.039	0.008
Mn	0.0001	0.00	0.001	0.001	0.00	0.00
Mg	0.38	0.65	0.52	0.68	0.44	0.47
Ca	0.48	0.62	0.58	0.82	0.53	0.53
Na	0.57	0.31	0.42	0.21	0.49	0.48
K	0.00	0.003	0.00	0.00	0.00	0.00
Cation sum	4.00	4.00	4.00	4.00	4.00	4.00

Table 5 Average pyroxene compositions from mafic eclogite for 6 oxygens. Diopside in sample 05-04D occurs within intergrowth with amphibole + plagioclase. Fe^{3+} recalculation after Droop (1987)

Protolith

The whole rock chemistry of the Berthelsen outcrop compared to the Polokongka La ridge outcrop show that while there are differences in bulk composition between mafic rocks hosted in the Puga Gneiss, with the Polokongka La eclogite plotting in the alkali basalt field (Figure 26). Whole rock major and trace element geochemistry of six samples from the Berthelsen eclogite boudin and the Polokongka La ridge sill were compared.

The Berthelsen eclogite has major element compositions corresponding to subalkaline basalts and the Polokongka La eclogite to alkali basalts (Figure 26a). Trace element characteristics of the both eclogites show an enrichment in large ion lithophile elements (LILEs) over high field strength elements (HFSEs) (Rb, Th, K). Ternary diagrams characterise the eclogites using immobile and incompatible elements as within plate basalts (WPB) to enriched mid–ocean ridge basalts (E–MORB) (Figure 26b–d). The Polokongka La ridge basalts are more alkaline in composition and higher Th/Y ratios, showing more of an affinity to WPBs. Their enrichment in Th could be related to the depth of melting but could also be a function of the more alkaline content of the rock.

The absence of an Eu anomaly in the Berthelsen outcrop suggests that plagioclase was not present in the source and the positive correlation of Mg number with Ni and Cr suggests olivine fractionation of mantle melts (Jonnalagadda *et al.*, 2017). The bulk composition is consistent with an attenuated continental lithosphere, which would have a slightly positive Nb anomaly and a slightly negative Zr anomaly with shallower melting (Pearce, 1996). These geochemical indicators are consistent with the low Ti/Y ratio and very low Zr, Ti and Y ratios in the Polokongka La ridge and Berthelsen eclogites.

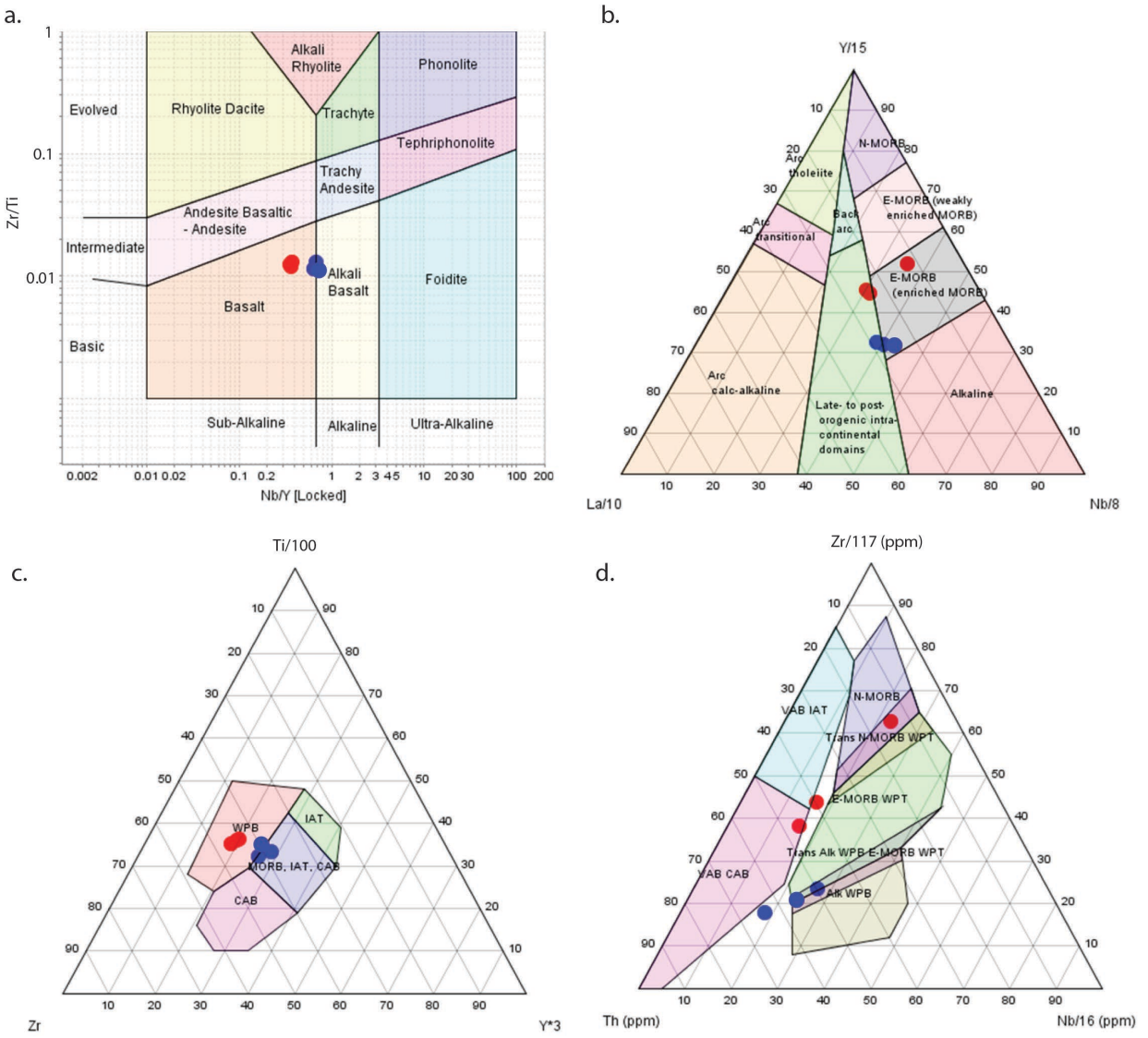


Figure 26 Bulk rock geochemistry of a transect of samples from the Berthelsen eclogite (red) and the Polokongka La ridge eclogite (blue). a. Mafic rock classification diagram from Pearce (1996) showing that the Polokongka La ridge eclogites are more alkali basalt than the Berthelsen eclogite. b. Tectonic classification of mafic rock diagram from Cabanis and Lecolle (1989) showing an enriched MORB and late to post orogenic intracontinental affinity in both eclogite outcrops. The Polokongka La ridge eclogite has a higher Nb and lower Y content.

The eclogite–facies mineral assemblage of the Polokongka La ridge eclogite also shows compositional banding and a larger abundance of clinozoisite, talc and white mica (including paragonite) than the Berthelsen eclogite, reflecting this difference in bulk composition. The Polokongka La pass eclogite preserves components of the protolith, preserving a porphyritic igneous texture in the pseudomorphs after plagioclase phenocrysts. These pseudomorphs contain abundant carbonate, clinozoisite and paragonite; however, the source of the carbonate is unknown.

Published studies from the Berthelsen outcrop report variations in mineral assemblage such as the absence of kyanite, coesite and glaucophane (St-Onge et al., 2013) which are present in other samples from the same outcrop (Wilke *et al.,* 2015). Differences in mineral assemblages could be attributed to variations in bulk composition of the protolith or alteration during retrogression. Compositional and mineralogical trends resulting from retrogression have been characterised and suggest that rare glaucophane cores in matrix amphiboles are an early retrograde phase, the presence of which could be controlled by variations in bulk composition of the protolith or could have been subsequently re-equilibrated during further amphibole growth. Kyanite has been identified in the matrix and as part of the peak assemblage in some published studies of the Berthelsen eclogite as well as in other eclogite bodies from the Tso Morari complex in this study but is absent in others.

The variation in kyanite abundance could be explained due to overprinting from retrograde metamorphism or by compositional heterogeneities in the protolith. Kyanite has also been observed to breakdown into hydrous phengite and talc. These radial clusters of phengite and talc are observed in kyanite–absent samples, suggesting that kyanite may have been overlooked as a peak assemblage phase due to the retrogressed nature of the sample. Compositional layering on the thin section scale is also observed in sample 05-04D, suggesting that compositional variations on the scale of a mafic boudin are also possible.

Thermobarometry and Phase Equilibrium Modelling

In addition to the petrographic observations and mineral chemistry described above, thermobarometric and phase equilibria techniques were employed in order to provide quantitative *P-T* constraints on the prograde history of mafic eclogites in the Tso Morari complex. Pressure–temperature conditions of equilibration can be calculated from observed mineral assemblages that preserve an original equilibrium mineral pairing. When interpreting equilibrium textures in a rock, length–scales of equilibration and time spent at those conditions should be considered; the longer the time spent at a particular *P-T* condition, the larger the volume of rock able to equilibrate. Initially, smaller volumes of rock may reach equilibrium in different parts of rock, forming a 'mosaic equilibrium', where careful petrographic observation is needed in order to determine which phases are in equilibrium. There are two main methods used to determine the changing *P-T–X* conditions of a system: conventional thermobarometry and phase equilibria modelling. Often, multiple methods are applied, with advantages and limitations of each technique.

Methods

Conventional Thermobarometry

Conventional thermobarometry is useful when trying to determine a single pressure and temperature of equilibration of a rock, where the bulk composition has changed by an unquantifiable amount e.g. strongly mylonitised rocks. Pressure and temperature conditions for a mineral assemblage can be calculated from the measured distribution of elements of particular phases. A good thermometer has a steep slope in *P-T* space, a large ΔS and a small ΔV. These are typically cation exchange reactions e.g. garnet-biotite (Ferry and Spear, 1978), garnet–clinopyroxene (Ravna, 2000). A good barometer has a shallow slope in *P-T* space, a small ΔS and a large ΔV. These are typically net transfer reactions e.g. garnet–clinopyroxene–phengite (Krogh Ravna *et al.*, 2004a). Single phase thermobarometry uses the concentration of a minor element in a single phase to establish pressure or temperature e.g. Si in phengite (Massonne and Schreyer, 1987), Ti in biotite (Henry *et al.*, 2005), Zr in rutile (Ferry *et al.*, 2007), Ti in quartz (Wark *et al.*, 2006).

Garnet-clinopyroxene thermometry

The distribution of Fe and Mg between garnet and clinopyroxene is temperature dependent and is frequently used as a thermometer in suitable rock types. The cation exchange reaction is as follows:

$$3Hedenbergite + Pyrope = Almandine + 3\ Diopside$$

Thermodynamic data for common mineral endmembers is readily available, allowing the temperature of equilibration at any given pressure to be determined by estimating the equilibrium constant (K_{eq}) for the reaction.

$$K_{eq} = \frac{(a_{|di})^3(a_{|Alm})}{(a_{|hed})^3(a_{|py})}$$

The activity of mineral endmembers depends on the solid solution between end members and a model describing the crystallographic sites over which the cations may mix. For ideal mixing, the activity of each component relates to the mole fraction, where the activity a of component i is the mole fraction of the cation j, to the power of the number of sites over which the cation can exchange.

$$a_i = (X_j)^{\alpha}$$

For the case of almandine garnet, where divalent cations mix over three sites and ideal mixing is assumed, the activity is expressed as:

$$a_{alm} = (X_{alm})^3 = (\frac{Fe}{Fe + Mg + Ca + Mn})^3$$

and the garnet–cpx thermometer equilibrium constant could be written as:

$$(K_{eq})^{1/3} = \left(\frac{X_{Mg}^{di} X_{Fe}^{alm}}{X_{Fe}^{hed} X_{Mg}^{py}}\right) = \frac{(Fe^{2+}/Mg)_{Grt}}{(Fe^{2+}/Mg)_{Cpx}} = K_D$$

Where K_D is the distribution coefficient without any exponents (Spear, 1993). The equilibrium reaction was originally calibrated at high *P-T* experiments (Råheim and Green, 1974; Ellis and Green, 1979; Pattison and Newton, 1989; Green and Adam, 1991) and updated calibrations were published by Powell (1985) and Ravna (2000). Often, we only have data for total Fe of a mineral and are required to estimate the ferric to ferrous

iron content of a mineral before applying thermometers such as the garnet-clinopyroxene Fe-Mg thermometer. For almandine garnet which contains a high amount of total Fe, all Fe can be treated as ferrous without affecting the calculated temperature significantly (Ravna, 2000). Clinopyroxenes have lower total Fe, so that the ferrous/ferric iron estimation has a more dramatic effect on calculated temperatures (Ravna, 2000). In this study, Fe^{3+} was calculated using the method of Droop (1987). Štípská and Powell (2005) suggest that a minimum uncertainty of ± 70 °C (1 S.D.) should be applied to temperatures obtained from the garnet–clinopyroxene thermometer mainly due to uncertainty regarding calculation of the XFe^{3+} ratio of both phases. For the garnet–clinopyroxene thermometer, the composition of the analysed garnet outer rim recording the highest pyrope composition was used in conjunction with the averaged matrix omphacite composition. In the case where two compositional clusters of omphacite are present, the average composition of the aegerine-rich cores was used.

Garnet–clinopyroxene–phengite–(kyanite)–(quartz) barometry

Many barometers depend on the large molar volume change between phases such as plagioclase and garnet or clinopyroxene e.g. jadeite + quartz = albite. Feldspars, however, are not stable in the eclogite facies, giving minimum estimates to the application of these barometers. In high–pressure rocks, it can also be difficult to prove that mineral phases of interest are in chemical equilibrium due to zoning and overprinting at lower pressures. The use of a barometer with the fewest number of phases is therefore most useful. The barometer which could be considered most useful at high pressures is the equilibrium pyrope + 2grossular = 6diopside + 3muscovite ($Al^{2}Mg^{-1}Si^{-1}$) as it involves 3 phases, is independent of water activity and silica saturation and involves no uncertainty related to Fe^{3+} estimation (Waters and Martin., 1993). The largest source of uncertainty when applying this barometer are the activity models for garnet and clinopyroxene (e.g Schmidt, 1993).

When used in conjunction with the garnet–clinopyroxene thermometer, a *P-T* estimate can be obtained. However, there is major uncertainty involved in the calculation of ferric Fe and therefore the temperature constraint from the garnet–clinopyroxene thermometer. By applying other relevant equilibria (with a different slope), independent of $Fe^{3+,}$ the intersection between these equilibria can be used as an independent estimate of *P* and *T*. In the system KCMASH (K_2O-CaO-MgO-Al_2O_3-SiO_2-H_2O), grossular and pyrope in garnet,

diopside in clinopyroxene, muscovite and celadonite in phengite, kyanite and coesite or quartz define invariant points from which three linearly independent net transfer reactions will define pressures and temperatures of equilibration. These include:

1. Kyanite–SiO_2–absent reaction: (GCP)

   $6CaMgSi_2O_6$ (diopside) + $3KAl_2AlSi_3O_{10}(OH)_2$ (muscovite) = $2Ca_3Al_2Si_2O_{12}$ (grossular) + $Mg3Al_2Si_3O_{12}$ (pyrope) + $3KAlMgSi_4O_{10}(OH)_2$ (celadonite)

2. Phengite–absent reaction (GCKS)

   $3CaMgSi_2O_6$ (diopside) + $2Al_2SiO_5$ (kyanite) = $Ca_3Al_2Si_2O_{12}$ (grossular) + $Mg3Al2Si_3O_{12}$ (pyrope) + $2SiO_2$ (coesite/quartz)

3. Clinopyroxene absent reaction (GPKS)

   $Mg_3Al_2Si_2O_{12}$ (pyrope) + $3KAl_2AlSi_3O_{10}(OH)_2$ (muscovite) + $4SiO_2$ (coesite/quartz) = $3KAlMgSi_4O_{10}(OH)_2$ (Al-celadonite)

Simple relations between ln K, pressure and temperature were retrieved by Krogh Ravna and Terry (2004) for each of these reactions, based on the database of Holland and Powell (1998). For a kyanite–phengite–quartz/coesite–bearing eclogite, these reactions will ideally intersect at a single *P-T* point, but the intersection of any two of the reactions will define a *P-T* point for a single sample. Combining reaction (1) and (2), average standard deviations for this intersection is ± 65°C and ± 3.2 kbar in the coesite stability field and ±82°C, 3 kbar in the quartz stability field (Krogh Ravna, 2004). For phengite–absent kyanite–bearing samples or kyanite–bearing samples where phengite is not thought to be in equilibrium with the peak assemblage, reaction 2 can be used in combination with the garnet–clinopyroxene thermometer. However, errors for this intersection are ±5.5 kbar, ± 40°C at 35 kbar, 700°C.

For the garnet–clinopyroxene–phengite–kyanite–quartz barometer, the composition of the analysed garnet outer rim recording the highest pyrope composition was used in conjunction with the averaged matrix omphacite composition, alongside an average matrix phengite composition. End–member activities were calculated by the spreadsheet GCKS (Krogh Ravna and Terry, 2004) using the garnet model of Ganguly *et al.* (1996) and the pyroxene model of Holland (1990) and phengite solid solution of Holland and Powell (1998). Ferric iron has been calculated assuming four cations and six oxygens for clinopyroxene, the phengite

formula normalised to twelve SiAlTiCrFeMnMg cations and garnet normalised to five CaMnFeMgAlTiCr cations where Ca + Mn + Fe^{2+} + Mg = 3 and Al + Ti + Cr + Fe^{3+} = 2.

Multi–equilibrium thermobarometry

Geothermobarometers provide single pressure or temperature conditions of equilibration. Greater confidence can be obtained by the simultaneous solution of multiple independent reactions between end–member phases in an equilibrium assemblage (Powell and Holland, 1994). In this study THERMOCALC version 3.33 and thermodynamic dataset ds55 (Powell and Holland, 1988; Holland and Powell, 1998) were used in Ave*PT* mode. Compositional analysis of phases thought to be in equilibrium at peak pressure were recalculated into end–member activities using the program AX (Holland and Powell, 2009). Considered phases that exhibit solid solution include garnet, omphacite, phengite and talc, whereas pure end–member compositions were used for quartz, rutile, lawsonite and H_2O (Table 10).

Ave*PT* also provides detailed statistical information on reliability and confidence of the calculated result (see Powell and Holland, 1994), allowing poor quality data to be excluded (i.e. a phase not actually in chemical equilibrium with the peak assemblage). In this study, endmembers with the largest e* were removed and the calculation rerun until all indices conformed to the χ^2 test (Powell and Holland, 1994). Ave*PT* also allows variation of the fluid composition over a range of XH_2O ($XH_2O = H_2O/(CO_2 + H_2O)$). This approach allows much more flexibility when compared to conventional thermobarometers.

Phase equilibrium modelling

Thermodynamic modelling using internally consistent thermodynamic datasets and programs such as Thermocalc (Powell *et al.*, 1998), Perplex (Connolly and Kerrick, 1987) or Theriak/Domino (De Capitani *et al.*, 1987) has become commonplace in metamorphic petrology. This approach considers mineral assemblages, mineral compositions and proportions for a rock of a given bulk composition, at different *P-T* conditions using an equilibrium approach. High–pressure metamorphic rocks commonly show chemical zoning in minerals and disequilibrium textures, indicating that consideration must be given to elemental fractionation and disequilibrium textures when trying to decipher the rock history. Advances on the equilibrium approach consider a series of equilibrium stages along a *P-T* path by fractionating various minerals or reaction–produced fluids, of differing proportions, out of the system as they grow (e.g. Lanari *et*

al., 2017). Examples of dehydration reactions and fractional crystallisation of solids in subduction zones involve a continuously changing effective bulk composition of the rock, strongly influencing major and trace element cycles in subduction zones. Predicting these fractionation effects allows prediction of timing of mineral growth and compositional zoning during the history of a specific rock.

Compositional zoning in minerals provides us with a direct window into the chemical conditions at the time of mineral growth as they reflect changes in pressure, temperature and chemical evolution of a rock. By comparing chemical zoning in minerals, with expected results from equilibrium modelling, we can gain insight into the succession of different metamorphic stages of a rock. Garnet is a useful mineral due to its refractory nature and slow intracrystalline diffusion, preserving chemical growth zones (O'Brien and Vrána, 1995), particularly in cold environments such as subduction zones. Garnet also forms an abundant mineral phase in a range of rock types over a large *P-T–X* range. It is also a rigid phase that is good at preserving ultrahigh–pressure minerals such as coesite during ultrahigh–pressure metamorphism. In this section thermodynamic forward models are used in order to investigate garnet growth and composition in a mafic eclogite from the Tso Morari complex, in order to gain insight into the mineralogical processes that cause complex growth zoning and the influence of fractionation of water and garnet growth during the metamorphic history of the rock.

Phase equilibria modelling was undertaken for sample 11-05, a mafic eclogite from the Polokongka La region. Phase equilibria models were calculated using the eleven component system MnO–N_2O–CaO–K_2O–FeO–MgO–Al_2O_3–SiO_2–H_2O–TiO_2–Fe_2O_3 (MnNCKFMASHTO) using Theriak Domino v.2015 (De Capitani *et al.*, 1987) with thermodynamic dataset ds55 (Powell and Holland, 1988; Holland and Powell, 1998; updated August 2004), adapted by Doug Tinkham (http://dtinkham.net/peq.html). The following activity composition models were used: Diener and Powell (2012) for amphibole and clinopyroxene. Holland and Powell (2003) for ternary plagioclase and K–feldspar. White *et al.* (2007) for garnet with added spessartine and biotite with added mnbi (ignoring mneast). Mahar *et al.* (1997) and Holland and Powell (1998) for chlorite with added mnchl as in Tinkham *et al.* (2001). Coggon and Holland *(*2002) for white mica with their prl and margarite members excluded due to the consistent overestimation of the stability of these end–members. White *et al.*, (2000, 2005) for ilmenite (Mn system). Holland and Powell (1998) for epidote.

The following pure phases that are not part of a converted solution model phases were added: H2O, CO2, quartz, coesite, kyanite, albite, rutile, sphene, zoisite, lawsonite, calcium carbonate.

MnO was included as a component due to the large effect on garnet stability, expanding it down temperature. It is acknowledged that other activity models for eclogite–bearing minerals e.g. white mica, amphibole, clinopyroxene, lack an Mn–bearing end member, precluding partitioning between these phases. However, negligible spessartine content in the outer garnet zones indicates that inclusion of MnO is not expected to have a significant effect on the position of grossular and pyrope isopleths, which are utilised for *P-T* determination, for garnet outer core or rim zones. A temperature of 700°C was used as an upper limit of phase diagrams as the higher temperature regions can be metastable with respect to melt–bearing assemblages. Melt models were not included due to the absence of appropriate models for mafic systems at low temperatures.

Phase diagrams were calculated as pixel maps rather than by calculating phase boundaries. This setting calculates all possible variables at the 'pixel' of interest, over a grid of predetermined size, allowing large amounts of data to be generated quickly. The output data files can then be represented on a grid as quantitative values. This method also provides a solution to the problem of the calculation getting 'stuck' when calculating phase boundaries, particularly those involving hydrous phases such as chlorite or felsic bulk compositions at high pressure.

Bulk composition calculation

The effective bulk composition used for phase equilibria modelling was calculated using mean microprobe analysis of homogeneous major phases in proportion to their modal volume in the rock (e.g. Palin *et al.*, 2017). X–ray fluorescence (XRF) analysis was not considered for determining bulk composition due to the requirement to consider smaller equilibration volumes in water–undersaturated systems and the requirement to exclude particular constituents during modelling. Garnet composition was estimated based on a representative garnet profile and an assumed spherical geometry. Fe^{3+} was estimated based on mineral stoichiometry using the method of Droop (1987). The anhydrous bulk composition was used to calculate phase diagrams with additional H_2O added to the anhydrous bulk (see below).

When calculating the bulk composition of a rock, the equilibration volume that influences mineral growth must be identified. This depends on the heterogeneous distribution of phases, the size and distribution of

poikiloblastic phases and can be limited by the slow diffusion of elements such as Al. Estimation of a suitable equilibration volume is a qualitative procedure and is the largest source of random error when estimating bulk compositions. In order to quantify this, a Monte–Carlo method was employed by randomly generating bulk compositions by varying the calculated modal mineral proportions (see Palin *et al.,* (2017)). Modal proportions of minerals were varied randomly from normal (Gaussian) distributions whose standard deviation is within 10% from the observed value. The resulting bulk composition was then input into Theriak-Domino with the water content of interest. In order to quantify the effect of the bulk composition uncertainty on garnet isopleths, the random bulk composition generation was repeated seven times and used to calculate the position of measured grossular and pyrope isopleths (see Figure 31). The resulting isopleth calculations are overlain on the same diagram to display the resulting variations in isopleth topology.

Results

Isochemical phase diagrams were constructed both with and without considering the effects of cation fractionation during garnet growth. The well preserved and sharp nature of the garnet zoning indicates that little diffusional modification has occurred, therefore we can assume that the composition of the garnet within these concentric zones reflects the prograde *P-T* conditions of garnet growth. However, petrographic observations interpreted above describe post–growth modification of garnet composition by the influx of fluids. This post–growth modification of garnet is identifiable as Mg-Fe embayments from the rim zones of garnet protruding inwards and are identifiable on EDS element maps as well as BSE images of garnet. It is therefore possible to identify areas of concentric garnet growth which are unaffected by Mg–embayments and are representative of prograde garnet growth, allowing for the selection of a representative profile which can be utilised in forward modelling of the rock. The core region has also been shown to occasionally preserve fine compositional textures. Identification of these fine features can be difficult to resolve, however analysis of a small number of garnets using high resolution mapping techniques highlights the variation in Ca within the core region, showing that the highest Ca patches are representative of the primary garnet growth (Waters *et al.*, 2020).

Garnet profiles across representative areas were used to model the prograde growth history of sample 11-05. Additionally, due to post–peak modification of Fe-Mg inclusions in garnet described above, such as

amphibole, inclusion assemblages are not relied upon to constrain the stability fields of garnet growth unless the inclusions have been demonstrated to represent prograde conditions, including textural observations such as grain size, proximity to fractures e.g. small isolated rutile grains, or changes in inclusions assemblage from core to rim, not associated with Mg–embayments e.g. paragonite + zoisite intergrowths at the garnet core-rim boundary.

Based on estimates from thin sections and BSE images, the average modal proportion of phases considered in the modelling of sample 11-05 is garnet 24%, omphacite 10.6%, coarse amphibole 3.2%, fine amphibole 14.9% (50% of symplectite proportion), plagioclase 14.9%, white mica 16%, clinozoisite 8%, kyanite 0.4%, rutile 0.1%, calcite 0.5%, quartz 8.2%. All bulk composition calculations utilised in modelling sample 11-05 are presented in Table 6. Water content during prograde garnet growth was estimated by the production of P–XH_2O, T–XH_2O and P–aH_2O phase diagrams as detailed below.

Bulk composition (mol%)	***Si***	***Al***	***Ca***	***Mg***	***Fe***	***Fe^{3+}***	***K***	***Na***	***Ti***	***Mn***	***H***
Calculated	55.83	22.02	10.7	7.96	8.70	1.14	2.14	5.54	0.11	0.14	0
1*	56.45	21.78	10.49	7.99	8.23	1.12	2.16	5.91	0.11	0.13	0
2*	55.67	21.64	10.61	8.36	9.06	1.04	2.03	5.28	0.11	0.15	0
3	56.20	22.64	10.45	7.45	8.65	1.14	2.33	5.63	0.1	0.15	0
4	55.33	22.11	10.83	8.00	9.24	1.11	2.13	5.09	0.11	0.16	0
5	56.09	22.17	10.51	7.97	8.32	1.10	2.22	5.72	0.12	0.14	0
6	55.85	21.77	10.94	7.89	8.59	1.19	1.93	5.71	0.11	0.14	0
7*	54.95	21.75	10.97	8.57	8.97	1.15	1.98	5.37	0.11	0.15	0

Table 6 showing the calculated bulk composition of sample 11-05 and the bulk compositions randomly generated using the Monte-Carlo method. Star denotes compositions with two isopleth intersections.

Determination of water content

Two petrological observations were used to constrain water conditions during garnet core growth: 1) Inclusion of hydrous minerals in garnet growth zones, 2) Observations of the changing style of garnet growth from core to rim. Inclusions trapped in garnet can give us an indication as to the prograde history of a rock. Prograde inclusion assemblages are hard to constrain in eclogites from the Tso Morari complex due to their common history of post peak modification of hydrous phases by the influx of fluid, as discussed above. Inclusions which occur away from fractures and altered zones in the garnet element maps are considered to be primary inclusions. These mostly consist of quartz and rutile in the garnet cores, occasionally with fine needles of zoisite. The consistent appearance of coarse zoisite and paragonite intergrowths at the garnet core-

rim boundary and the absence of such intergrowths in garnet cores suggests that lawsonite was a stable phase during garnet rim growth and subsequently broke down to form the pseudomorphs of zoisite and paragonite.

The change from grain boundary–dominated, skeletal garnet core growth to faceted garnet growth at the core-rim boundary (see Figure 14), suggests that garnet growth was initially controlled by the availability of constituents along the grain boundary network due to the limited availability of a fluid phase. This indicates that fluid–undersaturated conditions were present during garnet core growth in the absence of lawsonite as a stable phase. This is followed by the later appearance of pseudomorphs after hydrous lawsonite at the core-rim boundary, where garnet growth becomes faceted and replacement of its own inclusions occurs at a more pyrope–rich composition, equivalent to a later concentric garnet zone.

In order to determine the XH_2O of the system, T-XH_2O phase diagrams were constructed at 22 kbar and 26 kbar and P-XH_2O phase diagrams were constructed at 525°C. Results were compared to petrographic observations of primary mineral inclusions. Water undersaturated conditions of 6 mole of additional H_2O, in the range of 5–7 moles H_2O, were chosen to be representative of garnet core growth due to the absence of lawsonite at low pressure conditions (Figure 27).

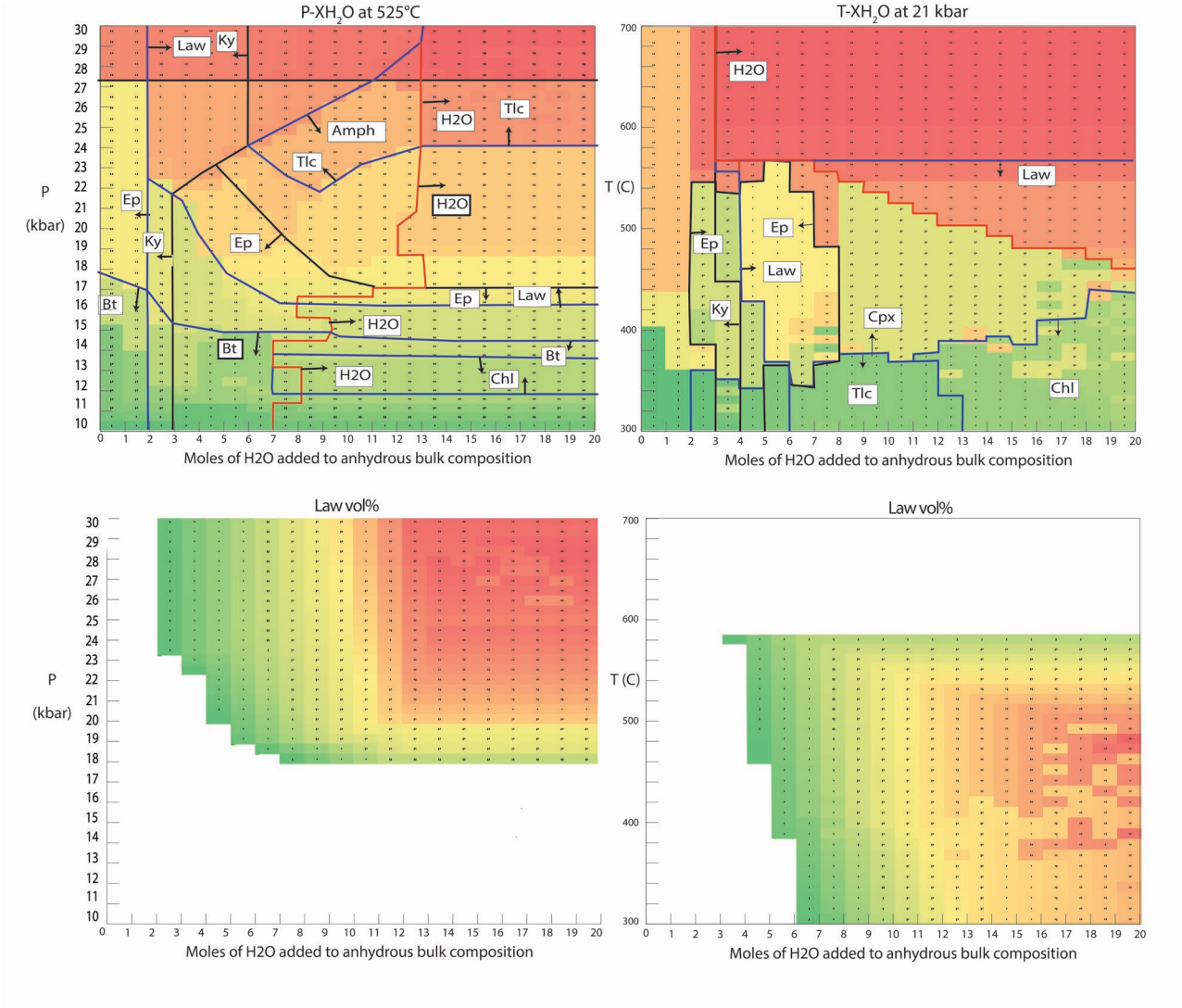


Figure 27 T-XH_2O and P-XH_2O phase diagrams showing stable assemblage fields (a,b) and lawsonite abundance (c,d). Colour scale reflects the range of numerical values in the grid where red = high and green = low. Red lines show H_2O saturation, blue lines show hydrous phases. The colour scale in c and d shows a greater modal abundance of lawsonite in red and a lower abundance in green. Lawsonite absent conditions require < 7 additional moles of H2O added to the anhydrous bulk composition for P=22 kbar and < 5 moles H_2O at P=26 kbar. Between 5 and 7 moles H_2O, no feldspar or lawsonite are present.

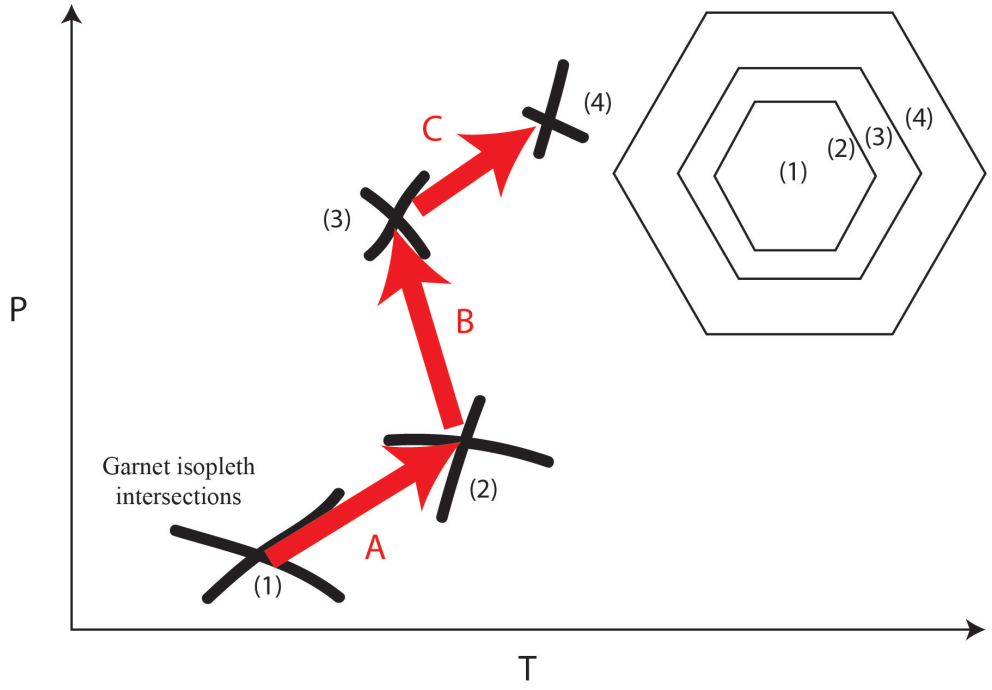
Fractionation of garnet

Based on the assumption that garnet growth begins in a rock matrix in which all of the minerals are chemically participating, the total bulk composition was used, with the estimated XH_2O, to construct a pseudosection using the software DOMINO, in order to model garnet core growth. In a chemically fractionated system, certain constituents are locked up in refractory phases such as garnet cores. These cores were removed from the total bulk composition successively for each garnet growth zone. Garnet growth zones were subdivided based on inclusion density and composition, as well as sharp changes in garnet composition from core to rim. Four zones of distinctive garnet growth were identified in sample 11-05 (see Figure 21).

Isopleths of pyrope and grossular were contoured in *P-T* space and the isopleth intersections for the garnet core zone, defined in Table 3, were used to determine a segment of *P-T* path, along which the rock evolved. Garnet and H_2O were then 100% fractionated out of the system by removing the predicted proportion of garnet of a specific composition, at each step along the *P-T* path. This was achieved using the software THERIAK. The fractionated bulk composition along this *P-T* path was then extracted and input into the software DOMINO, allowing us to model the growth of the next garnet zone using a fractionated bulk composition. This technique was repeated for successive garnet growth zones and allows not only continuous fractionation of garnet and H_2O during prograde garnet growth, but also allows isopleth intersections to be determined using an 'effective bulk composition' equivalent to the stage of garnet growth. Additionally, using this method, water saturation conditions and garnet resorption can be modified at specific points along the prograde evolution, in line with petrographic observations.

Bulk compositions	Notes	Si	Al	Ca	Mg	Fe	Fe^{3+}	K	Na	Ti	Mn	H
Inner core	Full bulk	55.83	22.02	10.70	7.96	8.70	1.14	2.14	5.54	0.11	0.14	6
Outer core	Grt removed 100%	46.21	15.64	7.68	7.29	2.91	1.11	2.14	5.54	0.11	0.00	6
Rim	Grt removed 100%	43.13	13.59	7.09	6.86	0.86	1.10	2.14	5.54	0.11	0.00	sat
Rim	Grt removed 50%	42.55	13.22	6.50	6.89	0.82	6.50	2.14	5.54	0.11	0.00	sat

Table 7 Fractionated bulk compositions for sample 11-05 in mol%, as input into Theriak Domino.



1. Using the full bulk composition (Table 7), calculate isopleth intersections using DOMINO for garnet compostion (1) and (2) to determine P-T path (A).

2. Calculate fractionated bulk composition after garnet outer core growth (2) using THERIAK after 100% fractionation of garnet along P-T (A).

3. Using fractionated bulk composition after garnet outer core growth (2), calculate isopleth intersections using DOMINO for garnet compostion (3) to determine P-T path (B).

4. Calculate fractionated bulk composition after garnet inner rim growth (3) using THERIAK after 100% fractionation of garnet along P-T (A) and (B).

5. Using fractionated bulk composition after garnet inner rim growth (3), calculate isopleth intersections using DOMINO for garnet compostion (4).

Figure 28 Cartoon detailing the garnet fractionation method described

Garnet core growth

In water saturated conditions, a garnet isopleth intersection for sample 11-05 is predicted at 20-21 kbar, 525-550°C (Figure 29c), comparable to the higher pressure intercept of Palin (2013) for sample L08-03A, at 20-25 kbar, 550-600°C (Figure 30b). In water undersaturated conditions (6 wt% H_2O), sample 11-05 shows only a single isopleth intersection at 11-14kbar, 400-470°C, showing a 10 kbar, 100°C shift in predicted *P-T* conditions (Figure 29a). A higher pressure intersect is close to occurring due to the extension of the grossular isopleth topology towards lower temperatures and higher pressures.

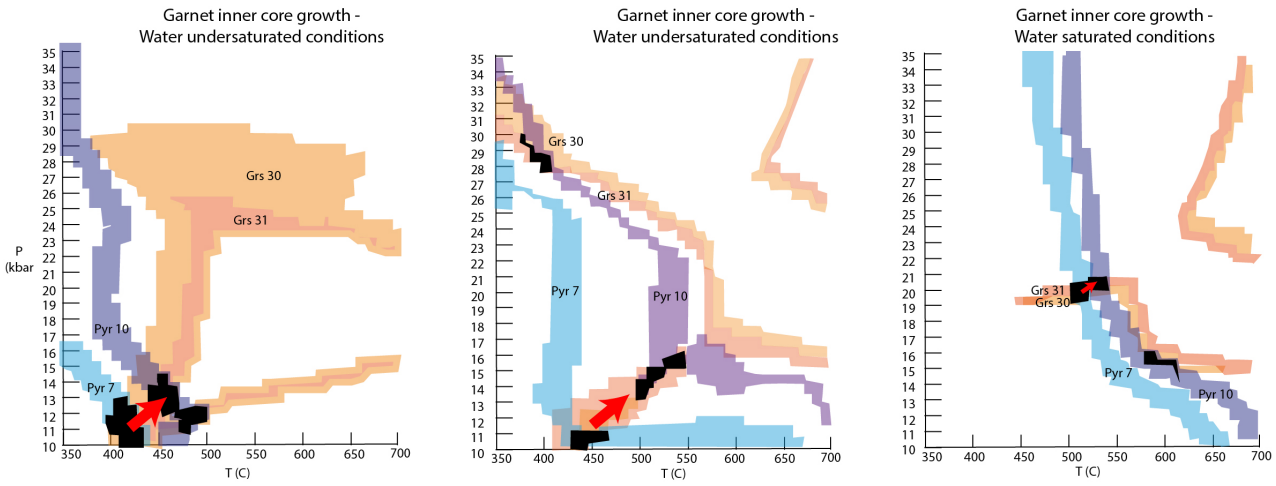


Figure 29 P-T pseudosection for sample 11-05 using a. water undersaturated bulk, 6 wt% H_2O, b. water undersaturated bulk, 9 wt% H_2O c. water saturated bulk. Coloured regions show the pyrope and grossular isopleths and the solid black regions show the isopleth intersections for the garnet inner core and the garnet inner core to outer core transition

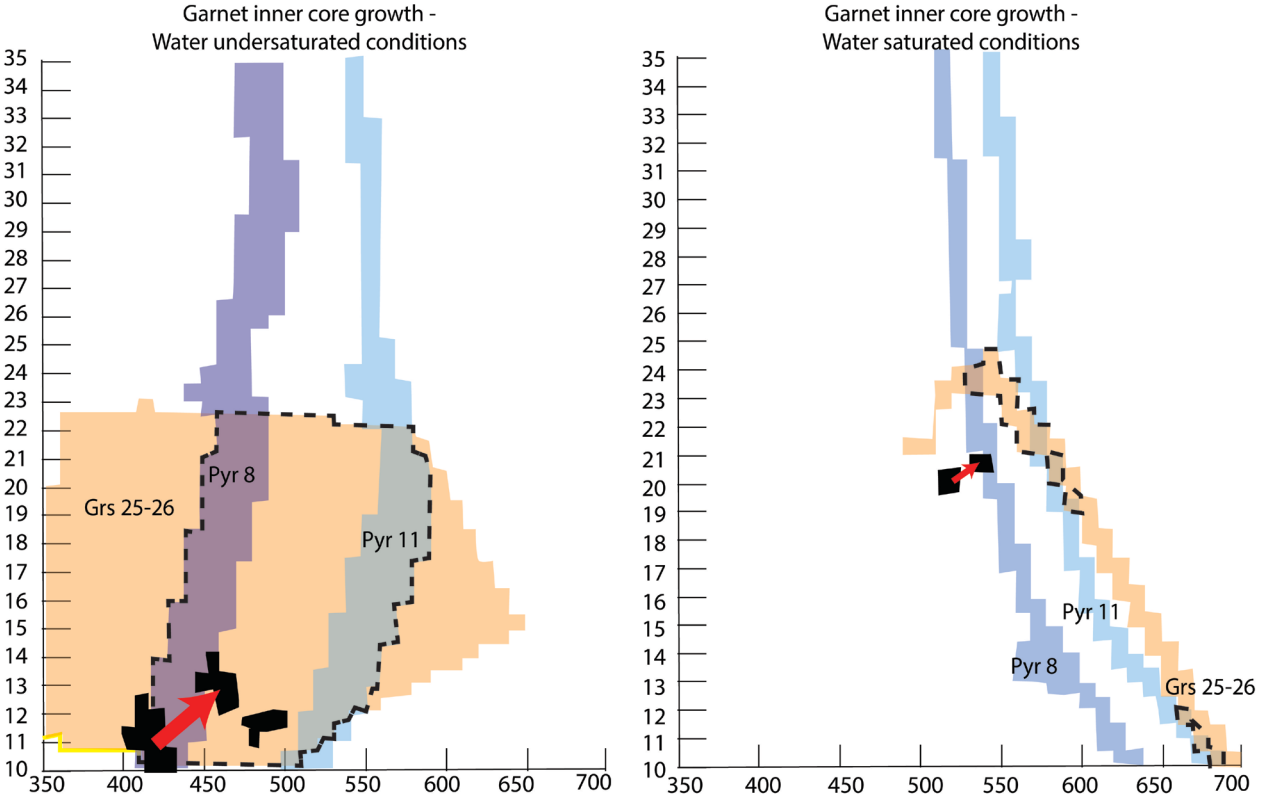


Figure 30 P-T pseudosection for sample L08-03A using bulk composition from St-Onge et al., (2013). A. Water undersaturated conditions with 3 mol% H_2O. B. Water saturated conditions with 50mol% H_2O. Black dashed region shows garnet isopleth intersections for sample L08-03A. Black solid region shows garnet isopleths intersections for sample 11-05 for comparison. Notes two possible intersections at 21kbar and 11 kbar in water saturated conditions.

A Monte-Carlo method was applied to the water undersaturated bulk composition of sample 11-05, in order to quantify the error associated with bulk composition calculation and the effect on the topology of the garnet compositional isopleths (see page 161, Bulk composition calculation). Figure 31 shows the measured garnet isopleths plotted using Theriak–Domino for seven bulk compositions randomly generated from the calculated bulk. The topology of the pyrope isopleths are not very variable, however the topology of the grossular isopleths vary significantly, particularly when isobaric. The isopleth intersection determined from the calculated bulk is common to all bulk compositions whereas, in some bulk compositions, the grossular isopleths extend up pressure and down temperature, occasionally forming a second intersection at pressures > 28 kbar and temperatures < 370°C. For the garnet isopleth intersection at lower pressures and temperatures (10-14 kbar, 400-500°C), assemblages are comprised of garnet, biotite, white mica, epidote, diopside, Na-Ca amphibole, quartz, rutile and kyanite. For the garnet isopleth intersection at higher pressure, lawsonite, garnet and glaucophane become more stable, paragonite disappears and talc is stable in the lower temperatures range.

The post peak alteration of ferro–magnesian mineral inclusions in garnet means that we cannot use the composition of these phases to verify which of the two observed intersections is most accurate. However, the absence of zoisite-paragonite intergrowths in the inclusion–rich core of garnet indicates that hydrous lawsonite was not a stable phase during garnet core growth. This observation is consistent with a garnet isopleth intersection in a lawsonite–absent assemblage field at 10-14 kbar, 400-500°C, an intersect that is not only petrologically validated, but also coincides with 100% of garnet isopleth intersections calculated using the Monte Carlo method, a factor which may therefore be an important consideration when faced with multiple garnet–isopleth intersections during pseudosection interpretation.

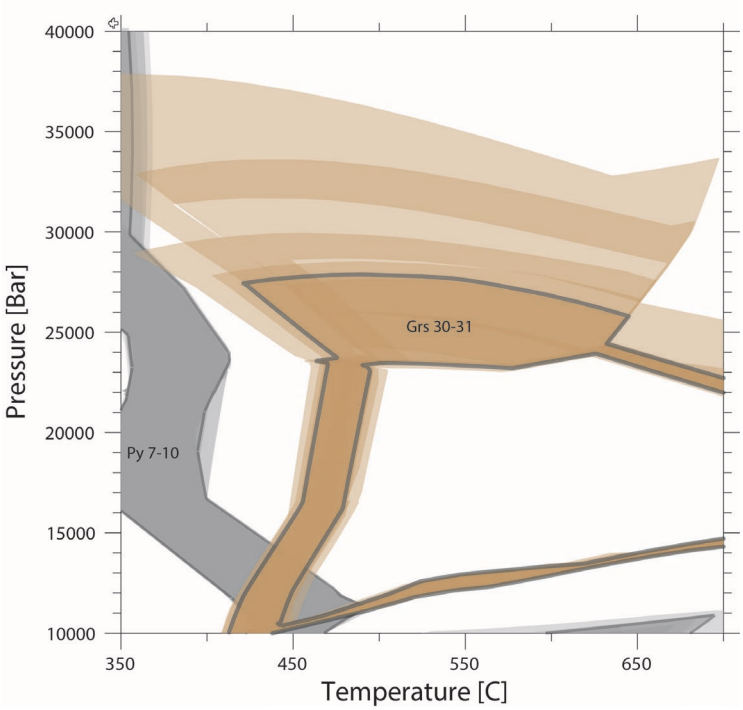


Figure 31 Pseudosection showing brown grossular (30-31%) and grey pyrope (7-10%) isopleths for sample 11-05. Isopleths plotted using the calculated bulk composition are outlined in grey. Isopleths plotted from randomly generated bulk compositions are shown in transparent shades of the same colour. See Table 6 for bulk compositions.

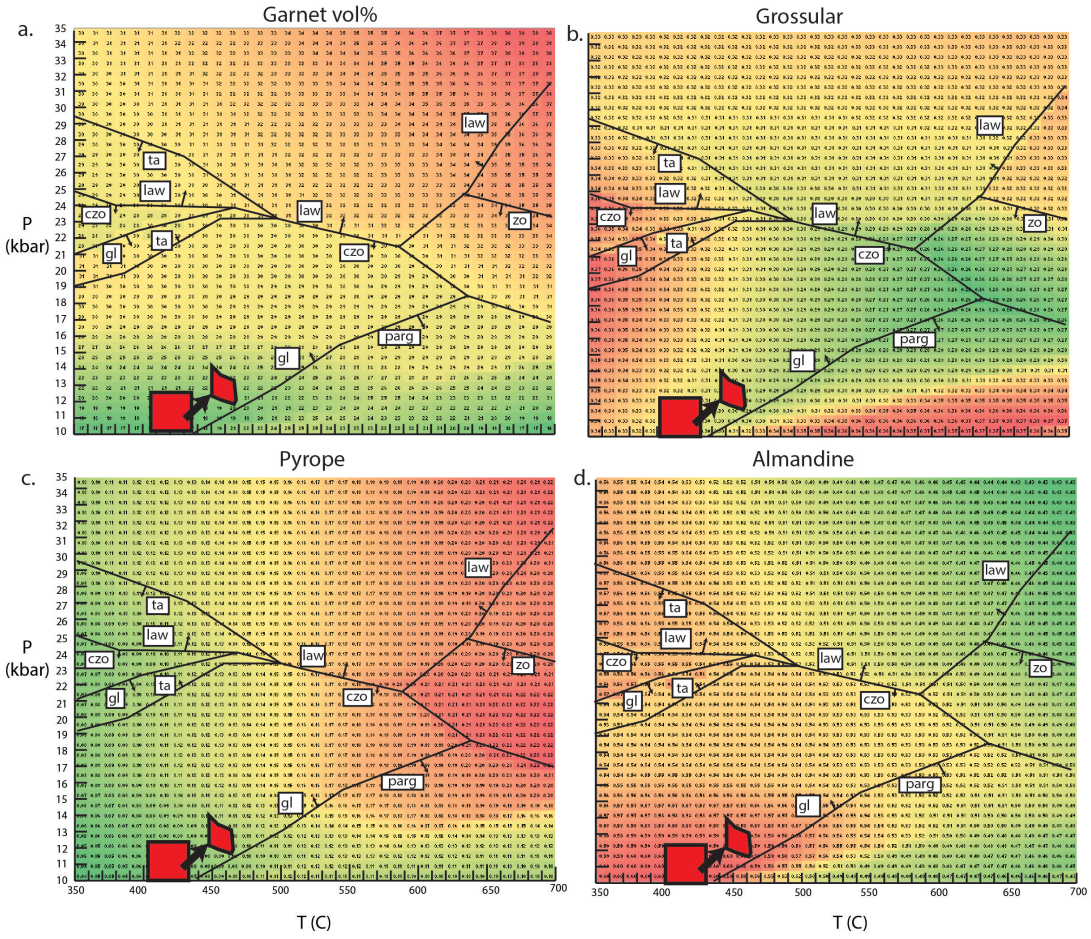


Figure 32 garnet mode (a) and garnet compositions (b–d) predicted for sample 11-05 based on an unfractionated bulk composition in water undersaturated conditions (6mol% H_2O). The red to green colour scale shows high to low values respectively. Mineral isograds are shown as solid black lines. Red areas denote garnet core isopleth intersection and black arrow marks predicted P-T path.

Following the determination of the conditions of garnet core growth, garnet can be fractionated from the bulk composition, with respect to the volume of garnet predicted by the models, in order to estimate the condition of garnet outer core growth. This has been estimated at 370-420°C, with an uncertain pressure estimate of 16.5-25 kbar due to the steeply oriented garnet isopleths (see Figure 33). Despite the wide range of predicted pressures, 10 model % of garnet growth is predicted to occur at any of the chosen isopleth intersections, compared to an observed 8.5%. The range of *P-T* paths predict similar changes in pyrope and grossular content along these paths which predict an approximately isothermal loading of the sample, resulting in an approximately constant predicted effective bulk composition along the range of isopleth intersections. The difference between high–pressure isopleth intersections compared to low–pressure intersections is the presence of talc, which is only predicted to be stable above 20 kbar.

An isothermally loaded *P-T* path predicts that garnet abundance will gradually increase, as garnet growth is controlled by equilibrium with amphibole. Growth rate of garnet slows towards the outer core of the garnet. This is shown by a large area of a single colour on the garnet mode diagram (Figure 33). As lawsonite becomes stable, amphibole is predicted to breakdown and garnet growth rate is predicted to accelerate as temperature increases. The almandine content of garnet is lower for garnets grown at higher pressure and temperature conditions. Grossular shows a more complex pattern influenced by changing mineral paragenesis, particularly related to the presence of a pargasitic amphibole at lower pressures, epidote group minerals below 24 kbar and lawsonite above 24 kbar. Pyrope content increases temperature in water saturated and water undersaturated models. Pyrope is observed to increase towards garnet rims, indicating a potential temperature increase towards the rims. We have demonstrated that the grossular isopleths, used for predicting pressures for garnet growth based on the intersection with pyrope isopleths, is highly variable depending on the mineral paragenesis along a *P-T* path. In order to determine the *P-T* conditions of garnet rim growth, it is therefore necessary to fractionate the garnet cores out of the total bulk composition, estimating a suitable effective bulk composition.

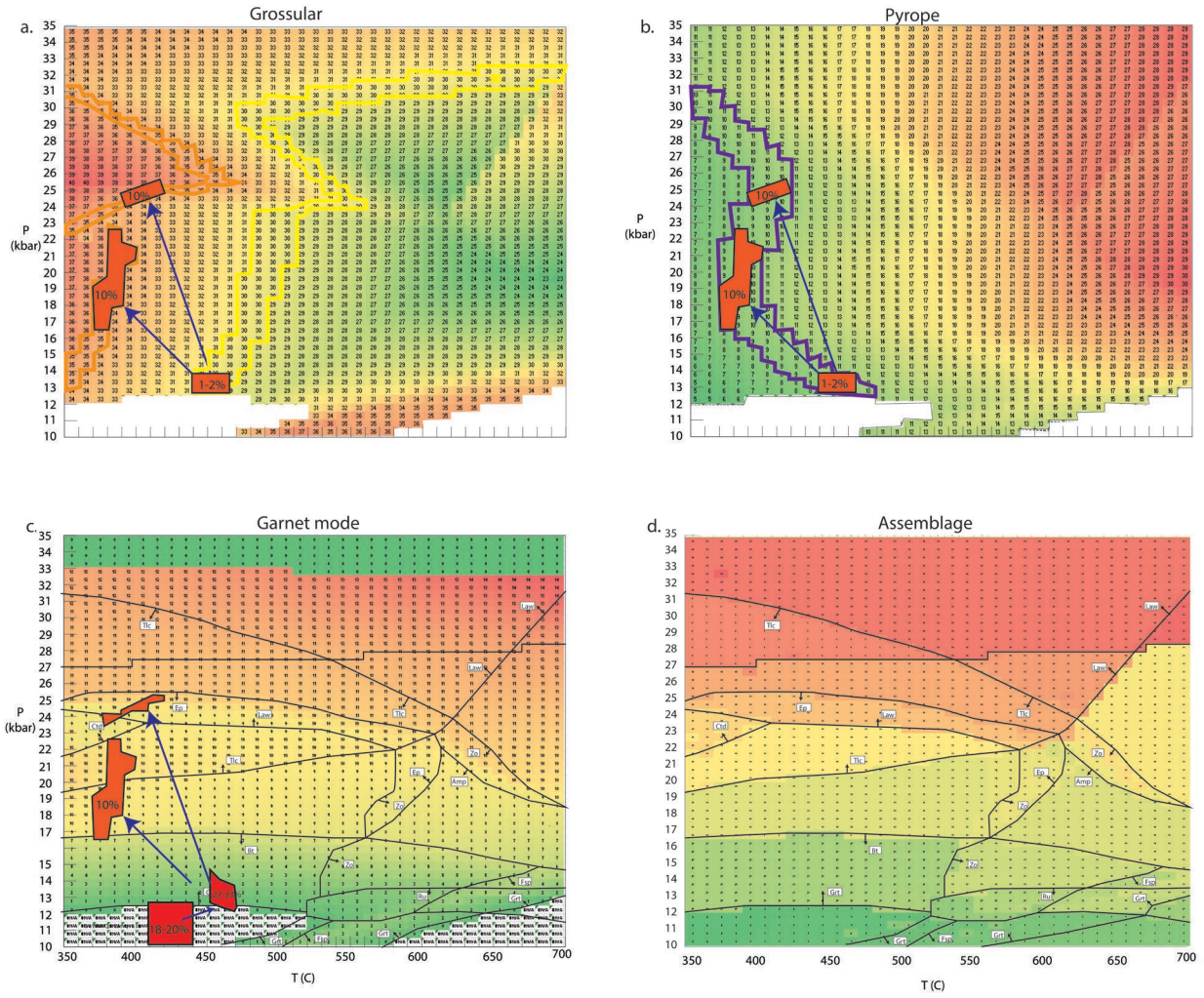


Figure 33 Sample 11-05 garnet outer core. Models based on a fractionated bulk composition in water undersaturated conditions (6mol% H_2O). Garnet compositions (a and b) and garnet modal abundance (c). The red to green colour scale shows high to low values respectively. Observed grossular isopleths of 30% (yellow) and 35% (orange) shown for the inner and outer zones of the garnet outer core respectively in a. Observed pyrope isopleths of 9–10% (blue) for the garnet outer core zone shown in b. Isopleth intersections for the outer core are shown as orange boxes with their corresponding garnet model abundances in a and b. Garnet inner core isopleth intersections with their corresponding garnet modal abundance shown in the red boxes in c. Isopleth intersections for the first garnet outer core growth ($Grs_{30}Pyr_{9–10}$) (shown in a) are consistent with the last growth of the garnet inner core (shown in c). d. Pseudosection showing assemblage fields with zero mode isopleths for major minerals plotted (also shown in c). Cpx present in all assemblages plotted. The red to green colour scale shows low to high variance respectively.

Pseudosections for garnet outer core growth (Figure 33) predict 30 modal % garnet growth to have occurred by the garnet core-rim boundary. Observed garnet modal abundance in this sample is 24%, indicating that either the models are overestimating garnet stability, or that garnet resorption occurred at the core-rim boundary. The presence of an irregular Mn– and Y–annulus at this boundary is consistent with garnet resorption having occurred, as the breakdown of garnet will liberate Mn and Y, which, in the absence of an alternate mineral sink, could back diffuse into the garnet, forming an annulus. Measured garnet compositions should preserve *P-T* conditions at the outer edge of the garnet core following resorption, therefore the predicted model proportion of garnet core growth based on isopleth intersection should be representative of *P-T* conditions prior to garnet resorption but represent an effective bulk composition after garnet has been resorbed which can be used to model garnet rim growth.

Garnet growth along a prograde *P-T* path in sample 11-05 is predicted to be gradual and constant. In order to instigate resorption of garnet along the prograde path, as predicted in sample 11-05, a change in effective bulk composition is required to shift the garnet mode % contours to higher pressure and temperatures. One way to change the effective bulk composition of a rock at a fixed pressure and temperature is to change the equilibration volume, increasing or decreasing the volume of rock that is 'available' to react. The addition of water increases the mobility of elements along grain boundaries, increasing the equilibration volume and changing the effective bulk composition of the rock. The appearance of pseudomorphs after hydrous lawsonite at the core-rim boundary of the Tso Morari eclogite and the presence of a Mn– and Y– annulus is consistent with the potential addition of water during prograde metamorphism. This change from water undersaturated to water saturated conditions at the core rim boundary, in order to explain the textures observed in the garnets, would need to push the garnet stability field to higher pressures and temperatures. The first growth of the garnet rim should preserve compositional intersections that are not consistent with the conditions preserved in the outer core of the garnet.

Garnet rim growth

Garnet rim *P-T* predictions using a fractionated bulk composition, with a water undersaturated core and a water undersaturated rim, does not produce any isopleth intersections. Modelling using the same bulk composition, with a water saturated rim (Figure 34) predicts an increase in pressure and a large increase in

temperature before garnet continues to grow at >26 kbar and >615°C. The closely spaced isopleths and the wedge shape of the garnet stability field make determination of garnet isopleth intersections difficult due to the uncertainty in the position of the isopleths. The high predicted grossular content also means that no isopleth intersections occur. The closely spaced pyrope and grossular isopleths reflect the breakdown of talc and lawsonite, hydrous minerals sensitive to water saturation conditions.

The P-T predictions using a water undersaturated core were compared to calculations using a water saturated core (Figure 33, dark grey box) and a water saturated rim with garnet cores fractionated out of the bulk composition (Figure 33, light grey box). In order to fractionate the garnet core out of the bulk composition, the composition of the garnet core was measured across a transect from core to inner rim and averaged over a sphere. A similar calculation was used to estimate the average bulk composition of the garnet rims. The garnet core and rim were then treated as two distinct phases in the bulk composition calculation where the composition of phases with respect to their modal abundance were used to calculate the bulk composition of the rock (as in methods, page 161).

Thermodynamic modelling of garnet rims in water saturated conditions after fractionation of the observed garnet core from the bulk composition, predicts garnet rim growth at ~27 kbar, 600°C (Figure 33, light grey box). In these models pyrope is predicted to increase and grossular to decrease rapidly towards the rim. These results are comparable to predictions without the effect of cation fractionation where observed grossular concentrations occur at pressures >26.5 kbar but predicted pyrope concentrations are too high. The predicted stable assemblage during garnet rim growth is garnet, phengite, omphacite, coesite, talc, lawsonite, rutile.

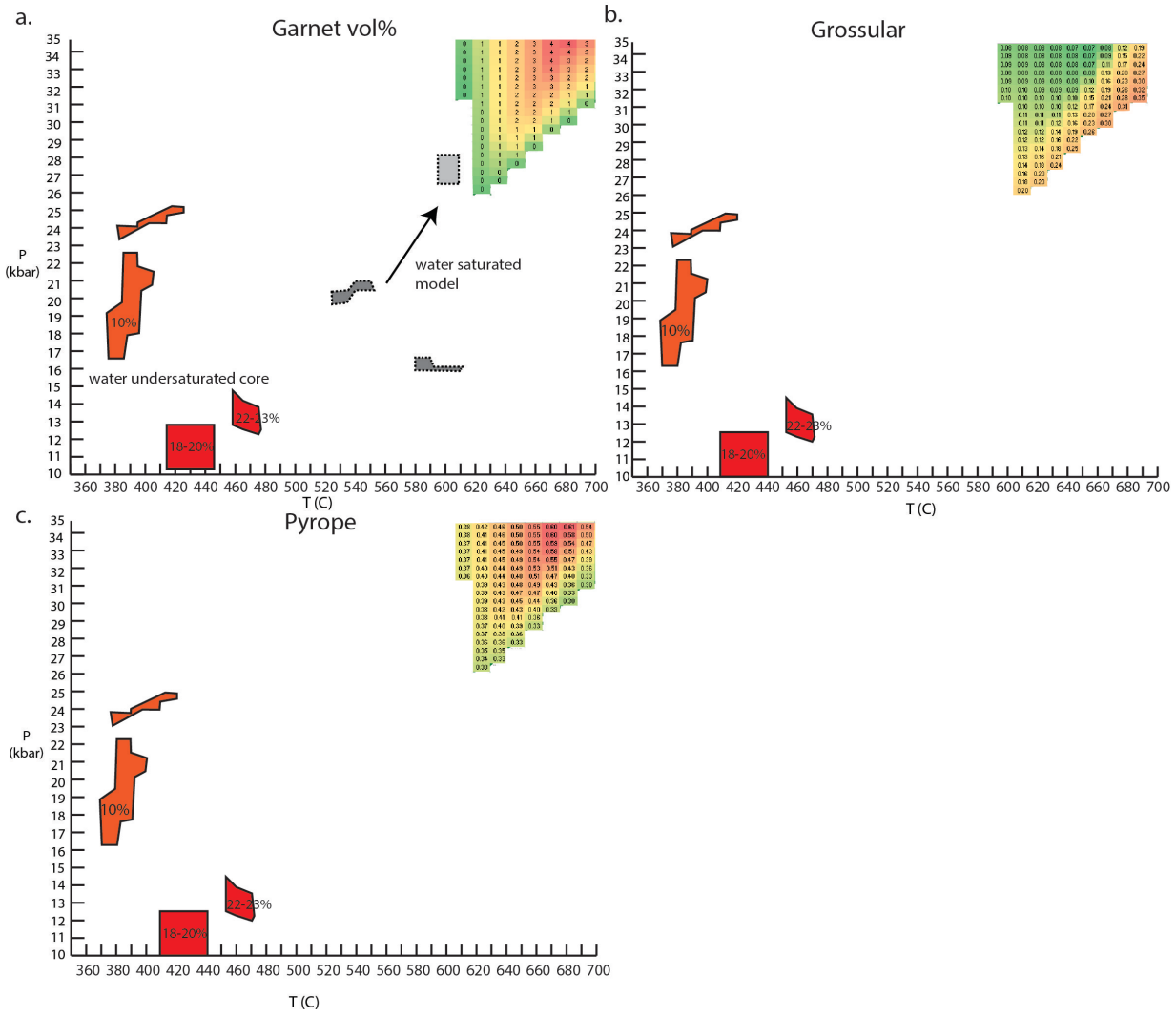


Figure 34 Sample 11-05 garnet rims growth. Garnet modal abundance (a), grossular (b) and pyrope (c) isopleths for inner rim conditions using a fractionated bulk composition. Red boxes correspond to garnet inner core isopleth intersections in water undersaturated conditions and their corresponding garnet abundances. Orange boxes correspond to garnet outer core isopleth intersections in water undersaturated conditions and their corresponding garnet abundance since the growth of the inner core. Dark grey and light grey dashed areas in a. show the observed isopleth intersections for a water saturated core calculated with the full bulk composition and a water saturated rim respectively, taking into account garnet core fractionation (see text).

Water activity

Previous modelling of the Tso Morari eclogites has assumed a pure water fluid with an activity of one. The presence of carbon–rich fluids can decrease water activity during metamorphism. It is difficult to determine the activity of water during peak metamorphism in these samples due to the amphibolite facies hydrous overprint. The presence of carbonate as a peak phase in these rocks suggests that the effect of water activity on metamorphism should be investigated.

Carbon was added as a component into the bulk composition based on 2% dolomite in sample 11-05. A simple H_2O-CO_2 mixing model (Fluid1) was adapted from DS6.1 and added to DS5 in the following format:

```
Fluid1   (SITE,MARGULES)    M(1):H2O,CO2

 H2O        H2O      1.0  0.0  0.0

 CO2        CO2      1.0  0.0  0.0
```

A P-XH_2O diagram was constructed at 525°C and shows that lawsonite–absent assemblages are stable at < 4 mol% H_2O at pressures > 25.5 kbar and < 8 mol% H_2O at pressures < 25.5 kbar (Figure 34d), suggesting that lawsonite-absent garnet cores grew in water-undersaturated conditions. Calculation of a *P-T* pseudosection in water undersaturated conditions (6 mol% H_2O) in the presence of a mixed fluid increases garnet stability (Figure 34a), increasing the modal abundance at a given *P-T*. The topology of the garnet pyrope isopleths are similar to the fluid–undersaturated conditions in the absence of CO_2 (compare Figure 34c to Figure 31c). The garnet grossular isopleth topology is different (compare Figure 34b to Figure 31b), with a much larger high–Ca field at low *P* and *T* and the values are much higher. Using the observed grossular and pyrope compositions of the garnet core, there is no isopleth intersection within the *P-T* window. However, these results shows that changing introducing CO_2 as a fluid phase affects the position of garnet isopleths and therefore could affect the apparent P-T conditions of garnet growth.

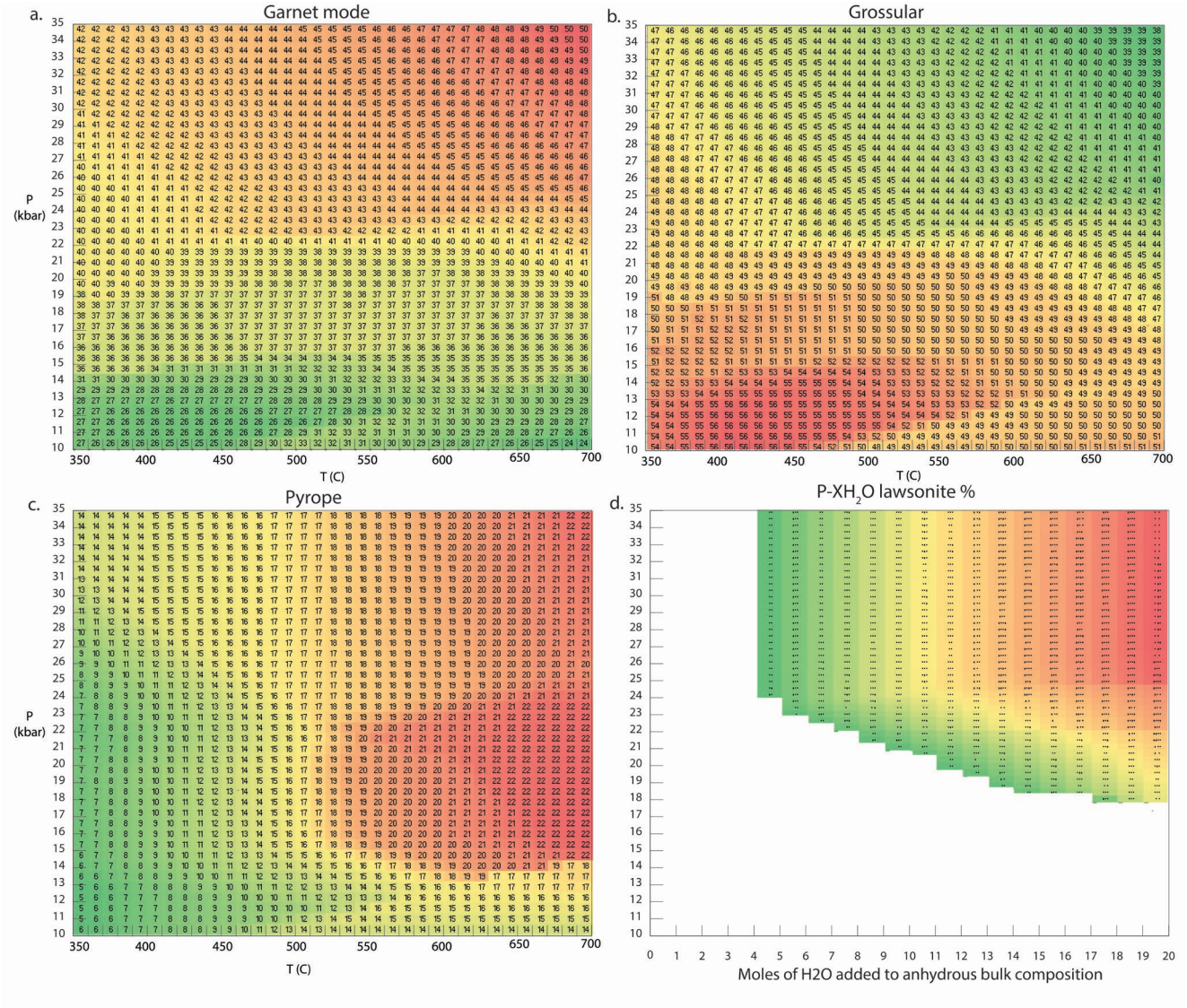


Figure 35 Sample 11-05 full bulk composition phase diagrams for $aH_2O<1$. a. Mode % garnet, b. Grossular isopleths, c, Pyrope isopleths, d, P-XH_2O diagram at 525°C showing lawsonite stability.

Conventional thermobarometry

The results of the garnet-clinopyroxene-phengite-kyanite-quartz/coesite equilibria are shown in Figure 36, with the input analyses shown in Table 8. Kyanite-quartz–absent (GCP), phengite–absent (GCKS) and clinopyroxene–absent (GKPS) equilibria all show relatively well constrained intersections. Equilibria for sample 11-05 (kyanite, quartz, phengite–bearing) also shows close agreement with the garnet-clinopyroxene thermometer, corrected for Fe^{3+} in clinopyroxene. Equilibria for sample a03-16 show a tight intersection, however there is a weaker agreement with the garnet-clinopyroxene thermometer. This may be explained by the fact that the garnet rim analysis did not necessarily target the most Mg–rich composition of garnet but analysed a Mg–embayment which postdates peak metamorphism. This problem may be present in all eclogite samples, where the thin Mg–rich rim may have been the most easily altered garnet composition. Equilibria for sample 05-04D show a tight intersection with falls within 1 S.D of the Fe^{3+} calculation for the garnet-clinopyroxene thermometer. Equilibria for sample 10-05 show a tight intersection in good agreement with the garnet-clinopyroxene thermometer.

Re-equilibration of garnet rims and matrix omphacite at post peak conditions would produce lower pressures than predicted. Fluid infiltration during the early retrograde history, of which there is evidence for in the garnet, amphibole and omphacite chemistry, would facilitate re-equilibration. These *P-T* estimates using conventional thermobarometry should therefore be considered as an estimate for the eclogite–facies assemblage preserved, and a minimum pressure estimate for the peak pressure obtained.

	05-04D			*a03–16*			*11-05*			*10–05*		
	Grt	**Omph**	**Phe**	**Grt**	**Omph**	**Phe**	**Grt**	**Omph**	**Phe**	**Grt**	**Omph**	**Phe**
SiO2	38.88	55.99	54.94	38.62	55.92	54.94	38.62	55.92	54.94	38.27	56.30	52.25
TiO2	0.03	0.04	0.22	0.03	0.03	0.22	0.03	0.03	0.22	0.03	0.04	0.31
Al2O3	21.61	10.06	25.06	21.93	10.05	25.06	21.93	10.05	25.06	21.78	11.22	29.08
FeO	24.81	3.03	1.16	24.68	5.33	1.16	24.68	5.33	1.16	26.10	2.54	1.66
MnO	0.29	0.02	0.003	0.3	0.01	0.03	0.3	0.01	0.03	0.29	0.01	0.00
MgO	7.67	9.81	5.74	9.44	8.36	5.74	9.44	8.36	5.74	7.64	9.09	4.24
CaO	6.12	15.31	0.03	5.84	13.84	0.03	5.84	13.84	0.03	5.86	14.25	0.04
Na2O		6.08	0.13		7.15	0.13		7.15	0.13		7.05	00.34
K2O			9.05			9.05			9.05			8.19
Total	99.41	99.91	96.30	100.84	100.96	96.35	100.84	100.69	96.35	99.97	100.49	96.10
Oxygens	12	6	22	12	6	22	12	6	22	12	6	22
Si	2.95	1.99	6.87	2.95	1.97	7.11	3.01	1.98	7.11	2.97	1.97	6.78
Al iv	1.97	0.01	1.14	1.97	0.03	0.89	1.97	0.02	0.89	1.99	0.03	1.23
Al vi		0.44	3.10		0.39	2.93		0.40	2.93		0.44	3.22
Ti	0.001	0.001	0.02	0.002	0.001	0.02	0.002	0.001	0.02	0.002	0.001	0.03
Fe3+		0.12			0.12			0.04			0.07	
Fe2+	1.87	0.02	0.14	1.58	0.03	0.13	1.61	0.05	0.13	1.69	0.01	0.18
Mn	0.02	0.00	0.001	0.02	0.00	0.003	0.02	0.001	0.003	0.02	0.00	0.00
Mg	0.79	0.40	0.09	1.07	0.44	1.11	0.89	0.52	1.11	0.88	0.48	0.82
Ca	0.47	0.47	0.001	0.48	0.52	0.004	0.51	0.58	0.004	0.49	0.54	0.01
Na		0.55	0.09		0.49	0.03		0.42	0.03		0.48	0.08
K			1.56			1.49			1.49			1.36
Cations	8.06	4.00	13.82	8.07	4.00	13.72	8.00	4.00	13.72	8.04	4.00	13.69

Table 8 Analysis used for Grt–Cpx–Phe–Ky–SiO_2 equilibria (Krogh Ravna and Terry, 2004). Wt% oxide of garnet composition of highest Mg content at Grt rim. Wt% oxide of average omphacite composition population with highest Na content. Wt% oxide of average phengite composition. Formula recalculation based on spreadsheet from Krogh Ravna and Terry (2004). Cpx composition calculated for ferric iron using the method of Droop (1987).

Sample	***P***	***T***	***Fe^{3+} pfu***	***Equilibria***	***Notes***
a03–16	27.15	495	0.124	GCP–GCKS	Ky observed
05–04D	26.83	475	0.040	GCP–GCKS	Ky inferred
05–04D	26.59	442	0.040	GCP–GC	
10–05	19.18	471	0.033	GCP–GCKS	Ky inferred
10–05	19.13	393	0.033	GC–GCP	
11-05	18.99	393	0.122	GCP–GCKS	Ky observed

Table 9 Results of conventional thermobarometry based on the intersection between the grt–cpx–phe equilibria and grt–cpx–ky–qz equilibria for all samples. Where kyanite is not observed, phe–talc clusters are present which are thought to be associated with the breakdown of kyanite in other samples. In these cases, the intersection of the grt–cpx–phe equilibria and grt–cpx thermometer is also shown. Mineral compositions used in the calculation shown in

The Ave*PT* function of THERMOCALC was used to calculate peak *P-T* conditions of equilibration for the garnet outer rims and other matrix phases considered part of the peak pressure assemblage. Peak phases that exhibit solid solution include garnet, omphacite, phengite, talc and pure endmembers used are coesite, rutile, lawsonite and H_2O. Ave*PT* results for analysed eclogite samples are presented in Table 10. For sample 11-05, talc, kyanite and white mica are observed in the matrix and predicted, using ave*PT*, to be present at peak conditions along with lawsonite. The ave*PT* results predict higher temperature and pressure estimates than the results from conventional thermobarometers (Figure 36). Decreasing the XH_2O used in the calculation decreases the sigfit value, as well as slightly decreasing the predicted temperature.

Ave*PT* results from samples 10-05 are also in close agreement with conventional thermobarometry. In sample 10-05, talc is not observed in the assemblage but is predicted in the ave*PT* predictions. Lawsonite is predicted to be present. Phengite is not predicted to be present and is observed in the matrix in clusters after kyanite. Paragonite was not excluded from the calculation as it is required to balance the Na endmembers, however the certainty of this endmember was increased, allowing equilibrium to be made over a larger range. Decreasing the XH_2O used in the calculation decreases the sigfit value, as well as slightly decreasing the predicted pressure and temperature.

Ave*PT* results of samples a03-16 and 05-04D are in close agreement with the garnet-clinopyroxene thermometer but predict high temperatures than the garnet-clinopyroxene-phengite equilibria. Ave*PT* results of sample a03-16 predict the presence of talc, lawsonite, phengite and kyanite in the matrix at peak conditions. White mica is predicted to be stable in the peak assemblage in these samples. In thin section, sample a03-16 has large laths of white mica and talc with faceted contacts with garnet rims. Decreasing the XH_2O used in the calculation decreases the sigfit value, as well as slightly decreasing the predicted temperature and increasing the predicted pressure.

Sample 05-04D has large laths of white mica and talc forming in clusters around kyanite and faceted contacts with garnet rims in the matrix. Ave*PT* results predict the presence of lawsonite, kyanite, celadonite and talc in the matrix at peak conditions. Decreasing the XH_2O used in the calculation decreases the sigfit value, as well as slightly decreasing the predicted temperature and increasing the predicted pressure. The presence of talc and white mica in the matrix of this sample as radial clusters around kyanite relicts is not consistent with the fact that talc and white mica are predicted to be present in the peak assemblage using avePT.

Sample	Calculation assemblage	XH_2O	T °C	S.D	P kbar	S.D	Sig fit	Corr	N	Endmembers excluded
11-05	Grt, cpx, wm, coe, ky, ta law, ru	1	597	17	25.5	2.0	1.47 (1.49)	0.757	7	q
	Grt, cpx, wm, coe, ky, ta law, ru	0.7	576	15	25.5	1.9	1.41	0.806	7	q
	Grt, cpx, wm, coe, ky, ta law, ru	0.5	565	14	25.6	1.9	1.38	0.960	7	q
10–05	Grt, cpx, coe, ky, ta, law, ru,	1	623	15	26.5	2.0	1.04	0.869	6	q, cel, fcel
	Grt, cpx, coe, ky, ta, law, ru,	0.7	605	13	27.3	2.0	0.97	0.874	6	q, cel, fcel
	Grt, cpx, coe, ky, ta, law, ru,	0.5	595	13	27.8	2.0	0.94	0.822	6	q, cel, fcel
a03–16	Grt, cpx, wm, coe, ky, ta, law, ru	1	647	16	27.1	2.2	1.60	0.859	5	q, cats
	Grt, cpx, wm, coe, ky, ta, law, ru	0.7	624	13	27.6	1.9	1.45	0.862	5	q, cats
	Grt, cpx, wm, coe, ky, ta, law, ru	0.5	612	12	27.9	1.8	1.39	0.869	5	q, cats
05–04D	Grt, cpx, wm, coe, ky, ta, law, ru,	1	685	27	30.2	3.1	1.67	0.875	7	q
	Grt, cpx, wm, coe, ky, ta, law, ru,	0.7	658	25	30.4	3.1	1.69	0.878	7	q
	Grt, cpx, wm, coe, ky, ta, law, ru,	0.5	642	24	30.5	3.1	1.71	0.884	7	q
L08-03A (Palin, 2013)	Grt, cpx, wm, ta, law, qz,	1	617	17	25.5	1.2	1.36	0.7	5	Fcel, ru, hed
	Grt, cpx, wm, ta, law, qz,	0.9	607	18	25.5	1.3	1.48	0.71	5	Fcel, ru, hed
	Grt, cpx, wm, ta, law, qz,	0.8	602	18	25.5	1.3	1.48	0.71	5	Fcel, ru, hed

Table 10 THERMOCALC AvePT results for mafic eclogite peak pressure assemblage. Sig Fit = significant fit (95% confidence limit), N = number of independent reactions used in calculation (after Powell and Holland, 1994)

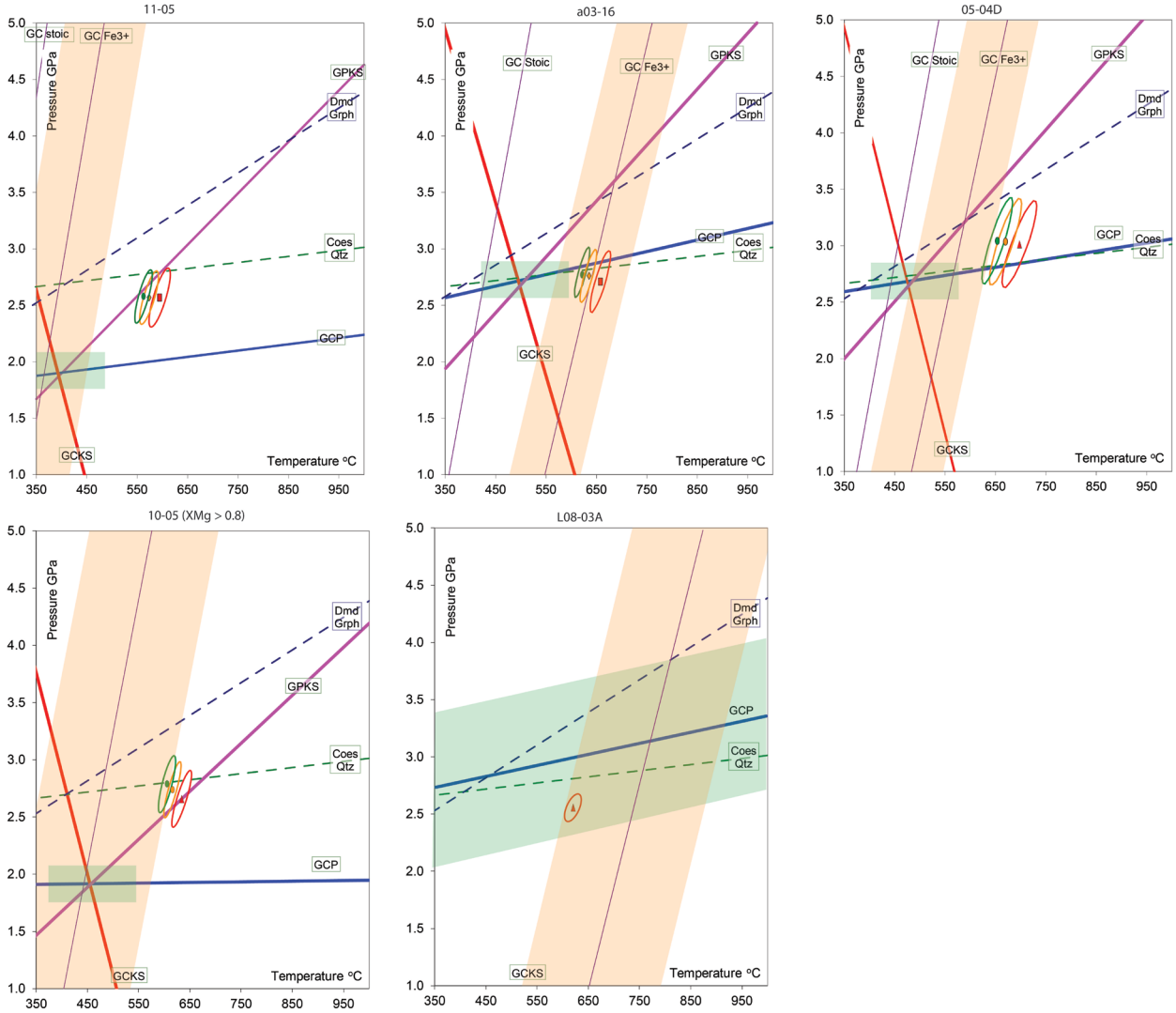


Figure 36 Results of conventional geobarometry for high pressure mineral assemblages from eclogite samples (see Table 8. Orange envelope around Grt–Cpx thermometer of ± 70°C showing uncertainty in Fe^{3+} calculation as suggested by Štípská & Powell (2005). Green boxes show average standard deviation reported by (Krogh Ravna et al., 2004b). Sample L08-03A results from Palin (2013). AvePT results plotted with error ellipses. Red ellipse XH_2O =1, orange ellipse XH_2O = 0.7, green ellipse XH_2O = 0.5

Discussion

Equilibrium models of garnet core growth

Previous attempts to determine the prograde conditions of garnet growth in mafic lithologies have focussed on variably preserved samples from the Berthelsen locality (e.g. Konrad-Schmolke *et al.*, 2008; St-Onge *et al.*, 2013; Chatterjee *et al.*, 2015). Initial *P-T* estimates for garnet core growth rely on the assumption of water saturated conditions and the preservation of primary inclusion chemistry and estimated *P-T* conditions using garnet isopleth intersections combined with amphibole and phengite inclusion chemistry (e.g. Palin, 2013; St-Onge et al., 2013, Konrad-Schmolke et al., 2008).

Locating stable assemblage fields when interpreting pseudosections for specific rock compositions is an approach advocated by Powell *et al.*, (2008). This approach relies not only on the robustness of mineral inclusions preserving primary inclusion chemistry as discussed above, but also the quality of solid solution models (e.g. Waters, 2019). Isopleth intersections within a given field have a smaller uncertainty and are less sensitive to bulk composition changes than assemblage fields, as they are governed by equilibria from a subset of phase components of the system (Waters, 2019), making them a more reliable indicator or *P-T* conditions of garnet growth. With this in mind, pseudosection modelling of sample 11-05 from the Polokongka La region, was undertaken and the resulting garnet isopleth intersections were compared to sample L08-03A of Palin (2013) using the same dataset and activity models. Following this, 'geological uncertainty' relating to bulk composition calculation was tested to demonstrate the effect of bulk composition on the position of garnet isopleths in *P-T* space.

Unpublished work by Palin (2013), which formed the basis for the work by St-Onge *et al.* (2013), shows that there are two possible garnet isopleth intersections for sample L08-03A at 21 kbar, 525°C and 11 kbar, 675°C. Neither of these isopleth intersections predict the observed amphibole inclusion assemblage, however the higher pressure intersect, which predicts glaucophane as the stable amphibole phase during prograde garnet growth, was considered correct due to the observed glaucophane in the core of matrix and inclusion amphibole.

High resolution BSE and EDS imaging of garnet has shown that the inclusion assemblage has been altered by later fluid–mediated retrograde metamorphism, which infiltrated the garnet cores forming the observed Mg-Ca channels and Mg–embayments and even atoll garnets (Figure 14). The chemistry of the amphibole inclusions has also been shown to exhibit a trend in compositions over a large range, similar to the trend recorded in the matrix amphiboles (Figure 23). These results indicate that the inclusion chemistry cannot be used as a primary indicator of prograde garnet growth and thus, we cannot rule out the lower pressure isopleth intercept predicted by Palin (2013).

The observed changes in mineral inclusion assemblages at the garnet core-rim boundary, thought to be representative of prograde conditions such as the appearance of lawsonite pseudomorphs, in conjunction with a changing style of garnet growth from skeletal to faceted separated by a Mn–annulus, suggest that garnet growth was initially water undersaturated. Published pseudosections of the Tso Morari eclogites assume water saturated conditions and the upper intersect of Palin (2013) also predicts lawsonite to be stable during prograde garnet growth. However, pseudomorphs after lawsonite, if present, are only observed in the garnet rims, suggesting that water undersaturated conditions need to be considered in the equilibrium models for garnet core growth. In order to understand the effects of H_2O saturation on the position of garnet isopleths, XH_2O was varied in the equilibrium models.

In H_2O–saturated conditions, garnet core isopleths intersect at roughly similar *P-T* conditions in samples 11-05 and L08-03A (21 kbar, 525°C), within the lawsonite stability field. L08-03A models also show a lower pressure intersect (11 kbar, 675°C) which is absent in sample 11-05 models. By changing the conditions from water saturated to undersaturated, a shift of approximately 100°C and 10 kbar is observed within the garnet core isopleth intersections in sample 11-05 (Figure 29). This shift to lower pressure and temperature estimates in water undersaturated conditions is also observed in sample L08-03A, however the exact shift cannot be precisely quantified due to the broad range of constant grossular content predicted in the models (Figure 30). For samples L08-03A and 11-05, the lower pressure intersect in water absent conditions lies within a lawsonite–absent assemblage field, consistent with petrographic observations. This large shift in predicted *P-T* conditions highlights the importance of estimating conditions of water saturation during prograde metamorphism.

Error associated with bulk composition determination has been estimated in the models using a Monte Carlo approach and applied to the garnet isopleth intersections. Two garnet isopleth intersections can be observed in water undersaturated conditions for sample 11-05 when the error in bulk composition calculation is considered, compared to a single intersection for the initial bulk composition calculation (Figure 31). The high–pressure intersection is only present in 12.5 % of generated bulk compositions. The low–pressure intersect is common to all bulk compositions and overlaps with the *P-T* conditions predicted for sample L08-03A, using the same water conditions and thermodynamic datasets, where only a single intersect is observed. The consistent prediction of the low–pressure intersect in mafic eclogites of different bulk composition and the absence of the high–pressure intersect in many of the models, suggests that garnet core growth is more likely to correspond to conditions of 10–14 kbar, 400–500°C.

The prograde *P-T* path recorded in garnet predicts an initial increase in pressure as the highest grossular values are preserved in the cores and gradually decrease without pyrope increasing. This is followed by heating, where pyrope content increases rapidly without a sharp change in grossular. This is consistent with water saturated models for sample L08-03A where initial loading is predicted to be approximately isothermal, followed by an approximately isobaric heating (Figure 11, St-Onge *et al*., 2013). In sample 11-05, isothermal loading in the garnet core (Figure 34), followed by isobaric heating as pyrope content increases, is also predicted. This loading then heating trajectory is independent of water saturation and fractionation but becomes more pronounced when fractionation of garnet is considered, as the first growth in the garnet cores occurs at lower pressure and temperature conditions. The presence of similar *P-T* trajectory in both sample L08-03A and 11-05, located 50 km apart, suggests that loading followed by heating is a feature common to the Tso Morari complex.

Pseudosection modelling predictions

Pseudosection modelling of the mafic eclogites from the Tso Morari complex has been attempted, where the bulk composition of an eclogite has been estimated and input into equilibrium thermodynamic models (e.g. St-Onge *et al.,* 2013; Konrad-Schmolke *et al.,* 2008). These models incorporate the fractionation of garnet during prograde growth along discrete steps. Fractionation changes the effective bulk composition of a rock during mineral growth and can cause discontinuous growth and recrystallisation of metamorphic minerals in high pressure rocks leading to strong compositional zoning in minerals such as garnet, a common mineral in ultrahigh–pressure rocks (Konrad-Schmolke *et al.,* 2008). The interpretation of garnet growth zones with respect to the *P-T* path of the rock using thermodynamic forward modelling is therefore essential for the determination of tectonic and metamorphic rates in ultrahigh–pressure rocks settings. Inverse modelling techniques have been investigated using a bulk composition of an unmetamorphosed Panjal Trap basalt and compared with theoretical *P-T–(t)* paths produced by thermomechanical models (Palin *et al.,* 2017). The models of Palin *et al.,* (2017) predict a peak assemblage of garnet + omphacite + phengite + rutile + coesite + lawsonite + minor talc at approximately 28 kbar.

De Sigoyer *et al.,* (1997) estimated peak pressures of the Berthelsen outcrop at 25 ± 3 kbar, 540 ± 50°C, based on the coexistence of garnet, omphacite and phengite with observed compositions, using conventional thermobarometry and the location of possible reactions between end–member phases. Studies such as *St-Onge et al.* (2013) estimated the peak pressure conditions in sample L08-03A of the Berthelsen eclogite at 25.5–27.5 kbar, 630-635°C, consistent with conditions just within the coesite stability field, based on the convergence of observed garnet isopleths using phase equilibria modelling. Peak temperature conditions predicted with cation fractionation occur at lower pressure (25.5 kbar) than results without cation fractionation (27.5 kbar) and record a decrease in pressure at the rim of the garnet from 26.5 to 25.5 kbar (Figure 12e, St-Onge *et al.,* 2013).

Garnet rim compositions recorded by de Sigoyer *et al.,* (1997) record a range in pyrope concentrations from 17–26%, whereas St-Onge *et al.* (2013) evaluated a larger number of garnet maps in addition to detailed transects from core to rim, with an average pyrope content of 34% at the garnet rim. The discrepancy in results presented in these two studies can be re interpreted based on the understanding of retrograde

metamorphism in the samples described in this study. The low and decreasing pyrope contents reported by de Sigoyer *et al.,* (1997), in the absence of element maps to confirm the textural distribution of pyrope in the garnet rims, is likely to reflect the analysis of garnet rim zones affected by later fluid–mediated alteration, resulting in re equilibration of the garnet rims at lower pressure conditions. In contrast, sample L08-03A preserves higher pyrope contents due to the lower degree of hydration and limited post–peak alteration of garnet compositions.

Chatterjee and Jagoutz (2015) estimated the peak *P-T* conditions of the Berthelsen eclogite at 22-23 kbar, 400-425°C. However, the bulk composition considered for initial garnet growth involved the "bulk compositions of the early assemblages using the mineral compositions and modes of the inclusions within the garnet core and an arbitrary contact zone of the host garnet surrounding the inclusions" (Chatterjee and Jagoutz, 2015). This approach does not consider the range of elements available to participate in reactions during the early prograde metamorphic history. Chatterjee and Jagoutz (2015) also used mineral composition isopleths to determine the conditions of garnet core and rim growth. Jadeite-rich pyroxene was assumed to be in equilibrium with the garnet cores, rather than the older, aegirine-rich pyroxene which has been documented to be present and overprinted by a later, jadeite-rich pyroxene in other eclogites from the Tso Morari complex. Consequently, the estimate for the initial garnet growth stage of 22-23 kbar, 400-425°C is not accurate. This initial *P-T* estimate was compared to estimates from conventional thermobarometry of 22-25 kbar, 458—480°C which relies on the preservation of compositions of primary inclusions such as omphacite and phengite, which, as discussed in this chapter, are not reliable due to fluid-mediated Fe-Mg alteration.

Results from sample 11-05 (this study) predict peak *P-T* conditions >26 kbar in water saturated conditions without cation fractionation. Taking cation fractionation into account lowers the predicted grossular content of the garnet, forming an intersection at 28 kbar, 600°C. These minimum pressure estimates are comparable to the estimates by St-Onge *et al.* (2013). When cation and H_2O fractionation is invoked along a predicted *P-T* path, garnet is not predicted to grow until >26 kbar, >625°C and no garnet isopleth intersections occur for rim conditions as the predicted grossular content is too high. This shift of the garnet stability field to higher pressures and temperatures may reflect the extreme fractionation involved in the method, where 100% of

garnet is resorbed at each step along the *P-T* path, depleting the effective bulk composition in garnet–forming elements. If garnet fractionation is less extreme, so that only 50% of garnet grown is removed from the effective bulk composition at every step in the model, garnet is stable at >23 kbar and >610°C and the modal abundance of garnet is < 3% below 700°C. Grossular isopleths in this model are also higher than observed grossular values in the garnet rim, providing no isopleth intersection.

Wilke *et al.* (2015) predicted that the peak conditions lie in the diamond stability field at 42 kbar, ~560°C due to the presence of the reaction magnesite → dolomite + aragonite. Projection of a *P-T* path to the diamond stability field predicts breakdown of lawsonite into minor amounts of garnet and omphacite (O'Brien, 2018b). In sample 11-05, very little garnet growth (< 1 mode %) is predicted in the diamond stability field in water saturated and water undersaturated conditions. The resulting garnet composition predicted also shows very little change, apart from a slight decrease in grossular content (2% in water saturated conditions). Any garnet growth at pressures within the diamond stability field would therefore be volumetrically minor, compositionally similar to garnet growth at 27 kbar and therefore have little effect on the density and metamorphic assemblage preserved within the rock. In the absence of abundant mineral growth at ultrahigh pressures, the phase change from carbon to diamond could still occur, increasing the density of the rock. Additionally, the highest pressures would be recorded in the thin outer zones of the garnet which are most easily lost to retrogression, and therefore control the preservation potential of minerals indicative of ultrahigh–pressure, such as coesite (Konrad-Schmolke *et al.,* 2008). It is therefore possible that, if the pressure increase from coesite to diamond stability field occurred, it may not have been preserved (O'Brien, 2018b).

Conventional thermobarometry vs petrographic observations

Conventional thermobarometry determines the pressure and temperature conditions between mineral phases in equilibrium. Matrix omphacite and the highest–Mg garnet has been interpreted to record the highest–pressure conditions preserved in the rock. If garnet growth in the coesite stability field is predicted to be relatively minor and easily altered, the pressures and temperatures related to garnet rim growth do not necessarily represent peak conditions but give an estimate of the conditions of garnet rim growth. Results from conventional thermobarometry can therefore be interpreted as minimum estimates.

Application of the garnet-clinopyroxene-phengite barometer to a suite of eclogite samples from across the dome produces results ranging of 18–28 kbar, 370–570°C. These results are consistently lower temperature than the results of ave*PT* calculations or temperatures predicted by the garnet-clinopyroxene thermometer and often lie outside of the uncertainty envelope related to the Fe^{3+} calculation of this thermometer. Ave*PT* results are more consistent with the intersection between the garnet-clinopyroxene-phengite barometer and the garnet-clinopyroxene thermometer corrected for Fe^{3+}. This intersection relies on the same garnet and clinopyroxene compositions and corresponds closely to the predicted *P-T* conditions for equilibration of the garnet rims estimated using phase equilibria modelling in water saturated conditions in samples 11-05 and L08-03A. Samples a03-16 shows the most consistent results when comparing ave*PT* results with the results from the garnet-clinopyroxene thermometer. In these samples, phengite is predicted to be a peak phase using ave*PT*. Ave*PT* results from all studied samples lie within 1 sigma error of each other in the range 23.5-33 kbar, 580-710°C.

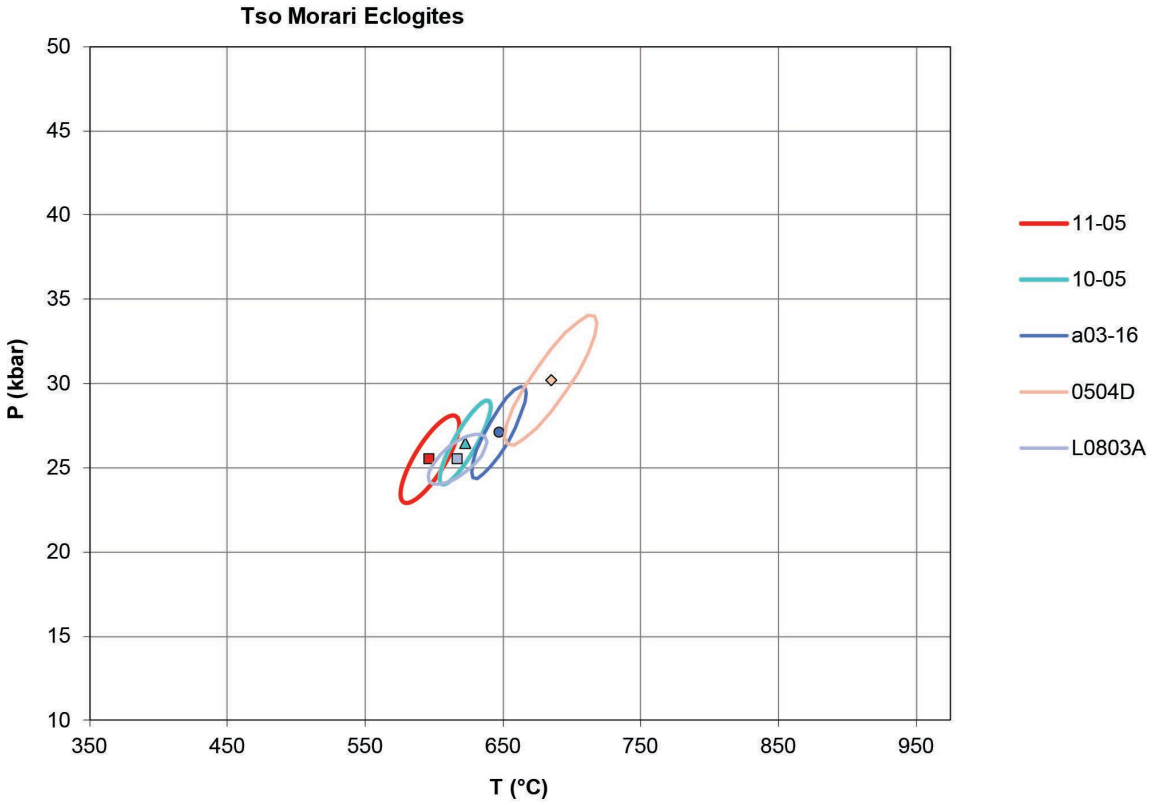


Figure 37 AvePT results from samples in this study and L08-03A from Palin (2013). Error ellipses are shown for 1.S.D.

For conventional barometry calculations, matrix omphacite was assumed to preserve conditions in equilibrium with the garnet rims. In the case where compositional zoning is preserved, the Fe^{3+} rich cores with high X_{Mg} are interpreted to represent prograde omphacite, more likely to be in equilibrium with the garnet rims than the rims affected by fluid-mediated alteration. Small and roughly equal amounts of Fe^{3+} and Fe^{2+} in the omphacite composition are very sensitive to ferric iron recalculation and therefore also affect thermometers and barometers which rely on clinopyroxene compositions, introducing a large amount of uncertainty. The ferric iron recalculation also assumes no Ca-eskola component (vacancies in the lattice M1 sites), due to the assumption that all cations sum to 4 per formula unit. The Ca-eskola component of pyroxene is temperature dependant and would not be expected at temperatures below 750°C (Konzett *et al.*, 2008), such as in the Tso Morari eclogites.

All mafic eclogite samples in this study contain phengite in the matrix in varying proportions. Phengite commonly forms in clusters in association with talc, often with relict kyanite or carbonate grains in the core, suggesting that the phengite and talc formed later than the peak pressure assemblage containing garnet and omphacite. Based on the textural observation that phengite is not in equilibrium with garnet and omphacite, the result predicted by the garnet-clinopyroxene-phengite barometer may not be representative of peak conditions.

Thermocalc calculation mode three was employed to determine the location of equilibria, specific to each sample, that could act as a useful geobarometer. A good geobarometer has a relatively shallow slope in *P-T* space, a small number of phases required to be in equilibrium and a small standard deviation, such as the garnet-clinopyroxene-phengite barometer, which, in sample 05-04D has a slope of 0.001 and involves three phases and a standard deviation (S.D) of 2.8 kbar. Alternative, phengite–absent equilibria, such as the reaction py + q+3law = 3di + 4ky + $6H_2O$, has a steeper slope of 0.073 and a S.D of 0.88 kbar involving five mineral phases or py + 6law = gr + 3di + 6ky + $12H_2O$, which has a slope of 0.086, a S.D of 0.72 and involves four mineral phases. The above–mentioned equilibria require an independent temperature estimate or intersecting equilibria in order to determine the *P-T* conditions in this sample. However, no alternative, independent phengite–absent equilibria are present in this sample, and the steep slope and uncertainty envelope around the garnet-clinopyroxene thermometer mean that pressure determination using this method is imprecise.

Ave*PT* calculations predict phengite to be in equilibrium with the garnet rims in samples 11-05 and 10–05, but do not predict phengite to be present in samples a03-16 and 05-04D. Similarly, sample 05-04D contains coarse talc in the matrix, often in association with phengite, but does not predict talc to be stable in the ave*PT* calculations. This inconsistency between observations and predictions shows that the models are able to predict seemingly feasible results, which are do not necessarily make sense within the textural context of the sample and must be interpreted with caution.

Lawsonite is predicted as a peak equilibrium phase in all samples in this study using ave*PT*. Lawsonite is unstable at low pressure and temperatures, reducing its preservation potential. Pseudomorphs after lawsonite have been identified in garnet rims in samples L08-03 and 05-04 but are not abundant. Pseudosection modelling of sample 11-05 in water saturated conditions predicts the peak modal abundance of lawsonite to be < 20% above 600°C, independent of pressure. Few mineral inclusions are trapped within garnet rims, reducing the likelihood of preserving and recognising pseudomorphs after lawsonite. Zoisite and paragonite intergrowths are absent in the matrix of these samples, perhaps indicating that lawsonite wasn't present in the matrix, however abundant hydrous amphibole and secondary clinozoisite are present in the matrix, resulting from retrograde hydration of the mafic eclogite. Later hydration could further reduce the preservation potential of pseudomorphs after lawsonite that are not entrapped in refractory minerals such as garnet. It is therefore possible that lawsonite was a peak phase in these samples, despite the small number of identifiable pseudomorphs preserved in garnet rims.

Coesite has been identified in the garnet rims of eclogites from the Berthelsen outcrop which have undergone little hydration (Sachan *et al.*, 2004). More hydrated samples from the Berthelsen outcrop are not reported to contain coesite but occasionally contains quartz inclusions in garnet with radial fractures. Radial fractures around quartz inclusions are particularly prevalent in the rims of garnet in sample 05-04D which also contains lawsonite pseudomorphs. The lack of preserved coesite in the garnet rims may related to the low preservation potential of coesite which decompresses to alpha quartz at lower pressures unless trapped in a rigid refractory mineral (Mosenfelder *et al.*, 2005). The degree of garnet growth at the *P*-*T* conditions of interest are predicted to be very low, reducing the chances of trapping coesite in garnet.

Composition of fluids during metamorphism

The rocks of the Tso Morari dome are extensively overprinted by fluid–mediated metamorphism in the amphibolite facies, producing hydrous minerals such as amphibole and mica. It is therefore difficult to determine the composition of the fluid present prior to this metamorphic overprint. Petrographic evidence for the addition of water at high–pressure has been discussed, along with the effect that the presence of water and a mixed fluid has on the garnet isopleths and the determination of *P-T* conditions, showing that the abundance and composition of the fluid during metamorphism is an important consideration that has not been extensively explored in previous studies to date.

The presence of carbonates as a peak phase in the mafic eclogites in these samples suggests that carbon was present in the bulk composition of these rocks during high pressure metamorphism, or that carbon was introduced as a fluid phase during metamorphism. Carbonate is also present as inclusions within garnet in sample 05-02, a granite gneiss from the north shore of Kiagar Tso suggesting that carbon was present during early prograde metamorphism of a range of lithologies.

Carbonate is common in basaltic rocks that have undergone alteration at low pressures and temperatures in the shallow crust (Staudigel *et al.*, 1981). This style of alteration must have a occurred after the intrusion of the basaltic dykes and must therefore be post Permian. Alternatively, carbon could have been added due to the addition of C-rich fluids during Himalayan metamorphism. The presence of carbonate–bearing channels within outcrops of eclogite with abundant symplectites after omphacite suggests that an externally–derived carbon–bearing fluid was present during symplectite formation in the early retrograde stages of metamorphism. The preservation of symplectites, which are disequilibrium textures, requires that fluid is present in small amounts to act as a kinetic facilitator and as a component for the reaction producing a hydrous product (Martin *et al.*, 2015). The juxtaposition of carbonate–bearing sediments from the Indian shelf sequence could be a possible source of carbon in this case. However, the analysis of fluid inclusions would be required to confirm the composition of the fluid during metamorphism.

Summary

Mafic eclogites from across the Tso Morari complex best preserve high pressure and prograde metamorphic conditions related to subduction of the leading edge of the Indian continental margin. Previous studies have focussed on limited eclogite exposures due to difficult accessibility and large area of the dome. In this study, detailed petrographic analysis and observations, combined with conventional thermobarometry and pseudosection modelling was undertaken on eclogite samples from a broad area of the Tso Morari complex, in order to determine the major variations in bulk composition, peak *P-T* conditions and the common prograde and retrograde trends and *P-T* conditions. All mafic eclogites studied show common retrograde metamorphic trends, allowing the bulk composition variations, peak assemblages and prograde features to be unravelled and compared.

Zoned garnet, omphacite and quartz are common features of the peak assemblage, whereas talc, phengite, kyanite and dolomite are present in varying abundances. Results of conventional thermobarometric calculations predict peak *P-T* conditions ranging from 19-30 kbar, 450–650°C and are mostly dependant on the presence of phengite as a peak phase. Ave*PT* estimates are more consistent suggesting that there is no resolvable difference in peak *P-T* conditions between samples, however the large pressure uncertainty on these calculations doesn't allow pressure differences of $< \pm 4$ kbar to be resolved.

There is evidence of initial post–peak hydration of the eclogites in the garnet mineral chemistry, which is linked to the replacement of amphibole inclusions in garnet and the growth of matrix amphibole cores, followed by growth of clinozoisite poikiloblasts. These initial stages of hydration occurred with minor breakdown of omphacite and garnet, which were still the predominant mineral phases in the rock. Exhumation to the lower crust resulted in a retrograde overprint within the amphibolite facies, corresponding to the amphibolite facies overprint in the surrounding felsic rocks and resulting in symplectite formation and further amphibole growth.

Conditions of prograde metamorphism are difficult to constrain petrographically due to alteration of prograde mineral assemblages. New equilibrium models of prograde metamorphism in water undersaturated conditions, constrained by garnet growth mechanisms and 'trustworthy' inclusion assemblages, produce *P-T*

estimates at much lower pressures and temperatures than previous models, defining an isothermal trajectory followed by isobaric heating. Predicted *P-T* conditions of garnet core growth are shown to be very sensitive to bulk composition and water saturation. This study highlights the importance of detailed petrographic study in order to confidently characterise the input parameters for thermodynamic modelling and estimation of *P-T* conditions. It also highlights the sensitivity of garnet isopleth position to water conditions in certain bulk compositions, previously thought to be the most robust indicator of prograde *P-T* conditions.

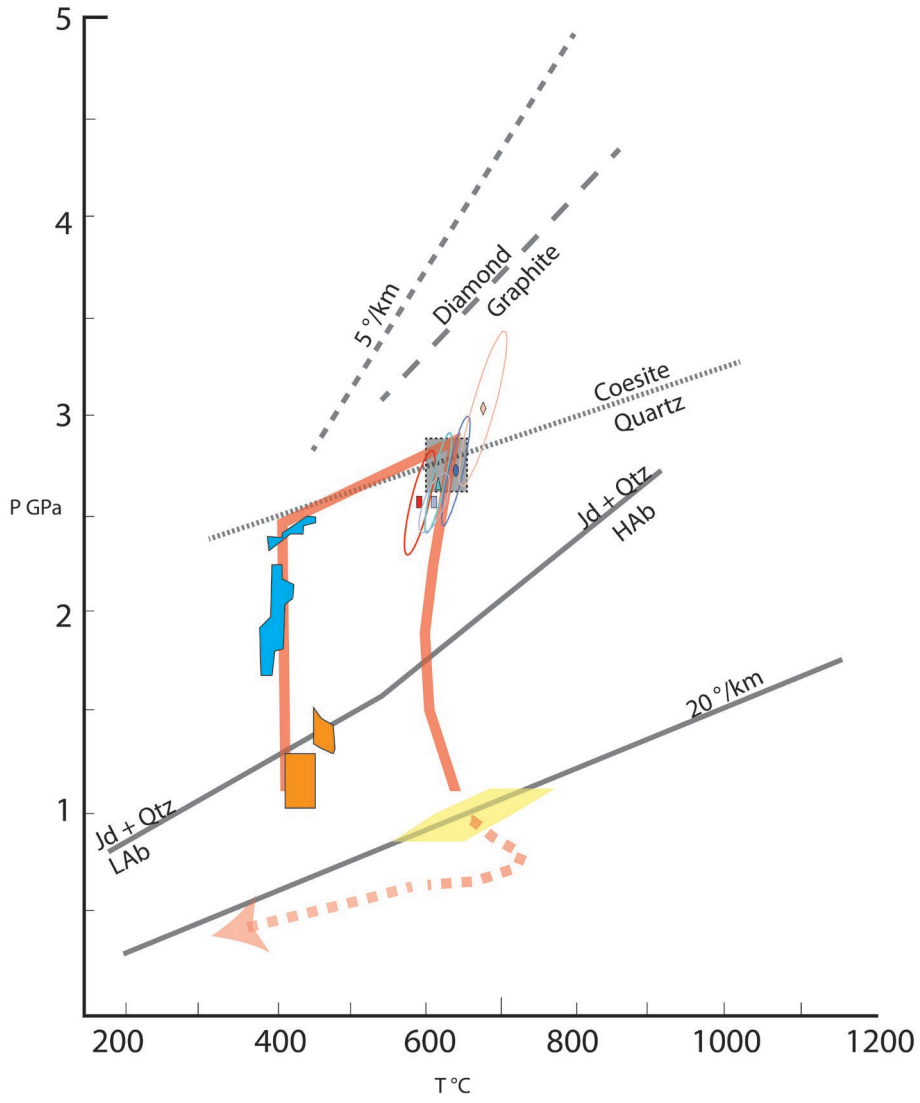


Figure 38 Summary of P-T results from sample 11-05. Orange and blue boxes show estimated P-T conditions for the garnet cores in sample 11-05 using pseudosection modelling for a water undersaturated core. Grey box shows the estimated P-T conditions for garnet rims in sample 11-05 using pseudosection modelling for a water saturated core and rim. Coloured ellipses show results of AvePT modelling for sample 11-05 (red), 10-05 (green), a03-16 (dark blue), 05-04D (orange) and L08-03A (grey). Yellow box shows results of Zr in Ru thermometry for 8-12kbar (see Chapter 7). Red arrow shows predicted P-T path. Dashed red arrow shows potential retrograde P-T path based on St-Onge et al. (2013), discussed in Chapters 7 and 8. Coesite to quartz (Bohlen and Boettcher, 1982), Albite to jadeite + quartz (Holland (1980), diamond to graphite (Bundy, 1980).

Chapter 4 - Eclogite-facies metamorphism in low–strain metagranites of the Tso Morari complex

Introduction

Mafic eclogites in exhumed continental crust often record depths of greater than 60 km. In high–pressure terranes, it is commonly observed that quartzofeldspathic rocks such as granites and sediments that host the eclogites record lower–pressure amphibolite facies conditions owing to extensive overprinting during deformation and metamorphism (e.g. Smith, 1984; Chopin, 1984; Young and Kylander-Clark, 2015) . Low–strain zones provide us with a unique window into the early tectonic history of felsic rocks in these terrains and can often preserve an extensive and protracted history.

The presence of minor ultrahigh–pressure mafic rocks within lower pressure felsic terrains, led to the early debate as to whether the whole tectonic unit experienced the same conditions or whether the mafic eclogites were introduced tectonically (Lappin, 1977; Smith, 1980; Cuthbert and Carswell, 1982). The observation that, in some cases, the host quartzofeldspathic rocks also preserve some transformation at eclogite facies conditions led to the understanding that the eclogites were metamorphosed *in situ*, and that there are other factors at play, such as water availability, residence time at depth, bulk composition and deformation that limit the transformation in felsic rocks (e.g. Austrheim, 1986; Koons et al., 1987; Rubie, 1990; Cuthbert *et al.*, 2000; Wain *et al.*, 2000). Debate continues as to whether rocks preserving lower–pressure assemblages, hosting high–pressure mafic eclogites, either persisted metastably throughout their high–pressure history, or else transformed and retrogressed pervasively so that little record of their high–pressure assemblage remains.

The Polokongka La granite is a coarse–grained peraluminous S-type granite with an A/CNK ratio in the range 0.88 – 1.98, which forms a low–strain zone within the Tso Morari complex (Girard and Bussy, 1999). Early accounts mapped the Polokongka La granite as a discrete granite body, presumed intrusive to the Puga Gneiss (Thakur and Virdi, 1979; Fuchs and Linner., 1996; Guillot *et al.*, 1997). However, Girard and Bussy (1999) and Epard and Steck (2008) emphasised the lack of observed intrusive relationships, the heterogeneous deformation and the continuous transition between undeformed granite and gneiss. Near identical U-Pb zircon

ages and morphology (Girard and Bussy, 1999) suggests that these lithologies belong to the same intrusive package.

Outcrops of macroscopically undeformed granite are present across the dome, ranging in size from 1 m – 1 km^2, and are often host to mafic eclogites (Chapter 2), suggesting that the entirety of the Tso Morari nappe underwent eclogite-facies metamorphism. However, there is currently no recorded evidence that the Puga Gneiss and granitoids from Tso Morari complex transformed to eclogite-facies assemblages.

This chapter describes the microstructure and petrology of low–strain domains within the Puga gneiss. It will be shown that low–strain zones within the Tso Morari metagranites preserve evidence of a history of emplacement, alteration and metamorphism spanning 480 Myr. Observations of mineral textures combined with mineral compositions within the granite are interpreted as a record of magmatic and magmatic-hydrothermal processes, high–pressure metamorphism and later metamorphism and deformation. Many of these features are preserved in localized textural domains in the rock, where local equilibrium was important and the dry conditions limit reaction progress but aided preservation potential.

The Polokongka La granite is observed to transition into the Puga Gneiss and garnet-mica schist towards the contact with a mafic dyke in the Polokongka La region. The Puga Gneiss preserves a high strain fabric which overprints earlier igneous features and is therefore considered in a separate chapter. The transition from granite to Puga Gneiss forms the link between these two chapters and is described in detail in chapter 5 along with detailed analysis of the metamorphic garnets in the Puga Gneiss.

Petrography and Mineral Compositions

Methods

Thin sections were made from 11 macroscopically undeformed granite samples from the Tso Morari complex (Table 1). Samples 11-01, 11-02, L08-04 and a05-10 were selected for detailed petrological analysis. Major element compositions of minerals that exhibit solid solutions were measured using a Cameca SX-5 field emission electron microprobe with a 15 keV acceleration potential, 20 nA beam current, 30 second count time per major element (30 second background) and 60 second count time on Ti (60 second background). A range of natural and synthetic oxide standards were used including albite (Na, Al, Si), MgO (Mg), wollastonite (Ca), andradite (Fe), Mn (Mn) and TiO2 (Ti) and analyses were verified against secondary mineral standards. Raw analyses were automatically corrected for atomic number, absorption and fluorescence using the phi-rho-z matrix correction routine (Merlet, 1994). Mineral spot analyses and line profiles were taken across white mica and garnet to determine the extent of intracrystalline compositional variation.

Sample number	*X*	*Y*	*Location*	*Rock type*	*Outcrop*	*Assemblage*	*Domains*
11-01	*78.369*	*33.235*	*Rulung valley*	*Cordierite granite*	*boulder*	*Kfs, Qz, Ab, Bt, Ms/Ph, Grt, Ky, Ilm, Rt, Ap, Zr, Mnz*	*1,2,3,4,5*
11-02	*78.369*	*33.235*	*Rulung valley*	*K-feldspar megacryst*	*boulder*	*Kfs, Qz, Ms/Ph, Bt, Ab, Grt, Ilm, Ap, Zr*	*1,2,3,4*
11-02c	*78.369*	*33.235*	*Rulung valley*	*Cordierite-Qtz enclave*	*boulder*	*Kfs, Qz, Ab, Bt, Ms/Ph, Grt, Ky, Ilm, Rt, Ap, Zr, Mnz*	*1,2,4,5*
a05-01	*78.241*	*33.240*	*Polokongka La*	*Granite*	*outcrop*	*Kfs, Qz, Ms/Ph, Bt, Ab, Grt, Ilm, Ep, Ap, Zr*	*1,2,3,4*
a05-02	*78.241*	*33.240*	*Polokongka La*	*Granite*	*outcrop*	*Kfs, Qz, Ms/Ph, Bt, Ab, Grt, Ilm, Ep, Ap, Zr*	*1,2,3,4*
a05-10a	*78.188*	*33.246*	*Polokongka La ridge*	*Grt-granite*	*boulder*	*Kfs, Qz, Ms/Phe, Bt, Ab, Grt, Ilm, Ap, Zr*	*1,2,3,4*
a05-17	*78.188*	*33.246*	*Polokongka La ridge*	*Granite*	*outcrop*	*Kfs, Qz, Ms/Ph, Bt, Ab, Ilm, Ep, Ap, Zr*	*1,2,3,4*
a10-06	*77.980*	*33.246013*	*Nuruchen*	*Granite*	*outcrop*	*Kfs, Qz, Ab, Ms/Ph, Bt, Grt, Ky, Ilm, Ap, Zr, Mnz*	*1,2,3,4,5*
a10-07	*77.980*	*33.246013*	*Nuruchen*	*Granite*	*outcrop*	*Kfs, Qz, Ab, Ms/Ph, Bt, Grt, Ky, Ilm, Ap, Zrn,*	*1,2,3,4,5*
a12-01	*77.989*	*33.232*	*Nuruchen*	*Granite*	*outcrop*	*Kfs, Qz, Ab, Ms/Ph, Bt, Grt, Ilm, Ap, Zrn,*	*1,2,3,4,5*
L08-04	*unknown*	*unknown*	*Polokongka La*	*Granite*	*unknown*	*Kfs, Qz, Ab, Ms/Ph, Bt, Czo, Ilm, Ap, Zrn*	*1,2,3,4*

Table 1 List of granite sample locations, rock type, assemblage and domains present. Description of different domains can be found in the text. Mineral abbreviations as in Whitney and Evans (2010).

Description

The macroscopically undeformed granites of the Tso Morari complex, such as the Polokongka La granite, are coarse–grained porphyritic granitic rocks that consist of quartz, alkali feldspar, white mica, biotite and albite ± garnet. The accessory mineral assemblage is dominated by apatite and zircon with monazite associated with specific altered domains, rutile as inclusions in mica and ilmenite forming rims around rutile and mica. Bifurcating needles of tourmaline are sometimes present, particularly along foliation planes of more deformed samples. The granite is characterised by coarse, euhedral, inclusion–rich alkali feldspar phenocrysts reaching up to 15 cm in length with a matrix grain size of 5 mm. Enclaves with diffuse edges and a rounded shape are numerous within the granite and can reach up to 50 cm in diameter. These rocks are fine to medium grained compared to a coarse–grained granite host.

The coarse–grained minerals, as seen in hand specimen, can be described under the microscope as mineral domains which retain some igneous characteristics such as textural relationships and mineral compositions (Figure 1). There are five textural domain types that commonly occur in all of the granite samples. These will first be described in objective, non-genetic terms:

1. Quartz–rich domain,
2. K-feldspar + white mica domain,
3. White mica + albite domain,
4. Mica domain,
5. Garnet + mica domain.

The quartz–rich domain consists of quartz grains, sometimes with a euhedral shape, of 3-4 mm with undulose extinction and/or fine deformation lamellae (Figure 2a-c). The grains often occur as clusters with face contacts, or as individual euhedral grains surrounded by other domains of similar size, retaining the igneous relationships with these domains (Figure 2a). In sample a05-10, the quartz–rich domains are polycrystalline within the euhedral domain shape (Figure 2f).

All other domain types preserve fine–grained polycrystalline aggregates. Domains of type 2 can occur as large domains of up to 15 cm which commonly enclose areas of the other four domain types. It often contains

a single K-feldspar megacryst with a perthitic texture which can be highly sericitised (Figure 2e). Type 2 domains are also associated with coarse grained white micas ~0.5-1 mm long (Figure 2d). The white mica has jagged outlines and a corroded rim containing a fine–grained white mica aggregate. Type 3 domains consist of a fine–grained aggregate of white mica + albite and appears darker than type 2 domains in plane polarised light, exhibiting zoning, with a dark core region and a pale rim (Figure 2f).

Type 4 domains vary in character across the samples. In the least altered samples (e.g. 11-01), this domain forms roughly rectangular regions, often occupied by a large single mica crystal of muscovite or biotite (Figure 4b-c), others are clusters of mica grains. Coarse rectangular biotite contain geometric arrays of rutile needles forming a sagenitic texture (c.f. Shau *et al.*, 1991) and rims of white mica + ilmenite which appear to replace the biotite. A second rim of white mica and a granular garnet corona can also be observed (Figure 4a). In other samples, biotite domains contain aggregates of red biotite clustered into a rectangular shape, surrounded by white mica + ilmenite rims. In samples a05-10, a10-06 and a10-07, these biotite domains are less well defined by shape; however, the coarse red biotite aggregates can be observed within the domain. The rim of this domain is often defined by 0.5 mm idioblastic garnets with distinct core and rim zones (Figure 4d-f). Idioblastic garnets after coarse biotite have been observed within type 2 domains, preserving rectangular inclusions within the domain. In sample a05-10, large garnet crystals completely replace coarse red biotite domains and have a rim of brown biotite.

Type 5 domains have curved but sharp boundaries, often composed of coarse aggregates of white mica and biotite which occasionally penetrate from the outer margin. Type 5 domains consists of fine–grained white mica with small irregular clusters of garnet and kyanite. These garnets are partially or completely replaced by biotite in more altered samples e.g. sample 11-02.

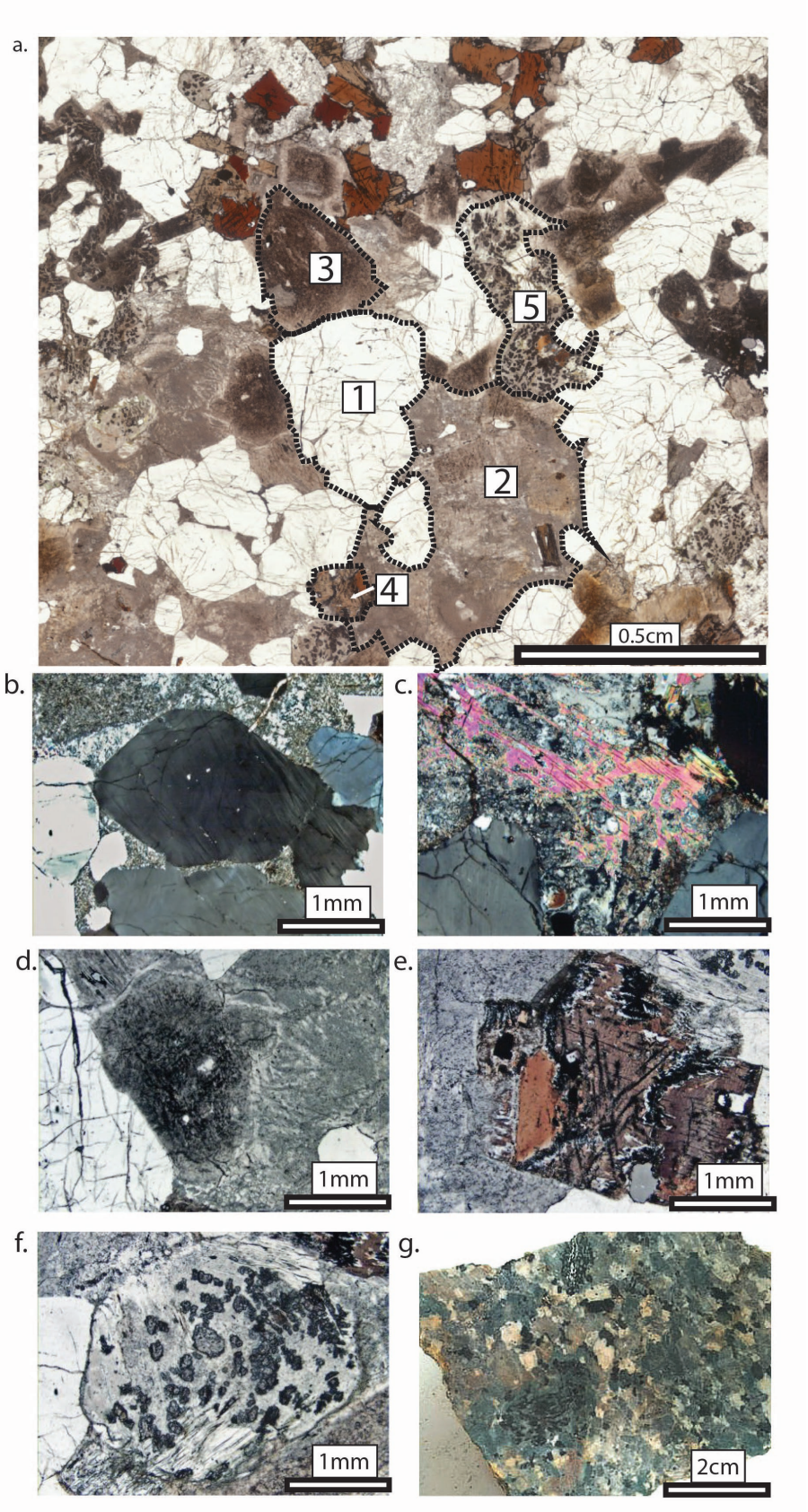


Figure 1 ***a.*** *Sample 11-01 showing the location of representative domains with igneous textural relationships, as referred to in the text* ***b.*** *Domain 1 – euhedral quartz with deformation twins* ***c*** *Domain 2 – K-feldspar + white mica* ***d*** *Domain 3 –white mica + albite* ***e.*** *Domain 4 –euhedral biotite.* ***f.*** *Domain 5 – white mica + garnet* ***g.*** *Sample a12-01 cut hand specimen, granite texture with skeletal biotite domains*

Quartz

Monocrystalline euhedral quartz grains are present in most granite samples from the Tso Morari complex. Single crystals of quartz exhibit low–strain internal features such as subgrain formation and incipient recrystallisation, which is often confined to grain boundaries (Figure 2b). Chessboard subgrains (0.5 mm width) are present within these grains (Figure 2b). Locally smaller subgrains have developed on a scale of <0.1 mm within the chess board subgrains. Quartz grain boundaries are commonly gently lobate at a scale of c. 0.1 mm as a result of minor grain-boundary migration.

Sample a05-10 shows different quartz textures to the other granites. Coarse igneous quartz domains are preserved, comparable in size and shape to those in neighbouring granite samples. However, they are dominantly composed of columnar quartz grains with a common shape orientation. Grain boundaries between columnar quartz grains are partially recrystallised and gently lobate, as a result of grain boundary migration.

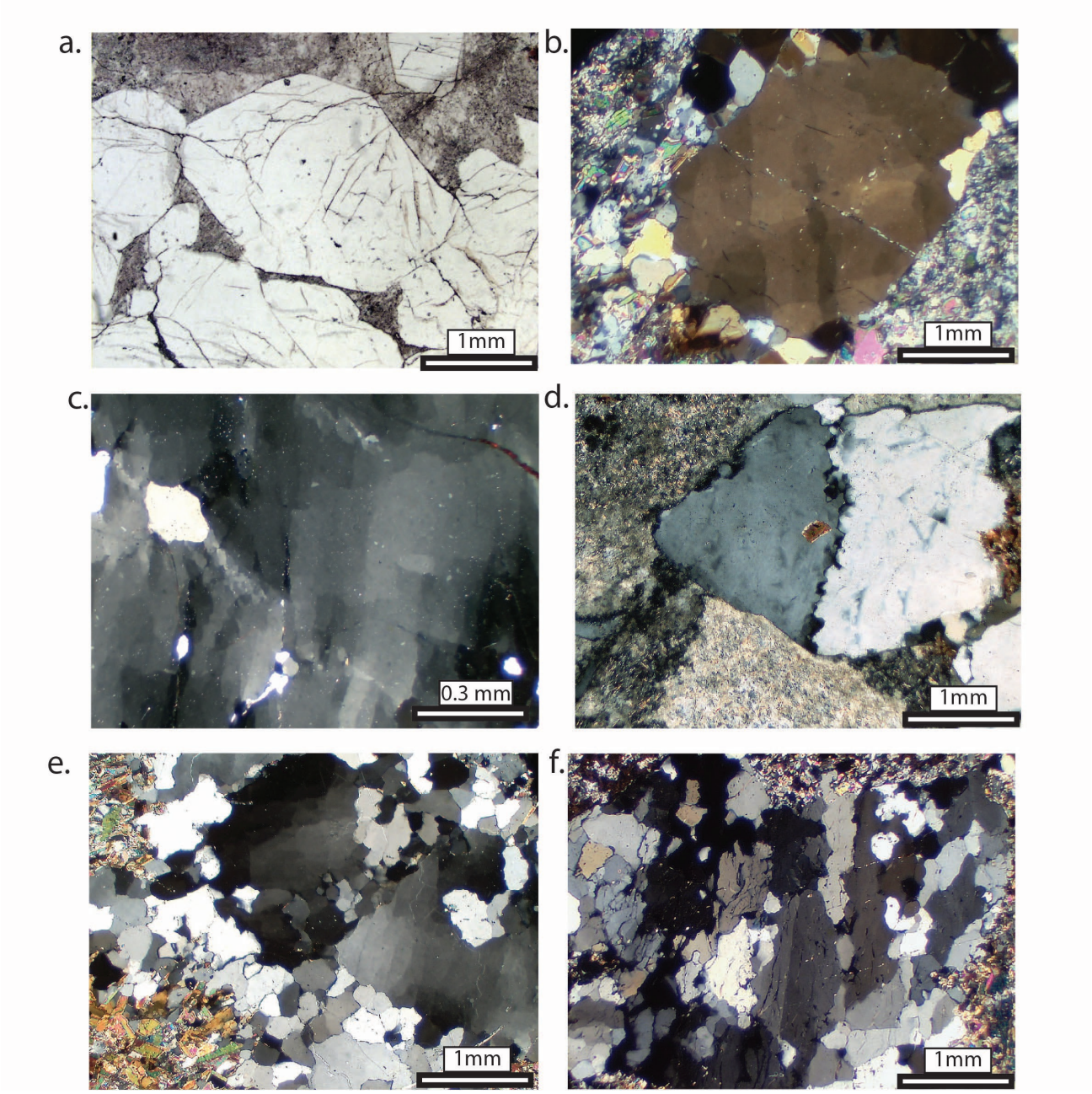


Figure 2 ***a-c*** *show variations in domain 1 quartz microstructures* ***a*** *Sample 11-01 showing euhedral quartz grains with face contacts* ***b*** *Sample a05-02 showing chess board subgrains strongly developed parallel to the quartz c-axis, with recrystallisation along grain boundaries* ***c*** *Sample a05-01 showing chess board subgrains within a relict quartz grain with some fine–grained recrystallisation internal to the grain.* ***d.*** *Sample a10-06 showing euhedral quartz grains with grains with irregular lobate grain boundaries.* ***e.*** *Sample a05-01 showing relict quartz grains with chess board subgrains and recrystallisation along grain boundaries.* ***f.*** *Sample a05-10 showing relict igneous quartz grains with a columnar texture and grain boundary migration along column boundaries*

Feldspar domains

There are two domains containing feldspars (type 2 & 3 domains) (Figure 1). The paler, cloudy domains corresponding to type 2 domains throughout sample 11-01 (Figure 1) contain K-feldspar (Or_{93}) with a fine string and bleb perthitic texture and microcline twinning. Rectangular inclusions of fine–grained white mica and albite intergrowths are observed in the K-feldspar. Mineral inclusions within K-feldspar phenocrysts have a smaller grain size compared to matrix phases, preserving similar mineralogical and textural relationships as in the equivalent matrix domains. A coarse generation of white mica is associated with type 2 domains, with a finer grained generation occurring around the rim of the coarser generation. In more altered samples, K-feldspar has partly broken down to form the white mica and plagioclase.

Type 3 domains often contain the assemblage white mica + albite in a fine–grained intergrowth. In less altered samples, islands of plagioclase are present with an anorthite content of 10-25%, preserved between channelised white mica structures. In sample L08-04 this domain also contains needles of clinozoisite in radial clusters.

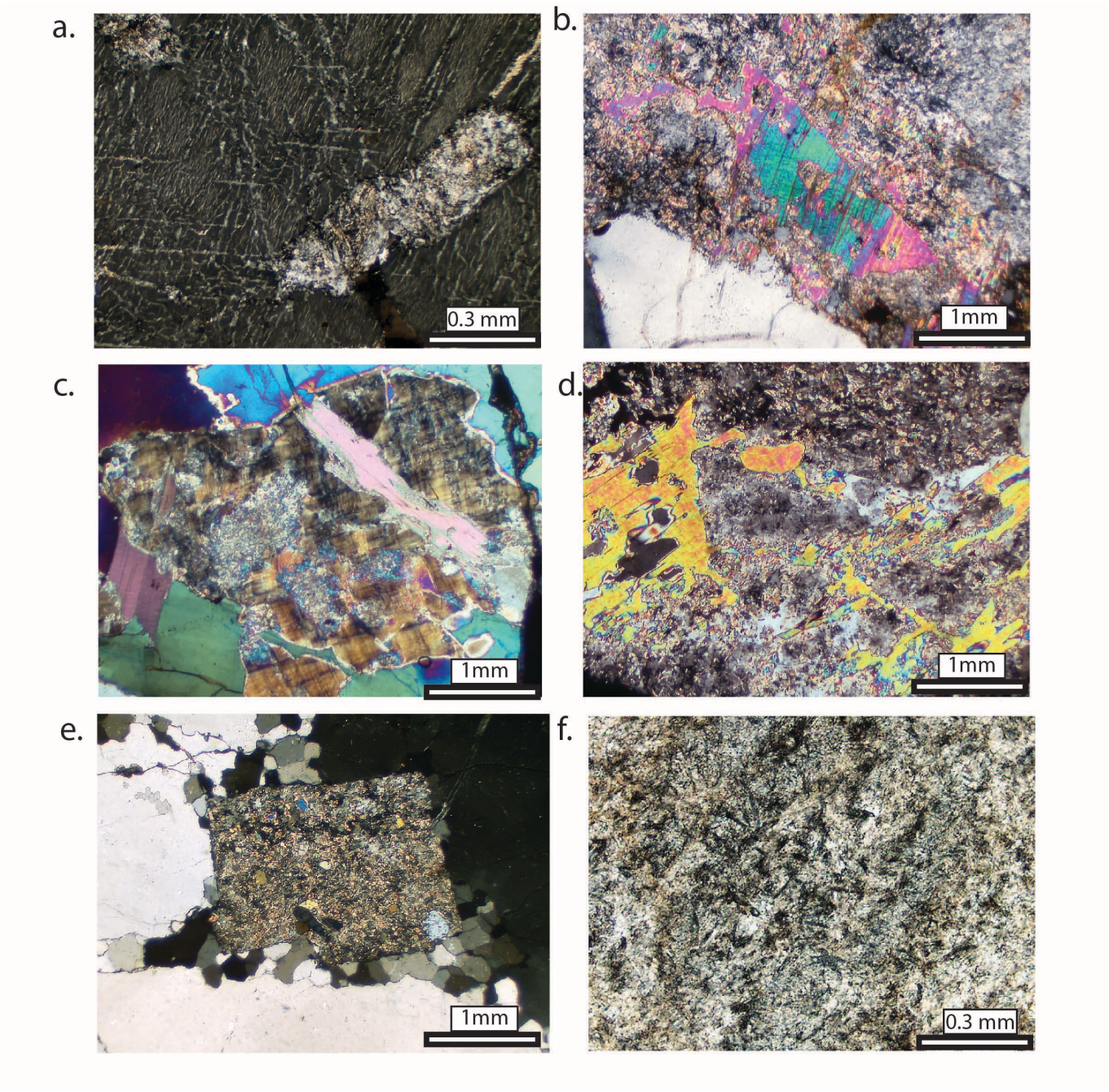


Figure 3 ***a.*** *Perthitic texture in K-feldspar with an approximately rectangular inclusion replaced by white mica* ***b.*** *Sample 11-02 domain 2, cloudy K-feldspar crystal with coarse white micas surrounded by finer phengitic white mica* ***c.*** *Sample L09-04 showing a relict microcline crystal with a large cross-cutting white mica and patchy domains of fine–grained white mica* ***d.*** *Sample a10-06 showing coarse–grained skeletal white mica with an irregular outline in a domain of fine–grained white mica + albite* ***e.*** *Sample a05-01 showing rectangular domain of white mica + albite surrounded by quartz with recrystallisation by grain boundary migration along grain boundaries.* ***f.*** *Sample L08-04 domain 3, albite + white mica with needles of clinozoisite in radial structures.*

Biotite

Biotite is the most abundant ferromagnesian mineral in the granites (Figure 4) and occurs in four textural generations:

(i) Coarse grained red-brown euhedral biotite (type 4 domains)

(ii) Red-brown biotite aggregates (type 4 domains)

(iii) Brown biotite after garnet

(iv) Coarse grained brown/colourless biotite around the edge of type 5 domains

Generation (i) is compositionally homogenous with a well–defined cleavage, a dark brown-red colour and a Ti content of 0.25-0.38 pfu and X_{Mg} of 0.21-0.39 (Figure 4b). Sagenitic rutile is sometimes present parallel to the cleavage planes. Trails of densely packed zircon inclusions and apatite crosscut the cleavage of the grains. The coarse–grained biotites have reaction coronas ~30 μm wide (Figure 4a-c) consisting of phengite (3.3-3.4 Si pfu) intergrown with fingers of ilmenite, surrounded by a continuous corona of granular garnet. Occasionally, this white mica – ilmenite intergrowth is surrounded by a second rim of white mica with a higher phengite content of 3.45-3.55 Si pfu. The coronas on biotite in contact with quartz are thinner but more continuous and have a narrow discontinuous phengite + ilmenite fringe.

Most granite samples preserve euhedral aggregates of biotite and white mica making up domain type 4, corresponding to biotite generation (ii) (Figure 4e). However, these are progressively replaced by aggregates of red-brown fine–grained biotite. These form distinct regions in samples a05-01 and a05-02, occupying a larger proportion of the rock (>20%) but not rectangular as in other samples. The aggregates are associated with phengitic white mica, and with garnet which partially replaces biotite in sample a05-10 (Figure 4e). Coarse–grained biotite (generation v) is also found around the edge of type 5 domains and is often colourless, with no Ti and a more magnesian composition (X_{Mg} 0.41-0.45). Fine–grained brown biotite forms coronas around garnet (generation iii) in domains 4 and 5 and has a low Ti content (0.09) and a high XMg (0.46-0.61). In altered samples such as a10-07, garnet is completely replaced by biotite.

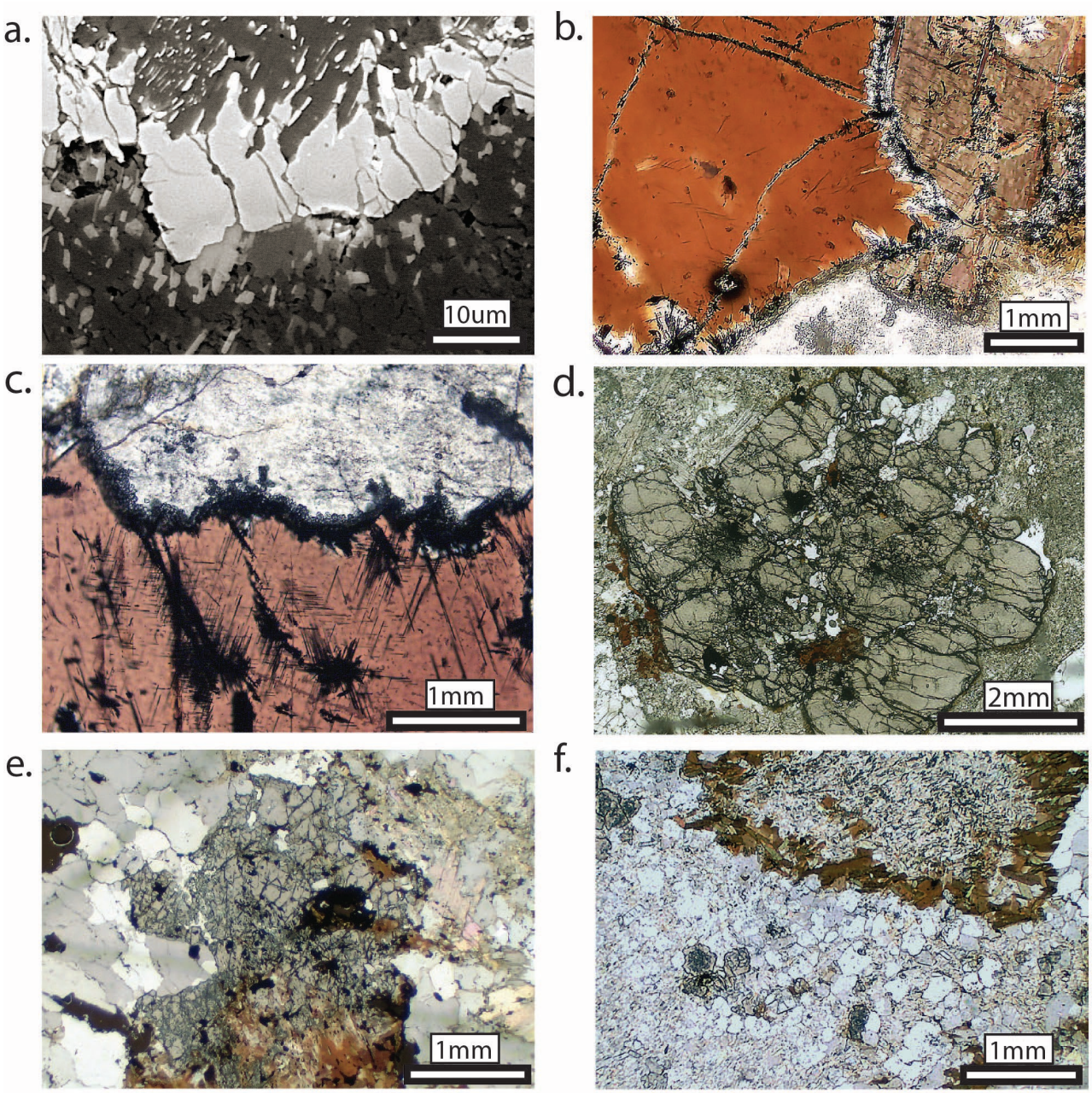


Figure 4 ***a*** *Sample 11-01, BSE image of zoned garnet rim and intergrown ilmenite and phengite around igneous biotite (top - domain 4) in contact with albite + white mica (bottom - domain 3)* ***b*** *Sample 11-01, red biotite cluster (domain 4) with phengite + ilmenite intergrowth replacing biotite along grain boundary* ***c*** *Photomicrograph of granular garnet texture around igneous biotite (domain 4).* ***d*** *Sample a05-10 course garnet with a thin rim of brown biotite.* ***e*** *Sample a05-10, garnet replacing red biotite aggregate in domain 4 with partial polarisation.* ***f*** *Sample a05-01, white mica with biotite aggregate around the rim (domain 4), often associated with garnets. Zoned garnets replacing rectangular inclusions in domain 2 (bottom).*

Sample	11-01				11-02					A05-10a					L08-04	
Domain	5				5			4		4					4	
Generation	iii	iii	iv	iv	iv	iv	iv	i	i	ii	ii	ii	ii	ii	i	i
SiO_2	38.10	38.93	38.39	36.68	37.29	37.23	34.98	34.53	35.15	37.03	37.31	36.05	36.50	37.07	32.99	33.06
TiO_2	0.00	0.03	1.76	2.26	0.01	0.02	0.01	2.59	2.42	2.72	2.68	2.75	2.54	2.81	2.28	2.31
Al_2O_3	20.22	20.33	19.29	18.76	18.46	18.09	19.69	18.13	18.06	16.87	16.16	17.41	17.50	16.33	17.74	18.19
FeO	17.37	18.02	15.86	14.33	20.13	21.21	21.65	22.87	22.42	21.47	20.79	21.48	21.08	21.11	24.99	24.25
MnO	0.16	0.13	0.10	0.04	0.17	0.22	0.23	0.26	0.23	0.06	0.06	0.02	0.03	0.03	0.28	0.27
MgO	11.87	11.20	12.55	12.85	9.31	9.33	8.55	7.27	7.23	8.73	9.10	8.22	9.04	8.86	4.24	4.30
CaO	0.07	0.14	0.03	0.03	0.03	0.02	0.19	0.02	0.07	0.00	0.06	0.03	0.01	0.01	0.04	0.00
Na_2O	0.08	0.08	0.05	0.04	0.09	0.09	0.16	0.08	0.08	0.09	0.13	0.06	0.08	0.13	0.07	0.05
K_2O	5.98	6.07	6.03	8.91	9.44	9.35	8.56	9.45	9.13	7.58	9.00	6.43	9.19	8.92	8.92	9.08
F	0.68	0.57	0.94	0.68	0.73	0.67	0.44	0.28	0.40	0.39	0.36	0.33	0.35	0.30	0.37	0.40
Cl	0.09	0.09	0.22	0.10	0.19	0.21	0.14	0.18	0.08	0.72	0.66	0.67	0.52	0.79	0.07	0.08
Total	94.63	95.59	95.21	94.67	95.84	96.44	94.60	95.66	95.26	95.66	96.31	93.45	96.84	96.36	91.98	91.99
Oxygens	22	22	22	22	22	22	22	22	22	22	22	22	22	22	22	22
Si	5.61	5.68	5.59	5.45	5.64	5.62	5.40	5.35	5.44	5.61	5.65	5.56	5.51	5.62	5.39	5.38
Ti	0.00	0.00	0.19	0.25	0.00	0.00	0.00	0.30	0.28	0.31	0.31	0.32	0.29	0.32	0.28	0.28
Al	3.51	3.50	3.31	3.29	3.29	3.22	3.59	3.31	3.29	3.01	2.89	3.17	3.11	2.92	3.42	3.49
Fe	2.14	2.20	1.93	1.78	2.55	2.68	2.80	2.96	2.90	2.72	2.63	2.77	2.66	2.68	3.41	3.30
Mn	0.02	0.02	0.01	0.00	0.02	0.03	0.03	0.03	0.03	0.01	0.01	0.00	0.00	0.00	0.04	0.04
Mg	2.60	2.44	2.72	2.85	2.10	2.10	1.97	1.68	1.67	1.97	2.05	1.89	2.03	2.00	1.03	1.04
Ca	0.01	0.02	0.01	0.00	0.01	0.00	0.03	0.00	0.01	0.00	0.01	0.01	0.00	0.00	0.01	0.00
Na	0.02	0.02	0.01	0.01	0.02	0.03	0.05	0.02	0.02	0.03	0.04	0.02	0.02	0.04	0.02	0.02
K	1.12	1.13	1.12	1.69	1.82	1.80	1.69	1.87	1.80	1.47	1.74	1.27	1.77	1.73	1.86	1.88
F	0.32	0.26	0.43	0.32	0.35	0.32	0.21	0.14	0.20	0.18	0.17	0.16	0.16	0.15	0.19	0.20
Cl	0.02	0.02	0.05	0.03	0.05	0.05	0.04	0.05	0.02	0.19	0.17	0.18	0.13	0.20	0.02	0.02
Cat.sum	15.04	15.00	14.89	15.33	15.44	15.49	15.55	15.54	15.44	15.13	15.32	15.01	15.40	15.31	15.46	15.43
X_{Mg}	0.55	0.53	0.58	0.61	0.45	0.44	0.41	0.36	0.36	0.42	0.44	0.41	0.43	0.43	0.23	0.24

Table 2 Representative data for biotites in the Tso Morari granites. Domains and biotite generations are described in the text.

White mica

White mica can be broadly subdivided into groups of coarse–grained muscovite and fine–grained phengite (Figure 5), both of which occur in domain types two to five and can be characterised into seven textural generations:

(i) Coarse–grained euhedral matrix muscovite (type 4 domains)

(ii) Coarse–grained muscovite associated with K-feldspar (type 2 domains)

(iii) Coarse–grained muscovite around the edge of type 5 domains

(iv) Fine–grained phengite rims around generation (ii)

(v) Fine–grained network of phengite (type 2 and 3 domains)

(vi) Fine–grained phengite corona around biotite (type 4 domains)

(vii) Fine–grained phengite with garnet + kyanite, in the centre of type 5 domains

Generation (i) is coarse–grained and has a similar composition to coarse–grained generations (ii) and (iii). These micas have the lowest phengite, highest paragonite content and break down into fine–grained phengitic white mica around their rim (Figure 5d-f). Fine grained generation (v) forms a network within domain types 2 and 3, as well as in the centre of domain type 5 (vii). These grains also plot along the celadonite exchange vector, with increasing Si and Mg pfu (Figure 5), ranging from 3.05-3.6 Si pfu. Fine–grained phengitic white micas is commonly associated with fine–grained albite, forming thin rims around biotite (type 4 domains).

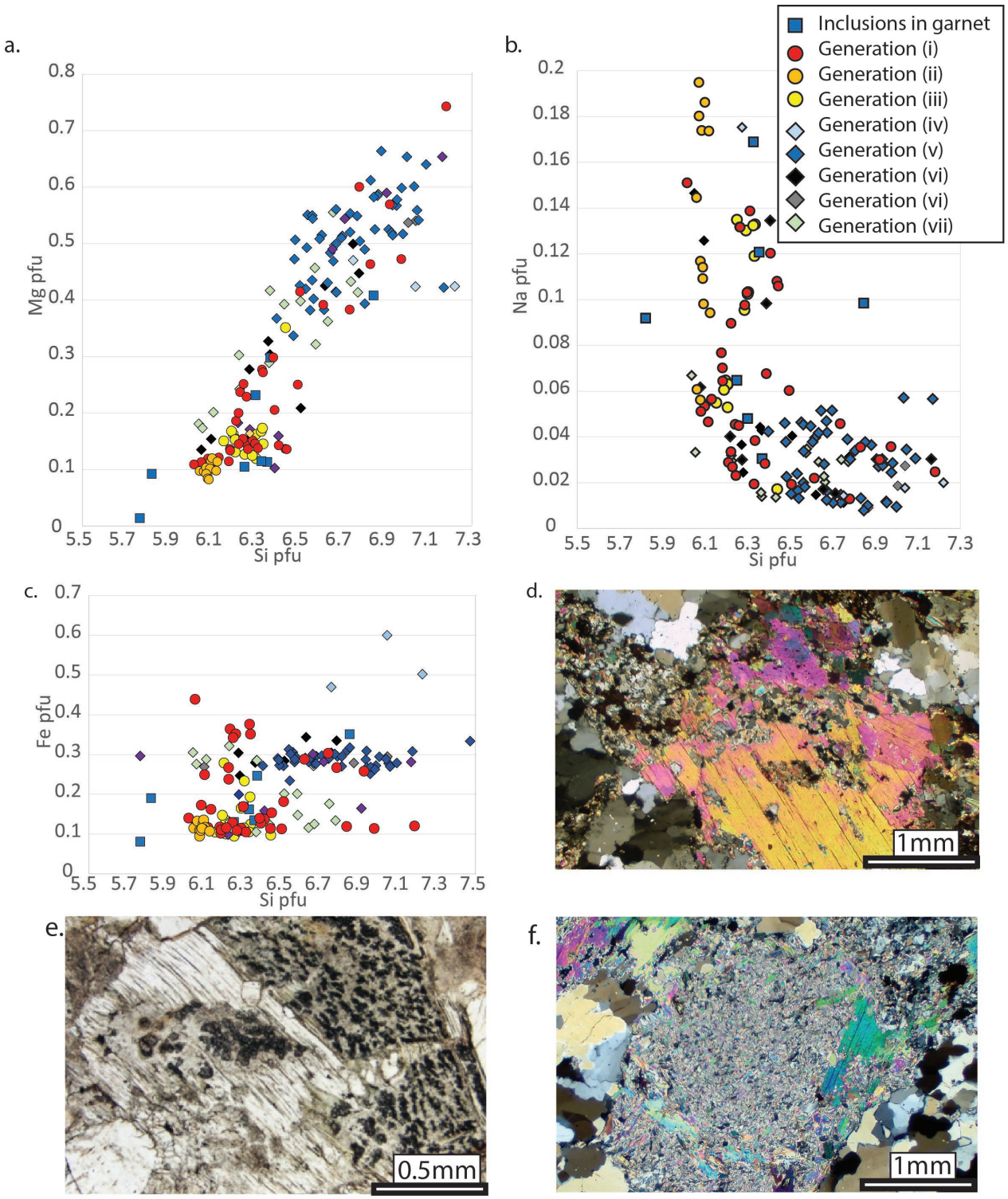


Figure 5 ***a-c*** *Mg, Na, Fe (respectively) vs Si pfu in white mica for all samples, circles = coarse–grained wm, diamonds = fine–grained wm. red circle = wm generation (i), orange circle = wm, generation (ii) in domain type 2, yellow circle = wm generation (iii) in domain type 5, black diamond = wm generation (vi), inner rim, grey diamond = wm generation (vi), outer wm, pale green diamond = wm generation (vii)in domain type 5, blue diamond = wm generation (v) in domain type 3, pale blue diamond = wm generation (iv) domain type 2* ***d*** *Sample a05-10, coarse white mica in domain type 2 with K-feldspar and fine white mica at the rim* ***e*** *Sample 11-01, coarse white mica in domain type 5 partially replaced by fine white mica and garnet* ***f*** *Sample a05-10, fine white mica aggregate in domain type 2 with remnants of coarse white mica*

Garnet

Multiple generations of garnet have been identified within the granite and Puga gneiss as described by Girard and Bussy (1999). The undeformed granites in this study contain three textural generations of garnet:

i) Thin (30μm) continuous zoned coronas around igneous biotite (Figure 4a),

ii) Small prograde garnets nucleated around coarse biotite aggregates (Figure 4d),

iii) Fe-Mg garnets with acicular kyanite inclusions within type 5 domains (Figure 6a).

Garnet coronas (i) around biotite (i) have a composition of $Alm_{54-80}Py_{3-7}Grs_{2-40}Sps_{2-4}$ with a gradient in grossular content from 2% in contact with the biotite to 40% in contact with albite. They are rarely preserved in the granite gneisses where biotite has broken down into aggregates of phengite and rutile/titanite. Garnets in type 5 domains (iii) are associated with assemblages of phengitic white mica and kyanite. These garnets are often replaced by biotite, particularly in enclaves within granite consisting of intergrown quartz and type 5 domains.

Cordierite

Type 5 domains contain multiple generations of micas including coarse biotite (iv) and white mica (iii) forming the rim of the domain, with fine grained phengite (vi) (3.15 to 3.4 Si pfu), kyanite needles, Fe-Mg garnet (iii) ($Alm_{72-79}Py_{20-26}Grs_{0.06-0.2}Sps_{1.3-2.5}$) and fine grained biotite (iii) in the centre of the domain (Figure 6). The composition of this domain type, based on element mapping, is shown in Table 3 and averages at the composition of cordierite with additional K and H_2O. Therefore, domains of type 5 are interpreted as pseudomorphs after cordierite. The bulk normative corundum of sample 11-01 is 14%, with a A/CNK ratio of 1.95. Enclaves are observed in the granite containing intergrowths of quartz with type 5 domains, with a fibrous texture at the intergrowth boundaries, ~100 μm wide, with a radial orientation.

Coarse white micas in type 5 domains have a phengite content of 3.05-3.17 Si pfu which closely correlates with the low phengite content of the coarse matrix white micas (i and ii). Biotite within type 5 domains is high in magnesium (X_{Mg} = 0.55) compared to igneous biotite (X_{Mg} = 0.32-0.40) and has a low Ti content compared to Ti–rich igneous biotites.

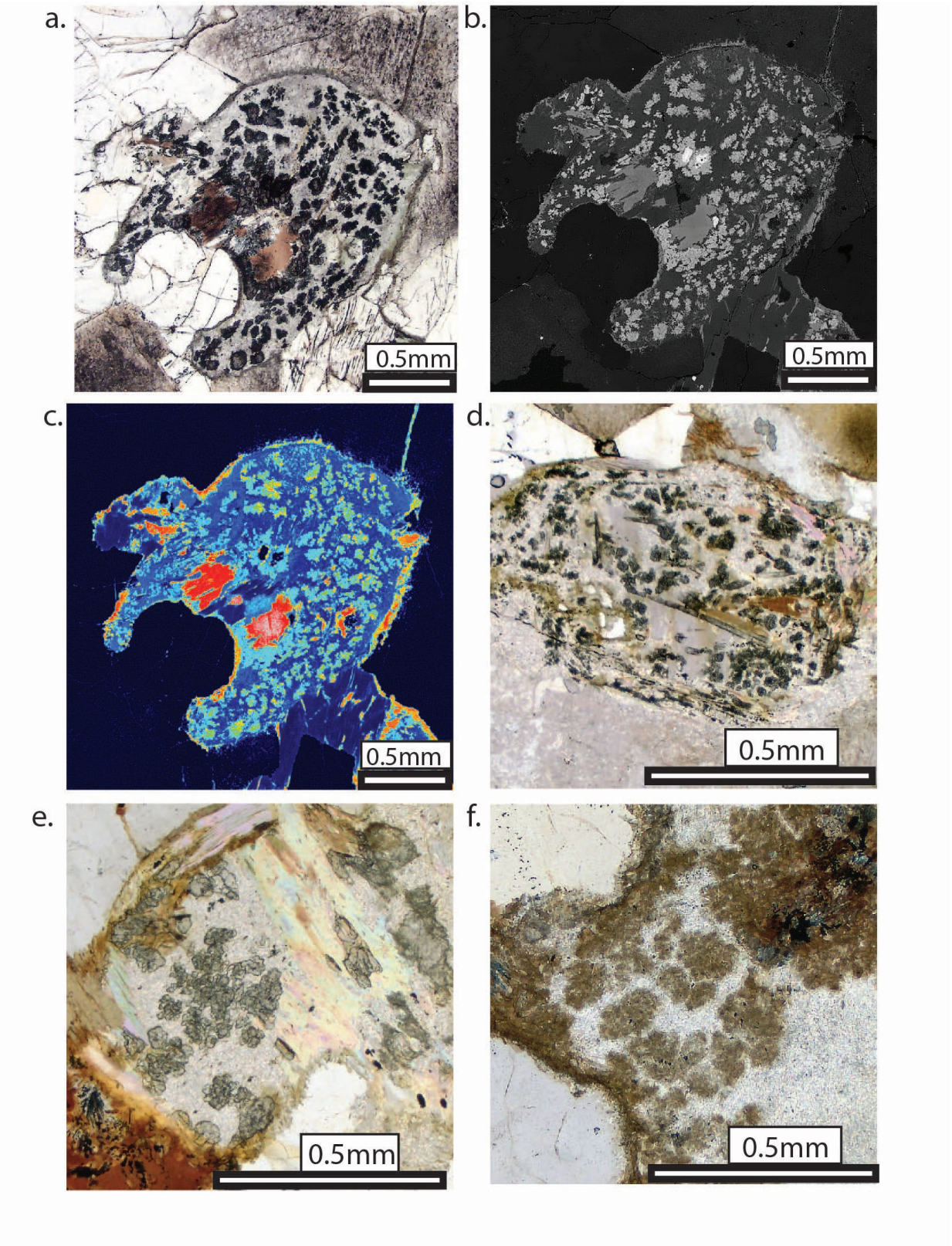


Figure 6 Sample 11-01 ***a*** *Photomicrograph of cordierite pseudomorph with large brown biotite, dark garnets and a matrix of fine grained white mica* ***b*** *BSE image of cordierite pseudomorph showing bright garnets and fine grained white mica matrix,* ***c*** *Mg-map of cordierite pseudomorph with red Mg-rich biotites, pale blue garnet and dark blue white mica* ***d and e*** *sample a10-07, domain type 5 with coarse biotite and white mica around the edge, partially replaced by fine white mica and garnet.* ***f.*** *Sample 11-02 showing garnets in domain type 5 completely replaced by brown biotite.*

	Oxide%		Cations pfu (18 oxygens)	Normalised to Si=5
SiO_2	44.069	Si	4.811	5.000
TiO_2	0.545	Ti	0.045	0.046
Al_2O_3	30.278	Al	3.897	4.050
FeO	12.791	Fe	1.168	1.214
MnO	0.859	Mn	0.079	0.083
MgO	3.754	Mg	0.611	0.635
CaO	0.471	Ca	0.055	0.057
Na_2O	0.750	Na	0.159	0.165
K_2O	6.482	K	0.903	0.938
Total	100	Cat.Sum	11.727	12.188
		Alkali sum		1.160

Table 3 Composition of domain 5 taken from representative element map

Geochronology

Methods

Monazite grains were identified in thin section using the a FEI Quanta 650 FEG E-Scanning electron microscope (E-SEM) at the University of Oxford with an accelerating voltage of 30 kV and a working distance of 15 mm. Images were taken using back scattered electron imaging to identify any zoning present. The U-Pb age of monazite was measured in situ using the Nu AttoM at the NERC Isotope Geoscience Laboratories (NIGL) using a spot size of 11-12 µm (See Appendix 2 for methods). Twenty-two spot analyses were made in monazite grains from sample 11-01. The primary standard reference material used was ‘Stern’ (Palin *et al.*, 2013; Horstwood *et al.*, 2016), the secondary reference materials were ‘Manangotry’ (Paquette *et al.*, 1994; Palin *et al.*, 2013) and 44069 (Aleinikoff *et al.*, 2006; Buick et al., 2011).

Results

Monazite grains are approximately 50 µm in diameter and occur as round grains with no zoning observed using backscatter electron imaging (Figure 7). Monazite is commonly associated with type 5 domains but are also found as inclusions in igneous micas, particularly biotite. The data reveal a variable amount of discordance, likely due to both incorporation of small amounts of common lead, and to minor disturbance of the isotope systematics during younger events. The latter is compatible with the fact the rock unit has undergone high pressure conditions during the Eocene. The weighted mean $^{206}Pb/^{238}U$ age of the concordant (>90%) analyses is taken as the date of monazite formation and yields a date of 473.6 ± 9.0 Ma (MSWD = 3.2). The high mean square weighted deviation (MSWD) indicates that even this age estimate, derived from concordant analyses, involves a degree of analytical scatter, probably due to analysis of domains comprising lead-loss or younger components.

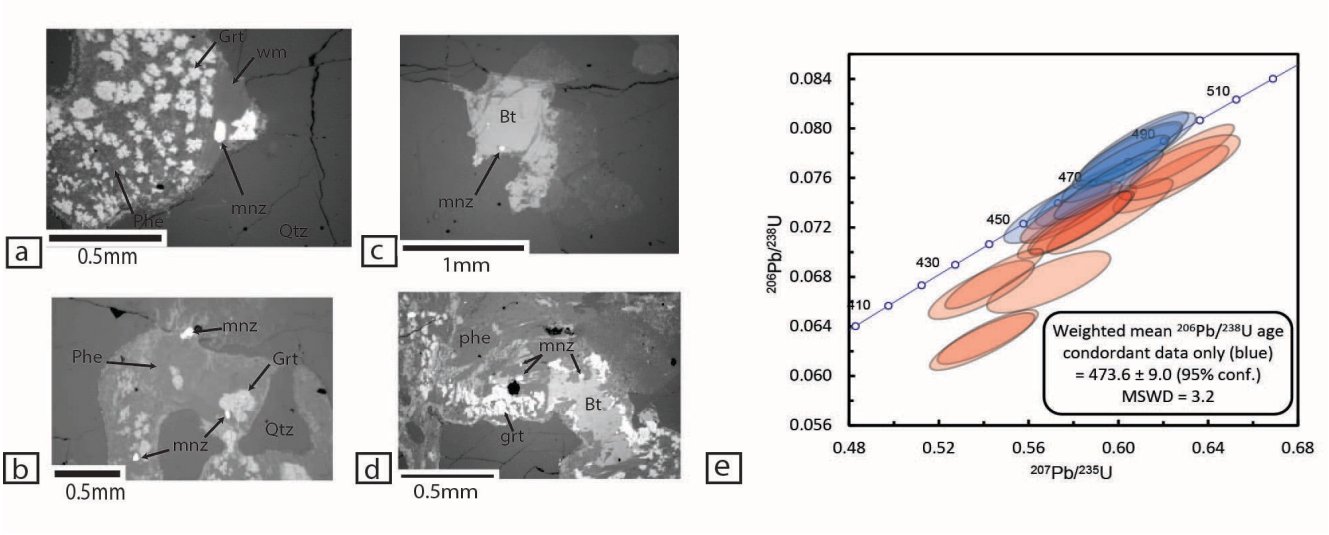


Figure 7 ***a-b,d*** *BSE images of monazite in pseudomorphs after cordierite* ***c*** *BSE image of monazite in igneous biotite* ***e*** *Tera Wasserburg plot showing concordant (blue) and non-concordant analyses of monazite (red)*

Phase equilibrium modelling

Methods

Phase equilibrium modelling was undertaken using the local bulk composition derived from domain 5 in sample 11-01 in order to determine the P-T conditions of metamorphism. The bulk composition (SI(41.77)AL(31.76)CA(0.05)MG(6.17)FE(10.51)F3(0.25)K(9.31)NA(0.27)TI(0.24)MN(0.22)H(40)O(?)) was calculated based on the average mineral compositions with respect to their modal abundances. Phase equilibrium models were calculated using the eleven component system MnO-N_2O-CaO-K_2O-FeO-MgO-Al_2O_3-SiO_2-H_2O-TiO_2-Fe_2O_3 (MnNCKFMASHTO) using Theriak/Domino v.2015 with thermodynamic dataset ds55 (Powell and Holland, 1988; Holland and Powell, 1998; updated August 2004), adapted by Doug Tinkham. For further discussion on this technique see chapter 3 methods section.

Results

Equilibrium models for the local bulk composition of domain 5 predict an observed garnet isopleth (pyrope 18-21% almandine 73-78%) intersection in the kyanite stability field at >625°C, 10-12 kbar. Kyanite is observed as inclusions in garnet and in the matrix of domain 5 suggesting that kyanite was stable during garnet growth.

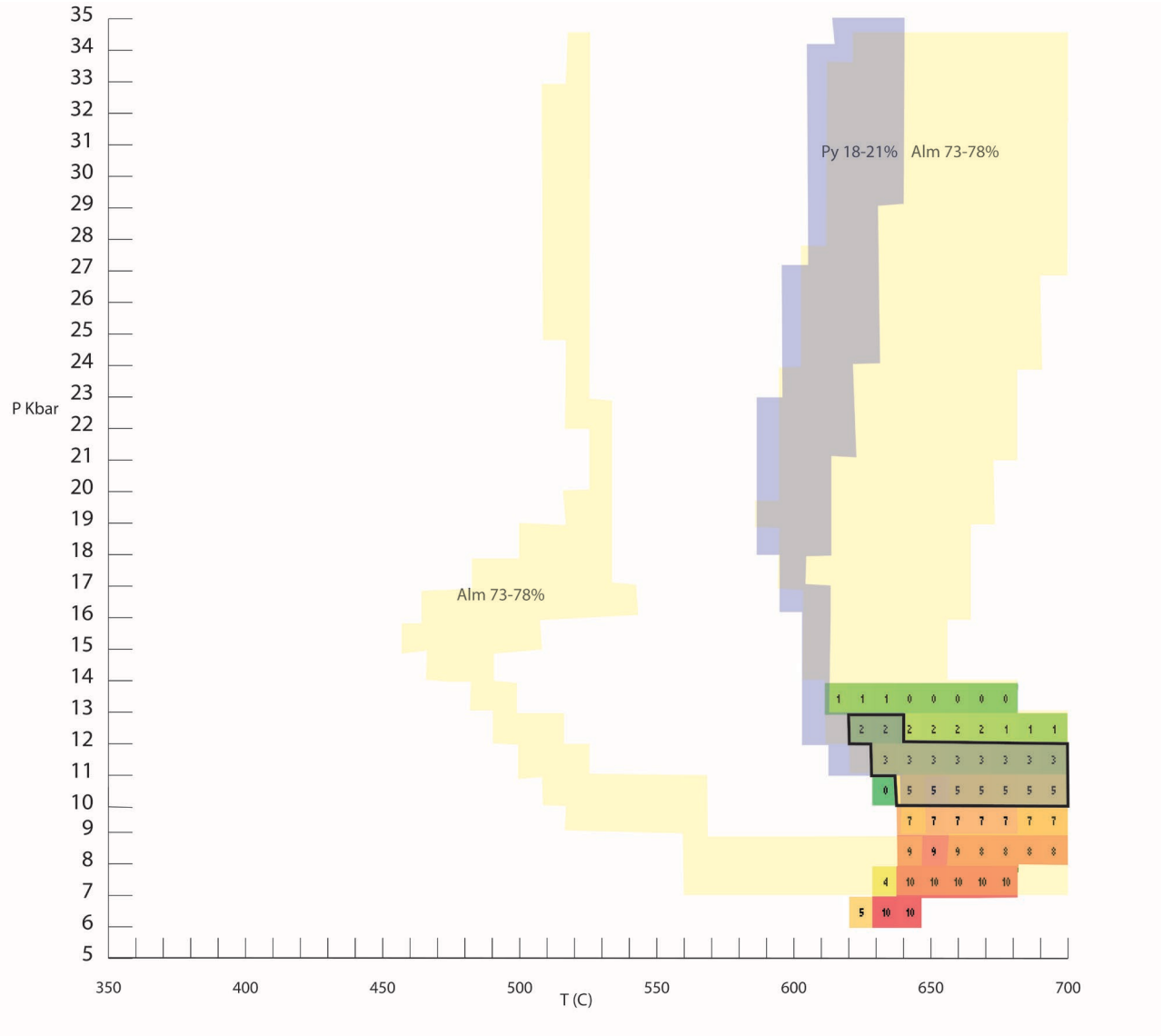


Figure 8 Phase equilibrium diagram for local bulk composition of domain 5 showing kyanite modal percentage. Colour scale shows low (green) to high (red) values. Pyrope isopleths for observed composition 18-21% (yellow) and almandine isopleths for observed composition 73-78% (blue) intersect in the kyanite stability field within blue box.

Interpretation

The textural domains described in the Tso Morari granitoids can be interpreted as the location of the primary igneous minerals, where igneous textural relationships have been preserved. Primary quartz, K-feldspar, biotite and muscovite are partially preserved in most samples, whereas plagioclase ± cordierite, although now pseudomorphed, make up part of the original assemblage.

Domain type 1

Microstructures in quartz domains show that the primary igneous quartz grains, although slightly deformed, have been preserved. Euhedral quartz grains in type 1 domains cluster into aggregates with interstitial feldspar, suggesting that quartz was one of the earliest minerals to crystallise in the magma. The grains preserve face contacts (Figure 2a), indicating that quartz underwent synneusis – the mutual attachment of crystals in a melt (Vance, 1969), allowing phenocrysts to develop without interference from adjacent grains (Swanson and Fenn, 1986).

Sample a05-10, from the Polokongka La region, preserves igneous quartz domains that comprise an aggregate of elongate quartz grains, in contrast to the single crystals preserved in other samples from the Tso Morari complex. The microstructure may be described as a columnar palisade texture (Figure 2f), similar to that seen in the matrix of the Dora Maira pyrope quartzite, which is interpreted to have nucleated and grown after coesite (Schertl et al., 1991). See chapter 6 for more detailed analysis of these textures.

High–temperature quartz microstructures in the form of chessboard subgrains are observed in granitoid samples from the Polokongka La region of Tso Morari complex (Figure 2b,c,e). These microstructures indicate that temperatures exceeded 600°C during deformation (Kruhl, 2003; Wallis et al., 2017). The chessboard subgrains are overprinted by lower temperature subgrain formation along chessboard subgrain boundaries producing finer grained subgrains, internal to the grain (Figure 2c). Recrystallisation is also occasionally evident along grain boundaries (Figure 2d and e).

Domain type 2

K-feldspar megacrysts in type 2 domains contain inclusions of single crystals and aggregates of domain type 1 (quartz), domain type 3 (white mica + albite) and domain type 3 (white mica + biotite) which are distinctly smaller than the matrix phases, providing an insight into the crystallisation history of the granite. The preserved K-feldspar is perthitic, occasionally showing microcline twinning (Figure 3c). This may indicate that the magma was wet enough for microcline to invert (Parsons *et al.*, 1971).

A generation of coarse–grained muscovite (generation ii) occurs within type 2 domains, where coarse skeletal white mica grains are replacing K-feldspar (Figure 9c and d). This is similar to the textures described in the

Land's End Granite where "secondary muscovite frequently penetrates the megacrysts along cleavage cracks or follows the direction of perthitic strings" (Booth, 1968). The Land's End Granite is a coarse–grained, porphyritic, two-mica peraluminous granite, which contains the diagnostic peraluminous minerals tourmaline, andalusite and cordierite which is strongly pinitised (Hawkes *et al.*, 1978). The Land's End Granite exhibits a range of late and post-magmatic alteration including mineralisation, tourmalinisation, greisenisation and kaolinisation (Exley *et al.*, 1982). Secondary muscovite after K-feldspar is thought to be associated with the late to post-magmatic alteration (Booth, 1968).

Coarse skeletal muscovite is also observed after K-feldspar in the anatectic 'biotite granite' from the Trois Seigneurs Massif, Pyrenees (Figure 9a and b). The Trois Seigneurs Massif contains a deep-seated syn-metamorphic granitoid suite, as described by Wickham (1987). The prevalence of muscovite after K-feldspar in hydrothermally altered granites, which have not undergone high–pressure metamorphism, and in the granites of the Tso Morari complex, suggests that the latter underwent a similar late– to post–magmatic history of hydrothermal alteration.

Fine–grained white mica from the Tso Morari granites shows different textural generations (iv to vi) plotting on a celadonite exchange vector towards a high Si and Mg content. These generations, which occur in domain types 2 and 5, are interpreted to have formed at relatively high–pressure conditions (c.f. Ernst, 1963). Coarse white mica replacing K-feldspar in type 2 domains has indistinct rims, partially replaced by fine–grained white mica, suggesting later modification and recrystallisation of the coarse white mica generation. The fine–grained white mica of type 2 domains (generation ii) may have formed under high–pressure conditions, or may have formed as a low temperature sericite as a result of the same post-magmatic pathway as the coarse–grained muscovite after K-feldspar, and, later converted to a higher-Si metamorphic state.

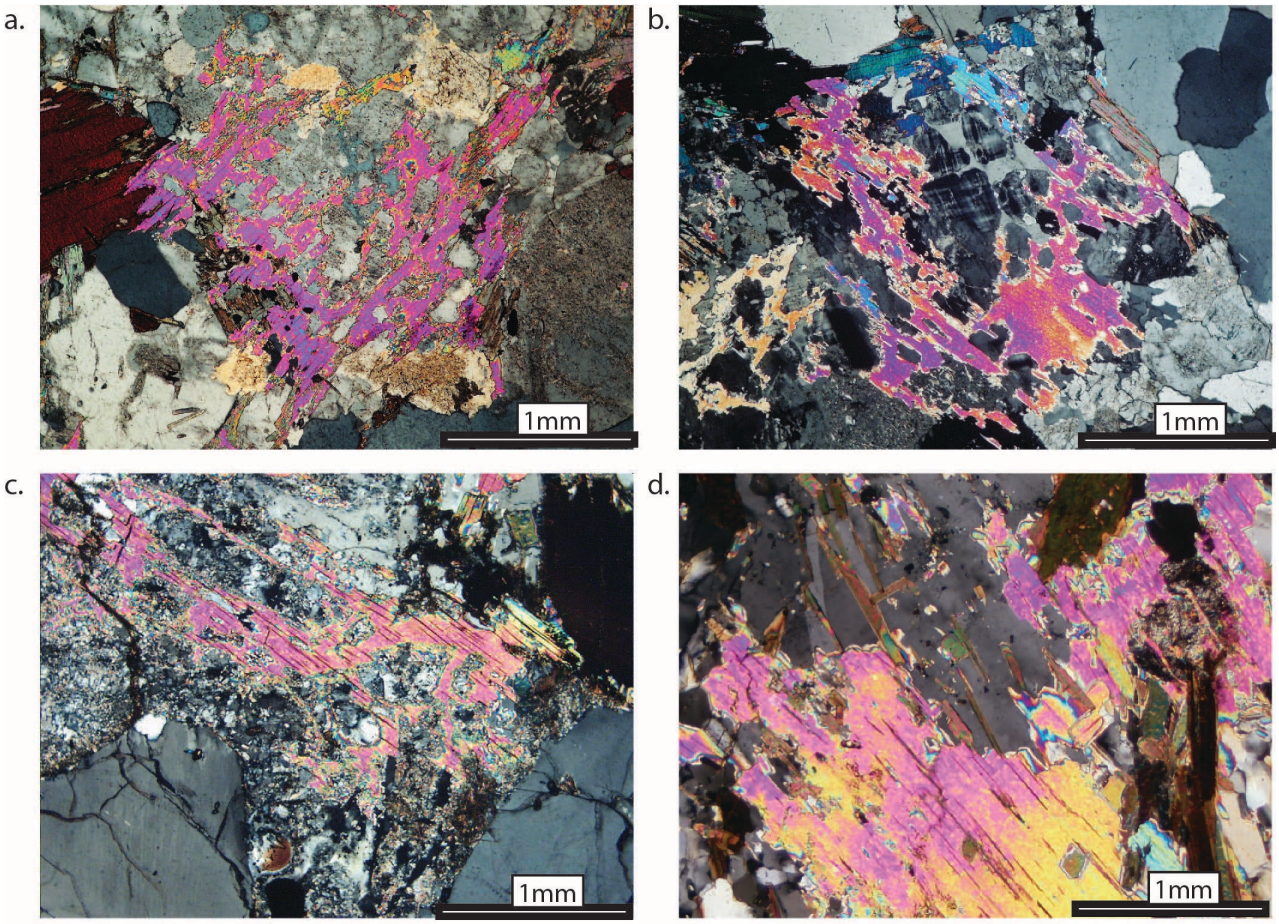


Figure 9 a. and b. Skeletal muscovite forming after K-feldspar in the biotite granite described by Wickham (1987) in the Trois Seigneurs Massif. c. Sample 11-02 from the Tso Morari complex showing skeletal muscovite after K-feldspar. d. Sample a05-02 showing coarse–grained irregular muscovite after K-feldspar.

Domain type 3

Sericitisation of plagioclase within the fine perthites of domain 2 or igneous plagioclase of domain 3 is observed. The original igneous plagioclase (domain 3) no longer contains Ca-bearing plagioclase but has been completely replaced by albite and white mica. The processes of albitisation and sericitisation are thought to take place in low temperature conditions (c.f. Meunier and Velde, 1982) and are thought to be directly linked, based on thermodynamic considerations as well as textural and chemical observations in granites (Plumper and Putnis, 2009). However, the presence of clinozoisite needles in equilibrated feldspar domains in high pressure metagranitoids such as the Monte Mucrone metaquartz-diorites (Koons et al., 1987) suggests that the considered plagioclase domain also equilibrated at relatively high pressures.

Domain type 4

A distinct, coarse–grained white mica generation with a celadonite– composition (generation i) occurs as matrix clusters in type 4 domains and is associated with coarse, Ti-rich biotite suggesting a high–temperature, magmatic origin. Mineral compositional data in the Polokongka La granite (sample 11-01), combined with textural observations, describe a double corona of phengite surrounding igneous biotite, with a corona of zoned garnet also forming around igneous biotite in contact with quartz or plagioclase.

Girard and Bussy (1999) first observed garnet + muscovite coronas around igneous biotite in the Polokongka La granite. An initial comparison was made with the coronas observed in the Monte Mucrone meta-quartz diorites of the Sesia zone, Alps, where zoned garnet, phengite and ilmenite form coronas around biotite (Oberhänsli *et al.*, 1985; Koons *et al.*, 1987). This feature is also observed in metagranites of high–pressure terranes such as the Brossasco metagranite (Biino *et al.*, 1992) and the Su Lu granite (Hirajima *et al.*, 1993). This reaction texture has been interpreted to from the breakdown of igneous biotite at eclogite–facies conditions (Oberhänsli *et al.*, 1985; Koons *et al.*, 1987). In the macroscopically undeformed granites of the Tso Morari complex, garnet and phengite coronas around biotite is documented to be a common, although volumetrically minor, texture in this study, indicating that all of these samples underwent a similar eclogite–facies metamorphic history.

In more altered granite samples from the Tso Morari complex, coarse igneous biotite with a high Ti content has broken down to form red biotite aggregates and are often partially replaced by skeletal garnets. In sample a05-10, garnet has begun to replace and pseudomorph these aggregates and even form large idioblastic garnets within the granite. Large idioblastic high-pressure garnets are also observed in the Puga Gneiss which derived from a granitic protolith (Chapter 4). The progression from thin coronitic rims of garnet (sample 11-01), to granular or skeletal replacement of red-brown biotite (sample a05-01) to euhedral garnets (sample a05-10) in increasingly altered samples, could represent a more complete transformation of biotite at eclogite facies conditions, facilitated by the availability of fluid at high pressure.

Domain type 5

A third generation of coarse–grained celadonite–poor (generation iii) occurs in type 5 domains, where coarse white mica + biotite often forms a rim around the edge of the domain or penetrates across the domain. White mica generation (iii) has a composition comparable to the igneous white mica (generation i), with a low celadonite content (Figure 5). The bulk composition of domain type 5 resembles a cordierite composition with additional potassium and H_2O, suggesting that it is related to the hydrothermal breakdown of cordierite.

It is common, in peraluminous granites, for cordierite to be unstable during the cooling history of a granite, causing it to break down during hydrothermal alteration to muscovite, phlogopite/biotite and/or chlorite e.g. the Peninsula granite (Farina *et al.*, 2012) and the Land's End granite (Booth, 1968. Exley et al., 1982). In the Peninsula granite, cordierite is a common phase in the enclaves within the granite, where it has been replaced by a mineral assemblage (Figure 10a) involving "aggregates of green-brown Ti-poor biotite and white mica as well as by very fine–grained mats of phyllosilicates varying under the polar microscope from grey to the typical third order blue of muscovite" (Farina *et al.*, 2012), i.e. by coarser-grained micas and by pinite. The occurrence of a fine–grained phyllosilicate, generally at the core of a cordierite pseudomorph, is a common feature of these coarse–grained enclaves.

The similarity in composition between the coarse white mica (iii) in the cordierite pseudomorphs, compared with the igneous white mica (i) (Figure 6), suggests that cordierite became unstable and broke down to form white mica and biotite during the late stage hydrothermal alteration of the granite. The biotite (iv) of type 5 domains has a high-Mg, low-Ti composition, consistent with formation from a cordierite breakdown reaction where the original cordierite was magnesium rich.

Metamorphism of pinitised pseudomorphs after cordierite produced the assemblage garnet + kyanite + phengite. The presence of kyanite, a high–pressure aluminosilicate polymorph, and phengitic white mica, indicates that metamorphism occurred at relatively high pressure. The Fe-Mg garnets contain no Ca or Mn, suggesting that the mineral compositions were controlled by the local bulk composition. The local availability of water from the original cordierite pseudomorph may have catalysed the reaction, allowing the complete

transformation of this domain, compared to partial transformation limited to grain boundaries elsewhere in the granite.

Pseudosection modelling of the cordierite pseudomorphs resulted in predicted P-T conditions of metamorphism at >625°C, 10-12 kbar. These conditions are consistent with the P-T conditions recorded in the amphibolite facies overprint in mafic eclogites by de Sigoyer *et al.*, (1997), St-Onge *et al.*, (2013), Palin *et al.*, (2014), Chatterjee and Jagoutz (2015) and Wilke *et al.*, (2015), suggesting that the metamorphic assemblage in this domain equilibrated on the retrograde path after emplacement in the crust. Lotout *et al*., (2017) and Godard (2009) describe domains of similar mineral assemblages in a granite from the high–pressure Lévézou massif in the southern French Massif Central and the Armorican massif, respectively. Pseudosection modelling using the local bulk composition of the cordierite pseudomorphs indicates that metamorphism occurred at 15-17 kbar, 650-670°C, at eclogite-facies conditions (Lotout *et al.*, 2019) and ~700°C, > 16 kbar (Godard, 2009). The metamorphic assemblages are interpreted to have formed following peak pressure conditions on the retrograde path.

Garnets are partially or completely replaced by brown biotite in the cordierite pseudomorphs in sample 11-02 (Figure 6f) and biotite is observed to form thin rims around garnet, which itself replaces high-Ti biotite, in sample a05-10 (Figure 4e). The breakdown of garnet to biotite suggests a later modification of garnet at lower temperatures, producing a low-Ti biotite generation. Fine grained, phengitic white mica commonly has thin rims of biotite + albite, formed from the breakdown of phengite under lower pressure conditions (Wain *et al.*, 2000).

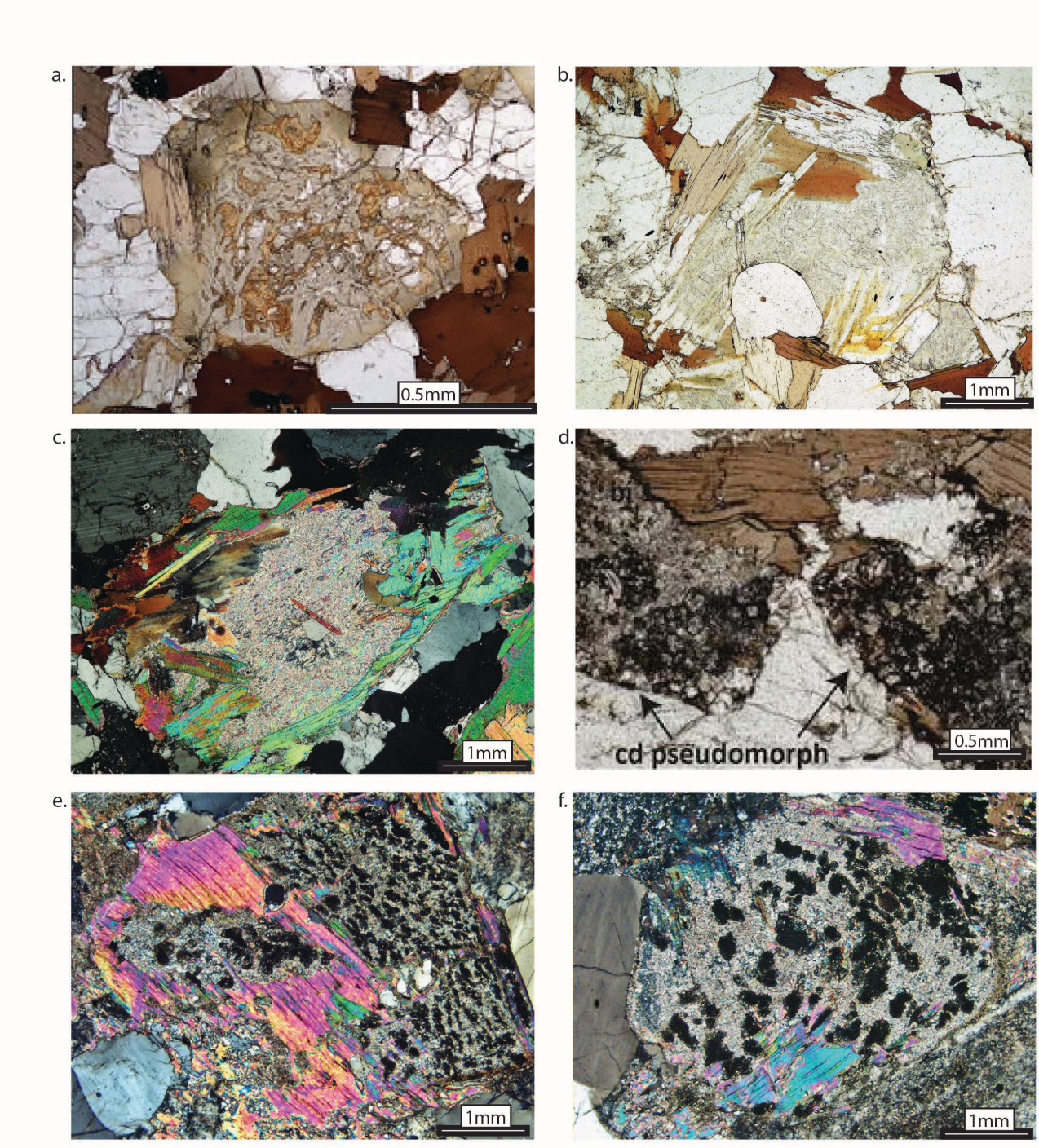


Figure 10 Cordierite pseudomorphs a. cordierite pseudomorph completely replaced by pinite from the Peninsula granite. Taken from Figure 4a, Farina *et al.*(2012)*. b. pinitised cordierite pseudomorph from biotite granite from the Trois Seigneurs Massif, with coarse–grained biotite and muscovite cross cutting the domain. c. pinitised cordierite pseudomorph from the Trois Seigneurs Massif, with coarse–grained biotite and white mica around the edge of the pseudomorph. d. cordierite pseudomorphed by fine–grained garnet + muscovite + kyanite from the high pressure Lévézou massif in the southern French Massif Central. Taken from Figure 3f,* Lotout *et al.* (2017)*. e. Sample 11-01 from the Tso Morari complex showing a coarse white mica grain penetrating across a cordierite pseudomorph. g. Sample 11-01 from the Tso Morari complex showing coarse white mica around the edge of a cordierite pseudomorph.*

Evolution of the Tso Morari granitoids

The granites of the Tso Morari complex record at least four stages in their evolution: magmatic, late magmatic, high pressure metamorphic and later metamorphic. The inferred mineral paragenesis for each stage are recorded in Table 4.

In the granites from the Tso Morari nappe, K-feldspar forms phenocrysts which crystallised early in the magmatic evolution of the granite. Quartz forms euhedral crystal shapes exhibiting quartz synneusis due to their early crystallisation. Cordierite formed an interstitial phase indicating that it crystallised late in the magmatic history of the granite. Cordierite is formed by crystallisation from peraluminous magmas at pressures < 5 kbar (Clemens *et al.*, 1981), placing an upper limit on the depth of crystallisation. The presence of magmatic muscovite in the Tso Morari metagranites also indicates that crystallisation must have occurred at pressures >3-4 kbar (c.f. Hyndman, 1981). Experimental data on peraluminous granite systems shows that K-feldspar is the last mineral to saturate in a magma of >4 wt% H_2O at 3-5 kbar, cordierite at <4 wt% H_2O and for quartz to crystallise before plagioclase pressures must exceed ~5 kbar. These factors indicate that the magma must have contained <4 wt% H_2O and formed at a depth of ~ 5 kbar.

Enclaves of cordierite + quartz within the granite along with bulk rock geochemical data, together with the presence of cordierite-quartz enclaves, indicate a peraluminous S-type composition and an origin by partial melting of sedimentary material (Girard and Bussy, 1999). The Polokongka La granite preserves textures related to late– and post–magmatic hydrothermal alteration, similar to those in many other unmetamorphosed peraluminous granites.

Close association of monazite with pseudomorphs after interstitial cordierite suggests that monazite formed in the late stages of crystallisation of the granite or is associated with the breakdown of cordierite. The U-Pb age of monazite of sample 11-01 is 473 ± 9 Ma and is consistent with the 479 ± 1 Ma U-Pb zircon age of the Polokongka La granite (Girard *et al.*, 1999). The monazite and zircon ages are interpreted as the age of crystallisation of the Polokongka La granite.

Magmatic stage	Late magmatic stage	High–pressure stage	Later modification
Quartz		Coesite?	Quartz
K-Feldspar	Muscovite	Phengite	
Plagioclase		clinozoisite	albite + white mica
Ti-biotite		Phengite + Ilmenite + garnet	
Muscovite		Phengite	biotite + albite
Cordierite	Muscovite + Mg–rich biotite	phengite + garnet + kyanite	biotite

Table 4 Table showing inferences of mineral paragenesis in the Tso Morari granites

Partial transformation of metagranitoids at high pressure

Macroscopically undeformed granites of the Tso Morari complex contain mineral compositions and textures preserving a magmatic and hydrothermal history, as well as preserving evidence of later metamorphism. Mineral assemblages such as phengite + garnet + ilmenite coronas around igneous biotite and garnet + kyanite + phengite pseudomorphs after cordierite, indicate that these granites underwent partial transformation in the eclogite facies. Transformation to an eclogite facies mineral assemblage involves the replacement of lower–pressure minerals, such as plagioclase, by higher density phases. The relative density of subducted material may determine the 'subductability' of the felsic rock, as well as the strength. For example, the presence of mica in the transformed assemblage could reduce the strength of the rock, acting as a weakening mechanism (e.g. Warren et al. 2013) and form a potential detachment surface which could influence the timing and style of exhumation.

Felsic rocks from ultrahigh–pressure terrains often record amphibolite facies conditions. However, low–strain zones have been shown to preserve a high–pressure metamorphic assemblage as a result of partial transformation. Preservation of igneous textural domains, despite further replacement of the igneous minerals, is observed in low–strain igneous rocks such as the Yankou metagranites of the Sulu province (Wallis *et al.*, 1997), the Monte Mucrone meta-quartz diorite of the Sesia Zone, Alps (Dal Piaz *et al.*, 1972; Oberhänsli *et al.*, 1985; Koons *et al.*, 1987), the Brossasco metagranites of the Dora Maira (Schertl *et al.*, 1991; Biino and Compangnoni., 1992), the Kokchetav Massif (Zhang *et al.*, 1997) and granulite-facies rocks

in the Western Gneiss Region of Norway (Wain *et al.*, 2001). In the Flaktraket mangerite-granulite complex of the Western Gneiss Region of Norway, >95% of the complex is thought to have preserved metastable igneous textures and coronas around the magmatic orthopyroxene during eclogite facies conditions (Wain *et al.*, 2001).

There are some marked differences between the Tso Morari metagranites and high–pressure metagranites from other terranes. For example, omphacite is expected to be the equilibrium pyroxene for felsic bulk compositions, formed from the breakdown of plagioclase at high pressures, but is absent in the feldspar domains of the Tso Morari granites. Koons et al (1987) observed jadeite cores and omphacite rims with zoisite and quartz, within domains replacing igneous plagioclase in the Monte Mucrone meta-quartz diorites. Static transformation in granite can be limited to regions such as igneous domains, where a local effective bulk composition is dominant and there is very little communication between domains. Subsequent mineral changes during growth in the Monte Mucrone meta-quartz diorites are interpreted to have grown as a result of partial equilibration of local mineral domains to the bulk composition as the equilibration volume enlarged, rather than due to changes in pressure and temperature (Koons *et al.,* 1987).

The absence of clinopyroxene in the plagioclase domains of the Tso Morari metagranitoids could be explained by the metastability of feldspar or the overprinting of high-pressure mineral assemblages during decompression. Garnet + phengite + ilmenite coronas around biotite are a common feature of partially transformed granites in high–pressure terrains. Koons et al. (1987) provided a detailed interpretation of this texture which can be summarised as follows: The asymmetrical chemical grossular zoning in garnet coronas in the Monte Mucrone meta-quartz diorites, is attributed to the influence of the breakdown of plagioclase into jadeite + quartz, which acts as a source for CaO and Al_2O_3. The breakdown of biotite adjacent to this, requires an input of CaO and Al_2O_3. The rate-determining step in this reaction is thought to be the diffusion of Al_2O_3 and CaO from the plagioclase domain to the biotite rim and could also explain the asymmetric zoning pattern seen in the garnet coronas. The non-completion of the biotite breakdown reaction could be due to the decrease in diffusive flux owing to the growth of garnet and muscovite coronas, lengthening diffusive pathways and therefore reducing the chemical potential gradients. Alternatively, the production of Al_2O_3 and CaO may have

ceased as the plagioclase breakdown reaction ran to completion. The presence of asymmetric chemical zoning in garnet may therefore be an indication of plagioclase breakdown.

Textures preserved in the plagioclase domains suggest that primary plagioclase was not preserved, however the lack of preserved clinopyroxene raises the question of whether clinopyroxene was present at high pressures in these rocks. The metastability of plagioclase is explored further in chapter 5 in the high-strain granite gneisses, where the composition of garnet grown at high pressure is explored as a potential indicator of plagioclase metastability.

Summary

Microstructural observations combined with mineral compositions are informative tools when unravelling a complex metamorphic history. Early and late magmatic-hydrothermal features are preserved in granites of the Tso Morari complex which experienced pressures of >26 kbar and temperatures of >600°C. Low–strain zones provide a unique window into these early histories. The microstructure of the igneous domains, the assemblages and mineral compositions in the Tso Morari granites reveal a complex evolution in which a peraluminous S-type granite was emplaced during the Ordovician (Girard and Busy, 1999) at depths equivalent to ~5 kbar, and hydrothermally altered during the late stages of emplacement at 473.6 ± 9 Ma. This granite was then subducted to high pressures during the Himalayan orogeny, where it partially transformed before being overprinted by amphibolite-facies metamorphism at >625°C, 10-12 kbar.

Previously, eclogite–facies metamorphism has been observed in the mafic rocks of the Tso Morari complex, hosted in predominantly amphibolite facies felsic rocks. The peak pressure of the Tso Morari complex has been estimated from the mafic eclogites at 26-42 kbar (de Sigoyer *et al.*, 1997; Guillot *et al.*, 1997b; Mukherjee *et al.*, 2004; St-Onge *et al.*, 2013; Chatterjee *et al.*, 2015; Wilke *et al.*, 2015). These estimates are within the coesite stability field and were first confirmed by the presence of coesite recorded in an eclogite boudin towards the northern boundary of the complex (Sachan *et al.*, 2004). However, evidence of high–pressure metamorphism has not been previously recorded in the host granite gneiss, owing to the pervasive amphibolite-facies overprint.

Undeformed granites are found throughout the Tso Morari complex and all preserve similar textural and compositional evidence of partial transformation during eclogite facies metamorphism, indicating that the entirety of the structurally distinct Tso Morari complex underwent high–pressure metamorphism during the Himalayan orogeny. The relatively low abundance of diagnostic high–pressure textures and preservation of igneous minerals such as mica indicates that metamorphic reactions were limited, perhaps by the availability of a fluid phase during subduction to eclogite facies depths, and controlled by the local bulk composition of the rock.

Chapter 5 – The transformation of continental crust during eclogite facies metamorphism

Introduction

The most extensive unit in the Tso Morari complex is the Puga Gneiss (Chapter 2, Figure 2), also known as the Tso Morari Gneiss (Epard and Steck, 2008). It was originally thought to be intruded by the Polokongka La granite (Thakur and Virdi, 1979; Fuchs and Linner., 1996; Guillot *et al.*, 1997). However, the lack of observed intrusive relationships, the existence of transitions between undeformed granite and high-strain gneiss, and near identical U-Pb zircon ages and morphology (Girard and Bussy, 1999) suggests that these lithologies belong to the same intrusive package. The Puga Gneiss is now represented as a single large unit on the geological maps of the Tso Morari dome (Chapter 2, Figure 2) but has been observed to be locally heterogeneous (Steck *et al.*, 1998; Girard and Bussy, 1999; Epard and Steck, 2008; St-Onge *et al.*, 2013; Buchs *et al.*, 2019). Muscovite–, biotite– and garnet–rich schists (Fuchs and Linner, 1996; Guillot *et al.*, 1997) are associated with metasedimentary xenoliths and partially assimilated pelite, quartzite and amphibolite, occurring as discontinuous bands concordant with the metamorphic fabric.

The Puga Gneiss is dominated by an intermediate–pressure metamorphic assemblage consisting of garnet, phengite, biotite, plagioclase, quartz and K-feldspar (Stutz, 1988; Epard *et al.*, 2008; St-Onge *et al.*, 2013). Metasedimentary xenoliths of metapelite and metagreywacke within the Puga Gneiss preserve biotite and kyanite/sillimanite textures replacing staurolite, phengite and chlorite, recording a temperature increase of up to 610 ± 30°C at 9 ± 3 kbar (de Sigoyer *et al.,* 1997), 650 ± 50°C at 9 ± 1 kbar (Girard, 2001) and 630°C ± 30°C at 9 ± 2 kbar (Guillot *et al.,* 1997). Thin cordierite coronas around garnet formed at 7.1 ± 1 kbar and 725 ± 50°C (St-Onge et al., 2013).

Mafic eclogite boudins within the Puga Gneiss and eclogite facies metasediments within the same structural unit led authors to conclude that the entirety of the Tso Morari complex was subducted to eclogite–facies depths (e.g. De Sigoyer *et al.*, 1997; Guillot *et al.*, 1997). Transformation of the Puga Gneiss during subduction may have influenced its strength and rheology. The transformation history of the subducted

continental crust is therefore important when considering the geodynamic evolution over time (Warren *et al.*, 2008a; Warren *et al.*, 2008b) (See Chapter 1).

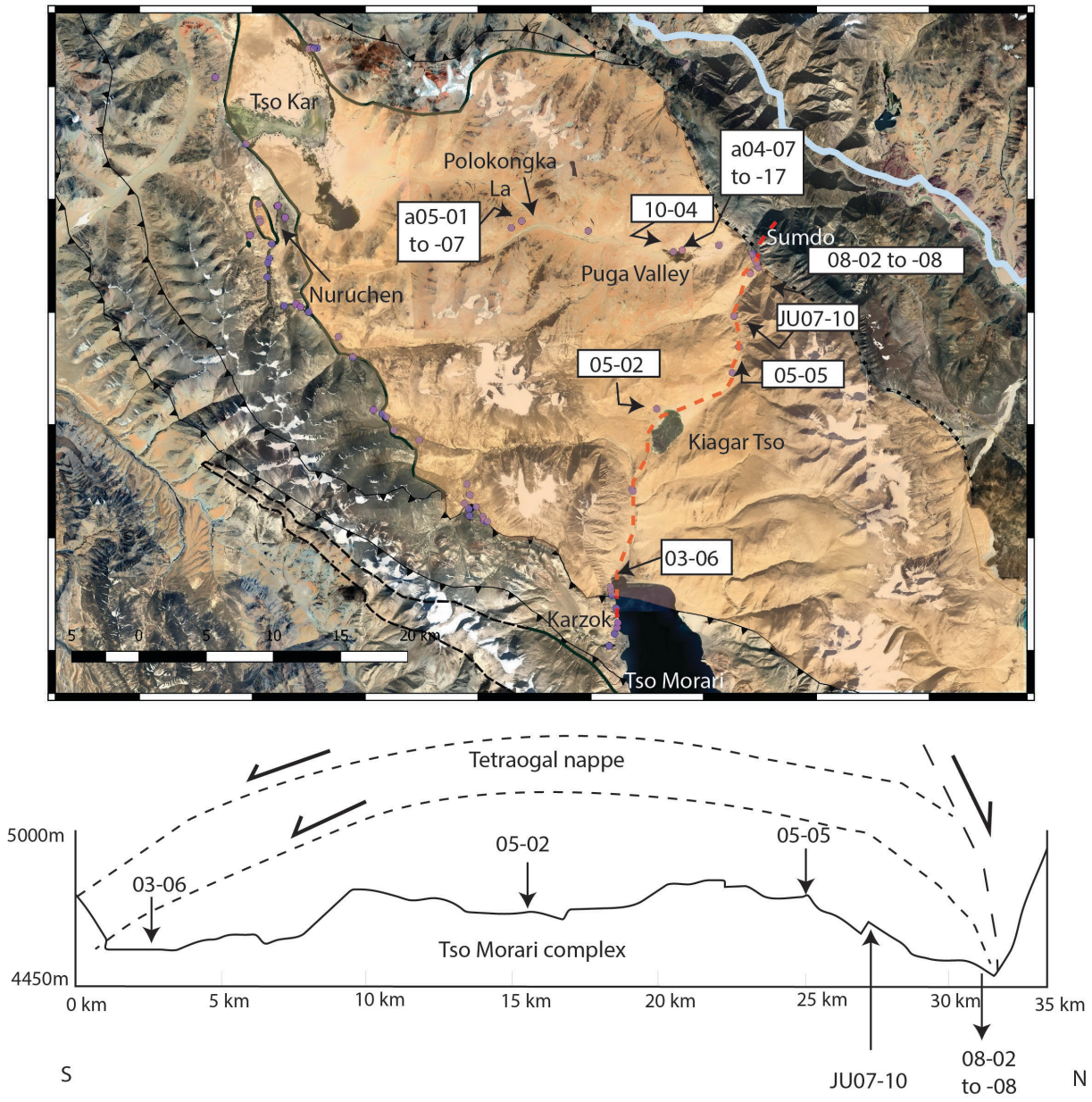


Figure 1 Map of the Tso Morari complex showing locations of Puga Gneiss sample. Shaded orange area marks outcrop area. Red dashed line denotes location of cross section. Cross section after Epard and Steck (2008). Sample locations marked to show relative stratigraphic height.

Sampling strategy and analytical methods

Whole Rock Geochemistry

Whole rock samples were prepared for major and trace element analysis by crushing with a tungsten carbide jaw crusher and grinding with a steel TEMA mill. Major and trace element data were obtained on fusion beads and pressed powder pellets respectively by XRF analysis, using the PANalytical Axios Advanced X-ray fluorescence spectrometer at the University of Leicester, UK. The PANalytical Axios has a 4Kw Rhodium anode end window ceramic technology x-ray tube. Total loss on ignition (LOI) was measured on pre-dried powders after ignition at 950°C for 1 hour. Calibrations were set using international rock reference material BH-1, WS-1, BCS375, BCS376, ARSiO2, ARAl2O3, MRG-1, NIM-D and BCS372/1 for major elements and BCS313/1, NIM-G, MRG-1, MA-N, STM-1, PCC-1, BHVO-1, G-2, GSP-1, BIR-1, BCR-1, S-ORE, JSd-1, JSd-2, JSd-3, BE-N, JR-1, JR-2, JR-3, MO=100, MO=90 for trace elements (See Appendix 3 for data).

Tectonic discrimination diagrams are geochemical tools that help to fingerprint bulk rock geochemistry and apply this to a tectonic setting. They can be used in conjunction with field relationships, petrology and mineralogy (Rollinson, 1993). For granitic rocks (to a plutonic rock with >5% modal quartz), Y+Nb vs Rb and Nb vs Y plots are used to discriminate between volcanic arc (VAG), syn-collisional (syn-COLG), within plate (WPG) and ocean ridge granites (ORG) (Pearce *et al.*, 1984). Flaws in the use of conventional tectonic discrimination diagrams, resulting in andesitic rocks often being plotted on mafic discrimination diagrams, are due to limited data, boundary fits that are not based on statistical rigour and the use of constant-sum data (Agrawal and Verma, 2007). The Pearce *et al.*, (1984) diagrams also use mobile elements such as Rb on their axes, which, in altered settings, could be under or over-estimated in a 'representative' sample. The low success rate for tectonic discrimination and limited plate tectonic settings, led Verma *et al.*, (2012) to conclude that these discrimination diagrams perform poorly when identifying collisional settings, particularly when discriminating between volcanic-arc and within plate settings.

A new multidimensional approach developed by Verma *et al.* (2011, 2012); Verma *et al.* (2013), has been proposed for correct discrimination of felsic and intermediate rocks. Three sets of diagrams are used based on all the major elements (FeO, Fe_2O_3, MnO, MgO, CaO, Na_2O, K_2O and P_2O_5 in wt%), a combination of

immobile major and trace elements (TiO_2, MgO and P_2O_5 in wt% and Nb, Ni, V, Y and Zr in ppm) or relatively immobile trace elements (La, Ce, Sm, Yb, Nb, Th, Y, Zr in ppm) (Verma, 2017). Each set of diagrams plots a set of five discrimination functions designed to discriminate between three or four tectonic settings. For each of these sets of plots, probability values are calculated based on the number and position of each point within a field, allowing for a quantitative interpretation of the robustness of the tectonic interpretation (See methods of Verma *et al.*, 2011).

This method also addresses the problem identified by Rollinson (1993), whereby the sum of the non SiO_2 major oxides are restricted to a total of 100%-SiO_2 wt%. This can mask geological correlations by introducing a negative bias known as the closure problem. Aitchison (1986) addresses this problem by looking at the ratio of major elements in order to compare their relative magnitudes on a logarithmic scale. Four sets of diagrams were developed for use on felsic rocks with $SiO_2 > 63\%$. These include two sets based on major elements, one for a combination of major and trace elements and one for trace elements (Verma *et al.*, 2013). These diagrams discriminate between island arc (IA), continental arc (CA), within-plate (WP) and continental collision (COL) settings, and are particularly useful when differentiating between very similar tectonic settings such as island and continental arcs.

The tectonic discrimination diagrams, not including the multi-dimensional plots, were plotted using the software IoGAS. The multi-dimensional tectonic discrimination diagrams were plotted using a series of programs freely downloadable from the website of the Institute of Renewable Energy at the National Autonomous University of Mexico (http://tlaloc.ier.unam.mx/index.html). The raw data was initially run through the program IgRoCS (Verma and Rivera-Gomax, 2013). This calculates the Fe-oxidation ratio adjustment as performed by Verma *et al.*, (2002). Following this, the adjusted values of major elements are calculated on an anhydrous basis using the method of Middlemost (1989). The samples were then divided into different classifications using the IUGS-TAS diagram (Bas and Steckeisen, 1991), splitting the rocks into mafic, intermediate and felsic classifications. The felsic samples were then put through the program TecDIA (Verma *et al.*, 2015) where the discrimination diagrams were produced and statistical analysis conducted.

Mineral chemistry

Major element compositions of minerals that exhibit solid solutions were measured using a Cameca SX–5 field emission electron microprobe with a 15 keV acceleration potential and 20 nA beam current. The following standards were used: synthetic TiO_2 (Ti), orthoclase (K), albite (Na, Si, Al), andradite (Fe), Mn metal (Mn), wollastonite (Ca), MgO (Mg), Cr metal (Cr), SrF_2 (F), BaFCl (Cl). Representative mineral analyses are presented in Table 3. Garnet maps were collected using a 170 nA current, 0.06 ms dwell time, 3 µm step size and 15 keV acceleration potential for the elements Al, Si, Ti, Y, Yb, P, Ca, Mn, Mg, Fe, Na.

Phase Equilibrium Modelling

Phase equilibrium models were calculated using the eleven component system MnO-N_2O-CaO-K_2O-FeO-MgO-Al_2O_3-SiO_2-H_2O-TiO_2-Fe_2O_3 (MnNCKFMASHTO) using Theriak/Domino v.2015 with thermodynamic dataset ds55 (Powell and Holland, 1988; Holland and Powell, 1998; updated August 2004), adapted by Doug Tinkham. For further discussion on this technique see chapter 3 methods section.

Results

Whole Rock Geochemistry

Results of whole rock XRF analysis are shown in Figure 2. Samples of undeformed granite, Puga gneiss and garnet-mica schists from within the Puga gneiss all plot within the rhyolite field with SiO_2 > 63%. These samples have different compositions from the pelitic metasediment collected from the metasedimentary sequence outside of the Puga Gneiss, in the west of the dome (Figure 2).

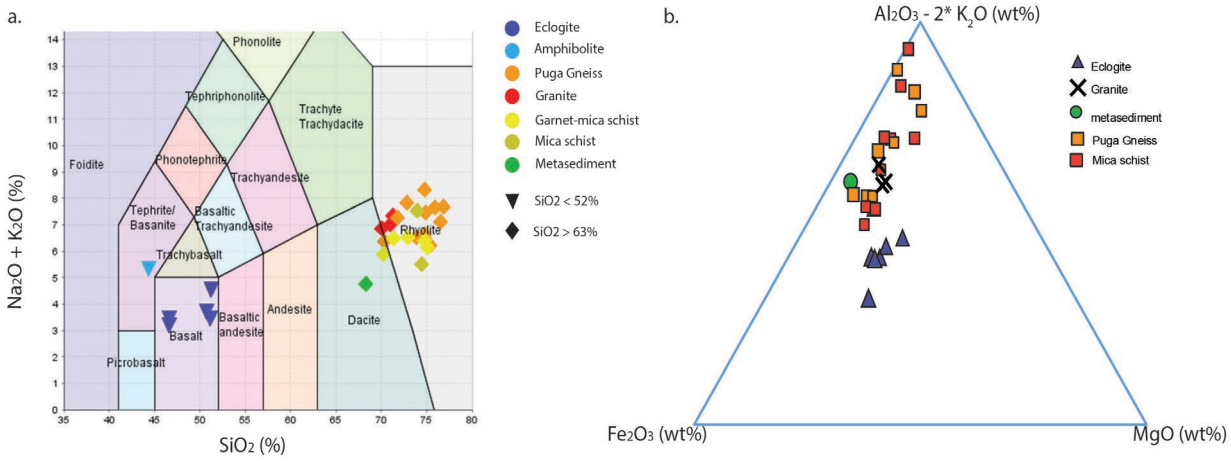


Figure 2 a. Classifications of whole rock samples using the IUGS-TAS diagram (Le Bas and Streckeisen, 1991). Puga gneiss samples, undeformed granites and garnet-mica schist from within the Puga Gneiss. b. AFM diagram for mafic and felsic samples. Gneisses derived from granitic protolith show a range in compositions trending to Al-rich, Fe– and Mg–poor.

Whole rock major element multi-dimensional plots and combined major- and trace-element multi-dimensional plots (Verma *et al.*, 2013) were constructed in order to interpret the tectonic setting in which the felsic intrusive rocks of the Tso Morari complex were formed. Major elements multi-dimensional plots (Figure 3) show a 77% probability of gneiss samples (n=19) and 76% probability of granite samples (n=3) falling in the collisional field, with 22% and 24% probability falling in the continental rift field and 1% and 0% probability falling in the continental arc field (Table 1). These percentages are calculated for a set of five diagrams, each of which take into account 4 of 5 different tectonic settings including: Island Arc (IA), Continental Arc (CA), Continental Rift (CR) field, Ocean Island (OI) and Collision group (Col). For each set of five discrimination diagrams, one calculation omits the most likely tectonic setting, reducing the probability that the data lies within a certain field. Table 1 shows that the least likely combination of tectonic settings is the IA-CA-CR+OI (Col excluded) plot. Exclusion of these data increases the probability of analyses lying in the collisional setting field to 93% of gneisses (n=19) and 100% (n=3) of granite.

The major and trace element combined plots show a spread of data, with a 57% probability of gneisses falling in the collisional field, 7% probability of falling in the continental rift + ocean island field and 1% probability of falling in the continental rift field (Figure 4). This increases to 91%, 1% and 7% probability after recalculation of the data, omitting the IA-CA-CR+OI plot which reduces the number of points in each field and reduced their probability. The granite data shows a similar split with 76% probability falling in the collisional field (increasing to 92%) and 24% probability falling in the continental arc setting (decreasing to 8%).

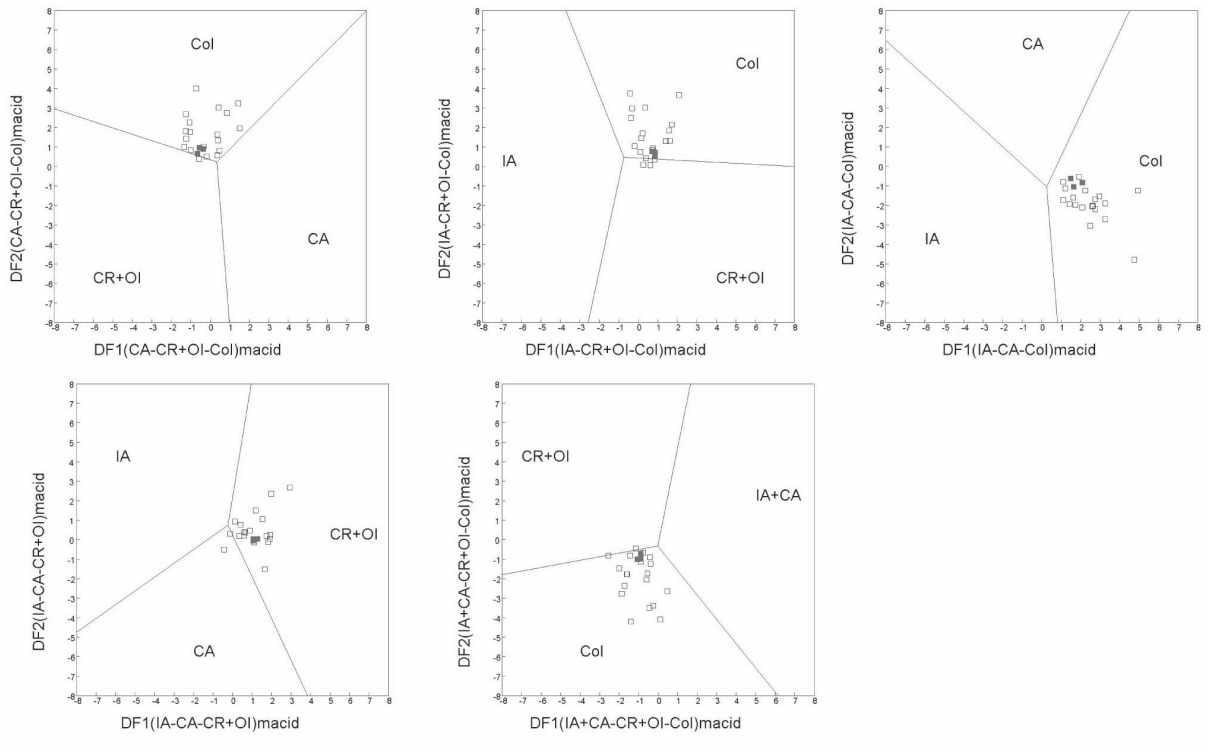


Figure 3 Tectonic discrimination diagrams for felsic rocks of the Tso Morari complex plotted using the method of Verma et al. (2015) for major elements. Island arc (IA), continental arc (CA), continental rift (CR), ocean-island (OI) and collision (Col) tectonic settings.

Rock type	*Tectonic diagram*	*Total #*	*Number of discriminated samples [mean ± 1 S.D.] [probability values]*				
			IA+CA	**IA**	**CA**	**CR+OI**	**Col**
gneiss	**(IA+CA-CR+OI-Col)**	19	0 (0)	---	---	1(0.5364)	18 [0.862±0.162] (0.5064-0.9997)
gneiss	**(IA-CA-CR+OI)**	19	**---**	***0 (0)***	***2 [0.592±0.208] (0.4442, 0.7391)***	***17 [0.870±0.133] (0.5867-0.9998)***	**---**
gneiss	**(IA-CA-Col)**	19	---	0 (0)	0 (0)	---	19 [0.973±0.048] (0.8279-1.0000)
gneiss	**(IA-CR+OI-Col)**	19	---	0 (0)	---	3 [0.612±0.089] (0.5090-0.6683)	16 [0.865±0.149] (0.5053-0.9991)
gneiss	**(CA-CR+OI-Col)**	19	---	---	0 (0)	1(0.5385)	18 [0.798±0.180] (0.4926-0.9990)
1. gneiss	**{Σn} {Σprob} [%prob]**	**95**	**{0} {0} [0%]**	**{0} {0} [0%]**	**{2} {1.1833} [1%]**	**{22} {17.7065} [22%]**	**{71} {62.2195} [77%]**
	Recal. Prob	**76**	**0%**	**0%**	**0%**	**7%**	**93%**
granite	**(IA+CA-CR+OI-Col)**	3	0 (0)	---	---	0 (0)	3 [0.691±0.082] (0.5972-0.7386)
granite	**(IA-CA-CR+OI)**	3	---	0 (0)	0 (0)	3 [0.8980±0.0262] (0.8785-0.9278)	---
granite	**(IA-CA-Col)**	3	---	0 (0)	0 (0)	---	3 [0.9527±0.0344] (0.9152-0.9827)
granite	**(IA-CR+OI-Col)**	3	---	0 (0)	---	0 (0)	3 [0.641±0.068] (0.5630-0.6869)
granite	**(CA-CR+OI-Col)**	3	---	---	0 (0)	0 (0)	3 [0.635±0.084] (0.5388-0.6902)
2. granite	**{Σn} {Σprob} [%prob]**	**15**	**{0} {0} [0%]**	**{0} {0} [0%]**	**{0} {0} [0%]**	**{3} {2.6941} [24%]**	**{12} {8.7595} [76%]**
	Recal. Prob	**12**	**0%**	**0%**	**0%**	**0%**	**100%**

Table 1 shows the results of statistical analysis of ln-transformed major element ratios after Verma et al., (2013). Each tectonic diagram omits one tectonic setting and shows the probability that n=19 gneiss samples or n=3 granite samples fall in specific fields. The shaded field calculates the probability that the samples lie within a specific field. The bold-italic field highlights one of the five plots which does not include the most likely field. The 'Recal. Prob' recalculates the total probability after exclusion of bold-italic field. Mean ± 1 S.D. = mean ± standard deviation of the probability estimates for all samples discriminated in a given tectonic setting, in reported in []. Σn = total number of sample plotting in a given tectonic field. Σprob = sum of the probability values for all samples falling in a given tectonic field. %prob = total probability of a given tectonic setting expressed in percent after assigning the probability of IA + CA to IA and CA.

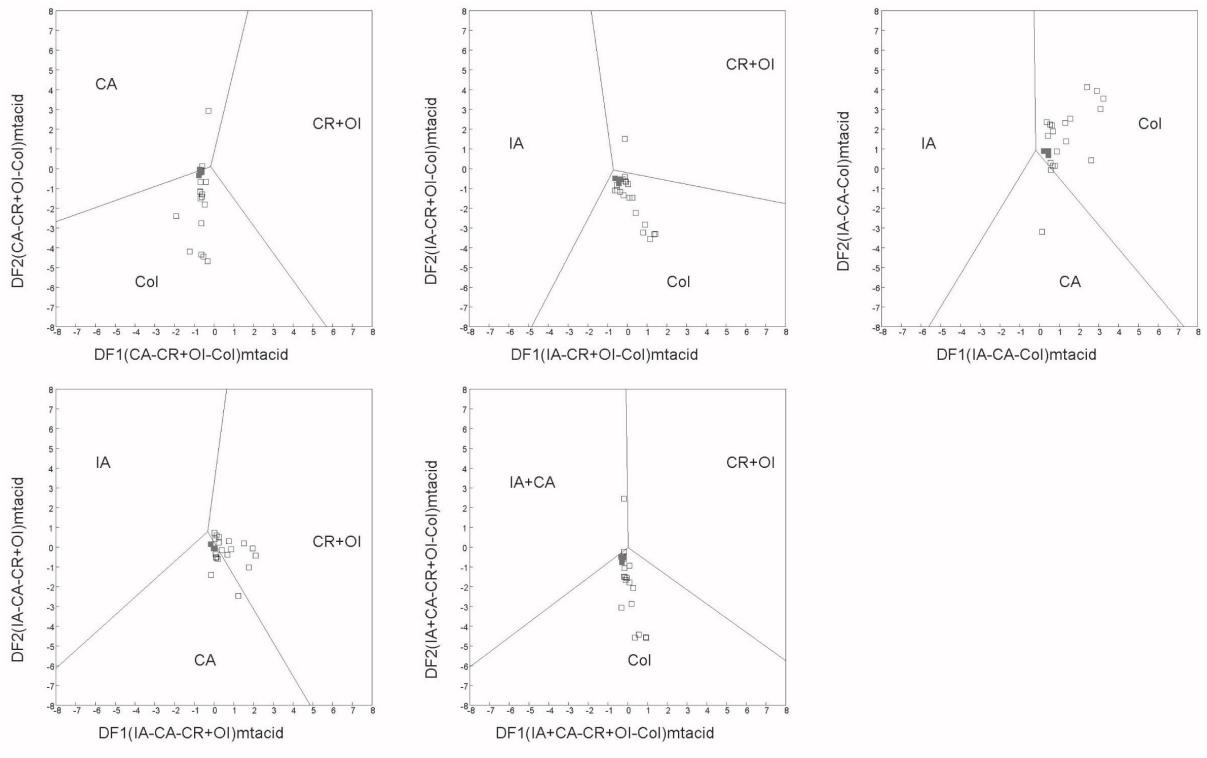


Figure 4 Tectonic discrimination diagrams for felsic rocks of the Tso Morari complex plotted using the method of Verma et al. (2015) for major and trace elements. Island arc (IA), continental arc (CA), continental rift (CR), ocean-island (OI) and collision (Col) tectonic settings.

Rock type	*Tectonic diagram*	*Total #*	*Number of discriminated samples*				
			IA+CA	**IA**	**CA**	**CR+OI**	**Col**
gneiss	**(IA+CA-CR+OI-Col)**	19	1(0.6029)	---	---	0 (0)	18 [0.821±0.197] (0.4125-0.9992)
gneiss	**(IA-CA-CR+OI)**	19	***---***	***0 (0)***	***6 [0.661±0.104] (0.5858-0.8682)***	***13 [0.718±0.173] (0.5076-0.9663)***	***---***
gneiss	**(IA-CA-Col)**	19	---	0 (0)	2 [0.743±0.335] (0.5059, 0.9793)	---	17 [0.842±0.165] (0.5316-0.9994)
gneiss	**(IA-CR+OI-Col)**	19	---	0 (0)	---	1(0.8917)	18 [0.832±0.147] (0.5676-0.9974)
gneiss	**(CA-CR+OI-Col)**	19	---	---	3 [0.581±0.231] (0.4235-0.8470)	0 (0)	16 [0.822±0.185] (0.4382-0.9977)
Gneiss	**{Σn} {Σprob} [%prob]**	**95**	**{1} {0.6029} [---]**	**{0} {0} [0%]**	**{11} {7.1928} [10%]**	**{14} {10.2260} [14%]**	**{69} {57.2174} [76%]**
	Recal. Prob	**76**	**1%**	**0%**	**7%**	**1%**	**91%**
granite	**(IA+CA-CR+OI-Col)**	3	0 (0)	---	---	0 (0)	3 [0.556±0.063] (0.5011-0.6253)
granite	**(IA-CA-CR+OI)**	3	---	0 (0)	3 [0.5173±0.0116] (0.5064-0.5294)	0 (0)	---
granite	**(IA-CA-Col)**	3	---	0 (0)	0 (0)	---	3 [0.579±0.055] (0.5206-0.6305)
granite	**(IA-CR+OI-Col)**	3	---	0 (0)	---	0 (0)	3 [0.610±0.071] (0.5372-0.6787)
granite	**(CA-CR+OI-Col)**	3	***---***	***---***	***1(0.4489)***	***0 (0)***	***2 [0.492±0.047] (0.4589, 0.5253)***
2. granite	**{Σn} {Σprob} [%prob]**	**15**	**{0} {0} [0%]**	**{0} {0} [0%]**	**{4} {2.0008} [24%]**	**{0} {0} [0%]**	**{11} {6.2162} [76%]**
	Recal. Prob	**12**	**0**	**0**	**8.33**	**0**	**92%**

Table 2 shows the results of statistical analysis of major and trace elements after Verma et al., (2013). Each tectonic diagram omits one tectonic setting and shows the probability that n=19 gneiss samples or n=3 granite samples fall in specific fields. The shaded field calculates the probability that the samples lie within a specific field. The bold-italic field highlights one of the five plots which does not include the most likely field. The 'Recal. Prob' recalculates the total probability after exclusion of bold-italic field. Mean ± 1 S.D. = mean ± standard deviation of the probability estimates for all samples discriminated in a given tectonic setting, in reported in []. Σn = total number of sample plotting in a given tectonic field. Σprob = sum of the probability values for all samples falling in a given tectonic field. %prob = total probability of a given tectonic setting expressed in percent after assigning the probability of IA + CA to IA and CA.

Petrography and Mineral Chemistry

Introduction

The following section presents a summary of common microstructural observations from the Puga Gneiss and features that relate to the granitoid protolith. This is followed by a longer section with a detailed description of petrography in a systematic geographical sequence, to illustrate particular local features, and also to bring out any significant variation with location and structural depth across the complex.

The gneissose banding in the Puga Gneiss is composed of quartz-rich bands and mica-rich bands that contain phengitic white mica, biotite and albite (Figure 5). Quartz occurs in polycrystalline ribbons or lenses in a strongly foliated fabric forming an L-tectonite, indicative of a high-strain fabric. Occasional relict quartz grains are present in the quartz ribbons, exhibiting undulose extinction and subgrain formation. The quartz in some samples has also undergone annealing by grain boundary migration, overprinting and coarsening the high strain fabric so that single quartz grains span the width of the ribbon. K-feldspar poikiloblasts, poikiloblastic albite lenses and polycrystalline albite aggregates are wrapped by mica. The poikiloblastic albite often contains white mica inclusions oriented obliquely to the fabric (Figure 6e). The rims of the albite poikiloblasts partially overgrow the wrapping schistosity.

White mica forms coarse lenticular aggregates (5x3 mm) which often contain idioblastic, sphenoidal inclusions of titanite (Figure 6c). Narrow bands of white mica are also present between quartzofeldspathic lenses in the matrix, part of the high strain fabric. Garnet-mica schists commonly occur in the Puga Gneiss at the high-strain margins of mafic sills (e.g. samples 05-02, 11-09 and a05-07). Sample 11-09 (Figure 5g) is strongly deformed and crenulated, containing white-mica lenses with clusters of rutile (rather than titanite) inclusions and poikiloblastic garnets wrapped by the matrix schistosity. Sample 05-02 also contains garnet poikiloblasts wrapped by a mica-rich matrix with a Si content of 3.0-3.35 Si pfu with the fine-grained margins of the coarse crystals recording a lower celadonite content (Figure 16e). Lamellae of biotite and albite can be observed in thin section to form along cleavage planes within the mica sheets.

Protolith

Despite its occasional schist-like appearance and high-Al bulk composition, the Puga gneiss has a granitic protolith and can be distinguished from a metasedimentary rock based on the presence of the following petrographic criteria: Coarse-grained cloudy apatite, zoned allanite, tourmaline needles, lenticular phengite with occasional titanite (or rutile) inclusion clusters, K-feldspar porphyroclasts, aggregates of Na-feldspar (see Figure 5) and an absence of carbonate, which is not uncommon in metasediments. However, many samples with these characteristics are much richer in white mica, and lack K-feldspar, compared to granitic protoliths, making identification in hand specimen difficult.

Figure 5 shows a suite of Puga Gneiss samples taken from across the dome, with examples of a 'classic′ Puga Gneiss, consisting of very coarse K-feldspar porphyroclasts and strong gneissose banding (Figure 5a and d). Feldspar commonly forms σ-type porphyroclasts, allowing the direction of shearing to be deciphered. Other samples show more intense deformation where dynamic recrystallisation is prevalent, reducing the grain size, have a larger proportion of biotite and white mica in the matrix (e.g. Figure 5a, e, f and g) and K feldspar augen with a high aspect ratio and an elongate shape (Figure 5f).

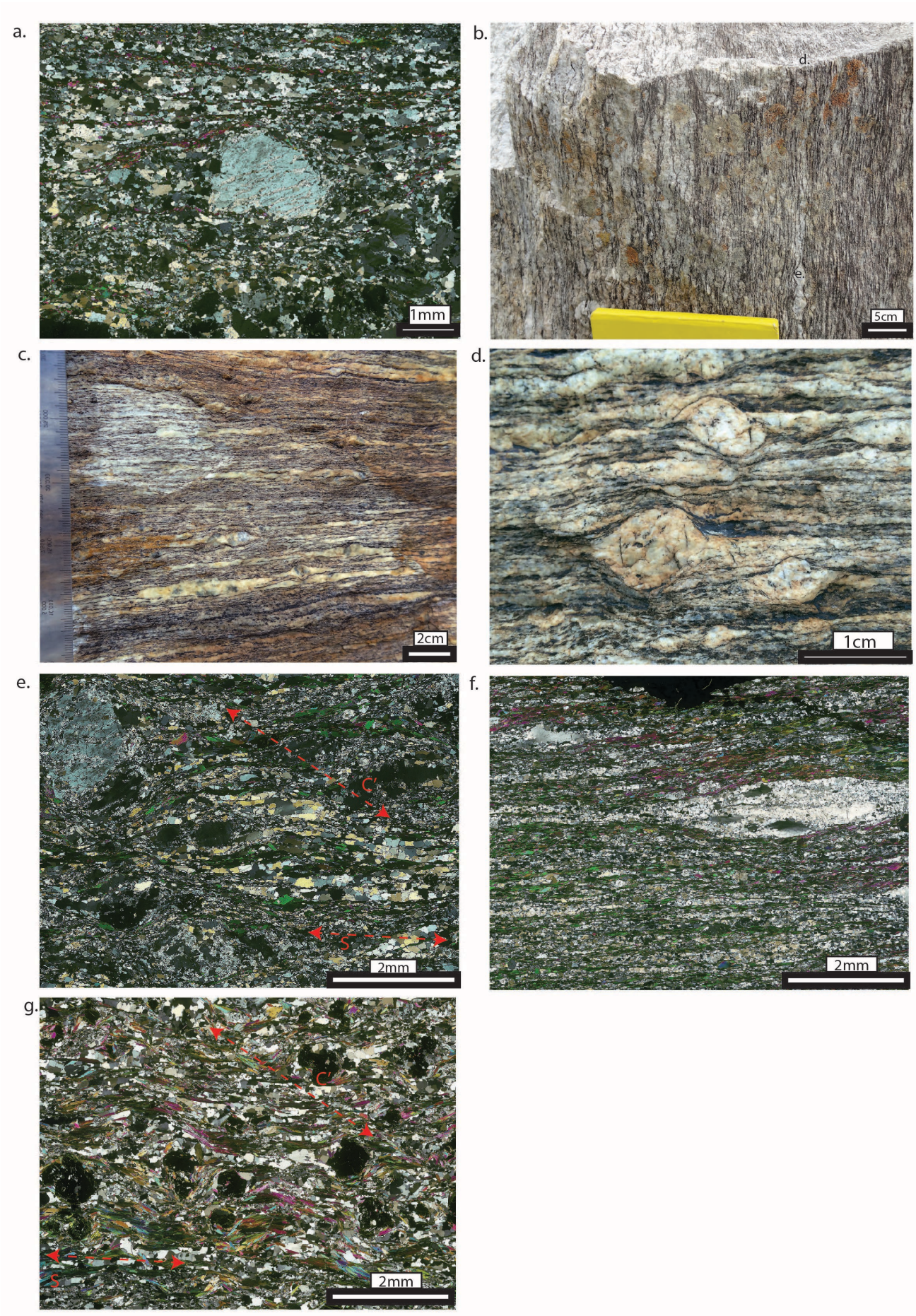

a.
1mm
b.
d.
e.
5cm
c.
2cm
d.
1cm
e.
C'
S
2mm
f.
2mm
g.
C'
S
2mm

Figure 5 (above) Field photos and photomicrographs showing variations in the Puga Gneiss. a. Photomicrograph of strongly foliated gneiss with K feldspar augen. b. Augen gneiss with compositional layering defined by variation in biotite abundance. Augens more sheared than in a. and retain a relatively spherical geometry to their sigma shape. c. Strongly sheared augen gneiss. Augen are elongate parallel to the foliation. d. sigma shaped augen of feldspar in the Puga Gneiss. e. Augen gneiss with K feldspar porphyroclasts, partially recrystallised. Mica, quartz and albite define foliation. C'-S fabric weakly developed. f. Relict porphyroclasts strongly recrystallised in a mica-rich gneiss with polycrystalline quartz ribbons and compositional layering. g. Sample 11-09. Garnet-mica gneiss from the sheared gneiss surrounding an eclogite boudin. Mica-rich schistosity wraps garnet poikiloblasts. Microfolds overprint schistosity.

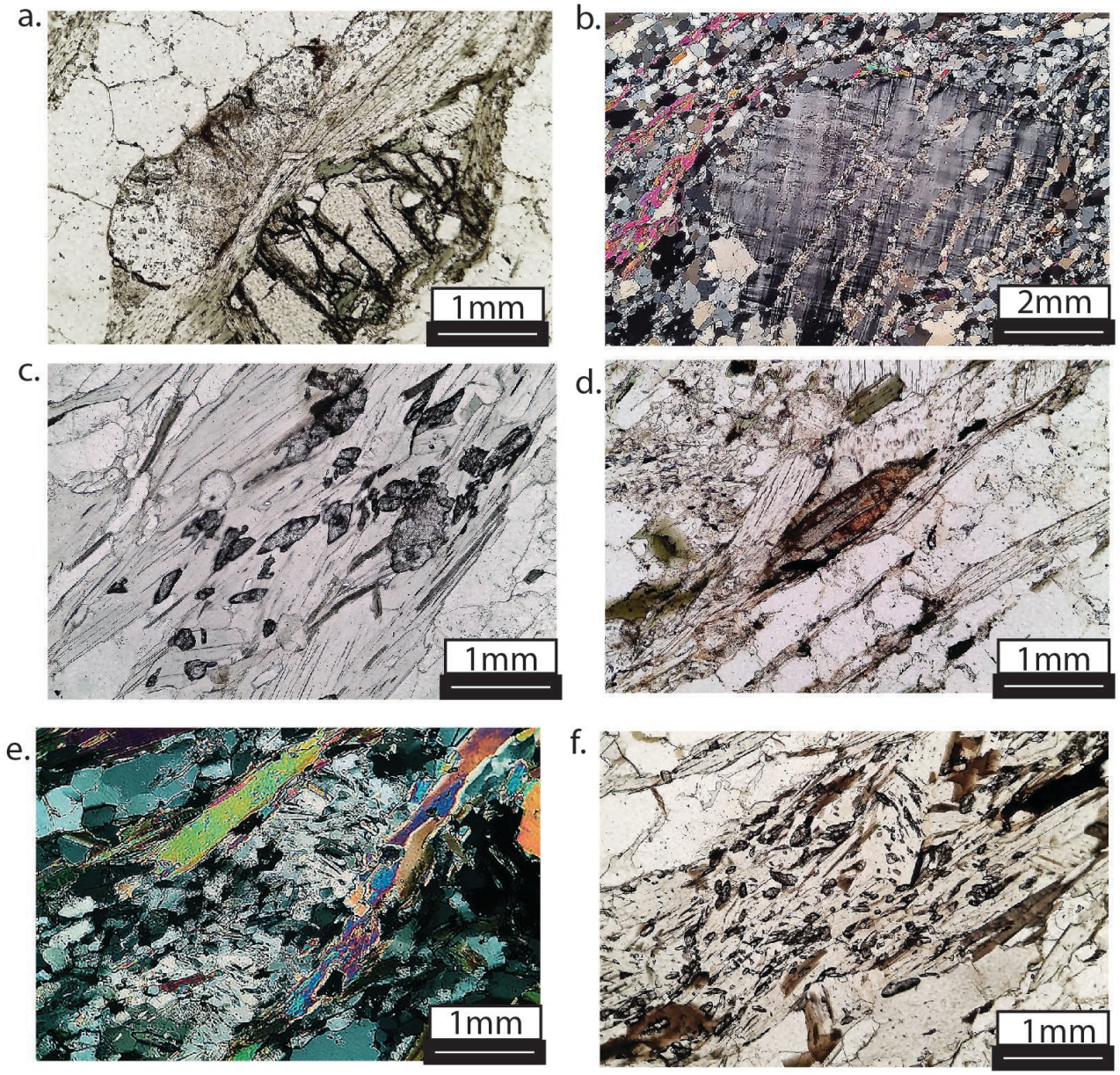


Figure 6 (above) Photomicrographs showing examples of petrographic criteria used for identification as Puga gneiss with a granitic protolith. a. Cloudy apatite next to mica- and garnet-rich band. d. brown allanite grain in mica rich layer. b. Microcline porphyroclast, wrapped by fabric, with crosscutting recrystallised bands. c. sphenoidal titanite inclusions in lenses of phengitic white mica. d. zoned brown allanite parallel to schistosity e. Albite poikiloblast with inclusions of white mica, in between two white mica sheets. f. sphenoidal titanite inclusions in lenses of phengitic white mica.

Polokongka La

In the Polokongka La region (Figure 1), mafic sills are hosted in undeformed granite which grades into a garnet-mica schist at the margins of the sills. This transition occurs over a distance of ~20 m and is exemplified by the suite of samples from a05-01 to a05-07 (locality 16/113, Figure 1), where a05-01 is the least deformed sample and a05-07 is a garnet mica schist from the sill margin (Figure 7 shows sample locations and figure 8 shows the variation in fabric and thin-section microstructure across the traverse). The bulk composition of these samples varies with the more Al-rich, Fe-, Mg-poor samples located closer to the mafic sill.

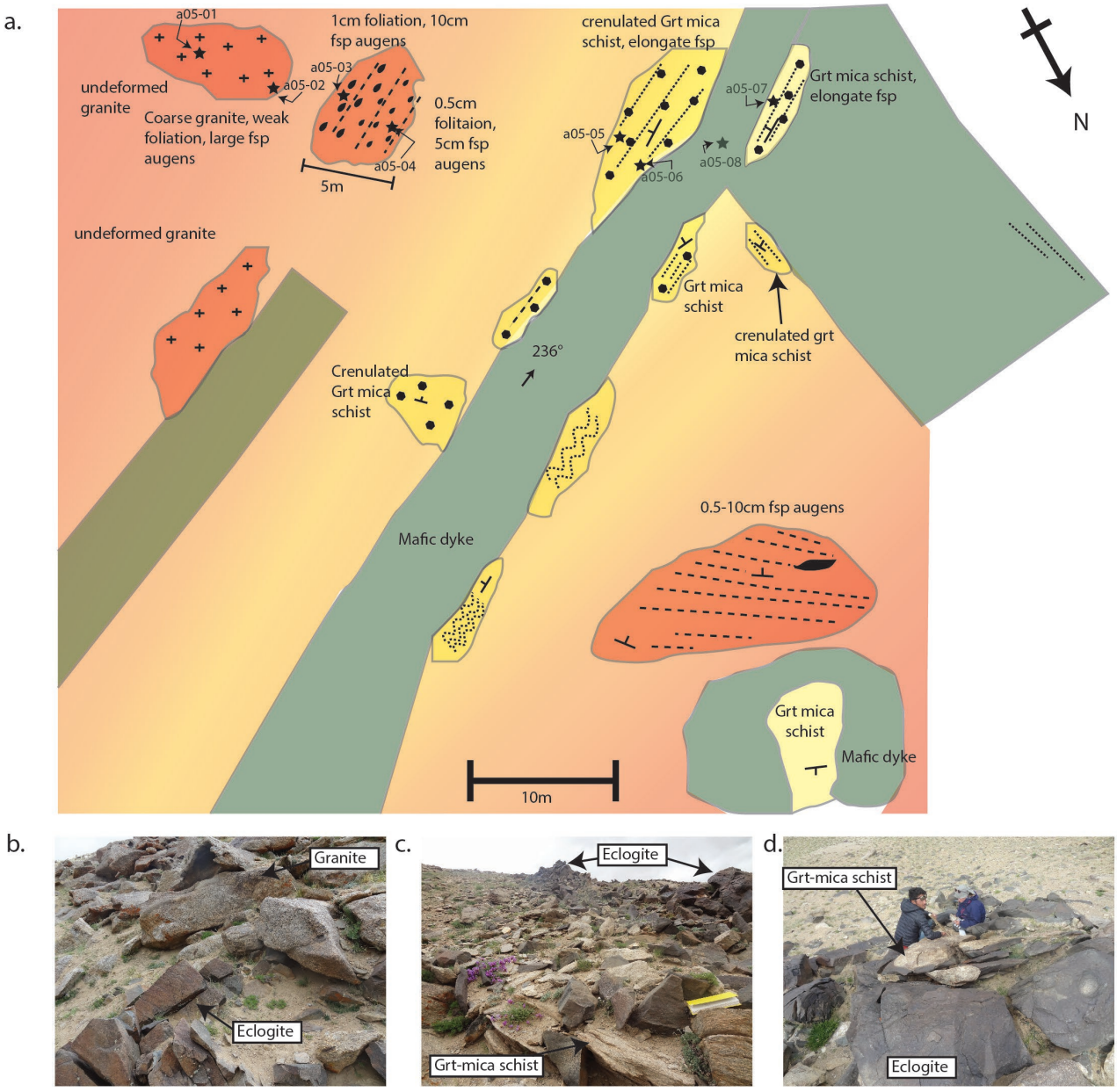
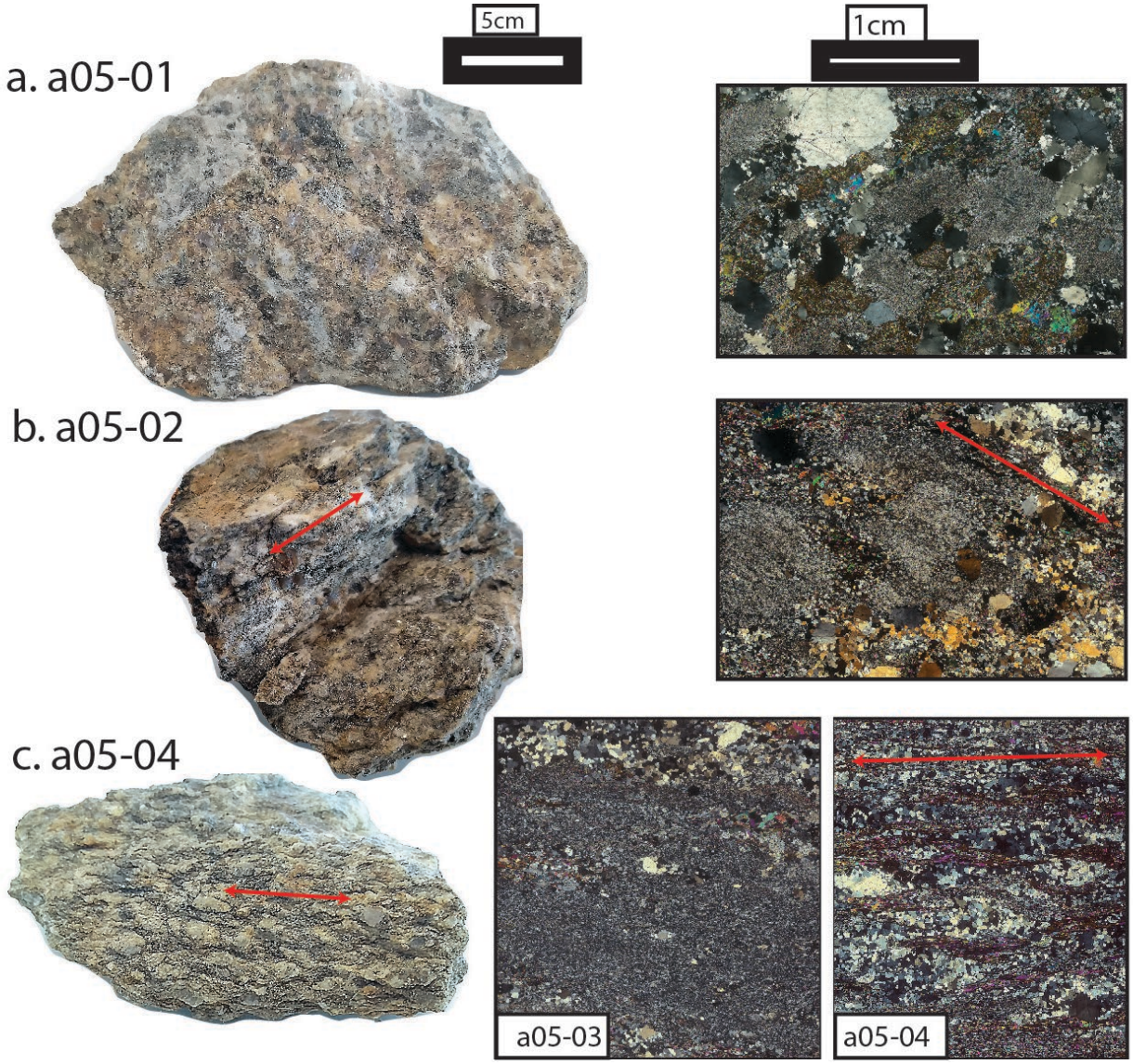


Figure 7 a. Exposure map showing a mafic sill (green) with a strongly deformed, crenulated margin. Foliation is weaker further from the sill. Location of samples indicated as stars. b. Brown eclogite dyke hosted in granite. c. Eclogite dyke with garnet-mica schist at contacts. d. Eclogite boudin with garnet-mica schist at contacts



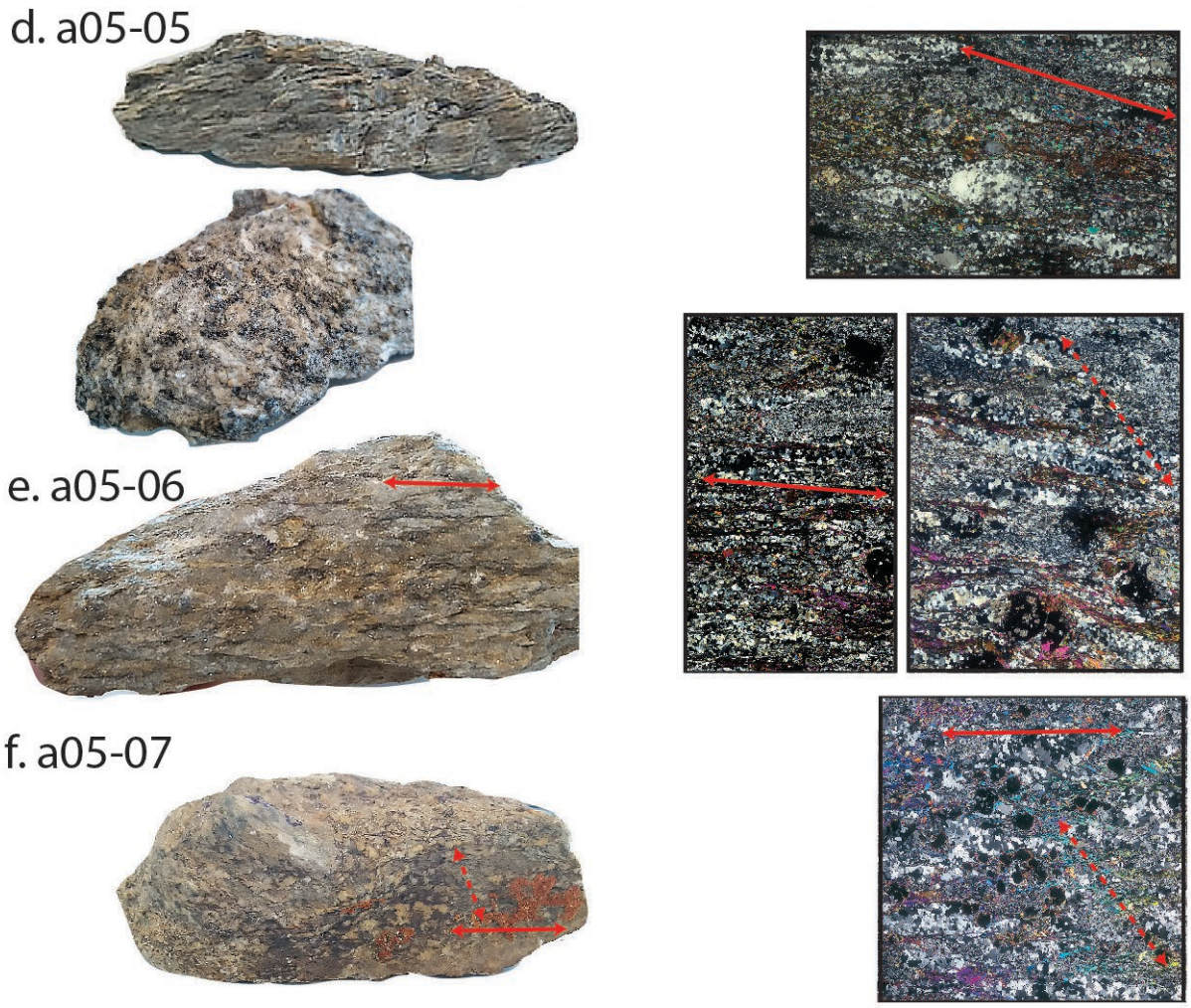


Figure 8 Suite of samples showing transect from macroscopically undeformed granite (a05-01) to garnet-mica schist (a05-07). Schistosity indicated by red solid arrow. Crenulation indicated by red dashed arrow. Location of samples shown in Figure 7.

Sample a05-01 is the least deformed sample from the transect, preserving igneous textural domains equivalent to domains 1 to 5 described in Chapter 3, representing a primary igneous assemblage of quartz, K-feldspar, plagioclase, muscovite, biotite ± cordierite. Primary quartz grains exhibit undulose extinction and recrystallisation along grain boundaries (Figure 9b). Altered feldspar domains contain fine-grained white mica and albite aggregates. Fine-grained white mica is present in the corroded rims of a coarse-grained white mica. Biotite is present as aggregates around the rims of anhedral domains (Figure 9a). The cores of these domains are rich in fine-grained white mica and epidote. Euhedral garnets (0.2 mm) are closely associated with the biotite-rich zones and grow on the interface between biotite and feldspar (Figure 9c). Biotite inclusions in altered feldspar domains

often contain abundant garnet, which can form polycrystalline pseudomorphs. The garnets have fine-grained inclusion-rich cores with inclusion-poor rims exhibiting faceted growth. Garnets are also present within altered feldspar domains composed of white mica, albite and epidote.

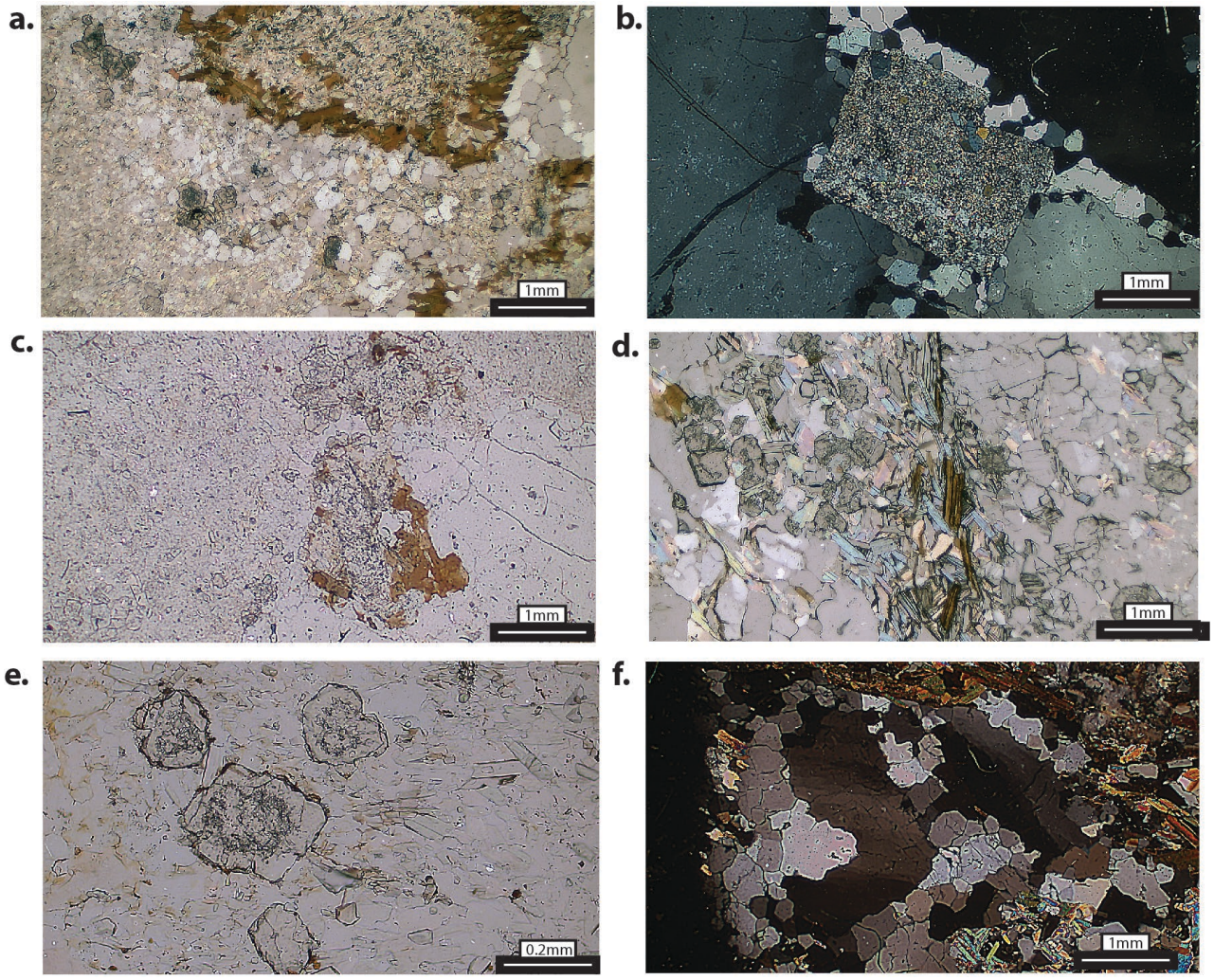
Sample a05-02 contains a weak foliation but retains vestiges of an igneous texture comparable to sample a05-01. Garnet occurs in biotite-rich domains adjacent to domains of albite + white mica (Figure 9d). Atoll garnets are present in the core of domains of white mica and albite after feldspar (Figure 9e). Quartz porphyroclasts are present but show extensive recrystallisation along grain boundaries (Figure 9f). Coarse-grained white mica is preserved as porphyroclasts, with a corroded rim composed of fine-grained white mica. Coarse albite poikiloblasts are present with numerous inclusions of white mica, biotite and epidote.

Samples a05-03 and a05-04 are augen gneisses from an outcrop which shows a progressive decrease in width of the augen from ~1-2 cm wide to 5 mm, associated with a decrease in thickness of quartz-rich bands. Feldspar-rich augen consist of K-feldspar or poikiloblastic albite with inclusions of aligned white mica, oriented obliquely to the external fabric (Figure 9g). Quartz porphyroclasts are rare and contain numerous subgrains and irregular grain boundaries subject to grain boundary migration (Figure 9i). Elongate recrystallised lenses of quartz and fine-grained albitic lenses are abundant and wrapped by a mica-rich foliation (Figure 9h). Garnet is present at the boundary between bands of poikiloblastic albite + white mica and quartz-rich lenses. Garnets contain white mica inclusions and often have a corroded outline, associated with biotite and epidote.

Sample a05-05 is located ~2m from the margin of the mafic sill and contains lenses of recrystallised quartz and lenses of albite + white mica (Figure 9j). Poikiloblastic albite is abundant in the albitic lenses. It contains inclusions of white mica and epidote and cuts across the rim of the mica-rich domains (Figure 9k and l).

Samples a05-06 and a05-07 were taken adjacent to the foliated margin of the mafic sill and have developed a crenulation, overprinting the schistosity. The alternating quartz and mica-rich bands (<0.1 mm) are thinner in width than in more distant samples. Recrystallised quartz is finer grained

and elongate, forming ribbon-like structures. Coarse garnets are wrapped by the schistosity, with polycrystalline quartz-rich strain shadows giving the porphyroclast a sigmoid shape (Figure 9m). The garnets commonly occur in biotite-rich domains between the quartz-rich ribbons and mica- + albite-rich domains, and they exhibit idioblastic crystal faces in contact with coarse grained white mica and biotite (Figure 9n). Corroded garnet rims are replaced by fine-grained biotite. Inclusions in garnet commonly consist of white mica and are often arranged in rectangular inclusion-rich domains, preserving the outline of altered feldspar (Figure 9o).



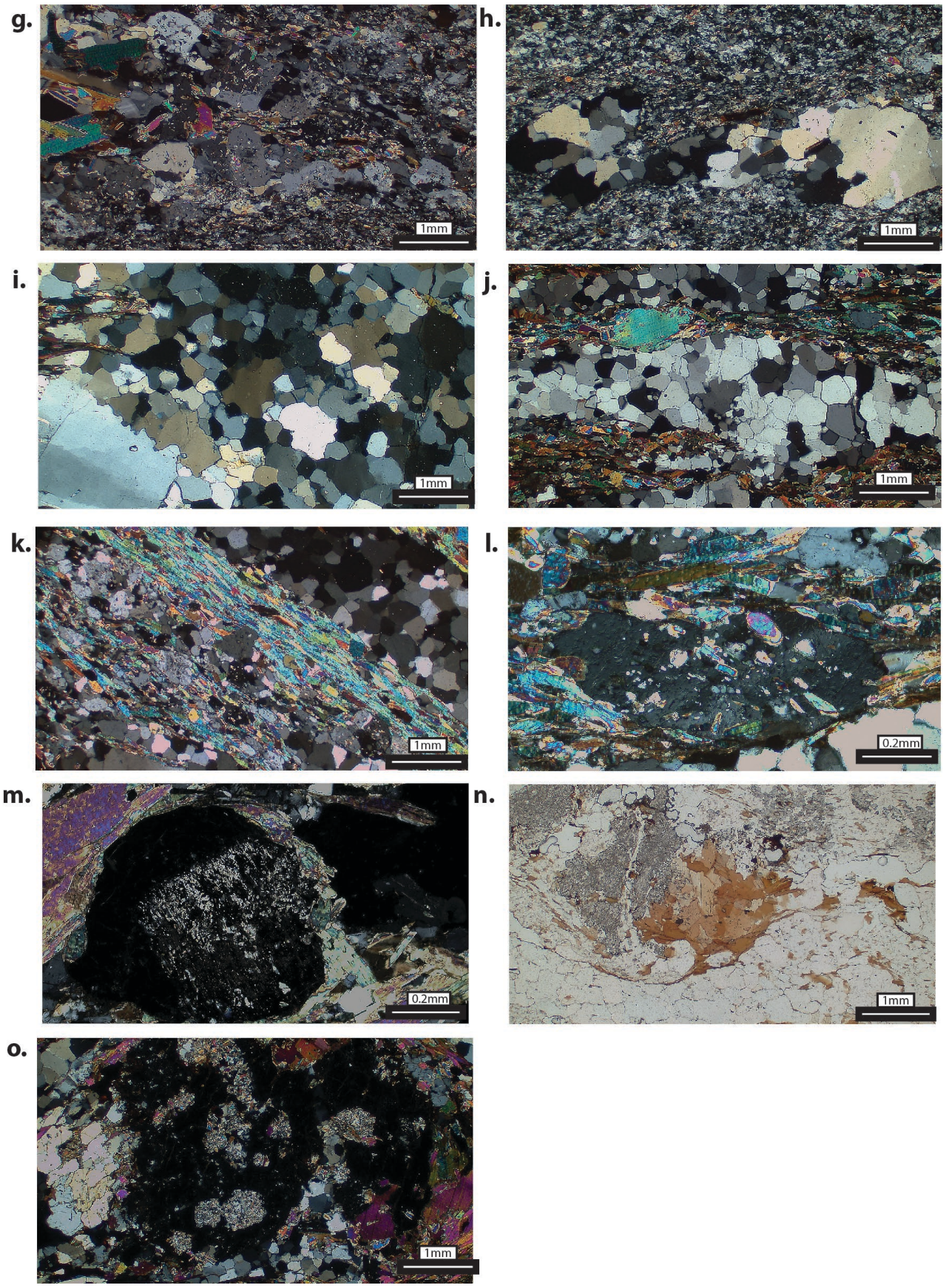

g.
1mm
h.
1mm
i.
1mm
j.
1mm
k.
1mm
l.
0.2mm
m.
0.2mm
n.
1mm
o.
1mm

Figure 9 ***a-c. Sample a05-01****. a. Domainal igneous texture with aggregates of white mica + albite with coarse biotite rims, associated with garnet. b. white mica + albite rectangular pseudomorph after K feldspar, surrounded by deformed quartz relicts and recrystallised quartz grains. c. garnet overgrowing coarse biotite between a quartz-rich and white mica + albite domain. d-f.* ***Sample a05-02****. d. Garnet associated with biotite and white mica. e. Atoll garnets in white mica + albite pseudomorph after plagioclase. f. Quartz porphyroclasts with recrystallised rims.* ***g-i. Sample a05-03*** *g. Poikiloblastic albite lens. h, recrystallised quartz ribbon next to albite + white mica lens. i. grain boundary migration of quartz porphyroclast.* ***j-l. Sample a05-05*** *j. recrystallised quartz lens with mica fish, k. mica-rich, poikiloblastic albite and quartz layers. l. Albite poikiloblast with obliquely aligned white mica inclusions.* ***m. Sample a05-07*** *rectangular inclusion patch in garnet inferred to replace an albite + white mica domain.* ***n-o. Sample a05-06*** *n. garnet replacing coarse biotite aggregate. o. inclusion patches in garnet, wrapped by fabric*

Puga Valley

Sample 10-04 (locality 16/106, Figure 1) is a strongly foliated schistose gneiss with approximately continuous, thin white mica crystals, fine bands of quartz ribbons and elongate lenses of quartz and feldspar aggregates (Figure 10b). Ribbons of quartz contain coarse grains which span the width of the narrow ribbon (Figure 10a), suggesting that quartz underwent recrystallisation and subsequent grain growth in the grain boundary migration regime. Quartz grain boundaries are lobate with some evidence of local undulose extinction. Feldspar aggregates show recrystallisation at a finer grain size than the quartz ribbons, with some evidence of post-deformation grain growth producing poikiloblastic feldspar grains. White mica lenses often contain coarse, bent crystals without polygonization and occasional zonation in birefringence, increasing towards the tips (Figure 10b). This rock contains garnet, which is skeletal in quartz-rich areas. Sample a04-02, also from the Puga Valley, shows coarse-grained, twinned inclusion-poor Na-plagioclase porphyroblasts which crosscut the white mica fabric.

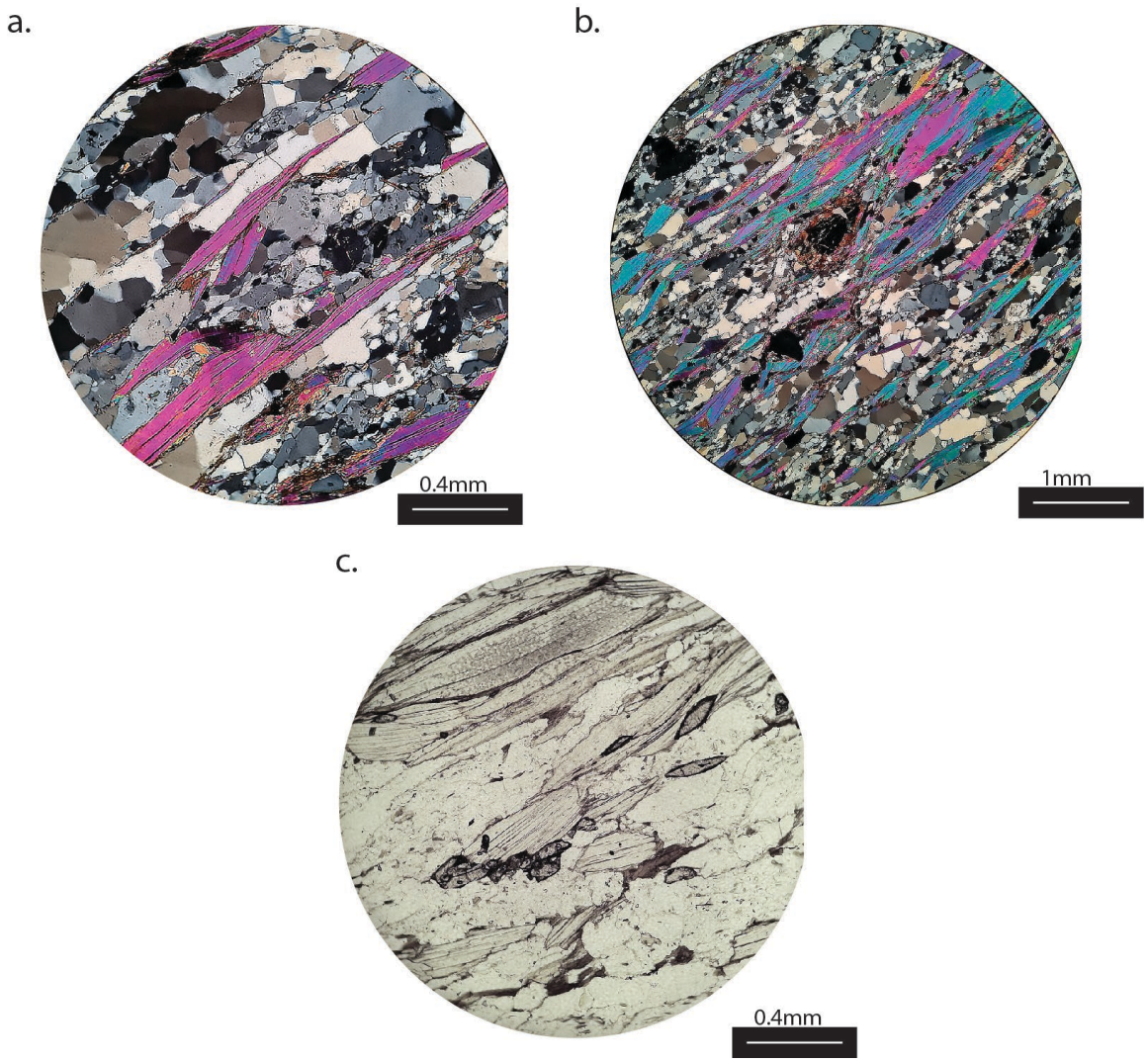


Figure 10 Sample 10-04. a. poikiloblastic albite wrapped by thin mica sheets in fabric. Subgrain rotation evident in quartz, with single crystals spanning thin ribbons. b. Thin bands of quartz-rich, feldspar-rich and mica-rich domains. Thicker stacks of white mica bend into local shear bands. garnet wrapped by fabric. c. Mica stacks associated with titanite grains

Ribil Valley

Compositional variations can be identified in the Puga Gneiss within a single outcrop at locality 16/73 (Figure 1) where distinct variations can be seen between less deformed leucogranite lenses (Figure 11e – sample 08-03) and strongly sheared, mica-rich gneisses which wrap the leucogranitic lenses (Figure 11d – sample 08-02).

Sample 08-02 is an example of a schistose Puga Gneiss, dominated by white mica trains separating elongate lenses of quartz and feldspar (Figure 12a and b). A few large white mica porphyroclasts are present, showing some zonation in birefringence, increasing towards the rim (Figure 12c). Broader

quartz ribbons preserve relict quartz porphyroclasts (~2 mm long) with an internal structure of equant subgrains which are of similar size (<100 μm) to the recrystallised grains in the rest of the ribbon (Figure 12b). The mica trains show evidence for stretching along the foliation in the form of discontinuous shear bands framing lenticular stacks of laths (Figure 12c). A few large, round, Na-feldspar poikiloblasts occur which are wrapped by the fabric and contains aligned white mica and quartz inclusions that are discordant to the external fabric (Figure 12a).

Sample 08-04 is wrapped by the main fabric in sample 08-02 and contains abundant deformed white mica porphyroclasts (Figure 12d-f). The overall fabric is less clearly organised into discrete ribbons of quartz, feldspar and white mica. Large twinned feldspar grains occur in lenticular domains with examples of poikiloblastic Na-feldspar with discordant aligned inclusions of white mica (Figure 12d). Quartz ribbons are thoroughly recrystallised although less abundant than sample 08-02. A large K feldspar porphyroclast has been replaced around its margin by large (up to 0.8 mm) sub-rectangular Na-feldspars (Figure 12g).

The compositional variations described above are cross-cut by a tourmaline-bearing augen gneiss with K-feldspar porphyroclasts with tartan twins (Figure 11f – sample 08-08). Na-feldspar, some with simple twins, cuts across the poikiloblastic feldspar and the enclosing fabric. Quartz has recrystallised in the subgrain rotation regime, similar to sample 08-02, and some recrystallisation of white mica is evident. Tourmaline is present within this sample, trapping small aligned inclusions, with some evidence of deformation. The metamorphic foliation cuts across the compositional variations described above, indicating that the foliation formed after the compositional variations or intrusive phases.

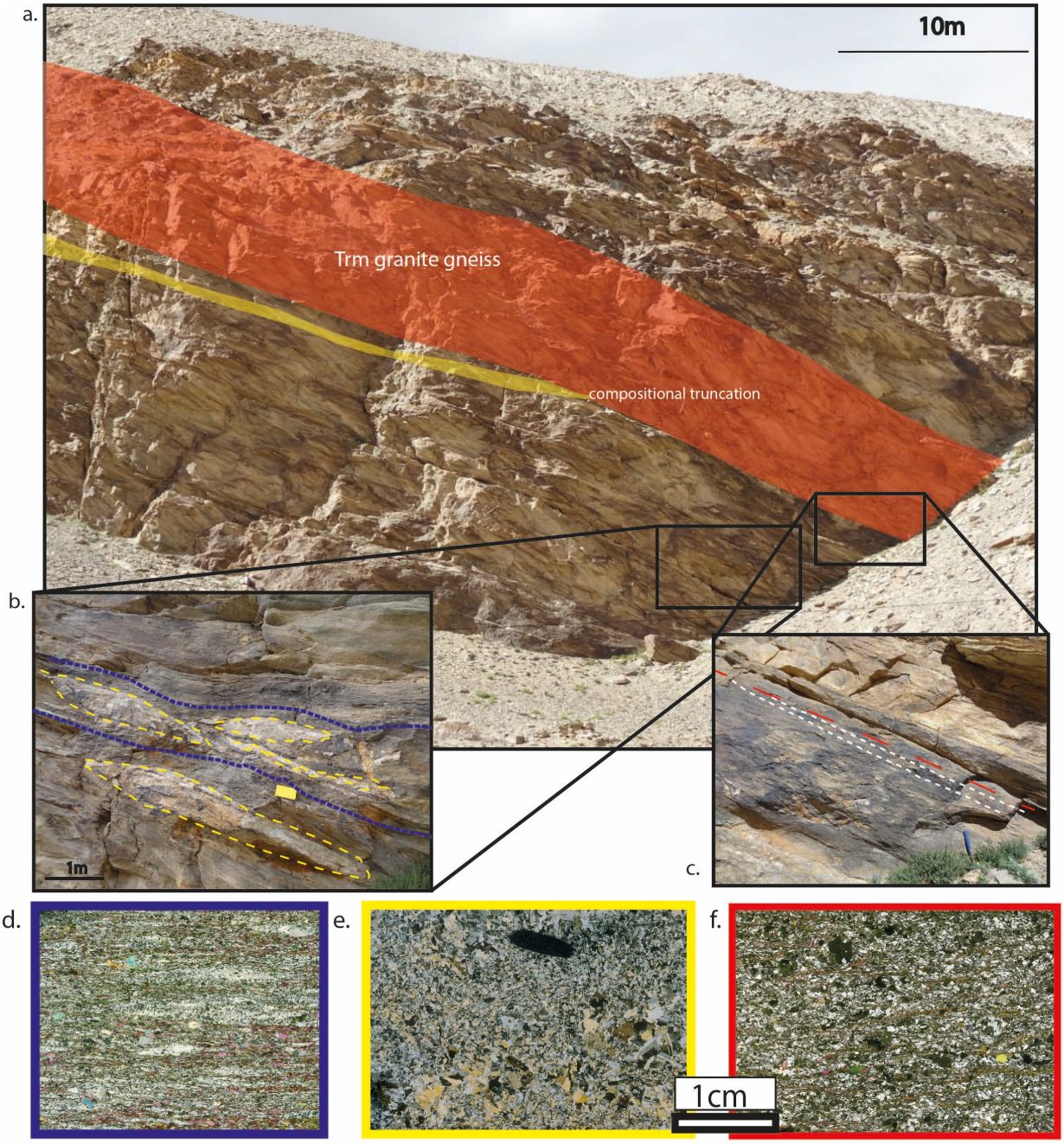
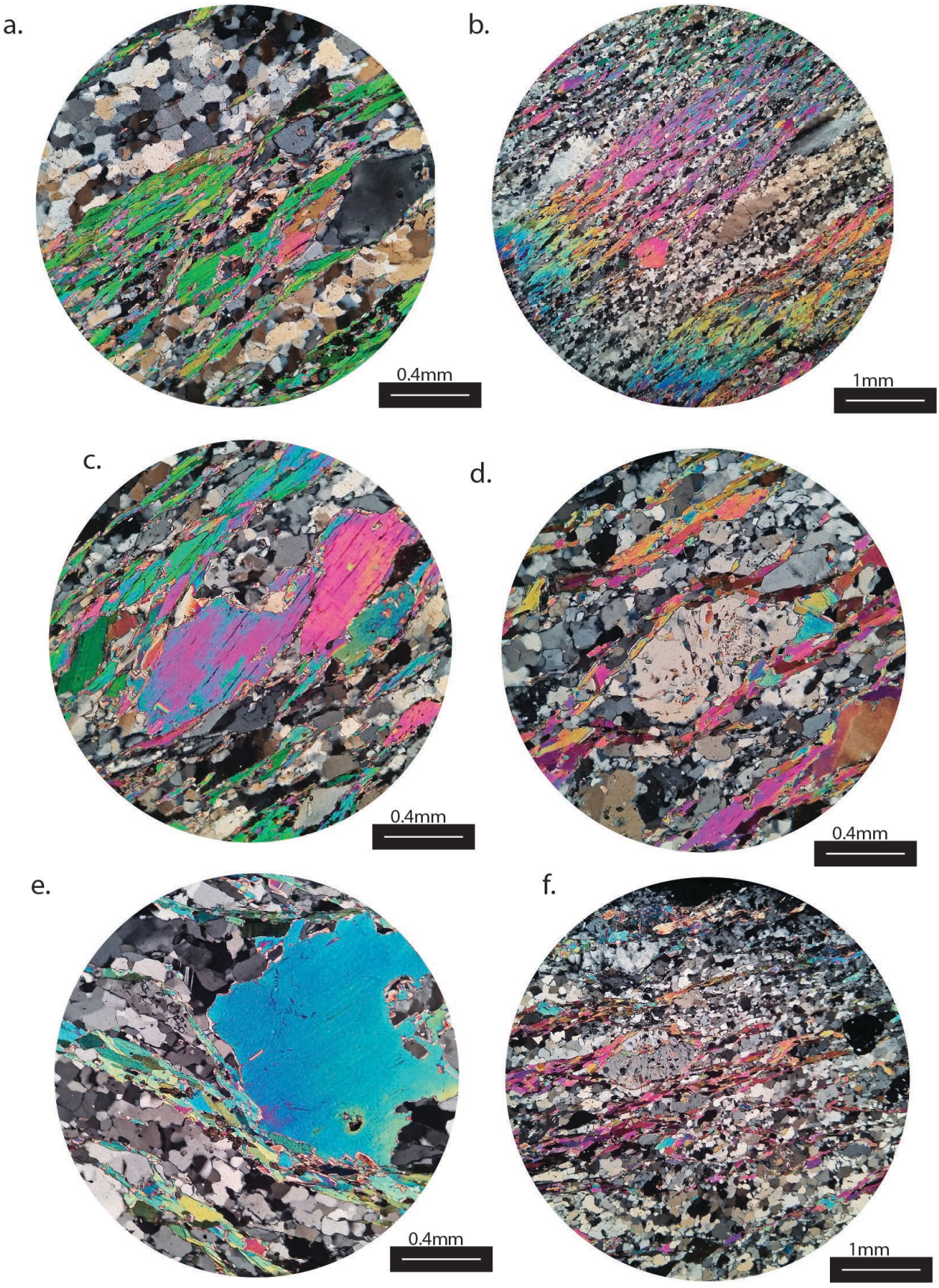


Figure 11 (above) a. outcrop from the Ribil valley (locality 16/73) showing several different compositions of augen gneiss. The fabric in the unit forming the base of the cliff is highlighted in a yellow band. This is truncated by the tourmaline-bearing augen gneiss (red). b. Close-up of the compositional variations within the bottom unit. Garnet-mica schist (blue) wraps around the leucocratic granitic rock (yellow). C. close-up of the contact between the bottom unit and the red unit with the metamorphic foliation shown as white dashed lines and the compositional variation show as a red dashed line. d. Sample 08-02 e. sample 08-03 and f. sample 08-8 show thin section photomicrographs of the blue, yellow and red gneisses respectively


a.
0.4mm
b.
1mm
c.
0.4mm
d.
0.4mm
e.
0.4mm
f.
1mm

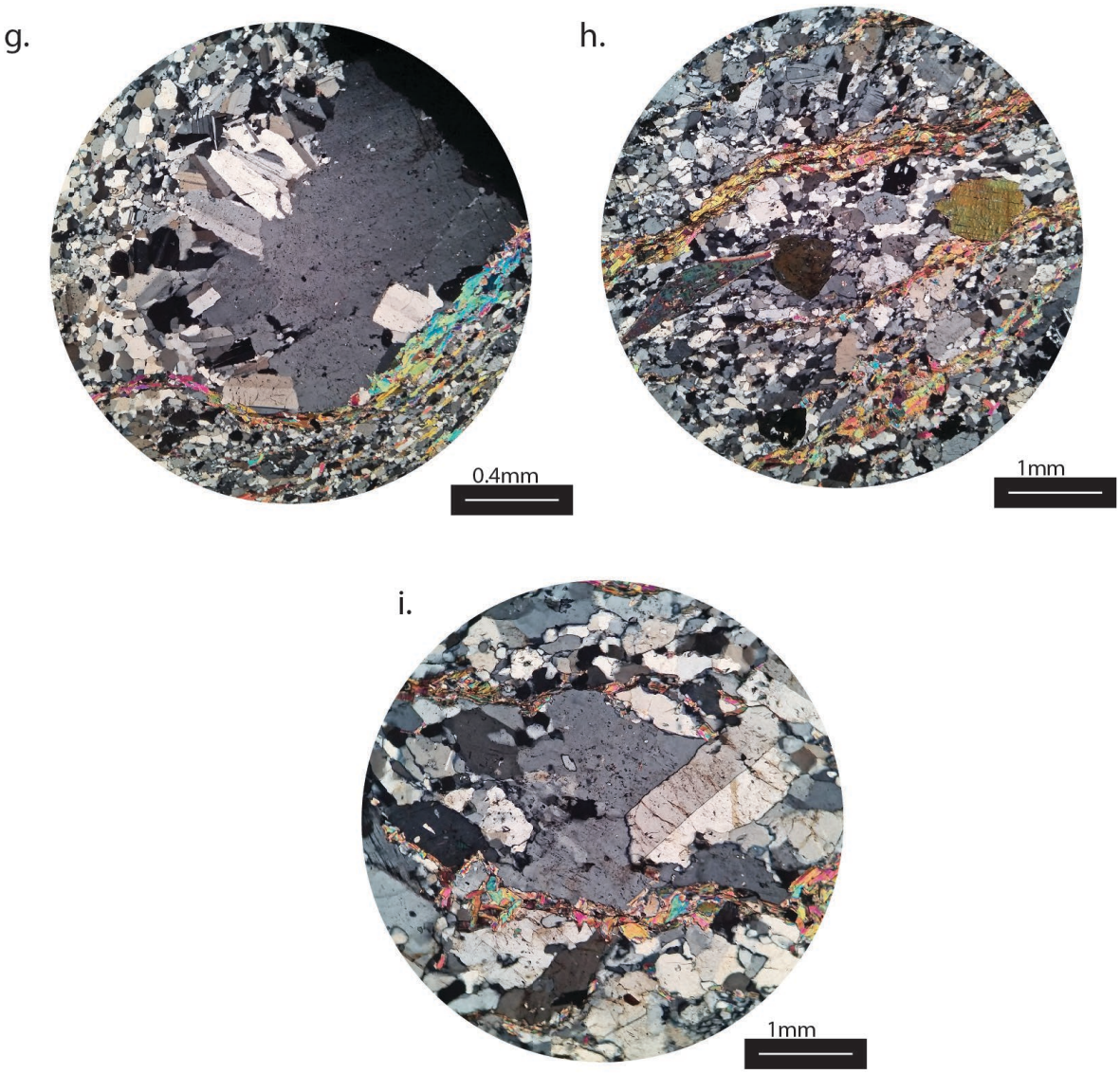


Figure 12 a-c. Sample 08-02. a. Recrystallised quartz ribbons, coarse feldspar porphyroclasts and relict mica lenses. b. Elongate quartz porphyroclasts showing subgrain rotation. Recrystallised quartz ribbons. white mica porphyroclasts and white mica sheets in matrix. c. White mica porphyroclasts. d-g. Sample 08-04 d. Feldspar poikiloblast wrapped by fabric. e. Mica porphyroclasts with thin mica sheets between quartz domains. Quartz exhibits subgrain rotation. f. feldspar, quartz and mica domains separated by thin mica sheets. g. K feldspar porphyroclasts partially replaced by simple twinned feldspar. h-i. sample 08-08. h. mica fabric wrapped feldspar domain and mica porphyroclasts. Zoned tourmaline postdates fabric. i. feldspar with simple twins overgrowing poikiloblastic feldspar.

Berthelsen outcrop

Sample JU-07 to JU-10 form a transect of samples taken from the Puga Gneiss surrounding the main eclogite boudin at the Berthelsen outcrop (locality 17/19, Figure 1). Sample JU-07 is taken from furthest from the boudin and forms a strongly foliated but granoblastic-textured schistose gneiss (Figure 13a). Quartz and feldspar have a similar grain size and flakes of white mica have an aspect ratio of 4:1. Sample JU-08 contains slightly broader white mica flakes with birefringence zoning (Figure 13b). Large, twinned Na-feldspars cross-cut other mineral phases. Quartz shows a range of grain sizes, often spanning the quartz ribbons, but occasionally forming finer domains. Equant subgrains within coarse quartz grains equate to the size of the fine quartz grains, implying recrystallisation near the grain boundary migration/subgrain rotation transition.

Sample JU-09, taken from closer to the eclogite boudin, is mica-rich, with narrow, lenticular mica flakes and quartz. Quartz of variable grain size contains lobate grain boundaries. Large grains show undulose extinction without the presence of tabular subgrain boundaries. Feldspar has a similar grain size to larger quartz grains with convex outlines and poikiloblastic cores, implying that they belong to a relatively late generation of growth. Sample JU-10, adjacent to the eclogite boudin, is fine-grained and schistose, containing narrow laths of white mica, aligned to the main fabric (Figure 13c). Fine-grained quartz and feldspar form monomineralic ribbons where quartz spans the width of the ribbons. Na-feldspar is mostly granular and fine-grained.

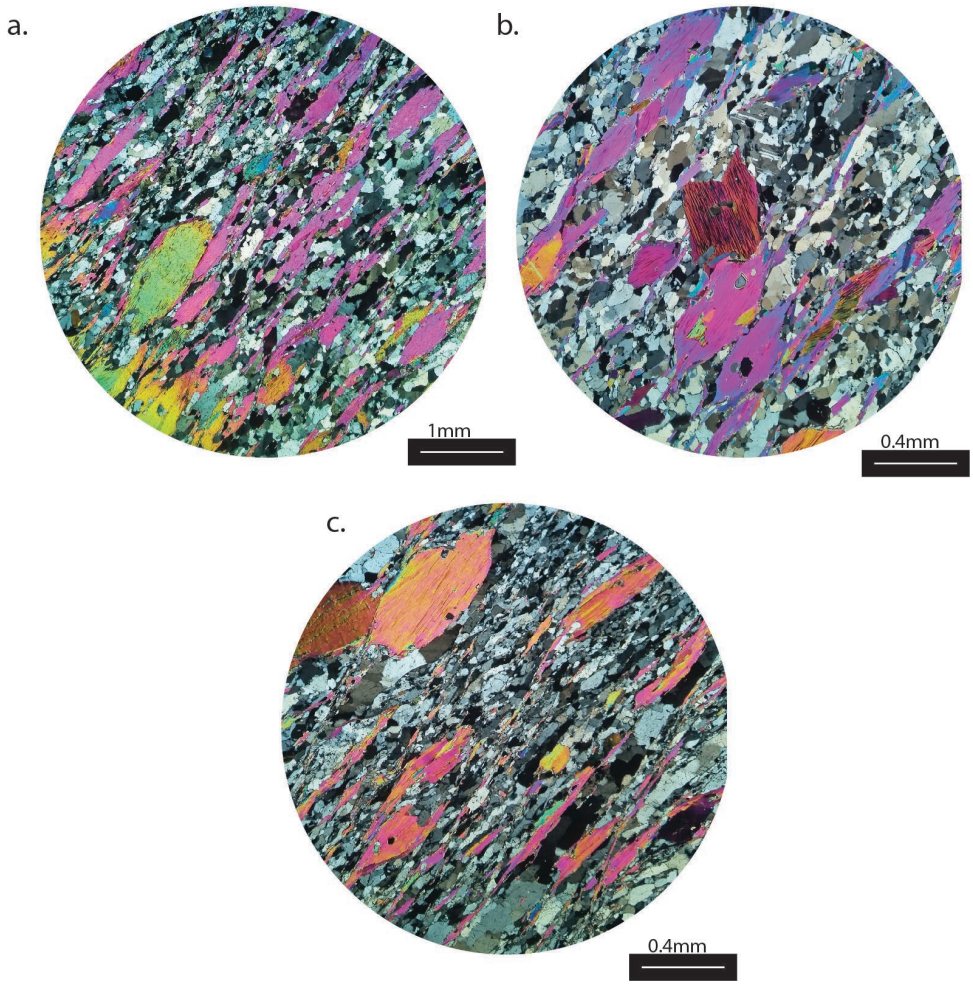


Figure 13 Transect JU07 to JU10. a. Sample JU07. Broad mica porphyroclasts. Quartz-rich domains with subgrain rotation. b. Sample JU08. Broad mica porphyroclasts. Quartz-rich domains with subgrain rotation. Thin mica sheets separating lenticular domains. Coarse twinned feldspar in feldspar domain. c. Sample JU10. Finer grained bands of quartz and feldspar. Subgrain rotation in quartz. Broad mica porphyroclasts show 'fish' geometries.

Kiagar La

Sample 05-05B and 05-05C (locality 16/53, Figure 1) are porphyroclastic gneisses from a heterogeneous outcrop of Puga gneiss, with variable mica content. Quartz is partly polygonised but now shows undulose extinction, tabular subgrains and lobate boundaries. Coarse K-feldspar porphyroclasts show microcline twinning, bordered by granular plagioclase. Zones and patches in the K-feldspar show fine-grained recrystallisation after original plagioclase inclusions. Rare garnets are found in feldspar domains. Some blocky white mica porphyroclasts are wrapped by the fabric and occasionally contain titanite inclusions. Tourmaline is occasionally present in large grains as subhedral original grains and poikiloblastic grains overgrowing the tectonic fabric.

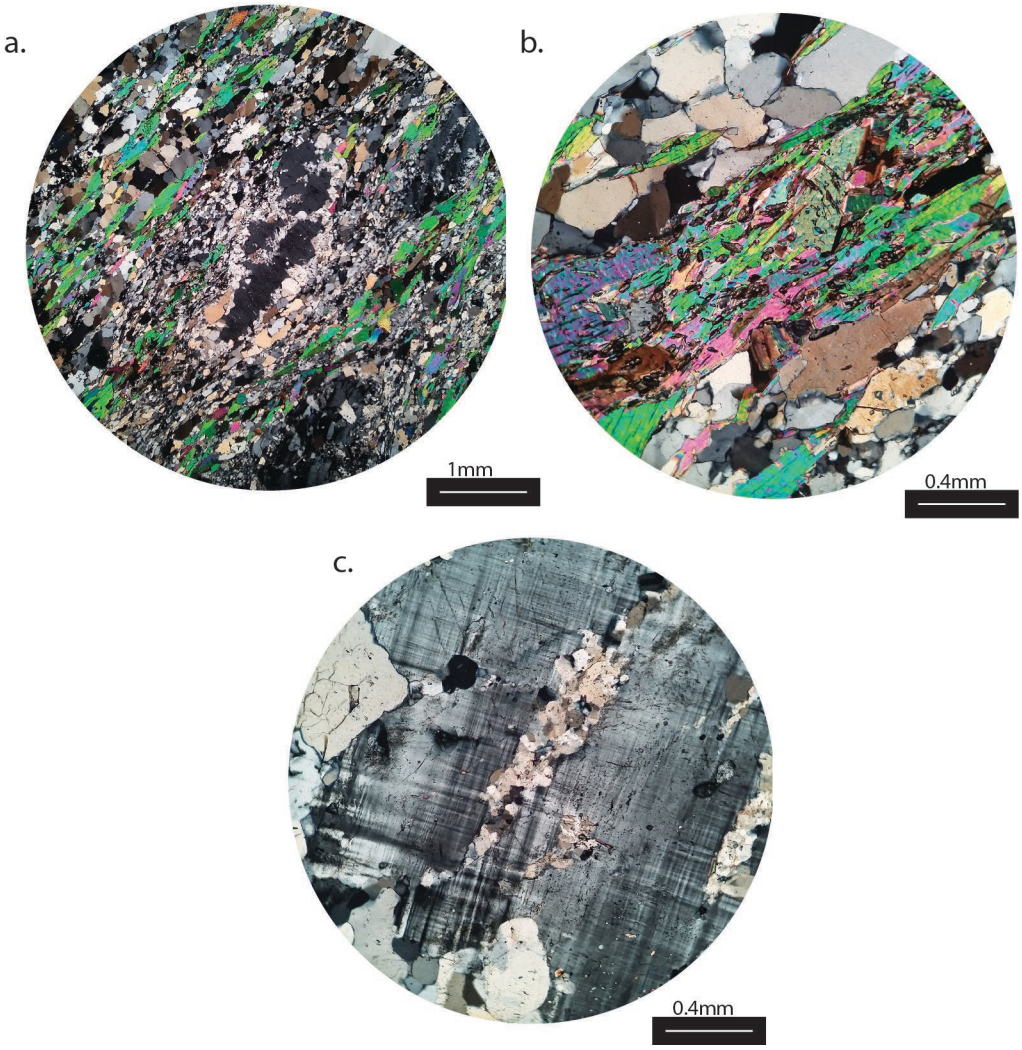


Figure 14 Sample 05-05C. a. σ-type K-feldspar porphyroclasts with granular plagioclase rim. Annealed quartz ribbons. Mica porphyroclasts sheared into thin mica bands. b. lenticular domains of white mica with titanite inclusions. Subgrain rotation evident in relict quartz. Cleaner annealed quartz at top. c. Microcline porphyroclasts with recrystallised feldspar domains.

Kiagar Tso

Sample 05-02 and 05-01 are taken from a Puga gneiss outcrop (locality 16/51, Figure 1), where the main fabric wraps the mafic eclogite boudins on the north shore of Kiagar Tso. These samples contain a schistosity defined by bands of white mica, Na-plagioclase and quartz (Figure 15b). Strongly developed foliation surfaces occur in quartz-rich domains with narrow mica trains, wrapped large rigid objects such as garnet (Figure 15g).

Quartz forms polycrystalline lenses with well annealed quartz grains and evidence of later undulose extinction, occasional tabular subgrains crossing larger grains and slightly lobate grain boundaries (Figure 15c and d). Lenticular white mica domains are composed of stacks of white mica sheets

(Figure 15d), parallel to the schistosity, often exhibiting an asymmetrical sigmoid shape, indicating direction of shearing. The terminations of the white mica lenses often curve into discontinuous C′ shear bands, indicating general shear motion with a component of flattening and shearing. White mica lenses occasionally contain idioblastic inclusions of titanite in domains with high titanium contents. Thin white mica trains, formed in a high strain fabric, separate quartz-rich domains. Elongate lenses of fine-grained albite have dusty alteration and contain small ragged flakes of white mica (Figure 15g). Slightly larger oval-shaped feldspar grains with obliquely aligned mica flakes form porphyroclasts, wrapped by a fabric of fine-grained feldspar and white mica. Garnet is present in feldspar-rich domains and is associated with biotite and light green chlorite.

Garnets within sample 05-02 are approximately 4-10 mm in diameter and occur in the mica rich regions of the rock. They contain abundant fractures infilled with white mica and have a corroded shape where garnet has broken down into biotite + white mica with occasional small xenotime crystals. Finer grained inclusions of quartz and rutile occur away from fractures and define a primary foliation, oblique to the matrix fabric. Kyanite is observed within the garnet core, adjacent to a staurolite grain, surrounded by white mica (Figure 15f). The occurrence of kyanite as inclusions surrounded by an altered rim indicated that it survived later fracturing and alteration of the garnet and that this is a primary inclusion.

Rutile inclusions in the garnet core define an early fabric which forms fold structures towards the core-rim boundary (Figure 15e). These fold structures are present in the lower left and right quadrants of the garnet (Figure 17b) and resemble millipede structures, thought to have formed in the matrix surrounding the garnet during syn-deformational growth and rotation of the fabric around the garnet (Bell *et al.*, 1986). These millipede structures are truncated by a thin, inclusion-poor rims, with planar rutile inclusions, preserving a fabric which wrapped around the garnet core.

Garnets exhibit concentric zonation in major and trace elements (Figure 16). The core region consists of an approximately constant composition of $Alm_{79}Grs_{12.5}Pyr_{5.5}Spss_{4\text{-}2.3}$ outlined by a faceted garnet shape, marked by a manganese- and yttrium-richer annulus. Following this, a calcium trough (10% Grs) can be observed with a faceted outline, indicating multiple nucleation points during growth of

the inner rim. The outer rim shows an increase in pyrope (to 16%) and grossular (to 13%) with a decrease in almandine (to 69%). Regions of high magnesium extend from the outer edge of the garnet crystal, replacing regions of the garnet rim and core and forming haloes around inclusions in garnet, cutting across the concentric zoning patterns.

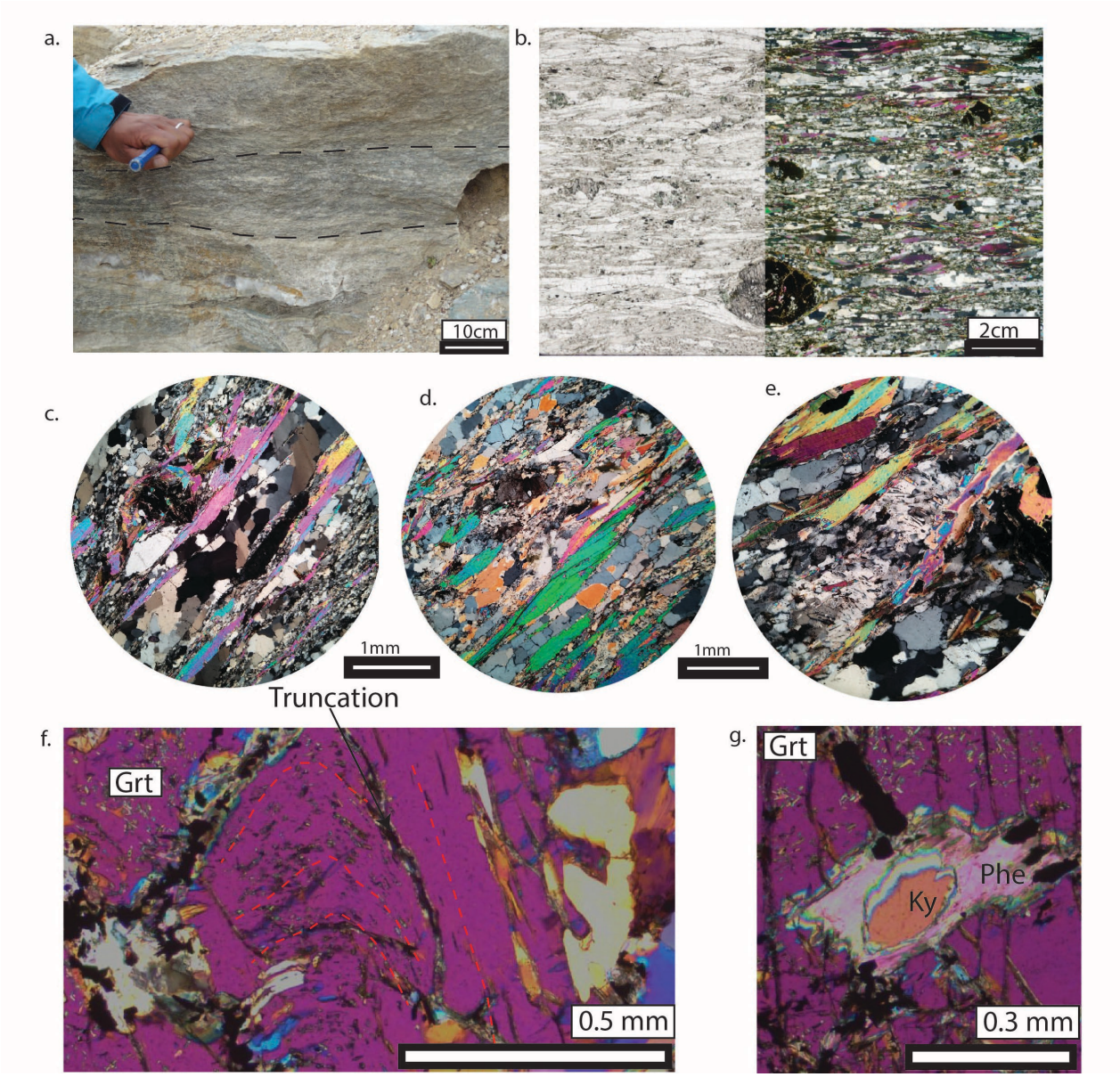


Figure 15 Sample 05-02 outcrop and thin section photographs. a. Outcrop showing compositional layering (black lines) due to variation in biotite content. Deformed quartz vein at bottom of outcrop. b. PPL and XPL Photomicrographs of sample 05-02. Garnets wrapped by fabric. Large garnet mapped in Figure 16. c. Small garnet wrapped by thin mica sheets. Subgrain rotation and undulose extinction in quartz domain. fine grain feldspar domain with white mica. d. Stacks of white mica wrapped by thin mica sheets. Annealed quartz ribbon. e. albite and white mica wrapping garnet poikiloblast. h. zoned idioblastic tourmaline grain wrapped by fabric. f. Rutile inclusion trail in garnet preserving an earlier crenulation cleavage, truncated by a planar fabric at the rim. g. Kyanite inclusion in garnet altered to white mica associated with a fracture network.

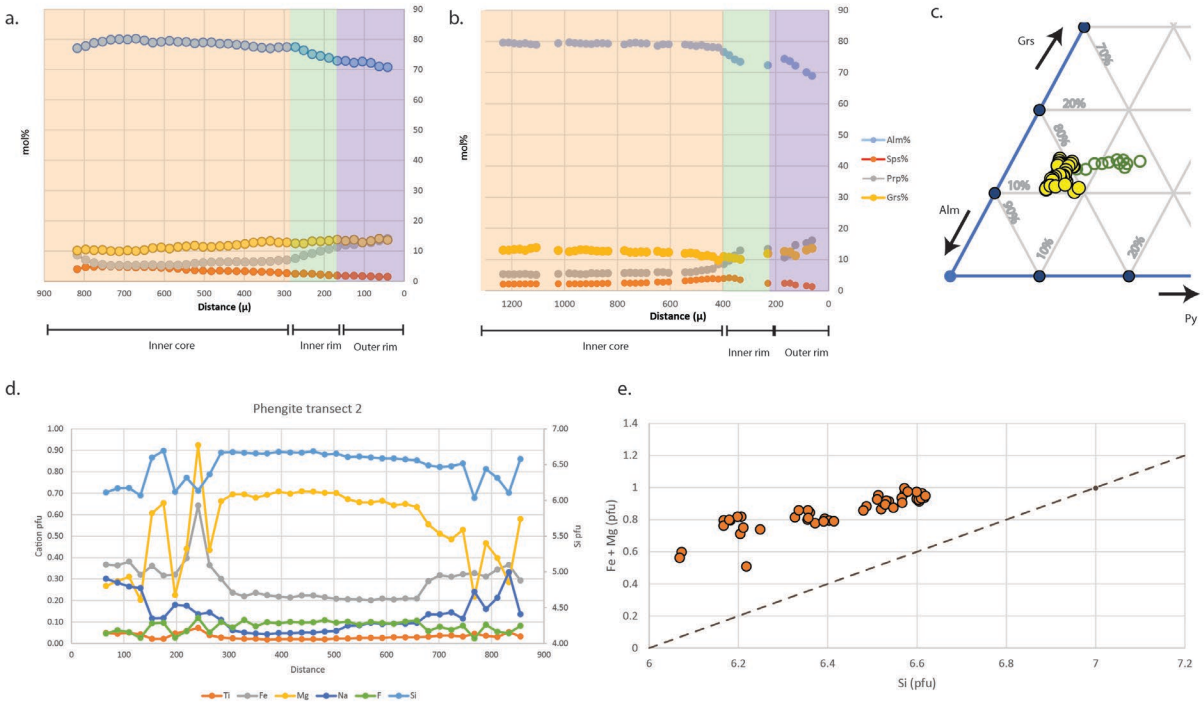


Figure 16: Sample 05-02 mineral chemistry. a. and b. Garnet zoning profiles from core (left) to rim (right). Inner core, inner rim and outer rim zones marked. c. Ternary diagram of transect across garnets. Solid yellow circles plot inner core region. Hollow green circles plot inner and outer rim regions. d. Transect across a coarse-grained phengite lath. e. Phengite analyses. Dashed line shows celadonite exchange vector from pure muscovite.

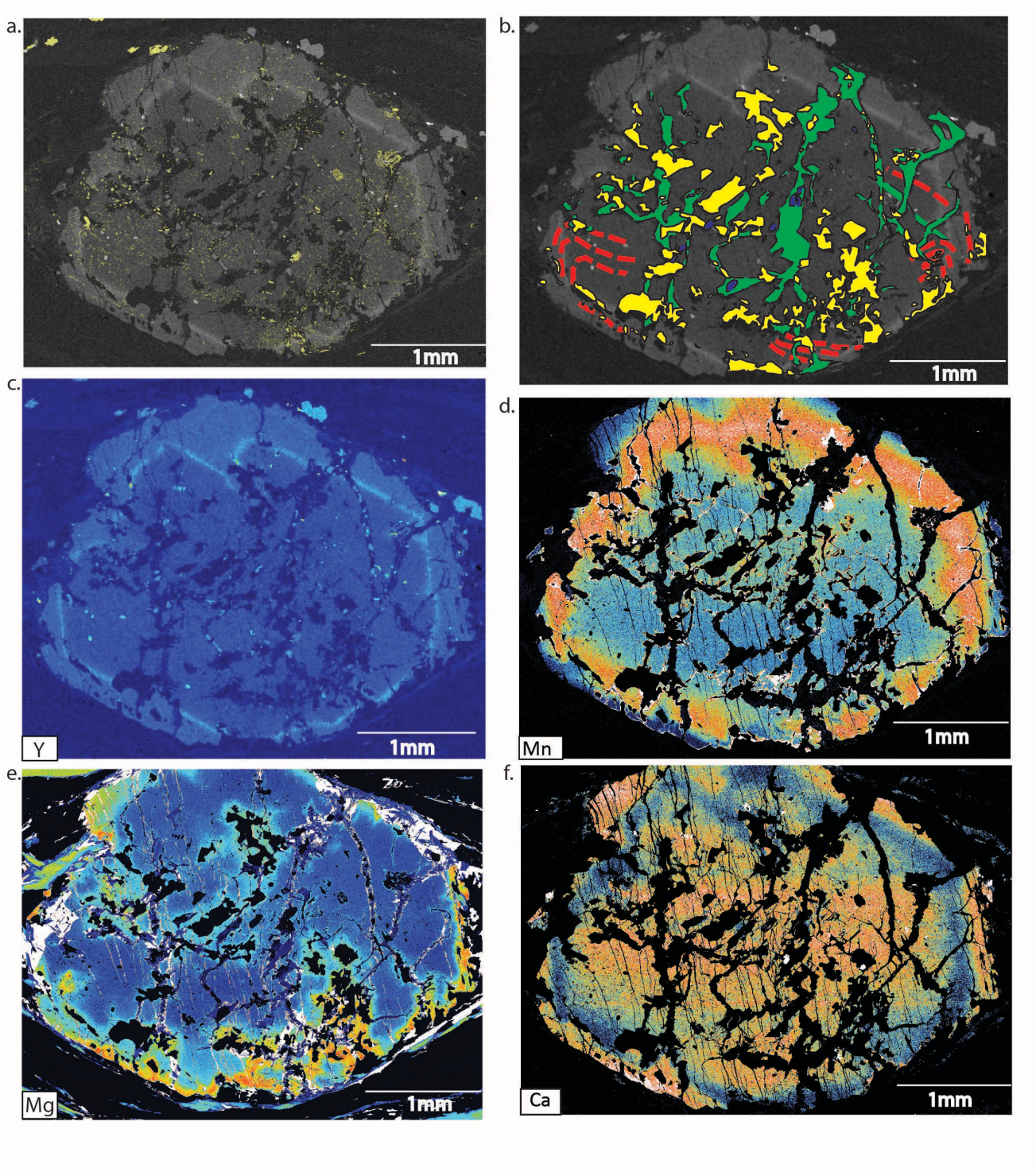


Figure 17. Sample 05-02 garnet. a. Ti map (yellow) overlying Y map, showing orientation of rutile inclusions and location of rectangular rutile clusters. b. Inclusion map of garnet. Background yttrium map shows the location of the core-rim boundary defined by the yttrium high. Red dotted lines follow rutile inclusion trails which show curved millipede structures within the garnet core and a truncating rim fabric. Superimposed inclusion map shows white mica (green) infilling fractures, quartz (yellow) and kyanite (blue). c. Yttrium map. d. Manganese map. e. Magnesium map. f. Calcium map

Mineral	*Phengite*	*Garnet core average*	*Garnet rim average*	*Biotite*	*Chlorite*
SiO_2	49.95	36.77	37.55	37.14	26.17
TiO_2	0.32	0.77	0.08	1.10	0.07
Al_2O_3	28.65	20.92	21.42	17.64	21.96
Cr_2O_3	0.01	0.04	0.02	0.01	0.01
FeO	2.62	34.37	32.22	15.73	21.69
MnO	0.00	1.13	0.99	0.09	0.19
MgO	2.85	1.53	3.13	12.87	17.60
CaO	0.00	4.16	4.39	0.01	0.03
Na_2O	0.51	0.04	0.05	0.10	0.07
K_2O	10.62	0.02	0.08	9.89	0.02
F	0.19	0.01	0.01	0.53	0.09
Cl_2O	0.00	0.00	0.00	0.08	0.02
Total	**95.72**	**99.92**	**99.93**	**94.95**	**86.86**
Ox	22	12	12	22	14
Si	6.413	2.990	2.996	5.563	2.708
Ti	0.032	0.005	0.005	0.124	0.005
Al	4.824	2.015	2.015	3.116	2.680
Cr	0.001	0.002	0.002	0.001	0.001
Fe^{3+}	0.00	0.000	0.000	0.110	0.000
Fe^{2+}	0.305	2.151	2.151	1.880	1.793
Mn	0.001	0.067	0.067	0.011	0.017
Mg	0.554	0.372	0.372	2.873	2.715
Ca	0.000	0.376	0.376	0.002	0.004
Na	0.144	0.007	0.007	0.030	0.014
K	1.811	0.008	0.008	1.889	0.003
F	0.074	0.001	0.001	0.251	0.030
Cl	0.000	0.001	0.001	0.020	0.002
Sum	**14.16**	**7.998**	**7.998**	**15.579**	**9.938**

Table 3 Representative mineral analyses from sample 05-02

Phase equilibrium modelling

Phase equilibrium modelling was undertaken on sample 05-02 in order to determine the P-T conditions of garnet growth with respect to the observed compositional zoning. The bulk composition (SI(78.676)AL(20.913)CA(0.391)MG(1.59)FE(1.901)F3(0.002)K(5.09)NA(7.751)TI(0.536)MN(0.027)H(0)O(?)) was calculated based on the average mineral compositions with respect to their modal abundances. P-XH_2O and T-XH_2O diagrams were constructed at 520°C, 22 kbar and 26 kbar respectively (Figure 18). The presence of kyanite as a primary inclusion in the garnet core indicates that water undersaturated conditions (~5 mol H_2O, equivalent ~10 atoms of H in the bulk composition where water saturation occurs at 7 moles H_2O, Figure 18) must have been present during garnet core growth (Figure 18a). In water saturated conditions, kyanite is not predicted to be in equilibrium with garnet.

Using the full bulk composition of sample 05-02, where all elements are available to react, and 2 moles H_2O added to the anhydrous bulk composition (4 H atoms in bulk composition, Figure 18), garnet compositional isopleths were modelled and compared to the measured garnet values of $Py_{5\text{-}7}Grs_{13}$ for the inner core. Calculated isopleths of these compositions intersect at P-T conditions of 350-430°C, 10-12 kbar (Figure 19a) in the assemblage field garnet + biotite + white mica + quartz + kyanite + microcline + rutile + clinopyroxene/plagioclase. However, rapidly changing grossular isopleths, corresponding to the breakdown of feldspar, mean that this intersection occurs over a very narrow range and could therefore be very sensitive to uncertainty in bulk composition.

Following fractionation of garnet cores from the total bulk composition, the resulting effective bulk composition for sample 05-02 contains very low Ca, so pseudosections predict a grossular content in garnet of < 2% above 15 kbar (Figure 19b). The low grossular content predicted, compared to observed values of 10-15%, suggests that the predicted mineral equilibria may not be representative of conditions preserved in the rock during prograde garnet growth. For example, plagioclase is predicted to break down to Ca-Na pyroxene at ~11 kbar. However, if plagioclase were to persist metastably to higher pressures, the growth of Ca-Na pyroxene would be suppressed.

Equilibrium thermodynamics provides a very good way of assessing metastable equilibrium stages and figuring out how far away they are from the 'final', most stable state (Anderson, 2005). It is important to

Considering the possibility of reactions removed from equilibrium could be considered important when inferring the P-T-t evolution of metamorphic rocks (Pattison et al., 2011). In order to test whether plagioclase could have persisted metastably to high pressures, clinopyroxene models were excluded in the thermodynamic database. The exclusion of clinopyroxene models is equivalent to suppressing and overstepping the nucleation of Ca-rich pyroxene and provides a way of modelling the metastability of plagioclase. Plagioclase in this example is metastable with respect to clinopyroxene but still able to react with the growing garnet and other phases in the rock. The resulting departure of equilibrium can be identified by measuring the composition of phases and seeing how they deviate from equilibrium models where the plagioclase breakdown reaction proceeded without being overstepped. From this, the effect on the position of isograds and the composition of the first crystals grown can be determined. Studies which consider the overstepping of equilibrium reactions have mostly been constrained in large thermal aureoles (e.g. Waters and Lovegrove, 2002; Pattison and Tinkham, 2009; Spear et al., 2014).

Theriak-Domino calculates the energy difference between the metastable Cpx-absent assemblage and the assemblage in which Cpx is notionally present but has a zero mode (where Cpx is "about to nucleate"). This energy difference is known as the macroscopic driving force for reaction or reaction affinity (Pattison et al., 2011). A large negative energy difference describes the departure of the system from equilibrium, such that if clinopyroxene were to nucleate, the energy of the system would be significantly reduced, indicating that it is energetically favourable for clinopyroxene to nucleate. The composition of Cpx "about to nucleate" can also be calculated as the composition that produces the maximum decrease in Gibbs free energy from the equilibrated, Cpx-absent assemblage (Spear et al., 2011).

Exclusion of clinopyroxene in the models for sample 05-02, using a fractionated bulk composition and water saturated conditions, results in the prediction of a much high grossular content above 20 kbar, decreasing with temperature (Figure 19c). Predicted grossular and pyrope isopleths are sub-parallel. Garnet isopleths corresponding to inner rim conditions of $Grs_{12\text{-}13}Py_{8\text{-}13}$ intersect at 575-610°C, 20-23 kbar. Garnet isopleths corresponding to outer rim conditions of $Grs_{14\text{-}15}Py_{17\text{-}18}$ intersect at 590-730°C, 20-33 kbar, for the same models.

At 575-610°C, 20-23 kbar, the driving force for nucleation of clinopyroxene is predicted to be around 11-13 kJ per mol oxygen, increasing to 20 kJ per mol oxygen at 30 kbar. Other studies, considering a variety of metamorphic minerals including garnet, andalusite and staurolite (e.g. Waters and Lovegrove, 2002; Spear and Pattison, 2017) have suggested values of energy overstepping at nucleation in the range 0.2 to 2 kJ per mole oxygen. This suggests that the nucleation of clinopyroxene would be energetically favourable even at relatively low pressures, apparently limiting the persistence of metastable plagioclase at higher pressures. Nevertheless, the observed grossular content of garnet appears to require the suppression of clinopyroxene. Models of 05-02 using the full bulk composition and water saturated conditions, used to estimate conditions of retrograde metamorphism, predict that albite is stable below 13 kbar at 500°C and <19 kbar at 600°C and low-Ti biotite is stable below 14 kbar at 600°C.

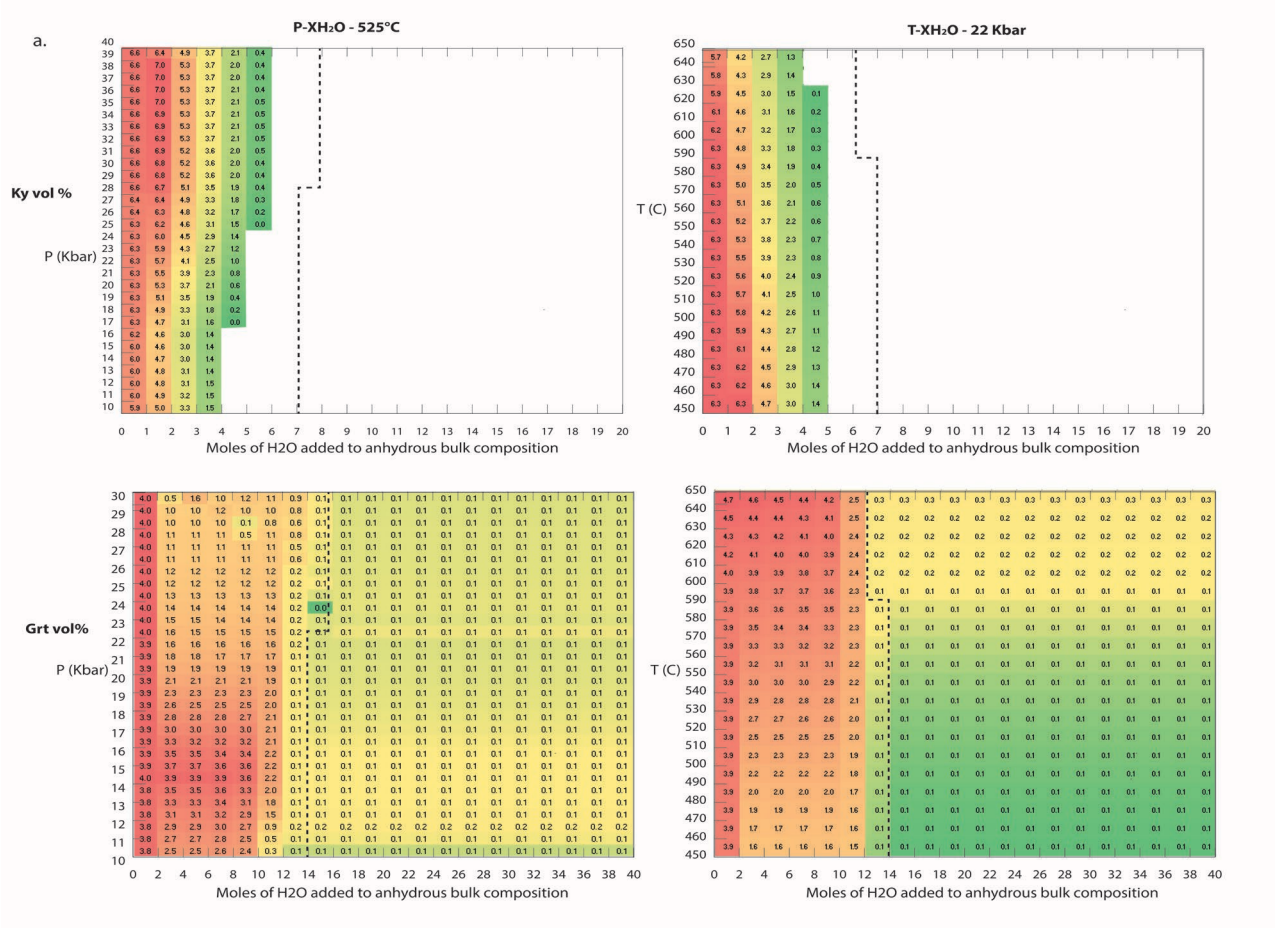


Figure 18 a. P-XH_2O Pixel map at 525°C showing volume % Kyanite and Garnet. Colour scale shows low (green) to high (red) values. b. T- XH_2O at 22 kbar showing volume % Kyanite and Garnet. Water saturation shown as dashed line. Colour scale reflects the range of numerical values in the grid where red = high and green = low. Anomalous low/high/zero values represent errors and time-out failures of the algorithm during calculation. X-axis shown moles of H2O added to the anhydrous bulk composition.

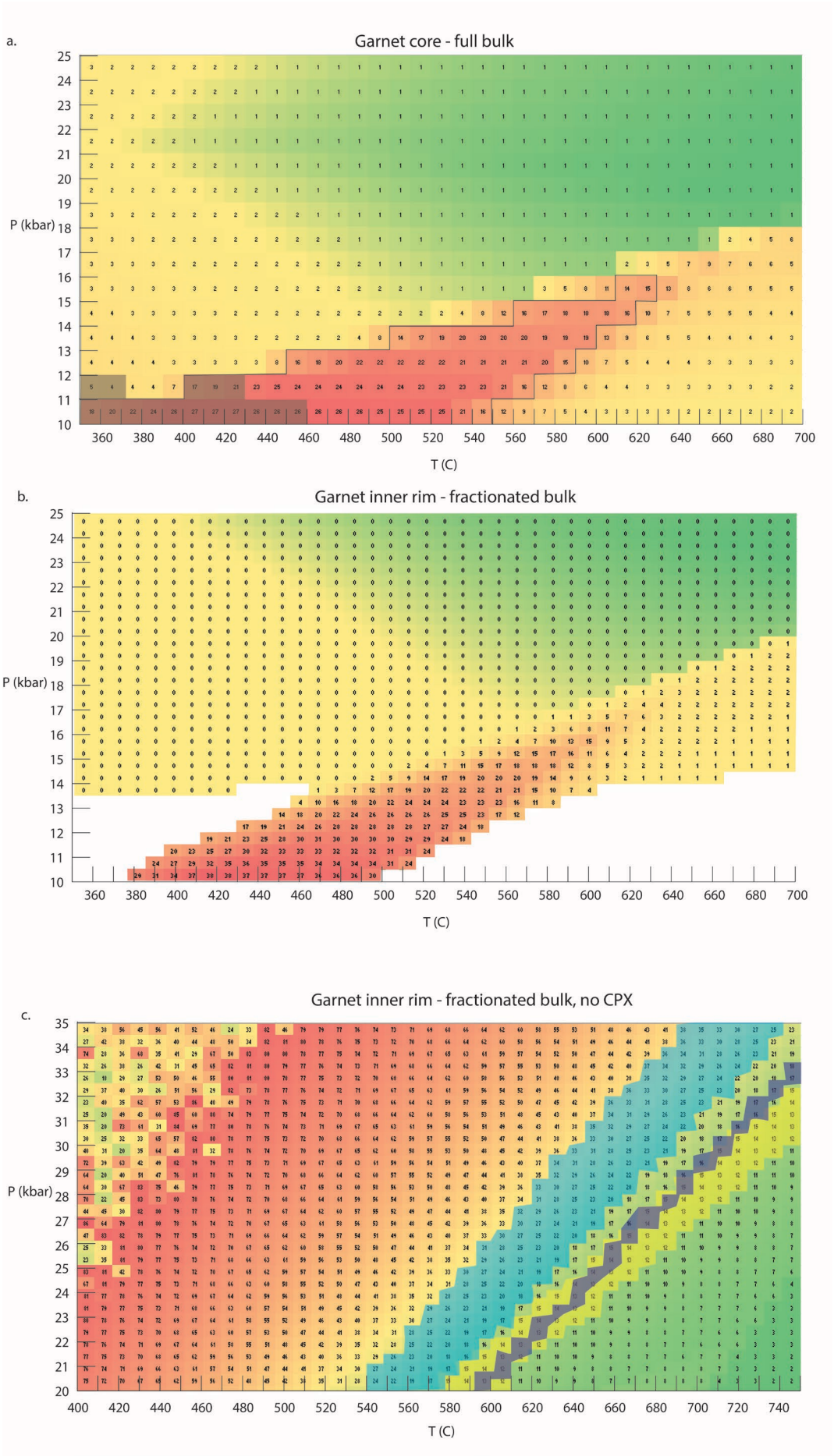

a.
Garnet core - full bulk
P (kbar)
T (C)
b.
Garnet inner rim - fractionated bulk
P (kbar)
T (C)
c.
Garnet inner rim - fractionated bulk, no CPX
P (kbar)
T (C)

Figure 19 Pixel maps - P-T diagram for sample 05-02 garnet grossular isopleths at 4 wt% H_2O. Colour scale shows low (green) to high (red) values. a. garnet core isopleths using the full unfractionated bulk composition. Black lines marks 13% grossular content. Grey box marks 5-7% pyrope. b. garnet inner rim grossular isopleths after fractionation of the garnet core. c. garnet inner rim grossular isopleths after fractionation of the garnet core with the clinopyroxene models suppressed. Pale blue zone (garnet inner rim) = 8-13% pyrope, dark blue zone (garnet outer rim) = 17-18% pyrope. Yellow zone = 12-15% grossular (garnet inner and outer rim)

Discussion

Protolith

Comparable U-Pb zircon ages of 482 ± 1 Ma for the Puga Gneiss and Polokongka La granite indicate that these lithologies belong to the same intrusive complex (Girard and Bussy, 1999). Field observations preserving cross cutting relationships (Figure 11) and geochemical variations in the Puga Gneiss, indicate that multiple different intrusive phases are present within the Tso Morari complex. The metamorphic foliation crosscuts and therefore postdates the compositional boundaries within the Puga Gneiss. Owing to the variation in deformation state throughout the complex forming irregularly distributed shear zones, these compositional variations are not easy to trace laterally.

The protolith of the Puga gneiss is granitic and can be identified by the presence of K-feldspar augen in hand specimen. Key criteria have been established to aid the identification of Puga Gneiss in thin section and in hand specimen. These criteria are particularly useful when trying to distinguish between a mica-schist, derived from deformation of the Puga Gneiss, and a mica-rich pelitic metasedimentary rock, which often form rafts within the Puga Gneiss. Strongly deformed Puga Gneiss no longer contains distinctive feldspar augen and contains a strong schistosity with abundant mica. The lack of distinguishing features, such as K feldspar augen in the deformed Puga Gneiss are a result of dynamic recrystallisation, reduction in grain size and development of a strong foliation.

Major and trace element analysis of whole rocks indicates that the granites and Puga Gneiss of the Tso Morari complex formed in a collisional tectonic setting. Suites of samples which include transects from low–strain to high–strain Puga Gneiss, indicate that more deformed samples trend towards a bulk composition relatively enriched in Al and/or depleted in Mg and Fe (Figure 2b) owing to alteration. Alteration of these samples can also be plotted using discriminate function analysis where the samples trend towards the collisional field with increasing alteration and deformation (Figure 3 and Figure 4).

Metamorphism of the Puga Gneiss

The overall microstructure in strongly foliated Puga gneiss is characterized by ribbons or lenticular domains of three types, dominated by quartz, white mica and sodic feldspar, respectively. Some samples show an augen texture, with porphyroclasts of K-feldspar, muscovite or quartz, up to several mm across.

Comparing common microstructural features in the Puga Gneiss in samples across the dome, shows a similar early metamorphic history in all samples, where primary plagioclase is absent, and metamorphic garnet is present. The relationship between mineral growth and deformation can be seen in transects of samples across strain gradients, such as JU-07 to JU-10 and a05-01 to a05-07. In transect a05-01 to a05-07, the breakdown of plagioclase occurred prior to garnet growth, subsequently followed by growth of feldspar poikiloblasts, which partly pre-date the formation of the main fabric. Primary K-feldspar has persisted in low–strain samples but underwent dynamic recrystallisation in high–strain samples. Quartz deformation and fabric formation took place in different quartz deformation regimes, dependant on structural position in the complex.

Coarse-grained zoisite and epidote are closely associated with low-Ti biotite in the matrix of samples located adjacent to mafic sills and cuts across the phengite-rich foliation. Biotite is sub-parallel to the foliation and is concentrated on the differentiated limbs of the crenulation cleavage, suggesting that the schistosity parallel growth is mimetic. Low-Ti biotite is also present as thin rims around phengite and garnet.

Garnet

The pattern of zoning within garnet in the Puga Gneiss is remarkably similar, although with different elemental concentrations, to zoning patterns in garnet from mafic eclogite samples (Chapter 3) across the dome. High-Mn cores indicate that the garnets are prograde and grew in the kyanite stability field, preserving kyanite inclusions in garnet cores. Phase equilibrium modelling of sample 05-02 shows that kyanite and garnet are predicted to coexist during prograde garnet core growth only in water undersaturated conditions. The presence of kyanite inclusions in the garnet core is consistent with a high-Al bulk composition of the Puga Gneiss achieved prior to garnet growth, following alteration of the S-type granite protolith. Kyanite and garnet then grew in equilibrium with an Al-rich bulk composition during subduction of the Indian margin.

The Mn and Y annulus at the core-rim boundary indicates that garnet resorption took place, followed by faceted garnet growth, defined by a low-Ca trough. This changing style of garnet growth is also observed to coincide with the appearance of lawsonite pseudomorphs in the mafic eclogites, suggesting a switch to water saturated conditions. This textural break also marks the shift from inclusion-rich to inclusion-poor garnet growth, signifying a change in the mechanism of garnet growth. The garnet rim preserves an increase in pyrope and grossular content, comparable to the rims on the mafic eclogites which are known to preserve coesite or polycrystalline inclusions after coesite. The comparison in garnet growth style, the change in water saturation and patterns in compositional zoning suggest that the high-Mg rims of the garnets within the Puga gneiss correspond to the highest pressure and temperatures recorded in the mafic eclogite, thought to be within the coesite stability field.

Syn-deformational microstructures within the garnet core in sample 05-02 indicate that early deformation (D1) within this sample occurred on the prograde path, prior to the growth of the high-pressure garnet rims. A later deformation event (D2) occurred post garnet growth, causing the matrix fabric to wrap around garnet porphyroblasts. A transect from undeformed granite to garnet-mica schist shows that nucleation of garnet occurred around biotite phenocrysts in the granite prior to the onset of deformation. The nucleation of garnet and phengite after igneous biotite is similar to the observations described in Chapter 4 and represent a reaction taking place in the eclogite facies (c.f. Koons *et al.*, 1987). The growth history of the garnet must therefore have taken place during prograde metamorphism at relatively high pressure, during subduction-related deformation.

The high variance assemblage preserved in the Puga Gneiss makes the application of conventional barometers difficult. The matrix assemblage is predominantly an amphibolite-facies assemblage which may not be in equilibrium with the refractory garnet poikiloblasts. Single element thermometers may be useful when trying to determine the peak temperature of the rock, as textural relationships between phases do not need to be assumed. The zirconium in rutile thermometer (Ferry *et al.*, 2007) has been employed on mafic and felsic rocks from the Tso Morari nappe in chapter 7.

In the absence of suitable phase relations for conventional thermobarometry, pseudosection modelling can be employed in order to determine the pressure and temperature conditions of equilibration. Using the full bulk

composition for sample 05-02 and water undersaturated conditions, observed garnet core isopleths intersect at 10-11 kbar, 350-440°C. This P-T intersection is comparable in pressure to the low-pressure garnet core isopleth intersection consistently observed in pseudosection models of the mafic eclogite samples in chapter 3, although approximately 50°C lower temperature. The lack of any isopleth intersections in the garnet rims reflects the very low Ca content of the bulk rock, uncertainty in the actual mineral assemblage and uncertainty in the effective bulk composition of the reacting system, preventing estimation of P-T conditions using mineral equilibria.

Feldspar

Textural and compositional relationships in the metagranite of the Tso Morari complex indicate that the breakdown of igneous K-feldspar and cordierite to coarse-grained mica is related to hydrothermal alteration of a granitic protolith by a post-magmatic fluid, prior to high pressure metamorphism (Chapter 4). Further alteration and metamorphism of the plagioclase and K-feldspar took place prior to garnet growth and is preserved as phengitic white mica + albite and phengitic white mica aggregates respectively. In low strain metagranites, primary plagioclase feldspar has already broken down. In the Puga Gneiss, fine-grained white mica aggregates are present within low strain lenses (augen) and as rectangular inclusions in garnet, preserving the earlier alteration texture after K-feldspar.

Sodic feldspar occurs in three textural types. The first and most typical type occurs in ribbons or lenticular domains as fine-grained aggregates that have a dusty appearance in thin section, in which feldspar is mixed with a small amount of very fine-grained white mica. It may be inferred that these represent the plagioclase content of the precursor granite, deformed and recrystallized. Because the metamorphic state of the granitic plagioclase is largely unknown – it may have been altered (sericitized) before UHP metamorphism, and it may or may not have transformed to an eclogite-facies assemblage – it is not possible to infer the conditions of deformation from its deformation style or recrystallised grain size, except that, as expected in quartzofeldspathic rocks deformed at around 500°C, the grain size is less than that of coexisting quartz.

The two other types of Na-feldspar are also found in these domains. The second type consists of small poikiloblasts (An < 4 %), where the inclusions are of muscovite with or without quartz. This texture is common in high–strain samples adjacent to mafic sills. The narrow mica flakes are commonly aligned at an

angle to the external foliation. However, there is no other evidence for a composite foliation in the Puga gneiss. These grains are contained within the foliation defined by white mica or are wrapped by the cleavage zones. However, they also commonly have convex, inclusion-free rim zones that in some cases appear to embay the framing mica flakes. The implication is that these grains have at least partly grown in place, after the deformation ceased.

'Stuffed plagioclase' textures have been observed in metatonalites and metadiorites from Hohe Tauern, Austria, consisting of minute inclusions of zoisite/clinozoisite and muscovite in calcic plagioclase. This texture is interpreted to have formed from the reactions anorthite + K feldspar + H_2O = zoisite + muscovite + quartz as a result of overprinting of a high–T, low–P igneous assemblage (Ackermand and Karl, 1972). The reaction muscovite + 2clinozoisite + 2quartz = sanidine + 4anorthite + H_2O can be pinpointed using THERMOCALC v3.33, thermodynamic dataset ds55 (Powell and Holland, 1988; Holland and Powell, 1998), sample 05-02 water saturated bulk composition and calculation mode 3 for pure phases. The reaction is predicted to occur below ~500°C, 4 kbar and 540°C, 6.6 kbar with anorthite forming on the low-pressure side of the reaction curve.

The third type of Na-feldspar consists of twinned, clear albite laths and porphyroblasts that overprint feldspar-rich domains, cutting across earlier fabrics and cleavage zones. They are also found as equant to oblong grains forming rims on K-feldspar porphyroclasts. Their larger size, clean texture and entirely post-tectonic relationships suggest that fluid-assisted recrystallization occurred in certain samples. This microstructure dominates one leucocratic sample, 08-03. Certain of these samples also show late recrystallization of white mica cleavage zones. The fact that samples from the same outcrop occurrence show a variation in the development of these late recrystallization features implies that fluid is channelized to some degree, rather than pervasive. These features are present throughout the complex but are more abundant in the structurally highest samples adjacent to the Zildat Shear Zone.

Quartz deformation regime constraints

Quartz deformation microstructures show regional variation in the quartz deformation mechanisms, which can be understood to relate to structural depth beneath the Zildat shear zone in the NE of the dome. Deformation temperatures can be estimated by assigning ranges of temperature to each quartz deformation

regime (bulging, subgrain rotation and grain boundary migration) (Stipp *et al.*, 2002; Passchier and Trouw, 2005) and comparing them to observed microstructures, producing a relative temperature scale.

Samples adjacent to the Zildat Shear Zone, such as samples 08-08, contain quartz ribbons recrystallized from elongate c. 2 mm grains to neoblasts of less than 100 μm in the subgrain rotation regime (c. 450 ± 50°C), and have not undergone further coarsening, as the neoblasts are of similar size to subgrains in the relict quartz. Sigma-type feldspar augen and asymmetrical mica lenses, parallel to the main matrix fabric, preserve a top-to-the-E sense of shear.

At intermediate structural depth, e.g. at the Berthelsen outcrop (JU samples) the recrystallization microstructures appear transitional between subgrain rotation (SGR) and grain boundary migration (GBM) regimes (i.e. c. 500°). At greater depths (samples 05-01, 05-02 and 05-05), large relict quartz grains are absent, and quartz tends to fill the width of the narrower quartz ribbons, so that a typical mean size is >200 μm. The grains commonly have gently lobate boundaries, but do not show the amoeboid shapes associated with active deformation in the GBM regime (cf. Passchier & Trouw, 2005). Moreover, these grains are not elongated along the ribbons, but are roughly equant and separated by thin white mica sheets from the relict high strain fabric. This suggests moderate post-deformational grain growth (annealing), which itself implies conditions within the GBM recrystallization regime (c. 550°C). Recrystallized quartz grains show a limited degree of later low-strain deformation at temperatures up to the onset of dislocation glide and climb, i.e. from smoothly undulose extinction to the development of tabular subgrains with small misorientations, formed during progressive cooling and deformation (Passchier and Trouw, 2005).

White mica occurs as a foliation-defining mineral and as porphyroclasts. The first type forms trains of flakes defining mica-rich cleavage zones, which are commonly lenticular, either as individual elongate grains, or as a stack of sub-parallel tabular grains, strongly aligned but tapering towards the tips of the lensoid domain. In some cases, the lenses define a low-angle S–C′ fabric, in which the flakes are aligned in S, while the tapering terminations are defined by C′ shear bands. Such microstructures imply an extension-related regime of general shear, with a component of flattening normal to the foliation. In some samples, lenticular domains of white mica contain abundant small grains of a Ti phase, generally titanite, suggesting that these may be derived by deformation and recrystallization of former igneous biotite.

The second distinct generation of white mica occurs as larger, more equant grains that form porphyroclasts, consistent with an origin inherited from the granitic precursor. Sigma-type mica porphyroclasts preserve a top-to-the-E sense of shear. In many samples, coarser white micas show internal variation in interference colour, generally concentric, such that tips and rims show higher birefringence than grain cores. Locally, muscovite flakes are deformed at their extremities by bending and kinking, but it is unclear how this relates to deformation in the adjacent matrix. In certain samples, muscovite in cleavage zones has been recrystallized to random neoblasts of small aspect ratio. This is a feature of rocks in which Na-feldspar neoblasts and late growth are also found.

Transformation of felsic rock at eclogite facies conditions

Felsic rocks require external hydration in order to equilibrate during prograde high–pressure metamorphism (Proyer, 2003). Experiments and equilibrium models show that metamorphism of granitic-granodioritic rocks at high pressure should produce assemblages containing garnet, phengite, quartz/coesite, jadeitic clinopyroxene, kyanite, rutile, zircon and allanite (Schmidt *et al.*, no date; Huang and Wyllie, 1981; Stern and Wyllie, 1981; Hermann, 2002; Proyer, 2003; Auzanneau *et al.*, 2006; Massonne, 2009). In bulk compositions containing more Ca and Fe, amphibole and epidote-group minerals will also be present below 30 kbar (Schmidt, 1993; Hermann, 2002).

Key transformations predicted at high pressure include: the breakdown of biotite and plagioclase to muscovite and garnet (e.g. Ghent & Stout, 1981), the breakdown of the calcic component of plagioclase to garnet/zoisite, kyanite and quartz (Goldsmith, 1982) and the increase in celadonite content of phengite from the reaction of K feldspar, biotite and quartz (Evans & Patrick, 1987; Massonne & Schreyer, 1987). The Ca-component of plagioclase decomposes at high pressure to form (clino)zoisite or grossular-rich garnet in fluid-consuming reactions.

Felsic rocks that preserve equilibrated high-pressure mineral assemblages include Alpine examples, such as the Monte Mucrone meta-quartz diorites of the Sesia zone (Compagnoni and Maffeo, 1973; Oberhänsli *et al.*, 1985; Koons *et al.*, 1987), metapelites from the Adula nappe (Heinrich, 1982) and the Brossasco metagranites of the Dora Maira massif (Biino *et al.*, 1992). Examples from the Western Gneiss region of Norway include the Bårdsholmen granulite facies complex (Engvik *et al.*, 2000) and quartzofeldspathic gneisses in the

Nordfjord-Stadlandet area (Wain *et al.*, 2000; Peterman *et al.*, 2009). Examples from the European Variscides include high-pressure relicts in metasediments of the Münchberg gneiss complex, Bavaria (Klemd *et al.*, 1991), jadeitic metagranites and orthogneiss from the Malpica-Tuy allochthon, NW Spain (Ibarguchi, 1995) and ortho- and para-gneisses from the southern Armorican Massif, France (Godard, 2009). Examples from Western China include orthogneisses from the North Qaidam metamorphic belt (Menold *et al.*, 2009).

Quartzofeldspathic rocks in these examples include a range in compositions including pelite, paragneiss, granite and granodioritic gneiss, which variably preserve different degrees of transformation and preservation during high-pressure metamorphism, depending largely on the water content of the rocks during high pressure metamorphism. For example, Young and Kylander-Clark (2015) showed that, in the Western Gneiss Region (WGR) of Norway, only the rare garnet-bearing pelitic rocks preserve parts of the high-pressure prograde metamorphism to near peak conditions with a mineral assemblage garnet + quartz + clinozoisite + kyanite + phengite, and pseudomorphs after coesite included in garnet and clinozoisite (Wain, 1997; Young and Kylander-Clark, 2015). The garnet-bearing pelites are overprinted by dehydration of white mica during exhumation. Less aluminous felsic rocks preserve evidence of high-pressure amphibolite facies conditions due to the presence of phengitic white mica, garnet, rutile and zoisite with abundant quartz, plagioclase and biotite.

In fluid-present systems, the transformation of felsic rocks can be controlled by the input of external fluids along channelised structures such as shear zones (e.g. Austrheim, 1986). In the Western Alps, preferential growth of high–pressure phases has been noted to occur along cracks or plagioclase grain boundaries, where the presence of fluid facilitates mass transfer (Gavin J. Wayte *et al.*, 1989). Different lithologies have different mechanical properties and thus are thought to predispose the boundaries to shearing. Eclogitisation of these boundaries and the breakdown of plagioclase can also lead to reaction weakening (Rubie, 1983) and further development of a shear zone as a conduit to fluids. In the absence of shearing, eclogitisation is still able to occur statically, but can be limited by fluid availability. Fluid-induced partial eclogitisation has been documented to take place along and surrounding eclogite facies shear zones in the granulite-facies Flatraket complex (Wain *et al.*, 2001) and surrounding a network of fluid pathways in the Bergen Arcs (Austrheim, 1987).

In the absence of fluid, non-transformation may preserve metamorphic assemblages and textures which predate the high-pressure history. Orthogneisses of the Western Gneiss Region commonly retain the igneous framework and the persistence of an Eu anomaly in zircon indicates that the plagioclase framework remained intact (Young and Kylander-Clark, 2015). The metastable persistence of plagioclase has been documented in the Western Gneiss Region (Mørk, 1985; Wain *et al.*, 2001), the western Alps (Koons *et al.*, 1987; Wayte *et al.*, 1989) and the Bergen Arcs (Austrheim and Griffin, 1985). In the Flatraket complex of the Western Gneiss Region, metastable plagioclase is preserved in between eclogite facies shear zones which equilibrated at 20-23 kbar (Wain et al., 2001). If the Flatraket complex experienced pressures equivalent to the adjacent UHP rocks (>28 kbar), quartz and plagioclase metastability is implied with an overstep of up to ~14 kbar (Wain et al., 2001). This magnitude of overstep is similar to the predicted overstep of the Tso Morari metagranites and gneisses if the peak pressure reached was ~27kbar.

Partial transformation under fluid-limited conditions can lead to coronitic textures such as in Monte Mucrone meta-quartz diorites (Koons *et al.,* 1987) and the Brossasco metagranites (Biino *et al.*, 1992). Metagranite and Puga Gneiss samples from the Tso Morari complex preserve evidence for partial transformation in the eclogite facies in the form of garnet + phengite rims around biotite (Chapter 4) (c.f. Koons *et al.*, 1987), phengitic white mica after feldspar and prograde compositional zoning patterns in garnet with relatively high-pressure rims. The formation of phengitic white mica at high pressure requires the breakdown of K feldspar and biotite in the presence of water. The continued presence of K-feldspar in the high pressure granitoids of the Tso Morari complex suggests that this breakdown reaction may have been limited by the abundance of water, impeding equilibration at high pressure (c.f. Young and Kylander-Clark, 2015). Reactions which form a hydrous high-pressure assemblage also cause dehydration upon exhumation, overprinting existing mineral assemblages. High-pressure mineral assemblages will be preserved only if re-equilibration during exhumation is inhibited (Rubie, 1983).

In equilibrium conditions, omphacite is predicted to be abundant. However, no clinopyroxene has been preserved in the metagranites or Puga Gneiss of the Tso Morari complex. Evidence for the formation of clinopyroxene from plagioclase is required in order to determine if the felsic rocks transformed pervasively to an eclogite-facies assemblage. Alternatively, textural evidence for the former presence of clinopyroxene,

or evidence for penetrative deformation and recrystallisation responsible for erasing the pre-existing mineralogy is required.

Clusters of clinozoisite needles are present in albite + white mica domains in rare granite samples, such as sample L08-04 (Chapter 4). This is comparable to local equilibration of feldspar domains observed in high pressure metagranites in the Alps, such as the Monte Mucrone meta-quartz diorite (Koons *et al.*, 1987), where plagioclase domains preserve the assemblage clinozoisite + jadeite + quartz. Jadeite breaks down at low pressures into the assemblage albite + white mica (Koons *et al.*, 1987), suggesting that the absence of jadeite could be explained by retrograde processes overprinting high–pressure mineral assemblages. The ultrahigh–pressure Su Lu metagranites record plagioclase domains that have been completely transformed into albite with tiny inclusions of epidote and muscovite and no jadeite (Hirajima *et al.*, 1993). Additionally, in New Caledonia, omphacite/jadeite is noted to be favoured in sodic rocks at high pressure, whereas zoisite is favoured in rocks with lower Na:Ca ratios (Black *et al.*, 1985), suggesting that clinopyroxene is not necessarily a stable phase in all high pressure mineral assemblages. Pseudomorphs of albite + muscovite after plagioclase in the Tso Morari metagranites may indicate that plagioclase transformed at high pressure and Na-cpx was replaced by muscovite + albite on retrogression. The absence of evidence for the former presence of jadeite makes this unlikely. However, the kinetics of the jadeite-albite transformation (e.g. Koons et al., 1987; Menold et al., 2009) indicate that it is possible that jadeite-bearing metagranite/gneiss from the Tso Morari complex was present but hasn't been observed. Rare clusters of clinozoisite needles indicate an effective bulk composition with a higher Ca content such as in sample L08-04.

Prograde grossular compositions in garnet rims are predicted to be very low in hydrous equilibrium models of sample 05-02 (Figure 19b), owing to the calculated presence of abundant Ca-rich clinopyroxene (>20% modal abundance). Observed grossular compositions in the garnet rim (10-15%) higher than predicted values suggest that the predicted mineral equilibria are not representative of reactions that occurred during the prograde history of the rock. Pseudosection models that suppress the nucleation of clinopyroxene (Figure 19c), representing the metastable persistence of plagioclase, predict grossular contents in garnet which are comparable to observed grossular compositions. Isopleths of the observed composition are subparallel in

these models and the intersection of grossular and pyrope isopleths occurs over a large range of pressure and temperature.

Primary plagioclase is not preserved in metagranites or the Puga Gneiss of the Tso Morari complex, suggesting that breakdown of plagioclase occurred. However, comparison of predicted vs observed grossular compositions in garnet suggest that complete transformation to a clinopyroxene-bearing assemblage did not occur at high pressure and plagioclase persisted metastably to high pressures. The magnitude of overstep recorded in the granites and orthogneisses of the Tso Morari complex is ~6-14 kbar, comparable to the rocks of the Flatraket complex in the Western Gneiss Region (Wain et al., 2001) and orthogneisses from the Luliang Shan in the North Qaidam metamorphic belt (Menold et al., 2009). Transformation of Ca-bearing plagioclase is therefore likely to have occurred at pressure conditions outside of the jadeite stability field, forming the local equilibrium assemblage of white mica + albite ± clinozoisite. Transformation of this domain may have been limited by fluid availability at high pressure, with isolated examples locally transforming to clinozoisite-bearing assemblages.

Summary

Samples of Puga Gneiss from different locations across the complex and varying deformation states have been studied in order to piece together the complex metamorphic history. The inferred relative timing of mineral growth in the Puga Gneiss is summarised in Figure 20, specific to a structurally deep sample which underwent deformation at temperatures > 550°C (e.g. 05-02), inferred from microstructural observations from deformed and undeformed samples across the complex.

The Puga Gneiss is formed from a heterogeneous, partially altered (hydrated) granitic protolith with the capacity to grow prograde garnet and kyanite. Evidence of high-pressure metamorphism is rare but is preserved in low–strain samples and prograde garnet poikiloblasts. The breakdown of feldspar to white mica and clinozoisite occurred in the absence of jadeite, prior to garnet growth at high pressure. Garnet core growth occurred in water–undersaturated conditions in the kyanite stability field and culminated in the growth of the garnet rims in hydrous, high–pressure conditions. The absence of jadeite-bearing assemblages and constraints on grossular content of high-pressure garnet from pseudosection modelling, indicates that plagioclase persisted metastably to high pressures. Metastable plagioclase is less dense and therefore more buoyant than an equilibrium assemblage containing jadeite, reducing the 'subductability' of the continental material. Hydrous breakdown of kyanite occurred after garnet growth, prior to fabric development. Poikiloblastic growth of plagioclase occurred prior to and postdating the main fabric forming event, forming lenses which partially overgrow the enclosing fabric which wraps around garnet poikiloblasts.

There is a significant difference in deformation mechanism and implied temperature of quartz recrystallisation between structurally low samples in the middle of the dome and structurally higher samples approaching the Zildat Shear Zone. Annealing of quartz took place in structurally deep samples, after the development of the high strain fabric (e.g. sample 05-02), whereas little annealing has taken place in structurally higher samples which record deformation in the subgrain rotation regime.

Retrograde metamorphism occurred following the development of the main fabric and includes the breakdown of garnet to form biotite, phengite breakdown to form biotite rims, growth of post-tectonic plagioclase porphyroblasts and epidote.

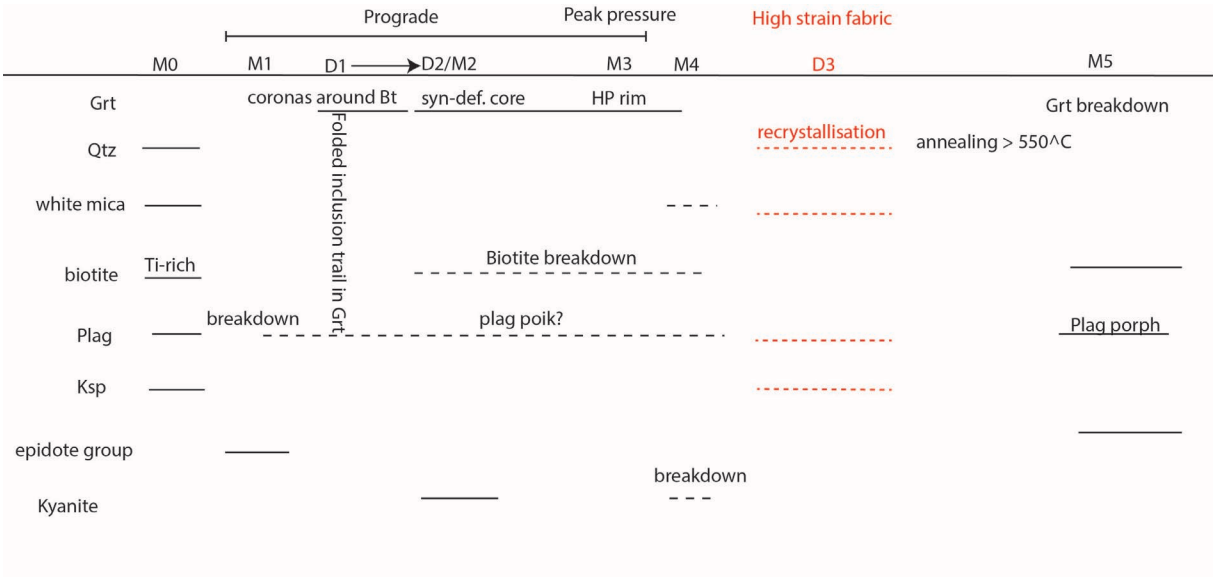


Figure 20 Microstructural observations summarised from samples across the Tso Morari complex, for a Puga Gneiss sample that underwent annealing at temperatures > 550°C.

Chapter 6 - EBSD analysis of palisade quartz textures: implications for coesite-quartz transformation

The contents of this chapter form the basis of the paper entitled "EBSD analysis of palisade quartz textures: implications for coesite-quartz transformation, Tso Morari complex, Himalaya" submitted to the Journal of Metamorphic Geology and currently *in review.* Co-author manuscript reviews were given by A. J. Parsons, G.E. Lloyd, D. J. Waters and R.M. Goddard.

Introduction

Ultrahigh–pressure conditions have been proposed in continental terranes such as the Alps (Chopin, 1984), the Himalaya (Sachan *et al.*, 2004), the Norwegian Caledonides (Smith, 1984), and the Dabie-Sulu region (Okay *et al.*, 1989). Such occurrences continue to drive debate over the extent and mechanisms by which continental crust may be subducted and exhumed during continental collision (e.g. Hacker and Gerya, 2013, Warren, 2013), and the importance of this process for orogenic cycles (e.g. Capitanio *et al.,* 2010; Afonso and Zlotnik, 2011). The dominantly felsic composition of ultrahigh–pressure continental terranes means that standard petrology-based techniques for determining peak pressures and temperatures are often not possible (e.g. O'Brien, 2018). In such cases, evidence for subduction to ultrahigh pressures is entirely dependent on the identification of coesite (Chopin, 1984; Smith, 1984). However, the low preservation potential of coesite, which rapidly transforms to quartz on decompression (Mosenfelder *et al.*, 1997; Perrillat *et al.*, 2003), makes detection of ultrahigh–pressure conditions in felsic rocks extremely difficult (e.g. Palin *et al.,* 2017), and direct evidence of coesite is mostly preserved as rare inclusions within minerals in mafic rocks (e.g. Wain, 1997). Here, we document previously unreported crystallographically constrained microstructures in quartz grains from a granite in the Tso Morari ultrahigh–pressure complex in Ladakh, NW Indian Himalaya that define transformation of coesite to quartz. These microstructures support previous studies that argue for subduction of Indian continental crust to ultrahigh pressures at onset of the Himalayan orogeny (O'Brien *et al.,* 1999; O'Brien, 2006; St-Onge *et al.*, 2013).

Palisade quartz as a replacement of coesite was originally recognized in the pyrope quartzite of the Dora Maira massif in the western Alps (Chopin, 1984). In these rocks, palisade quartz forms a rim of radially arranged elongate grains surrounding coesite inclusions within garnet and kyanite (e.g. Figure 1f and g). Schertl et al. (1991) also observed matrix palisade quartz in embayments into garnet and in quartz bands separated by folia of coarse–grained phengite. These were inferred to form by nucleation and growth of quartz from the margins of these bands inwards, from the external boundary of coesite domains towards a central medial line (Lenze and Stöckhert, 2008), similar to the formation of syntaxial veins. However, the formation mechanisms of palisade quartz textures are poorly understood and, thus far, their identification has been based purely on qualitative criteria (e.g. Lenze & Stöckhert, 2008). Previous studies of palisade quartz using electron backscatter diffraction (EBSD) techniques (Lenze and Stöckhert (2007, 2008)) proposed that the crystallography of coesite has no control over the nucleation and growth of quartz. However, these preliminary studies did not investigate the domainal fabric and grain boundary misorientation of quartz palisade microstructures. Similarly, no systematic crystallographic relationship is preserved in quartz grains in relation to old coesite in shear deformation experiments by Richter et al. (2016). In these experiments, the resulting fine-grained quartz shows a strong crystallographic preferred orientation, suggesting that the CPO is either inherited from precursor coesite, or deformation microstructures have overprinted preexisting relationships in quartz, forming a CPO.

Thermobarometric estimates from mafic eclogites (e.g. de Sigoyer et al., 1997; St-Onge et al., 2013), and the discovery of coesite inclusions in garnet rim zones within mafic eclogite boudins (Sachan et al., 2004), suggest that the mafic rocks of the Tso Morari complex experienced ultrahigh–pressure conditions of over 26 kbar (O'Brien et al., 1999; O'Brien, 2006; St-Onge et al., 2013). Despite the lack of evidence for ultrahigh–pressure metamorphism in the abundant felsic rocks of the Tso Morari complex, the distribution of mafic pods with evidence for ultrahigh–pressure metamorphism suggest that the whole of the Tso Morari complex subducted to ultrahigh pressures. This suggestion is supported by the discovery of rare eclogite-facies mineral assemblages preserved in metasedimentary rocks (Guillot et al., 1997) and evidence of partial transformation of primary igneous phases in low strain metagranites, limited by a lack of fluids needed to drive metamorphic reactions (Bidgood et al., 2018).

New petrographic EBSD and misorientation analyses of palisade quartz in the matrix of a granite from the Tso Morari complex is presented in order to investigate the crystallographic relationships of the coesite-quartz transformation. Several previously unreported textural observations are documented, including quartz palisade domains with outlines defined by relict igneous quartz grain shapes. This study provides the first detailed misorientation analysis of palisade quartz, from which the first reported evidence of twinning in coesite recorded in quartz is described. The observations presented suggest that the coesite-to-quartz transformation is crystallographically controlled and that palisade quartz textures may be quantitatively defined by specific crystallographic criteria, providing a new criterion, in cases where coesite is no longer preserved, for the identification of ultrahigh–pressure rocks and for deep subduction of continental terranes. The preservation of these microstructures is attributed to the relatively undeformed nature of the host rock and it is postulated that similar crystallographic relationships may exist between quartz palisade grains in other ultrahigh–pressure terranes which are yet to be investigated with misorientation analyses.

Sample description

Deformation in the Tso Morari nappe is highly heterogeneous, and local areas of undeformed granite grade laterally into strongly deformed orthogneissic mylonites (Girard and Bussy, 1999; Epard and Steck, 2008). In this chapter, a macroscopically undeformed S-type granite from the Tso Morari complex in the region of Polokongka La (WGS84 78.1882°E 33.2465°N) is analysed. This granite has an assemblage of quartz, K-feldspar, biotite, and white mica, with fine–grained domains of phengite + albite and phengite + garnet + kyanite that pseudomorph igneous plagioclase and cordierite respectively (see Chapter 4). Quartz in the granite typically occurs as distinct, 3-4 mm euhedral relict igneous grains, or as aggregates of recrystallized quartz that have collectively retained the original shapes of igneous quartz grains, as defined by surrounding feldspar domains. Some quartz grains exhibit synneusis, indicative of crystallization early in the magmatic history (see chapter 4, figure 3a). Specimen a05-10, collected from the Polokongka La granite forms the focus of this study. This sample contains isolated domains of recrystallized quartz grains, each of which originally formed as a single igneous quartz crystal, comparable in size and shape to the relict igneous

quartz grains in the surrounding undeformed granite (Figure 1). Many of these recrystallized quartz grains preserve palisade textures which consist of elongate grains spanning the igneous quartz domain.

The elongate larger grains that make up the palisade texture are ~0.5-2 mm in length and ~0.2-0.3 mm in width and have a strong grain shape alignment of grain long-axes observed across the thin-section. Intra-crystalline deformation features in these grains include undulose extinction, subgrain boundaries, and locally chessboard subgrains which are indicative of low-strain deformation at temperatures greater than 550-600°C (Kruhl, 1996; Wallis *et al.*, 2019). The grain boundaries are commonly lobate, on a scale of 0.05-0.1 mm. Smaller equant grains, ~0.05-0.1 mm in diameter, also occur in the quartz domains and are interpreted to have formed by dynamic recrystallisation of elongate grains (e.g. Passchier and Trouw, 2005).

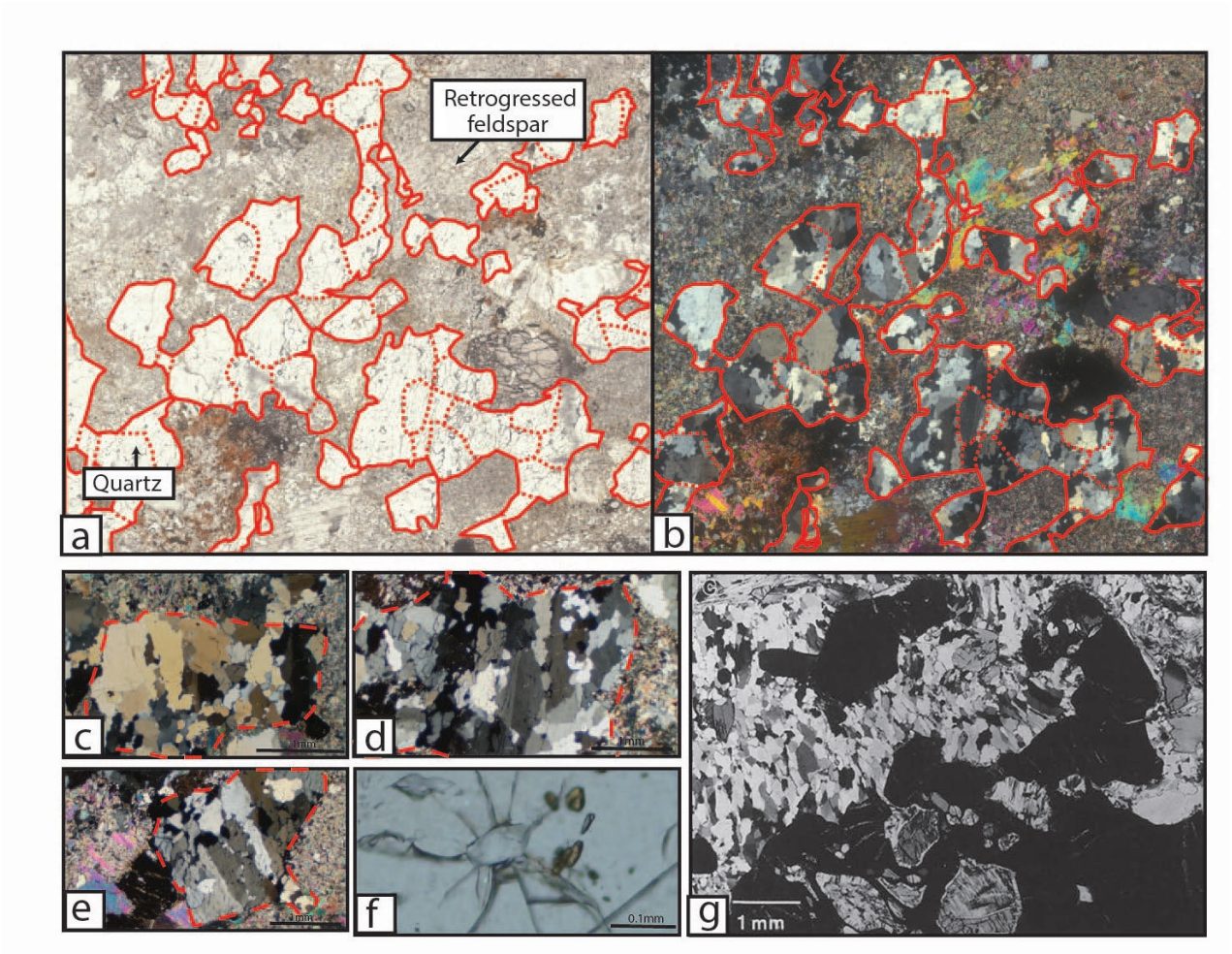


Figure 1- Sample a05-10 is a garnet-bearing granite boulder taken from the Polokongka La region of the Tso Morari complex, which forms an area of ~1 km² undeformed granite outcrop, 78.1882°E 33.2465°N (see figure 2). Photomicrographs a. and b. of sample a05-10 show distinct igneous quartz domains surrounded by fine grained mica aggregates, representing the original feldspar domains (Bidgood et al., 2019). Palisade quartz textures span the igneous domain. Intracrystalline deformation is present within the palisades. Grain boundary migration and subgrain formation is dominant along the grain boundaries of the palisades. c-e. Photomicrographs of sample a05-10 showing

palisade quartz textures confined to igneous quartz domain outlined by the red dotted lines. f. Photomicrograph of a polycrystalline quartz inclusion in garnet surrounded by radial fractures from sample 05-04, a mafic eclogite in the Tso Morari complex, 78.3610°E 33.1627°N. g. Photomicrograph of the Dora Maira Pyrope Quartzite from Schertl et al., 1991. Palisade quartz textures are replacing high relief coesite inclusions in garnet (isotropic) and coarser palisade quartz textures are preserved in the matrix, oriented perpendicular to quartz-garnet interface.

Crystallographic preferred orientation and grain boundary misorientation analysis

Methods

Quartz microstructures were initially investigated by optical microscopy in a petrographic polished thin section (30 μm thick). The quartz crystal preferred orientation (CPO) was determined using electron backscatter diffraction (EBSD) collected on an FEI Quanta 650 FEG E-Scanning electron microscope (E-SEM) equipped with Oxford Instruments Aztec (version 3.3) acquisition software and a NordlysNano EBSD camera. The sample was mapped at low vacuum (50 Pa), tilted to 70°, with an accelerating voltage of 30 kV and a working distance of 15 mm. In order to reduce the mapping time, the step size was 20 μm and pixels were binned (2 x 2 binning).

EBSD data were processed using Oxford Instruments Channel5 software. Isolated 'wildspikes' ≤ 1 pixels were removed. Non-indexed points which were surrounded by ≥ 6 indexed points were given the average orientation of their neighbours. Grain boundaries were defined by a misorientation of 10°.

Crystal axes and poles to crystal plane are plotted on pole figures with lower hemisphere projections and contoured in units of multiples of uniform distribution (m.u.d.). Pole figures were constructed for <*a*> and [*c*] crystallographic axes, and {*m*} {*r*} and {*z*} poles to planes. The <*a*> axes were plotted as a plane, rather than a direction, to avoid being plotted on opposite hemispheres. Grain boundary misorientations were calculated using the Channel 5 Tango software.

Results

Within each quartz domain, crystallographic axis orientations are organized into at least two 'single crystal' populations, each defined by a distinct point-maximum of *c*-axis orientations (Figure 3a,d). Each population of *c*-axis orientations derives from a texturally and spatially distinct subdomain of the larger domain (Figure 3b and c). Within each subdomain, grain boundary misorientation analysis demonstrates that adjacent palisade grains are typically misorientated with respect to each other by an equivalent misorientation angle/axis pair of 60°/[0001] (i.e. red lines on Figures. 3a,b,c and 4), corresponding to the location of the optically identified palisade quartz grain boundaries. This is consistent with *r*- and *z*-poles to planes orientations ($\{10\bar{1}1\}$ and $\{01\bar{1}1\}$ respectively), which both form six point-maxima around a single *c*-axis point-maximum, rather than the conventional three point-maxima displayed by a single crystal of quartz (Figures 3e,f, 5g,h). Populations of *c*-axis orientations from adjacent subdomains are misorientated by ~90°/<a> with respect to each other (Figure 3d, 5b). Boundaries between these subdomains bisect the encompassing quartz domain.

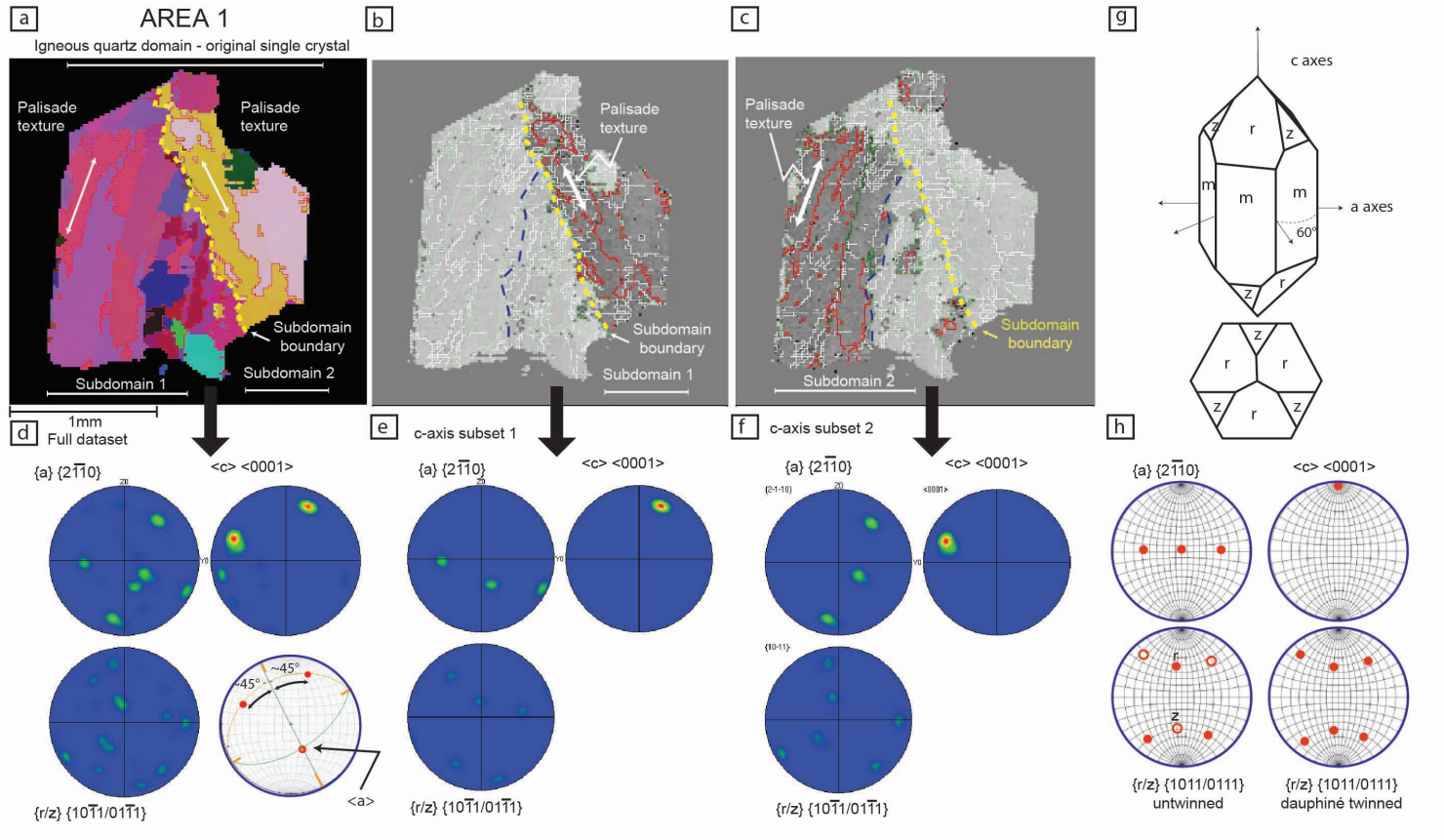


Figure 2 Results of EBSD and misorientation analysis of Area 1. All pole figures are lower hemisphere projections. a. Euler map showing orientation of individual grains. Yellow line marks the boundary between subdomains with different c-axis orientations, blue line marks a complex zone not defined by the c-axis subsets. Misorientations of 60° around [0001] are shown as red lines. b. Subdomain 1 band contrast and grain boundary map showing the grains corresponding to the c-axis orientation in e (dark grey). c. Subdomain 2 band contrast and grain boundary map showing the grains corresponding to the c-axis orientation in f (dark grey). d. Pole figure of full domain shown in a. showing <c> <0001> axis and {a} {2$\bar{1}\bar{1}$0} and {r/z} {10$\bar{1}$1}/{01$\bar{1}\bar{1}$} planes. Distinct c-axis clusters (red filled circles), which can be identified on the <c> axis plot which plot along a great circle, 90° apart, approximately bisected by the trace of the subdomain boundary marked by the yellow line. The pole to the great circle is shown as an unfilled circle. e. Pole figure of subdomain 1. Subsets defined by c-axis clusters shown in d. f. Pole figure of subdomain 2. Subsets defined by c-axis clusters shown in d. For further EBSD subsets of sample a05-10 see supporting information file 2. g. schematic cartoon of an ideal untwinned quartz crystal. h. Schematic pole figure for a single crystal of quartz with a vertical c-axis showing 6 a-axes (poles to m planes) around c axis at 60° to each other and the poles to 3 r/z planes around the c-axis at 134° to each other

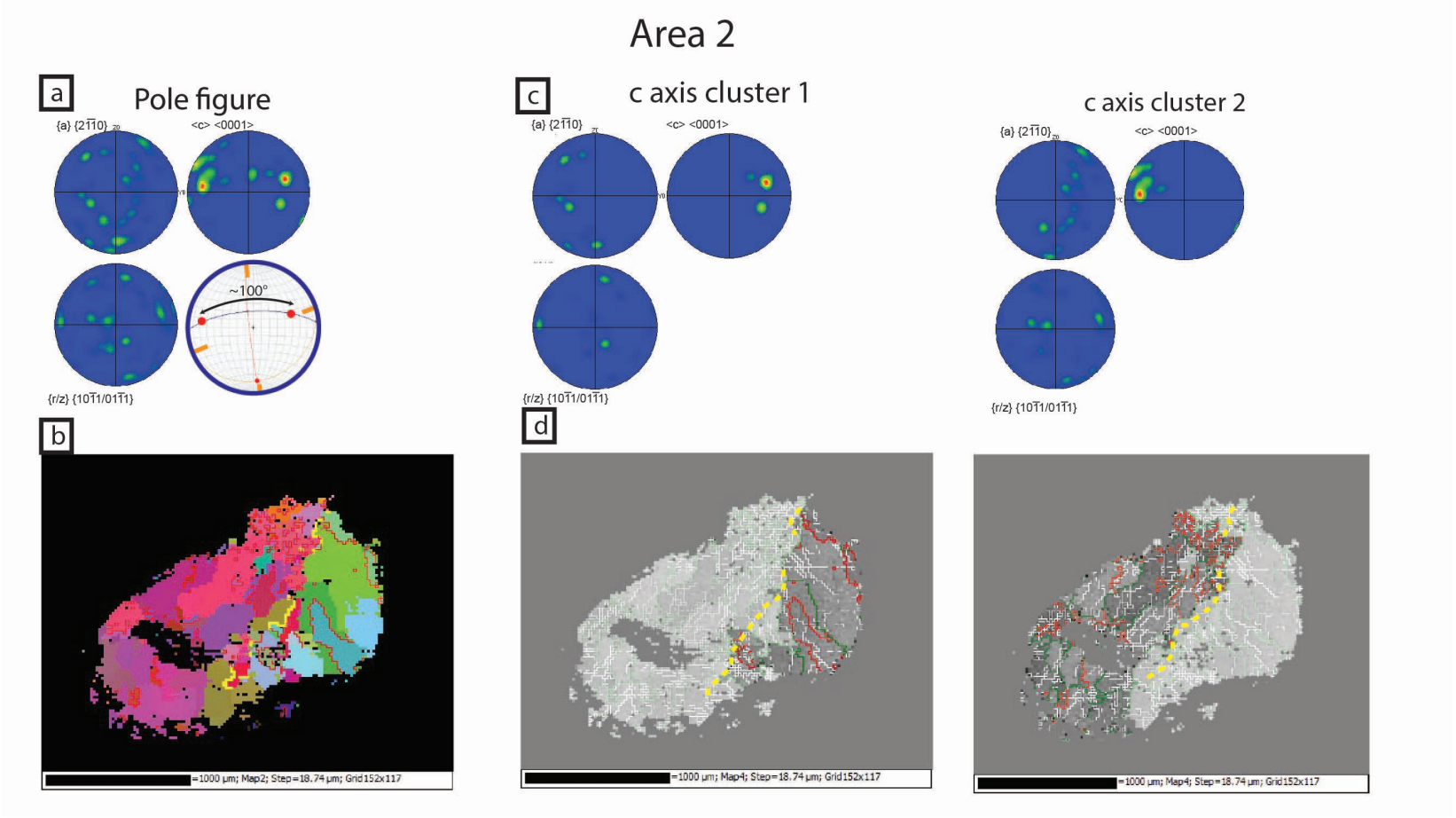


Figure 3. Further EBSD subset of sample a05-10. All pole figures are lower hemisphere projections. Area 2. a. Pole figure showing <c> <0001> axis and {a} $\{2\bar{1}\bar{1}0\}$ *and {r/z}* $\{10\bar{1}1/\{01\bar{1}\bar{1}\}$ *planes. Two distinct c-axis clusters (filled circles) can be identified on the <c> axis plot which plot along a great circle, 90° apart, approximately bisected by the trace of the subdomain boundary marked by the yellow line. The pole to the great circle is shown as a smaller unfilled circle. b. Euler map showing orientation of individual grains. Misorientations of 60° around [0001] are shown as red lines and misorientations of 90° ± 20° about (021) are shown as yellow lines. c. Pole figures showing 'single crystal' populations. Subsets defined by c-axis clusters shown in a. d. Clusters of grains corresponding to c-axis subsets. Yellow line marks the boundary between subdomains.*

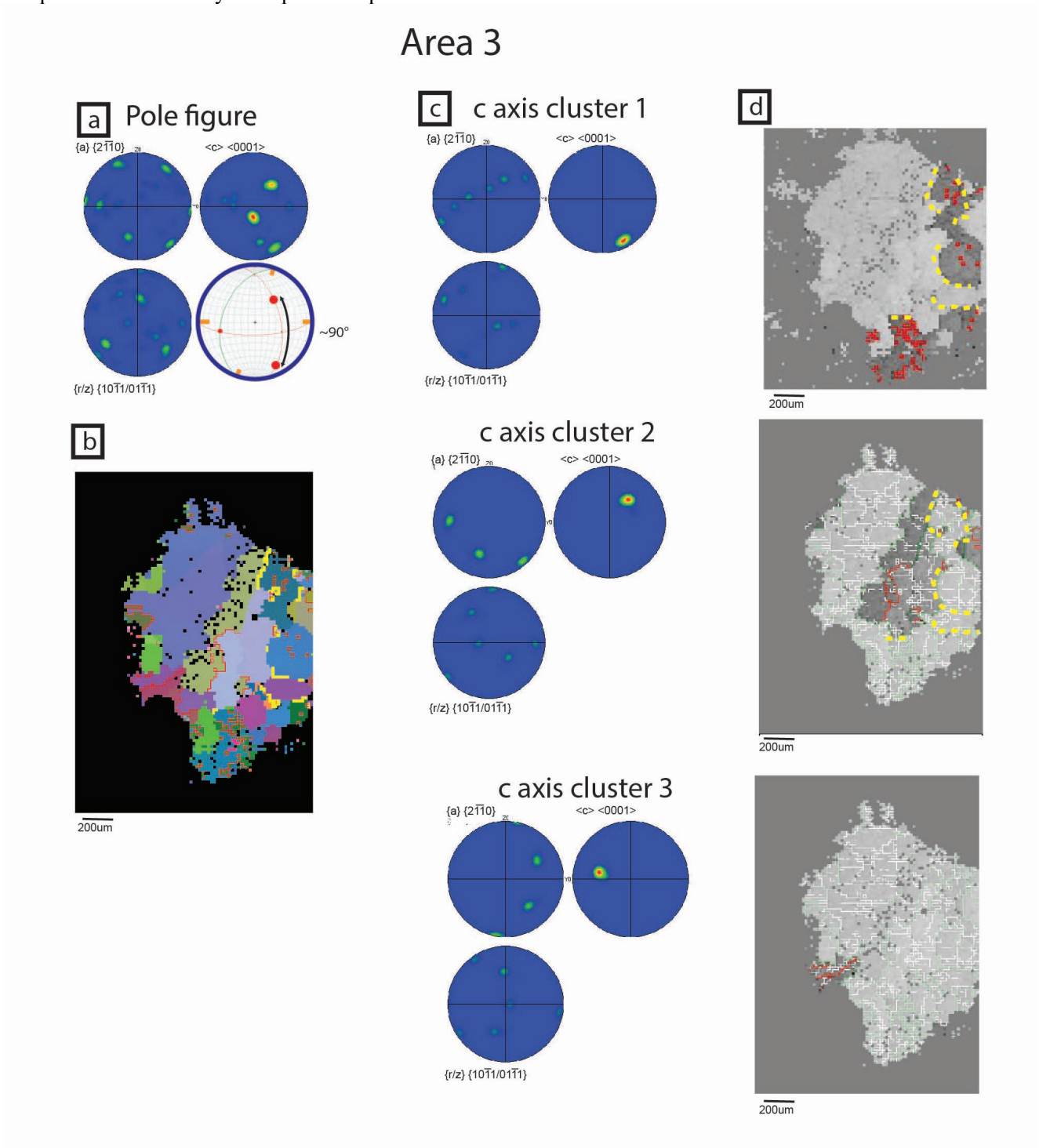


Figure 4 - Further EBSD subset of sample a05-10. All pole figures are lower hemisphere projections. Area 3. a. Pole figure showing <c> <0001> axis and {a} {2$\bar{1}\bar{1}$0} and {r/z} {10$\bar{1}$1/{01$\bar{1}\bar{1}$} planes. Two distinct c-axis clusters (filled circles) can be identified on the <c> axis plot which plot along a great circle, 90° apart, approximately bisected by the trace of the subdomain boundary marked by the yellow line. The pole to the great circle is shown as a smaller unfilled circle. b. Euler map showing orientation of individual grains. Misorientations of 60° around [0001] are shown as red lines and misorientations of 90° ± 20° about (021) are shown as yellow lines. c. Pole figures showing 'single crystal' populations. Subsets defined by c-axis clusters shown in a. d. Clusters of grains corresponding to c-axis subsets. Yellow line marks the boundary between subdomains.

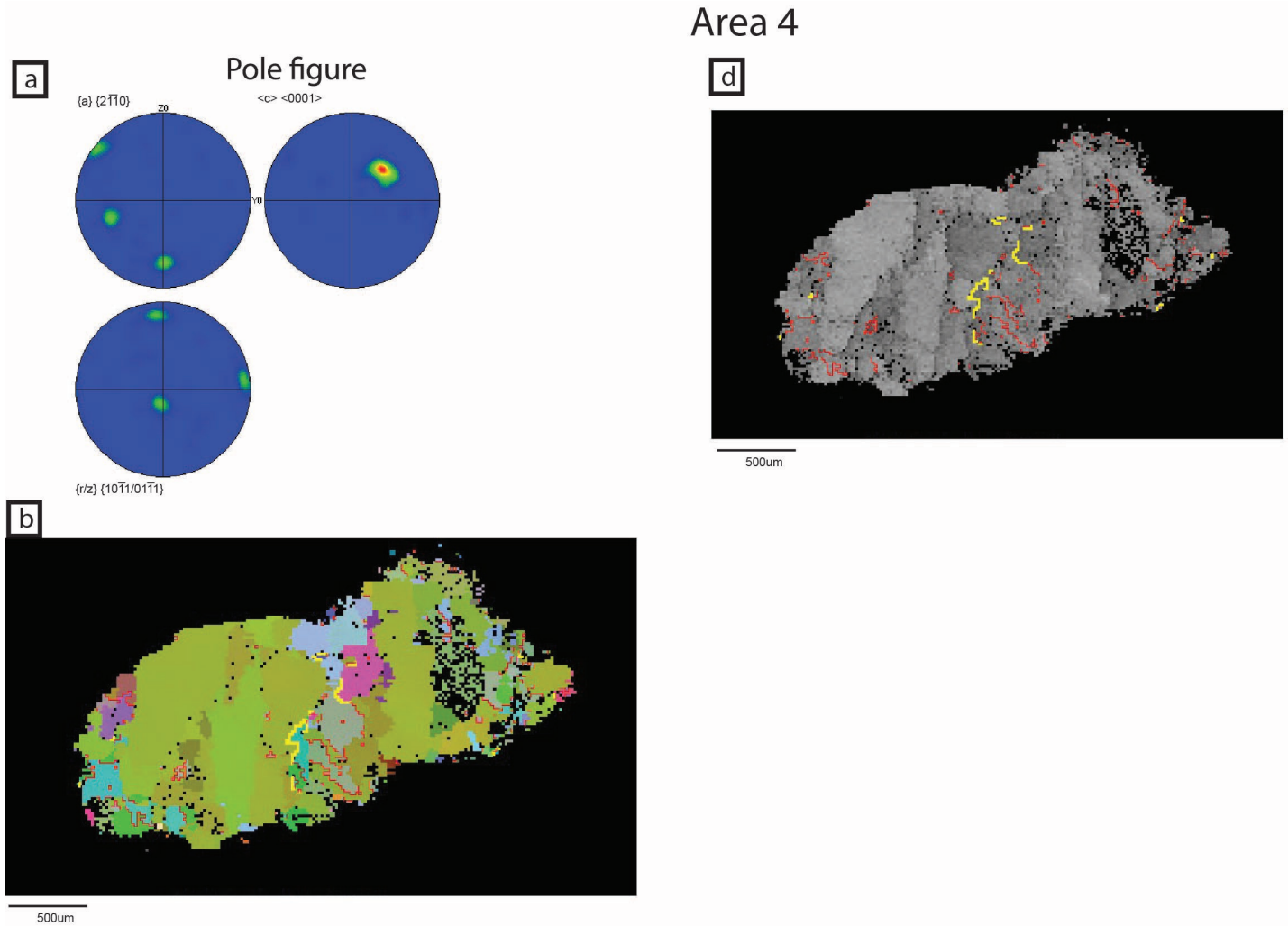


Figure 5 Further EBSD subset of sample a05-10. All pole figures are lower hemisphere projections. Area 4. a. Pole figure showing <c> <0001> axis and {a} $\{2\bar{1}\bar{1}0\}$ *and {r/z}* $\{10\bar{1}1/\{01\bar{1}1\}$ *planes. One c-axis cluster can be identified on the <c> axis plot, representing a 'single, untwinned, crystal' population with 3 r/z planes b. Euler map showing orientation of individual grains and c. band contrast map. Misorientations of 60° around [0001] are shown as red lines and misorientations of 90° ± 20° about (021) are shown as yellow lines.*

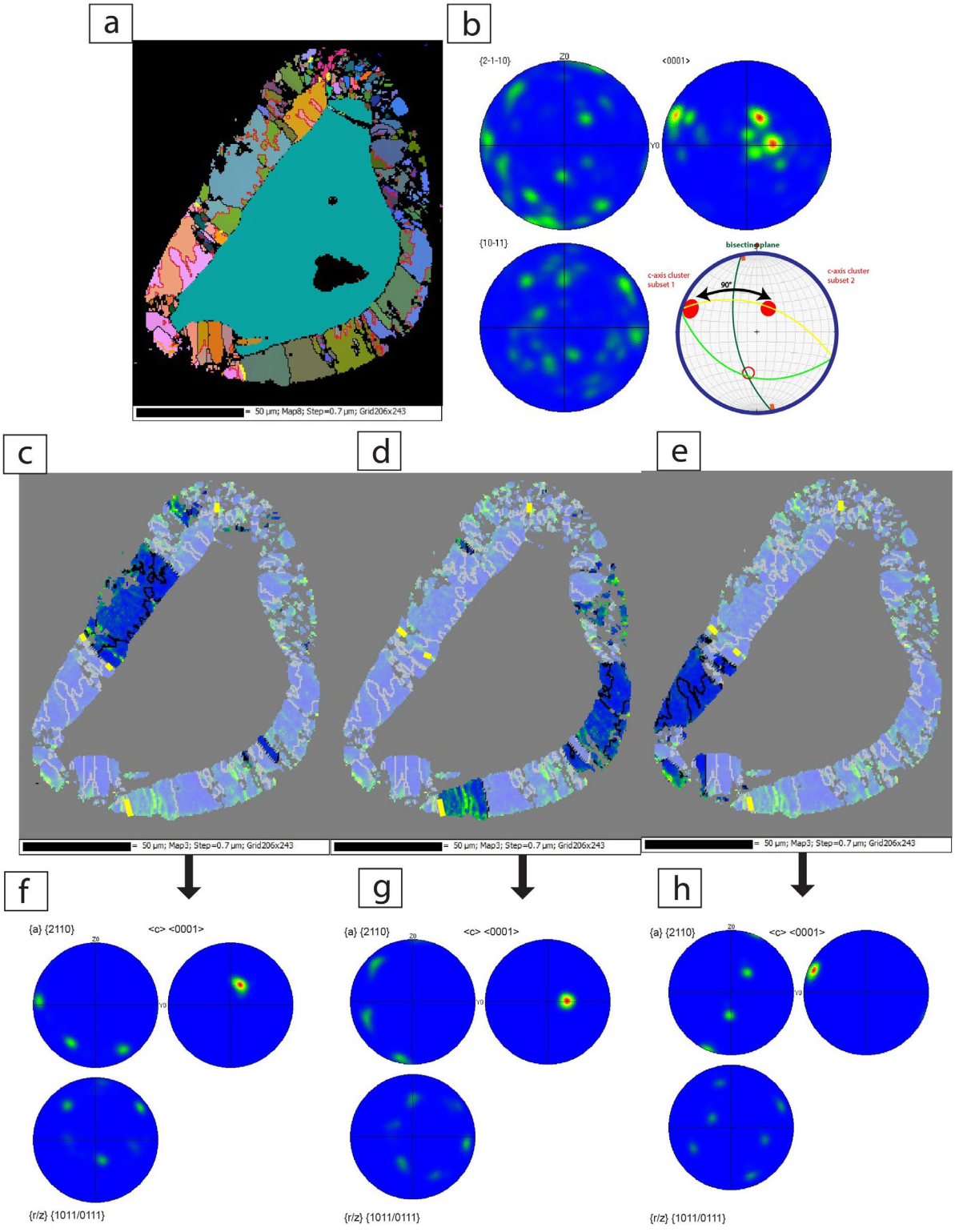


Figure 6 Sample DW09-53A from the Dora Maira Pyrope Quartzite. a. Euler map of coesite inclusion (teal) in garnet. Misorientations of 60°/[0001] are shown as red lines and $90^{\circ}/[02\bar{2}1]$ *are shown as yellow lines. b. quartz pole figure showing multiple c-axis clusters within the dataset. Clusters corresponding to subsets in c and e are plotted on a single steronet. c-e. Quartz grain map showing the grains which corresponds to the c-axis orientations below (blue). f-h. Subsets defined by c-axis clusters corresponding to grains above.*

Discussion

We suggest that the palisade quartz grains within sample a05-10 are consistent with complete transformation of original igneous quartz grains to coesite, followed by complete coesite-to-quartz transformation during decompression. Each igneous quartz grain is defined by a texturally and crystallographically distinct domain of recrystallized quartz which can be observed throughout the sample. Individual domains have different and unrelated crystallographic orientations, suggesting that the CPO within the domains is not deformation related, as this would produce crystallographically preferred orientations.

Crystallographically controlled nucleation of quartz from coesite

Within a single domain, large portions of the subdomain boundary approximate a misorientation angle/axis pair between adjacent subdomains of $90^{\circ}/[02\bar{2}1]$ (yellow lines in Fig. 4). This misorientation angle/axis pair lies within the 90°/(021) twinning plane of coesite (Jacob *et al.*, 2009; Schertl et al., 1991). We propose that the formation of two subdomains of quartz bisected by a boundary of this orientation has been inherited from a single grain of former twinned coesite.

Domain specific single crystal CPOs and inherited twinning relationships from former coesite preserved in quartz favour a crystallographic control on the nucleation of quartz from coesite. We therefore suggest that the systematically arranged orientations of palisade quartz grains within subdomains of a larger single domain are crystallographically controlled by the intra-crystalline structure and orientation of the precursor coesite. We suggest that the pseudohexagonal arrangement down [010] of coesite may provide a template for epitaxial nucleation and topotaxial growth of quartz palisades, where the *c*-axis of quartz would correspond to the inherited [010] axis of coesite (see table 2 in Jacob et al., 2009). Based on this hypothesis, quartz *c*-axes inherited from coesite should be orientated at c. 45° to the trace of the coesite twin plane (see figure 6). This relationship is consistently observed in sample a05-10 (see stereonet Figure 3d).

The consistent relationship between the location and orientation of the subdomain boundary with a misorientation equivalent to twinning in coesite, suggests that the crystallographic relationship between adjacent subdomains is an inherited record of twinning in the precursor coesite grains. This observation is at odds with Lenze and Stöckhert (2008), who interpreted the CPO of palisade quartz as randomly orientated

when plotted for a region of matrix quartz and for polycrystalline quartz inclusions. However, their study did not investigate domainal fabrics or grain boundary misorientation of quartz palisade microstructures as described in our study.

Palisade grain boundary misorientations

The misorientation of 60°/[0001] recorded between adjacent palisade grains is consistent with a dauphiné twin relationship (Green *et al.*, 1970; Tullis, 1970), which is defined by a 180° (equivalent to 60°) rotation about the c-axis in trigonal quartz (Frondel, 1945). Dauphiné twins are internal boundaries that cannot be observed optically. The 60°/[0001] misorientations that we observe occur across palisade grain boundaries.

Dauphiné twins can form in response to deviatoric stresses (e.g. Thomas and Wooster, 1951; Tullis, 1970; Lloyd, 2000; Pehl and Wenk, 2005); however, the undeformed nature of sample a05-10 and the different and unrelated crystallographic orientations between quartz domains makes this mechanism improbable. Instead, the presence of dauphiné twin-like relationships in a05-10 can be explained as a response to either (1) beta- to alpha-quartz transition (Putnis, 1992; Nord, 1994; Piazolo et al., 2005); or (2) a feature of the epitaxial nucleation of quartz on a coesite precursor. Given that pressure–temperature estimates from the Tso Morari complex record a retrograde path directly from the coesite stability field to that of alpha-quartz, the beta–alpha quartz transition can explain the presence of the dauphiné twin-like relationships only if beta-quartz formed as a kinetically favored metastable intermediate phase during nucleation and growth of alpha-quartz from coesite. There are currently no experimental observations which suggests that the metastable nucleation of beta quartz, within the alpha quartz stability field, is favourable.

Alternatively, we suggest that an alpha-quartz grain nucleating epitaxially on coesite may adopt one of two orientations derived from the precursor coesite that are related to each other by the dauphiné twin law. This is consistent with the nucleation and growth hypothesis observed during the coesite-quartz transition in experimental studies by Mosenfelder and Bohlen (1997), where characteristic microtextures are observed, similar to those in natural UHP rocks. Crystallographically controlled nucleation of quartz after coesite followed by interface-controlled growth would result in a palisade aggregate in which adjacent grains have a dauphiné twin-like relationship, which we observe in sample a05-10. This hypothesis also explains why the observed dauphine twin-like misorientations occur across palisade grain boundaries.

The coesite-quartz transformation involves a 7% increase in volume (Van Der Molen *et al.*, 1986) which, when combined with the hypothesised nucleation and growth mechanism, may slightly distort pre-existing igneous textural relationships. However, the domainal structure of quartz orientations, observed misorientations between grains and inherited crystallographic relationships would remain a common feature within each polycrystalline quartz domain.

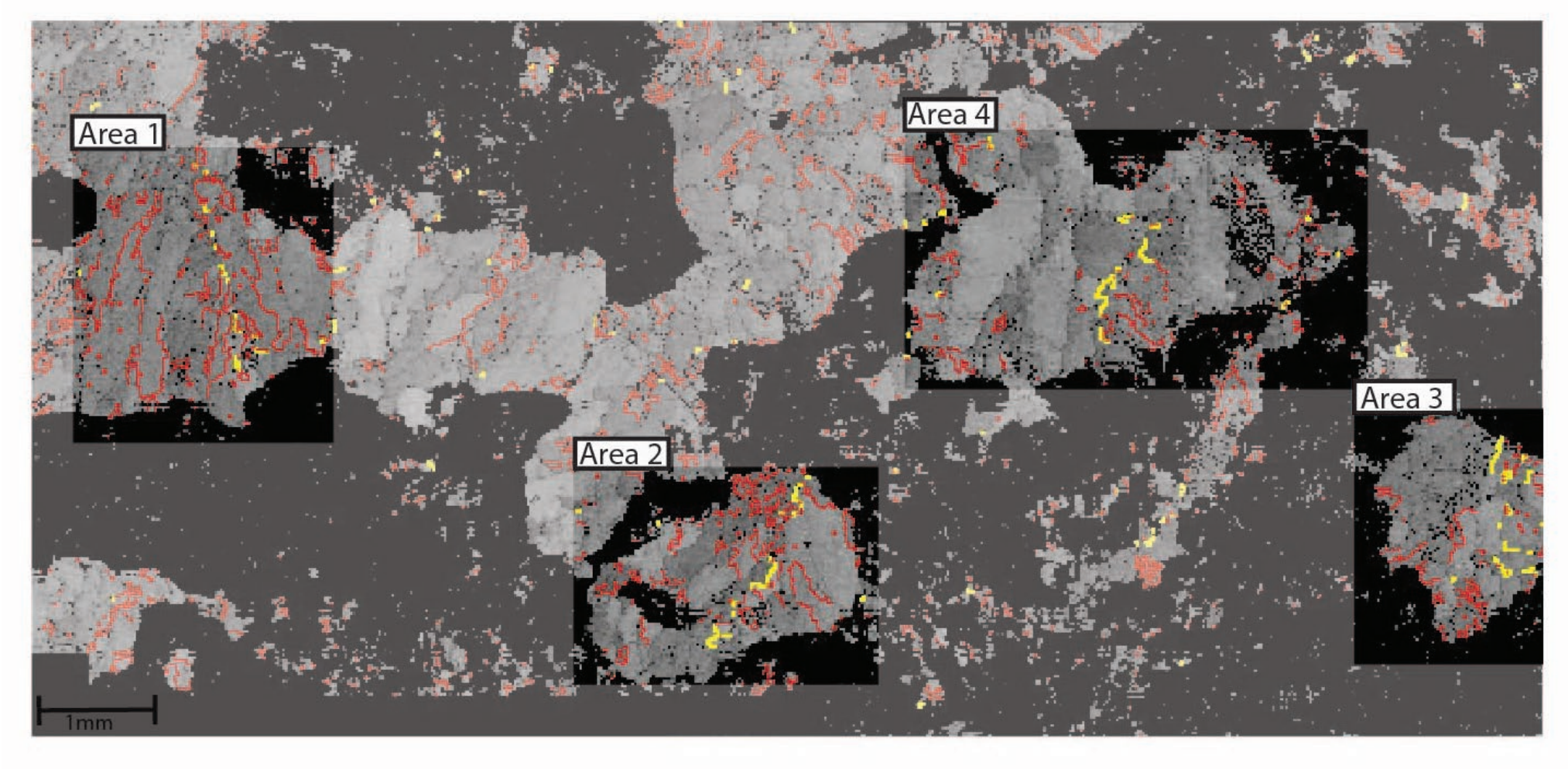


Figure 7 Band contrast map showing targeted areas. Misorientations of 60°/[0001] are shown as red lines and misorientations of $90^{\circ}/[02\bar{2}1]$ *are shown as yellow lines. The yellow lines are not continuous but define the boundary between texturally distinct subdomains of palisade quartz grains within each larger encompassing domain.*

Peak pressure of the Tso Morari complex

The preservation of microstructures after coesite confirm that sample a05-10 from the centre of the Tso Morari complex was subducted to UHP. However, microstructures after coesite are not a common feature in the granites of the Tso Morari dome and single quartz crystals, which did not undergo transformation to coesite, microstructures are observed in samples from within the Polokongka La region. The ease at which the coesite-forming reaction occurs (Perrillat, 2008) suggests that the entirety of the Polokongka La region, if subducted to the coesite stability field, would show quartz microstructures indicative of transformation to quartz from coesite. However, Mosenfelder et al. (2005) highlighted the importance of fluid for catalysing the coesite to quartz reaction, suggesting that dry conditions could aid the preservation of coesite. If fluid also acts as a catalyst for the quartz to coesite reaction, the dry conditions preserved in the Tso Morari metagranites could therefore have caused the coesite-forming reaction to have been overstepped. However, the potential magnitude of overstep able to be maintained by quartz grains is currently unknown.

The presence of untransformed quartz and textures after coesite in the Polokongka La region of the Tso Morari dome, may indicate that some areas achieved UHP conditions whereas others did not. Heterogeneous distribution of pressure within subducted crustal material could push some regions into the coesite stability field if the depth of subduction is equivalent to the quartz-coesite transition at approximately 26 kbar at their metamorphic peak. The feasibility of this hypothesis with respect to the predicted magnitude of crustal overpressures, potential subdivision of the Tso Morari complex and investigating other factor affecting the coesite-quartz transitions are discussed in chapter 8 in the section entitled ‘Peak Metamorphism’.

Implications for the investigation of continental subduction to ultrahigh–pressure conditions

The formation and preservation of peak-metamorphic textures in ultrahigh–pressure terranes depends on, (1) stresses, temperature and the availability of fluids needed to mediate prograde metamorphic reactions at ultrahigh–pressure conditions (e.g. Austrheim, 1987; Terry and Heidelbach, 2006), and (2) lack of exhumation-related deformation and metamorphism that would otherwise overprint and remove any record of peak conditions (e.g. Palin *et al.*, 2014). Ultrahigh–pressure indicators may therefore be easier to find in

the least deformed regions of an ultrahigh–pressure terrane, such as low–strain granitic and mafic boudins, despite the entire terrane having undergone subduction to ultrahigh–pressure depths (e.g. Palin et al., 2014).

In other ultrahigh–pressure terranes, evidence of transformation of mineral assemblages at ultrahigh–pressure conditions is typically widespread but not abundant (e.g. Cuthbert *et al.*, 2000). For example, the Western Gneiss Region (WGR) of Norway is a well-studied high-pressure terrane occupying 30,000 km^2, ~5000 km^2 of which is considered ultrahigh–pressure. There are fifteen confirmed occurrences of coesite and microdiamond that are considered indigenous to the crust (Smith, 1984; Smith and Lappin, 1989; Wain, 1997; Cuthbert *et al.*, 2000; Wain *et al.*, 2000; Carswell *et al.*, 2001, 2003; Root *et al.*, 2005; Vrijmoed *et al.*, 2006; Schönig *et al.*, 2018). The number of coesite and diamond occurrences is very small considering the size of the terrane. There are also numerous occurrences of polycrystalline quartz in the WGR which are thought to have formed after coesite (see Peterman *et al.*, 2009, figure 1) and are corroborated by *P-T* estimates from conventional thermobarometry and pseudosection modelling in rocks of suitable bulk composition. Additionally, in the Greenland Caledonides, coesite inclusions have been found included in zircons from one outcrop (McClelland *et al.*, 2006), suggesting that the polycrystalline quartz, found as inclusions in garnet-bearing gneisses that host eclogites facies mafic rocks throughout the province, are indicative of ultrahigh–pressure conditions (Gilotti and Krogh Ravna, 2002).

The above-mentioned occurrences of quartz-after-coesite microstructures are based on qualitative assessments of optically visible microstructures. A quantitative approach to identifying these microstructures would give a better understanding of the extent of the ultrahigh–pressure terrane and allow a more detailed tectonic interpretation to be presented. Even within a well-studied terrane such as the WGR, a reliable, quantitative indicator of the former presence of coesite could increase the number of known ultrahigh–pressure localities and would not be reliant upon less robust indicators such as conventional thermobarometric constraints and thermodynamic modelling. A quantitative approach to identifying the former presence of coesite would be particularly useful in the host quartzofeldspathic gneisses of the WGR, where evidence for ultrahigh–pressure is limited to polycrystalline quartz inclusions in garnet and clinozoisite (Wain, 1997). That such microstructures and their critical crystallographic relationships have until now not been described and evaluated is understandable. Misorientation analysis is not commonly applied to such material, and the preservation of the microstructures relies on the relatively low state of strain in the metagranite.

Quartz microstructures in low strain granitoids have not been comprehensively studied in any ultrahigh–pressure terrane, including the Polokongka La region of the Tso Morari nappe. We suggest therefore that palisade quartz may be recognizable in other low strain granitoids within ultrahigh–pressure terranes with targeted sampling. The isolated occurrence of palisade quartz in sample a05-10 of the Polokongka La granite represents a crucial observation for understanding the pressure-temperature evolution of this ultrahigh–pressure terrane. Matrix palisade quartz after coesite is infrequently described, and previously its identification has been based purely upon a qualitative set of criteria. Palisade textures could also be readily mistaken for a deformation-related shape fabric, raising the possibility that some occurrences of ultrahigh–pressure conditions have been overlooked, or misidentified. In contrast, our observations provide a quantitative, crystallographically defined set of criteria by which quartz-after-coesite microstructures may be identified and used as an indicator of ultrahigh–pressure conditions. Additional EBSD studies of palisade quartz textures from other ultrahigh–pressure occurrences are required in order to confirm this observation. However, we believe that the current absence of comparable studies reflects the limited attention given to felsic lithologies, and specifically the lack of EBSD-based misorientation analyses of palisade quartz textures and the coesite-to-quartz transformation.

The study of subducted continental fragments is important for understanding the geodynamic processes of deep subduction. Our observations of dauphiné twin-like relationships and inherited coesite twinning, which formed during crystallographically controlled nucleation and growth of palisade quartz, may be a common and defining feature of quartz-after-coesite, and in the absence of coesite, may represent the only quantitative indicator of ultrahigh–pressure conditions. Further testing of our proposed ultrahigh–pressure indicator should be recognized as an essential target for future studies of orogenesis and continental subduction, particularly in low-strain enclaves of felsic and siliceous rocks of continental terranes.

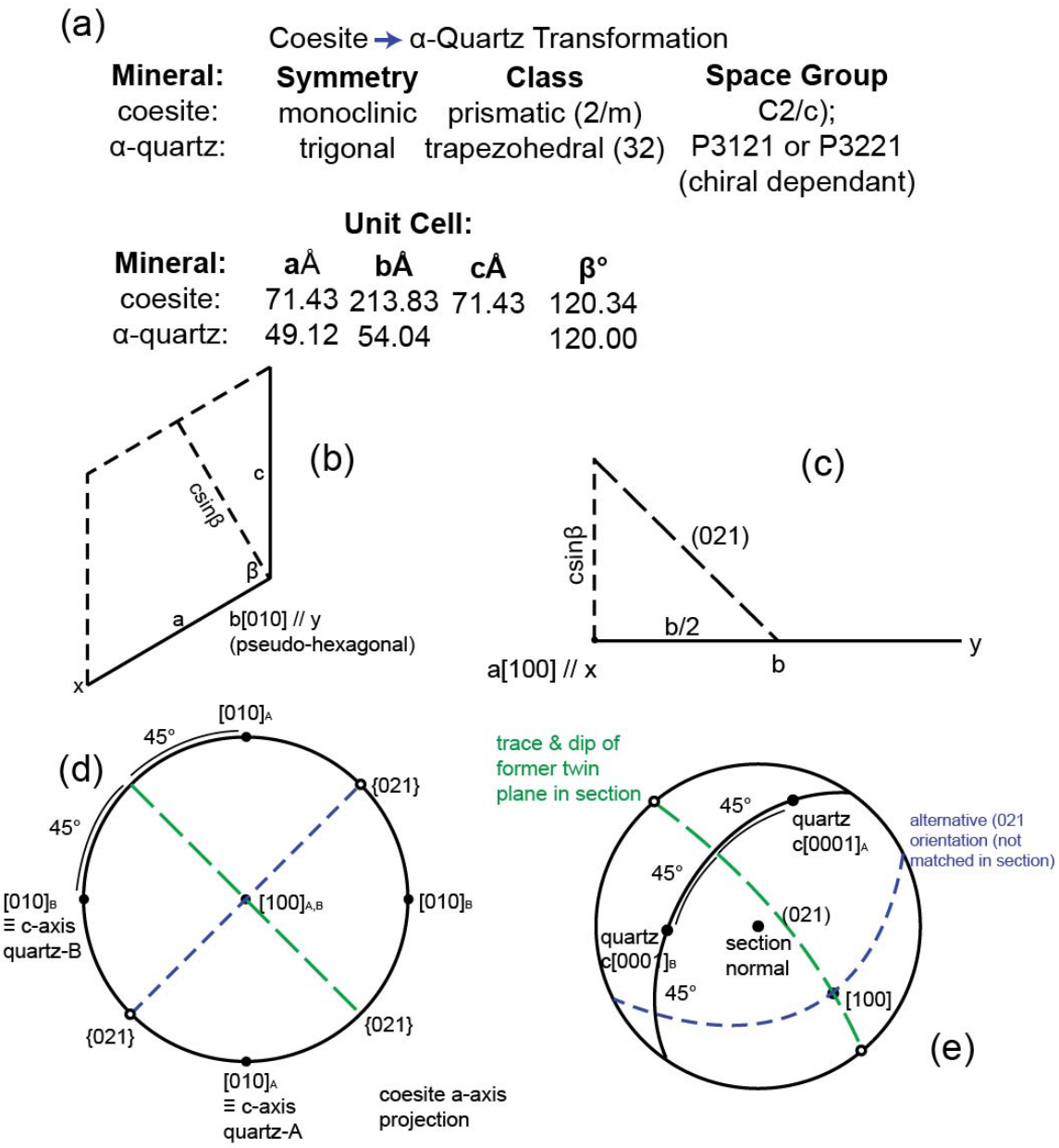


Figure 8 a. Summary of coesite and α-quartz crystallography. b. coesite unit cell down b[010]. c. coesite unit cell a[100], csinβ ≈ b/2. d. stereographic projection of coesite showing (021) twin planes and orientation of coesite [010] and quartz c-axis. e. stereographic projection of coesite showing a dipping (021) twin plane. Quartz c-axis inherited from coesite is orientated at 45° to (021) along [010]. Two possible orientations of the (021) twin plane are shown.

Summary

An undeformed metagranite sample from the ultrahigh–pressure Tso Morari complex contains discrete domains of recrystallized quartz with palisade textures. The findings in this study document several previously unreported textural observations by combining optical microscopy, EBSD, and misorientation analysis. Each quartz domain originally formed a single igneous quartz crystal that transformed to coesite during subduction to ultrahigh–pressure depths and then transformed back to quartz with palisade textures during exhumation. EBSD and misorientation analysis indicate that quartz CPOs preserve elements of the pseudo-hexagonal arrangements in precursor coesite, demonstrating that there was a crystallographic control during the nucleation and growth of palisade quartz after coesite, where the c-axis of quartz is aligned with the pseudohexagonal [010] axis of coesite. The observations in this study are believed to be the first reported evidence of twinning in former coesite inherited in daughter grains of quartz. The crystallographic patterns observed provide the first quantitative approach of using CPO to identify and define palisade quartz textures. Such observations are an important addition to interpreting the limited examples of palisade quartz textures in the matrix of natural samples and provide a useful indicator of burial to ultrahigh–pressure conditions in terrains where coesite preservation is limited.

Chapter 7 - Geochronology of the Tso Morari nappe

This chapter was written by A.K. Bidgood. U-Pb LA-ICP-MS geochronology was performed by A.K. Bidgood at NIGL with assistance from N.M.W Roberts. U-Pb CA-ID-TIMS geochronology was performed by S. Tapster at NIGL, with sample preparation by A.K. Bidgood. Mass spectrometer technical specifications and working conditions given in Appendix 2 were provided by N.M.W Roberts and S. Tapster.

Introduction

The exhumation rates of ultrahigh–pressure terranes are mostly constrained by peak metamorphic ages on minerals formed at mantle depths, combined with $^{40}Ar/^{39}Ar$ cooling ages recorded at mid crustal levels. The difference in depth and temperature (>300°C) and uncertainty over the *P-T* path traversed by the samples during exhumation limits our understanding of the geodynamic context and exhumation mechanisms involved. Identifying these mechanisms ideally requires a measure of the rates of cooling and decompression, and interpretation of any spatial variation.

Current ages of metamorphism of the Tso Morari nappe range from 70-35 Ma (De Sigoyer *et al*., 2000; Leech *et al*., 2007; St-Onge *et al*., 2013; Donaldson *et al*., 2013) and 31-29 Ma (De Sigoyer *et al*., 2000), with the ages of high pressure metamorphism in the range of 54-42 Ma (Leech *et al*., 2007; St-Onge *et al*., 2013; Donaldson *et al*., 2013). A gap exists between older metamorphic ages of >40 Ma ages and the younger Ar-Ar and fission track ages of < 30 Ma (Schlup *et al.*, 2003) (Figure 1). New U-Pb ages of titanite and rutile in this study, fall within this gap, providing a constraint on the age that these rocks attained at crustal depths during exhumation.

The rutile and titanite data provide constraints on a part of the geochronological history of the Tso Morari complex that currently is lacking in age data but is extensively recorded in retrograde metamorphic microstructures and in amphibole and garnet chemistry. In particular, one eclogite sample (a03-12) provided high-precision zircon Chemical Abrasion Isotope Dilution Thermal Ion Mass Spectrometry (CA-ID-TIMS) ages together with Laser Ablation Inductively Coupled Plasma Mass Spectrometry (LA-ICP-MS) rutile and titanite ages and trace element data, allowing a more detailed interpretation of the *P-T-t* path of this rock.

Rutile and titanite ages across the nappe provide a new dataset which can be used in conjunction with temperature estimates from the Zr content of rutile to further constrain the exhumation of the Tso Morari nappe.

Geochronology of the Tso Morari eclogites

Ultrahigh pressure metamorphism in the Tso Morari complex is currently estimated at 53-37 Ma. Despite various efforts at dating eclogite facies metamorphism in the Tso Morari dome, a consensus has not been reached. Initial estimates by De Sigoyer *et al*. (2000) used Sm-Nd isochron ages on garnet-glaucophane-whole rock (WR), Lu-Hf garnet-omphacite-WR, Sm-Nd garnet-amphibole-WR and U-Pb in allanite techniques, yielding ages of 55 ± 7 Ma, 55 ± 12 Ma, 47 ± 11 Ma and 55 ± 17 Ma, respectively. These estimates attempted to date minerals which can definitively be linked to a metamorphic stage. However, these estimates all lie within the same uncertainty window as the stages related to exhumation of the Tso Morari dome at 48 ± 2 Ma (Ar-Ar phengite), 45 ± 11 Ma (Rb-Sr phengite-apatite-rutile metapelite) (De Sigoyer *et al.*, 2000).

Three studies, Leech *et al*., 2007; St-Onge *et al*., 2013 and Donaldson *et al*., 2013 have used in-situ U-Pb zircon techniques on rocks from the Tso Morari nappe. Leech *et al*. (2007) presents three clusters of ages for growth stages in zircon rims, analysed by SHRIMP U-Pb of zircon separates, from quartzofeldspathic gneisses from within the Tso Morari nappe. These age clusters are thought to represent ultrahigh–pressure metamorphism at 53.3 ± 0.7 Ma, followed by further eclogite facies metamorphism and an amphibolite facies overprint at 45.2 ± 0.7 Ma. St-Onge *et al*. (2013) present SHRIMP U-Pb *in situ* zircon ages, providing petrological context for the ages of the zircons due to their location within host phases, in combination with petrological modelling. Zircon inclusions in garnet cores give ages of 58 ± 2.2 Ma (n=2) and zircons in the matrix give ages of 50.8 ± 1.4 Ma (n=4), bracketing ultrahigh–pressure metamorphism.

Donaldson *et al.* (2013) used LA-SS-ICP-MS to measure the U-(Th)-Pb and REE abundances of in situ zircon from two mafic eclogites, located ~10 km apart. Zircon grains of approximately 12-30 μm were measured using a spot size of 12-14 μm increasing the uncertainty on the analyses to 5%. The resulting age for sample DD71710-2B, located in the Berthelsen outcrop and the same location of sample L08-03A (St-Onge *et al*., 2013), yielded an age of 44.2 ± 1.2 Ma (n=61), whereas sample CM71710-4, located at the bridge outcrop to the south (equivalent to sample AB04-05), yielded an age of 45.3 ± 1.6 Ma (n=37). The age data presented

by Donaldson *et al.,* (2013) is thought to represent multiple populations of zircon growth, despite the REE patterns displaying similar characteristics of flat, heavy REEs and no Eu anomaly, and is interpreted to represent protracted zircon growth or recrystallisation in the eclogite facies during prograde/ultrahigh–pressure metamorphism.

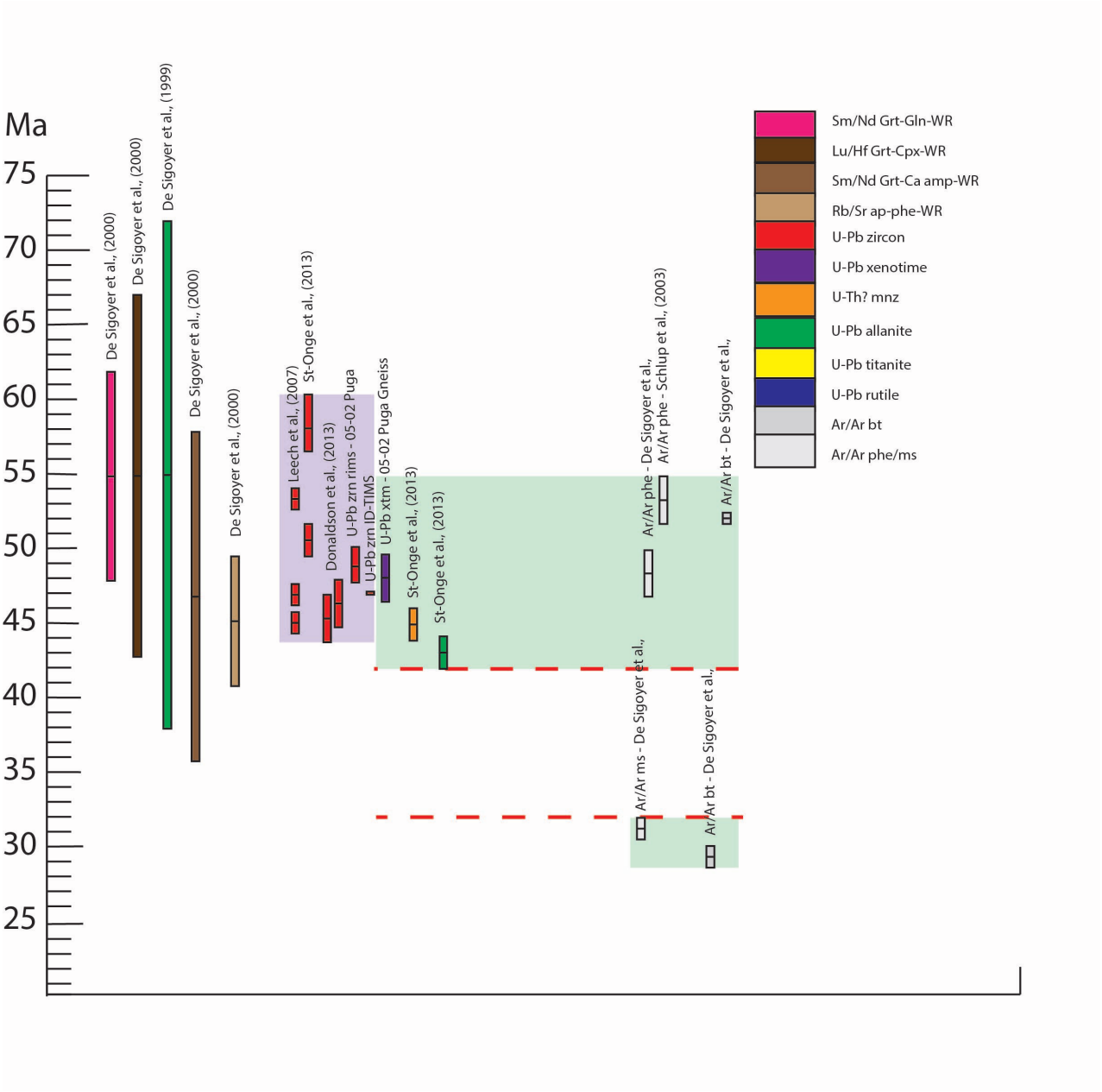


Figure 1 Summary of geochronology results for the Tso Morari complex. Colours refer to mineral and dating method. Purple box denotes high pressure ages, green box denotes ages within the crust. Red dashed lines highlight the absence of current published data between 42-32 Ma.

Methods

Radioisotopic dating

A detailed description of methods used can be found in Appendix 2 with the raw data in Appendix 3. Zircon, rutile and titanite grains were separated at the Geochronology and Tracers Facility, British Geological Survey (formerly known as the NERC Isotope Geosciences Laboratory, NIGL). Zircon grains from the heavy, non-magnetic fraction were imaged via cathodoluminescence (CL) using an FEI Quanta 650 FEG E-Scanning electron microscope (E-SEM) at the University of Oxford, using a 10 kV electron beam, 16mm working distance and a beam current of 0.49nA. Zircon grains from the felsic rocks were also mounted on sticky tape in order to analyse the <10 μm thick rims. Rutile and titanite grains chosen for analysis were picked from the non-magnetic fraction and were imaged via backscatter electron imaging to determine the homogeneity of the grains chosen for analysis. None of the rutile grains showed any evidence of zoning and grains containing inclusions of zircon or alteration to titanite were avoided.

U-(Th)-Pb isotopes in monazite, zircon, xenotime and rutile were analysed at the Geochronology and Tracers Facility, British Geological Survey, using a Nu Instruments AttoM HR sector-field single-collector inductively coupled plasma mass spectrometer (SC-ICP-MS). Details of the technical aspects and geochronological applications of the Nu Attom ICP-MS are found in (Roberts *et al.*, 2011). Xenotime grains in sample 05-02 were analysed in thin section in order to preserve the petrographic relationships observed.

Individual zircon grains were extracted after LA-ICP-MS analysis from the epoxy resin for further analysis by CA-ID-TIMS at the Geochronology and Tracers Facility; these U-Pb analyses follow analytical and data reduction methods described by Tapster *et al*. (2016) and utilised the ET535 EARTHTIME mixed tracer (Condon *et al*. 2015).

Zirconium in Rutile thermometry

Mineral compositions were obtained on rutile separates from a Cameca SX-five field-emission electron probe micro-analyser (EPMA) equipped with wavelength dispersive spectrometers, including 2 spectrometers with large PET crystals, at the Department of Earth Sciences, University of Oxford. Zr, Nb, Cr and Fe were analysed at an accelerating voltage of 15 KV with a current of 200 nA and counting times of 300s on peak and 150s on background position with a 2 μm beam. Si and Ca were measured using EDS to determine whether any titanite was picked up in the analysis. A matrix correction was applied to all analysis assuming a matrix composition of TiO_2. Elements were calibrated using a range of natural and synthetic standards.

The primary standard used for Zr analysis was R632 with a Zr content of 4294 ± 196 ppm (Axelsson *et al.*, 2018). Individual rutile grains for this standard have a homogeneous composition of a range of trace elements including Zr, U, Pb, Cr, Fe, V, Mo, Sb, Sn, Hf, Ta and W, making this a suitable reference material for age and temperature determinations (Axelsson *et al*, 2018). The secondary standard used was R10 rutile standard with a Zr content of 759 μg/g (Luvizotto *et al.*, 2009). Synthetic TiO2 was used as a blank.

The elements Fe, Nb and Cr were measured during the analysis to determine the geochemical clusters of different samples. Data exhibiting excursions in Fe, Ca and Si content were excluded. Data with much larger Zr concentrations than analyses on the same grain were also excluded due to the confirmed presence of zircon inclusions.

Temperature calculations were made using the thermometer of Tomkins *et al.* (2007) with an independent pressure estimate of 10 kbar, corresponding to the pressure of the amphibolite facies overprint as predicted by St-Onge *et al*. (2011). Pressures of 8 kbar, 12 kbar and 27 kbar were also used to determine the pressure dependence of the thermometer at measured Zr concentrations and form an envelope around the range of predicted pressures for the amphibolite facies overprint recorded in the eclogites and host felsic rocks.

Spectrometer	Element	Crystal	Peak	Background	Standard
1	Nb	PET	65397	+1000 - 1400	LiNbO3
2	Fe	LIF	48079	± 1000	Andradite
3	Zr	LPET	69415	+800 -500	R632 rutile
4	Cr	PET	26200	± 1000	Cr
5	Zr	LPET	69377	+800 -500	R632 rutile

Table 1 Analytical conditions used in Zr in rutile analysis

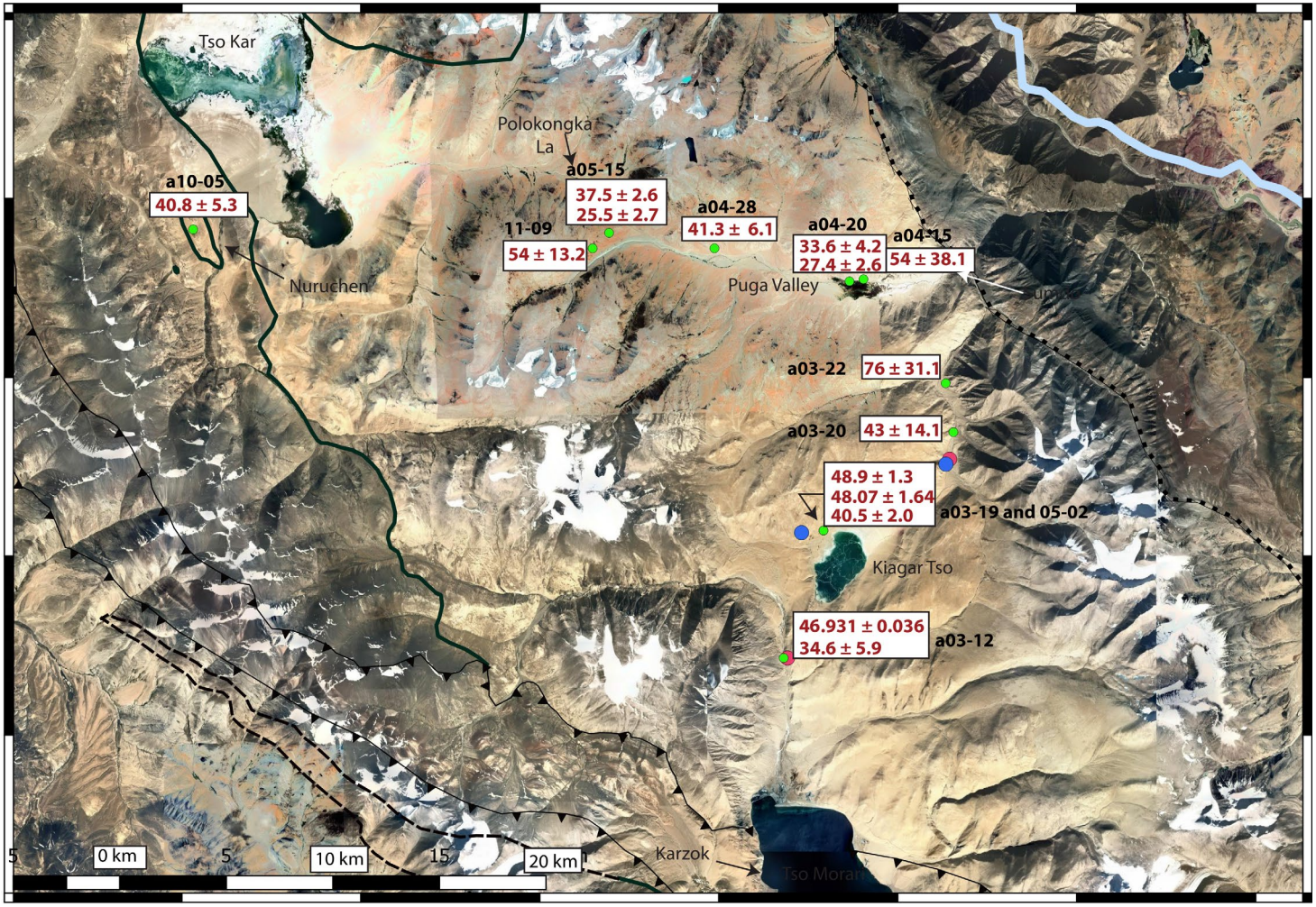


Figure 2 Map of sample locations for geochronology. Large blue dots = Donaldson et al., (2015). Large red dots = Leech et al., (2007). Red number = U-Pb zircon, purple number = U-Pb xenotime, Green number = U-Pb titanite, Blue number = U-Pb rutile

Mineral	Sample	Rock Type	Age	2s[1]	2s[2]	MSWD	Y-int	2s	Comment
Xenotime	0502	Gneiss	48.07	0.79	1.64	3.0	0.80	0.13	Lower intercept 206Pb/238U age
Titanite	A04-20	Eclogite	33.6	4.1	4.2	24.0	0.760	0.040	Lower intercept 206Pb/238U age
Titanite	A05-15	Eclogite	37.5	2.3	2.6	7.3	0.779	0.016	Lower intercept 206Pb/238U age, 1 rejected
Rutile	A03-12	Eclogite	34.6	5.7	5.9	2.2	0.635	0.040	Lower intercept 206Pb/238U age
Rutile	A03-20	Eclogite	43	14	14.1	1.8	0.798	0.055	Lower intercept 206Pb/238U age
Rutile	A04-15	Eclogite	54	38	38.1	1.9	0.840	0.018	Lower intercept 206Pb/238U age
Rutile	A10-05	Eclogite	40.8	5.0	5.3	2.0	0.830	0.035	Lower intercept 206Pb/238U age
Rutile	A05-15	Eclogite	25.5	2.5	2.7	3.0	0.797	0.014	Lower intercept 206Pb/238U age
Rutile	0502	Gneiss	40.5	1.1	2.0	2.0	0.728	0.017	Lower intercept 206Pb/238U age
Rutile	1109	Gneiss	54	13	13.2	3.4	0.834	0.026	Lower intercept 206Pb/238U age
Rutile	16-05	Eclogite							*no age determined*
Rutile	A03-19	Eclogite	34.1	3.5	3.8	4.0	0.809	0.036	Lower intercept 206Pb/238U age
Rutile	A03-22	Eclogite	76	31	31.1	3.5	0.834	0.031	Lower intercept 206Pb/238U age
Rutile	A04-20	Eclogite	27.4	3.0	3.2	2.6	0.783	0.020	Lower intercept 206Pb/238U age, 1 rejected
Rutile	A04-28	Eclogite	41.3	5.9	6.1	4.7	0.915	0.008	Lower intercept 206Pb/238U age
Rutile	JU13a	Eclogite							*no age determined*
Zircon	0502	Gneiss	482.1	4.2	8.4	2.1	*Na*	*Na*	weighted mean 206Pb/238U age of concordant analyses, 2 of 19 rejected
Zircon	0502	Gneiss	48.9	1.1	1.3	1.1	*Na*	*Na*	weighted mean 206Pb/238U age of youngest rims, n = 3
Zircon	A03-12	Eclogite	47.55	0.61	0.94	0.59	*Na*	*Na*	lower intercept 206Pb/238U age, anchored at 0.84 ± 0.02, 1 of 10 rejected
Zircon	A04-28	Eclogite	491	32	33	0.21	*Na*	*Na*	weighted mean 207Pb/206Pb age of upper concordant analyses, n = 3
Zircon	A12-14	Calc-pelite							inherited ages only

Table 2 Summary of LA-ICP-MS U-Pb geochronology results

Results

Mafic Eclogite

Zircon

Zircon grains were extracted from sample a03-12, located by the bridge at locality 16/41. Sample a03-12 is a mafic eclogite with the assemblage garnet + omphacite + phengite + rutile + talc + quartz + Na-Ca amphibole with amphibole-plagioclase symplectite replacing omphacite and titanite replacing rutile. In thin section, zircon grains are found as clustered inclusions in single crystal quartz and omphacite grains (Figure 4).

Separated zircon grains from sample a03-12 are translucent and colourless with heterogeneous rounded and euhedral grain shapes. They have complex zoning patterns, dominated by fir-tree and sector zoning, with only weak oscillatory igneous-type zoning. Several darker core regions may represent older zircon growth. Only a small percentage of grains have discordant bright rims (Figure 5). In other samples, zircon has been identified in thin section, with a grain size of <8 µm, a rounded shape and thin, bright metamorphic rims.

In samples a05-15 and a04-28 from the Puga Valley and sample a10-05 from Nuruchen in the west of the dome, spongey textured, inclusion-rich zircons are present in the non-magnetic separates, with inclusions of phengitic white mica, rutile, Na-cpx and ZrO_2. These rounded zircons are larger than the euhedral zircons in sample a03-12, ~100 µm in diameter.



Figure 3 Photomicrographs from Sample a03-16 showing clusters of zircon and rutile included in A. omphacite, B. and C. quartz.

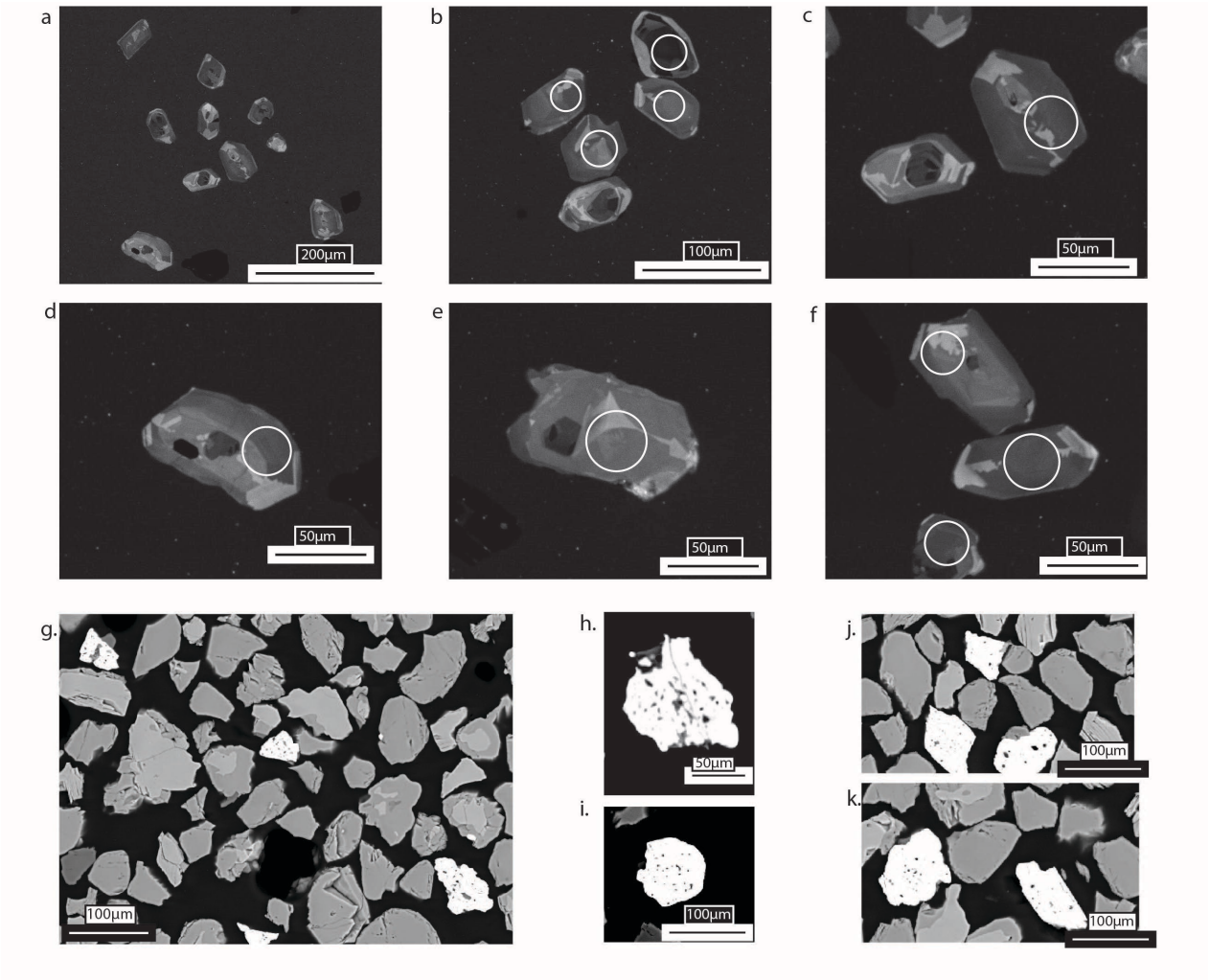


Figure 4 a. to f. Cathodoluminescence imaging of zircon grains from sample a03-12 showing location of U-Pb analysis spots. G. to k. BSE images of round spongey zircon morphologies from mafic eclogites g. Sample a05-15. h. Sample a04-28. i. Sample a10-05. J. Sample a05-15. K. sample a05-15

Laser spot analysis on 20 zircons was performed in sample a03-12, to determine the trace element patterns of the zircon cores. REE data are plotted as chondrite-normalised values (Figure 4). The REE patterns of zircon cores are consistent across multiple grains with no Eu anomaly, flat HREE patterns and depleted LREEs.

Due to the small size of the zircons and low U concentrations (13.5-1528 ppm), the radiogenic to common Pb ratios are low, resulting in laser ablation analyses distributed between common Pb and Concordia ($^{207}Pb/^{206}Pb$ = 0.0479 – 0.1413). The samples have low Th/U ratios (<0.01) and similar individual REE patterns. ^{207}Pb-corrected dates span the range of 46.6-50.8 Ma, peaking at 47.55 Ma ± 0.94 Ma (Figure 4).

The mean square of weighted deviates (MSWD) value is 0.59 with n = 10 with 1 rejected value, indicating that the results represent a single population. Zircon grains were extracted from the resin mounts and prepared as single grain aliquots for CA-ID-TIMS. The TIMS results provides three reproducible fractions yielding a weighted mean (Th-corrected) $^{206}Pb/^{238}U$ date of 46.931 ± 0.036 Ma (n=3, MSWD =1.6).

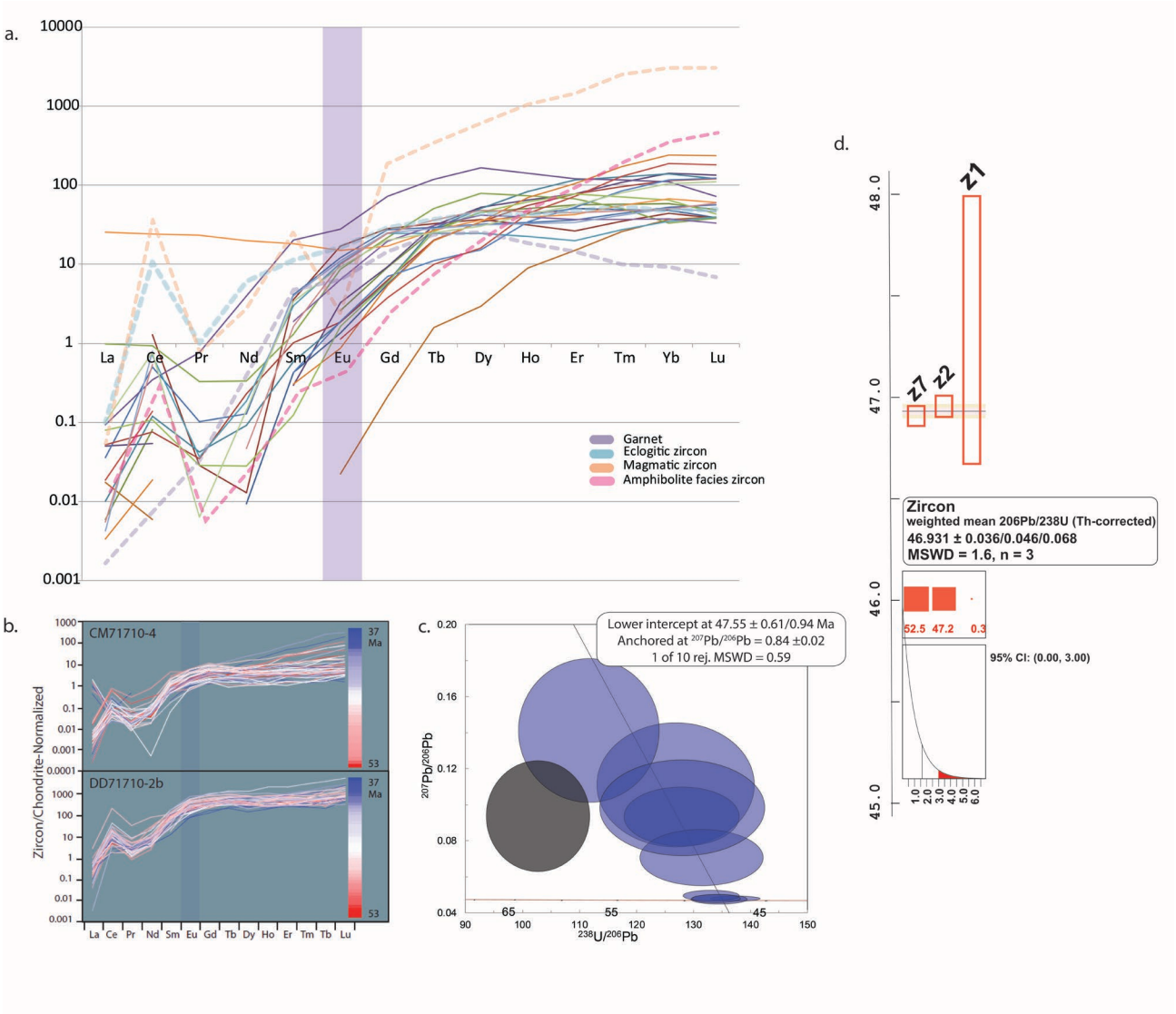


Figure 5. Sample a03-12 zircon data (solid lines). Thicker dashed lines refer to REE patterns in zircons in key, taken from Rubatto (2017). a. REE in zircon plots. b. REE plots from Donaldson et al., 2013. c. Tera-Wasserburg plot of LA-ICP-MS U-Pb data with lower intercept $^{206}Pb/^{238}U$ age and 1 sigma (%) error ellipses on data points. First uncertainty = analytical uncertainty only; second uncertainty = systematic uncertainties propogated d. Weighted mean $^{206}Pb/^{238}U$ age of 3 zircon grains using ID-TIMS

Titanite

Titanite often forms as thin rims around rutile and along fractures in rutile in the eclogites and Puga Gneiss of the Tso Morari nappe. Individual titanite grains and rims around rutile grains were analysed by LA-ICP-MS. Uranium concentrations averaging 346 ppm in sample a04-20 and 242 ppm in sample a05-15. U-Pb ages, based on the lower intercept of a free regression through all of the data, give a weighted mean age of 33.6 ± 4.2 Ma (MSWD = 24, n = 24) for sample a04-20 and 37.5 ± 2.6 Ma (MSWD = 7.3, n = 18) for sample a05-15. The MSWD for these samples is high and the precision on the individual data are relatively good. This indicates that the large uncertainty (and high MSWD) on the data is not limited by the data precision, so that the scatter observed may represent natural heterogeneity in the titanite age data. For sample a04-20, the data were divided into clusters that lie on potentially distinct regression lines, giving lower intercepts of 41.7± 8.0 Ma and 34.1 ± 4.2 Ma. These regression lines have very different slopes, unconstrained by an upper intercept, so the older array falls outside the uncertainty limits of the aggregate age.

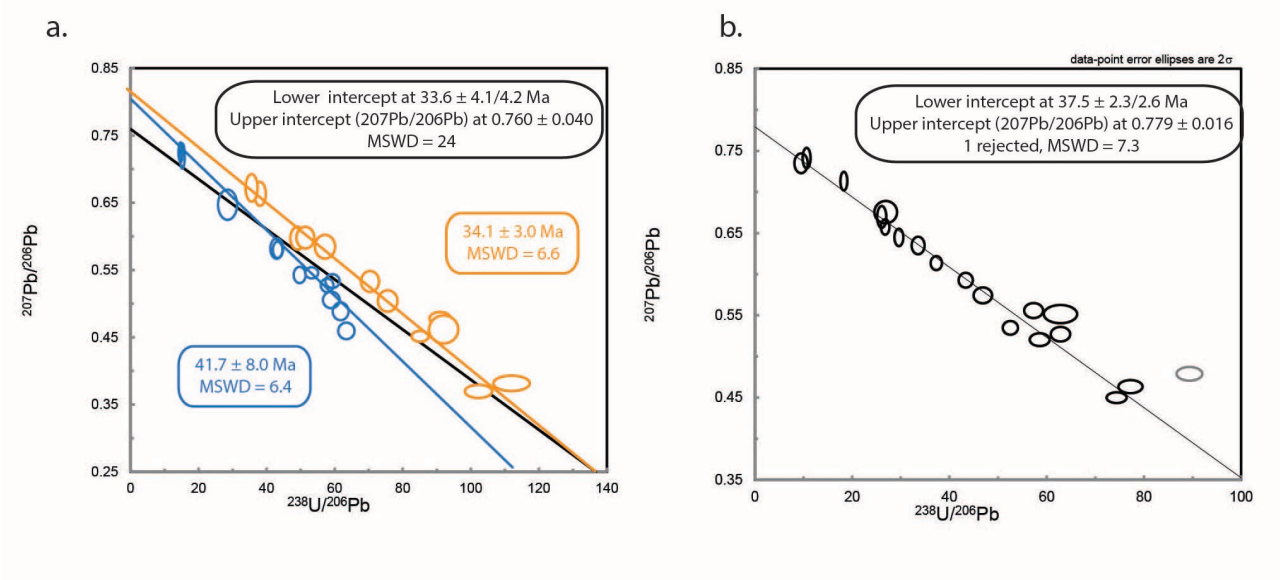


Figure 6 U-Pb titanite results shown as Tera-Wasserburg plots. First uncertainty = analytical uncertainty only; second uncertainty = systematic uncertainties propogated a. Sample a04-20. Black = free regression through all data. orange and blue = data subdivided into potentially distinct regression lines. b. Sample a05-15. Grey = excluded data

Rutile

Rutile separates from 11 mafic eclogite samples and one sample of Puga gneiss were analysed using LA-ICP-MS. The mafic eclogite samples contain a large proportion of common lead, producing large uncertainties in the data (Figure 8). Mean uranium concentrations in rutile for mafic eclogite samples are very low (<3 ppm) whereas the rutile grains from the Puga Gneiss (sample 05-02) contain a mean of 40.2 ppm U. Concentrations of Pb are variable, with the mean of most samples falling below 0.4 ppm with a maximum value of 3.6 ppm. Sample a04-28 contains higher values of Pb with a mean of 10.8 ppm and a maximum of 75.5 ppm. Puga Gneiss sample 05-02 contains a mean Pb concentration of 0.8 ppm and a maximum of 6.6 ppm.

Rutile U-Pb ages range from 25.5 ± 2.7 Ma to 54 ± 13 Ma and are plotted on Figure 8. Samples 16-05 and JU13 did not produce an isochron and samples a03-22 and a04-15 contain very large uncertainties. These samples are not considered further. The MSWD of the remaining 8 samples are large, ranging from 1.8 to 4.7.

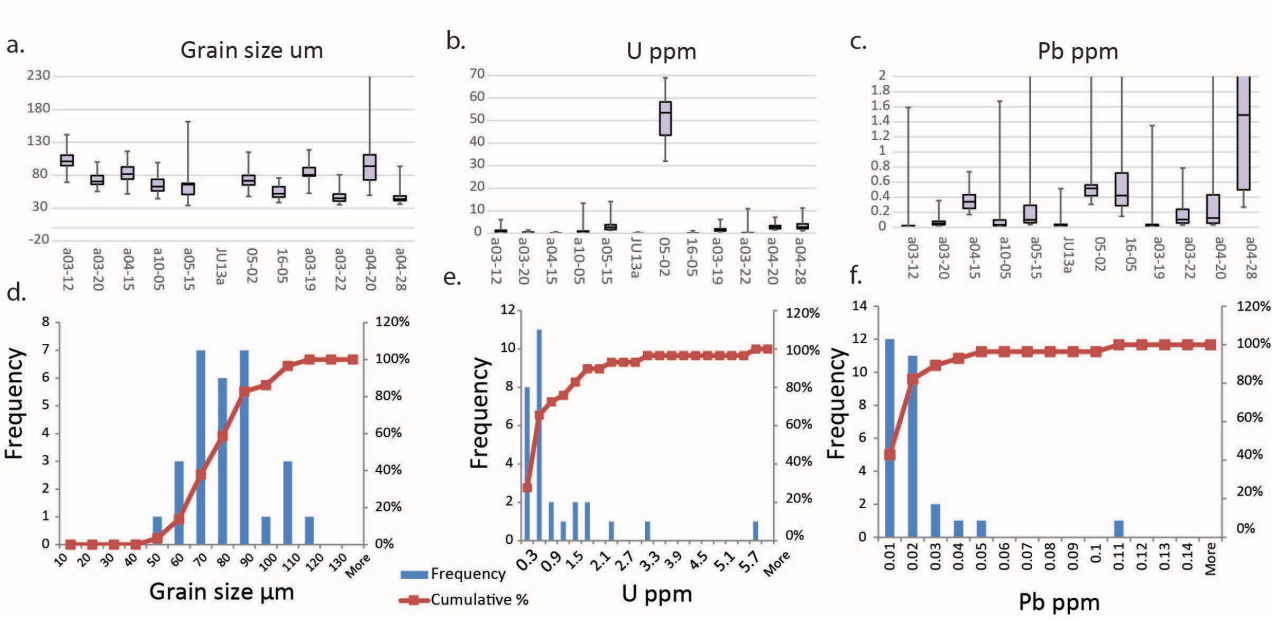


Figure 7 LA-ICP-MS data from rutile separates. Sample 05-02 from Puga Gneiss. All other samples mafic eclogites. a. Box plot showing grain size statistics per sample. b. Box plot showing ppm Uranium statistics per sample. a. Box plot showing ppm Lead statistics per sample. d. e. and f. Sample a03-12 histograms for grain size, U ppm and Pb ppm showing variation within a sample.

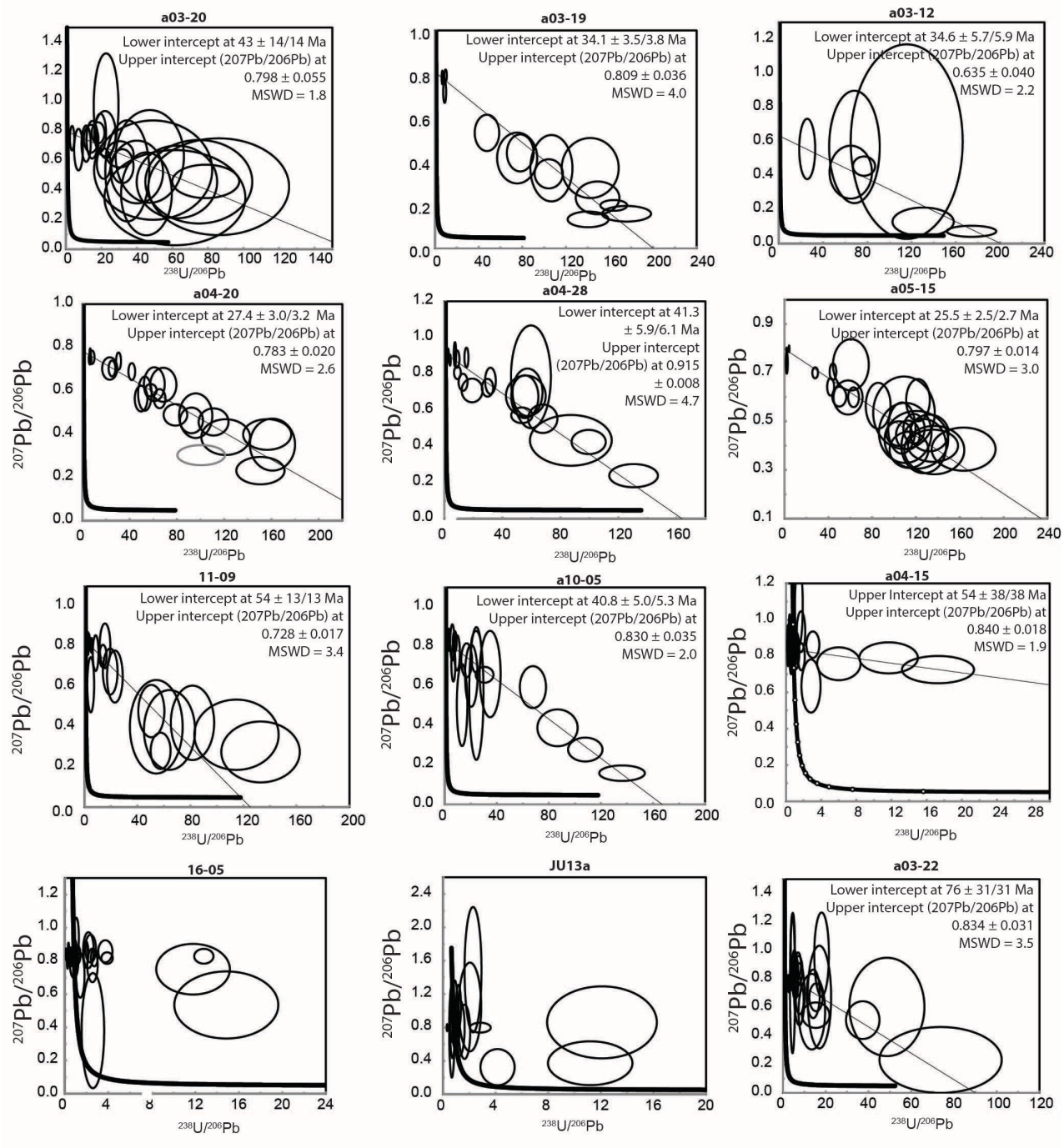


Figure 8 U-Pb rutile geochronology shown as Tera-Wasserburg plots, for 12 eclogite samples from the Tso Morari nappe. Uncertainties are quoted as in Figure 6. Due to their large uncertainties, samples a04-15, a16-05, Ju13 and a03-22 are not considered further. Data plotted with 2σ uncertainties

		a03-12	a03-20	a04-15	a10-05	a05-15	JU13a	05-02	16-05	a03-19	a03-22	a04-20	a04-28
Pb ppm	mean	0.07	0.06	0.28	0.13	0.87	0.07	0.79	0.61	0.11	0.14	0.38	10.79
	min	0.00	0.00	0.09	0.00	0.01	0.00	0.19	0.00	0.01	0.01	0.01	0.04
	Q1	0.01	0.02	0.17	0.01	0.04	0.01	0.30	0.15	0.01	0.03	0.03	0.27
	median	0.01	0.04	0.26	0.02	0.08	0.02	0.40	0.28	0.02	0.08	0.10	1.26
	Q3	0.02	0.07	0.35	0.09	0.27	0.03	0.45	0.58	0.03	0.21	0.41	11.13
	max	1.59	0.34	0.66	1.67	10.67	0.50	6.59	3.64	1.35	0.76	2.69	75.53
U ppm	mean	0.92	0.40	0.13	1.20	2.99	0.03	40.20	0.14	1.36	0.49	2.35	2.68
	min	0.07	0.21	0.01	0.04	1.02	0.00	20.36	0.01	0.40	0.04	1.00	0.31
	Q1	0.29	0.27	0.03	0.19	1.34	0.00	31.96	0.04	0.71	0.10	1.53	1.20
	median	0.49	0.31	0.06	0.33	2.40	0.01	41.94	0.07	1.06	0.14	2.33	1.90
	Q3	1.12	0.45	0.12	0.84	3.48	0.01	46.75	0.13	1.69	0.21	2.87	3.27
	max	5.85	1.41	0.64	13.27	13.78	0.48	57.43	1.10	5.80	10.85	6.56	10.32
Grain Size µm	mean	77.91	62.93	60.75	54.52	47.75		55.77	46.38	57.87	41.99	75.79	42.46
	min	44.21	44.78	29.41	32.79	17.60		30.43	30.51	26.32	29.27	25.64	30.49
	Q1	69.47	55.56	51.84	44.44	34.17		47.83	38.66	52.63	35.09	49.29	36.04
	median	75.79	59.70	59.41	51.28	49.18		54.35	43.86	54.35	39.22	70.30	38.18
	Q3	85.44	68.89	70.28	62.14	51.11		62.50	54.39	65.22	45.51	87.64	43.22
	max	116.50	89.55	94.12	87.50	145.16		97.83	67.86	92.39	75.00	217.82	88.04

Table 3 LA-ICP-MS data of rutile separates

Puga Gneiss

Sample 05-02 is an orthogneiss with an Al-rich granitic protolith and is thought to be representative of the garnet-bearing Puga Gneiss. Zircon grains in this sample show oscillatory zoning and a euhedral shape, reminiscent of igneous zircon. Thin, bright rims (< 20 μm) are present on zircons exhibiting igneous textures. LA-ICP-MS analysis of zircon cores yields an age of 482 ± 8.4 Ma (Figure 8a and b), comparable to the ages of 479 ± 1 Ma from zircon in the Puga Gneiss and Polokongka La granite (Girard and Bussy, 1999). Analysis of the zircon rims shows a Himalayan overprint at around 48.9 ± 1.3 Ma (Figure 8c and d).

Rare xenotime grains have been observed in this sample adjacent to the garnet rims. The outer edge of the garnet shows a corroded shape which crosscuts the internal concentric zoning, indicating that garnet breakdown occurred following the growth of the high-pressure rims (see chapter 6), liberating Y for xenotime growth. The U-Pb xenotime age is therefore likely to record the age of garnet breakdown at 48.07 ± 1.64 Ma. Rutile from this sample yield U-Pb ages of 40.5 ± 2.0 Ma, providing a more precise measurement than rutile from the mafic eclogites due to the higher U content (Figure 6).

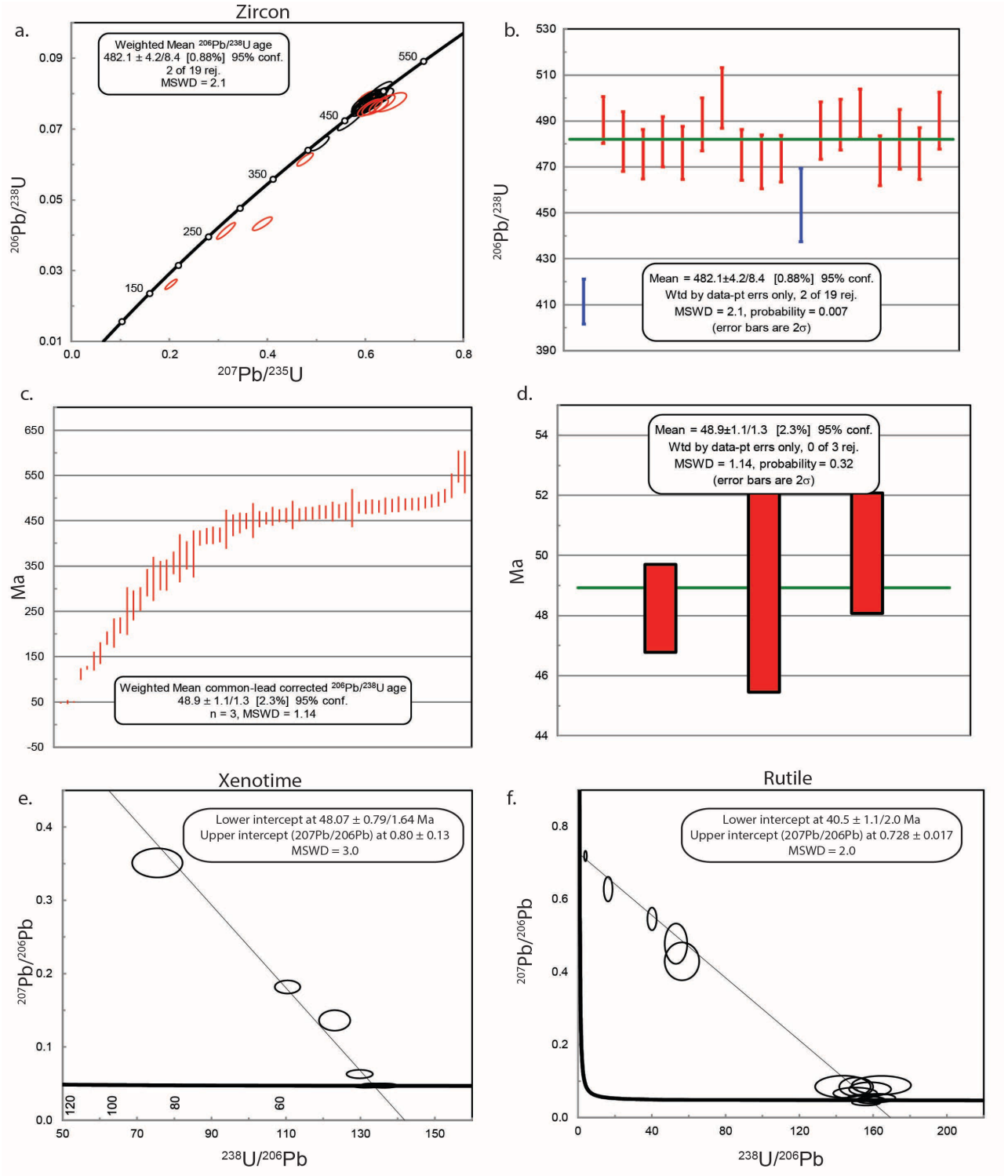


Figure 9 Sample 05-02 zircon date from the Puga Gneiss. a. Wetherill concordia plot showing U-Pb zircon core ages. b. Weighted average plot of concordant (>90%) zircon core $^{206}Pb/^{238}U$ ages. c. Rank-plot of all $^{206}Pb/^{238}U$ zircon ages. An older age plateau represents the zircon cores at ~480 Ma. The youngest ages represent thin rims, and converge on a Himalayan age. d. Weighted average $^{206}Pb/^{238}U$ age of the three youngest zircon ages. e. Tera-Wasserburg plot of xenotime U-Pb analyses. f. Tera-Wasserburg plot of rutile U-Pb analyses. Uncertainties as in Figure 6. Box heights and uncertainty ellipses are 2σ uncertainties.

Zirconium in rutile thermometry

Results from the zirconium in rutile thermometer show a continuous distribution of Zr concentrations, without any obvious clustering in Zr content, across all samples of mafic eclogites (Figure 9b). The data plots as three different geochemical clusters with varying Nb content (Figure 9e). Rutile from the felsic gneiss (sample 05-02 - square) has the highest Nb content. Sample a03-19, a mafic eclogite taken from the same locality as sample 05-02, shows a lower Nb concentration but a similar Zr concentration shown by an overlapping interquartile range (Figure 9d and e). The mafic samples are divided into two clusters with distinct Nb concentrations. Samples a04-20 and a05-15 have higher Nb concentrations from 1500 to 4000 ppm Nb. The lower Nb (<1000 ppm) cluster shows a range of Zr concentrations from 20 to 120 ppm. Sample a10-05 has the highest Nb concentration of the lower Nb cluster, closely followed by a03-20, whilst samples a03-22, JU13, a16-05 and a04-15 have the lowest concentration of Nb. Sample a04-28 shows two distinct clusters of data including a tight cluster at around 600 ppm Nb, 20-80 ppm Zr, overlapping with the lower Nb samples, and a more diffuse cluster at 1700-3700 ppm Nb, 20-145 ppm Zr, overlapping with the higher Nb samples.

Zirconium in rutile concentrations show an asymmetric distribution of values with overlapping ranges. The median values vary from 24 to 89 ppm (Figure 9d). Multiple spots were analysed from individual grains and show no significant variation in Zr content, suggesting homogenous chemical compositions across individual grains. Temperature estimates at 8 kbar, 10 kbar and 12 kbar are plotted using the calibration of Tompkins *et al*. (2007) on Figure 11. Average temperatures show a median temperature in the range between 648 ± 85.8 °C (SD) and 729 ± 75.5 °C, calculated at 10 kbar. The standard error or the mean for temperatures calculated at 8, 10 and 12 kbar are plotted to allow comparison of the mean value between samples.

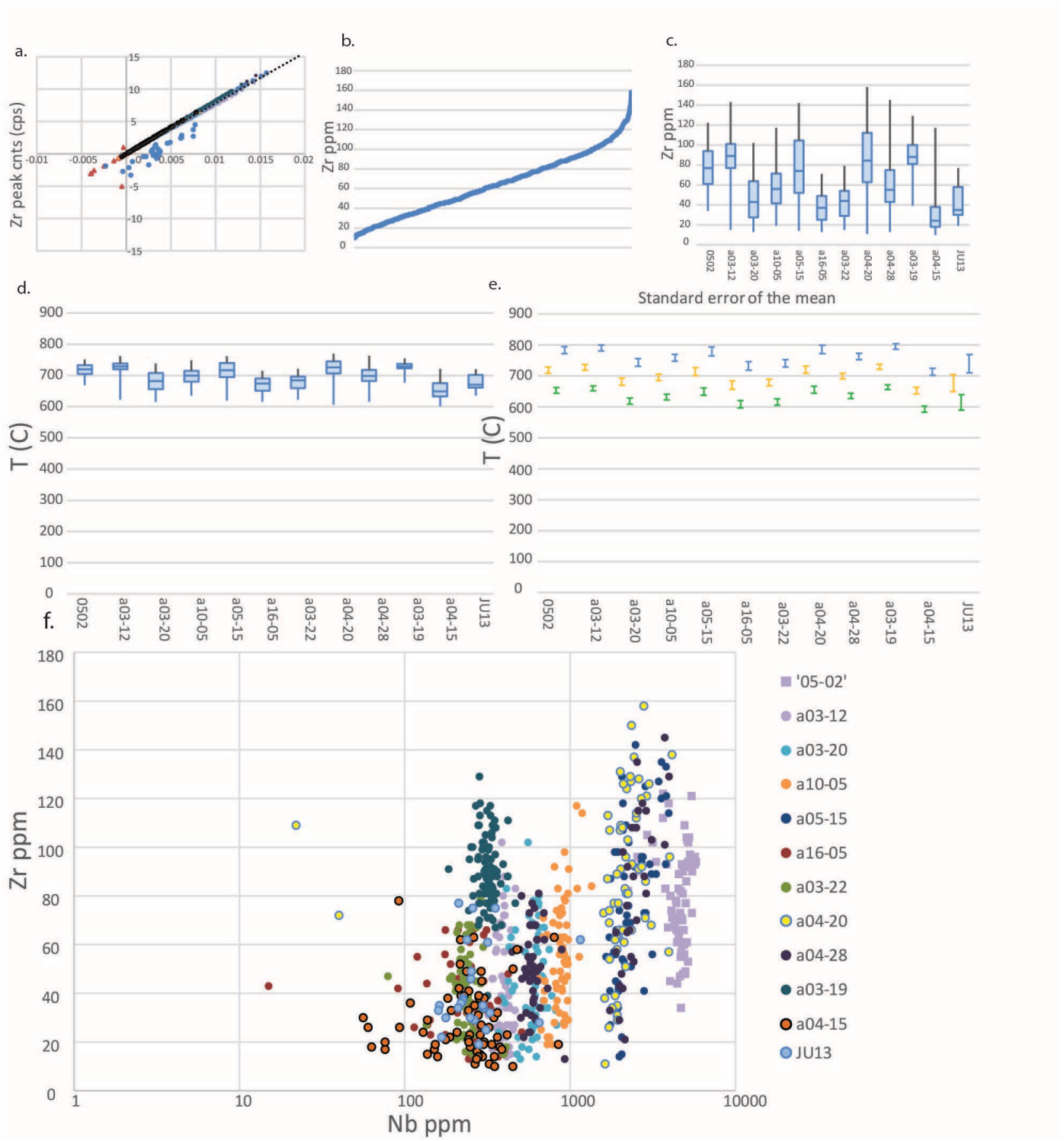


Figure 10 Zr in rutile results. a. y-axis = total Zr counts minus background counts. x-axis = Zr wt%. Sample data should lie on the black dashed line from zero Zr (TiO2 blank) to secondary standard R10. Sample JU13 (pale blue dots) lies below this line. b. Zr ppm plotted in order of increasing Zr content showing a continuous population. c. box plot of Zr ppm data for all samples. d. box plot of temperature using the calibration of Tompkins et al (2007) calibration at 10 kbar. e. standard error of the mean for temperatures calculated using Tompkins et al., (2007) for 8 kbar (green), 10 kbar (orange) and 12 kbar (blue) f. Zr ppm vs Nb ppm for all samples. Symbols: standard = triangles, granite gneiss = squares, mafic eclogite/amphibolite = circles.

Zr wt%												
	0502	**a03-12**	**a03-20**	**a10-05**	**a05-15**	**a16-05**	**a03-22**	**a04-20**	**a04-28**	**a03-19**	**a04-15**	**JU13**
n	**71**	**71**	**86**	**74**	**59**	**61**	**81**	**66**	**80**	**90**	**74**	**27**
mean	0.0078	0.0090	0.0046	0.0057	0.0078	0.0038	0.0043	0.0085	0.0061	0.0090	0.0029	0.0042
min	0.0034	0.0015	0.0013	0.0019	0.0014	0.0013	0.0015	0.0011	0.0013	0.0039	0.0010	0.0019
Q1	0.0061	0.0077	0.0028	0.0042	0.0052	0.0025	0.0029	0.0063	0.0043	0.0081	0.0018	0.0030
med	0.0077	0.0089	0.0043	0.0056	0.0074	0.0037	0.0044	0.0085	0.0055	0.0088	0.0024	0.0035
Q3	0.0094	0.0101	0.0064	0.0072	0.0105	0.0049	0.0054	0.0112	0.0075	0.0100	0.0038	0.0058
max	0.0122	0.0143	0.0102	0.0117	0.0142	0.0071	0.0079	0.0158	0.0145	0.0129	0.0117	0.0077
SD	0.1161	0.0987	0.1225	0.1180	0.1292	0.1343	0.1235	0.1240	0.1105	0.1039	0.1218	0.1951
T °C		**P =**	**10**									
	0502	**a03-12**	**a03-20**	**a10-05**	**a05-15**	**a16-05**	**a03-22**	**a04-20**	**a04-28**	**a03-19**	**a04-15**	**JU13**
mean	718.63	727.33	681.23	695.53	714.40	670.50	678.31	720.50	699.25	729.34	653.00	677.12
min	668.75	622.80	615.22	635.61	619.13	615.22	622.80	606.53	615.22	676.92	601.65	635.61
Q1	704.57	719.62	656.37	680.67	694.51	650.90	659.45	706.38	682.82	722.95	632.64	661.42
med	719.62	729.21	682.82	699.16	717.02	673.77	684.22	725.75	698.03	728.46	648.63	670.47
Q3	732.88	737.74	707.39	714.78	740.05	690.84	696.88	744.97	717.90	737.07	675.37	701.14
max	750.75	761.96	738.41	747.84	761.46	714.33	721.31	769.12	762.95	754.66	720.47	719.62
SD	85.84	75.46	88.68	86.22	98.45	94.43	87.36	95.32	82.79	77.16	84.48	134.44

Table 4 Results of Zr in Rutile thermometry. Statistical parameters for Zr ppm and temperature (Tomkins et al., 2007) for all samples.

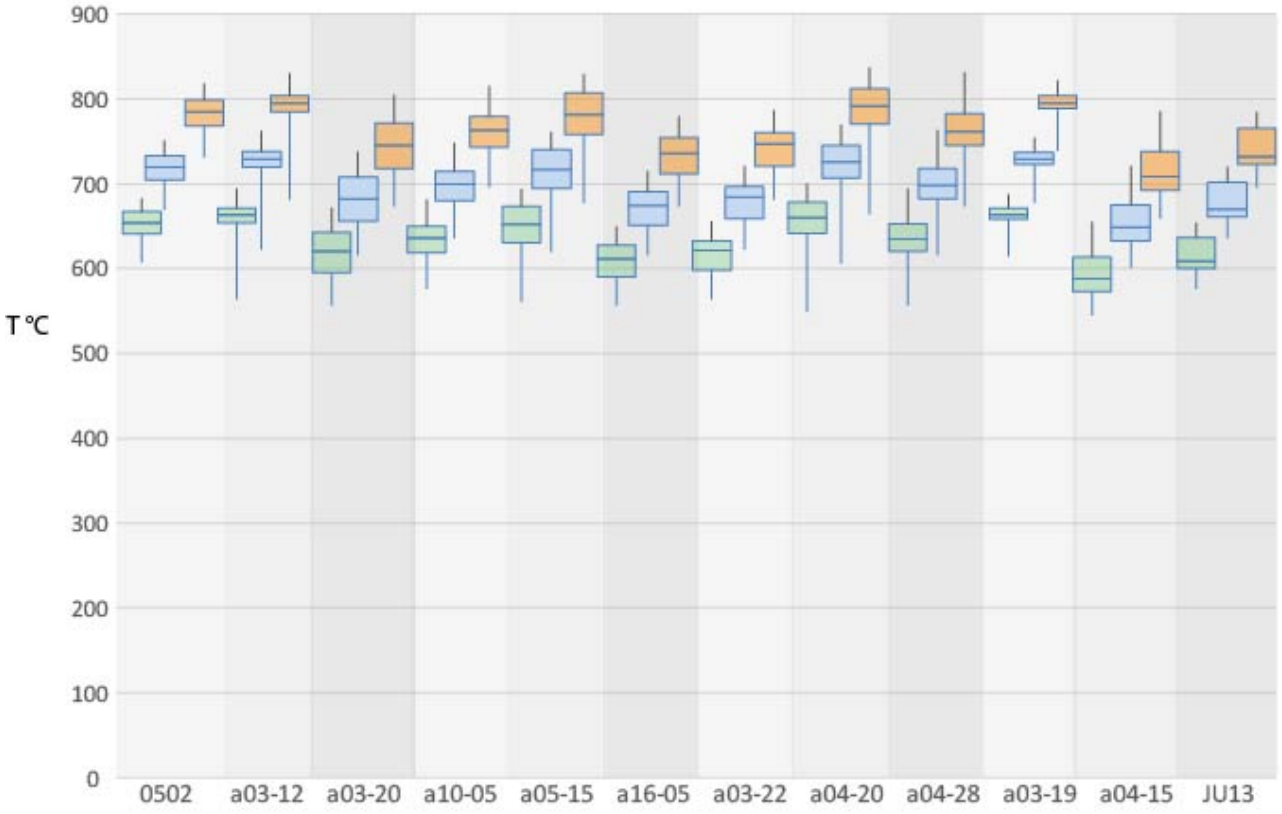


Figure 11 Box plot of Zr in rutile thermometry results at 8kbar (green), 10kbar (blue) and 12kbar (orange)

Discussion

Zircon

REE profiles, particularly mid to heavy REEs, can be used for recognising the conditions of growth of metamorphic zircon due to the partitioning of REEs into co-existing minerals. Garnet is the major host of HREEs. Zircon coexisting with garnet therefore shows a flat HREE pattern, whereas magmatic zircon that crystallised in the absence of garnet will show relatively enriched HREEs (e.g. Schaltegger *et al.*, 1999; Rubatto, 2002). The presence of an Eu anomaly relative to other REEs in zircon is thought to be due to the greater partitioning of Eu into coexisting feldspar (Schaltegger *et al*., 1999; Rubatto, 2002). In eclogitic assemblages, the lack of Eu anomaly is attributed to the breakdown of plagioclase into jadeite + quartz and is often coupled with flat HREE profiles indicating the presence of garnet (Rubatto, 2002; Rubatto and Hermann, 2003). Metamorphic zircon growing in the presence of LREE-rich phases such as titanite, allanite or monazite can also show a depleted LREE profile (Rubatto *et al.*, 2009). REE signatures are dependent on bulk rock composition, the volume percent of co-existing minerals and the presence of coexisting phases controlling the HREE or Eu budget. REE profiles of zircons from mafic eclogite sample a03-12 show flat HREE patterns and a lack of Eu anomaly, suggesting crystallisation in garnet present, plagioclase absent conditions, consistent with crystallisation in the eclogite facies. The concentration of LREEs is relatively depleted, comparable to amphibolite facies zircon (Rubatto, 2017). In eclogite-facies mafic rocks, zirconium for the growth of eclogite-facies zircon is sourced, in some cases, from the breakdown of ilmenite forming rutile as the high pressure TiO_2 phase (Bingen *et al.*, 2001).

Leech *et al.*, (2007) documented three clusters of ages for growth stages in zircon from quartzofeldspathic gneisses from within the Tso Morari nappe based on the analysis of zircon rims (SHRIMP). <20 μm wide zircon rims were identified by CL imaging of zircon separates and analysed using a 30 μm sport size. The age clusters presented are thought to represent ultrahigh–pressure metamorphism at 53.3 ± 0.7Ma, followed by further eclogite facies metamorphism and an amphibolite facies overprint at 45.2 ± 0.7Ma. However, there is no petrographic evidence presented to support this interpretation, such as inclusions in zircons or trace element data (O'Brien, 2006). Zircon morphology

and zoning, along with a core age of 480.9 ±3 Ma and a range of zircon rim ages, suggest that the zircon rim age could in fact be a mixed age influenced by analysis of the zircon cores. Furthermore, the first recorded stage of zircon crystallisation proposed by Leech *et al*. (2007) is interpreted to represent ultrahigh–pressure metamorphism. This is in contrast to the reaction sequence published by various authors from the well preserved mafic eclogites, which show that there was at least one stage of eclogite-facies metamorphism prior to peak pressures. The ages published by Leech *et al*. (2007) therefore represent periods of zircon growth in the quartzofeldspathic rocks of the Tso Morari nappe, but yield no petrographic information as to what these ages represent in the metamorphic history of the rock.

Complex zoning within zircons grains from mafic eclogites indicates potentially protracted periods of zircon growth. Laser spot analysis targeting the cores and mantles of zircon from a03-12 provided Himalayan ages, suggesting that these zircon grains are entirely composed of metamorphic zircon, rather than preserving an older history. The zircon CA-ID-TIMS age from mafic eclogite sample a03-12 is 46.931 ± 0.036 Ma, this provides the most robust estimate of the timing of metamorphic zircon growth from Tso Morari thus far. This age is significantly younger than the SHRIMP U-Pb zircon age of 58.0 ± 2.2 Ma included in garnet cores and younger than the matrix zircon age of 50.8 ± 1.4 Ma in the Berthelsen outcrop, thought to bracket ultrahigh–pressure metamorphism (St-Onge *et al.*, 2013). This age overlaps with the LA-ICP-MS age of 45.3 ± 1.6 Ma (MSWD = 3.4, n = 47) from near to Kiagar La ~13 km to the NE (Donaldson *et al.*, 2013, sample DD71710-2B) and is slightly older than the 44.2 ± 1.2 Ma (MSWD = 2.4, n = 61) age from NW of Kiagar Tso (Donaldson *et al.*, 2013, sample CM71710-4), ~9 km NE of sample a03-12.

Results by Donaldson *et al*., (2013) show seemingly distinct ages from the two different outcrops, with flat HREE and no Eu anomaly, consistent with growth in the absence of plagioclase and the presence of garnet. Although 64% of their dates were obtained from zircon inclusions in garnet and omphacite, these dates are comparable to those of matrix grains, and the upper limit of the data peak (ca. 47 Ma) is interpreted as the oldest age of ultrahigh–pressure metamorphism. However, the data are dominated by analyses with variable proportions of common Pb, so that the lower intercept age depends on the position of the regression line and upper intersect projection.

The spread of data from Donaldson *et al*. (2013) (n=60) is interpreted as a record of protracted prograde zircon growth. Protracted zircon crystallisation would produce zonation within individual zircon crystals, producing a mixed age and a spread in the data. The tight and reproduceable age in sample a03-12 (n=3) indicates that a single population of zircon growth occurred in this sample. These results do not support the continuous crystallisation hypothesis suggested by Donaldson *et al*. (2013). In order to add confidence to the interpretation that zircon crystallisation in the eclogite facies was not protracted, more zircon grains should be analysed via the same high precision CA-ID-TIMS method.

St-Onge et al. (2013) analysed a sample size of n=4 zircon grains in the matrix, whereas Donaldson et al., (2013) was able to analyse a larger number of grains in situ. However, sample a03-12 U-Pb ID-TIMS age does not lie within error of sample L08-03 (St-Onge et al., 2013) and sample CM71710-4 (Donaldson et al., 2013) suggesting a real variation of zircon crystallisation ages between samples. Zircon crystallisation in mafic eclogite samples is interpreted to have occurred in the eclogite facies. The variation in zircon crystallisation ages could be attributed to slight variations in bulk composition liberating Zr from a source mineral at different P-T conditions, the presence of fluids catalysing the reaction that results in zircon crystallisation or variation in the timing of the achievement of peak pressure conditions. Episodes of fluid infiltration are known to have occurred on the initial retrograde path in the eclogite facies (Palin et al., 2014), suggesting that the variation in U-Pb zircon ages between samples in the complex could potentially reflect the variation in timing of fluid infiltration in the eclogite facies. However, other hypotheses relating to bulk composition variations and peak pressure gradients cannot be ruled out.

The original aim of this chapter was to place better constraints on the P-T-t history of the Tso Morari complex. However, zircons from only one mafic eclogite were obtained in the heavy mineral separates and zircons identified in situ in other samples were too small (<4μm) to analyse. The U-Pb ID-TIMS age of sample a03-12 was therefore compared to results from previous studies. However, the results from St-Onge et al. (2013) and Donaldson et al., (2013) are based on less accurate in situ dating methods (SHRIMP and LA-SS-ICP-MS respectively). In order to determine whether the precise and

reproducible age from sample a03-12 is representative of the entire Tso Morari complex, more analyses using a high precision method such as ID-TIMS are required.

Xenotime

Pb diffusion in xenotime is very slow and measured Pb isotope signatures are thought to be representative of growth conditions in sub-solidus rocks (Cherniak, 2006). Xenotime is observed in Puga gneiss sample 05-02 as a breakdown product of garnet and records a U-Pb age of 48.07 ± 1.64 Ma. Garnet is likely to breakdown at pressures less than ~10 kbar based on the total bulk composition of sample 05-02 in water-undersaturated conditions (Figure 4, Chapter 8). Sample 05-02 also records thin metamorphic rims around igneous zircon with an age of 48.9 ± 1.3. This is slightly older than the ID-TIMS age of 46.931 ± 0.036 Ma eclogite facies zircon recorded in a mafic eclogite 9km to the SW.

Titanite

Laser ablation data from titanite grains have a high MSWD, allowing multiple different age interpretations. Precise individual analyses coupled with a large MSWD on the mean age indicate that there is perhaps more than one generation of titanite growth recorded in a single sample. Trace element analyses of titanite grains would help to distinguish whether multiple generations were present within a sample. Titanite ages from the sample a05-15 (Polokongka La ridge) and a04-20 (Puga School) show overlapping ages in the range of 40.1-29.4 Ma, indicating that titanite is recording a similar process over a similar time period in both samples, located 5.7 km apart.

The closure temperature (T_c) of titanite has been estimated at >650°C (Cherniak, 1993; Frost *et al.*, 2001). The T_c of titanite is dependent on grain size and cooling rate. Thus, titanite grains that remained below the T_c or are large enough to retain their Pb will record the time of growth and grains that are small enough will record the time the rock fell below the T_c. The T_c of titanite of 100 μm diameter is experimentally determined to be ~600°C for the U-Pb system (Cherniak, 1993). The T_c of titanite has since been acknowledged to be in excess of 800°C in a suite of natural samples in which the thermal evolution is well constrained (Kohn *et al.*, 2011). Early estimates of titanite T_c reflect the difficulty in relating titanite ages to specific temperatures, as titanite is able to crystallise over a large temperature

range (Kohn, 2017). Peak amphibolite facies conditions of metamorphism in the Tso Morari nappe are predicted to be ~705-755°C (St-Onge et al., 2013), suggesting that titanite grains in this sample record a cooling age related to the T_c of titanite. However, titanite that grew below the T_c would record the age of growth of titanite.

In the mafic eclogites from the Tso Morari nappe, titanite is observed to form as rims around rutile grains. In sample 11-05, titanite is predicted to be stable during prograde growth, breaking down to form rutile at high pressures, and forming from the breakdown of rutile during re-equilibration at lower pressure. Titanite grains analysed by LA-ICP-MS are therefore also thought to have formed due to the breakdown of rutile under amphibolite facies conditions. This reaction is predicted to occur at ~ 530°C for sample 11-05 based on phase equilibria modelling (discussed in chapter 5), water saturated conditions and an unfractionated bulk composition (Figure 11). Peak temperature (705-755°C) is predicted to occur at 45.3 ± 1.1 Ma at the Berthelsen outcrop (St-Onge *et al*., 2013) and in the range of 600-800°C across the whole nappe based on Zr in rutile thermometry. Predicted growth of titanite at temperatures below the T_c therefore suggests that the U-Pb age of titanite records titanite growth at a temperature well below the peak temperature, during retrograde metamorphism. The overlapping ages recorded between two samples indicate that titanite grew approximately over the same interval during the exhumation of these samples and provides an indication of residence time in the lower-middle crust.

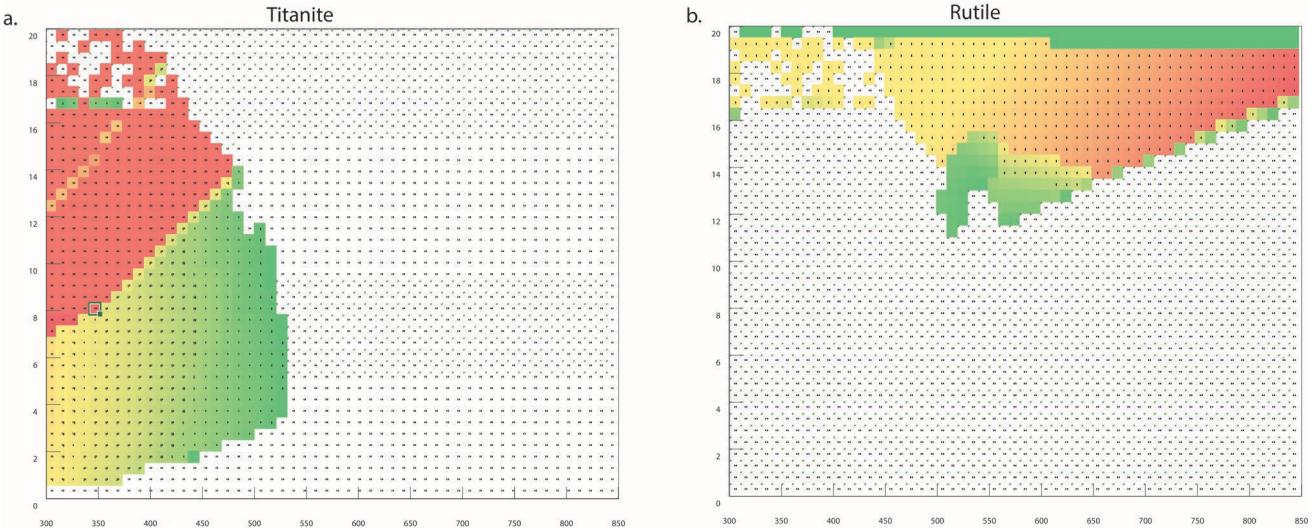


Figure 12 Phase equilibrium models of sample 11-05 showing titanite and rutile stability. Colour scale shows relative modal values from low (green) to higher (red).

Rutile

U-Pb age

Large uncertainties in the U-Pb rutile data and large MSWDs makes tectonic interpretation difficult for this dataset. Samples 05-02 (Puga Gneiss) and a03-19 (mafic eclogite), collected from the same locality, show different and apparently resolvable lower intercept ages. However, high concentrations of common lead, a high MSWD, and poorer precision with a possibly significant spread on more radiogenic analyses suggests that these data could feasibly overlap. Additionally, analyses with high proportions of common Pb can help to pin the upper intersect on a free regression, but large uncertainties on these data add uncertainty to this upper intersect.

The closure temperature (T_c) of rutile is poorly understood and is suggested, from experimental data, to be similar to that of titanite (Cherniak, 2000). However, natural data suggests it could be much lower (Mezger *et al.*, 1989) owing to the presence of ilmenite exsolution lamellae reducing the length scale of effective diffusion (Kylander-Clark *et al.*, 2008). Estimated T_c of rutile ranges from 400°C (Mezger *et al.*, 1989) to 540-630°C (Cherniak, 2000; Vry *et al.*, 2006). These temperatures vary from core to rim of large rutile crystals (Mezger *et al.*, 1989). Li *et al.*, (2013) determined that the cores of the largest rutile grains record temperatures close to those of metamorphic zircon, whereas the rim temperatures are consistent with the closure of the muscovite Rb-Sr system at ~500°C. The T_c of rutile is thought to be dependent on the rate of cooling, so that the slow-cooled terranes record lower temperatures.

Rutile is thought to be the peak titanium-bearing phase during eclogite-facies metamorphism and is present in all eclogite samples. The U-Pb age of rutile can therefore be interpreted as the age of cooling during exhumation, at a closure temperature lower than the maximum temperature recorded by Zr in rutile analysis. Rutile LA-ICP-MS U-Pb data show a large proportion of common Pb, resulting in large uncertainties in the U-Pb Tera Wasserburg intercept age. Most of the rutile data falls within the range 40-30 Ma, ~10-20 myr after the eclogite facies zircon ages, representing the time the Tso Morari nappe was exhumed through the lower crust.

In sample a04-20 (locality 16/105), the rutile age of 27.4 ± 3.2 Ma is younger (although overlapping within uncertainty) than the titanite age of 33.6 ± 4.2 Ma. Similarly, sample a05-15 (locality 16/113) records a rutile age of 25.5 ± 2.7 Ma and an older titanite age of 37.5 ± 2.6 Ma. The similarity of the titanite and rutile ages supports the interpretation that the Tso Morari nappe was exhumed to the lower crust by ~40-30 Ma. If titanite growth occurs below the Tc of titanite, locking in radiogenic Pb, and above the Tc of rutile, the resulting ages of the titanite rims could be older than the rutile cores. Alternatively, if titanite ages are recording a Tc which is lower than the Tc for rutile, or rutile is recording a growth age, titanite rims would be younger than rutile cores. Rutile ages in samples a04-20 and a05-15 are consistently younger than the titanite ages by ~7-17 and 0-13.5 myr respectively, suggesting that the T_c of rutile is lower than temperature at which titanite grew (~530°C).

Zirconium in Rutile

Rutile grains show homogeneous Zr concentrations across the dome, suggesting that the peak temperature was consistent throughout the nappe and concentrations of <1000 ppm Nb in eight samples of mafic eclogite. Three samples (a04-20, a05-15 and a04-28) of mafic eclogite show higher Nb concentrations. These samples lie within the Puga Valley, suggesting that the variation in trace element composition of rutile has a systematic spatial distribution. The variation in Nb content of rutile grains is likely related to bulk compositional variations among samples from the Puga valley and elsewhere in the dome. Alternatively, the presence of both high and low Nb concentration clusters in sample a04-15 from the Puga valley, could be related to the presence of two generations of rutile preserved in this samples, with different trace element signatures.

Zr in rutile temperatures recorded in mafic rocks have been shown to be consistent with previously published temperature data obtained using conventional thermobarometry (e.g. Tual et al., 2018; Rehman et al., 2019). Maximum Zr in rutile concentration from mafic granulites from the Khondalite Belt in China were interpreted as the peak temperature of granulite facies metamorphism (Jiao et al., 2011). Pape et al. (2016) reported that most rutile grains in a granulite from the Ivrea-Verbano Zone, northern Italy, recorded peak temperatures, with some of the grains affected by post peak Zr

modification. Tual et al. (2018) recorded Zr in rutile temperatures from rutile inclusions in garnet, comparable to the temperature estimate from the composition of the enclosing garnet zones.

The studies mentioned above indicate that Zr concentrations are homogenous within individual grains but there are often variations between grains making interpretation difficult. Rutile is known to grow under a range of P-T conditions, at different times during a single P-T path and Zr concentrations in rutile are known to be affected by local fluid-controlled diffusion rates (e.g. Zack et al., 2004; Zack and Koojiman, 2017; Tual et al., 2018; Rehman et al., 2019). However, studies also suggest that the maximum Zr content recorded represents peak metamorphic temperatures (e.g. Ewing et al., 2013; Koojiman et al., 2012; Miller et al., 2007; Pape et al., 2016; Zack and Koojiman, 2017; Zack and Luvizotto, 2006). The Zr in rutile thermometer is also pressure dependant, requiring an independent estimate of pressure (Tomkins *et al.*, 2007).

The average temperature for Zr in rutile thermometry is in the range of 670-720°C at 10 kbar for all samples from the Tso Morari complex, with little variation (Figure 12). Coarse-grained rutile separates, likely sourced from the abundant matrix grains, were analysed in this study. Rutile grains are also observed as fine-grained inclusions in all phases in the mafic eclogites, suggesting that rutile formed early in the prograde history of the rock. The prograde P-T history of the rock experienced pressures and temperatures of ~27-28 kbar, ~645°C (Chapter 3). Interpretation of the Zr content of rutile at pressures of 27 kbar, using the calibration of Tomkins *et al.*, (2007), suggests temperatures in the range 1170-1289°C. Such high temperatures are considered unreasonable at these pressures based on the known P-T history of the rock which is thought to be <645°C at 27.5 kbar (St-Onge et al., 2013; Chapter 3, this study).

Zr in rutile temperature estimates at 8-12 kbar are consistent with peak temperatures recorded by conventional thermobarometry and phase equilibrium modelling in mafic eclogites (de Sigoyer *et al.*, 1997; Guillot *et al.*, 1997; St-Onge *et al.*, 2013; Chatterjee *et al.*, 2015; Wilke *et al.*, 2015)(Figure 13), with the exception of St-Onge et al. (2013) who record higher temperatures at 7-8.4 kbar in a sample of felsic gneiss. The lower limit of rutile stability is predicted to be at ~10-12 kbar (Figure 13), 500-700°C, based on pseudosection modelling of sample 11-05 (see Chapter 3 for details on the modelling and bulk

composition) using the full bulk composition in water saturated conditions. Predicted Zr in rutile temperatures at 8-12 kbar lie outside of the rutile stability field, suggesting that diffusional resetting of pre-existing rutile may have occurred, rather than growth of new rutile grains in the range of 8-12 kbar, 670-720°C.

Diffusional resetting of Zr in rutile is thought to be possible down to the closure temperature of Pb at 635°C (200µm elongate grain, cooling rate 1°C.Ma^{-1}) owing to the similarity in Zr diffusion in rutile (Sasaki et al., 1985; Cherniak, 2000). Zr in rutile was shown not to have been reset in rocks from Alpe Arami, Italy, despite peak temperatures of 800°C, thought to be due to the fast cooling rates (100°C.Ma^{-1}) (Olker et al., 2003). Diffusional resetting requires a reservoir to facilitate ion exchange (Cherniak, 2000). This could be provided by the addition of fluid and the breakdown of Zr-bearing phases such as clinopyroxene (Lundstrom *et al.*, 1994), coinciding with emplacement of the UHP rocks into crustal conditions.

Due to the difficulty in collecting large volumes of hard, fresh mafic rock from which rutile grains were separated, more retrogressed samples were considered for geochronological analysis than for petrological analysis. Zr in rutile thermometry has been shown to be sensitive to the degree of retrogression in eclogites, with more retrogressed eclogites preserving lower temperatures (Rehman *et al.*, 2017). Temperatures obtained by this method can therefore be considered as minimum estimates of peak temperature.

The higher temperatures of St-Onge et al. (2013) of 705-755°C at 7.-8.4 kbar are not reflected in the Zr in rutile temperatures. There are several possible reasons for this apparent discrepancy. Firstly, the higher temperatures could be a result of inaccuracies in the thermodynamic dataset used, limitations in the activity models or incorrect assumptions made about the activity or concentration of H_2O used in the calculations. A second possibility is that the peak temperature is higher than that recorded by Zr in rutile. Peak temperature estimates of rocks from the Tso Morari complex are discussed further in Chapter 8.

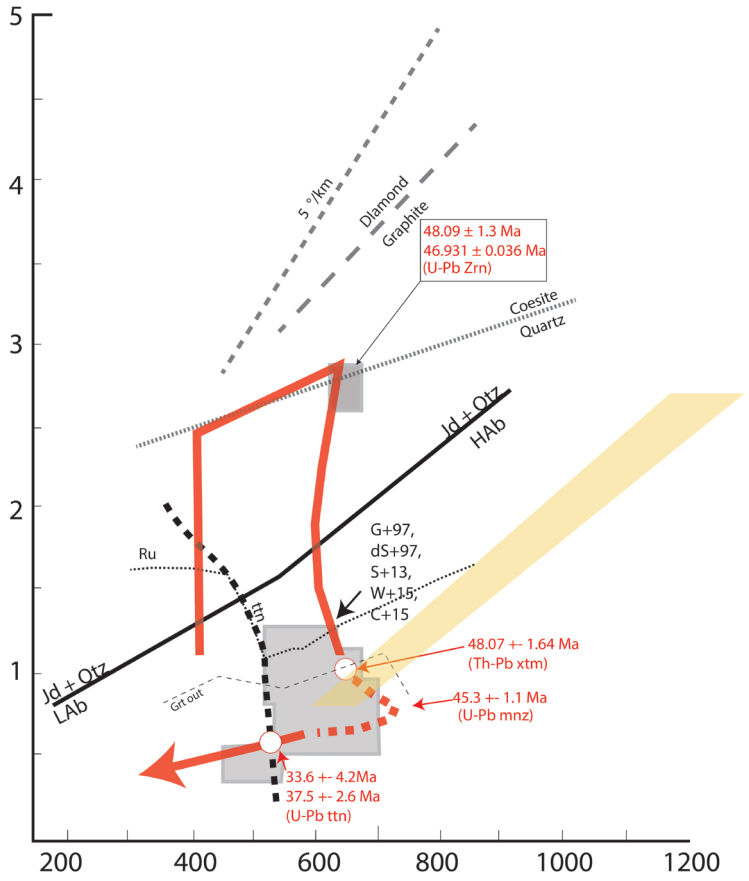


Figure 13 Summary of P-T results and proposed P-T paths for the Tso Morari. Red arrow shows proposed P-T path from Chapter 3. Dark grey box shows peak P-T estimate from chapter 3. Light grey box shows published P-T predictions for Tso Morari eclogites : G + 97 (Guillot et al., 1997), dS + 97 (de Sigoyer et al., 1997), S + 13 (St-Onge et al., 2013), CJ15 (Chatterjee and Jagoutz, 2015), W + 15 (Wilke et al., 2015). Dotted line shoes lower limit of rutile stability based on pseudosection modelling of mafic eclogite sample 11-05 in water saturated conditions. Thick dashed line upper limit of titanite (ttn) stability field based on pseudosection modelling of mafic eclogite sample 11-05 in water saturated conditions. Thin dashed line shows lower limit of garnet stability field based on pseudosection modelling of granite gneiss sample 05-02, in water saturated conditions. Yellow box shows results of Zr in Ru thermometry for 8-27kbar. Coesite to quartz (Bohlen and Boettcher, 1982), Albite to jadeite + quartz (Holland (1980), diamond to graphite (Bundy, 1980).

Upper crustal constraints

The Rb-Sr age of phengite (pinned by apatite) from the Polokongka La region, in the north-central part of the dome, records an age of 45.5 ± 4.4 Ma at a closure temperature of ~550°C (e.g. Cliff, 1993; Freeman *et al.*, 1997). This age is comparable to titanite growth ages at ~530°C of 33.6 ± 4.2 Ma and 37.5 ± 2.6 Ma, in samples from the Puga valley.

Ar-Ar ages in white mica and biotite are thought to record a closure temperature of 425°C, for a 100 µm radius at 10 kbar (Purdy *et al.*, 1976; Harrison *et al.*, 2009), and <350°C (Harrison *et al.*, 1985)

respectively. The closure temperature of Ar in muscovite depends on cooling rate and effective grain size (Harrison *et al.*, 2009), but are thought to record an upper crustal age. The Ar-Ar age of muscovite (31.1 ± 0.3 Ma) is ~2 myr older than the Ar-Ar age of biotite (29 ± 0.4 and 29.3 ± 0.3 Ma) in metasediments from the south-western edge of the complex (De Sigoyer *et al.,* 2000), consistent with cooling through the closure temperatures. Ar-Ar of phengite from the north side of the complex, adjacent to the Zildat shear zone, records ages of 48 ± 2 Ma (de Sigoyer *et al.*, 2000) and 53.8 ± 0.13 Ma (Schlup *et al.*, 2003). The ages are determined from samples from the Zildat valley and produce results which are several million years apart, overlapping with the ages of eclogite facies metamorphism, suggesting that these samples may contain excess Ar, recording anomalously old ages.

Zircon fission track data taken from a transect through Kiagar Tso to Tso Morari suggest that the whole region, including the Tetraogal and Mata nappes, cooled through 300-200°C between 47-32 Ma (Schlup *et al*., 2003). Fission track dating of apatite (Schlup *et al*., 2003) shows that the Tso Morari nappe underwent rapid cooling below 110-60°C at ~7.5 Ma close to the Zildat fault in the north and ~26 Ma in the south west.

Variation across the dome

Zircon U-Pb ages show approximately constant ages, within uncertainty, across the Tso Morari nappe, suggesting that high pressure metamorphism was contemporaneous across the dome. The age of garnet breakdown in crustal conditions (48.07 ± 1.64 Ma, U-Pb xenotime) in sample 05-02 overlaps with the age of eclogite facies zircon crystallisation (46.931 ± 0.036 Ma) in sample a03-12, suggesting that exhumation to crustal conditions took place very quickly, within 0.5 to 1 Myr.

Titanite and rutile ages are interpreted to represent the time when then rocks were exhumed to crustal depths. Titanite ages from the central part of the dome suggest that at 40 Ma, the temperature was > 500°C, in the amphibolite facies. The overlapping titanite ages of two different samples from the Puga valley, suggests that their exhumation history was the same between 40-29 Ma.

Ar-Ar analysis of biotite and muscovite (De Sigoyer *et al*., 2000) show that the western part of the Tso Morari nappe was at upper crustal levels (<5 kbar) at ~30 Ma. The gradient in Ar-Ar and Rb-Sr ages of

mica from the north to the south of the complex (De Sigoyer et al., 2000; Schlup et al., 2003) suggest that the greenschist-facies retrogression in the centre of the Tso Morari nappe (48-53 Ma) is older than the south-western part of the nappe (29-31 Ma).

Rutile and titanite U-Pb ages fall within the range of 47-22 Ma and are younger than the U-Pb zircon ages. The rutile and titanite U-Pb ages are also younger than and overlapping with the Ar-Ar phengite and Rb-Sr phengite ages from the northern side of the complex, but older than and overlapping with the Ar-Ar muscovite and biotite ages from the south west side of the complex. In order to determine whether a gradient exists in the exhumation ages of the Tso Morari complex to up c. 30 Ma, higher resolution titanite data from a larger distribution of samples are needed.

Schlup *et al*., (2003) suggested that by 47-32 Ma, the Tso Morari complex had been exhumed through 300-200°C to a depth of c. 10 km, based on zircon fission track data, during which time the Mata nappe had undergone cooling at shallow structural levels (3-5 km) (fission track of apatite, Schlup *et al*., 2003). These results imply that the Tso Morari, Tetraogal and Mata nappes were situated close together when undergoing uplift through 300°C. Apatite fission track data indicate ages of 23.4 ± 1.1 Ma in the south west of the complex and 7.6 ± 0.8 Ma in the centre of the complex (Schlup et al., 2003). The gradient in apatite fission track ages implies tilting of the complex, combined with increased exhumation, linked to brittle reactivation of the Ribil-Zildat fault over the period 25 to 5 Ma.

The time elapsed between peak metamorphism and emplacement in the base of the crust is much shorter than the predicted duration of residence in the lower crust, contributing to the characteristic kinked exhumation path. Age data suggests that samples from the Tso Morari nappe were exhumed quickly from ultrahigh–pressure depths in <1 Myr, before stalling in the lower crust for 10-20 Myr. The mechanism by which the rocks were exhumed to and from the lower crust must therefore have been different.

Summary

Determination of the U-Pb age of eclogite facies zircon crystallisation in one sample, produces a precise estimate on the timing of high-pressure metamorphism at 46.93 ± 0.04 Ma. Xenotime, titanite and rutile U-Pb ages are interpreted to represent the time when then rocks were exhumed to crustal depths. These data provide constraints on a part of the geochronological history of the Tso Morari complex, from 47 to 22 Ma, that currently is lacking in age data but is extensively recorded in retrograde metamorphic microstructures and in amphibole and garnet chemistry. Rutile and titanite ages across the complex provide a new dataset which can be used in conjunction with temperature estimates from the Zr content of rutile to further constrain the exhumation-style of the Tso Morari nappe.

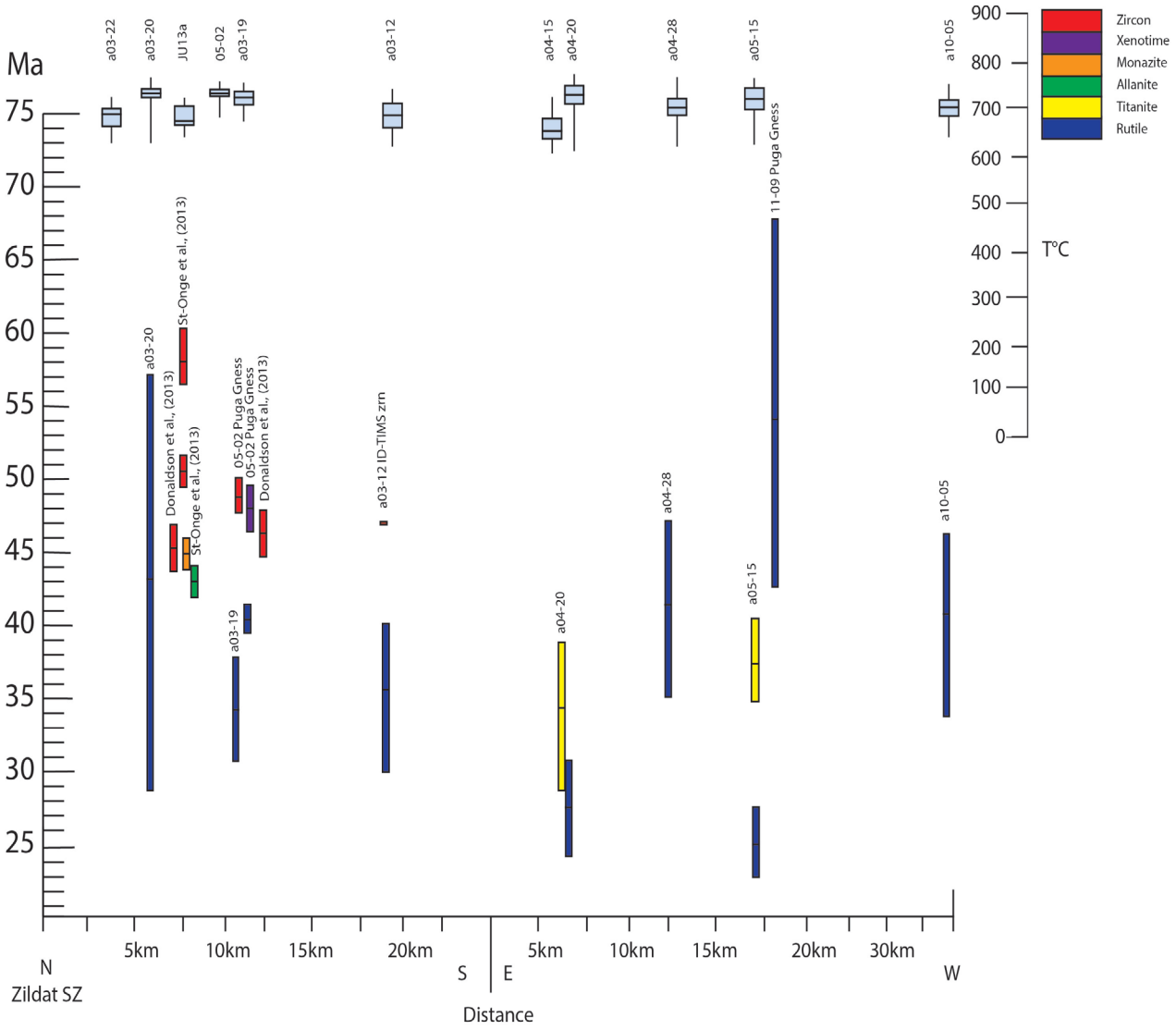


Figure 14 Age vs distance plot showing geochronological data in two transects from N-S and E-W with corresponding Zr in rutile data. Data from mafic eclogites unless specified otherwise.

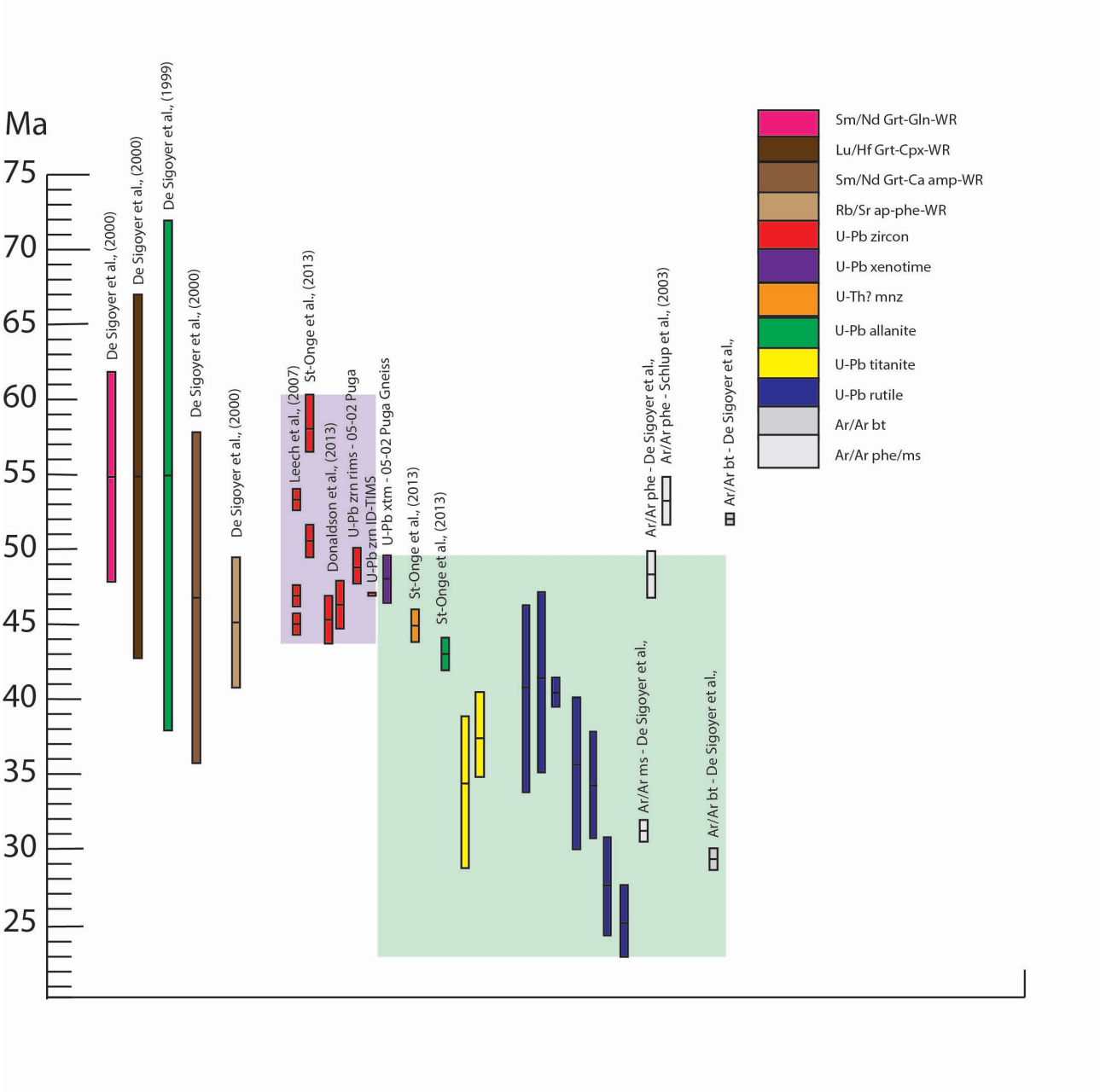


Figure 15 Summary of geochronology results for the Tso Morari nappe. Colours refer to mineral and dating method. Purple box denotes high pressure ages, green box denotes ages within the crust

Chapter 8 – Tectonic synthesis

This chapter summarises the tectonic constraints using field structural, geochemical, thermobarometric and geochronological data presented in Chapters 2-7. All these data can be compared with data from the Kaghan and Stak regions of northern Pakistan (e.g. Pognante *et al.*, 1993; O'Brien *et al.,* 1999; Parrish *et al.*, 2006; Lanari *et al.*, 2013) and integrated into a tectonic model to explain ultrahigh–pressure rocks along the North-western Himalaya, concentrating on potential processes involved in the subduction and exhumation of ultrahigh–pressure (UHP) rocks.

In order to understand the evolution of ultrahigh–pressure terranes, it is important to characterise the tectonostratigraphy, as well as the structural and metamorphic evolution of different rock types over time and their relationship to surrounding geological units. Metasediments of the Indus suture zone and their structural relationship with respect to surrounding units such as suture zone ophiolites (e.g. the Nidar ophiolite), give an account of the pre- and early history of the India-Asia collision (e.g. Buchs and Epard, 2019). Geochemistry and geochronology of igneous and volcanic rocks provide constraints on crustal scale processes (e.g. St-Onge *et al.*, 2010). Stratigraphic horizons, such a basement-cover interface, can act as detachment surfaces, allowing buoyancy-driven exhumation of crustal material from UHP conditions. High-strain zones can localise on stratigraphic horizons, pre-existing structural horizons or even zones of metamorphic weakening, such as fluid alteration pathways.

Previous studies of the Tso Morari complex have highlighted a paucity of spatial and temporal data, making tectonic synthesis difficult. Unanswered questions are still debated regarding the volume and mechanisms by which continental material can be subducted, the cause of detachment of continental material from a dense anchor and the style of exhumation. Exhumed ultrahigh–pressure terranes such as Tso Morari are the only direct evidence for processes that occurred at depth. It is therefore important to piece together a model for the formation of UHP terranes such as Tso Morari, in order to understand the potential mechanisms driving the subduction, detachment and exhumation.

Summary

By studying a range of lithologies from different structural positions in the Tso Morari complex, the most complete record of the metamorphic evolution of the complex through time can be deciphered. The Puga Gneiss is the most abundant lithology in the Tso Morari complex and had a partially altered (hydrated) granitic protolith with the capability to grow prograde garnet and kyanite. Low –strain metagranites preserve a complex history of magmatic emplacement, hydrothermal alteration, high-pressure metamorphism and later amphibolite-facies alteration, indicating that low strain zones provide a valuable window into metamorphic processes that occurred prior to deformation. Partial transformation in low–strain metagranites is documented to be a widespread feature, indicating that the entire complex experienced conditions in the eclogite facies. The metamorphic history recorded in garnet in the Puga Gneiss is essentially the same as that in the mafic eclogite, implying that these units underwent the same prograde history (**Error! Reference source not found.**). The prograde path records initial loading followed by heating to peak conditions in the coesite stability field. Subsequent isothermal decompression took place over ~1 Myr to crustal levels, followed by slower exhumation through the crust.

The prograde path is constrained by garnet compositions, garnet growth mechanisms and 'trustworthy' inclusion assemblages, indicating a switch from water–undersaturated to water–saturated conditions. Pressure–Temperature estimates for prograde garnet core growth occur at much lower pressures and temperatures than previous models. P-T estimates also show that the availability of fluid during metamorphism is an important consideration that has not been extensively explored in previous studies to date. This study highlights the importance of detailed petrographic study in order to confidently characterise the input parameters for thermodynamic modelling and estimation of P–T conditions. It also highlights the sensitivity of garnet isopleth positions to water saturation in certain bulk compositions, previously thought to be the most robust indicator of prograde P–T conditions.

The ultrahigh-pressure history of the complex is best preserved in mafic eclogites hosted in the Puga Gneiss. However, fluid-mediated retrogression makes estimating peak *P-T* conditions difficult using conventional methods. The best guide to peak pressure is the evidence for local, sporadic conversion of quartz to coesite. Evidence for ultrahigh-pressure metamorphism, in the form of preserved coesite inclusions in garnet, has

previously been identified in two outcrops of mafic eclogite. Pseudomorphs after coesite are present in the matrix of a metagranite from the centre of the complex. However, adjacent metagranites preserve quartz textures which have not transformed to coesite. The discrepancy in apparent peak pressures suggests that overpressure may have been important in transforming only some of the quartz to coesite, after the complex was subducted to ~ 26 kbar. It is unlikely that the complex spent long in, or traversed far into, the realm of UHP conditions, because of the indications that most of the quartz and feldspar failed to transform to coesite and Na-Cpx respectively.

High precision U-Pb dating of zircon using CA-ID-TIMS produced a more precise age of eclogite-facies metamorphism at 46.9 ± 0.04 Ma. This is comparable to the age of ultrahigh-pressure metamorphism of the Kaghan eclogites at 46.4 ± 0.1 Ma, located 450 km to the west, indicating synchronous subduction of the two ultrahigh-pressure localities in the subducted northern Indian continental margin. Xenotime, titanite and rutile U-Pb ages are interpreted to represent the time when then rocks were exhumed to crustal depths. Fast initial exhumation of < 1 Myr is estimated, followed by slower exhumation from the base of the crust over 10-20 Myr, providing constraints on a part of the geochronological history of the Tso Morari complex, from 47 to 22 Ma, that currently is lacking in age data but is extensively recorded in retrograde metamorphic microstructures and in amphibole and garnet chemistry.

There is limited evidence of early, prograde deformation fabrics in the Puga gneiss, except where rarely preserved in garnet, which means that very little is known about the state of strain within the complex at the subduction stage. The present high-strain fabric wraps prograde minerals (notably garnet) and formed in, or continued to develop under, conditions where sodic feldspar was stable, i.e. in the crustal realm. There was sufficient time, after slowing of the exhumation rate from HP/UHP conditions, for quartz fabrics and some feldspar in the deeper levels of the complex to undergo annealing and growth at c. 550°C in the crustal regime. This happened before further cooling and exhumation, of which there is little recorded evidence internally in the gneiss, except near its margins, so the later exhumation is most likely related to movements on the larger-scale nappe boundaries.

It is also important to acknowledge observations and interpretations that appear to be inconsistent with the proposed *P-T* history for the Tso Morari complex. These can be summarised as follows: 1. The relationships

involving magnesite and dolomite in the mafic eclogites are taken to imply peak pressures in the diamond field (Wilke *et al.,* 2015). This is inconsistent with the hypothesis that the Tso Morari complex only just reached UHP conditions as well as the observation that most of the quartz and feldspar failed to transform to coesite and Na-Cpx respectively. 2. The high temperature assigned to sample L08-03F (St-Onge *et al.*, 2013) for the formation of cordierite coronas around garnet and 'leucosomes'. Evidence for a high temperature overprint is lacking in the mineralogical record of low-pressure metamorphism in the broad variety of felsic and mafic compositions. 3. Zircon ages in the range 58-50 Ma, thought to be representative of peak (U)HP conditions (Leech *et al.*, 2007). However, no petrographic evidence is presented in support of this interpretation.

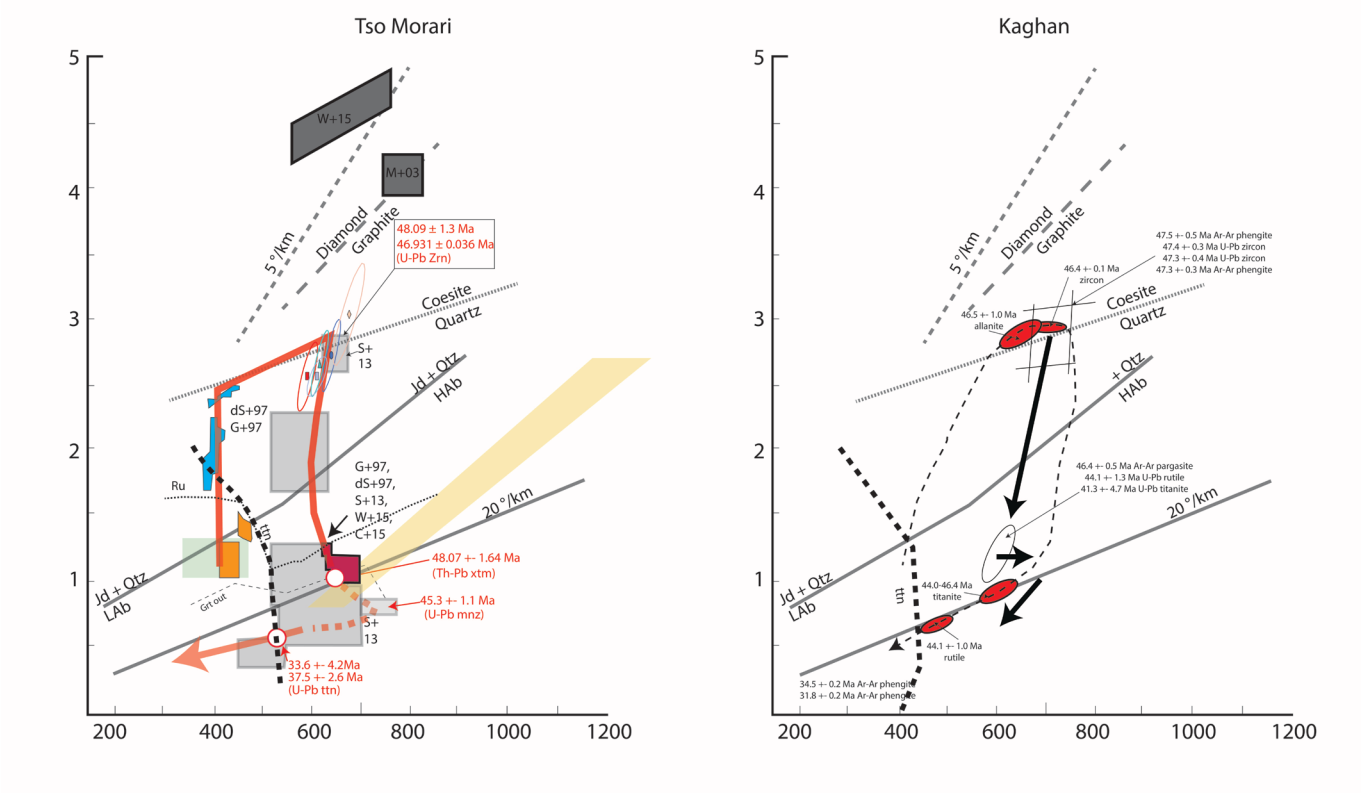


Figure 1 ***a.*** *Summary of P-T results and proposed P-T paths for the Tso Morari and Kaghan eclogites modified from O'Brien (2018a). Green box shows results of Grt-Cpx-Phe thermobarometry for sample 11-05. Orange and blue boxes show estimated P-T conditions for sample 11-05 using pseudosection modelling. Grey box of peak P-T conditions by S+13 overlaps with the peak P-T estimated for sample 11-05 in water saturated conditions. Coloured ellipses show results of AvePT modelling for sample 11-05. Yellow box shows results of Zr in Ru thermometry for 8-12kbar. Thick black dashed line shows upper limit of titanite (ttn) stability field based on pseudosection modelling of mafic eclogite sample 11-05 in water saturated conditions. Thin black dotted line shows lower limit of rutile (Ru) stability field based on pseudosection modelling of mafic eclogite sample 11-05 in water saturated conditions. Thin black dashed line shows lower limit of garnet stability field based on pseudosection modelling of granite gneiss sample 05-02, in water saturated conditions. Red arrow shows predicted P-T path. Dark and light grey boxes for published P-T predictions for Tso Morari eclogites. Coesite to quartz (Bohlen and Boettcher, 1982), Albite to jadeite + quartz (Holland (1980), diamond to graphite (Bundy, 1980). P-T estimates: G + 97 (Guillot et al., 1997), dS + 97 (de Sigoyer et al., 1997), M + 03 (Mukherjee et al., 2003), S + 13 (St-Onge et al., 2013), CJ15 (Chatterjee and*

Jagoutz, 2015), W + 15 (Wilke et al., 2015), W+10 (Wilke et al., 2010). ***b.*** *Summary of P-T results and proposed P-T paths for the Himalayan eclogites modified from* Wilke *et al.*(2010) *and* Parrish *et al.* (2006)*. The upper limit of titanite stability was calculated using the bulk composition of coesite eclogite (Wilke et al., 2010) and the thermodynamic modelling described in chapter 3.*

The North Indian margin

The structural and metamorphic history of the Tso Morari dome shows that the continental passive margin of India was subducted to UHP conditions (Steck *et al.*, 1998). The northern passive margin of Greater India was very long lived, with the oldest sediments deposited in the Proterozoic and the youngest sediments in the Eocene. An unconformity has been identified in the Palaeozoic stratigraphy of the Tethyan Himalaya, relating to an orogenic event close to the Cambo-Ordovician boundary known as the Bhimpedian or Kurgiakh orogeny (Garzanti *et al.*, 1986). The unconformity is marked by the change in sedimentary facies showing a marine transgression accompanied by the appearance of intercalated tuffaceous material from an immature island arc. By the middle Ordovician, eroded continental material was being deposited in alluvial fans, derived from erosion of the newly formed orogenic belt.

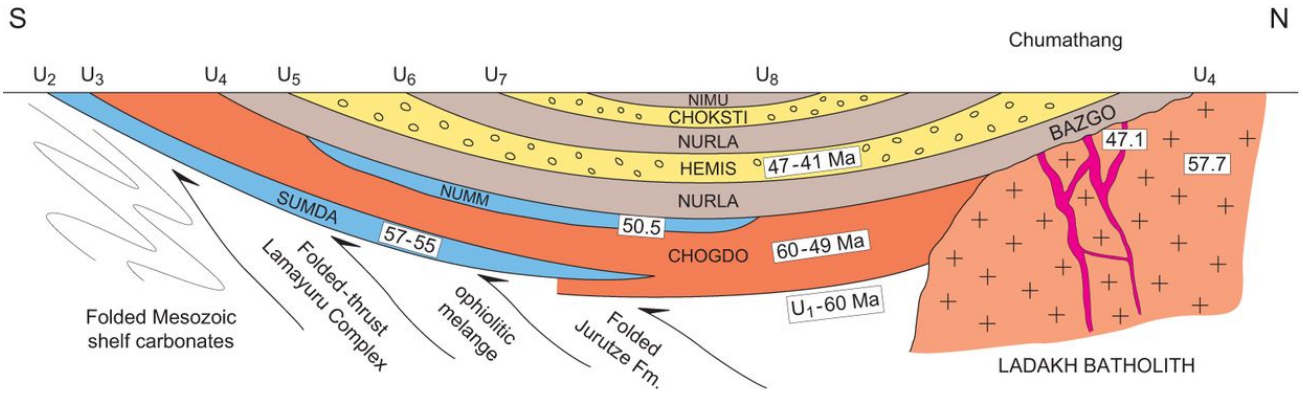
Further evidence of crustal thickening in the Ordovician comes from S-type granites which occur in the Lesser Himalaya (e.g. Mansehra, Mandi and Kathmandu granite), and pre-Himalayan ages within the Greater Himalaya (e.g. Nanga Parbat, Kinnaur Kailas and Ama Drime) and the north Himalayan domes (Tso Morari, Kangmar and Kampa domes). Evidence from metagranitoids in the Tso Morari complex suggest that these granites also underwent hydrothermal alteration during the Ordovician (chapter 4). Recent U-Pb geochronology of metamorphic rocks provides evidence of the Bhimpedian orogeny (482.4 ± 7.9 Ma and 464.5 ± 4.0 Ma, U-Pb monazite) in the Pakistan Himalaya (Palin *et al.*, 2018). The metamorphic, stratigraphic and geochronological results link rocks of the Pakistan Himalaya with the Lesser Himalaya and the Higher Himalaya, indicating that they all form part of a single contiguous plate. Flood basalt volcanism is prevalent in the NW Indian Himalaya and is linked to the Permian continental flood basalts known as the Panjal traps, formed in an extensional setting (Garzanti *et al.*, 1999). The north Indian passive margin also underwent extension and associated magmatism in the Early Cretaceous, as defined by the Comei large igneous province (Zhu *et al.*, 2009) and the Wolong volcanics (Hu *et al.*, 2010).

Timing of continental collision

The timing of continental subduction with respect to continental collision is important when trying to understand large scale plate motions and subduction dynamics. The timing of the collision of India with Asia is debated and has been determined using proxies such as the final marine sediments recorded along the Indus suture zone and north Indian plate margin (Green et al., 2008) and the first deposition of Asian-derived sediments in the Indus molasse basin (Hu *et al.*, 2015) (see chapter 1). Proxy data from the region of NW India allows a more direct comparison to be made with the data from the Tso Morari dome.

In the region of Chumathang in the Indus suture zone, north of the Tso Morari dome, the base of the Chogdo formation, comprised of sandstones, siltstones and mudstones, is dated at 60 Ma based on the presence of detrital zircons (Garzanti *et al.*, 1988). This unit lies above an unconformity which truncates folded metasediments related to the ophiolite obduction-related deformation. The terrestrial sediments of the Chogdo formation are interbedded with marine limestones indicating that the marine to terrestrial transition was underway during 60 – 50.5 Ma. The youngest marine sediments have been dated using Nummulitic limestones at 50.5 Ma (Green *et al.*, 2008). After 50.5 Ma, conglomerates and fluvial sediments were deposited. The transition to terrestrial sediments indicates that uplift and erosion was underway by this time and has been considered as a minimum age for continental collision (e.g. St-Onge *et al.*, 2010).

However, the deposition of limestone at 50.5 Ma could have occurred on the Indian continental shelf, rather than the Tethys ocean (e.g. Hu *et al.*, 2016). Additionally, sediments deposited in the Chumathang region suggest that terrestrial material was being deposited from 60 Ma (Garzanti *et al.*, 1988). Elsewhere in the Himalaya, proxies for the timing of continental collision predict collision to have occurred ~10 Myr earlier than the predicted subduction of Tso Morari. For example, the earliest arrival of Indian continental lithosphere to the subduction zone has been determined at 59 ± 1 Ma based on the identification of Asian-derived zircons in deep marine Palaeocene sedimentary rocks on the Greater Indian continental rise (DeCelles *et al.*, 2014; Wu *et al.*, 2014; Hu *et al.*, 2015; Metcalf *et al.*, 2017). Additionally, prograde Barrovian metamorphic ages from the North Himalayan domes at 56-54 Ma require that some collision and crustal thickening must have occurred at this time (Smit *et al.*, 2014).



U8 ~2 Ma. Quaternary alluvial terraces overlying folded Nimu Fm; Zanskar river.
U7 ~ ? Base of Nimu Fm. Ending of massive conglomerates; return to fine-grained sandstones, mudstones, siltstones.
U6 ~41 Ma. Return to Nurla facies floodplain muds, silts and lower-energy rivers.
U5 ~47 Ma Base of Hemis - Choksti conglomerates, high-energy fluvial channels derived from north; uplift Ladakh batholith.?Initiation of Indus River.
U4 50.5 Ma. Final marine transgression (Nummultic limestones), followed by sub-aerial fluvial and floodplain deposition (Nurla Fm.).
U3 ~54 Ma. Marine to continental transition (top Sumda Fm.).
U2 ~57 Ma. Neo-autochthonous marine transgression
U1 60 Ma. Base of Chogdo Fm purple-red sandstones, siltstones, mudstones (60-49 Ma detrital zircons). Unconformity truncates folded and thrust Lamayuru, Nindam, Jurutze, Tar Fms. End of ophiolite-obduction-related deformation.
--- Late Cretaceous-Paleocene thrusts, folds ---

Figure 2 Restoration of the Indus Group molasse basin along the Indus Suture Zone, taken from Searle (2019), after Searle et al., (1988) and St-Onge et al. (2010). Time constraints are from biostratigraphy (Green et al., 2008), detrital zircon ages (Clift et al., 2002) and U-Pb zircon geochronology from Ladakh granites (St-Onge et al., 2010)

Competing models for the India-Asia collision

There are three competing and mutually exclusive models for the India-Asia collision (Figure 3). Early models proposed a single subduction zone configuration of the Indian continent beneath Asia (Gansser, 1966; Le Fort, 1975; Sengör *et al.*, 1996). Within a plate kinematic framework, the single subduction zone configuration places the northern margin of Greater India 3000 km south of the southern Asian margin at the estimated time of collision (e.g. Van Hinsbergen *et al.*, 2012, 2019), despite horizontal estimates of shortening in the region of 1000km (Matte *et al.*, 1997). Other studies hypothesise a double subduction configuration in order to be consistent with the plate kinematic reconstructions, requiring the closure of two suture zones (e.g. Replumaz *et al.*, 2010, 2014; Jagoutz *et al.*, 2015). The feasibility of single vs. double subduction zone configurations are discussed in Parsons *et al.* (2019). Discussion as to the feasibility of each of the competing models for the India-Asia is found in Parsons *et al.,* (2019) and is summarised briefly below.

The minimum area reconstruction assumes that the area of Greater India was attached to the rest of India and has a north-south width of <1000 km prior to collision, assuming that most of the continental crust is

preserved in the bedrock record (e.g. Yakovlev and Clark, 2014). This model invokes a double subduction model in order to be consistent with the proposed timing of the collision of Greater India with Asia and predicts a 'soft' collision with an arc at 59 ± 1 Ma followed by 'hard' collision at ~45-30 Ma. The minimum area reconstruction model is consistent the restored location of the southern margin of Asia, decelerations in Indian plate velocity, temporal changes in magma geochemistry in the Kohistan and Ladakh blocks (e.g. Bouilhol *et al.*, 2013; Jagoutz *et al.*, 2018) and is able to explain most of the seismic anomalies beneath the Himalaya (Parsons et al., 2019). However, this model is inconsistent with bedrock evidence.

The enlarged-area reconstruction of Greater India assumes that the area of Greater India was contiguous with the rest of India, with a single subduction zone configuration and a north-south width of >3000 km (e.g. Hu *et al.*, 2016; Ingalls *et al.*, 2016; Van Hinsbergen *et al.*, 2019). The enlarged-area Greater India reconstruction models are consistent with the timing of subduction and collision recorded in the bedrock, palaeomagnetic and plate kinematic data, and is able to explain all of the seismic anomalies beneath the Himalaya. However, this model indicates that the pre-collisional area of Greater India is not entirely present in the bedrock record (e.g. Yakovlev *et al.*, 2014; Ingalls *et al.*, 2016), requiring complete subduction of a large portion of continental lithosphere, at least ~2000 km by ~ 2500 km in area, the feasibility of which is disputed (e.g. Rowley *et al.*, 2017; van Hinsbergen *et al.*, 2017).

The Greater India Basin reconstruction invokes rifting of the northern margin of Greater India in the early Cretaceous, prior to collision at ~60-50 Ma, forming a microcontinent. Collision of Asia with this microcontinent was followed by subduction of the Greater India Basin oceanic lithosphere (van Hinsbergen *et al.* 2012; 2019; Zhou and Su, 2019). The Greater India Basin reconstruction models are consistent with mantle tomography and plate kinematics and does not require subduction of large areas of continental crust (e.g. van Hinsbergen *et al.,* 2019). However, this model is inconsistent with the location and geochemistry of subduction-related magmatism and requires the presence of a suture zone along the Himalayan Main Central Thrust, for which there is no observable evidence (e.g. Searle, 2018).

None of the proposed models for the India-Asia collision are entirely consistent with bedrock evidence, plate kinematic reconstructions and mantle tomography. Most studies interpret their data in the context of just one of these models, with little discussion as to the validity of other models and the assumptions involved.

Interpretation of data from Tso Morari is discussed below with reference to different end member models and their assumptions.

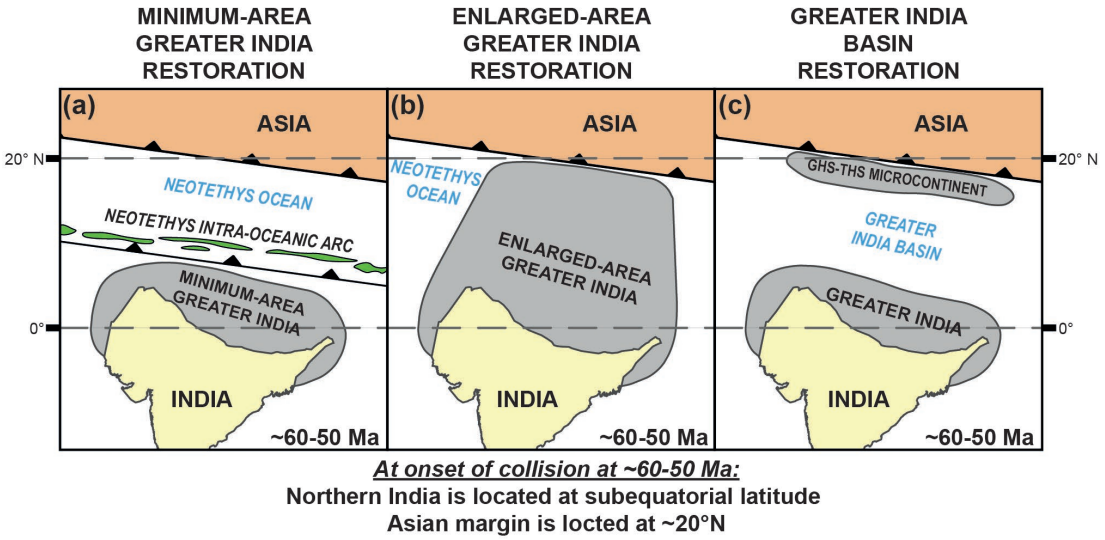


Figure 3 Greater India restorations for models of the India-Asia collision taken from Parsons *et al.*, (2019)*, figure 4. a. Minimum-area reconstruction. b. Enlarged-area reconstruction. c. Greater India Basin reconstruction. GHS – Greater Himalayan Sequence; THS – Tethyan Himalayan Sequence.*

Subduction of continental crust

Using the new and precise age for eclogite-facies metamorphism at 46.9 Ma (Chapter 7) and assumptions about the subduction angle and rate of subduction, we are able to estimate the timing of initiation and duration of subduction of the Tso Morari complex. The rate of subduction can be estimated from the rate of northward motion of India, derived from plate reconstruction models from Matthews *et al.*, (2016). Starting at 46.9 Ma, the horizontal distance moved can be back-calculated (Table 2) and compared to the down-dip distance subducted. The angle of subduction of India beneath Asia during continental collision has been approximated as four endmember dips of 20°, 45°, 70° and 90° and the down-dip distance calculated for each endmember dip for a vertical distance of 100 km (28 kbar, coesite stability field) and 150 km (42 kbar, diamond stability field) (table 1).

The results show that, in the most extreme scenario where the subduction angle is 20° (cf. Kaneko *et al.*, 2003) and peak pressure is 42 kbar it would have taken 4.1 myr to subduct 439 km of continental lithosphere (compare table 1, down-dip distance with cumulative km starting at 46.9 Ma, Table 2). The subduction of the

Tso Morari complex therefore probably initiated at ~50 Ma. Additionally, subduction to 42 kbar at 46.9 Ma, with a subduction angle of 45°, 70° and 90° would produce estimates for subduction initiation at 49.2 Ma, 48.8 Ma and 48.5 Ma respectively. These calculations assume no shortening of the subducted slab and no large northern extension of the Tso Morari complex.

Kaneko *et al.,* (2003) observed coesite included in zircon rims in felsic gneisses from the Kaghan valley, with a U-Pb zircon age of 46.2 ± 0.7 Ma (95% confidence errors, n=8). Parrish et al (2006) reported U-Pb geochronology of zircon from coesite-bearing mafic eclogites with an ID-TIMS zircon age of 46.4 ± 0.1 Ma. In the granite gneiss of the Kaghan valley, $^{232}Th/^{204}Pb$-$^{208}Pb/^{204}Pb$ isochron ages of allanite record a weighted mean age of 46.5 ± 1.0 Ma (MSWD = 0.21), interpreted to represent growth of the 2 volumetrically dominant zones consistent with growth during prograde to peak UHP metamorphism (Parrish *et al.*, 2006). The similarity in prograde/peak UHP of the Kaghan valley and the eclogite facies age recorded in Tso Morari, located 450 km apart, indicates synchronous subduction of the two UHP localities in the subducted northern Indian continental margin.

The minimum area Greater India reconstruction model (Parsons *et al.,* 2019) consists of two, simultaneously active, north-dipping subduction zones (Figure 3), invokes a 'soft' collision with an intra-oceanic arc at 59 ± 1 Ma with northward subduction of the NeoTethys oceanic lithosphere, followed by collision of Asia with greater India. Collision of India with the Neotethys intraoceanic island arc at 59 Ma would account for the prograde metamorphism recorded in the North Himalayan domes at 56-54 Ma (e.g. Smit *et al.*, 2014). Subsequent collision with the Lhasa and Karakoram terranes would then coincide with continental subduction of the leading edge of the continent at 50-46.9 Ma. Assuming that UHP metamorphism occurred at 46.9 Ma, with no crustal thickening prior to UHP metamorphism, initiation of continental subduction is predicted to occur at ~ 50 Ma. This places the Tso Morari dome on the leading edge of the margin of Greater India prior to collision.

The enlarged-area Greater India model invokes collision of India and Asia at 59 Ma and is consistent with prograde metamorphism in the Greater Himalayan Sequence at 56-54 Ma. In order to explain subduction and UHP metamorphism at ~50-47 Ma, the Tso Morari dome would not lie on the leading edge of the continental margin. Using the plate velocity models of Matthews *et al.*, (2016), we can reconstruct the relative position

of the Tso Morari rocks with respect to the leading edge of Greater India, assuming continental collision occurred at 59 Ma and that all shortening was accommodated in a single subduction zone (Table 2 – calculated for vertical subduction). In this model, ~1630 km of continental plate would have been subducted by 47 Ma, placing the Tso Morari rocks ~1446 km from the continental margin of Greater India, requiring an extensional detachment with a metamorphic discontinuity within the Indian plate, between the Indus Suture Zone and the Tso Morari complex. However, in order for this model to work, large volumes of buoyant continental material would have to be subducted to mantle depths.

Although the subduction of large volumes of continental material seems unfeasible, thermodyamic modelling of phase changes (Parsons *et al.,* 2019) suggest that felsic rock can become negatively buoyant at ~8.5-9 GPa (~250- 300 km depth) (Afonso and Zlotnik, 2011; Kawai and Tsuchiya, 2013; Kawai *et al.*, 2013). Subduction of material to this depth would define a 'depth of no return', coinciding with the stishovite-in isograd. The feasibility of subducting large volumes of thinned continental lithosphere to extreme depths has not been quantified, however, in order for material to be subducted to this depth it must not detach from the subducting slab or the underlying continental lithosphere, and must be cold and thin enough to be subducted. Large volumes of seismically fast material have been imaged beneath Tibet in the mantle transition zone and are consistent with the predicted behaviour of subducted continental lithosphere (Schaeffer and Lebedev, 2013; Parsons *et al.*, 2019).

The Greater India Basin hypothesis invokes a 'soft' collision with a microcontinent in the Greater Indian Basin at 59 Ma and does not require subduction of large volumes of continental material. In this model, subduction and UHP metamorphism of the Tso Morari complex at ~50-47 Ma would place the Tso Morari complex on the leading edge of Greater India prior to collision.

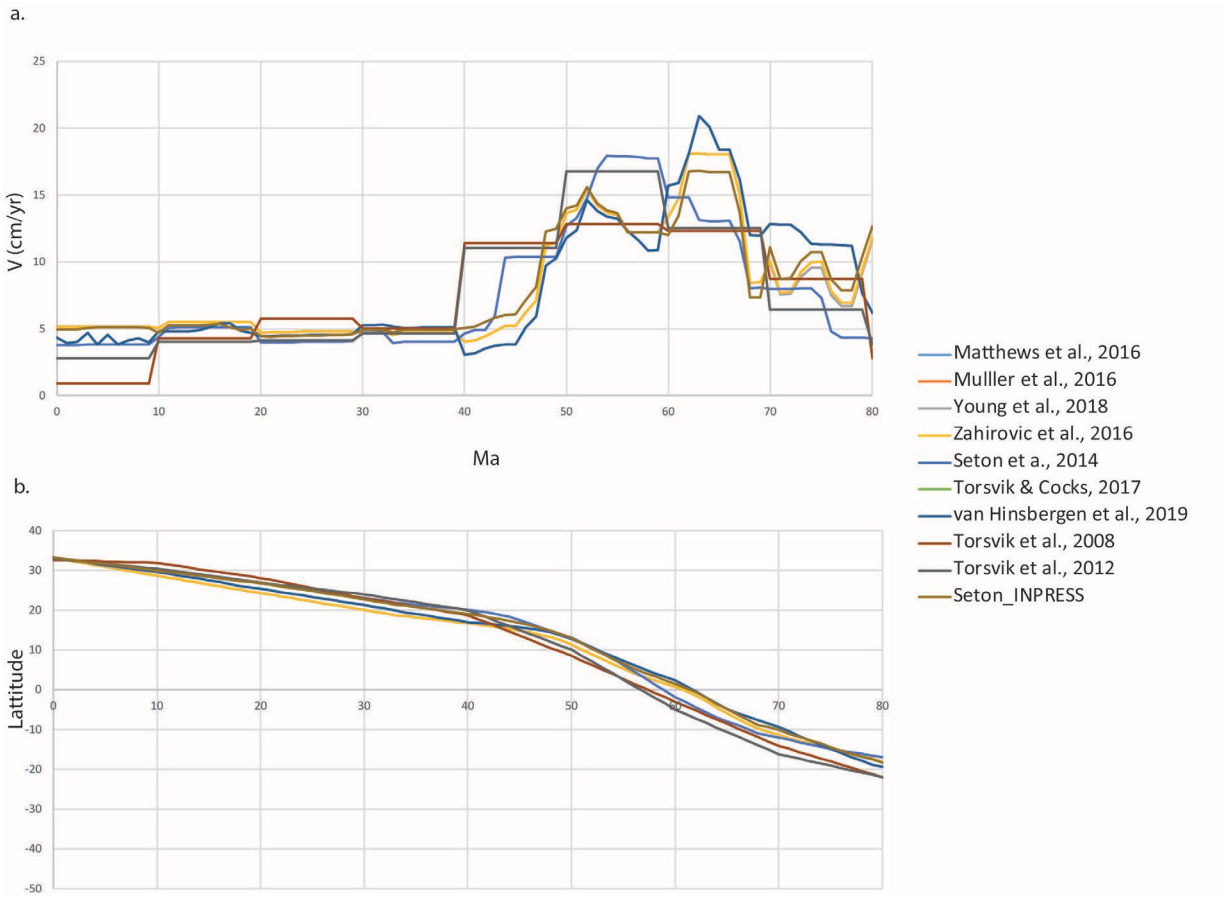


Figure 4 a. Velocity of India over time. b. Latitude of India over time. (Torsvik *et al.*, 2008, 2012, 2017; Seton *et al.*, 2014; Matthews *et al.*, 2016; Müller *et al.*, 2016; Zahirovic *et al.*, 2016; Young *et al.*, 2018; Van Hinsbergen *et al.*, 2019)

Subduction angle	Horizontal distance (km) at 28 kbar (d = 100km)	Horizontal distance (km) at 42 kbar (d = 150km)
20	292	439
45	141	212
70	106	160
90	100	150

Table 1 Calculation of horizontal distance (d) subducted at 100km vertical depth (h) and 150km vertical depth based on different angles of dip (a). d = h/sin(a)

Ma	*Lat*	*Long*	*V mag (cm/yr)*	*Distance (90° dip) in 1 Myr*	*cumulative km (90° dip) - peak eclogite backwards*	*cumulative km (90° dip) - 59 Ma forwards*
59	1.5791	63.5192	12.23	122	1634	122.26
58	2.4452	64.1935	12.22	122	1512	244.42
57	3.3143	64.8629	12.21	122	1389	366.49
56	4.1864	65.5275	12.20	122	1267	488.45
55	5.2909	66.0308	13.50	135	1145	623.49
54	6.4254	66.5073	13.69	137	1010	760.35
53	7.6144	66.972	14.20	142	873	902.321
52	8.9263	67.42	15.42	154	731	1056.48
51	10.1752	67.4609	13.91	139	577	1195.58
50	11.3919	67.3105	13.64	136	438	1332.02
49	12.3679	67.6381	11.44	114	301	1446.37
48	13.2226	68.1789	11.18	112	187	1558.18
47	13.8436	68.3388	7.13	71	76	1629.44
46.9	14.3995	68.3972	6.22	62	4*	1691.64

Table 2 Velocity estimated for the northward motion of India based on palaeomagnetic models from Matthews *et al.*, (2016)*. Lat and Long calculated for a reference point in the western syntaxis within a fixed mantle reference frame. Horizontal distance calculated for 1 Myr intervals. Cumulative distance subducted (assuming 90° dip) calculated starting at peak pressure metamorphism at 46.9 Ma and working back in time. * calculated for the period 46.931-47 Ma. Cumulative distance subducted calculated starting at 59Ma and working forward in time. Cumulative distance of subducted material calculated assuming a 90° dip*

Differences observed in UHP terranes around the world have shown that burial and exhumation of UHP material does not always take place during the same stage of the orogenic cycles (Kylander-Clark *et al.*, 2012). In the Alps, the timing of UHP metamorphism (35.4 ± 1 Ma, U-Pb zircon, whiteschist, Gebauer *et al.*, 1997) is thought to take place not long after continental collision, the effects of which were underway by c. 33 Ma (e.g. Liati and Gebauer, 2003; Rubatto *et al.*, 2009). UHP terranes such as the Dora Maira are thought to have a very short residence time at UHP (<3 Myr) (Rubatto *et al.*, 2001).

In older and larger orogens such as within the Western Gneiss region of the Norwegian Caledonides or the Chinese Dabie Sulu, geochronological data suggests much longer timescales of subduction and exhumation (ca. 25 Myr) and high-pressure metamorphism occurring tens of Ma after the onset of continental collision (Kylander-Clark *et al.*, 2012). In contrast, high pressure rocks of the As Sifah unit in Oman record eclogite-facies metamorphism at 78.95 ± 0.13 Ma (U-Pb zircon, Warren *et al.*, 2005) owing to subduction of the leading edge of the Arabian continent, where no continental collision has occurred (Agard *et al.*, 2010). Whereas in North Qaidam, continental subduction of arc material to UHP (468-463 Ma, Song *et al.*, 2004) is thought to have occurred beneath an island arc (active 486-438 Ma, Xu *et al.*, 2000) following obduction of an ophiolite at 500 ± 17 Ma (Shi *et al.*, 2004).

Tso Morari forms one of the larger of the 'small terranes' which were exhumed rapidly following a short residence time at peak pressure (Kylander-Clark et al., 2012) (see Chapter 1). The timing of peak metamorphism coincides roughly with the onset of continental collision but postdates the first arrival of continental material to the suture zone, as well as postdating ophiolite obduction. Mapping out the northward velocity of India using palaeomagnetic data (Figure 4) shows that it decreased at approximately 62 Ma and again at 52-50 Ma and underwent a change in direction at ~ 47-43 Ma (Torsvik et al., 2008, 2012, 2017; Seton et al., 2014; Matthews et al., 2016; Müller et al., 2016; Zahirovic et al., 2016; Young et al., 2018; Van Hinsbergen et al., 2019). The reduction in velocity could be explained by the arrival of buoyant continental material at the subduction zone, which is more difficult to subduct than dense ocean crust. Interpretation of these data suggest that UHP metamorphism took place either ~15 Myr or ~ 3-5 Myr after a reduction in velocity, with a change in direction of India coincident with peak UHP metamorphism.

The timing and duration of continental subduction in the Himalaya is most consistent with UHP terranes in the Alps, such as the Dora Maira. However, uncertainties relating to the onset of continental collision and the complex collision models in the Himalaya make comparison between orogens difficult.

Loading/burial then heating

Initial *P-T* path predictions, based on unfractionated phase equilibrium models of the Tso Morari eclogites, predict loading followed by heating at ~ 27-28 kbar (Figure 1). More advanced modelling techniques change the exact position and shape of the *P-T* path predicted. However, the overall topology of *P-T* paths produced is consistent, producing a path indicative of loading followed by heating (see chapter 3). Predicted mineral assemblages pass through the lawsonite stability field, consistent with observations of lawsonite pseudomorphs in the Tso Morari eclogites.

A thermomechanical model of Eocene subduction in the Himalaya predicts *P-T* paths of subducted upper crustal material along a cold path, indicating loading and burial followed by heating (Palin *et al.*, 2017, figure 6). However, these models are not specific to continental material. General models of continental subduction (Burov *et al.*, 2013) predict that continental subduction can occur only in cold strong lithosphere (T_{moho} < 550°C) with high convergence rates, and dense crustal UHP material is not always exhumed to the surface.

Sizova *et al.*, (2012) showed that the shape of the *P-T* path depends on the length of ocean slab attached to the continent. Shorter oceanic slabs (such as the 400 km long slab in model I of Sizova *et al.,* 2012) predict concurrent heating and loading, whereas longer slabs (600 km long slab of model II) are dominated by loading until they reach near-peak pressures (Sizova *et al.*, 2012, figure 2). Particle *P-T-t* paths produced in models of subduction (e.g. Sizova *et al.*, 2012; Burov *et al.*, 2013) generally begin at surface conditions and may therefore not be good estimates for continental material, which may have been derived from deeper and hotter levels in the crust, prior to subduction.

Peak metamorphism

Pressure determinations from mineral assemblages rely on the assumption that two or more phases are in equilibrium and that the recorded pressure is equivalent to the lithostatic pressure, providing information on the depth of burial. Field evidence based on the discrepancies in pressure estimates within UHP terranes suggest that tectonic overpressure of up to 1.5 GPa more than lithostatic pressure can be reached in rocks such as orogenic peridotites, which commonly record pressures much higher than the crustal rocks in which they are hosted (Vrijmoed *et al.*, 2009; Brueckner *et al.*, 2010; Li *et al.*, 2010). However, overpressure can only be assumed in these examples if UHP metamorphism in the peridotites is concurrent with metamorphism in the surrounding terrane. This raises questions as to whether the lithosphere could withstand such large overpressures and whether barometers used to provide such estimates are accurate measures of depth of burial. Thermomechanical 2D numerical models of continental subduction/collision zones suggest that local overpressures would be in the range of 3-4 kbar greater than lithostatic pressure in subducted crustal material (Gerya *et al.*, 2008; Li *et al.*, 2010).

In a terrane subject to overpressure, a heterogeneous distribution of stress would be expected to produce areas of contrasting peak pressures. When considering overpressure, it is important to consider the scales and timescales involved. For metamorphic minerals to record pressures equivalent to the tectonic overpressure invoked, the overpressure must be maintained long enough that metamorphic reactions occur. In subduction zone settings, continuous subduction could potentially maintain large differential stresses for the duration of subduction, rather than experiencing a finite displacement or shortening. Pressure estimates in eclogite-facies rocks have uncertainties in the order of 1-2 kbar, similar to potential overpressure estimates in subducted crustal material of 3-4 kbar, making it difficult to determine whether rocks record pressures greater than lithostatic (Warren, 2012).

Pseudomorphs preserved following the nucleation and growth of quartz after coesite provide an important indication of pressure. Transformation of quartz to coesite is a polymorphic reaction that has small uncertainties on the pressure at which this transformation occurs (Mosenfelder *et al.*, 1997), is thought to take place relatively quickly in relation to geological timescales, and does not require the presence of additional reactants and diffusional processes (Perrillat *et al.*, 2003). The former presence of coesite is therefore a

particularly useful pressure indicator in the absence of growth of metamorphic phases at high pressures. However, the quartz to coesite reaction is relatively sluggish compared to the reverse reaction and may depend on the availability of fluid to catalyse the reaction, allowing metastable persistence of quartz above the quartz-coesite transition.

The preservation of microstructures after coesite confirm that sample a05-10 from the centre of the Tso Morari complex was subducted to UHP. However, microstructures after coesite are not a common feature in the granites of the Tso Morari dome and single quartz crystals, which did not undergo transformation to coesite, microstructures are observed in samples from within the Polokongka La region. The presence of untransformed quartz and textures after coesite in the Polokongka La region of the Tso Morari dome, may indicate that some areas achieved UHP conditions whereas others did not. The ease at which the coesite-breakdown reaction occurs suggests that the entirety of the Polokongka La region, if subducted to the coesite stability field, would show quartz microstructures indicative of transformation to quartz from coesite.

The discrepancy in quartz microstructural observations could be explained in one of three ways: 1. the presence of shear zones within the Tso Morari complex, subdividing the complex into regions of lower and higher pressure. 2. If the peak pressure during subduction lies approximately at the quartz-coesite transition, tectonic overpressure could push some regions into the coesite stability field. 3. Additional factors such as deformation or fluid interaction may be required to progress the quartz to coesite transition.

The Tso Morari complex has been interpreted as a coherent tectonic unit (Epard and Steck, 2008). The subdivision of the Tso Morari complex into regions of lower and higher pressure is difficult to test in the field owing to the poor exposure across the dome, heterogeneous deformation state of the Puga Gneiss and the lack of phases present in the felsic material required in conventional thermobarometry. However, partial transformation of granites from across the complex indicates that a large proportion of the dome experienced a similar metamorphic history, suggesting that the Tso Morari complex was subducted and exhumed as a relatively coherent unit.

A hypothesis worth exploring, based on the record in metagranites, is that the rocks of the Tso Morari complex were approximately at the quartz-coesite transition at their metamorphic peak, so that just some of

the locally over-pressured rocks transformed to coesite. Heterogeneous distribution of pressure within subducted crustal material could push some regions into the coesite stability field if the depth of subduction is equivalent to the quartz-coesite transition at approximately 26 kbar.

Alternatively, the quartz-coesite boundary may have been slightly overstepped, but additional factors such as a critical amount of low-strain deformation, or a small amount of fluid interaction, triggered the transformation in certain restricted domains. The presence of fluid is known to have a catalytic effect on reactions (Rubie, 1986) and H_2O increases the diffusion rate of oxygen in silicates (Elphick and Graham, 1988). Additionally, fluids may reduce the activation energy required to break Si-O bonds, enhancing nucleation. The quartz to coesite reaction is relatively sluggish compared to the reverse reaction and may depend on the availability of fluid to catalyse the reaction (Mosenfelder and Bohlen, 1997; Perrillat *et al.*, 2003), allowing metastable persistence of quartz above the quartz-coesite transition. However, the magnitude of overstep that can be sustained by metastable quartz is unknown. The fast reaction kinetics determined from experiments such as Mosenfelder and Bohlen (1997) and Perrillat et al. (2003) indicate that a large overstep may not be sustained, suggesting that the peak pressure of the complex could lie just above the quartz-coesite transition, with the progress of the quartz to coesite reaction limited to restricted domains where factors such as fluids were available.

Peak pressure estimates for the eclogites from the Tso Morari complex are in the range of 26-40 kbar (e.g. St-Onge et al., 2013; Wilke et al., 2015). Peak pressure estimates of >40 kbar are reliant on equilibrium relations between magnesite and dolomite, which may be considered tenuous in the absence of post-coesite microstructures as seen in other UHP terranes. The discrepancy in these peak–pressure estimates is currently unresolved (O'Brien, 2018) (see chapter 3).

Detachment

Buoyancy driven exhumation of UHP material is thought to take place following detachment of crustal material at depth (Ernst, 1997; Hermann *et al.*, 2001; Parrish *et al.*, 2006; Warren *et al.*, 2008c, 2008a; Beaumont *et al.*, 2009). Small UHP terranes such as Tso Morari and Dora Maira, are composed only of mid- to upper-crustal material, suggesting that detachment occurred. Thermomechanical models of continental subduction by Burov *et al.,* (2013) predict that in slower convergence settings, relatively weak UHP rocks of

the upper plate may decouple from the strong, underlying lower plate. Rheological changes and fluid-exchanges associated with low to middle pressure phase changes along the subduction interface are thought to be responsible for weakening associated with detachment of crustal units (Burov *et al.*, 2013).

Detachment or weakening mechanisms include transformation weakening, increases in temperature, hydration, melting, grain size reduction or the development of a foliation (Warren *et al.*, 2008b) (see Chapter 1). The presence of fluids during subduction can be responsible for weakening crustal rocks by catalysing metamorphic reactions, facilitating melting or acting as a lubricant. Hydrous phases in the peak assemblage of the Tso Morari eclogites indicate that fluids were present during subduction. However, the fact that transformation of felsic rocks was incomplete suggests that fluid infiltration was limited. During the early stages of exhumation, fluids derived from the dehydration of hydrous phases such as talc, and externally derived fluids, generated amphibole- and clinozoisite-bearing assemblages at ~23 and ~19 kbar (Palin *et al.*, 2014). Symplectites formed after omphacite, indicating *P-T* conditions in the lower crust and the presence of some fluid, but not enough to saturate grain boundaries or form a free interconnected phase. Strain localisation, such as at the margins of the Tso Morari mafic dykes where syn-deformational garnet growth occurred at high pressures (chapter 5), provides opportunities for fluid infiltration.

Transformation in the eclogite facies to a mechanically weak assemblage, such as the common mica-bearing assemblages, would influence the strength and anisotropy of the subducted unit. Transformation in the eclogite facies has been shown to be volumetrically minor in felsic rocks in the Tso Morari complex, often limited by the dry conditions (see chapter 4 and chapter 5), making transformation weakening an unlikely detachment mechanism.

Primary plagioclase is absent from the Puga Gneiss. Bulk geochemical trends and replacement textures suggest that igneous plagioclase broke down to form white mica + albite ± clinozoisite (Chapter 5). However, this ‘alteration’ could have happened at any stage in the history of the rocks, whether late- or post-magmatic, metamorphic, or accompanying high-strain deformation. Clinopyroxene is expected to form from the breakdown of plagioclase at high pressure equilibrium conditions. The absence of clinopyroxene observed after plagioclase, and a grossular content in garnet which is not consistent with growth in the presence of clinopyroxene (Chapter 5), suggests that plagioclase persisted metastably to high pressures during

subduction. Models of crustal strength that assume feldspar-absent assemblages (Stöckhert *et al.*, 1998) or transformation of continental material under equilibrium conditions during subduction, are therefore not realistic.

Isothermal decompression

For a sample of Puga Gneiss (e.g. sample 05-02) at 28 kbar and 550°C, the hydrous assemblage clinopyroxene, garnet, rutile, carpholite, white mica and coesite predicted in water saturated conditions has a bulk density of >3.08 $g.cm^{-3}$ in the presence of clinopyroxene and >2.89 $g.cm^{-3}$ in the unlikely case that plagioclase persisted metastably. In water undersaturated conditions the assemblage clinopyroxene, garnet, white mica, K feldspar, coesite, kyanite and rutile has a bulk density of 3.10 $g.cm^{-3}$. Puga Gneiss at this depth is positively buoyant with respect to the mantle which has a density of 3.35 $g.cm^{-3}$. During subduction of continental crust, following detachment at depth, it is therefore expected that the positive buoyancy force exerted by a large slab of continental crust would drive exhumation to a depth of neutral buoyancy. Exhumation via this mechanism is predicted to be rapid, occurring within 3 Myr of subduction to peak pressure (Duretz *et al.*, 2013).

The exhumation rate of the Tso Morari eclogites can be estimated based on the precise age of peak pressure metamorphism at ~28 kbar, measured by U-Pb of zircon, and the age of garnet breakdown at ~10 kbar in crustal conditions, measured by U-Pb of xenotime. The precise age of zircon growth, provided by ID-TIMS of zircon, would ideally be used in conjunction with the age of garnet breakdown within the same sample or location. However, sample a03-12 (ID-TIMS zircon) and 05-02 (LA-ICP-MS xenotime) are located ~9 km apart and the weighted mean average of the xenotime age in sample 05-02 is older than the zircon age in sample a03-12, despite petrological evidence indicating that this should not be the case. This discrepancy can be explained by the large uncertainty on the xenotime measurement which overlaps with the zircon age, indicating that the whole unit exhumed rapidly, within error of these measurements.

Assuming a peak pressure (M2) of ~28 kbar at 48.09 ± 1.3 Ma (LA-ICP-MS, U-Pb zircon, sample 05-02) and the ~10 kbar breakdown of garnet (LA-ICP-MS, U-Pb xenotime, sample 05-02) at 48.07 ± 1.64 Ma, the

slowest estimated vertical exhumation rate predicted is 6 mm.a^{-1}. Extrapolation of *P-T* paths into the diamond stability field (Wilke *et al.*, 2015) increases the slowest rates of exhumation from ~6 mm.a^{-1} to ~10.8 mm.a^{-1}.

Estimates of exhumation rate by other authors are in the range of 12-80 mm.a^{-1} (O'Brien and Sachan, 2000; Massonne *et al.*, 2003; Parrish *et al.*, 2006; St-Onge *et al.*, 2013). Sharp compositional boundaries, preserved between garnet inner and outer core zones, imply that UHP metamorphism in the Tso Morari complex was short lived, allowing constraints to be placed on exhumation rates by diffusion modelling of zoned garnets, of 23-45 mm.a^{-1} from eclogite to amphibolite facies (O'Brien *et al.*, 2000). Fast rates of decompression have also been estimated from UHP to lower crustal conditions in the Tso Morari complex; St-Onge et al., (2013) predicted an exhumation rate of 12 mm.a^{-1} based on peak M2 conditions (28 kbar, 640-650°C at 50.8 ± 1.4 Ma) to the breakdown of garnet (12.5 kbar, 690 ± 25°C at 45.3 ± 1.1 Ma). Similarly, Parrish et al., (2006) predicted an initial exhumation rate in the range of 25 to 80 mma^{-1} in the Kaghan eclogites based on peak pressure conditions (>100 km, 46.4 ± 0.1 Ma) to lower crustal depths (<35 km, 45.6 to 47.7 Ma).

The lower crustal age constraint in the Kaghan eclogite is based on titanite age data, thought to represent crustal conditions at 30 kbar and temperatures > 600°C (Parrish *et al.,* 2006). However, pressure–temperature conditions equating to titanite stability or U-Pb closure temperature were not constrained. The U-Pb age of titanite from the Tso Morari eclogites is interpreted to date a growth age of titanite during cooling through a temperature well below peak temperature (Chapter 7). Therefore, understanding the extent of the stability field of titanite allows a more direct comparison between the titanite age in Kaghan (Parrish *et al.,* 2006) with the titanite age in Tso Morari (Chapter 7).

Thermodynamic modelling of the Kaghan coesite eclogite described in Wilke *et al.*, (2010) was employed in water saturated conditions, using the same dataset and activity models as the thermodynamic modelling of the Tso Morari eclogites in Chapter 3. In the Kaghan eclogite, titanite is predicted to be stable below 450°C compared to 530°C in the Tso Morari eclogite (Figure 1b). Based on the assumption that the titanite ages from Kaghan also records a growth age during cooling, the initial exhumation rate of ~25 mm.a^{-1} can therefore be considered a minimum. Short-lived UHP metamorphism and rapid exhumation is a common feature of many UHP terranes including the Dora Maira (Chopin *et al.*, 1991), Zermatt–Saas (Amato Ł *et al.*, 1999), Kaghan (Parrish *et al.*, 2006), Kokchetav (Hermann *et al.*, 2001).

Temperatures achieved after exhumation to crustal levels

St-Onge *et al*. (2013) documented an increase in temperature (M4) to 705-755°C, 7-8.4 kbar, based on a non-fractionated isochemical phase diagram calculated for the assemblage garnet-cordierite-sillimanite-biotite-plagioclase-quartz-melt, within a felsic rock from the Berthelsen outcrop of the Tso Morari complex. Th-Pb SHRIMP dating of monazite cores with allanite rims was interpreted to constrain the timing of M4 metamorphism at 45.3 ± 1.1 Ma. This temperature increase predicts peak conditions above the solidus and is consistent with cordierite rims around garnet, interpreted as a decompression texture and the presence of 'leucosomes', interpreted as a melting texture. St-Onge et al., (2013) estimated a melt fraction of 10-15% based on the volume of albite + quartz 'leucosomes' in the gneiss. However, evidence of melting elsewhere in the abundant Puga Gneiss has not been observed. The Puga Gneiss contains albite + quartz leucocratic bands which formed as a product of syn-metamorphic deformation and could have been mistaken for leucosomes formed through anatexis. Quartz microstructures in Puga Gneiss samples from across the complex preserve maximum temperatures in the core of the complex, indicative of post-deformation annealing of quartz at ~550°C.

The petrographic relationships and mineral compositions preserved in the mafic eclogites of the Tso Morari complex record temperatures of <600°C during isothermal decompression from peak pressure (Palin *et al.*, 2014), with no evidence of a high temperature overprint. Observed fine-grained breakdown products of omphacite in Tso Morari eclogites (Chapter 3) contain albite and indicate temperatures <550°C. These symplectites are clinopyroxene-absent intergrowths, contrasting to the lamellar pyroxene-bearing symplectites observed in the mafic eclogites of the Western Gneiss Region formed at temperatures of 700-550°C (e.g. Martin, 2019). The textural and compositional differences between intergrowths after omphacite in the Tso Morari eclogites and symplectites after omphacite in other UHP terranes such as the Western Gneiss Region, suggest that the Tso Morari eclogites did not form at such high temperatures.

Magnesiohornblende rims around matrix amphiboles also record amphibolite facies conditions of < 12 kbar, (Palin *et al.*, 2014). Temperature estimates from conventional thermobarometric techniques, such as amphibole-plagioclase thermometry of symplectites, have not been applied to the Tso Morari eclogites owing

to the lack of a Ca-component in plagioclase in the symplectites, preventing this exchange equilibrium from being used.

Zr in rutile thermometry records peak temperatures achieved during the *P-T* history of the rock. At 8 kbar, the average peak temperatures recorded by the eclogites of the Tso Morari complex are in the range of 592-659°C, consistent with deformation of quartz in the grain boundary migration regime (Passchier and Trouw, 2005) in the host Puga Gneiss. Sample 05-02 (Puga Gneiss) records a Zr in rutile temperature of 653°C. The Zr in rutile temperatures are higher than temperature estimates at peak pressure and sit just above the wet solidus (625°C) in the Puga Gneiss and just below the muscovite dehydration reaction (670°C). Peak temperatures recorded by the Zr content of rutile from multiple lithologies and sample locations are consistently lower than the temperature estimates by St-Onge et al., (2013) from the Berthelsen outcrop. The lack of melt textures in the Puga Gneiss and low Zr in rutile temperatures in the mafic eclogites and Puga Gneiss suggest that melting did not occur in these lithologies in the Tso Morari complex and temperatures are unlikely to have reached 705-755°C as suggested by St-Onge et al., (2013).

An increase in temperature is predicted in a mafic eclogite from the Kaghan valley from 580-630°C at 10-17 kbar to 650-720°Cat ~12 kbar (Wilke *et al.*, 2010a) between ~ 40 and 30 Ma (Wilke *et al.*, 2010b) (Figure 1b). The higher temperature estimates (650-720°C) are based on amphibole-plagioclase thermometry and are consistent with temperature estimates based on Zr content in matrix rutile (706-729°C). Rutile from fresh eclogites in the Kaghan valley yield slightly higher average temperatures than heavily retrogressed eclogites (~679-691°C) (Rehman *et al.*, 2019). In contrast, however, the *P-T* estimates of 580-630°C at 10-17 kbar are derived only from Na in the A-site of glaucophane (580—630°C) which forms in the cores of zoned matrix amphibole (Wilke *et al.*, 2010a). However, Na in sodic amphibole is pressure-dependent, a factor which does not seem to have been investigated above 17 kbar in the study by Wilke *et al.,* (2010a).

The Tso Morari and Kaghan eclogites are thought to have similar bulk compositions and followed comparable subduction-related *P-T*-t paths. Glaucophane cores of matrix amphiboles in the Tso Morari eclogites, similar in composition and texture to those observed in the Kaghan eclogites, are thought to have formed at high pressure, early in the retrograde history of the eclogite (de Sigoyer *et al.*, 1997). These similarities suggest

that glaucophane in the Kaghan eclogites could have formed under similar conditions to that in the Tso Morari eclogites, removing the temperature constraint of 580-630°C on the initial retrograde path. The peak temperatures recorded by amphibole-plagioclase thermometry and Zr in rutile thermometry in the Kaghan eclogites overlap and are comparable to the temperature predicted at peak pressure, suggesting that isothermal decompression to crustal conditions may have occurred without an increase in temperature

Mafic boudins in the Tso Morari complex preserve an eclogite facies core with hydrated and retrogressed rims. Zoned matrix amphiboles and symplectites after omphacite have been linked to the isothermal decompression and subsequent amphibolite-facies history of the rocks. The lower–pressure overprint consists of biotite, epidote and Na-plagioclase, formed in greenschist- to epidote-amphibolite-facies conditions. There is no evidence of a high temperature amphibolite-facies overprint in the mineral compositions of the mafic rocks. The preservation of early retrograde features in the core of the boudins and the extensive greenschist-facies overprint in the rims suggests that a high temperature overprint was not experienced by the mafic lithologies. In summary, the mineralogical record of low-pressure metamorphism in the broad variety of felsic and mafic compositions casts doubt on the suggestions of a high-temperature episode in the Tso Morari complex at crustal levels.

Exhumation from the lower crust

A decrease in exhumation rate at 8-12 kbar is recorded in the Tso Morari complex (e.g. de Sigoyer *et al.*, 2000; St-Onge *et al.*, 2013) and is consistent with a change in exhumation mechanism from rapid, buoyancy driven initial exhumation to the lower crust, followed by a mechanism with a slower rate of exhumation. The rate of exhumation from the lower crust to the surface can be constrained by dating minerals which record temperatures or growth below 700°C at low pressures, such as U-Pb titanite, U-Pb rutile, Ar-Ar phengite, Ar-Ar biotite, fission track zircon etc. New U-Pb data from titanite and rutile (chapter 7) combined with published Ar-Ar and fission track ages (de Sigoyer *et al.*, 2000; Schlup *et al.*, 2003) indicate that this period of exhumation lasted ~10-15 Myr.

U-Pb ages of rutile contain large overlapping uncertainties making it difficult to resolve spatial variations across the dome. However, the peak temperatures recorded by Zr in rutile are consistent across the dome,

indicating that there was no significant thermal gradient across the Tso Morari complex when it resided in the lower crust.

Exhumation mechanisms:

Physical/analogue and numerical modelling provides insight into how rocks could be exhumed from UHP depths. However, there is a lack of precise empirical data from known occurrences to verify the models, particularly on the rates of these processes. Combined petrographic, geochronological data and field mapping provide an insight into exhumation of a specific terrane over time and can be compared to models to test their validity. Proposed exhumation models include 1. eduction (Andersen *et al.*, 1991), 2. exhumation of a relatively coherent unit along the subduction channel (Chemenda *et al.*, 1995), 3. exhumation of relatively coherent crustal stacks separated by shear zone (Sizova *et al.*, 2012), 4. ductile exhumation within a subduction channel melange (Burov *et al.*, 2001; Gerya *et al.*, 2008; Warren *et al.*, 2008c; Yamato *et al.*, 2008; Beaumont *et al.*, 2009), 5. microplate rotation (Webb *et al.*, 2008) and 6. diapiric exhumation (Chatterjee *et al.*, 2015) (see chapter 1 for a review of exhumation mechanisms).

Key features of the Tso Morari complex include short-lived metamorphism at peak pressure conditions followed by fast, buoyancy driven initial exhumation to lower crustal conditions, as well as the presence of relatively coherent and undeformed units within the Puga Gneiss separated by wide zones of ductile deformation. Complex exhumation-related deformation styles within the Puga Gneiss make it difficult to identify the location of potential shear zones juxtaposing relatively coherent units. Similarities in garnet compositions and zoning trends indicate that the prograde high-pressure *P-T* history is uniform across the Tso Morari complex (chapter 3 and 5), suggesting that the entire unit behaved relatively coherently during subduction. It is difficult to resolve the spatial variation in the timing of high-pressure metamorphism in the Tso Morari complex due to the insufficiently high precision of zircon ages. New ID-TIMS data (chapter 7) more precisely dates high pressure metamorphism but the lack of spatial resolution prevents interpretation with respect to exhumation mechanisms.

Consideration of data from the Tso Morari dome allows certain exhumation mechanisms, such as eduction and diapiric exhumation, to be discounted. A distinguishing factor of the eduction model is the predicted

long-lived duration of UHP metamorphism and the slow exhumation rates (Andersen *et al.*, 1991). This is not consistent with the short-lived metamorphism and fast, buoyancy driven initial exhumation recorded in the Tso Morari dome. During exhumation, the eclogites of the Tso Morari complex follow an isothermal decompression trend, showing a rapid decrease in pressure with little decrease in temperature. This is not consistent with the diapiric exhumation model proposed by Chatterjee and Jagoutz (2015) which predicts an increase of temperature due to passage through the mantle wedge during exhumation.

Rapid exhumation predicted from peak pressures to lower crustal conditions, as recorded in samples from localities 16/41 (the Bridge) and 16/51 (Kiagar Tso), is consistent with rapid buoyancy-driven exhumation along the subduction channel, a feature of exhumation models including Chemenda *et al.* (1995), Sizova *et al.* (2012) and Beaumont and Jamieson (2009). The Chemenda *et al.,* (1995) model simulates exhumation of a coherent tectonic block which would contain uniform *P-T*-t paths within the block. Exhumation of relatively coherent crustal stacks is simulated in the Sizova *et al.* (2012) model which results in the juxtaposition of coherent blocks with contrasting *P-T* paths, separated by shear zones. Ductile exhumation within a subduction channel melange (England and Holland, 1979; Mancktelow, 1995) is simulated in models which result in contrasting *P-T-t* conditions within units (Beaumont and Jamieson, 2009). Relatively coherent and undeformed units within the Puga Gneiss, separated by wide zones of ductile deformation, suggests that the style of exhumation is partially analogous to both the Chemenda-style exhumation of relatively coherent blocks (Sizova *et al.*, 2012) and the ductile exhumation within a subduction channel melange (Beaumont *et al.*, 2009). However, further insight into the exhumation-style of the Tso Morari dome requires a greater spatial distribution of *P-T-t* data.

The history of the Indian crust in Ladakh

Prior to continental collision, the northern margin of India was covered by a Neoproterozoic to Ordovician passive margin sequence, intruded by Ordovician granites, and overlain by a thick Permian–Mesozoic shelf carbonate sequence. Parts of the continental crust were subducted to peak eclogite facies depths by 46.9 Ma, prior to peak kyanite grade metamorphism in the Greater Himalayan Sequence in Zanskar at 33-31 Ma (Vance *et al.*, 1999; Walker *et al.*, 1999). The Tetraogal nappe, which now lies structurally above the Tso Morari complex, was metamorphosed to amphibolite facies conditions.

By 40-30 Ma, the Tso Morari dome was exhumed to upper crustal levels (<300°C) and underwent a uniform and approximately similar uplift history across the dome (Schlup *et al.*, 2003), suggesting that the Tso Morari, Tetraogal and Mata nappes were juxtaposed to their current relative structural positions by this time. Deformation in the Himalayan orogen continued to propagate towards the southwest after 30 Ma, stacking the GHS above the LHS. Extrusion of the GHS beneath the South Tibetan detachment was underway and peak sillimanite-grade conditions were achieved at ~21 – 19.5 Ma in Zanskar (Noble and Searle, 1995) and at ~28 – 19 Ma in the Everest region (Cottle *et al.*, 2009), facilitated by crustal stacking and burial. Crustal thickening would have aided the exhumation of the Tso Morari dome and thickened crust is hypothesised to underlie the dome. Underplating of Asia by the rigid Indian lower crust would also have aided exhumation.

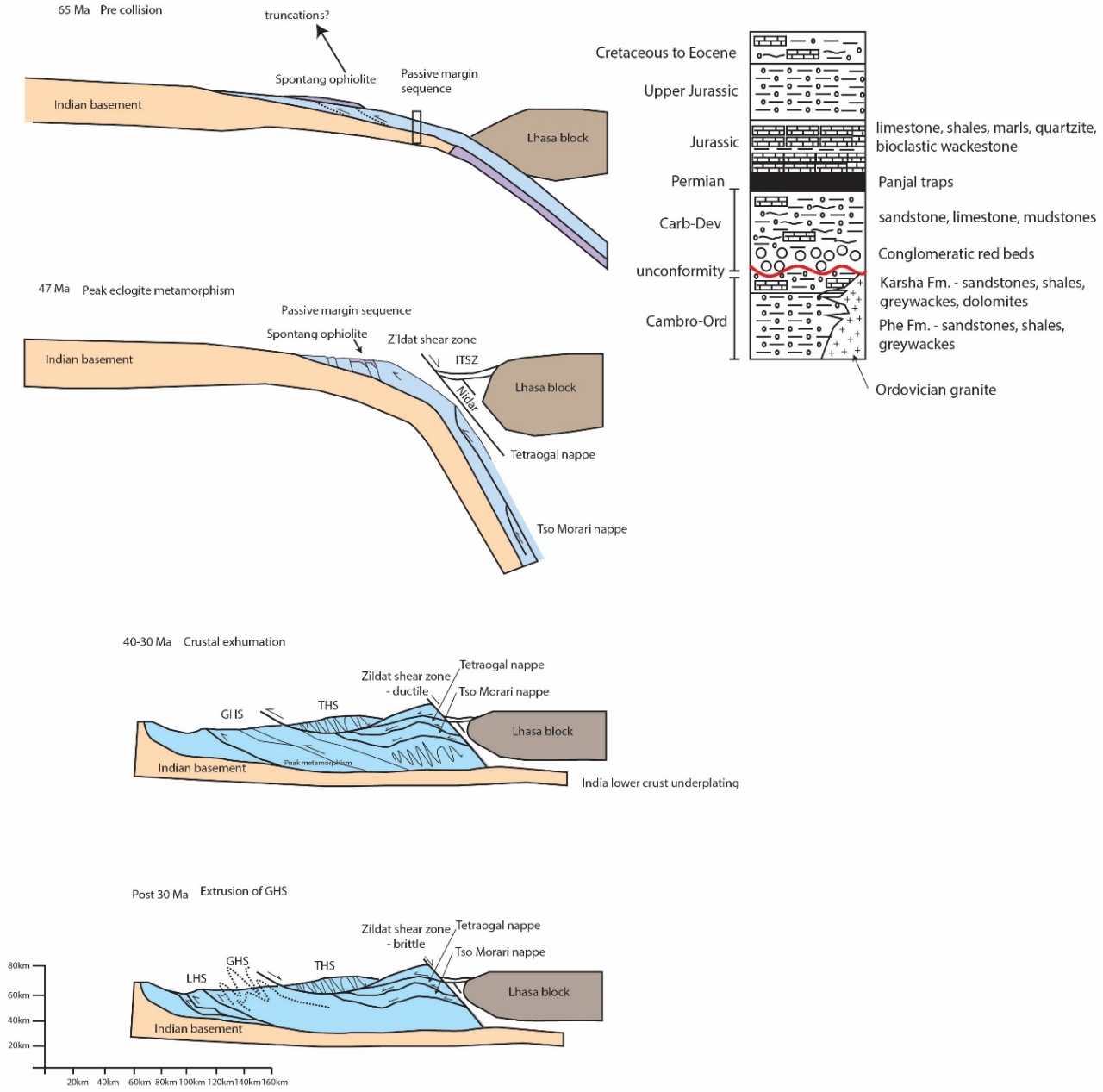


Figure 5 Model for the evolution of the western Himalaya showing four stages: a. the northern margin of India prior to continental collision including a generalised representation of the stratigraphy. b. Continental subduction of India to peak eclogite facies conditions. c. Exhumation of the Tso Morari complex to crustal levels, coincident with peak Barrovian metamorphism in the GHS. d. Extrusion of the GHS and southward propagation of deformation in the Himalaya.

Future work

Exploring crystallographic controls on the coesite-quartz transition

Preservation of quartz microstructures after coesite, in the absence of coesite, could provide the only evidence of subduction to UHP. The EDSD technique in Chapter 6 provides a useful tool for confirming the former presence of coesite. Future work would apply this technique to known coesite-bearing UHP rocks in order to test the validity of this method. Samples from this suite either contain coesite as inclusions within the same thin section (e.g., the Dora Maira Pyrope quartzite) or are immediately adjacent to coesite bearing samples (e.g., the Otnheim mangarite, western Gneiss Region of Norway). EBSD analyses of these coesite bearing samples will allow quantification of the matrix quartz textures to further test the universal applicability of the quartz misorientation-based UHP indicator. Additional samples from localities within collisional orogens where UHP conditions are debated but not yet confirmed will also be examined.

To further probe the microstructural control of parent coesite on daughter quartz, a D-DIA experimental setup will be used and conducted at the Advanced Photon Source at ANL using beamline 6-B,M-B. The D-DIA is a solid-medium deformation apparatus able to generate pressures and temperatures within the coesite stability field. Synchrotron light offers the unique possibility of identifying the transient formation of coesite *in-situ* using X-ray diffraction (Figure 2). Therefore, this experimental set-up is the only way in which we can ensure fully retrograded samples have passed through the coesite stability field.

The experiments will be conducted on quartz single crystals in two different orientations. For each initial quartz orientation, three experiments are required so that all relevant microstructural features can be examined *ex-situ*. First, an experiment will be run to examine the textures in coesite transformed from the single crystal. Quenching the experiment to room temperature at elevated pressures will prevent the coesite from transforming during depressurization. The second experiment will follow the same initial heating and pressurization path, but after deformation, the newly-created coesite will be taken back through the α-quartz transition at temperatures that allow the coesite-to-quartz transition to occur. The third experiment will also take coesite back to quartz but will first transition through the β-quartz field before ending in the α-quartz field. This latter path will constrain any effects of Dauphiné twinning, which is known to occur as a result of the α–β transition.

Bulk composition effects of granite alteration

The suite of samples described in Chapter 5 provides an important insight into the timing of deformation, metamorphic reactions and the change in bulk rock geochemistry during the progressive transformation from a metagranite to a garnet-mica schist. Bulk rock XRF data was acquired from this transect in this thesis. Analysis of this data with respect to the normative components provides a test for correlations, allowing the change in bulk composition with deformation to be potentially linked to 'predicted' mineral reactions.

For example:

(1) Muscovite after K feldspar reaction which reduces bulk K2O and increases normative corundum.

$$3KAlSi_3O_8 + 2H^+ \rightarrow KAl_3Si_3O_{10}(OH)_2 + 6SiO_2 + 2K^+$$

(2) Sericitisation of plagioclase which reduces Na2O, increases normative corundum and could work mutually with the alteration of K-feldspar to limit the bulk change in K2O.

$$3NaAlSi_3O_8 + K^+ + 2H^+ \rightarrow KAl_3Si_3O_{10}(OH)_2 + 6SiO_2 + 3Na^+$$

(3) Transformation of Ca-bearing plagioclase to albite which could couple with the 'sericitization' reaction to moderate the bulk change of SiO2.

$$CaAl_2Si_2O_8 + 4SiO_2 + 2Na^+ \rightarrow 2NaAlSi_3O_8 + Ca^{2+}$$

In a granite where biotite is the only significant ferromagnesian mineral, the normative hypersthene represents the total Fe^{2+} + Mg content. However, the K content of the actual biotite contributes to the normative orthoclase. It would be useful to subtract this component of 'orthoclase' to determine the model normative feldspar content of the rock. Normative corundum is expected to reflect muscovite content to a significant degree, as the dominant Al-rich mineral in a granitic composition.

Constraining the exhumation history of the Tso Morari complex

Eclogite facies zircon ages in this thesis were obtained using ID-TIMS for a single sample (a03-12) for n=3. Additional zircons will be run from this sample in order to increase the reliability this this result. The inclusions in the inclusion-rich zircons described in mafic eclogites in Chapter 7 will be identified via raman spectroscopy in order to constrain the coexisting mineral assemblage and analysed via CA-ID-TIMS, increasing the number of samples of mafic eclogite containing zircons studied.

ID-TIMS analysis of rutile grains has already been attempted during this thesis (by Simon Tapster at BGS) but were found to have a very low U content, a very high proportion of common lead and in some cases produced an insoluble precipitate. Titanite grains were observed, during U-Pb laser dating in this thesis, to contain a higher proportion of U. U-Pb dating of titanite grains from multiple mafic eclogites from across the complex will be attempted using ID-TIMS in order to get a more precise constraint on the exhumation of the complex.

References

Ackermand, D. and Karl, F. (1972). Experimental studies on the formation of inclusions in plagioclases from metatonalites, Hohe Tauern, Austria (lower temperature stability limit of the paragenesis anorthite plus potash feldspar). Contributions to Mineralogy and Petrology, 35(1), 11–21.

Afonso, J., & Zlotnik, S. (2011). The subductability of continental lithosphere: The before and after story. Arc-Continent Collision, 53–86.

Agard, P., Searle, M. P., Alsop, G. I., & Dubacq, B. (2010). Crustal stacking and expulsion tectonics during continental subduction: P-T deformation constraints from Oman. Tectonics, 29(5). https://doi.org/10.1029/2010TC002669

Agrawal, S., & Verma, S. P. (2007). Comment on 'Tectonic classification of basalts with classification trees" by Pieter Vermeesch (2006). https://doi.org/10.1016/j.gca.2007.03.036

Ahmad, T., Tanaka, T., Sachan, H., & Mukherjee, P. (2006). Petrogenesis of coesite bearing Tso Morari eclogites: isotopic and elemental constraints. Journal of Asian Earth Sciences, 26, 121.

Aitchison, J. (1986). The statistical analysis of compositional data (1st edition). Chapman and Hall, London.

Aitchison, J. C., Ali, J. R., & Davis, A. M. (2007). When and where did India and Asia collide? Journal of Geophysical Research, 112(B5), B05423. https://doi.org/10.1029/2006JB004706

Aleinikoff, J. N., Schenck, W. S., Plank, M. O., Srogi, L. A., Fanning, C. M., Kamo, S. L., & Bosbyshell, H. (2006). Deciphering igneous and metamorphic events in high-grade rocks of the Wilmington complex, Delaware: Morphology, cathodoluminescence and backscattered electron zoning, and SHRIMP U-Pb geochronology of zircon and monazite. Bulletin of the Geological Society of America, 118(1–2), 39–64. https://doi.org/10.1130/B25659.1

Amato Ł, J. M., Johnson, C. M., Baumgartner, L. P., & Beard, B. L. (1999). Rapid exhumation of the Zermatt-Saas ophiolite deduced from high-precision Sm-Nd and Rb-Sr geochronology. Earth and Planetary Science Letters (Vol. 171).

Ambrose, T., Larson, K., Guilmette, C., Cottle, J., Buckingham, H., & Rai, S. (2015). Lateral extrusion, underplating, and out-of-sequence thrusting within the Himalayan metamorphic core, Kanchenjunga, Nepal. Lithosphere, 7(4), 441–464.

Anderson, G. M. (2005). Thermodynamics of natural systems. Cambridge University Press.

Andersen, T., & Austrheim, H. (2008). The Caledonian Infrastructure in the Fjord-ergion of Western Norway: With Special Emphasis on Formation and Exhumation of High-and Ultrahigh-pressure Rocks, Late-to Post-orogenic Tectonic Processes and Basin Formation. In Field Trip Guidebook 33 IGC excursion No 29, 88 (August 15–22nd).

Andersen, T.B., Jamtveit, B., Dewey, J. F., & Swensson, E. (1991). Subduction and eduction of continental crust: major mechanisms during continent-continent collision and orogenic extensional collapse, a model based on the south Norwegian Caledonides. Terra Nova, 3(3), 303–310.

Austrheim, H. (1986). Eclogitization of lower crustal granulites by fluid migration through shear zones. Earth and Planetary Science Letters, 81, 221–232.

Austrheim, H., & Griffin, W. (1985). Shear deformation and eclogite formation withi granulite-facies anorthosites of the Bergen Arcs, Western Norway. Chemical Geology, 50(1–3), 267–281.

Auzanneau, E., Vielzeuf, D., & Schmidt, M. W. (2006). Experimental evidence of decompression melting during exhumation of subducted continental crust. Contributions to Mineralogy and Petrology, 152(2), 125–148. https://doi.org/10.1007/s00410-006-0104-5

Avigad, D., Chopin, C., & Le Bayon, R. (2003). Thrusting and Extension in the Southern Dora-Maira Ultra-High-Pressure Massif (Western Alps): View from Below the Coesite-Bearing Unit. The Journal of Geology, 111(1), 57–70. https://doi.org/10.1086/344664

Axelsson, E., Pape, J., Berndt, J., Corfu, F., Mezger, K., & Raith, M. M. (2018). Rutile R632 - A New Natural Reference Material for U-Pb and Zr Determination. Geostandards and Geoanalytical Research, 42(3), 319–338. https://doi.org/10.1111/ggr.12213

Babeyko, A., & Sobolev, S. (2005). Quantifying different modes of the late Cenozoic shortening in the central Andes. Geology, 33(8), 621–624. Retrieved from https://pubs.geoscienceworld.org/gsa/geology/article-abstract/33/8/621/103764

Barnhoorn, A., Bystricky, M., Burlini, L., & K Kunze. (2004). The role of recrystallisation on the deformation behaviour of calcite rocks: large strain torsion experiments on Carrara marble. Journal of Structural Geology, 26(5), 885–903. Retrieved from https://www.sciencedirect.com/science/article/pii/S0191814103001925

Bas, M. Le, & Streckeisen, A. (1991). The IUGS systematics of igneous rocks. Journal of the Geological Society, 148(5), 825–833.

Bassoulet, J., Bellier, J., & Colchen, M. (1978). Decouverte de Cretace superieur calcaire pelagique dans le Zanskar (Himalaya du Ladakh). Bulletin de La Société Géologique de France, 7(6), 961–964.

Baud, A., Arn, R., Bugnon, P., & Crisinel, A. (1982). Le contact Gondwana-péri-Gondwana dans le Zanskar oriental (Ladakh, Himalaya). Bulletin de La Société Geologique de France, 24(2), 341–361.

Bearth, P. (1959). Uber Eklogite, Glaucophanschiefer und metamorphen Pillowlaven. Schweizerische Mineralogische Und Petrographische Mitteilungen, 39, 267–286.

Beaumont, C., Jamieson, R. A., Butler, J. P., & Warren, C. J. (2009). Crustal structure: A key constraint on the mechanism of ultra-high-pressure rock exhumation. Earth and Planetary Science Letters (Vol. 287). https://doi.org/10.1016/j.epsl.2009.08.001

Bédard, É., Hébert, R., Guilmette, C., Lesage, G., Wang, C., & Dostal, J. (2009). Petrology and geochemistry of the Saga and Sangsang ophiolitic massifs, Yarlung Zangbo Suture Zone, Southern Tibet: evidence for an arc–back-arc origin. Lithos, 113(1–2), 48–67. Retrieved from https://www.sciencedirect.com/science/article/pii/S0024493709000309

Bell, T. H., Rubenach, M. J., & Fleming, P. D. (1986). Porphyroblast nucleation, growth and dissolution in regional metamorphic rocks as a function of deformation partitioning during foliation development. Journal of Metamorphic Geology, 4(1), 37–67. https://doi.org/10.1111/j.1525-1314.1986.tb00337.x

Bercovici, D., & Ricard, Y. (2012). Mechanisms for the generation of plate tectonics by two-phase grain-damage and pinning. Physics of the Earth and Planetary Interiors, 202, 27–55. Retrieved from https://www.sciencedirect.com/science/article/pii/S0031920112000854

Berthelsen, A. (1953). On the geology of the Rupshu district, N.W. Himalaya: A contribution to the Problem of the Central Gneisses. Meddelelser Fra Dansk Geologisk Forening (Kobenhavn), 12, 351–414.

Bhargava, O. (1987). Stratigraphy, microfacies and paleoenvironment of the Lilang Group (Scythian-Dogger), Spiti Valley, Himachal Himalaya, India. Journal of the Palaeontological Society, 25, 91–107. Retrieved from http://www.palaeontologicalsociety.in/vol32/v9.pdf

Biino, G., & Compangnoni, R. (1992). Very-high pressure meta-morphism of the Brossasco coronite metagranite, southern Dora Maira Massif, Western Alps. Schweizerische Mineralogische Und Petrographische Mitteilungen, 72, 347–363. Retrieved from https://ci.nii.ac.jp/naid/80006845685/

Bingen, B., Austrheim, H., & Whitehouse, M. (2001). Ilmenite as a source for zirconium during high-grade metamorphism? Textural evidence from the Caledonides of western Norway and implications for zircon geochronology. Journal of Petrology, 42(2), 355–375.

Black, P. M., Brothers, R. N., & Yokoyama, K. (1985). Mineral parageneses in eclogite-facies meta-acidites in northern New Caledonia. Eclogites and Eclogite-facies Rocks (Smith, DC, Vol. 12). Elsevier.

Booth, B. (1968). Petrogenetic significance of alkali feldspar megacrysts and their inclusions in Cornubian granites. Nature, 217(5133), 1036.

Bouilhol, P., Jagoutz, O., Hanchar, J. M., & Dudas, F. O. (2013). Dating the India–Eurasia collision through arc magmatic records. Earth and Planetary Science Letters, 366, 163–175.

Bowring, J. F., McLean, N. M., and Bowring, S. A., (2011), Engineering cyber infrastructure for U-Pb geochronology: Tripoli and U-Pb_Redux: Geochemistry Geophysics Geosystems, v. 12.

Bracciali, L. et al. (2013) 'UPb LA-(MC)-ICP-MS dating of rutile: New reference materials and applications to sedimentary provenance', Chemical Geology, 347, pp. 82–101.

Braden, Z., Godin, L., & Cottle, J. M. (2017). Segmentation and rejuvenation of the Greater Himalayan sequence in western Nepal revealed by in situ U–Th/Pb monazite petrochronology. Lithos, 284–285, 751–765. https://doi.org/10.1016/j.lithos.2017.04.023

Brookfield, M. (1993). The Himalayan passive margin from Precambrian to Cretaceous times. Sedimentary Geology, 84(1–3), 1–35. Retrieved from https://www.sciencedirect.com/science/article/pii/0037073893900424

Brookfield, M., & Andrews-Speed, C. (1984). Sedimentology, petrography and tectonic significance of teh shelf, flysch and molasse clastic deposits across the Indus suture zone, Ladakh, NW India. Sedimentary Geology, 40(4), 249–286.

Brown, W. H., Fyfe, W. S., & Turner, F. J. (1962). Aragonite in California glaucophane schists, and the kinetics of the aragonite—calcite transformation. Journal of Petrology, 3(3), 566–582.

Brueckner, H., Carswell, D., Griffin, W., Medaris Jr, L., Van Roermund, H., & Cuthbert, S. (2010). The mantle and crustal evolution of two garnet peridotite suites from the Western Gneiss Region, Norwegian Caledonides: an isotopic investigation. Lithos, 117(1–4), 1–19. Retrieved from https://www.sciencedirect.com/science/article/pii/S002449371000023X

Brun, J., & Faccenna, C. (2008). Exhumation of high-pressure rocks driven by slab rollback. Earth and Planetary Science Letters, 272(1–2), 1–7. Retrieved from https://www.sciencedirect.com/science/article/pii/S0012821X08001416

Buchs, N., & Epard, J.-L. (2019). Geology of the eastern part of the Tso Morari nappe, the Nidar Ophiolite and the surrounding tectonic units (NW Himalaya, India). Journal of Maps, 15(2), 38–48. https://doi.org/10.1080/17445647.2018.1541196

Buick, I. S., Lana, C., & Gregory, C. (2011). A LA-ICP-MS and SHRIMP U/Pb age constraint on the timing of REE mineralisation associated with Bushveld granites, South Africa. South African Journal of Geology, 114(1), 1–14. https://doi.org/10.2113/gssajg.1141.1

Burg, J.-P., & Bouilhol, P. (2018). Timeline of the South-Tibet--Himalayan belt: the geochronological record of subduction, collision, and underthrusting from zircon and monazite U-Pb ages. Canadian Journal of Earth Sciences. https://doi.org/10.1139/cjes-2018-0174

Burov, E., Francois, T., Yamato, P., & Wolf, S. (2013). Mechanisms of continental subduction and exhumation of HP and UHP rocks. Gondwana Research, 25(2), 464–493.

Burov, E., Jolivet, L., Pourhiet, L. Le, & Poliakov, A. (2001). A thermomechanical model of exhumation of high pressure (HP) and ultra-high pressure (UHP) metamorphic rocks in Alpine-type collision belts. Tectonophysics.

Burtman, V., & Molnar, P. (1993). Geological and geophysical evidence for deep subduction of continental crust beneath the Pamir.

Butler, J., Beaumont, C., & Jamieson, R. (2011). Crustal emplacement of exhuming (ultra) high-pressure rocks: Will that be pro-or retro-side? Geology, 39(7), 635–638. Retrieved from https://pubs.geoscienceworld.org/gsa/geology/article-abstract/39/7/635/130591

Bystricky, M., Kunze, K., Burlini, L., & JP Burg. (2000). High shear strain of olivine aggregates: Rheological and seismic consequences. Science, 290(5496), 1564–1567. Retrieved from https://science.sciencemag.org/content/290/5496/1564.short

Cabanis, B., & Lecolle, M. (1989). The La/10-Y/15-Nb/8 diagram: A tool for distinguishing volcanic series and discovering crustal mixing and/or contamination: Comptes Rendus de l'Academie des Sciences, serie 2. Science de La Terre, 30, 309.

Caldwell, W. (2008). Field excursion. In 23rd Himalaya-Karakoram-Tibet conference.

Capitanio, F., Morra, G., Goes, S., & Weinberg, R. (2010). India–Asia convergence driven by the subduction of the Greater Indian continent. Nature Geoscience, 3(2), 136. Retrieved from https://www.nature.com/articles/ngeo725

Carosi, R., Lombardo, B., Molli, G., Musumeci, G., & Pertusati, P. C. (1998). The South Tibetan detachment system in the Rongbuk valley, Everest region. Deformation features and geological implications. Journal of Asian Earth Sciences, 16(2–3), 299–311.

Carosi, R., Montomoli, C., Rubatto, D., & Visonà, D. (2010). Late Oligocene high-temperature shear zones in the core of the Higher Himalayan Crystallines (Lower Dolpo, western Nepal). Tectonics, 29(4), n/a-n/a. https://doi.org/10.1029/2008TC002400

Carosi, R., Montomoli, C., Tiepolo, M., & Peruzzo, L. (2012). Miocene andalusite leucogranite in central-east Himalaya (Everest–Masang Kang area): low-pressure melting during heating. Lithos, 144(`), 194–208.

Carosi, R., Montomoli, C., Iaccarino, S., Massonne, H.J., Rubatto, D., Langone, A., Gemignani, L. and Visonà, D., (2016). Middle to late Eocene exhumation of the Greater Himalayan Sequence in the Central Himalayas: Progressive accretion from the Indian plate. Bulletin, 128(11–12), 1571–1592. Retrieved from https://pubs.geoscienceworld.org/gsa/gsabulletin/article-abstract/128/11-12/1571/185307

Carswell, D. A., Brueckner, H.K., Cuthbert, S. J., Krogh, T. E., Mehta, K., O'Brien, P. J., & Tucker, R. D. (2001). Coesite preservation within zircons in the Hareidland eclogite and the timing of ultra-high pressure metamorphism in the Western Gneiss Region of Norway. In In Fluid/Slab/Mantle Interactions and Ultrahigh-P Minerals: UHPM Workshop (extended abstracts). Waseda University, Tokyo (pp. 111–115).

Carswell, D. A., Tucker, R. D., O'Brien, P. J., & Krogh, T. E. (2003). Coesite micro-inclusions and the U/Pb age of zircons from the Hareidland Eclogite in the Western Gneiss Region of Norway. Lithos, 67(3–4), 181–190.

Catlos, E. J., Harrison, T. M., Kohn, M. J., Grove, M., Ryerson, F. J., Manning, C. E., & Upreti, B. N. (2001). Geochronologic and thermobarometric constraints on the evolution of the Main Central Thrust, central Nepal Himalaya. Journal of Geophysical Research: Solid Earth, 106(B8), 16177–16204. https://doi.org/10.1029/2000JB900375

Chamberlain, C. P., Zeitler, P. K., & Erickson, E. (1991). Constraints on the Tectonic Evolution of the Northwestern Himalaya from Geochronologic and Petrologic Studies of Babusar Pass, Pakistan. The Journal of Geology, 99(6), 829–849. https://doi.org/10.1086/629555

Chan, G., Aitchison, J., Crowley, Q., Horstwood, M., Searle, M., RR, P., & Chan, J. (2015). U–Pb zircon ages for Yarlung Tsangpo suture zone ophiolites, southwestern Tibet and their tectonic implications. Gondwana Research, 27(2), 719–732. Retrieved from https://www.sciencedirect.com/science/article/pii/S1342937X13002219

Chatterjee, N., & Jagoutz, O. (2015). Exhumation of the UHP Tso Morari eclogite as a diapir rising through the mantle wedge. Contributions to Mineralogy and Petrology, 169(1), 3. Retrieved from http://link.springer.com/article/10.1007/s00410-014-1099-y

Chaudry, M. N., & Ghazanfar, M. (1987). Geology, structure and geomorphology of upper Kaghan valley, Northwestern Himalaya, Pakistan. Geological Bulletin University of Punjab, 22, 13–57.

Chauvet, F., Lapierre, H., Bosch, D., Guillot, S., Mascle, G., Vannay, J.C., Cotten, J., Brunet, P. and Keller, F., (2008). Geochemistry of the Panjal Traps basalts (NW Himalaya): records of the Pangea Permian break-up. Bulletin de La Société Géologique de France, 179(4), 383–395.

Chemenda, A., Mattauer, M., & Bokun, A. (1996). Continental subduction and a mechanism for exhumation of high-pressure metamorphic rocks: new modelling and field data from Oman. Earth and Planetary Science Letters, 143(1–4), 173–182. Retrieved from https://www.sciencedirect.com/science/article/pii/0012821X96001239

Chemenda, A., Mattauer, M., & Malavieille, J. (1995). A mechanism for syn-collisional rock exhumation and associated normal faulting: results from physical modelling. Earth and Planetary. Retrieved from http://www.sciencedirect.com/science/article/pii/0012821X9500042B

Cherniak, D. (1993). Lead diffusion in titanite and preliminary results on the effects of radiation damage on Pb transport. Chemical Geology, 110(1–3), 177–194. Retrieved from https://www.sciencedirect.com/science/article/pii/000925419390253F

Cherniak, D. (2006). Pb and rare earth element diffusion in xenotime. Lithos, 88(1–4), 1–14. Retrieved from https://www.sciencedirect.com/science/article/pii/S0024493705001866

Cherniak, D. (2000). Pb diffusion in rutile. Contributions to Mineralogy and Petrology, 139(2), 198–207. https://doi.org/10.1007/PL00007671

Chew, D. M., Petrus, J. A. and Kamber, B. S. (2014) 'U-Pb LA-ICPMS dating using accessory mineral standards with variable common Pb', Chemical Geology, 363, pp. 185–199. doi: 10.1016/j.chemgeo.2013.11.006.

Chopin, C. (1987). Very-High-Pressure Metamorphism in the Western Alps: Implications for Subduction of Continental Crust. Philosophical Transactions of the Royal Society A: Mathematical, Physical and Engineering Sciences, 321(1557), 183–197. https://doi.org/10.1098/rsta.1987.0010

Chopin, C, Henry, C., & Michard, A. (1991). Geology and petrology of the coesite-bearing terrain, Dora Maira massif, Western Alps. European Journal of Mineralogy, 3(2), 263–291.

Chopin, Christian. (1984). Coesite and pure pyrope in high-grade blueschists of the Western Alps: a first record and some consequences. Contributions to Mineralogy and Petrology, 86(2), 107–118. https://doi.org/10.1007/BF00381838

Chopin, Christian. (2003). Ultrahigh-pressure metamorphism: tracing continental crust into the mantle. Earth and Planetary Science Letters, 212(1–2), 1–14. https://doi.org/10.1016/S0012-821X(03)00261-9

Clemens, J., & Wall, V. (1981). Origin and crystallization of some peraluminous (S-type) granitic magmas. The Canadian Mineralogist, 19(1), 111–131. Retrieved from https://pubs.geoscienceworld.org/canmin/article-abstract/19/1/111/11467

Cliff, R. A. (1993). Isotopic dating of metamorphism and cooling. Proceedings VI Summer School, Earth and Planetary Science, Sienna, 131–140.

Clift, P., Carter, A., Krol, M., & Kirby, E. (2002). Constraints on India-Eurasia collision in the Arabian sea region taken from the Indus Group, Ladakh Himalaya, India. Geological Society, London, Special Publications, 195(1), 97–116. Retrieved from https://sp.lyellcollection.org/content/195/1/97.short

Cloos, M., & Shreve, R. L. (1988). Subduction-channel model of prism accretion, melange formation, sediment subduction, and subduction erosion at convergent plate margins: 2. Implications and discussion. Pure and Applied Geophysics PAGEOPH, 128(3–4), 501–545. https://doi.org/10.1007/BF00874549

Coggon, R., & Holland, T. (2002). Mixing properties of phengitic micas and revised garnet-phengite thermobarometers. Journal of Metamorphic Geology. Retrieved from http://onlinelibrary.wiley.com/doi/10.1046/j.1525-1314.2002.00395.x/full

Colchen, M., Mascle, G., & Delaygue, G. (1994). Lithostratigraphy and age of the formations of the Tso Morari dome. Journal of the Nepal Geological Society, 10, 1–23.

Compagnoni. R., & B. Maffeo. (1973). Jadeite-bearing metagranitoids and related rocks in the Mont Mucrone area (Sesia-Lanzo Zone, Western Italian Alps). Schweizerische Mineralogische Und Petrographische Mitteilungen, 53, 355–378.

Compagnoni, R., & Hirajima, T. (2001). Superzoned garnets in the coesite-bearing Brossasco-Isasca Unit, Dora-Maira massif, Western Alps, and the origin of the whiteschists. Lithos, 57(4), 219–236.

Condon, D. J., B. Schoene, N. M. McLean, S. A. Bowring, and R. R. Parrish (2015). "Metrology and Traceability of U-Pb Isotope Dilution Geochronology (EARTHTIME Tracer Calibration Part I)." Geochimica et Cosmochimica Acta.

Connolly, J. A. D., & Kerrick, D. M. (1987). An algorithm and computer program for calculating composition phase diagrams. Calphad, 11(1), 1–55.

Corfield, R. I., & Searle, M.P. (2000). Crustal shortening estimates across the north Indian continental margin, Ladakh, NW India. Geological Society, London, Special Publications, 170(1), 395–410.

Corfield, R. I., Searle, M. P., & Green, O. R. (1999). Photang thrust sheet: an accretionary complex structurally below the Spontang ophiolite constraining timing and tectonic environment of ophiolite obduction, Ladakh Himalaya, NW India. Journal of the Geological Society, 156(5), 1031–1044.

Corfield, R. I., Searle, M. P., & Pedersen, R. B. (2001). Tectonic setting, origin, and obduction history of the Spontang Ophiolite, Ladakh Himalaya, NW India. The Journal of Geology, 109(6), 715–736.

Corrie, S., Kohn, M., & Vervoort, J. (2010). Young eclogite from the Greater Himalayan Sequence, Arun Valley, eastern Nepal: P–T–t path and tectonic implications. Earth and Planetary Science Letters, 289(3–4), 406–416. Retrieved from http://www.sciencedirect.com/science/article/pii/S0012821X09006918

Cottle, J., Jessup, M., Newell, D., & Horstwood, M. (2009). Geochronology of granulitized eclogite from the Ama Drime Massif: Implications for the tectonic evolution of the South Tibetan Himalaya. Retrieved from http://onlinelibrary.wiley.com/doi/10.1029/2008TC002256/full

Cottle, J. M., Searle, M. P., Horstwood, M. S. A., & Waters, D. J. (2009). Timing of Midcrustal Metamorphism, Melting, and Deformation in the Mount Everest Region of Southern Tibet Revealed by U(-Th)-Pb Geochronology. The Journal of Geology, 117(6), 643–664. https://doi.org/10.1086/605994

Crowley, J. L., Waters, D. J., Searle, M. P., & Bowring, S. A. (2009). Pleistocene melting and rapid exhumation of the Nanga Parbat massif, Pakistan: Age and P–T conditions of accessory mineral growth in migmatite and leucogranite. Earth and Planetary Science Letters, 288(3–4), 408–420.

Cuthbert, S. J., & Carswell, D. A. (1982). Petrology and tectonic setting of eclogites and related rocks from the Dalsfjord area, Sunnfjord, west Norway. Terra Cognita, 2, 315–316.

Cuthbert, S. J., Carswell, D. A., Krogh-Ravna, E. J., & Wain, A. (2000). Eclogites and eclogites in the Western Gneiss region, Norwegian Caledonides. Lithos, 52(1–4), 165–195. https://doi.org/10.1016/S0024-4937(99)00090-0

Dal Piaz, G. V, Hunziker, J. C., & Martinotti, G. (1972). La Zona Sesia - Lanzo e l'evoluzione tettonico-metamorfica delle Alpi Nordoccidentali interne. Memorie Della Società Geoligica Italiana Memorie Della Società Geologica Italiana, 11, 433–460. Retrieved from https://ci.nii.ac.jp/naid/10026535850/

Davis, P. B., & Whitney, D. L. (2006). Petrogenesis of lawsonite and epidote eclogite and blueschist, Sivrihisar Massif, Turkey. Journal of Metamorphic Geology, 24(9), 823–849.

De Bresser, J., Ter Heege, J., & Spiers, C. (2001). Grain size reduction by dynamic recrystallization: can it result in major rheological weakening? International Journal of Earth Sciences, 90(1), 28–45. https://doi.org/10.1007/s005310000149

De Capitani, C., & Brown, T. H. (1987). The computation of chemical equilibrium in complex systems containing non-ideal solutions. Geochimica et Cosmochimica Acta, 51(10), 2639–2652.

de Sigoyer, J;, Chavagnac, V., & Blichert-Toft, J. (2000). Dating the Indian continental subduction and collisional thickening in the northwest Himalaya: Multichronology of the Tso Morari eclogites. Geology, 28(6), 487–490. Retrieved from http://geology.gsapubs.org/content/28/6/487.short

de Sigoyer, J;, & Guillot, S. (1997). Glaucophane-bearing eclogites in the Tso Morari dome (eastern Ladakh, NW Himalaya). European Journal of …, 128(2–3), 197–212.

de Sigoyer, Julia, Guillot, S., & Dick, P. (2004). Exhumation of the ultrahigh-pressure Tso Morari unit in eastern Ladakh (NW Himalaya): A case study. Tectonics, 23(3), n/a-n/a. https://doi.org/10.1029/2002TC001492

DeCelles, P. G., Kapp, P., Gehrels, G. E., & Ding, L. (2014). Paleocene-Eocene foreland basin evolution in the Himalaya of southern Tibet and Nepal: Implications for the age of initial India-Asia collision. Tectonics, 33(5), 824–849. https://doi.org/10.1002/2014TC003522

DeCelles, P., Gehrels, G., Quade, J., Ojha, T., Kapp, P., & Upreti, B. (1998). Neogene foreland basin deposits, erosional unroofing, and the kinematic history of the Himalayan fold-thrust belt, western Nepal. Geological Society of America Bulletin, 110(1), 2–21. Retrieved from https://pubs.geoscienceworld.org/gsa/gsabulletin/article-abstract/110/1/2/183281

Diener, J. F. A., & Powell, R. (2012). Revised activity–composition models for clinopyroxene and amphibole. Journal of Metamorphic Geology, 30(2), 131–142.

Ding, H., Zhang, Z., Dong, X., Tian, Z., Xiang, H., Mu, H., Gou, Z., Shui, X., Li, W. and Mao, L., (2016). Early Eocene (c. 50 Ma) collision of the Indian and Asian continents: Constraints from the North Himalayan metamorphic rocks, southeastern Tibet. Earth and Planetary Science Letters, 435, 64–73. Retrieved from https://www.sciencedirect.com/science/article/pii/S0012821X15007694

Dobretsov, N. L., Sobolev, N. V., Shatsky, V. S., Coleman, R. G., & Ernst, W. G. (1995). Geotectonic evolution of diamondiferous paragneisses, Kokchetav Complex, northern Kazakhstan: The geologic enigma of ultrahigh-pressure crustal rocks within a Paleozoic foldbelt. The Island Arc, 4(4), 267–279. https://doi.org/10.1111/j.1440-1738.1995.tb00149.x

Donaldson, D. G., Webb, A. A. G., Menold, C. A., Kylander-Clark, A. R. C., & Hacker, B. R. (2013). Petrochronology of Himalayan ultrahigh-pressure eclogite. Geology, 41(8), 835–838. https://doi.org/10.1130/G33699.1

Draganits, E., Grasemann, B., Frank, W., Miller, C., & Wiesmayr, G. (1998). The sedimentary protoliths of the HHC in the Chamba-Lahaul Area (NW-Himalayas, India). 13th Himalaya Karakorum Tibet Workshop, 20–22.

Droop, G. (1987). A general equation for estimating Fe3+ concentrations in ferromagnesian silicates and oxides from microprobe analyses, using stoichiometric criteria. Mineralogical Magazine, 51(361), 431–435.

Duretz, T., & Gerya, T. (2013). Slab detachment during continental collision: Influence of crustal rheology and interaction with lithospheric delamination. Tectonophysics, 602, 124–140. Retrieved from http://www.sciencedirect.com/science/article/pii/S0040195113000061

Duretz, T., Gerya, T., Kaus, B., & Andersen, T. (2012). Thermomechanical modeling of slab eduction. Journal of Geophysical, 117(B8). Retrieved from http://onlinelibrary.wiley.com/doi/10.1029/2012JB009137/full

Duretz, T., & Schmalholz, S. (2012). Dynamics of slab detachment. Geochemistry, Geophysics, 13(3). Retrieved from http://onlinelibrary.wiley.com/doi/10.1029/2011GC004024/full

Ellis, D. J., & Green, D. H. (1979). An experimental study of the effect of Ca upon garnet-clinopyroxene Fe-Mg exchange equilibria. Contributions to Mineralogy and Petrology, 71(1), 13–22.

Elphick, S. C., & Graham, C. M. (1988). The effect of hydrogen on oxygen diffusion in quartz: evidence for fast proton transients?. Nature, 335(6187), 243–245.

England, P. C., & Holland, T. J. B. (1979). Archimedes and the Tauern eclogites: the role of buoyancy in the preservation of exotic eclogite blocks. Earth and Planetary Science Letters, 44(2), 287–294. https://doi.org/10.1016/0012-821X(79)90177-8

Engvik, A. K., Austrheim, H., & Andersen, T. B. (2000). Structural, mineralogical and petrophysical effects on deep crustal rocks of fluid-limited polymetamorphism, Western Gneiss Region, Norway. Journal of the Geological Society, London, 157, 121–134.

Epard, J., & Steck, A. (2004). The Eastern prolongation of the Zanskar Shear Zone (Western Himalaya). Eclogae Geologicae Helvetiae, 97(2), 193–212. https://doi.org/10.1007/s00015-004-1116-7

Epard, J., & Steck, A. (2008). Structural development of the Tso Morari ultra-high pressure nappe of the Ladakh Himalaya. Tectonophysics, 451(1–4), 242–264.

Ernst, W. (1997). Buoyancy-driven, rapid exhumation of ultrahigh-pressure metamorphosed continental crust. *Proceedings of the National Academy of Sciences*, *94*(18), pp.9532-9537. Retrieved from http://www.pnas.org/content/94/18/9532.short

Ernst, W. G. (1963). Significance of phengitic micas from low-grade schists. American Mineralogist: Journal of Earth and Planetary Materials, 48(11–12), 1357–1373.

Essene, E. J., & Fyfe, W. S. (1967). Omphacite in Californian metamorphic rocks. Contributions to Mineralogy and Petrology, 15(1), 1–23. https://doi.org/10.1007/BF01167213

Ewing, T. A., Hermann, J., & Rubatto, D. (2013). The robustness of the Zr-in-rutile and Ti-in-zircon thermometers during high-temperature metamorphism (Ivrea-Verbano Zone, northern Italy). Contributions to Mineralogy and Petrology, 165(4), 757–779.

Exley, C. S., Stone, M., & Lees, G. L. (1982). Petrology of the granites and minor intrusions. Igneous Rocks of the British Isles, 293–302.

Faccenda, M., Minelli, G., & Gerya, T. (2009). Coupled and decoupled regimes of continental collision: numerical modeling. Earth and Planetary Science Letters, 278(3–4), 337–349. Retrieved from https://www.sciencedirect.com/science/article/pii/S0012821X08007693

Farina, F., Stevens, G., & Villaros, A. (2012). Multi-batch, incremental assembly of a dynamic magma chamber: the case of the Peninsula pluton granite (Cape Granite Suite, South Africa). Mineralogy and Petrology, 106(3–4), 193–216. Retrieved from https://ezproxy-prd.bodleian.ox.ac.uk:7073/content/pdf/10.1007%2Fs00710-012-0224-8.pdf

Faure, M., Lin, W., Schärer, U., Shu, L., Sun, Y., & Arnaud N. (2003). Continental subduction and exhumation of UHP rocks. Structural and geochronological insights from the Dabieshan (East China). Lithos, 70(3–4), 213–241. Retrieved from https://www.sciencedirect.com/science/article/pii/S0024493703001002

Ferry, J. M., & Watson, E. B. (2007). New thermodynamic models and revised calibrations for the Ti-in-zircon and Zr-in-rutile thermometers. Contributions to Mineralogy and Petrology, 154(4), 429–437. https://doi.org/10.1007/s00410-007-0201-0

Ferry, J. T., & Spear, F. S. (1978). Experimental calibration of the partitioning of Fe and Mg between biotite and garnet. Contributions to Mineralogy and Petrology, 66(2), 113–117.

Fontan, D., Schouppe, M., Hunziker, C. J., Martinotti, G., & Verkaeren, J. (2000). Metamorphic evolution, 40Ar-39Ar chronology and tectonic model for the Neelum valley, Azad Kashmir, NE Pakistan. Geological Society, London, Special Publications, 170(1), 431-453.

Le Fort, P., Guillot, S., & Pêcher, A. (1997). HP metamorphic belt along the Indus suture zone of NW Himalaya: new discoveries and significance. Comptes Rendus de l'Académie Des. Retrieved from http://www.sciencedirect.com/science/article/pii/S1251805097827553

Freeman, S. R., Inger, S., Butler, R. W. H., & Cliff, R. A. (1997). Dating deformation using Rb-Sr in white mica: Greenschist facies deformation ages from the Entrelor shear zone, Italian Alps. Tectonics, 16(1), 57–76.

Frondel, C. (1945). Secondary Dauphiné twinning in quartz. American Mineralogist: Journal of Earth and Planetary Materials, 30(5–6), 447–460.

Frost, B., Chamberlain, K., & Schumacher, J. (2001). Sphene (titanite): phase relations and role as a geochronometer. Chemical Geology, 172(1–2), 131–148. Retrieved from https://www.sciencedirect.com/science/article/pii/S0009254100002400

Fuchs, G., & Linner, M. (1996). On the geology of the suture zone and Tso Morari dome in Eastern Ladakh (Himalaya). Jahrbuch Der Geologischen Bundesanstalt, 139(191), 207. Retrieved from https://www.researchgate.net/profile/Manfred_Linner/publication/268401848_On_the_Geology_of_the_Suture_Zone_and_Tso_Morari_Dome_in_Eastern_Ladakh_Himalaya/links/570784c808ae04e9708f02eb.pdf

Gaetani, M., Casnedi, R., Fois, E., Garzanti, E., Jadoul, F., Nicora, A., & Tintori, A. (1985). Stratigraphy on the Tethys Himalaya in Zanskar, Ladakh. Rivista Italiana Di Palaeotologia e Stratigrafia, 91, 443–478.

Gaetani, M., & Garzanti, E. (1991). Multicyclic history of the northern India continental margin (northwestern Himalaya). American Association of Petroleum Geologists Bulleti, 75(9), 1427–1446.

Gaetani, M., Garzanti, E., & Tintori, A. (1990). Permo-Carboniferous stratigraphy in SE Zanskar and NW Lahul (NW Himalaya, India). Eclogae Geologicae Helvetiae, 83, 143–161.

Ganguly, J., Cheng, W., & Tirone, M. (1996). Thermodynamics of aluminosilicate garnet solid solution: new experimental data, an optimized model, and thermometric applications. Contributions to Mineralogy and Petrology, 126(1–2), 137–151.

Gansser, A. (1964). Geology of the Himalayas.

Gansser, A. (1966). The Indian Ocean and the Himalayas, a geological interpretation: Eclogae Geol. Eclogae Geologicae Helvetiae, 67, 479–507.

Garzanti, Eduardo, Casnedi, R., & Jadoul, F. (1986). Sedimentary evidence of a Cambro-Ordovician orogenic event in the northwestern Himalaya. Sedimentary Geology, 48(3–4), 237–265. https://doi.org/10.1016/0037-0738(86)90032-1

Garzanti, E, & Van Haver, T. (1988). The Indus clastics: forearc basin sedimentation in the Ladakh Himalaya (India). Sedimentary Geology, 59(3–4), 237–249. Retrieved from https://www.sciencedirect.com/science/article/pii/0037073888900784

Garzanti, E, Jadoul, F., & Nicora, A. (1995). Triassic of Spiti (Tethys Himalaya, N India). Rivista Italiana Di Palaeotologia e Stratigrafia, 101(3). Retrieved from https://riviste.unimi.it/index.php/RIPS/article/view/8588

Garzanti, E, Fort, P. Le, & Sciunnach, D. (1999). First report of Lower Permian basalts in South Tibet: tholeiitic magmatism during break-up and incipient opening of Neotethys. Journal of Asian Earth Sciences, 17(4), 533–546. Retrieved from https://www.sciencedirect.com/science/article/pii/S1367912099000085

Gebauer, D., Schertl, H., Brix, M., & Schreyer, W. (1997). 35 Ma old ultrahigh-pressure metamorphism and evidence for very rapid exhumation in the Dora Maira Massif, Western Alps. Lithos. Retrieved from http://www.sciencedirect.com/science/article/pii/S0024493797820026

Gerstenberger, H., and Haase, G., (1997), A highly effective emitter substance for mass spectrometric Pb isotope ratio determinations: Chemical Geology, v. 136, p. 309- 312.

Gerya, T, & Stöckhert, B. (2006). Two-dimensional numerical modelling of tectonic and metamorphic histories at active continental margins. International Journal of Earth Sciences, 95(2), 250–274. Retrieved from http://link.springer.com/article/10.1007/s00531-005-0035-9

Gerya, TV, Perchuk, L., & Burg, J. (2008). Transient hot channels: perpetrating and regurgitating ultrahigh-pressure, high-temperature crust–mantle associations in collision belts. Lithos, 103(1–2), 236–256. Retrieved from https://www.sciencedirect.com/science/article/pii/S0024493707002277

Gerya, T. V., & Meilick, F. I. (2011). Geodynamic regimes of subduction under an active margin: effects of rheological weakening by fluids and melts. Journal of Metamorphic Geology, 29(1), 7–31. https://doi.org/10.1111/j.1525-1314.2010.00904.x

Gilotti, J. A., & Krogh Ravna, E. J. (2002). First evidence for ultrahigh-pressure metamorphism in the North- East Greenland Caledonides. Geology, 30(6), 551. https://doi.org/10.1130/0091-7613(2002)030<0551:FEFUPM>2.0.CO;2

Girard, M. (2001). Metamorphism and tectonics of the transition between non metamorphic Tethayan Himalaya sediments and the North Himalayan Crystalline Zone (Rupshu. Retrieved from http://www.unil.ch/files/live/sites/iste/files/shared/X.Library/Memoirs of Geology/35 - Girard (2001).pdf

Girard, M., & Bussy, F. (1999). Late Pan-African magmatism in the Himalaya: new geochronological and geochemical data from the Ordovician Tso Morari metagranites (Ladakh, NW India). Schweizerische Mineralogische Und Petrographische Mitteilungen, 79, 399–418.

Godard, G. (2009). Two orogenic cycles recorded in eclogite-facies gneiss from the southern Armorican Massif (France). European Journal of Mineralogy, 21(6), 1173–1190. https://doi.org/10.1127/0935-1221/2009/0021-1984

Godin, L., & Harris, L. B. (2014). Tracking basement cross-strike discontinuities in the Indian crust beneath the Himalayan orogen using gravity data–relationship to upper crustal faults. Geophysical Journal International, 198(1), 198–215.

Godin, L., Parrish, R. R., Brown, R. L., & Hodges, K. V. (2001). Crustal thickening leading to exhumation of the Himalayan metamorphic core of central Nepal: Insight from U-Pb geochronology and 40Ar/39Ar thermochronology. Tectonics, 20(5), 729–747.

Gordon, S., Little, T., Hacker, B., Bowring, S., Korchinski, M., Baldwin, S., & Kylander-Clark, A. (2012). Multi-stage exhumation of young UHP–HP rocks: Timescales of melt crystallization in the D'Entrecasteaux Islands, southeastern Papua New Guinea. Earth and Planetary Science Letters, 351, 237–246. Retrieved from http://www.sciencedirect.com/science/article/pii/S0012821X12003731

Goscombe, B., Gray, D., & Foster, D. (2018). Metamorphic response to collision in the Central Himalayan Orogen. Gondwana Research, 57, 191–265. Retrieved from https://www.sciencedirect.com/science/article/pii/S1342937X18300224

Greco, A., & Spencer, D. (1993). A section through the Indian plate, Kaghan valley, NW Himalaya, Pakistan. Geological Society, London, Special Publications, 74(1), 221–236. Retrieved from https://sp.lyellcollection.org/content/74/1/221.short

Green, H. W., Griggs, D. T., & Christie, J. M. (1970). Syntectonic and annealing recrystallization of fine-grained quartz aggregates. In In Experimental and Natural Rock Deformation/Experimentelle und natürliche Gesteinsverformung (pp. 272–335). Springer, Berlin, Heidelberg.

Green, O., Searle, M., Corfield, R., & Corfield, R. (2008). Cretaceous-Tertiary carbonate platform evolution and the age of the India-Asia collision along the Ladakh Himalaya (Northwest India). The Journal of Geology, 116(4), 331–353. Retrieved from http://www.jstor.org/stable/10.1086/588831

Green, T. H., & Adam, J. (1991). Assessment of the garnet–clinopyroxene Fe–Mg exchange thermometer using new experimental data. Journal of Metamorphic Geology, 9(3), 341–347.

Groppo, C., Lombardo, B., Rolfo, F., & Pertusati, P. (2007). Clockwise exhumation path of granulitized eclogites from the Ama Drime range (Eastern Himalayas). Journal of Metamorphic Geology, 25(1), 51–75. https://doi.org/10.1111/j.1525-1314.2006.00678.x

Groppo, C., Rolfo, F., Sachan, H., & Rai, S. (2016). Petrology of blueschist from the Western Himalaya (Ladakh, NW India): exploring the complex behavior of a lawsonite-bearing system in a paleo-accretionary. Lithos, 252, 41–56. Retrieved from https://www.sciencedirect.com/science/article/pii/S0024493716000864

Grujic, D., Warren, C., & Wooden, J. (2011). Rapid synconvergent exhumation of Miocene-aged lower orogenic crust in the eastern Himalaya. Lithosphere, 3(5), 346–366. Retrieved from https://pubs.geoscienceworld.org/gsa/lithosphere/article-abstract/3/5/346/145603

Guillot, S, Sigoyer, J. De, & Lardeaux, J. (1997). Eclogitic metasediments from the Tso Morari area (Ladakh, Himalaya): Evidence for continental subduction during India-Asia convergence. Contributions to Mineralogy and Petrology, 128(2–3), 197–212.

Guillot, S, Hattori, K., & Sigoyer, J. de. (2000). Mantle wedge serpentinization and exhumation of eclogites: insights from eastern Ladakh, northwest Himalaya. Geology. Retrieved from http://geology.gsapubs.org/content/28/3/199.short

Guillot, S., Garzanti, E., Baratoux, D., Marquer, D., Mahéo, G., & De Sigoyer, J. (2003). Reconstructing the total shortening history of the NW Himalaya. Geochemistry, Geophysics, Geosystems, 4(7).

Guillot, S., Mahéo, G., de Sigoyer, J., Hattori, K. H., & Pêcher, A. (2008). Tethyan and Indian subduction viewed from the Himalayan high- to ultrahigh-pressure metamorphic rocks. Tectonophysics, 451(1–4), 225–241. https://doi.org/10.1016/j.tecto.2007.11.059

Guillot, Stéphane, Hattori, K., Agard, P., Schwartz, S., & Vidal, O. (2009). Exhumation Processes in Oceanic and Continental Subduction Contexts: A Review. In Subduction zone geodynamics (pp. 175–205). https://doi.org/10.1007/978-3-540-87974-9_10

Hacker, B.R., Ratschbacher, L., Webb, L., McWilliams, M.O., Ireland, T., Calvert, A., Dong, S., Wenk, H.R. and Chateigner, D., (2000). Exhumation of ultrahigh-pressure continental crust in east central China: Late Triassic-Early Jurassic tectonic unroofing. Journal of Geophysical Research: Solid Earth, 105(B6), 13339–13364.

Hacker, B.R., Calvert, A., Zhang, R.Y., Ernst, W.G. and Liou, J.G., (2003). Ultrarapid exhumation of ultrahigh-pressure diamond-bearing metasedimentary rocks of the Kokchetav Massif, Kazakhstan? Lithos, 70(3–4), 61–75. Retrieved from https://www.sciencedirect.com/science/article/pii/S0024493703000926

Hacker, B. (2006). Pressures and temperatures of ultrahigh-pressure metamorphism: implications for UHP tectonics and H2O in subducting slabs. International Geology Review. Retrieved from http://www.tandfonline.com/doi/abs/10.2747/0020-6814.48.12.1053

Hacker, Bradley R., Andersen, T. B., Johnston, S., Kylander-Clark, A. R. C., Peterman, E. M., Walsh, E. O., & Young, D. (2010). High-temperature deformation during continental-margin subduction & exhumation: The ultrahigh-pressure Western Gneiss Region of Norway. Tectonophysics, 480(1), 149–171. https://doi.org/10.1016/j.tecto.2009.08.012

Hacker, Bradley R., & Gerya, T. V. (2013). Paradigms, new and old, for ultrahigh-pressure tectonism. Tectonophysics, 603, 79–88. https://doi.org/10.1016/j.tecto.2013.05.026

Hacker, Bradley R., Gerya, T. V., & Gilotti, J. a. (2013). Formation and exhumation of ultrahigh-pressure terranes. Elements, 9(4), 289–293. https://doi.org/10.2113/gselements.9.4.289

Hamilton, W. (1979). Tectonics of the Indonesian region.

Handy, M. R. (1990). The solid-state flow of polymineralic rocks. Journal of Geophysical Research, 95(B6), 8647. https://doi.org/10.1029/JB095iB06p08647

Harris, N., Ayres, M., & Massey, J. (1995). Geochemistry of granitic melts produced during the incongruent melting of muscovite: implications for the extraction of Himalayan leucogranite magmas. Journal of Geophysical Research: Solid Earth, 100(B8), 15767–15777.

Harris, R. (2003). Geodynamic patterns of ophiolites and marginal basins in the Indonesian and New Guinea regions. Geological Society, London, Special Publications, 218(1), 481–505.

Harrison, T., Duncan, I., & Mcdougall, I. (1985). Diffusion of 40Ar in biotite: temperature, pressure and compositional effects. Geochimica et Cosmochimica Acta, 49(11), 2461–2468. Retrieved from https://www.sciencedirect.com/science/article/pii/0016703785902467

Harrison, T. M., Célérier, J., Aikman, A. B., Hermann, J., & Heizler, M. T. (2009). Diffusion of 40 Ar in muscovite. Geochimica et Cosmochimica Acta, 73(4), 1039–1051. https://doi.org/10.1016/j.gca.2008.09.038

Haver, T. Van. (1984). Etude stratigraphique, sédimentologique et structurale d'un bassin d'avant arc: exemple du bassin de l'Indus, Ladakh, Himalaya. Université Scientifique et Médicale de Grenoble. Retrieved from https://tel.archives-ouvertes.fr/tel-00641418/

Hawkes, J., & Dangerfield, J. (1978). The Variscan granites of south-west England: a progress report. Proceedings of the Ussher Society, 4(2), 158–171. Retrieved from http://www.ussher.org.uk/journal/70s/1978/Vol 4, Part 2, 1978.pdf#page=52

Hayden, H. (1904). The Geology of Spiti, with parts of Bashar and Rupshu. Memoir of the Geological Survey of India, 36, 1–129.

Heaman, L. M. (2009) 'The application of U–Pb geochronology to mafic, ultramafic and alkaline rocks: an evaluation of three mineral standards.', Chemical Geology, 261(1–2), pp. 43–52.

Hébert, R., Bezard, R., Guilmette, C., Dostal, J., Wang, C., & Lio, Z. (2012). The Indus–Yarlung Zangbo ophiolites from Nanga Parbat to Namche Barwa syntaxes, southern Tibet: First synthesis of petrology, geochemistry, and geochronology with incidences on geodynamic reconstructions of Neo-Tethys. Gondwana Research, 22(2), 377–397. Retrieved from https://www.sciencedirect.com/science/article/pii/S1342937X11002838

Heinrich, C. (1982). Kyanite-eclogite to amphibolite facies evolution of hydrous mafic and pelitic rocks, Adula nappe, Central Alps. Contributions to Mineralogy and Petrology, 81, 30–38.

Henry, D. J., Guidotti, C. V., & Thomson, J. A. (2005). The Ti-saturation surface for low-to-medium pressure metapelitic biotites: Implications for geothermometry and Ti-substitution mechanisms. American Mineralogist, 90(2–3), 316–328. https://doi.org/10.2138/am.2005.1498

Hermann, J., Rubatto, D., Korsakov, A., & Shatsky, V. S. (2001). Multiple zircon growth during fast exhumation of diamondiferous, deeply subducted continental crust (Kokchetav Massif, Kazakhstan). Contributions to Mineralogy and Petrology, 141(1), 66–82.

Hermann, J. (2002). Allanite: thorium and light rare earth element carrier in subducted crust. Chemical Geology, 192(3–4), 289–306.

Heuret, A., & Lallemand, S. (2005). Plate motions, slab dynamics and back-arc deformation. Physics of the Earth and Planetary Interiors, 149(1–2), 31–51. Retrieved from https://www.sciencedirect.com/science/article/pii/S0031920104003462

Hiess, J., Condon, D. J., McLean, N., and Noble, S. R., (2012), U-238/U-235 Systematics in Terrestrial Uranium-Bearing Minerals: Science, v. 335, no. 6076, p. 1610-1614.

Hirajima, T., Wallis, S. R., Zhai, M., & Ye, K. (1993). Eclogitized metagranitoid from the Su-Lu ultra-high pressure (UHP) province, eastern China. Proceedings of the Japan Academy, Series B, 69(10), 249–254. Retrieved from https://www.jstage.jst.go.jp/article/pjab1977/69/10/69_10_249/_article/-char/ja/

Hodges, K. (2000). Tectonics of the Himalaya and southern Tibet from two perspectives. Geological Society of America Bulletin, 112(3), 324–350. Retrieved from https://pubs.geoscienceworld.org/gsa/gsabulletin/article-abstract/112/3/324/183584

Holland, T. J. (1990). Activities of components in omphacitic solid solutions. Contributions to Mineralogy and Petrology, 105(4), 446–453.

Holland, T. J. B., & Powell, R. (1998). An internally consistent thermodynamic data set for phases of petrological interest. Journal of Metamorphic Geology, 16(3), 309–343. https://doi.org/10.1111/j.1525-1314.1998.00140.x

Holland, T., & Powell, R. (2003). Activity–composition relations for phases in petrological calculations: an asymmetric multicomponent formulation. Contributions to Mineralogy and Petrology, 145(4), 492–501.

Holland, T, & Powell, R. (2009). AX: A program to calculate activities of mineral end-members from chemical analyses.

Holyoke, C., & Tullis, J. (2006). Formation and maintenance of shear zones. Geology, 34(2), 105–108. Retrieved from https://pubs.geoscienceworld.org/gsa/geology/article-abstract/34/2/105/129428

Honegger, K., Dietrich, V., Frank, W., Gansser, A., Thoni, M., & Trommsdorff, V. (1982). Magmatism and metamorphism in the Ladakh Himalayas (the Indus-Tsangpo suture zone). Earth and Planetary Science Letters, 60(2), 253–292. Retrieved from https://www.sciencedirect.com/science/article/pii/0012821X82900073

Honegger, K., Le Fort, P., Mascle, G., & Zimmermann, J.-L. (1989). The blueschists along the Indus Suture Zone in Ladakh, NW Himalaya. Journal of Metamorphic Geology, 7(1), 57–72. https://doi.org/10.1111/j.1525-1314.1989.tb00575.x

Horstwood, M. S. A., Košler, J., Gehrels, G., Jackson, S. E., McLean, N. M., Paton, C., … Schoene, B. (2016). Community-Derived Standards for LA-ICP-MS U-(Th-)Pb Geochronology – Uncertainty Propagation, Age Interpretation and Data Reporting. Geostandards and Geoanalytical Research, 40(3), 311–332. https://doi.org/10.1111/j.1751-908X.2016.00379.x

Hu, X., Jansa, L., Chen, L., Griffin, W. L., O'Reilly, S. Y., & Wang, J. (2010). Provenance of Lower Cretaceous Wölong volcaniclastics in the Tibetan Tethyan Himalaya: Implications for the final breakup of eastern Gondwana. Sedimentary Geology, 223(3–4), 193–205.

Hu, XM, Garzanti, E., An, W., & Hu, X. (2015). Provenance and drainage system of the Early Cretaceous volcanic detritus in the Himalaya as constrained by detrital zircon geochronology. Journal of Palaeogeography, 4(1), 85–98. Retrieved from https://www.sciencedirect.com/science/article/pii/S2095383615300122

Hu, X, Garzanti, E., Wang, J., Huang, W., An, W., & Webb, A. (2016). The timing of India-Asia collision onset–Facts, theories, controversies. Earth-Science Reviews, 160, 264–299. Retrieved from https://www.sciencedirect.com/science/article/pii/S0012825216302033

Huang, W., & Wyllie, P. (1981). Phase relationships of S-type granite with H2O to 35 kbar: Muscovite granite from Harney Peak, South Dakota. Journal of Geophysical Research, 86(B11), 10515–10529. Retrieved from https://agupubs.onlinelibrary.wiley.com/doi/abs/10.1029/JB086iB11p10515%4010.1002/%28ISSN%292169-9356.GANDR1

Hubbard, M., Spencer, D., & West, D. (1995). Tectonic exhumation of the Nanga Parbat massif, northern Pakistan. Earth and Planetary Science Letters, 133(1–2), 213–225. Retrieved from https://www.sciencedirect.com/science/article/pii/0012821X9500075N

Humphris, S., & Thompson, G. (1978). Hydrothermal alteration of oceanic basalts by seawater. Geochimica et Cosmochimica Acta, 42(1), 107–125. Retrieved from https://www.sciencedirect.com/science/article/pii/0016703778902211

Hunen, J. van, & Allen, M. (2011). Continental collision and slab break-off: a comparison of 3-D numerical models with observations. Earth and Planetary Science Letters, 302(1–2), 27–37. Retrieved from https://www.sciencedirect.com/science/article/pii/S0012821X10007429

Hyndman, D. W. (1981). Controls on source and depth of emplacement of granitic magma. Geology, 9(6), 244–249.

Iaccarino, S., Montomoli, C., Carosi, R., Massonne, H., Langone, A., & Visona, D. (2015). Pressure–temperature–time–deformation path of kyanite-bearing migmatitic paragneiss in the Kali Gandaki valley (Central Nepal): Investigation of Late. Lithos, 231, 103–121. Retrieved from https://www.sciencedirect.com/science/article/pii/S0024493715002042

Ibarguchi, J. (1995). Petrology of jadeite metagranite and associated orthogneiss from the Malpica-Tuy allochthon (Northwest Spain). European Journal of Mineralogy, 403–416. Retrieved from https://www.schweizerbart.de/papers/ejm/detail/7/83560

Ingalls, M., Rowley, D., Currie, B., & Colman, A. (2016). Large-scale subduction of continental crust implied by India–Asia mass-balance calculation. Nature Geo, 9(11), 848. Retrieved from https://www.nature.com/articles/ngeo2806

Jackson, S. E. et al. (2004) 'The application of laser ablation-inductively coupled plasma-mass spectrometry to in situ U-Pb zircon geochronology', Chemical Geology, 211(1–2), pp. 47–69. doi: 10.1016/j.chemgeo.2004.06.017.

Jacob, D., Cordier, P., Morniroli, J.-P., & Schertl, H.-P. (2009). Application of precession electron diffraction to the characterization of (021) twinning in pseudo-hexagonal coesite. American Mineralogist, 94, 684–692.

Jaffey, A. H., Flynn, K. F., Glendeni.Le, Bentley, W. C., and Essling, A. M., (1971), Precision Measurement of Half-Lives and Specific Activities of U-235 and U-238: Physical Review C, v. 261 4, no. 5, p. 1889-&.

Jagoutz, O., Royden, L., Holt, A. F., & Becker, T. W. (2015). Anomalously fast convergence of India and Eurasia caused by double subduction. Nature Geoscience. Nature Geoscience, 8, 475.

Jagoutz, O., Bouilhol, P., Schaltegger, U., & Müntener, O. (2018). The isotopic evolution of the Kohistan Ladakh arc from subduction initiation to continent arc collision. Geological Society, London, Special Publications, 483.

Jessup, M. J., Newell, D. L., Cottle, J. M., Berger, A. L., & Spotila, J.A . (2009). Orogen-parallel extension and exhumation enhanced by denudation in the trans-Himalayan Arun River gorge, Ama Drime Massif, Tibet-Nepal. Geology. Geology, 36(7), 587–590.

Jolivet, L., Raimbourg, H., Labrousse, L., Avigad, D., Leroy, Y., Austrheim, H., & Andersen, T. B. (2005). Softening trigerred by eclogitization, the first step toward exhumation during continental subduction. Earth and Planetary Science Letters, 237(3–4), 532–547. https://doi.org/10.1016/j.epsl.2005.06.047

Jonnalagadda, M.K., Karmalkar, N. R., & Duraiswami, R. A. (2017a). Geochemistry of eclogites of the Tso Morari complex, Ladakh, NW Himalayas: insights into trace element behavior during subduction and exhumation. Geoscience Frontiers.

Jonnalagadda, Mallika K, Karmalkar, N. R., Duraiswami, R. A., Harshe, S., Gain, S., & Griffin, W. L. (2017b). Formation of atoll garnets in the UHP eclogites of the Tso Morari Complex, Ladakh, Himalaya. Journal of Earth System Science, 126(8), 107. https://doi.org/10.1007/s12040-017-0887-y

Jonnalagadda, M. K., Karmalkar, N. R., & Duraiswami, R. A. (2019). Geochemistry of eclogites of the Tso Morari complex, Ladakh, NW Himalayas: insights into trace element behavior during subduction and exhumation. Geoscience Frontiers, 10(3), 811–826.

Jordan, P. (1988). The rheology of polymineralic rocks — an approach. Geologische Rundschau, 77(1), 285–294. https://doi.org/10.1007/BF01848690

Kaneko, Y., Maruyama, S., Terabayashi, M., Yamamoto, H., Ishikawa, M., Anma, R., Parkinson, C.D., Ota, T., Nakajima, Y., Katayama, I. and Yamamoto, J., (2000). Geology of the Kokchetav UHP-HP metamorphic belt, Northern Kazakhstan. The Island Arc, 9(3), 264–283. https://doi.org/10.1046/j.1440-1738.2000.00278.x

Kaneko, Y., Katayama, I., Yamamoto, H., Misawa, K., Ishikawa, M., Rehman, H.U., Kausar, A.B. and Shiraishi, K. (2003). Timing of Himalayan ultrahigh-pressure metamorphism: sinking rate and subduction angle of the Indian continental crust beneath Asia. Journal of Metamorphic Geology, 21(6), 589–599. https://doi.org/10.1046/j.1525-1314.2003.00466.x

Kapp, P., & DeCelles, P. (2019). Mesozoic–Cenozoic geological evolution of the Himalayan-Tibetan orogen and working tectonic hypotheses. American Journal of Science, 319(3), 159–254. Retrieved from http://www.ajsonline.org/content/319/3/159.short

Kawai, K., & Tsuchiya, T. (2013a). First-principles study on the high-pressure phase transition and elasticity of KAlSi3O8 hollandite. American Mineralogist, 98(1), 207–218. Retrieved from https://pubs.geoscienceworld.org/ssa/ammin/article/98/1/207/45737

Kawai, K., Yamamoto, S., Tsuchiya, T., & Maruyama, S. (2013b). The second continent: existence of granitic continental materials around the bottom of the mantle transition zone. Geoscience Frontiers, 4(1), 1–6. Retrieved from https://www.sciencedirect.com/science/article/pii/S1674987112001065

Kellett, Dawn A., Grujic, D., Coutand, I., Cottle, J., & Mukul, M. (2013). The South Tibetan detachment system facilitates ultra rapid cooling of granulite-facies rocks in Sikkim Himalaya. Tectonics, 32(2), 252–270. https://doi.org/10.1002/tect.20014

Kellett, D, Grujic, D., Mottram, C., Mukul, M., & Larson, K. (2014a). Virtual field guide for the Darjeeling-Sik-kim Himalaya, India. (Eds. C. Montomoli, R. Carosi, R. Law, S. Singh, & S. M. Rai,), Geological field trips in the Himalaya, Karakoram and Tibet, Journal of the Virtual Explorer.

Kellett, DA, Cottle, J., & Smit, M. (2014b). Eocene deep crust at Ama Drime, Tibet: Early evolution of the Himalayan orogen. Lithosphere, 6(4), 220–229. Retrieved from https://pubs.geoscienceworld.org/gsa/lithosphere/article-abstract/6/4/220/145700

Kellett, D.A., Cottle, J. M., & Larson, K. P. (2019). The South Tibetan Detachment System: history, advances, definition and future directions. Geological Society, London, Special Publications, 483(1), 377–400.

Klemd, R., Matthes, S., & Okrusch, M. (1991). High-pressure relics in meta-sediments intercalated with the Weissenstein eclogite, Münchberg gneiss complex, Bavaria. Contributions to Mineralogy and Petrology, 107(3), 328–342. https://doi.org/10.1007/BF00325102

Kohn, M. (2017). Titanite petrochronology. Reviews in Mineralogy and Geochemistry, 83(1), 419–441.

Kohn, M., & Corrie, S. (2011). Preserved Zr-temperatures and U–Pb ages in high-grade metamorphic titanite: evidence for a static hot channel in the Himalayan orogen. Earth and Planetary Science Letters, 311(1–2), 136–143.

Konrad-Schmolke, M., O'Brien, P., & Capitani, C. de. (2008a). Garnet growth at high-and ultrahigh-pressure conditions and the effect of element fractionation on mineral modes and composition. Lithos, 103(3–4), 309–332.

Konrad-Schmolke, M., Zack, T., & O'Brien, P. (2008b). Combined thermodynamic and rare earth element modelling of garnet growth during subduction: examples from ultrahigh-pressure eclogite of the Western Gneiss. Earth and Planetary.

Konzett, J., Frost, D. J., Proyer, A., & Ulmer, P. (2008). The Ca-Eskola component in eclogitic clinopyroxene as a function of pressure, temperature and bulk composition: an experimental study to 15 GPa with possible implications for the formation of oriented SiO2-inclusions in omphacite. Contributions to Mineralogy and Petrology, 155(2), 215–228. https://doi.org/10.1007/s00410-007-0238-0

Kooijman, E., Smit, M. A., Mezger, K., & Berndt, J. (2012). Trace element systematics in granulite facies rutile: implications for Zr geothermometry and provenance studies. Journal of Metamorphic Geology, 30(4), 397–412. https://doi.org/10.1111/j.1525-1314.2012.00972.x

Koons, P. O., Rubie, D. C., & Frueh-Green, G. (1987). The Effects of Disequilibrium and Deformation on the Mineralogical Evolution of Quartz Diorite During Metamorphism in the Eclogite Facies. Journal of Petrology, 28(4), 679–700. https://doi.org/10.1093/petrology/28.4.679

Kouketsu, Y., Hattori, K., Guillot, S., & Rayner, N. (2016). Eocene to Oligocene retrogression and recrystallization of the Stak eclogite in northwest Himalaya. Lithos, 240, 155–166. Retrieved from https://www.sciencedirect.com/science/article/pii/S0024493715004053

Kouketsu, Y., Hattori, K., & Guillot, S. (2017). Protolith of the Stak eclogite in the northwestern Himalaya. Italian Journal of Geosciences, 136(1), 64–72. Retrieved from https://pubs.geoscienceworld.org/italianjgeo/article-abstract/136/1/64/309276

Krabbendam, M., Wain, A., & Andersen, T. (2000). Pre-Caledonian granulite and gabbro enclaves in the Western Gneiss Region, Norway: indications of incomplete transition at high pressure. Geological Magazine, 137(3), 235–255.

Krogh, T.E., (1973), A low contamination method for hydrothermal decomposition of zircon and extraction of U and Pb for isotopic age determination: Geochim. Cosmochim. Acta, v. 37, p. 485-494.

Krogh Ravna, E. J., & Terry, M. P. (2004). Geothermobarometry of UHP and HP eclogites and schists - an evaluation of equilibria among garnet-clinopyroxene-kyanite-phengite-coesite/quartz. Journal of Metamorphic Geology, 22(6), 579–592. https://doi.org/10.1111/j.1525-1314.2004.00534.x

Kruhl, J. H. (1996). Prism-and basal-plane parallel subgrain boundaries in quartz: A microstructural geothermobarometer. Journal of Metamorphic Geology, 14(5), 581–589.

Kruhl, J. H. (2003). Prism- and basal-plane parallel subgrain boundaries in quartz: a microstructural geothermobarometer. Journal of Metamorphic Geology, 14(5), 581–589. https://doi.org/10.1046/j.1525-1314.1996.00413.x

Kylander-Clark, A., Hacker, B., & Mattinson, J. (2008). Slow exhumation of UHP terranes: titanite and rutile ages of the Western Gneiss Region, Norway. Earth and Planetary Science Letters, 272(3–4), 531–540. Retrieved from http://www.sciencedirect.com/science/article/pii/S0012821X08003464

Kylander-Clark, A., Hacker, B., Johnson, C., Beard, B., & Mahlen, N. (2009). Slow subduction of a thick ultrahigh-pressure terrane. Tectonics, 28(2). Retrieved from https://agupubs.onlinelibrary.wiley.com/doi/abs/10.1029/2007TC002251

Kylander-Clark, A. R. C., Hacker, B. R., & Mattinson, C. G. (2012). Size and exhumation rate of ultrahigh-pressure terranes linked to orogenic stage. Earth and Planetary Science Letters (Vol. 321). https://doi.org/10.1016/j.epsl.2011.12.036

Labrousse, L., Jolivet, L., Andersen, T. B., Agard, P., Hébert, R., Maluski, H., & Schärer, U. (2004). Pressure-temperature-time deformation history of the exhumation of ultrahigh pressure rocks in the Western Gneiss Region, Norway. In Special Paper 380: Gneiss Domes in Orogeny (Vol. 380, pp. 155–183). Geological Society of America. https://doi.org/10.1130/0-8137-2380-9.155

Lanari, P., Riel, N., Guillot, S., Vidal, O., & Schwartz, S. (2013). Deciphering high-pressure metamorphism in collisional context using microprobe mapping methods: Application to the Stak eclogitic massif (northwest Himalaya). Geology, 41(2), 111–114. Retrieved from http://geology.gsapubs.org/content/41/2/111.short

Lanari, P., Giuntoli, F., Loury, C., Burn, M., & Engi, M. (2017). An inverse modeling approach to obtain P–T conditions of metamorphic stages involving garnet growth and resorption. European Journal of Mineralogy, 29(2), 181–199.

Lappin, M. A. (1977). Crustal and in situ origin of Norwegian eclogites. Nature, 269(5630), 730–730. https://doi.org/10.1038/269730a0

Lardeaux, J., Ledru, P., Daniel, I., & S Duchene. (2001). The Variscan French Massif Central—a new addition to the ultra-high pressure metamorphic "club": exhumation processes and geodynamic consequences. Tectonophysics, 332(1–2), 143–167. Retrieved from https://www.sciencedirect.com/science/article/pii/S0040195100002535

Larson, K. P., & Cottle, J. M. (2015). Initiation of crustal shortening in the Himalaya. Terra Nova, 27(3), 169–174. https://doi.org/10.1111/ter.12145

Le Fort, P. (1975). Himalayas: the collided range. Present knowledge of the continental arc. American Journal of Science, 275, 1–44.

Le Fort, P., Cuney, M., Deniel, C., France-Lanord, C., Sheppard, S. M. F., Upreti, B. N., & Vidal, P. (1987). Crustal generation of the Himalayan leucogranites. Tectonophysics, 134(1–3), 39–57.

Lee, J., Hacker, B., & Wang, Y. (2004). Evolution of North Himalayan gneiss domes: structural and metamorphic studies in Mabja Dome, southern Tibet. Journal of Structural Geology, 26(12), 2297–2316.

Leech, M., Singh, S., & Jain, A. (2005). The onset of India–Asia continental collision: early, steep subduction required by the timing of UHP metamorphism in the western Himalaya. Earth and Planetary Letters, 234(1–2), 83–97. Retrieved from http://www.sciencedirect.com/science/article/pii/S0012821X05001573

Leech, M. L., Singh, S., & Jain, A. K. (2007). Continuous metamorphic zircon growth and interpretation of U-Pb SHRIMP dating: An example from the Western Himalaya. International Geology Review, 49(4), 313–328. https://doi.org/10.2747/0020-6814.49.4.313

Lenze, A., & Stöckhert, B. (2008). Microfabrics of quartz formed from coesite (Dora-Maira Massif, Western Alps). European Journal of Mineralogy, 20(5), 811–826. Retrieved from https://pubs.geoscienceworld.org/eurjmin/article-abstract/20/5/811/62578

Li, Q. L., Yang, Y. N., Shi, Y. H., & Lin, W. (2013). Eclogite rutile U–Pb dating: constraint for formation and evolution of continental collisional orogen. Chin Sci Bull, 58,. Chin Sci Bull, 58, 2279–2284.

Li, S.-M., Wang, Q., Zhu, D.-C., Stern, R. J., Cawood, P. A., Sui, Q.-L., & Zhao, Z. (2018). One or Two Early Cretaceous Arc Systems in the Lhasa Terrane, Southern Tibet. Journal of Geophysical Research: Solid Earth, 123, 3391–3413.

Li, Z., & Gerya, T. V. (2009). Polyphase formation and exhumation of high-to ultrahigh-pressure rocks in continental subduction zone: Numerical modeling and application to the Sulu ultrahigh-pressure terrane in eastern China. Journal of. Geophysical Research: Solid Earth, 114(B9).

Li, ZH, Gerya, T., & Burg, J. (2010). Influence of tectonic overpressure on P–T paths of HP–UHP rocks in continental collision zones: thermomechanical modelling. Journal of Metamorphic Geology, 28(3), 227–247.

Liati, A., & Gebauer, D. (2003). Geochronological constraints for the time of metamorphism in the Gruf Complex (Central Alps) and implications for the Adula-Cima Lunga nappe system. S. Wiss Bulletin of Mineralogy and Petrology, 83(2), 159–172.

Liou, J. G., Tsujimori, T., Zhang, R. Y., Katayama, I., & Maruyama, S. (2004). Global UHP Metamorphism and Continental Subduction/Collision: The Himalayan Model. International Geology Review, 46(1), 1–27. https://doi.org/10.2747/0020-6814.46.1.1

Little, T., Hacker, B., Gordon, S., & Baldwin, S. (2011). Diapiric exhumation of Earth's youngest (UHP) eclogites in the gneiss domes of the D'Entrecasteaux Islands, Papua New Guinea. Tectonophysics, 510(1–2), 39–68. Retrieved from http://www.sciencedirect.com/science/article/pii/S0040195111002228

Lloyd, G. E. (2000). Grain boundary contact effects during faulting of quartzite: an SEM/EBSD analysis. Journal of Structural Geology, 22(11–12), 1675–1693. https://doi.org/10.1016/S0191-8141(00)00069-9

Lombardo, B., & Rolfo, F. (2000a). Glaucophane and barroisite eclogites from the Upper Kaghan nappe: implications for the metamorphic history of the NW Himalaya. Journal of Geodynamics, 30(1–2), 37–60. Retrieved from http://sp.lyellcollection.org/content/170/1/411.short

Lombardo, B., & Rolfo, F. (2000b). Two contrasting eclogite types in the Himalayas: implications for the Himalayan orogeny. Journal of Geodynamics. Retrieved from http://www.sciencedirect.com/science/article/pii/S0264370799000265

Lotout, C., Pitra, P., Poujol, M., & Van Den Driessche, J. (2017). Ordovician magmatism in the Lévézou massif (French Massif Central): tectonic and geodynamic implications. International Journal of Earth Sciences, 106(2), 501–515. https://doi.org/10.1007/s00531-016-1387-z

Lotout, C., Pitra, P., Poujol, M., Ruffet, G., Anczkiewicz, R., & Van den Driessche, J. (2019). Emplacement, burial, exhumation–deciphering the fate of the Lévézou massif via petrochronological studies of felsic and mafic eclogites. Retrieved from https://hal-insu.archives-ouvertes.fr/insu-02064556/

Ludwig, K. (2008) 'Isoplot version 4.15: a geochronological toolkit for microsoft Excel.', Berkeley Geochronology Center, Special Publication, 4, pp. 247–270.

Lundstrom, C. C., Shaw, H. F., Ryerson, F. J., Phinney, D. L., Gill, J. B., & Williams, Q. (1994). Compositional controls on the partitioning of U, Th, Ba, Pb, Sr and Zr between clinopyroxene and haplobasaltic melts: implications for uranium series disequilibria in basalts. Earth and Planetary Science Letters, 128(3–4), 407–423.

Luvizotto, G.L., Zack, T., Meyer, H.P., Ludwig, T., Triebold, S., Kronz, A., Münker, C., Stockli, D.F., Prowatke, S., Klemme, S. and Jacob, D.E., (2009). Rutile crystals as potential trace element and isotope mineral standards for microanalysis. Chemical Geology, 261(3–4), 346–369. https://doi.org/10.1016/j.chemgeo.2008.04.012

Mahar, E. M., Baker, J. M., Powell, R., Holland, T. J. B., & Howell, N. (1997). The effect of Mn on mineral stability in metapelites. Journal of Metamorphic Geology, 15(2), 223–238.

Mahéo, G., Bertrand, H., Guillot, S., Mascle, G., Pecher, A., Picard, C., & de Sigoyer, J. (2000). Témoins d'un arc immature téthysien dans les ophiolites du Sud Ladakh (NW Himalaya, Inde). Comptes Rendus de l'Académie Des Sciences-Series IIA-Earth and Planetary Science, 330(4), 289–295. Retrieved from https://www.sciencedirect.com/science/article/pii/S1251805000001300

Mancktelow, N. S. (1995). Nonlithostatic pressure during sediment subduction and the development and exhumation of high pressure metamorphic rocks. Journal of Geophysical Research: Solid Earth, 100(B1), 571–583.

Martin, A. (2017). A review of Himalayan stratigraphy, magmatism, and structure. Gondwana Research, 49, 42–80. Retrieved from https://www.sciencedirect.com/science/article/pii/S1342937X17302332

Martin, C. (2019). P–T conditions of symplectite formation in the eclogites from the Western Gneiss Region (Norway). Geological Society, London, Special Publications, 478(1), 197–216.

Martin, Céline, & Duchêne, S. (2015). Residual water in hydrous minerals as a kinetic factor for omphacite destabilization into symplectite in the eclogites of Vårdalsneset (WGR, Norway). Lithos, 232, 162–173. https://doi.org/10.1016/J.LITHOS.2015.06.021

Mascle, G. (1986). Structure et evolution des bassins d'episuture et de perisuture lies a la chaine himalayenne. Bull Centres Rech Explor-Prod Elf-Aquitaine, 10, 181–203. Retrieved from https://ci.nii.ac.jp/naid/10016973287/

Mascle, H. (1985). L'Himalaya resulte-t-il du telescopage de trois chaines? Bulletin de La Société Géologique de France, 1(3), 289–304. Retrieved from https://pubs.geoscienceworld.org/sgf/bsgf/article-abstract/I/3/289/123136

Massonne, H.-J., & Schreyer, W. (1987). Phengite geobarometry based on the limiting assemblage with K-feldspar, phlogopite, and quartz. Contributions to Mineralogy and Petrology, 96(2), 212–224. https://doi.org/10.1007/BF00375235

Massonne, H. (2009). Hydration, dehydration, and melting of metamorphosed granitic and dioritic rocks at high-and ultrahigh-pressure conditions. Earth and Planetary Science Letters. Retrieved from http://www.sciencedirect.com/science/article/pii/S0012821X09005627

Massonne, H., & O'Brien, P. (2003). The Bohemian massif and the NW Himalaya. Ultrahigh Pressure Metamorphism.

Massonne, H., Willner, A., & Gerya, T. (2007). Densities of metapelitic rocks at high to ultrahigh pressure conditions: What are the geodynamic consequences? Earth and Planetary Science Letters, 256(1–2), 12–27. Retrieved from https://www.sciencedirect.com/science/article/pii/S0012821X07000131

Matte, P., Mattauer, M., Olivet, J. M., & Griot, D.A. (1997). Continental subductions beneath Tibet and the Himalayan orogeny: a review. Terra Nova, 9(5–6), 264-270.

Matthews, K. J., Dietmar Müller, R., & Sandwell, D. T. (2016). Oceanic microplate formation records the onset of India-Eurasia collision. Earth and Planetary Science Letters, 433, 204–214. https://doi.org/10.1016/j.epsl.2015.10.040

Mattinson, J.M., (2005), Zircon U-Pb chemical-abrasion ("CA-TIMS") method: combined annealing and multi-step dissolution analysis for improved precision and accuracy of zircon ages: Chem. Geol., v. 220, p. 47-56.

Mattinson, C., Wooden, J., Liou, J., Bird, D., & Wu, C. (2006). Age and duration of eclogite-facies metamorphism, North Qaidam HP/UHP terrane, Western China. American Journal of Science, 306(9), 683–711. Retrieved from http://www.ajsonline.org/content/306/9/683.short

McClelland, W., Power, S., Gilotti, J., Mazdab, F., & Wopenka, B. (2006). U-Pb SHRIMP geochronology and trace-element geochemistry of coesite-bearing zircons, North-East Greenland Caledonides. Special Papers - Geological Society of America, 403, 23.

McLean, N. M., Bowring, J. F., and Bowring, S. A., (2011), An algorithm for U-Pb isotope dilution data reduction and uncertainty propagation: Geochemistry Geophysics Geosystems, v. 12.

McLean, Noah M., Daniel J. Condon, Blair Schoene, and Samuel A. Bowring (2015). "Evaluating uncertainties in the calibration of isotopic reference materials and multi-element isotopic tracers (EARTHTIME Tracer Calibration Part II)."Geochimica et Cosmochimica Acta.

Menold, C. A., Manning, C. E., Yin, A., Tropper, P., Chen, X.-H., & Wang, X.-F. (2009). Metamorphic evolution, mineral chemistry and thermobarometry of orthogneiss hosting ultrahigh-pressure eclogites in the North Qaidam metamorphic belt, Western China. Journal of Asian Earth Sciences, 35, 273–284. https://doi.org/10.1016/j.jseaes.2008.12.008

Merlet, C. (1994). An accurate computer correction program for quantitative electron probe microanalysis. Microchimica Acta, 114(1), 363–376.

Metcalf, K., & Kapp, P. (2017). The Yarlung suture mélange, Lopu Range, southern Tibet: Provenance of sandstone blocks and transition from oceanic subduction to continental collision. Gondwana Research, 48, 15–33. Retrieved from https://www.sciencedirect.com/science/article/pii/S1342937X1630301X

Meunier, A., & Velde, B. (1982). Phengitization, sericitization and potassium-beidellite in a hydrothermally-altered granite. Clay Minerals, 17(3), 285–299. Retrieved from https://www.cambridge.org/core/journals/clay-minerals/article/phengitization-sericitization-and-potassiumbeidellite-in-a-hydrothermallyaltered-granite/96C7C78B1D4E37155976D4D049C76896

Mezger, K., Hanson, G., & SR Bohlen. (1989). High-precision UPb ages of metamorphic rutile: application to the cooling history of high-grade terranes. Earth and Planetary Science Letters, 96(1–2), 106–118. Retrieved from https://www.sciencedirect.com/science/article/pii/0012821X8990126X

Middlemost, E. (1989). Iron oxidation ratios, norms and the classification of volcanic rocks. Chemical Geology, 77(1), 19–26. Retrieved from https://www.sciencedirect.com/science/article/pii/0009254189900119

Miller, C., Zanetti, A., Thöni, M., & Konzett, J. (2007). Eclogitisation of gabbroic rocks: redistribution of trace elements and Zr in rutile thermometry in an Eo-Alpine subduction zone (Eastern Alps). Chemical Geology, 239(1–2), 96–123.

Molnar, P., & Gray, D. (1979). Subduction of continental lithosphere: Some constraints and uncertainties. Geology, 7(1), 58–62. Retrieved from https://pubs.geoscienceworld.org/gsa/geology/article-abstract/7/1/58/195520

Morimoto, N. (1988). Nomenclature of Pyroxenes. Mineralogy and Petrology, 39(1), 55–76. https://doi.org/10.1007/BF01226262

Mørk, M. B. E. (1985). Incomplete high P–T metamorphic transitions within the Kvamsøy pyroxenite complex, west Norway: a case study of disequilibrium. Journal of Metamorphic Geology, 3(3), 245–264. https://doi.org/10.1111/j.1525-1314.1985.tb00320.x

Mosenfelder, J., & Bohlen, S. (1997). Kinetics of the coesite to quartz transformation. Earth and Planetary Science Letters, 153(1–2), 133–147.

Mosenfelder, J., Schertl, H., Smyth, J., & JG, L. (2005). Factors in the preservation of coesite: The importance of fluid infiltration. American Mineralogist, 90(5–6), 779–789. Retrieved from https://pubs.geoscienceworld.org/msa/ammin/article-abstract/90/5-6/779/44397

Mottram, C.M., Warren, C.J., Regis, D., Roberts, N.M., Harris, N.B., Argles, T.W. and Parrish, R.R., (2014) 'Developing an inverted Barrovian sequence; insights from monazite petrochronology.', Earth and Planetary Science Letters, 403, pp. 418–431.

Mukherjee, B., & Sachan, H. (2003). Carbonate-bearing UHPM rocks from the Tso-Morari region, Ladakh, India: petrological implications. International Geology Review, 1, 49–69. Retrieved from http://www.tandfonline.com/doi/abs/10.2747/0020-6814.45.1.49

Mukherjee, B., & Sachan, H. (2004). Garnet response diamond pressure metamorphism from Tso-Morari region, Ladakh, India. Himalayan Journal of Science.

Mukherjee, B., & Sachan, H. (2009). Fluids in coesite-bearing rocks of the Tso Morari Complex, NW Himalaya: evidence for entrapment during peak metamorphism and subsequent uplift. Geological Magazine, 146(6), 876–889.

Müller, R.D., Seton, M., Zahirovic, S., Williams, S.E., Matthews, K.J., Wright, N.M., Shephard, G.E., Maloney, K.T., Barnett-Moore, N., Hosseinpour, M. and Bower, D.J., (2016). Ocean Basin Evolution and Global-Scale Plate Reorganization Events Since Pangea Breakup. Annual Review of Earth and Planetary Sciences, 44(1), 107–138. https://doi.org/10.1146/annurev-earth-060115-012211

Murphy, M., & Mark Harrison, T. (1999). Relationship between leucogranites and the Qomolangma detachment in the Rongbuk Valley, south Tibet. Geology, 27(9), 831–834. Retrieved from https://pubs.geoscienceworld.org/gsa/geology/article-abstract/27/9/831/190362

Nábělek, J., Hetényi, G., Vergne, J., Sapkota, S., Kafle, B., Jiang, M., Su, H., Chen, J. and Huang, B.S., (2009). Underplating in the Himalaya-Tibet collision zone revealed by the Hi-CLIMB experiment. Science, 325(5946), 1371–1374. Retrieved from https://science.sciencemag.org/content/325/5946/1371.short

Najman, Y., Appel, E., Boudagher-Fadel, M., Bown, P., Carter, A., Garzanti, E., Godin, L., Han, J., Liebke, U., Oliver, G. and Parrish, R., (2010). Timing of India-Asia collision: Geological, biostratigraphic, and palaeomagnetic constraints. Journal of Geophysical Research, 115(B12), B12416. https://doi.org/10.1029/2010JB007673

Nakazawa, K., & Kapoor, H. M. (1973). Spilitic pillow lava in Panjal trap of Kashmir, India. Memoirs of the Faculty of Science, Kyoto University, Series of Geology and Mineralogy, 39, 83–98.

Nanda, M. M., & Singh, M. P. (1977). Stratigraphy and sedimentation of the Zanskar area, Ladakh and adjoining parts fo the Lahul region of Himachal Pradesh. Himalayan Geology, 6, 365–388.

Noble, S., & Searle, M. (1995). Age of crustal melting and leucogranite formation from U-Pb zircon and monazite dating in the western Himalaya, Zanskar, India. Geology, 23(12), 1135–1138. Retrieved from https://pubs.geoscienceworld.org/gsa/geology/article-abstract/23/12/1135/206243

Nord, G. L. (1994). Transformation-induced twin boundaries in minerals. Phase Transitions, 48(1–3), 107–134. https://doi.org/10.1080/01411599408200356

Norton, I. O., & Sclater, J. G. (1979). A model for the evolution of the Indian Ocean and the breakup of Gondwanaland. Journal of Geophysical Research: Solid Earth, 84(B12), 6803–6830. https://doi.org/10.1029/JB084iB12p06803

O'Brien, P. J. (2006). The age of deep, steep continental subduction in the NW Himalaya: Relating zircon growth to metamorphic history. Comment on: "The onset of India–Asia continental collision: Early, steep subduction required by the timing of UHP metamorphism in the western. Earth and Planetary Science Letters, 245(3–4), 814–816. https://doi.org/10.1016/j.epsl.2006.03.033

O'Brien, P.J., & Vrána, S. (1995). Eclogites with a short-lived granulite facies overprint in the Moldanubian Zone, Czech Republic: petrology, geochemistry and diffusion modelling of garnet zoning. Geologische Rundschau, 84(3), 473–488.

O'Brien, P., Zotov, N. and Law, R. (1999). First discovery of coesite in the Kaghan eclogites (Pakistan); implications for Himalayan evolution. Terra Nova, 2, 109–111.

O'Brien, P., & Sachan, H. (2000). Diffusion modelling in garnet from Tso Morari eclogite and implications for exhumation models. Earth Science Frontiers, 7, 25–27. Retrieved from http://d.wanfangdata.com.cn/periodical_dxqy2000z1010.aspx

O'Brien, P., Zotov, N., Law, R., Khan, M., & Jan, M. (2001). Coesite in Himalayan eclogite and implications for models of India-Asia collision. Geology, 29(5), 435–438. Retrieved from http://geology.gsapubs.org/content/29/5/435.short

O'Brien, P. (2018a). Eclogites and other high-pressure rocks in the Himalaya: a review. Geological Society, London, Special Publications, 483, SP483.13.

O'Brien, P. (2018b). Tso Morari coesite eclogite: pseudosection predictions v. the preserved record and implications for tectonometamorphic models. Geological Society, London, Special Publications, 474(1), 5–24.

Oberhänsli, R., Hunziker, J. C., Martinotti, G., & Stern, W. B. (1985). Geochemistry, geochronology and petrology of Monte Mucrone: An example of EO-alpine eclogitization of Permian granitoids in the Sesia-Lanzo Zone, Western Alps, Italy. Chemical Geology: Isotope Geoscience Section, 52(2), 165–184. https://doi.org/10.1016/0168-9622(85)90016-8

Oberhänsli, R. (2013). High-pressure–low-temperature evolution in the Indus-Tsangpo Suture along the Kohistan Arc (Kaghan Valley, NE Pakistan). Episodes, 36(2), 87–93.

Okay, A., Xu, S., & Sengor, A. (1989). Coesite from the Dabie Shan eclogites, central China. European Journal of Mineralogy, 1(4), 595–598. Retrieved from

Okay, A., & Şengör, A. C. (1992). Evidence for intracontinental thrust-related exhumation of the ultra-high-pressure rocks in China. Geology, 20(5), 411–414. Retrieved from https://pubs.geoscienceworld.org/gsa/geology/article-abstract/20/5/411/205719

Olker, B., Altherr, R., & Paquin, J. (2003). Fast exhumation of the ultrahigh-pressure Alpe Arami garnet peridotite (Central Alps, Switzerland): constraints from geospeedometry and thermal modelling. Journal of Metamorphic Geology, 21(4), 395–402.

Palin, R.M., Searle, M.P., Waters, D.J., Parrish, R.R., Roberts, N.M.W., Horstwood, M.S.A., Yeh, M.W., Chung, S.L. and Anh, T.T., (2013). A geochronological and petrological study of anatectic paragneiss and associated granite dykes from the Day Nui Con Voi metamorphic core complex, North Vietnam: Constraints on the timing of metamorphism within the Red River shear zone. Journal of Metamorphic Geology, 31(4), 359–387. https://doi.org/10.1111/jmg.12025

Palin, R. M., St-Onge, M. R., Waters, D. J., Searle, M. P., & Dyck, B. (2014). Phase equilibria modelling of retrograde amphibole and clinozoisite in mafic eclogite from the Tso Morari massif, northwest India: constraining the P - T - M (H 2 O) conditions of exhumation. Journal of Metamorphic Geology, 32(7), 675–693. https://doi.org/10.1111/jmg.12085

Palin, R., Reuber, G., White, R., Kaus, B., & Weller, O. (2017). Subduction metamorphism in the Himalayan ultrahigh-pressure Tso Morari massif: an integrated geodynamic and petrological modelling approach. Earth and Planetary Science Letters, 467, 108–119. Retrieved from https://www.sciencedirect.com/science/article/pii/S0012821X17301656

Palin, R., Treloar, P., Searle, M., & Wald, T. (2018). U-Pb monazite ages from the Pakistan Himalaya record pre-Himalayan Ordovician orogeny and Permian continental breakup. Bulletin, 130(11–12), 2047–2061. Retrieved from https://pubs.geoscienceworld.org/gsa/gsabulletin/article-abstract/543303/UPb-monazite-ages-from-the-Pakistan-Himalaya

Pape, J., Mezger, K., & Robyr, M. (2016). A systematic evaluation of the Zr-in-rutile thermometer in ultra-high temperature (UHT) rocks. Contributions to Mineralogy and Petrology, 171(5), 44.

Paquette, J.-L., Nédélec, A., Moine, B., & Rakotondrazafy, M. (1994). U-Pb, Single Zircon Pb-Evaporation, and Sm-Nd Isotopic Study of a Granulite Domain in SE Madagascar. The Journal of Geology, 102(5), 523–538. https://doi.org/10.1086/629696

Parrish, R. R. (1990) 'U–Pb dating of monazite and its application to geological problems.', Canadian Journal of Earth Sciences, 27(11), pp. 1431–1450.

Parrish, R., & Hodges, V. (1996). Isotopic constraints on the age and provenance of the Lesser and Greater Himalayan sequences, Nepalese Himalaya. Geological Society of America Bulletin, 108(7), 904–911. Retrieved from https://pubs.geoscienceworld.org/gsa/gsabulletin/article-abstract/108/7/904/183184

Parrish, R., Gough, S., Searle, M., & Waters, D. (2006). Plate velocity exhumation of ultrahigh-pressure eclogites in the Pakistan Himalaya. Geology. Retrieved from http://geology.gsapubs.org/content/34/11/989.short

Parsons, A., Phillips, R., Lloyd, G., Law, R., Searle, M., & Walshaw, R. (2016). Mid-crustal deformation of the Annapurna-Dhaulagiri Himalaya, central Nepal: An atypical example of channel flow during the Himalayan orogeny. Geosphere, 12(3), 985–1015. Retrieved from https://pubs.geoscienceworld.org/gsa/geosphere/article-abstract/12/3/985/132429

Parsons, A J, Hosseini, K., Palin, R., & Sigloch, K. (2019). Geological, geophysical and plate kinematic constraints for models of the India-Asia collision. Earth Science Reviews, in review.

Parsons, I., & Boyd, R. (1971). Distribution of potassium feldspar polymorphs in intrusive sequences. Mineralogical Magazine, 38(295), 295–311. Retrieved from http://citeseerx.ist.psu.edu/viewdoc/download?doi=10.1.1.627.2518&rep=rep1&type=pdf

Passchier, C. W., & Trouw, R. A. J. (2005). Deformation Mechanisms. In Microtectonics (pp. 25–66). Berlin/Heidelberg: Springer-Verlag. https://doi.org/10.1007/3-540-29359-0_3

Pattison, D. R. M., & Newton, R. C. (1989). Reversed experimental calibration of the garnet-clinopyroxene Fe—Mg exchange thermometer. Contributions to Mineralogy and Petrology, 101(1), 87–103.

Pattison, D. R. M., & Tinkham, D. K. (2009). Interplay between equilibrium and kinetics in prograde metamorphism of pelites: an example from the Nelson aureole, British Columbia. Journal of Metamorphic Geology, 24(7), 249–279.

Pattison, D. R., De Capitani, C., & Gaidies, F. (2011). Petrological consequences of variations in metamorphic reaction affinity. Journal of Metamorphic Geology, 29(9), 953–977.

Pearce, JA, Harris, N., & Tindle, A. (1984). Trace element discrimination diagrams for the tectonic interpretation of granitic rocks. Journal of Petrology, 25(956–983).

Pearce, J. (1996). Sources and settings of granitic rocks. Episodes, 19, 120–125.

Pehl, J., & Wenk, H. (2005). Evidence for regional Dauphiné twinning in quartz from the Santa Rosa mylonite zone in Southern California. A neutron diffraction study. Journal of Structural Geology, 27(10), 1741–1749.

Perrillat, J., Daniel, I., Lardeaux, J., & Cardon, H. (2003). Kinetics of the coesite–quartz transition: application to the exhumation of ultrahigh-pressure rocks. Journal of Petrology, 44(4), 773–788.

Peterman, E., Hacker, B., & Baxter, E. (2009). Phase transformations of continental crust during subduction and exhumation: Western Gneiss Region, Norway. European Journal of Mineralogy, 21(6), 1097–1118. Retrieved from https://pubs.geoscienceworld.org/eurjmin/article-abstract/21/6/1097/69417

Piazolo, S., Prior, D. J., & Holness, M. D. (2005). The use of combined cathodoluminescence and EBSD analysis: a case study investigating grain boundary migration mechanisms in quartz. Journal of Microscopy, 217(2), 152–161. https://doi.org/10.1111/j.1365-2818.2005.01423.x

Plank, T., & Langmuir, C. (1993). Tracing trace elements from sediment input to volcanic output at subduction zones. Nature, 362(6422), 739. Retrieved from https://www.nature.com/articles/362739a0

Plumper, O., & Putnis, A. (2009). The Complex Hydrothermal History of Granitic Rocks: Multiple Feldspar Replacement Reactions under Subsolidus Conditions. Journal of Petrology, 50(5), 967–987. https://doi.org/10.1093/petrology/egp028

Pognante, U. (1985). Coronitic reactions and ductile shear zones in eclogitised ophiolite metagabbro, Western Alps, North Italy. Chemical Geology, 50(1–3), 99–109. Retrieved from https://www.sciencedirect.com/science/article/pii/0009254185901147

Pognante, U., & Spencer, D. (1991). First report of eclogites from the Himalayan belt, Kaghan valley (northern Pakistan). European Journal of Mineralogy, 3, 613–618. Retrieved from http://www.schweizerbart.de/papers/ejm/detail/3/82653/%23

Pognante, U., Benna, P., & Fort, P. Le. (1993). High-pressure metamorphism in the High Himalayan crystallines of the Stak valley, northeastern Nanga Parbat-Haramosh syntaxis,

Pakistan Himalaya. Geological Society, London,. Retrieved from http://sp.lyellcollection.org/content/74/1/161.short

Powell, R. (1985). Regression diagnostics and robust regression in geothermometer/geobarometer calibration: the garnet-clinopyroxene geothermometer revisited. Journal of Metamorphic Geology, 3(3), 231–243.

Powell, R., & Holland, T. (1994). Optimal geothermometry and geobarometry. American Mineralogist, 79(1–2), 20-133.

Powell, R., & Holland, T. J. B. (1988). An internally consistent dataset with uncertainties and correlations: 3. Applications to geobarometry, worked examples and a computer program. Journal of Metamorphic Geology, 6(2), 173–204.

Powell, R., & Holland, T. (2008). On thermobarometry. Journal of Metamorphic Geology, 26(2), 155–179. Retrieved from http://onlinelibrary.wiley.com/doi/10.1111/j.1525-1314.2007.00756.x/full

Powell, R., & Powell, R. (1998). Calculating phase diagrams involving solid solutions via non-linear equations, with examples using THERMOCALC. Journal of Metamorphic Geology, 16, 577–588. https://doi.org/10.1111/j.1525-1314.1998.00157.x

Proyer, A. (2003). The preservation of high-pressure rocks during exhumation: metagranites and metapelites. Lithos, 70(3–4), 183–194. https://doi.org/10.1016/S0024-4937(03)00098-7

Puga, E., Federico, A. D., & Demant, A. (1995). The eclogitized pillows of the Betic Ophiolitic Association: relics of the Tethys Ocean floor incorporated in the Alpine chain after subduction. Terra Nova, 7(1), 31–43. https://doi.org/10.1111/j.1365-3121.1995.tb00665.x

Purdy, J., & Jager, E. (1976). K-Ar ages on rock forming minerals from Central Alps. Memoire de Padova.

Putnis, A. (1992). An introduction to mineral sciences. Retrieved from https://books.google.co.uk/books?hl=en&lr=&id=yMGzmOqYescC&oi=fnd&pg=PR19&dq=putnis+1992+quartz&ots=wivzuBpxRt&sig=N2LjovTRWQiLldMImSgT3Wl7-DQ

Råheim, A., & Green, D. H. (1974). Experimental determination of the temperature and pressure dependence of the Fe-Mg partition coefficient for coexisting garnet and clinopyroxene. Contributions to Mineralogy and Petrology, 48(3), 179–203.

Raimbourg, H., Jolivet, L., & Leroy, Y. (2007). Consequences of progressive eclogitization on crustal exhumation, a mechanical study. Geophysical Journal International, 168(1), 379–401. Retrieved from https://academic.oup.com/gji/article-abstract/168/1/379/2141017

Rajkumar, A. (2015). Prograde histories in high-P to ultra-high-P metamorphic rocks from Tibet and northern India. University of Sydney.

Ranalli, G. (2000). Rheology of the crust and its role in tectonic reactivation. Journal of Geodynamics, 30(1–2), 3–15. Retrieved from https://www.sciencedirect.com/science/article/pii/S0264370799000241

Ravna, K. (2000). The garnet–clinopyroxene Fe2+–Mg geothermometer: an updated calibration. Journal of Metamorphic Geology, 18(2), 211–219.

Rehman, H., Kobayash, K., Tsujimori, T., Ota, T., Yamamoto, H., Nakamura, E., & Kaneko, Y. (2013). Ion microprobe U–Th–Pb geochronology and study of micro-inclusions in zircon

from the Himalayan high-and ultrahigh-pressure eclogites, Kaghan Valley of Pakistan. Journal of Asian Earth Sciences, 63, 179–196.

Rehman, H., Lee, H., Chung, S., Khan, T., & O'Brien, P. (2016). Source and mode of the Permian Panjal Trap magmatism: evidence from zircon U–Pb and Hf isotopes and trace element data from the Himalayan ultrahigh. Lithos, 260, 286–299.

Rehman, Hafiz U., Jan, M. Q., Khan, T., Yamamoto, H., & Kaneko, Y. (2017). Varieties of the Himalayan eclogites: A pictorial review of textural and petrological features. Island Arc, 26(5), e12209. https://doi.org/10.1111/iar.12209

Rehman, H.U., Iizuka, Y., Lee, H.Y., Chung, S.L., Duan, Z., Wei, C., Khan, T., Zafar, T. and Yamamoto, H., (2019). Zirconium in rutile thermometry of the Himalayan ultrahigh-pressure eclogites and their retrogressed counterparts, Kaghan Valley, Pakistan. Lithos, 344–345, 86–99. https://doi.org/10.1016/j.lithos.2019.06.017

Replumaz, A., Negredo, A. M., Guillot, S., & Villaseñor, A. (2010). Multiple episodes of continental subduction during India/Asia convergence: Insight from seismic tomography and tectonic reconstruction. Tectonophysics, 483, 125–134.

Replumaz, A., Capitanio, F. A., Guillot, S., Negredo, A. M., & Villaseñor, A. (2014). The coupling of Indian subduction and Asian continental tectonics. Gondwana Research, 26, 608–626.

Richter, B., Stünitz, H., & Heilbronner, R. (2016). Stresses and pressures at the quartz-to-coesite phase transformation in shear deformation experiments. Journal of Geophysical Research: Solid Earth, 121(11), 8015–8033. https://doi.org/10.1002/2016JB013084

Riel, N., Hattori, K., Guillot, S., Rayner, N., Davis, B., Latif, M., & Kausar, A. (2008). SHRIMP zircon ages of eclogites in the Stak massif, northern Pakistan. Himalayan Journal of Science, 5(7), 119–120. Retrieved from https://www.nepjol.info/index.php/HJS/article/view/1308/1288

Roberts, N., Horstwood, M., Condorelli, V., & Noble, S. (2011). Technical Aspects and Geochronological Applications of the Nu Attom ICP-MS. In 14th Indian Society of Mass Spectrometry Symposium cum Workshop.

Roberts, N. M., Thomas, R. J. and Jacobs, J. (2016) 'Geochronological constraints on the metamorphic sole of the Semail ophiolite in the United Arab Emirates.', Geoscience Frontiers, 7(4), pp. 609–619.

Robinson, D. M., & Martin, A. J. (2014a). Reconstructing the Greater Indian margin: A balanced cross section in central Nepal focusing on the Lesser Himalayan duplex. Tectonics, 33(11), 2143–2168. https://doi.org/10.1002/2014TC003564

Robinson, P., Roberts, D., Gee, D. G., & Solli, A. (2014b). A major synmetamorphic Early Devonian thrust and extensional fault system in the Mid Norway Caledonides: relevance to exhumation of HP and UHP rocks. Geological Society, London, Special Publications, 390(1), 241–270.

Roecker, S. W. (1982). Velocity structure of the Pamir-Hindu Kush Region: Possible evidence of subducted crust. Journal of Geophysical Research: Solid Earth, 87(B2), 945–959. https://doi.org/10.1029/JB087iB02p00945

Rolfo, F., Carosi, R., Montomoli, C., & Visonà, D. (2008). Discovery of granulitized eclogite in North Sikkim expands the eastern Himalaya high-pressure province. Himalayan Journal of

Science, 5(7), 126–127. Retrieved from https://www.nepjol.info/index.php/HJS/article/view/1312/1292

Rollinson, H. (1993). Using geochemical data: evaluation. Presentation, Interpretation. Singapore. Ongman.

Root, D. B., Hacker, B. R., Gans, P. B., Ducea, M. N., Eide, E. A., & Mosenfelder, J. L. (2005). Discrete ultrahigh-pressure domains in the Western Gneiss Region, Norway: implications for formation and exhumation. Journal of Metamorphic Geology, 23(1), 45–61. https://doi.org/10.1111/j.1525-1314.2005.00561.x

Rowley, D., & Ingalls, M. (2017). Reply to 'Unfeasible subduction?'. Nature Geoscience, 10, 879–880.

Rubatto, D, & Hermann, J. (2001). Exhumation as fast as subduction? Geology, 29(1), 3–6. Retrieved from https://pubs.geoscienceworld.org/gsa/geology/article-abstract/29/1/3/191937

Rubatto, Daniela. (2002). Zircon trace element geochemistry: partitioning with garnet and the link between U–Pb ages and metamorphism. Chemical Geology, 184(1), 123–138. https://doi.org/10.1016/S0009-2541(01)00355-2

Rubatto, Daniela, & Hermann, J. (2003). Zircon formation during fluid circulation in eclogites (Monviso, Western Alps): Implications for Zr and Hf budget in subduction zones. Geochimica et Cosmochimica Acta, 67(12), 2173–2187. https://doi.org/10.1016/S0016-7037(02)01321-2

Rubatto, Daniela, Hermann, J., Berger, A., & Engi, M. (2009). Protracted fluid-induced melting during Barrovian metamorphism in the Central Alps. Contributions to Mineralogy and Petrology, 158(6), 703–722. https://doi.org/10.1007/s00410-009-0406-5

Rubatto, D. (2017). Zircon: the metamorphic mineral. Reviews in Mineralogy and Geochemistry, 83, 261–295. Retrieved from https://pubs.geoscienceworld.org/msa/rimg/article-abstract/83/1/261/520746

Rubie, D. (1983). Reaction-enhanced ductility: The role of solid-solid univariant reactions in deformation of the crust and mantle. Tectonophysics, 96(3–4), 331–352. Retrieved from https://www.sciencedirect.com/science/article/pii/0040195183902251

Rubie, D.C. (1986). The catalysis of mineral reactions by water and restrictions on the presence of aqueous fluid during metamorphism. Mineralogical Magazine, 50(357), 399–415.

Rubie, D. C. (1990). Role of kinetics in the formation and preservation of eclogites. In Eclogite facies rocks (pp. 111–140). Retrieved from https://ci.nii.ac.jp/naid/10026535967/

Sachan, K., Bodnar, R., Islam, R., & Szabo, C. (1999). Exhumation history of eclogites from the Tso-Morari Crystalline Complex in Eastern Ladakh: mineralogical and fluid inclusion constraints. Geological Society Of. Retrieved from http://www.geosocindia.org/index.php/jgsi/article/view/68998

Sachan, H.K., Mukherjee, B.K., Ogasawara, Y., Maruyama, S., Pandey, A.K., Muko, A., Yoshioka, N. and Ishida, H., (2001). Discovery of coesite from Indian Himalaya: consequences on Himalayan tectonics. In In Ultrahigh-Pressure Minerals (UHPM) Workshop, Waseda Univ., Tokyo, Japan.

Sachan, Himanshu K., Mukherjee, B. K., Ogasawara, Y., Maruyama, S., Ishida, H., Muko, A., & Yoshioka, N. (2004). Discovery of coesite from Indus Suture Zone (ISZ), Ladakh, India: Evidence for deep subduction. European Journal of Mineralogy, 16(2), 235–240. https://doi.org/10.1127/0935-1221/2004/0016-0235

Sasaki, J., Peterson, N. L., & Hoshino, K. (1985). Tracer impurity diffusion in single-crystal rutile (TiO2− x). Journal of Physics and Chemistry of Solids, 46(11), 1267–1283.

Schaef, H. T., Mcgrail, B. P., & Owen, A. T. (2008). Basalt-CO 2-H 2 O Interactions and Variability in Carbonate Mineralization Rates. Energy Procedia, 1(1), 4899–4906. https://doi.org/10.1016/j.egypro.2009.02.320

Schaeffer, A. J., & Lebedev, S. (2013). Global shear speed structure of the upper mantle and transition zone. Geophysical Journal International, 194(1), 417–449.

Schaltegger, U., Fanning, C. M., Günther, D., Maurin, J. C., Schulmann, K., & Gebauer, D. (1999). Growth, annealing and recrystallization of zircon and preservation of monazite in high-grade metamorphism: Conventional and in-situ U-Pb isotope, cathodoluminescence and microchemical evidence. Contributions to Mineralogy and Petrology, 134(2–3), 186–201. https://doi.org/10.1007/s004100050478

Schärer, U., (1984). The effect of initial 230Th disequilibrium on young U-Pb ages: the Makalu case, Himalaya. Earth and Planetary Science Letters 67, 191-204.

Schärer, U., Hamet, J., & Allègre, C. (1984). The Transhimalaya (Gangdese) plutonism in the Ladakh region: a UPb and RbSr study. Earth and Planetary Science Letters, 67(3), 327–339. Retrieved from https://www.sciencedirect.com/science/article/pii/0012821X84901729

Schertl, H.-P., Schreyer, W., & Chopin, C. (1991). The pyrope-coesite rocks and their country rocks at Parigi, Dora Maira Massif, Western Alps: detailed petrography, mineral chemistry and PT-path. Contributions to Mineralogy and Petrology, 108(1–2), 1–21. https://doi.org/10.1007/BF00307322

Schlup, M., & Carter, A. (2003). Exhumation history of eastern Ladakh revealed by 40Ar/39Ar and fission-track ages: the Indus River–Tso Morari transect, NW Himalaya. *Journal of the Geological Society*, *160*(3), pp.385-399. Retrieved from http://jgs.lyellcollection.org/content/160/3/385.short

Schmid, R., Romer, R., L Franz, Oberhänsli, R., & Martinotti, G. (2003). Basement-Cover Sequences within the UHP unit of the Dabie Shan. Journal of Metamorphic Geology, 21(6), 531–538.

Schmidt, M. (1993). Phase relations and compositions in tonalite as a function of pressure: an experimental study at 650 C. American Journal of Science, 293, 1011–1060. Retrieved from http://earth.geology.yale.edu/~ajs/1993/10.1993.01Schmidt.pdf

Schmidt, M. W., Vielzeuf, D., & Auzanneau, E. (2004). Melting and dissolution of subducting crust at high pressures: the key role of white mica. Earth and Planetary Science Letters, 228(1–2), 65–84.

Schmitz, M. D. and Bowring, S. A. (2001) 'U-Pb zircon and titanite systematics of the Fish Canyon Tuff: an assessment of high-precision U-Pb geochronology and its application to young volcanic rocks.', Geochimica et Cosmochimica Acta, 65(15), pp. 2571–2587.

Scholl, D., & Huene, R. von. (2007). Crustal recycling at modern subduction zones applied to the past—Issues of growth and preservation of continental basement crust, mantle geochemistry, and. Geological Society of America Memoirs, 200, 9–32.

Scholz, C. H., & Campos, J. (1995). On the mechanism of seismic decoupling and back arc spreading at subduction zones. Journal of Geophysical Research: Solid Earth, 100(B11), 22103–22115. https://doi.org/10.1029/95JB01869

Schönig, J., Meinhold, G., von Eynatten, H., & Lünsdorf, N. (2018). Tracing ultrahigh-pressure metamorphism at the catchment scale. Scientific Reports, 8(1), 2931. Retrieved from https://www.nature.com/articles/s41598-018-21262-8

Searle, M.P., Cooper, D.J.W., Rex, A.J. and Colchen, M., (1988). Collision tectonics of the Ladakh-Zanskar Himalaya. *Philosophical Transactions of the Royal Society of London. Series A, Mathematical and Physical Sciences*, *326*(1589), pp.117-150.

Searle, MP, Waters, D., Rex, D., & Wilson, R. (1992). Pressure, temperature and time constraints on Himalayan metamorphism from eastern Kashmir and western Zanskar. Journal of the Geological Society, 149(5), 753–773.

Searle, MP, Waters, D., Martin, H., & Rex, D. (1994). Structure and metamorphism of blueschist–eclogite facies rocks from the northeastern Oman Mountains. Journal of the Geological Society, 151(3), 555–576.

Searle, M, Corfield, R., Stephenson, B., & Mccarron, J. (1997). Structure of the North Indian continental margin in the Ladakh–Zanskar Himalayas: implications for the timing of obduction of the Spontang ophiolite, India–Asia collision and deformation events in the Himalaya. Geological Magazine, 134(3), 297–316.

Searle, MP. (1999). Emplacement of Himalayan leucogranites by magma injection along giant sill complexes: examples from the Cho Oyu, Gyachung Kang and Everest. Journal of Asian Earth Sciences, 17(5–5), 773–783.

Searle, MP, Noble, S., Hurford, A., & Rex, D. (1999). Age of crustal melting, emplacement and exhumation history of the Shivling leucogranite, Garhwal Himalaya. Geological Magazine, 136(5), 513–525.

Searle, MP, Simpson, R., Law, R., Parrish, R., & Waters, D. (2003). The structural geometry, metamorphic and magmatic evolution of the Everest massif, High Himalaya of Nepal–South Tibet. Journal of the Geological Society, 160(3), 345–366.

Searle, MP, Stephenson, B., Walker, J., & Walker, C. (2007). Restoration of the Western Himalaya: implications for metamorphic protoliths, thrust and normal faulting, and channel flow models. Episodes, 30(4), 242.

Searle, M. P., Law, R. D., Godin, L., Larson, K. P., Streule, M. J., Cottle, J. M., & Jessup, M. J. (2008). Defining the Himalayan main central thrust in Nepal. Journal of the Geological Society, 165(2), 523–534.

Searle, MP, Cottle, J., Streule, M., & Waters, D. (2009). Crustal melt granites and migmatites along the Himalaya: melt source, segregation, transport and granite emplacement mechanisms. Earth and Environmental Science Transactions of the Royal Society of Edinburgh, 100(1–2), 219–233.

Searle, M. P., Elliott, J. R., Phillips, R. J., & Chung, S. L. (2011). Crustal–lithospheric structure and continental extrusion of Tibet. Journal of the Geological Society, 168, 633–672.

Searle, MP. (2015). 6.11 Mountain Building, Tectonic Evolution, Rheology, and Crustal Flow in the Himalaya, Karakoram, and Tibet.

Searle, M. P. (2019). Timing of subduction initiation, arc formation, ophiolite obduction and India–Asia collision in the Himalaya. Geological Society, London, Special Publications, 483(1), 19–37.

Semprich, J., Simon, N. S. C., & Podladchikov, Y. Y. (2010). Density variations in the thickened crust as a function of pressure, temperature, and composition. International Journal of Earth Sciences, 99(7), 1487–1510. https://doi.org/10.1007/s00531-010-0557-7

Sengör, A. C., & Natal'In, B. A. (1996). Turkic-type orogeny and its role in the making of the continental crust. Annual Review of Earth and Planetary Sciences, 24(1), 263–337.

Seton, M., Whittaker, J.M., Wessel, P., Müller, R.D., DeMets, C., Merkouriev, S., Cande, S., Gaina, C., Eagles, G., Granot, R. and Stock, J., (2014). Community infrastructure and repository for marine magnetic identifications. Geochemistry, Geophysics, Geosystems, 15(4), 1629–1641. https://doi.org/10.1002/2013GC005176

Shau, Y. H., Yang, H. Y., & Peacor, D. R. (1991). On oriented titanite and rutile inclusions in sagenitic biotite. American Mineralogist, 76(7–8), 1205–1217.

Shellnutt, J. G., Bhat, G. M., Wang, K. L., Brookfield, M. E., Jahn, B. M., & Dostal, J. (2014). Petrogenesis of the flood basalts from the Early Permian Panjal Traps, Kashmir, India: Geochemical evidence for shallow melting of the mantle. Lithos, 204, 159–171.

Shi, R., Yang, J., Cailai, W., Iizuka, T., & Hirata, T. (2004). Island arc volcanic rocks in the North Qaidam UHP metamorphic belt. Acta Geologica Sinica - Chinese Edition, 78(1), 52–64.

de Sigoyer, JB. (1998). Mécanismes d'exhumation des roches de haute pression basse température en contexte de convergence continentale: Tso Morari, Himalaya. Retrieved from https://tel.archives-ouvertes.fr/tel-00877529/

de Sigoyer, J, Guillot, S., & Dick, P. (2004). Exhumation of the ultrahigh-pressure Tso Morari unit in eastern Ladakh (NW Himalaya): A case study. Tectonics. Retrieved from http://onlinelibrary.wiley.com/doi/10.1029/2002TC001492/full

Simpson, R., Parrish, R., Searle, M., & Waters, D. (2000). Two episodes of monazite crystallization during metamorphism and crustal melting in the Everest region of the Nepalese Himalaya. Geology, 28(5), 403–406.

Sippl, C., Schurr, B., Yuan, X., Mechie, J., Schneider, F.M., Gadoev, M., Orunbaev, S., Oimahmadov, I., Haberland, C., Abdybachaev, U. and Minaev, V., (2013). Geometry of the Pamir-Hindu Kush intermediate-depth earthquake zone from local seismic data. Journal of Geophysical Research: Solid Earth, 118(4), 1438–1457. https://doi.org/10.1002/jgrb.50128

Sizova, E., Gerya, T., & Brown, M. (2012). Exhumation mechanisms of melt-bearing ultrahigh pressure crustal rocks during collision of spontaneously moving plates. Journal of Metamorphic Geology, 30(9), 927–955. https://doi.org/10.1111/j.1525-1314.2012.01004.x

Sláma, J. et al. (2008) 'Plešovice zircon — A new natural reference material for U – Pb and Hf isotopic microanalysis', 249, pp. 1–35. doi: 10.1016/j.chemgeo.2007.11.005.

Smit, M., Hacker, B., & Lee, J. (2014). Tibetan garnet records early Eocene initiation of thickening in the Himalaya. Geology, 42(7), 591–594. Retrieved from https://pubs.geoscienceworld.org/gsa/geology/article-abstract/42/7/591/131606

Smith, David C. (1980). A tectonic mélange of foreign eclogites and ultramafites in West Norway. Nature, 287(5780), 366–367. https://doi.org/10.1038/287366a0

Smith, David C. (1984). Coesite in clinopyroxene in the Caledonides and its implications for geodynamics. Nature, 310(5979), 641–644. https://doi.org/10.1038/310641a0

Smith, David C., & Lappin, M. A. (1989). Coesite in the Straumen kyanite-eclogite pod, Norway. Terra Nova, 1(1), 47–56. https://doi.org/10.1111/j.1365-3121.1989.tb00325.x

Smith, H. A., Chamberlain, C. P., & Zeitler, P. K. (1994). Timing and Duration of Himalayan Metamorphism within the Indian Plate, Northwest Himalaya, Pakistan. The Journal of Geology, 102(5), 493–508. https://doi.org/10.1086/629694

Smye, A., Bickle, M., Holland, T., Parrish, R., & Condon, D. (2011). Rapid formation and exhumation of the youngest Alpine eclogites: a thermal conundrum to Barrovian metamorphism. Earth and Planetary Science Letters, 306(3–4), 193–204.

Song, S., Zhang, L., & Niu, Y. (2004). Ultra-deep origin of garnet peridotite from the North Qaidam ultrahigh-pressure belt, Northern Tibetan Plateau, NW China. American Mineralogist, 89(8–9), 1330–1336. https://doi.org/10.2138/am-2004-8-922

Spear, F. S. (1993). Metamorphic phase equilibria and pressure-temperature-time paths. Mineralogical Society of America, Monograph Series, Washington, D.C.

Spear, F. S., Thomas, J. B., & Hallett, B. W. (2014). Overstepping the garnet isograd: a comparison of QuiG barometry and thermodynamic modeling. Contributions to Mineralogy and Petrology, 168(3), 1059.

Spear, F. S., & Pattison, D. R. (2017). The implications of overstepping for metamorphic assemblage diagrams (MADs). Chemical Geology, 457, 38–46.

Spencer, C., Dyck, B., Mottram, C., Roberts, N., Wao, W., & Martin, E. (2019). Deconvolving the pre-Himalayan Indian margin–Tales of crustal growth and destruction. Geoscience Frontiers, 10(3), 863–872. Retrieved from https://www.sciencedirect.com/science/article/pii/S1674987118300677

Spencer, D. A., Tonarini, S., & Pognante, U., (1995). Geochemical and Sr-Nd isotopic characterisation of Higher Himalayan eclogites (and associated metabasites). European Journal of Mineralogy, 89–102.

Spencer, K.J., Hacker, B.R., Kylander-Clark, A.R.C., Andersen, T.B., Cottle, J.M., Stearns, M.A., Poletti, J.E. and Seward, G.G.E., (2013) 'Campaign-style titanite U–Pb dating by laser-ablation ICP: Implications for crustal flow, phase transformations and titanite closure.', Chemical Geology, 341, pp. 84–101.

Spring, L., Bussy, F., Vannay, J. C., Huon, S., & Cosca, M.A. (1993). Early Permian granitic dykes of alkaline affinity in the Indian High Himalaya of Upper Lahul and SE Zanskar: geochemical characterization and geotectonic implications. Geological Society, London, Special Publications, 74(1), 251–264.

St-Onge, M R, Rayner, N., Palin, R. M., Searle, M. P., & Waters, D. J. (2013). Integrated pressure – temperature – time constraints for the Tso Morari dome (Northwest India): implications

for the burial and exhumation path of UHP units in the western Himalaya. Journal of Metamorphic Geology, 31(5), 469–504. https://doi.org/10.1111/jmg.12030

St-Onge, Marc R, Rayner, N., & Searle, M. P. (2010). Zircon age determinations for the Ladakh batholith at Chumathang (Northwest India): Implications for the age of the India-Asia collision in the Ladakh Himalaya. https://doi.org/10.1016/j.tecto.2010.09.010

Stacey, J. T. and Kramers, 1. (1975) 'Approximation of terrestrial lead isotope evolution by a two-stage model. Earth and planetary science letters, 26(2)', Earth and Planetary Science letters, 26(2), pp. 207–221.

Staudigel, H., Hart, S. R., & Richardson, S. H. (1981). Alteration of the oceanic crust: processes and timing. Earth andPlanetary Science Letters (Vol. 52).

Steck, A. (2003). Geology of the NW Indian Himalaya. Eclogae Geologicae Helvetiae, 96(2), 147–196.

Steck, A., Spring, L., Vannay, J., Masson, H., & Stutz, E. (1993). Geological Transect Across the Northwestern Himalaya in Eastern Ladakh and Lahul–A Model for the Continental Collision of India and Asia.

Steck, A., Epard, J. L., Vannay, J. C., Hunziker, J., Girard, M., Morard, A., & Robyr, M. (1998). Geological transect across the Tso Morari and Spiti areas: The nappe structures of the Tethys Himalaya. Eclogae Geologicae Helvetiae, 91, 103–121.

Stern, C., & Wyllie, P. (1981). Phase relationships of I-type granite with H2O to 35 kilobars: The Dinkey Lakes biotite-granite from the Sierra Nevada Batholith. Journal of Geophysical Research, 86(B11), 10412–10422.

Stipp, M., Stunitz, H., Heilbronner, R., & Schmid, S. M. (2002). The eastern Tonale fault zone: a 'natural laboratory'for crystal plastic deformation of quartz over a temperature range from 250 to 700 C. Journal of Structural Geology, 24(12), 1861–1884.

Štípská, P., & Powell, R. (2005). Constraining the P–T path of a MORB-type eclogite using pseudosections, garnet zoning and garnet-clinopyroxene thermometry: an example from the Bohemian Massif. Journal of Metamorphic Geology, 23(8), 725–743.

Stöckhert, B., & Renner, J. (1998). Rheology of Crustal Rocks at Ultrahigh Pressure. In When continents collide: geodynamics and geochemistry of ultrahigh-pressure rocks (pp. 57–95). Springer, Dordrecht. https://doi.org/10.1007/978-94-015-9050-1_3

Stöckhert, B. (2002). Stress and deformation in subduction zones: insight from the record of exhumed metamorphic rocks. Geological Society, London, Special Publications, 200(1), 255–274. https://doi.org/10.1144/GSL.SP.2001.200.01.15

Stöckhert, B., & Gerya, T. V. (2005). Pre-collisional high pressure metamorphism and nappe tectonics at active continental margins: a numerical simulation. Terra Nova, 17(2), 102–110. https://doi.org/10.1111/j.1365-3121.2004.00589.x

Stoliczka, F. (1865). Geological Sections Across the Himalayan Mountains, from Wang-Tu-Bridge on the River Sutlej to Sungdo on the Indus: With an Account of the Foramtion in Spiti: Accompanied by a Revision of All Known Fossils from the District. Government of India.

Stutz, E. (1988). Géologie de la chaîne de Nyimaling aux confins du Ladakh et du Rupshu (NW-Himalaya, Inde): évolution paléogéographique et tectonique d'un segment de la marge.

Retrieved from http://www.unil.ch/files/live/sites/iste/files/shared/X.Library/Memoirs of Geology/03 - Stutz (1988).pdf

Stutz, E, & Steck, A. (1986). La terminaison occidentale du Cristallin du Tso Morari (Haut-Himalaya; Ladakh Méridional, Inde): subdivision et tectonique de nappe. Eclogae Geologicae Helvetiae, 79. Retrieved from https://serval.unil.ch/notice/serval:BIB_C4E29BC25B2B

Stutz, Edgar, & Thöni, M. (1987). The lower Paleozoic Nyimaling Granite in the Indian Himalaya (Ladakh): New Rb/Sr data versus zircon typology. Geologische Rundschau, 76(2), 307–315. https://doi.org/10.1007/BF01821076

Swanson, S. E., & Fenn, P. M. (1986). Quartz crystallization in igneous rocks. American Mineralogist1, 71(3–4), 331–342.

Tao, R., L., Z., Fei, Y., & Liu, Q. (2014). The effect of Fe on the stability of dolomite at high pressure: Experimental study and petrological observation in eclogite from southwestern Tianshan, China. Geochimica et Cosmochimica Acta, 143, 253–267.

Tapster, S., Condon, D.J., Naden, J., Noble, S.R., Petterson, M.G., Roberts, N.M.W., Saunders, A.D. & Smith, D.J., (2016). Rapid thermal rejuvenation of high-crystallinity magma linked to porphyry copper deposit formation; evidence from the Koloula Porphyry Prospect, Solomon Islands. Earth and Planetary Science Letters, 442, 206-217.

Terry, M. P., & Heidelbach, F. (2006). Deformation-enhanced metamorphic reactions and the rheology of high-pressure shear zones, Western Gneiss Region, Norway. Journal of Metamorphic Geology, 24(1), 3–18.

Terry, M., & Robinson, P. (2004). Geometry of eclogite-facies structural features: implications for production and exhumation of UHP and HP rocks, Western Gneiss Region, Norway. Tectonics, 23, TC2001.

Thakur, V., & Virdi, N. (1979). Lithostratigraphy, structural framework, deformation and metamorphism of the southeastern region of Ladakh, Kashmir Himalaya, India. Himalayan Geology, 9, 63–78.

Thakur, V. (1983). Palaeotectonic evolution of Indus-Tsangpo suture zone in Ladakh and southern Tibet. Geology of Indus Suture Zone of Ladakh. Wadia Institute of Himalayan Geology, Dehra Dun, India,. pp.195-204.

Thakur, V., & Bhat, M. (1983). Interpretation of tectonic environment of Nidar ophiolite: a geochemical approach. Geology of the Indus Suture Zone of Ladakh. 21-31.

Thakur, V. C. (1983). Deformation and metamorphism of the Tso Morari crystalline complex. Geology of the Indus Suture Zone of Ladakh. Wadia Institute of Himalayan Geology, Dehra Dun, India, 1–8.

Thakur, V., & Misra, D. (1984). Tectonic framework of the Indus and Shyok suture zones in eastern Ladakh, northwest Himalaya. Tectonophysics, 101(3–4), 207–220. Retrieved from https://www.sciencedirect.com/science/article/pii/0040195184901148

Thomas, L. A., & Wooster, W. A. (1951). Piezoerescence—the growth of Dauphiné twinning in quartz under stress. Proc. R. Soc. Lond. A, 208(1092), 43–62.

Tinkham, D. K., Zuluaga, C. A., & Stowell, H. H. (2001). Metapelite phase equilibria modelling in MnNCKFMASH: the effect of variable Al2O3 and MgO/(MgO+ FeO) on mineral stability. Geological Materials Research, 3(1), 1–42.

Tirel, C., Brun, J., Burov, E., Wortel, M., & Lebedev, S. (2013). A plate tectonics oddity: Caterpillar-walk exhumation of subducted continental crust. Geology, 41(5), 555–558. Retrieved from https://pubs.geoscienceworld.org/gsa/geology/article-abstract/41/5/555/131177

Tobgay, T., McQuarrie, N., Long, S., Kohn, M., & Corrie, S. (2012). The age and rate of displacement along the Main Central Thrust in the western Bhutan Himalaya. Earth and Planetary Science Letters, 319, 146–158. Retrieved from https://www.sciencedirect.com/science/article/pii/S0012821X11007199

Tomkins, H. S., Powell, R., & Ellis, D. J. (2007). The pressure dependence of the zirconium-in-rutile thermometer. Journal of Metamorphic Geology, 25(6), 703–713. https://doi.org/10.1111/j.1525-1314.2007.00724.x

Torsvik, Trond H., Müller, R. D., Van Der Voo, R., Steinberger, B., & Gaina, C. (2008). Global plate motion frames: Toward a unified model. Reviews of Geophysics, 46(3). https://doi.org/10.1029/2007RG000227

Torsvik, T.H., Van der Voo, R., Preeden, U., Mac Niocaill, C., Steinberger, B., Doubrovine, P.V., Van Hinsbergen, D.J., Domeier, M., Gaina, C., Tohver, E. and Meert, J.G., (2012). Phanerozoic polar wander, palaeogeography and dynamics. Earth Science Reviews, 114(3–4), 325–368.

Torsvik, T.H., & Cocks, L. R. M. (2017). The integration of palaeomagnetism, the geological record and mantle tomography in the location of ancient continents. Geological Magazine, 1–9. https://doi.org/10.1017/S001675681700098X

Tsujimori, T., Sisson, V., Liou, J., & Harlow, G. (2006). Very-low-temperature record of the subduction process: A review of worldwide lawsonite eclogites. Lithos, 92(3–4), 609–624. Retrieved from https://www.sciencedirect.com/science/article/pii/S002449370600140X

Tullis, J. (1970). Quartz: preferred orientation in rocks produced by Dauphiné twinning. Science, 168(3937), 1342–1344.

van Der Molen, I., & Van Roermund, H. (1986). The pressure path of solid inclusions in minerals: The retention of coesite inclusions during uplift. *Lithos*, *19*(3–4), 317–324. https://doi.org/10.1016/0024-4937(86)90030-7

van Ufford, A., & Cloos, M. (2005). Cenozoic tectonics of New Guinea. AAPG Bulletin, 89(1), 119–140. Retrieved from https://pubs.geoscienceworld.org/gsa/aapgbull/article/89/1/119/40183

van Hinsbergen, D. J. J., Lippert, P. C., & Huang, W. (2017). Unfeasible subduction? Nature Geoscience, 10, 878–879.

van Hinsbergen, D., & Lippert, P. (2012). Greater India Basin hypothesis and a two-stage Cenozoic collision between India and Asia. Proceedings of the National Academy of Sciences, 109(20), 7659–7664. Retrieved from https://www.pnas.org/content/109/20/7659.short

van Hinsbergen, D., Lippert, P., Li, S., Huang, W., Advokaat, E., & Spakman, W. (2019). Reconstructing Greater India: Paleogeographic, kinematic, and geodynamic perspectives.

Tectonophysics, 760, 69–94. Retrieved from https://www.sciencedirect.com/science/article/pii/S0040195118301331

Vance, D., & Harris, N. (1999). Timing of prograde metamorphism in the Zanskar Himalaya. Geology, 27(5), 395–398. Retrieved from https://pubs.geoscienceworld.org/gsa/geology/article-abstract/27/5/395/186333

Vance, D., & O'Nions, R.K. (1990). Isotopic chronometry of zoned garnets: growth kinetics and metamorphic histories. Earth and Planetary Science Letters, 97(3–4), 227–240.

Vance, J. A. (1969). On synneusis. Contributions to Mineralogy and Petrology, 24(1), 7–29.

Vannay, J. (1993). Geochemistry of the continental basalts within the Tethyan Himalaya of Lahul-Spiti and SE Zanskar, northwest India. Geological Society, London, Special Publications, 74(1), 237–249.

Vannay, J.-C., & Hodges, K. V. (2003). Tectonometamorphic evolution of the Himalayan metamorphic core between the Annapurna and Dhaulagiri, central Nepal. Journal of Metamorphic Geology, 14(5), 635–656. https://doi.org/10.1046/j.1525-1314.1996.00426.x

Verma, S.P., Torres-Alvarado, I.S., & Sotelo-Rodríguez, Z. T. (2002). SINCLAS: standard igneous norm and volcanic rock classification system. Computers & Geosciences, 28(5), 711–715.

Verma, Surendra P, & Agrawal, S. (2011). New tectonic discrimination diagrams for basic and ultrabasic volcanic rocks through log-transformed ratios of high field strength elements and implications for petrogenetic processes. Revista Mexicana de Ciencias Geológicas.

Verma, SK, Pandarinath, K., & Verma, S. (2012). Statistical evaluation of tectonomagmatic discrimination diagrams for granitic rocks and proposal of new discriminant-function-based multi-dimensional diagrams for acid rocks. International Geology Review, 54(3), 325–347.

Verma, SP, & Rivera-Gomez, M. (2013). Computer programs for the classification and nomenclature of igneous rocks. Episodes, 36(2), 115–124.

Verma, Surendra P., Pandarinath, K., Verma, S. K., & Agrawal, S. (2013). Fifteen new discriminant-function-based multi-dimensional robust diagrams for acid rocks and their application to Precambrian rocks. Lithos, 168–169, 113–123. https://doi.org/10.1016/J.LITHOS.2013.01.014

Verma, Surendra P, Cruz-Huicochea, R., Díaz-González, L., & Verma, S. K. (2015). A new computer program TecDIA for multidimensional tectonic discrimination of intermediate and acid magmas and its application to the Bohemian Massif, Czech Republic. Journal of Geosciences, 60(4), 203–218. https://doi.org/10.3190/jgeosci.201

Virdi, N., Thakur, V., & Azmi, R. (1978). Discovery and significance of Permian microfossils in the Tso Morari crystallines of Ladakh, J & K, India. Himalayan Geology, 8, 993–1000. Retrieved from https://scholar.google.co.uk/scholar?q=tso+morari&btnG=&hl=en&as_sdt=0%2C5#9

Vogt, K., & Gerya, T. (2014). From oceanic plateaus to allochthonous terranes: numerical modelling. Gondwana Research, 25(2), 494–508. Retrieved from https://www.sciencedirect.com/science/article/pii/S1342937X12003516

von Huene, R., & Scholl, D. W. (1991). Observations at convergent margins concerning sediment subduction, subduction erosion, and the growth of continental crust. Reviews of Geophysics, 29(3), 279. https://doi.org/10.1029/91RG00969

Vrijmoed, J., Smith, D., & Van Roermund, H. (2006). Microdiamond (in situ) in the Svartberget peridotite, Vestlandet, Norway, confirmed by Raman Microscopy. In Geo-Raman '06, 7th International Conference on Raman Spectroscopy, Applied to Earth and Planetary Sciences (pp. 85–86).

Vrijmoed, J., Austrheim, H., John, T., & Podladchikov, Y. (2008). Metasomatism of the UHP Svartberget olivine-websterite body in the Western Gneiss Complex, Norway. Geochimica et Cosmochimica Acta Supplement, 72(989). Retrieved from

Vrijmoed, J., Podladchikov, Y., Anderson, T., & Hartz, E. (2009). An alternative model for ultra-high pressure in the Svartberget Fe-Ti garnet-peridotite, Western Gneiss Region, Norway. European Journal of Mineralogy, 21(6), 1119–1133.

Vry, J., & Baker, J. (2006). LA-MC-ICPMS Pb–Pb dating of rutile from slowly cooled granulites: confirmation of the high closure temperature for Pb diffusion in rutile. Geochimica et Cosmochimica Acta, 70(7), 1807–1820

Wain, A. (1997). New evidence for coesite in eclogite and gneisses: Defining an ultrahigh-pressure province in the Western Gneiss region of Norway. Geology, 25(10), 927–930. https://doi.org/10.1130/0091-7613(1997)025

Wain, A., Waters, D., Jephcoat, A., & Olijynk, H. (2000). The high-pressure to ultrahigh-pressure eclogite transition in the Western Gneiss Region, Norway. European Journal of Mineralogy, 12(3), 667–687. https://doi.org/10.1127/0935-1221/2000/0012-0667

Wain, A. L., Waters, D. J., & Austrheim, H. (2001). Metastability of granulites and processes of eclogitisation in the UHP region of western Norway. Journal of Metamorphic Geology, 19(5), 609–625. https://doi.org/10.1046/j.0263-4929.2001.00333.x

Walker, J. D., Martin, M. W., Bowring, S. A., Searle, M. P., Waters, D. J., & Hodges, K. V. (1999). Metamorphism, Melting, and Extension: Age Constraints from the High Himalayan Slab of Southeast Zanskar and Northwest Lahaul. The Journal of Geology, 107(4), 473–495. https://doi.org/10.1086/314360

Walker, C. B., Searle, M. P., & Waters, D. J. (2001). An integrated tectonothermal model for the evolution of the High Himalaya in western Zanskar with constraints from thermobarometry and metamorphic modeling. Tectonics, 20(6), 810–833. https://doi.org/10.1029/2000TC001249

Wallis, D., Parsons, A., & Hansen, L. (2017). Quantifying geometrically necessary dislocations in quartz using HR-EBSD: application to chessboard subgrain boundaries. Journal of Structural Geology. Retrieved from https://www.sciencedirect.com/science/article/pii/S0191814117302973

Wallis, D., Parsons, A. J., & Hansen, L. N. (2019). Quantifying geometrically necessary dislocations in quartz using HR-EBSD: application to chessboard subgrain boundaries. Journal of Structural Geology, 125, 235–247.

Wallis, S.R., Ishiwatari, A., Hirajima, T., Ye, K., Guo, J., Nakamura, D., Kato, T., Zhai, M., Enami, M., Cong, B. and Banno, S., (1997). Occurrence and field relationships of ultrahigh-pressure metagranitoid and coesite eclogite in the Su-Lu terrane, eastern China. Journal of the Geological Society, 154(1), 45–54. https://doi.org/10.1144/gsjgs.154.1.0045

Walsh, E., & Hacker, B. (2004). The fate of subducted continental margins: Two-stage exhumation of the high-pressure to ultrahigh-pressure Western Gneiss Region, Norway. Journal of Metamorphic Geology, 22(7), 671–687.

Wang, J. M., Zhang, J. J., & Wang, X. X. (2013). Structural kinematics, metamorphic P-T profiles and zircon geochronology across the Greater Himalayan Crystalline Complex in south-central Tibet: implication for a revised channel flow. Journal of Metamorphic Geology, 31(6), 607–628. https://doi.org/10.1111/jmg.12036

Wang, Y., Zhang, L., Zhang, J., & Wei, C. (2017). The youngest eclogite in central Himalaya: P–T path, U–Pb zircon age and its tectonic implication. Gondwana Research, 41, 188–206. Retrieved from https://www.sciencedirect.com/science/article/pii/S1342937X15002713

Wark, D., & Watson, E. (2006). TitaniQ: a titanium-in-quartz geothermometer. Contributions to Mineralogy and Petrology, 152(6), 743.754.

Warren, Clare J., Parrish, R. R., Waters, D. J., & Searle, M. P. (2005). Dating the geologic history of Oman's Semail ophiolite: Insights from U-Pb geochronology. Contributions to Mineralogy and Petrology, 150(4), 403–422. https://doi.org/10.1007/s00410-005-0028-5

Warren, Clare J., Beaumont, C., & Jamieson, R. A. (2008a). Deep subduction and rapid exhumation: Role of crustal strength and strain weakening in continental subduction and ultrahigh-pressure rock exhumation. Tectonics, 27(6), n/a-n/a. https://doi.org/10.1029/2008TC002292

Warren, Clare J., Beaumont, C., & Jamieson, R. A. (2008b). Formation and exhumation of ultra-high-pressure rocks during continental collision: Role of detachment in the subduction channel. Geochemistry, Geophysics, Geosystems, 9(4), https://doi.org/10.1029/2007GC001839

Warren, C.J., Beaumont, C., & Jamieson, R. A. (2008c). Modelling tectonic styles and ultra-high pressure (UHP) rock exhumation during the transition from oceanic subduction to continental collision. Earth and Planetary Science Letters (Vol. 267). https://doi.org/10.1016/j.epsl.2007.11.025

Warren, C. J., Grujic, D., Kellett, D. A., Cottle, J., Jamieson, R. A., & Ghalley, K. S. (2011). Probing the depths of the India-Asia collision: U-Th-Pb monazite chronology of granulites from NW Bhutan. Tectonics, 30(2). https://doi.org/10.1029/2010TC002738

Warren, C., Hanke, F., & Kelley, S. (2012). When can muscovite 40Ar/39Ar dating constrain the timing of metamorphic exhumation? Chemical Geology, 291, 79–86. Retrieved from https://www.sciencedirect.com/science/article/pii/S0009254111003871

Warren, C J. (2013). Exhumation of (ultra-)high-pressure terranes: concepts and mechanisms. Solid Earth, 4, 75–92. https://doi.org/10.5194/se-4-75-2013

Waters, D. (2019). Metamorphic constraints on the tectonic evolution of the High Himalaya in Nepal: the art of the possible. Geological Society, London, Special Publications, 483. Retrieved from https://sp.lyellcollection.org/content/early/2019/02/07/SP483-2018-187.abstract

Waters, D., & Martin, H. (1993). The Garnet-Cpx-Phengite Barometer. Terra Abstracts, 5(1), 410–411.

Waters, D. J., & Lovegrove, D. P. (2002). Assessing the extent of disequilibrium and overstepping of prograde metamorphic reactions in metapelites from the Bushveld Complex aureole,

South Africa. Journal of Metamorphic Geology, 20(1), 135–149. https://doi.org/10.1046/j.0263-4929.2001.00350.x

Waters, David J., Utting, J., & Bidgood, A. K. (2020). Eclogite garnets and their inclusion suites: prograde growth and post-entrapment modification. Journal of Metamorphic Geology, In prep.

Wayte, G.J., Worden, R. H., Rubie, D. C., & Droop, G. T. (1989). A TEM study of disequilibrium plagioclase breakdown at high pressure: the role of infiltrating fluid. Contributions to Mineralogy and Petrology, 101(4), 426–437.

Webb, L., Baldwin, S., Little, T., & Fitzgerald, P. (2008). Can microplate rotation drive subduction inversion? Geology, 36(10), 823–826. Retrieved from https://pubs.geoscienceworld.org/gsa/geology/article-abstract/36/10/823/29728

White, R. W., Powell, R., Holland, T. J. B., & Worley, B. A. (2000). The effect of TiO2 and Fe2O3 on metapelitic assemblages at greenschist and amphibolite facies conditions: mineral equilibria calculations in the system K2O-FeO-MgO-Al2O3-SiO2-H2O-TiO2-Fe2O3. Journal of Metamorphic Geology, 18(5), 497–511.

White, R. W., Pomroy, N. E., & Powell, R. (2005). An in situ metatexite–diatexite transition in upper amphibolite facies rocks from Broken Hill, Australia. Journal of Metamorphic Geology, 23(7), 579–602.

White, R. W., Powell, R., & Holland, T. J. B. (2007). Progress relating to calculation of partial melting equilibria for metapelites. Journal of Metamorphic Geology, 25(5), 511–527.

White, S., & Knipe, R. (1978). Transformation-and reaction-enhanced ductility in rocks. Journal of the Geological Society, 135(5), 513–516.

Whitney, D. L., & Evans, B. W. (2010). Abbreviations for names of rock-forming minerals. American Mineralogist, 95(1), 185–187.

Wickham, S. M. (1987). Crustal Anatexis and Granite Petrogenesis During Low-pressure Regional Metamorphism: The Trois Seigneurs Massif, Pyrenees, France. Journal of Petrology, 28(1), 127–169.

Wiedenbeck, M. et al. (1995) ‘three natural zircon standards for U-TH-Pb, Lu-Hf, element and REE analyses’, 19

Wiedenbeck, M. et al. (2004) ‘Further Characterisation of the 91500 Zircon Crystal’, Geostandards and Geoanalytical Research, 28, pp. 9–39.

Wilke, F., O’Brien, P., Altenberger, U., Konrad-Schmolke, M., & Khan, M. (2010). Multi-stage reaction history in different eclogite types from the Pakistan Himalaya and implications for exhumation processes. Lithos, 114(1–2), 70–85. Retrieved from https://www.sciencedirect.com/science/article/pii/S0024493709003284

Wilke, F., O’Brien, P., Gerdes, A., Tinnerman, M., Sudo, M., & Khan, M. (2010). The multistage exhumation history of the Kaghan Valley UHP series, NW Himalaya, Pakistan from U-Pb and 40Ar/39Ar ages. European Journal of Mineralogy, 22(5), 703–719.

Wilke, F., Sobel, E., O’Brien, P., & -, D. S. (2012). Apatite fission track and (U–Th)/He ages from the higher Himalayan crystallines, Kaghan Valley, Pakistan: implications for an eocene plateau and oligocene. Journal of Asian Earth Sciences, 59, 14–23.

Wilke, F., O'Brien, P., Schmidt, A., & Ziemann, M. (2015). Subduction, peak and multi-stage exhumation metamorphism: Traces from one coesite-bearing eclogite, Tso Morari, western Himalaya. Lithos, 231, 77–91. Retrieved from http://www.sciencedirect.com/science/article/pii/S0024493715002066

Woodhead, J. D. and Hergt, J. M. (2001) 'Strontium, neodymium and lead isotope analyses of NIST glass certified reference materials: SRM 610, 612, 614.', Geostandards Newsletter, 25(2–3), pp. 261–266.

Wu, F.-Y., Ji, W.-Q., Wang, J.-G., Liu, C.-Z., Chung, S.-L., & Clift, P. D. (2014). Zircon u–pb and hf isotopic constraints on the onset time of india-asia collision. American Journal of Science, 314, 548–579.

Wu, Y., Fei, Y., Jin, Z., & Liu, X. (2009). The fate of subducted upper continental crust: an experimental study. Earth and Planetary Science Letters, 282(1–4), 275–284.

Wyss, M., Hermann, J., & Steck, A. (1999). Structural and metamorphic evolution of the northern Himachal Himalaya, NW India (Spiti-eastern Lahul-Parvati valley traverse). Eclogae Geologicae Helvetiae, 92(1), 3–44. https://doi.org/10.5169/seals-168645

Xu, Z. Q., Zhang, J. X., & Li, H. B. (2000). Architecture and orogeny of the northern Qilian orogenic belt, NW China. Journal of the Geological Society of China (Taiwan), 43(1), 125–141.

Xu, Z., Wang, Q., Ji, S., Chen, J., Zeng, L., Yang, J., Chen, F., Liang, F. and Wenk, H.R., (2006). Petrofabrics and seismic properties of garnet peridotite from the UHP Sulu terrane (China): implications for olivine deformation mechanism in a cold and dry subducting continental slab. Tectonophysics, 421(1–2), 111–127.

Yakovlev, P. V., & Clark, M. K. (2014). Conservation and redistribution of crust during the Indo-Asian collision. Tectonics, 33(6), 1016–1027. https://doi.org/10.1002/2013TC003469

Yamato, P., Burov, E., Agard, P., Le Pourhiet, L., & Jolivet, L. (2008). HP-UHP exhumation during slow continental subduction: Self-consistent thermodynamically and thermomechanically coupled model with application to the Western Alps. Earth and Planetary Science Letters, 271(1–4), 63–74.

Yin, K., & Harrison, P. J. (2000). Influences of flood and ebb tides on nutrient fluxes and chlorophyll on an intertidal flat. Marine Ecology Progress Series, 196, 75–85.

Yin, A. (2006). Cenozoic tectonic evolution of the Himalayan orogen as constrained by along-strike variation of structural geometry, exhumation history, and foreland. Earth-Science Reviews, 76(1–2), 1–131.

Yin, An, Manning, C. E., Lovera, O., Menold, C. A., Chen, X., & Gehrels, G. E. (2007). Early Paleozoic Tectonic and Thermomechanical Evolution of Ultrahigh-Pressure (UHP) Metamorphic Rocks in the Northern Tibetan Plateau, Northwest China. International Geology Review, 49(8), 681–716. https://doi.orFg/10.2747/0020-6814.49.8.681

Young, D. J. (2018). Structure of the (ultra) high-pressure Western Gneiss Region, Norway: Imbrication during Caledonian continental margin subduction. GSA Bulletin, 130(5–6), 926–940.

Young, A., Flament, N., Maloney, K., & Williams, S. (2018). Global kinematics of tectonic plates and subduction zones since the late Paleozoic Era. Geoscience Frontiers, 10(3), 989–1013.

Young, D., & Kylander-Clark, A. (2015). Does continental crust transform during eclogite facies metamorphism? Journal of Metamorphic. Retrieved from http://onlinelibrary.wiley.com/doi/10.1111/jmg.12123/full

Zack, T., Moraes, R. D., & Kronz, A. (2004). Temperature dependence of Zr in rutile: empirical calibration of a rutile thermometer. Contributions to Mineralogy and Petrology, 148(4), 471–488.

Zack, T., & Kooijman, E. (2017). Petrology and geochronology of rutile. Reviews in Mineralogy and Geochemistry, 83(1), 443–467.

Zack, T., & Luvizottow, G. L. (2006). Application of rutile thermometry to eclogites. Mineralogy and Petrology, 88(1–2), 69–85.

Zahirovic, S., Matthews, K. J., Flament, N., Muller, R. D., Hill, K. C., Seton, M., & Gurnis, M. (2016). Tectonic evolution and deep mantle structure of the eastern Tethys since the latest Jurassic Publication Details. Earth-Sc, 162(293–337).

Zeitler, P., Sutter, J., Williams, I., Zartman, R., & Tahirkheli, R. (1989). Geochronology and temperature history of the Nanga Parbat–Haramosh massif, Pakistan. Geological Society of America Special Papers, 232, 1–22.

Zhang, R. Y., Hirajima, T., Banno, S., B., C., & Liou, J. (1995). Petrology of ultrahigh-pressure rocks from the southern Su-Lu region, eastern China. Journal of Metamorphic Geology, 13(5), 659–675.

Zhang, R. Y., Liou, J. G., Ernst, W. G., Coleman, R. G., Sobolev, N. V., & Shatsky, V. S. (1997). Metamorphic evolution of diamond-bearing and associated rocks from the Kokchetav Massif, northern Kazakhstan. Journal of Metamorphic Geology, 15(4), 479–496. https://doi.org/10.1111/j.1525-1314.1997.00035.x

Zhao, Z. Y., Fang, A. M., & Yu, L. J. (2003). High- to ultrahigh-pressure (UHP) ductile shear zones in the Sulu UHP metamorphic belt, China: implications for continental subduction and exhumation. Terra Nova, 15(5), 322–329. https://doi.org/10.1046/j.1365-3121.2003.00500.x

Zhu, D.-C., Chung, S.-L., Mo, X.-X., Zhao, Z.-D., Niu, Y., Song, B., & Yang, Y.-H. (2009). The 132 Ma Comei-Bunbury large igneous province: Remnants identified in present-day southeastern Tibet and southwestern Australia. Geology, 37, 583–586.

Appendix

Appendix 1 – Sample Locations

Locality number 2016	Locality number 2017	Name of outcrop	Waypoint	Longitude	Latitude	Samples	Geochron sample	Petrological sample
16/3	–	N of Karzok	3	78.370174	33.211574	01–01a, b		
16/27	–	NW shore of Tso Morari	27	78.259106	33.000797	03–02, 03–03		
16/41	17/15	The Bridge	29	78.275886	33.067799	04–01 to 04–07, a03–01 to a–03–12	a03–07 and a03–12	a03–05 and a03–09
16/51	17/17	Kiagar Tso	31	78.295858	33.121413	05–01, 05–02, a03–13 to a03–19	a03–19	a03–16
16/52	–	Kiagar La river confluence	33	78.355712	33.145521	05–03		
16/53	17/18	Kiagar La stream bed	34	78.361079	33.162646	05–04a–d 05–05a–c, a03–20	a03–20	05–04b, c, d
–	17/19	Berthelsen outcrop	19	78.357175	33.183358	a03–21 to a03–25, JU05 to JU13a	a03–22	JU11 to JU13a
16/73	–	Road to Ribil Sumdo	47	78.368897	33.235048	08–01 to 08–08		08–01 to 08–04, 08–08
16/62	–	Ribil sumdo village	37	78.376391	33.215384			
16/71	–	East of Ribil village, E of Zildat	45	78.379905	33.215391			
16/61	–	Ribil Valley	41	78.371456	33.225109	06–01		
16/610	–	Sumdo village	44	78.368897	33.235048			
16/81	–	west of Sumdo	49	78.370174	33.211574			
16/91	17/20	Eastern puga valley	53	78.368897	33.235048	09–01 to 09–05, a04–01 to a04–05		
16/106	17/21	Puga hot springs	61	78.368897	33.235048	10–01 to 10–04, a04–06 to a04–17	a04–15	a04–13
16/105	17/22	Puga school	59	78.368897	33.235048	10–05, a04–18 to a04–20	a04–20	10–05
16/114	17/23	Puga valley halfway to the top	81	78.368897	33.235048	13–01 to 13–03, a04–21 to a04–25	?	
16/115	17/25	Polokongka La pass	82	78.368897	33.235048	13–04, 13–05, a04–26 to a04–32, a05–01 to a 05–08	a04–28	a04–30 and a04–31
16/113	17/28	Polokongka La ridge	66	78.368897	33.235048	11–05 to 11–09, a05–11 to a05–17	a05–15	11–05 to 11–07
–	17/29	Thukje	26	78.018911	33.361317	a06–01 to a06–03		
–	17/31 –	North of Ponganagu – N end of transect	27	78.022718	33.361493	a07–01 to a 07–08		

Appendix 1 – Sample Locations

Locality number 2016	Locality number 2017	Name of outcrop	Waypoint	Longitude	Latitude	Samples	Geochron sample	Petrological sample
	17/37 –	North of Ponganagu – amphibolite in puga gneiss						
–	17/41	North of Ponganagu	40	77.960958	33.389391	a07–01 to a 07–08		a07–06
–	17/44	Ridge west of Ponganagu	43	77.944287	33.342213	a08–01 to a08–04		
–	17/55	Road to Nuruchen	56	77.968609	33.297771	a09–01 to a09–08		
–		Nuruchen	87					
–	17/67 –	Ridge east of Nuruchen	69	78.239795	33.237862	a11–01 to a11–09		
–	17/76		79	78.239795	33.237862	a11–01 to a11–09		a11–09
–	17/67 –	Small ridge west of Nuruchen	69	78.184245	33.243527	a10–01 to a10–08		
–	17/73		76	77.999637	33.24937	a10–01 to a10–08		
–	17/79 –	Big ridge west of Nuruchen	84	78.162729	33.272054	a12–02 and a12–03		
–	17/81 –		86	77.989563	33.230158	a12–06 to a12–13	a12–14	
–	17/83 –		88	77.993915	33.248381	a12–15		
–	17/86		91	77.976552	33.283477			
–	17/94 –	East Bank of river south of Nuruchen	94	78.239795	33.237862	a13–01 to a13–03		
–	17/97		97	78.239795	33.237862	a13–01 to a13–03		
–	17/107	Spanlung river – metasediments	108	78.014864	33.188068	a14–01 to a14–03, a15–01		
–	17/109	Spanlung river – Puga Gneiss	111	78.018676	33.186004			
–	17/111	Rajun Karu	113	78.0423	33.169462			
–	17/117	Kyamuri La	119	78.060466	33.143782	a16–01 to a16–05		
–	17/121	South of Kyamuri La	124	78.086397	33.107179			
–	17/122	Gyama Barma	126	78.14463	33.071266			
–	17/127	South of Gyama Barma	131	78.257717	32.96328	a17–02, a18–01		
–	17/130 –	Walk to Karzok	126	78.14463	33.071266			
–	17/134 –		138	78.173677	33.032959			
–	17/137	Yarlung Nyau	141	78.177971	33.017069			
16/01	–	Karzok	1	78.025369	33.361718			
	17/1 –	South of Karzok	1	77.960916	33.38997	a02–02 to a 02–11		
	17/14		14	78.257717	32.96328	a02–02 to a 02–11		
	17/1	Rupshu	1a	78.257717	32.96328	a01–01 to a01–16		

Appendix 2 – Radioisotopic dating methods

Appendix 2 – Radioisotopic dating methods

Mineral separation

Zircon, rutile and titanite were separated using a tungsten-carbide jaw-crusher and a steel disk mill at the Geochronology and Tracers Facility, British Geological Survey (formerly the NERC Isotope Geoscience Laboratories, NIGL). Samples were then sieved to extract the <500 μm fraction and separated using a Rodger's table to separate heavy from light material. The heavy material was then further processed using a Frantz magnetic separator. The non-magnetic fraction was further separated using diodomethane heavy liquid separation and the heavy, non-magnetic fraction was collected. Individual grains were then picked and mounted in 25 mm round epoxy resin disks and polished to half-crystal depth. Zircon grains were imaged via cathodoluminescence (CL) using an FEI Quanta 650 FEG E-Scanning electron microscope (E-SEM) using a 20kV electron beam, 10mm working distance and a beam current of 20nA. Zircon grains from the felsic rocks were also mounted on sticky tape in order to analyse the <10μm thick rims.

Rutile grains chosen for analysis were picked from the non-magnetic fraction which concentrates grains without mineral inclusions. Grains were also picked from slightly more magnetic fractions which had a higher U content. Rutile grains were imaged via backscatter electron imaging to determine the homogeneity of the grains chosen for analysis. None of the rutile grains showed any evidence of zoning and grains containing inclusions of zircon or alteration to titanite were avoided.

Lasar Ablation

U-(Th)-Pb isotopes in monazite, zircon, xenotime and rutile grains were analysed at the Geochronology and Tracers Facility using a Nu Instruments AttoM HR sector-field single-ion-collector inductively coupled plasma mass spectrometer (SC-ICP-MS). Details of the technical aspects and geochronological applications of the Nu Attom ICP-MS are found in Roberts *et al*. (2011). The analytical procedure for zircon and rutile are previously described in Roberts *et al.* (2016) and for monazite in Mottram *et al.* (2014). Zircon grains were subsequently extracted from the epoxy resin for further analysis. Xenotime grains in sample 05-02 were analysed in thin section in order to preserve the petrographic relationships observed.

Samples were ablated with a New Wave Research 193UC laser ablation system using a New Wave Research TV2 cell. The setup achieves a washout time of < 1 second, by combining a moveable cup with an ablation volume of ca. 3-4 cm^3 and < 1 m tubing to the plasma torch. The ICP-MS is used in peak-jumping mode with the measured masses being: ^{204}Pb, ^{206}Pb, ^{207}Pb, ^{208}Pb, ^{232}Th and ^{235}U (for zircon and xenotime) or ^{238}U (rutile and titanite). ^{238}U is calculated where

not measured using the measured ^{235}U mass and the currently accepted value of 137.818 (Hiess et al., 2012. Each data integration records 80 sweeps of the measured masses, roughly equating to 0.3 seconds.

Data were processed using the time-resolved analysis on the Nu Instruments' software, an in-house Excel spreadsheet for data reduction and uncertainty propagation, and Isoplot version v4 (Ludwig, 2008) for data age plotting and calculation. Data were normalised using a standard-sample-bracketing technique. Normalisation factors were calculated based on measured/accepted value for the $^{207}Pb/^{206}Pb$, $^{206}Pb/^{238}U$ and $^{208}Pb/^{232}Th$ ratios of a reference material analysed at regular intervals during the session. Reference materials were also used as secondary standards and processed as unknowns to validate the precision and accuracy for an individual session; these data are also used to assess the long-term excess variance overtime that allows for the propagation of uncertainties (as per Horstwood *et al.*, 2016).

The ablation parameters for rutile were a 25 second ablation using a repetition rate of 6 Hz, a 32 μm static spot size with a laser fluence of ~3 J/cm^2. The reference materials used were PCA (1865 ± 7.5 Ma, Bracciali et al., 2013), Sugluk (1719 ± 14 Ma, Bracciali *et al.*, 2013), R10 (1090 Ma, Luvizotto et al., 2009) and R19 (490 Ma, Zack et al., 2008). Which was used as a primary reference material varied per analytical session, as the materials are variably heterogeneous. The pooled results from all analytical sessions are as follows: PCA = 1859 ± 25 Ma (MSWD = 1.1, n = 16 of 16), Sugluk = 1714 ± 30 Ma (MSWD = 1.3; n = 15 of 16); R10 = 1100 ± 7 Ma (MSWD = 2.6; 68 of 73) and R19 = 466 ± 4 Ma (MSWD = 1.3, n = 15 of 15).

The ablation parameters for titanite were 25 second ablation time using a repetition rate of 6 Hz, a 32 μm static spot size and with a laser fluence of ~3 J/cm^2. The reference material Khan titanite (522.2 ± 2.2 Ma, Heaman, 2009) was used as a primary reference material for U-Pb ratios, and NIST612 silicate glass was used as a primary reference material for Pb-Pb ratios (using Woodhead and Hergt, 2001 values). Ontario-2 (1054 ± 8 Ma, Spencer *et al.*, 2013) and Fish Canyon Tuff (28.40 ± 0.02 Ma; Schmitz and Bowring, 2001) were used as secondary reference materials, and gave ages of 1035 ± 8 Ma (MSWD = 0.9) and 28.3 ± 1.5 Ma (MSWD = 1.5), respectively.

The ablation parameters for zircon were a 23-25 second ablation time using a repetition rate of 5-6Hz, a 20-27μm static spot size and with a laser fluence of ~2.1-2.5 J/cm^2. The 91500 reference material (1065 Ma, Wiedenbeck *et al.*, 1995, 2004) was used as a primary reference material and Plešovice (337 Ma, Sláma *et al.*, 2008) and GJ1 (609 Ma, Jackson *et al.*, 2004) were used as secondary reference materials.

The ablation parameters for xenotime were a 20 second ablation time using a repetition rate of 6 Hz, a 15 μm spot size with a laser fluence of ~3 J/cm^2. FC-1 xenotime (54.5 ± 0.3 Ma, Parrish, 1990) was used as a reference material, and

only monazite reference materials were run in the same session as secondary reference materials as no other matrix-matched xenotime materials were available.

Corrections

All ages are calculated as lower intercept ages on Tera-Wasserburg plots, using free regressions. Additional common lead corrected age data in the tables are calculated using a ^{207}Pb-based correction (see Chew *et al.,* (2014), and assuming a Stacey and Kramers (1975) model lead composition for that age. An additional correction is applied to the common-lead corrected aged that accounts for any excess ^{206}Pb derived from ^{230}Th; this uses an estimated whole-rock value of 3.8. For all minerals, U-Pb age uncertainties include propagation of the analytical uncertainties, and the session-based reproducibility as an excess variance uncertainty. Data were screened for occurrences of mixed analyses where two zones had inadvertently been measured.

CA-ID-TIMS

Chemical abrasion Isotope dilution thermal ionisation mass spectrometry Uranium lead geochronology (CA-ID-TIMS) analysis was undertaken at the Geochronology and Tracers Facility, British Geological Survey, Keyworth. The methodology for analytical procedure, instrument conditions, corrections and data reduction follows that outlined in detail in Tapster et al., (2016).

Zircon were plucked from an epoxy mount prepared at NIGL were thermally annealed at ~900˚C over a period of ~60 hrs in quartz dishes following Mattinson et al., (2005). Aliquots were fluxed in Teflon beakers and 4N HNO_3 at 90˚C for 1–2 hrs before being ultrasonically cleaned and rinsed and loaded into 300 µl Teflon microcapsules. Aliquots selected for chemical abrasion were leached inside a Parr vessel for 12 hours at 180˚C (Mattinson et al., 2005) before further rinsing stages with 4N HNO_3 and 6N HCl. All zircons were spiked with the mixed ^{205}Pb- ^{233}U- ^{235}U (ET535) EARTHTIME tracer solution (Condon et al., 2015; Mclean et al., 2015) and dissolved at 220˚C in ~200 µl 29N HF and trace 4N HNO_3 for ~80 hrs in a Parr vessel. Samples were evaporated and converted to chlorides by dissolving overnight in 3N HCl at 180˚C. Chemical separation of U and Pb was achieved using standard HCl based anion exchange procedures (Krogh, 1973) using Teflon columns and Bio-Rad AG-1 8x resin. Combined U-Pb fractions were dried down with ~10 µl of H_3PO_4. Samples were loaded on a zone-refined Re filament in a silica gel matrix (Gerstenberger and Haase, 1997).

Isotope ratio measurements were made using a Thermo Triton thermal ionization mass-spectrometer (TIMS). Pb was measured in peak hopping (dynamic) mode on a single MassCom secondary electron multiplier (SEM) for lower beam

intensities. Linearity and dead time corrections on the SEM were monitored using repeated analyses of the NBS 982, NBS 981 and U 500 standards. U was run as an oxide (UO_2) and measured in static mode on Faraday detectors equipped with $10^{12}\Omega$ resistors. Raw U and Pb data were filtered using the Tripoli software program (Bowring et al., 2011). The Pb measurements were filtered for isobaric interferences of $BaPO_3$ and Tl using the monitoring masses of 201 and 203. The U mass fractionation was calculated in real-time based on the isotopic composition of the double spiked 'ET535 v.3.0' tracer, Pb mass fractionation was attributed a value of 0.14 ± 0.02 %/amu Uranium oxide measurements were corrected for isobaric interferences using an $^{18}O/^{16}O$ value of 0.00205. Data reduction, date calculation/presentation and uncertainty propagation was done in ET_Redux (McLean et al., 2011) with the U decay constants of Jaffey et al., (1971), the $^{238}U/^{235}U$ ratio of Hiess et al. (2012) and the decay constants of Cheng et al., (2000) for ^{230}Th. Uranium blanks were assumed to be 0.1 ± 0.01 pg (1σ). Common Pb was attributed entirely to laboratory blank using a calculated Pb isotopic composition for the laboratory blank of $^{206}Pb/^{204}Pb$= 18.10 ± 0.27%, $^{207}Pb/^{204}Pb$ = 15.55 ± 0.14% and $^{208}Pb/^{204}Pb$ = 37.82 ± 0.41% (1σ uncertainties). $^{206}Pb/^{238}U$ dates were corrected for initial ^{230}Th disequilibrium (Schärer, 1984) using a value of Th/U[magma] = 3.5, the low Th/U of the zircon results in variation of this value having negligible effects on the $^{206}Pb/^{238}U$ dates.

Best estimate of crystallisation age was selected from the youngest population where n=> 3 of concordant data at the level of stated 2σ precision where the weighted mean age had a statistically acceptable MSWD (Mean Square Weighted Deviate) for the given population size. Uncertainties on the best age interpretations are presented in the form ± x/y/z (2σ), where x = analytical uncertainty only for comparison with other samples from this ID-TIMS data set and others also using the EARTHTIME tracers; y = analytical and tracer calibration uncertainty for comparison with U-Pb data sets that do not use EARTHTIME tracers; z = total uncertainty including U decay constants for comparison with dates yielded by other radio-isotopic systems.

Appendix 2 – Radioisotopic dating methods

Laboratory and Sample Preparation	
Laboratory name	NERC Isotope Geosciences Laboratory (BGS, Keyworth)
Sample type/mineral	Monazite, zircon, titanite, rutile & xenotime
Sample preparation	Monazite & xenotime - *in situ* polished section
	Zircon - Conventional mineral separation, 1 inch resin mount, polished to half thickness for core analysis, mounted on sticky tape for rim analysis
	Rutile and titanite - Conventional mineral separation, 1 inch resin mount, polished to half thickness for core analysis.
Imaging	Zircon - cathodoluminescence imaging (SEM-CL) at the NIGL
	Rutile and titanite – BSE imaging at Oxford University
Laser ablation system	
Make, Model and type	?
Ablation cell and volume	?
Laser wavelength (nm)	193 nm
Pulse width (ns)	4 ns
Fluence (J cm^{-2})	2.0 Jcm^{-2} (monazite)
	2.1-2.5 Jcm^{-2} (zircon)
	2.7 Jcm^{-2} (rutile)
	2.7 Jcm^{-2} (titanite)
Repetition rate (Hz)	3-7 Hz (monazite)
	5-6 Hz (zircon)
	6 Hz (rutile)
	6 Hz (titanite)
Ablation duration (s)	22-25 s (monazite)
	23-25 s (zircon)
	25 s (rutile)
	25 s (titanite)
Ablation pit depth/ablation rate	150nm per pulse
Spot diameter (µm) nominal/actual	11-12 µm (monazite)
	20-27 µm (zircon)
	32 µm (rutile)
	25 µm (titanite)
Sampling mode/pattern Carrier gas	Static spot ablation

Appendix 2 – Radioisotopic dating methods

Cell carrier gas flow (l min-1)	0.8 l/min
ICP-MS Instrument	
Make, Model and type	Nu Instruments AttoM SC-SF-ICP-MS
Sample introduction	Free air aspiration of desolvator
RF power (W)	1300 W
Make-up gas flow (l min-1)	0.7 l/min
Detection system	Discrete dynode MassCom ion counter
Masses measured	202, 204, 206, 207, 208, 232, 235 (additional masses 2016 monazite analyses: 164 & 174)
Integration time per peak/dwell times (ms); quadrupole settling time between mass jumps	200 µs for ^{202}Hg, ^{204}Hg, ^{206}Pb, ^{208}Pb, ^{232}Th and 800 µs for ^{207}Pb and ^{235}U
Total integration time per output data point (s)	0.3 seconds
'Sensitivity' as useful yield (%, element)	~0.2% on U
IC Dead time (ns)	15 ns
Data Processing	
Gas blank	>60 s on-peak zero subtracted
Calibration strategy	Standard sample bracketing using matrix-matched reference materials (see text for details)
Reference Material information	Zircon: 91500 1065 Ma (Wiedenbeck *et al.*, 1995, 2004), Plešovice 337.13 Ma (Sláma *et al.*, 2008), GJ-1 602.3 ± 1Ma ^{206}Pb/^{238}U age 609.2 ± 0.7 Ma ^{207}Pb/^{206}Pb age (Horstwood et al., 2016; Jackson *et al.* (2004). Rutile: R10 1095.2 ± 4.7 Ma and R19 490 Ma (Luvizotto *et al.*, 2009; Zack et al., 2008), Sugluk-4 (1719 Ma; Bracciali et al., 2013) and PCA (1865 Ma; Bracciali et al., 2013). Monazite: Stern 507 Ma, Manangotry 559 Ma and Moacyr 507 Ma (Palin et al., 2013) and 44069 425 Ma (Aleinikoff *et al.*, 2006). Titanite: Khan 522 Ma (Heaman, 2009), Ontario-2 1054 Ma (Spencer et al., 2013) and Fish Canyon Tuff 28 Ma (Schmitz & Bowring, 2001).
Data processing package used/Correction for LIEF	Nu Instruments TRA acquisition software, in-house spreadsheet data normalisation, uncertainty propagation and age calculation. LIEF correction assumes reference material and samples behave identically.
Mass discrimination	^{206}Pb/^{238}U, ^{207}Pb/^{206}Pb and ^{208}Pb/^{232}Th normalised to reference material
Common-Pb correction, composition and uncertainty	No common lead correction applied – results based on intercept ages in Tera-Wasserburg plots.
Uncertainty level and propagation	Ages are quoted at 2s absolute, propagation is by quadratic addition. Reproducibility and age uncertainty of reference material and common-Pb composition uncertainty are propagated where appropriate.

Appendix 3

Radioisotopic data

The following data obtained during geochronological analysis supplement the relevant tables ppresented in chapter 7

Zircon

Spot	Date	comments	^{204}Pb	^{206}Pb	^{207}Pb	^{208}Pb	^{232}Th	^{238}U	Th/U	Pb ppm	Th ppm	U ppm	$^{238}U/^{206}Pb$	1s %	$^{207}Pb/^{206}Pb$	1s %	$^{207}Pb/^{235}U$	1s %	$^{206}Pb/^{238}U$	1s %
91500_01	14/05/2018	20um, 66%, 20sec, 7Hz, 2J	-3	54642	4123	5932	97151	371187	0.4	16.6	33.5	94.4	5.7343	1.70	0.0754	1.25	1.8130	2.11	0.1744	1.70
91500_02	14/05/2018		6	49004	3719	5177	86996	320637	0.4	14.9	30.0	81.5	5.6212	1.38	0.0751	1.02	1.8412	1.71	0.1779	1.38
91500_03	14/05/2018		-41	44944	3408	4592	76622	294430	0.4	13.6	26.4	74.9	5.5930	1.42	0.0755	1.08	1.8605	1.78	0.1788	1.42
91500_04	14/05/2018		4	48054	3527	4789	84018	316935	0.4	14.5	29.0	80.6	5.5521	1.75	0.0731	1.03	1.8152	2.04	0.1801	1.75
91500_05	14/05/2018		15	55033	4271	5817	99911	352018	0.4	16.7	34.4	89.5	5.5423	1.46	0.0762	1.09	1.8946	1.82	0.1804	1.46
91500_06	14/05/2018		-31	51358	3885	5404	91529	332417	0.4	15.6	31.5	84.5	5.4826	1.37	0.0746	1.21	1.8761	1.83	0.1824	1.37
91500_07	14/05/2018		-36	49244	3726	5087	86235	323952	0.4	14.9	29.7	82.4	5.5148	1.64	0.0745	1.28	1.8624	2.08	0.1813	1.64
91500_08	14/05/2018		86	49257	3666	5221	83231	321443	0.4	15.0	28.7	81.7	5.5996	1.44	0.0743	1.10	1.8284	1.81	0.1786	1.44
91500_09	14/05/2018		101	51333	3910	5737	91037	334728	0.4	15.7	31.4	85.1	5.5830	1.34	0.0755	1.19	1.8632	1.79	0.1791	1.34
91500_10	14/05/2018		60	53504	4095	5773	95118	346472	0.4	16.3	32.8	88.1	5.4983	1.76	0.0746	0.97	1.8694	2.01	0.1819	1.76
91500_11	14/05/2018		-46	53062	3990	5757	93574	348488	0.4	16.1	32.2	88.6	5.5974	1.42	0.0749	1.19	1.8438	1.86	0.1787	1.42
91500_12	14/05/2018		87	53868	3996	5736	93487	349109	0.4	16.4	32.2	88.8	5.5427	1.59	0.0737	1.02	1.8321	1.89	0.1804	1.59
91500_13	14/05/2018		23	40288	3080	3830	64587	264494	0.3	12.1	22.3	67.3	5.6262	2.00	0.0762	1.20	1.8666	2.33	0.1777	2.00
91500_14	14/05/2018		8	47394	3600	4910	84227	309254	0.4	14.4	29.0	78.6	5.5240	1.90	0.0750	0.98	1.8722	2.14	0.1810	1.90
91500_15	14/05/2018		88	50869	3822	5575	98406	319952	0.4	15.5	33.9	81.4	5.3339	1.42	0.0747	1.04	1.9303	1.76	0.1875	1.42
91500_16	14/05/2018		-31	51008	3902	5405	96630	331927	0.4	15.5	33.3	84.4	5.5213	1.58	0.0745	1.31	1.8593	2.06	0.1811	1.58
91500_17	14/05/2018		-25	50839	3865	5415	98643	324324	0.4	15.5	34.0	82.5	5.4617	1.56	0.0756	0.87	1.9077	1.79	0.1831	1.56
91500_18	14/05/2018		-5	42780	3144	4312	77366	277564	0.4	12.9	26.7	70.6	5.5029	1.51	0.0734	1.17	1.8392	1.91	0.1817	1.51
91500_19	14/05/2018		-8	36142	2740	3420	59285	241009	0.3	10.9	20.4	61.3	5.6287	1.76	0.0750	1.24	1.8361	2.15	0.1777	1.76
91500_20	14/05/2018		-86	44925	3297	4624	81313	295678	0.4	13.6	28.0	75.2	5.6108	1.66	0.0729	1.20	1.7903	2.05	0.1782	1.66
91500_21	14/05/2018		-72	47084	3606	5284	85061	318440	0.4	14.4	29.3	81.0	5.7117	1.52	0.0756	1.05	1.8235	1.84	0.1751	1.52
91500_22	14/05/2018		29	48583	3755	5273	87235	317425	0.4	14.8	30.1	80.7	5.5707	1.49	0.0763	1.13	1.8866	1.87	0.1795	1.49
91500_23	14/05/2018		83	49752	3741	5303	90440	334165	0.4	15.1	31.2	85.0	5.6977	1.63	0.0748	0.98	1.8087	1.90	0.1755	1.63
91500_24	14/05/2018		-11	50315	3826	5337	92441	335578	0.4	15.3	31.9	85.3	5.6256	1.49	0.0756	1.11	1.8517	1.86	0.1778	1.49
91500_25	14/05/2018		50	50617	3836	5440	91505	334201	0.4	15.4	31.5	85.0	5.6781	1.42	0.0749	0.90	1.8191	1.69	0.1761	1.42
91500_26	14/05/2018		70	43332	3192	4502	77357	285846	0.4	13.1	26.7	72.7	5.5365	1.35	0.0750	1.16	1.8662	1.78	0.1806	1.35
91500_01	16/05/2018		39	89295	6672	9392	144972	567823	0.4	11.3	24.8	61.1	5.6090	1.69	0.0743	1.05	1.8250	1.99	0.1783	1.69
91500_02	16/05/2018		52	86407	6521	8830	136980	534243	0.4	11.0	23.5	57.5	5.4526	1.68	0.0740	1.02	1.8704	1.97	0.1834	1.68
91500_03	16/05/2018		8	98596	7523	10888	164862	620073	0.4	12.6	28.3	66.7	5.5429	1.52	0.0751	1.22	1.8665	1.95	0.1804	1.52
91500_04	16/05/2018		-90	104362	7938	11145	174720	667391	0.4	13.3	29.9	71.8	5.6286	1.63	0.0747	0.99	1.8295	1.91	0.1777	1.63
91500_05	16/05/2018		-9	103952	7870	11128	176617	672685	0.4	13.2	30.3	72.4	5.5555	1.87	0.0734	1.07	1.8203	2.15	0.1800	1.87
91500_06	16/05/2018		87	78414	5915	7786	120973	498282	0.4	9.9	20.7	53.6	5.4856	1.84	0.0748	0.93	1.8800	2.06	0.1823	1.84
91500_07	16/05/2018		23	94337	7231	10076	154667	610336	0.4	12.0	26.5	65.7	5.5586	1.63	0.0750	1.04	1.8603	1.93	0.1799	1.63
91500_08	16/05/2018		30	110424	8410	11024	155548	725047	0.3	14.0	26.7	78.0	5.7281	1.80	0.0748	1.41	1.7994	2.28	0.1746	1.80
91500_09	16/05/2018		39	157050	11986	16347	227772	1012564	0.4	20.0	39.0	109.0	5.6271	1.67	0.0758	1.41	1.8557	2.18	0.1777	1.67
91500_10	16/05/2018		51	146192	11257	15734	213001	968519	0.4	18.6	36.5	104.2	5.6613	1.83	0.0768	1.58	1.8698	2.42	0.1766	1.83
91500_11	16/05/2018		30	130503	10157	13884	188823	869276	0.3	16.6	32.4	93.6	5.7232	1.72	0.0777	1.31	1.8719	2.16	0.1747	1.72
91500_12	16/05/2018		4	143371	10700	15408	197143	939601	0.3	18.2	33.8	101.1	5.5862	1.57	0.0744	1.14	1.8354	1.94	0.1790	1.57
91500_13	16/05/2018		62	145805	10879	15268	201025	951921	0.3	18.5	34.5	102.4	5.5397	1.62	0.0743	1.15	1.8496	1.98	0.1805	1.62
91500_14	16/05/2018		111	140787	10784	14882	193671	925086	0.3	17.9	33.2	99.6	5.5313	1.66	0.0758	1.22	1.8897	2.06	0.1808	1.66
GJ-1_01	14/05/2018		-48	82067	4932	950	26129	992491	0.0	22.6	9.0	252.4	10.4731	1.30	0.0603	0.97	0.7929	1.62	0.0955	1.30
GJ-1_02	14/05/2018		97	88823	5371	1093	28528	1075050	0.0	24.5	9.8	273.4	10.3405	1.20	0.0597	0.94	0.7953	1.52	0.0967	1.20
GJ-1_03	14/05/2018		-71	92836	5690	1139	29861	1121246	0.0	25.6	10.3	285.1	10.2993	1.22	0.0602	1.21	0.8051	1.72	0.0971	1.22
GJ-1_04	14/05/2018		-66	87089	5288	992	28684	1083774	0.0	24.0	9.9	275.6	10.6615	1.30	0.0614	1.07	0.7935	1.69	0.0938	1.30
GJ-1_05	14/05/2018		-35	89340	5410	987	27528	1067903	0.0	24.6	9.5	271.6	10.1823	1.08	0.0601	1.26	0.8140	1.66	0.0982	1.08
GJ-1_06	14/05/2018		16	88731	5322	1020	28259	1085770	0.0	24.4	9.7	276.1	10.4883	1.17	0.0596	1.13	0.7830	1.62	0.0953	1.17
GJ-1_07	14/05/2018		27	84310	5036	990	26214	1027140	0.0	23.2	9.0	261.2	10.5164	1.26	0.0603	1.06	0.7902	1.65	0.0951	1.26
GJ-1_08	14/05/2018		-66	90024	5453	979	28004	1064988	0.0	24.8	9.7	270.8	10.1079	1.26	0.0601	1.12	0.8191	1.68	0.0989	1.26
GJ-1_09	14/05/2018		48	91223	5550	1076	29787	1123767	0.0	25.2	10.3	285.8	10.4491	1.26	0.0600	0.81	0.7910	1.50	0.0957	1.26
GJ-1_10	14/05/2018		44	92265	5698	1105	29913	1120517	0.0	25.5	10.3	285.0	10.3350	1.30	0.0609	1.21	0.8127	1.78	0.0968	1.30
GJ-1_11	14/05/2018		-123	88446	5410	1049	27863	1072243	0.0	24.4	9.6	272.7	10.3811	1.29	0.0600	1.00	0.7970	1.64	0.0963	1.29
GJ-1_12	14/05/2018		47	86551	5225	994	27477	1056110	0.0	23.9	9.5	268.6	10.2924	1.23	0.0595	1.02	0.7967	1.60	0.0972	1.23
GJ-1_13	14/05/2018		68	91903	5640	1002	29365	1099825	0.0	25.3	10.1	279.7	10.1263	1.28	0.0609	1.19	0.8282	1.75	0.0988	1.28
GJ-1_14	14/05/2018		26	87289	5266	1005	27909	1043561	0.0	24.1	9.6	265.4	10.2497	1.30	0.0596	1.08	0.8017	1.69	0.0976	1.30
GJ-1_15	14/05/2018		-61	82519	5111	1033	29755	977796	0.0	22.8	10.3	248.7	10.1788	1.14	0.0609	0.95	0.8245	1.48	0.0982	1.14
GJ-1_16	14/05/2018		77	86906	5247	1049	30872	1006063	0.0	24.0	10.6	255.9	9.9362	1.27	0.0603	0.90	0.8367	1.56	0.1006	1.27
GJ-1_17	14/05/2018		95	86442	5294	967	30876	1016731	0.0	23.8	10.6	258.6	9.9639	1.27	0.0598	1.05	0.8270	1.65	0.1004	1.27
GJ-1_18	14/05/2018		-13	85005	5149	1075	29241	1012679	0.0	23.5	10.1	257.5	10.2609	1.23	0.0606	1.11	0.8135	1.65	0.0975	1.23
GJ-1_19	14/05/2018		28	88615	5265	1104	30143	1059797	0.0	24.4	10.4	269.5	10.2273	1.18	0.0597	1.17	0.8046	1.66	0.0978	1.18
GJ-1_20	14/05/2018		-14	86899	5393	977	30220	1050038	0.0	24.0	10.4	267.0	10.3160	1.22	0.0609	0.95	0.8140	1.55	0.0969	1.22
GJ-1_21	14/05/2018		52	86558	5236	971	29036	1044299	0.0	23.9	10.0	265.6	10.3365	1.31	0.0603	1.08	0.8043	1.70	0.0967	1.31
GJ-1_22	14/05/2018		-3	86803	5136	1023	29080	1034372	0.0	23.9	10.0	263.1	10.3706	1.53	0.0592	1.21	0.7870	1.95	0.0964	1.53
GJ-1_23	14/05/2018		45	86792	5199	999	29553	1042789	0.0	23.9	10.2	265.2	10.2195	1.40	0.0601	1.02	0.8106	1.73	0.0979	1.40
GJ-1_24	14/05/2018		34	87274	5278	1063	28723	1051260	0.0	24.1	9.9	267.3	10.4852	1.30	0.0616	0.99	0.8094	1.63	0.0954	1.30
GJ-1_25	14/05/2018		56	80816	4898	1040	27689	993648	0.0	22.3	9.5	252.7	10.4168	1.30	0.0603	0.94	0.7972	1.61	0.0960	1.30
GJ-1_26	14/05/2018		43	82477	4950	920	27690	999449	0.0	22.7	9.5	254.2	10.2787	1.48	0.0606	1.14	0.8128	1.87	0.0973	1.48
GJ-1_01	16/05/2018		89	187685	11528	2226	60248	2200848	0.0	21.7	10.3	236.9	10.2602	1.62	0.0603	1.05	0.8102	1.93	0.0975	1.62
GJ-1_02	16/05/2018		88	194168	11949	2338	62043	2296354	0.0	22.4	10.6	247.1	10.5035	1.52	0.0609	0.95	0.7990	1.79	0.0952	1.52
GJ-1_03	16/05/2018		20	193606	11834	2113	61214	2274870	0.0	22.3	10.5	244.8	10.3559	1.54	0.0600	0.95	0.7978	1.80	0.0966	1.54
GJ-1_04	16/05/2018		30	196449	11896	2152	62150	2249516	0.0	22.7	10.7	242.1	10.1182	1.67	0.0590	1.02	0.8041	1.96	0.0988	1.67
GJ-1_05	16/05/2018		103	193915	11907	2277	60974	2355996	0.0	22.4	10.4	253.6	10.3833	1.43	0.0601	0.92	0.7972	1.70	0.0963	1.43
GJ-1_06	16/05/2018		10	252089	15453	2900	78375	2954135	0.0	29.1	13.4	317.9	10.1089	1.45	0.0604	0.95	0.8232	1.74	0.0989	1.45
GJ-1_07	16/05/2018		43	206451	12456	2295	64926	2433506	0.0	23.8	11.1	261.9	10.0568	1.42	0.0593	0.95	0.8125	1.71	0.0994	1.42
GJ-1_08	16/05/2018		60	295938	18072	3453	78060	3617689	0.0	34.2	13.4	389.3	10.5564	1.76	0.0595	1.10	0.7765	2.08	0.0947	1.76
GJ-1_09	16/05/2018		-1	292610	17737	3378	77423	3608230	0.0	33.8	13.3	388.3	10.5699	1.74	0.0597	1.19	0.7779	2.11	0.0946	1.74
GJ-1_10	16/05/2018		121	293826	18094	3418	77700	3575595	0.0	33.9	13.3	384.8	10.4942	1.70	0.0611	1.09	0.8025	2.02	0.0953	1.70
GJ-1_11	16/05/2018		35	299249	18164	3396	78431	3578245	0.0	34.5	13.4	385.1	10.2607	1.56	0.0594	1.03	0.7984	1.87	0.0975	1.56
GJ-1_12	16/05/2018		39	287053	17830	3309	76543	3490208	0.0	33.2	13.1	375.6	10.3885	1.54	0.0612	1.05	0.8116	1.86	0.0963	1.54
GJ-1_13	16/05/2018		3	287719	17583	3376	75299	3563014	0.0	33.2	12.9	383.5	10.3512	1.66	0.0604	1.21	0.8036	2.05	0.0966	1.66
GJ-1_14	16/05/2018		-56	293614	17759	3461	74692	3559591	0.0	33.9	12.8	383.1	10.3659	1.69	0.0607	1.49	0.8069	2.25	0.0965	1.69
Ples_01	14/05/2018		124	131636	7149	3880	198031	2866256	0.1	36.7	68.2	728.9	18.8572	1.11	0.0541	0.86	0.3956	1.40	0.0530	1.11
Ples_02	14/05/2018		25	136078	7373	4121	208821	2983478	0.1	37.9	72.0	758.7	18.4131	1.14	0.0535	0.92	0.4005	1.46	0.0543	1.14
Ples_03	14/05/2018		38	134870	7252	4399	224324	2973949	0.1	37.7	77.3	756.3	18.8531	1.06	0.0538	0.84	0.3932	1.35	0.0530	1.06
Ples_04	14/05/2018		74	139680	7344	4203	218293	3041831	0.1	38.9	75.2	773.6	18.6723	1.37	0.0532	1.12	0.3929	1.77	0.0536	1.37
Ples_05	14/05/2018		93	135718	7523	4658	204613	2934106	0.1	38.0	70.5	746.2	18.2659	1.05	0.0557	0.95	0.4200	1.41	0.0547	1.05
Ples_06	14/05/2018		41	120380	6520	3379	177867	2633460	0.1	33.5	61.3	669.7	18.5801	1.19	0.0533	0.89	0.3955	1.49	0.0538	1.19
Ples_07	14/05/2018		62	97395	5288	2639	139709	2092727	0.1	27.1	48.1	532.2	18.2037	1.12	0.0534	0.90	0.4045	1.44	0.0549	1.12
Ples_08	14/05/2018		-3	95834	5192	2643	140106	2102059	0.1	26.7	48.3	534.6	18.6032	1.13	0.0541	1.04	0.4008	1.53	0.0538	1.13
Ples_09	14/05/2018		16	112847	6119	3313	164196	2486839	0.1	31.4	56.6	632.4	18.7532	1.23	0.0535	0.78	0.3929	1.45	0.0533	1.23
Ples_10	14/05/2018		76	93045	5066	2661	133683	2029270	0.1	25.9	46.1	516.1	18.7134	1.12	0.0536	0.94	0.3948	1.46	0.0534	1.12
Ples_11	14/05/2018		74	114815	6182	3144	166166	2528975	0.1	31.9	57.3	643.1	18.7441	1.01	0.0541	0.86	0.3981	1.33	0.0534	1.01
Ples_12	14/05/2018		23	130494	6918	4088	211655	2863370	0.1	36.4	72.9	728.2	18.4166	1.32	0.0524	0.92	0.3923	1.61	0.0543	1.32
Ples_13	14/05/2018		33	128966	6895	4103	206686	2761711	0.1	36.0	71.2	702.3	18.1809	1.21	0.0529	0.78	0.4010	1.44	0.0550	1.21
Ples_14	14/05/2018		71	138043	7327	4243	209722	2944065	0.1	38.5	72.3	748.7	18.1408	1.12	0.0535	0.99	0.4064	1.50	0.0551	1.12
Ples_15	14/05/2018		41	114300	6193	3186	188460	2411973	0.1	31.8	64.9	613.4	17.8467	1.12	0.0538	0.81	0.4157	1.38	0.0560	1.12
Ples_16	14/05/2018		-61	117712	6272	3285	191127	2492296	0.1	32.7	65.9	633.8	17.9489	1.22	0.0528	0.91	0.4055	1.52	0.0557	1.22
Ples_17	14/05/2018		-5	93751	5091	2710	151363	1987802	0.1	26.1	52.2	505.5	17.9090	1.19	0.0540	0.97	0.4155	1.54	0.0558	1.19
Ples_18	14/05/2018		34	111758	6142	3345	175646	2444781	0.1	31.2	60.5	621.7	18.7361	1.09	0.0542	0.81	0.3983	1.36	0.0534	1.09
Ples_19	14/05/2018		133	95040	5106	2705	145336	2060600	0.1	26.4	50.1	524.0	18.6008	1.18	0.0537	1.05	0.3982	1.58	0.0538	1.18
Ples_20	14/05/2018		66	113017	6058	3169	175747	2425781	0.1	31.4	60.6	616.9	18.3613	1.08	0.0535	0.92	0.4019	1.42	0.0545	1.08
Ples_21	14/05/2018		5	109972	5799	3305	173154	2394666	0.1	30.6	59.7	609.0	18.6658	1.33	0.0525	0.91	0.3878	1.61	0.0536	1.33
Ples_22	14/05/2018		94	103744	5411	3049	162659	2248657	0.1	28.8	56.1	571.9	18.5335	1.12	0.0529	0.92	0.3932	1.45	0.0540	1.12
Ples_23	14/05/2018		-14	108081	5765	3207	173147	2432827	0.1	30.1	59.7	618.7	19.0955	1.15	0.0532	0.94	0.3838	1.49	0.0524	1.15
Ples_24	14/05/2018		8	113326	6188	3718	190129	2489078	0.1	31.7	65.5	633.0	18.7627	1.12	0.0539	0.88	0.3960	1.42	0.0533	1.12
Ples_25	14/05/2018		46	96983	5332	2931	156548	2137757	0.1	27.1	53.9	543.7	18.6264	1.12	0.0540	1.03	0.3999	1.52	0.0537	1.12
Ples_26	14/05/2018		15	88833	4783	2581	140447	1990544	0.1	24.7	48.4	506.2	19.0134	1.14	0.0535	0.90	0.3877	1.45	0.0526	1.14

	Zircon																				
Spot	Rho	$^{207}Pb/^{206}Pb$	2s abs	$^{206}Pb/^{238}U$	2s abs	$^{207}Pb/^{235}U$	2s abs	6-38/7-6	6-38/7-35	*f206*	1s %	$^{206}Pb^*/^{238}U$	1s %	206/238-Pb	2s [Ma]	Th/U min.	Th/U wr.	f	r. 206/238 a	*2s [Mo]*
91500_01	0.81	1080	50	1036	32	1050	27	4.1	1.3	0.002	1.25	0.1740	1.7	1034	32.3	0.4	3.8	0.09	**1034.6**	***32.3***
91500_02	0.80	1071	41	1055	27	1060	22	1.5	0.5	0.001	1.02	0.1778	1.4	1055	26.7	0.4	3.8	0.10	**1055.0**	***26.7***
91500_03	0.79	1082	43	1060	28	1067	23	2.0	0.6	0.001	1.08	0.1786	1.4	1059	27.6	0.4	3.8	0.09	**1059.7**	***27.6***
91500_04	0.86	1017	42	1068	34	1051	26	-4.9	-1.6	-0.002	1.03	0.1805	1.8	1070	34.6	0.4	3.8	0.09	**1070.1**	***34.6***
91500_05	0.80	1100	44	1069	29	1079	24	2.8	0.9	0.001	1.09	0.1802	1.5	1068	28.7	0.4	3.8	0.10	**1068.2**	***28.7***
91500_06	0.75	1059	49	1080	27	1073	24	-2.0	-0.7	-0.001	1.21	0.1826	1.4	1081	27.3	0.4	3.8	0.10	**1081.3**	***27.3***
91500_07	0.79	1056	52	1074	32	1068	27	-1.8	-0.6	-0.001	1.28	0.1815	1.6	1075	32.4	0.4	3.8	0.09	**1075.3**	***32.4***
91500_08	0.79	1049	45	1059	28	1056	24	-0.9	-0.3	0.000	1.10	0.1787	1.4	1060	28.1	0.4	3.8	0.09	**1059.9**	***28.1***
91500_09	0.75	1081	48	1062	26	1068	23	1.8	0.6	0.001	1.19	0.1790	1.3	1061	26.1	0.4	3.8	0.10	**1061.5**	***26.1***
91500_10	0.88	1057	39	1077	35	1070	26	-1.9	-0.6	-0.001	0.97	0.1820	1.8	1078	34.8	0.4	3.8	0.10	**1078.3**	***34.8***
91500_11	0.77	1065	48	1060	28	1061	24	0.5	0.1	0.000	1.19	0.1786	1.4	1059	27.8	0.4	3.8	0.10	**1059.6**	***27.8***
91500_12	0.84	1033	41	1069	31	1057	25	-3.5	-1.2	-0.002	1.02	0.1807	1.6	1071	31.4	0.4	3.8	0.10	**1071.1**	***31.4***
91500_13	0.86	1100	48	1055	39	1069	30	4.2	1.4	0.002	1.20	0.1774	2.0	1053	38.6	0.3	3.8	0.09	**1052.8**	***38.6***
91500_14	0.89	1070	40	1073	37	1071	28	-0.3	-0.1	0.000	0.98	0.1811	1.9	1073	37.4	0.4	3.8	0.10	**1073.0**	***37.4***
91500_15	0.81	1061	42	1108	29	1092	23	-4.4	-1.5	-0.002	1.04	0.1879	1.4	1110	28.9	0.4	3.8	0.11	**1110.1**	***28.9***
91500_16	0.77	1055	53	1073	31	1067	27	-1.7	-0.6	-0.001	1.31	0.1813	1.6	1074	31.3	0.4	3.8	0.10	**1074.2**	***31.3***
91500_17	0.87	1085	35	1084	31	1084	24	0.1	0.0	0.000	0.87	0.1831	1.6	1084	31.0	0.4	3.8	0.11	**1084.0**	***31.0***
91500_18	0.79	1026	47	1076	30	1060	25	-4.9	-1.6	-0.002	1.17	0.1821	1.5	1079	30.1	0.4	3.8	0.10	**1078.9**	***30.1***
91500_19	0.82	1068	50	1054	34	1058	28	1.3	0.4	0.001	1.24	0.1775	1.8	1054	34.0	0.3	3.8	0.09	**1053.8**	***34.0***
91500_20	0.81	1011	49	1057	32	1042	26	-4.6	-1.5	-0.002	1.20	0.1786	1.7	1059	32.4	0.4	3.8	0.10	**1059.6**	***32.4***
91500_21	0.82	1084	42	1040	29	1054	24	4.0	1.3	0.002	1.05	0.1747	1.5	1038	29.0	0.4	3.8	0.10	**1038.4**	***29.0***
91500_22	0.80	1102	45	1064	29	1076	25	3.4	1.1	0.002	1.13	0.1792	1.5	1063	29.1	0.4	3.8	0.10	**1062.8**	***29.1***
91500_23	0.86	1062	40	1042	31	1049	25	1.9	0.6	0.001	0.98	0.1754	1.6	1042	31.2	0.4	3.8	0.10	**1041.8**	***31.2***
91500_24	0.80	1084	45	1055	29	1064	24	2.7	0.9	0.001	1.11	0.1775	1.5	1053	28.8	0.4	3.8	0.10	**1053.7**	***28.8***
91500_25	0.84	1067	36	1046	27	1052	22	2.0	0.6	0.001	0.90	0.1759	1.4	1045	27.3	0.4	3.8	0.10	**1045.1**	***27.3***
91500_26	0.76	1068	47	1070	27	1069	23	-0.2	-0.1	0.000	1.16	0.1806	1.4	1070	26.6	0.4	3.8	0.10	**1070.7**	***26.6***
91500_01	0.85	1049	42	1058	33	1054	26	-0.8	-0.3	0.000	1.05	0.1784	1.7	1058	32.8	0.4	3.8	0.11	**1058.2**	***32.8***
91500_02	0.85	1042	41	1086	33	1071	26	-4.2	-1.4	-0.002	1.02	0.1838	1.7	1088	33.6	0.4	3.8	0.11	**1087.8**	***33.6***
91500_03	0.78	1070	49	1069	30	1069	25	0.1	0.0	0.000	1.22	0.1804	1.5	1069	29.9	0.4	3.8	0.11	**1069.4**	***29.9***
91500_04	0.85	1061	40	1054	32	1056	25	0.6	0.2	0.000	0.99	0.1776	1.6	1054	31.7	0.4	3.8	0.11	**1054.2**	***31.7***
91500_05	0.87	1024	43	1067	37	1053	28	-4.2	-1.4	-0.002	1.07	0.1804	1.9	1069	36.8	0.4	3.8	0.11	**1069.2**	***36.8***
91500_06	0.89	1064	37	1079	37	1074	27	-1.5	-0.5	-0.001	0.93	0.1824	1.8	1080	36.6	0.4	3.8	0.10	**1080.5**	***36.6***
91500_07	0.84	1069	42	1066	32	1067	25	0.3	0.1	0.000	1.04	0.1799	1.6	1066	31.9	0.4	3.8	0.11	**1066.6**	***31.9***
91500_08	0.79	1063	57	1037	34	1045	29	2.4	0.8	0.001	1.41	0.1744	1.8	1036	34.3	0.3	3.8	0.09	**1036.4**	***34.3***
91500_09	0.76	1089	56	1054	32	1065	28	3.2	1.0	0.002	1.41	0.1774	1.7	1053	32.3	0.4	3.8	0.09	**1053.2**	***32.3***
91500_10	0.76	1116	63	1049	35	1070	31	6.1	2.0	0.003	1.58	0.1761	1.8	1046	35.0	0.4	3.8	0.09	**1045.8**	***35.0***
91500_11	0.80	1140	52	1038	33	1071	28	8.9	3.1	0.005	1.31	0.1739	1.7	1034	32.7	0.3	3.8	0.09	**1033.8**	***32.7***
91500_12	0.81	1052	46	1062	31	1058	25	-0.9	-0.3	0.000	1.14	0.1791	1.6	1062	30.7	0.3	3.8	0.09	**1062.3**	***30.7***
91500_13	0.81	1051	46	1070	32	1063	26	-1.8	-0.6	-0.001	1.15	0.1807	1.6	1071	31.8	0.3	3.8	0.09	**1070.9**	***31.8***
91500_14	0.81	1091	49	1071	33	1077	27	1.8	0.6	0.001	1.22	0.1806	1.7	1070	32.6	0.3	3.8	0.09	**1070.6**	***32.6***
GJ-1_01	0.80	613	42	588	15	593	14	4.0	0.8	0.001	0.97	0.0954	1.3	587	14.6	0.0	3.8	0.01	**587.6**	***14.6***
GJ-1_02	0.79	592	41	595	14	594	14	-0.6	-0.2	0.000	0.94	0.0967	1.2	595	13.6	0.0	3.8	0.01	**595.3**	***13.6***
GJ-1_03	0.71	610	52	597	14	600	15	2.0	0.4	0.000	1.21	0.0971	1.2	597	13.9	0.0	3.8	0.01	**597.3**	***13.9***
GJ-1_04	0.77	653	46	578	14	593	15	11.5	2.6	0.003	1.07	0.0936	1.3	577	14.3	0.0	3.8	0.01	**576.7**	***14.3***
GJ-1_05	0.65	609	54	604	12	605	15	0.8	0.1	0.000	1.26	0.0982	1.1	604	12.5	0.0	3.8	0.01	**604.0**	***12.5***
GJ-1_06	0.72	589	49	587	13	587	14	0.3	0.0	0.000	1.13	0.0953	1.2	587	13.1	0.0	3.8	0.01	**587.2**	***13.1***
GJ-1_07	0.77	614	46	586	14	591	15	4.7	1.0	0.001	1.06	0.0950	1.3	585	14.1	0.0	3.8	0.01	**585.2**	***14.1***
GJ-1_08	0.75	606	48	608	15	608	15	-0.3	-0.1	0.000	1.12	0.0989	1.3	608	14.6	0.0	3.8	0.01	**608.4**	***14.6***
GJ-1_09	0.84	603	35	589	14	592	13	2.2	0.4	0.000	0.81	0.0957	1.3	589	14.2	0.0	3.8	0.01	**589.1**	***14.2***
GJ-1_10	0.73	637	52	595	15	604	16	6.6	1.4	0.001	1.21	0.0966	1.3	595	14.7	0.0	3.8	0.01	**594.7**	***14.7***
GJ-1_11	0.79	605	43	593	15	595	15	2.0	0.4	0.000	1.00	0.0963	1.3	593	14.6	0.0	3.8	0.01	**592.8**	***14.6***
GJ-1_12	0.77	585	44	598	14	595	14	-2.1	-0.5	0.000	1.02	0.0972	1.2	598	14.0	0.0	3.8	0.01	**598.2**	***14.0***
GJ-1_13	0.73	634	51	607	15	613	16	4.2	0.9	0.001	1.19	0.0987	1.3	607	14.8	0.0	3.8	0.01	**606.7**	***14.8***
GJ-1_14	0.77	590	47	600	15	598	15	-1.7	-0.4	0.000	1.08	0.0976	1.3	600	14.8	0.0	3.8	0.01	**600.5**	***14.8***
GJ-1_15	0.77	635	41	604	13	611	14	4.9	1.1	0.001	0.95	0.0981	1.1	603	13.1	0.0	3.8	0.01	**603.7**	***13.1***
GJ-1_16	0.82	615	39	618	15	617	14	-0.5	-0.1	0.000	0.90	0.1007	1.3	618	15.0	0.0	3.8	0.01	**618.4**	***15.0***
GJ-1_17	0.77	596	46	617	15	612	15	-3.4	-0.7	-0.001	1.05	0.1004	1.3	617	14.9	0.0	3.8	0.01	**617.1**	***14.9***
GJ-1_18	0.74	624	48	599	14	604	15	3.9	0.8	0.001	1.11	0.0974	1.2	599	14.0	0.0	3.8	0.01	**599.2**	***14.0***
GJ-1_19	0.71	593	51	601	14	599	15	-1.4	-0.3	0.000	1.17	0.0978	1.2	602	13.6	0.0	3.8	0.01	**601.7**	***13.6***
GJ-1_20	0.79	637	41	596	14	605	14	6.3	1.4	0.001	0.95	0.0968	1.2	596	13.8	0.0	3.8	0.01	**595.8**	***13.8***
GJ-1_21	0.77	615	47	595	15	599	15	3.3	0.7	0.001	1.08	0.0967	1.3	595	14.8	0.0	3.8	0.01	**595.1**	***14.8***
GJ-1_22	0.78	575	53	593	17	589	17	-3.2	-0.7	-0.001	1.21	0.0965	1.5	594	17.4	0.0	3.8	0.01	**594.0**	***17.4***
GJ-1_23	0.81	607	44	602	16	603	16	0.9	0.2	0.000	1.02	0.0978	1.4	602	16.0	0.0	3.8	0.01	**601.9**	***16.0***
GJ-1_24	0.80	660	42	587	15	602	15	11.0	2.5	0.003	0.99	0.0951	1.3	586	14.5	0.0	3.8	0.01	**586.0**	***14.5***
GJ-1_25	0.81	613	41	591	15	595	14	3.6	0.7	0.001	0.94	0.0959	1.3	590	14.7	0.0	3.8	0.01	**590.7**	***14.7***
GJ-1_26	0.79	626	49	598	17	604	17	4.4	0.9	0.001	1.14	0.0972	1.5	598	16.8	0.0	3.8	0.01	**598.2**	***16.8***
GJ-1_01	0.84	615	45	600	18	603	17	2.5	0.5	0.001	1.05	0.0974	1.6	599	18.5	0.0	3.8	0.01	**599.4**	***18.5***
GJ-1_02	0.85	635	41	586	17	596	16	7.7	1.7	0.002	0.95	0.0950	1.5	585	16.9	0.0	3.8	0.01	**585.5**	***16.9***
GJ-1_03	0.85	602	41	594	17	596	16	1.3	0.2	0.000	0.95	0.0965	1.5	594	17.4	0.0	3.8	0.01	**594.3**	***17.4***
GJ-1_04	0.85	568	44	608	19	599	18	-6.9	-1.4	-0.001	1.02	0.0990	1.7	608	19.4	0.0	3.8	0.01	**608.5**	***19.4***
GJ-1_05	0.84	606	40	593	16	595	15	2.2	0.4	0.000	0.92	0.0963	1.4	592	16.1	0.0	3.8	0.01	**592.7**	***16.1***
GJ-1_06	0.84	617	41	608	17	610	16	1.5	0.3	0.000	0.95	0.0989	1.5	608	16.8	0.0	3.8	0.01	**608.1**	***16.8***
GJ-1_07	0.83	578	41	611	17	604	15	-5.8	-1.2	-0.001	0.95	0.0995	1.4	612	16.6	0.0	3.8	0.01	**612.0**	***16.6***
GJ-1_08	0.85	585	48	583	20	583	18	0.2	0.0	0.000	1.10	0.0947	1.8	583	19.6	0.0	3.8	0.01	**583.6**	***19.6***
GJ-1_09	0.83	591	52	583	19	584	19	1.4	0.3	0.000	1.19	0.0946	1.7	583	19.3	0.0	3.8	0.01	**582.8**	***19.3***
GJ-1_10	0.84	643	47	587	19	598	18	8.8	1.9	0.002	1.09	0.0951	1.7	586	18.9	0.0	3.8	0.01	**585.8**	***18.9***
GJ-1_11	0.83	583	45	599	18	596	17	-2.8	-0.6	-0.001	1.03	0.0975	1.6	600	17.9	0.0	3.8	0.01	**600.0**	***17.9***
GJ-1_12	0.83	645	45	592	17	603	17	8.2	1.8	0.002	1.05	0.0961	1.5	591	17.3	0.0	3.8	0.01	**591.6**	***17.3***
GJ-1_13	0.81	616	52	594	19	599	18	3.5	0.7	0.001	1.21	0.0965	1.7	594	18.8	0.0	3.8	0.01	**594.3**	***18.8***
GJ-1_14	0.75	628	64	594	19	601	20	5.5	1.2	0.001	1.49	0.0964	1.7	593	19.1	0.0	3.8	0.01	**593.2**	***19.1***
Ples_01	0.79	376	39	333	7	338	8	11.5	1.6	0.001	0.86	0.0530	1.1	333	7.2	0.1	3.8	0.02	**332.8**	***7.2***
Ples_02	0.78	350	41	341	8	342	8	2.6	0.3	0.000	0.92	0.0543	1.1	341	7.6	0.1	3.8	0.02	**341.0**	***7.6***
Ples_03	0.79	362	38	333	7	337	8	7.9	1.0	0.001	0.84	0.0530	1.1	333	6.9	0.1	3.8	0.03	**333.0**	***6.9***
Ples_04	0.77	339	51	336	9	336	10	0.7	0.1	0.000	1.12	0.0536	1.4	336	9.0	0.1	3.8	0.03	**336.4**	***9.0***
Ples_05	0.74	439	42	344	7	356	8	21.8	3.5	0.003	0.95	0.0546	1.0	343	7.0	0.1	3.8	0.02	**342.8**	***7.0***
Ples_06	0.80	343	40	338	8	338	9	1.4	0.1	0.000	0.89	0.0538	1.2	338	7.9	0.1	3.8	0.02	**338.0**	***7.9***
Ples_07	0.78	347	41	345	8	345	8	0.6	0.0	0.000	0.90	0.0549	1.1	345	7.5	0.1	3.8	0.02	**344.9**	***7.5***
Ples_08	0.74	375	47	338	7	342	9	10.0	1.4	0.001	1.04	0.0537	1.1	337	7.4	0.1	3.8	0.02	**337.3**	***7.4***
Ples_09	0.84	348	35	335	8	336	8	3.9	0.5	0.000	0.78	0.0533	1.2	335	8.0	0.1	3.8	0.02	**334.9**	***8.0***
Ples_10	0.77	355	42	336	7	338	8	5.4	0.7	0.001	0.94	0.0534	1.1	335	7.3	0.1	3.8	0.02	**335.6**	***7.3***
Ples_11	0.76	377	39	335	7	340	8	11.1	1.5	0.001	0.86	0.0533	1.0	335	6.6	0.1	3.8	0.02	**334.8**	***6.6***
Ples_12	0.82	304	42	341	9	336	9	-12.2	-1.4	-0.001	0.92	0.0544	1.3	341	8.8	0.1	3.8	0.03	**341.4**	***8.8***
Ples_13	0.84	325	36	345	8	342	8	-6.3	-0.8	-0.001	0.78	0.0550	1.2	345	8.1	0.1	3.8	0.03	**345.5**	***8.1***
Ples_14	0.75	350	45	346	8	346	9	1.2	0.1	0.000	0.99	0.0551	1.1	346	7.6	0.1	3.8	0.03	**346.0**	***7.6***
Ples_15	0.81	364	37	351	8	353	8	3.4	0.4	0.000	0.81	0.0560	1.1	351	7.6	0.1	3.8	0.03	**351.5**	***7.6***
Ples_16	0.80	321	41	350	8	346	9	-9.0	-1.1	-0.001	0.91	0.0558	1.2	350	8.3	0.1	3.8	0.03	**350.0**	***8.3***
Ples_17	0.77	371	44	350	8	353	9	5.5	0.7	0.001	0.97	0.0558	1.2	350	8.1	0.1	3.8	0.03	**350.2**	***8.1***
Ples_18	0.80	377	37	335	7	340	8	11.2	1.5	0.001	0.81	0.0533	1.1	335	7.1	0.1	3.8	0.03	**334.9**	***7.1***
Ples_19	0.75	360	47	338	8	340	9	6.4	0.8	0.001	1.05	0.0537	1.2	337	7.8	0.1	3.8	0.03	**337.5**	***7.8***
Ples_20	0.76	352	42	342	7	343	8	2.9	0.3	0.000	0.92	0.0544	1.1	342	7.2	0.1	3.8	0.03	**341.9**	***7.2***
Ples_21	0.83	308	41	336	9	333	9	-9.2	-1.1	-0.001	0.91	0.0536	1.3	337	8.7	0.1	3.8	0.03	**336.9**	***8.7***
Ples_22	0.77	323	42	339	7	337	8	-4.8	-0.6	0.000	0.92	0.0540	1.1	339	7.4	0.1	3.8	0.03	**339.1**	***7.4***
Ples_23	0.77	337	43	329	7	330	8	2.2	0.2	0.000	0.94	0.0524	1.1	329	7.4	0.1	3.8	0.03	**329.1**	***7.4***
Ples_24	0.79	367	40	335	7	339	8	8.8	1.2	0.001	0.88	0.0532	1.1	334	7.3	0.1	3.8	0.03	**334.6**	***7.3***
Ples_25	0.74	373	46	337	7	342	9	9.6	1.3	0.001	1.03	0.0536	1.1	337	7.3	0.1	3.8	0.03	**336.9**	***7.3***
Ples_26	0.78	349	41	330	7	333	8	5.4	0.7	0.001	0.90	0.0526	1.1	330	7.3	0.1	3.8	0.03	**330.4**	***7.3***

Zircon

Spot	Date	comments	^{204}Pb	^{206}Pb	^{207}Pb	^{208}Pb	^{232}Th	^{238}U	Th/U	Pb ppm	Th ppm	U ppm	$^{238}U/^{206}Pb$	1s %	$^{207}Pb/^{206}Pb$	1s %	$^{207}Pb/^{235}U$	1s %	$^{206}Pb/^{238}U$	1s %
Ples_01	16/05/2018		115	308276	16465	11339	580880	6576407	0.1	36.2	99.5	707.8	18.7081	1.47	0.0539	0.90	0.3968	1.72	0.0535	1.47
Ples_02	16/05/2018		8	324601	17779	12690	604934	6838058	0.1	38.2	103.7	735.9	18.5433	1.65	0.0536	1.18	0.3983	2.03	0.0539	1.65
Ples_03	16/05/2018		39	297516	15777	8891	478306	6372788	0.1	34.7	82.0	685.9	18.6421	1.42	0.0523	0.96	0.3867	1.71	0.0536	1.42
Ples_04	16/05/2018		11	236062	13115	7661	317826	4878966	0.1	27.6	54.5	525.1	17.9348	1.55	0.0546	0.95	0.4196	1.82	0.0558	1.55
Ples_05	16/05/2018		94	444040	24219	15940	760459	9315054	0.1	52.1	130.3	1002.5	18.1008	1.45	0.0540	0.95	0.4115	1.74	0.0552	1.45
Ples_06	16/05/2018		31	289890	15490	9450	431543	5816871	0.1	33.9	74.0	626.0	17.5302	1.54	0.0528	0.87	0.4149	1.77	0.0570	1.54
Ples_07	16/05/2018		-18	103675	5671	2924	145702	2244701	0.1	12.1	25.0	241.6	18.2660	1.46	0.0538	1.09	0.4061	1.82	0.0547	1.46
Ples_08	16/05/2018		-15	338363	18019	8834	324308	7600245	0.1	39.3	55.6	818.0	19.1219	1.91	0.0532	1.43	0.3831	2.39	0.0523	1.91
Ples_09	16/05/2018		77	305986	16529	8171	292993	6510651	0.1	35.6	50.2	700.7	18.6134	2.08	0.0540	1.60	0.4001	2.62	0.0537	2.08
Ples_10	16/05/2018		4	392648	20871	14492	468618	8538069	0.1	46.1	80.3	918.9	18.9042	2.10	0.0528	1.71	0.3851	2.71	0.0529	2.10
Ples_11	16/05/2018		33	259528	13795	9113	400036	5801441	0.1	30.4	68.6	624.4	18.6688	1.53	0.0530	1.11	0.3911	1.89	0.0536	1.53
Ples_12	16/05/2018		253	302036	18568	12422	321416	6679709	0.1	35.8	55.1	718.9	18.3482	2.05	0.0593	1.22	0.4451	2.38	0.0545	2.05
Ples_13	16/05/2018		84	378469	21889	14389	425665	8084231	0.1	44.6	72.9	870.0	17.7817	1.82	0.0574	1.33	0.4445	2.26	0.0562	1.82
Ples_14	16/05/2018		123	410830	22618	16310	597711	9108950	0.1	48.4	102.4	980.3	18.5256	2.06	0.0534	1.36	0.3974	2.47	0.0540	2.06
0502_01b	14/05/2018	heavily discordant	-13	359279	19943	5545	217960	5309457	0.1	98.9	75.1	1350.2	12.6923	1.03	0.0554	0.82	0.6016	1.32	0.0788	1.03
0502_02a	14/05/2018	heavily discordant	31	222452	12414	2744	112824	6436942	0.0	61.1	38.9	1637.0	24.2581	2.27	0.0554	0.98	0.3149	2.48	0.0412	2.27
0502_12a	14/05/2018		-18	176708	9997	2869	107712	3143643	0.0	48.7	37.1	799.5	15.1761	1.24	0.0558	0.83	0.5067	1.49	0.0659	1.24
0502_18b	14/05/2018		-9	312927	17642	6494	244637	4663895	0.1	86.7	84.3	1186.1	12.6505	1.07	0.0561	0.75	0.6111	1.30	0.0790	1.07
0502_11a	14/05/2018		-12	56804	3214	4532	175275	861626	0.3	16.6	60.4	219.1	12.9072	1.40	0.0562	1.30	0.6002	1.91	0.0775	1.40
0502_12b	14/05/2018		58	266063	15261	7421	290982	4115191	0.1	74.2	100.3	1046.5	13.0630	1.17	0.0562	0.90	0.5932	1.48	0.0766	1.17
0502_06	14/05/2018		5	75280	4273	4184	164325	1138168	0.2	21.5	56.6	289.4	12.9090	1.18	0.0562	0.84	0.6003	1.45	0.0775	1.18
0502_02b	14/05/2018		-54	92594	5200	4561	172475	1406625	0.2	26.3	59.4	357.7	13.0449	1.26	0.0562	0.80	0.5941	1.49	0.0767	1.26
0502_20a	14/05/2018		-32	81794	4681	5225	198109	1216662	0.2	23.6	68.3	309.4	12.7002	1.23	0.0563	1.14	0.6109	1.67	0.0787	1.23
0502_13a	14/05/2018	heavily discordant	-26	75835	4265	1406	53851	3343818	0.0	21.0	18.6	850.4	38.2428	2.19	0.0563	1.09	0.2029	2.44	0.0261	2.19
0502_04	14/05/2018	heavily discordant	-21	488641	27549	7555	302729	9357033	0.0	134.7	104.3	2379.6	16.3014	1.21	0.0563	0.75	0.4763	1.42	0.0613	1.21
0502_15a	14/05/2018		52	125413	7183	5693	216072	1852267	0.2	35.6	74.5	471.1	12.3975	1.37	0.0566	0.93	0.6292	1.65	0.0807	1.37
0502_08a	14/05/2018		46	202371	11446	7526	300521	3082400	0.1	56.9	103.6	783.9	13.0715	1.20	0.0566	0.77	0.5972	1.43	0.0765	1.20
0502_16	14/05/2018		-23	59602	3352	3373	126198	899902	0.2	17.1	43.5	228.9	13.1569	1.29	0.0568	0.97	0.5949	1.62	0.0760	1.29
0502_20b	14/05/2018		21	115161	6559	3609	136569	1761918	0.1	32.2	47.1	448.1	13.1189	1.12	0.0568	0.96	0.5968	1.48	0.0762	1.12
0502_17a	14/05/2018		-50	364051	20735	6547	253230	5904305	0.1	100.6	87.3	1501.5	13.7218	1.83	0.0569	0.82	0.5712	2.00	0.0729	1.83
0502_14b	14/05/2018		36	73215	4180	2886	107580	1096371	0.1	20.6	37.1	278.8	12.7772	1.34	0.0569	1.06	0.6141	1.71	0.0783	1.34
0502_03	14/05/2018		-11	217326	12450	5312	204951	3226248	0.1	60.4	70.6	820.5	12.7056	1.18	0.0569	0.65	0.6177	1.35	0.0787	1.18
0502_01a	14/05/2018		96	106021	6048	6061	244901	1574533	0.2	30.4	84.4	400.4	12.5753	1.12	0.0570	0.82	0.6250	1.39	0.0795	1.12
0502_10	14/05/2018		-9	359059	20510	4787	183743	5532295	0.0	98.8	63.3	1406.9	13.1441	1.19	0.0574	0.71	0.6014	1.38	0.0761	1.19
0502_19	14/05/2018		-51	40440	2326	3096	121099	615615	0.3	11.8	41.7	156.6	12.8806	1.39	0.0574	1.24	0.6143	1.86	0.0776	1.39
0502_07	14/05/2018		-8	419975	24125	6551	255704	6448482	0.1	115.9	88.1	1639.9	13.0534	1.23	0.0577	0.76	0.6090	1.44	0.0766	1.23
0502_11b	14/05/2018		-3	47622	2712	5241	209950	710641	0.4	14.3	72.4	180.7	12.6601	1.31	0.0577	1.38	0.6280	1.91	0.0790	1.31
0502_05	14/05/2018	heavily discordant	-30	60089	3521	3104	116085	925515	0.2	17.2	40.0	235.4	13.1495	1.27	0.0581	1.09	0.6088	1.67	0.0760	1.27
0502_09	14/05/2018	heavily discordant	18	99018	5784	6015	217934	1507687	0.2	28.5	75.1	383.4	13.1060	1.23	0.0589	1.28	0.6199	1.77	0.0763	1.23
0502_08a	14/05/2018	heavily discordant	-10	76347	4525	4511	170492	1165264	0.2	22.0	58.8	296.3	12.9685	1.31	0.0597	1.06	0.6340	1.69	0.0771	1.31
0502_20c	14/05/2018	heavily discordant	-2	49490	3043	26845	1017787	757363	1.8	20.4	350.7	192.6	12.8908	1.41	0.0609	1.49	0.6510	2.05	0.0776	1.41
0502_14a	14/05/2018	heavily discordant	72	165210	11088	5983	102707	4392177	0.0	46.9	35.4	1117.0	23.1207	1.78	0.0653	1.18	0.3893	2.13	0.0433	1.78
0502_18a	14/05/2018	Inherited	-38	136952	10006	18254	347061	984306	0.5	42.5	119.6	250.3	6.1817	1.35	0.0732	0.92	1.6327	1.63	0.1618	1.35
0502_02c	14/05/2018	Inherited	-1	590083	47311	193629	2906578	4021992	1.0	213.7	1001.6	1022.8	5.7142	1.89	0.0794	0.68	1.9144	2.01	0.1750	1.89
0502_13b	14/05/2018	Inherited	99	68206	5522	9529	150555	475229	0.4	21.4	51.9	120.9	5.9283	1.35	0.0809	0.96	1.8797	1.66	0.1687	1.35
0502_15b	14/05/2018	Inherited	-58	664833	81102	81243	790347	2540042	0.4	212.7	272.4	646.0	3.2386	1.15	0.1196	0.86	5.0909	1.44	0.3088	1.15
0502_17b	14/05/2018	Inherited	41	576880	95261	146220	1144429	1739347	0.9	210.4	394.4	442.3	2.5435	1.25	0.1625	0.82	8.8031	1.49	0.3932	1.25
~~0502_21~~	~~14/05/2018~~	~~rej - visible change in ratio~~	~~-9~~	~~42378~~	~~2506~~	~~4057~~	~~135541~~	~~1949647~~	~~0.1~~	~~12.6~~	~~46.7~~	~~495.8~~	~~35.1964~~	~~10.82~~	~~0.0638~~	~~2.85~~	~~0.2498~~	~~11.19~~	0.0284	~~10.82~~
0502_rim_14	16/05/2018		26	77901	3767	148	23704	12014150	0.0	8.8	4.1	1293.0	133.3722	1.53	0.0474	1.12	0.0490	1.89	0.0075	1.53
0502_rim_06	16/05/2018		-112	222691	11996	952	96072	33203840	0.0	25.4	16.5	3573.5	129.7370	4.14	0.0486	1.22	0.0516	4.32	0.0077	4.14
0502_rim_42	16/05/2018		-44	189825	9613	1358	82377	28645100	0.0	21.6	14.1	3082.9	128.0724	2.03	0.0498	1.93	0.0536	2.80	0.0078	2.03
0502_rim_49	16/05/2018		-4	346830	19708	8040	262605	24673000	0.0	40.3	45.0	2655.4	56.8271	5.88	0.0562	2.47	0.1362	6.38	0.0176	5.88
0502_rim_63	16/05/2018		87	175233	10271	7500	179456	10409300	0.0	20.8	30.8	1120.3	50.3906	1.65	0.0576	1.19	0.1575	2.03	0.0198	1.65
0502_rim_53	16/05/2018		34	381374	20981	6658	224189	20988030	0.0	44.0	38.4	2258.8	45.4023	7.68	0.0538	1.13	0.1633	7.77	0.0220	7.68
0502_rim_29	16/05/2018		-12	100151	6184	10306	232633	5077602	0.1	12.6	39.9	546.5	39.8232	7.92	0.0614	1.50	0.2126	8.06	0.0251	7.92
0502_rim_62	16/05/2018		30	240845	13260	8477	289855	9868556	0.0	28.3	49.7	1062.1	33.1016	3.83	0.0558	1.10	0.2323	3.98	0.0302	3.83
0502_rim_16	16/05/2018		41	280385	15761	5225	179538	11433990	0.0	32.4	30.8	1230.6	31.1973	8.24	0.0555	0.89	0.2450	8.29	0.0321	8.24
0502_rim_52	16/05/2018		17	605887	35003	9004	260853	20040280	0.0	69.9	44.7	2156.8	28.8133	4.15	0.0567	1.25	0.2712	4.34	0.0347	4.15
0502_rim_57	16/05/2018		-24	166051	9272	7029	227707	9386356	0.0	19.6	39.0	1010.2	25.1232	10.74	0.0557	1.69	0.3057	10.87	0.0398	10.74
0502_rim_39	16/05/2018		80	185348	10403	5873	212647	5520664	0.1	21.7	36.4	594.1	23.9109	6.41	0.0555	0.98	0.3197	6.48	0.0418	6.41
0502_rim_60	16/05/2018		52	409594	22848	6570	230131	11514660	0.0	47.3	39.4	1239.2	22.6973	4.84	0.0556	1.03	0.3379	4.94	0.0441	4.84
0502_rim_58	16/05/2018		24	669749	37384	20414	577131	15510160	0.1	78.3	98.9	1669.2	20.0015	4.99	0.0568	1.17	0.3913	5.13	0.0500	4.99
0502_rim_43	16/05/2018		59	369280	20976	6986	239206	8407458	0.0	42.8	41.0	904.8	19.4565	7.81	0.0565	0.98	0.4003	7.87	0.0514	7.81
0502_rim_12	16/05/2018		86	300847	17372	6868	243526	6980127	0.1	35.0	41.7	751.2	19.0384	5.11	0.0569	0.87	0.4119	5.19	0.0525	5.11
0502_rim_10	16/05/2018		64	419192	23839	9833	399180	9663481	0.1	48.7	68.4	1040.0	19.0079	5.37	0.0563	0.83	0.4085	5.43	0.0526	5.37
0502_rim_64	16/05/2018		112	261805	15411	12333	294629	5620961	0.1	31.2	50.5	604.9	17.4960	3.58	0.0577	1.45	0.4549	3.86	0.0572	3.58
0502_rim_19	16/05/2018		193	261510	17594	7173	217684	8481633	0.0	30.8	37.3	912.8	16.9671	7.52	0.0585	1.12	0.4755	7.60	0.0589	7.52
0502_rim_56	16/05/2018		32	335310	18947	9684	321656	7160314	0.1	39.2	55.1	770.6	16.7247	4.29	0.0565	1.05	0.4653	4.42	0.0598	4.29
0502_rim_01	16/05/2018		-11	588091	33376	11697	435945	11181400	0.1	68.1	74.7	1203.4	16.6054	7.10	0.0557	0.91	0.4625	7.16	0.0602	7.10
0502_rim_41	16/05/2018		2	830081	47518	17760	572081	14534400	0.1	96.4	98.0	1564.2	15.1150	2.07	0.0575	1.01	0.5242	2.30	0.0662	2.07
0502_rim_54	16/05/2018		62	1885267	107533	27819	886372	31641790	0.0	217.5	151.9	3405.4	14.9808	2.19	0.0570	0.99	0.5243	2.41	0.0668	2.19
0502_rim_02	16/05/2018		109	667346	38834	7407	278852	11495020	0.0	76.8	47.8	1237.1	14.9316	2.39	0.0567	0.91	0.5234	2.56	0.0670	2.39
0502_rim_45	16/05/2018		72	606059	34624	7974	233422	10587530	0.0	69.8	40.0	1139.5	14.8845	2.03	0.0570	1.18	0.5276	2.34	0.0672	2.03
0502_rim_18	16/05/2018		88	192186	11052	4386	158128	4086203	0.1	22.3	27.1	439.8	14.4750	5.22	0.0554	1.07	0.5278	5.33	0.0691	5.22
0502_rim_17	16/05/2018		103	643722	37627	5059	183606	10552910	0.0	73.9	31.5	1135.7	14.1551	2.81	0.0567	1.02	0.5518	2.99	0.0706	2.81
0502_rim_20	16/05/2018		-18	421465	24169	13493	492328	7094502	0.1	49.4	84.4	763.5	13.9851	2.68	0.0568	0.97	0.5598	2.84	0.0715	2.68
0502_rim_44	16/05/2018		39	283464	16175	9984	317816	4686444	0.1	33.3	54.5	504.4	13.8670	2.04	0.0566	1.21	0.5624	2.38	0.0721	2.04
0502_rim_33	16/05/2018		-63	184393	10605	11049	385721	2954452	0.2	22.2	66.1	318.0	13.8084	4.45	0.0567	1.12	0.5658	4.59	0.0724	4.45
0502_rim_47	16/05/2018		-29	783609	44404	5305	171594	12835070	0.0	89.7	29.4	1381.3	13.7185	2.04	0.0568	1.19	0.5708	2.36	0.0729	2.04
0502_rim_03	16/05/2018		44	563792	32355	5681	212192	8819345	0.0	64.8	36.4	949.2	13.6511	1.57	0.0569	0.97	0.5744	1.84	0.0733	1.57
0502_rim_51	16/05/2018		17	259499	14591	9450	303262	4221381	0.1	30.5	52.0	454.3	13.5406	2.33	0.0560	1.27	0.5695	2.65	0.0739	2.33
0502_rim_46	16/05/2018		-1	413619	23772	10607	349902	6508350	0.1	48.2	60.0	700.4	13.4659	1.60	0.0573	1.24	0.5861	2.02	0.0743	1.60
0502_rim_40	16/05/2018		77	278318	16165	10241	314327	4375679	0.1	32.8	53.9	470.9	13.4344	1.82	0.0576	1.32	0.5913	2.25	0.0744	1.82
0502_rim_25	16/05/2018		-10	134862	7719	8061	291480	2267052	0.2	16.2	50.0	244.0	13.4462	3.50	0.0569	1.13	0.5828	3.68	0.0744	3.50
0502_rim_48	16/05/2018		103	2791104	163500	7010	215770	43676450	0.0	318.8	37.0	4700.6	13.4361	1.65	0.0570	1.01	0.5849	1.93	0.0744	1.65
0502_rim_61	16/05/2018		29	343594	19661	9548	295055	5251777	0.1	40.1	50.6	565.2	13.3487	1.70	0.0569	1.16	0.5880	2.06	0.0749	1.70
0502_rim_15	16/05/2018		-77	117872	6704	6198	224137	1843445	0.2	14.1	38.4	198.4	13.3531	1.57	0.0559	0.91	0.5770	1.81	0.0749	1.57
0502_rim_09	16/05/2018		-15	158414	9053	4614	170680	2417510	0.1	18.5	29.3	260.2	13.2613	1.78	0.0563	0.90	0.5853	1.99	0.0754	1.78
0502_rim_50	16/05/2018		37	1014866	57967	14979	423584	15737190	0.0	117.1	72.6	1693.7	13.2473	1.59	0.0570	0.90	0.5929	1.83	0.0755	1.59
0502_rim_28	16/05/2018		73	161769	9402	4486	152596	2547314	0.1	18.9	26.2	274.1	13.2117	2.42	0.0573	1.10	0.5975	2.65	0.0757	2.42
0502_rim_35	16/05/2018		30	302707	17596	14431	515846	4609434	0.2	36.0	88.4	496.1	13.1979	1.73	0.0571	0.95	0.5963	1.97	0.0758	1.73
0502_rim_30	16/05/2018		95	380260	21394	6709	243203	6375261	0.1	44.0	41.7	686.1	13.2076	2.17	0.0553	0.86	0.5770	2.33	0.0757	2.17
0502_rim_23	16/05/2018		75	203970	12159	18630	538158	2984971	0.3	25.3	92.2	321.3	12.9728	4.56	0.0589	0.97	0.6260	4.66	0.0771	4.56
0502_rim_38	16/05/2018		-20	690891	39699	9025	325662	10305220	0.1	79.6	55.8	1109.1	12.9758	1.44	0.0566	0.87	0.6015	1.68	0.0771	1.44
0502_rim_04	16/05/2018		-35	540368	30649	3699	130926	7977234	0.0	61.9	22.4	858.5	12.9301	1.71	0.0564	0.92	0.6013	1.94	0.0773	1.71
0502_rim_21	16/05/2018		43	377719	20389	7920	285598	5690059	0.1	43.7	48.9	612.4	12.9332	1.77	0.0555	0.89	0.5911	1.98	0.0773	1.77
0502_rim_11	16/05/2018		53	588270	33686	11178	379970	8820794	0.1	68.1	65.1	949.3	12.9177	1.42	0.0559	0.85	0.5965	1.65	0.0774	1.42
0502_rim_34	16/05/2018		-50	133448	7714	6543	233765	1917588	0.2	15.9	40.1	206.4	12.8747	2.00	0.0565	1.10	0.6052	2.28	0.0777	2.00
0502_rim_27	16/05/2018		8	782301	44484	12515	438041	11779730	0.1	90.3	75.1	1267.8	12.8451	1.59	0.0567	0.88	0.6088	1.82	0.0779	1.59
0502_rim_08	16/05/2018		-10	98363	5734	8969	335432	1409768	0.4	12.2	57.5	151.7	12.7664	1.83	0.0577	0.99	0.6233	2.08	0.0783	1.83
0502_rim_07	16/05/2018		42	248536	14441	20561	730503	3636427	0.3	30.5	125.2	391.4	12.7771	1.43	0.0569	0.88	0.6138	1.68	0.0783	1.43
0502_rim_37	16/05/2018		-35	172394	9881	7258	265138	2569418	0.2	20.4	45.4	276.5	12.7762	1.42	0.0562	0.89	0.6060	1.68	0.0783	1.42
0502_rim_36	16/05/2018		4	473196	26891	6847	251110	7056470	0.1	54.6	43.0	759.4	12.7672	1.54	0.0557	0.87	0.6012	1.77	0.0783	1.54
0502_rim_26	16/05/2018		1	425138	23413	7936	277928	6243026	0.1	49.1	47.6	671.9	12.6765	1.36	0.0558	0.85	0.6068	1.61	0.0789	1.36
0502_rim_31	16/05/2018		-17	210794	12098	5193	181662	3078313	0.1	24.5	31.1	331.3	12.5769	1.54	0.0568	0.91	0.6227	1.79	0.0795	1.54
0502_rim_32	16/05/2018		142	414409	22927	16686	584123	5887237	0.2	48.9	100.1	633.6	12.4750	1.67	0.0562	1.04	0.6213	1.97	0.0802	1.67
0502_rim_13	16/05/2018		13	404900	22939	10604	392564	5882020	0.1	47.2	67.3	633.0	12.3144	1.55	0.0559	0.80	0.6256	1.75	0.0812	1.55
0502_rim_22	16/05/2018		51	423989	25644	14015	432184	5408333	0.1	49.9	74.1	582.1	11.7207	2.70	0.0592	1.01	0.6962	2.88	0.0853	2.70
0502_rim_59	16/05/2018		337	850468	60490	32513	521021	11385220	0.1	101.5	89.3	1225.3	10.6831	3.30	0.0705	1.36	0.9092	3.57	0.0936	3.30
0502_rim_05	16/05/2018		64	629917	43026	46603	868131	7997881	0.2	77.4	148.8	860.8	10.9637	4.42	0.0677	1.08	0.8507	4.55	0.0912	4.42
A03-12_01	14/05/2018		112	36600	1760	106	31440	6008708	0.0071	9.9	10.8	1528.1	137.3781	1.30	0.0480	1.20	0.0482	1.77	0.0073	1.30
A03-12_02	14/05/2018		-36	473	51	16	158	72441	0.0030	0.1	0.1	18.4	126.8910	4.43	0.1111	12.68	0.1207	13.43	0.0079	4.43
A03-12_03	14/05/2018		24	371	56	60	396	53082	0.0101	0.1	0.1	13.5	111.6845	4.51	0.1413	11.54	0.1744	12.39	0.0090	4.51

Zircon

Spot	Rho	$^{207}Pb/^{206}Pb$	2s abs	$^{206}Pb/^{238}U$	2s abs	$^{207}Pb/^{235}U$	2s abs	6-38/7-6	6-38/7-35	*f206*	1s %	$^{206}Pb^*/^{238}U$	1s %	206/238-Pb	2s [Ma]	Th/U min.	Th/U wr.	f	r. 206/238 a	*2s [Ma]*
Ples_01	0.85	365	41	336	10	339	10	8.1	1.1	0.001	0.90	0.0534	1.5	335	9.6	0.1	3.8	0.04	**335.6**	***9.6***
Ples_02	0.81	354	53	339	11	340	12	4.4	0.5	0.000	1.18	0.0539	1.7	338	10.9	0.1	3.8	0.04	**338.6**	***10.9***
Ples_03	0.83	299	44	337	9	332	10	-12.7	-1.5	-0.001	0.96	0.0537	1.4	337	9.3	0.1	3.8	0.03	**337.4**	***9.3***
Ples_04	0.85	396	43	350	11	356	11	11.7	1.7	0.001	0.95	0.0557	1.6	349	10.5	0.1	3.8	0.03	**349.5**	***10.5***
Ples_05	0.84	373	43	347	10	350	10	7.0	0.9	0.001	0.95	0.0552	1.4	346	9.8	0.1	3.8	0.03	**346.5**	***9.8***
Ples_06	0.87	319	39	358	11	352	10	-12.0	-1.5	-0.001	0.87	0.0571	1.5	358	10.7	0.1	3.8	0.03	**358.2**	***10.7***
Ples_07	0.80	364	49	344	10	346	11	5.6	0.7	0.001	1.09	0.0547	1.5	343	9.8	0.1	3.8	0.03	**343.5**	***9.8***
Ples_08	0.80	335	65	329	12	329	13	2.0	0.2	0.000	1.43	0.0523	1.9	329	12.3	0.1	3.8	0.02	**328.7**	***12.3***
Ples_09	0.79	372	72	337	14	342	15	9.4	1.3	0.001	1.60	0.0537	2.1	337	13.6	0.1	3.8	0.02	**337.2**	***13.6***
Ples_10	0.78	321	78	332	14	331	15	-3.4	-0.5	0.000	1.71	0.0529	2.1	332	13.6	0.1	3.8	0.02	**332.5**	***13.6***
Ples_11	0.81	328	50	336	10	335	11	-2.7	-0.4	0.000	1.11	0.0536	1.5	336	10.1	0.1	3.8	0.03	**336.6**	***10.1***
Ples_12	0.86	576	53	342	14	374	15	40.6	8.5	0.007	1.22	0.0541	2.0	340	13.4	0.1	3.8	0.02	**339.8**	***13.4***
Ples_13	0.81	505	58	353	13	373	14	30.2	5.6	0.005	1.33	0.0560	1.8	351	12.4	0.1	3.8	0.02	**351.2**	***12.4***
Ples_14	0.83	347	62	339	14	340	14	2.2	0.3	0.000	1.36	0.0540	2.1	339	13.6	0.1	3.8	0.03	**339.0**	***13.6***
0502_01b	0.78	429	36	489	10	478	10	-14.1	-2.2	-0.002	0.82	0.0789	1.0	490	9.8	0.1	3.8	0.01	**490.0**	***9.8***
0502_02a	0.92	430	44	260	12	278	12	39.4	6.3	0.005	0.98	0.0410	2.3	259	11.5	0.0	3.8	0.01	**259.3**	***11.5***
0502_12a	0.83	444	37	411	10	416	10	7.4	1.2	0.001	0.83	0.0658	1.2	411	9.8	0.0	3.8	0.01	**411.1**	***9.8***
0502_18b	0.82	456	33	490	10	484	10	-7.5	-1.3	-0.001	0.75	0.0791	1.1	491	10.1	0.1	3.8	0.02	**491.1**	***10.1***
0502_11a	0.73	461	57	481	13	477	14	-4.4	-0.8	-0.001	1.30	0.0775	1.4	481	13.0	0.3	3.8	0.07	**481.5**	***13.0***
0502_12b	0.79	461	40	476	11	473	11	-3.1	-0.6	0.000	0.90	0.0766	1.2	476	10.7	0.1	3.8	0.03	**475.9**	***10.7***
0502_06	0.81	461	37	481	11	477	11	-4.3	-0.7	-0.001	0.84	0.0775	1.2	481	10.9	0.2	3.8	0.05	**481.4**	***10.9***
0502_02b	0.84	462	35	476	12	474	11	-3.1	-0.6	0.000	0.80	0.0767	1.3	476	11.5	0.2	3.8	0.04	**476.5**	***11.5***
0502_20a	0.73	464	50	489	12	484	13	-5.3	-0.9	-0.001	1.14	0.0788	1.2	489	11.5	0.2	3.8	0.06	**489.1**	***11.5***
0502_13a	0.90	464	48	166	7	188	8	64.1	11.3	0.009	1.09	0.0259	2.2	165	7.1	0.0	3.8	0.01	**165.1**	***7.1***
0502_04	0.85	466	33	384	9	396	9	17.6	3.0	0.003	0.75	0.0612	1.2	383	8.9	0.0	3.8	0.01	**383.0**	***8.9***
0502_15a	0.83	476	41	500	13	496	13	-5.1	-0.9	-0.001	0.93	0.0807	1.4	500	13.2	0.2	3.8	0.04	**500.6**	***13.2***
0502_08a	0.84	478	34	475	11	475	11	0.5	0.1	0.000	0.77	0.0765	1.2	475	11.0	0.1	3.8	0.03	**475.3**	***11.0***
0502_16	0.80	483	43	472	12	474	12	2.3	0.4	0.000	0.97	0.0760	1.3	472	11.7	0.2	3.8	0.05	**472.2**	***11.7***
0502_20b	0.76	484	42	474	10	475	11	2.2	0.3	0.000	0.96	0.0762	1.1	473	10.2	0.1	3.8	0.03	**473.6**	***10.2***
0502_17a	0.91	486	36	453	16	459	15	6.8	1.2	0.001	0.82	0.0728	1.8	453	16.0	0.1	3.8	0.02	**453.2**	***16.0***
0502_14b	0.79	489	47	486	13	486	13	0.6	0.1	0.000	1.06	0.0783	1.3	486	12.5	0.1	3.8	0.03	**485.9**	***12.5***
0502_03	0.88	489	29	488	11	488	10	0.2	0.0	0.000	0.65	0.0787	1.2	488	11.1	0.1	3.8	0.02	**488.6**	***11.1***
0502_01a	0.81	493	36	493	11	493	11	-0.1	-0.1	0.000	0.82	0.0795	1.1	493	10.7	0.2	3.8	0.06	**493.4**	***10.7***
0502_10	0.86	505	31	473	11	478	10	6.4	1.1	0.001	0.71	0.0760	1.2	472	10.8	0.0	3.8	0.01	**472.4**	***10.8***
0502_19	0.75	507	54	482	13	486	14	5.0	0.9	0.001	1.24	0.0776	1.4	482	12.9	0.3	3.8	0.07	**481.8**	***12.9***
0502_07	0.85	518	33	476	11	483	11	8.1	1.5	0.001	0.76	0.0765	1.2	475	11.2	0.1	3.8	0.01	**475.4**	***11.2***
0502_11b	0.69	518	61	490	12	495	15	5.4	1.0	0.001	1.38	0.0789	1.3	490	12.4	0.4	3.8	0.11	**489.8**	***12.4***
0502_05	0.76	533	48	472	12	483	13	11.3	2.1	0.002	1.09	0.0759	1.3	472	11.5	0.2	3.8	0.04	**471.8**	***11.5***
0502_09	0.69	565	56	474	11	490	14	16.1	3.2	0.003	1.28	0.0761	1.2	473	11.2	0.2	3.8	0.05	**472.8**	***11.2***
0502_08a	0.78	591	46	479	12	499	13	19.0	4.0	0.004	1.06	0.0768	1.3	477	12.0	0.2	3.8	0.05	**477.3**	***12.0***
0502_20c	0.69	635	64	482	13	509	16	24.2	5.4	0.005	1.49	0.0772	1.4	479	12.9	1.8	3.8	0.48	**479.4**	***12.9***
0502_14a	0.83	784	49	273	10	334	12	65.2	18.2	0.017	1.18	0.0425	1.7	268	9.2	0.0	3.8	0.01	**268.5**	***9.2***
0502_18a	0.83	1020	37	967	24	983	20	5.3	1.7	0.002	0.92	0.1614	1.4	964	24.2	0.5	3.8	0.13	**964.7**	***24.2***
0502_02c	0.94	1182	27	1040	36	1086	27	12.0	4.3	0.007	0.68	0.1738	1.9	1033	35.8	1.0	3.8	0.26	**1033.4**	***35.8***
0502_13b	0.81	1218	38	1005	25	1074	22	17.5	6.4	0.010	0.96	0.1670	1.3	995	24.6	0.4	3.8	0.11	**995.6**	***24.6***
0502_15b	0.80	1951	31	1735	35	1835	24	11.1	5.4	0.017	0.86	0.3035	1.1	1709	33.8	0.4	3.8	0.11	**1709.0**	***33.8***
0502_17b	0.84	2481	28	2137	45	2318	27	13.9	7.8	0.039	0.82	0.3780	1.2	2067	42.4	0.9	3.8	0.23	**2067.2**	***42.4***
~~0502_21~~	~~0.97~~	~~735~~	~~121~~	~~181~~	~~38~~	~~226~~	~~44~~	~~75.4~~	~~20.2~~	~~0.018~~	~~2.85~~	~~0.0279~~	~~10.6~~	~~177~~	~~37.1~~	~~0.1~~	3.8	~~0.02~~	~~**177.6**~~	~~***37.1***~~
0502_rim_14	0.81	70	53	48	1	49	2	31.2	0.8	0.001	1.12	0.0075	1.5	48	1.5	0.0	3.8	0.00	48.2	*1.5*
0502_rim_06	0.96	127	57	49	4	51	4	60.9	3.1	0.002	1.22	0.0077	4.1	49	4.1	0.0	3.8	0.00	**49.5**	***4.1***
0502_rim_42	0.72	184	90	50	2	53	3	72.8	5.3	0.003	1.93	0.0078	2.0	50	2.0	0.0	3.8	0.00	**50.1**	***2.0***
0502_rim_49	0.92	459	110	112	13	130	15	75.5	13.3	0.010	2.47	0.0174	5.8	111	12.8	0.0	3.8	0.00	**111.5**	***12.8***
0502_rim_63	0.81	514	52	127	4	148	6	75.3	14.7	0.011	1.19	0.0196	1.6	125	4.0	0.0	3.8	0.01	**125.4**	***4.0***
0502_rim_53	0.99	363	51	140	21	154	22	61.3	8.6	0.006	1.13	0.0219	7.6	140	21.0	0.0	3.8	0.00	**139.7**	***21.0***
0502_rim_29	0.98	654	64	160	25	196	28	75.6	18.3	0.015	1.50	0.0247	7.8	157	24.2	0.1	3.8	0.02	**157.6**	***24.2***
0502_rim_62	0.96	444	49	192	14	212	15	56.8	9.5	0.007	1.10	0.0300	3.8	190	14.3	0.0	3.8	0.01	**190.6**	***14.3***
0502_rim_16	0.99	431	40	203	33	222	33	52.8	8.6	0.007	0.89	0.0318	8.2	202	32.5	0.0	3.8	0.01	**202.2**	***32.5***
0502_rim_52	0.96	480	55	220	18	244	19	54.2	9.7	0.008	1.25	0.0344	4.1	218	17.7	0.0	3.8	0.01	**218.4**	***17.7***
0502_rim_57	0.99	441	75	252	53	271	50	43.0	7.1	0.006	1.69	0.0396	10.7	250	52.2	0.0	3.8	0.01	**250.4**	***52.2***
0502_rim_39	0.99	431	44	264	33	282	31	38.8	6.2	0.005	0.98	0.0416	6.4	263	32.8	0.1	3.8	0.02	**263.0**	***32.8***
0502_rim_60	0.98	438	46	278	26	296	25	36.6	6.0	0.005	1.03	0.0438	4.8	277	26.0	0.0	3.8	0.01	**276.8**	***26.0***
0502_rim_58	0.97	483	52	314	31	335	29	34.9	6.2	0.005	1.17	0.0497	5.0	313	30.3	0.1	3.8	0.02	**313.1**	***30.3***
0502_rim_43	0.99	473	43	323	49	342	45	31.6	5.5	0.005	0.98	0.0512	7.8	322	48.6	0.0	3.8	0.01	**321.8**	***48.6***
0502_rim_12	0.99	488	38	330	33	350	30	32.4	5.8	0.005	0.87	0.0523	5.1	328	32.5	0.1	3.8	0.01	**328.6**	***32.5***
0502_rim_10	0.99	466	37	331	35	348	32	29.1	5.0	0.004	0.83	0.0524	5.3	329	34.2	0.1	3.8	0.02	**329.3**	***34.2***
0502_rim_64	0.93	520	64	358	25	381	24	31.1	5.9	0.005	1.45	0.0569	3.6	357	24.6	0.1	3.8	0.02	**356.7**	***24.6***
0502_rim_19	0.99	550	49	369	54	395	49	32.9	6.5	0.006	1.12	0.0586	7.5	367	53.1	0.0	3.8	0.01	**367.3**	***53.1***
0502_rim_56	0.97	471	46	374	31	388	28	20.5	3.5	0.003	1.05	0.0596	4.3	373	31.0	0.1	3.8	0.02	**373.4**	***31.0***
0502_rim_01	0.99	441	41	377	52	386	45	14.6	2.3	0.002	0.91	0.0601	7.1	376	51.6	0.1	3.8	0.02	**376.4**	***51.6***
0502_rim_41	0.90	510	44	413	17	428	16	19.1	3.5	0.003	1.01	0.0660	2.1	412	16.4	0.1	3.8	0.02	**411.9**	***16.4***
0502_rim_54	0.91	491	44	417	18	428	17	15.2	2.7	0.002	0.99	0.0666	2.2	416	17.6	0.0	3.8	0.01	**415.8**	***17.6***
0502_rim_02	0.93	480	40	418	19	427	18	13.0	2.2	0.002	0.91	0.0668	2.4	417	19.2	0.0	3.8	0.01	**417.3**	***19.2***
0502_rim_45	0.86	491	52	419	16	430	16	14.6	2.6	0.002	1.18	0.0670	2.0	418	16.4	0.0	3.8	0.01	**418.4**	***16.4***
0502_rim_18	0.98	430	48	431	43	430	37	-0.2	-0.1	0.000	1.07	0.0691	5.2	431	43.3	0.1	3.8	0.02	**430.8**	***43.3***
0502_rim_17	0.94	479	45	440	24	446	21	8.1	1.4	0.001	1.02	0.0706	2.8	440	23.8	0.0	3.8	0.01	**439.7**	***23.8***
0502_rim_20	0.94	484	43	445	23	451	21	8.0	1.4	0.001	0.97	0.0714	2.7	445	22.9	0.1	3.8	0.03	**444.9**	***22.9***
0502_rim_44	0.86	475	54	449	18	453	17	5.6	0.9	0.001	1.21	0.0721	2.0	449	17.7	0.1	3.8	0.03	**448.7**	***17.7***
0502_rim_33	0.97	479	50	451	39	455	33	6.0	1.0	0.001	1.12	0.0724	4.4	450	38.6	0.2	3.8	0.05	**450.5**	***38.6***
0502_rim_47	0.86	484	52	454	18	459	17	6.4	1.1	0.001	1.19	0.0728	2.0	453	17.8	0.0	3.8	0.01	**453.3**	***17.8***
0502_rim_03	0.85	487	43	456	14	461	14	6.5	1.1	0.001	0.97	0.0732	1.6	455	13.7	0.0	3.8	0.01	**455.5**	***13.7***
0502_rim_51	0.88	450	56	459	21	458	19	-2.0	-0.4	0.000	1.27	0.0739	2.3	459	20.6	0.1	3.8	0.03	**459.6**	***20.6***
0502_rim_46	0.79	502	54	462	14	468	15	8.0	1.4	0.001	1.24	0.0742	1.6	461	14.2	0.1	3.8	0.02	**461.4**	***14.2***
0502_rim_40	0.81	516	58	463	16	472	17	10.3	1.9	0.002	1.32	0.0743	1.8	462	16.2	0.1	3.8	0.03	**462.2**	***16.2***
0502_rim_25	0.95	486	50	462	31	466	27	4.9	0.8	0.001	1.13	0.0743	3.5	462	31.1	0.2	3.8	0.05	**462.3**	***31.1***
0502_rim_48	0.85	492	45	463	15	468	14	6.0	1.0	0.001	1.01	0.0744	1.6	462	14.7	0.0	3.8	0.00	**462.5**	***14.7***
0502_rim_61	0.82	490	51	466	15	470	15	4.9	0.8	0.001	1.16	0.0749	1.7	465	15.2	0.1	3.8	0.02	**465.5**	***15.2***
0502_rim_15	0.86	448	41	466	14	462	13	-3.8	-0.7	-0.001	0.91	0.0749	1.6	466	14.1	0.2	3.8	0.05	**466.0**	***14.1***
0502_rim_09	0.89	465	40	469	16	468	15	-0.8	-0.2	0.000	0.90	0.0754	1.8	469	16.1	0.1	3.8	0.03	**468.9**	***16.1***
0502_rim_50	0.87	491	40	469	14	473	14	4.5	0.8	0.001	0.90	0.0754	1.6	469	14.4	0.0	3.8	0.01	**469.0**	***14.4***
0502_rim_28	0.91	502	48	470	22	476	20	6.4	1.1	0.001	1.10	0.0756	2.4	470	21.8	0.1	3.8	0.03	**470.1**	***21.8***
0502_rim_35	0.88	495	42	471	16	475	15	5.0	0.9	0.001	0.95	0.0757	1.7	470	15.7	0.2	3.8	0.05	**470.6**	***15.7***
0502_rim_30	0.93	424	38	470	20	463	17	-10.9	-1.7	-0.001	0.86	0.0758	2.2	471	19.7	0.1	3.8	0.02	**471.3**	***19.7***
0502_rim_23	0.98	564	42	479	42	494	36	15.2	3.0	0.003	0.97	0.0769	4.5	477	41.7	0.3	3.8	0.08	**477.6**	***41.7***
0502_rim_38	0.85	477	39	479	13	478	13	-0.3	-0.1	0.000	0.87	0.0771	1.4	479	13.2	0.1	3.8	0.01	**478.8**	***13.2***
0502_rim_04	0.88	469	41	480	16	478	15	-2.4	-0.4	0.000	0.92	0.0774	1.7	480	15.8	0.0	3.8	0.01	**480.6**	***15.8***
0502_rim_21	0.89	431	40	480	16	472	15	-11.3	-1.8	-0.002	0.89	0.0774	1.8	481	16.4	0.1	3.8	0.02	**481.0**	***16.4***
0502_rim_11	0.86	449	38	481	13	475	12	-7.1	-1.2	-0.001	0.85	0.0775	1.4	481	13.1	0.1	3.8	0.02	**481.3**	***13.1***
0502_rim_34	0.88	474	49	482	19	481	17	-1.8	-0.3	0.000	1.10	0.0777	2.0	482	18.5	0.2	3.8	0.05	**482.5**	***18.5***
0502_rim_27	0.88	482	39	483	15	483	14	-0.3	-0.1	0.000	0.88	0.0779	1.6	483	14.8	0.1	3.8	0.02	**483.5**	***14.8***
0502_rim_08	0.88	520	43	486	17	492	16	6.5	1.2	0.001	0.99	0.0782	1.8	486	17.1	0.4	3.8	0.10	**485.8**	***17.1***
0502_rim_07	0.85	488	39	486	13	486	13	0.4	0.0	0.000	0.88	0.0783	1.4	486	13.4	0.3	3.8	0.08	**485.9**	***13.4***
0502_rim_37	0.85	460	39	486	13	481	13	-5.7	-1.0	-0.001	0.89	0.0783	1.4	486	13.3	0.2	3.8	0.04	**486.4**	***13.3***
0502_rim_36	0.87	440	39	486	14	478	13	-10.5	-1.7	-0.001	0.87	0.0784	1.5	487	14.5	0.1	3.8	0.01	**487.0**	***14.5***
0502_rim_26	0.85	445	38	489	13	482	12	-10.0	-1.6	-0.001	0.85	0.0790	1.4	490	12.9	0.1	3.8	0.02	**490.3**	***12.9***
0502_rim_31	0.86	485	40	493	15	492	14	-1.7	-0.3	0.000	0.91	0.0795	1.5	493	14.7	0.1	3.8	0.02	**493.5**	***14.7***
0502_rim_32	0.85	462	46	497	16	491	15	-7.6	-1.3	-0.001	1.04	0.0803	1.7	498	16.0	0.2	3.8	0.04	**497.8**	***16.0***
0502_rim_13	0.89	448	36	503	15	493	14	-12.2	-2.0	-0.002	0.80	0.0813	1.6	504	15.1	0.1	3.8	0.03	**504.3**	***15.1***
0502_rim_22	0.94	575	44	528	27	536	24	8.2	1.6	0.002	1.01	0.0852	2.7	527	27.3	0.1	3.8	0.03	**527.2**	***27.3***
0502_rim_59	0.92	942	56	577	36	657	34	38.8	12.2	0.014	1.36	0.0923	3.3	569	35.4	0.1	3.8	0.02	**569.3**	***35.4***
0502_rim_05	0.97	859	45	563	47	625	42	34.5	10.0	0.011	1.08	0.0902	4.4	557	46.4	0.2	3.8	0.05	**557.0**	***46.4***
A03-12_01	0.73	100	57	47	1	48	2	53.5	2.1	0.001	1.20	0.0073	1.3	47	1.2	0.0	3.8	0.00	**46.8**	***1.2***
A03-12_02	0.33	1817	460	51	4	116	29	97.2	56.2	0.081	12.68	0.0072	4.2	47	3.9	0.0	3.8	0.00	**46.6**	***3.9***
A03-12_03	0.36	2243	399	57	5	163	37	97.4	64.8	0.119	11.54	0.0079	4.2	51	4.2	0.0	3.8	0.00	**50.8**	***4.2***

Zircon

Spot	Date	comments	^{204}Pb	^{206}Pb	^{207}Pb	^{208}Pb	^{232}Th	^{238}U	Th/U	Pb ppm	Th ppm	U ppm	$^{238}U/^{206}Pb$	1s %	$^{207}Pb/^{206}Pb$	1s %	$^{207}Pb/^{235}U$	1s %	$^{206}Pb/^{238}U$	1s %
A03-12_04	14/05/2018		29	1064	100	23	344	162408	0.0029	0.3	0.1	41.3	127.9610	3.22	0.0935	7.15	0.1007	7.84	0.0078	3.22
A03-12_06	14/05/2018		-104	13305	647	25	3049	2115142	0.0020	3.6	1.1	537.9	134.5214	1.49	0.0476	2.29	0.0488	2.73	0.0074	1.49
A03-12_08	14/05/2018		109	653	71	145	15216	82810	0.2490	0.2	5.2	21.1	102.7341	3.60	0.0938	13.40	0.1258	13.88	0.0097	3.60
A03-12_09	14/05/2018		38	822	67	-18	306	130448	0.0032	0.2	0.1	33.2	131.4298	3.35	0.0707	9.02	0.0741	9.62	0.0076	3.35
A03-12_10	14/05/2018		-92	9640	467	3	7844	1502395	0.0071	2.6	2.7	382.1	133.1604	1.51	0.0495	2.43	0.0513	2.86	0.0075	1.51
A03-12_11	14/05/2018		-65	557	53	53	291	84982	0.0046	0.2	0.1	21.6	128.0577	4.61	0.0984	11.01	0.1059	11.93	0.0078	4.61
A03-12_12	14/05/2018		-93	13723	664	20	16760	2162688	0.0105	3.7	5.8	550.0	134.0154	1.31	0.0479	1.96	0.0493	2.36	0.0075	1.31
~~A03-12_05~~	14/05/2018	~~rej - low Pb counts~~	~~0~~	~~42~~	~~5~~	~~2~~	~~15~~	~~5025~~	~~0.0~~	~~0.0~~	~~0.0~~	~~1.3~~	~~146.8344~~	~~28.38~~	~~0.1577~~	~~130.89~~	~~0.1480~~	~~133.93~~	0.0068	~~28.38~~
~~A03-12_07~~	14/05/2018	~~rej - low Pb counts~~	~~1~~	~~150~~	~~33~~	~~-3~~	~~105~~	~~19181~~	~~0.0~~	~~0.0~~	~~0.0~~	~~4.9~~	~~97.6370~~	~~13.36~~	~~0.1450~~	~~40.35~~	~~0.2046~~	~~42.50~~	0.0102	~~13.36~~
~~A03-12_13~~	14/05/2018	~~rej - low Pb counts~~	~~-62~~	~~51~~	~~25~~	~~-33~~	~~32~~	~~4987~~	~~0.0~~	~~0.0~~	~~0.0~~	~~1.3~~	~~82.9056~~	~~35.14~~	~~0.1992~~	~~55.37~~	~~0.3311~~	~~65.58~~	0.0121	~~35.14~~
A04-15_01	14/05/2018		21	40599	3065	1186	11973	371870	0.0	11.5	4.1	94.6	9.3726	6.13	0.0787	1.73	1.1575	6.37	0.1067	6.13
A04-15_02	14/05/2018		13	320226	20619	2835	89548	4289821	0.0	88.4	30.9	1090.9	11.2198	1.36	0.0642	0.80	0.7891	1.58	0.0891	1.36
A04-15_03	14/05/2018		74	467983	32953	5687	135928	4154566	0.0	130.3	46.8	1056.5	7.5779	1.32	0.0704	0.86	1.2799	1.58	0.1320	1.32
A04-28_01	14/05/2018		-20	43239	2450	2263	85856	713649	0.2	12.3	29.6	181.5	13.9918	1.36	0.0572	1.48	0.5636	2.01	0.0715	1.36
A04-28_02a	14/05/2018		123	3203	200	245	199468	1751908	0.2	0.9	68.7	445.5	454.4449	1.77	0.0621	4.36	0.0188	4.70	0.0022	1.77
A04-28_02b	14/05/2018		19	3014	197	268	164920	1469374	0.2	0.9	56.8	373.7	422.3446	1.64	0.0635	5.03	0.0207	5.30	0.0024	1.64
A04-28_03a	14/05/2018		24	42569	3051	5662	155845	616236	0.3	13.2	53.7	156.7	12.5767	1.50	0.0715	2.89	0.7834	3.26	0.0795	1.50
A04-28_03b	14/05/2018		8	85438	4947	1003	34141	1327519	0.0	23.5	11.8	337.6	13.2847	1.51	0.0571	1.17	0.5928	1.91	0.0753	1.51
A04-28_04a	14/05/2018		19	2736	162	101	2343	470529	0.0	0.8	0.8	119.7	146.0080	1.72	0.0583	4.39	0.0550	4.71	0.0068	1.72
A04-28_04b	14/05/2018		-81	84333	4629	19733	2916954	6781066	0.6	27.9	1005.2	1724.5	65.0487	2.92	0.0552	1.11	0.1170	3.13	0.0154	2.92
A04-28_05	14/05/2018		6	96354	5555	2119	81906	1455508	0.1	26.7	28.2	370.2	12.7641	1.29	0.0566	1.29	0.6110	1.82	0.0783	1.29
A12-14_01	14/05/2018		-6	31399	2780	4004	45626	252486	0.2	9.8	15.7	64.2	6.8945	1.60	0.0829	2.78	1.6575	3.21	0.1450	1.60
A12-14_02a	14/05/2018		146	280705	45714	3683	22302	741261	0.0	84.9	7.7	188.5	2.2440	1.54	0.1616	0.79	9.9262	1.73	0.4456	1.54
A12-14_02b	14/05/2018		28	70179	11728	12867	95634	183485	0.7	24.4	33.0	46.7	2.2239	1.73	0.1649	0.97	10.2169	1.98	0.4497	1.73
A12-14_03	14/05/2018		50	21050	1799	6990	100883	118789	1.2	7.7	34.8	30.2	4.7652	2.33	0.0857	1.77	2.4776	2.93	0.2099	2.33
A12-14_05	14/05/2018		-9	96387	7126	29268	425962	757922	0.8	34.1	146.8	192.7	6.1749	2.67	0.0738	1.07	1.6472	2.88	0.1619	2.67
A12-14_06	14/05/2018		24	69835	4365	10070	302666	791954	0.5	21.7	104.3	201.4	9.6757	1.61	0.0626	1.20	0.8914	2.01	0.1034	1.61
A12-14_08	14/05/2018		86	221800	37555	32743	243895	569156	0.6	75.1	84.0	144.7	2.1650	1.42	0.1660	0.98	10.5701	1.72	0.4619	1.42
A12-14_10a	14/05/2018		25	164591	12022	10094	181760	1096213	0.2	48.0	62.6	278.8	5.6607	1.62	0.0723	0.93	1.7608	1.87	0.1767	1.62
A12-14_10b	14/05/2018		-16	205167	14929	13913	256522	1401513	0.2	60.2	88.4	356.4	5.7871	1.92	0.0722	1.04	1.7186	2.19	0.1728	1.92
A12-14_11	14/05/2018		83	68397	4180	43455	1375123	949821	2.0	29.8	473.9	241.5	11.3201	2.09	0.0607	0.98	0.7393	2.31	0.0883	2.09
A12-14_12	14/05/2018		82	101513	7168	19768	287716	730027	0.5	33.0	99.2	185.7	6.3359	2.13	0.0731	1.26	1.5898	2.47	0.1578	2.13
A12-14_13	14/05/2018		18	22052	2095	3981	38324	138113	0.4	7.2	13.2	35.1	5.2850	2.17	0.0988	1.98	2.5757	2.94	0.1892	2.17
A12-14_14	14/05/2018		1	217011	16046	3305	38579	1557493	0.0	60.8	13.3	396.1	5.8731	1.87	0.0738	1.10	1.7325	2.17	0.1703	1.87
A12-14_15	14/05/2018		36	444367	70256	17750	212735	2127785	0.1	136.9	73.3	541.1	4.2606	2.57	0.1611	1.11	5.2101	2.79	0.2347	2.57
A12-14_17	14/05/2018		17	394712	47531	10747	103280	1370062	0.1	116.5	35.6	348.4	2.9628	2.20	0.1194	1.01	5.5527	2.42	0.3375	2.20
A12-14_18	14/05/2018		-4	323950	24122	70741	1135384	1901060	0.8	107.7	391.3	483.5	5.0505	1.64	0.0748	1.09	2.0410	1.97	0.1980	1.64
A12-14_19	14/05/2018		63	211876	15657	2602	41747	1383491	0.0	59.2	14.4	351.8	5.5791	2.01	0.0740	0.95	1.8290	2.23	0.1792	2.01
A12-14_20	14/05/2018		-51	21065	1644	12009	220207	148778	2.0	8.9	75.9	37.8	6.0587	1.81	0.0780	1.75	1.7750	2.52	0.1651	1.81
A12-14_21	14/05/2018		56	14297	1232	4626	62599	88696	1.0	5.2	21.6	22.6	5.2724	2.72	0.0883	1.91	2.3084	3.33	0.1897	2.72
A12-14_22	14/05/2018		91	242033	21325	48821	556070	1170470	0.6	80.3	191.6	297.7	4.1697	2.63	0.0867	0.92	2.8644	2.78	0.2398	2.63
A12-14_23	14/05/2018		8	51659	3769	5473	107705	369184	0.4	15.7	37.1	93.9	6.0228	2.00	0.0728	1.24	1.6652	2.35	0.1660	2.00
A12-14_24	14/05/2018		119	123121	9755	24069	374644	722878	0.7	40.4	129.1	183.8	4.9157	1.57	0.0782	0.78	2.1935	1.75	0.2034	1.57
A12-14_25	14/05/2018		15	107506	9920	27825	341175	475784	1.0	37.3	117.6	121.0	3.7755	1.84	0.0925	1.21	3.3752	2.20	0.2649	1.84
A12-14_04	14/05/2018	rej - heavily discordant	149	1557	1227	3332	16072	30429	0.7	1.6	5.5	7.7	15.8165	5.24	0.7892	2.42	6.8765	5.77	0.0632	5.24
A12-14_07	14/05/2018	rej - heavily discordant	83	3962	1980	5217	23916	68406	0.5	2.9	8.2	17.4	14.2727	3.77	0.5041	1.91	4.8672	4.23	0.0701	3.77
A12-14_09	14/05/2018	rej - heavily discordant	166	2153	1362	3465	13769	40215	0.5	1.8	4.7	10.2	16.0518	4.26	0.6298	2.08	5.4071	4.74	0.0623	4.26
A12-14_16	14/05/2018	rej - heavily discordant	149	1650	1204	3294	15601	12689	1.7	1.6	5.4	3.2	5.0540	9.93	0.7308	2.48	19.9290	10.24	0.1979	9.93

	Zircon																		
Spot	Rho	$^{207}Pb/^{206}Pb$	2s abs	$^{206}Pb/^{238}U$	2s abs	$^{207}Pb/^{235}U$	2s abs	6-38/7-6	6-38/7-35	*f206*	1s %	$^{206}Pb^*/^{238}U$	1s %	206/238-Pb	2s [Ma]	Th/U min.	Th/U wr.	f	r. 206/238 a	*2s [Ma]*
A03-12_04	0.41	1499	270	50	3	97	14	96.7	48.5	0.059	7.15	0.0074	3.1	47	2.9	0.0	3.8	0.00	**47.4**	***2.9***
A03-12_06	0.54	82	109	48	1	48	3	41.7	1.3	0.001	2.29	0.0074	1.5	48	1.4	0.0	3.8	0.00	**47.8**	***1.4***
A03-12_08	0.26	1503	507	62	4	120	31	95.8	48.1	0.059	13.40	0.0092	3.5	59	4.1	0.2	3.8	0.07	58.9	*4.1*
A03-12_09	0.35	948	369	49	3	73	13	94.8	32.7	0.030	9.02	0.0074	3.3	47	3.1	0.0	3.8	0.00	**47.5**	***3.1***
A03-12_10	0.53	173	113	48	1	51	3	72.1	5.0	0.003	2.43	0.0075	1.5	48	1.4	0.0	3.8	0.00	**48.2**	***1.4***
A03-12_11	0.39	1594	411	50	5	102	23	96.9	50.9	0.065	11.01	0.0073	4.4	47	4.1	0.0	3.8	0.00	**47.0**	***4.1***
A03-12_12	0.55	96	93	48	1	49	2	49.9	1.9	0.001	1.96	0.0075	1.3	48	1.2	0.0	3.8	0.00	**48.0**	***1.2***
~~A03-12_05~~	~~0.21~~	~~2431~~	~~4437~~	~~44~~	~~25~~	~~140~~	~~301~~	~~98.2~~	~~68.8~~	~~0.140~~	~~130.89~~	~~0.0059~~	~~30.5~~	~~38~~	~~22.9~~	~~0.0~~	3.8	~~0.00~~	~~**37.8**~~	~~***22.9***~~
~~A03-12_07~~	~~0.31~~	~~2287~~	~~1388~~	~~66~~	~~17~~	~~189~~	~~137~~	~~97.1~~	~~65.2~~	~~0.123~~	~~40.35~~	~~0.0090~~	~~12.7~~	~~58~~	~~14.6~~	~~0.0~~	3.8	~~0.00~~	~~**57.7**~~	~~***14.6***~~
~~A03-12_13~~	~~0.54~~	~~2820~~	~~1809~~	~~77~~	~~54~~	~~290~~	~~287~~	~~97.3~~	~~73.4~~	~~0.192~~	~~55.37~~	~~0.0097~~	~~30.3~~	~~63~~	~~37.6~~	~~0.0~~	3.8	~~0.00~~	~~**62.7**~~	~~***37.6***~~
A04-15_01	0.96	1165	69	654	76	781	67	43.9	16.3	0.022	1.73	0.1044	6.0	640	72.7	0.0	3.8	0.01	**640.3**	***72.7***
A04-15_02	0.86	750	34	550	14	591	14	26.6	6.8	0.007	0.80	0.0885	1.4	547	14.1	0.0	3.8	0.01	**546.8**	***14.1***
A04-15_03	0.84	939	35	799	20	837	18	14.9	4.5	0.006	0.86	0.1312	1.3	795	19.7	0.0	3.8	0.01	**795.0**	***19.7***
A04-28_01	0.68	500	65	445	12	454	15	11.0	1.9	0.002	1.48	0.0713	1.4	444	11.6	0.2	3.8	0.04	**444.4**	***11.6***
A04-28_02a	0.38	679	186	14	1	19	2	97.9	25.3	0.020	4.36	0.0022	1.7	14	0.5	0.2	3.8	0.04	**14.0**	***0.5***
A04-28_02b	0.31	724	214	15	1	21	2	97.9	26.8	0.022	5.03	0.0023	1.6	15	0.5	0.2	3.8	0.04	**15.0**	***0.5***
A04-28_03a	0.46	972	118	493	14	587	29	49.2	16.0	0.018	2.89	0.0781	1.5	485	13.8	0.3	3.8	0.09	**484.8**	***13.8***
A04-28_03b	0.79	497	52	468	14	473	14	5.9	1.0	0.001	1.17	0.0752	1.5	467	13.6	0.0	3.8	0.01	**467.6**	***13.6***
A04-28_04a	0.37	542	192	44	2	54	5	91.9	19.1	0.014	4.39	0.0068	1.7	43	1.5	0.0	3.8	0.00	**43.5**	***1.5***
A04-28_04b	0.93	421	50	98	6	112	7	76.6	12.5	0.009	1.11	0.0152	2.9	97	5.6	0.6	3.8	0.15	**97.6**	***5.6***
A04-28_05	0.71	476	57	486	12	484	14	-2.2	-0.4	0.000	1.29	0.0784	1.3	486	12.0	0.1	3.8	0.02	**486.6**	***12.0***
A12-14_01	0.50	1267	109	873	26	992	40	31.1	12.0	0.018	2.78	0.1424	1.6	858	25.2	0.2	3.8	0.06	**858.3**	***25.2***
A12-14_02a	0.89	2473	27	2376	61	2428	31	3.9	2.1	0.012	0.79	0.4402	1.5	2352	59.5	0.0	3.8	0.01	**2352.2**	***59.5***
A12-14_02b	0.87	2506	32	2394	69	2455	36	4.5	2.5	0.014	0.97	0.4432	1.7	2365	67.0	0.7	3.8	0.19	**2365.5**	***67.0***
A12-14_03	0.80	1331	69	1228	52	1266	42	7.7	3.0	0.005	1.77	0.2087	2.3	1222	51.4	1.2	3.8	0.30	**1222.2**	***51.4***
A12-14_05	0.93	1036	43	968	48	988	36	6.6	2.1	0.003	1.07	0.1615	2.7	965	47.6	0.8	3.8	0.20	**965.1**	***47.6***
A12-14_06	0.80	694	51	634	19	647	19	8.7	2.0	0.002	1.20	0.1031	1.6	633	19.3	0.5	3.8	0.14	**632.9**	***19.3***
A12-14_08	0.82	2518	33	2448	57	2486	31	2.8	1.5	0.009	0.98	0.4576	1.4	2429	56.6	0.6	3.8	0.15	**2429.5**	***56.6***
A12-14_10a	0.87	995	38	1049	31	1031	24	-5.4	-1.7	-0.002	0.93	0.1771	1.6	1051	31.4	0.2	3.8	0.06	**1051.3**	***31.4***
A12-14_10b	0.88	991	42	1028	36	1015	28	-3.7	-1.2	-0.002	1.04	0.1731	1.9	1029	36.5	0.2	3.8	0.07	**1029.3**	***36.5***
A12-14_11	0.91	629	42	546	22	562	20	13.3	2.9	0.003	0.98	0.0881	2.1	544	21.7	2.0	3.8	0.52	**544.3**	***21.7***
A12-14_12	0.86	1016	51	945	37	966	30	7.1	2.2	0.003	1.26	0.1573	2.1	942	37.1	0.5	3.8	0.14	**942.2**	***37.1***
A12-14_13	0.74	1601	74	1117	44	1294	42	30.2	13.7	0.027	1.98	0.1840	2.1	1089	42.1	0.4	3.8	0.10	**1089.3**	***42.1***
A12-14_14	0.86	1037	45	1014	35	1021	28	2.2	0.7	0.001	1.10	0.1701	1.9	1013	34.8	0.0	3.8	0.01	**1012.9**	***34.8***
A12-14_15	0.92	2467	37	1359	63	1854	47	44.9	26.7	0.093	1.11	0.2129	2.3	1244	52.5	0.1	3.8	0.04	**1244.5**	***52.5***
A12-14_17	0.91	1947	36	1875	71	1909	41	3.7	1.8	0.006	1.01	0.3355	2.2	1865	70.3	0.1	3.8	0.03	**1865.3**	***70.3***
A12-14_18	0.83	1063	44	1165	35	1129	26	-9.5	-3.1	-0.005	1.09	0.1990	1.6	1170	35.1	0.8	3.8	0.21	**1170.0**	***35.1***
A12-14_19	0.90	1043	38	1063	39	1056	29	-1.9	-0.7	-0.001	0.95	0.1794	2.0	1064	39.4	0.0	3.8	0.01	**1064.0**	***39.4***
A12-14_20	0.72	1148	70	985	33	1036	32	14.2	5.0	0.008	1.75	0.1638	1.8	978	32.5	2.0	3.8	0.53	**978.1**	***32.5***
A12-14_21	0.82	1389	73	1120	56	1215	46	19.4	7.8	0.014	1.91	0.1870	2.7	1105	54.3	1.0	3.8	0.25	**1105.2**	***54.3***
A12-14_22	0.94	1353	35	1386	65	1373	41	-2.4	-1.0	-0.002	0.92	0.2403	2.6	1388	65.4	0.6	3.8	0.17	**1388.4**	***65.4***
A12-14_23	0.85	1008	50	990	37	995	29	1.7	0.5	0.001	1.24	0.1659	2.0	990	36.5	0.4	3.8	0.10	**989.8**	***36.5***
A12-14_24	0.89	1153	31	1194	34	1179	24	-3.5	-1.2	-0.002	0.78	0.2038	1.6	1196	34.2	0.7	3.8	0.18	**1196.2**	***34.2***
A12-14_25	0.84	1477	46	1515	50	1499	34	-2.6	-1.1	-0.002	1.21	0.2655	1.8	1518	49.8	1.0	3.8	0.26	**1518.2**	***49.8***
A12-14_04	0.91	4902	69	395	40	2096	97	91.9	81.1	0.938	2.42	0.0039	2.3	25	1.2	0.7	3.8	0.19	**25.3**	***1.2***
A12-14_07	0.89	4253	56	437	32	1797	69	89.7	75.7	0.568	1.91	0.0302	2.0	192	7.4	0.5	3.8	0.12	**192.2**	***7.4***
A12-14_09	0.90	4578	60	390	32	1886	78	91.5	79.3	0.731	2.08	0.0167	1.9	107	4.0	0.5	3.8	0.12	**107.1**	***4.0***
A12-14_16	0.97	4793	71	1164	208	3088	181	75.7	62.3	0.846	2.48	0.0305	2.6	194	9.9	1.7	3.8	0.44	**194.0**	***9.9***

Monazite

Spot	comments	^{204}Pb cps	^{206}Pb cps	^{207}Pb cps	^{208}Pb cps	^{232}Th cps	^{238}U cps	Th/U	Pb ppm	Th ppm	U ppm	^{238}U/^{206}Pb	1s %	^{207}Pb/^{206}Pb	1s %	^{208}Pb/^{206}Pb	1s %	^{207}Pb/^{235}U	1s %	^{206}Pb/^{238}U	1s %
11-01a_M01		66	702781	40825	3635215	134739800	8026367	12.3	1840	75509	4014	13.46	1.3	0.057	0.77	5.155	2.26	0.581	1.55	0.074	1.34
11-01a_M04	discordant	119	357932	22771	3609858	153108900	4793836	23.4	1677	85803	2397	15.84	1.4	0.062	0.90	9.926	1.54	0.542	1.69	0.063	1.43
11-01a_M06	discordant	19	187136	11727	2967060	100573600	2321269	31.8	1330	56362	1161	14.80	1.5	0.061	1.28	15.99	1.55	0.569	1.98	0.068	1.51
11-01a_M07		116	978514	56985	2722014	98058940	10937225	6.6	1579	54953	5469	13.37	1.5	0.057	0.94	2.781	2.49	0.588	1.74	0.075	1.47
11-01a_M08	discordant	84	238956	14335	3296316	128094400	2986148	31.5	1492	71785	1493	14.94	1.5	0.058	1.04	13.80	1.59	0.539	1.79	0.067	1.45
11-01a_M09		37	1347397	76854	2697157	97031960	14689727	4.8	1732	54377	7346	12.84	1.3	0.056	0.77	2.544	7.67	0.605	1.52	0.078	1.31
11-01a_M12	discordant	79	420602	25054	2507553	94719010	5032209	13.8	1241	53081	2516	13.81	1.7	0.058	0.81	5.824	1.76	0.582	1.86	0.072	1.68
11-01a_M13		35	794716	42963	3682517	130510500	8492279	11.3	1899	73139	4247	12.78	1.6	0.056	0.85	5.053	6.95	0.608	1.78	0.078	1.56
11-01a_M14	discordant	159	850219	51629	3404438	127155600	9443615	9.9	1810	71258	4722	13.18	1.5	0.060	0.83	3.981	1.35	0.623	1.69	0.076	1.47
11-01a_M15		69	442515	25489	2970679	108239400	5091752	15.6	1445	60658	2546	13.65	1.4	0.057	0.97	7.056	3.74	0.573	1.72	0.073	1.41
11-01a_M16	discordant	74	160365	10295	3304838	127914200	2159809	43.4	1460	71684	1080	15.94	1.5	0.062	0.93	20.42	1.43	0.539	1.77	0.063	1.50
11-01a_M17		-1	627487	35309	2864278	108004000	6787138	11.7	1482	60526	3394	12.73	1.5	0.056	0.75	4.652	1.81	0.607	1.64	0.079	1.46
11-01a_M18	discordant	45	198683	11970	2963468	106275100	2329981	33.4	1334	59557	1165	13.72	1.7	0.059	0.89	15.12	1.85	0.596	1.92	0.073	1.71
11-01a_M20	discordant	36	329971	19497	3042871	109010800	3560394	22.4	1426	61090	1780	12.86	1.4	0.059	0.67	9.206	1.39	0.628	1.51	0.078	1.35
11-01a_M21		-3	631207	36073	4925744	180789900	6867813	19.3	2350	101315	3434	12.85	1.4	0.056	0.84	9.413	8.08	0.604	1.65	0.078	1.42
11-01a_M22	discordant	70	348356	20389	2900190	111038500	3999248	20.4	1374	62226	2000	13.66	1.4	0.057	0.79	8.314	2.58	0.579	1.59	0.073	1.38
11-01a_M25	discordant	164	489887	29625	2541185	95276370	5403989	12.9	1286	53393	2702	13.01	1.4	0.059	1.07	5.421	4.44	0.627	1.76	0.077	1.41
11-01a_M26	discordant	4	751345	44250	2169891	85732270	8639001	7.3	1246	48045	4320	13.82	1.5	0.059	0.69	2.809	1.89	0.584	1.62	0.072	1.46
11-01a_M29	discordant	80	358773	21228	4149684	151224700	4157926	26.7	1903	84747	2079	13.81	1.4	0.058	0.77	11.68	1.93	0.583	1.62	0.072	1.42
11-01a_M30	discordant	91	232364	13800	2534857	100728600	2908034	25.4	1169	56449	1454	14.74	1.5	0.058	0.76	11.09	1.56	0.545	1.64	0.068	1.46
11-01a_M31		95	1038285	60526	2995951	107505000	11682844	6.7	1721	60246	5842	13.03	1.4	0.057	0.76	2.920	1.64	0.599	1.63	0.077	1.44
11-01a_M34		46	534050	30746	2168119	79739050	5910780	9.9	1148	44686	2956	13.25	1.5	0.057	0.70	4.042	1.84	0.596	1.66	0.075	1.51
~~11-01a_M02~~	~~high cm pb spike~~	~~257~~	~~549219~~	~~36148~~	~~3004574~~	~~125351300~~	~~6718123~~	~~13.7~~	1509	70247	3359	~~14.49~~	~~1.7~~	~~0.063~~	~~1.15~~	~~5.480~~	~~2.32~~	~~0.599~~	~~2.05~~	~~0.069~~	~~1.70~~
~~11-01a_M05~~	~~drilled through~~	~~569~~	~~604569~~	~~44577~~	~~2749431~~	~~103935300~~	~~7181410~~	~~10.6~~	1428	58246	3591	~~13.88~~	~~2.1~~	~~0.083~~	~~8.81~~	~~4.588~~	~~2.02~~	~~0.828~~	~~9.05~~	~~0.072~~	~~2.07~~
~~11-01a_M32~~	~~zircon~~	~~-20~~	~~277588~~	~~18329~~	~~49069~~	~~837994~~	~~1559915~~	~~0.4~~	145	470	780	~~6.72~~	~~2.0~~	~~0.065~~	~~1.12~~	~~0.178~~	~~5.06~~	~~1.339~~	~~2.31~~	~~0.149~~	~~2.02~~
44069_01		-39	608047	33625	2186349	86094600	7941370	7.9	1188	48248	3971	15.26	1.4	0.054	0.77	3.564	1.61	0.486	1.58	0.066	1.38
44069_02		209	685370	38501	2197531	87602050	8856685	7.3	1228	49092	4429	15.37	1.3	0.055	0.76	3.196	1.67	0.491	1.52	0.065	1.32
44069_03		73	692548	38879	2035610	79194090	8816460	6.6	1163	44381	4409	15.31	1.3	0.055	0.75	2.949	1.58	0.499	1.50	0.065	1.29
44069_04		61	645418	36498	2013431	82663160	8131996	7.5	1133	46325	4066	14.91	1.4	0.055	0.73	3.117	1.46	0.511	1.62	0.067	1.44
44069_05		138	614294	34518	1713122	69987830	7663863	6.7	993	39221	3832	14.78	1.4	0.056	0.66	2.796	1.63	0.518	1.54	0.068	1.39
44069_06		110	648316	36578	1491940	60501880	7993462	5.5	915	33905	3997	14.66	1.5	0.055	0.87	2.286	1.37	0.520	1.75	0.068	1.51
44069_07		143	648449	36351	1319514	53811360	7874642	5.0	842	30156	3938	14.47	1.3	0.055	0.83	2.111	1.89	0.522	1.58	0.069	1.34
44069_08		-10	734103	40231	1567872	61497760	8816904	5.1	984	34464	4409	14.19	1.3	0.055	0.67	2.167	1.31	0.530	1.50	0.070	1.34
44069_09		13	898667	50617	2012870	81745970	10704932	5.6	1245	45811	5353	14.20	1.4	0.055	0.86	2.234	1.75	0.535	1.63	0.070	1.38
44069_10		20	563299	31491	1712416	67881730	6809776	7.3	970	38041	3405	14.32	1.4	0.055	0.95	3.032	1.69	0.530	1.71	0.070	1.42
44069_11		11	568882	31708	1418700	57649460	6924963	6.1	849	32307	3463	14.38	1.5	0.055	0.96	2.582	1.74	0.523	1.78	0.070	1.50
44069_12		-86	544452	30617	1317287	53908630	6580058	6.0	795	30211	3290	14.34	1.4	0.055	0.89	2.445	1.60	0.530	1.63	0.070	1.37
44069_13		17	514043	28848	1306513	51239970	6216268	6.0	777	28715	3108	14.47	1.3	0.055	0.75	2.574	1.72	0.526	1.54	0.069	1.34
FC-1_04		-79	331923	15743	391061	116071900	31102288	2.7	310	65047	15553	110.15	1.4	0.047	1.07	1.191	2.70	0.058	1.78	0.009	1.42
FC-1_05		78	248765	12061	374542	116034600	22918516	3.7	267	65026	11460	109.61	1.4	0.048	1.02	1.551	2.22	0.060	1.77	0.009	1.45
FC-1_06		5	107232	5170	378899	112762700	9658979	8.6	206	63193	4830	108.63	1.4	0.048	1.30	3.577	1.75	0.061	1.93	0.009	1.43
FC-1_07		3	305971	14528	346539	113765100	27706826	3.0	280	63754	13855	107.24	1.4	0.046	0.86	1.140	1.79	0.060	1.67	0.009	1.43
FC-1_08		63	336101	15854	394239	121583700	30211484	3.0	314	68136	15107	105.92	1.4	0.046	0.75	1.165	2.18	0.060	1.55	0.009	1.35
FC-1_09		83	328354	15380	380588	125370700	29622280	3.1	304	70258	14812	106.19	1.4	0.046	0.79	1.179	2.42	0.060	1.60	0.009	1.39
FC-1_10		81	308415	14650	368241	117682000	27896824	3.1	290	65949	13950	108.70	1.4	0.047	0.82	1.193	2.68	0.059	1.63	0.009	1.41
FC-1A_01		-4	284054	15131	309495	96530610	24966670	2.8	256	54096	12484	105.42	1.5	0.052	1.13	1.093	2.86	0.069	1.88	0.009	1.51
FC-1A_02		584	289334	21755	341443	95760650	25055929	2.8	274	53665	12529	103.35	1.4	0.073	1.39	1.154	2.49	0.097	1.99	0.010	1.43
FC-1A_03		1464	299049	37205	383193	94221940	23624261	2.9	302	52802	11813	94.71	1.5	0.118	4.42	1.311	2.63	0.172	4.67	0.011	1.52
FC-1B_01		79	212591	10174	355139	108357800	18900107	4.2	243	60724	9451	105.66	1.4	0.047	0.94	1.677	2.48	0.061	1.72	0.009	1.44
FC-1B_02		-72	228298	10941	307975	99237570	20787464	3.5	230	55613	10395	107.67	1.4	0.047	0.98	1.361	2.68	0.060	1.72	0.009	1.42
FC-1B_03		69	238463	11574	342884	107155600	20974316	3.7	249	60050	10488	104.34	1.4	0.048	0.91	1.425	2.94	0.063	1.68	0.010	1.41
Man_01		97	373896	22846	9983874	297373300	3668805	59.4	4362	166649	1835	11.83	1.4	0.060	0.95	26.65	1.45	0.704	1.71	0.085	1.43
Man_02		-122	371637	23224	10182720	296009000	3652068	59.4	4445	165884	1826	11.60	1.6	0.061	1.02	27.03	1.31	0.727	1.90	0.086	1.60
Man_03		-71	370475	22765	10064850	297930000	3578938	61.0	4395	166961	1790	11.36	1.5	0.060	0.83	27.08	1.34	0.730	1.68	0.088	1.46
Man_04		164	407133	25901	11032900	318894300	3858615	60.6	4818	178709	1929	11.22	1.4	0.062	0.84	27.21	1.34	0.767	1.66	0.089	1.43
Man_05		76	414223	25377	11111590	317385600	3983003	58.4	4854	177864	1992	11.41	1.4	0.060	1.05	26.82	1.26	0.727	1.78	0.088	1.44
Man_06		136	406958	25912	11255880	321052500	3876232	60.7	4912	179919	1938	11.19	1.4	0.062	1.06	27.33	1.45	0.767	1.77	0.089	1.41
Man_07		53	378472	23301	10149210	300177700	3550472	62.0	4434	168221	1775	10.98	1.4	0.060	0.86	26.50	1.23	0.757	1.68	0.091	1.45
Man_08		81	382820	23115	10170100	309726800	3639457	62.4	4444	173572	1820	11.27	1.4	0.059	0.83	26.08	1.20	0.723	1.64	0.089	1.42
Man_09		33	382742	23600	9984253	307361700	3538628	63.7	4366	172247	1769	10.91	1.5	0.061	0.93	25.94	1.27	0.764	1.76	0.092	1.50
Man_10		60	354604	21978	9426092	281596300	3347752	61.7	4119	157808	1674	11.26	1.5	0.061	0.98	26.63	1.26	0.742	1.77	0.089	1.48
Man_11		173	362494	22392	9502867	286745100	3384542	62.1	4155	160693	1692	11.01	1.5	0.061	0.99	25.90	1.39	0.759	1.81	0.091	1.51
Man_12		-8	364310	21956	9659959	288750000	3409017	62.1	4222	161816	1705	11.13	1.4	0.060	0.83	26.45	1.34	0.737	1.63	0.090	1.40
Man_13		129	352885	21639	9340743	278919900	3309533	61.8	4082	156308	1655	11.20	1.4	0.060	0.94	26.61	1.47	0.734	1.71	0.089	1.43
Stern_04		165	652257	37231	3570753	121265300	6414120	13.9	1790	67957	3207	11.71	1.4	0.056	0.88	5.487	1.50	0.658	1.67	0.085	1.42
Stern_05		26	763968	43220	4237639	133583700	7703251	12.7	2120	74861	3852	11.99	1.3	0.056	0.79	5.559	1.28	0.642	1.54	0.083	1.33
Stern_06		166	756627	43951	4277857	136699700	7857038	12.8	2134	76607	3929	12.35	1.4	0.056	0.82	5.613	1.44	0.629	1.62	0.081	1.39
Stern_07		110	738538	43175	4089956	135173800	7492297	13.2	2047	75752	3746	12.05	1.4	0.058	0.91	5.571	1.44	0.658	1.68	0.083	1.42
Stern_08		42	678637	38635	3778660	123615300	6700126	13.5	1889	69274	3350	12.05	1.4	0.056	0.90	5.593	1.54	0.643	1.70	0.083	1.45
Stern_09		102	595226	33843	3294014	108857600	5974554	13.4	1649	61004	2988	12.03	1.6	0.057	1.29	5.565	1.59	0.648	2.02	0.083	1.55
Stern_10		-111	659320	38595	3707660	123861200	6818340	13.3	1851	69412	3409	12.35	1.5	0.057	1.05	5.577	1.43	0.640	1.83	0.081	1.50
Stern_11		25	656595	37319	3722065	120950400	6676517	13.3	1856	67781	3339	12.09	1.5	0.057	1.07	5.681	1.37	0.646	1.81	0.083	1.46
Stern_12		-68	619839	35444	3498999	117875800	6302450	13.7	1746	66058	3152	12.07	1.5	0.057	0.87	5.590	1.56	0.652	1.77	0.083	1.54
Stern_13		-35	553142	32098	3194411	105554400	5735189	13.5	1588	59153	2868	12.31	1.6	0.057	1.06	5.704	1.54	0.636	1.90	0.081	1.58
SternA_01		-58	674617	38703	3752624	123983300	7240118	12.6	1877	69481	3620	12.82	1.7	0.057	1.11	5.564	1.59	0.613	2.05	0.078	1.73
SternA_02		-11	681331	38661	3875600	124040400	7243413	12.6	1931	69513	3622	12.71	1.5	0.056	0.95	5.695	1.42	0.608	1.77	0.079	1.49
SternA_03		-26	659787	37991	3816055	125401600	7260230	12.7	1897	70275	3630	13.02	1.6	0.057	1.01	5.708	1.47	0.601	1.88	0.077	1.59
SternB_01		265	698234	40138	3799692	133558300	7387689	13.3	1907	74847	3694	12.58	1.5	0.057	0.88	5.449	1.52	0.619	1.72	0.079	1.47
SternB_02		110	647118	37611	3579120	125166000	6751660	13.6	1792	70143	3376	12.34	1.5	0.057	0.99	5.457	1.47	0.637	1.76	0.081	1.46
SternB_03		-35	724858	41219	3904110	134924400	7624657	13.0	1962	75612	3813	12.65	1.4	0.056	0.84	5.461	1.32	0.615	1.65	0.079	1.42

	Monazite																			
Spot	Rho	$^{208}Pb/^{232}U$	1s %	$^{207}Pb/^{206}Pb$	2s abs	$^{206}Pb/^{238}U$	2s abs	$^{207}Pb/^{235}U$	2s abs	$^{208}Pb/^{232}U$	2s abs	scordance	*f206*	1s %	*f208*	1s %	pr.Th-Pb Ag	2s abs	'.206/238	2s abs
11-01a_M01	0.87	0.022	1.54	481.1	17.1	462.1	11.9	465.1	11.5	450	14	4.0	0.00	0.77	0.00	2.39	**449.6**	***13.7***	**461.6**	***11.9***
11-01a_M04	0.84	0.020	1.53	683.2	19.3	394.7	10.9	439.6	12.0	395	12	42.2	0.01	0.90	0.00	1.78	**394.2**	***11.9***	**390.5**	***10.7***
11-01a_M06	0.76	0.025	1.68	642.7	27.4	421.5	12.3	457.4	14.5	496	16	34.4	0.01	1.28	0.00	2.01	**495.3**	***16.5***	**417.8**	***12.1***
11-01a_M07	0.84	0.023	1.63	493.7	20.6	465.0	13.2	469.7	13.0	460	15	5.8	0.00	0.94	0.00	2.66	**459.5**	***14.8***	**464.6**	***13.2***
11-01a_M08	0.81	0.022	1.66	545.5	22.6	417.7	11.7	437.7	12.6	432	14	23.4	0.00	1.04	0.00	1.90	**431.5**	***14.2***	**415.3**	***11.7***
11-01a_M09	0.86	0.023	1.46	468.5	17.1	483.4	12.2	480.6	11.6	467	13	-3.2	0.00	0.77	0.00	7.71	**467.0**	***13.4***	**483.6**	***12.2***
11-01a_M12	0.90	0.022	1.92	539.6	17.7	450.8	14.6	465.5	13.8	449	17	16.5	0.00	0.81	0.00	1.94	**448.6**	***17.0***	**449.3**	***14.5***
11-01a_M13	0.88	0.024	1.65	467.0	18.8	485.8	14.6	482.3	13.6	470	15	-4.0	0.00	0.85	0.00	7.00	**470.1**	***15.4***	**485.9**	***14.6***
11-01a_M14	0.87	0.022	1.56	589.5	17.9	471.5	13.4	492.0	13.1	447	14	20.0	0.00	0.83	0.00	1.58	**446.1**	***13.7***	**469.6**	***13.3***
11-01a_M15	0.82	0.023	1.46	482.4	21.5	455.7	12.4	460.0	12.6	457	13	5.5	0.00	0.97	0.00	3.86	**457.3**	***13.2***	**455.1**	***12.4***
11-01a_M16	0.85	0.022	1.44	686.4	19.9	392.4	11.4	438.0	12.5	433	12	42.8	0.01	0.93	0.00	1.70	**432.7**	***12.3***	**387.5**	***11.2***
11-01a_M17	0.89	0.023	1.60	455.2	16.7	487.4	13.7	481.6	12.5	452	14	-7.1	0.00	0.75	0.00	1.96	**451.8**	***14.3***	**487.7**	***13.7***
11-01a_M18	0.89	0.024	1.76	580.0	19.2	453.6	14.9	474.9	14.5	474	16	21.8	0.00	0.89	0.00	2.05	**473.5**	***16.5***	**451.0**	***14.8***
11-01a_M20	0.90	0.023	1.55	553.8	14.7	482.7	12.6	495.1	11.8	460	14	12.8	0.00	0.67	0.00	1.55	**460.1**	***14.1***	**481.1**	***12.5***
11-01a_M21	0.86	0.023	1.33	465.4	18.5	483.1	13.2	479.9	12.5	453	12	-3.8	0.00	0.84	0.00	8.13	**452.7**	***11.9***	**483.0**	***13.2***
11-01a_M22	0.87	0.022	1.51	506.2	17.5	455.5	12.1	463.8	11.8	441	13	10.0	0.00	0.79	0.00	2.70	**440.4**	***13.2***	**454.3**	***12.1***
11-01a_M25	0.80	0.022	1.57	575.1	23.2	477.2	12.9	494.3	13.7	444	14	17.0	0.00	1.07	0.00	4.57	**443.7**	***13.7***	**475.5**	***12.8***
11-01a_M26	0.90	0.021	1.77	550.6	15.2	450.3	12.7	466.9	12.0	420	15	18.2	0.00	0.69	0.00	2.01	**418.7**	***14.6***	**448.8**	***12.6***
11-01a_M29	0.88	0.023	1.57	545.7	16.9	450.5	12.3	466.3	12.0	454	14	17.4	0.00	0.77	0.00	2.08	**453.3**	***14.0***	**448.6**	***12.3***
11-01a_M30	0.89	0.021	1.48	539.7	16.6	423.1	11.9	441.5	11.7	425	12	21.6	0.00	0.76	0.00	1.73	**425.1**	***12.5***	**421.0**	***11.8***
11-01a_M31	0.88	0.023	1.38	476.7	16.9	476.6	13.2	476.5	12.3	458	13	0.0	0.00	0.76	0.00	1.81	**458.3**	***12.5***	**476.6**	***13.2***
11-01a_M34	0.91	0.023	1.79	502.7	15.3	468.9	13.6	474.5	12.5	459	16	6.7	0.00	0.70	0.00	1.97	**458.8**	***16.2***	**468.3**	***13.6***
~~11-01a_M02~~	~~0.83~~	~~0.020~~	~~1.62~~	~~706.4~~	~~24.4~~	~~430.1~~	~~14.1~~	~~476.3~~	~~15.5~~	~~404~~	~~13~~	~~39.1~~	~~0.01~~	~~1.15~~	~~0.00~~	~~2.59~~	**~~402.1~~**	***~~12.9~~***	**~~426.0~~**	***~~12.9~~***
~~11-01a_M05~~	~~0.23~~	~~0.022~~	~~1.73~~	~~1277.6~~	~~171.7~~	~~448.4~~	~~17.9~~	~~612.2~~	~~80.0~~	~~439~~	~~15~~	~~64.9~~	~~0.03~~	~~8.81~~	~~0.02~~	~~9.04~~	**~~432.3~~**	***~~14.6~~***	**~~433.3~~**	***~~16.9~~***
~~11-01a_M32~~	~~0.87~~	~~0.049~~	~~5.38~~	~~785.5~~	~~23.4~~	~~893.7~~	~~33.6~~	~~862.9~~	~~26.5~~	~~963~~	~~101~~	~~-13.8~~	~~0.00~~	~~1.12~~	~~-0.05~~	~~5.18~~	**~~1011.7~~**	***~~111.5~~***	**~~897.5~~**	***~~22.9~~***
44069_01	0.87	0.021	1.57	365.2	17.3	409.1	10.9	402.4	10.4	421	13	-12.0	0.00	0.77	0.00	1.78	**421.0**	***13.1***	**409.5**	***10.9***
44069_02	0.87	0.021	1.82	403.5	17.0	406.3	10.4	405.7	10.1	423	15	-0.7	0.00	0.76	0.00	1.83	**422.9**	***15.2***	**406.3**	***10.4***
44069_03	0.86	0.021	1.60	427.6	16.8	408.0	10.2	410.8	10.1	428	14	4.6	0.00	0.75	0.00	1.75	**427.4**	***13.5***	**407.7**	***10.2***
44069_04	0.89	0.020	1.51	423.2	16.3	418.4	11.7	419.0	11.0	406	12	1.1	0.00	0.73	0.00	1.64	**405.6**	***12.1***	**418.3**	***11.7***
44069_05	0.91	0.021	1.84	433.6	14.6	422.1	11.4	423.7	10.6	411	15	2.7	0.00	0.66	0.00	1.76	**411.1**	***15.0***	**421.9**	***11.4***
44069_06	0.87	0.021	1.72	423.9	19.4	425.5	12.5	425.1	12.1	412	14	-0.4	0.00	0.87	0.00	1.62	**412.1**	***14.0***	**425.5**	***12.5***
44069_07	0.85	0.021	1.97	403.1	18.5	430.9	11.2	426.4	10.9	420	16	-6.9	0.00	0.83	0.00	2.07	**420.6**	***16.4***	**431.3**	***11.2***
44069_08	0.89	0.021	1.74	393.1	15.1	439.0	11.4	431.6	10.5	425	15	-11.7	0.00	0.67	0.00	1.47	**425.2**	***14.6***	**439.6**	***11.4***
44069_09	0.85	0.021	1.58	414.9	19.3	438.8	11.7	434.9	11.5	416	13	-5.8	0.00	0.86	0.00	1.95	**416.2**	***13.0***	**439.2**	***11.7***
44069_10	0.83	0.021	1.76	413.4	21.3	435.2	12.0	431.6	12.0	422	15	-5.3	0.00	0.95	0.00	1.94	**422.7**	***14.7***	**435.5**	***12.0***
44069_11	0.84	0.021	1.75	394.3	21.6	433.4	12.6	427.1	12.4	418	15	-9.9	0.00	0.96	0.00	1.99	**418.7**	***14.5***	**433.9**	***12.6***
44069_12	0.84	0.021	1.65	418.3	19.8	434.5	11.5	431.8	11.4	413	13	-3.9	0.00	0.89	0.00	1.82	**413.3**	***13.5***	**434.7**	***11.5***
44069_13	0.87	0.022	1.84	420.5	16.7	430.9	11.2	429.1	10.7	433	16	-2.5	0.00	0.75	0.00	1.88	**432.9**	***15.7***	**431.0**	***11.2***
FC-1_04	0.80	0.003	2.45	27.9	25.6	58.3	1.6	57.5	2.0	58	3	-108.4	0.00	1.07	0.00	2.91	**58.1**	***2.9***	**58.3**	***1.7***
FC-1_05	0.82	0.003	2.12	82.2	24.1	58.5	1.7	59.1	2.0	55	2	28.8	0.00	1.02	0.00	2.44	**55.3**	***2.3***	**58.5**	***1.7***
FC-1_06	0.74	0.003	2.04	93.6	30.8	59.1	1.7	59.9	2.2	57	2	36.9	0.00	1.30	0.00	2.18	**56.5**	***2.3***	**58.9**	***1.7***
FC-1_07	0.86	0.003	1.90	14.3	20.6	59.8	1.7	58.7	1.9	52	2	-317.4	0.00	0.86	0.00	1.98	**52.1**	***2.0***	**59.9**	***1.7***
FC-1_08	0.87	0.003	2.25	13.6	18.0	60.6	1.6	59.4	1.8	55	2	-346.8	0.00	0.75	0.00	2.31	**55.2**	***2.5***	**60.7**	***1.6***
FC-1_09	0.87	0.003	2.30	1.5	18.9	60.4	1.7	59.0	1.8	52	2	-3935.4	0.00	0.79	0.00	2.55	**51.9**	***2.4***	**60.5**	***1.7***
FC-1_10	0.87	0.003	2.38	23.7	19.6	59.0	1.7	58.2	1.8	53	3	-149.2	0.00	0.82	0.00	2.80	**53.5**	***2.5***	**59.1**	***1.7***
FC-1A_01	0.80	0.003	2.78	305.0	25.7	60.9	1.8	67.3	2.5	54	3	80.0	0.01	1.13	0.01	3.08	**53.5**	***2.9***	**60.5**	***1.8***
FC-1A_02	0.72	0.003	2.56	1014.4	28.2	62.1	1.8	94.3	3.6	60	3	93.9	0.03	1.39	0.06	2.85	**56.5**	***2.7***	**60.1**	***1.7***
FC-1A_03	0.33	0.003	2.98	1925.7	79.2	67.7	2.0	160.9	13.8	67	4	96.5	0.09	4.42	0.14	5.14	**57.2**	***3.0***	**61.7**	***1.8***
FC-1B_01	0.84	0.003	2.43	31.2	22.6	60.7	1.7	60.0	2.0	56	3	-94.7	0.00	0.94	0.00	2.65	**56.0**	***2.7***	**60.8**	***1.7***
FC-1B_02	0.82	0.003	2.68	35.1	23.5	59.6	1.7	59.0	2.0	53	3	-69.6	0.00	0.98	0.00	2.86	**53.2**	***2.8***	**59.6**	***1.7***
FC-1B_03	0.84	0.003	2.81	90.0	21.7	61.5	1.7	62.2	2.0	53	3	31.7	0.00	0.91	0.00	3.08	**53.4**	***3.0***	**61.4**	***1.7***
Man_01	0.83	0.028	1.58	618.6	20.5	523.2	14.3	541.2	14.3	557	17	15.4	0.00	0.95	0.00	1.74	**556.9**	***17.4***	**520.1**	***14.2***
Man_02	0.84	0.028	1.43	644.2	21.8	533.2	16.4	554.5	16.1	558	16	17.2	0.00	1.02	0.00	1.66	**558.2**	***15.7***	**529.7**	***16.3***
Man_03	0.87	0.028	1.43	609.4	17.9	544.0	15.2	556.6	14.3	563	16	10.7	0.00	0.83	0.00	1.57	**562.9**	***15.9***	**541.3**	***15.2***
Man_04	0.86	0.029	1.34	690.9	17.9	550.2	15.0	578.2	14.5	586	15	20.4	0.00	0.84	0.00	1.58	**585.8**	***15.5***	**546.0**	***14.9***
Man_05	0.81	0.029	1.41	609.7	22.6	541.7	15.0	554.7	15.1	582	16	11.2	0.00	1.05	0.00	1.64	**582.0**	***16.2***	**538.9**	***14.9***
Man_06	0.80	0.029	1.44	683.7	22.7	551.6	14.9	577.9	15.5	579	16	19.3	0.00	1.06	0.00	1.80	**578.6**	***16.4***	**547.6**	***14.8***
Man_07	0.86	0.028	1.47	614.5	18.6	562.0	15.6	572.4	14.6	556	16	8.5	0.00	0.86	0.00	1.50	**555.5**	***16.2***	**559.5**	***15.5***
Man_08	0.86	0.027	1.38	571.2	18.2	548.1	14.9	552.4	13.9	544	15	4.0	0.00	0.83	0.00	1.46	**543.9**	***14.8***	**546.1**	***14.8***
Man_09	0.85	0.027	1.37	621.7	20.1	565.1	16.2	576.3	15.4	544	15	9.1	0.00	0.93	0.00	1.58	**543.8**	***14.7***	**562.4**	***16.1***
Man_10	0.83	0.028	1.47	624.9	21.1	548.4	15.5	563.3	15.2	555	16	12.2	0.00	0.98	0.00	1.60	**555.0**	***16.1***	**545.4**	***15.5***
Man_11	0.84	0.028	1.45	626.1	21.4	560.4	16.2	573.4	15.7	553	16	10.5	0.00	0.99	0.00	1.71	**552.7**	***15.8***	**557.6**	***16.2***
Man_12	0.86	0.028	1.46	585.5	18.1	554.5	14.9	560.4	14.0	557	16	5.3	0.00	0.83	0.00	1.58	**557.3**	***16.0***	**552.3**	***14.8***
Man_13	0.83	0.028	1.47	591.6	20.4	551.4	15.1	559.1	14.6	554	16	6.8	0.00	0.94	0.00	1.75	**554.4**	***16.1***	**549.1**	***15.0***
Stern_04	0.85	0.025	1.70	449.8	19.5	528.1	14.4	513.4	13.4	495	17	-17.4	0.00	0.88	0.00	1.74	**495.4**	***16.6***	**529.1**	***14.5***
Stern_05	0.86	0.026	1.48	445.8	17.5	516.6	13.2	503.5	12.2	523	15	-15.9	0.00	0.79	0.00	1.50	**523.7**	***15.3***	**517.5**	***13.2***
Stern_06	0.86	0.026	1.55	468.0	18.2	501.9	13.4	495.7	12.6	520	16	-7.3	0.00	0.82	0.00	1.66	**520.3**	***15.9***	**502.3**	***13.5***
Stern_07	0.84	0.025	1.61	511.2	19.9	514.1	14.0	513.4	13.5	508	16	-0.6	0.00	0.91	0.00	1.71	**508.3**	***16.2***	**514.0**	***14.0***
Stern_08	0.85	0.026	1.63	459.3	19.9	514.1	14.3	503.9	13.4	512	16	-11.9	0.00	0.90	0.00	1.78	**512.5**	***16.5***	**514.7**	***14.3***
Stern_09	0.77	0.025	1.76	473.3	28.5	514.7	15.3	507.0	16.0	503	17	-8.8	0.00	1.29	0.00	2.05	**503.7**	***17.5***	**515.1**	***15.4***
Stern_10	0.82	0.025	1.58	503.6	23.1	502.1	14.5	502.1	14.4	501	16	0.3	0.00	1.05	0.00	1.77	**501.2**	***15.7***	**501.8**	***14.5***
Stern_11	0.81	0.026	1.56	476.6	23.6	512.4	14.3	505.7	14.3	516	16	-7.5	0.00	1.07	0.00	1.74	**516.5**	***15.9***	**512.8**	***14.4***
Stern_12	0.87	0.025	1.72	496.0	19.2	513.0	15.2	509.7	14.1	494	17	-3.4	0.00	0.87	0.00	1.78	**494.4**	***16.8***	**513.0**	***15.2***
Stern_13	0.83	0.025	1.61	485.4	23.4	503.5	15.3	500.1	14.9	500	16	-3.7	0.00	1.06	0.00	1.87	**499.6**	***15.9***	**503.6**	***15.3***
SternA_01	0.84	0.025	1.54	494.1	24.4	484.2	16.1	485.7	15.7	501	15	2.0	0.00	1.11	0.00	1.94	**501.3**	***15.3***	**483.8**	***16.1***
SternA_02	0.84	0.026	1.50	454.8	21.2	488.1	14.0	482.1	13.5	520	15	-7.3	0.00	0.95	0.00	1.71	**520.1**	***15.4***	**488.4**	***14.0***
SternA_03	0.84	0.025	1.53	481.9	22.4	476.9	14.6	477.6	14.2	500	15	1.0	0.00	1.01	0.00	1.79	**500.2**	***15.1***	**476.6**	***14.6***
SternB_01	0.86	0.024	1.64	473.5	19.6	493.1	14.0	489.5	13.2	478	15	-4.1	0.00	0.88	0.00	1.76	**477.9**	***15.5***	**493.2**	***14.0***
SternB_02	0.83	0.024	1.35	493.7	21.8	502.3	14.1	500.6	13.8	472	13	-1.7	0.00	0.99	0.00	1.77	**472.0**	***12.6***	**502.2**	***14.1***
SternB_03	0.86	0.024	1.52	470.1	18.6	490.4	13.4	486.6	12.6	486	15	-4.3	0.00	0.84	0.00	1.56	**485.8**	***14.6***	**490.5**	***13.4***

Xenotime

	comments	^{204}Pb	206Pb	207Pb	^{208}Pb	^{232}Th	^{238}U	Pbppm	Uppm	^{238}U/^{206}Pb	1σ %	^{207}Pb/^{206}Pb	1σ %	^{207}Pb/^{235}U	1σ %	^{206}Pb/^{238}U	1σ %	Rho	^{207}Pb/^{206}Pb	2σ abs
0502_xt_01		426	24390.23	4579.757	10559	1038327	22939	21.7	1776.8	110.413	1.26	0.182	2.01	0.227	2.37	0.009	1.26	0.53	2669	33
0502_xt_03		372	15424.69	5367.691	13697	206910	9972	18.9	772.4	75.453	3.66	0.351	2.31	0.641	4.33	0.013	3.66	0.85	3711	35
0502_xt_05		113	14030.99	662.5608	303	98062	16044	8.2	1242.7	135.799	1.16	0.048	1.98	0.049	2.29	0.007	1.16	0.50	97	47
0502_xt_06		109	16609.12	779.4385	304	104825	18241	9.7	1412.9	131.097	0.85	0.046	1.39	0.048	1.62	0.008	0.85	0.52	-2	33
0502_xt_07		74	12679.67	599.7679	315	102126	14670	7.5	1136.3	136.230	1.16	0.047	2.35	0.048	2.62	0.007	1.16	0.44	49	56
0502_xt_08		-59	15863.07	1013.317	984	120239	17269	9.8	1337.6	129.793	1.11	0.063	3.73	0.067	3.89	0.008	1.11	0.29	709	79
0502_xt_09		-112	28085.82	1321.644	839	289710	31174	16.6	2414.7	132.842	0.93	0.046	1.64	0.048	1.88	0.008	0.93	0.49	22	39
0502_xt_10		-20	25833.99	1236.328	724	242998	29006	15.3	2246.7	133.335	0.91	0.048	1.55	0.050	1.79	0.007	0.91	0.51	119	36
0502_xt_11		5	10195.21	1364.146	2333	32566	10597	7.6	820.8	123.066	1.39	0.136	4.18	0.152	4.41	0.008	1.39	0.32	2179	73
0502_mnz_01	mnz in aln - high cm-Pb	17522	410099.1	285129.9	806799	18381010	16781	824.7	1299.8	4.629	1.85	0.690	0.63	20.534	1.95	0.216	1.85	0.95	4709	9
0502_xt_02	hit zircon	-51	49665.61	2990.819	3097	224926	19172	30.6	1485.0	46.205	2.85	0.060	1.50	0.180	3.22	0.022	2.85	0.89	621	32
0502_xt_04	hit zircon	94	26970.07	1927.551	1873	18508	3661	16.9	283.5	15.711	1.93	0.072	1.88	0.633	2.70	0.064	1.93	0.72	991	38
0502_xt_12	clipped edge of zircon	-87	40985.41	2083.558	1835	571358	50049	24.7	3876.7	146.372	0.86	0.050	1.67	0.047	1.88	0.007	0.86	0.46	208	39
FC1_xnt_01		-94	125753.3	5999.072	6279	1834765	123901	75.8	9597.1	118.730	0.72	0.047	0.86	0.055	1.12	0.008	0.72	0.64	74	20
FC1_xnt_02		26	119537.9	5753.878	6578	1967790	119716	72.4	9273.0	117.781	0.81	0.047	0.79	0.055	1.13	0.008	0.81	0.71	61	19
FC1_xnt_03		-60	121550.2	5733.807	6519	1953893	121341	73.5	9398.8	118.568	0.75	0.047	0.83	0.055	1.12	0.008	0.75	0.67	44	20
FC1_xnt_04		-33	138453	6634.792	6851	2054273	137678	83.4	10664.2	119.313	0.68	0.048	0.80	0.055	1.05	0.008	0.68	0.65	100	19
FC1_xnt_05		67	134780.2	6459.448	6774	1928685	132287	81.3	10246.7	116.657	0.80	0.048	0.89	0.057	1.19	0.009	0.80	0.67	97	21
FC1_xnt_06		47	142294	6752.379	7212	2009539	136724	85.8	10590.4	115.943	0.89	0.048	0.89	0.057	1.26	0.009	0.89	0.71	81	21
FC1_xnt_07		-32	149153	7094.883	7824	2131319	145995	90.1	11308.5	115.919	0.85	0.047	0.88	0.056	1.23	0.009	0.85	0.70	57	21
FC1_xnt_08		297	144859.9	8911.599	13000	2050921	136037	91.6	10537.2	113.741	1.44	0.061	9.16	0.074	9.27	0.009	1.44	0.15	650	197
Man_Mnz_01		61	255264.2	15631.84	6440383	216723900	23640	3684.9	1831.1	11.012	0.49	0.061	0.48	0.760	0.69	0.091	0.49	0.71	629	10
Man_Mnz_02		63	247383.9	15196.07	6233227	215570800	22905	3566.6	1774.2	11.043	0.38	0.060	0.55	0.754	0.67	0.091	0.38	0.57	619	12
Man_Mnz_03		58	226627.7	14081.6	6091306	203123700	21204	3476.7	1642.5	11.095	0.68	0.062	0.67	0.774	0.95	0.090	0.68	0.71	686	14
Man_Mnz_04		-54	234589.9	14106.36	6397236	209698100	22192	3649.0	1718.9	11.240	0.42	0.060	0.49	0.736	0.64	0.089	0.42	0.65	603	11
Man_Mnz_05		-6	276949.3	16857.79	6858263	222040500	25078	3926.9	1942.5	10.824	0.57	0.061	0.60	0.773	0.82	0.092	0.57	0.69	630	13
Man_Mnz_06		80	266583.2	16163.69	6578178	219216900	24520	3767.1	1899.3	10.974	0.50	0.061	0.78	0.762	0.93	0.091	0.50	0.54	629	17
Man_Mnz_07		50	267832.3	16265.14	6713590	219606200	24713	3842.2	1914.2	10.835	0.56	0.061	0.61	0.770	0.83	0.092	0.56	0.67	624	13
Man_Mnz_08		45	259208.8	16189.32	6430556	212212000	23883	3682.0	1850.0	10.847	0.54	0.061	0.66	0.780	0.85	0.092	0.54	0.63	652	14
NISt612_01		243	6749.659	6107.307	14960	15544	198	15.3	15.4	3.548	0.97	0.910	1.02	35.370	1.41	0.282	0.97	0.69	5105	14
NISt612_02		316	6924.71	6149.142	14934	15259	202	15.4	15.6	3.443	1.15	0.893	1.48	35.743	1.87	0.290	1.15	0.61	5078	21
NISt612_03		407	6808.947	6382.287	15248	16513	202	15.6	15.7	3.540	1.19	0.926	1.01	36.059	1.56	0.283	1.19	0.76	5129	14
NISt612_04		316	6707.238	5947.826	14105	15425	194	14.7	15.1	3.524	1.20	0.900	1.10	35.180	1.63	0.284	1.20	0.74	5088	16
Stern_Mnz_01		97	513026	29908.23	2852343	98011310	53273	1864.2	4126.5	12.382	0.59	0.058	0.49	0.644	0.76	0.081	0.59	0.77	523	11
Stern_Mnz_02		-8	313455.2	18007.25	1920368	66336950	30567	1236.4	2367.7	11.384	0.77	0.057	0.62	0.692	0.99	0.088	0.77	0.78	497	14
Stern_Mnz_03		67	470499.9	27631.66	2673005	93646570	49632	1741.2	3844.4	12.335	0.80	0.058	0.51	0.647	0.95	0.081	0.80	0.84	526	11
Stern_Mnz_04		97	458779.1	26998.28	2672458	95271960	47217	1734.1	3657.3	12.184	0.57	0.059	0.51	0.664	0.76	0.082	0.57	0.75	554	11
Stern_Mnz_05		74	521213.9	30429.18	2995097	97277630	53444	1947.4	4139.7	12.013	0.77	0.058	0.45	0.667	0.89	0.083	0.77	0.86	534	10
Stern_Mnz_06		-45	525803.4	30807.44	3015823	96613070	52756	1961.5	4086.4	12.055	1.06	0.058	0.58	0.666	1.21	0.083	1.06	0.88	538	13
Stern_Mnz_07		27	427066.1	25074.71	2805557	99347580	45791	1788.7	3546.9	13.046	2.23	0.059	0.64	0.622	2.32	0.077	2.23	0.96	561	14
Stern_Mnz_08		-16	403796.3	23743.4	2568948	88668880	40212	1645.3	3114.7	11.784	0.87	0.058	0.53	0.682	1.01	0.085	0.87	0.86	542	11

Xenotime

	$^{206}Pb/^{238}U$	2σ abs	$^{207}Pb/^{235}U$	2σ abs	6-38/7-6	6-38/7-35	*f206*	1s %	$^{206}Pb^*/^{238}U$	1s %	Cor.206/238-Pb Age	2s [Ma]	Th/U min.	Th/U wr.	f	Cor. 206/238 age	*2s [Ma]*
0502_xt_01	58	1	208	9	97.8	72.0	0.170	2.01	0.0075	1.1	48	1.1	0.6	3.8	0.15	**48.4**	***1.1***
0502_xt_03	85	6	503	34	97.7	83.1	0.382	2.31	0.0082	2.4	53	2.5	0.3	3.8	0.07	**52.7**	***2.5***
0502_xt_05	47	1	48	2	51.4	2.0	0.001	1.98	0.0074	1.2	47	1.1	0.1	3.8	0.02	**47.4**	***1.1***
0502_xt_06	49	1	48	2	2744.7	-2.1	-0.001	1.39	0.0076	0.8	49	0.8	0.1	3.8	0.02	**49.2**	***0.8***
0502_xt_07	47	1	47	2	3.9	0.0	0.000	2.35	0.0073	1.2	47	1.1	0.1	3.8	0.02	**47.3**	***1.1***
0502_xt_08	49	1	66	5	93.0	24.8	0.020	3.73	0.0075	1.1	48	1.1	0.1	3.8	0.02	**48.6**	***1.1***
0502_xt_09	48	1	48	2	-118.5	-1.1	-0.001	1.64	0.0075	0.9	48	0.9	0.1	3.8	0.03	**48.5**	***0.9***
0502_xt_10	48	1	50	2	59.5	2.8	0.002	1.55	0.0075	0.9	48	0.9	0.1	3.8	0.03	**48.2**	***0.9***
0502_xt_11	52	1	144	12	97.6	63.8	0.112	4.18	0.0072	1.3	46	1.2	0.0	3.8	0.01	**46.4**	***1.2***
0502_mnz_01	1261	42	3117	37	73.2	59.5	0.715	0.63	0.0615	0.7	385	5.2	14.0	3.8	3.69	**384.6**	***5.2***
0502_xt_02	138	8	168	10	77.8	18.0	0.015	1.50	0.0213	2.8	136	7.6	0.2	3.8	0.04	**136.1**	***7.6***
0502_xt_04	398	15	498	21	59.9	20.1	0.022	1.88	0.0623	1.9	389	14.3	0.1	3.8	0.02	**389.6**	***14.3***
0502_xt_12	44	1	47	2	78.9	6.5	0.004	1.67	0.0068	0.9	44	0.7	0.1	3.8	0.04	**43.8**	***0.7***
FC1_xnt_01	54	1	54	1	27.3	0.8	0.001	0.86	0.0084	0.7	54	0.8	0.2	3.8	0.05	**54.2**	***0.8***
FC1_xnt_02	55	1	55	1	10.6	0.2	0.000	0.79	0.0085	0.8	54	0.9	0.2	3.8	0.06	**54.6**	***0.9***
FC1_xnt_03	54	1	54	1	-22.1	-0.4	0.000	0.83	0.0084	0.8	54	0.8	0.2	3.8	0.05	**54.3**	***0.8***
FC1_xnt_04	54	1	55	1	46.3	1.8	0.001	0.80	0.0084	0.7	54	0.7	0.2	3.8	0.05	**53.9**	***0.7***
FC1_xnt_05	55	1	56	1	43.3	1.7	0.001	0.89	0.0086	0.8	55	0.9	0.2	3.8	0.05	**55.1**	***0.9***
FC1_xnt_06	55	1	56	1	32.0	1.0	0.001	0.89	0.0086	0.9	55	1.0	0.2	3.8	0.05	**55.4**	***1.0***
FC1_xnt_07	55	1	55	1	3.3	0.0	0.000	0.88	0.0086	0.9	55	0.9	0.2	3.8	0.05	**55.5**	***0.9***
FC1_xnt_08	56	2	73	13	91.3	22.5	0.018	9.16	0.0086	1.4	55	1.6	0.2	3.8	0.05	**55.5**	***1.6***
Man_Mnz_01	560	5	574	6	11.0	2.4	0.002	0.48	0.0906	0.5	559	5.2	117.4	3.8	30.90	**556.2**	***5.2***
Man_Mnz_02	559	4	571	6	9.8	2.1	0.002	0.55	0.0904	0.4	558	4.1	120.5	3.8	31.72	**554.8**	***4.1***
Man_Mnz_03	556	7	582	8	18.9	4.5	0.004	0.67	0.0897	0.7	554	7.2	122.7	3.8	32.28	**550.9**	***7.2***
Man_Mnz_04	549	4	560	6	8.9	1.9	0.002	0.49	0.0888	0.4	548	4.4	121.0	3.8	31.85	**545.5**	***4.4***
Man_Mnz_05	570	6	582	7	9.6	2.1	0.002	0.60	0.0922	0.6	569	6.1	113.4	3.8	29.84	**565.7**	***6.1***
Man_Mnz_06	562	5	575	8	10.6	2.3	0.002	0.78	0.0909	0.5	561	5.3	114.5	3.8	30.13	**558.1**	***5.3***
Man_Mnz_07	569	6	580	7	8.8	1.9	0.002	0.61	0.0921	0.6	568	6.0	113.8	3.8	29.95	**565.3**	***6.0***
Man_Mnz_08	569	6	585	8	12.8	2.9	0.003	0.66	0.0919	0.5	567	5.8	113.8	3.8	29.95	**564.2**	***5.8***
NISt612_01	1601	27	3649	27	68.6	56.1	0.940	1.02	0.0170	1.0	109	2.1	1.0	3.8	0.26	**109.0**	***2.1***
NISt612_02	1644	33	3659	36	67.6	55.1	0.915	1.48	0.0247	1.4	157	4.2	1.0	3.8	0.25	**157.5**	***4.2***
NISt612_03	1604	34	3668	30	68.7	56.3	0.957	1.01	0.0120	1.0	77	1.5	1.0	3.8	0.28	**77.2**	***1.5***
NISt612_04	1610	34	3644	32	68.4	55.8	0.926	1.10	0.0210	1.0	134	2.7	1.0	3.8	0.27	**134.1**	***2.7***
Stern_Mnz_01	501	6	504	6	4.2	0.8	0.001	0.49	0.0807	0.6	500	5.6	23.6	3.8	6.20	**499.9**	***5.6***
Stern_Mnz_02	543	8	534	8	-9.2	-1.7	-0.001	0.62	0.0880	0.8	544	8.0	27.8	3.8	7.31	**543.0**	***8.0***
Stern_Mnz_03	502	8	507	8	4.5	0.8	0.001	0.51	0.0810	0.8	502	7.7	24.2	3.8	6.36	**501.7**	***7.7***
Stern_Mnz_04	508	6	517	6	8.3	1.6	0.001	0.51	0.0820	0.6	508	5.5	25.8	3.8	6.80	**507.3**	***5.5***
Stern_Mnz_05	515	8	519	7	3.4	0.6	0.001	0.45	0.0832	0.8	515	7.6	23.3	3.8	6.13	**514.7**	***7.6***
Stern_Mnz_06	514	10	518	10	4.6	0.8	0.001	0.58	0.0829	1.1	513	10.5	23.5	3.8	6.17	**512.9**	***10.5***
Stern_Mnz_07	476	20	491	18	15.2	3.0	0.003	0.64	0.0764	2.2	475	20.3	27.8	3.8	7.31	**474.3**	***20.3***
Stern_Mnz_08	525	9	528	8	3.1	0.6	0.001	0.53	0.0848	0.9	525	8.7	28.2	3.8	7.43	**524.2**	***8.7***

Titanite

		comments	^{204}Pb	^{206}Pb	^{207}Pb	^{208}Pb	^{232}Th	^{238}U		Pbppm		Uppm	$^{238}U/^{206}Pb$	1s %	$^{207}Pb/^{206}Pb$	1s %	$^{207}Pb/^{235}U$	1s %	$^{206}Pb/^{238}U$	1s %	Rho
16-05_01	19/03/2019		7550	151707	124679	304741	578	3696		9.691		0.868	0.0198	7.19	0.8158	0.71	5692.784	7.22	50.6321	7.19	1.00
16-05_02	19/03/2019		7997	159273	130868	320061	28302	18521		10.174		4.350	0.1089	4.42	0.8131	0.82	1028.747	4.49	9.1799	4.42	0.98
16-05_03	19/03/2019		14484	238722	229161	537520	0	1248		15.249		0.293	-0.0008	19.63	0.9422	0.59	-157908.114	19.64	-1216.119	19.63	1.00
16-05_04	19/03/2019		4509	87410	72436	178320	167	3414		5.583		0.802	0.0327	6.38	0.8217	0.78	3467.205	6.43	30.6167	6.38	0.99
16-05_05	19/03/2019		5613	111909	92197	224293	734	9606		7.148		2.256	0.0811	5.30	0.8154	0.78	1386.207	5.35	12.3351	5.30	0.99
16-05_06	19/03/2019		4406	84257	69581	171260	430	2203		5.382		0.517	-0.0027	22.25	0.8161	0.71	-41313.287	22.27	-367.3327	22.25	1.00
A04_20_01	19/03/2019		478	11826	5576	14454	46206	1069539	0.04	0.755	10.853	251.220	90.9508	1.40	0.4781	0.81	0.7245	1.62	0.0110	1.40	0.87
A04_20_02	19/03/2019		624	16073	7732	19072	68515	1467652	0.05	1.027	16.093	344.732	92.0140	1.90	0.4617	1.84	0.6915	2.65	0.0109	1.90	0.72
A04_20_03	19/03/2019		640	28520	10853	27112	111939	3243390	0.03	1.822	26.293	761.828	111.9682	1.95	0.3816	1.22	0.4697	2.31	0.0089	1.95	0.85
A04_20_04	19/03/2019		691	16780	12343	31899	13395	247597	0.05	1.072	3.146	58.157	14.7120	1.75	0.7251	0.82	6.7930	1.93	0.0680	1.75	0.91
A04_20_05	19/03/2019		310	9713	6492	16467	37981	377219	0.10	0.620	8.921	88.604	38.0565	1.82	0.6632	1.09	2.4017	2.12	0.0263	1.82	0.86
A04_20_06	19/03/2019		712	20838	12576	30737	28698	1033943	0.03	1.331	6.741	242.859	49.0897	1.78	0.5973	1.16	1.6768	2.13	0.0204	1.78	0.84
A04_20_07	19/03/2019		1429	37603	22107	57118	46887	1920833	0.02	2.402	11.013	451.178	51.3769	2.09	0.5981	1.10	1.6043	2.37	0.0195	2.09	0.89
A04_20_08	19/03/2019		640	17661	9390	23944	33520	1253803	0.03	1.128	7.873	294.501	70.3795	1.54	0.5330	1.19	1.0437	1.94	0.0142	1.54	0.79
A04_20_09	19/03/2019		878	41455	15493	38729	176983	4278263	0.04	2.648	41.571	1004.906	102.2644	1.61	0.3696	1.08	0.4981	1.94	0.0098	1.61	0.83
A04_20_10	19/03/2019		602	13019	8762	21840	10088	460877	0.02	0.832	2.370	108.254	35.5735	2.03	0.6721	1.24	2.6038	2.38	0.0281	2.03	0.85
A04_20_11	19/03/2019		1274	41093	19135	49980	214332	2614778	0.08	2.625	50.344	614.176	63.4221	1.54	0.4595	1.10	0.9985	1.89	0.0158	1.54	0.82
A04_20_12	19/03/2019		926	22440	14642	37522	49303	681414	0.07	1.433	11.581	160.055	28.5151	4.01	0.6470	1.42	3.1272	4.25	0.0351	4.01	0.94
A04_20_13	19/03/2019		472	13740	7069	18604	64121	1035865	0.06	0.878	15.061	243.311	75.5636	1.56	0.5039	1.29	0.9191	2.02	0.0132	1.56	0.77
A04_20_14	19/03/2019		886	25658	13079	33982	103140	1524446	0.07	1.639	24.226	358.072	59.0003	1.70	0.5055	0.99	1.1807	1.97	0.0169	1.70	0.86
A04_20_15	19/03/2019		1272	37390	18207	47245	180659	2307625	0.08	2.388	42.434	542.030	61.7367	1.54	0.4886	1.11	1.0906	1.90	0.0162	1.54	0.81
A04_20_16	19/03/2019		928	20861	15253	40031	30991	320060	0.10	1.333	7.279	75.178	15.2507	1.85	0.7193	1.06	6.5005	2.13	0.0656	1.85	0.87
A04_20_17	19/03/2019		775	21804	12803	33417	40126	947624	0.04	1.393	9.425	222.584	42.9565	1.80	0.5818	1.06	1.8667	2.09	0.0233	1.80	0.86
A04_20_18	19/03/2019		1170	38505	21312	54137	100824	1913041	0.05	2.460	23.682	449.348	49.6969	1.45	0.5426	0.91	1.5048	1.71	0.0201	1.45	0.85
A04_20_19	19/03/2019		861	30095	16134	40796	96126	1729187	0.06	1.922	22.579	406.163	57.7692	1.31	0.5273	0.78	1.2578	1.53	0.0173	1.31	0.86
A04_20_20	19/03/2019		842	29822	13453	34500	185955	2540299	0.07	1.905	43.678	596.682	85.0972	1.20	0.4514	0.73	0.7311	1.41	0.0118	1.20	0.85
A04_20_21	19/03/2019		196	5141	3008	7738	12654	296173	0.04	0.328	2.972	69.567	57.1380	2.13	0.5846	1.23	1.4101	2.46	0.0175	2.13	0.86
A04_20_22	19/03/2019		768	24764	13610	34561	70705	1305376	0.05	1.582	16.608	306.615	53.2340	1.46	0.5458	0.62	1.4131	1.59	0.0188	1.46	0.92
A04_20_23	19/03/2019		718	20913	12207	31292	21530	908993	0.02	1.336	5.057	213.510	43.2291	1.33	0.5801	0.85	1.8494	1.58	0.0231	1.33	0.84
A04_20_24	19/03/2019		767	22974	12506	31902	57162	1380680	0.04	1.467	13.426	324.303	59.3563	1.44	0.5335	0.79	1.2386	1.64	0.0168	1.44	0.88
A05-15_01	19/03/2019		771	18745	11966	31111	42555	630486	0.07	1.197		148.093	33.5611	1.62	0.6350	0.69	2.6075	1.76	0.0298	1.62	0.92
A05-15_02	19/03/2019		1107	29733	16086	42152	103445	1556989	0.07	1.899		365.716	52.5319	1.21	0.5348	0.64	1.4030	1.37	0.0190	1.21	0.89
A05-15_04	19/03/2019		1365	28309	19308	50126	57723	778183	0.07	1.808		182.785	26.9039	3.54	0.6755	0.82	3.4604	3.63	0.0372	3.54	0.97
A05-15_05	19/03/2019		900	22038	14278	37429	62938	647792	0.10	1.408		152.158	29.6082	1.26	0.6448	0.67	3.0013	1.43	0.0338	1.26	0.88
A05-15_06	19/03/2019		888	21335	10036	25552	101554	1640783	0.06	1.363		385.398	77.2377	1.31	0.4633	0.70	0.8267	1.49	0.0129	1.31	0.88
A05-15_07	19/03/2019		788	18284	13676	37416	308984	194221	1.59	1.168		45.620	10.6302	3.13	0.7413	0.69	9.6102	3.21	0.0941	3.13	0.98
A05-15_08	19/03/2019		790	24438	14157	36069	45641	1150646	0.04	1.561		270.271	46.8707	1.66	0.5743	0.69	1.6886	1.79	0.0213	1.66	0.92
A05-15_09	19/03/2019		1509	32421	24237	63513	33722	372886	0.09	2.071		87.586	9.4992	5.94	0.7350	0.67	10.6633	5.97	0.1053	5.94	0.99
A05-15_10	19/03/2019		677	25263	13215	34309	111290	1493649	0.07	1.614		350.838	58.5653	1.43	0.5204	0.61	1.2247	1.55	0.0171	1.43	0.92
A05-15_11	19/03/2019		799	19655	11045	28388	92845	1132672	0.08	1.255		266.049	57.3114	1.38	0.5558	0.67	1.3366	1.54	0.0174	1.38	0.90
A05-15_12	19/03/2019		726	18257	12067	31793	101663	491422	0.21	1.166		115.428	26.7868	1.34	0.6575	0.58	3.3830	1.46	0.0373	1.34	0.92
A05-15_13	19/03/2019		792	18774	13636	36240	64913	342022	0.19	1.199		80.336	18.2908	1.59	0.7133	0.65	5.3744	1.72	0.0547	1.59	0.93
A05-15_14	19/03/2019		931	25551	14092	37137	265347	1703311	0.16	1.632		400.085	62.8329	2.23	0.5515	0.82	1.2097	2.38	0.0159	2.23	0.94
A05-15_15	19/03/2019		540	19486	10316	26923	110829	1224099	0.09	1.245		287.524	62.8425	1.30	0.5271	0.69	1.1560	1.47	0.0159	1.30	0.88
A05-15_16	19/03/2019		652	15723	10676	27735	29815	410327	0.07	1.004		96.380	26.0795	1.48	0.6696	0.81	3.5388	1.69	0.0383	1.48	0.88
A05-15_17	19/03/2019	outlier?	381	13814	6650	16507	12013	1218501	0.01	0.882		286.209	89.3605	1.21	0.4789	0.71	0.7386	1.41	0.0112	1.21	0.86
A05-15_18	19/03/2019		755	20678	12389	32085	95159	897428	0.11	1.321		210.794	43.3504	1.38	0.5927	0.62	1.8843	1.51	0.0231	1.38	0.91
A05-15_19	19/03/2019		847	21080	13049	34161	108302	783396	0.14	1.347		184.009	37.3041	1.28	0.6135	0.57	2.2667	1.40	0.0268	1.28	0.91
A05-15_20	19/03/2019		1043	39323	17759	44224	241140	2925703	0.08	2.512		687.208	74.3874	1.13	0.4499	0.60	0.8335	1.28	0.0134	1.13	0.88
~~A05-15_03~~	~~19/03/2019~~	~~rej - inclusion~~	~~20388~~	~~2888048~~	~~465550~~	~~1358704~~	~~45285300~~	~~121529200~~	0.37	~~184.480~~		~~28545.568~~	~~41.7940~~	~~1.64~~	~~0.1571~~	~~2.68~~	~~0.5181~~	~~3.14~~	~~0.0239~~	~~1.64~~	~~0.52~~
FCT_01	19/03/2019		352	8521	3950	16259	2373326	923400		0.544		216.894	108.0586	1.26	0.4639	0.91	0.5917	1.55	0.0093	1.26	0.81
FCT_02	19/03/2019		361	8660	4036	16020	2396733	939663		0.553		220.714	108.6807	1.30	0.4588	0.80	0.5818	1.52	0.0092	1.30	0.85
FCT_03	19/03/2019		363	8374	3900	16123	2347124	901457		0.535		211.740	107.9783	1.34	0.4612	0.74	0.5886	1.53	0.0093	1.34	0.87
FCT_04	19/03/2019		216	8479	4041	16148	2305792	934808		0.542		219.574	109.8360	1.32	0.4691	0.78	0.5886	1.53	0.0091	1.32	0.86
FCT_05	19/03/2019		224	8483	4141	16416	2314927	861816		0.542		202.429	101.7225	1.30	0.4833	0.99	0.6548	1.64	0.0098	1.30	0.80
FCT_06	19/03/2019		305	9365	4995	17490	2052556	812076		0.598		190.746	86.7029	3.18	0.5233	1.22	0.8318	3.41	0.0115	3.18	0.93
FCT_07	19/03/2019		273	8131	3881	16092	2258915	826638		0.519		194.166	101.6309	1.40	0.4776	0.96	0.6477	1.69	0.0098	1.40	0.83
FCT_08	19/03/2019		214	8844	4005	16425	2253556	963661		0.565		226.351	109.9548	1.37	0.4539	1.03	0.5689	1.71	0.0091	1.37	0.80
Khan_01	19/03/2019		1047	913063	67665	261241	4023730	10626230		58.324		2495.959	11.6078	1.21	0.0734	1.11	0.8712	1.65	0.0861	1.21	0.74
Khan_02	19/03/2019		287	897212	56423	231647	4078887	10768120		57.311		2529.286	11.9875	1.16	0.0625	0.42	0.7183	1.24	0.0834	1.16	0.94
Khan_03	19/03/2019		284	906769	56785	234791	4137838	10753170		57.922		2525.773	11.8208	1.12	0.0620	0.41	0.7232	1.20	0.0846	1.12	0.94
Khan_04	19/03/2019		373	903792	56710	236178	4128426	10731010		57.731		2520.569	11.8197	1.13	0.0620	0.41	0.7225	1.20	0.0846	1.13	0.94
Khan_05	19/03/2019		282	899670	56438	234581	3939525	10779300		57.468		2531.912	11.9433	1.10	0.0620	0.45	0.7160	1.19	0.0837	1.10	0.93
Khan_06	19/03/2019		342	893508	55931	230933	3939715	10827980		57.075		2543.347	12.0676	1.13	0.0619	0.40	0.7071	1.20	0.0829	1.13	0.94
Khan_07	19/03/2019		469	895699	58894	236843	3898638	10736340		57.214		2521.820	11.9449	1.10	0.0652	0.42	0.7526	1.18	0.0837	1.10	0.93
Khan_08	19/03/2019		365	906599	57321	234088	3968556	10951360		57.911		2572.327	12.0971	1.19	0.0627	0.40	0.7149	1.26	0.0827	1.19	0.95
NIST614_01	19/03/2019		8581	146167	136114	325036	221489	158439		38.794		37.215	1.0817	1.50	0.9145	0.49	116.5246	1.58	0.9245	1.50	0.95
NIST614_02	19/03/2019		8809	147737	134467	324440	218544	158799		38.751		37.300	1.0594	1.68	0.9029	0.48	117.4574	1.75	0.9439	1.68	0.96
NIST614_03	19/03/2019		8553	147648	134664	320117	218545	157750		38.481		37.053	1.0836	1.59	0.9045	0.53	115.0421	1.67	0.9228	1.59	0.95
NIST614_04	19/03/2019		8457	146597	133544	318739	219683	161576		38.255		37.952	1.0860	1.66	0.9072	0.50	115.1326	1.73	0.9208	1.66	0.96
Ont1_01	19/03/2019		965	321467	37431	238704	1818069	1724922		20.534		405.161	5.3295	1.20	0.1155	0.46	2.9866	1.28	0.1876	1.20	0.93
Ont1_02	19/03/2019		1063	319344	37099	236541	1799103	1724086		20.399		404.964	5.3785	1.21	0.1152	0.49	2.9524	1.30	0.1859	1.21	0.93
Ont1_03	19/03/2019		999	318871	36726	233774	1781483	1688134		20.368		396.520	5.3022	1.21	0.1142	0.45	2.9688	1.29	0.1886	1.21	0.94
Ont1_04	19/03/2019		970	312754	36713	230006	1781231	1686135		19.978		396.051	5.3356	1.16	0.1155	0.45	2.9831	1.25	0.1874	1.16	0.93
Ont2_01	19/03/2019		1013	184997	25198	177530	1327194	997246		11.817		234.240	5.3438	1.25	0.1356	0.73	3.4969	1.45	0.1871	1.25	0.86
Ont2_02	19/03/2019		952	182298	25059	174257	1287601	960734		11.645		225.663	5.1886	1.34	0.1366	0.76	3.6280	1.54	0.1927	1.34	0.87
Ont2_03	19/03/2019		825	181158	24002	174704	1310114	980738		11.572		230.362	5.3891	1.21	0.1310	0.46	3.3504	1.30	0.1856	1.21	0.93
Ont2_04	19/03/2019		770	185435	24278	174964	1327873	995677		11.845		233.871	5.3256	1.22	0.1297	0.56	3.3571	1.34	0.1878	1.22	0.91
Ont2_05	19/03/2019		883	160823	22013	148252	1170201	862280		10.273		202.538	5.3660	1.34	0.1369	1.00	3.5151	1.67	0.1864	1.34	0.80
Ont2_06	19/03/2019		690	154619	20502	145279	1131061	830484		9.877		195.070	5.3417	1.21	0.1306	0.50	3.3689	1.31	0.1872	1.21	0.92
Ont2_07	19/03/2019		685	159201	20869	150192	1166082	849782		10.169		199.602	5.3634	1.17	0.1301	0.51	3.3418	1.28	0.1865	1.17	0.92
Ont2_08	19/03/2019		657	156560	21030	150065	1184114	839211		10.001		197.119	5.3691	1.23	0.1326	0.51	3.4045	1.33	0.1863	1.23	0.92

	Titanite																		
	$^{207}Pb/^{206}Pb$	2s abs	$^{206}Pb/^{238}U$	2s abs	$^{207}Pb/^{235}U$	2s abs	6-38/7-6	6-38/7-35	*f206*	1s %	$^{206}Pb^*/^{238}U$	1s %	206/238-Pb	2s [Ma]	Th/U min.	Th/U wr.	f	DT. 206/238 age	*2s [Ma]*
16-05_01	4950	20	25426	850	8780	137	-413.7	-189.6	-181.142	0.71	9222.2417	1315.7	58852	21320.2	0.2	3.8	0.04	**58861.9**	***21320.2***
16-05_02	4945	23	14958	494	7044	87	-202.5	-112.4	-20.388	0.82	196.3380	95.9	34069	6883.0	1.5	3.8	0.40	**34074.3**	***6883.0***
16-05_03	5154	17	#VALUE!	#VALUE!	#VALUE!	#VALUE!	#VALUE!	#VALUE!	#VALUE!	0.59	#VALUE!	#VALUE!	#VALUE!	#VALUE!	0.0	3.8	0.00	**#VALUE!**	***#VALUE!***
16-05_04	4960	22	22264	751	8277	123	-348.9	-169.0	-130.989	0.78	4041.0842	848.0	53534	18616.8	0.0	3.8	0.01	**53543.0**	***18616.8***
16-05_05	4949	22	16699	603	7346	103	-237.4	-127.3	-35.630	0.78	451.8351	196.0	39423	10258.6	0.1	3.8	0.02	**39429.6**	***10258.6***
16-05_06	4950	20	#VALUE!	#VALUE!	#VALUE!	#VALUE!	#VALUE!	#VALUE!	#VALUE!	0.71	#VALUE!	#VALUE!	#VALUE!	#VALUE!	0.2	3.8	0.05	**#VALUE!**	***#VALUE!***
A04_20_01	4175	24	70	2	553	14	98.3	87.3	0.545	0.81	0.0050	0.8	32	0.5	0.0	3.8	0.01	**32.3**	***0.5***
A04_20_02	4123	55	70	3	534	22	98.3	86.9	0.524	1.84	0.0052	1.3	33	0.9	0.0	3.8	0.01	**33.3**	***0.9***
A04_20_03	3838	37	57	2	391	15	98.5	85.3	0.423	1.22	0.0052	1.2	33	0.8	0.0	3.8	0.01	**33.2**	***0.8***
A04_20_04	4781	23	424	14	2085	34	91.1	79.7	0.854	0.82	0.0099	0.7	64	0.9	0.1	3.8	0.01	**63.6**	***0.9***
A04_20_05	4653	31	167	6	1243	30	96.4	86.5	0.779	1.09	0.0058	0.9	37	0.7	0.1	3.8	0.03	**37.5**	***0.7***
A04_20_06	4501	34	130	5	1000	27	97.1	87.0	0.695	1.16	0.0062	1.0	40	0.8	0.0	3.8	0.01	**40.0**	***0.8***
A04_20_07	4503	32	124	5	972	29	97.2	87.2	0.696	1.10	0.0059	1.0	38	0.8	0.0	3.8	0.01	**38.1**	***0.8***
A04_20_08	4335	35	91	3	726	20	97.9	87.5	0.614	1.19	0.0055	0.9	35	0.7	0.0	3.8	0.01	**35.3**	***0.7***
A04_20_09	3790	33	63	2	410	13	98.3	84.7	0.408	1.08	0.0058	1.0	37	0.8	0.0	3.8	0.01	**37.3**	***0.8***
A04_20_10	4672	36	179	7	1302	34	96.2	86.3	0.790	1.24	0.0059	1.1	38	0.8	0.0	3.8	0.01	**38.1**	***0.8***
A04_20_11	4116	33	101	3	703	19	97.5	85.7	0.521	1.10	0.0076	0.9	49	0.9	0.1	3.8	0.02	**48.6**	***0.9***
A04_20_12	4617	41	222	17	1439	63	95.2	84.6	0.757	1.42	0.0085	1.5	55	1.6	0.1	3.8	0.02	**54.8**	***1.6***
A04_20_13	4253	38	85	3	662	19	98.0	87.2	0.578	1.29	0.0056	1.0	36	0.7	0.1	3.8	0.02	**36.0**	***0.7***
A04_20_14	4257	29	108	4	792	21	97.5	86.3	0.579	0.99	0.0071	0.9	46	0.8	0.1	3.8	0.02	**45.9**	***0.8***
A04_20_15	4207	33	104	3	749	20	97.5	86.2	0.558	1.11	0.0072	0.9	46	0.8	0.1	3.8	0.02	**46.1**	***0.8***
A04_20_16	4770	30	409	15	2046	37	91.4	80.0	0.847	1.06	0.0100	0.9	64	1.2	0.1	3.8	0.03	**64.5**	***1.2***
A04_20_17	4463	31	148	5	1069	27	96.7	86.1	0.675	1.06	0.0076	0.9	49	0.9	0.0	3.8	0.01	**48.7**	***0.9***
A04_20_18	4361	27	128	4	932	21	97.1	86.2	0.626	0.91	0.0075	0.8	48	0.8	0.1	3.8	0.01	**48.5**	***0.8***
A04_20_19	4319	23	111	3	827	17	97.4	86.6	0.607	0.78	0.0068	0.7	44	0.6	0.1	3.8	0.01	**43.9**	***0.6***
A04_20_20	4090	22	75	2	557	12	98.2	86.5	0.511	0.73	0.0057	0.7	37	0.5	0.1	3.8	0.02	**37.0**	***0.5***
A04_20_21	4470	36	112	5	893	29	97.5	87.5	0.680	1.23	0.0056	1.1	36	0.8	0.0	3.8	0.01	**36.2**	***0.8***
A04_20_22	4370	18	120	3	894	19	97.3	86.6	0.630	0.62	0.0069	0.7	45	0.6	0.1	3.8	0.01	**44.8**	***0.6***
A04_20_23	4459	25	147	4	1063	21	96.7	86.1	0.673	0.85	0.0076	0.7	49	0.7	0.0	3.8	0.01	**48.7**	***0.7***
A04_20_24	4336	23	108	3	818	18	97.5	86.8	0.615	0.79	0.0065	0.7	42	0.6	0.0	3.8	0.01	**41.8**	***0.6***
A05-15_01	4590	20	189	6	1303	26	95.9	85.5	0.742	0.69	0.0077	0.7	49	0.6	0.1	3.8	0.02	**49.4**	***0.6***
A05-15_02	4340	19	122	3	890	16	97.2	86.3	0.616	0.64	0.0073	0.6	47	0.6	0.1	3.8	0.02	**47.1**	***0.6***
A05-15_04	4680	24	235	16	1518	56	95.0	84.5	0.793	0.82	0.0077	1.0	49	1.0	0.1	3.8	0.02	**49.4**	***1.0***
A05-15_05	4612	19	214	5	1408	21	95.4	84.8	0.754	0.67	0.0083	0.6	53	0.6	0.1	3.8	0.03	**53.4**	***0.6***
A05-15_06	4128	21	83	2	612	14	98.0	86.4	0.526	0.70	0.0061	0.7	39	0.6	0.1	3.8	0.02	**39.5**	***0.6***
A05-15_07	4813	20	580	35	2398	57	88.0	75.8	0.873	0.69	0.0120	0.7	77	1.1	1.6	3.8	0.42	**76.7**	***1.1***
A05-15_08	4444	20	136	4	1004	23	96.9	86.4	0.666	0.69	0.0071	0.7	46	0.7	0.0	3.8	0.01	**45.9**	***0.7***
A05-15_09	4801	19	645	72	2494	105	86.6	74.1	0.863	0.67	0.0144	1.0	92	1.8	0.1	3.8	0.02	**92.2**	***1.8***
A05-15_10	4300	18	109	3	812	17	97.5	86.6	0.598	0.61	0.0069	0.7	44	0.6	0.1	3.8	0.02	**44.2**	***0.6***
A05-15_11	4397	20	112	3	862	18	97.5	87.1	0.643	0.67	0.0062	0.7	40	0.5	0.1	3.8	0.02	**40.1**	***0.5***
A05-15_12	4641	17	236	6	1500	23	94.9	84.3	0.770	0.58	0.0086	0.5	55	0.6	0.2	3.8	0.05	**55.2**	***0.6***
A05-15_13	4758	19	343	11	1881	29	92.8	81.8	0.840	0.65	0.0087	0.6	56	0.7	0.2	3.8	0.05	**56.2**	***0.7***
A05-15_14	4385	24	102	5	805	26	97.7	87.4	0.638	0.82	0.0058	1.0	37	0.7	0.2	3.8	0.04	**37.2**	***0.7***
A05-15_15	4319	20	102	3	780	16	97.6	87.0	0.607	0.69	0.0063	0.7	40	0.5	0.1	3.8	0.02	**40.3**	***0.5***
A05-15_16	4667	23	243	7	1536	26	94.8	84.2	0.786	0.81	0.0082	0.7	53	0.7	0.1	3.8	0.02	**52.9**	***0.7***
A05-15_17	4178	21	72	2	562	12	98.3	87.2	0.546	0.71	0.0051	0.7	33	0.4	0.0	3.8	0.00	**32.8**	***0.4***
A05-15_18	4490	18	147	4	1076	20	96.7	86.3	0.689	0.62	0.0072	0.6	46	0.6	0.1	3.8	0.03	**46.2**	***0.6***
A05-15_19	4540	16	171	4	1202	19	96.2	85.8	0.715	0.57	0.0076	0.5	49	0.5	0.1	3.8	0.04	**49.1**	***0.5***
A05-15_20	4085	18	86	2	616	12	97.9	86.0	0.509	0.60	0.0066	0.6	42	0.5	0.1	3.8	0.02	**42.5**	***0.5***
~~A05-15_03~~	~~2425~~	~~91~~	~~152~~	~~5~~	~~424~~	~~22~~	~~93.7~~	~~64.0~~	~~0.136~~	~~2.68~~	~~0.0207~~	~~1.5~~	~~132~~	~~3.8~~	~~0.4~~	~~3.8~~	~~0.10~~	**~~122.0~~**	***~~2.8~~***
FCT_01	4130	27	59	1	472	12	98.6	87.4	0.528	0.91	0.0044	0.8	28	0.4	2.6	3.8	0.68	**28.2**	***0.4***
FCT_02	4114	24	59	2	466	11	98.6	87.3	0.521	0.80	0.0044	0.7	28	0.4	2.6	3.8	0.67	**28.4**	***0.4***
FCT_03	4122	22	59	2	470	11	98.6	87.4	0.524	0.74	0.0044	0.7	28	0.4	2.6	3.8	0.69	**28.4**	***0.4***
FCT_04	4147	23	58	2	470	11	98.6	87.6	0.534	0.78	0.0042	0.7	27	0.4	2.5	3.8	0.65	**27.3**	***0.4***
FCT_05	4191	29	63	2	511	13	98.5	87.7	0.552	0.99	0.0044	0.8	28	0.5	2.7	3.8	0.71	**28.4**	***0.5***
FCT_06	4308	36	74	5	615	31	98.3	88.0	0.603	1.22	0.0046	1.5	29	0.9	2.5	3.8	0.67	**29.5**	***0.9***
FCT_07	4174	28	63	2	507	13	98.5	87.6	0.545	0.96	0.0045	0.8	29	0.5	2.7	3.8	0.72	**28.8**	***0.5***
FCT_08	4098	31	58	2	457	13	98.6	87.2	0.515	1.03	0.0044	0.9	28	0.5	2.3	3.8	0.62	**28.4**	***0.5***
Khan_01	1024	45	533	12	636	15	48.0	16.3	0.019	1.11	0.0845	1.2	523	11.9	0.4	3.8	0.10	**523.1**	***11.9***
Khan_02	690	18	517	12	550	10	25.2	6.0	0.006	0.42	0.0829	1.2	513	11.4	0.4	3.8	0.10	**513.6**	***11.4***
Khan_03	675	18	524	11	553	10	22.4	5.3	0.005	0.41	0.0841	1.1	521	11.2	0.4	3.8	0.10	**521.0**	***11.2***
Khan_04	673	18	524	11	552	10	22.2	5.2	0.005	0.41	0.0842	1.1	521	11.2	0.4	3.8	0.10	**521.1**	***11.2***
Khan_05	676	19	518	11	548	10	23.3	5.5	0.006	0.45	0.0833	1.1	516	10.9	0.4	3.8	0.10	**515.8**	***10.9***
Khan_06	671	17	513	11	543	10	23.6	5.5	0.006	0.40	0.0824	1.1	510	11.0	0.4	3.8	0.10	**510.7**	***11.0***
Khan_07	782	18	518	11	570	10	33.7	9.0	0.009	0.42	0.0829	1.1	514	10.7	0.4	3.8	0.10	**513.7**	***10.7***
Khan_08	700	17	512	12	548	11	26.8	6.5	0.007	0.40	0.0821	1.2	509	11.6	0.4	3.8	0.10	**508.9**	***11.6***
NIST614_01	5112	14	4220	93	4840	31	17.4	12.8	0.917	0.49	0.0765	0.5	475	4.3	1.4	3.8	0.37	**475.6**	***4.3***
NIST614_02	5093	14	4285	104	4848	35	15.9	11.6	0.889	0.48	0.1050	0.5	644	5.8	1.4	3.8	0.36	**644.1**	***5.8***
NIST614_03	5096	15	4215	97	4827	33	17.3	12.7	0.899	0.53	0.0933	0.5	575	5.5	1.4	3.8	0.36	**575.1**	***5.5***
NIST614_04	5100	14	4208	102	4828	34	17.5	12.8	0.905	0.50	0.0878	0.5	543	5.0	1.4	3.8	0.36	**542.9**	***5.0***
Ont1_01	1888	17	1109	24	1404	19	41.3	21.1	0.049	0.46	0.1785	1.1	1059	22.2	1.1	3.8	0.28	**1058.9**	***22.2***
Ont1_02	1883	18	1099	24	1395	20	41.6	21.2	0.049	0.49	0.1768	1.1	1050	22.2	1.0	3.8	0.27	**1049.9**	***22.2***
Ont1_03	1868	16	1114	25	1400	19	40.4	20.4	0.047	0.45	0.1797	1.2	1066	22.7	1.1	3.8	0.28	**1065.8**	***22.7***
Ont1_04	1888	16	1107	24	1403	19	41.3	21.1	0.049	0.45	0.1783	1.1	1058	21.6	1.1	3.8	0.28	**1057.7**	***21.6***
																		1058.1	***22.2***
Ont2_01	2172	25	1106	25	1527	23	49.1	27.6	0.074	0.73	0.1733	1.2	1030	22.0	1.3	3.8	0.35	**1030.4**	***22.0***
Ont2_02	2184	27	1136	28	1556	24	48.0	27.0	0.074	0.76	0.1785	1.2	1059	24.1	1.3	3.8	0.35	**1059.0**	***24.1***
Ont2_03	2112	16	1097	24	1493	20	48.0	26.5	0.069	0.46	0.1728	1.1	1028	21.5	1.3	3.8	0.35	**1027.8**	***21.5***
Ont2_04	2094	20	1109	25	1494	21	47.0	25.8	0.067	0.56	0.1753	1.1	1041	22.0	1.3	3.8	0.35	**1041.4**	***22.0***
Ont2_05	2188	35	1102	27	1531	26	49.6	28.0	0.076	1.00	0.1722	1.2	1024	23.4	1.4	3.8	0.36	**1024.6**	***23.4***
Ont2_06	2106	18	1106	25	1497	20	47.5	26.1	0.068	0.50	0.1745	1.1	1037	21.7	1.4	3.8	0.36	**1037.2**	***21.7***
Ont2_07	2099	18	1102	24	1491	20	47.5	26.1	0.067	0.51	0.1739	1.1	1034	20.9	1.4	3.8	0.36	**1033.8**	***20.9***
Ont2_08	2133	18	1101	25	1505	21	48.4	26.9	0.071	0.51	0.1731	1.1	1029	21.8	1.4	3.8	0.37	**1029.4**	***21.8***

RUTILE

		comments	^{204}Pb	^{206}Pb	^{207}Pb	^{208}Pb	^{232}Th	^{238}U	Pb ppm	U ppm	$^{238}U/^{206}Pb$	1s %	$^{207}Pb/^{206}Pb$	1s %	$^{207}Pb/^{235}U$	1s %	$^{206}Pb/^{238}U$	1s %	Rho
PCA_01	16/05/2018		bd	26430	4467	3493	bd	76336	0.021	4.985	2.9605	3.17	0.1594	4.05	7.4186	5.14	0.3378	3.17	0.62
PCA_02	16/05/2018		bd	30638	3653	569	bd	90524	0.021	5.911	2.9257	3.22	0.1193	1.87	5.6177	3.73	0.3418	3.22	0.86
PCA_03	16/05/2018		bd	27831	3172	67	bd	84850	0.019	5.541	3.0764	3.25	0.1135	1.55	5.0846	3.60	0.3251	3.25	0.90
PCA_04	16/05/2018		bd	24329	2838	226	bd	75957	0.017	4.960	3.1737	3.20	0.1206	1.67	5.2352	3.61	0.3151	3.20	0.89
PCA_05	16/05/2018		bd	33026	3776	60	bd	96414	0.023	6.296	2.9749	3.32	0.1153	1.59	5.3402	3.68	0.3361	3.32	0.90
PCA_06	16/05/2018		bd	34393	4016	53	bd	103847	0.024	6.781	3.0246	3.21	0.1169	1.86	5.3264	3.72	0.3306	3.21	0.86
PCA_07	16/05/2018		bd	32017	3750	86	bd	97047	0.022	6.337	2.9953	3.26	0.1155	1.73	5.3126	3.69	0.3339	3.26	0.88
PCA_08	16/05/2018		bd	31893	3698	98	bd	97348	0.022	6.357	3.0520	3.17	0.1175	1.50	5.3053	3.51	0.3277	3.17	0.90
PCA_09	16/05/2018		bd	38980	4594	126	bd	118019	0.027	7.706	3.0179	3.22	0.1182	1.60	5.3970	3.59	0.3314	3.22	0.90
PCA_10	16/05/2018		bd	39058	4435	59	bd	114632	0.027	7.485	2.9493	3.16	0.1131	1.45	5.2865	3.48	0.3391	3.16	0.91
PCA_11	16/05/2018		bd	55938	6425	330	bd	161436	0.038	10.542	2.8489	3.55	0.1140	1.70	5.5126	3.93	0.3510	3.55	0.90
PCA_12	16/05/2018		bd	37163	4111	142	bd	108172	0.025	7.063	2.9618	3.10	0.1128	1.52	5.2479	3.45	0.3376	3.10	0.90
PCA_13	16/05/2018		bd	75477	8844	443	bd	240088	0.052	15.677	3.1853	3.18	0.1171	1.64	5.0646	3.58	0.3139	3.18	0.89
PCA_14	16/05/2018		bd	29313	3312	106	bd	84953	0.020	5.547	2.9067	3.27	0.1138	1.44	5.3959	3.58	0.3440	3.27	0.92
PCA_15	16/05/2018		bd	35109	4057	156	bd	101665	0.024	6.639	2.9030	3.19	0.1166	1.51	5.5333	3.53	0.3445	3.19	0.90
PCA_16	16/05/2018		bd	41160	4762	100	bd	118363	0.028	7.729	2.8345	3.37	0.1129	1.55	5.4913	3.71	0.3528	3.37	0.91
R10_01	07/07/2017		-39	44153	3356	-36	-4	1770	7.00	35.29	5.144	1.86	0.076	1.36	2.046	2.31	0.194	1.86	0.81
R10_02	07/07/2017		-21	44502	3455	-25	6	1737	7.07	34.64	4.983	1.70	0.077	1.21	2.126	2.09	0.201	1.70	0.82
R10_03	07/07/2017		44	44856	3435	6	10	1804	7.12	35.98	5.120	1.84	0.076	0.97	2.042	2.08	0.195	1.84	0.88
R10_04	07/07/2017		5	42933	3284	-18	-4	1766	6.81	35.22	5.247	1.89	0.075	1.03	1.978	2.15	0.191	1.89	0.88
R10_05	07/07/2017		-18	43881	3358	49	-1	1787	6.97	35.62	5.170	1.72	0.076	0.83	2.020	1.91	0.193	1.72	0.90
R10_06	07/07/2017		-79	45415	3366	19	-1	1828	7.20	36.44	5.158	1.80	0.074	1.03	1.971	2.07	0.194	1.80	0.87
R10_07	07/07/2017		44	44389	3418	9	18	1799	7.05	35.88	5.154	1.70	0.076	0.70	2.025	1.83	0.194	1.70	0.92
R10_08	07/07/2017		46	44665	3406	-2	46	1808	7.09	36.05	5.170	1.73	0.075	0.93	2.006	1.96	0.193	1.73	0.88
R10_09	07/07/2017		-97	17964	1369	22	1	644	2.85	12.84	5.298	2.02	0.076	1.84	1.972	2.74	0.189	2.02	0.74
R10_10	07/07/2017		57	18328	1436	5	-3	635	2.92	12.66	5.207	2.47	0.078	1.84	2.051	3.08	0.192	2.47	0.80
R10_11	07/07/2017		92	17736	1352	23	-3	612	2.82	12.20	5.131	1.90	0.077	2.14	2.058	2.86	0.195	1.90	0.66
R10_12	07/07/2017		-87	18557	1459	39	-3	676	2.96	13.47	5.395	1.61	0.077	1.92	1.968	2.51	0.185	1.61	0.64
R10_13	07/07/2017		54	15905	1214	10	-1	560	2.53	11.16	5.267	1.87	0.076	2.38	1.995	3.03	0.190	1.87	0.62
R10_14	07/07/2017		86	14774	1113	3	-1	541	2.34	10.79	5.430	1.48	0.073	1.73	1.863	2.28	0.184	1.48	0.65
R10_15	07/07/2017		14	15648	1257	5	20	534	2.49	10.65	5.122	2.12	0.078	1.50	2.100	2.59	0.195	2.12	0.82
R10_01	16/05/2018		bd	98369	7458	40	bd	532263	6.423	34.756	5.4013	3.46	0.0758	1.61	1.9349	3.82	0.1851	3.46	0.91
R10_02	16/05/2018		bd	98438	7870	65	bd	543757	6.428	35.507	5.5364	3.26	0.0796	1.51	1.9822	3.59	0.1806	3.26	0.91
R10_03	16/05/2018		bd	104056	7687	26	bd	527429	6.795	34.440	5.1297	3.30	0.0732	1.37	1.9673	3.58	0.1949	3.30	0.92
R10_04	16/05/2018		bd	99401	7901	921	337	521428	6.491	34.048	5.2043	3.39	0.0784	1.31	2.0758	3.64	0.1922	3.39	0.93
R10_05	16/05/2018		bd	93227	7395	577	1271	498916	6.088	32.578	5.3628	3.19	0.0774	1.55	1.9884	3.55	0.1865	3.19	0.90
R10_06	16/05/2018		bd	100190	7677	58	bd	530633	6.542	34.650	5.2849	3.30	0.0767	1.44	1.9990	3.60	0.1892	3.30	0.92
R10_07	16/05/2018		bd	101225	7728	60	bd	531953	6.610	34.736	5.2442	3.28	0.0761	1.41	1.9987	3.57	0.1907	3.28	0.92
R10_08	16/05/2018		bd	100387	7663	44	bd	538743	6.555	35.179	5.3859	3.20	0.0762	1.37	1.9506	3.48	0.1857	3.20	0.92
R10_09	16/05/2018		bd	103322	7881	16	bd	536968	6.747	35.063	5.1809	3.22	0.0751	1.38	1.9991	3.50	0.1930	3.22	0.92
R10_10	16/05/2018		bd	97242	7472	18	bd	526914	6.350	34.407	5.4566	3.32	0.0765	1.35	1.9310	3.59	0.1833	3.32	0.93
R10_11	16/05/2018		bd	105276	8259	44	bd	545151	6.874	35.598	5.1056	3.36	0.0785	1.50	2.1183	3.68	0.1959	3.36	0.91
R10_12	16/05/2018		bd	195471	14887	9	bd	1159567	12.764	75.718	5.9676	3.31	0.0750	1.56	1.7325	3.66	0.1676	3.31	0.90
R10_13	16/05/2018		bd	172724	13099	67	bd	964966	11.279	63.011	5.6479	3.28	0.0752	1.33	1.8352	3.54	0.1771	3.28	0.93
R10_14	16/05/2018		bd	190882	14757	49	bd	1102486	12.464	71.991	5.8152	3.22	0.0762	1.54	1.8061	3.57	0.1720	3.22	0.90
R10_15	16/05/2018		bd	109506	8456	86	bd	578191	7.151	37.755	5.2452	3.53	0.0764	1.60	2.0075	3.88	0.1907	3.53	0.91
R10_16	16/05/2018		bd	194479	14633	46	bd	1141891	12.699	74.564	5.9106	3.14	0.0748	1.38	1.7442	3.43	0.1692	3.14	0.92
R10_01	18/03/2018		bd	69873	5308	23	bd	248706	12.544	41.483	5.3383	1.51	0.0758	1.16	1.9557	1.90	0.1873	1.51	0.79
R10_02	18/03/2018		bd	68230	5204	32	bd	242832	12.254	40.503	5.4124	1.87	0.0764	1.14	1.9455	2.19	0.1848	1.87	0.86
R10_03	18/03/2018		bd	56396	4450	21	bd	207236	10.152	34.566	5.5725	1.79	0.0771	1.16	1.9072	2.13	0.1795	1.79	0.84
R10_04	18/03/2018		bd	59298	4588	32	bd	223331	10.661	37.251	5.4149	1.35	0.0765	0.98	1.9469	1.67	0.1847	1.35	0.81
R10_05	18/03/2018		bd	52162	3953	28	bd	189140	9.364	31.548	5.3912	1.64	0.0754	1.01	1.9281	1.93	0.1855	1.64	0.85
R10_06	18/03/2018		bd	47002	3705	15	bd	165767	8.460	27.649	5.2979	1.54	0.0781	1.00	2.0309	1.84	0.1888	1.54	0.84
R10_07	18/03/2018		bd	48037	3706	88	bd	179560	8.645	29.950	5.4845	1.40	0.0767	1.00	1.9266	1.72	0.1823	1.40	0.81
R10_08	18/03/2018		bd	39544	3110	28	bd	152370	7.119	25.415	5.4803	1.65	0.0770	1.12	1.9372	2.00	0.1825	1.65	0.83
R10_09	18/03/2018		bd	39361	3026	41	bd	150279	7.077	25.066	5.4243	1.58	0.0750	1.11	1.9056	1.93	0.1844	1.58	0.82
R10_10	18/03/2018		bd	37330	2886	30	bd	142051	6.713	23.694	5.5256	1.38	0.0763	1.05	1.9037	1.73	0.1810	1.38	0.80
R10_11	18/03/2018		bd	31657	2465	26	bd	120714	5.696	20.135	5.3858	1.18	0.0766	1.19	1.9611	1.68	0.1857	1.18	0.70
R10_12	18/03/2018		bd	36317	2763	23	bd	136342	6.522	22.741	5.3198	1.47	0.0761	1.28	1.9715	1.94	0.1880	1.47	0.75
R10_01	19/03/2019		80299	80299	6131	15	-1	306761	9.050	32.116	5.5961	1.57	0.0752	0.93	1.8508	1.82	0.1787	1.57	0.86
R10_02	19/03/2019		81779	81779	6268	-15	5	302167	9.216	31.635	5.4038	1.65	0.0754	0.90	1.9236	1.88	0.1851	1.65	0.88
R10_03	19/03/2019		75714	75714	5928	3	-1	272637	8.548	28.544	5.2767	1.67	0.0757	1.13	1.9778	2.01	0.1895	1.67	0.83
R10_04	19/03/2019		69023	69023	5291	30	-1	254712	7.783	26.667	5.3962	1.48	0.0757	0.89	1.9342	1.72	0.1853	1.48	0.86
R10_05	19/03/2019		68008	68008	5397	9	-1	248530	7.686	26.020	5.3067	1.58	0.0764	0.92	1.9841	1.83	0.1884	1.58	0.86
R10_06	19/03/2019		63327	63327	4871	-9	10	225492	7.139	23.608	5.0718	1.79	0.0753	1.16	2.0466	2.13	0.1972	1.79	0.84
R10_07	19/03/2019		56973	56973	4421	30	3	224121	6.431	23.464	5.8337	1.65	0.0763	0.75	1.8035	1.81	0.1714	1.65	0.91
R10_08	19/03/2019		53516	53516	4095	13	3	199635	6.033	20.901	5.5153	1.84	0.0756	1.06	1.8880	2.13	0.1813	1.84	0.87
R10_09	19/03/2019		52060	52060	4004	29	-1	192223	5.873	20.125	5.4418	1.59	0.0762	0.91	1.9300	1.83	0.1838	1.59	0.87
R10_10	19/03/2019		85571	85571	6683	112	2	347145	8.880	33.375	5.7239	1.92	0.0773	0.83	1.8614	2.09	0.1747	1.92	0.92
R10_11	19/03/2019		88306	88306	6946	77	10	346559	9.165	33.318	5.5424	1.77	0.0772	0.85	1.9185	1.96	0.1804	1.77	0.90
R10_12	19/03/2019		92424	92424	7161	88	-1	357902	9.583	34.409	5.4815	1.82	0.0762	0.94	1.9171	2.05	0.1824	1.82	0.89
R10_13	19/03/2019		73566	73566	5736	48	9	277484	7.629	26.678	5.1947	2.00	0.0778	0.81	2.0653	2.16	0.1925	2.00	0.93
R10_14	19/03/2019		77742	77742	6151	49	0	286562	8.070	27.550	5.1482	1.87	0.0775	0.87	2.0737	2.06	0.1942	1.87	0.91
R10_15	19/03/2019		71704	71704	5571	47	0	276452	7.434	26.578	5.5338	1.89	0.0762	0.85	1.8981	2.08	0.1807	1.89	0.91
R10_16	19/03/2019		84671	84671	6693	84	10	328101	8.792	31.544	5.3567	1.79	0.0773	0.83	1.9889	1.97	0.1867	1.79	0.91
R10_17	19/03/2019		78335	78335	6041	86	10	289050	8.120	27.790	5.1872	1.95	0.0763	1.01	2.0284	2.20	0.1928	1.95	0.89
R10_18	19/03/2019		80783	80783	6343	63	-1	315661	8.382	30.348	5.3690	1.80	0.0758	0.94	1.9464	2.03	0.1863	1.80	0.89
R10_19	19/03/2019		82588	82588	6310	78	12	313057	8.554	30.098	5.2496	2.05	0.0761	0.84	1.9982	2.21	0.1905	2.05	0.92
R10_20	19/03/2019		80659	80659	6229	38	-1	313541	8.357	30.144	5.2720	1.80	0.0759	0.97	1.9830	2.05	0.1897	1.80	0.88
R10_21	19/03/2019		79090	79090	6033	42	-1	305115	8.188	29.334	5.2123	1.89	0.0746	1.16	1.9737	2.22	0.1919	1.89	0.85
R10_22	19/03/2019		75333	75333	5788	64	4	314823	7.805	30.267	5.8024	1.80	0.0759	0.67	1.8025	1.92	0.1723	1.80	0.94
R10_23	19/03/2019		79627	79627	6265	48	15	320866	8.262	30.848	5.5688	1.91	0.0771	0.77	1.9073	2.06	0.1796	1.91	0.93
R10_24	19/03/2019		77675	77675	5962	43	8	316360	8.045	30.415	5.6985	1.75	0.0751	0.85	1.8175	1.94	0.1755	1.75	0.90
R10_25	19/03/2019		75551	75551	5894	40	11	309159	7.834	29.723	5.5788	1.59	0.0769	0.78	1.8988	1.77	0.1792	1.59	0.90
R10_26	19/03/2019		83573	83573	6353	32	12	313474	8.649	30.138	5.2302	1.74	0.0755	0.76	1.9891	1.90	0.1912	1.74	0.92
R10_27	19/03/2019		83635	83635	6579	60	29	326332	8.679	31.374	5.3501	1.74	0.0766	0.83	1.9743	1.93	0.1869	1.74	0.90
R10_28	19/03/2019		71914	71914	5485	38	8	284248	7.445	27.328	5.4076	1.68	0.0755	0.84	1.9233	1.87	0.1849	1.68	0.89
R10_29	19/03/2019		71567	71567	5600	69	3	296895	7.426	28.544	5.6587	1.52	0.0767	0.70	1.8690	1.67	0.1767	1.52	0.91
R10_30	19/03/2019		80293	80293	6160	59	12	314092	8.317	30.197	5.3896	1.68	0.0762	0.82	1.9493	1.87	0.1855	1.68	0.90
Sugluk_01	16/05/2018		bd	72161	7679	77	bd	241075	0.049	15.742	3.3461	3.20	0.1066	1.37	4.3913	3.48	0.2989	3.20	0.92
Sugluk_02	16/05/2018		bd	73695	7860	105	bd	238442	0.050	15.570	3.2390	3.20	0.1069	1.39	4.5493	3.49	0.3087	3.20	0.92
Sugluk_03	16/05/2018		bd	75646	8341	228	bd	245004	0.052	15.998	3.1840	3.21	0.1080	1.53	4.6760	3.55	0.3141	3.21	0.90
Sugluk_04	16/05/2018		bd	72001	7674	48	bd	233722	0.049	15.262	3.2575	3.27	0.1056	1.44	4.4665	3.57	0.3070	3.27	0.92
Sugluk_05	16/05/2018		bd	72234	7633	60	bd	226768	0.049	14.808	3.1749	3.21	0.1043	1.46	4.5278	3.53	0.3150	3.21	0.91
Sugluk_06	16/05/2018		bd	68106	7403	85	bd	227533	0.046	14.858	3.3423	3.30	0.1070	1.51	4.4137	3.63	0.2992	3.30	0.91
Sugluk_07	16/05/2018		bd	75162	8083	270	bd	227043	0.051	14.826	3.0791	3.25	0.1052	1.35	4.7088	3.52	0.3248	3.25	0.92
Sugluk_08	16/05/2018		bd	74401	7934	26	bd	247768	0.050	16.179	3.3455	3.12	0.1051	1.49	4.3287	3.45	0.2989	3.12	0.90
Sugluk_09	16/05/2018		bd	72623	7611	-2	bd	228183	0.049	14.900	3.1632	3.29	0.1054	1.42	4.5920	3.59	0.3161	3.29	0.92
Sugluk_10	16/05/2018		bd	69741	7534	3	bd	231243	0.047	15.100	3.3461	3.35	0.1082	1.52	4.4569	3.68	0.2989	3.35	0.91
Sugluk_11	16/05/2018		bd	63772	6677	41	INF	203683	0.043	13.300	3.2254	3.24	0.1047	1.54	4.4732	3.59	0.3100	3.24	0.90
Sugluk_12	16/05/2018		bd	68516	7533	64	1	227690	0.047	14.868	3.2728	3.17	0.1081	1.48	4.5532	3.49	0.3055	3.17	0.91
Sugluk_13	16/05/2018		bd	139108	14698	39	INF	490446	0.094	32.025	3.5248	3.17	0.1059	1.41	4.1399	3.47	0.2837	3.17	0.91
Sugluk_14	16/05/2018		bd	142241	15530	26	1	501543	0.097	32.750	3.4792	3.33	0.1070	1.40	4.2379	3.61	0.2874	3.33	0.92
Sugluk_15	16/05/2018		bd	80501	8543	46	7	240109	0.055	15.679	2.9429	3.26	0.1066	1.47	4.9901	3.57	0.3398	3.26	0.91
Sugluk_16	16/05/2018		bd	133664	14371	41	INF	435843	0.091	28.460	3.2353	3.28	0.1065	1.51	4.5365	3.61	0.3091	3.28	0.91
PCA_01	19/03/2019		72083	72083	8407	-31	-1	159245	8.424	16.672	3.3168	1.73	0.1160	1.10	4.8199	2.05	0.3015	1.73	0.84
PCA_02	19/03/2019		72888	72888	8873	-26	-1	159696	8.557	16.719	3.1899	1.69	0.1191	1.12	5.1445	2.03	0.3135	1.69	0.83
PCA_03	19/03/2019		71578	71578	8233	-23	-1	150567	8.353	15.764	3.1334	1.70	0.1137	1.14	5.0026	2.04	0.3191	1.70	0.83
PCA_04	19/03/2019		68085	68085	8157	64	10	146652	7.989	15.354	3.1615	1.70	0.1175	1.05	5.1209	2.00	0.3163	1.70	0.85

RUTILE

	$^{207}Pb/^{206}Pb$	2s abs	$^{206}Pb/^{238}U$	2s abs	$^{207}Pb/^{235}U$	2s abs	c. % 6-38/	c. %6-38/7	*f206*	1s %	$^{206}Pb^*/^{238}U$	1s %	?06/238-Pb	2s [Ma]	Th/U min.	Th/U wr.	f	. 206/238	*2s [Ma]*
PCA_01	2449	137	1876	102	2163	88	23.4	13.3	0.052	4.05	0.3203	3.0	1791	93.6	0.0	3.8	0.00	**1791.5**	***93.6***
PCA_02	1945	67	1895	105	1919	62	2.6	1.2	0.006	1.87	0.3398	3.2	1886	103.8	0.0	3.8	0.00	**1885.9**	***103.8***
PCA_03	1856	56	1814	102	1834	59	2.3	1.0	-0.001	1.55	0.3253	3.3	1815	102.2	0.0	3.8	0.00	**1815.7**	***102.2***
PCA_04	1964	60	1766	98	1858	60	10.1	5.0	0.007	1.67	0.3127	3.2	1754	97.0	0.0	3.8	0.00	**1754.6**	***97.0***
PCA_05	1884	57	1868	107	1875	61	0.9	0.4	0.001	1.59	0.3357	3.3	1866	106.5	0.0	3.8	0.00	**1866.2**	***106.5***
PCA_06	1909	67	1841	102	1873	62	3.6	1.7	0.003	1.86	0.3296	3.2	1836	101.6	0.0	3.8	0.00	**1836.6**	***101.6***
PCA_07	1887	62	1857	104	1871	61	1.6	0.7	0.002	1.73	0.3333	3.3	1854	104.0	0.0	3.8	0.00	**1854.8**	***104.0***
PCA_08	1918	54	1827	100	1870	58	4.8	2.3	0.004	1.50	0.3264	3.2	1821	99.5	0.0	3.8	0.00	**1821.1**	***99.5***
PCA_09	1929	57	1845	102	1884	60	4.4	2.1	0.005	1.60	0.3298	3.2	1837	101.6	0.0	3.8	0.00	**1837.7**	***101.6***
PCA_10	1850	52	1882	102	1867	58	-1.7	-0.8	-0.001	1.45	0.3394	3.2	1884	102.5	0.0	3.8	0.00	**1884.3**	***102.5***
PCA_11	1863	61	1939	118	1903	65	-4.1	-1.9	0.000	1.70	0.3511	3.5	1940	117.7	#VALUE!	3.8	#VALUE!	**#VALUE!**	***117.7***
PCA_12	1845	55	1875	100	1860	57	-1.7	-0.8	-0.001	1.52	0.3381	3.1	1878	100.3	#VALUE!	3.8	#VALUE!	**#VALUE!**	***100.3***
PCA_13	1912	59	1760	97	1830	59	7.9	3.8	0.003	1.64	0.3129	3.2	1755	96.8	#VALUE!	3.8	#VALUE!	**#VALUE!**	***96.8***
PCA_14	1861	52	1906	107	1884	59	-2.4	-1.2	0.000	1.44	0.3441	3.3	1907	107.2	0.0	3.8	0.00	**1906.9**	***107.2***
PCA_15	1904	54	1908	104	1906	59	-0.2	-0.1	0.003	1.51	0.3435	3.2	1903	103.9	0.0	3.8	0.00	**1903.8**	***103.9***
PCA_16	1847	56	1948	112	1899	62	-5.5	-2.6	-0.001	1.55	0.3532	3.4	1950	112.5	#VALUE!	3.8	#VALUE!	**#VALUE!**	***112.5***
R10_01	1104	27	1145	39	1131	31	-3.7	-1.3	-0.002	1.36	0.1948	1.9	1147	39.1	0.0	3.8	0.00	**1147.4**	***39.1***
R10_02	1118	24	1179	37	1157	28	-5.5	-1.9	-0.003	1.21	0.2013	1.7	1182	36.8	0.0	3.8	0.00	**1182.4**	***36.8***
R10_03	1091	19	1150	39	1129	28	-5.4	-1.8	-0.003	0.97	0.1959	1.8	1153	38.7	0.0	3.8	0.00	**1153.4**	***38.7***
R10_04	1076	21	1124	39	1108	29	-4.5	-1.5	-0.002	1.03	0.1910	1.9	1127	39.0	0.0	3.8	0.00	**1127.1**	***39.0***
R10_05	1089	17	1140	36	1122	26	-4.6	-1.6	-0.002	0.83	0.1939	1.7	1142	35.9	0.0	3.8	0.00	**1142.8**	***35.9***
R10_06	1035	21	1142	37	1106	27	-10.3	-3.3	-0.005	1.03	0.1948	1.8	1148	37.8	0.0	3.8	0.00	**1147.8**	***37.8***
R10_07	1088	14	1143	35	1124	25	-5.1	-1.7	-0.003	0.70	0.1945	1.7	1146	35.6	0.0	3.8	0.00	**1146.2**	***35.6***
R10_08	1075	19	1140	36	1118	26	-6.0	-2.0	-0.003	0.93	0.1940	1.7	1143	36.2	0.0	3.8	0.00	**1143.3**	***36.2***
R10_09	1090	37	1115	41	1106	36	-2.2	-0.8	-0.001	1.84	0.1890	2.0	1116	41.4	0.0	3.8	0.00	**1116.0**	***41.4***
R10_10	1134	37	1132	51	1133	41	0.2	0.0	0.000	1.84	0.1920	2.5	1132	51.1	0.0	3.8	0.00	**1132.6**	***51.1***
R10_11	1111	43	1148	40	1135	38	-3.3	-1.2	-0.002	2.14	0.1953	1.9	1150	40.0	0.0	3.8	0.00	**1150.1**	***40.0***
R10_12	1123	38	1096	32	1105	33	2.4	0.8	0.001	1.92	0.1851	1.6	1095	32.3	0.0	3.8	0.00	**1095.1**	***32.3***
R10_13	1102	48	1121	38	1114	40	-1.7	-0.6	-0.001	2.38	0.1900	1.9	1121	38.4	0.0	3.8	0.00	**1121.8**	***38.4***
R10_14	1024	35	1090	30	1068	30	-6.4	-2.0	-0.003	1.73	0.1847	1.5	1093	29.7	0.0	3.8	0.00	**1093.0**	***29.7***
R10_15	1148	30	1150	44	1149	35	-0.2	-0.1	0.000	1.50	0.1952	2.1	1150	44.4	0.0	3.8	0.00	**1150.0**	***44.4***
R10_01	1091	65	1095	69	1093	50	-0.4	-0.2	0.000	1.61	0.1852	3.5	1095	69.4	0.0	3.8	0.00	**1095.5**	***69.4***
R10_02	1188	59	1070	64	1109	47	9.9	3.5	0.004	1.51	0.1798	3.2	1066	63.5	0.0	3.8	0.00	**1066.4**	***63.5***
R10_03	1020	56	1148	69	1104	47	-12.5	-4.0	-0.003	1.37	0.1956	3.3	1152	69.5	0.0	3.8	0.00	**1151.8**	***69.5***
R10_04	1157	52	1133	70	1141	49	2.0	0.7	0.003	1.31	0.1916	3.4	1130	69.8	0.0	3.8	0.00	**1130.3**	***69.8***
R10_05	1131	62	1102	64	1112	47	2.5	0.8	0.002	1.55	0.1862	3.2	1101	64.2	0.0	3.8	0.00	**1100.8**	***64.2***
R10_06	1112	57	1117	67	1115	48	-0.4	-0.2	0.001	1.44	0.1891	3.3	1116	67.3	0.0	3.8	0.00	**1116.6**	***67.3***
R10_07	1096	57	1125	67	1115	47	-2.6	-0.9	0.000	1.41	0.1907	3.3	1125	67.3	0.0	3.8	0.00	**1125.3**	***67.3***
R10_08	1101	55	1098	64	1099	46	0.3	0.1	0.000	1.37	0.1856	3.2	1098	64.3	0.0	3.8	0.00	**1097.9**	***64.3***
R10_09	1073	55	1138	67	1115	46	-6.1	-2.0	-0.001	1.38	0.1932	3.2	1139	67.0	0.0	3.8	0.00	**1139.0**	***67.0***
R10_10	1107	54	1085	66	1092	47	2.0	0.7	0.001	1.35	0.1832	3.3	1084	65.9	0.0	3.8	0.00	**1084.5**	***65.9***
R10_11	1159	59	1153	71	1155	50	0.5	0.1	0.003	1.50	0.1953	3.4	1150	70.3	0.0	3.8	0.00	**1150.2**	***70.3***
R10_12	1069	63	999	61	1021	46	6.6	2.2	-0.001	1.56	0.1678	3.3	1000	61.0	0.0	3.8	0.00	**1000.0**	***61.0***
R10_13	1074	54	1051	63	1058	45	2.2	0.7	-0.001	1.33	0.1772	3.3	1052	63.3	0.0	3.8	0.00	**1052.1**	***63.3***
R10_14	1101	62	1023	61	1048	46	7.1	2.4	0.000	1.54	0.1719	3.2	1023	60.6	0.0	3.8	0.00	**1022.9**	***60.6***
R10_15	1106	64	1125	73	1118	51	-1.7	-0.6	0.000	1.60	0.1906	3.5	1124	72.5	0.0	3.8	0.00	**1124.7**	***72.5***
R10_16	1063	55	1008	58	1025	43	5.2	1.7	-0.001	1.38	0.1694	3.1	1009	58.5	0.0	3.8	0.00	**1009.2**	***58.5***
R10_01	1089	46	1107	31	1100	25	-1.7	-0.6	-0.001	1.16	0.1875	1.5	1108	30.8	0.0	3.8	0.00	**1108.0**	***30.8***
R10_02	1106	45	1093	38	1097	29	1.2	0.4	0.001	1.14	0.1847	1.9	1092	37.5	0.0	3.8	0.00	**1092.6**	***37.5***
R10_03	1124	46	1064	35	1084	28	5.4	1.8	0.003	1.16	0.1790	1.8	1061	34.8	0.0	3.8	0.00	**1061.6**	***34.8***
R10_04	1108	39	1092	27	1097	22	1.4	0.4	0.001	0.98	0.1845	1.3	1092	27.0	0.0	3.8	0.00	**1092.0**	***27.0***
R10_05	1080	41	1097	33	1091	25	-1.6	-0.6	-0.001	1.01	0.1856	1.6	1098	33.1	0.0	3.8	0.00	**1097.9**	***33.1***
R10_06	1149	40	1115	31	1126	25	3.0	1.0	0.002	1.00	0.1885	1.5	1113	31.3	0.0	3.8	0.00	**1113.3**	***31.3***
R10_07	1113	40	1080	28	1090	23	3.0	1.0	0.001	1.00	0.1821	1.4	1078	27.7	0.0	3.8	0.00	**1078.5**	***27.7***
R10_08	1122	45	1080	33	1094	26	3.7	1.2	0.002	1.12	0.1821	1.6	1079	32.6	0.0	3.8	0.00	**1078.8**	***32.6***
R10_09	1069	45	1091	32	1083	25	-2.1	-0.7	-0.001	1.11	0.1845	1.6	1092	31.7	0.0	3.8	0.00	**1092.0**	***31.7***
R10_10	1104	42	1072	27	1082	23	2.8	0.9	0.001	1.05	0.1807	1.4	1071	27.2	0.0	3.8	0.00	**1071.2**	***27.2***
R10_11	1112	48	1098	24	1102	22	1.2	0.4	0.001	1.19	0.1856	1.2	1097	23.8	0.0	3.8	0.00	**1097.5**	***23.8***
R10_12	1098	51	1110	30	1106	26	-1.2	-0.4	-0.001	1.28	0.1881	1.5	1111	29.9	0.0	3.8	0.00	**1111.3**	***29.9***
R10_01	1073	37	1060	31	1064	24	1.2	0.4	0.001	0.93	0.1786	1.6	1059	30.5	0.0	3.8	0.00	**1059.5**	***30.5***
R10_02	1080	36	1095	33	1089	25	-1.4	-0.5	-0.001	0.90	0.1852	1.7	1095	33.3	0.0	3.8	0.00	**1095.5**	***33.3***
R10_03	1088	45	1119	34	1108	27	-2.8	-1.0	-0.001	1.13	0.1898	1.7	1120	34.3	0.0	3.8	0.00	**1120.5**	***34.3***
R10_04	1088	35	1096	30	1093	23	-0.7	-0.3	0.000	0.89	0.1854	1.5	1096	29.8	0.0	3.8	0.00	**1096.6**	***29.8***
R10_05	1105	37	1113	32	1110	24	-0.7	-0.3	0.000	0.92	0.1885	1.6	1113	32.1	0.0	3.8	0.00	**1113.6**	***32.1***
R10_06	1077	46	1160	38	1131	29	-7.7	-2.6	-0.004	1.16	0.1980	1.8	1164	38.3	0.0	3.8	0.00	**1164.6**	***38.3***
R10_07	1104	30	1020	31	1047	23	7.6	2.6	0.004	0.75	0.1708	1.6	1016	30.8	0.0	3.8	0.00	**1016.5**	***30.8***
R10_08	1083	43	1074	36	1077	28	0.8	0.3	0.000	1.06	0.1812	1.8	1074	36.3	0.0	3.8	0.00	**1074.0**	***36.3***
R10_09	1101	36	1087	32	1092	24	1.2	0.4	0.001	0.91	0.1837	1.6	1087	31.6	0.0	3.8	0.00	**1087.2**	***31.6***
R10_10	1129	33	1038	37	1068	27	8.1	2.8	0.004	0.83	0.1740	1.9	1034	36.5	0.0	3.8	0.00	**1034.2**	***36.5***
R10_11	1125	34	1069	35	1088	26	5.0	1.7	0.003	0.85	0.1800	1.8	1067	34.5	0.0	3.8	0.00	**1067.0**	***34.5***
R10_12	1102	38	1080	36	1087	27	1.9	0.6	0.001	0.94	0.1822	1.8	1079	36.0	0.0	3.8	0.00	**1079.5**	***36.0***
R10_13	1143	32	1135	42	1137	29	0.7	0.2	0.000	0.81	0.1924	2.0	1135	41.5	0.0	3.8	0.00	**1134.8**	***41.5***
R10_14	1133	35	1144	39	1140	28	-1.0	-0.4	-0.001	0.87	0.1943	1.9	1145	39.0	0.0	3.8	0.00	**1145.2**	***39.0***
R10_15	1101	34	1071	37	1080	27	2.7	0.9	0.001	0.85	0.1805	1.9	1069	37.2	0.0	3.8	0.00	**1069.7**	***37.2***
R10_16	1129	33	1103	36	1112	26	2.3	0.8	0.001	0.83	0.1865	1.8	1102	36.1	0.0	3.8	0.00	**1102.4**	***36.1***
R10_17	1104	40	1136	41	1125	29	-2.9	-1.0	-0.002	1.01	0.1931	2.0	1138	40.6	0.0	3.8	0.00	**1138.3**	***40.6***
R10_18	1091	38	1101	36	1097	27	-1.0	-0.3	0.000	0.94	0.1863	1.8	1102	36.4	0.0	3.8	0.00	**1101.8**	***36.4***
R10_19	1098	34	1124	42	1115	30	-2.4	-0.8	-0.001	0.84	0.1907	2.0	1125	42.2	0.0	3.8	0.00	**1125.6**	***42.2***
R10_20	1091	39	1120	37	1110	27	-2.6	-0.9	-0.001	0.97	0.1899	1.8	1121	37.0	0.0	3.8	0.00	**1121.3**	***37.0***
R10_21	1059	47	1131	39	1107	29	-6.8	-2.2	-0.003	1.16	0.1925	1.9	1135	39.4	0.0	3.8	0.00	**1135.2**	***39.4***
R10_22	1092	27	1025	34	1046	25	6.1	2.0	0.003	0.67	0.1718	1.8	1022	33.9	0.0	3.8	0.00	**1022.3**	***33.9***
R10_23	1123	31	1065	37	1084	27	5.2	1.8	0.003	0.77	0.1791	1.9	1062	37.1	0.0	3.8	0.00	**1062.2**	***37.1***
R10_24	1072	34	1042	34	1052	25	2.8	0.9	0.001	0.85	0.1752	1.7	1041	33.4	0.0	3.8	0.00	**1041.2**	***33.4***
R10_25	1118	31	1063	31	1081	23	4.9	1.6	0.003	0.78	0.1788	1.6	1060	30.9	0.0	3.8	0.00	**1060.6**	***30.9***
R10_26	1082	30	1128	36	1112	25	-4.3	-1.4	-0.002	0.76	0.1916	1.7	1130	36.1	0.0	3.8	0.00	**1130.4**	***36.1***
R10_27	1112	33	1105	35	1107	26	0.7	0.2	0.000	0.83	0.1868	1.7	1104	35.2	0.0	3.8	0.00	**1104.6**	***35.2***
R10_28	1081	34	1094	34	1089	25	-1.2	-0.4	-0.001	0.84	0.1850	1.7	1094	33.7	0.0	3.8	0.00	**1094.7**	***33.7***
R10_29	1114	28	1049	29	1070	22	5.9	2.0	0.003	0.70	0.1762	1.5	1046	29.1	0.0	3.8	0.00	**1046.3**	***29.1***
R10_30	1101	33	1097	34	1098	25	0.4	0.1	0.000	0.82	0.1855	1.7	1097	33.7	0.0	3.8	0.00	**1097.3**	***33.7***
					1101	42													
Sugluk_01	1742	50	1686	94	1711	56	3.3	1.5	0.001	1.37	0.2985	3.2	1684	94.1	0.0	3.8	0.00	**1684.3**	***94.1***
Sugluk_02	1748	51	1734	97	1740	56	0.7	0.3	0.002	1.39	0.3083	3.2	1732	96.4	0.0	3.8	0.00	**1732.6**	***96.4***
Sugluk_03	1766	56	1761	98	1763	58	0.3	0.1	0.003	1.53	0.3132	3.2	1756	97.7	0.0	3.8	0.00	**1756.8**	***97.7***
Sugluk_04	1724	53	1726	98	1725	58	-0.1	-0.1	0.000	1.44	0.3070	3.3	1726	98.2	0.0	3.8	0.00	**1726.3**	***98.2***
Sugluk_05	1702	54	1765	98	1736	57	-3.7	-1.7	-0.002	1.46	0.3154	3.2	1767	98.7	0.0	3.8	0.00	**1767.8**	***98.7***
Sugluk_06	1750	55	1687	97	1715	58	3.6	1.6	0.002	1.51	0.2987	3.3	1685	97.1	0.0	3.8	0.00	**1685.2**	***97.1***
Sugluk_07	1718	50	1813	102	1769	57	-5.5	-2.5	0.000	1.35	0.3249	3.2	1814	101.9	0.0	3.8	0.00	**1814.1**	***101.9***
Sugluk_08	1716	55	1686	92	1699	55	1.7	0.8	-0.001	1.49	0.2991	3.1	1687	91.9	0.0	3.8	0.00	**1687.2**	***91.9***
Sugluk_09	1721	52	1771	101	1748	58	-2.9	-1.3	0.000	1.42	0.3162	3.3	1771	101.2	0.0	3.8	0.00	**1771.6**	***101.2***
Sugluk_10	1769	55	1686	99	1723	59	4.7	2.2	0.003	1.52	0.2980	3.3	1681	98.2	0.0	3.8	0.00	**1681.5**	***98.2***
Sugluk_11	1709	57	1741	98	1726	58	-1.9	-0.9	-0.001	1.54	0.3104	3.2	1743	98.3	#VALUE!	3.8	#VALUE!	**#VALUE!**	***98.3***
Sugluk_12	1768	54	1719	95	1741	57	2.8	1.3	0.003	1.48	0.3047	3.2	1714	94.4	0.0	3.8	0.00	**1714.7**	***94.4***
Sugluk_13	1730	52	1610	90	1662	55	6.9	3.1	0.000	1.41	0.2836	3.2	1610	89.6	#VALUE!	3.8	#VALUE!	**#VALUE!**	***89.6***
Sugluk_14	1749	51	1629	95	1681	58	6.9	3.1	0.002	1.40	0.2870	3.3	1626	94.9	0.0	3.8	0.00	**1626.7**	***94.9***
Sugluk_15	1741	54	1886	106	1818	59	-8.3	-3.7	0.001	1.47	0.3394	3.3	1884	105.4	0.0	3.8	0.00	**1884.3**	***105.4***
Sugluk_16	1740	55	1736	99	1738	58	0.2	0.1	0.001	1.51	0.3088	3.3	1735	99.0	#VALUE!	3.8	#VALUE!	**#VALUE!**	***99.0***
PCA_01	1895	40	1699	51	1788	34	10.4	5.0	0.015	1.10	0.2970	1.7	1676	50.0	0.0	3.8	0.00	**1676.6**	***50.0***
PCA_02	1942	40	1758	52	1843	34	9.5	4.6	0.015	1.12	0.3089	1.7	1735	50.5	0.0	3.8	0.00	**1735.6**	***50.5***
PCA_03	1860	41	1786	53	1820	34	4.0	1.9	0.006	1.14	0.3173	1.7	1776	52.2	0.0	3.8	0.00	**1776.8**	***52.2***
PCA_04	1918	38	1772	52	1840	33	7.6	3.7	0.012	1.05	0.3126	1.7	1754	51.3	0.0	3.8	0.00	**1754.1**	***51.3***

RUTILE

		comments	^{204}Pb	^{206}Pb	^{207}Pb	^{208}Pb	^{232}Th	^{238}U	Pb ppm	U ppm	$^{238}U/^{206}Pb$	1s %	$^{207}Pb/^{206}Pb$	1s %	$^{207}Pb/^{235}U$	1s %	$^{206}Pb/^{238}U$	1s %	Rho
PCA_05	19/03/2019		64943	64943	7718	132	-1	140165	7.621	14.674	3.1500	1.97	0.1180	1.01	5.1630	2.21	0.3175	1.97	0.89
PCA_06	19/03/2019		64484	64484	7474	52	-1	145058	7.539	15.187	3.3494	1.46	0.1152	1.05	4.7397	1.80	0.2986	1.46	0.81
PCA_07	19/03/2019		69010	69010	8243	130	-1	161160	8.102	16.873	3.4600	1.59	0.1175	0.88	4.6794	1.82	0.2890	1.59	0.87
PCA_08	19/03/2019		64350	64350	7455	18	-1	146091	7.519	15.295	3.3029	1.84	0.1139	0.98	4.7507	2.08	0.3028	1.84	0.88
PCA_09	19/03/2019		73797	73797	8778	64	1	166498	7.945	16.007	3.2051	1.75	0.1169	1.40	5.0246	2.24	0.3120	1.75	0.78
PCA_10	19/03/2019		72241	72241	8736	103	-1	157911	7.795	15.182	3.1088	1.90	0.1196	1.00	5.3018	2.15	0.3217	1.90	0.89
PCA_11	19/03/2019		75716	75716	9028	94	-1	159785	8.156	15.362	2.9371	2.03	0.1166	1.10	5.4714	2.31	0.3405	2.03	0.88
R19_01	07/07/2017		0	10536	630	-25	-4	1111	1.64	22.15	13.447	1.28	0.059	2.21	0.600	2.56	0.074	1.28	0.50
R19_02	07/07/2017		26	11026	621	-9	2	1133	1.72	22.59	13.136	1.01	0.056	1.93	0.582	2.18	0.076	1.01	0.46
R19_03	07/07/2017		-81	10710	609	-38	2	1124	1.66	22.41	13.578	1.15	0.057	2.31	0.577	2.58	0.074	1.15	0.44
R19_04	07/07/2017		-60	10877	640	-25	-4	1121	1.70	22.35	13.225	1.17	0.057	1.78	0.596	2.13	0.076	1.17	0.55
R19_05	07/07/2017		-160	10309	590	30	-1	1087	1.61	21.68	13.379	1.26	0.056	2.35	0.579	2.67	0.075	1.26	0.47
R19_06	07/07/2017		-2	10375	624	29	-1	1101	1.63	21.96	13.576	1.20	0.059	2.17	0.604	2.48	0.074	1.20	0.48
R19_07	07/07/2017		31	10456	599	26	-1	1100	1.63	21.93	13.380	1.18	0.056	2.38	0.580	2.65	0.075	1.18	0.45
R19_08	07/07/2017		-15	10335	629	-1	-1	1093	1.62	21.79	13.500	1.06	0.059	1.85	0.602	2.14	0.074	1.06	0.50
R19_09	07/07/2017		92	4237	246	23	-3	373	0.66	7.43	13.556	2.11	0.058	3.95	0.594	4.48	0.074	2.11	0.47
R19_10	07/07/2017		23	4355	234	-6	-3	373	0.68	7.43	12.797	2.20	0.052	4.32	0.556	4.85	0.078	2.20	0.45
R19_11	07/07/2017		-69	4204	260	20	-3	366	0.66	7.30	13.116	2.14	0.060	4.28	0.634	4.79	0.076	2.14	0.45
R19_12	07/07/2017		-61	4469	236	-22	-3	376	0.69	7.50	12.901	2.34	0.054	3.92	0.576	4.57	0.078	2.34	0.51
R19_13	07/07/2017		63	3598	206	-9	-1	319	0.56	6.36	13.193	2.07	0.057	3.65	0.594	4.19	0.076	2.07	0.49
R19_14	07/07/2017		-57	3621	214	7	-1	314	0.57	6.26	13.004	2.23	0.057	2.90	0.607	3.66	0.077	2.23	0.61
R19_15	07/07/2017		64	3605	194	-7	-1	313	0.56	6.25	13.232	1.68	0.055	4.22	0.572	4.54	0.076	1.68	0.37
A03-12_Rut_01	16/05/2018		351	7553	4773	11987	730	4365	0.015	0.285	0.5827	8.71	0.6258	1.85	147.9965	8.90	1.7160	8.71	0.98
A03-12_Rut_05	16/05/2018		bd	67	42	94	INF	8295	0.000	0.542	115.6047	17.87	0.5990	38.98	0.7142	42.88	0.0087	17.87	0.42
A03-12_Rut_11	16/05/2018		bd	247	31	62	79	35862	0.000	2.342	130.4582	8.67	0.1281	26.75	0.1354	28.12	0.0077	8.67	0.31
A03-12_Rut_17	16/05/2018		bd	631	270	681	1164	48060	0.001	3.138	77.0588	5.31	0.4552	5.09	0.8141	7.36	0.0130	5.31	0.72
A03-12_Rut_18	16/05/2018		bd	119	57	56	47	7798	0.000	0.509	65.0445	12.03	0.4198	15.12	0.8895	19.33	0.0154	12.03	0.62
A03-12_Rut_19	16/05/2018		bd	126	59	214	18	8802	0.000	0.575	68.3817	13.65	0.5680	23.74	1.1447	27.38	0.0146	13.65	0.50
A03-12_Rut_25	16/05/2018		bd	190	94	261	4	5817	0.000	0.380	25.7250	11.46	0.5561	13.03	2.9794	17.35	0.0389	11.46	0.66
A03-12_Rut_28	16/05/2018		bd	509	43	85	357	89631	0.000	5.853	174.1532	5.24	0.0724	18.38	0.0573	19.11	0.0057	5.24	0.27
~~A03-12_Rut_24~~	~~16/05/2018~~	~~rej - neg. Ratio~~	~~bd~~	~~48~~	~~38~~	~~88~~	~~3~~	~~2977~~	~~0.000~~	~~0.194~~	~~60.8234~~	~~20.40~~	~~-0.3300~~	~~110.90~~	~~-0.7478~~	~~112.76~~	~~0.0164~~	~~20.40~~	~~0.18~~
~~A03-12_Rut_02~~	~~16/05/2018~~	~~rej - low Pb counts~~	~~bd~~	~~169~~	~~22~~	~~18~~	~~1~~	~~25032~~	~~0.000~~	~~1.635~~	~~147.8441~~	~~7.79~~	~~0.1075~~	~~32.30~~	~~0.1002~~	~~33.23~~	~~0.0068~~	~~7.79~~	~~0.23~~
~~A03-12_Rut_03~~	~~16/05/2018~~	~~rej - low Pb counts~~	~~bd~~	~~73~~	~~14~~	~~52~~	~~1~~	~~6988~~	~~0.000~~	~~0.456~~	~~101.4347~~	~~19.11~~	~~0.2190~~	~~46.62~~	~~0.2975~~	~~50.39~~	~~0.0099~~	~~19.11~~	~~0.38~~
~~A03-12_Rut_04~~	~~16/05/2018~~	~~rej - low Pb counts~~	~~bd~~	~~68~~	~~18~~	~~53~~	~~1~~	~~7050~~	~~0.000~~	~~0.460~~	~~92.0313~~	~~14.52~~	~~0.0232~~	~~974.93~~	~~0.0348~~	~~975.04~~	~~0.0109~~	~~14.52~~	~~0.01~~
~~A03-12_Rut_06~~	~~16/05/2018~~	~~rej - low Pb counts~~	~~bd~~	~~64~~	~~17~~	~~89~~	~~62~~	~~4432~~	~~0.000~~	~~0.289~~	~~82.6861~~	~~17.26~~	~~0.1835~~	~~69.13~~	~~0.3059~~	~~71.25~~	~~0.0121~~	~~17.26~~	~~0.24~~
~~A03-12_Rut_07~~	~~16/05/2018~~	~~rej - low Pb counts~~	~~bd~~	~~177~~	~~15~~	~~78~~	~~15~~	~~20244~~	~~0.000~~	~~1.322~~	~~117.9463~~	~~7.41~~	~~0.1254~~	~~28.94~~	~~0.1466~~	~~29.87~~	~~0.0085~~	~~7.41~~	~~0.25~~
~~A03-12_Rut_08~~	~~16/05/2018~~	~~rej - low Pb counts~~	~~bd~~	~~86~~	~~16~~	~~87~~	~~58~~	~~13455~~	~~0.000~~	~~0.879~~	~~161.2383~~	~~11.32~~	~~0.4182~~	~~42.37~~	~~0.3575~~	~~43.85~~	~~0.0062~~	~~11.32~~	~~0.26~~
~~A03-12_Rut_09~~	~~16/05/2018~~	~~rej - low Pb counts~~	~~bd~~	~~177~~	~~29~~	~~64~~	~~82~~	~~21613~~	~~0.000~~	~~1.411~~	~~119.3172~~	~~10.65~~	~~0.1691~~	~~23.46~~	~~0.1953~~	~~25.77~~	~~0.0084~~	~~10.65~~	~~0.41~~
~~A03-12_Rut_10~~	~~16/05/2018~~	~~rej - low Pb counts~~	~~bd~~	~~131~~	~~19~~	~~97~~	~~154~~	~~22997~~	~~0.000~~	~~1.502~~	~~170.2442~~	~~9.93~~	~~0.1587~~	~~32.17~~	~~0.1285~~	~~33.67~~	~~0.0059~~	~~9.93~~	~~0.30~~
~~A03-12_Rut_12~~	~~16/05/2018~~	~~rej - low Pb counts~~	~~bd~~	~~54~~	~~21~~	~~68~~	~~20~~	~~6818~~	~~0.000~~	~~0.445~~	~~114.7855~~	~~18.83~~	~~0.0856~~	~~207.28~~	~~0.1028~~	~~208.13~~	~~0.0087~~	~~18.83~~	~~0.09~~
~~A03-12_Rut_13~~	~~16/05/2018~~	~~rej - low Pb counts~~	~~bd~~	~~62~~	~~14~~	~~51~~	~~INF~~	~~8939~~	~~0.000~~	~~0.584~~	~~125.4436~~	~~15.70~~	~~0.1759~~	~~59.37~~	~~0.1932~~	~~61.41~~	~~0.0080~~	~~15.70~~	~~0.26~~
~~A03-12_Rut_14~~	~~16/05/2018~~	~~rej - low Pb counts~~	~~bd~~	~~38~~	~~6~~	~~29~~	~~1~~	~~4338~~	~~0.000~~	~~0.283~~	~~167.4527~~	~~39.86~~	~~-0.0910~~	~~124.51~~	~~-0.0749~~	~~130.74~~	~~0.0060~~	~~39.86~~	~~0.30~~
~~A03-12_Rut_15~~	~~16/05/2018~~	~~rej - low Pb counts~~	~~bd~~	~~89~~	~~20~~	~~97~~	~~96~~	~~9394~~	~~0.000~~	~~0.613~~	~~103.1635~~	~~12.13~~	~~0.1914~~	~~33.62~~	~~0.2556~~	~~35.74~~	~~0.0097~~	~~12.13~~	~~0.34~~
~~A03-12_Rut_16~~	~~16/05/2018~~	~~rej - low Pb counts~~	~~bd~~	~~25~~	~~9~~	~~41~~	~~1~~	~~1060~~	~~0.000~~	~~0.069~~	~~61.3038~~	~~64.81~~	~~-0.3320~~	~~39.97~~	~~-0.7464~~	~~76.14~~	~~0.0163~~	~~64.81~~	~~0.85~~
~~A03-12_Rut_20~~	~~16/05/2018~~	~~rej - low Pb counts~~	~~bd~~	~~48~~	~~7~~	~~19~~	~~4~~	~~7355~~	~~0.000~~	~~0.480~~	~~139.9500~~	~~20.72~~	~~0.1692~~	~~87.01~~	~~0.1667~~	~~89.44~~	~~0.0071~~	~~20.72~~	~~0.23~~
~~A03-12_Rut_21~~	~~16/05/2018~~	~~rej - low Pb counts~~	~~bd~~	~~41~~	~~8~~	~~18~~	~~5~~	~~6016~~	~~0.000~~	~~0.393~~	~~150.4503~~	~~33.67~~	~~0.1251~~	~~113.47~~	~~0.1146~~	~~118.36~~	~~0.0066~~	~~33.67~~	~~0.28~~
~~A03-12_Rut_22~~	~~16/05/2018~~	~~rej - low Pb counts~~	~~bd~~	~~55~~	~~10~~	~~45~~	~~INF~~	~~7553~~	~~0.000~~	~~0.493~~	~~127.7385~~	~~24.35~~	~~-0.0250~~	~~639.75~~	~~-0.0269~~	~~640.22~~	~~0.0078~~	~~24.35~~	~~0.04~~
~~A03-12_Rut_23~~	~~16/05/2018~~	~~rej - low Pb counts~~	~~bd~~	~~33~~	~~13~~	~~46~~	~~bd~~	~~1599~~	~~0.000~~	~~0.104~~	~~96.0989~~	~~61.53~~	~~0.2630~~	~~35.13~~	~~0.3772~~	~~70.86~~	~~0.0104~~	~~61.53~~	~~0.87~~
~~A03-12_Rut_26~~	~~16/05/2018~~	~~rej - low Pb counts~~	~~bd~~	~~38~~	~~14~~	~~44~~	~~20~~	~~4377~~	~~0.000~~	~~0.286~~	~~125.0946~~	~~28.42~~	~~0.1606~~	~~112.66~~	~~0.1769~~	~~116.19~~	~~0.0080~~	~~28.42~~	~~0.24~~
~~A03-12_Rut_27~~	~~16/05/2018~~	~~rej - low Pb counts~~	~~bd~~	~~123~~	~~12~~	~~53~~	~~4~~	~~17171~~	~~0.000~~	~~1.121~~	~~145.5948~~	~~10.37~~	~~0.1325~~	~~38.10~~	~~0.1254~~	~~39.48~~	~~0.0069~~	~~10.37~~	~~0.26~~
~~A03-12_Rut_29~~	~~16/05/2018~~	~~rej - low Pb counts~~	~~bd~~	~~-6~~	~~4~~	~~44~~	~~9~~	~~2199~~	~~0.000~~	~~0.144~~	~~-148.7619~~	~~52.65~~	~~-0.2158~~	~~107.35~~	~~0.1999~~	~~119.57~~	~~-0.0067~~	~~52.65~~	~~0.44~~
A03-20_Rut_03	16/05/2018		bd	257	212	502	439	3864	0.001	0.252	14.8176	8.80	0.7410	7.00	6.8916	11.24	0.0675	8.80	0.78
A03-20_Rut_04	16/05/2018		bd	117	57	114	184	8061	0.000	0.526	62.5021	14.80	0.4558	22.01	1.0050	26.52	0.0160	14.80	0.56
A03-20_Rut_05	16/05/2018		bd	63	31	164	25	4960	0.000	0.324	86.0527	18.81	0.4235	31.56	0.6782	36.74	0.0116	18.81	0.51
A03-20_Rut_06	16/05/2018		bd	66	30	105	127	4967	0.000	0.324	74.8445	16.43	0.4571	25.21	0.8418	30.09	0.0134	16.43	0.55
A03-20_Rut_07	16/05/2018		bd	583	437	1141	39452	9423	0.001	0.615	14.2061	11.74	0.7483	5.14	7.2594	12.81	0.0704	11.74	0.92
A03-20_Rut_08	16/05/2018		bd	302	236	615	405	6060	0.001	0.396	19.4025	6.69	0.7882	6.68	5.5987	9.46	0.0515	6.69	0.71
A03-20_Rut_09	16/05/2018		bd	282	107	255	3074	21595	0.000	1.410	78.7323	9.79	0.4595	10.04	0.8043	14.02	0.0127	9.79	0.70
A03-20_Rut_10	16/05/2018		bd	256	185	518	180	7107	0.001	0.464	30.3809	10.41	0.6426	5.63	2.9149	11.83	0.0329	10.41	0.88
A03-20_Rut_11	16/05/2018		bd	313	188	513	1329	6933	0.001	0.453	21.3155	7.49	0.5795	7.21	3.7467	10.40	0.0469	7.49	0.72
A03-20_Rut_12	16/05/2018		bd	98	68	141	40	4618	0.000	0.302	47.2351	16.63	0.6284	20.36	1.8334	26.29	0.0212	16.63	0.63
A03-20_Rut_13	16/05/2018		bd	385	271	561	211	3199	0.001	0.209	7.0980	14.04	0.6742	8.52	13.0908	16.43	0.1409	14.04	0.85
A03-20_Rut_14	16/05/2018		bd	116	84	167	407	5134	0.000	0.335	39.9682	15.06	0.5232	16.54	1.8039	22.37	0.0250	15.06	0.67
A03-20_Rut_15	16/05/2018		bd	88	52	143	519	4313	0.000	0.282	61.3713	26.40	0.3496	37.59	0.7851	45.93	0.0163	26.40	0.57
A03-20_Rut_16	16/05/2018		bd	94	65	140	22	3373	0.000	0.220	34.5549	14.64	0.5304	26.31	2.1152	30.11	0.0289	14.64	0.49
A03-20_Rut_17	16/05/2018		bd	96	54	91	481	4247	0.000	0.277	49.1122	27.66	0.5358	25.58	1.5034	37.68	0.0204	27.66	0.73
A03-20_Rut_18	16/05/2018		bd	197	185	430	280	4080	0.000	0.266	22.0412	11.14	0.7823	7.97	4.8916	13.70	0.0454	11.14	0.81
A03-20_Rut_19	16/05/2018		bd	247	135	312	186	6987	0.000	0.456	31.8269	8.02	0.5628	8.33	2.4371	11.56	0.0314	8.02	0.69
A03-20_Rut_20	16/05/2018		bd	373	258	628	688	4062	0.001	0.265	11.4037	9.24	0.7144	7.01	8.6339	11.59	0.0877	9.24	0.80
A03-20_Rut_22	16/05/2018		bd	95	38	145	288	4478	0.000	0.292	45.3535	12.86	0.3754	30.51	1.1408	33.11	0.0220	12.86	0.39
A03-20_Rut_23	16/05/2018		bd	951	503	1452	906	13865	0.002	0.905	18.1242	8.17	0.7875	3.71	5.9884	8.97	0.0552	8.17	0.91
A03-20_Rut_24	16/05/2018		bd	167	134	275	238	3863	0.000	0.252	22.6433	12.60	0.9703	14.92	5.9060	19.53	0.0442	12.60	0.65
A03-20_Rut_25	16/05/2018		bd	1354	1075	2796	419	4801	0.003	0.313	3.4786	14.30	0.7516	4.49	29.7771	14.99	0.2875	14.30	0.95
~~A03-20_Rut_01~~	~~16/05/2018~~	~~rej - low Pb counts~~	~~bd~~	~~35~~	~~17~~	~~76~~	~~bd~~	~~3387~~	~~0.000~~	~~0.221~~	~~105.3947~~	~~33.59~~	~~-0.2287~~	~~104.40~~	~~-0.2991~~	~~109.67~~	~~0.0095~~	~~33.59~~	~~0.31~~
~~A03-20_Rut_02~~	~~16/05/2018~~	~~rej - large uncertainty~~	~~bd~~	~~56~~	~~30~~	~~135~~	~~15~~	~~5902~~	~~0.000~~	~~0.385~~	~~122.9583~~	~~21.04~~	~~0.4516~~	~~67.84~~	~~0.5061~~	~~71.03~~	~~0.0081~~	~~21.04~~	~~0.30~~
~~A03-20_Rut_21~~	~~16/05/2018~~	~~rej - large uncertainty~~	~~d~~	~~34~~	~~33~~	~~-9~~	~~16~~	~~3670~~	~~0.000~~	~~0.240~~	~~96.1273~~	~~34.74~~	~~0.1753~~	~~94.88~~	~~0.2514~~	~~101.04~~	~~0.0104~~	~~34.74~~	~~0.34~~
A04-15_Rut_01	16/05/2018		bd	1073	917	2249	14	920	0.003	0.060	0.9369	12.48	0.8133	2.93	119.6338	12.82	1.0673	12.48	0.97
A04-15_Rut_02	16/05/2018		bd	618	435	1411	21	8008	0.002	0.523	11.6736	11.67	0.7899	4.42	9.3254	12.48	0.0857	11.67	0.94
A04-15_Rut_03	16/05/2018		bd	476	350	1013	3	265	0.001	0.017	0.6006	12.17	0.7883	4.62	180.9116	13.01	1.6651	12.17	0.93
A04-15_Rut_04	16/05/2018		bd	979	936	2112	1729	6034	0.002	0.394	3.0585	9.85	0.8625	3.45	38.8637	10.44	0.3270	9.85	0.94
A04-15_Rut_05	16/05/2018		bd	1972	1619	4065	812	3333	0.005	0.218	1.1915	9.73	0.8255	2.38	95.4799	10.02	0.8393	9.73	0.97
A04-15_Rut_06	16/05/2018		bd	750	586	1593	bd	377	0.002	0.025	0.5226	11.71	0.8478	6.06	223.5697	13.19	1.9134	11.71	0.89
A04-15_Rut_07	16/05/2018		bd	1175	1016	2416	339	1650	0.003	0.108	0.9865	9.36	0.8661	3.57	121.0018	10.02	1.0137	9.36	0.93
A04-15_Rut_08	16/05/2018		bd	692	585	1360	36	514	0.002	0.034	0.7612	11.90	0.8210	4.43	148.6374	12.70	1.3136	11.90	0.94
A04-15_Rut_09	16/05/2018		bd	978	531	2038	bd	195	0.002	0.013	0.2056	16.32	0.8570	5.35	574.4186	17.18	4.8632	16.32	0.95
A04-15_Rut_10	16/05/2018		bd	1532	1236	2977	303	3708	0.004	0.242	1.1025	13.92	0.7987	2.21	99.8466	14.09	0.9070	13.92	0.99
A04-15_Rut_11	16/05/2018		bd	1606	1448	3450	12	935	0.004	0.061	0.5750	8.51	0.8539	2.61	204.6546	8.90	1.7391	8.51	0.96
A04-15_Rut_12	16/05/2018		bd	757	621	1615	285	1364	0.002	0.089	1.7083	11.50	0.9339	4.92	75.3442	12.51	0.5854	11.50	0.92
A04-15_Rut_13	16/05/2018		bd	1765	1429	3680	39	571	0.004	0.037	0.3403	13.45	0.8705	2.71	352.5317	13.72	2.9385	13.45	0.98
A04-15_Rut_14	16/05/2018		bd	1190	952	2275	25	1015	0.003	0.066	0.9045	7.09	0.8391	3.68	127.8434	7.99	1.1056	7.09	0.89
A04-15_Rut_15	16/05/2018		bd	615	477	1078	7	9811	0.001	0.641	17.2919	9.69	0.7251	4.23	5.7794	10.57	0.0578	9.69	0.92
A04-15_Rut_16	16/05/2018		bd	731	631	1254	20	1162	0.002	0.076	1.1086	15.34	0.8310	5.13	103.3073	16.17	0.9020	15.34	0.95
A04-15_Rut_17	16/05/2018		bd	842	666	1858	6	224	0.002	0.015	0.2588	11.09	0.8401	4.29	447.3873	11.89	3.8643	11.09	0.93
A04-15_Rut_18	16/05/2018		259	2530	2183	5343	70	1792	0.006	0.117	0.5152	15.88	0.8135	2.26	217.6116	16.04	1.9411	15.88	0.99
A04-15_Rut_19	16/05/2018		bd	410	357	901	28	623	0.001	0.041	1.4629	12.45	1.0783	8.37	101.5834	15.00	0.6836	12.45	0.83
A04-15_Rut_20	16/05/2018		bd	362	254	772	39	979	0.001	0.064	2.8464	15.59	0.6349	9.42	30.7389	18.21	0.3513	15.59	0.86
A04-15_Rut_21	16/05/2018		bd	983	882	2185	286	1767	0.002	0.115	1.7479	9.09	0.7962	3.86	62.7792	9.87	0.5721	9.09	0.92
A04-15_Rut_22	16/05/2018		bd	1894	1682	4117	69	566	0.005	0.037	0.3005	5.94	0.8348	3.50	382.9223	6.90	3.3283	5.94	0.86
A04-15_Rut_23	16/05/2018		bd	584	483	1133	31	4339	0.001	0.283	6.0092	16.85	0.7573	4.87	17.3678	17.54	0.1664	16.85	0.96
A04-15_Rut_24	16/05/2018		bd	1433	1027	3053	32	840	0.003	0.055	0.5680	13.36	0.8588	2.83	208.3737	13.65	1.7606	13.36	0.98
A04-15_Rut_25	16/05/2018		bd	955	868	2101	bd	521	0.002	0.034	0.4244	10.79	0.9289	4.41	301.6719	11.65	2.3565	10.79	0.93
A04-15_Rut_26	16/05/2018		bd	1252	979	2741	17	444	0.003	0.029	0.3310	10.16	0.8387	3.39	349.2147	10.71	3.0212	10.16	0.95
A10-05_01	18/03/2018		827	827	103	159	2871	92828	0.182	15.483	136.1989	5.26	0.1584	10.14	0.1603	11.42	0.0073	5.26	0.46
A10-05_02	18/03/2018		262	262	203	462	4	4151	0.155	0.692	24.0842	7.03	0.7740	5.58	4.4291	8.98	0.0415	7.03	0.78
A10-05_04	18/03/2018		bd	108	61	131	bd	1348	0.050	0.225	20.4315	9.56	0.6525	9.84	4.4011	13.72	0.0489	9.56	0.70

RUTILE

	$^{207}Pb/^{206}Pb$	2s abs	$^{206}Pb/^{238}U$	2s abs	$^{207}Pb/^{235}U$	2s abs	c. % 6-38/c.	%6-38/7	*f206*	1s %	$^{206}Pb^*/^{238}U$	1s %	²06/238-Pb	2s [Ma]	Th/U min.	Th/U wr.	f	·. 206/238	*2s [Ma]*
PCA_05	1926	36	1777	61	1847	37	7.7	3.7	0.012	1.01	0.3137	1.9	1759	59.6	0.0	3.8	0.00	**1759.2**	***59.6***
PCA_06	1883	38	1684	43	1774	30	10.6	5.1	0.015	1.05	0.2941	1.4	1662	41.9	0.0	3.8	0.00	**1662.2**	***41.9***
PCA_07	1918	32	1637	46	1764	30	14.7	7.2	0.021	0.88	0.2829	1.6	1606	44.0	0.0	3.8	0.00	**1606.3**	***44.0***
PCA_08	1862	35	1705	55	1776	34	8.4	4.0	0.012	0.98	0.2992	1.8	1687	53.7	0.0	3.8	0.00	**1687.5**	***53.7***
PCA_09	1909	50	1751	53	1823	37	8.3	4.0	0.012	1.40	0.3081	1.7	1732	52.3	0.0	3.8	0.00	**1731.9**	***52.3***
PCA_10	1950	36	1798	59	1869	36	7.8	3.8	0.012	1.00	0.3177	1.9	1778	58.1	0.0	3.8	0.00	**1778.9**	***58.1***
PCA_11	1905	40	1889	66	1896	39	0.8	0.4	0.001	1.10	0.3400	2.0	1887	65.8	0.0	3.8	0.00	**1887.1**	***65.8***
R19_01	551	48	462	11	477	19	16.1	3.2	0.003	2.21	0.0741	1.3	461	11.3	0.0	3.8	0.00	**461.3**	***11.3***
R19_02	433	43	473	9	466	16	-9.3	-1.5	-0.001	1.93	0.0762	1.0	474	9.2	0.0	3.8	0.00	**473.7**	***9.2***
R19_03	487	51	458	10	463	19	5.9	1.0	0.001	2.31	0.0736	1.1	458	10.1	0.0	3.8	0.00	**457.9**	***10.1***
R19_04	501	39	470	11	475	16	6.2	1.1	0.001	1.78	0.0755	1.2	469	10.6	0.0	3.8	0.00	**469.6**	***10.6***
R19_05	460	52	465	11	464	20	-1.0	-0.2	0.000	2.35	0.0748	1.3	465	11.3	0.0	3.8	0.00	**464.9**	***11.3***
R19_06	584	47	458	11	479	19	21.5	4.4	0.004	2.17	0.0734	1.2	456	10.5	0.0	3.8	0.00	**456.5**	***10.5***
R19_07	463	53	465	11	464	20	-0.3	-0.1	0.000	2.38	0.0747	1.2	465	10.6	0.0	3.8	0.00	**464.8**	***10.6***
R19_08	565	40	461	9	478	16	18.5	3.7	0.003	1.85	0.0738	1.1	459	9.4	0.0	3.8	0.00	**459.3**	***9.4***
R19_09	545	86	459	19	473	33	15.8	3.1	0.003	3.95	0.0736	2.1	458	18.6	0.0	3.8	0.00	**457.7**	***18.6***
R19_10	271	99	485	21	449	35	-79.1	-8.0	-0.006	4.32	0.0786	2.2	488	20.8	0.0	3.8	0.00	**488.2**	***20.8***
R19_11	616	93	474	19	499	37	23.1	5.0	0.005	4.28	0.0759	2.1	471	19.3	0.0	3.8	0.00	**471.7**	***19.3***
R19_12	369	88	481	22	462	33	-30.5	-4.2	-0.003	3.92	0.0778	2.4	483	21.8	0.0	3.8	0.00	**483.1**	***21.8***
R19_13	486	80	471	19	473	31	3.1	0.5	0.000	3.65	0.0758	2.1	471	18.7	0.0	3.8	0.00	**470.9**	***18.7***
R19_14	502	64	478	20	482	28	4.9	0.9	0.001	2.90	0.0768	2.2	477	20.4	0.0	3.8	0.00	**477.4**	***20.4***
R19_15	408	94	470	15	459	33	-15.0	-2.3	-0.002	4.22	0.0757	1.7	471	15.2	0.0	3.8	0.00	**470.7**	***15.2***
A03-12_Rut_01	4569	54	6441	673	5081	165	-41.0	-26.8	0.731	1.85	0.4619	2.7	2448	109.3	0.0	3.8	0.01	**2448.6**	***109.3***
A03-12_Rut_05	4506	1133	56	20	547	310	98.8	89.9	0.697	38.98	0.0026	27.7	17	9.3	#VALUE!	3.8	#VALUE!	**#VALUE!**	***9.3***
A03-12_Rut_11	2073	942	49	8	129	66	97.6	61.8	0.102	26.75	0.0069	8.2	44	7.3	0.0	3.8	0.00	**44.3**	***7.3***
A03-12_Rut_17	4102	151	83	9	605	65	98.0	86.3	0.515	5.09	0.0063	3.7	40	3.0	0.0	3.8	0.00	**40.5**	***3.0***
A03-12_Rut_18	3982	453	98	23	646	170	97.5	84.8	0.471	15.12	0.0081	9.6	52	9.9	0.0	3.8	0.00	**52.4**	***9.9***
A03-12_Rut_19	4428	693	94	25	775	260	97.9	87.9	0.658	23.74	0.0050	16.3	32	10.5	0.0	3.8	0.00	**32.3**	***10.5***
A03-12_Rut_25	4397	381	246	55	1402	235	94.4	82.5	0.643	13.03	0.0139	9.3	89	16.4	0.0	3.8	0.00	**89.0**	***16.4***
A03-12_Rut_28	996	747	37	4	57	21	96.3	34.7	0.032	18.38	0.0056	5.1	36	3.6	0.0	3.8	0.00	**35.8**	***3.6***
~~A03-12_Rut_24~~	~~#NUM!~~	~~#NUM!~~	~~105~~	~~42~~	~~-1399~~	~~#VALUE!~~	~~#NUM!~~	~~107.5~~	~~-0.476~~	~~110.90~~	~~0.0243~~	~~60.8~~	~~155~~	~~183.0~~	~~0.0~~	~~3.8~~	~~0.00~~	~~**154.7**~~	~~***183.0***~~
~~A03-12_Rut_02~~	~~1758~~	~~1182~~	~~43~~	~~7~~	~~97~~	~~60~~	~~97.5~~	~~55.2~~	~~0.076~~	~~32.30~~	~~0.0062~~	~~7.6~~	~~40~~	~~6.1~~	~~0.0~~	~~3.8~~	~~0.00~~	~~**40.3**~~	~~***6.1***~~
~~A03-12_Rut_03~~	~~2973~~	~~1502~~	~~63~~	~~24~~	~~264~~	~~211~~	~~97.9~~	~~76.1~~	~~0.217~~	~~46.62~~	~~0.0077~~	~~18.1~~	~~50~~	~~17.8~~	~~0.0~~	~~3.8~~	~~0.00~~	~~**49.7**~~	~~***17.8***~~
~~A03-12_Rut_04~~	~~#NUM!~~	~~#NUM!~~	~~70~~	~~20~~	~~35~~	~~512~~	~~#NUM!~~	~~-100.8~~	~~-0.030~~	~~974.93~~	~~0.0112~~	~~32.9~~	~~72~~	~~46.7~~	~~0.0~~	~~3.8~~	~~0.00~~	~~**71.9**~~	~~***46.7***~~
~~A03-12_Rut_06~~	~~2685~~	~~2286~~	~~77~~	~~27~~	~~271~~	~~292~~	~~97.1~~	~~71.4~~	~~0.172~~	~~69.13~~	~~0.0100~~	~~18.6~~	~~64~~	~~23.7~~	~~0.0~~	~~3.8~~	~~0.00~~	~~**64.3**~~	~~***23.7***~~
~~A03-12_Rut_07~~	~~2035~~	~~1024~~	~~54~~	~~8~~	~~139~~	~~75~~	~~97.3~~	~~60.8~~	~~0.099~~	~~28.94~~	~~0.0076~~	~~7.3~~	~~49~~	~~7.1~~	~~0.0~~	~~3.8~~	~~0.00~~	~~**49.2**~~	~~***7.1***~~
~~A03-12_Rut_08~~	~~3976~~	~~1269~~	~~40~~	~~9~~	~~310~~	~~211~~	~~99.0~~	~~87.2~~	~~0.469~~	~~42.37~~	~~0.0033~~	~~20.7~~	~~21~~	~~8.8~~	~~0.0~~	~~3.8~~	~~0.00~~	~~**21.3**~~	~~***8.8***~~
~~A03-12_Rut_09~~	~~2548~~	~~786~~	~~54~~	~~11~~	~~181~~	~~82~~	~~97.9~~	~~70.3~~	~~0.154~~	~~23.46~~	~~0.0071~~	~~9.7~~	~~46~~	~~8.8~~	~~0.0~~	~~3.8~~	~~0.00~~	~~**45.7**~~	~~***8.8***~~
~~A03-12_Rut_10~~	~~2442~~	~~1089~~	~~38~~	~~7~~	~~123~~	~~75~~	~~98.5~~	~~69.2~~	~~0.141~~	~~32.17~~	~~0.0050~~	~~9.7~~	~~32~~	~~6.3~~	~~0.0~~	~~3.8~~	~~0.00~~	~~**32.6**~~	~~***6.3***~~
~~A03-12_Rut_12~~	~~1330~~	~~8023~~	~~56~~	~~21~~	~~99~~	~~333~~	~~95.8~~	~~43.7~~	~~0.049~~	~~207.28~~	~~0.0083~~	~~20.6~~	~~53~~	~~21.8~~	~~0.0~~	~~3.8~~	~~0.00~~	~~**53.3**~~	~~***21.8***~~
~~A03-12_Rut_13~~	~~2614~~	~~1976~~	~~51~~	~~16~~	~~179~~	~~184~~	~~98.0~~	~~71.5~~	~~0.163~~	~~59.37~~	~~0.0067~~	~~16.3~~	~~43~~	~~13.9~~	~~#VALUE!~~	~~3.8~~	~~#VALUE!~~	~~**#VALUE!**~~	~~***13.9***~~
~~A03-12_Rut_14~~	~~#NUM!~~	~~#NUM!~~	~~38~~	~~30~~	~~-79~~	~~-242~~	~~#NUM!~~	~~148.5~~	~~-0.174~~	~~124.51~~	~~0.0070~~	~~51.6~~	~~45~~	~~46.2~~	~~0.0~~	~~3.8~~	~~0.00~~	~~**45.2**~~	~~***46.2***~~
~~A03-12_Rut_15~~	~~2754~~	~~1105~~	~~62~~	~~15~~	~~231~~	~~138~~	~~97.7~~	~~73.1~~	~~0.182~~	~~33.62~~	~~0.0079~~	~~11.7~~	~~51~~	~~11.8~~	~~0.0~~	~~3.8~~	~~0.00~~	~~**51.0**~~	~~***11.8***~~
~~A03-12_Rut_16~~	~~#NUM!~~	~~#NUM!~~	~~104~~	~~133~~	~~-1393~~	~~#VALUE!~~	~~#NUM!~~	~~107.5~~	~~-0.479~~	~~39.97~~	~~0.0241~~	~~97.7~~	~~154~~	~~290.0~~	~~0.0~~	~~3.8~~	~~0.00~~	~~**153.8**~~	~~***290.0***~~
~~A03-12_Rut_20~~	~~2550~~	~~2915~~	~~46~~	~~19~~	~~157~~	~~231~~	~~98.2~~	~~70.7~~	~~0.154~~	~~87.01~~	~~0.0060~~	~~22.1~~	~~39~~	~~17.1~~	~~0.0~~	~~3.8~~	~~0.00~~	~~**38.9**~~	~~***17.1***~~
~~A03-12_Rut_21~~	~~2030~~	~~4017~~	~~43~~	~~29~~	~~110~~	~~221~~	~~97.9~~	~~61.2~~	~~0.099~~	~~113.47~~	~~0.0060~~	~~32.3~~	~~39~~	~~24.8~~	~~0.0~~	~~3.8~~	~~0.00~~	~~**38.6**~~	~~***24.8***~~
~~A03-12_Rut_22~~	~~#NUM!~~	~~#NUM!~~	~~50~~	~~24~~	~~-28~~	~~-444~~	~~#NUM!~~	~~281.3~~	~~-0.091~~	~~639.75~~	~~0.0085~~	~~63.9~~	~~55~~	~~69.4~~	~~#VALUE!~~	~~3.8~~	~~#VALUE!~~	~~**#VALUE!**~~	~~***69.4***~~
~~A03-12_Rut_23~~	~~3265~~	~~1105~~	~~67~~	~~81~~	~~325~~	~~333~~	~~98.0~~	~~79.5~~	~~0.273~~	~~35.13~~	~~0.0076~~	~~45.8~~	~~49~~	~~44.2~~	~~0.0~~	~~3.8~~	~~0.00~~	~~**48.7**~~	~~***44.2***~~
~~A03-12_Rut_26~~	~~2462~~	~~3808~~	~~51~~	~~29~~	~~165~~	~~304~~	~~97.9~~	~~69.0~~	~~0.143~~	~~112.66~~	~~0.0068~~	~~29.2~~	~~44~~	~~25.6~~	~~0.0~~	~~3.8~~	~~0.00~~	~~**44.1**~~	~~***25.6***~~
~~A03-12_Rut_27~~	~~2131~~	~~1334~~	~~44~~	~~9~~	~~120~~	~~86~~	~~97.9~~	~~63.2~~	~~0.108~~	~~38.10~~	~~0.0061~~	~~10.1~~	~~39~~	~~7.9~~	~~0.0~~	~~3.8~~	~~0.00~~	~~**39.5**~~	~~***7.9***~~
~~A03-12_Rut_29~~	~~#NUM!~~	~~#NUM!~~	~~-43~~	~~-46~~	~~185~~	~~341~~	~~#NUM!~~	~~123.5~~	~~-0.332~~	~~107.35~~	~~-0.0090~~	~~78.6~~	~~-58~~	~~-92.3~~	~~0.0~~	~~3.8~~	~~0.00~~	~~**-57.9**~~	~~***-92.3***~~
A03-20_Rut_03	4812	200	421	71	2098	182	91.3	79.9	0.876	7.00	0.0084	6.2	54	6.6	0.0	3.8	0.01	**53.7**	***6.6***
A03-20_Rut_04	4104	654	102	30	706	239	97.5	85.5	0.516	22.01	0.0077	13.4	50	13.3	0.0	3.8	0.00	**49.8**	***13.3***
A03-20_Rut_05	3995	944	74	28	526	264	98.1	85.8	0.475	31.56	0.0061	18.0	39	14.0	0.0	3.8	0.00	**39.3**	***14.0***
A03-20_Rut_06	4109	749	86	28	620	247	97.9	86.2	0.518	25.21	0.0064	15.3	41	12.6	0.0	3.8	0.00	**41.5**	***12.6***
A03-20_Rut_07	4826	147	439	99	2144	206	90.9	79.5	0.885	5.14	0.0081	4.7	52	4.9	1.1	3.8	0.29	**51.8**	***4.9***
A03-20_Rut_08	4901	191	324	42	1916	151	93.4	83.1	0.936	6.68	0.0033	6.3	21	2.7	0.0	3.8	0.00	**21.4**	***2.7***
A03-20_Rut_09	4116	298	81	16	599	120	98.0	86.4	0.521	10.04	0.0061	7.0	39	5.5	0.0	3.8	0.01	**39.2**	***5.5***
A03-20_Rut_10	4607	163	209	43	1386	165	95.5	84.9	0.752	5.63	0.0082	5.0	52	5.2	0.0	3.8	0.00	**52.5**	***5.2***
A03-20_Rut_11	4457	210	296	43	1581	154	93.4	81.3	0.672	7.21	0.0154	5.4	98	10.6	0.1	3.8	0.01	**98.5**	***10.6***
A03-20_Rut_12	4575	590	135	44	1057	297	97.0	87.2	0.734	20.36	0.0056	15.6	36	11.2	0.0	3.8	0.00	**36.3**	***11.2***
A03-20_Rut_13	4677	246	850	220	2686	270	81.8	68.4	0.792	8.52	0.0293	7.4	186	26.9	0.0	3.8	0.00	**186.4**	***26.9***
A03-20_Rut_14	4308	486	159	47	1047	257	96.3	84.8	0.601	16.54	0.0100	11.6	64	14.8	0.0	3.8	0.01	**64.1**	***14.8***
A03-20_Rut_15	3705	1145	104	54	588	345	97.2	82.3	0.382	37.59	0.0101	21.7	65	27.9	0.0	3.8	0.01	**64.7**	***27.9***
A03-20_Rut_16	4328	772	184	53	1154	348	95.8	84.1	0.610	26.31	0.0113	17.0	72	24.5	0.0	3.8	0.00	**72.4**	***24.5***
A03-20_Rut_17	4343	750	130	71	932	379	97.0	86.1	0.617	25.58	0.0078	19.0	50	18.9	0.0	3.8	0.01	**50.2**	***18.9***
A03-20_Rut_18	4890	227	286	62	1801	208	94.2	84.1	0.928	7.97	0.0032	7.4	21	3.1	0.0	3.8	0.00	**21.0**	***3.1***
A03-20_Rut_19	4415	243	199	31	1254	154	95.5	84.1	0.651	8.33	0.0110	6.1	70	8.5	0.0	3.8	0.00	**70.4**	***8.5***
A03-20_Rut_20	4760	201	542	95	2300	192	88.6	76.4	0.843	7.01	0.0138	6.1	88	10.7	0.0	3.8	0.01	**88.4**	***10.7***
A03-20_Rut_22	3813	923	141	36	773	307	96.3	81.8	0.415	30.51	0.0129	14.7	83	24.1	0.0	3.8	0.00	**82.8**	***24.1***
A03-20_Rut_23	4899	106	346	55	1974	145	92.9	82.5	0.935	3.71	0.0036	3.5	23	1.6	0.0	3.8	0.00	**23.2**	***1.6***
A03-20_Rut_24	5195	420	279	68	1962	293	94.6	85.8	1.166	14.92	-0.0073	17.5	-47	-16.7	0.0	3.8	0.00	**-47.3**	***-16.7***
A03-20_Rut_25	4833	129	1629	399	3479	259	66.3	53.2	0.890	4.49	0.0317	4.3	201	17.0	0.0	3.8	0.01	**201.4**	***17.0***
~~A03-20_Rut_01~~	~~#NUM!~~	~~#NUM!~~	~~61~~	~~41~~	~~-361~~	~~-2790~~	~~#NUM!~~	~~116.9~~	~~-0.348~~	~~104.40~~	~~0.0128~~	~~58.1~~	~~82~~	~~93.9~~	~~0.0~~	~~3.8~~	~~0.00~~	~~**82.1**~~	~~***93.9***~~
~~A03-20_Rut_02~~	~~4090~~	~~2018~~	~~52~~	~~22~~	~~416~~	~~396~~	~~98.7~~	~~87.4~~	~~0.511~~	~~67.84~~	~~0.0040~~	~~36.2~~	~~26~~	~~18.4~~	~~0.0~~	~~3.8~~	~~0.00~~	~~**35.7**~~	~~***18.4***~~
~~A03-20_Rut_21~~	~~2609~~	~~3160~~	~~67~~	~~46~~	~~228~~	~~346~~	~~97.4~~	~~70.7~~	~~0.162~~	~~94.88~~	~~0.0087~~	~~32.9~~	~~56~~	~~36.6~~	~~0.0~~	~~3.8~~	~~0.00~~	~~**56.1**~~	~~***36.6***~~
A04-15_Rut_01	4945	83	4682	781	4866	230	5.3	3.8	0.968	2.93	0.0346	2.9	219	12.4	0.0	3.8	0.00	**219.4**	***12.4***
A04-15_Rut_02	4904	126	530	118	2371	206	89.2	77.6	0.938	4.42	0.0053	4.2	34	2.9	0.0	3.8	0.00	**34.2**	***2.9***
A04-15_Rut_03	4901	132	6319	912	5284	234	-28.9	-19.6	0.936	4.62	0.1065	4.4	652	54.3	0.0	3.8	0.00	**652.3**	***54.3***
A04-15_Rut_04	5029	98	1824	306	3742	188	63.7	51.3	1.030	3.45	-0.0097	3.6	-63	-4.5	0.1	3.8	0.02	**-62.8**	***-4.5***
A04-15_Rut_05	4966	68	3928	548	4640	184	20.9	15.3	0.983	2.38	0.0143	2.3	92	4.3	0.1	3.8	0.02	**91.7**	***4.3***
A04-15_Rut_06	5004	172	6893	922	5497	237	-37.7	-25.4	1.011	6.06	-0.0214	6.1	-139	-17.3	0.0	3.8	0.00	**-139.4**	***-17.3***
A04-15_Rut_07	5035	101	4512	580	4878	184	10.4	7.5	1.034	3.57	-0.0348	3.7	-228	-17.2	0.1	3.8	0.01	**-228.0**	***-17.2***
A04-15_Rut_08	4959	126	5407	817	5085	228	-9.0	-6.3	0.977	4.43	0.0298	4.3	189	16.2	0.0	3.8	0.00	**189.4**	***16.2***
A04-15_Rut_09	5020	152	11402	1545	6453	299	-127.1	-76.7	1.023	5.35	-0.1109	5.5	-758	-88.9	0.0	3.8	0.00	**-758.0**	***-88.9***
A04-15_Rut_10	4919	63	4161	802	4685	250	15.4	11.2	0.949	2.21	0.0461	2.2	290	12.6	0.0	3.8	0.01	**290.6**	***12.6***
A04-15_Rut_11	5014	74	6496	661	5408	166	-29.5	-20.1	1.019	2.61	-0.0327	2.7	-214	-11.6	0.0	3.8	0.00	**-214.2**	***-11.6***
A04-15_Rut_12	5141	139	2971	525	4402	224	42.2	32.5	1.120	4.92	-0.0702	5.7	-469	-55.5	0.1	3.8	0.01	**-468.9**	***-55.5***
A04-15_Rut_13	5042	77	8837	1179	5958	246	-75.3	-48.3	1.040	2.71	-0.1170	2.9	-802	-49.2	0.0	3.8	0.00	**-802.2**	***-49.2***
A04-15_Rut_14	4990	105	4800	463	4933	149	3.8	2.7	1.000	3.68	-0.0001	3.7	-1	-0.1	0.0	3.8	0.00	**-0.6**	***-0.1***
A04-15_Rut_15	4781	121	362	68	1943	168	92.4	81.4	0.856	4.23	0.0083	3.9	53	4.1	0.0	3.8	0.00	**53.5**	***4.1***
A04-15_Rut_16	4976	146	4145	876	4719	282	16.7	12.2	0.990	5.13	0.0091	5.1	58	5.9	0.0	3.8	0.00	**58.3**	***5.9***
A04-15_Rut_17	4991	122	10198	1046	6200	216	-104.3	-64.5	1.001	4.29	-0.0053	4.3	-34	-3.0	0.0	3.8	0.00	**-34.2**	***-3.0***
A04-15_Rut_18	4945	64	6954	1227	5470	281	-40.6	-27.1	0.968	2.26	0.0625	2.2	391	17.0	0.0	3.8	0.00	**391.1**	***17.0***
A04-15_Rut_19	5343	234	3358	621	4702	264	37.1	28.6	1.302	8.37	-0.2065	11.5	-1491	-399.0	0.0	3.8	0.00	**-1491.5**	***-399.0***
A04-15_Rut_20	4590	272	1941	502	3511	307	57.7	44.7	0.742	9.42	0.0905	8.1	559	85.7	0.0	3.8	0.00	**558.9**	***85.7***
A04-15_Rut_21	4915	110	2916	413	4219	180	40.7	30.9	0.946	3.86	0.0309	3.7	196	14.2	0.0	3.8	0.01	**196.2**	***14.2***
A04-15_Rut_22	4982	99	9445	564	6042	131	-89.6	-56.3	0.995	3.50	0.0175	3.5	112	7.7	0.0	3.8	0.01	**112.1**	***7.7***
A04-15_Rut_23	4843	139	992	303	2955	291	79.5	66.4	0.897	4.87	0.0172	4.7	110	10.2	0.0	3.8	0.00	**109.8**	***10.2***
A04-15_Rut_24	5022	80	6546	1014	5426	244	-30.3	-20.6	1.025	2.83	-0.0440	2.9	-290	-17.3	0.0	3.8	0.00	**-290.0**	***-17.3***
A04-15_Rut_25	5133	124	7806	909	5801	212	-52.1	-34.6	1.114	4.41	-0.2675	5.1	-2007	-242.5	0.0	3.8	0.00	**-2006.9**	***-242.5***
A04-15_Rut_26	4989	96	8971	916	5949	197	-79.8	-50.8	1.000	3.39	0.0010	3.4	6	0.4	0.0	3.8	0.00	**6.5**	***0.4***
A10-05_01	2438	343	47	5	151	32	98.1	68.8	0.141	10.14	0.0063	4.7	41	3.8	0.0	3.8	0.01	**40.7**	***3.8***
A10-05_02	4875	159	262	36	1718	139	94.6	84.7	0.920	5.58	0.0033	5.2	21	2.2	0.0	3.8	0.00	**21.5**	***2.2***
A10-05_04	4629	284	308	57	1713	205	93.3	82.0	0.763	9.84	0.0116	7.8	74	11.6	0.0	3.8	0.00	**74.6**	***11.6***

RUTILE

		comments	^{204}Pb	^{206}Pb	^{207}Pb	^{208}Pb	^{232}Th	^{238}U	Pb ppm	U ppm	$^{238}U/^{206}Pb$	1s %	$^{207}Pb/^{206}Pb$	1s %	$^{207}Pb/^{235}U$	1s %	$^{206}Pb/^{238}U$	1s %	Rho
A10-05_08	18/03/2018		2113	2113	1519	3531	140	4233	1.195	0.706	3.0610	8.74	0.8351	2.77	37.5988	9.17	0.3267	8.74	0.95
A10-05_09	18/03/2018		799	799	639	1380	108	9053	0.470	1.510	16.8441	10.02	0.7309	4.82	5.9803	11.12	0.0594	10.02	0.90
A10-05_10	18/03/2018		6074	6074	4262	9851	4286	139572	3.367	23.280	30.6312	9.10	0.6574	2.50	2.9578	9.44	0.0326	9.10	0.96
A10-05_11	18/03/2018		433	433	224	484	116	2221	0.190	0.370	9.5041	9.15	0.7685	4.76	11.1439	10.32	0.1052	9.15	0.89
A10-05_15	18/03/2018		bd	123	80	180	185	3000	0.064	0.500	34.8842	9.41	0.6613	13.55	2.6125	16.50	0.0287	9.41	0.57
A10-05_16	18/03/2018		628	628	406	954	bd	2503	0.332	0.418	5.8451	11.11	0.8213	4.57	19.3645	12.01	0.1711	11.11	0.92
A10-05_18	18/03/2018		bd	174	100	212	16	7501	0.081	1.251	67.7646	6.06	0.5949	7.29	1.2100	9.48	0.0148	6.06	0.64
A10-05_19	18/03/2018		784	784	590	1432	124	2689	0.468	0.449	6.6389	9.31	0.7130	5.14	14.8014	10.63	0.1506	9.31	0.88
A10-05_22	18/03/2018		bd	87	54	109	23	1477	0.042	0.246	24.3167	9.20	0.5625	24.43	3.1882	26.11	0.0411	9.20	0.35
A10-05_24	18/03/2018		bd	69	46	111	4	608	0.038	0.101	13.3498	12.39	0.5039	16.87	5.2017	20.93	0.0749	12.39	0.59
A10-05_26	18/03/2018		1037	1037	871	2080	711	6700	0.665	1.118	7.7359	7.73	0.8256	2.62	14.7085	8.16	0.1293	7.73	0.95
A10-05_27	18/03/2018		bd	206	50	114	617	15582	0.062	2.599	107.9683	5.00	0.2783	8.89	0.3552	10.20	0.0093	5.00	0.49
A10-05_28	18/03/2018		bd	168	78	162	108	8827	0.068	1.472	86.6447	7.30	0.3884	9.81	0.6178	12.23	0.0115	7.30	0.60
~~A10-05_03~~	~~18/03/2018~~		~~bd~~	~~83~~	~~47~~	~~93~~	~~23~~	~~1986~~	~~0.037~~	~~0.331~~	~~32.3747~~	~~13.26~~	~~0.3038~~	~~29.20~~	~~1.2932~~	~~32.07~~	~~0.0309~~	~~13.26~~	~~0.41~~
~~A10-05_05~~	~~18/03/2018~~		~~bd~~	~~167~~	~~48~~	~~94~~	~~70~~	~~17400~~	~~0.051~~	~~2.902~~	~~147.0642~~	~~5.20~~	~~0.2706~~	~~10.73~~	~~0.2536~~	~~11.92~~	~~0.0068~~	~~5.20~~	~~0.44~~
~~A10-05_06~~	~~18/03/2018~~		~~bd~~	~~61~~	~~31~~	~~68~~	~~bd~~	~~3570~~	~~0.027~~	~~0.595~~	~~83.3584~~	~~10.76~~	~~0.5186~~	~~29.61~~	~~0.8575~~	~~31.51~~	~~0.0120~~	~~10.76~~	~~0.34~~
~~A10-05_07~~	~~18/03/2018~~		~~bd~~	~~49~~	~~27~~	~~48~~	~~4~~	~~2078~~	~~0.021~~	~~0.347~~	~~58.3319~~	~~15.65~~	~~0.2092~~	~~53.53~~	~~0.4942~~	~~55.77~~	~~0.0171~~	~~15.65~~	~~0.28~~
~~A10-05_12~~	~~18/03/2018~~		~~bd~~	~~26~~	~~27~~	~~63~~	~~bd~~	~~457~~	~~0.019~~	~~0.076~~	~~26.3686~~	~~24.10~~	~~0.3448~~	~~34.05~~	~~1.8024~~	~~41.72~~	~~0.0379~~	~~24.10~~	~~0.58~~
~~A10-05_13~~	~~18/03/2018~~		~~bd~~	~~42~~	~~23~~	~~32~~	~~4~~	~~1703~~	~~0.016~~	~~0.284~~	~~59.6619~~	~~15.80~~	~~0.2253~~	~~39.93~~	~~0.5205~~	~~42.94~~	~~0.0168~~	~~15.80~~	~~0.37~~
~~A10-05_14~~	~~18/03/2018~~		~~bd~~	~~129~~	~~21~~	~~30~~	~~78~~	~~11569~~	~~0.030~~	~~1.930~~	~~135.9169~~	~~5.90~~	~~0.1650~~	~~24.42~~	~~0.1673~~	~~25.12~~	~~0.0074~~	~~5.90~~	~~0.24~~
~~A10-05_17~~	~~18/03/2018~~		~~bd~~	~~48~~	~~21~~	~~37~~	~~bd~~	~~3812~~	~~0.018~~	~~0.636~~	~~119.2739~~	~~11.83~~	~~0.3105~~	~~29.72~~	~~0.3588~~	~~31.99~~	~~0.0084~~	~~11.83~~	~~0.37~~
~~A10-05_20~~	~~18/03/2018~~		~~bd~~	~~26~~	~~15~~	~~18~~	~~24~~	~~2458~~	~~0.010~~	~~0.410~~	~~141.5606~~	~~23.12~~	~~-0.0494~~	~~285.82~~	~~-0.0481~~	~~286.76~~	~~0.0071~~	~~23.12~~	~~0.08~~
~~A10-05_21~~	~~18/03/2018~~		~~bd~~	~~40~~	~~15~~	~~38~~	~~bd~~	~~1645~~	~~0.016~~	~~0.274~~	~~66.1819~~	~~15.55~~	~~0.2011~~	~~48.86~~	~~0.4187~~	~~51.27~~	~~0.0151~~	~~15.55~~	~~0.30~~
~~A10-05_23~~	~~18/03/2018~~		~~bd~~	~~133~~	~~24~~	~~45~~	~~123~~	~~11575~~	~~0.034~~	~~1.931~~	~~124.3893~~	~~7.20~~	~~0.1542~~	~~15.97~~	~~0.1708~~	~~17.52~~	~~0.0080~~	~~7.20~~	~~0.41~~
~~A10-05_25~~	~~18/03/2018~~		~~bd~~	~~48~~	~~30~~	~~63~~	~~bd~~	~~1840~~	~~0.024~~	~~0.307~~	~~46.3540~~	~~14.51~~	~~0.3769~~	~~28.82~~	~~1.1205~~	~~32.26~~	~~0.0216~~	~~14.51~~	~~0.45~~
~~A10-05_29~~	~~18/03/2018~~		~~bd~~	~~72~~	~~33~~	~~57~~	~~45~~	~~3518~~	~~0.027~~	~~0.587~~	~~73.4453~~	~~11.58~~	~~0.4041~~	~~38.97~~	~~0.7583~~	~~40.65~~	~~0.0136~~	~~11.58~~	~~0.28~~
A5-15_01	18/03/2018		8199	8199	5692	14750	12646	144947	4.777	24.177	27.9518	3.79	0.6996	1.31	3.4492	4.01	0.0358	3.79	0.94
A5-15_02	18/03/2018		1801	1801	1131	2799	7987	50197	0.956	8.373	42.0702	3.08	0.6420	2.30	2.1030	3.85	0.0238	3.08	0.80
A5-15_03	18/03/2018		392	392	162	383	432	33928	0.156	5.659	132.2350	5.42	0.4523	6.82	0.4713	8.71	0.0076	5.42	0.62
A5-15_04	18/03/2018		bd	156	55	123	7	14516	0.056	2.421	136.7724	8.18	0.3820	10.64	0.3849	13.42	0.0073	8.18	0.61
A5-15_05	18/03/2018		bd	181	83	160	176	12995	0.071	2.167	107.1091	4.75	0.4722	9.10	0.6075	10.27	0.0093	4.75	0.46
A5-15_06	18/03/2018		bd	164	65	176	162	13536	0.068	2.258	120.3990	9.85	0.4240	11.43	0.4854	15.09	0.0083	9.85	0.65
A5-15_07	18/03/2018		bd	223	65	202	158	25277	0.082	4.216	163.5394	7.29	0.3857	9.40	0.3250	11.89	0.0061	7.29	0.61
A5-15_08	18/03/2018		341	341	144	355	362	26026	0.140	4.341	112.6402	3.93	0.4438	5.47	0.5430	6.73	0.0089	3.93	0.58
A5-15_09	18/03/2018		330	330	162	378	772	27113	0.145	4.522	121.8827	3.62	0.5871	6.05	0.6639	7.05	0.0082	3.62	0.51
A5-15_10	18/03/2018		517	517	316	897	368	19645	0.288	3.277	57.9877	9.37	0.5982	4.79	1.4216	10.52	0.0172	9.37	0.89
A5-15_11	18/03/2018		1168	1168	790	1961	2386	34571	0.654	5.766	44.2051	2.81	0.7038	1.98	2.1944	3.44	0.0226	2.81	0.82
A5-15_12	18/03/2018		bd	144	66	116	14	13112	0.054	2.187	135.6204	6.89	0.3998	6.75	0.4063	9.65	0.0074	6.89	0.71
A5-15_13	18/03/2018		550	550	249	617	183	37528	0.236	6.259	104.7058	4.59	0.4497	4.60	0.5919	6.50	0.0096	4.59	0.71
A5-15_14	18/03/2018		34107	34107	26640	68566	41899	47289	21.569	7.888	1.9875	4.90	0.7890	0.73	54.7087	4.95	0.5031	4.90	0.99
A5-15_15	18/03/2018		19877	19877	15920	39165	137905	51555	12.503	8.599	4.1256	2.94	0.7983	0.70	26.6664	3.02	0.2424	2.94	0.97
A5-15_16	18/03/2018		bd	189	75	146	64	16136	0.068	2.691	127.2069	6.57	0.3982	11.42	0.4314	13.18	0.0079	6.57	0.50
A5-15_18	18/03/2018		424	424	188	404	68	32532	0.169	5.426	113.6345	6.36	0.3831	7.91	0.4646	10.15	0.0088	6.36	0.63
A5-15_19	18/03/2018		1703	1703	1063	2650	4436	56916	0.903	9.493	50.0087	5.20	0.6016	2.76	1.6580	5.88	0.0200	5.20	0.88
A5-15_20	18/03/2018		481	481	232	522	474	37359	0.206	6.231	118.2185	3.35	0.4699	5.27	0.5478	6.25	0.0085	3.35	0.54
A5-15_21	18/03/2018		332	332	149	318	210	24526	0.133	4.091	109.0592	10.53	0.5356	11.35	0.6768	15.49	0.0092	10.53	0.68
A5-15_22	18/03/2018		314	314	133	353	278	23342	0.133	3.893	110.1844	8.88	0.4525	11.14	0.5660	14.25	0.0091	8.88	0.62
A5-15_24	18/03/2018		473	473	258	802	484	20249	0.256	3.377	60.5931	11.02	0.7325	5.89	1.6662	12.49	0.0165	11.02	0.88
A5-15_25	18/03/2018		5417	5417	4475	11019	198	12903	3.488	2.152	2.0105	18.82	0.7395	2.40	50.6961	18.97	0.4974	18.82	0.99
A5-15_26	18/03/2018		241	241	123	322	110	13666	0.114	2.279	85.5200	5.42	0.5642	6.84	0.9092	8.72	0.0117	5.42	0.62
A5-15_27	18/03/2018		837	837	509	1288	1106	35912	0.439	5.990	63.0373	3.22	0.5992	2.77	1.3100	4.25	0.0159	3.22	0.76
~~A5-15_17~~	~~18/03/2018~~		~~bd~~	~~116~~	~~29~~	~~54~~	~~bd~~	~~11738~~	~~0.033~~	~~1.958~~	~~148.5112~~	~~8.01~~	~~0.2507~~	~~22.84~~	~~0.2327~~	~~24.21~~	~~0.0067~~	~~8.01~~	~~0.33~~
~~A5-15_23~~	~~18/03/2018~~		~~bd~~	~~87~~	~~23~~	~~62~~	~~28~~	~~10747~~	~~0.029~~	~~1.793~~	~~175.0445~~	~~7.48~~	~~0.3240~~	~~23.75~~	~~0.2551~~	~~24.90~~	~~0.0057~~	~~7.48~~	~~0.30~~
JU13a_04	18/03/2018		bd	70	63	138	bd	102	0.045	0.017	2.2875	11.47	1.4929	20.55	89.9432	23.53	0.4371	11.47	0.49
JU13a_05	18/03/2018		bd	38	30	63	bd	304	0.022	0.051	12.0884	14.09	0.8613	20.47	9.8199	24.85	0.0827	14.09	0.57
JU13a_06	18/03/2018		bd	70	36	82	bd	505	0.031	0.084	11.1945	11.72	0.3717	28.87	4.5765	31.15	0.0893	11.72	0.38
JU13a_09	18/03/2018		bd	54	44	101	bd	57	0.033	0.009	1.2313	13.90	0.7947	17.66	88.9571	22.47	0.8122	13.90	0.62
JU13a_10	18/03/2018		bd	46	30	73	bd	137	0.025	0.023	4.1511	12.77	0.3241	27.34	10.7611	30.17	0.2409	12.77	0.42
JU13a_11	18/03/2018		515	515	431	1010	bd	207	0.326	0.034	0.7518	11.59	0.8478	10.94	155.4208	15.94	1.3301	11.59	0.73
JU13a_12	18/03/2018		1654	1654	1290	3166	bd	338	1.019	0.056	0.3237	5.34	0.7986	2.16	340.0289	5.76	3.0895	5.34	0.93
JU13a_13	18/03/2018		bd	167	129	297	bd	127	0.099	0.021	1.1810	6.60	1.0473	10.33	122.2193	12.26	0.8468	6.60	0.54
JU13a_14	18/03/2018		bd	107	78	165	bd	63	0.058	0.010	0.9061	9.97	0.9549	17.47	145.2326	20.12	1.1036	9.97	0.50
JU13a_15	18/03/2018		bd	86	78	173	bd	46	0.056	0.008	0.6800	12.02	0.7570	30.06	153.4344	32.37	1.4706	12.02	0.37
JU13a_16	18/03/2018		bd	79	59	150	bd	46	0.048	0.008	0.7246	10.74	0.8377	19.74	159.3261	22.47	1.3800	10.74	0.48
JU13a_17	18/03/2018		bd	52	39	77	bd	71	0.028	0.012	1.6408	10.81	0.7478	17.75	62.8110	20.78	0.6094	10.81	0.52
JU13a_18	18/03/2018		bd	38	35	79	bd	64	0.025	0.011	2.0513	17.02	1.0457	20.80	70.2593	26.88	0.4875	17.02	0.63
JU13a_19	18/03/2018		1432	1432	1124	2480	255	5063	0.840	0.844	2.8361	11.48	0.7982	3.02	38.7869	11.87	0.3526	11.48	0.97
JU13a_20	18/03/2018		bd	132	95	253	bd	84	0.080	0.014	1.0073	10.65	0.7575	9.51	103.6405	14.28	0.9927	10.65	0.75
~~JU13a_07~~	~~18/03/2018~~	~~rej - large uncertainty~~	~~bd~~	~~51~~	~~38~~	~~94~~	~~bd~~	~~64~~	~~0.030~~	~~0.011~~	~~2.0024~~	~~13.87~~	~~0.0660~~	~~198.81~~	~~4.5447~~	~~199.29~~	~~0.4994~~	~~13.87~~	~~0.07~~
~~JU13a_08~~	~~18/03/2018~~	~~rej - large uncertainty~~	~~bd~~	~~34~~	~~29~~	~~50~~	~~bd~~	~~53~~	~~0.019~~	~~0.009~~	~~2.1470~~	~~20.30~~	~~0.1029~~	~~143.56~~	~~6.6077~~	~~144.99~~	~~0.4658~~	~~20.30~~	~~0.14~~
~~JU13a_01~~	18/03/2018	~~neg. Ratio~~	~~bd~~	~~36~~	~~17~~	~~49~~	~~bd~~	~~5~~	0.017	0.001	~~-0.0368~~	~~32.60~~	~~0.2389~~	~~64.31~~	~~-893.7344~~	~~72.10~~	-27.1483	~~32.60~~	~~0.45~~
~~JU13a_02~~	18/03/2018	~~neg. Ratio~~	~~bd~~	~~34~~	~~11~~	~~-7~~	~~bd~~	~~3~~	0.006	0.000	~~-0.0755~~	~~49.80~~	~~0.0872~~	~~77.93~~	~~-159.2101~~	~~92.48~~	-13.2412	~~49.80~~	~~0.54~~
~~JU13a_03~~	18/03/2018	~~neg. Ratio~~	~~bd~~	~~58~~	~~51~~	~~117~~	~~bd~~	~~1~~	0.038	0.000	~~-0.0217~~	~~16.90~~	~~1.2885~~	~~22.52~~	########	~~28.15~~	-46.0236	~~16.90~~	~~0.60~~
0502_Rutile_02	07/07/2017		-118	549	47	58	76	599	0.10	11.95	164.504	3.98	0.089	11.82	0.074	12.47	0.006	3.98	0.32
0502_Rutile_03	07/07/2017		-1	777	64	91	59	811	0.14	16.16	158.359	2.94	0.078	9.95	0.068	10.38	0.006	2.94	0.28
0502_Rutile_05	07/07/2017		11	2014	1113	2921	9777	548	0.89	10.93	40.106	2.54	0.546	2.33	1.876	3.45	0.025	2.54	0.74
0502_Rutile_06	07/07/2017		161	450	37	30	178	451	0.08	8.99	143.598	4.28	0.085	14.59	0.081	15.21	0.007	4.28	0.28
0502_Rutile_07	07/07/2017		1026	23507	16470	43156	4605	591	12.26	11.78	4.031	7.42	0.719	0.81	24.572	7.47	0.248	7.42	0.99
0502_Rutile_08	07/07/2017		73	5426	3417	9244	15555	564	2.67	11.24	16.305	5.94	0.628	2.21	5.306	6.34	0.061	5.94	0.94
0502_Rutile_09	07/07/2017		-7	1019	500	1370	1357	350	0.43	6.99	53.102	4.69	0.478	4.73	1.240	6.66	0.019	4.69	0.70
0502_Rutile_10	07/07/2017		-137	1275	63	7	19	1580	0.20	31.50	158.807	1.98	0.048	7.96	0.042	8.21	0.006	1.98	0.24
0502_Rutile_11	07/07/2017		-13	1431	75	-9	8	1707	0.22	34.05	154.760	2.25	0.054	6.75	0.048	7.11	0.006	2.25	0.32
0502_Rutile_12	07/07/2017		15	1428	62	-7	17	1763	0.22	35.16	156.215	2.00	0.041	7.72	0.036	7.97	0.006	2.00	0.25
0502_Rutile_15	07/07/2017		43	1783	819	2186	3309	746	0.71	14.88	56.333	6.78	0.429	4.95	1.050	8.39	0.018	6.78	0.81
0502_Rutile_16	07/07/2017		-40	939	60	15	-3	1095	0.15	21.84	150.287	3.23	0.067	9.69	0.061	10.22	0.007	3.23	0.32
0502_Rutile_17	07/07/2017		47	1051	59	28	15	1323	0.17	26.38	162.785	2.33	0.054	8.86	0.046	9.16	0.006	2.33	0.25
0502_Rutile_18	07/07/2017		-59	1163	85	77	33	1347	0.20	26.87	150.821	2.48	0.084	12.40	0.077	12.65	0.007	2.48	0.20
~~0502_Rutile_01~~	~~07/07/2017~~	~~burnt through the grain~~	~~48~~	~~487~~	~~80~~	~~207~~	~~389~~	~~434~~	~~0.11~~	~~8.65~~	~~107.371~~	~~8.48~~	~~0.187~~	~~11.48~~	~~0.241~~	~~14.27~~	~~0.009~~	~~8.48~~	~~0.59~~
~~0502_Rutile_04~~	~~07/07/2017~~	~~burnt through the grain~~	~~-74~~	~~553~~	~~64~~	~~91~~	~~1022~~	~~605~~	~~0.10~~	~~12.06~~	~~158.453~~	~~5.69~~	~~0.128~~	~~10.85~~	~~0.111~~	~~12.25~~	~~0.006~~	~~5.69~~	~~0.46~~
~~0502_Rutile_13~~	~~07/07/2017~~	~~rej - low Pb counts~~	4	~~692~~	~~22~~	~~11~~	~~-3~~	~~668~~	~~0.11~~	~~13.32~~	~~149.350~~	~~3.11~~	~~0.031~~	~~23.80~~	~~0.028~~	~~24.00~~	~~0.007~~	~~3.11~~	~~0.13~~
~~0502_Rutile_14~~	~~07/07/2017~~	~~rej - low Pb counts~~	~~28~~	~~632~~	~~19~~	~~-2~~	~~-3~~	~~581~~	~~0.10~~	~~11.59~~	~~140.402~~	~~4.55~~	~~0.035~~	~~19.03~~	~~0.035~~	~~19.56~~	~~0.007~~	~~4.55~~	~~0.23~~
1109_Rutile_02	07/07/2017		82	9289	1795	3238	8109	4532	2.11	90.37	57.490	5.34	0.280	13.16	0.672	14.20	0.017	5.34	0.38
1109_Rutile_03	07/07/2017		121	1211	857	2132	16959	120	0.62	2.39	13.982	7.94	0.752	3.04	7.415	8.50	0.072	7.94	0.93
1109_Rutile_04	07/07/2017		264	3595	2887	7464	11184	70	2.06	1.40	2.771	6.59	0.827	1.30	41.146	6.71	0.361	6.59	0.98
1109_Rutile_05	07/07/2017		111	3543	2906	7327	1827	56	2.03	1.12	2.110	8.60	0.803	1.66	52.442	8.76	0.474	8.60	0.98
1109_Rutile_06	07/07/2017		-135	108	44	72	7	41	0.03	0.81	50.499	7.95	0.478	11.15	1.305	13.69	0.020	7.95	0.58
1109_Rutile_09	07/07/2017		41	120	26	67	-3	114	0.03	2.28	132.893	9.10	0.275	22.56	0.285	24.33	0.008	9.10	0.37
1109_Rutile_12	07/07/2017		-15	336	257	671	35	55	0.19	1.10	19.446	11.65	0.675	6.96	4.783	13.57	0.051	11.65	0.86
1109_Rutile_13	07/07/2017		-68	751	539	1297	150	47	0.38	0.93	8.451	10.47	0.767	4.74	12.507	11.49	0.118	10.47	0.91
1109_Rutile_14	07/07/2017		-29	233	162	458	5	39	0.13	0.78	22.976	10.54	0.650	8.16	3.901	13.32	0.044	10.54	0.79
1109_Rutile_15	07/07/2017		-93	49	28	58	-3	19	0.02	0.38	54.198	15.00	0.400	23.78	1.017	28.11	0.018	15.00	0.53
1109_Rutile_16	07/07/2017		6	65	29	39	-3	54	0.02	1.08	114.734	11.33	0.360	19.86	0.433	22.86	0.009	11.33	0.50
1109_Rutile_17	07/07/2017		53	1354	1182	2902	1275	31	0.80	0.61	3.275	10.03	0.822	2.07	34.600	10.24	0.305	10.03	0.98
1109_Rutile_18	07/07/2017		100	1697	1394	3365	209	27	0.95	0.55	2.538	14.04	0.815	2.89	44.252	14.34	0.394	14.04	0.98
1109_Rutile_19	07/07/2017		12	2190	1858	4509	2827	83	1.26	1.65	5.307	4.44	0.806	1.86	20.921	4.82	0.188	4.44	0.92
1109_Rutile_21	07/07/2017		34	94	60	111	-3	49	0.04	0.98	64.180	12.27	0.384	21.13	0.825	24.43	0.016	12.27	0.50

RUTILE

	$^{207}Pb/^{206}Pb$	2s abs	$^{206}Pb/^{238}U$	2s abs	$^{207}Pb/^{235}U$	2s abs	c. % 6-38/c.	%6-38/7	*f206*	1s %	$^{206}Pb*/^{238}U$	1s %	²06/238-Pb	2s [Ma]	Th/U min.	Th/U wr.	f	·. 206/238	*2s [Ma]*
A10-05_08	4983	79	1822	272	3709	167	63.4	50.9	0.994	2.77	0.0019	2.8	12	0.7	0.0	3.8	0.01	**12.2**	***0.7***
A10-05_09	4793	138	372	72	1973	177	92.2	81.2	0.863	4.82	0.0081	4.4	52	4.5	0.0	3.8	0.00	**52.2**	***4.5***
A10-05_10	4640	72	207	37	1397	134	95.5	85.2	0.771	2.50	0.0075	2.8	48	2.7	0.0	3.8	0.01	**48.2**	***2.7***
A10-05_11	4864	136	645	111	2535	176	86.7	74.6	0.910	4.76	0.0095	4.4	61	5.3	0.1	3.8	0.01	**60.9**	***5.3***
A10-05_15	4649	391	182	34	1304	217	96.1	86.0	0.776	13.55	0.0064	10.7	41	8.8	0.1	3.8	0.02	**41.4**	***8.8***
A10-05_16	4959	130	1018	206	3060	209	79.5	66.7	0.979	4.57	0.0036	4.5	23	2.1	0.0	3.8	0.00	**23.2**	***2.1***
A10-05_18	4496	212	94	11	805	100	97.9	88.3	0.693	7.29	0.0045	5.4	29	3.1	0.0	3.8	0.00	**29.2**	***3.1***
A10-05_19	4757	147	904	155	2803	184	81.0	67.7	0.832	5.14	0.0252	4.6	161	14.4	0.0	3.8	0.01	**160.8**	***14.4***
A10-05_22	4414	713	260	47	1454	340	94.1	82.1	0.648	24.43	0.0145	16.2	93	29.7	0.0	3.8	0.00	**92.7**	***29.7***
A10-05_24	4253	497	466	110	1853	306	89.1	74.9	0.568	16.87	0.0324	11.0	205	44.2	0.0	3.8	0.00	**205.6**	***44.2***
A10-05_26	4967	75	784	113	2797	144	84.2	72.0	0.986	2.62	0.0018	2.6	12	0.6	0.1	3.8	0.03	**12.0**	***0.6***
A10-05_27	3353	278	59	6	309	53	98.2	80.7	0.292	8.89	0.0066	4.4	42	3.7	0.0	3.8	0.01	**42.2**	***3.7***
A10-05_28	3865	296	74	11	488	91	98.1	84.9	0.431	9.81	0.0066	5.9	42	5.0	0.0	3.8	0.00	**42.3**	***5.0***
~~A10-05_03~~	~~3490~~	~~903~~	~~196~~	~~51~~	~~843~~	~~313~~	~~94.4~~	~~76.7~~	~~0.321~~	~~29.20~~	~~0.0210~~	~~13.0~~	~~134~~	~~34.3~~	~~0.0~~	~~3.8~~	~~0.00~~	~~**134.0**~~	~~***24.3***~~
~~A10-05_05~~	~~3309~~	~~336~~	~~44~~	~~5~~	~~229~~	~~48~~	~~98.7~~	~~81.0~~	~~0.283~~	~~10.73~~	~~0.0049~~	~~4.8~~	~~31~~	~~3.0~~	~~0.0~~	~~3.8~~	~~0.00~~	~~**21.5**~~	~~***2.0***~~
~~A10-05_06~~	~~4295~~	~~870~~	~~77~~	~~16~~	~~629~~	~~259~~	~~98.2~~	~~87.8~~	~~0.597~~	~~29.61~~	~~0.0048~~	~~18.2~~	~~31~~	~~11.3~~	~~0.0~~	~~3.8~~	~~0.00~~	~~**31.2**~~	~~***11.3***~~
~~A10-05_07~~	~~2899~~	~~1736~~	~~110~~	~~34~~	~~408~~	~~319~~	~~96.2~~	~~73.1~~	~~0.203~~	~~53.53~~	~~0.0137~~	~~16.5~~	~~87~~	~~28.7~~	~~0.0~~	~~3.8~~	~~0.00~~	~~**87.6**~~	~~***28.7***~~
~~A10-05_12~~	~~3684~~	~~1039~~	~~240~~	~~113~~	~~1046~~	~~436~~	~~93.5~~	~~77.1~~	~~0.371~~	~~34.05~~	~~0.0238~~	~~19.7~~	~~152~~	~~59.0~~	~~0.0~~	~~3.8~~	~~0.00~~	~~**152.0**~~	~~***59.0***~~
~~A10-05_13~~	~~3019~~	~~1282~~	~~107~~	~~33~~	~~425~~	~~262~~	~~96.5~~	~~74.8~~	~~0.224~~	~~39.93~~	~~0.0130~~	~~15.2~~	~~83~~	~~25.1~~	~~0.0~~	~~3.8~~	~~0.00~~	~~**83.4**~~	~~***25.1***~~
~~A10-05_14~~	~~2508~~	~~821~~	~~47~~	~~6~~	~~157~~	~~71~~	~~98.1~~	~~69.9~~	~~0.149~~	~~24.42~~	~~0.0063~~	~~6.2~~	~~40~~	~~5.0~~	~~0.0~~	~~3.8~~	~~0.00~~	~~**40.3**~~	~~***5.0***~~
~~A10-05_17~~	~~3524~~	~~917~~	~~54~~	~~13~~	~~311~~	~~159~~	~~98.5~~	~~82.7~~	~~0.333~~	~~29.72~~	~~0.0056~~	~~12.7~~	~~36~~	~~9.1~~	~~0.0~~	~~3.8~~	~~0.00~~	~~**36.0**~~	~~***9.1***~~
~~A10-05_20~~	~~#NUM!~~	~~#NUM!~~	~~45~~	~~21~~	~~-50~~	~~-348~~	~~#NUM!~~	~~190.6~~	~~-0.122~~	~~285.82~~	~~0.0079~~	~~43.4~~	~~51~~	~~43.9~~	~~0.0~~	~~3.8~~	~~0.00~~	~~**51.0**~~	~~***43.9***~~
~~A10-05_21~~	~~2835~~	~~1594~~	~~97~~	~~30~~	~~355~~	~~268~~	~~96.6~~	~~72.8~~	~~0.193~~	~~48.86~~	~~0.0122~~	~~15.7~~	~~78~~	~~24.3~~	~~0.0~~	~~3.8~~	~~0.00~~	~~**78.3**~~	~~***24.3***~~
~~A10-05_23~~	~~2393~~	~~544~~	~~52~~	~~7~~	~~160~~	~~51~~	~~97.8~~	~~67.8~~	~~0.135~~	~~15.97~~	~~0.0070~~	~~6.6~~	~~45~~	~~5.9~~	~~0.0~~	~~3.8~~	~~0.00~~	~~**44.8**~~	~~***5.9***~~
~~A10-05_25~~	~~3819~~	~~872~~	~~138~~	~~39~~	~~763~~	~~298~~	~~96.4~~	~~82.0~~	~~0.415~~	~~28.82~~	~~0.0126~~	~~14.7~~	~~81~~	~~23.5~~	~~0.0~~	~~3.8~~	~~0.00~~	~~**81.0**~~	~~***23.5***~~
~~A10-05_29~~	~~3925~~	~~1171~~	~~87~~	~~20~~	~~573~~	~~305~~	~~97.8~~	~~84.8~~	~~0.451~~	~~38.97~~	~~0.0075~~	~~18.7~~	~~48~~	~~17.9~~	~~0.0~~	~~3.8~~	~~0.00~~	~~**48.1**~~	~~***17.9***~~
A5-15_01	4730	38	227	17	1516	61	95.2	85.0	0.824	1.31	0.0063	1.3	40	1.0	0.1	3.8	0.02	**40.5**	***1.0***
A5-15_02	4606	67	151	9	1150	52	96.7	86.8	0.752	2.30	0.0059	1.9	38	1.4	0.2	3.8	0.04	**38.0**	***1.4***
A5-15_03	4093	203	49	5	392	55	98.8	87.6	0.513	6.82	0.0037	4.4	24	2.1	0.0	3.8	0.00	**23.8**	***2.1***
A5-15_04	3840	321	47	8	331	73	98.8	85.8	0.424	10.64	0.0042	6.5	27	3.5	0.0	3.8	0.00	**27.2**	***3.5***
A5-15_05	4157	270	60	6	482	76	98.6	87.6	0.538	9.10	0.0043	5.4	28	3.0	0.0	3.8	0.00	**27.9**	***3.0***
A5-15_06	3997	342	53	10	402	95	98.7	86.7	0.477	11.43	0.0043	7.5	28	4.2	0.0	3.8	0.00	**28.0**	***4.2***
A5-15_07	3854	284	39	6	286	58	99.0	86.2	0.429	9.40	0.0035	5.8	22	2.6	0.0	3.8	0.00	**22.6**	***2.6***
A5-15_08	4065	163	57	4	440	47	98.6	87.1	0.502	5.47	0.0044	3.4	28	1.9	0.0	3.8	0.00	**28.5**	***1.9***
A5-15_09	4476	176	53	4	517	56	98.8	89.8	0.684	6.05	0.0026	4.3	17	1.4	0.0	3.8	0.01	**16.8**	***1.4***
A5-15_10	4504	139	110	20	898	118	97.6	87.7	0.697	4.79	0.0052	4.4	34	2.9	0.0	3.8	0.00	**33.7**	***2.9***
A5-15_11	4739	57	144	8	1179	47	97.0	87.8	0.831	1.98	0.0038	1.7	25	0.8	0.1	3.8	0.02	**24.7**	***0.8***
A5-15_12	3908	203	47	6	346	55	98.8	86.3	0.447	6.75	0.0041	4.9	26	2.5	0.0	3.8	0.00	**26.4**	***2.5***
A5-15_13	4084	137	61	6	472	48	98.5	87.0	0.509	4.60	0.0047	3.2	30	2.0	0.0	3.8	0.00	**30.2**	***2.0***
A5-15_14	4902	21	2627	208	4082	94	46.4	35.6	0.909	0.73	0.0458	0.8	288	4.5	0.9	3.8	0.23	**288.5**	***4.5***
A5-15_15	4919	20	1399	73	3371	57	71.6	58.5	0.944	0.70	0.0135	0.7	87	1.2	2.7	3.8	0.70	**86.7**	***1.2***
A5-15_16	3902	344	50	7	364	78	98.7	86.1	0.444	11.42	0.0044	6.3	28	3.5	0.0	3.8	0.00	**28.2**	***3.5***
A5-15_18	3844	239	56	7	387	63	98.5	85.4	0.425	7.91	0.0051	5.0	33	3.2	0.0	3.8	0.00	**32.6**	***3.2***
A5-15_19	4512	80	128	13	993	72	97.2	87.1	0.701	2.76	0.0060	2.5	38	1.9	0.1	3.8	0.02	**38.5**	***1.9***
A5-15_20	4149	156	54	4	444	44	98.7	87.8	0.535	5.27	0.0039	3.2	25	1.6	0.0	3.8	0.00	**25.4**	***1.6***
A5-15_21	4342	333	59	12	525	120	98.6	88.8	0.618	11.35	0.0035	8.1	23	3.6	0.0	3.8	0.00	**22.6**	***3.6***
A5-15_22	4094	331	58	10	455	100	98.6	87.2	0.513	11.14	0.0044	7.2	28	4.1	0.0	3.8	0.00	**28.5**	***4.1***
A5-15_24	4796	169	106	23	996	147	97.8	89.4	0.868	5.89	0.0022	5.3	14	1.5	0.0	3.8	0.01	**14.1**	***1.5***
A5-15_25	4810	69	2603	759	4006	321	45.9	35.0	0.832	2.40	0.0835	3.7	517	37.0	0.0	3.8	0.00	**517.2**	***37.0***
A5-15_26	4418	200	75	8	657	81	98.3	88.6	0.654	6.84	0.0040	4.8	26	2.5	0.0	3.8	0.00	**26.1**	***2.5***
A5-15_27	4506	81	101	6	850	48	97.7	88.1	0.698	2.77	0.0048	2.2	31	1.3	0.0	3.8	0.01	**30.9**	***1.3***
~~A5-15_17~~	~~3189~~	~~723~~	~~43~~	~~7~~	~~212~~	~~89~~	~~98.6~~	~~79.6~~	~~0.258~~	~~22.84~~	~~0.0050~~	~~8.4~~	~~32~~	~~5.4~~	~~0.0~~	~~3.8~~	~~0.00~~	~~**32.2**~~	~~***5.4***~~
~~A5-15_23~~	~~3589~~	~~730~~	~~37~~	~~5~~	~~231~~	~~98~~	~~99.0~~	~~84.1~~	~~0.351~~	~~23.75~~	~~0.0037~~	~~9.6~~	~~24~~	~~4.6~~	~~0.0~~	~~3.8~~	~~0.00~~	~~**24.0**~~	~~***4.6***~~
JU13a_04	5794	566	2338	435	4580	388	59.7	49.0	1.827	20.55	-0.3614	38.7	-2891	-3716.6	0.1	3.8	0.02	**-2891.3**	***-3716.6***
JU13a_05	5027	580	512	137	2418	378	89.8	78.8	1.029	20.47	-0.0024	21.1	-15	-6.5	0.0	3.8	0.00	**-15.3**	***-6.5***
JU13a_06	3798	874	552	123	1745	419	85.5	68.4	0.410	28.87	0.0527	13.7	331	87.9	0.0	3.8	0.00	**331.0**	***87.9***
JU13a_09	4912	503	3833	757	4569	373	22.0	16.1	0.945	17.66	0.0448	16.7	283	91.8	0.0	3.8	0.00	**283.0**	***91.8***
JU13a_10	3590	840	1391	312	2503	446	61.2	44.4	0.350	27.34	0.1565	12.7	937	217.3	0.0	3.8	0.00	**937.6**	***217.3***
JU13a_11	5004	311	5453	801	5130	279	-9.0	-6.3	1.012	10.94	-0.0158	11.1	-103	-22.9	0.0	3.8	0.01	**-102.4**	***-22.9***
JU13a_12	4919	62	9079	501	5922	110	-84.6	-53.3	0.950	2.16	0.1556	2.1	932	35.8	0.0	3.8	0.00	**932.6**	***35.8***
JU13a_13	5302	289	3954	379	4888	221	25.4	19.1	1.264	10.33	-0.2234	13.2	-1630	-507.8	0.0	3.8	0.00	**-1629.8**	***-507.8***
JU13a_14	5172	492	4794	642	5062	341	7.3	5.3	1.147	17.47	-0.1623	20.1	-1142	-522.5	0.0	3.8	0.00	**-1141.6**	***-522.5***
JU13a_15	4843	859	5831	862	5117	504	-20.4	-13.9	0.897	30.06	0.1512	27.0	908	441.7	0.0	3.8	0.00	**908.2**	***441.7***
JU13a_16	4987	561	5590	757	5155	375	-12.1	-8.4	0.999	19.74	0.0013	19.7	8	3.2	0.0	3.8	0.00	**8.2**	***3.2***
JU13a_17	4825	508	3068	507	4220	348	36.4	27.3	0.885	17.75	0.0698	15.8	435	131.3	0.0	3.8	0.00	**435.0**	***131.3***
JU13a_18	5300	583	2560	682	4332	432	51.7	40.9	1.262	20.80	-0.1276	26.6	-880	-522.8	0.0	3.8	0.00	**-880.3**	***-522.8***
JU13a_19	4919	86	1947	375	3740	211	60.4	47.9	0.949	3.02	0.0179	2.9	115	6.6	0.1	3.8	0.01	**114.7**	***6.6***
JU13a_20	4844	272	4445	650	4722	253	8.2	5.9	0.898	9.51	0.1015	8.6	623	101.4	0.1	3.8	0.02	**623.3**	***101.4***
~~JU13a_07~~	~~807~~	~~8321~~	~~2611~~	~~570~~	~~1739~~	~~1473~~	~~-223.4~~	~~-50.1~~	~~0.024~~	~~198.81~~	~~0.4873~~	~~14.4~~	~~2559~~	~~579.9~~	~~0.0~~	~~3.8~~	~~0.00~~	~~**2559.4**~~	~~***579.9***~~
~~JU13a_08~~	~~1678~~	~~5304~~	~~2465~~	~~782~~	~~2060~~	~~1277~~	~~-46.9~~	~~-19.6~~	~~0.071~~	~~143.56~~	~~0.4327~~	~~21.4~~	~~2318~~	~~784.7~~	~~0.0~~	~~3.8~~	~~0.00~~	~~**2318.5**~~	~~***784.7***~~
~~JU13a_01~~	~~3112~~	~~2048~~	~~#VALUE!~~	~~#VALUE!~~	~~#VALUE!~~	~~#VALUE!~~	~~#VALUE!~~	~~#VALUE!~~	0.243	64.31	-20.5622	29.2	#VALUE!	#VALUE!	-0.1	3.8	-0.03	**#NUM!**	***#VALUE!***
~~JU13a_02~~	~~1366~~	~~3001~~	~~#VALUE!~~	~~#VALUE!~~	~~#VALUE!~~	~~#VALUE!~~	~~#VALUE!~~	~~#VALUE!~~	0.051	77.93	-12.5650	47.4	#VALUE!	#VALUE!	-0.2	3.8	-0.06	**#NUM!**	***#VALUE!***
~~JU13a_03~~	~~5591~~	~~624~~	~~#VALUE!~~	~~#VALUE!~~	~~#VALUE!~~	~~#VALUE!~~	~~#VALUE!~~	~~#VALUE!~~	1.568	22.52	26.1639	36.6	21285	3440.3	-0.6	3.8	-0.15	**21288.8**	***3440.3***
0502_Rutile_02	1401	226	39	3	73	17	97.2	46.4	0.053	11.82	0.0058	3.8	37	2.8	0.0	3.8	0.00	**37.1**	***2.8***
0502_Rutile_03	1149	198	41	2	67	13	96.5	39.2	0.040	9.95	0.0061	2.8	39	2.2	0.0	3.8	0.00	**39.1**	***2.2***
0502_Rutile_05	4370	34	159	8	1073	45	96.4	85.2	0.629	2.33	0.0092	1.7	59	2.1	0.2	3.8	0.06	**59.4**	***2.1***
0502_Rutile_06	1312	283	45	4	79	23	96.6	43.7	0.048	14.59	0.0066	4.1	43	3.5	0.0	3.8	0.00	**42.7**	***3.5***
0502_Rutile_07	4769	12	1428	187	3291	136	70.0	56.6	0.821	0.81	0.0444	1.5	280	8.1	0.1	3.8	0.03	**280.4**	***8.1***
0502_Rutile_08	4574	32	384	44	1870	103	91.6	79.5	0.729	2.21	0.0166	2.3	106	4.8	0.4	3.8	0.10	**106.4**	***4.8***
0502_Rutile_09	4174	70	120	11	819	72	97.1	85.3	0.544	4.73	0.0086	3.3	55	3.7	0.1	3.8	0.01	**55.3**	***3.7***
0502_Rutile_10	108	188	40	2	42	7	62.7	2.7	0.002	7.96	0.0063	2.0	40	1.6	0.0	3.8	0.00	**40.5**	***1.6***
0502_Rutile_11	383	152	42	2	48	7	89.1	13.4	0.009	6.75	0.0064	2.2	41	1.8	0.0	3.8	0.00	**41.2**	***1.8***
0502_Rutile_12	-278	196	41	2	36	6	114.8	-13.6	-0.007	7.72	0.0064	2.0	41	1.7	0.0	3.8	0.00	**41.5**	***1.7***
0502_Rutile_15	4015	74	113	15	729	84	97.2	84.4	0.482	4.95	0.0092	4.2	59	5.0	0.1	3.8	0.02	**59.1**	***5.0***
0502_Rutile_16	827	202	43	3	60	12	94.8	29.0	0.025	9.69	0.0065	3.2	42	2.6	0.0	3.8	0.00	**41.8**	***2.6***
0502_Rutile_17	362	200	39	2	45	8	89.1	12.7	0.009	8.86	0.0061	2.3	39	1.8	0.0	3.8	0.00	**39.2**	***1.8***
0502_Rutile_18	1303	241	43	2	75	18	96.7	43.6	0.048	12.40	0.0063	2.4	41	2.0	0.0	3.8	0.00	**40.7**	***2.0***
~~0502_Rutile_01~~	~~2720~~	~~189~~	~~60~~	~~10~~	~~219~~	~~55~~	~~97.8~~	~~72.7~~	~~0.177~~	~~11.48~~	~~0.0077~~	~~7.3~~	~~49~~	~~7.1~~	~~0.0~~	~~3.8~~	~~0.00~~	~~**49.3**~~	~~***7.1***~~
~~0502_Rutile_04~~	~~2071~~	~~191~~	~~41~~	~~5~~	~~107~~	~~25~~	~~98.0~~	~~62.2~~	~~0.103~~	~~10.85~~	~~0.0057~~	~~5.2~~	~~36~~	~~3.8~~	~~0.0~~	~~3.8~~	~~0.01~~	~~**36.5**~~	~~***2.8***~~
~~0502_Rutile_13~~	~~-1101~~	~~722~~	~~43~~	~~3~~	~~28~~	~~13~~	~~103.9~~	~~-52.3~~	~~-0.021~~	~~23.80~~	~~0.0068~~	~~3.2~~	~~44~~	~~2.8~~	~~0.0~~	~~3.8~~	~~0.00~~	~~**44.0**~~	~~***2.8***~~
~~0502_Rutile_14~~	~~-685~~	~~527~~	~~46~~	~~4~~	~~35~~	~~13~~	~~106.7~~	~~-32.3~~	~~-0.015~~	~~19.03~~	~~0.0072~~	~~4.6~~	~~46~~	~~4.3~~	~~0.0~~	~~3.8~~	~~0.00~~	~~**46.5**~~	~~***4.3***~~
1109_Rutile_02	3365	205	111	12	522	110	96.7	78.7	0.293	13.16	0.0123	5.4	79	8.4	0.0	3.8	0.01	**78.9**	***8.4***
1109_Rutile_03	4834	43	445	68	2163	142	90.8	79.4	0.889	3.04	0.0079	2.8	51	2.9	1.9	3.8	0.51	**50.9**	***2.9***
1109_Rutile_04	4969	18	1987	221	3799	125	60.0	47.7	0.952	1.30	0.0173	1.3	111	2.8	2.2	3.8	0.58	**110.7**	***2.8***
1109_Rutile_05	4927	24	2501	347	4040	161	49.2	38.1	0.890	1.66	0.0520	1.8	327	11.2	0.4	3.8	0.12	**327.2**	***11.2***
1109_Rutile_06	4175	165	126	20	848	146	97.0	85.1	0.544	11.15	0.0090	7.1	58	8.1	0.0	3.8	0.00	**58.1**	***8.1***
1109_Rutile_09	3332	353	48	9	254	104	98.5	81.0	0.288	22.56	0.0054	9.2	34	6.3	0.0	3.8	0.00	**34.6**	***6.3***
1109_Rutile_12	4678	100	323	73	1782	206	93.1	81.9	0.791	6.96	0.0107	6.0	69	8.2	0.0	3.8	0.00	**69.0**	***8.2***
1109_Rutile_13	4862	68	721	141	2643	196	85.2	72.7	0.904	4.74	0.0113	4.4	73	6.4	0.0	3.8	0.01	**72.7**	***6.4***
1109_Rutile_14	4625	118	275	56	1614	195	94.1	83.0	0.760	8.16	0.0104	6.7	67	8.9	0.0	3.8	0.00	**67.0**	***8.9***
1109_Rutile_15	3910	357	118	35	713	253	97.0	83.5	0.445	23.78	0.0102	13.5	66	17.6	0.0	3.8	0.00	**65.8**	***17.6***
1109_Rutile_16	3751	302	56	13	365	131	98.5	84.7	0.396	19.86	0.0053	10.4	34	7.0	0.0	3.8	0.00	**34.0**	***7.0***
1109_Rutile_17	4961	29	1718	296	3627	184	65.4	52.6	0.955	2.07	0.0137	2.0	88	3.5	0.6	3.8	0.15	**87.7**	***3.5***
1109_Rutile_18	4948	41	2142	493	3871	251	56.7	44.7	0.927	2.89	0.0287	2.9	182	10.3	0.1	3.8	0.03	**182.5**	***10.3***
1109_Rutile_19	4932	27	1113	90	3135	89	77.4	64.5	0.949	1.86	0.0096	1.8	62	2.2	0.5	3.8	0.12	**61.8**	***2.2***
1109_Rutile_21	3848	319	100	24	611	203	97.4	83.7	0.425	21.13	0.0090	11.4	57	13.1	0.0	3.8	0.00	**57.6**	***13.1***

RUTILE

		comments	^{204}Pb	^{206}Pb	^{207}Pb	^{208}Pb	^{232}Th	^{238}U	Pb ppm	U ppm	$^{238}U/^{206}Pb$	1s %	$^{207}Pb/^{206}Pb$	1s %	$^{207}Pb/^{235}U$	1s %	$^{206}Pb/^{238}U$	1s %	Rho
1109_Rutile_26	07/07/2017		-124	121	44	101	-3	75	0.04	1.49	81.542	8.19	0.420	18.03	0.709	19.80	0.012	8.19	0.41
1109_Rutile_27	07/07/2017		143	1919	1562	3601	1131	72	1.04	1.43	4.748	22.13	0.609	9.23	17.687	23.98	0.211	22.13	0.92
1109_Rutile_29	07/07/2017		-140	265	179	463	47	26	0.13	0.53	15.511	10.59	0.803	5.67	7.137	12.01	0.064	10.59	0.88
~~1109_Rutile_01~~	~~07/07/2017~~	~~low Pb counts~~	~~3~~	~~38~~	~~10~~	~~-1~~	~~-3~~	~~59~~	~~0.01~~	~~1.18~~	~~206.532~~	~~18.28~~	~~0.081~~	~~121.58~~	~~0.054~~	~~122.94~~	~~0.005~~	~~18.28~~	~~0.15~~
~~1109_Rutile_07~~	~~07/07/2017~~	~~low Pb counts~~	~~62~~	~~38~~	~~6~~	~~-10~~	~~-3~~	~~42~~	~~0.00~~	~~0.84~~	~~150.298~~	~~16.30~~	~~0.172~~	~~41.82~~	~~0.158~~	~~44.88~~	~~0.007~~	~~16.30~~	~~0.36~~
~~1109_Rutile_08~~	~~07/07/2017~~	~~low Pb counts~~	~~-77~~	~~28~~	~~5~~	~~-4~~	~~-3~~	~~41~~	~~0.00~~	~~0.83~~	~~206.223~~	~~23.59~~	~~-0.097~~	~~154.38~~	~~-0.065~~	~~156.17~~	~~0.005~~	~~23.59~~	~~0.15~~
~~1109_Rutile_10~~	~~07/07/2017~~	~~biotite~~	~~1251~~	~~24115~~	~~20454~~	~~50748~~	~~-3~~	~~0~~	~~14.06~~	~~0.00~~	~~0.000~~	~~20.06~~	~~0.837~~	~~0.56~~	~~########~~	~~20.07~~	~~########~~	~~20.06~~	~~1.00~~
~~1109_Rutile_11~~	~~07/07/2017~~	~~low Pb counts~~	~~-50~~	~~53~~	~~5~~	~~-12~~	~~-3~~	~~68~~	~~0.01~~	~~1.36~~	~~172.612~~	~~16.13~~	~~0.063~~	~~232.51~~	~~0.050~~	~~233.07~~	~~0.006~~	~~16.13~~	~~0.07~~
~~1109_Rutile_20~~	~~07/07/2017~~	~~low Pb counts~~	~~88~~	~~52~~	~~11~~	~~12~~	~~-3~~	~~39~~	~~0.01~~	~~0.78~~	~~102.505~~	~~12.83~~	~~0.243~~	~~53.03~~	~~0.327~~	~~54.57~~	~~0.010~~	~~12.83~~	~~0.24~~
~~1109_Rutile_22~~	~~07/07/2017~~	~~low Pb counts~~	~~21~~	~~130~~	~~23~~	~~40~~	~~-3~~	~~105~~	~~0.03~~	~~2.08~~	~~111.278~~	~~8.73~~	~~0.180~~	~~24.90~~	~~0.223~~	~~26.39~~	~~0.009~~	~~8.73~~	~~0.33~~
~~1109_Rutile_23~~	~~07/07/2017~~	~~low Pb counts~~	~~41~~	~~112~~	~~18~~	~~15~~	~~74~~	~~129~~	~~0.02~~	~~2.57~~	~~151.027~~	~~7.09~~	~~0.179~~	~~25.70~~	~~0.163~~	~~26.66~~	~~0.007~~	~~7.09~~	~~0.27~~
~~1109_Rutile_24~~	~~07/07/2017~~	~~low Pb counts~~	~~26~~	~~32~~	~~10~~	~~30~~	~~-3~~	~~29~~	~~0.01~~	~~0.57~~	~~113.011~~	~~23.98~~	~~0.161~~	~~95.91~~	~~0.196~~	~~98.86~~	~~0.009~~	~~23.98~~	~~0.24~~
~~1109_Rutile_25~~	~~07/07/2017~~	~~low Pb counts~~	~~32~~	~~40~~	~~17~~	~~20~~	~~-3~~	~~33~~	~~0.01~~	~~0.65~~	~~113.281~~	~~17.40~~	~~0.273~~	~~140.17~~	~~0.333~~	~~141.25~~	~~0.009~~	~~17.40~~	~~0.12~~
~~1109_Rutile_28~~	~~07/07/2017~~	~~low Pb counts~~	~~33~~	~~96~~	~~2~~	~~-15~~	~~-3~~	~~96~~	~~0.01~~	~~1.92~~	~~144.260~~	~~10.82~~	~~-0.010~~	~~448.50~~	~~-0.010~~	~~448.63~~	~~0.007~~	~~10.82~~	~~0.02~~
16-05_01	19/03/2019		560	560	477	1260	9	382	0.221	0.037	0.8958	9.63	0.8591	3.35	132.1686	10.20	1.1163	9.63	0.94
16-05_02	19/03/2019		361	361	243	708	18	266	0.126	0.026	0.9466	7.84	0.8191	4.50	119.2518	9.04	1.0564	7.84	0.87
16-05_03	19/03/2019		9738	9738	8053	20065	282	2361	3.640	0.227	0.3461	4.44	0.8248	1.27	328.4672	4.62	2.8897	4.44	0.96
16-05_04	19/03/2019		2608	2608	2189	5498	13	1018	0.990	0.098	0.5233	4.92	0.8222	1.63	216.5327	5.19	1.9109	4.92	0.95
16-05_05	19/03/2019		203	203	134	374	6	188	0.068	0.018	1.4250	11.22	0.7136	7.71	69.0194	13.61	0.7018	11.22	0.82
16-05_06	19/03/2019		5535	5535	4657	11775	121	2802	2.112	0.269	0.6846	2.73	0.8146	1.46	163.9839	3.10	1.4607	2.73	0.88
16-05_07	19/03/2019		7378	7378	5918	15283	87	1035	2.748	0.099	0.1929	6.17	0.8236	1.39	588.3100	6.33	5.1831	6.17	0.98
16-05_08	19/03/2019		4673	4673	3824	9613	250	400	1.741	0.038	0.1208	10.60	0.8419	1.69	960.3190	10.74	8.2767	10.60	0.99
16-05_09	19/03/2019		614	614	487	1335	5	808	0.234	0.078	1.9331	5.01	0.8437	3.75	60.1525	6.26	0.5173	5.01	0.80
16-05_10	19/03/2019		1045	1045	892	2220	3	590	0.400	0.057	0.7889	5.49	0.8320	2.36	145.3367	5.98	1.2675	5.49	0.92
16-05_11	19/03/2019		459	459	390	1140	28	1451	0.191	0.139	2.3704	8.50	0.8750	3.90	50.8750	9.35	0.4219	8.50	0.91
16-05_12	19/03/2019		497	497	407	1088	77	1605	0.192	0.154	3.7297	7.13	0.8586	3.17	31.7272	7.80	0.2681	7.13	0.91
16-05_13	19/03/2019		3063	3063	2573	6450	1769	9059	1.162	0.871	3.8885	5.51	0.8177	1.74	28.9815	5.78	0.2572	5.51	0.95
16-05_14	19/03/2019		2286	2286	1945	4945	133	937	0.882	0.090	0.4793	6.02	0.8428	1.94	242.3632	6.33	2.0865	6.02	0.95
16-05_16	19/03/2019		626	626	493	1231	2	401	0.226	0.039	0.8680	6.91	0.8532	4.01	135.4680	7.99	1.1520	6.91	0.86
16-05_17	19/03/2019		623	623	494	1217	7	863	0.224	0.083	1.9237	4.12	0.8287	3.41	59.3672	5.35	0.5198	4.12	0.77
16-05_18	19/03/2019		95	95	51	115	54	1202	0.025	0.116	14.8501	13.15	0.5353	15.43	4.9675	20.27	0.0673	13.15	0.65
16-05_19	19/03/2019		1918	1918	1558	3784	6	420	0.698	0.040	0.3408	7.30	0.8578	2.51	346.9125	7.72	2.9346	7.30	0.95
16-05_20	19/03/2019		876	876	706	1777	8	1826	0.323	0.176	2.7150	4.72	0.8202	2.60	41.6352	5.39	0.3683	4.72	0.88
16-05_21	19/03/2019		752	752	632	1570	71	1067	0.284	0.103	1.1926	8.62	0.8372	2.58	96.7461	9.00	0.8385	8.62	0.96
16-05_22	19/03/2019		298	298	242	625	1	576	0.112	0.055	2.5453	7.71	0.7739	5.35	41.9063	9.38	0.3929	7.71	0.82
16-05_23	19/03/2019		732	732	640	1537	7	445	0.280	0.043	0.8480	18.04	0.7832	4.47	127.2806	18.58	1.1792	18.04	0.97
16-05_24	19/03/2019		1018	1018	823	2026	6	430	0.372	0.041	0.5908	8.04	0.8233	2.71	192.0495	8.49	1.6926	8.04	0.95
16-05_25	19/03/2019		453	453	393	870	19	563	0.165	0.054	1.0464	9.67	0.9426	5.15	124.1512	10.95	0.9557	9.67	0.88
16-05_26	19/03/2019		1203	1203	1010	2532	8	11461	0.456	1.102	12.7853	2.83	0.8289	2.20	8.9350	3.58	0.0782	2.83	0.79
16-05_27	19/03/2019		1241	1241	989	2538	11	387	0.458	0.037	0.2567	8.97	0.8041	2.54	431.7094	9.32	3.8955	8.97	0.96
16-05_28	19/03/2019		153	153	108	262	277	1900	0.050	0.183	11.7929	11.73	0.7507	8.30	8.7733	14.37	0.0848	11.73	0.82
16-05_29	19/03/2019		777	777	628	1599	109	704	0.289	0.068	1.1153	5.69	0.8107	2.91	100.1853	6.39	0.8967	5.69	0.89
16-05_30	19/03/2019		334	334	272	622	8	465	0.118	0.045	2.1729	9.16	0.8655	5.11	54.8926	10.49	0.4602	9.16	0.87
16-05_31	19/03/2019		50	50	38	85	5	93	0.017	0.009	2.5837	16.39	0.3805	37.24	20.2989	40.69	0.3870	16.39	0.40
~~16-05_15~~	~~19/03/2019~~	~~low Pb counts~~	~~19~~	~~19~~	~~2~~	~~7~~	~~1~~	~~372~~	~~0.003~~	~~0.036~~	~~35.1134~~	~~33.42~~	~~0.0425~~	~~195.81~~	~~0.1670~~	~~198.64~~	~~0.0285~~	~~33.42~~	~~0.17~~
A03-19_01	19/03/2019		140	140	62	151	-1	7246	0.034	0.697	78.1335	6.42	0.4380	7.92	0.7726	10.20	0.0128	6.42	0.63
A03-19_03	19/03/2019		184	184	37	79	-1	19728	0.029	1.897	149.1046	5.49	0.2319	13.24	0.2143	14.33	0.0067	5.49	0.38
A03-19_04	19/03/2019		147	147	48	107	28	11397	0.029	1.096	106.7570	7.38	0.3679	16.92	0.4750	18.46	0.0094	7.38	0.40
A03-19_06	19/03/2019		210	210	104	224	51	10627	0.052	1.022	75.2911	9.98	0.4148	11.49	0.7592	15.21	0.0133	9.98	0.66
A03-19_07	19/03/2019		332	332	41	84	503	28422	0.044	2.733	140.4114	5.47	0.1331	11.06	0.1306	12.33	0.0071	5.47	0.44
A03-19_12	19/03/2019		155	155	43	109	99	15734	0.029	1.513	142.3369	7.50	0.3688	15.26	0.3571	17.00	0.0070	7.50	0.44
A03-19_13	19/03/2019		217	217	79	189	613	14939	0.047	1.436	104.2986	5.08	0.3422	7.98	0.4522	9.45	0.0096	5.08	0.54
A03-19_15	19/03/2019		236	236	40	95	60	27865	0.036	2.679	175.6616	5.23	0.1589	9.22	0.1247	10.60	0.0057	5.23	0.49
A03-19_20	19/03/2019		3616	3616	2921	7453	937	17025	1.345	1.637	6.6649	4.08	0.7842	1.62	16.2152	4.39	0.1500	4.08	0.93
A03-19_23	19/03/2019		3331	3331	2431	6113	64	21811	1.142	2.097	9.6115	4.97	0.7936	1.39	11.3793	5.16	0.1040	4.97	0.96
A03-19_27	19/03/2019		527	527	109	272	204	60353	0.087	5.802	163.9668	3.06	0.1972	5.14	0.1657	5.98	0.0061	3.06	0.51
A03-19_31	19/03/2019		1885	1885	1420	3613	9	11804	0.665	1.135	8.7886	6.30	0.7179	2.85	11.2572	6.92	0.1138	6.30	0.91
A03-19_32	19/03/2019		394	394	208	489	71	15508	0.105	1.491	47.5977	9.65	0.5302	6.43	1.5351	11.60	0.0210	9.65	0.83
~~A03-19_02~~	~~19/03/2019~~	~~low Pb counts~~	~~76~~	~~76~~	~~21~~	~~66~~	~~-1~~	~~5467~~	~~0.016~~	~~0.526~~	~~103.6280~~	~~9.09~~	~~0.3678~~	~~20.05~~	~~0.4892~~	~~22.01~~	~~0.0096~~	~~9.09~~	~~0.41~~
~~A03-19_05~~	~~19/03/2019~~	~~low Pb counts~~	~~90~~	~~90~~	~~29~~	~~98~~	~~-1~~	~~6245~~	~~0.021~~	~~0.600~~	~~97.2439~~	~~8.00~~	~~0.2706~~	~~34.39~~	~~0.3836~~	~~35.31~~	~~0.0103~~	~~8.00~~	~~0.23~~
~~A03-19_08~~	~~19/03/2019~~	~~low Pb counts~~	~~219~~	~~219~~	~~23~~	~~58~~	~~33~~	~~24271~~	~~0.029~~	~~2.333~~	~~159.4555~~	~~4.78~~	~~0.0994~~	~~16.62~~	~~0.0859~~	~~17.29~~	~~0.0063~~	~~4.78~~	~~0.28~~
~~A03-19_09~~	~~19/03/2019~~	~~low Pb counts~~	~~97~~	~~97~~	~~12~~	~~31~~	~~-1~~	~~10084~~	~~0.013~~	~~0.970~~	~~155.4163~~	~~9.16~~	~~0.0902~~	~~32.68~~	~~0.0800~~	~~33.94~~	~~0.0064~~	~~9.16~~	~~0.27~~
~~A03-19_10~~	~~19/03/2019~~	~~low Pb counts~~	~~74~~	~~74~~	~~18~~	~~36~~	~~-1~~	~~7265~~	~~0.012~~	~~0.698~~	~~145.7875~~	~~10.64~~	~~0.2517~~	~~30.81~~	~~0.2379~~	~~32.59~~	~~0.0069~~	~~10.64~~	~~0.33~~
~~A03-19_11~~	~~19/03/2019~~	~~low Pb counts~~	~~51~~	~~51~~	~~14~~	~~41~~	~~-1~~	~~4855~~	~~0.010~~	~~0.467~~	~~136.8399~~	~~14.07~~	~~0.2335~~	~~50.13~~	~~0.2351~~	~~52.06~~	~~0.0073~~	~~14.07~~	~~0.27~~
~~A03-19_14~~	~~19/03/2019~~	~~low Pb counts~~	~~136~~	~~136~~	~~29~~	~~66~~	~~20~~	~~17729~~	~~0.022~~	~~1.704~~	~~189.0292~~	~~5.80~~	~~0.2009~~	~~16.14~~	~~0.1465~~	~~17.15~~	~~0.0053~~	~~5.80~~	~~0.34~~
~~A03-19_16~~	~~19/03/2019~~	~~low Pb counts~~	~~100~~	~~100~~	~~17~~	~~37~~	~~-1~~	~~11782~~	~~0.015~~	~~1.133~~	~~166.8070~~	~~7.89~~	~~0.1297~~	~~26.23~~	~~0.1072~~	~~27.39~~	~~0.0060~~	~~7.89~~	~~0.29~~
~~A03-19_17~~	~~19/03/2019~~	~~low Pb counts~~	~~73~~	~~73~~	~~13~~	~~16~~	~~-1~~	~~8626~~	~~0.010~~	~~0.829~~	~~169.1129~~	~~9.03~~	~~0.2033~~	~~30.89~~	~~0.1657~~	~~32.18~~	~~0.0059~~	~~9.03~~	~~0.28~~
~~A03-19_18~~	~~19/03/2019~~	~~low Pb counts~~	~~60~~	~~60~~	~~4~~	~~9~~	~~-1~~	~~5100~~	~~0.007~~	~~0.490~~	~~117.8264~~	~~12.05~~	~~0.1445~~	~~42.87~~	~~0.1690~~	~~44.53~~	~~0.0085~~	~~12.05~~	~~0.27~~
~~A03-19_19~~	~~19/03/2019~~	~~low Pb counts~~	~~35~~	~~35~~	~~10~~	~~17~~	~~-1~~	~~4140~~	~~0.006~~	~~0.398~~	~~174.6079~~	~~17.73~~	~~-0.0803~~	~~106.28~~	~~-0.0634~~	~~107.75~~	~~0.0057~~	~~17.73~~	~~0.16~~
~~A03-19_21~~	~~19/03/2019~~	~~low Pb counts~~	~~99~~	~~99~~	~~14~~	~~37~~	~~-1~~	~~7807~~	~~0.014~~	~~0.751~~	~~128.3582~~	~~8.70~~	~~0.1662~~	~~41.10~~	~~0.1785~~	~~42.01~~	~~0.0078~~	~~8.70~~	~~0.21~~
~~A03-19_22~~	~~19/03/2019~~	~~low Pb counts~~	~~142~~	~~142~~	~~11~~	~~11~~	~~-1~~	~~18971~~	~~0.016~~	~~1.824~~	~~186.1293~~	~~4.93~~	~~0.0634~~	~~24.20~~	~~0.0470~~	~~24.70~~	~~0.0054~~	~~4.93~~	~~0.20~~
~~A03-19_24~~	~~19/03/2019~~	~~low Pb counts~~	~~61~~	~~61~~	~~10~~	~~18~~	~~-1~~	~~7708~~	~~0.009~~	~~0.741~~	~~184.3089~~	~~10.34~~	~~0.1184~~	~~64.39~~	~~0.0885~~	~~65.22~~	~~0.0054~~	~~10.34~~	~~0.16~~
~~A03-19_25~~	~~19/03/2019~~	~~low Pb counts~~	~~76~~	~~76~~	~~14~~	~~34~~	~~-1~~	~~6568~~	~~0.012~~	~~0.631~~	~~126.6164~~	~~9.81~~	~~0.1470~~	~~48.26~~	~~0.1601~~	~~49.25~~	~~0.0079~~	~~9.81~~	~~0.20~~
~~A03-19_26~~	~~19/03/2019~~	~~low Pb counts~~	~~96~~	~~96~~	~~11~~	~~40~~	~~-1~~	~~10747~~	~~0.014~~	~~1.033~~	~~167.4901~~	~~8.05~~	~~0.2534~~	~~31.72~~	~~0.2085~~	~~32.72~~	~~0.0060~~	~~8.05~~	~~0.25~~
~~A03-19_28~~	~~19/03/2019~~	~~low Pb counts~~	~~77~~	~~77~~	~~7~~	~~28~~	~~-1~~	~~10128~~	~~0.011~~	~~0.974~~	~~187.1311~~	~~9.51~~	~~0.0496~~	~~67.15~~	~~0.0365~~	~~67.82~~	~~0.0053~~	~~9.51~~	~~0.14~~
~~A03-19_29~~	~~19/03/2019~~	~~low Pb counts~~	~~95~~	~~95~~	~~10~~	~~25~~	~~-1~~	~~13891~~	~~0.013~~	~~1.335~~	~~200.7266~~	~~6.68~~	~~0.0701~~	~~31.49~~	~~0.0481~~	~~32.19~~	~~0.0050~~	~~6.68~~	~~0.21~~
~~A03-19_30~~	~~19/03/2019~~	~~low Pb counts~~	~~120~~	~~120~~	~~15~~	~~22~~	~~-1~~	~~17287~~	~~0.015~~	~~1.662~~	~~204.9726~~	~~6.99~~	~~0.1337~~	~~21.39~~	~~0.0899~~	~~22.50~~	~~0.0049~~	~~6.99~~	~~0.31~~
~~A03-19_33~~	~~19/03/2019~~	~~low Pb counts~~	~~56~~	~~56~~	~~11~~	~~43~~	~~-1~~	~~5832~~	~~0.011~~	~~0.561~~	~~152.3765~~	~~11.96~~	~~0.1288~~	~~53.01~~	~~0.1165~~	~~54.34~~	~~0.0066~~	~~11.96~~	~~0.22~~
~~A03-19_34~~	~~19/03/2019~~	~~low Pb counts~~	~~68~~	~~68~~	~~10~~	~~30~~	~~-1~~	~~8247~~	~~0.010~~	~~0.793~~	~~174.9608~~	~~10.15~~	~~0.1176~~	~~52.58~~	~~0.0926~~	~~53.55~~	~~0.0057~~	~~10.15~~	~~0.19~~
~~A03-19_35~~	~~19/03/2019~~	~~low Pb counts~~	~~72~~	~~72~~	~~13~~	~~27~~	~~-1~~	~~7726~~	~~0.011~~	~~0.743~~	~~162.4110~~	~~9.08~~	~~0.2148~~	~~31.82~~	~~0.1823~~	~~33.09~~	~~0.0062~~	~~9.08~~	~~0.27~~
~~A03-19_36~~	~~19/03/2019~~	~~low Pb counts~~	~~49~~	~~49~~	~~6~~	~~36~~	~~-1~~	~~6317~~	~~0.009~~	~~0.607~~	~~180.6035~~	~~13.65~~	~~0.1550~~	~~44.76~~	~~0.1183~~	~~46.80~~	~~0.0055~~	~~13.65~~	~~0.29~~
~~A03-19_37~~	~~19/03/2019~~	~~low Pb counts~~	~~197~~	~~197~~	~~18~~	~~14~~	~~-1~~	~~29664~~	~~0.022~~	~~2.852~~	~~221.0443~~	~~5.48~~	~~0.0726~~	~~20.86~~	~~0.0453~~	~~21.57~~	~~0.0045~~	~~5.48~~	~~0.25~~
~~A03-19_38~~	~~19/03/2019~~	~~low Pb counts~~	~~219~~	~~219~~	~~28~~	~~89~~	~~721~~	~~17909~~	~~0.032~~	~~1.722~~	~~130.8128~~	~~7.32~~	~~0.1525~~	~~15.99~~	~~0.1607~~	~~17.59~~	~~0.0076~~	~~7.32~~	~~0.42~~
A03-22_01	19/03/2019		745	745	662	1482	13	532	0.278	0.051	0.9038	7.83	0.8827	2.74	134.6032	8.30	1.1064	7.83	0.94
A03-22_02	19/03/2019		704	704	537	1363	102	1013	0.250	0.097	1.6600	6.08	0.7657	3.05	63.5715	6.81	0.6024	6.08	0.89
A03-22_04	19/03/2019		71	71	52	108	128	2171	0.022	0.209	48.6193	14.75	0.6028	23.40	1.7086	27.66	0.0206	14.75	0.53
A03-22_05	19/03/2019		354	354	282	670	-1	1886	0.126	0.181	7.2494	10.50	0.8612	4.71	16.3720	11.51	0.1379	10.50	0.91
A03-22_06	19/03/2019		91	91	73	165	46	1337	0.032	0.129	17.0292	13.19	0.6720	21.93	5.4386	25.59	0.0587	13.19	0.52
A03-22_07	19/03/2019		236	236	202	545	1962	1008	0.094	0.097	5.9840	7.71	0.8467	5.24	19.4994	9.32	0.1671	7.71	0.83
A03-22_08	19/03/2019		123	123	85	223	25	1495	0.041	0.144	18.0613	7.73	0.9717	12.38	7.4145	14.59	0.0554	7.73	0.53
A03-22_09	19/03/2019		115	115	63	160	238	2733	0.032	0.263	37.3128	8.57	0.5103	10.61	1.8848	13.64	0.0268	8.57	0.63
A03-22_10	19/03/2019		804	804	647	1628	145	1428	0.296	0.137	2.7055	5.34	0.7675	3.23	39.0965	6.25	0.3696	5.34	0.86
A03-22_13	19/03/2019		178	178	121	310	30	1477	0.058	0.142	14.1219	8.96	0.6947	10.02	6.7793	13.45	0.0708	8.96	0.67
A03-22_15	19/03/2019		647	647	502	1228	17	1456	0.229	0.140	3.0149	4.88	0.7639	3.28	34.9180	5.88	0.3317	4.88	0.83
A03-22_16	19/03/2019		498	498	399	980	251	2830	0.180	0.272	6.8938	9.22	0.7536	4.05	15.0664	10.07	0.1451	9.22	0.92
A03-22_17	19/03/2019		1698	1698	646	1462	3295	112834	0.366	10.848	15.3159	17.17	0.5448	6.70	4.9026	18.43	0.0653	17.17	0.93
A03-22_19	19/03/2019		100	100	75	187	60	394	0.035	0.038	7.6551	12.91	0.6918	12.89	12.4553	18.24	0.1306	12.91	0.71
A03-22_20	19/03/2019		2093	2093	1668	4168	537	3261	0.762	0.314	1.5301	10.23	0.7937	1.78	71.4941	10.38	0.6536	10.23	0.99
A03-22_22	19/03/2019		96	96	59	181	9	1096	0.032	0.105	13.4874	18.82	0.5694	19.05	5.8188	26.78	0.0741	18.82	0.70
A03-22_23	19/03/2019		229	229	172	440	77	1316	0.081	0.127	5.7585	9.88	0.7884	6.87	18.8678	12.03	0.1737	9.88	0.82
A03-22_24	19/03/2019		1104	1104	950	2265	93	863	0.415	0.083	1.0375	5.26	0.8544	2.23	113.5033	5.71	0.9639	5.26	0.92
A03-22_25	19/03/2019		126	126	109	208	-1	426	0.043	0.041	4.4546	10.97	0.7563	25.84	23.3992	28.08	0.2245	10.97	0.39
A03-22_26	19/03/2019		577	577	478	1170	465	3518	0.214	0.338	7.0606	7.88	0.8980	3.97	17.5283	8.83	0.1416	7.88	0.89
A03-22_27	19/03/2019		856	856	729	1795	2311	1439	0.325	0.138	4.0847	5.03	0.8271	3.30	27.9049	6.01	0.2448	5.03	0.84
A03-22_28	19/03/2019		419	419	318	752	442	3074	0.143	0.296	7.8304	9.85	0.6552	6.45	11.5325	11.77	0.1277	9.85	0.84
A03-22_29	19/03/2019		200	200	176	445	7	560	0.079	0.054	4.5571	8.71	1.0516	8.20	31.8041	11.96	0.2194	8.71	0.73

RUTILE

	$^{207}Pb/^{206}Pb$	2s abs	$^{206}Pb/^{238}U$	2s abs	$^{207}Pb/^{235}U$	2s abs	c. % 6-38/c.	%6-38/7	*f206*	1s %	$^{206}Pb^*/^{238}U$	1s %	²06/238-Pb	2s [Ma]	Th/U min.	Th/U wr.	f	·. 206/238	*2s [Ma]*
1109_Rutile_26	3981	270	79	13	544	155	98.0	85.6	0.471	18.03	0.0065	9.5	42	7.9	0.0	3.8	0.00	**41.8**	***7.9***
1109_Rutile_27	4530	134	1232	478	2973	380	72.8	58.6	0.680	9.23	0.0674	9.5	421	76.6	0.2	3.8	0.06	**420.9**	***76.6***
1109_Rutile_29	4927	81	403	82	2129	194	91.8	81.1	0.956	5.67	0.0028	5.4	18	2.0	0.0	3.8	0.01	**18.3**	***2.0***
1109_Rutile_01	1230	2386	31	11	54	121	97.5	42.0	0.044	121.58	0.0046	18.3	30	10.8	0.0	3.8	0.00	**29.9**	***10.8***
1109_Rutile_07	2575	699	43	14	149	117	98.3	71.2	0.158	41.82	0.0056	15.2	36	10.9	0.0	3.8	0.00	**36.1**	***10.9***
1109_Rutile_08	#NUM!	#NUM!	31	15	-68	-248	#NUM!	145.8	-0.182	154.38	0.0057	39.5	37	29.0	0.0	3.8	0.00	**36.9**	***29.0***
1109_Rutile_10	4986	8	#VALUE!	#VALUE!	#VALUE!	#VALUE!	#VALUE!	#VALUE!	#VALUE!	0.56	#VALUE!	#VALUE!	#VALUE!	#VALUE!	-1.2	3.8	-0.33	**#VALUE!**	***#VALUE!***
1109_Rutile_11	714	4940	37	12	50	205	94.8	25.5	0.021	232.51	0.0057	16.5	36	12.0	0.0	3.8	0.00	**36.6**	***12.0***
1109_Rutile_20	3139	843	63	16	287	242	98.0	78.2	0.247	53.03	0.0073	16.3	47	15.3	0.0	3.8	0.00	**47.3**	***15.3***
1109_Rutile_22	2650	413	58	10	204	93	97.8	71.7	0.168	24.90	0.0075	8.4	48	8.0	0.0	3.8	0.00	**48.2**	***8.0***
1109_Rutile_23	2640	427	43	6	153	73	98.4	72.3	0.167	25.70	0.0055	7.3	35	5.2	0.0	3.8	0.00	**35.6**	***5.2***
1109_Rutile_24	2466	1620	57	27	182	285	97.7	68.8	0.144	95.91	0.0076	24.7	49	23.9	0.0	3.8	0.00	**48.8**	***23.9***
1109_Rutile_25	3326	2195	57	20	292	542	98.3	80.6	0.286	140.17	0.0063	42.0	40	33.8	0.0	3.8	0.00	**40.6**	***33.8***
1109_Rutile_28	#NUM!	#NUM!	45	10	-10	-95	#NUM!	543.4	-0.072	448.50	0.0074	34.4	48	32.7	0.0	3.8	0.00	**47.9**	***32.7***
16-05_01	5023	95	4833	624	4967	187	3.8	2.7	0.757	3.35	0.2713	3.4	1547	94.2	20.7	3.8	5.44	**1547.1**	***94.2***
16-05_02	4955	128	4648	500	4863	167	6.2	4.4	0.655	4.50	0.3641	4.0	2002	136.2	0.1	3.8	0.03	**2001.9**	***136.2***
16-05_03	4965	36	8756	412	5887	89	-76.4	-48.7	-1.257	1.27	6.5233	10.1	13009	1044.7	0.0	3.8	0.00	**13011.0**	***1044.7***
16-05_04	4961	46	6888	404	5465	100	-38.8	-26.0	0.011	1.63	1.8903	4.9	6842	398.2	0.0	3.8	0.01	**6843.1**	***398.2***
16-05_05	4758	221	3427	570	4314	241	28.0	20.6	0.675	7.71	0.2279	6.4	1323	150.3	0.2	3.8	0.05	**1323.6**	***150.3***
16-05_06	4947	41	5805	206	5184	61	-17.3	-12.0	0.346	1.46	0.9557	1.9	4324	115.9	0.0	3.8	0.00	**4324.8**	***115.9***
16-05_07	4963	40	11744	635	6477	121	-136.6	-81.3	-6.176	1.39	37.1929	45.1	23482	4064.6	0.2	3.8	0.06	**23485.8**	***4064.6***
16-05_08	4994	48	14359	1117	6974	197	-187.5	-105.9	-16.750	1.69	146.9109	190.3	32210	10085.4	1.6	3.8	0.42	**32215.4**	***10085.4***
16-05_09	4997	106	2688	216	4177	118	46.2	35.6	0.939	3.75	0.0314	3.5	199	13.9	0.0	3.8	0.00	**199.4**	***13.9***
16-05_10	4977	67	5278	384	5063	114	-6.0	-4.2	0.564	2.36	0.5532	2.7	2839	124.6	0.0	3.8	0.00	**2839.1**	***124.6***
16-05_11	5049	110	2269	317	4010	171	55.1	43.4	1.010	3.90	-0.0041	3.9	-26	-2.1	0.0	3.8	0.00	**-26.4**	***-2.1***
16-05_12	5022	90	1531	192	3542	143	69.5	56.8	1.013	3.17	-0.0034	3.2	-22	-1.4	0.0	3.8	0.01	**-21.8**	***-1.4***
16-05_13	4953	49	1475	144	3453	108	70.2	57.3	0.957	1.74	0.0112	1.7	72	2.4	0.0	3.8	0.01	**71.8**	***2.4***
16-05_14	4996	55	7265	505	5579	121	-45.4	-30.2	-0.179	1.94	2.4593	7.1	8000	620.5	1.4	3.8	0.36	**8001.8**	***620.5***
16-05_16	5013	114	4941	460	4992	150	1.5	1.0	0.833	4.01	0.1923	3.5	1134	73.1	0.0	3.8	0.00	**1133.8**	***73.1***
16-05_17	4972	97	2698	179	4164	102	45.7	35.2	0.916	3.41	0.0437	3.1	276	16.9	0.0	3.8	0.00	**276.0**	***16.9***
16-05_18	4341	452	420	106	1814	295	90.3	76.8	0.609	15.43	0.0263	10.7	168	35.3	0.0	3.8	0.01	**167.7**	***35.3***
16-05_19	5021	71	8830	666	5942	145	-75.9	-48.6	-1.325	2.51	6.8241	17.3	13262	1699.1	0.0	3.8	0.01	**13263.8**	***1699.1***
16-05_20	4957	74	2022	162	3810	102	59.2	46.9	0.940	2.60	0.0219	2.5	140	6.8	0.0	3.8	0.00	**139.9**	***6.8***
16-05_21	4986	73	3925	488	4653	167	21.3	15.6	0.812	2.58	0.1577	2.7	944	46.4	0.1	3.8	0.03	**944.4**	***46.4***
16-05_22	4875	153	2136	274	3817	171	56.2	44.0	0.868	5.35	0.0517	4.8	325	30.1	0.0	3.8	0.00	**325.3**	***30.1***
16-05_23	4891	127	5022	1149	4929	319	-2.7	-1.9	1.090	4.47	-0.1058	5.1	-721	-78.7	0.0	3.8	0.01	**-720.8**	***-78.7***
16-05_24	4963	77	6385	621	5344	158	-28.7	-19.5	0.228	2.71	1.3068	6.2	5388	440.3	0.0	3.8	0.00	**5389.4**	***440.3***
16-05_25	5154	145	4324	582	4904	200	16.1	11.8	0.962	5.15	0.0359	5.0	227	22.2	0.0	3.8	0.01	**227.4**	***22.2***
16-05_26	4972	63	485	26	2331	63	90.2	79.2	0.989	2.20	0.0008	2.2	5	0.2	0.0	3.8	0.00	**5.6**	***0.2***
16-05_27	4929	72	10239	860	6163	173	-107.7	-66.1	-3.086	2.54	15.9173	37.5	18233	3439.5	0.8	3.8	0.21	**18235.6**	***3439.5***
16-05_28	4831	237	525	117	2315	233	89.1	77.3	0.886	8.30	0.0097	7.5	62	9.2	0.0	3.8	0.01	**62.1**	***9.2***
16-05_29	4941	83	4126	338	4688	121	16.5	12.0	0.737	2.91	0.2356	2.6	1364	63.9	0.4	3.8	0.11	**1364.0**	***63.9***
16-05_30	5033	145	2441	362	4085	190	51.5	40.3	0.987	5.11	0.0061	5.0	39	3.9	0.0	3.8	0.01	**39.3**	***3.9***
16-05_31	3834	1125	2109	564	3106	583	45.0	32.1	0.328	37.24	0.2601	16.4	1491	423.5	0.3	3.8	0.07	**1490.9**	***423.5***
16-05_15	-195	9802	181	118	157	457	193.0	-15.5	-0.009	195.81	0.0287	33.8	183	120.5	0.0	3.8	0.00	**182.8**	***120.5***
A03-19_01	4045	236	82	10	581	86	98.0	85.9	0.494	7.92	0.0065	5.1	42	4.2	-0.1	3.8	-0.01	**41.7**	***4.2***
A03-19_03	3065	423	43	5	197	50	98.6	78.1	0.234	13.24	0.0051	5.2	33	3.4	0.0	3.8	0.00	**33.1**	***3.4***
A03-19_04	3783	513	60	9	395	114	98.4	84.8	0.406	16.92	0.0056	8.1	36	5.8	0.0	3.8	0.00	**35.9**	***5.8***
A03-19_06	3963	344	85	17	574	125	97.9	85.2	0.464	11.49	0.0071	7.5	46	6.9	0.0	3.8	0.00	**45.8**	***6.9***
A03-19_07	2139	387	46	5	125	29	97.9	63.3	0.109	11.06	0.0063	5.0	41	4.1	0.0	3.8	0.00	**40.9**	***4.1***
A03-19_12	3787	462	45	7	310	87	98.8	85.4	0.407	15.26	0.0042	7.6	27	4.1	0.0	3.8	0.00	**26.9**	***4.1***
A03-19_13	3673	244	62	6	379	58	98.3	83.8	0.373	7.98	0.0060	4.4	39	3.4	0.0	3.8	0.01	**38.7**	***3.4***
A03-19_15	2444	312	37	4	119	24	98.5	69.3	0.142	9.22	0.0049	4.7	31	2.9	0.0	3.8	0.00	**31.5**	***2.9***
A03-19_20	4893	46	901	68	2890	81	81.6	68.8	0.924	1.62	0.0114	1.5	73	2.2	0.0	3.8	0.00	**73.1**	***2.2***
A03-19_23	4910	40	638	60	2555	92	87.0	75.0	0.941	1.39	0.0061	1.3	39	1.1	0.0	3.8	0.00	**39.6**	***1.1***
A03-19_27	2803	168	39	2	156	17	98.6	74.8	0.190	5.14	0.0049	2.7	32	1.7	0.0	3.8	0.00	**31.9**	***1.7***
A03-19_31	4767	82	695	82	2545	121	85.4	72.7	0.840	2.85	0.0182	2.6	116	6.0	0.0	3.8	0.00	**116.6**	***6.0***
A03-19_32	4327	189	134	26	945	133	96.9	85.8	0.610	6.43	0.0082	5.4	53	5.7	0.0	3.8	0.00	**52.7**	***5.7***
A03-19_02	3783	608	62	11	404	137	98.4	84.7	0.406	20.05	0.0057	9.8	37	7.2	0.0	3.8	0.00	**37.0**	***7.2***
A03-19_05	3310	1078	66	10	330	182	98.0	80.0	0.282	34.39	0.0074	11.3	47	10.6	0.0	3.8	0.00	**47.5**	***10.6***
A03-19_08	1613	619	40	4	84	27	97.5	51.8	0.067	16.62	0.0059	4.6	38	3.5	0.0	3.8	0.00	**37.7**	***3.5***
A03-19_09	1430	1247	41	8	78	50	97.1	47.1	0.055	32.68	0.0061	8.8	39	6.9	0.0	3.8	0.00	**39.2**	***6.9***
A03-19_10	3195	975	44	9	217	120	98.6	79.7	0.259	30.81	0.0051	11.2	33	7.3	0.0	3.8	0.00	**32.8**	***7.3***
A03-19_11	3076	1601	47	13	214	184	98.5	78.1	0.236	50.13	0.0056	16.0	36	11.4	0.0	3.8	0.00	**36.0**	***11.4***
A03-19_14	2834	526	34	4	139	44	98.8	75.5	0.195	16.14	0.0043	5.6	27	3.1	0.0	3.8	0.00	**27.5**	***3.1***
A03-19_16	2094	922	39	6	103	52	98.2	62.7	0.105	26.23	0.0054	7.6	34	5.2	0.0	3.8	0.00	**34.6**	***5.2***
A03-19_17	2853	1006	38	7	156	89	98.7	75.6	0.198	30.89	0.0047	9.5	30	5.8	0.0	3.8	0.00	**30.6**	***5.8***
A03-19_18	2282	1476	54	13	159	123	97.6	65.6	0.123	42.87	0.0074	11.8	48	11.2	0.0	3.8	0.00	**47.9**	***11.2***
A03-19_19	#NUM!	#NUM!	37	13	-66	-160	#NUM!	155.4	-0.161	106.28	0.0066	26.7	43	22.7	0.0	3.8	0.00	**42.8**	***22.7***
A03-19_21	2520	1381	50	9	167	122	98.0	70.0	0.151	41.10	0.0066	9.6	43	8.2	0.0	3.8	0.00	**42.6**	***8.2***
A03-19_22	723	1027	35	3	47	22	95.2	25.9	0.021	24.20	0.0053	4.8	34	3.3	0.0	3.8	0.00	**33.9**	***3.3***
A03-19_24	1932	2306	35	7	86	102	98.2	59.5	0.091	64.39	0.0049	11.1	32	7.0	0.0	3.8	0.00	**31.8**	***7.0***
A03-19_25	2312	1656	51	10	151	129	97.8	66.4	0.126	48.26	0.0069	10.5	44	9.3	0.0	3.8	0.00	**44.4**	***9.3***
A03-19_26	3206	1003	38	6	192	109	98.8	80.0	0.261	31.72	0.0044	10.2	28	5.8	0.0	3.8	0.00	**28.5**	***5.8***
A03-19_28	177	3132	34	7	36	47	80.6	5.7	0.004	67.15	0.0053	9.5	34	6.5	0.0	3.8	0.00	**34.3**	***6.5***
A03-19_29	931	1293	32	4	48	30	96.6	32.9	0.030	31.49	0.0048	6.6	31	4.1	0.0	3.8	0.00	**31.2**	***4.1***
A03-19_30	2147	747	31	4	87	37	98.5	64.1	0.110	21.39	0.0043	6.6	28	3.7	0.0	3.8	0.00	**28.0**	***3.7***
A03-19_33	2082	1866	42	10	112	109	98.0	62.3	0.104	53.01	0.0059	12.1	38	9.1	0.0	3.8	0.00	**37.9**	***9.1***
A03-19_34	1920	1886	37	7	90	88	98.1	59.2	0.090	52.58	0.0052	10.4	33	6.9	0.0	3.8	0.00	**33.6**	***6.9***
A03-19_35	2942	1028	40	7	170	99	98.7	76.7	0.212	31.82	0.0048	9.8	31	6.1	0.0	3.8	0.00	**31.3**	***6.1***
A03-19_36	2402	1522	36	10	114	96	98.5	68.6	0.137	44.76	0.0048	13.3	31	8.1	0.0	3.8	0.00	**30.8**	***8.1***
A03-19_37	1003	847	29	3	45	19	97.1	35.3	0.033	20.86	0.0044	5.3	28	3.0	0.0	3.8	0.00	**28.3**	***3.0***
A03-19_38	2374	545	49	7	151	48	97.9	67.6	0.133	15.99	0.0066	6.7	43	5.7	0.1	3.8	0.02	**42.7**	***5.7***
A03-22_01	5061	78	4803	510	4985	155	5.1	3.7	0.837	2.74	0.1802	2.6	1068	51.5	81.0	3.8	21.31	**1066.5**	***51.5***
A03-22_02	4859	87	3040	288	4232	128	37.4	28.2	0.795	3.05	0.1237	2.7	752	38.6	0.1	3.8	0.01	**752.3**	***38.6***
A03-22_04	4515	680	131	38	1012	304	97.1	87.0	0.702	23.40	0.0061	17.0	39	13.3	0.0	3.8	0.01	**39.5**	***13.3***
A03-22_05	5026	134	833	162	2899	199	83.4	71.3	1.029	4.71	-0.0040	4.9	-26	-2.5	0.0	3.8	0.00	**-25.7**	***-2.5***
A03-22_06	4672	632	368	94	1891	365	92.1	80.5	0.786	21.93	0.0125	17.5	80	27.8	0.0	3.8	0.01	**80.5**	***27.8***
A03-22_07	5002	149	996	141	3067	166	80.1	67.5	1.007	5.24	-0.0012	5.3	-8	-0.8	2.6	3.8	0.68	**-7.6**	***-0.8***
A03-22_08	5197	348	347	52	2163	232	93.3	83.9	1.176	12.38	-0.0098	14.6	-63	-18.6	0.0	3.8	0.00	**-63.2**	***-18.6***
A03-22_09	4271	312	170	29	1076	167	96.0	84.2	0.584	10.61	0.0112	7.1	72	10.2	0.0	3.8	0.01	**71.7**	***10.2***
A03-22_10	4863	92	2028	183	3748	117	58.3	45.9	0.864	3.23	0.0501	2.9	315	17.7	0.2	3.8	0.05	**315.2**	***17.7***
A03-22_13	4720	288	441	76	2083	214	90.7	78.8	0.814	10.02	0.0131	8.3	84	13.9	0.0	3.8	0.00	**84.3**	***13.9***
A03-22_15	4856	94	1847	155	3636	110	62.0	49.2	0.867	3.28	0.0440	2.9	277	15.8	0.0	3.8	0.00	**277.5**	***15.8***
A03-22_16	4837	116	873	149	2819	176	81.9	69.0	0.884	4.05	0.0169	3.7	108	8.0	0.0	3.8	0.01	**108.0**	***8.0***
A03-22_17	4367	196	408	134	1803	271	90.7	77.4	0.622	6.70	0.0247	7.7	157	24.0	0.0	3.8	0.00	**157.5**	***24.0***
A03-22_19	4714	371	791	189	2639	295	83.2	70.0	0.803	12.89	0.0257	10.7	164	34.4	0.6	3.8	0.15	**163.7**	***34.4***
A03-22_20	4911	51	3242	501	4349	189	34.0	25.5	0.819	1.78	0.1185	2.4	722	32.1	0.0	3.8	0.01	**722.0**	***32.1***
A03-22_22	4432	556	461	165	1949	382	89.6	76.3	0.652	19.05	0.0258	14.0	164	45.4	0.0	3.8	0.00	**164.4**	***45.4***
A03-22_23	4901	196	1032	186	3035	209	78.9	66.0	0.927	6.87	0.0127	6.4	81	10.3	0.0	3.8	0.01	**81.2**	***10.3***
A03-22_24	5015	63	4351	324	4814	109	13.2	9.6	0.785	2.23	0.2073	2.1	1214	46.0	0.2	3.8	0.04	**1214.6**	***46.0***
A03-22_25	4842	739	1306	254	3244	437	73.0	59.8	0.876	25.84	0.0278	22.7	176	78.5	0.0	3.8	0.00	**176.6**	***78.5***
A03-22_26	5086	112	854	125	2964	157	83.2	71.2	1.079	3.97	-0.0111	4.3	-72	-6.3	0.0	3.8	0.00	**-72.2**	***-6.3***
A03-22_27	4969	94	1412	126	3416	112	71.6	58.7	0.971	3.30	0.0070	3.2	45	2.9	3.9	3.8	1.03	**45.0**	***2.9***
A03-22_28	4636	186	775	142	2567	199	83.3	69.8	0.755	6.45	0.0312	5.4	198	21.2	0.1	3.8	0.02	**198.5**	***21.2***
A03-22_29	5308	230	1279	199	3544	212	75.9	63.9	1.292	8.20	-0.0641	10.9	-427	-97.0	0.1	3.8	0.02	**-427.2**	***-97.0***

RUTILE

		comments	^{204}Pb	^{206}Pb	^{207}Pb	^{208}Pb	^{232}Th	^{238}U	Pb ppm	U ppm	$^{238}U/^{206}Pb$	1s %	$^{207}Pb/^{206}Pb$	1s %	$^{207}Pb/^{235}U$	1s %	$^{206}Pb/^{238}U$	1s %	Rho
A03-22_30	19/03/2019		250	250	189	508	401	1209	0.091	0.116	4.5174	10.95	0.8188	5.06	24.9796	12.06	0.2214	10.95	0.91
A03-22_31	19/03/2019		291	291	252	614	18	1242	0.111	0.119	5.3544	8.03	0.8825	5.53	22.7142	9.75	0.1868	8.03	0.82
A03-22_32	19/03/2019		226	226	158	399	91	1976	0.075	0.190	15.4621	8.27	0.6704	5.94	5.9754	10.19	0.0647	8.27	0.81
A03-22_33	19/03/2019		113	113	48	127	18	6353	0.028	0.611	73.7487	15.84	0.2306	40.97	0.4310	43.93	0.0136	15.84	0.36
~~A03-22_03~~	~~19/03/2019~~	~~low Pb counts~~	~~49~~	~~49~~	~~21~~	~~35~~	~~78~~	~~1251~~	~~0.010~~	~~0.120~~	~~37.5439~~	~~14.23~~	~~0.4060~~	~~22.77~~	~~1.4902~~	~~26.85~~	~~0.0266~~	~~14.23~~	~~0.53~~
~~A03-22_11~~	~~19/03/2019~~	~~low Pb counts~~	~~44~~	~~44~~	~~14~~	~~28~~	~~39~~	~~2384~~	~~0.008~~	~~0.229~~	~~87.0894~~	~~16.60~~	~~0.1879~~	~~37.29~~	~~0.2943~~	~~40.82~~	~~0.0114~~	~~16.60~~	~~0.41~~
~~A03-22_12~~	~~19/03/2019~~	~~low Pb counts~~	~~20~~	~~20~~	~~19~~	~~26~~	~~-1~~	~~1075~~	~~0.006~~	~~0.103~~	~~80.2346~~	~~35.23~~	~~0.1144~~	~~95.52~~	~~0.1964~~	~~101.81~~	~~0.0125~~	~~35.23~~	~~0.35~~
~~A03-22_14~~	~~19/03/2019~~	~~low Pb counts~~	~~44~~	~~44~~	~~21~~	~~37~~	~~-1~~	~~489~~	~~0.010~~	~~0.047~~	~~11.2872~~	~~18.82~~	~~0.2263~~	~~42.45~~	~~2.7636~~	~~46.44~~	~~0.0886~~	~~18.82~~	~~0.41~~
~~A03-22_18~~	~~19/03/2019~~	~~low Pb counts~~	~~36~~	~~36~~	~~19~~	~~50~~	~~-1~~	~~1494~~	~~0.010~~	~~0.144~~	~~58.7889~~	~~16.38~~	~~0.4325~~	~~24.58~~	~~1.0138~~	~~29.54~~	~~0.0170~~	~~16.38~~	~~0.55~~
~~A03-22_21~~	~~19/03/2019~~	~~low Pb counts~~	~~44~~	~~44~~	~~24~~	~~68~~	~~38~~	~~1295~~	~~0.013~~	~~0.124~~	~~39.5812~~	~~15.71~~	~~0.3567~~	~~39.74~~	~~1.2419~~	~~42.74~~	~~0.0253~~	~~15.71~~	~~0.37~~
A04-20_03	19/03/2019		180	180	71	167	88	12376	0.040	1.190	95.8819	5.99	0.4847	8.68	0.6967	10.54	0.0104	5.99	0.57
A04-20_04	19/03/2019		283	283	131	354	345	17707	0.074	1.702	92.3280	4.31	0.4630	5.23	0.6911	6.78	0.0108	4.31	0.64
A04-20_05	19/03/2019		5162	5162	3989	10607	19424	24352	1.900	2.341	6.5767	3.43	0.7679	1.47	16.0924	3.73	0.1521	3.43	0.92
A04-20_06	19/03/2019		1305	1305	969	2532	1228	24170	0.462	2.324	25.0598	4.68	0.7028	2.12	3.8652	5.14	0.0399	4.68	0.91
A04-20_07	19/03/2019		275	275	156	383	447	10353	0.078	0.995	52.8568	4.41	0.5866	5.49	1.5294	7.04	0.0189	4.41	0.63
A04-20_08	19/03/2019		308	308	170	441	369	10864	0.088	1.045	49.6548	4.41	0.5635	4.30	1.5641	6.16	0.0201	4.41	0.72
A04-20_09	19/03/2019		260	260	93	268	543	29205	0.060	2.808	156.3787	5.31	0.3978	7.26	0.3506	9.00	0.0064	5.31	0.59
A04-20_10	19/03/2019		604	604	333	832	1512	28587	0.170	2.748	65.3495	3.08	0.5634	3.20	1.1881	4.44	0.0153	3.08	0.69
A04-20_11	19/03/2019		7346	7346	5558	15093	1513	32139	2.692	3.090	6.4594	6.87	0.7457	1.35	15.9096	7.00	0.1548	6.87	0.98
A04-20_12	19/03/2019		4622	4622	3837	12142	621	34410	1.981	3.308	8.0145	11.42	0.7546	1.69	12.9767	11.55	0.1248	11.42	0.99
A04-20_13	19/03/2019		446	446	209	503	1090	24995	0.111	2.403	78.7472	5.20	0.4885	4.15	0.8549	6.65	0.0127	5.20	0.78
A04-20_14	19/03/2019		1312	1312	971	2514	1382	29513	0.461	2.837	30.5780	2.79	0.7368	2.20	3.3210	3.55	0.0327	2.79	0.78
A04-20_15	19/03/2019		1015	1015	798	1515	978	17213	0.320	1.655	23.1015	11.35	0.7026	3.00	4.1918	11.74	0.0433	11.35	0.97
A04-20_16	19/03/2019		1716	1716	1051	2763	2057	68198	0.532	6.557	57.8405	3.52	0.6023	1.94	1.4352	4.02	0.0173	3.52	0.88
A04-20_17	19/03/2019		331	331	213	543	412	13774	0.104	1.324	60.8534	5.91	0.6301	5.07	1.4271	7.79	0.0164	5.91	0.76
A04-20_19	19/03/2019		430	430	277	698	225	21489	0.135	2.066	68.4913	6.61	0.6274	5.12	1.2625	8.36	0.0146	6.61	0.79
A04-20_20	19/03/2019		1296	1296	897	2353	6837	38139	0.437	3.667	41.7910	2.78	0.6883	2.32	2.2699	3.62	0.0239	2.78	0.77
A04-20_21	19/03/2019	outlier?	390	390	180	523	277	32649	0.105	3.139	100.5190	8.20	0.3025	6.26	0.4148	10.32	0.0099	8.20	0.79
A04-20_22	19/03/2019		397	397	180	432	285	31263	0.097	3.006	111.0248	4.65	0.4558	5.61	0.5658	7.29	0.0090	4.65	0.64
A04-20_18	19/03/2019		122	122	47	121	98	11151	0.028	1.072	121.2733	6.95	0.3858	8.73	0.4385	11.16	0.0082	6.95	0.62
A04-20_25	19/03/2019		155	155	51	93	171	17903	0.029	1.721	160.8744	4.85	0.3511	13.97	0.3007	14.79	0.0062	4.85	0.33
A04-20_26	19/03/2019		158	158	33	63	50	16660	0.024	1.602	150.6798	5.53	0.2309	11.18	0.2112	12.48	0.0066	5.53	0.44
~~A04-20_01~~	~~19/03/2019~~	~~low Pb counts~~	~~186~~	~~186~~	~~10~~	~~-8~~	~~73~~	~~29140~~	~~0.018~~	~~2.802~~	~~222.3832~~	~~5.10~~	~~0.0576~~	~~25.67~~	~~0.0357~~	~~26.17~~	~~0.0045~~	~~5.10~~	~~0.19~~
~~A04-20_02~~	~~19/03/2019~~	~~low Pb counts~~	~~206~~	~~206~~	~~10~~	~~4~~	~~4~~	~~29897~~	~~0.021~~	~~2.874~~	~~205.0844~~	~~4.69~~	~~0.0495~~	~~23.90~~	~~0.0332~~	~~24.35~~	~~0.0049~~	~~4.69~~	~~0.19~~
~~A04-20_23~~	~~19/03/2019~~	~~low Pb counts~~	~~108~~	~~108~~	~~11~~	~~19~~	~~31~~	~~15687~~	~~0.013~~	~~1.508~~	~~194.0008~~	~~7.41~~	~~0.0683~~	~~36.14~~	~~0.0485~~	~~36.89~~	~~0.0052~~	~~7.41~~	~~0.20~~
~~A04-20_24~~	~~19/03/2019~~	~~low Pb counts~~	~~83~~	~~83~~	~~4~~	~~6~~	~~9~~	~~12404~~	~~0.009~~	~~1.193~~	~~211.8743~~	~~9.89~~	~~0.0797~~	~~70.90~~	~~0.0518~~	~~71.58~~	~~0.0047~~	~~9.89~~	~~0.14~~
A04-28_01	19/03/2019		16910	16910	15257	35550	3271	64113	6.510	6.164	2.3708	11.64	0.9092	1.40	52.8550	11.72	0.4218	11.64	0.99
A04-28_02	19/03/2019		47184	47184	43983	104789	1319	36817	18.839	3.540	1.0937	3.64	0.9324	1.13	117.4922	3.81	0.9144	3.64	0.95
A04-28_03	19/03/2019		2128	2128	1870	3730	946	18475	0.743	1.776	12.8622	9.80	0.7535	2.54	8.0734	10.12	0.0777	9.80	0.97
A04-28_04	19/03/2019		492	492	260	539	332	29061	0.124	2.794	87.1816	13.21	0.4329	13.22	0.6843	18.69	0.0115	13.21	0.71
A04-28_05	19/03/2019		147	147	93	217	117	5892	0.044	0.566	57.3098	7.36	0.6979	7.68	1.6784	10.63	0.0174	7.36	0.69
A04-28_06	19/03/2019		1576	1576	1226	2654	106	19754	0.525	1.899	19.1036	15.47	0.7082	3.77	5.1094	15.93	0.0523	15.47	0.97
A04-28_07	19/03/2019		64769	64769	64707	157625	2997	37740	27.602	3.628	0.3518	9.13	0.9283	0.91	363.6582	9.18	2.8424	9.13	1.00
A04-28_08	19/03/2019		1744	1744	1660	3552	21	9240	0.669	0.888	7.2816	4.59	0.9080	2.99	17.1862	5.48	0.1373	4.59	0.84
A04-28_09	19/03/2019		769	769	606	1412	112	16500	0.268	1.586	31.7337	4.76	0.7611	3.89	3.3055	6.15	0.0315	4.76	0.77
A04-28_10	19/03/2019		4969	4969	4505	11146	860	13104	1.982	1.260	3.8733	4.86	0.8762	1.45	31.1773	5.07	0.2582	4.86	0.96
A04-28_11	19/03/2019		27618	27618	25212	62961	1232	25042	11.132	2.408	0.9325	6.52	0.9099	0.96	134.4777	6.59	1.0724	6.52	0.99
A04-28_12	19/03/2019		22046	22046	19629	47461	6655	107327	8.570	10.319	2.0734	17.79	0.8853	1.16	58.8441	17.82	0.4823	17.79	1.00
A04-28_13	19/03/2019		2300	2300	2070	5019	-1	24383	0.903	2.344	15.1990	3.73	0.8896	2.51	8.0668	4.49	0.0658	3.73	0.83
A04-28_14	19/03/2019		145	145	75	179	61	6337	0.038	0.609	59.6646	9.42	0.7836	14.79	1.8100	17.53	0.0168	9.42	0.54
A04-28_15	19/03/2019		622	622	279	679	1142	43012	0.152	4.135	99.4832	4.84	0.4238	6.44	0.5870	8.05	0.0101	4.84	0.60
A04-28_16	19/03/2019		255	255	50	117	606	21643	0.041	2.081	130.4613	5.26	0.2381	10.98	0.2515	12.18	0.0077	5.26	0.43
A04-28_17	19/03/2019		1443	1443	1158	3040	-1	8421	0.542	0.810	8.5991	8.40	0.8814	2.23	14.1268	8.69	0.1163	8.40	0.97
A04-28_18	19/03/2019		29245	29245	25557	62846	19907	24969	11.311	2.401	1.1982	6.37	0.8721	0.74	100.3123	6.41	0.8346	6.37	0.99
A04-28_19	19/03/2019		189933	189933	178644	417016	2308	3246	75.528	0.312	0.0299	5.39	0.9223	0.51	4254.160	5.42	33.4677	5.39	1.00
A04-28_20	19/03/2019		154060	154060	145683	344114	557	12929	61.901	1.243	0.1271	6.52	0.9305	0.63	1009.194	6.55	7.8697	6.52	1.00
A04-28_21	19/03/2019		175593	175593	168949	392709	660	9356	70.880	0.899	0.0699	4.94	0.9295	0.56	1833.638	4.97	14.3146	4.94	0.99
A04-28_22	19/03/2019		7681	7681	6836	17124	35	3229	3.042	0.310	0.6140	8.05	0.9204	1.20	206.5887	8.14	1.6287	8.05	0.99
A04-28_23	19/03/2019		28749	28749	27054	64095	2743	34032	11.527	3.272	0.7614	10.64	0.9078	0.68	164.3276	10.66	1.3134	10.64	1.00
A04-28_24	19/03/2019		49457	49457	44738	106660	9651	105999	19.310	10.191	1.0533	16.38	0.8984	0.58	117.5619	16.39	0.9494	16.38	1.00
A04-28_25	19/03/2019		321	321	197	422	1145	12449	0.090	1.197	55.4516	6.89	0.6736	7.16	1.6743	9.93	0.0180	6.89	0.69
A04-28_26	19/03/2019		274	274	165	378	749	15598	0.079	1.500	56.1352	9.96	0.6781	6.77	1.6648	12.04	0.0178	9.96	0.83
A04-28_27	19/03/2019		26639	26639	24238	56788	2201	78746	10.351	7.571	1.4634	10.86	0.8986	0.61	84.6327	10.88	0.6834	10.86	1.00
A04-28_28	19/03/2019		987	987	648	1549	676	36103	0.306	3.471	53.4067	5.61	0.5710	3.08	1.4735	6.40	0.0187	5.61	0.88
A04-28_29	19/03/2019		320	320	173	382	1006	15162	0.084	1.458	67.8368	6.07	0.5521	5.81	1.1217	8.40	0.0147	6.07	0.72
A04-28_30	19/03/2019		20407	20407	19786	47304	147	23523	8.412	2.262	1.5717	8.10	0.9182	0.87	80.5161	8.15	0.6362	8.10	0.99
A04-28_31	19/03/2019		6775	6775	7280	17463	245	6856	3.030	0.659	1.3045	10.51	0.9102	1.27	96.1640	10.58	0.7666	10.51	0.99
A04-28_32	19/03/2019		3382	3382	2871	6871	2439	32374	1.262	3.112	8.9689	10.68	0.8064	1.80	12.3914	10.83	0.1115	10.68	0.99
A04-28_33	19/03/2019		826	826	637	1744	1647	17445	0.308	1.677	29.7575	5.38	0.7230	2.76	3.3486	6.05	0.0336	5.38	0.89

RUTILE

	$^{207}Pb/^{206}Pb$	2s abs	$^{206}Pb/^{238}U$	2s abs	$^{207}Pb/^{235}U$	2s abs	c. % 6-38/	c. %6-38/7	*f206*	1s %	$^{206}Pb*/^{238}U$	1s %	²06/238-Pb	2s [Ma]	Th/U min.	Th/U wr.	f	·. 206/238	*2s [Ma]*
A03-22_30	4955	144	1289	251	3307	212	74.0	61.0	0.963	5.06	0.0082	4.9	53	5.1	0.2	3.8	0.04	**52.7**	***5.1***
A03-22_31	5061	157	1104	161	3215	174	78.2	65.7	1.055	5.53	-0.0102	5.9	-66	-7.8	0.0	3.8	0.00	**-66.2**	***-7.8***
A03-22_32	4669	171	404	64	1972	163	91.3	79.5	0.784	5.94	0.0140	5.0	90	8.9	0.0	3.8	0.01	**89.7**	***8.9***
A03-22_33	3056	1311	87	27	364	238	97.2	76.1	0.231	40.97	0.0104	15.4	67	20.5	0.0	3.8	0.00	**67.0**	***20.5***
~~A03-22_03~~	~~3931~~	~~684~~	~~169~~	~~47~~	~~926~~	~~283~~	~~95.7~~	~~81.7~~	~~0.451~~	~~22.77~~	~~0.0146~~	~~12.9~~	~~94~~	~~23.9~~	~~0.1~~	~~3.8~~	~~0.01~~	~~**93.7**~~	~~***23.9***~~
~~A03-22_11~~	~~2724~~	~~1229~~	~~73~~	~~24~~	~~262~~	~~173~~	~~97.3~~	~~72.2~~	~~0.177~~	~~37.29~~	~~0.0093~~	~~15.2~~	~~60~~	~~18.1~~	~~0.0~~	~~3.8~~	~~0.00~~	~~**60.1**~~	~~***18.1***~~
~~A03-22_12~~	~~1870~~	~~3446~~	~~80~~	~~56~~	~~182~~	~~293~~	~~95.7~~	~~56.2~~	~~0.084~~	~~95.52~~	~~0.0114~~	~~33.3~~	~~73~~	~~48.2~~	~~0.0~~	~~3.8~~	~~0.00~~	~~**73.3**~~	~~***48.2***~~
~~A03-22_14~~	~~3026~~	~~1362~~	~~547~~	~~195~~	~~1346~~	~~528~~	~~81.9~~	~~59.3~~	~~0.211~~	~~42.45~~	~~0.0699~~	~~17.3~~	~~436~~	~~144.5~~	~~0.0~~	~~3.8~~	~~0.00~~	~~**435.9**~~	~~***144.5***~~
~~A03-22_18~~	~~4026~~	~~734~~	~~109~~	~~35~~	~~711~~	~~264~~	~~97.3~~	~~84.7~~	~~0.486~~	~~24.58~~	~~0.0087~~	~~14.6~~	~~56~~	~~16.3~~	~~0.0~~	~~3.8~~	~~-0.01~~	~~**56.2**~~	~~***16.2***~~
~~A03-22_21~~	~~3736~~	~~1209~~	~~161~~	~~50~~	~~820~~	~~394~~	~~95.7~~	~~80.4~~	~~0.389~~	~~39.74~~	~~0.0154~~	~~18.2~~	~~99~~	~~35.6~~	~~0.1~~	~~3.8~~	~~0.02~~	~~**98.9**~~	~~***35.6***~~
A04-20_03	4195	257	67	8	537	84	98.4	87.5	0.554	8.68	0.0047	5.5	30	3.3	0.0	3.8	0.00	**30.1**	***3.3***
A04-20_04	4127	155	69	6	533	55	98.3	87.0	0.526	5.23	0.0051	3.4	33	2.3	0.0	3.8	0.00	**33.1**	***2.3***
A04-20_05	4863	42	912	58	2882	69	81.2	68.3	0.902	1.47	0.0149	1.4	95	2.6	0.6	3.8	0.15	**95.5**	***2.6***
A04-20_06	4737	61	252	23	1606	80	94.7	84.3	0.828	2.12	0.0069	1.9	44	1.7	0.1	3.8	0.01	**44.2**	***1.7***
A04-20_07	4475	160	121	11	942	83	97.3	87.2	0.682	5.49	0.0060	4.0	39	3.1	0.1	3.8	0.03	**38.8**	***3.1***
A04-20_08	4417	126	129	11	956	74	97.1	86.6	0.652	4.30	0.0070	3.2	45	2.9	0.0	3.8	0.01	**45.1**	***2.9***
A04-20_09	3901	218	41	4	305	46	98.9	86.5	0.444	7.26	0.0036	4.4	23	2.0	0.0	3.8	0.00	**23.0**	***2.0***
A04-20_10	4416	93	98	6	795	48	97.8	87.7	0.653	3.20	0.0053	2.3	34	1.6	0.1	3.8	0.01	**34.3**	***1.6***
A04-20_11	4821	39	928	118	2871	126	80.8	67.7	0.872	1.35	0.0199	1.5	127	3.7	0.0	3.8	0.01	**126.9**	***3.7***
A04-20_12	4838	48	758	161	2678	197	84.3	71.7	0.887	1.69	0.0141	2.0	90	3.5	0.0	3.8	0.00	**90.2**	***3.5***
A04-20_13	4207	123	81	8	627	60	98.1	87.0	0.558	4.15	0.0056	3.3	36	2.3	0.1	3.8	0.02	**36.2**	***2.3***
A04-20_14	4804	63	207	11	1486	54	95.7	86.0	0.872	2.20	0.0042	2.0	27	1.0	0.0	3.8	0.01	**27.0**	***1.0***
A04-20_15	4736	86	273	60	1672	176	94.2	83.7	0.828	3.00	0.0075	3.2	48	3.0	0.1	3.8	0.03	**48.1**	***3.0***
A04-20_16	4514	56	110	8	904	47	97.6	87.8	0.702	1.94	0.0051	1.7	33	1.1	0.0	3.8	0.00	**33.2**	***1.1***
A04-20_17	4579	147	105	12	900	89	97.7	88.3	0.738	5.07	0.0043	4.0	28	2.2	0.1	3.8	0.04	**27.8**	***2.2***
A04-20_19	4573	148	93	12	829	91	98.0	88.7	0.734	5.12	0.0039	4.1	25	2.1	0.0	3.8	0.00	**25.1**	***2.1***
A04-20_20	4706	67	152	8	1203	50	96.8	87.3	0.811	2.32	0.0045	2.0	29	1.1	0.1	3.8	0.03	**29.2**	***1.1***
A04-20_21	3483	194	64	10	352	60	98.2	81.9	0.323	6.26	0.0067	5.9	43	5.1	0.0	3.8	0.00	**43.4**	***5.1***
A04-20_22	4104	167	58	5	455	52	98.6	87.3	0.517	5.61	0.0043	3.7	28	2.0	0.0	3.8	0.00	**28.1**	***2.0***
A04-20_18	3855	263	53	7	369	67	98.6	85.7	0.429	8.73	0.0047	5.5	30	3.3	0.0	3.8	0.00	**30.4**	***3.3***
A04-20_25	3712	426	40	4	267	67	98.9	85.0	0.385	13.97	0.0038	6.2	25	3.0	0.0	3.8	0.00	**24.7**	***3.0***
A04-20_26	3058	358	43	5	195	43	98.6	78.1	0.233	11.18	0.0051	5.0	33	3.3	0.0	3.8	0.00	**32.9**	***3.3***
~~A04-20_01~~	~~516~~	~~1127~~	~~29~~	~~3~~	~~36~~	~~18~~	~~94.4~~	~~18.8~~	~~0.014~~	~~25.67~~	~~0.0044~~	~~5.0~~	~~29~~	~~2.9~~	~~0.2~~	~~3.8~~	~~0.06~~	~~**28.6**~~	~~***2.9***~~
~~A04-20_02~~	~~170~~	~~1116~~	~~31~~	~~3~~	~~33~~	~~16~~	~~81.6~~	~~5.6~~	~~0.004~~	~~23.90~~	~~0.0049~~	~~4.7~~	~~31~~	~~2.9~~	~~0.0~~	~~3.8~~	~~0.00~~	~~**31.4**~~	~~***2.9***~~
~~A04-20_23~~	~~877~~	~~1496~~	~~33~~	~~5~~	~~48~~	~~34~~	~~96.2~~	~~31.1~~	~~0.027~~	~~36.14~~	~~0.0050~~	~~7.3~~	~~32~~	~~4.7~~	~~0.0~~	~~3.8~~	~~0.00~~	~~**32.4**~~	~~***4.7***~~
~~A04-20_24~~	~~1189~~	~~2800~~	~~30~~	~~6~~	~~51~~	~~69~~	~~97.4~~	~~40.8~~	~~0.042~~	~~70.90~~	~~0.0045~~	~~9.9~~	~~29~~	~~5.8~~	~~0.0~~	~~3.8~~	~~0.00~~	~~**29.2**~~	~~***5.8***~~
A04-28_01	5103	39	2269	430	4048	210	55.5	44.0	1.061	1.40	-0.0257	1.6	-168	-5.6	2.2	3.8	0.58	**-167.7**	***-5.6***
A04-28_02	5139	32	4186	220	4848	74	18.5	13.7	0.953	1.13	0.0433	1.1	273	5.8	0.1	3.8	0.02	**273.3**	***5.8***
A04-28_03	4836	73	483	90	2239	168	90.0	78.4	0.890	2.54	0.0085	2.5	55	2.7	0.1	3.8	0.03	**54.8**	***2.7***
A04-28_04	4027	395	74	19	529	144	98.2	86.1	0.488	13.22	0.0059	9.3	38	7.0	0.0	3.8	0.00	**37.9**	***7.0***
A04-28_05	4726	221	112	16	1000	127	97.6	88.9	0.824	7.68	0.0031	6.5	20	2.6	0.1	3.8	0.03	**19.9**	***2.6***
A04-28_06	4748	108	329	98	1838	240	93.1	82.1	0.834	3.77	0.0087	4.1	56	4.5	0.0	3.8	0.00	**55.9**	***4.5***
A04-28_07	5133	26	8678	817	5990	171	-69.1	-44.9	-1.177	0.91	6.1869	19.9	12714	1900.1	0.0	3.8	0.01	**12716.0**	***1900.1***
A04-28_08	5101	85	830	71	2945	100	83.7	71.8	1.093	2.99	-0.0127	3.3	-82	-5.5	0.0	3.8	0.00	**-82.3**	***-5.5***
A04-28_09	4851	111	200	19	1482	92	95.9	86.5	0.904	3.89	0.0030	3.5	20	1.4	0.0	3.8	0.00	**19.7**	***1.4***
A04-28_10	5051	41	1481	127	3525	95	70.7	58.0	1.039	1.45	-0.0100	1.5	-65	-2.0	0.1	3.8	0.02	**-64.9**	***-2.0***
A04-28_11	5104	27	4698	421	4984	125	8.0	5.8	0.894	0.96	0.1141	1.1	697	14.5	0.0	3.8	0.01	**696.8**	***14.5***
A04-28_12	5066	33	2537	706	4155	305	49.9	38.9	1.011	1.16	-0.0055	1.2	-35	-0.8	0.0	3.8	0.00	**-35.3**	***-0.8***
A04-28_13	5072	71	411	30	2239	78	91.9	81.7	1.069	2.51	-0.0046	2.7	-29	-1.6	0.0	3.8	0.00	**-29.3**	***-1.6***
A04-28_14	4892	422	107	20	1049	207	97.8	89.8	0.933	14.79	0.0011	13.8	7	2.0	0.0	3.8	0.01	**7.3**	***2.0***
A04-28_15	3996	193	64	6	469	59	98.4	86.3	0.476	6.44	0.0053	4.0	34	2.7	0.0	3.8	0.00	**33.9**	***2.7***
A04-28_16	3107	350	49	5	228	49	98.4	78.4	0.242	10.98	0.0058	4.8	37	3.6	0.1	3.8	0.01	**37.5**	***3.6***
A04-28_17	5059	63	709	112	2758	153	86.0	74.3	1.057	2.23	-0.0067	2.4	-43	-2.1	0.0	3.8	0.00	**-43.0**	***-2.1***
A04-28_18	5044	21	3912	363	4689	121	22.4	16.6	0.873	0.74	0.1057	1.0	648	12.7	0.3	3.8	0.07	**648.1**	***12.7***
A04-28_19	5123	14	22820	642	8484	104	-345.4	-169.0	-142.299	0.51	4795.898	776.0	54638	18078.5	5.5	3.8	1.44	**54646.8**	***18078.5***
A04-28_20	5136	18	14070	706	7024	125	-174.0	-100.3	-15.126	0.63	126.9067	105.6	31273	7284.2	0.0	3.8	0.00	**31278.5**	***7284.2***
A04-28_21	5134	16	17591	569	7630	96	-242.6	-130.5	-46.701	0.56	682.8143	237.0	42080	11257.3	0.1	3.8	0.03	**42087.0**	***11257.3***
A04-28_22	5120	34	6230	613	5418	152	-21.7	-15.0	0.226	1.20	1.2614	6.2	5260	433.8	0.0	3.8	0.01	**5261.0**	***433.8***
A04-28_23	5101	19	5407	735	5187	195	-6.0	-4.2	0.617	0.68	0.5030	4.1	2627	174.3	0.0	3.8	0.00	**2627.2**	***174.3***
A04-28_24	5086	16	4303	954	4849	286	15.4	11.3	0.877	0.58	0.1170	2.1	713	28.1	0.0	3.8	0.01	**713.6**	***28.1***
A04-28_25	4676	206	115	16	999	119	97.5	88.5	0.793	7.16	0.0037	5.9	24	2.8	0.8	3.8	0.21	**24.1**	***2.8***
A04-28_26	4685	195	114	22	995	142	97.6	88.6	0.799	6.77	0.0036	5.8	23	2.7	0.0	3.8	0.01	**23.2**	***2.7***
A04-28_27	5087	17	3357	545	4519	198	34.0	25.7	0.974	0.61	0.0179	0.7	115	1.5	0.0	3.8	0.00	**114.6**	***1.5***
A04-28_28	4436	90	120	13	920	75	97.3	87.0	0.662	3.08	0.0063	2.8	41	2.3	0.0	3.8	0.01	**40.8**	***2.3***
A04-28_29	4387	170	94	11	764	86	97.8	87.6	0.639	5.81	0.0053	4.3	34	2.9	0.2	3.8	0.04	**34.4**	***2.9***
A04-28_30	5117	25	3174	394	4468	151	38.0	29.0	1.020	0.87	-0.0129	0.9	-84	-1.5	0.0	3.8	0.00	**-83.9**	***-1.5***
A04-28_31	5105	36	3668	563	4647	193	28.1	21.1	0.964	1.27	0.0276	1.3	176	4.5	0.1	3.8	0.03	**175.8**	***4.5***
A04-28_32	4933	51	681	137	2635	185	86.2	74.1	0.957	1.80	0.0048	1.8	31	1.1	0.0	3.8	0.00	**30.7**	***1.1***
A04-28_33	4777	79	213	23	1492	90	95.5	85.7	0.855	2.76	0.0049	2.5	31	1.6	0.2	3.8	0.05	**31.5**	***1.6***

ID-TIMS ZIRCON : Sample A0312

	Dates (Ma)										Composition				Isotopic Ratios							Fraction
Fraction	206Pb/ 238U <Th> a	±2σ abs	206Pb/ 238U b	±2σ abs	207Pb/ 235U b	±2σ abs	207Pb/ 206Pb b	±2σ abs	Corr. coef.	% disc c	Th/ U d	Pb* (pg) e	Pbc (pg) f	Pb*/ Pbc g	206Pb/ 204Pb h	206Pb/ 238U i	±2σ %	207Pb/ 235U i	±2σ %	207Pb/ 206Pb i	±2σ %	Fraction
Zircon																						
z1	47.331	0.659	47.22	0.66	55.86	8.52	443.77	336.87	0.42	89.36	0.010	0.15	0.23	0.65	63.419651	0.007352	1.403145	0.056550	15.680438	0.055809	15.149746	z1
z2	46.955	0.052	46.85	0.05	47.24	0.53	67.21	26.01	0.53	30.30	0.002	1.24	0.12	10.75	765.591530	0.007294	0.111581	0.047623	1.147557	0.047377	1.092447	z2
z7	46.908	0.049	46.80	0.05	47.34	0.40	74.73	18.89	0.74	37.38	0.002	1.97	0.10	19.36	1365.945472	0.007286	0.105816	0.047725	0.870043	0.047527	0.794085	z7

a Corrected for initial Th/U disequilibrium using radiogenic 208Pb and Th/U[magma] = 5.

b Isotopic dates calculated using the decay constants λ238 = 1.5512500000E-10 and λ235 = 9.8485000000E-10 (Jaffey et al. 1971).

c % discordance = 100 - (100 * (206Pb/238U date) / (207Pb/206Pb date))

d Th contents calculated from radiogenic 208Pb and the 230Th-corrected 206Pb/238U date of the sample, assuming concordance between the U-Pb and Th-Pb systems.

e Total mass of radiogenic Pb.

f Total mass of common Pb.

g Ratio of radiogenic Pb (including 208Pb) to common Pb.

h Measured ratio corrected for fractionation and spike contribution only.

i Measured ratios corrected for fractionation, tracer and blank.

Appendix 4 – Whole rock XRF data

Sample	Ju07	Ju07a	Ju08	Ju09	Ju10	Ju11	Ju13	Ju13a	a04-07	a04-09	a04-10	a01-11	a04-16	a04-17
Type	Gneiss	Gneiss	Gneiss	Gneiss	Gneiss	amphibolite	eclogite	eclogite	Gneiss	Gneiss	Gneiss	Granite	Gneiss	Gneiss
SiO_2	73.80	75.28	74.76	74.71	76.44	44.35	46.57	46.55	74.74	75.04	73.84	70.90	74.35	72.72
TiO_2	0.27	0.15	0.06	0.06	0.05	2.42	2.52	2.40	0.20	0.29	0.24	0.45	0.21	0.27
Al_2O_3	14.19	13.88	15.08	14.15	14.41	15.22	15.83	14.94	12.94	12.99	13.38	13.65	13.26	13.46
Fe_2O_3	2.67	1.31	1.26	1.19	0.66	13.82	14.28	13.62	2.09	2.31	2.05	2.48	1.62	1.68
MnO	0.06	0.02	0.05	0.03	0.02	0.18	0.19	0.19	0.03	0.04	0.03	0.05	0.02	0.03
MgO	0.77	1.38	0.09	0.36	0.08	6.90	6.59	6.65	0.78	0.65	0.83	1.02	1.37	0.64
CaO	0.27	1.06	0.47	0.89	0.42	7.76	10.50	11.11	0.42	0.62	0.64	2.47	0.60	1.14
Na_2O	1.74	4.10	4.99	3.73	5.11	2.48	2.72	3.13	3.49	3.39	2.53	2.77	2.60	2.49
K_2O	4.82	2.14	2.49	2.95	2.02	2.87	0.49	0.37	2.95	2.77	5.03	4.25	2.93	5.37
P_2O_5	0.19	0.18	0.26	0.21	0.24	0.34	0.27	0.29	0.13	0.15	0.16	0.16	0.13	0.19
SO_3	<0.001	<0.001	0.00	0.00	<0.001	0.02	0.04	0.04	0.01	<0.001	0.01	0.01	0.01	0.01
LOI	**1.70**	**0.97**	**1.15**	**1.66**	**0.98**	**2.59**	**0.94**	**1.90**	**1.24**	**1.41**	**1.42**	**0.88**	**1.99**	**1.66**
Total	**100.49**	**100.47**	**100.66**	**99.93**	**100.42**	**98.95**	**100.96**	**101.18**	**99.02**	**99.67**	**100.15**	**99.09**	**99.07**	**99.67**
As	<0.4	2.5	<0.4	<0.4	0.2	9.6	6.5	<0.7	0.7	0.7	<0.4	11.6	1.5	6.1
Ba	69.8	69.6	16.5	39.7	11.2	84.6	64.0	31.6	150.7	175.6	230.5	620.7	118.0	278.4
Ce	27.0	31.0	0.5	4.2	3.8	27.7	31.0	31.2	44.8	51.4	22.2	46.1	42.7	50.8
Co	27.7	56.6	29.1	35.3	113.5	68.5	141.2	79.3	23.2	23.1	24.0	65.1	41.6	24.8
Cr	5.6	-0.8	<0.6	<0.6	<0.6	191.2	225.1	194.8	0.5	6.1	2.4	4.2	1.0	12.2
Cs	32.1	7.9	2.9	12.2	3.4	59.2	11.2	10.2	11.0	7.0	7.1	12.9	9.0	17.9
Cu	<0.6	10.3	<0.5	<0.5	<0.5	45.6	71.6	37.4	0.2	<0.5	<0.5	<0.5	<0.5	1.2
Ga	19.5	17.2	23.8	17.4	18.6	21.9	23.1	24.6	15.2	15.9	15.9	16.9	15.8	16.2
La	11.9	13.9	2.4	3.6	1.5	4.2	9.7	9.1	25.4	24.6	8.8	23.5	21.7	23.3
Mo	0.7	1.2	0.5	0.5	0.5	2.1	2.2	2.0	0.7	0.6	0.7	0.6	0.7	1.3
Nb	16.9	12.8	16.6	15.5	10.9	9.7	9.6	9.4	8.9	11.4	11.8	12.4	9.2	12.4
Nd	15.0	15.4	2.6	4.1	4.8	13.8	18.5	18.9	24.0	24.3	13.4	25.0	22.8	23.7
Ni	6.2	11.9	1.0	9.7	0.0	81.3	95.7	81.6	4.2	4.5	4.8	6.3	4.4	5.8

Appendix 4 – Whole rock XRF data

Pb	3.7	14.7	10.5	8.0	17.4	10.6	4.5	5.6	7.0	3.7	24.0	17.5	4.8	12.1
Rb	489.3	112.1	227.8	236.8	158.3	267.0	42.0	31.1	142.7	137.8	223.5	214.8	138.3	230.5
Sb	<0.9	<0.8	0.5	0.5	0.1	<1.2	<1.2	0.7	0.0	0.3	<0.9	<1.0	<0.9	0.1
Sc	5.6	4.0	7.6	7.1	2.9	27.3	35.8	32.3	3.8	7.2	4.4	10.3	3.6	5.8
Se	<0.6	<0.5	<0.5	<0.5	<0.5	<0.8	<0.9	<0.9	<0.5	<0.5	<0.6	<0.6	<0.5	<0.6
Sn	20.3	10.5	11.5	18.5	15.7	0.8	1.0	<1.2	3.4	5.2	4.2	3.4	5.1	3.2
Sr	20.3	59.9	20.8	80.7	35.3	223.4	345.0	374.7	16.7	21.7	36.8	104.6	21.7	44.7
Th	7.1	12.5	5.5	3.6	1.1	1.8	1.4	0.4	14.5	16.4	12.8	18.0	13.5	16.2
U	1.6	5.3	0.4	2.3	1.0	3.4	1.5	0.7	2.4	3.5	2.2	1.4	3.3	4.1
V	22.3	10.5	2.1	2.8	<0.8	344.5	371.7	358.7	16.3	21.1	18.8	54.1	20.5	21.2
Y	28.6	23.4	9.5	12.9	6.3	26.4	27.2	25.4	41.9	42.7	42.3	46.7	28.9	48.1
Zn	81.7	15.5	34.9	23.7	18.7	92.6	99.9	102.3	34.7	33.8	29.2	38.6	12.2	34.4
Zr	91.7	71.2	27.9	41.7	11.7	175.5	186.4	188.9	89.0	112.4	109.4	153.2	102.0	114.1

Appendix 4 – Whole rock XRF data

Sample	a05-01	a05-02	a05-03	a05-04	a05-05	a05-06	a05-07	a08-02	03-06	05-05c	08-07	11-05	11-06	11-07
Type	Granite	Granite	Gneiss	Gneiss	Gneiss	Gneiss	Gneiss	metasediment	Gneiss	Gneiss	Gneiss	Eclogite	Eclogite	Eclogite
SiO_2	70.00	71.15	71.71	70.23	71.25	72.86	70.18	68.25	75.78	76.79	74.68	50.70	51.16	51.16
TiO_2	0.50	0.36	0.36	0.51	0.50	0.52	0.57	0.88	0.17	0.10	0.07	1.46	1.50	0.95
Al_2O_3	14.77	14.50	14.63	13.64	14.20	13.82	14.84	16.75	13.02	11.79	13.77	16.53	15.76	16.97
Fe_2O_3	2.78	2.66	1.95	3.60	3.65	3.20	4.46	4.55	1.18	1.15	0.48	12.59	11.53	9.94
MnO	0.04	0.05	0.04	0.05	0.05	0.04	0.07	0.00	0.02	0.02	0.01	0.19	0.16	0.16
MgO	1.23	0.86	0.88	1.25	1.26	1.16	1.40	0.59	0.31	0.21	0.35	6.73	6.60	7.37
CaO	1.28	0.98	0.99	1.06	1.32	0.71	1.10	0.59	0.50	0.46	0.76	8.11	9.21	8.40
Na_2O	2.58	3.36	3.31	2.76	1.83	3.39	1.95	0.33	2.76	2.72	3.47	2.34	2.83	3.60
K_2O	4.32	4.03	4.00	3.64	4.67	3.18	3.97	4.47	4.93	4.99	4.90	1.39	0.66	0.97
P_2O_5	0.17	0.15	0.15	0.16	0.16	0.18	0.15	0.04	0.16	0.16	0.26	0.18	0.19	0.16
SO_3	0.02	0.00	0.00	0.00	0.00	0.00	0.00	<0.001	<0.001	<0.001	0.01	<0.001	0.02	0.01
LOI	**1.49**	**1.75**	**1.49**	**2.85**	**1.51**	**1.25**	**1.53**	**1.93**	**0.85**	**0.86**	**1.16**	**0.64**	**1.04**	**1.06**
Total	**99.18**	**99.85**	**99.51**	**99.74**	**100.41**	**100.30**	**100.23**	**98.37**	**99.69**	**99.24**	**99.94**	**100.86**	**100.66**	**100.74**
As	0.7	<0.5	<0.5	<0.5	0.1	<0.5	<0.5	<0.5	4.9	1.2	7.9	0.1	3.1	1.9
Ba	687.1	610.8	776.7	646.5	637.4	566.6	727.1	268.4	129.5	29.4	93.6	284.2	119.1	199.9
Ce	74.4	62.0	60.4	67.1	53.9	56.9	63.3	61.6	32.7	-0.6	9.7	32.7	23.0	18.0
Co	51.3	51.7	37.2	39.5	31.5	53.8	39.8	37.5	45.7	55.5	19.1	115.5	106.1	92.0
Cr	28.3	16.5	27.9	31.9	31.0	31.7	33.5	117.6	<0.6	<0.6	<0.6	163.5	262.0	226.2
Cs	6.4	2.1	8.7	9.4	8.8	8.9	5.3	24.5	18.1	8.1	10.7	8.6	5.9	3.2
Cu	8.1	6.8	5.5	17.4	7.3	8.8	22.0	17.8	<0.5	1.3	0.5	26.3	29.3	3.4
Ga	18.8	16.5	18.4	17.6	18.4	17.0	20.3	25.1	16.8	17.2	17.5	21.8	22.1	20.0
La	40.8	31.8	29.9	30.3	26.2	26.4	32.1	26.1	13.7	1.2	6.0	13.4	11.5	9.5
Mo	1.2	1.1	1.2	1.0	1.3	1.0	1.5	1.3	1.0	0.7	0.8	1.4	1.5	1.7
Nb	15.4	10.9	13.7	15.1	14.3	15.4	15.9	13.1	12.5	13.5	13.3	15.9	15.7	10.3
Nd	33.7	27.8	24.8	28.7	26.2	25.4	29.4	23.4	14.3	3.5	5.9	16.5	14.3	11.0
Ni	15.0	10.8	18.0	33.5	15.6	14.3	17.4	36.2	3.0	0.6	3.6	142.4	130.9	155.2
Pb	20.4	9.8	16.7	10.2	60.5	4.6	10.7	48.3	25.7	28.5	19.0	3.8	6.8	4.4
Rb	220.6	184.6	231.1	224.7	240.7	147.5	188.1	200.3	349.1	313.1	332.2	86.2	33.7	48.0

Appendix 4 – Whole rock XRF data

Sb	0.6	<0.6	<0.6	<0.6	<0.6	0.2	0.5	0.2	<0.9	0.0	0.9	<1.2	<1.1	<1.1
Sc	5.9	5.6	5.9	6.4	6.6	10.4	10.7	15.3	4.0	3.4	4.2	22.3	25.7	21.1
Se	<0.6	<0.6	<0.6	<0.6	<0.6	<0.6	<0.6	<0.6	<0.6	<0.6	<0.5	<0.8	<0.8	<0.8
Sn	3.9	2.5	3.7	3.6	4.3	2.5	4.8	9.2	9.3	14.4	10.1	<1.1	<1.1	<1.0
Sr	113.5	78.7	82.3	73.8	133.6	72.0	110.1	52.1	27.2	23.8	18.7	234.2	282.4	286.9
Th	20.0	16.3	16.5	18.8	18.0	15.7	18.6	16.8	14.0	2.0	4.3	3.5	2.3	1.2
U	3.0	2.7	2.8	3.2	3.0	2.6	3.6	2.5	3.8	3.2	2.4	1.5	0.7	0.3
V	57.2	38.8	52.1	62.6	56.9	58.3	62.9	139.5	10.8	3.1	4.9	219.1	233.5	181.3
Y	45.1	33.5	29.4	37.5	31.2	30.7	35.5	21.6	26.9	6.7	17.1	23.6	21.7	16.3
Zn	59.3	42.9	61.5	80.8	61.7	43.9	67.1	96.9	31.7	23.4	19.2	113.9	91.8	92.2
Zr	180.1	119.2	162.6	168.5	158.3	158.6	180.3	178.8	79.9	7.0	39.2	113.6	101.4	66.0

Appendix 4 – Whole rock XRF data

XRF major element data and recommended values for international reference material. Highlighted row show recommended values taken from http://georem.mpch-mainz.gwdg.de/

IRM	Material	SiO2	TiO2	Al2O3	Fe2O3	MnO	MgO	CaO	Na2O	K2O	P2O5	SO3	Total
BH-1	***Bardon Hill microgranodiorite***	***68.07***	***0.43***	***14.35***	***5.81***	***0.14***	***2.50***	***3.53***	***3.94***	***0.87***	***0.07***	***0.00***	
BH-1	Bardon Hill microgranodiorite	68.73	0.41	14.60	5.82	0.14	2.68	3.59	3.68	0.84	0.07	0.06	100.63
BH-1	Bardon Hill microgranodiorite	68.88	0.41	14.59	5.82	0.14	2.65	3.60	3.66	0.84	0.07	0.06	100.73
BH-1	Bardon Hill microgranodiorite	68.83	0.41	14.56	5.82	0.14	2.65	3.59	3.66	0.84	0.07	0.06	100.65
BH-1	Bardon Hill microgranodiorite	68.82	0.41	14.59	5.83	0.14	2.67	3.60	3.67	0.84	0.07	0.06	100.70
BH-1	Bardon Hill microgranodiorite	66.60	0.41	13.97	5.78	0.13	2.57	3.53	3.83	0.83	0.07	0.07	97.79
BH-1	Bardon Hill microgranodiorite	68.41	0.41	14.40	5.82	0.14	2.67	3.57	3.70	0.84	0.07	0.03	100.07
BH-1	Bardon Hill microgranodiorite	68.48	0.41	14.36	5.83	0.14	2.66	3.60	3.68	0.84	0.07	0.06	100.12
BH-1	Bardon Hill microgranodiorite	68.44	0.41	14.31	5.74	0.13	2.66	3.58	3.67	0.84	0.07	0.05	99.90
BH-1	Bardon Hill microgranodiorite	68.44	0.41	14.31	5.74	0.13	2.66	3.58	3.67	0.84	0.07	0.05	99.90
BH-1	Bardon Hill microgranodiorite	68.85	0.41	14.49	5.83	0.14	2.67	3.59	3.69	0.84	0.07	0.05	100.63
BH-1	Bardon Hill microgranodiorite	68.47	0.41	14.32	5.83	0.14	2.67	3.57	3.71	0.84	0.07	0.04	100.06
BH-1	Bardon Hill microgranodiorite	67.50	0.41	14.20	5.84	0.14	2.64	3.58	3.65	0.84	0.07	0.03	98.90
BH-1	Bardon Hill microgranodiorite	68.34	0.42	14.33	5.82	0.14	2.66	3.57	3.68	0.84	0.07	0.03	99.88
BH-1	Bardon Hill microgranodiorite	68.41	0.41	14.31	5.83	0.14	2.66	3.57	3.69	0.83	0.07	0.03	99.95
BH-1	Bardon Hill microgranodiorite	68.44	0.41	14.35	5.83	0.14	2.66	3.57	3.68	0.84	0.07	0.02	100.01
BH-1	Bardon Hill microgranodiorite	68.40	0.41	14.31	5.83	0.14	2.67	3.57	3.68	0.83	0.07	0.02	99.95
BH-1	Bardon Hill microgranodiorite	67.03	0.40	14.39	5.83	0.14	2.65	3.49	3.68	0.81	0.06	0.02	98.50
BH-1	Bardon Hill microgranodiorite	68.31	0.41	14.32	5.83	0.14	2.64	3.56	3.69	0.83	0.07	0.02	99.82
BH-1	Bardon Hill microgranodiorite	68.45	0.41	14.34	5.83	0.14	2.66	3.58	3.68	0.83	0.07	0.02	100.01
Avg.		***68.31***	***0.41***	***14.37***	***5.82***	***0.14***	***2.66***	***3.57***	***3.69***	***0.84***	***0.07***	***0.04***	
St.Dev		***0.6***	***0.0***	***0.2***	***0.0***	***0.0***	***0.0***	***0.0***	***0.0***	***0.0***	***0.0***	***0.0***	
RSD (%)		***0.9***	***1.0***	***1.1***	***0.5***	***1.1***	***0.9***	***0.7***	***1.0***	***0.8***	***3.2***	***42.9***	
WS-1	***Whin Sill dolerite***	***51.31***	***2.54***	***14.04***	***13.51***	***0.18***	***5.31***	***8.87***	***3.10***	***1.36***	***0.30***	***0.00***	
WS-1	Whin Sill dolerite	52.33	2.50	14.24	13.50	0.17	5.43	8.79	2.87	1.32	0.31	0.15	101.62
WS-1	Whin Sill dolerite	52.39	2.49	14.24	13.51	0.17	5.42	8.79	2.83	1.33	0.31	0.15	101.64
WS-1	Whin Sill dolerite	52.30	2.50	14.21	13.51	0.17	5.42	8.80	2.81	1.32	0.31	0.16	101.52
WS-1	Whin Sill dolerite	52.13	2.51	14.18	13.54	0.17	5.39	8.83	2.84	1.33	0.31	0.17	101.39
WS-1	Whin Sill dolerite	50.57	2.52	13.65	13.59	0.17	5.22	8.63	3.02	1.30	0.31	0.18	99.17
WS-1	Whin Sill dolerite	51.69	2.53	13.96	13.56	0.17	5.35	8.82	2.81	1.32	0.31	0.17	100.69

Appendix 4 – Whole rock XRF data

IRM	Material	SiO2	TiO2	Al2O3	Fe2O3	MnO	MgO	CaO	Na2O	K2O	P2O5	SO3	Total
WS-1	Whin Sill dolerite	51.89	2.52	13.94	13.55	0.17	5.38	8.78	2.84	1.33	0.31	0.16	100.86
WS-1	Whin Sill dolerite	51.53	2.52	13.98	13.46	0.17	5.36	8.79	2.82	1.32	0.31	0.17	100.42
WS-1	Whin Sill dolerite	51.53	2.52	13.98	13.46	0.17	5.36	8.79	2.82	1.32	0.31	0.17	100.42
WS-1	Whin Sill dolerite	52.00	2.52	14.00	13.55	0.17	5.38	8.80	2.84	1.32	0.31	0.16	101.05
WS-1	Whin Sill dolerite	51.66	2.52	13.91	13.57	0.17	5.37	8.79	2.82	1.32	0.31	0.16	100.60
WS-1	Whin Sill dolerite	51.57	2.53	13.98	13.58	0.17	5.41	8.72	2.85	1.32	0.31	0.16	100.61
WS-1	Whin Sill dolerite	51.36	2.51	13.74	13.56	0.17	5.34	8.76	2.79	1.31	0.30	0.07	99.91
WS-1	Whin Sill dolerite	51.42	2.51	13.74	13.56	0.17	5.37	8.76	2.77	1.31	0.30	0.07	99.98
WS-1	Whin Sill dolerite	51.49	2.51	13.80	13.59	0.17	5.35	8.75	2.78	1.32	0.30	0.07	100.12
WS-1	Whin Sill dolerite	51.42	2.52	13.80	13.57	0.17	5.38	8.76	2.78	1.31	0.30	0.07	100.08
WS-1	Whin Sill dolerite	51.64	2.52	13.80	13.56	0.17	5.36	8.74	2.77	1.31	0.30	0.07	100.24
WS-1	Whin Sill dolerite	51.37	2.51	13.70	13.56	0.17	5.35	8.74	2.79	1.31	0.30	0.06	99.89
WS-1	Whin Sill dolerite	50.97	2.51	13.61	13.56	0.17	5.31	8.74	2.75	1.29	0.30	0.06	99.28
Avg.		***51.64***	***2.51***	***13.92***	***13.55***	***0.17***	***5.37***	***8.77***	***2.82***	***1.32***	***0.31***	***0.13***	
St.Dev		***0.5***	***0.0***	***0.2***	***0.0***	***0.0***	***0.0***	***0.0***	***0.1***	***0.0***	***0.0***	***0.0***	
RSD (%)		***0.9***	***0.4***	***1.4***	***0.3***	***0.9***	***0.9***	***0.5***	***2.1***	***0.7***	***1.3***	***37.4***	
BCS375	***feldspar***	***67.10***	***0.38***	***19.80***	***0.12***	***0.00***	***0.50***	***0.89***	***10.40***	***0.79***	***0.00***	***0.00***	
BCS375	feldspar	67.56	0.38	20.17	0.12	0.00	0.03	0.84	10.21	0.76	0.03	0.06	100.16
BCS375	feldspar	67.75	0.38	20.18	0.12	0.00	0.03	0.84	10.13	0.77	0.03	0.06	100.28
BCS375	feldspar	67.63	0.37	20.14	0.12	0.00	0.03	0.84	10.12	0.76	0.03	0.06	100.10
BCS375	feldspar	67.58	0.38	20.20	0.12	0.00	0.04	0.85	10.25	0.76	0.03	0.06	100.26
BCS375	feldspar	67.50	0.38	20.00	0.12	0.00	0.04	0.85	10.86	0.77	0.03	0.07	100.62
BCS375	feldspar	67.21	0.38	19.95	0.12	0.00	0.04	0.86	10.20	0.76	0.03	0.07	99.61
BCS375	feldspar	67.37	0.38	19.97	0.12	0.00	0.04	0.84	10.22	0.76	0.02	0.06	99.77
BCS375	feldspar	67.25	0.38	20.09	0.12	0.00	0.04	0.85	10.23	0.76	0.02	0.06	99.80
BCS375	feldspar	67.25	0.38	20.09	0.12	0.00	0.04	0.85	10.23	0.76	0.02	0.06	99.80
BCS375	feldspar	67.70	0.38	20.08	0.12	0.00	0.03	0.84	10.23	0.76	0.02	0.06	100.23
BCS375	feldspar	67.31	0.38	20.00	0.12	0.00	0.04	0.85	10.22	0.77	0.03	0.06	99.77
BCS375	feldspar	67.32	0.38	20.05	0.12	0.00	0.04	0.86	10.24	0.76	0.03	0.07	99.87
BCS375	feldspar	67.31	0.38	19.96	0.11	0.00	0.02	0.82	10.20	0.76	0.02	0.03	99.61
BCS375	feldspar	67.28	0.38	19.97	0.11	0.00	0.02	0.83	10.22	0.76	0.02	0.03	99.62
BCS375	feldspar	67.31	0.38	20.08	0.11	0.00	0.02	0.83	10.25	0.76	0.02	0.02	99.79
BCS375	feldspar	67.37	0.38	19.98	0.11	0.00	0.01	0.82	10.25	0.76	0.02	0.02	99.73

Appendix 4 – Whole rock XRF data

IRM	Material	SiO2	TiO2	Al2O3	Fe2O3	MnO	MgO	CaO	Na2O	K2O	P2O5	SO3	Total
BCS375	feldspar	67.60	0.38	20.05	0.11	0.00	0.02	0.82	10.22	0.76	0.02	0.02	100.01
BCS375	feldspar	67.28	0.38	19.93	0.11	0.00	0.01	0.83	10.22	0.76	0.02	0.02	99.56
BCS375	feldspar	67.25	0.37	19.98	0.11	0.00	0.01	0.82	10.19	0.76	0.02	0.02	99.54
Avg.		***67.41***	***0.38***	***20.05***	***0.12***	***0.00***	***0.03***	***0.84***	***10.25***	***0.76***	***0.02***	***0.05***	
St.Dev		***0.2***	***0.0***	***0.1***	***0.0***	***0.0***	***0.0***	***0.0***	***0.2***	***0.0***	***0.0***	***0.0***	
RSD (%)		***0.3***	***0.5***	***0.4***	***1.0***	***17.7***	***39.0***	***1.5***	***1.5***	***0.5***	***10.3***	***38.8***	
BCS376	***feldspar***	***67.10***	***0.00***	***17.70***	***0.10***	***0.00***	***0.03***	***0.54***	***2.83***	***11.20***	***0.00***		
BCS376	feldspar	67.45	0.01	18.05	0.10	0.00	0.05	0.50	2.87	11.27	0.02	0.07	100.40
BCS376	feldspar	67.54	0.01	18.10	0.11	0.00	0.05	0.51	2.83	11.27	0.02	0.08	100.52
BCS376	feldspar	67.62	0.01	18.08	0.10	0.00	0.05	0.51	2.84	11.28	0.02	0.07	100.59
BCS376	feldspar	67.50	0.01	18.09	0.11	0.00	0.05	0.51	2.85	11.27	0.02	0.07	100.48
BCS376	feldspar	67.23	0.01	17.39	0.11	0.00	0.05	0.51	3.02	11.36	0.02	0.09	99.79
BCS376	feldspar	67.08	0.01	17.84	0.11	0.00	0.05	0.50	2.88	11.25	0.02	0.06	99.79
BCS376	feldspar	67.27	0.01	17.88	0.11	0.00	0.05	0.50	2.88	11.25	0.02	0.07	100.05
BCS376	feldspar	67.16	0.01	17.97	0.10	0.00	0.05	0.50	2.87	11.26	0.02	0.07	100.02
BCS376	feldspar	67.16	0.01	17.97	0.10	0.00	0.05	0.50	2.87	11.26	0.02	0.07	100.02
BCS376	feldspar	67.66	0.01	17.99	0.10	0.00	0.05	0.50	2.87	11.28	0.02	0.07	100.55
BCS376	feldspar	67.17	0.01	17.81	0.10	0.00	0.05	0.50	2.87	11.25	0.02	0.06	99.84
BCS376	feldspar	67.76	0.01	18.04	0.10	0.00	0.05	0.51	2.90	11.30	0.02	0.06	100.75
BCS376	feldspar	67.12	0.01	17.82	0.10	0.00	0.02	0.48	2.85	11.28	0.01	0.03	99.72
BCS376	feldspar	67.09	0.01	17.79	0.10	0.00	0.02	0.48	2.84	11.28	0.01	0.03	99.65
BCS376	feldspar	67.15	0.01	17.85	0.10	0.00	0.02	0.48	2.84	11.28	0.01	0.03	99.78
BCS376	feldspar	67.09	0.00	17.84	0.10	0.00	0.02	0.48	2.85	11.28	0.01	0.03	99.70
BCS376	feldspar	67.59	0.01	17.88	0.10	0.00	0.02	0.48	2.86	11.31	0.01	0.02	100.27
BCS376	feldspar	67.13	0.01	17.78	0.10	0.00	0.02	0.47	2.85	11.27	0.01	0.02	99.66
BCS376	feldspar	67.20	0.01	17.84	0.10	0.00	0.02	0.47	2.84	11.28	0.01	0.02	99.79
Avg.		***67.31***	***0.01***	***17.89***	***0.10***	***0.00***	***0.04***	***0.49***	***2.87***	***11.28***	***0.02***	***0.06***	
St.Dev		***0.2***	***0.0***	***0.2***	***0.0***	***0.0***	***0.0***	***0.0***	***0.0***	***0.0***	***0.0***	***0.0***	
RSD (%)		***0.3***	***28.4***	***0.9***	***3.3***	***20.8***	***38.1***	***3.0***	***1.4***	***0.2***	***21.5***	***41.2***	
ARSiO2	***SiO2***	***100.00***	***0.00***	***0.00***	***0.00***	***0.00***	***0.00***	***0.00***	***0.00***	***0.00***	***0.00***		
ARSiO2	SiO2	99.86	0.00	0.01	0.00	0.00	-0.01	0.01	0.16	0.01	0.01	0.02	100.07

Appendix 4 – Whole rock XRF data

IRM	Material	SiO2	TiO2	Al2O3	Fe2O3	MnO	MgO	CaO	Na2O	K2O	P2O5	SO3	Total
ARSiO2	SiO2	99.99	0.01	0.00	0.00	0.00	0.00	0.00	0.16	0.01	0.01	0.02	100.19
ARSiO2	SiO2	99.91	0.01	0.00	0.00	0.00	0.00	0.00	0.15	0.01	0.01	0.02	100.09
ARSiO2	SiO2	99.85	0.00	0.00	0.00	0.00	0.00	0.01	0.16	0.01	0.01	0.02	100.05
ARSiO2	SiO2	96.75	0.02	0.46	0.02	0.00	0.14	0.13	0.27	0.03	0.02	0.23	98.07
ARSiO2	SiO2	98.43	0.03	0.70	0.03	0.00	0.20	0.19	0.31	0.04	0.03	0.26	100.23
ARSiO2	SiO2	99.16	0.02	0.49	0.02	0.00	0.15	0.13	0.25	0.03	0.02	0.19	100.46
ARSiO2	SiO2	99.06	0.02	0.59	0.02	0.00	0.17	0.16	0.27	0.03	0.02	0.23	100.57
ARSiO2	SiO2	99.06	0.02	0.59	0.02	0.00	0.17	0.16	0.27	0.03	0.02	0.23	100.57
ARSiO2	SiO2	99.57	0.02	0.57	0.02	0.00	0.17	0.16	0.27	0.03	0.02	0.21	101.07
ARSiO2	SiO2	98.96	0.02	0.60	0.03	0.00	0.17	0.16	0.28	0.03	0.02	0.22	100.49
ARSiO2	SiO2	99.66	0.02	0.63	0.03	0.00	0.19	0.17	0.28	0.04	0.02	0.23	101.28
ARSiO2	SiO2	99.21	0.00	-0.04	0.00	0.00	0.00	0.01	0.09	0.00	0.00	0.03	99.31
ARSiO2	SiO2	99.16	0.00	-0.06	0.00	0.00	-0.01	0.01	0.08	0.00	0.00	0.02	99.23
ARSiO2	SiO2	99.21	0.01	-0.06	0.00	0.00	-0.01	0.01	0.09	0.00	0.00	0.02	99.28
ARSiO2	SiO2	99.17	0.00	-0.06	0.00	0.00	-0.01	0.01	0.09	0.00	0.00	0.02	99.22
ARSiO2	SiO2	99.67	0.00	-0.06	0.00	0.00	-0.01	0.01	0.09	0.00	0.00	0.02	99.72
ARSiO2	SiO2	99.22	0.00	-0.07	0.00	0.00	-0.01	0.01	0.08	0.00	0.00	0.02	99.26
ARSiO2	SiO2	99.29	0.00	-0.07	0.00	0.00	-0.01	0.01	0.09	0.00	0.00	0.01	99.33
Avg.		***99.22***											
St.Dev		***0.7***											
RSD (%)		***0.7***											
ARAl2O3	***Al2O3***	***0.00***	***0.00***	***99.95***	***0.00***	***0.00***	***0.00***	***0.00***	***0.00***	***0.00***	***0.00***		
ARAl2O3	Al2O3	0.04	0.01	99.54	0.01	0.00	0.01	0.00	0.06	0.01	0.01	0.02	99.71
ARAl2O3	Al2O3	0.03	0.01	100.20	0.01	0.00	0.01	0.00	0.06	0.01	0.01	0.02	100.35
ARAl2O3	Al2O3	0.02	0.01	100.03	0.00	0.00	0.01	0.00	0.07	0.01	0.01	0.02	100.19
ARAl2O3	Al2O3	0.02	0.01	100.31	0.00	0.00	0.02	0.00	0.07	0.00	0.01	0.02	100.47
ARAL2O3	Al2O3	0.08	0.01	96.98	0.01	0.00	0.04	0.02	0.07	0.00	0.01	0.05	97.25
ARAL2O3	Al2O3	0.08	0.00	99.62	0.01	0.00	0.05	0.01	0.06	0.00	0.00	0.04	99.87
ARAL2O3	Al2O3	0.08	0.01	99.59	0.00	0.00	0.04	0.01	0.06	0.00	0.01	0.04	99.84
ARAL2O3	Al2O3	0.08	0.01	100.20	0.00	0.00	0.04	0.01	0.06	0.00	0.01	0.04	100.44
ARAL2O3	Al2O3	0.08	0.01	100.20	0.00	0.00	0.04	0.01	0.06	0.00	0.01	0.04	100.44
ARAL2O3	Al2O3	0.09	0.01	100.17	0.00	0.00	0.04	0.02	0.06	0.00	0.01	0.03	100.44
ARAL2O3	Al2O3	0.08	0.01	99.37	0.00	0.00	0.04	0.01	0.06	0.00	0.01	0.03	99.62

Appendix 4 – Whole rock XRF data

IRM	Material	SiO2	TiO2	Al2O3	Fe2O3	MnO	MgO	CaO	Na2O	K2O	P2O5	SO3	Total
ARAL2O3	Al2O3	0.08	0.00	100.25	0.00	0.00	0.04	0.01	0.06	0.00	0.00	0.03	100.49
ARAL2O3	Al2O3	0.09	0.01	99.52	0.00	0.00	0.05	0.02	0.06	0.00	0.01	0.03	99.79
ARAL2O3	Al2O3	0.08	0.00	99.38	0.00	0.00	0.04	0.02	0.06	0.00	0.00	0.03	99.64
ARAL2O3	Al2O3	0.09	0.01	99.92	0.01	0.00	0.04	0.02	0.06	0.00	0.00	0.03	100.17
ARAL2O3	Al2O3	0.08	0.01	99.76	0.00	0.00	0.05	0.02	0.06	0.00	0.00	0.03	100.01
ARAL2O3	Al2O3	0.09	0.00	100.12	0.01	0.00	0.04	0.02	0.05	0.00	0.00	0.03	100.38
ARAL2O3	Al2O3	-0.02	0.00	99.68	0.00	0.00	0.02	0.00	0.05	0.00	0.00	0.01	99.76
ARAL2O3	Al2O3	-0.02	0.01	99.68	0.00	0.00	0.04	0.00	0.05	0.00	0.00	0.01	99.77
Avg.				***99.71***									
St.Dev				***0.7***									
RSD (%)				***0.7***									
MRG-1	***gabbro***	***39.59***	***3.82***	***8.57***	***18.16***	***0.17***	***13.72***	***14.90***	***0.75***	***0.18***	***0.08***	***0.15***	
MRG-1	gabbro	39.49	3.87	8.53	18.24	0.16	13.71	15.03	0.84	0.20	0.06	0.17	100.29
MRG-1	gabbro	39.77	3.89	8.54	18.25	0.16	13.88	15.01	0.84	0.19	0.06	0.18	100.77
MRG-1	gabbro	39.76	3.89	8.53	18.26	0.16	13.83	15.03	0.85	0.20	0.07	0.19	100.74
MRG-1	gabbro	39.76	3.87	8.57	18.26	0.16	13.89	15.02	0.87	0.20	0.07	0.19	100.85
MRG-1	gabbro	39.04	3.94	8.49	18.47	0.16	13.17	15.13	0.90	0.20	0.07	0.36	99.93
MRG-1	gabbro	39.83	3.92	8.69	18.26	0.15	13.58	15.04	0.86	0.20	0.07	0.31	100.92
MRG-1	gabbro	39.79	3.91	8.74	18.27	0.15	13.62	15.05	0.87	0.20	0.07	0.32	101.01
MRG-1	gabbro	39.83	3.92	8.75	18.26	0.15	13.67	15.05	0.86	0.20	0.07	0.32	101.09
MRG-1	gabbro	39.83	3.92	8.75	18.26	0.15	13.67	15.05	0.86	0.20	0.07	0.32	101.09
MRG-1	gabbro	40.06	3.92	8.73	18.28	0.15	13.67	15.07	0.86	0.20	0.07	0.30	101.30
MRG-1	gabbro	39.79	3.92	8.67	18.26	0.15	13.61	15.07	0.86	0.20	0.07	0.30	100.90
MRG-1	gabbro	40.19	3.89	8.81	18.26	0.15	13.78	14.98	0.86	0.20	0.07	0.30	101.51
MRG-1	gabbro	39.47	3.91	8.53	18.29	0.15	13.67	15.03	0.79	0.19	0.07	0.25	100.35
MRG-1	gabbro	39.50	3.91	8.51	18.28	0.15	13.67	15.02	0.80	0.19	0.07	0.27	100.37
MRG-1	gabbro	39.49	3.92	8.54	18.31	0.15	13.68	15.02	0.79	0.19	0.07	0.25	100.41
MRG-1	gabbro	39.53	3.90	8.51	18.28	0.15	13.69	15.05	0.79	0.19	0.07	0.26	100.43
MRG-1	gabbro	39.62	3.91	8.52	18.29	0.15	13.69	15.04	0.79	0.19	0.07	0.27	100.53
MRG-1	gabbro	39.43	3.91	8.38	18.29	0.15	13.77	14.99	0.73	0.18	0.06	0.18	100.08
MRG-1	gabbro	39.51	3.92	8.38	18.27	0.15	13.76	14.97	0.73	0.18	0.06	0.18	100.11
Avg.		***39.67***	***3.91***	***8.59***	***18.28***	***0.15***	***13.68***	***15.03***	***0.83***	***0.20***	***0.07***	***0.26***	

Appendix 4 – Whole rock XRF data

St.Dev		***0.3***	***0.0***	***0.1***	***0.0***	***0.0***	***0.2***	***0.0***	***0.0***	***0.0***	***0.0***	***0.1***	
RSD (%)		***0.6***	***0.4***	***1.5***	***0.3***	***1.3***	***1.1***	***0.2***	***5.9***	***3.0***	***5.3***	***23.9***	
IRM	**Material**	**SiO2**	**TiO2**	**Al2O3**	**Fe2O3**	**MnO**	**MgO**	**CaO**	**Na2O**	**K2O**	**P2O5**	**SO3**	**Total**
NIM-D	***dunite***	***38.60***	***0.02***	***0.30***	***16.80***	***0.22***	***43.11***	***0.28***	***0.04***	***0.01***	***0.01***	***0.20***	
NIM-D	dunite	39.18	0.03	0.95	17.10	0.24	42.21	0.46	0.04	0.03	0.02	0.23	100.51
NIM-D	dunite	39.50	0.04	0.96	17.09	0.24	42.69	0.47	0.04	0.03	0.02	0.24	101.33
NIM-D	dunite	39.50	0.04	0.97	17.09	0.24	42.54	0.47	0.03	0.03	0.02	0.26	101.19
NIM-D	dunite	39.41	0.04	1.00	17.10	0.24	42.66	0.48	0.03	0.04	0.02	0.26	101.28
NIM-D	dunite	39.37	0.04	0.89	17.23	0.23	41.87	0.49	0.09	0.04	0.02	0.30	100.57
NIM-D	dunite	39.28	0.04	1.03	17.11	0.23	42.24	0.54	0.11	0.04	0.03	0.30	100.95
NIM-D	dunite	39.33	0.04	0.90	17.13	0.23	42.53	0.49	0.07	0.03	0.02	0.25	101.02
NIM-D	dunite	39.27	0.03	0.93	17.11	0.23	42.63	0.49	0.07	0.04	0.02	0.27	101.09
NIM-D	dunite	39.27	0.03	0.93	17.11	0.23	42.63	0.49	0.07	0.04	0.02	0.27	101.09
NIM-D	dunite	39.55	0.04	0.94	17.11	0.23	42.63	0.51	0.07	0.04	0.02	0.25	101.41
NIM-D	dunite	39.30	0.04	0.94	17.12	0.23	42.45	0.51	0.08	0.04	0.02	0.26	101.00
NIM-D	dunite	39.46	0.04	1.02	17.13	0.23	42.84	0.53	0.10	0.04	0.02	0.29	101.71
NIM-D	dunite	38.61	0.02	0.32	17.07	0.23	43.28	0.34	-0.08	0.01	0.01	0.07	99.88
NIM-D	dunite	38.76	0.03	0.31	17.09	0.23	43.26	0.33	-0.07	0.01	0.01	0.07	100.02
NIM-D	dunite	38.72	0.02	0.31	17.10	0.23	43.28	0.33	-0.09	0.01	0.01	0.07	100.02
NIM-D	dunite	38.18	0.02	0.31	17.10	0.23	43.26	0.34	-0.08	0.01	0.01	0.07	99.45
NIM-D	dunite	38.85	0.02	0.33	17.09	0.23	43.35	0.34	-0.07	0.01	0.01	0.08	100.26
NIM-D	dunite	38.62	0.02	0.19	17.08	0.23	43.50	0.29	-0.12	0.00	0.01	0.02	99.87
NIM-D	dunite	38.70	0.03	0.19	17.07	0.23	43.49	0.30	-0.12	0.01	0.00	0.02	99.92
Avg.		***39.10***	***0.03***	***0.71***	***17.11***	***0.23***	***42.81***	***0.43***	***0.01***	***0.03***	***0.02***	***0.19***	
St.Dev		***0.4***	***0.0***	***0.3***	***0.0***	***0.0***	***0.5***	***0.1***	***0.1***	***0.0***	***0.0***	***0.1***	
RSD (%)		***1.0***	***19.0***	***47.9***	***0.2***	***0.8***	***1.1***	***20.1***	***846.0***	***48.4***	***44.0***	***56.3***	
BCS372/1	***cement***	***20.30***	***0.27***	***5.37***	***3.42***	***0.03***	***1.31***	***65.30***	***0.10***	***0.75***	***0.07***	***2.95***	
BCS372/1	cement	20.12	0.27	5.31	3.43	0.04	1.36	65.56	0.23	0.77	0.08	2.66	99.83
BCS372/1	cement	20.27	0.27	5.34	3.43	0.04	1.37	65.66	0.24	0.77	0.08	2.85	100.31
BCS372/1	cement	20.23	0.27	5.33	3.42	0.04	1.36	65.60	0.23	0.77	0.08	2.91	100.25
BCS372/1	cement	20.26	0.27	5.35	3.42	0.04	1.37	65.56	0.24	0.77	0.08	2.92	100.29
BCS372/1	cement	20.48	0.28	5.41	3.46	0.04	1.38	65.79	0.25	0.78	0.09	3.37	101.32
BCS372/1	cement	20.48	0.28	5.43	3.43	0.03	1.43	65.26	0.24	0.78	0.09	2.84	100.29
BCS372/1	cement	20.48	0.28	5.41	3.43	0.03	1.43	65.31	0.23	0.77	0.09	2.93	100.38

Appendix 4 – Whole rock XRF data

IRM	Material	SiO2	TiO2	Al2O3	Fe2O3	MnO	MgO	CaO	Na2O	K2O	P2O5	SO3	Total
BCS372/1	cement	20.46	0.28	5.43	3.43	0.03	1.43	65.30	0.22	0.77	0.09	2.94	100.38
BCS372/1	cement	20.46	0.28	5.43	3.43	0.03	1.43	65.30	0.22	0.77	0.09	2.94	100.38
BCS372/1	cement	20.60	0.28	5.43	3.43	0.03	1.43	65.41	0.23	0.77	0.09	2.74	100.44
BCS372/1	cement	20.48	0.27	5.41	3.43	0.03	1.42	65.31	0.23	0.78	0.09	2.78	100.23
BCS372/1	cement	20.60	0.27	5.43	3.44	0.03	1.43	65.42	0.23	0.76	0.08	2.81	100.51
BCS372/1	cement	20.11	0.27	5.19	3.44	0.03	1.38	65.31	0.17	0.76	0.08	2.76	99.51
BCS372/1	cement	20.12	0.27	5.17	3.44	0.03	1.38	65.42	0.17	0.76	0.08	3.01	99.86
BCS372/1	cement	20.12	0.27	5.22	3.44	0.03	1.39	65.25	0.17	0.76	0.08	2.79	99.53
BCS372/1	cement	20.07	0.27	5.13	3.44	0.03	1.37	65.47	0.17	0.76	0.08	2.80	99.60
BCS372/1	cement	20.23	0.27	5.22	3.43	0.03	1.39	65.37	0.17	0.77	0.08	2.83	99.79
BCS372/1	cement	20.12	0.27	5.22	3.44	0.03	1.39	65.34	0.17	0.76	0.08	2.85	99.67
BCS372/1	cement	20.11	0.27	5.22	3.44	0.03	1.37	65.35	0.17	0.76	0.08	2.86	99.66
Avg.		***20.31***	***0.27***	***5.32***	***3.43***	***0.03***	***1.40***	***65.42***	***0.21***	***0.77***	***0.08***	***2.87***	
St.Dev		***0.2***	***0.0***	***0.1***	***0.0***	***0.0***	***0.0***	***0.1***	***0.0***	***0.0***	***0.0***	***0.1***	
RSD (%)		***0.9***	***1.0***	***2.0***	***0.2***	***3.6***	***2.0***	***0.2***	***15.6***	***0.7***	***3.5***	***5.1***	
Blank	***Li-Tetraborate***	***0.00***	***0.00***	***0.00***	***0.00***	***0.00***	***0.00***	***0.00***	***0.00***	***0.00***	***0.00***	***0.00***	
Blank	Li-Tetraborate	0.00	0.01	0.03	0.02	0.00	0.06	0.01	0.14	0.00	0.01	0.02	0.30
Blank	Li-Tetraborate	0.00	0.00	0.03	0.02	0.00	0.06	0.01	0.13	0.00	0.01	0.02	0.29
Blank	Li-Tetraborate	0.00	0.00	0.03	0.02	0.00	0.06	0.01	0.14	0.01	0.01	0.02	0.29
blank	Li-Tetraborate	0.00	0.00	0.02	0.02	0.00	0.06	0.01	0.14	0.01	0.01	0.02	0.28
Blank	Li-Tetraborate	0.24	0.01	0.22	0.02	0.00	0.12	0.03	0.15	0.00	0.01	0.05	0.85
Blank	Li-Tetraborate	0.27	0.01	0.25	0.02	0.00	0.12	0.04	0.14	0.00	0.01	0.05	0.91
Blank	Li-Tetraborate	0.23	0.01	0.23	0.02	0.00	0.12	0.03	0.13	0.00	0.01	0.04	0.82
Blank	Li-Tetraborate	0.22	0.01	0.24	0.02	0.00	0.12	0.03	0.13	0.00	0.01	0.04	0.82
Blank	Li-Tetraborate	0.22	0.01	0.24	0.02	0.00	0.12	0.03	0.13	0.00	0.01	0.04	0.82
Blank	Li-Tetraborate	0.22	0.00	0.24	0.02	0.00	0.12	0.03	0.13	0.00	0.01	0.04	0.82
Blank	Li-Tetraborate	0.22	0.01	0.23	0.02	0.00	0.12	0.03	0.13	0.00	0.01	0.04	0.80
Blank	Li-Tetraborate	0.26	0.01	0.25	0.02	0.00	0.12	0.04	0.13	0.00	0.01	0.05	0.88
Blank	Li-Tetraborate	0.08	0.00	0.17	0.02	0.00	0.10	0.02	0.11	0.00	0.00	0.02	0.53
Blank	Li-Tetraborate	0.06	0.00	0.16	0.02	0.00	0.10	0.02	0.11	0.00	0.00	0.02	0.51
Blank	Li-Tetraborate	0.07	0.00	0.17	0.02	0.00	0.10	0.02	0.10	0.00	0.00	0.02	0.51
Blank	Li-Tetraborate	0.06	0.00	0.16	0.02	0.00	0.10	0.02	0.11	0.00	0.00	0.01	0.51
Blank	Li-Tetraborate	0.06	0.00	0.17	0.02	0.00	0.10	0.02	0.11	0.00	0.00	0.02	0.51

Appendix 4 – Whole rock XRF data

Blank	Li-Tetraborate	0.05	0.00	0.16	0.02	0.00	0.10	0.02	0.10	0.00	0.00	0.01	0.47
Blank	Li-Tetraborate	0.06	0.00	0.17	0.02	0.00	0.10	0.02	0.11	0.00	0.00	0.01	0.50

Appendix 4 – Whole rock XRF data

XRF trace element data and recommended values for international reference material. Highlighted row shows recommended values taken from http://georem.mpch-mainz.gwdg.de/

IRM	Material	Rb	Sr	Y	Zr	Nb	Mo	Pb	Th	U	Ga	Zn	Cu	Ni	Co	Cr	V	Sc	Ba	La	Ce	Nd	Cs	As	Sb	Se	Sn	W
NIM-G	***Granite***	***312.0***	***12.5***	***14 1.0***	***296.0***	***55.7***	***3.0***	***35.7***	***53.9***	***15.0***	***27 .0***	***52.3***	***16.8***	***8.0***	***4.0***	***12.0***	***2.0***	***1.2***	***115.0***	***109 .0***	***19 5.0***	***72.0***	***0.9***	***15.0***	***0.6***	***-***	***4.0***	***-***
NIM-G	Granite	319.1	10.5	14 3.3	286.3	54.9	1.1	39.0	51.2	16.5	27 .8	54.9	16.3	7.9	1.8	19.4	2.3	0.1	111.4	119 .3	20 9.7	76.6	4.7	13.1	0.5	-0.5	5.8	7.1
NIM-G	Granite	319.2	10.4	14 3.7	286.8	55.0	1.1	38.7	51.3	16.5	28 .2	54.5	15.6	8.6	0.3	17.5	2.8	0.8	107.5	118 .5	20 9.9	75.8	7.3	13.2	2.0	-0.1	4.8	7.5
NIM-G	Granite	317.7	11.3	14 3.0	284.4	55.2	1.0	37.7	51.1	15.8	28 .3	54.2	16.5	8.6	0.2	20.5	1.0	1.3	112.9	121 .9	20 6.3	76.5	4.7	12.4	1.1	-0.1	5.5	6.8
Avg.		***318.6***	***10.7***	***14 3.3***	***285.8***	***55.0***	***1.1***	***38.5***	***51.2***	***16.2***	***28 .1***	***54.5***	***16.1***	***8.4***	***0.8***	***19.1***	***2.1***	***0.7***	***110.6***	***119 .9***	***20 8.6***	***76.3***	***5.5***	***12.9***	***1.2***	***-0.2***	***5.4***	***7.1***
St.Dev		***0.8***	***0.5***	***0.3***	***1.3***	***0.2***	***0.1***	***0.7***	***0.1***	***0.4***	***0.2***	***0.3***	***0.5***	***0.4***	***0.9***	***1.5***	***0.9***	***0.6***	***2.8***	***1.8***	***2.0***	***0.4***	***1.5***	***0.4***	***0.8***	***0.2***	***0.5***	***0.3***
RSD (%)		***0.3***	***4.5***	***0.2***	***0.4***	***0.3***	***4.8***	***1.8***	***0.2***	***2.4***	***0.9***	***0.6***	***3.0***	***4.5***	***117 .8***	***7.8***	***46.1***	***85.7***	***2.5***	***1.5***	***1.0***	***0.6***	***26.9***	***3.5***	***66.5***	***-112 .4***	***9.6***	***4.9***
MRG-1	***Gabbro***	***8.5***	***266.0***	***14.0***	***108.0***	***20.0***	***0.9***	***10.0***	***0.9***	***0.2***	***17 .0***	***191.0***	***134.0***	***193.0***	***87.0***	***430.0***	***52 6.0***	***55.0***	***51.0***	***9.8***	***28.0***	***19.2***	***0.6***	***0.7***	***0.9***	***0.2***	***3.6***	***0.3***
MRG-1	Gabbro	8.6	275.0	14.0	110.9	22.2	2.8	5.4	1.0	1.2	17 .6	215.8	135.4	193.6	85.8	461.6	54 8.6	55.8	51.0	9.0	32.1	18.9	2.3	-0.3	0.0	0.5	4.1	-2.0
MRG-1	Gabbro	8.7	274.5	14.3	110.8	21.7	2.7	5.2	1.8	0.7	18 .5	214.7	135.2	195.9	87.7	458.9	54 7.8	56.3	51.0	4.7	28.9	16.7	3.4	1.3	0.7	0.7	3.2	-2.2
MRG-1	Gabbro	9.1	275.0	14.2	107.6	21.6	2.7	4.6	0.7	0.7	19 .0	215.4	135.2	194.5	87.5	457.7	54 7.6	57.0	51.3	4.5	29.6	17.7	-1.1	0.9	-0.6	0.4	2.9	-1.6
Avg.		***8.8***	***274.9***	***14.2***	***109.7***	***21.9***	***2.7***	***5.1***	***1.2***	***0.9***	***18 .4***	***215.3***	***135.2***	***194.7***	***87.0***	***459.4***	***54 8.0***	***56.4***	***51.1***	***6.1***	***30.2***	***17.8***	***1.5***	***0.6***	***0.0***	***0.5***	***3.4***	***-1.9***
St.Dev		***0.3***	***0.3***	***0.2***	***1.9***	***0.3***	***0.1***	***0.4***	***0.5***	***0.3***	***0.7***	***0.6***	***0.1***	***1.2***	***1.1***	***2.0***	***0.6***	***0.6***	***0.2***	***2.5***	***1.7***	***1.1***	***2.3***	***0.8***	***0.6***	***0.1***	***0.6***	***0.3***
RSD (%)		***2.9***	***0.1***	***1.3***	***1.7***	***1.5***	***2.2***	***8.1***	***46.5***	***37.5***	***3.8***	***0.3***	***0.1***	***0.6***	***1.2***	***0.4***	***0.1***	***1.0***	***0.3***	***42.0***	***5.5***	***6.0***	***153 .2***	***128 .8***	***177 1.2***	***26.1***	***18.2***	***-16.4***
MA-N	***Granite***	***3600.0***	***84.0***	***0.4***	***25.0***	***173.0***	***0.3***	***29.0***	***1.4***	***12.5***	***59 .0***	***220.0***	***140.0***	***3.0***	***0.5***	***3.0***	***0.2***	***0.2***	***42.0***	***0.5***	***0.9***	***0.4***	***640 .0***	***13.0***	***1.7***	***0.0***	***900.0***	***70.0***
MA-N	Granite	3600.4	85.6	0.2	25.5	165.1	-0.2	28.9	1.5	12.6	58 .0	226.6	139.0	25.0	-1.6	10.3	8.4	-2.8	54.1	6.0	10.9	1.5	639 .9	12.8	-0.7	0.8	829.7	69.0
MA-N	Granite	3600.6	85.7	0.6	25.7	165.0	-0.2	29.0	1.3	12.5	57 .5	225.1	138.9	26.6	-0.4	9.6	7.7	-3.5	54.3	7.0	8.8	2.5	639 .8	13.5	3.5	1.3	833.8	68.3

Appendix 4 – Whole rock XRF data

IRM	Material	Rb	Sr	Y	Zr	Nb	Mo	Pb	Th	U	Ga	Zn	Cu	Ni	Co	Cr	V	Sc	Ba	La	Ce	Nd	Cs	As	Sb	Se	Sn	W
MA-N	Granite	3599.4	86.7	0.2	23.6	165.5	-0.2	28.9	1.4	12.5	57.8	225.7	139.4	25.1	-2.1	9.7	9.2	-2.1	56.7	5.2	8.6	1.5	639.6	12.2	1.3	1.3	829.8	68.4
Avg.		***3600.1***	***86.0***	***0.3***	***24.9***	***165.2***	***-0.2***	***28.9***	***1.4***	***12.5***	***57.8***	***225.8***	***139.1***	***25.6***	***-1.4***	***9.9***	***8.4***	***-2.8***	***55.0***	***6.1***	***9.4***	***1.8***	***639.8***	***12.8***	***1.4***	***1.1***	***831.1***	***68.5***
St.Dev		***0.7***	***0.6***	***0.3***	***1.2***	***0.3***	***0.0***	***0.1***	***0.1***	***0.0***	***0.2***	***0.7***	***0.3***	***0.9***	***0.9***	***0.4***	***0.7***	***0.7***	***1.4***	***0.9***	***1.3***	***0.6***	***0.1***	***0.7***	***2.1***	***0.3***	***2.3***	***0.4***
RSD (%)		***0.0***	***0.7***	***77.9***	***4.7***	***0.2***	***-11.6***	***0.2***	***5.2***	***0.3***	***0.4***	***0.3***	***0.2***	***3.4***	***-64.0***	***3.9***	***8.9***	***-25.4***	***2.6***	***14.6***	***13.7***	***32.2***	***0.0***	***5.2***	***156.3***	***25.5***	***0.3***	***0.6***
STM-1	***Nepheline syenite***	***118.0***	***700.0***	***46.0***	***1380.0***	***268.0***	***5.2***	***17.7***	***31.0***	***9.1***	***36.0***	***235.0***	***4.6***	***3.0***	***0.9***	***4.3***	***8.7***	***0.6***	***560.0***	***150.0***	***259.0***	***79.0***	***1.5***	***4.6***	***1.7***	***0.0***	***6.8***	***3.6***
STM-1	Nepheline syenite	116.5	712.6	43.6	1378.1	257.9	5.7	17.7	30.4	7.8	37.3	226.9	12.7	5.1	2.9	13.1	2.5	1.4	561.9	144.0	251.8	78.3	6.8	6.2	2.1	-0.3	8.0	2.4
STM-1	Nepheline syenite	116.9	712.6	43.7	1377.4	258.1	5.8	16.7	31.1	7.9	37.5	227.0	12.5	3.9	2.0	13.6	1.9	1.7	573.3	144.1	254.0	80.1	6.1	7.0	1.2	-1.0	8.8	1.5
STM-1	Nepheline syenite	116.7	713.8	43.4	1374.2	258.6	5.7	17.1	31.2	7.9	36.6	227.7	13.1	5.5	2.1	14.3	2.4	0.9	574.0	146.5	254.3	79.9	5.0	6.3	1.2	0.4	8.0	3.0
Avg.		***116.7***	***713.0***	***43.6***	***1376.6***	***258.2***	***5.7***	***17.2***	***30.9***	***7.9***	***37.1***	***227.2***	***12.8***	***4.9***	***2.4***	***13.7***	***2.3***	***1.3***	***569.7***	***144.9***	***253.4***	***79.4***	***6.0***	***6.5***	***1.5***	***-0.3***	***8.3***	***2.3***
St.Dev		***0.2***	***0.7***	***0.1***	***2.1***	***0.4***	***0.1***	***0.5***	***0.4***	***0.1***	***0.4***	***0.4***	***0.3***	***0.8***	***0.5***	***0.6***	***0.3***	***0.4***	***6.8***	***1.4***	***1.3***	***1.0***	***0.9***	***0.5***	***0.5***	***0.7***	***0.4***	***0.8***
RSD (%)		***0.2***	***0.1***	***0.3***	***0.2***	***0.1***	***1.2***	***2.7***	***1.4***	***1.0***	***1.2***	***0.2***	***2.3***	***16.9***	***21.0***	***4.4***	***13.2***	***31.8***	***1.2***	***1.0***	***0.5***	***1.3***	***15.0***	***7.0***	***35.6***	***-224.2***	***5.4***	***34.0***
PCC-1	***Peridotite***	***0.1***	***0.4***	***0.1***	***0.2***	***1.0***	***2.0***	***10.0***	***0.0***	***0.0***	***0.7***	***42.0***	***10.0***	***2380.0***	***112.0***	***2730.0***	***31.0***	***8.4***	***1.2***	***0.1***	***0.1***	***0.0***	***0.0***	***0.1***	***1.3***	***0.0***	***1.6***	***0.0***
PCC-1	Peridotite	2.1	-0.3	0.6	0.9	1.5	0.6	9.1	-0.3	-0.3	1.2	48.5	17.0	2381.3	112.8	2729.7	32.4	8.0	3.0	-0.5	-0.5	0.9	-2.7	-0.5	1.3	-0.1	0.3	-9.5
PCC-1	Peridotite	2.0	-0.3	0.5	1.2	1.5	0.6	8.6	-0.4	0.6	1.3	47.1	16.3	2381.5	111.1	2730.6	32.6	7.9	4.5	0.9	-7.4	-1.4	-1.3	-0.6	0.6	-0.6	0.1	-9.7
PCC-1	Peridotite	2.6	0.1	0.9	-0.6	1.7	0.5	8.5	0.0	1.0	1.6	48.6	16.7	2382.4	112.2	2729.0	32.6	7.7	1.9	-1.9	-5.1	-0.7	-5.1	-0.1	0.9	-0.2	0.5	-11.3
Avg.		***2.2***	***-0.2***	***0.7***	***0.5***	***1.5***	***0.6***	***8.7***	***-0.2***	***0.4***	***1.4***	***48.1***	***16.7***	***2381.7***	***112.0***	***2729.8***	***32.5***	***7.9***	***3.1***	***-0.5***	***-4.3***	***-0.4***	***-3.0***	***-0.4***	***0.9***	***-0.3***	***0.3***	***-10.2***
St.Dev		***0.3***	***0.3***	***0.2***	***1.0***	***0.1***	***0.1***	***0.3***	***0.2***	***0.7***	***0.2***	***0.8***	***0.4***	***0.6***	***0.9***	***0.8***	***0.1***	***0.2***	***1.3***	***1.4***	***3.5***	***1.2***	***1.9***	***0.3***	***0.4***	***0.3***	***0.2***	***1.0***

Appendix 4 – Whole rock XRF data

RSD (%)		*14.5*	*-131.7*	*32.4*	*191.2*	*8.9*	*12.8*	*3.6*	*-88.8*	*155.5*	*14.6*	*1.7*	*2.2*	*0.0*	*0.8*	*0.0*	*0.3*	*2.2*	*41.5*	*-267.4*	*-81.3*	*-314.4*	*-62.6*	*-68.3*	*40.5*	*-80.8*	*62.2*	*-9.5*
IRM	**Material**	**Rb**	**Sr**	**Y**	**Zr**	**Nb**	**Mo**	**Pb**	**Th**	**U**	**Ga**	**Zn**	**Cu**	**Ni**	**Co**	**Cr**	**V**	**Sc**	**Ba**	**La**	**Ce**	**Nd**	**Cs**	**As**	**Sb**	**Se**	**Sn**	**W**
BHVO-1	***Basalt***	***9.5***	***399.2***	***26.2***	***174.6***	***18.5***	***1.1***	***2.0***	***1.2***	***0.4***	***21.3***	***105.1***	***137.2***	***120.0***	***44.9***	***287.6***	***313.8***	***31.4***	***134.4***	***15.4***	***38.1***	***24.8***	***0.1***	***0.6***	***0.2***	***0.1***	***2.1***	***0.2***
BHVO-1	Basalt	9.8	395.2	27.6	181.5	19.4	1.4	3.8	0.8	0.6	20.1	121.6	162.8	125.9	44.0	278.8	297.2	30.8	131.5	12.9	37.8	25.3	1.9	0.6	0.9	0.3	0.9	-1.3
BHVO-1	Basalt	9.7	394.9	27.8	180.4	19.5	1.6	2.7	1.3	0.9	19.8	121.4	160.4	125.1	43.4	274.1	299.0	30.6	135.5	12.6	42.8	24.4	0.5	-0.1	1.4	0.4	1.8	-1.9
BHVO-1	Basalt	10.7	397.5	28.1	177.5	19.5	1.5	4.0	1.3	0.3	20.9	121.2	161.3	124.9	45.7	279.1	296.2	29.8	139.6	14.4	38.0	23.3	1.8	0.6	-1.0	0.9	1.7	-2.4
Avg.		***10.1***	***395.9***	***27.8***	***179.8***	***19.5***	***1.5***	***3.5***	***1.1***	***0.6***	***20.3***	***121.4***	***161.5***	***125.3***	***44.4***	***277.3***	***297.4***	***30.4***	***135.5***	***13.3***	***39.6***	***24.3***	***1.4***	***0.4***	***0.4***	***0.5***	***1.5***	***-1.9***
St.Dev		***0.5***	***1.4***	***0.2***	***2.1***	***0.0***	***0.1***	***0.7***	***0.3***	***0.3***	***0.6***	***0.2***	***1.2***	***0.5***	***1.2***	***2.8***	***1.4***	***0.5***	***4.1***	***1.0***	***2.8***	***1.0***	***0.7***	***0.4***	***1.3***	***0.3***	***0.5***	***0.5***
RSD (%)		***5.4***	***0.4***	***0.9***	***1.2***	***0.2***	***5.0***	***20.9***	***26.4***	***48.8***	***2.7***	***0.1***	***0.8***	***0.4***	***2.7***	***1.0***	***0.5***	***1.7***	***3.0***	***7.3***	***7.2***	***4.1***	***52.9***	***101.9***	***285.0***	***59.4***	***35.9***	***-29.0***
G-2	***Granite***	***168.5***	***474.9***	***9.9***	***319.0***	***12.0***	***0.4***	***30.0***	***24.5***	***2.0***	***23.3***	***83.5***	***11.0***	***3.5***	***4.5***	***7.9***	***35.1***	***3.7***	***1860.0***	***88.4***	***161.2***	***53.8***	***1.4***	***0.3***	***0.1***	***0.1***	***1.7***	***0.1***
G-2	Granite	167.4	471.2	8.8	309.3	12.3	0.4	29.7	24.2	1.9	22.8	80.4	11.4	1.8	4.2	14.3	38.4	3.4	1867.2	98.9	169.8	53.9	-4.6	-0.4	0.5	-0.6	1.8	-1.0
G-2	Granite	167.6	469.5	7.9	309.0	12.4	0.5	29.2	24.0	1.9	21.9	81.1	11.3	2.8	3.2	13.4	37.1	3.8	1867.1	100.8	169.0	53.5	-5.1	-0.4	-0.3	-0.5	0.4	-2.5
G-2	Granite	166.7	471.3	8.7	306.3	12.2	0.5	29.3	24.2	1.8	21.8	79.9	11.6	3.2	4.5	16.7	36.8	3.2	1873.0	102.1	166.7	53.2	-4.5	0.3	-0.4	-0.4	1.5	-0.7
Avg.		***167.2***	***470.7***	***8.5***	***308.2***	***12.3***	***0.5***	***29.4***	***24.1***	***1.9***	***22.2***	***80.5***	***11.5***	***2.6***	***4.0***	***14.8***	***37.5***	***3.5***	***1869.1***	***100.6***	***168.5***	***53.6***	***-4.8***	***-0.2***	***-0.1***	***-0.5***	***1.2***	***-1.4***
St.Dev		***0.5***	***1.0***	***0.5***	***1.7***	***0.1***	***0.0***	***0.3***	***0.1***	***0.1***	***0.6***	***0.6***	***0.1***	***0.7***	***0.7***	***1.7***	***0.9***	***0.3***	***3.4***	***1.6***	***1.6***	***0.4***	***0.3***	***0.4***	***0.5***	***0.1***	***0.7***	***0.9***
RSD (%)		***0.3***	***0.2***	***5.6***	***0.5***	***0.8***	***6.3***	***0.9***	***0.5***	***4.5***	***2.6***	***0.8***	***1.2***	***28.2***	***16.8***	***11.5***	***2.3***	***9.3***	***0.2***	***1.6***	***0.9***	***0.7***	***-7.1***	***-258.4***	***-614.8***	***-20.7***	***59.9***	***-68.8***
GSP-1	***Granodiorite***	***254.0***	***234.0***	***26.0***	***565.0***	***27.9***	***0.8***	***55.0***	***106.0***	***2.5***	***23.0***	***104.0***	***33.0***	***8.8***	***6.6***	***13.0***	***53.0***	***6.2***	***1310.0***	***184.0***	***39.0***	***196.0***	***1.0***	***0.1***	***3.2***	***0.1***	***6.6***	***0.3***
GSP-1	Granodiorite	257.8	236.0	24.7	568.2	26.9	2.1	59.5	95.4	2.1	22.1	97.5	35.8	9.7	5.9	9.0	53.0	6.0	1314.1	141.3	329.8	152.1	3.5	-0.4	3.2	-0.9	7.2	-0.7

Appendix 4 – Whole rock XRF data

IRM	Material	Rb	Sr	Y	Zr	Nb	Mo	Pb	Th	U	Ga	Zn	Cu	Ni	Co	Cr	V	Sc	Ba	La	Ce	Nd	Cs	As	Sb	Se	Sn	W
GSP-1	Granodiorite	258.3	237.2	24.6	568.0	27.0	2.0	60.1	95.9	2.5	22.5	99.4	36.5	10.6	8.5	8.4	51.5	5.5	1312.6	140.1	332.1	153.2	2.2	-2.3	4.0	-0.6	8.0	-0.1
GSP-1	Granodiorite	257.6	238.1	24.6	565.4	27.0	2.1	59.4	95.9	2.1	22.7	99.6	36.4	11.0	6.2	9.4	51.9	6.5	1318.6	143.4	326.3	153.5	0.2	-0.1	2.4	0.0	8.5	-0.9
Avg.		***257.9***	***237.1***	***24.6***	***567.2***	***26.9***	***2.1***	***59.7***	***95.7***	***2.2***	***22.4***	***98.8***	***36.2***	***10.4***	***6.8***	***8.9***	***52.1***	***6.0***	***1315.1***	***141.6***	***329.4***	***152.9***	***2.0***	***-0.9***	***3.2***	***-0.5***	***7.9***	***-0.5***
St.Dev		***0.4***	***1.0***	***0.1***	***1.6***	***0.1***	***0.1***	***0.4***	***0.3***	***0.2***	***0.3***	***1.2***	***0.4***	***0.6***	***1.4***	***0.5***	***0.7***	***0.5***	***3.1***	***1.7***	***2.9***	***0.7***	***1.7***	***1.2***	***0.8***	***0.4***	***0.7***	***0.4***
RSD (%)		***0.1***	***0.4***	***0.2***	***0.3***	***0.3***	***3.8***	***0.7***	***0.3***	***10.9***	***1.4***	***1.2***	***1.1***	***6.1***	***20.9***	***5.4***	***1.4***	***8.2***	***0.2***	***1.2***	***0.9***	***0.5***	***84.0***	***-126.9***	***25.4***	***-92.0***	***8.3***	***-79.4***
BIR-1	***Basalt***	***0.2***	***108.6***	***15.6***	***14.8***	***0.6***	***0.1***	***3.0***	***0.0***	***0.0***	***15.5***	***70.4***	***120.7***	***168.9***	***52.2***	***392.9***	***320.6***	***43.2***	***6.8***	***0.6***	***1.9***	***2.4***	***0.0***	***0.2***	***0.5***	***0.0***	***0.7***	***0.0***
BIR-1	Basalt	1.9	108.5	17.6	15.1	2.5	0.7	4.5	0.9	0.8	16.1	68.5	127.4	171.0	52.7	378.6	314.4	39.9	15.7	-1.2	2.2	2.4	-1.8	-0.5	-1.1	0.1	1.0	-0.8
BIR-1	Basalt	2.0	108.9	17.5	15.5	2.6	0.9	4.1	0.4	0.5	14.4	69.3	127.3	171.3	50.9	380.2	313.8	40.6	13.5	0.3	3.0	2.9	-1.8	0.6	-0.4	-0.8	-0.3	0.9
BIR-1	Basalt	2.8	109.4	17.7	13.6	2.5	0.6	2.7	-1.0	-0.3	15.5	69.3	127.3	169.6	49.8	379.0	312.4	39.1	16.7	-0.6	3.8	0.7	-1.0	-0.6	0.3	-0.7	-1.0	-0.2
Avg.		***2.2***	***108.9***	***17.6***	***14.7***	***2.5***	***0.8***	***3.8***	***0.1***	***0.3***	***15.3***	***69.0***	***127.3***	***170.6***	***51.1***	***379.3***	***313.5***	***39.8***	***15.3***	***-0.5***	***3.0***	***2.0***	***-1.5***	***-0.2***	***-0.4***	***-0.5***	***-0.1***	***0.0***
St.Dev		***0.5***	***0.5***	***0.1***	***1.0***	***0.1***	***0.2***	***1.0***	***1.0***	***0.6***	***0.9***	***0.4***	***0.0***	***0.9***	***1.5***	***0.8***	***1.0***	***0.7***	***1.7***	***0.8***	***0.8***	***1.1***	***0.4***	***0.7***	***0.7***	***0.5***	***1.0***	***0.9***
RSD (%)		***21.8***	***0.4***	***0.6***	***6.8***	***2.5***	***22.5***	***25.3***	***1196.3***	***169.8***	***5.6***	***0.6***	***0.0***	***0.5***	***2.9***	***0.2***	***0.3***	***1.9***	***10.8***	***-146.0***	***27.5***	***57.3***	***-29.6***	***-399.2***	***-174.0***	***-110.1***	***-1133.6***	***-1881.1***
BCR-1	***Basalt***	***46.6***	***334.9***	***36.9***	***190.3***	***12.7***	***1.5***	***13.4***	***5.8***	***1.7***	***22.2***	***128.5***	***19.6***	***11.7***	***37.6***	***13.5***	***404.4***	***32.4***	***683.3***	***25.5***	***53.9***	***28.7***	***1.0***	***0.6***	***0.6***	***0.1***	***2.4***	***0.4***
BCR-1	Basalt	49.0	332.6	38.2	198.6	13.2	2.6	13.9	5.6	1.9	22.6	124.0	40.8	10.0	36.3	14.8	383.4	28.2	713.1	25.6	57.6	29.8	1.4	1.3	1.0	-0.3	0.1	1.3
BCR-1	Basalt	48.6	332.4	38.3	198.5	13.2	2.4	13.9	6.5	1.4	22.0	123.2	40.5	10.3	38.6	9.3	384.7	29.9	724.7	26.7	58.8	31.8	-1.3	1.3	-0.9	0.8	1.3	0.8
BCR-1	Basalt	48.9	333.8	38.7	195.8	13.4	2.0	13.5	5.6	1.3	22.6	124.5	40.5	11.1	37.2	4.7	388.2	28.9	713.4	25.1	56.7	28.8	-0.8	0.5	1.6	-0.1	2.4	0.6
Avg.		***48.8***	***332.9***	***38.4***	***197.7***	***13.3***	***2.3***	***13.8***	***5.9***	***1.5***	***22.4***	***123.9***	***40.6***	***10.5***	***37.4***	***9.6***	***385.4***	***29.0***	***717.1***	***25.8***	***57.7***	***30.1***	***-0.2***	***1.0***	***0.6***	***0.1***	***1.3***	***0.9***

Appendix 4 – Whole rock XRF data

St.Dev		*0.2*	*0.7*	*0.3*	*1.6*	*0.1*	*0.3*	*0.3*	*0.5*	*0.3*	*0.3*	*0.7*	*0.2*	*0.6*	*1.2*	*5.1*	*2.5*	*0.9*	*6.6*	*0.8*	*1.0*	*1.5*	*1.4*	*0.5*	*1.3*	*0.6*	*1.2*	*0.4*
RSD (%)		*0.5*	*0.2*	*0.7*	*0.8*	*0.8*	*12.7*	*1.9*	*8.9*	*19.9*	*1.5*	*0.5*	*0.4*	*5.4*	*3.1*	*52.6*	*0.6*	*3.1*	*0.9*	*3.2*	*1.8*	*5.1*	*-590.9*	*45.3*	*223.8*	*403.9*	*92.9*	*41.1*
IRM	**Material**	**Rb**	**Sr**	**Y**	**Zr**	**Nb**	**Mo**	**Pb**	**Th**	**U**	**Ga**	**Zn**	**Cu**	**Ni**	**Co**	**Cr**	**V**	**Sc**	**Ba**	**La**	**Ce**	**Nd**	**Cs**	**As**	**Sb**	**Se**	**Sn**	**W**
JSd-1	*Stream sediment*	*67.4*	*340.0*	*14.8*	*132.0*	*11.1*	*0.5*	*12.9*	*4.4*	*1.0*	*17.2*	*96.5*	*22.2*	*7.0*	*11.2*	*22.0*	*76.0*	*10.9*	*520.0*	*18.6*	*34.4*	*17.8*	*2.0*	*2.4*	*0.5*	*0.1*	*2.8*	*0.5*
JSd-1	Stream sediment	65.5	330.7	14.9	126.0	12.0	0.6	12.6	3.4	0.4	16.6	89.5	22.2	5.9	12.5	19.2	79.6	10.5	537.4	13.6	26.8	15.9	-0.7	2.1	-0.2	-0.1	0.6	-0.9
JSd-1	Stream sediment	65.7	330.2	14.6	126.1	12.0	0.4	12.5	3.6	0.8	16.2	89.6	22.3	6.5	11.3	18.5	80.9	10.5	528.8	14.8	27.6	16.5	0.2	2.1	-0.3	0.1	1.6	0.7
JSd-1	Stream sediment	65.6	331.4	15.0	124.7	12.2	0.6	12.4	3.4	1.0	16.7	89.8	22.6	6.5	12.2	18.3	78.2	9.8	537.1	14.1	26.7	15.6	-2.0	1.9	0.1	0.0	1.5	-0.3
Avg.		*65.6*	*330.8*	*14.8*	*125.6*	*12.1*	*0.5*	*12.5*	*3.5*	*0.7*	*16.5*	*89.6*	*22.4*	*6.3*	*12.0*	*18.6*	*79.6*	*10.3*	*534.4*	*14.1*	*27.0*	*16.0*	*-0.8*	*2.0*	*-0.1*	*0.0*	*1.2*	*-0.2*
St.Dev		*0.1*	*0.6*	*0.2*	*0.8*	*0.1*	*0.1*	*0.1*	*0.1*	*0.3*	*0.3*	*0.2*	*0.2*	*0.3*	*0.6*	*0.5*	*1.4*	*0.4*	*4.9*	*0.6*	*0.5*	*0.5*	*1.1*	*0.1*	*0.2*	*0.1*	*0.5*	*0.8*
RSD (%)		*0.2*	*0.2*	*1.3*	*0.6*	*1.0*	*16.3*	*0.7*	*3.6*	*43.4*	*1.5*	*0.2*	*0.9*	*5.3*	*5.2*	*2.4*	*1.7*	*3.9*	*0.9*	*4.2*	*1.9*	*2.9*	*-134.0*	*6.2*	*-150.8*	*362.5*	*44.5*	*-486.6*
JSd-2	*Stream sediment*	*26.9*	*202.0*	*17.4*	*111.0*	*4.6*	*11.5*	*146.0*	*2.3*	*1.1*	*15.3*	*2056.0*	*1114.0*	*92.8*	*48.4*	*108.0*	*1240.0*	*17.5*	*1199.0*	*11.3*	*23.4*	*13.2*	*1.1*	*38.6*	*11.6*	*18.8*	*32.5*	*4.7*
JSd-2	Stream sediment	27.5	202.6	19.3	113.8	5.6	14.6	149.6	3.9	1.6	16.2	2055.9	1120.7	100.0	48.2	109.7	1396.0	19.8	1122.0	9.2	16.7	11.0	-3.6	42.6	13.1	22.5	37.2	2.1
JSd-2	Stream sediment	27.2	202.3	19.7	114.4	5.5	14.6	149.7	3.5	0.6	15.3	2055.9	1120.5	98.8	47.2	111.5	1412.0	19.8	1122.9	9.0	17.6	10.7	-6.0	39.8	11.6	22.5	36.7	1.3
JSd-2	Stream sediment	28.1	203.4	19.7	112.4	5.9	14.8	148.6	3.7	1.4	14.1	2056.0	1120.4	100.4	47.7	110.4	1373.0	18.2	1120.0	10.8	15.4	6.4	-5.3	39.6	13.2	22.1	36.5	2.2
Avg.		*27.6*	*202.8*	*19.6*	*113.5*	*5.7*	*14.6*	*149.3*	*3.7*	*1.2*	*15.2*	*2056.0*	*1120.5*	*99.7*	*47.7*	*110.5*	*1394.0*	*19.3*	*1121.7*	*9.7*	*16.6*	*9.4*	*-5.0*	*40.6*	*12.6*	*22.3*	*36.8*	*1.9*
St.Dev		*0.4*	*0.6*	*0.2*	*1.0*	*0.2*	*0.1*	*0.6*	*0.2*	*0.5*	*1.0*	*0.0*	*0.2*	*0.8*	*0.5*	*0.9*	*2.0*	*0.9*	*1.5*	*1.0*	*1.1*	*2.6*	*1.2*	*1.7*	*0.9*	*0.2*	*0.4*	*0.5*
RSD (%)		*1.6*	*0.3*	*1.0*	*0.9*	*3.5*	*0.9*	*0.4*	*5.3*	*42.6*	*6.9*	*0.0*	*0.0*	*0.8*	*1.1*	*0.8*	*1.4*	*4.8*	*0.1*	*10.1*	*6.7*	*27.4*	*-24.4*	*4.1*	*7.1*	*1.0*	*1.1*	*26.5*
JSd-3	*Stream sediment*	*285.0*	*58.7*	*14.9*	*124.0*	*7.8*	*1.6*	*82.1*	*9.7*	*1.7*	*13.5*	*136.0*	*426.0*	*19.6*	*12.7*	*35.3*	*72.0*	*10.5*	*462.0*	*19.8*	*42.0*	*15.7*	*30.6*	*252.0*	*2.3*	*1.3*	*195.0*	*179.0*

Appendix 4 – Whole rock XRF data

IRM	Material	Rb	Sr	Y	Zr	Nb	Mo	Pb	Th	U	Ga	Zn	Cu	Ni	Co	Cr	V	Sc	Ba	La	Ce	Nd	Cs	As	Sb	Se	Sn	W
JSd-3	Stream sediment	279.3	54.8	14.4	126.4	8.7	1.6	81.5	10.9	1.5	12.9	127.8	360.0	19.2	12.8	31.5	76.1	11.9	480.4	19.8	45.2	16.5	30.2	260.0	2.0	0.4	197.3	132.3
JSd-3	Stream sediment	279.0	55.2	14.6	126.5	8.8	1.6	81.1	10.7	1.5	13.0	126.2	357.6	19.4	13.1	31.5	76.2	9.9	477.7	18.7	45.2	16.1	29.7	260.6	1.4	0.5	198.1	130.7
JSd-3	Stream sediment	278.1	55.8	14.9	124.5	8.9	1.7	80.5	10.9	1.7	12.8	126.3	357.1	20.6	12.9	31.8	75.8	11.6	478.6	21.7	50.8	18.2	31.1	252.0	1.4	0.8	198.1	130.9
Avg.		***278.8***	***55.3***	***14.6***	***125.8***	***8.8***	***1.6***	***81.0***	***10.8***	***1.6***	***12.9***	***126.8***	***358.3***	***19.7***	***12.9***	***31.6***	***76.0***	***11.1***	***478.9***	***20.1***	***47.1***	***16.9***	***30.3***	***257.5***	***1.6***	***0.6***	***197.8***	***131.3***
St.Dev		***0.6***	***0.5***	***0.2***	***1.1***	***0.1***	***0.1***	***0.5***	***0.1***	***0.1***	***0.1***	***0.9***	***1.6***	***0.8***	***0.2***	***0.2***	***0.2***	***1.1***	***1.4***	***1.5***	***3.2***	***1.1***	***0.7***	***4.8***	***0.3***	***0.2***	***0.5***	***0.9***
RSD (%)		***0.2***	***0.9***	***1.7***	***0.9***	***1.2***	***3.6***	***0.6***	***1.1***	***7.4***	***0.9***	***0.7***	***0.4***	***3.8***	***1.3***	***0.5***	***0.2***	***9.6***	***0.3***	***7.6***	***6.8***	***6.6***	***2.4***	***1.9***	***20.9***	***32.2***	***0.2***	***0.7***
BE-N	***Basalt***	***47.6***	***1392.0***	***29.4***	***272.9***	***113.2***	***2.8***	***4.1***	***10.6***	***2.4***	***17.2***	***122.9***	***68.8***	***269.7***	***59.0***	***353.1***	***231.9***	***22.6***	***1039.0***	***82.6***	***153.0***	***66.4***	***0.7***	***1.9***	***0.3***	***0.1***	***1.7***	***28.0***
BE-N	Basalt	44.0	1384.6	29.6	277.6	108.4	2.0	4.1	10.6	2.4	16.5	118.3	75.1	277.1	59.7	330.8	230.2	24.3	1081.5	85.7	155.2	66.3	0.7	3.3	1.0	-0.3	1.3	28.4
BE-N	Basalt	43.8	1385.4	29.5	276.5	108.4	1.9	3.2	10.7	2.4	16.6	118.6	74.5	274.4	59.1	336.6	228.0	23.5	1082.4	85.3	154.8	65.6	-0.1	4.6	-1.1	0.5	1.4	28.2
BE-N	Basalt	44.3	1386.2	29.5	275.0	108.2	2.4	4.1	10.6	2.4	18.0	115.7	74.0	272.5	59.7	338.4	230.5	25.7	1076.1	85.8	159.6	66.9	1.2	3.9	1.4	-1.5	2.1	30.1
Avg.		***44.1***	***1385.4***	***29.5***	***276.4***	***108.3***	***2.1***	***3.8***	***10.6***	***2.4***	***17.0***	***117.5***	***74.5***	***274.7***	***59.5***	***335.3***	***229.6***	***24.5***	***1080.0***	***85.6***	***156.5***	***66.2***	***0.6***	***3.9***	***0.4***	***-0.4***	***1.6***	***28.9***
St.Dev		***0.2***	***0.8***	***0.1***	***1.3***	***0.1***	***0.3***	***0.5***	***0.0***	***0.0***	***0.8***	***1.6***	***0.5***	***2.3***	***0.3***	***4.0***	***1.4***	***1.1***	***3.4***	***0.2***	***2.7***	***0.7***	***0.6***	***0.6***	***1.3***	***1.0***	***0.4***	***1.0***
RSD (%)		***0.5***	***0.1***	***0.2***	***0.5***	***0.1***	***11.8***	***14.2***	***0.4***	***1.5***	***4.9***	***1.4***	***0.7***	***0.8***	***0.6***	***1.2***	***0.6***	***4.6***	***0.3***	***0.3***	***1.7***	***1.0***	***106.6***	***16.5***	***304.8***	***-239.0***	***25.4***	***3.5***
JR-1	***Rhyolite***	***257.0***	***29.1***	***45.1***	***99.9***	***15.2***	***3.3***	***19.3***	***26.7***	***8.9***	***16.1***	***30.6***	***2.7***	***1.7***	***0.8***	***2.8***	***7.0***	***5.1***	***50.3***	***19.7***	***47.2***	***23.3***	***20.8***	***16.3***	***1.2***	***0.0***	***2.9***	***1.6***
JR-1	Rhyolite	250.1	26.0	45.3	101.6	16.3	2.1	17.9	26.7	7.8	15.6	28.0	-0.7	3.8	-0.7	-1.1	7.1	3.0	44.4	20.0	45.0	23.9	21.4	15.2	1.1	-0.4	3.4	3.0
JR-1	Rhyolite	250.9	26.5	44.9	101.3	16.2	2.2	18.0	25.9	8.0	15.4	27.7	-0.2	3.4	-1.2	2.8	7.1	4.6	45.8	19.2	45.7	25.9	21.2	15.8	1.3	-0.1	3.2	3.3
JR-1	Rhyolite	249.2	26.8	45.0	99.6	16.6	2.4	17.3	27.1	7.7	15.3	28.2	-0.1	4.2	0.9	3.7	7.8	5.3	46.0	20.6	45.7	25.5	21.3	16.6	1.1	0.0	2.4	3.1
Avg.		***250.1***	***26.4***	***45.1***	***100.9***	***16.4***	***2.2***	***17.8***	***26.6***	***7.8***	***15.4***	***28.0***	***-0.3***	***3.8***	***-0.3***	***1.8***	***7.3***	***4.3***	***45.4***	***19.9***	***45.5***	***25.1***	***21.3***	***15.9***	***1.2***	***-0.2***	***3.0***	***3.1***

Appendix 4 – Whole rock XRF data

St.Dev		*0.9*	*0.4*	*0.2*	*1.1*	*0.2*	*0.2*	*0.4*	*0.6*	*0.1*	*0.2*	*0.2*	*0.3*	*0.4*	*1.1*	*2.6*	*0.4*	*1.2*	*0.9*	*0.7*	*0.4*	*1.0*	*0.1*	*0.7*	*0.1*	*0.2*	*0.5*	*0.1*
RSD (%)		*0.3*	*1.4*	*0.5*	*1.1*	*1.4*	*6.8*	*2.3*	*2.2*	*1.6*	*1.0*	*0.8*	*-87.5*	*9.8*	*-340.1*	*143.2*	*5.7*	*27.8*	*1.9*	*3.5*	*0.9*	*4.1*	*0.6*	*4.6*	*9.5*	*-145.4*	*17.7*	*4.2*

IRM	Material	Rb	Sr	Y	Zr	Nb	Mo	Pb	Th	U	Ga	Zn	Cu	Ni	Co	Cr	V	Sc	Ba	La	Ce	Nd	Cs	As	Sb	Se	Sn	W
JR-2	*Rhyolite*	*303.0*	*8.1*	*51.1*	*96.3*	*18.7*	*3.4*	*21.5*	*31.4*	*10.9*	*17.9*	*27.8*	*1.4*	*2.0*	*0.5*	*3.1*	*3.0*	*5.6*	*39.5*	*16.3*	*38.8*	*20.4*	*25.0*	*19.2*	*1.5*	*0.0*	*3.5*	*5.2*
JR-2	Rhyolite	295.8	6.4	50.2	97.6	19.1	1.9	20.6	31.6	9.6	15.5	26.5	-1.2	3.9	-0.4	1.4	3.3	6.4	32.4	16.3	35.6	21.4	24.4	19.3	1.8	0.0	4.0	4.5
JR-2	Rhyolite	295.6	6.7	50.9	97.9	19.4	2.0	21.4	31.1	9.5	16.8	27.1	-1.2	4.1	-0.8	3.3	3.4	5.6	30.2	16.4	38.6	23.7	27.5	18.8	2.5	-0.8	3.6	4.5
JR-2	Rhyolite	294.2	6.9	50.1	96.0	19.3	2.0	20.7	31.2	9.6	16.0	26.9	-0.6	4.2	-0.9	2.8	2.1	5.4	31.9	19.0	38.4	22.5	26.8	18.4	1.9	-0.4	3.9	3.5
Avg.		*295.2*	*6.7*	*50.4*	*97.2*	*19.3*	*2.0*	*20.9*	*31.3*	*9.6*	*16.1*	*26.8*	*-1.0*	*4.1*	*-0.7*	*2.5*	*2.9*	*5.8*	*31.5*	*17.2*	*37.5*	*22.5*	*26.2*	*18.8*	*2.1*	*-0.4*	*3.8*	*4.2*
St.Dev		*0.9*	*0.2*	*0.4*	*1.0*	*0.1*	*0.1*	*0.5*	*0.3*	*0.1*	*0.7*	*0.3*	*0.4*	*0.1*	*0.2*	*1.0*	*0.7*	*0.5*	*1.2*	*1.5*	*1.7*	*1.2*	*1.6*	*0.4*	*0.4*	*0.4*	*0.2*	*0.6*
RSD (%)		*0.3*	*3.7*	*0.8*	*1.1*	*0.7*	*2.9*	*2.2*	*0.9*	*0.6*	*4.1*	*1.0*	*-35.3*	*3.5*	*-33.8*	*40.5*	*24.9*	*9.4*	*3.7*	*8.9*	*4.5*	*5.2*	*6.2*	*2.3*	*19.5*	*-108.4*	*5.7*	*13.9*
JR-3	*Rhyolite*	*453.0*	*10.4*	*172.0*	*1678.0*	*535.0*	*0.5*	*32.8*	*112.0*	*21.1*	*36.6*	*209.0*	*2.9*	*1.6*	*1.0*	*3.5*	*4.2*	*0.5*	*65.8*	*179.0*	*327.0*	*107.0*	*10.0*	*1.1*	*0.2*	*0.0*	*17.4*	*7.8*
JR-3	Rhyolite	465.5	7.1	172.3	1680.2	542.1	-0.1	35.6	112.1	20.6	37.9	193.5	2.9	4.3	3.2	-5.9	1.5	0.9	56.5	169.5	316.6	103.9	8.4	-0.3	0.8	-0.2	20.8	7.7
JR-3	Rhyolite	465.1	7.3	171.8	1681.1	542.1	-0.2	36.4	112.3	20.7	38.7	191.8	2.3	4.5	2.4	-4.0	2.3	1.0	53.8	168.9	314.1	102.5	7.5	0.4	-0.8	-0.3	20.1	9.4
JR-3	Rhyolite	462.8	7.4	170.8	1674.3	542.0	-0.5	35.5	112.9	20.6	38.5	192.9	4.6	8.0	3.2	-4.6	1.2	0.7	52.9	171.0	316.1	102.3	8.2	0.8	1.0	-0.1	19.9	7.4
Avg.		*464.5*	*7.3*	*171.7*	*1678.5*	*542.1*	*-0.3*	*35.8*	*112.4*	*20.6*	*38.4*	*192.7*	*3.3*	*5.6*	*3.0*	*-4.8*	*1.7*	*0.9*	*54.4*	*169.8*	*315.6*	*102.9*	*8.0*	*0.3*	*0.4*	*-0.2*	*20.2*	*8.1*
St.Dev		*1.5*	*0.1*	*0.8*	*3.7*	*0.1*	*0.2*	*0.5*	*0.4*	*0.1*	*0.4*	*0.9*	*1.2*	*2.1*	*0.5*	*1.0*	*0.6*	*0.1*	*1.9*	*1.1*	*1.3*	*0.8*	*0.5*	*0.5*	*1.0*	*0.1*	*0.5*	*1.1*
RSD (%)		*0.3*	*1.9*	*0.5*	*0.2*	*0.0*	*-74.1*	*1.5*	*0.4*	*0.3*	*1.1*	*0.5*	*36.2*	*37.0*	*15.9*	*-19.8*	*34.0*	*14.8*	*3.5*	*0.6*	*0.4*	*0.8*	*5.6*	*184.4*	*278.5*	*-45.5*	*2.3*	*13.2*
TY-G	*As Ref.*	*-*	*-*	*-*	*-*	*-*	*-*	*-*	*-*	*-*	*-*	*-*	*-*	*-*	*-*	*-*	*-*	*-*	*-*	*-*	*-*	*-*	*-*	*0.0*	*0.0*	*0.0*	*0.0*	*400.0*

Appendix 4 – Whole rock XRF data

IRM	Material	Rb	Sr	Y	Zr	Nb	Mo	Pb	Th	U	Ga	Zn	Cu	Ni	Co	Cr	V	Sc	Ba	La	Ce	Nd	Cs	As	Sb	Se	Sn	W
TY-G		-	-	-	-	-	-	-	-	-	-	-	-	-	-	-	-	-	-	-	-	-	-	0.0	0.0	-2.7	-0.5	394.7
TY-G		-	-	-	-	-	-	-	-	-	-	-	-	-	-	-	-	-	-	-	-	-	-	0.5	0.4	-2.1	0.2	393.9
TY-G		-	-	-	-	-	-	-	-	-	-	-	-	-	-	-	-	-	-	-	-	-	-	0.6	-1.0	-2.3	-0.4	392.5
Avg.		-	-	-	-	-	-	-	-	-	-	-	-	-	-	-	-	-	-	-	-	-	-	***0.4***	***-0.2***	***-2.4***	***-0.2***	***393.7***
St.Dev		-	-	-	-	-	-	-	-	-	-	-	-	-	-	-	-	-	-	-	-	-	-	***0.3***	***0.7***	***0.3***	***0.4***	***1.1***
RSD (%)		-	-	-	-	-	-	-	-	-	-	-	-	-	-	-	-	-	-	-	-	-	-	***84.4***	***-385.6***	***-12.7***	***-186.3***	***0.3***
GS-N	***Granite***	***185.0***	***570.0***	***16.0***	***235.0***	***21.0***	***1.2***	***53.0***	***41.0***	***7.5***	***22.0***	***48.0***	***20.0***	***32.8***	***65.0***	***54.0***	***65.0***	***7.3***	***1400.0***	***75.0***	***135.0***	***49.0***	***5.4***	***1.6***	***0.7***	***0.0***	***3.0***	***450.0***
GS-N	Granite	-	-	-	-	-	-	-	-	-	-	-	-	-	-	-	-	-	-	-	-	-	-	2.0	0.2	-3.0	1.8	454.5
GS-N	Granite	-	-	-	-	-	-	-	-	-	-	-	-	-	-	-	-	-	-	-	-	-	-	0.5	0.3	-2.8	3.4	455.1
GS-N	Granite	-	-	-	-	-	-	-	-	-	-	-	-	-	-	-	-	-	-	-	-	-	-	1.4	0.4	-2.8	2.7	456.2
Avg.		-	-	-	-	-	-	-	-	-	-	-	-	-	-	-	-	-	-	-	-	-	-	***1.3***	***0.3***	***-2.9***	***2.7***	***455.3***
St.Dev		-	-	-	-	-	-	-	-	-	-	-	-	-	-	-	-	-	-	-	-	-	-	***0.8***	***0.1***	***0.1***	***0.8***	***0.9***
RSD (%)		-	-	-	-	-	-	-	-	-	-	-	-	-	-	-	-	-	-	-	-	-	-	***58.8***	***42.1***	***-3.2***	***29.7***	***0.2***
ZW-C	***Zinnwaldite***	***8500.0***	***17.0***	***33.0***	***82.0***	***198.0***	***4.3***	***80.0***	***43.0***	***20.0***	***99.0***	***1050.0***	***42.0***	***11.0***	***2.0***	***56.0***	***6.0***	***42.0***	***69.0***	***30.0***	***94.0***	***25.0***	***2600.0***	***31.0***	***4.2***	***0.0***	***1377.0***	***320.0***
ZW-C	Zinnwaldite	-	-	-	-	-	-	-	-	-	-	-	-	-	-	-	-	-	-	-	-	-	-	35.3	-9.4	-2.6	1416.5	352.4
ZW-C	Zinnwaldite	-	-	-	-	-	-	-	-	-	-	-	-	-	-	-	-	-	-	-	-	-	-	35.5	-2.1	-1.7	1426.8	352.0
ZW-C	Zinnwaldite	-	-	-	-	-	-	-	-	-	-	-	-	-	-	-	-	-	-	-	-	-	-	34.1	-6.2	-2.6	1429.0	354.0
Avg.		-	-	-	-	-	-	-	-	-	-	-	-	-	-	-	-	-	-	-	-	-	-	***35.0***	***-5.9***	***-2.3***	***1424.1***	***352.8***

Appendix 4 – Whole rock XRF data

St.Dev		-	-	-	-	-	-	-	-	-	-	-	-	-	-	-	-	-	-	-	-	-	-	***0.8***	***3.7***	***0.5***	***6.7***	***1.1***
RSD (%)		-	-	-	-	-	-	-	-	-	-	-	-	-	-	-	-	-	-	-	-	-	-	***2.2***	***-61.8***	***-23.2***	***0.5***	***0.3***
IRM	**Material**	**Rb**	**Sr**	**Y**	**Zr**	**Nb**	**Mo**	**Pb**	**Th**	**U**	**Ga**	**Zn**	**Cu**	**Ni**	**Co**	**Cr**	**V**	**Sc**	**Ba**	**La**	**Ce**	**Nd**	**Cs**	**As**	**Sb**	**Se**	**Sn**	**W**
Mica-Fe	***Biotite***	***2200.0***	***5.0***	***48.0***	***800.0***	***270.0***		***13.0***																***3.0***	***0.0***	***0.0***	***70.0***	***15.0***
Mica-Fe	Biotite	-	-	-	-	-	-	-	-	-	-	-	-	-	-	-	-	-	-	-	-	-	-	3.2	-2.0	-0.8	90.3	9.0
Mica-Fe	Biotite	-	-	-	-	-	-	-	-	-	-	-	-	-	-	-	-	-	-	-	-	-	-	1.8	-2.7	-1.5	90.4	7.1
Mica-Fe	Biotite	-	-	-	-	-	-	-	-	-	-	-	-	-	-	-	-	-	-	-	-	-	-	1.9	-1.9	-0.8	87.8	8.7
Avg.		-	-	-	-	-	-	-	-	-	-	-	-	-	-	-	-	-	-	-	-	-	-	***2.3***	***-2.2***	***-1.0***	***89.5***	***8.3***
St.Dev		-	-	-	-	-	-	-	-	-	-	-	-	-	-	-	-	-	-	-	-	-	-	***0.8***	***0.4***	***0.4***	***1.5***	***1.0***
RSD (%)		-	-	-	-	-	-	-	-	-	-	-	-	-	-	-	-	-	-	-	-	-	-	***34.5***	***-19.5***	***-39.0***	***1.7***	***12.2***

Appendix 5

Electron microprobe analyses

The following data supplement the relevant tables presented in chapters 3, 5 and 6.
Excluded data (e.g. low totals or mixed analysis) indicated with a strikethrough and negative values replaced with red zeros
Mineral abbreviations after Whitney and Evans (2010)
Block colour refers to data collected over a single transect (distance along transect in um)

Metagranite

Sample	Spot	SiO2	TiO2	Al2O3	FeO	MnO	MgO	CaO	Na2O	K2O	F	Cl	Total	Min	distance (um)
11-01	1 / 1 .	35.00	3.18	18.15	22.26	0.08	7.06	0.07	0.07	9.37	0.40	0.08	95.71	Bt	
11-01	2 / 1 .	36.21	3.12	18.76	21.83	0.06	7.32	0.05	0.10	8.36	0.41	0.07	96.29	Bt	
11-01	3 / 1 .	35.88	2.81	18.72	21.09	0.05	7.59	0.07	0.06	9.17	0.41	0.07	95.91	Bt	
11-01	4 / 1 .	35.23	3.21	17.78	23.50	0.06	6.87	0.09	0.11	8.69	0.37	0.16	96.07	Bt	
11-01	5 / 1 .	34.58	3.13	18.07	23.57	0.07	6.70	0.08	0.05	9.08	0.47	0.10	95.92	Bt	
11-01	6 / 1 .	35.45	3.31	18.23	22.61	0.09	7.26	0.01	0.07	9.33	0.52	0.08	96.96	Bt	
11-01	8 / 1 .	51.89	0.07	40.88	1.17	0.02	0.80	0.04	0.56	4.96	0.11	0.00	100.51	Ms	
11-01	9 / 1 .	47.62	0.02	37.90	1.06	0.00	0.59	0.01	0.31	8.05	0.07	0.01	95.64	Ms	
11-01	10 / 1 .	52.09	0.00	40.58	1.28	0.00	0.84	0.00	0.42	5.53	0.08	0.00	100.80	Ms	
11-01	11 / 1 .	47.39	0.12	36.29	1.54	0.02	0.79	0.00	0.18	7.99	0.10	0.00	94.41	Ms	
11-01	12 / 1 .	48.91	0.02	38.05	0.98	0.02	0.76	0.03	0.41	5.10	0.05	0.01	94.34	Ms	
11-01	14 / 1 .	52.60	0.08	40.80	1.02	0.00	0.77	0.00	0.60	5.00	0.10	0.00	100.94	Ms	
11-01	15 / 1 .	48.43	0.09	38.30	1.02	0.01	0.72	0.00	0.28	8.18	0.14	0.01	97.19	Ms	
11-01	16 / 1 .	51.73	0.10	40.68	1.09	0.00	0.76	0.00	0.56	5.35	0.08	0.00	100.34	Ms	
11-01	17 / 1 .	47.44	0.15	37.32	1.05	0.00	0.69	0.00	0.26	8.57	0.05	0.00	95.53	Ms	
11-01	18 / 1 .	37.59	0.11	21.73	30.16	1.58	1.21	8.40	0.03	0.39	0.00	0.01	101.15	Grt	
11-01	19 / 1 .	37.20	0.12	21.63	33.33	1.75	1.64	3.83	0.07	0.03	0.00	0.01	99.61	Grt	
11-01	20 / 1 .	37.45	0.09	21.87	30.40	1.10	1.39	7.71	0.05	0.03	0.01	0.00	100.10	Grt	
11-01	21 / 1 .	38.11	0.06	22.08	23.76	0.83	0.74	13.67	0.04	0.07	0.09	0.01	99.45	Grt	
11-01	22 / 1 .	37.36	0.07	21.55	34.63	1.87	1.82	2.93	0.04	0.02	0.00	0.00	100.25	Grt	
11-01	23 / 1 .	37.23	0.11	21.39	35.01	1.84	1.77	2.53	0.04	0.01	0.03	0.00	99.97	Grt	
11-01	24 / 1 .	37.09	0.14	21.22	37.27	2.33	1.40	0.68	0.05	0.03	0.00	0.00	100.17	Grt	
11-01	25 / 1 .	47.39	0.75	35.01	2.23	0.03	0.80	0.01	0.10	7.52	0.14	0.01	93.98	Ms	
11-01	26 / 1 .	52.29	0.72	36.05	2.73	0.00	1.13	0.03	0.17	4.65	0.12	0.02	97.90	Ms	
11-01	27 / 1 .	50.82	0.86	30.59	3.16	0.02	2.19	0.03	0.06	8.01	0.44	0.01	96.18	Ms	
11-01	28 / 1 .	55.67	0.95	33.07	3.29	0.01	2.47	0.05	0.13	3.45	0.38	0.03	99.49	Ms	
11-01	29 / 1 .	51.34	1.28	28.50	2.77	0.00	2.55	0.02	0.04	8.53	0.44	0.01	95.47	Ms	
11-01	30 / 1 .	57.95	0.82	30.48	2.65	0.05	2.98	0.01	0.12	4.17	0.35	0.00	99.59	Ms	
11-01	31 / 1 .	53.61	0.71	28.63	2.75	0.00	3.08	0.02	0.04	7.78	0.58	0.01	97.20	Ms	
11-01	32 / 1 .	57.90	0.76	31.04	2.76	0.02	2.98	0.01	0.08	3.97	0.38	0.01	99.90	Ms	
11-01	33 / 1 .	47.98	0.03	37.54	1.16	0.00	0.84	0.01	0.26	8.22	0.14	0.00	96.17	Ms	
11-01	34 / 1 .	52.86	0.08	40.69	1.17	0.01	0.81	0.00	0.57	4.53	0.08	0.00	100.80	Ms	
11-01	35 / 1 .	48.53	0.12	37.89	1.02	0.00	0.81	0.01	0.25	8.19	0.15	0.00	96.97	Ms	
11-01	36 / 1 .	52.24	0.08	40.85	1.04	0.01	0.73	0.01	0.56	4.96	0.07	0.00	100.55	Ms	
11-01	37 / 1 .	48.04	0.01	38.46	0.89	0.00	0.79	0.00	0.22	8.32	0.14	0.00	96.86	Ms	
11-01	38 / 1 .	51.96	0.02	41.36	0.97	0.01	0.71	0.01	0.58	5.11	0.06	0.00	100.80	Ms	
11-01	39 / 1 .	50.11	0.00	34.29	2.17	0.00	1.83	0.03	0.07	8.21	0.28	0.01	97.01	Ms	
11-01	40 / 1 .	51.00	0.08	39.43	1.60	0.00	0.65	0.02	0.43	5.09	0.11	0.01	98.41	Ms	
11-01	42 / 1 .	50.59	0.02	39.45	1.30	0.02	0.67	0.01	0.40	5.30	0.13	0.01	97.91	Ms	
11-01	43 / 1 .	47.96	0.01	37.55	1.07	0.01	0.68	0.01	0.25	8.32	0.12	0.00	95.98	Ms	
11-01	44 / 1 .	52.01	0.00	40.24	1.46	0.00	0.90	0.02	0.44	4.92	0.18	0.01	100.16	Ms	
11-01	45 / 1 .	49.12	0.00	34.12	2.63	0.02	2.16	0.03	0.06	8.30	0.21	0.01	96.64	Ms	
11-01	46 / 1 .	53.99	0.01	36.15	1.98	0.01	2.52	0.01	0.14	4.38	0.24	0.01	99.42	Ms	
11-01	47 / 1 .	50.45	0.01	36.53	1.00	0.00	1.54	0.03	0.06	8.45	0.20	0.00	98.27	Ms	
11-01	48 / 1 .	56.59	0.00	35.39	1.34	0.00	2.32	0.01	0.13	4.61	0.25	0.00	100.64	Ms	
11-01	49 / 1 .	50.51	0.00	35.00	1.16	0.02	2.07	0.03	0.06	8.14	0.31	0.00	97.29	Ms	
11-01	50 / 1 .	38.10	0.00	20.22	17.37	0.16	11.87	0.07	0.08	5.98	0.68	0.09	94.63	Bt	
11-01	51 / 1 .	48.28	0.01	36.67	1.41	0.02	1.33	0.02	0.11	8.45	0.15	0.01	96.46	Ms	
11-01	52 / 1 .	38.93	0.03	20.33	18.02	0.13	11.20	0.14	0.08	6.07	0.57	0.09	95.59	Bt	
11-01	54 / 1 .	37.72	0.07	22.27	34.46	0.83	5.21	0.03	0.04	0.02	0.03	0.00	100.65	Grt	
11-01	55 / 1 .	37.98	0.00	22.32	34.57	0.64	5.05	0.09	0.01	0.01	0.03	0.00	100.70	Grt	
11-01	56 / 1 .	38.03	0.00	22.56	33.78	1.08	5.18	0.08	0.01	0.05	0.00	0.00	100.76	Grt	
11-01	57 / 1 .	38.67	0.00	22.44	32.61	0.58	6.44	0.09	0.00	0.07	0.00	0.00	100.83	Grt	
11-01	58 / 1 .	38.31	0.00	22.40	33.36	0.76	6.15	0.05	0.01	0.02	0.00	0.00	101.01	Grt	
11-01	59 / 1 .	38.12	0.00	22.63	34.17	1.45	4.37	0.07	0.02	0.07	0.00	0.00	100.87	Grt	
11-01	60 / 1 .	55.65	0.01	34.83	1.74	0.00	2.40	0.02	0.13	4.60	0.37	0.01	99.77	Ms	
11-01	61 / 1 .	47.60	0.03	36.22	1.20	0.01	1.24	0.02	0.12	8.64	0.25	0.01	95.33	Ms	
11-01	62 / 1 .	38.39	1.76	19.29	15.86	0.10	12.55	0.03	0.05	6.03	0.94	0.22	95.21	Bt	
11-01	63 / 1 .	36.68	2.26	18.76	14.33	0.04	12.85	0.03	0.04	8.91	0.68	0.10	94.67	Bt	
11-01	65 / 1 .	47.21	0.41	37.01	0.96	0.01	0.86	0.02	0.24	7.52	0.12	0.01	94.36	Ms	
11-01	66 / 1 .	51.63	0.07	39.52	0.98	0.00	0.92	0.02	0.56	5.19	0.15	0.01	99.04	Ms	
11-01	67 / 1 .	46.77	0.11	36.28	1.74	0.02	0.77	0.15	0.21	7.34	0.15	0.02	93.56	Ms	
11-01	68 / 1 .	51.88	0.08	39.63	0.92	0.01	0.95	0.01	0.50	5.33	0.11	0.01	99.43	Ms	
11-01	69 / 1 .	51.05	0.01	33.99	1.89	0.01	2.10	0.02	0.06	7.93	0.31	0.01	97.38	Ms	
11-01	70 / 1 .	54.25	0.00	36.23	1.14	0.01	1.99	0.01	0.12	4.52	0.25	0.01	98.54	Ms	
11-01	71 / 1 .	52.83	0.00	32.75	1.19	0.00	2.64	0.08	0.08	7.76	0.50	0.01	97.85	Ms	
11-01	72 / 1 .	54.75	0.01	37.43	1.47	0.03	1.80	0.03	0.15	4.60	0.22	0.01	100.49	Ms	
11-01	73 / 1 .	65.65	0.02	19.38	0.02	0.00	0.00	0.00	0.57	13.95	0.00	0.00	99.56	Kfsp	
11-01	74 / 1 .	69.34	0.01	20.51	0.03	0.00	0.00	0.00	0.94	9.69	0.00	0.01	100.50	Kfsp	
11-01	75 / 1 .	65.53	0.02	19.13	0.02	0.02	0.00	0.00	0.66	13.96	0.00	0.00	99.29	Kfsp	
11-01	77 / 1 .	63.46	0.01	24.98	0.48	0.01	0.05	0.58	4.62	3.29	0.09	0.01	97.57	kfsp	
11-01	78 / 1 .	53.14	0.22	39.30	1.61	0.02	0.75	0.00	0.19	4.59	0.21	0.01	100.03	kfsp	
11-01	79 / 1 .	48.30	0.03	36.40	1.51	0.00	0.70	0.02	0.07	8.24	0.07	0.01	95.34	kfsp	
11-01	81 / 1 .	65.77	0.00	21.66	0.02	0.01	0.00	3.06	3.64	0.08	0.00	0.00	94.21	plag	
11-01	82 / 1 .	65.74	0.00	23.93	0.86	0.03	0.03	3.30	8.21	0.13	0.06	0.01	102.30	plag	
11-01	85 / 1 .	64.64	0.00	20.67	0.17	0.02	0.01	1.82	3.46	0.06	0.05	0.01	90.90	plag	
11-01	86 / 1 .	61.78	0.01	26.65	0.87	0.01	0.17	2.87	4.98	1.07	0.01	0.01	98.43	plag	

Metagranite

Sample	Spot	SiO2	TiO2	Al2O3	FeO	MnO	MgO	CaO	Na2O	K2O	F	Cl	Total	Min	distance (um)
11-01	88 / 1 .	64.73	0.00	24.22	0.03	0.02	0.01	3.52	7.72	0.08	0.00	0.01	100.33	plag	
11-02	2 / 1 .	38.47	0.09	17.51	20.08	0.21	9.72	0.00	0.07	9.65	0.74	0.18	96.71	Bt	
11-02	3 / 1 .	49.43	0.00	34.11	2.65	0.02	1.58	0.00	0.17	10.56	0.09	0.00	98.60	Ms	
11-02	4 / 1 .	46.21	0.04	37.44	1.19	0.00	0.69	0.00	0.58	10.51	0.04	0.00	96.70	Ms	
11-02	5 / 1 .	48.55	0.02	34.73	2.82	0.03	1.44	0.00	0.15	10.67	0.18	0.01	98.57	Ms	
11-02	6 / 1 .	46.24	0.00	36.76	1.15	0.00	0.78	0.00	0.49	10.43	0.09	0.00	95.95	Ms	
11-02	7 / 1 .	49.19	0.00	34.05	2.59	0.01	1.70	0.00	0.18	10.21	0.13	0.00	98.07	Ms	
11-02	8 / 1 .	34.92	0.01	19.16	21.90	0.20	8.57	0.29	0.10	8.54	0.48	0.15	94.32	Ms	
11-02	9 / 1 .	34.98	0.01	19.69	21.65	0.23	8.55	0.19	0.16	8.56	0.44	0.14	94.60	Bt	
11-02	10 / 1 .	35.24	0.01	18.91	21.23	0.18	8.62	0.07	0.05	9.41	0.61	0.23	94.56	Bt	
11-02	11 / 1 .	35.92	0.02	19.17	21.29	0.19	8.99	0.03	0.05	9.76	0.67	0.20	96.28	Bt	
11-02	12 / 1 .	37.29	0.01	18.46	20.13	0.17	9.31	0.03	0.09	9.44	0.73	0.19	95.84	Bt	
11-02	13 / 1 .	37.23	0.02	18.09	21.21	0.22	9.33	0.02	0.09	9.35	0.67	0.21	96.44	Bt	
11-02	14 / 1 .	36.35	0.03	19.30	20.78	0.22	9.01	0.00	0.09	9.56	0.61	0.16	96.08	Bt	
11-02	15 / 1 .	36.66	0.03	20.11	20.41	0.21	8.47	0.00	0.09	9.74	0.61	0.23	96.56	Bt	
11-02	16 / 1 .	46.81	0.01	33.67	2.89	0.03	1.53	0.01	0.12	11.16	0.19	0.02	96.44	Ms	
11-02	17 / 1 .	46.27	0.00	36.86	2.80	0.03	0.93	0.01	0.26	10.48	0.12	0.01	97.75	Ms	
11-02	18 / 1 .	45.66	0.00	36.07	2.49	0.04	0.88	0.00	0.13	11.06	0.12	0.01	96.45	Ms	
11-02	19 / 1 .	47.68	0.00	36.99	2.69	0.02	1.06	0.00	0.22	10.59	0.15	0.01	99.37	Ms	
11-02	20 / 1 .	50.49	0.00	29.35	2.46	0.01	2.83	0.00	0.09	11.13	0.29	0.00	96.65	Ms	
11-02	21 / 1 .	34.53	2.59	18.13	22.87	0.26	7.27	0.02	0.08	9.45	0.28	0.18	95.66	Bt	
11-02	22 / 1 .	35.06	2.36	17.60	22.54	0.24	7.43	0.00	0.07	9.36	0.47	0.18	95.30	Bt	
11-02	23 / 1 .	35.15	2.42	18.06	22.42	0.23	7.23	0.07	0.08	9.13	0.40	0.08	95.26	Bt	
11-02	24 / 1 .	35.22	2.77	18.03	21.94	0.28	7.19	0.03	0.09	9.39	0.41	0.09	95.44	Bt	
11-02	25 / 1 .	35.17	2.61	17.64	22.54	0.29	7.29	0.01	0.06	9.40	0.37	0.13	95.52	Bt	
11-02	1 / 1 .	68.07	0.00	20.60	0.02	0.03	0.00	0.72	8.19	0.09	0.00	0.00	97.68	plag	
11-02	3 / 1 .	67.33	0.00	21.10	0.04	0.00	0.00	1.32	8.11	0.09	0.03	0.00	98.00	plag	
11-02	4 / 1 .	57.60	0.04	29.55	1.65	0.01	0.86	0.60	4.04	7.22	0.08	0.00	101.67	Ms	
11-02	5 / 1 .	59.33	0.02	25.88	0.96	0.01	0.47	0.49	4.77	4.14	0.00	0.01	96.08	Ms	
11-02	6 / 1 .	48.63	0.01	35.60	1.85	0.01	0.85	0.12	0.70	10.20	0.10	0.01	98.08	Ms	
11-02	7 / 1 .	68.03	0.00	20.50	0.01	0.00	0.00	0.46	9.35	0.10	0.00	0.00	98.40	plag	
11-02	9 / 1 .	68.07	0.07	20.65	0.00	0.00	0.00	0.48	9.86	0.05	0.02	0.00	99.19	plag	
11-02	10 / 1 .	47.90	0.02	34.83	3.53	0.01	1.48	0.00	0.20	10.06	0.10	0.02	98.16	kfsp	
11-02	11 / 1 .	46.91	0.00	34.36	2.37	0.01	1.22	0.00	0.10	11.38	0.10	0.01	96.44	kfsp	
11-02	12 / 1 .	48.46	0.01	35.38	2.27	0.01	1.24	0.00	0.20	10.36	0.13	0.00	98.04	kfsp	
11-02	13 / 1 .	95.02	0.01	4.12	0.29	0.03	0.17	0.00	0.01	1.35	0.02	0.00	101.01	Qtz	
11-02	14 / 1 .	90.67	0.01	6.40	0.43	0.00	0.20	0.02	0.02	1.82	0.01	0.00	99.58	Qtz	
11-02	15 / 1 .	51.75	0.00	31.65	2.21	0.02	0.98	0.00	0.13	10.04	0.19	0.01	96.98	Ms	
a05-10A	1 / 1 .	51.49	0.08	30.28	2.75	0.01	2.15	0.00	0.06	8.05	0.26	0.01	95.15	Ms	0
a05-10A	1 / 2 .	54.38	0.16	32.80	2.95	0.01	2.02	0.01	0.19	4.53	0.15	0.02	97.22	Ms	10.24
a05-10A	1 / 3 .	50.96	0.26	29.46	2.58	0.04	2.09	0.04	0.09	8.32	0.14	0.03	94.01	Ms	20.41
a05-10A	1 / 4 .	52.99	0.24	30.53	2.80	0.01	1.95	0.06	0.16	6.00	0.08	0.08	94.89	Ms	30.59
a05-10A	1 / 5 .	46.97	0.11	20.42	2.48	0.01	1.76	0.08	0.18	7.09	0.00	0.06	79.13	Ms	40.82
a05-10A	1 / 6 .	58.61	0.01	24.11	0.77	0.01	0.01	0.26	6.93	0.10	0.03	0.03	90.86	Ms	51
a05-10A	1 / 7 .	72.69	0.00	18.77	0.11	0.00	0.00	0.11	4.25	0.09	0.00	0.00	95.98	Ms	61.19
a05-10A	1 / 8 .	78.11	0.01	21.03	0.09	0.00	0.00	0.34	10.28	0.07	0.00	0.00	109.92	Ms	71.41
a05-10A	1 / 9 .	73.01	0.00	18.66	0.09	0.01	0.00	0.16	4.15	0.09	0.03	0.00	96.18	Ms	81.6
a05-10A	1 / 10 .	59.40	0.25	30.41	2.65	0.00	2.88	0.00	0.11	4.23	0.22	0.04	100.18	Ms	91.78
a05-10A	1 / 11 .	51.16	0.23	31.63	2.52	0.00	1.87	0.05	0.17	8.26	0.17	0.05	96.11	Ms	102.01
a05-10A	1 / 12 .	59.50	0.05	24.36	0.71	0.02	0.46	0.24	5.26	2.92	0.00	0.08	93.57	Ms	112.19
a05-10A	1 / 13 .	54.91	0.17	27.09	2.46	0.00	2.98	0.04	0.04	7.81	0.33	0.13	95.95	Ms	122.38
a05-10A	1 / 14 .	56.58	0.23	30.11	2.93	0.01	2.60	0.08	0.14	4.59	0.19	0.10	97.55	Ms	132.6
a05-10A	1 / 15 .	54.20	0.23	26.85	2.62	0.01	3.10	0.18	0.05	7.68	0.31	0.06	95.29	Ms	142.79
a05-10A	1 / 16 .	55.79	0.25	35.09	2.59	0.01	1.85	0.05	0.19	4.69	0.11	0.04	100.67	Ms	152.97
a05-10A	1 / 17 .	48.11	0.23	27.99	5.35	0.01	2.35	0.03	0.08	8.38	0.14	0.08	92.74	Ms	163.19
a05-10A	1 / 18 .	55.56	0.28	31.42	2.38	0.00	2.20	0.00	0.19	6.14	0.13	0.06	98.36	Ms	173.38
a05-10A	1 / 19 .	55.23	0.21	26.07	2.59	0.03	2.87	0.00	0.05	8.06	0.35	0.05	95.53	Ms	183.57
a05-10A	1 / 20 .	58.45	0.28	29.76	2.69	0.00	2.79	0.00	0.12	3.95	0.23	0.04	98.29	Ms	193.79
a05-10A	1 / 21 .	50.48	0.22	28.66	2.34	0.00	2.13	0.02	0.08	8.71	0.23	0.05	92.92	Ms	203.98
a05-10A	1 / 22 .	58.22	0.20	29.68	2.64	0.02	2.76	0.00	0.11	3.91	0.22	0.04	97.79	Ms	214.16
a05-10A	1 / 42 .	53.77	0.22	29.01	2.10	0.03	1.98	0.07	0.99	4.15	0.12	0.04	92.49	Ms	418.14
a05-10A	1 / 43 .	~~45.00~~	~~0.12~~	~~21.70~~	~~2.57~~	~~0.01~~	~~2.14~~	~~0.21~~	~~1.21~~	~~6.28~~	~~0.14~~	~~0.08~~	~~79.48~~		428.33
a05-10A	1 / 44 .	68.13	0.00	20.19	0.07	0.01	0.00	0.29	9.62	0.07	0.03	0.01	98.40	fsp	438.55
a05-10A	1 / 45 .	~~65.05~~	~~0.00~~	~~17.71~~	~~0.07~~	~~0.00~~	~~0.00~~	~~0.34~~	~~5.56~~	~~0.09~~	~~0.00~~	~~0.00~~	88.76	fsp	448.73
a05-10A	1 / 46 .	63.28	0.04	20.90	1.80	0.03	0.65	0.27	5.96	2.28	0.00	0.06	95.26	fsp	458.92
a05-10A	1 / 47 .	~~47.57~~	~~0.23~~	~~27.19~~	~~2.33~~	~~0.01~~	~~2.29~~	~~0.01~~	~~0.06~~	~~7.99~~	~~0.12~~	~~0.05~~	87.84	Ms	469.14
a05-10A	1 / 48 .	~~50.41~~	~~0.25~~	~~29.18~~	~~2.35~~	~~0.03~~	~~2.09~~	~~0.02~~	~~0.16~~	~~4.50~~	~~0.12~~	~~0.03~~	89.13	Ms	479.33
a05-10A	1 / 49 .	~~46.72~~	~~0.18~~	~~27.03~~	~~2.47~~	~~0.00~~	~~2.33~~	~~0.05~~	~~0.08~~	~~8.00~~	~~0.27~~	~~0.06~~	87.20	Ms	489.51
a05-10A	1 / 50 .	52.06	0.19	27.96	2.63	0.00	2.69	0.02	0.15	4.19	0.25	0.05	90.19	Ms	499.74
a05-10A	1 / 51 .	~~46.30~~	~~0.20~~	~~26.07~~	~~2.43~~	~~0.02~~	~~2.48~~	~~0.04~~	~~0.05~~	~~7.74~~	~~0.18~~	~~0.08~~	85.59	Ms	509.92
a05-10A	1 / 52 .	65.55	0.00	19.23	0.11	0.03	0.06	0.30	9.59	0.22	0.02	0.02	95.13	fsp	520.11
a05-10A	1 / 1 .	35.42	0.51	18.03	19.15	0.02	6.76	0.08	0.01	8.66	0.34	0.45	89.42	Bt	0
a05-10A	1 / 2 .	37.02	0.04	21.57	31.58	0.35	1.65	6.11	0.07	0.08	0.00	0.08	98.55	Grt	19.48
a05-10A	1 / 3 .	39.44	0.03	20.97	32.19	0.31	1.97	6.49	0.03	0.00	0.00	0.00	101.41	Grt	38.96
a05-10A	1 / 4 .	~~29.27~~	~~0.04~~	~~19.87~~	~~29.94~~	~~0.23~~	~~1.67~~	~~5.25~~	~~0.07~~	~~0.03~~	~~0.01~~	~~0.05~~	~~86.42~~	Grt	58.44
a05-10A	1 / 5 .	39.57	0.05	20.86	32.38	0.24	2.16	6.12	0.02	0.02	0.02	0.01	101.44	Grt	77.92
a05-10A	1 / 6 .	39.74	0.06	20.99	31.41	0.18	2.28	7.01	0.02	0.01	0.03	0.00	101.72	Grt	97.4
a05-10A	1 / 7 .	39.85	0.06	21.04	31.83	0.15	2.28	6.69	0.00	0.00	0.04	0.01	101.94	Grt	116.88
a05-10A	1 / 8 .	39.76	0.06	21.07	31.92	0.14	2.43	6.58	0.02	0.00	0.02	0.00	101.99	Grt	136.36
a05-10A	1 / 9 .	39.91	0.06	21.07	31.80	0.18	2.24	6.65	0.02	0.01	0.05	0.00	101.99	Grt	155.84
a05-10A	1 / 10 .	39.83	0.07	20.94	31.52	0.16	2.26	7.13	0.01	0.00	0.00	0.00	101.87	Grt	175.32
a05-10A	1 / 11 .	39.84	0.07	21.04	31.20	0.17	2.07	7.40	0.02	0.00	0.04	0.00	101.84	Grt	194.8

Metagranite

Sample	Spot	SiO2	TiO2	Al2O3	FeO	MnO	MgO	CaO	Na2O	K2O	F	Cl	Total	Min	distance (um)
a05-10A	1 / 12 .	39.70	0.08	21.07	31.56	0.17	2.11	7.14	0.02	0.01	0.00	0.00	101.84	Grt	214.28
a05-10A	1 / 13 .	39.75	0.07	20.97	31.61	0.18	2.01	7.20	0.01	0.01	0.00	0.01	101.77	Grt	233.76
a05-10A	1 / 14 .	39.61	0.07	20.93	31.57	0.17	2.05	7.33	0.01	0.01	0.03	0.00	101.79	Grt	253.24
a05-10A	1 / 15 .	39.69	0.08	21.06	31.83	0.20	1.93	7.05	0.03	0.00	0.02	0.00	101.88	Grt	272.72
a05-10A	1 / 16 .	39.74	0.09	20.86	30.96	0.17	1.82	8.03	0.01	0.00	0.00	0.00	101.67	Grt	292.2
a05-10A	1 / 17 .	39.79	0.12	21.06	31.36	0.20	1.77	7.62	0.02	0.00	0.04	0.00	101.98	Grt	311.68
a05-10A	1 / 18 .	39.44	0.07	20.89	32.24	0.21	1.80	6.92	0.01	0.00	0.00	0.01	101.55	Grt	331.16
a05-10A	1 / 19 .	39.76	0.08	20.88	32.37	0.20	1.69	6.94	0.01	0.00	0.00	0.00	101.90	Grt	350.64
a05-10A	1 / 20 .	39.50	0.09	20.88	31.78	0.18	1.70	7.43	0.01	0.00	0.06	0.01	101.62	Grt	370.12
a05-10A	1 / 21 .	39.66	0.09	20.95	32.56	0.21	1.67	7.03	0.00	0.00	0.01	0.00	102.19	Grt	389.6
a05-10A	1 / 22 .	39.52	0.07	20.89	32.90	0.19	1.65	6.81	0.01	0.00	0.09	0.00	102.12	Grt	409.09
a05-10A	1 / 23 .	39.62	0.07	20.71	32.66	0.19	1.53	6.72	0.02	0.00	0.02	0.00	101.54	Grt	428.56
a05-10A	1 / 24 .	39.70	0.07	20.90	31.82	0.18	1.53	7.22	0.03	0.00	0.00	0.03	101.47	Grt	448.05
a05-10A	1 / 25 .	39.67	0.11	20.80	32.20	0.21	1.51	7.18	0.03	0.00	0.00	0.00	101.69	Grt	467.53
a05-10A	1 / 26 .	39.51	0.08	20.91	32.47	0.21	1.47	6.97	0.04	0.00	0.00	0.00	101.60	Grt	487.01
a05-10A	1 / 27 .	39.50	0.07	20.81	32.66	0.20	1.41	6.87	0.03	0.00	0.00	0.00	101.49	Grt	506.49
a05-10A	1 / 28 .	~~24.34~~	~~0.09~~	~~17.58~~	~~31.62~~	~~0.20~~	~~0.71~~	~~6.20~~	~~0.05~~	~~0.15~~	~~0.00~~	~~0.07~~	~~80.99~~		525.97
a05-10A	1 / 29 .	~~31.43~~	~~0.08~~	~~17.01~~	~~26.22~~	~~0.08~~	~~5.07~~	~~4.13~~	~~0.17~~	~~3.88~~	~~0.02~~	~~0.57~~	~~88.67~~		545.45
a05-10A	1 / 30 .	39.66	0.09	21.44	32.67	0.25	1.26	7.06	0.01	0.03	0.02	0.00	102.47	Grt	564.93
a05-10A	1 / 31 .	39.68	0.09	20.70	32.82	0.24	1.21	6.94	0.02	0.01	0.02	0.01	101.73	Grt	584.41
a05-10A	1 / 32 .	39.45	0.06	20.79	33.08	0.26	1.25	6.78	0.02	0.01	0.00	0.00	101.68	Grt	603.89
a05-10A	1 / 33 .	39.50	0.08	20.76	32.87	0.23	1.17	6.93	0.03	0.00	0.06	0.00	101.62	Grt	623.37
a05-10A	1 / 34 .	39.33	0.13	20.69	32.68	0.30	1.15	7.18	0.04	0.00	0.00	0.00	101.48	Grt	642.85
a05-10A	1 / 35 .	39.47	0.11	20.88	32.87	0.27	1.06	7.03	0.03	0.00	0.05	0.00	101.77	Grt	662.33
a05-10A	1 / 36 .	39.51	0.13	20.78	31.62	0.33	1.08	8.18	0.03	0.01	0.00	0.00	101.64	Grt	681.81
a05-10A	1 / 37 .	39.52	0.14	20.80	32.05	0.32	1.04	7.86	0.04	0.00	0.02	0.00	101.80	Grt	701.29
a05-10A	1 / 38 .	39.38	0.16	20.95	31.28	0.28	1.05	8.54	0.03	0.00	0.00	0.00	101.65	Grt	720.77
a05-10A	1 / 39 .	39.53	0.15	20.84	31.16	0.33	0.98	8.62	0.03	0.01	0.04	0.00	101.68	Grt	740.25
a05-10A	1 / 40 .	39.48	0.14	20.75	31.74	0.34	1.06	8.12	0.04	0.00	0.00	0.00	101.68	Grt	759.73
a05-10A	1 / 41 .	39.47	0.16	20.60	30.99	0.34	1.04	8.72	0.01	0.01	0.01	0.01	101.37	Grt	779.21
a05-10A	1 / 42 .	39.58	0.16	20.89	31.11	0.34	1.01	8.69	0.06	0.01	0.00	0.00	101.83	Grt	798.69
a05-10A	1 / 43 .	39.76	0.17	20.76	30.50	0.34	0.99	9.19	0.03	0.01	0.00	0.00	101.72	Grt	818.17
a05-10A	1 / 44 .	39.66	0.20	20.73	30.93	0.34	1.01	8.95	0.06	0.00	0.00	0.01	101.88	Grt	837.65
a05-10A	1 / 45 .	39.58	0.18	20.72	30.52	0.38	1.01	9.27	0.05	0.00	0.03	0.00	101.74	Grt	857.13
a05-10A	1 / 46 .	39.57	0.15	20.79	30.87	0.41	1.07	8.89	0.03	0.00	0.06	0.00	101.84	Grt	876.61
a05-10A	1 / 47 .	39.59	0.04	20.87	31.96	0.48	1.11	7.74	0.04	0.00	0.01	0.00	101.82	Grt	896.09
a05-10A	1 / 48 .	39.27	0.17	21.24	30.83	0.48	1.11	8.63	0.04	0.00	0.00	0.00	101.74	Grt	915.57
a05-10A	1 / 49 .	39.05	0.18	20.45	30.53	0.47	1.06	8.96	0.04	0.00	0.03	0.02	100.80	Grt	935.05
a05-10A	1 / 50 .	39.47	0.16	20.74	30.68	0.54	1.13	8.75	0.01	0.00	0.00	0.00	101.40	Grt	954.53
a05-10A	1 / 51 .	39.48	0.20	20.67	30.58	0.51	1.05	8.92	0.03	0.01	0.00	0.00	101.43	Grt	974.01
a05-10A	1 / 52 .	39.71	0.17	20.80	30.72	0.58	1.16	8.65	0.01	0.00	0.03	0.00	101.81	Grt	993.49
a05-10A	1 / 53 .	39.55	0.19	20.81	30.71	0.63	1.15	8.49	0.03	0.01	0.00	0.00	101.54	Grt	1012.97
a05-10A	1 / 54 .	39.77	0.17	20.67	30.53	0.62	1.15	8.85	0.01	0.02	0.03	0.00	101.82	Grt	1032.45
a05-10A	1 / 55 .	39.75	0.18	20.80	31.02	0.63	1.19	8.44	0.04	0.00	0.06	0.00	102.11	Grt	1051.93
a05-10A	1 / 56 .	39.54	0.16	20.70	31.07	0.65	1.18	8.20	0.05	0.01	0.01	0.00	101.57	Grt	1071.41
a05-10A	1 / 57 .	39.61	0.17	20.76	31.13	0.59	1.23	8.08	0.06	0.00	0.05	0.01	101.69	Grt	1090.89
a05-10A	1 / 58 .	39.55	0.15	20.65	30.47	0.61	1.15	8.80	0.03	0.01	0.00	0.00	101.43	Grt	1110.37
a05-10A	1 / 59 .	~~30.47~~	~~0.15~~	~~23.01~~	~~30.45~~	~~0.59~~	~~0.85~~	~~8.02~~	~~0.02~~	~~0.00~~	~~0.02~~	~~0.03~~	~~93.61~~		1129.85
a05-10A	1 / 60 .	39.65	0.18	20.78	30.17	0.54	1.24	9.00	0.02	0.00	0.07	0.00	101.64	Grt	1149.33
a05-10A	1 / 61 .	39.74	0.24	20.68	29.76	0.56	1.16	9.36	0.04	0.00	0.06	0.00	101.57	Grt	1168.81
a05-10A	1 / 62 .	98.96	0.00	1.84	2.16	0.16	0.06	0.74	0.01	0.00	0.00	0.02	103.88	Qtz	1188.29
a05-10A	1 / 63 .	105.01	0.00	0.03	0.42	0.04	0.01	0.03	0.00	0.01	0.00	0.00	105.51	Qtz	1207.77
a05-10A	1 / 64 .	~~33.74~~	~~0.04~~	~~3.27~~	~~24.94~~	~~0.69~~	~~0.84~~	~~4.58~~	~~0.10~~	~~0.05~~	~~0.03~~	~~0.08~~	~~68.36~~		1227.25
a05-10A	1 / 65 .	~~33.09~~	~~0.13~~	~~17.50~~	~~30.57~~	~~0.32~~	~~4.04~~	~~0.54~~	~~0.04~~	~~5.59~~	~~0.05~~	~~0.81~~	~~92.67~~		1246.74
a05-10A	1 / 66 .	39.74	0.07	20.90	31.11	1.09	1.49	7.40	0.03	0.00	0.00	0.00	101.82	Grt	1266.22
a05-10A	1 / 67 .	37.52	0.40	20.05	30.45	1.08	1.91	5.82	0.04	3.10	0.03	0.17	100.57	Grt	1285.69
a05-10A	1 / 68 .	39.70	0.21	20.75	29.63	1.24	1.36	8.79	0.06	0.00	0.04	0.00	101.79	Grt	1305.17
a05-10A	1 / 69 .	40.25	0.17	15.86	30.44	1.34	1.47	8.18	0.05	0.00	0.00	0.00	97.76	Grt	1324.66
a05-10A	1 / 70 .	39.67	0.06	20.98	31.37	1.43	1.52	6.78	0.01	0.01	0.01	0.00	101.85	Grt	1344.14
a05-10A	1 / 71 .	39.68	0.21	20.80	30.23	1.51	1.38	7.94	0.04	0.01	0.00	0.00	101.79	Grt	1363.62
a05-10A	1 / 72 .	40.58	0.08	20.78	31.29	1.72	1.58	6.67	0.03	0.00	0.02	0.00	102.77	Grt	1383.1
a05-10A	1 / 73 .	39.48	0.16	20.78	30.40	1.67	1.36	7.77	0.04	0.01	0.01	0.00	101.67	Grt	1402.58
a05-10A	1 / 74 .	39.40	0.11	21.03	30.92	1.72	1.44	7.31	0.05	0.00	0.04	0.00	102.02	Grt	1422.06
a05-10A	1 / 75 .	39.58	0.10	20.87	31.08	1.74	1.41	7.18	0.04	0.01	0.00	0.01	101.95	Grt	1441.54
a05-10A	1 / 76 .	39.31	0.12	20.90	32.38	1.87	1.49	5.74	0.04	0.01	0.00	0.00	101.86	Grt	1461.02
a05-10A	1 / 77 .	~~26.58~~	~~0.17~~	~~14.26~~	~~24.99~~	~~1.48~~	~~0.64~~	~~7.18~~	~~0.04~~	~~0.04~~	~~0.00~~	~~0.06~~	~~75.45~~		1480.5
a05-10A	1 / 78 .	~~33.00~~	~~0.14~~	~~3.74~~	~~25.42~~	~~1.38~~	~~1.12~~	~~6.16~~	~~0.09~~	~~0.06~~	~~0.00~~	~~0.03~~	~~71.14~~		1499.98
a05-10A	1 / 79 .	39.45	0.17	20.69	30.70	1.75	1.29	7.37	0.01	0.01	0.02	0.01	101.44	Grt	1519.46
a05-10A	1 / 80 .	39.30	0.09	20.86	32.10	2.00	1.34	5.98	0.03	0.01	0.03	0.00	101.75	Grt	1538.94
a05-10A	1 / 81 .	39.63	0.22	20.55	31.30	2.21	1.12	6.89	0.05	0.00	0.02	0.00	101.99	Grt	1558.42
a05-10A	1 / 82 .	39.42	0.20	20.68	30.10	2.07	1.16	8.00	0.06	0.00	0.00	0.00	101.70	Grt	1577.9
a05-10A	1 / 83 .	39.71	0.12	20.77	29.65	2.23	1.05	8.36	0.00	0.00	0.00	0.00	101.82	Grt	1597.38
a05-10A	1 / 84 .	39.50	0.08	20.99	30.03	2.63	1.10	7.94	0.03	0.01	0.02	0.00	102.32	Grt	1616.86
a05-10A	1 / 85 .	32.87	0.08	32.56	25.32	1.83	0.94	6.62	0.14	0.02	0.00	0.10	100.47	Grt	1636.34
a05-10A	1 / 86 .	39.51	0.14	20.70	29.80	2.66	1.10	7.93	0.01	0.00	0.01	0.01	101.88	Grt	1655.82
a05-10A	1 / 87 .	39.49	0.10	20.87	29.46	2.72	0.95	8.18	0.02	0.00	0.01	0.00	101.81	Grt	1675.3
a05-10A	1 / 88 .	39.40	0.19	20.69	29.18	2.83	0.97	8.71	0.08	0.00	0.00	0.02	102.01	Grt	1694.78
a05-10A	1 / 89 .	39.54	0.23	20.49	28.43	2.71	0.92	9.05	0.03	0.01	0.06	0.00	101.48	Grt	1714.26
a05-10A	1 / 90 .	39.40	0.07	20.97	30.05	3.08	1.03	7.43	0.01	0.00	0.00	0.00	102.05	Grt	1733.74
a05-10A	1 / 91 .	39.50	0.24	20.68	28.58	2.89	0.91	8.76	0.04	0.00	0.03	0.00	101.63	Grt	1753.22
a05-10A	1 / 1 .	~~35.42~~	~~0.51~~	~~18.03~~	~~19.15~~	~~0.02~~	~~6.76~~	~~0.08~~	~~0.01~~	~~8.66~~	~~0.34~~	~~0.45~~	~~89.42~~		0
a05-10A	1 / 2 .	37.02	0.04	21.57	31.58	0.35	1.65	6.11	0.07	0.08	0.00	0.08	98.55	Grt	19.48
a05-10A	1 / 3 .	39.44	0.03	20.97	32.19	0.31	1.97	6.49	0.03	0.00	0.00	0.00	101.41	Grt	38.96
a05-10A	1 / 4 .	~~29.27~~	~~0.04~~	~~19.87~~	~~29.94~~	~~0.23~~	~~1.67~~	~~5.25~~	~~0.07~~	~~0.03~~	~~0.01~~	~~0.05~~	~~86.42~~		58.44

Metagranite

Sample	Spot	SiO2	TiO2	Al2O3	FeO	MnO	MgO	CaO	Na2O	K2O	F	Cl	Total	Min	distance (um)
a05-10A	1 / 5 .	39.57	0.05	20.86	32.38	0.24	2.16	6.12	0.02	0.02	0.02	0.01	101.44	Grt	77.92
a05-10A	1 / 6 .	39.74	0.06	20.99	31.41	0.18	2.28	7.01	0.02	0.01	0.03	0.00	101.72	Grt	97.4
a05-10A	1 / 7 .	39.85	0.06	21.04	31.83	0.15	2.28	6.69	0.00	0.00	0.04	0.01	101.94	Grt	116.88
a05-10A	1 / 8 .	39.76	0.06	21.07	31.92	0.14	2.43	6.58	0.02	0.00	0.02	0.00	101.99	Grt	136.36
a05-10A	1 / 9 .	39.91	0.06	21.07	31.80	0.18	2.24	6.65	0.02	0.01	0.05	0.00	101.99	Grt	155.84
a05-10A	1 / 10 .	39.83	0.07	20.94	31.52	0.16	2.26	7.13	0.01	0.00	0.00	0.00	101.87	Grt	175.32
a05-10A	1 / 11 .	39.84	0.07	21.04	31.20	0.17	2.07	7.40	0.02	0.00	0.04	0.00	101.84	Grt	194.8
a05-10A	1 / 12 .	39.70	0.08	21.07	31.56	0.17	2.11	7.14	0.02	0.01	0.00	0.00	101.84	Grt	214.28
a05-10A	1 / 13 .	39.75	0.07	20.97	31.61	0.18	2.01	7.20	0.01	0.01	0.00	0.01	101.77	Grt	233.76
a05-10A	1 / 14 .	39.61	0.07	20.93	31.57	0.17	2.05	7.33	0.01	0.01	0.03	0.00	101.79	Grt	253.24
a05-10A	1 / 15 .	39.69	0.08	21.06	31.83	0.20	1.93	7.05	0.03	0.00	0.02	0.00	101.88	Grt	272.72
a05-10A	1 / 16 .	39.74	0.09	20.86	30.96	0.17	1.82	8.03	0.01	0.00	0.00	0.00	101.67	Grt	292.2
a05-10A	1 / 17 .	39.79	0.12	21.06	31.36	0.20	1.77	7.62	0.02	0.00	0.04	0.00	101.98	Grt	311.68
a05-10A	1 / 18 .	39.44	0.07	20.89	32.24	0.21	1.80	6.92	0.01	0.00	0.00	0.01	101.55	Grt	331.16
a05-10A	1 / 19 .	39.76	0.08	20.88	32.37	0.20	1.69	6.94	0.01	0.00	0.00	0.00	101.90	Grt	350.64
a05-10A	1 / 20 .	39.50	0.09	20.88	31.78	0.18	1.70	7.43	0.01	0.00	0.06	0.01	101.62	Grt	370.12
a05-10A	1 / 21 .	39.66	0.09	20.95	32.56	0.21	1.67	7.03	0.00	0.00	0.01	0.00	102.19	Grt	389.6
a05-10A	1 / 22 .	39.52	0.07	20.89	32.90	0.19	1.65	6.81	0.01	0.00	0.09	0.00	102.12	Grt	409.09
a05-10A	1 / 23 .	39.62	0.07	20.71	32.66	0.19	1.53	6.72	0.02	0.00	0.02	0.00	101.54	Grt	428.56
a05-10A	1 / 24 .	39.70	0.07	20.90	31.82	0.18	1.53	7.22	0.03	0.00	0.00	0.03	101.47	Grt	448.05
a05-10A	1 / 25 .	39.67	0.11	20.80	32.20	0.21	1.51	7.18	0.03	0.00	0.00	0.00	101.69	Grt	467.53
a05-10A	1 / 26 .	39.51	0.08	20.91	32.47	0.21	1.47	6.97	0.04	0.00	0.00	0.00	101.60	Grt	487.01
a05-10A	1 / 27 .	39.50	0.07	20.81	32.66	0.20	1.41	6.87	0.03	0.00	0.00	0.00	101.49	Grt	506.49
a05-10A	1 / 28 .	24.34	~~0.09~~	~~17.58~~	~~31.62~~	~~0.20~~	~~0.71~~	~~6.20~~	~~0.05~~	~~0.15~~	~~0.00~~	~~0.07~~	~~80.99~~		525.97
a05-10A	1 / 29 .	31.43	~~0.08~~	~~17.01~~	~~26.22~~	~~0.08~~	~~5.07~~	~~4.13~~	~~0.17~~	~~3.88~~	~~0.02~~	~~0.57~~	~~88.67~~		545.45
a05-10A	1 / 30 .	39.66	0.09	21.44	32.67	0.25	1.26	7.06	0.01	0.03	0.02	0.00	102.47	Grt	564.93
a05-10A	1 / 31 .	39.68	0.09	20.70	32.82	0.24	1.21	6.94	0.02	0.01	0.02	0.01	101.73	Grt	584.41
a05-10A	1 / 32 .	39.45	0.06	20.79	33.08	0.26	1.25	6.78	0.02	0.01	0.00	0.00	101.68	Grt	603.89
a05-10A	1 / 33 .	39.50	0.08	20.76	32.87	0.23	1.17	6.93	0.03	0.00	0.06	0.00	101.62	Grt	623.37
a05-10A	1 / 34 .	39.33	0.13	20.69	32.68	0.30	1.15	7.18	0.04	0.00	0.00	0.00	101.48	Grt	642.85
a05-10A	1 / 35 .	39.47	0.11	20.88	32.87	0.27	1.06	7.03	0.03	0.00	0.05	0.00	101.77	Grt	662.33
a05-10A	1 / 36 .	39.51	0.13	20.78	31.62	0.33	1.08	8.18	0.03	0.01	0.00	0.00	101.64	Grt	681.81
a05-10A	1 / 37 .	39.52	0.14	20.80	32.05	0.32	1.04	7.86	0.04	0.00	0.02	0.00	101.80	Grt	701.29
a05-10A	1 / 38 .	39.38	0.16	20.95	31.28	0.28	1.05	8.54	0.03	0.00	0.00	0.00	101.65	Grt	720.77
a05-10A	1 / 39 .	39.53	0.15	20.84	31.16	0.33	0.98	8.62	0.03	0.01	0.04	0.00	101.68	Grt	740.25
a05-10A	1 / 40 .	39.48	0.14	20.75	31.74	0.34	1.06	8.12	0.04	0.00	0.00	0.00	101.68	Grt	759.73
a05-10A	1 / 41 .	39.47	0.16	20.60	30.99	0.34	1.04	8.72	0.01	0.01	0.01	0.01	101.37	Grt	779.21
a05-10A	1 / 42 .	39.58	0.16	20.89	31.11	0.34	1.01	8.69	0.06	0.01	0.00	0.00	101.83	Grt	798.69
a05-10A	1 / 43 .	39.76	0.17	20.76	30.50	0.34	0.99	9.19	0.03	0.01	0.00	0.00	101.72	Grt	818.17
a05-10A	1 / 44 .	39.66	0.20	20.73	30.93	0.34	1.01	8.95	0.06	0.00	0.00	0.01	101.88	Grt	837.65
a05-10A	1 / 45 .	39.58	0.18	20.72	30.52	0.38	1.01	9.27	0.05	0.00	0.03	0.00	101.74	Grt	857.13
a05-10A	1 / 46 .	39.57	0.15	20.79	30.87	0.41	1.07	8.89	0.03	0.00	0.06	0.00	101.84	Grt	876.61
a05-10A	1 / 47 .	39.59	0.04	20.87	31.96	0.48	1.11	7.74	0.04	0.00	0.01	0.00	101.82	Grt	896.09
a05-10A	1 / 48 .	39.27	0.17	21.24	30.83	0.48	1.11	8.63	0.04	0.00	0.00	0.00	101.74	Grt	915.57
a05-10A	1 / 49 .	39.05	0.18	20.45	30.53	0.47	1.06	8.96	0.04	0.00	0.03	0.02	100.80	Grt	935.05
a05-10A	1 / 50 .	39.47	0.16	20.74	30.68	0.54	1.13	8.75	0.01	0.00	0.00	0.00	101.40	Grt	954.53
a05-10A	1 / 51 .	39.48	0.20	20.67	30.58	0.51	1.05	8.92	0.03	0.01	0.00	0.00	101.43	Grt	974.01
a05-10A	1 / 52 .	39.71	0.17	20.80	30.72	0.58	1.16	8.65	0.01	0.00	0.03	0.00	101.81	Grt	993.49
a05-10A	1 / 53 .	39.55	0.19	20.81	30.71	0.63	1.15	8.49	0.03	0.01	0.00	0.00	101.54	Grt	1012.97
a05-10A	1 / 54 .	39.77	0.17	20.67	30.53	0.62	1.15	8.85	0.01	0.02	0.03	0.00	101.82	Grt	1032.45
a05-10A	1 / 55 .	39.75	0.18	20.80	31.02	0.63	1.19	8.44	0.04	0.00	0.06	0.00	102.11	Grt	1051.93
a05-10A	1 / 56 .	39.54	0.16	20.70	31.07	0.65	1.18	8.20	0.05	0.01	0.01	0.00	101.57	Grt	1071.41
a05-10A	1 / 57 .	39.61	0.17	20.76	31.13	0.59	1.23	8.08	0.06	0.00	0.05	0.01	101.69	Grt	1090.89
a05-10A	1 / 58 .	39.55	0.15	20.65	30.47	0.61	1.15	8.80	0.03	0.01	0.00	0.00	101.43	Grt	1110.37
a05-10A	1 / 59 .	~~30.47~~	~~0.15~~	~~23.01~~	~~30.45~~	~~0.59~~	~~0.85~~	~~8.02~~	~~0.02~~	~~0.00~~	~~0.02~~	~~0.03~~	~~93.61~~		1129.85
a05-10A	1 / 60 .	39.65	0.18	20.78	30.17	0.54	1.24	9.00	0.02	0.00	0.07	0.00	101.64	Grt	1149.33
a05-10A	1 / 61 .	39.74	0.24	20.68	29.76	0.56	1.16	9.36	0.04	0.00	0.06	0.00	101.57	Grt	1168.81
a05-10A	1 / 62 .	98.96	0.00	1.84	2.16	0.16	0.06	0.74	0.01	0.00	0.00	0.02	103.88	Qtz	1188.29
a05-10A	1 / 63 .	105.01	0.00	0.03	0.42	0.04	0.01	0.03	0.00	0.01	0.00	0.00	105.51	Qtz	1207.77
a05-10A	1 / 64 .	~~33.74~~	~~0.04~~	~~3.27~~	~~24.94~~	~~0.69~~	~~0.84~~	~~4.58~~	~~0.10~~	~~0.05~~	~~0.03~~	~~0.08~~	~~68.36~~		1227.25
a05-10A	1 / 65 .	~~33.09~~	~~0.13~~	~~17.50~~	~~30.57~~	~~0.32~~	~~4.04~~	~~0.54~~	~~0.04~~	~~5.59~~	~~0.05~~	~~0.81~~	~~92.67~~		1246.74
a05-10A	1 / 66 .	39.74	0.07	20.90	31.11	1.09	1.49	7.40	0.03	0.00	0.00	0.00	101.82	Grt	1266.22
a05-10A	1 / 67 .	37.52	0.40	20.05	30.45	1.08	1.91	5.82	0.04	3.10	0.03	0.17	100.57	Grt	1285.69
a05-10A	1 / 68 .	39.70	0.21	20.75	29.63	1.24	1.36	8.79	0.06	0.00	0.04	0.00	101.79	Grt	1305.17
a05-10A	1 / 69 .	40.25	0.17	15.86	30.44	1.34	1.47	8.18	0.05	0.00	0.00	0.00	97.76	Grt	1324.66
a05-10A	1 / 70 .	39.67	0.06	20.98	31.37	1.43	1.52	6.78	0.01	0.01	0.01	0.00	101.85	Grt	1344.14
a05-10A	1 / 71 .	39.68	0.21	20.80	30.23	1.51	1.38	7.94	0.04	0.01	0.00	0.00	101.79	Grt	1363.62
a05-10A	1 / 72 .	40.58	0.08	20.78	31.29	1.72	1.58	6.67	0.03	0.00	0.02	0.00	102.77	Grt	1383.1
a05-10A	1 / 73 .	39.48	0.16	20.78	30.40	1.67	1.36	7.77	0.04	0.01	0.01	0.00	101.67	Grt	1402.58
a05-10A	1 / 74 .	39.40	0.11	21.03	30.92	1.72	1.44	7.31	0.05	0.00	0.04	0.00	102.02	Grt	1422.06
a05-10A	1 / 75 .	39.58	0.10	20.87	31.08	1.74	1.41	7.18	0.04	0.01	0.00	0.01	101.95	Grt	1441.54
a05-10A	1 / 76 .	39.31	0.12	20.90	32.38	1.87	1.49	5.74	0.04	0.01	0.00	0.00	101.86	Grt	1461.02
a05-10A	1 / 77 .	~~26.58~~	~~0.17~~	~~14.26~~	~~24.99~~	~~1.48~~	~~0.64~~	~~7.18~~	~~0.04~~	~~0.04~~	~~0.00~~	~~0.06~~	~~75.45~~		1480.5
a05-10A	1 / 78 .	33.00	0.14	3.74	25.42	1.38	1.12	6.16	0.09	0.06	0.00	0.03	71.14	Grt	1499.98
a05-10A	1 / 79 .	39.45	0.17	20.69	30.70	1.75	1.29	7.37	0.01	0.01	0.02	0.01	101.44	Grt	1519.46
a05-10A	1 / 80 .	39.30	0.09	20.86	32.10	2.00	1.34	5.98	0.03	0.01	0.03	0.00	101.75	Grt	1538.94
a05-10A	1 / 81 .	39.63	0.22	20.55	31.30	2.21	1.12	6.89	0.05	0.00	0.02	0.00	101.99	Grt	1558.42
a05-10A	1 / 82 .	39.42	0.20	20.68	30.10	2.07	1.16	8.00	0.06	0.00	0.00	0.00	101.70	Grt	1577.9
a05-10A	1 / 83 .	39.71	0.12	20.77	29.65	2.23	1.05	8.36	0.00	0.00	0.00	0.00	101.82	Grt	1597.38
a05-10A	1 / 84 .	39.50	0.08	20.99	30.03	2.63	1.10	7.94	0.03	0.01	0.02	0.00	102.32	Grt	1616.86
a05-10A	1 / 85 .	32.87	0.08	32.56	25.32	1.83	0.94	6.62	0.14	0.02	0.00	0.10	100.47	Grt	1636.34
a05-10A	1 / 86 .	39.51	0.14	20.70	29.80	2.66	1.10	7.93	0.01	0.00	0.01	0.01	101.88	Grt	1655.82
a05-10A	1 / 87 .	39.49	0.10	20.87	29.46	2.72	0.95	8.18	0.02	0.00	0.01	0.00	101.81	Grt	1675.3
a05-10A	1 / 88 .	39.40	0.19	20.69	29.18	2.83	0.97	8.71	0.08	0.00	0.00	0.02	102.01	Grt	1694.78

Metagranite

Sample	Spot	SiO2	TiO2	Al2O3	FeO	MnO	MgO	CaO	Na2O	K2O	F	Cl	Total	Min	distance (um)
a05-10A	1 / 89 .	39.54	0.23	20.49	28.43	2.71	0.92	9.05	0.03	0.01	0.06	0.00	101.48	Grt	1714.26
a05-10A	1 / 90 .	39.40	0.07	20.97	30.05	3.08	1.03	7.43	0.01	0.00	0.00	0.00	102.05	Grt	1733.74
a05-10A	1 / 91 .	39.50	0.24	20.68	28.58	2.89	0.91	8.76	0.04	0.00	0.03	0.00	101.63	Grt	1753.22
a05-10A	1 / 1 .	57.30	0.18	27.22	2.49	0.04	2.48	0.00	0.14	8.47	0.35	0.03	98.70	Ms	
a05-10A	2 / 1 .	56.19	0.22	30.09	2.85	0.04	3.17	0.01	0.05	3.82	0.28	0.05	96.77	Ms	
a05-10A	3 / 1 .	56.76	0.23	30.83	2.39	0.01	2.06	0.00	0.19	7.66	0.25	0.02	100.39	Ms	
a05-10A	4 / 1 .	50.37	0.41	38.32	1.07	0.02	0.60	0.00	0.22	4.72	0.00	0.00	95.70	Ms	
a05-10A	5 / 1 .	54.55	0.05	35.24	1.11	0.01	0.74	0.02	0.45	7.84	0.16	0.03	100.20	Ms	
a05-10A	6 / 1 .	51.18	0.31	36.81	1.62	0.00	0.98	0.01	0.12	4.55	0.12	0.02	95.71	Ms	
a05-10A	7 / 1 .	58.21	0.23	29.21	2.68	0.00	2.84	0.01	0.16	8.14	0.24	0.03	101.75	Ms	
a05-10A	8 / 1 .	54.63	0.28	30.84	2.88	0.04	2.93	0.01	0.05	3.60	0.19	0.06	95.49	Ms	
a05-10A	9 / 1 .	59.12	0.32	28.51	2.68	0.00	3.09	0.00	0.13	7.75	0.25	0.02	101.89	Ms	
a05-10A	10 / 1 .	54.79	0.23	31.30	2.60	0.04	2.61	0.01	0.07	3.91	0.15	0.02	95.73	Ms	
a05-10A	11 / 1 .	59.80	0.18	26.58	2.76	0.00	3.44	0.01	0.13	7.44	0.30	0.18	100.82	Ms	
a05-10A	12 / 1 .	50.62	0.19	38.74	1.13	0.00	0.64	0.01	0.21	4.92	0.12	0.00	96.57	Ms	
a05-10A	13 / 1 .	58.54	0.28	30.17	2.32	0.00	2.53	0.02	0.15	7.90	0.25	0.01	102.17	Ms	
a05-10A	14 / 1 .	51.75	0.73	36.51	1.30	0.02	0.77	0.14	0.37	5.49	0.08	0.10	97.23	Ms	
a05-10A	15 / 1 .	54.89	0.46	35.52	1.13	0.00	0.78	0.01	0.51	8.03	0.14	0.00	101.46	Ms	
a05-10A	16 / 1 .	51.01	0.49	38.44	1.07	0.01	0.61	0.00	0.19	4.66	0.11	0.00	96.58	Ms	
a05-10A	17 / 1 .	55.27	0.12	34.18	1.57	0.00	1.36	0.01	0.25	8.12	0.17	0.01	101.05	Ms	
a05-10A	18 / 1 .	51.35	0.19	38.65	1.15	0.00	0.65	0.00	0.23	4.74	0.07	0.00	97.03	Ms	
a05-10A	19 / 1 .	61.62	0.16	25.81	2.61	0.01	4.06	0.00	0.10	7.66	0.45	0.06	102.54	Ms	
a05-10A	20 / 1 .	51.85	0.01	37.27	1.46	0.02	1.06	0.02	0.14	4.84	0.12	0.03	96.80	Ms	
a05-10A	21 / 1 .	54.69	0.25	35.13	1.23	0.00	0.74	0.03	0.44	7.80	0.08	0.05	100.41	Ms	
a05-10A	22 / 1 .	51.28	0.70	39.18	1.01	0.01	0.53	0.00	0.26	4.79	0.01	0.00	97.73	Ms	
a05-10A	23 / 1 .	54.91	0.66	35.26	1.24	0.01	0.87	0.00	0.57	8.00	0.13	0.00	101.64	Ms	
a05-10A	24 / 1 .	51.79	1.19	36.28	1.50	0.00	0.97	0.00	0.16	5.20	0.10	0.01	97.22	Ms	
a05-10A	25 / 1 .	54.55	0.74	35.74	0.96	0.00	0.56	0.03	0.41	7.82	0.08	0.02	100.88	Ms	
a05-10A	26 / 1 .	38.98	2.72	16.03	21.47	0.06	8.73	0.00	0.09	7.58	0.39	0.72	96.77	Bt	
a05-10A	27 / 1 .	39.27	2.68	15.35	20.79	0.06	9.10	0.06	0.13	9.00	0.36	0.66	97.46	Bt	
a05-10A	28 / 1 .	37.94	2.75	16.54	21.48	0.02	8.22	0.03	0.06	6.43	0.33	0.67	94.47	Bt	
a05-10A	29 / 1 .	38.42	2.54	16.62	21.08	0.03	9.04	0.01	0.08	9.19	0.35	0.52	97.89	Bt	
a05-10A	30 / 1 .	38.78	2.85	16.19	21.47	0.03	8.58	0.00	0.09	6.57	0.28	0.70	95.54	Bt	
a05-10A	31 / 1 .	39.02	2.81	15.51	21.11	0.03	8.86	0.01	0.13	8.92	0.30	0.79	97.50	Bt	
a05-10A	32 / 1 .	55.49	0.33	30.89	2.79	0.00	2.87	0.03	0.06	3.69	0.17	0.05	96.37	Ms	
a05-10A	33 / 1 .	61.25	0.27	26.15	2.74	0.00	3.56	0.01	0.13	7.73	0.34	0.04	102.22	Ms	
a05-10A	34 / 1 .	55.22	0.37	31.60	2.65	0.00	2.59	0.01	0.07	3.96	0.25	0.02	96.75	Ms	
a05-10A	35 / 1 .	58.35	0.35	27.99	2.89	0.00	3.18	0.00	0.13	8.07	0.37	0.12	101.43	Ms	
a05-10A	36 / 1 .	52.77	0.18	37.18	1.57	0.01	0.92	0.06	0.12	4.79	0.07	0.02	97.69	Ms	
a05-10A	37 / 1 .	54.11	0.13	35.06	1.75	0.00	1.11	0.00	0.28	8.13	0.11	0.02	100.69	Ms	
a05-10A	38 / 1 .	53.70	0.29	33.08	2.42	0.00	2.18	0.03	0.08	4.37	0.18	0.03	96.35	Ms	
a05-10A	39 / 1 .	58.50	0.35	28.19	2.77	0.00	3.07	0.00	0.12	7.58	0.42	0.04	101.02	Ms	
a05-10A	40 / 1 .	40.08	0.13	24.81	21.75	4.22	0.87	6.25	0.17	1.65	0.02	0.01	99.97	Grt	
a05-10A	41 / 1 .	~~29.38~~	~~0.06~~	~~17.40~~	~~35.68~~	~~1.34~~	~~2.78~~	~~0.45~~	~~0.13~~	~~3.41~~	~~0.05~~	~~0.56~~	~~91.23~~		
a05-10A	42 / 1 .	~~33.86~~	~~0.02~~	~~19.84~~	~~28.16~~	~~4.47~~	~~1.97~~	~~9.19~~	~~0.01~~	~~0.05~~	~~0.01~~	~~0.01~~	~~97.59~~	mix	
a05-10A	43 / 1 .	~~12.47~~	~~0.00~~	~~4.41~~	~~16.49~~	~~2.34~~	~~8.95~~	~~22.62~~	~~0.00~~	~~0.00~~	~~0.00~~	~~0.00~~	~~67.23~~	mix	
a05-10A	44 / 1 .	39.61	0.01	62.47	1.07	0.10	0.02	0.04	0.00	0.09	0.00	0.01	103.38	ky mix	
a05-10A	45 / 1 .	34.39	0.01	62.61	1.70	0.11	0.02	0.14	0.02	0.01	0.00	0.11	99.08	ky mix	
a05-10A	46 / 1 .	51.78	0.13	34.41	2.28	0.00	1.55	0.01	0.12	4.24	0.17	0.02	94.70	ms	
a05-10A	47 / 1 .	57.07	0.20	28.98	3.33	0.05	2.17	0.13	0.40	7.18	0.23	0.04	99.78	ms	
a05-10A	48 / 1 .	39.92	0.00	63.80	0.59	0.02	0.01	0.01	0.00	0.00	0.00	0.00	104.33	ms	
a05-10A	49 / 1 .	0.03	99.66	0.03	0.48	0.02	0.00	0.03	0.01	0.00	0.23	0.00	100.47	Ru	
a05-10A	50 / 1 .	51.33	0.12	35.52	1.57	0.03	1.21	0.00	0.19	4.60	0.14	0.00	94.71	Ms	
a05-10A	51 / 1 .	52.40	0.18	35.03	1.27	0.00	0.60	0.00	0.49	7.52	0.08	0.01	97.55	Ms	
a05-10A	52 / 1 .	50.97	0.16	36.57	1.21	0.00	0.55	0.01	0.26	5.16	0.00	0.00	94.85	Ms	
a05-10A	53 / 1 .	60.33	0.22	25.75	3.13	0.00	3.34	0.02	0.18	7.60	0.27	0.06	100.87	Ms	
a05-10A	54 / 1 .	57.23	0.22	28.36	3.12	0.01	3.26	0.01	0.09	3.67	0.28	0.06	96.32	Ms	
a05-10A	55 / 1 .	51.10	0.19	33.75	1.49	0.02	0.59	0.07	0.67	8.66	0.08	0.09	96.73	Ms	
a05-10A	56 / 1 .	47.58	0.62	39.08	1.77	0.02	0.48	0.13	0.37	5.95	0.10	0.12	96.23	Ms	
a05-10A	57 / 1 .	57.84	0.27	26.40	3.05	0.01	3.23	0.03	0.14	8.18	0.23	0.10	99.48	Ms	
a05-10A	58 / 1 .	48.93	0.07	43.01	0.78	0.06	0.08	0.71	2.02	1.05	0.03	0.00	96.73	Ms	
L08-04	1 / 1 .	46.39	0.10	37.24	0.94	0.04	0.46	0.00	0.46	10.86	0.16	0.01	96.66	Ms	
L08-04	2 / 1 .	46.58	0.16	37.90	1.14	0.05	0.50	0.00	0.24	10.19	0.09	0.00	96.87	Ms	
L08-04	3 / 1 .	64.74	0.01	19.28	0.02	0.00	0.01	0.01	0.70	16.01	0.00	0.01	100.78	kfeld	
L08-04	4 / 1 .	67.55	0.00	20.88	0.03	0.00	0.00	1.05	9.32	0.19	0.00	0.01	98.96	plag	
L08-04	5 / 1 .	46.22	0.12	37.56	1.16	0.02	0.50	0.00	0.81	10.32	0.13	0.00	96.80	ms	
L08-04	6 / 1 .	46.80	0.12	38.22	1.06	0.02	0.50	0.01	0.58	9.82	0.04	0.00	97.17	ms	
L08-04	7 / 1 .	64.89	0.00	19.10	0.01	0.01	0.00	0.05	0.58	16.21	0.07	0.00	100.92	kfeld	
L08-04	8 / 1 .	45.41	0.12	36.57	1.19	0.00	0.54	0.00	0.42	9.22	0.21	0.00	93.66	ms	
L08-04	1 / 1 .	~~18.87~~	~~0.02~~	~~22.11~~	~~0.76~~	~~0.03~~	~~0.36~~	~~0.02~~	~~0.50~~	~~6.84~~	~~0.18~~	~~0.00~~	~~49.69~~		
L08-04	2 / 1 .	44.94	0.09	35.85	1.11	0.03	0.57	0.00	0.37	10.15	0.15	0.00	93.25	ms	
L08-04	3 / 1 .	46.47	0.14	37.19	1.23	0.00	0.62	0.01	0.73	9.20	0.11	0.01	95.72	ms	
L08-04	4 / 1 .	63.72	0.00	19.32	0.00	0.00	0.00	0.01	0.65	16.10	0.04	0.00	99.81	kfeld	
L08-04	5 / 1 .	46.96	0.06	38.04	1.08	0.00	0.54	0.00	0.78	9.70	0.15	0.01	97.32	Ms	
L08-04	6 / 1 .	46.36	0.07	37.14	1.00	0.00	0.52	0.00	0.45	10.75	0.07	0.00	96.35	Ms	
L08-04	7 / 1 .	47.14	0.22	38.19	1.05	0.02	0.48	0.00	0.72	9.67	0.11	0.01	97.62	Ms	
L08-04	8 / 1 .	44.90	0.11	36.28	0.84	0.00	0.42	0.03	0.21	10.43	0.12	0.00	93.32	Ms	
L08-04	9 / 1 .	46.05	0.15	37.35	0.99	0.02	0.42	0.02	0.68	9.05	0.14	0.01	94.88	Ms	
L08-04	10 / 1 .	46.74	0.10	36.84	1.04	0.02	0.59	0.02	0.37	10.48	0.20	0.02	96.41	Ms	
L08-04	11 / 1 .	47.91	0.20	38.21	1.00	0.00	0.52	0.00	0.70	9.43	0.18	0.01	98.17	Ms	
L08-04	12 / 1 .	~~0.00~~	~~0.00~~	~~0.01~~	~~0.00~~	~~0.00~~	~~0.02~~	~~0.00~~	~~0.13~~	~~0.14~~	~~0.01~~	~~0.00~~	~~-0.67~~		
L08-04	13 / 1 .	48.75	0.25	28.66	3.87	0.05	1.94	0.51	0.08	9.59	0.45	0.01	94.16	Ms	
L08-04	14 / 1 .	69.09	0.14	17.02	3.03	0.05	1.71	0.10	0.06	6.73	0.38	0.01	98.32	ms	

Metagranite

Sample	Spot	SiO2	TiO2	Al2O3	FeO	MnO	MgO	CaO	Na2O	K2O	F	Cl	Total	Min	distance (um)
L08-04	15 / 1 .	72.93	0.09	15.24	1.89	0.05	0.91	0.20	0.25	8.44	0.21	0.00	100.20	ms	
L08-04	16 / 1 .	50.08	0.14	27.00	4.17	0.06	2.34	0.09	0.06	10.93	0.59	0.01	95.45	ms	
L08-04	17 / 1 .	54.17	0.11	25.80	5.52	0.08	2.19	0.07	0.07	10.07	0.40	0.01	98.50	ms	
L08-04	18 / 1 .	62.16	0.14	21.90	3.15	0.05	1.63	0.09	0.05	9.36	0.40	0.01	98.93	ms	
L08-04	19 / 1 .	57.30	0.21	25.15	4.76	0.05	2.26	0.26	0.08	10.28	0.55	0.01	100.92	ms	
L08-04	20 / 1 .	32.95	4.84	17.67	26.56	0.49	3.96	0.00	0.04	9.16	0.45	0.08	96.19	Bt	
L08-04	21 / 1 .	33.98	2.85	18.52	26.23	0.37	4.13	0.01	0.04	9.62	0.39	0.08	96.21	Bt	
L08-04	22 / 1 .	33.60	3.05	18.40	25.92	0.35	4.09	0.02	0.06	9.56	0.42	0.08	95.56	Bt	
L08-04	23 / 1 .	33.62	3.12	17.94	26.05	0.39	4.36	0.06	0.06	9.53	0.35	0.07	95.54	Bt	
L08-04	27 / 1 .	47.13	0.19	38.14	1.31	0.01	0.59	0.00	0.83	9.97	0.17	0.00	98.34	ms	
L08-04	28 / 1 .	45.72	0.09	37.45	1.27	0.02	0.56	0.00	0.59	10.52	0.16	0.00	96.36	ms	

Puga Gneiss

Sample	Spot	SiO2	TiO2	Al2O3	Cr2O3	FeO	MnO	MgO	CaO	Na2O	K2O	F	Cl	Total	Min	distance (u
05-02	All SiO2 increased by 1/0.95, i.e. 95% --> 100%, Al reduced by same factor															
05-02	1 / 1 .	36.79	1.02	17.95	0.01	15.94	0.12	12.28	0.00	0.11	10.18	0.55	0.05	94.75	Bt	
05-02	2 / 1 .	100.98	0.02	0.01	0.01	0.03	0.01	0.00	0.01	0.00	0.00	0.00	0.00	101.05	Qz	
05-02	3 / 1 .	~~32.13~~	~~1.33~~	~~15.61~~	~~0.01~~	~~17.32~~	~~0.17~~	~~9.44~~	~~0.04~~	~~0.08~~	~~8.35~~	~~0.50~~	~~0.07~~	~~84.83~~	xBt	
05-02	4 / 1 .	36.49	1.44	17.51	0.05	18.54	0.19	10.77	0.03	0.09	10.09	0.44	0.09	95.53	Bt	
05-02	5 / 1 .	~~31.40~~	~~1.30~~	~~15.49~~	~~0.06~~	~~16.63~~	~~0.22~~	~~9.47~~	~~0.00~~	~~0.09~~	~~8.53~~	~~0.45~~	~~0.05~~	~~83.47~~	xBt	
05-02	6 / 1 .	36.57	1.28	17.52	0.03	16.85	0.15	12.23	0.01	0.07	10.11	0.52	0.08	95.18	Bt	
05-02	7 / 1 .	~~0.00~~	~~50.59~~	~~0.05~~	~~0.07~~	~~40.30~~	~~0.04~~	~~0.00~~	~~0.00~~	~~0.00~~	~~0.02~~	~~0.00~~	~~0.01~~	91.02	Ilm	
05-02	8 / 1 .	0.10	53.93	0.37	0.02	41.22	0.23	0.00	0.03	0.01	0.02	0.00	0.00	95.93	Ilm	
05-02	9 / 1 .	0.07	55.55	0.37	0.05	39.07	0.23	0.00	0.03	0.00	0.02	0.00	0.00	95.36	Ilm	
05-02	10 / 1 .	36.67	1.49	18.07	0.00	16.26	0.11	11.93	0.00	0.10	10.21	0.49	0.07	95.13	Bt	
05-02	11 / 1 .	~~0.05~~	~~11.39~~	~~0.07~~	~~0.08~~	~~76.84~~	~~0.14~~	~~0.02~~	~~0.01~~	~~0.00~~	~~0.12~~	~~0.00~~	~~0.01~~	~~88.72~~	Hem?	
05-02	12 / 1 .	36.20	1.10	17.82	0.09	16.15	0.10	12.60	0.01	0.09	9.98	0.51	0.05	94.46	Bt	
05-02	13 / 1 .	26.09	0.13	21.64	0.01	19.83	0.20	18.54	0.00	0.03	0.05	0.10	0.03	86.58	Chl	
05-02	14 / 1 .	25.57	0.07	22.12	0.00	20.29	0.20	18.21	0.02	0.01	0.01	0.09	0.00	86.54	Chl	
05-02	15 / 1 .	37.04	1.40	17.66	0.03	16.11	0.14	12.60	0.03	0.08	10.08	0.55	0.09	95.55	Bt	
05-02	16 / 1 .	0.01	0.13	0.14	0.00	91.37	0.04	0.00	0.00	0.00	0.00	0.00	0.00	91.67	Mag	
05-02	17 / 1 .	27.77	0.09	21.73	0.03	20.72	0.16	16.42	0.08	0.43	0.04	0.06	0.03	87.53	Chl	
05-02	18 / 1 .	25.10	0.05	22.23	0.02	24.84	0.22	14.94	0.05	0.02	0.00	0.12	0.03	87.57	Chl	
05-02	19 / 1 .	26.06	0.07	22.06	0.03	20.69	0.23	17.65	0.02	0.01	0.00	0.08	0.00	86.84	Chl	
05-02	20 / 1 .	~~36.69~~	~~0.00~~	~~0.00~~	~~0.00~~	~~0.78~~	~~0.00~~	~~0.00~~	~~0.04~~	~~0.00~~	~~0.00~~	~~0.00~~	~~0.00~~	~~36.85~~	x	
05-02	1 / 1 .	37.39	1.12	17.34	0.00	15.78	0.08	13.25	0.00	0.14	10.04	0.59	0.09	95.55	Bt	
05-02	2 / 1 .	36.63	1.08	17.45	0.00	15.19	0.06	12.74	0.08	0.11	10.13	0.47	0.07	93.78	Bt	
05-02	3 / 1 .	36.97	1.04	17.69	0.03	15.91	0.07	12.92	0.01	0.11	10.03	0.55	0.11	95.17	Bt	
05-02	4 / 1 .	35.58	1.10	17.69	0.01	17.35	0.05	12.93	0.04	0.08	8.48	0.59	0.07	93.70	Bt	
05-02	5 / 1 .	37.22	1.29	17.30	0.01	16.30	0.11	12.82	0.01	0.07	10.01	0.53	0.07	95.50	Bt	
05-02	6 / 1 .	37.35	1.13	17.01	0.00	15.99	0.08	13.59	0.02	0.10	9.51	0.53	0.08	95.16	Bt	
05-02	7 / 1 .	37.59	1.31	17.54	0.00	14.80	0.07	13.48	0.03	0.10	9.91	0.53	0.07	95.19	Bt	
05-02	8 / 1 .	37.39	1.52	17.61	0.03	15.45	0.08	13.20	0.00	0.15	9.93	0.47	0.05	95.68	Bt	
05-02	9 / 1 .	37.54	1.65	17.48	0.01	15.17	0.06	13.24	0.00	0.11	10.14	0.49	0.07	95.75	Bt	
05-02	10 / 1 .	37.19	1.55	17.34	0.02	15.58	0.05	13.09	0.00	0.10	10.16	0.51	0.08	95.42	Bt	
05-02	11 / 1 .	37.18	0.97	17.40	0.02	16.54	0.12	12.47	0.03	0.11	9.85	0.45	0.08	95.02	Bt	
05-02	12 / 1 .	40.12	0.99	19.07	0.02	14.04	0.09	10.82	0.02	0.08	9.85	0.46	0.09	95.44	Bt	
05-02	13 / 1 .	36.98	1.19	17.65	0.01	15.67	0.10	12.97	0.05	0.10	10.06	0.57	0.09	95.17	Bt	
05-02	14 / 1 .	37.57	1.18	17.58	0.03	14.65	0.10	13.34	0.01	0.12	9.76	0.48	0.08	94.69	Bt	
05-02	15 / 1 .	37.75	1.25	17.35	0.00	14.95	0.11	13.61	0.00	0.13	10.00	0.52	0.08	95.48	Bt	
05-02	16 / 1 .	38.24	1.21	17.09	0.01	14.55	0.08	13.85	0.00	0.17	9.94	0.52	0.07	95.50	Bt	
05-02	17 / 1 .	37.49	1.27	17.55	0.01	14.73	0.08	13.42	0.00	0.13	10.10	0.48	0.08	95.11	Bt	
05-02	1 / 1 .	37.53	1.27	17.80	0.02	14.87	0.10	13.42	0.00	0.14	10.03	0.54	0.09	95.56	Bt	
05-02	2 / 1 .	26.43	0.00	21.95	0.00	19.27	0.16	18.53	0.02	0.01	0.02	0.07	0.01	86.43	Chl	
05-02	3 / 1 .	26.15	0.04	21.97	0.00	19.20	0.17	18.90	0.05	0.00	0.02	0.12	0.02	86.55	Chl	
05-02	4 / 1 .	36.65	0.41	18.12	0.03	15.63	0.12	13.04	0.05	0.11	9.73	0.46	0.08	94.20	Bt	
05-02	5 / 1 .	35.07	0.47	17.97	0.00	16.92	0.04	13.32	0.00	0.07	8.57	0.56	0.11	92.80	Bt	
05-02	6 / 1 .	36.95	0.39	18.10	0.00	15.76	0.06	13.00	0.00	0.08	10.10	0.55	0.06	94.80	Bt	
05-02	7 / 1 .	37.24	0.62	17.75	0.00	15.34	0.02	12.73	0.02	0.09	9.97	0.57	0.11	94.18	Bt	
05-02	8 / 1 .	36.93	0.69	17.81	0.00	15.56	0.05	12.93	0.00	0.07	10.10	0.65	0.09	94.56	Bt	
05-02	9 / 1 .	37.53	0.73	17.40	0.03	15.44	0.03	13.26	0.00	0.08	10.15	0.63	0.08	95.07	Bt	
05-02	10 / 1 .	37.20	0.80	17.59	0.00	15.83	0.06	12.57	0.03	0.09	9.56	0.66	0.06	94.12	Bt	
05-02	1 / 1 .	101.90	0.01	0.01	0.02	0.02	0.00	0.00	0.00	0.01	0.00	0.01	0.00	101.99	Qz	0
05-02	1 / 2 .	~~80.52~~	~~0.00~~	~~11.37~~	~~0.01~~	~~0.08~~	~~0.00~~	~~0.01~~	~~0.41~~	~~5.92~~	~~0.13~~	~~0.03~~	~~0.07~~	~~98.48~~	x	21.95
05-02	1 / 3 .	69.07	0.01	20.05	0.01	0.05	0.02	0.00	0.47	11.81	0.06	0.02	0.00	101.56	Ab	43.86
05-02	1 / 4 .	46.84	0.48	32.47	0.00	3.32	0.00	1.36	0.00	1.17	9.88	0.11	0.01	95.59	Ms/Ph	65.78
05-02	1 / 5 .	47.53	0.45	32.09	0.00	3.30	0.01	1.48	0.00	1.10	9.99	0.15	0.01	96.01	Ms/Ph	87.71
05-02	1 / 6 .	47.18	0.50	31.55	0.00	3.44	0.01	1.57	0.01	1.02	9.99	0.12	0.01	95.35	Ms/Ph	109.63
05-02	1 / 7 .	46.62	0.42	33.55	0.01	2.90	0.00	1.03	0.02	1.00	9.91	0.06	0.01	95.49	Ms/Ph	131.55
05-02	1 / 8 .	50.93	0.21	27.41	0.00	3.29	0.01	3.11	0.02	0.45	10.27	0.22	0.02	95.84	Ms/Ph	153.49
05-02	1 / 9 .	51.77	0.21	26.73	0.01	2.88	0.02	3.36	0.01	0.46	10.07	0.23	0.01	95.66	Ms/Ph	175.41
05-02	1 / 10 .	46.88	0.45	32.78	0.13	2.90	0.00	1.15	0.06	0.70	10.19	0.06	0.00	95.25	Ms/Ph	197.33
05-02	1 / 11 .	48.24	0.57	29.53	0.02	3.58	0.01	2.23	0.00	0.68	10.47	0.13	0.00	95.39	Ms/Ph	219.26
05-02	1 / 12 .	46.15	0.70	27.37	0.00	5.70	0.03	4.62	0.00	0.52	10.41	0.27	0.02	95.67	Ms/Ph	241.18
05-02	1 / 13 .	48.79	0.38	29.63	0.01	3.30	0.03	2.21	0.01	0.56	10.54	0.12	0.00	95.52	Ms/Ph	263.11
05-02	1 / 14 .	51.60	0.27	26.79	0.02	2.74	0.00	3.41	0.00	0.43	10.44	0.24	0.00	95.81	Ms/Ph	285.03
05-02	1 / 15 .	51.63	0.24	26.65	0.03	2.16	0.00	3.57	0.00	0.24	11.07	0.18	0.01	95.67	Ms/Ph	306.96
05-02	1 / 16 .	51.76	0.21	26.84	0.03	2.02	0.01	3.58	0.00	0.20	11.16	0.26	0.00	95.92	Ms/Ph	328.89
05-02	1 / 17 .	51.46	0.21	26.84	0.00	2.15	0.00	3.48	0.00	0.18	11.17	0.19	0.01	95.59	Ms/Ph	350.81
05-02	1 / 18 .	51.50	0.18	26.83	0.00	2.05	0.00	3.55	0.00	0.17	11.30	0.24	0.00	95.67	Ms/Ph	372.73
05-02	1 / 19 .	51.88	0.20	26.70	0.04	2.00	0.00	3.65	0.00	0.19	11.23	0.22	0.00	95.98	Ms/Ph	394.66
05-02	1 / 20 .	51.68	0.21	26.70	0.00	1.95	0.01	3.58	0.00	0.19	11.30	0.24	0.01	95.76	Ms/Ph	416.58
05-02	1 / 21 .	51.62	0.20	26.72	0.02	2.04	0.00	3.64	0.01	0.20	11.11	0.23	0.01	95.71	Ms/Ph	438.52
05-02	1 / 22 .	51.87	0.20	26.64	0.02	2.05	0.00	3.64	0.00	0.20	11.08	0.23	0.01	95.82	Ms/Ph	460.44
05-02	1 / 23 .	51.33	0.19	27.05	0.00	1.96	0.00	3.60	0.00	0.22	10.94	0.26	0.01	95.41	Ms/Ph	482.37
05-02	1 / 24 .	51.60	0.23	26.97	0.04	1.91	0.00	3.61	0.00	0.23	11.05	0.23	0.00	95.76	Ms/Ph	504.29
05-02	1 / 25 .	51.36	0.23	27.62	0.00	1.89	0.03	3.46	0.00	0.32	10.94	0.24	0.01	95.98	Ms/Ph	526.21
05-02	1 / 26 .	51.36	0.26	27.59	0.03	1.88	0.00	3.39	0.00	0.33	10.95	0.21	0.01	95.86	Ms/Ph	548.14
05-02	1 / 27 .	51.28	0.27	27.71	0.00	1.84	0.00	3.38	0.00	0.38	10.95	0.24	0.00	95.89	Ms/Ph	570.06
05-02	1 / 28 .	50.96	0.25	27.62	0.00	1.91	0.00	3.41	0.00	0.35	10.98	0.23	0.00	95.60	Ms/Ph	591.99
05-02	1 / 29 .	50.89	0.29	27.70	0.03	1.86	0.00	3.30	0.00	0.36	10.86	0.22	0.00	95.37	Ms/Ph	613.92
05-02	1 / 30 .	50.98	0.28	27.85	0.00	1.92	0.01	3.34	0.00	0.36	10.94	0.24	0.00	95.81	Ms/Ph	635.84
05-02	1 / 31 .	50.64	0.29	27.87	0.00	1.91	0.01	3.25	0.00	0.37	10.87	0.25	0.00	95.34	Ms/Ph	657.77
05-02	1 / 32 .	49.85	0.31	28.48	0.01	2.63	0.02	2.83	0.02	0.53	10.56	0.14	0.01	95.31	Ms/Ph	679.69
05-02	1 / 33 .	49.72	0.36	28.69	0.01	2.89	0.01	2.61	0.00	0.52	10.56	0.18	0.01	95.46	Ms/Ph	701.62

Puga Gneiss

Sample	Spot	SiO2	TiO2	Al2O3	Cr2O3	FeO	MnO	MgO	CaO	Na2O	K2O	F	Cl	Total	Min	distance (u
05-02	1 / 34 .	49.79	0.36	28.81	0.00	2.82	0.01	2.47	0.00	0.56	10.49	0.15	0.01	95.38	Ms/Ph	723.55
05-02	1 / 35 .	50.50	0.32	28.54	0.05	2.94	0.02	2.72	0.00	0.45	10.46	0.20	0.01	96.11	Ms/Ph	745.47
05-02	1 / 36 .	46.05	0.44	33.25	0.04	2.94	0.02	1.10	0.00	0.93	10.32	0.06	0.02	95.13	Ms/Ph	767.4
05-02	1 / 37 .	49.55	0.35	29.31	0.00	2.82	0.00	2.39	0.00	0.62	10.31	0.21	0.01	95.44	Ms/Ph	789.32
05-02	1 / 38 .	48.55	0.30	30.59	0.04	3.12	0.00	2.03	0.00	0.83	10.07	0.13	0.01	95.61	Ms/Ph	811.24
05-02	1 / 39 .	47.01	0.53	32.61	0.02	3.33	0.00	1.46	0.01	1.29	9.71	0.11	0.00	96.03	Ms/Ph	833.17
05-02	1 / 40 .	50.88	0.32	27.89	0.01	2.68	0.00	2.98	0.00	0.53	10.37	0.20	0.02	95.77	Ms/Ph	855.09
05-02	1 / 1 .	~~75.04~~	~~0.05~~	~~6.99~~	~~0.00~~	~~9.72~~	~~0.11~~	~~4.95~~	~~0.05~~	~~0.00~~	~~0.11~~	~~0.02~~	~~0.01~~	~~97.03~~	x	0
05-02	1 / 2 .	~~39.86~~	~~0.05~~	~~22.62~~	~~0.00~~	~~26.91~~	~~0.39~~	~~4.63~~	~~3.79~~	~~0.04~~	~~2.12~~	~~0.12~~	~~0.04~~	~~100.45~~	Grt+	20.92
05-02	1 / 3 .	38.05	0.00	21.73	0.03	30.90	0.57	4.10	4.81	0.03	0.00	0.00	0.00	100.22	Grt	41.81
05-02	1 / 4 .	37.69	0.04	21.46	0.00	31.49	0.68	3.89	4.63	0.04	0.00	0.02	0.00	99.92	Grt	62.71
05-02	1 / 5 .	37.93	0.14	21.51	0.02	31.27	0.73	3.78	4.82	0.05	0.00	0.02	0.00	100.25	Grt	83.6
05-02	1 / 6 .	~~10.02~~	~~70.00~~	~~6.46~~	~~0.00~~	~~10.77~~	~~0.27~~	~~1.24~~	~~1.33~~	~~0.00~~	~~0.00~~	~~0.02~~	~~0.01~~	~~100.08~~	(Rt)	104.5
05-02	1 / 7 .	37.49	0.06	21.32	0.00	32.85	1.04	2.93	4.36	0.03	0.00	0.00	0.01	100.09	Grt	125.4
05-02	1 / 8 .	37.33	0.04	21.18	0.02	32.80	1.02	2.66	4.37	0.04	0.01	0.00	0.00	99.47	Grt	146.3
05-02	1 / 9 .	37.38	0.03	21.25	0.04	32.97	1.04	2.62	4.34	0.05	0.02	0.00	0.01	99.73	Grt	167.2
05-02	1 / 10 .	~~43.06~~	~~0.06~~	~~26.27~~	~~0.05~~	~~14.13~~	~~0.27~~	~~4.11~~	~~0.89~~	~~0.15~~	~~9.24~~	~~0.23~~	~~0.09~~	~~98.43~~	x	188.09
05-02	1 / 11 .	~~38.62~~	~~0.03~~	~~22.15~~	~~0.02~~	~~30.10~~	~~0.95~~	~~3.17~~	~~3.88~~	~~0.07~~	~~1.48~~	~~0.04~~	~~0.03~~	~~100.52~~	Grt+	208.99
05-02	1 / 12 .	37.60	0.02	21.49	0.00	31.99	1.08	3.23	4.30	0.03	0.00	0.00	0.00	99.73	Grt	229.89
05-02	1 / 13 .	101.32	0.05	0.02	0.00	0.38	0.02	0.00	0.02	0.00	0.01	0.00	0.00	101.80	Qz	250.79
05-02	1 / 14 .	~~39.33~~	~~59.35~~	~~0.44~~	~~0.05~~	~~3.47~~	~~0.02~~	~~0.03~~	~~0.03~~	~~0.02~~	~~0.07~~	~~0.00~~	~~0.01~~	~~102.81~~	x	271.69
05-02	1 / 15 .	99.01	0.12	1.08	0.02	1.06	0.02	0.01	0.04	0.01	0.02	0.08	0.05	101.46	Qz	292.59
05-02	1 / 16 .	37.57	0.08	21.24	0.01	32.48	1.50	3.24	3.52	0.07	0.00	0.00	0.01	99.69	Grt	313.49
05-02	1 / 17 .	37.38	0.06	21.28	0.00	32.94	1.71	2.86	3.65	0.06	0.00	0.00	0.00	99.91	Grt	334.39
05-02	1 / 18 .	37.20	0.05	21.23	0.04	33.48	1.77	2.41	3.73	0.05	0.00	0.00	0.00	99.97	Grt	355.29
05-02	1 / 19 .	37.15	0.07	21.06	0.03	33.80	1.69	2.14	3.81	0.04	0.00	0.03	0.00	99.80	Grt	376.19
05-02	1 / 20 .	~~37.76~~	~~0.09~~	~~20.93~~	~~0.01~~	~~32.63~~	~~1.51~~	~~2.02~~	~~3.21~~	~~0.05~~	~~1.22~~	~~0.06~~	~~0.07~~	~~99.52~~	Grt+	397.09
05-02	1 / 21 .	37.01	0.06	21.00	0.03	34.54	1.67	1.76	3.80	0.02	0.00	0.01	0.00	99.86	Grt	417.99
05-02	1 / 22 .	37.21	0.05	20.90	0.03	34.55	1.61	1.68	3.94	0.04	0.01	0.00	0.00	100.01	Grt	438.88
05-02	1 / 23 .	37.14	0.07	21.01	0.01	34.71	1.54	1.62	3.85	0.03	0.03	0.00	0.00	100.03	Grt	459.78
05-02	1 / 24 .	36.97	0.09	21.03	0.03	34.61	1.49	1.54	4.11	0.03	0.00	0.00	0.00	99.87	Grt	480.68
05-02	1 / 25 .	37.02	0.10	20.96	0.05	34.73	1.39	1.48	4.20	0.02	0.00	0.03	0.00	99.93	Grt	501.58
05-02	1 / 26 .	37.10	0.10	20.96	0.06	34.75	1.35	1.48	4.14	0.05	0.00	0.02	0.00	100.00	Grt	522.48
05-02	1 / 27 .	37.07	0.11	21.02	0.01	34.86	1.30	1.45	4.22	0.04	0.00	0.01	0.00	100.07	Grt	543.38
05-02	1 / 28 .	~~30.33~~	~~15.59~~	~~17.68~~	~~0.07~~	~~29.05~~	~~1.05~~	~~1.49~~	~~3.24~~	~~0.03~~	~~0.62~~	~~0.02~~	~~0.02~~	~~99.18~~	x	564.28
05-02	1 / 29 .	36.95	0.11	20.99	0.02	34.95	1.21	1.44	4.30	0.03	0.00	0.00	0.00	99.98	Grt	585.18
05-02	1 / 30 .	36.95	0.10	20.99	0.03	34.72	1.16	1.48	4.24	0.03	0.00	0.01	0.02	99.72	Grt	606.08
05-02	1 / 31 .	37.22	0.10	21.00	0.03	34.17	1.17	1.47	4.34	0.02	0.00	0.01	0.04	99.54	Grt	626.98
05-02	1 / 32 .	~~23.45~~	~~0.98~~	~~12.60~~	~~0.03~~	~~56.08~~	~~0.62~~	~~0.86~~	~~2.19~~	~~0.02~~	~~0.23~~	~~0.02~~	~~0.02~~	~~97.09~~	x	647.88
05-02	1 / 33 .	37.23	0.12	20.98	0.05	34.92	1.09	1.42	4.31	0.02	0.00	0.00	0.00	100.13	Grt	668.78
05-02	1 / 34 .	36.45	3.04	20.57	0.02	34.08	1.02	1.39	4.22	0.01	0.00	0.00	0.00	100.78	Grt+	689.68
05-02	1 / 35 .	34.56	6.70	19.57	0.02	32.88	0.96	1.33	4.01	0.03	0.00	0.00	0.01	100.08	Grt+	710.58
05-02	1 / 36 .	37.01	0.21	21.05	0.05	35.00	1.04	1.44	4.29	0.03	0.00	0.02	0.00	100.15	Grt	731.48
05-02	1 / 37 .	37.08	0.16	20.99	0.08	34.94	1.05	1.41	4.49	0.03	0.00	0.02	0.00	100.23	Grt	752.37
05-02	1 / 38 .	~~36.07~~	~~2.38~~	~~20.44~~	~~0.03~~	~~34.12~~	~~0.97~~	~~1.34~~	~~4.53~~	~~0.04~~	~~0.00~~	~~0.04~~	~~0.00~~	~~99.94~~	Grt+	773.27
05-02	1 / 39 .	~~29.16~~	~~20.21~~	~~17.03~~	~~0.02~~	~~28.32~~	~~0.81~~	~~1.15~~	~~3.54~~	~~0.02~~	~~0.00~~	~~0.00~~	~~0.00~~	~~100.23~~	x	794.17
05-02	1 / 40 .	~~33.87~~	~~10.95~~	~~18.87~~	~~0.07~~	~~31.83~~	~~0.91~~	~~1.28~~	~~4.02~~	~~0.02~~	~~0.00~~	~~0.02~~	~~0.00~~	~~101.85~~	x	815.07
05-02	1 / 41 .	37.15	0.18	21.01	0.07	34.91	0.98	1.39	4.39	0.03	0.00	0.02	0.00	100.13	Grt	835.97
05-02	1 / 42 .	37.01	0.15	20.95	0.13	34.99	0.98	1.38	4.43	0.04	0.00	0.02	0.00	100.06	Grt	856.87
05-02	1 / 43 .	36.96	0.17	20.91	0.08	34.80	0.95	1.41	4.49	0.05	0.01	0.00	0.01	99.82	Grt	877.77
05-02	1 / 44 .	~~35.87~~	~~3.12~~	~~20.37~~	~~0.04~~	~~33.88~~	~~0.94~~	~~1.29~~	~~4.43~~	~~0.03~~	~~0.00~~	~~0.03~~	~~0.01~~	~~100.01~~	Grt+	898.67
05-02	1 / 45 .	37.16	0.20	20.90	0.05	34.98	0.93	1.32	4.57	0.02	0.00	0.01	0.01	100.16	Grt	919.57
05-02	1 / 46 .	36.93	0.18	20.90	0.04	34.93	0.96	1.37	4.44	0.03	0.01	0.00	0.00	99.79	Grt	940.47
05-02	1 / 47 .	37.01	0.28	21.04	0.04	34.99	0.94	1.38	4.34	0.03	0.00	0.00	0.00	100.01	Grt	961.37
05-02	1 / 48 .	~~36.87~~	~~0.15~~	~~20.67~~	~~0.07~~	~~34.13~~	~~0.93~~	~~1.73~~	~~4.25~~	~~0.02~~	~~0.54~~	~~0.05~~	~~0.03~~	~~99.41~~	Grt+	982.27
05-02	1 / 49 .	37.07	0.13	21.00	0.06	35.09	0.96	1.35	4.51	0.02	0.00	0.01	0.00	100.19	Grt	1003.17
05-02	1 / 50 .	37.13	0.15	21.02	0.05	34.96	0.93	1.33	4.53	0.01	0.00	0.01	0.00	100.10	Grt	1024.06
05-02	1 / 51 .	~~38.19~~	~~0.03~~	~~2.66~~	~~0.07~~	~~3.20~~	~~0.05~~	~~0.09~~	~~0.32~~	~~0.00~~	~~0.65~~	~~0.00~~	~~0.00~~	~~44.83~~	x	1044.96
05-02	1 / 52 .	~~36.93~~	~~0.01~~	~~0.00~~	~~0.00~~	~~1.05~~	~~0.04~~	~~0.00~~	~~0.01~~	~~0.00~~	~~0.00~~	~~0.00~~	~~0.01~~	~~37.45~~	x	1065.86
05-02	1 / 53 .	37.30	0.12	21.07	0.07	34.74	0.93	1.27	4.80	0.02	0.02	0.00	0.00	100.34	Grt	1086.76
05-02	1 / 54 .	36.82	0.19	20.96	0.08	34.86	0.95	1.30	4.70	0.04	0.01	0.01	0.01	99.93	Grt	1107.66
05-02	1 / 55 .	36.85	0.17	20.79	0.04	34.93	0.94	1.34	4.50	0.04	0.01	0.01	0.00	99.62	Grt	1128.56
05-02	1 / 56 .	37.26	0.08	20.95	0.04	34.94	0.93	1.33	4.63	0.01	0.02	0.03	0.00	100.22	Grt	1149.46
05-02	1 / 57 .	36.98	0.13	21.03	0.05	35.05	0.92	1.32	4.61	0.04	0.00	0.03	0.00	100.12	Grt	1170.36
05-02	1 / 58 .	36.95	0.13	20.93	0.05	35.10	0.92	1.32	4.52	0.03	0.00	0.01	0.01	99.96	Grt	1191.26
05-02	1 / 59 .	36.59	0.16	21.05	0.02	34.75	0.88	1.31	4.48	0.03	0.00	0.05	0.00	99.29	Grt	1212.15
05-02	1 / 60 .	36.98	0.22	20.91	0.00	35.10	0.93	1.34	4.53	0.06	0.00	0.00	0.01	100.05	Grt	1233.05
05-02	2 / 1 .	~~45.95~~	~~0.11~~	~~33.92~~	~~0.01~~	~~3.36~~	~~0.03~~	~~0.85~~	~~0.36~~	~~0.53~~	~~3.86~~	~~0.07~~	~~0.06~~	~~89.05~~	x	0
05-02	2 / 2 .	37.66	0.05	21.61	0.01	31.74	0.63	3.58	4.81	0.05	0.01	0.00	0.00	100.15	Grt	20.96
05-02	2 / 3 .	37.72	0.01	21.36	0.00	31.71	0.64	3.39	4.94	0.05	0.00	0.01	0.01	99.82	Grt	41.93
05-02	2 / 4 .	37.28	0.48	21.44	0.08	32.21	0.70	3.23	4.68	0.04	0.00	0.00	0.00	100.13	Grt	62.89
05-02	2 / 5 .	37.36	0.08	21.39	0.10	32.39	0.72	3.23	4.52	0.04	0.00	0.01	0.01	99.85	Grt	83.86
05-02	2 / 6 .	37.38	0.14	21.39	0.01	32.14	0.77	3.06	4.81	0.04	0.00	0.00	0.01	99.75	Grt	104.83
05-02	2 / 7 .	37.44	0.02	21.45	0.05	32.44	0.77	3.01	4.68	0.04	0.01	0.01	0.00	99.91	Grt	125.79
05-02	2 / 8 .	37.16	0.04	21.41	0.04	32.46	0.80	2.89	4.82	0.06	0.00	0.00	0.00	99.69	Grt	146.76
05-02	2 / 9 .	37.36	0.04	21.18	0.05	32.82	0.84	2.69	4.69	0.05	0.00	0.00	0.00	99.72	Grt	167.72
05-02	2 / 10 .	37.26	0.01	21.28	0.06	33.13	0.95	2.52	4.63	0.04	0.00	0.00	0.00	99.87	Grt	188.68
05-02	2 / 11 .	37.08	0.02	21.22	0.05	33.49	1.06	2.31	4.64	0.07	0.00	0.00	0.01	99.96	Grt	209.65
05-02	2 / 12 .	37.30	0.03	21.17	0.08	33.84	1.09	2.14	4.37	0.05	0.01	0.02	0.00	100.08	Grt	230.61
05-02	2 / 13 .	37.01	0.01	21.19	0.00	34.04	1.04	1.87	4.35	0.04	0.00	0.01	0.00	99.53	Grt	251.58
05-02	2 / 14 .	37.17	0.05	21.16	0.00	34.13	1.13	1.75	4.45	0.02	0.00	0.03	0.01	99.89	Grt	272.55

Puga Gneiss

Sample	Spot	SiO2	TiO2	Al2O3	Cr2O3	FeO	MnO	MgO	CaO	Na2O	K2O	F	Cl	Total	Min	distance (u
05-02	2 / 15 .	36.98	0.06	21.16	0.00	34.19	1.21	1.73	4.48	0.06	0.00	0.00	0.00	99.85	Grt	293.51
05-02	2 / 16 .	36.87	0.04	21.10	0.03	34.02	1.30	1.64	4.63	0.05	0.00	0.00	0.01	99.67	Grt	314.47
05-02	2 / 17 .	37.04	0.04	21.08	0.05	34.04	1.33	1.63	4.54	0.03	0.00	0.00	0.00	99.77	Grt	335.44
05-02	2 / 18 .	36.97	0.03	21.08	0.00	34.11	1.35	1.60	4.43	0.04	0.00	0.02	0.01	99.62	Grt	356.4
05-02	2 / 19 .	36.98	0.05	21.08	0.02	34.42	1.40	1.58	4.29	0.04	0.00	0.00	0.02	99.89	Grt	377.37
05-02	2 / 20 .	36.91	0.01	21.17	0.00	34.48	1.40	1.62	4.16	0.04	0.00	0.00	0.00	99.74	Grt	398.34
05-02	2 / 21 .	36.80	0.03	21.14	0.04	34.68	1.43	1.59	4.07	0.03	0.00	0.00	0.01	99.80	Grt	419.3
05-02	2 / 22 .	36.85	0.00	21.13	0.00	34.43	1.46	1.59	4.00	0.04	0.00	0.00	0.01	99.47	Grt	440.27
05-02	2 / 23 .	37.08	0.01	21.04	0.00	34.66	1.40	1.56	3.92	0.04	0.00	0.01	0.00	99.70	Grt	461.23
05-02	2 / 24 .	37.06	0.05	21.19	0.02	34.77	1.46	1.53	3.96	0.03	0.00	0.03	0.00	100.10	Grt	482.19
05-02	2 / 25 .	36.64	0.15	21.14	0.02	34.47	1.53	1.47	4.06	0.03	0.00	0.00	0.00	99.50	Grt	503.16
05-02	2 / 26 .	36.87	0.01	21.03	0.09	34.62	1.60	1.37	3.97	0.03	0.01	0.00	0.00	99.60	Grt	524.13
05-02	2 / 27 .	36.98	0.01	21.05	0.00	34.60	1.73	1.32	3.91	0.04	0.00	0.00	0.00	99.63	Grt	545.09
05-02	2 / 28 .	36.89	0.01	21.19	0.02	35.08	1.82	1.34	3.75	0.03	0.01	0.00	0.00	100.13	Grt	566.06
05-02	2 / 29 .	36.83	0.08	21.08	0.08	34.69	1.86	1.29	3.85	0.05	0.00	0.00	0.00	99.80	Grt	587.02
05-02	2 / 30 .	36.75	0.56	21.07	0.02	34.49	1.94	1.34	3.78	0.05	0.00	0.00	0.00	99.97	Grt	607.98
05-02	2 / 31 .	36.83	0.26	21.10	0.04	34.76	1.95	1.33	3.55	0.04	0.00	0.01	0.00	99.84	Grt	628.95
05-02	2 / 32 .	36.73	0.04	21.13	0.01	35.18	1.91	1.30	3.46	0.04	0.00	0.00	0.01	99.79	Grt	649.91
05-02	2 / 33 .	36.87	0.06	21.15	0.02	35.01	1.94	1.29	3.53	0.03	0.00	0.00	0.00	99.89	Grt	670.88
05-02	2 / 34 .	36.78	0.03	21.15	0.01	34.97	2.00	1.30	3.41	0.03	0.01	0.04	0.00	99.72	Grt	691.85
05-02	2 / 35 .	36.63	0.06	21.18	0.03	34.84	2.05	1.29	3.44	0.05	0.00	0.01	0.00	99.55	Grt	712.81
05-02	2 / 36 .	37.02	0.03	21.24	0.03	34.65	2.05	1.37	3.57	0.05	0.00	0.01	0.01	100.03	Grt	733.78
05-02	2 / 37 .	36.83	0.03	21.13	0.04	34.44	2.02	1.51	3.54	0.04	0.02	0.00	0.00	99.57	Grt	754.74
05-02	2 / 38 .	37.12	0.04	21.21	0.03	34.10	1.97	1.74	3.63	0.03	0.01	0.00	0.00	99.88	Grt	775.7
05-02	2 / 39 .	37.00	0.04	21.33	0.03	33.95	1.69	2.18	3.54	0.07	0.00	0.00	0.00	99.81	Grt	796.67
05-02	2 / 40 .	37.14	0.08	21.32	0.01	33.62	1.57	2.46	3.46	0.04	0.00	0.00	0.00	99.68	Grt	817.64
05-02	1 / 1 .	101.40	0.00	0.00	0.00	0.01	0.00	0.00	0.01	0.00	0.00	0.00	0.00	101.38	Qz	0
05-02	1 / 2 .	101.27	0.00	0.00	0.00	0.01	0.01	0.00	0.03	0.00	0.00	0.01	0.00	101.32	Qz	21.93
05-02	1 / 3 .	100.00	0.00	0.81	0.00	0.23	0.03	0.01	0.01	0.00	0.17	0.01	0.00	101.24	Qz	43.87
05-02	1 / 4 .	48.73	0.37	30.12	0.00	3.16	0.00	2.06	0.00	0.73	10.32	0.09	0.00	95.52	Ms/Ph	65.81
05-02	1 / 5 .	47.79	0.51	32.33	0.04	2.95	0.01	1.47	0.01	0.72	10.42	0.10	0.01	96.31	Ms/Ph	87.74
05-02	1 / 6 .	68.51	0.01	20.18	0.00	0.09	0.00	0.02	0.33	11.44	0.28	0.01	0.00	100.83	Ab	109.68
05-02	1 / 7 .	69.21	0.01	19.99	0.03	0.06	0.02	0.00	0.16	11.70	0.10	0.01	0.00	101.29	Ab	131.61
05-02	1 / 8 .	66.53	0.01	21.09	0.01	0.20	0.00	0.06	0.83	10.55	0.74	0.00	0.00	100.02	Ab	153.55
05-02	1 / 9 .	46.78	0.40	32.93	0.00	3.07	0.00	1.25	0.00	1.02	10.27	0.06	0.01	95.72	Ms/Ph	175.48
05-02	1 / 10 .	48.70	0.39	30.88	0.03	3.13	0.00	1.95	0.00	0.68	10.29	0.15	0.00	96.13	Ms/Ph	197.42
05-02	1 / 11 .	47.13	0.39	33.51	0.01	2.89	0.00	1.10	0.01	0.58	10.60	0.10	0.01	96.30	Ms/Ph	219.35
05-02	1 / 12 .	47.53	0.45	32.29	0.03	2.76	0.00	1.38	0.00	0.81	10.53	0.08	0.00	95.79	Ms/Ph	241.29
05-02	1 / 13 .	46.69	0.40	32.41	0.01	3.33	0.01	1.44	0.00	1.08	10.23	0.09	0.01	95.63	Ms/Ph	263.22
05-02	1 / 14 .	49.56	0.29	28.80	0.00	3.29	0.02	2.53	0.00	0.63	10.43	0.16	0.00	95.61	Ms/Ph	285.16
05-02	1 / 15 .	50.00	0.24	29.04	0.00	2.88	0.00	2.52	0.00	0.72	10.15	0.16	0.01	95.63	Ms/Ph	307.09
05-02	1 / 16 .	49.70	0.24	29.14	0.04	3.01	0.02	2.47	0.00	0.59	10.53	0.12	0.00	95.80	Ms/Ph	329.03
05-02	1 / 17 .	49.80	0.33	29.02	0.00	2.93	0.00	2.39	0.00	0.45	10.66	0.15	0.00	95.65	Ms/Ph	350.96
05-02	1 / 18 .	51.33	0.22	26.79	0.02	3.22	0.01	3.22	0.00	0.45	10.42	0.16	0.00	95.71	Ms/Ph	372.9
05-02	1 / 19 .	51.16	0.24	26.55	0.01	3.45	0.02	3.22	0.00	0.47	10.36	0.20	0.00	95.59	Ms/Ph	394.83
05-02	1 / 20 .	37.49	1.46	17.66	0.02	15.18	0.05	13.23	0.00	0.11	10.01	0.52	0.09	95.58	Bt	416.77
05-02	1 / 21 .	51.19	0.19	26.40	0.00	3.15	0.01	3.20	0.00	0.46	10.07	0.21	0.02	94.78	Ms/Ph	438.7
05-02	1 / 22 .	46.45	0.53	33.00	0.02	2.97	0.01	1.24	0.00	0.74	10.61	0.07	0.01	95.60	Ms/Ph	460.64
05-02	1 / 23 .	51.68	0.15	26.81	0.02	2.36	0.00	3.52	0.00	0.38	10.53	0.19	0.00	95.55	Ms/Ph	482.57
05-02	1 / 24 .	47.93	0.49	30.32	0.00	3.73	0.00	2.02	0.00	0.92	10.21	0.11	0.00	95.67	Ms/Ph	504.51
05-02	1 / 25 .	48.21	0.55	30.20	0.01	3.62	0.01	2.09	0.00	0.93	10.34	0.17	0.01	96.04	Ms/Ph	526.45
05-02	1 / 26 .	48.37	0.47	29.98	0.01	3.66	0.00	2.19	0.00	0.79	10.45	0.12	0.01	95.95	Ms/Ph	548.38
05-02	1 / 27 .	48.53	0.51	30.31	0.00	3.30	0.00	2.05	0.00	0.73	10.43	0.11	0.01	95.89	Ms/Ph	570.32
05-02	1 / 28 .	50.70	0.28	27.17	0.01	3.14	0.03	3.17	0.00	0.51	10.33	0.18	0.01	95.44	Ms/Ph	592.25
05-02	1 / 29 .	47.91	0.47	30.47	0.02	3.58	0.00	1.93	0.00	0.80	10.31	0.13	0.01	95.56	Ms/Ph	614.19
05-02	1 / 30 .	46.89	0.43	33.92	0.00	2.79	0.00	1.03	0.02	1.00	10.21	0.09	0.01	96.32	Ms/Ph	636.12
05-02	1 / 31 .	46.45	0.40	32.87	0.02	3.06	0.01	1.16	0.06	0.75	10.38	0.11	0.03	95.24	Ms/Ph	658.06
05-02	1 / 32 .	51.05	0.31	27.64	0.00	2.94	0.01	2.86	0.00	0.43	10.45	0.18	0.00	95.75	Ms/Ph	679.99
05-02	1 / 33 .	50.98	0.32	27.14	0.03	3.03	0.00	3.04	0.00	0.52	10.39	0.18	0.01	95.53	Ms/Ph	701.93
05-02	1 / 34 .	50.93	0.29	27.31	0.00	2.70	0.01	3.18	0.00	0.46	10.50	0.20	0.01	95.46	Ms/Ph	723.86
05-02	1 / 35 .	50.81	0.29	27.19	0.01	2.98	0.02	3.06	0.00	0.47	10.36	0.19	0.00	95.28	Ms/Ph	745.8
05-02	1 / 36 .	51.26	0.28	27.46	0.00	2.12	0.01	3.49	0.00	0.42	10.60	0.21	0.00	95.71	Ms/Ph	767.73
05-02	1 / 37 .	43.87	0.61	25.25	0.01	5.74	0.00	4.57	0.05	0.47	9.13	0.24	0.13	89.93	Ms/Ph	789.67
05-02	1 / 38 .	49.53	0.33	28.71	0.00	3.04	0.02	2.74	0.00	0.59	10.56	0.19	0.01	95.58	Ms/Ph	811.6
05-02	1 / 39 .	50.90	0.30	27.21	0.00	2.73	0.01	3.23	0.00	0.45	10.35	0.20	0.01	95.29	Ms/Ph	833.54
05-02	1 / 40 .	49.10	0.34	29.10	0.02	3.22	0.00	2.40	0.02	0.55	10.33	0.15	0.00	95.15	Ms/Ph	855.47
05-02	1 / 41 .	49.88	0.32	28.69	0.04	2.80	0.00	2.61	0.00	0.61	10.48	0.17	0.00	95.50	Ms/Ph	877.41
05-02	1 / 42 .	52.03	0.23	26.69	0.02	1.91	0.01	3.83	0.00	0.25	10.71	0.20	0.01	95.77	Ms/Ph	899.34
05-02	1 / 43 .	51.74	0.19	26.71	0.00	1.89	0.01	3.70	0.00	0.21	10.85	0.22	0.01	95.42	Ms/Ph	921.28
05-02	1 / 44 .	51.94	0.21	26.85	0.00	2.05	0.02	3.73	0.00	0.19	10.79	0.21	0.00	95.90	Ms/Ph	943.21
05-02	1 / 45 .	51.25	0.21	26.31	0.01	2.00	0.00	3.67	0.00	0.21	11.04	0.23	0.02	94.82	Ms/Ph	965.15
05-02	1 / 46 .	51.87	0.22	26.68	0.00	1.93	0.01	3.74	0.00	0.19	10.98	0.20	0.01	95.74	Ms/Ph	987.09
05-02	1 / 47 .	52.09	0.21	26.73	0.00	1.87	0.00	3.84	0.00	0.22	10.96	0.21	0.00	95.99	Ms/Ph	1009.02
05-02	1 / 48 .	51.79	0.22	26.45	0.00	2.28	0.01	3.65	0.00	0.27	10.71	0.24	0.01	95.51	Ms/Ph	1030.95
05-02	1 / 49 .	51.30	0.26	27.47	0.00	1.93	0.01	3.59	0.00	0.31	10.79	0.24	0.01	95.76	Ms/Ph	1052.89
05-02	1 / 50 .	50.75	0.29	27.72	0.02	2.18	0.00	3.37	0.00	0.35	10.74	0.19	0.00	95.48	Ms/Ph	1074.83
05-02	1 / 51 .	51.34	0.28	27.38	0.02	2.33	0.01	3.25	0.00	0.40	10.58	0.18	0.01	95.69	Ms/Ph	1096.76
05-02	1 / 52 .	50.94	0.30	28.00	0.00	2.02	0.01	3.35	0.00	0.43	10.71	0.22	0.00	95.85	Ms/Ph	1118.7
05-02	1 / 53 .	51.14	0.24	26.84	0.00	2.88	0.02	3.23	0.00	0.37	10.51	0.19	0.00	95.31	Ms/Ph	1140.63
05-02	1 / 54 .	51.62	0.22	26.65	0.00	2.91	0.00	3.43	0.00	0.33	10.40	0.18	0.00	95.65	Ms/Ph	1162.57
05-02	1 / 55 .	50.88	0.29	26.39	0.01	2.92	0.00	3.38	0.00	0.32	10.40	0.20	0.02	94.68	Ms/Ph	1184.5

Puga Gneiss

Sample	Spot	SiO2	TiO2	Al2O3	Cr2O3	FeO	MnO	MgO	CaO	Na2O	K2O	F	Cl	Total	Min	distance (u
05-02	1 / 56 .	50.94	0.31	27.58	0.00	3.14	0.00	3.06	0.00	0.48	10.16	0.17	0.00	95.71	Ms/Ph	1206.44
05-02	1 / 57 .	47.88	0.33	29.91	0.01	3.61	0.01	2.18	0.00	0.79	10.24	0.18	0.01	95.07	Ms/Ph	1228.37
05-02	1 / 58 .	47.84	0.39	30.24	0.02	3.45	0.01	2.18	0.00	0.94	10.01	0.12	0.00	95.13	Ms/Ph	1250.31
05-02	1 / 59 .	49.49	0.39	29.21	0.00	2.99	0.01	2.78	0.01	0.87	9.74	0.14	0.00	95.56	Ms/Ph	1272.24
05-02	1 / 60 .	49.76	0.31	29.29	0.02	2.39	0.00	2.88	0.00	0.89	9.90	0.15	0.02	95.50	Ms/Ph	1294.18
05-02	1 / 61 .	50.18	0.32	28.96	0.06	2.01	0.02	3.01	0.00	0.87	9.96	0.15	0.00	95.45	Ms/Ph	1316.11
05-02	1 / 62 .	50.36	0.27	28.97	0.01	1.89	0.00	3.07	0.00	0.82	10.06	0.18	0.00	95.53	Ms/Ph	1338.05
05-02	1 / 63 .	49.97	0.30	29.05	0.03	2.17	0.00	2.88	0.01	0.48	10.26	0.16	0.00	95.23	Ms/Ph	1359.98
05-02	1 / 64 .	51.52	0.27	27.30	0.00	2.69	0.00	3.21	0.00	0.48	10.19	0.22	0.00	95.76	Ms/Ph	1381.92
05-02	1 / 1 .	100.68	0.00	0.01	0.02	0.00	0.00	0.01	0.02	0.00	0.02	0.00	0.00	100.73	Qz	
05-02	1 / 2 .	99.06	0.01	0.00	0.00	0.00	0.01	0.00	0.01	0.00	0.00	0.02	0.00	99.08	Qz	
05-02	1 / 3 .	99.38	0.00	0.01	0.00	0.00	0.02	0.00	0.01	0.00	0.00	0.00	0.00	99.38	Qz	
05-02	1 / 4 .	100.27	0.02	0.01	0.01	0.00	0.00	0.00	0.00	0.00	0.00	0.00	0.00	100.25	Qz	
05-02	1 / 5 .	100.15	0.00	0.01	0.00	0.00	0.00	0.00	0.00	0.01	0.00	0.00	0.00	100.16	Qz	
05-02	1 / 6 .	100.34	0.00	0.00	0.00	0.01	0.00	0.00	0.01	0.00	0.01	0.01	0.00	100.39	Qz	
05-02	1 / 7 .	100.26	0.00	0.02	0.00	0.02	0.01	0.00	0.00	0.00	0.00	0.00	0.00	100.29	Qz	
05-02	1 / 8 .	100.65	0.01	0.00	0.00	0.01	0.00	0.00	0.01	0.00	0.00	0.02	0.00	100.69	Qz	
05-02	1 / 9 .	99.68	0.00	0.01	0.00	0.01	0.00	0.01	0.00	0.01	0.01	0.00	0.00	99.72	Qz	
05-02	1 / 10 .	100.70	0.00	0.01	0.00	0.00	0.00	0.00	0.01	0.00	0.00	0.00	0.00	100.67	Qz	
05-02	1 / 11 .	98.96	0.01	0.04	0.00	0.06	0.00	0.00	0.01	0.00	0.01	0.01	0.01	99.08	Qz	
05-02	1 / 12 .	~~49.69~~	~~0.20~~	~~36.34~~	~~0.00~~	~~3.03~~	~~0.00~~	~~1.00~~	~~0.00~~	~~0.79~~	~~6.50~~	~~0.05~~	~~0.00~~	~~97.58~~	x	
05-02	1 / 13 .	100.76	0.00	0.10	0.02	0.20	0.00	0.02	0.01	0.01	0.02	0.00	0.00	101.11	Qz	
05-02	1 / 14 .	99.51	0.00	0.01	0.04	0.06	0.01	0.00	0.02	0.00	0.01	0.00	0.01	99.65	Qz	
05-02	1 / 15 .	99.84	0.00	0.02	0.00	0.02	0.00	0.00	0.00	0.00	0.00	0.00	0.01	99.87	Qz	
05-02	1 / 16 .	99.58	0.00	0.01	0.03	0.03	0.01	0.00	0.00	0.00	0.00	0.00	0.00	99.64	Qz	

Eclogites

Sample	Spot	SiO2	TiO2	Al2O3	FeO	MnO	MgO	CaO	Na2O	K2O	Total	Min	distance
10-05	~~1 / 1 .~~	~~47.75~~	~~0.20~~	~~9.17~~	~~8.00~~	~~0.07~~	~~14.31~~	~~8.12~~	~~3.43~~	~~0.42~~	~~91.46~~	amph	
10-05	~~2 / 1 .~~	~~44.63~~	~~0.30~~	~~11.51~~	~~11.14~~	~~0.09~~	~~10.97~~	~~7.47~~	~~3.79~~	~~0.37~~	~~90.27~~	amph	
10-05	3 / 1 .	57.03	0.03	11.61	3.59	0.02	7.91	12.25	7.72	0.00	100.16	prx	
10-05	4 / 1 .	55.83	0.05	8.88	6.08	0.17	7.96	14.92	6.32	0.00	100.21	prx	
10-05	5 / 1 .	55.60	0.04	8.79	7.26	0.04	7.56	14.56	6.79	0.02	100.65	prx	
10-05	6 / 1 .	55.58	0.04	8.97	7.34	0.03	7.27	13.56	7.27	0.00	100.05	prx	
10-05	7 / 1 .	56.98	0.04	11.59	2.20	0.01	8.72	13.61	7.28	0.00	100.44	prx	
10-05	8 / 1 .	55.60	0.07	8.11	6.69	0.02	8.28	14.42	6.47	0.01	99.66	prx	
10-05	9 / 1 .	49.22	0.26	11.25	10.53	0.06	12.80	8.25	4.06	0.41	96.84	amph	
10-05	10 / 1 .	47.75	0.17	11.73	12.48	0.10	11.19	8.98	3.46	0.33	96.20	amph	
10-05	11 / 1 .	54.33	0.14	12.12	9.07	0.10	10.70	9.55	4.44	0.25	100.69	amph	
10-05	12 / 1 .	48.02	0.24	12.27	12.55	0.10	10.87	8.69	3.81	0.34	96.89	amph	
10-05	13 / 1 .	47.87	0.17	11.76	12.19	0.10	11.29	9.43	3.22	0.34	96.38	amph	
10-05	14 / 1 .	47.79	0.24	12.14	12.41	0.11	10.91	8.75	3.51	0.33	96.19	amph	
10-05	15 / 1 .	48.01	0.25	12.19	12.44	0.12	10.94	8.96	3.48	0.33	96.71	amph	
10-05	16 / 1 .	48.25	0.22	11.82	12.46	0.12	10.96	8.58	3.74	0.30	96.44	amph	
10-05	17 / 1 .	47.64	0.18	11.61	12.35	0.11	11.24	9.04	3.51	0.31	95.99	amph	
10-05	18 / 1 .	55.77	0.04	8.74	7.04	0.03	7.92	14.35	6.85	0.00	100.74	prx	
10-05	19 / 1 .	56.29	0.03	11.19	2.82	0.02	9.09	14.06	7.17	0.02	100.71	prx	
10-05	20 / 1 .	47.99	0.31	12.40	11.96	0.10	11.27	8.24	4.05	0.32	96.65	amph	
10-05	21 / 1 .	65.17	0.01	21.81	0.22	0.02	0.14	2.91	9.29	0.08	99.65	plag	
10-05	22 / 1 .	66.32	0.00	21.28	0.18	0.02	0.21	2.58	9.77	0.05	100.41	plag	
10-05	23 / 1 .	47.78	0.14	11.08	11.91	0.10	12.23	10.17	2.75	0.35	96.51	amph	
10-05	24 / 1 .	47.66	0.16	11.58	12.17	0.10	11.77	9.83	2.68	0.39	96.33	amph	
10-05	25 / 1 .	~~54.01~~	~~0.21~~	~~26.43~~	~~1.14~~	~~0.00~~	~~5.41~~	~~0.00~~	~~0.14~~	~~8.46~~	~~95.79~~	?	
10-05	26 / 1 .	39.10	0.16	28.46	5.25	0.06	0.00	24.61	0.06	0.07	97.72	czo	
10-05	27 / 1 .	38.50	0.16	27.62	5.58	0.03	0.00	25.10	0.00	0.06	97.05	czo	
10-05	28 / 1 .	36.10	0.10	20.07	15.40	0.10	12.57	0.02	0.14	9.53	94.03	bt	
10-05	29 / 1 .	49.02	0.17	11.19	11.87	0.11	11.60	8.50	3.70	0.27	96.43	amph	
10-05	30 / 1 .	56.15	0.04	10.37	2.48	0.01	9.68	14.73	6.53	0.01	99.99	amph	
10-05	31 / 1 .	0.05	0.28	0.04	0.14	0.13	0.02	64.16	0.01	0.02	64.87	calcite	
10-05	32 / 1 .	74.74	0.02	16.44	0.93	0.01	2.70	3.74	5.71	0.03	104.32	amph	0
10-05	32 / 2 .	45.00	0.13	13.31	12.70	0.10	10.79	10.41	3.13	0.45	96.03	amph	3.17
10-05	32 / 3 .	45.28	0.16	13.45	12.74	0.12	10.54	10.29	3.19	0.45	96.21	amph	6.34
10-05	32 / 4 .	45.56	0.15	13.23	12.65	0.14	10.70	10.12	3.10	0.40	96.07	amph	9.51
10-05	32 / 5 .	46.33	0.18	12.49	12.51	0.14	11.09	9.65	3.31	0.40	96.08	amph	12.68
10-05	32 / 6 .	47.56	0.20	11.78	12.52	0.11	11.27	9.39	3.39	0.35	96.56	amph	15.85
10-05	32 / 7 .	48.32	0.24	11.96	12.53	0.13	10.87	8.87	3.55	0.32	96.78	amph	19.03
10-05	32 / 8 .	48.11	0.29	11.80	12.45	0.10	11.15	8.84	3.72	0.32	96.78	amph	22.2
10-05	32 / 9 .	47.89	0.32	12.31	12.50	0.10	10.83	8.39	3.75	0.33	96.43	amph	25.37
10-05	32 / 10 .	47.47	0.35	12.59	12.58	0.07	10.76	8.46	3.84	0.36	96.46	amph	28.54
10-05	32 / 11 .	47.60	0.35	12.53	12.36	0.14	10.95	8.72	3.77	0.37	96.79	amph	31.71
10-05	32 / 12 .	48.34	0.32	11.95	11.79	0.10	11.68	8.44	3.90	0.34	96.86	amph	34.88
10-05	32 / 13 .	48.07	0.31	11.73	11.48	0.09	12.05	8.60	3.67	0.38	96.38	amph	38.05
10-05	32 / 14 .	49.50	0.25	10.87	11.08	0.11	12.33	8.54	3.72	0.34	96.73	amph	41.22
10-05	32 / 15 .	50.61	0.24	9.50	10.33	0.08	13.53	8.51	3.63	0.32	96.75	amph	44.39
10-05	32 / 16 .	50.01	0.27	10.55	10.71	0.09	13.02	8.07	3.86	0.36	96.94	amph	47.56
10-05	32 / 17 .	50.57	0.26	9.83	10.32	0.09	13.43	7.97	3.84	0.33	96.63	amph	50.73
10-05	32 / 18 .	50.31	0.26	9.94	10.29	0.08	13.23	8.26	3.77	0.35	96.50	amph	53.91
10-05	32 / 19 .	50.62	0.24	10.10	10.22	0.10	13.33	8.13	3.78	0.37	96.89	amph	57.08
10-05	32 / 20 .	50.97	0.25	9.38	10.03	0.07	13.80	7.98	3.75	0.36	96.58	amph	60.25
10-05	32 / 21 .	50.76	0.22	9.80	10.49	0.11	13.41	8.24	3.76	0.35	97.13	amph	63.42
10-05	32 / 22 .	50.69	0.22	9.67	10.22	0.10	13.62	8.27	3.75	0.41	96.95	amph	66.59
10-05	32 / 23 .	50.55	0.23	9.72	10.10	0.08	13.64	8.38	3.68	0.40	96.77	amph	69.76
10-05	32 / 24 .	50.89	0.23	9.54	9.80	0.08	13.74	8.08	3.80	0.39	96.54	amph	72.93
10-05	32 / 25 .	51.88	0.19	7.42	9.46	0.04	15.18	9.16	3.24	0.33	96.90	amph	76.1
10-05	32 / 26 .	51.32	0.22	9.05	10.38	0.09	13.60	8.09	3.82	0.37	96.94	amph	79.27
10-05	32 / 27 .	50.83	0.23	9.37	10.97	0.11	13.36	8.19	3.55	0.38	97.00	amph	82.44
10-05	32 / 28 .	50.65	0.22	9.43	10.52	0.08	13.36	8.46	3.46	0.39	96.59	amph	85.62
10-05	32 / 29 .	51.07	0.20	9.25	10.46	0.09	13.53	8.30	3.57	0.37	96.84	amph	88.79
10-05	32 / 30 .	51.05	0.21	8.79	10.65	0.10	13.79	8.24	3.47	0.38	96.68	amph	91.96
10-05	32 / 31 .	51.42	0.18	8.90	10.10	0.09	14.01	8.20	3.54	0.38	96.83	amph	95.13
10-05	32 / 32 .	51.65	0.20	8.95	9.91	0.11	14.07	8.37	3.45	0.41	97.11	amph	98.3
10-05	32 / 33 .	51.92	0.17	8.41	9.07	0.08	15.00	8.45	3.48	0.39	96.97	amph	101.47
10-05	32 / 34 .	51.39	0.17	9.30	8.06	0.07	15.35	8.80	3.71	0.40	97.26	amph	104.64
10-05	32 / 35 .	51.00	0.15	9.64	7.26	0.02	15.80	8.97	3.78	0.40	97.03	amph	107.81
10-05	32 / 36 .	50.80	0.17	10.11	6.97	0.06	15.62	8.93	3.77	0.44	96.86	amph	110.98
10-05	32 / 37 .	50.49	0.17	10.46	7.10	0.04	15.60	8.95	3.92	0.41	97.16	amph	114.15
10-05	32 / 38 .	50.67	0.18	9.91	7.94	0.06	15.08	8.64	3.86	0.39	96.74	amph	117.33
10-05	32 / 39 .	51.77	0.17	8.44	8.99	0.08	14.75	8.25	3.64	0.35	96.44	amph	120.5
10-05	32 / 40 .	51.81	0.17	8.68	9.46	0.09	14.36	7.82	3.46	0.32	96.17	amph	123.67

Eclogites

Sample	Spot	SiO2	TiO2	Al2O3	FeO	MnO	MgO	CaO	Na2O	K2O	Total	Min	distance
10-05	32 / 41 .	50.72	0.23	9.69	10.03	0.09	13.61	8.24	3.58	0.37	96.56	amph	126.84
10-05	32 / 42 .	50.54	0.24	9.77	10.09	0.08	13.72	8.47	3.62	0.37	96.91	amph	130.01
10-05	32 / 43 .	50.54	0.22	10.01	10.14	0.09	13.40	7.96	3.69	0.36	96.41	amph	133.18
10-05	32 / 44 .	50.19	0.25	9.98	10.31	0.10	13.40	8.36	3.66	0.36	96.60	amph	136.35
10-05	32 / 45 .	49.93	0.28	10.53	10.88	0.09	13.24	8.41	3.63	0.36	97.34	amph	139.52
10-05	32 / 46 .	49.16	0.29	10.75	11.40	0.12	12.39	8.66	3.46	0.40	96.62	amph	142.69
10-05	32 / 47 .	48.43	0.31	11.27	11.88	0.12	11.88	8.87	3.55	0.43	96.73	amph	145.86
10-05	32 / 48 .	48.20	0.30	11.31	12.04	0.12	11.44	8.66	3.56	0.35	95.98	amph	149.03
10-05	32 / 49 .	48.26	0.30	11.55	12.23	0.11	11.35	8.31	3.80	0.35	96.26	amph	152.21
10-05	32 / 50 .	48.60	0.30	11.45	12.27	0.09	11.32	8.40	3.78	0.34	96.56	amph	155.38
10-05	32 / 51 .	47.73	0.31	11.99	12.56	0.12	11.06	8.80	3.57	0.35	96.48	amph	158.55
10-05	32 / 52 .	48.35	0.29	11.87	12.25	0.13	11.20	8.66	3.75	0.29	96.78	amph	161.72
10-05	32 / 53 .	48.08	0.30	12.27	12.91	0.09	10.76	8.56	3.80	0.33	97.09	amph	164.89
10-05	32 / 54 .	48.05	0.17	11.60	12.91	0.11	10.85	8.84	3.57	0.33	96.42	amph	168.06
10-05	32 / 55 .	47.34	0.17	11.83	12.72	0.06	11.08	9.32	3.37	0.33	96.21	amph	171.23
10-05	32 / 56 .	47.27	0.15	11.66	12.57	0.12	11.33	9.81	3.22	0.35	96.49	amph	174.4
10-05	32 / 57 .	46.39	0.13	12.19	12.69	0.10	11.36	10.51	3.04	0.39	96.80	amph	177.57
10-05	32 / 58 .	47.92	0.10	11.24	12.46	0.08	9.79	10.30	2.68	0.40	94.97	amph	180.74
10-05	32 / 59 .	56.56	0.03	10.69	2.39	0.02	9.23	14.71	6.55	0.06	100.26	amph	183.91
10-05	32 / 60 .	56.78	0.03	10.58	2.13	0.00	9.66	15.18	6.63	0.00	100.99	amph	187.09
10-05	33 / 1 .	55.95	0.04	8.71	5.27	0.02	8.98	14.50	6.74	0.00	100.19	amph	0
10-05	33 / 2 .	48.27	0.32	12.65	11.59	0.10	11.24	8.57	3.98	0.29	97.01	amph	3.19
10-05	33 / 3 .	48.78	0.29	11.63	11.08	0.08	12.10	8.60	3.90	0.37	96.82	amph	6.37
10-05	33 / 4 .	48.99	0.27	10.51	10.58	0.06	13.05	8.34	3.79	0.39	95.97	amph	9.56
10-05	33 / 5 .	52.70	0.15	7.27	10.28	0.11	14.82	9.08	2.63	0.28	97.33	amph	12.74
10-05	33 / 6 .	51.98	0.16	8.97	9.10	0.09	14.68	8.49	3.53	0.37	97.37	amph	15.93
10-05	33 / 7 .	51.00	0.16	10.11	8.10	0.07	15.11	8.80	3.69	0.38	97.42	amph	19.12
10-05	33 / 8 .	51.01	0.15	10.15	7.82	0.07	15.33	8.93	3.72	0.40	97.59	amph	22.3
10-05	33 / 9 .	50.76	0.17	10.01	7.48	0.08	15.40	9.08	3.59	0.43	97.00	amph	25.49
10-05	33 / 10 .	50.72	0.17	10.04	7.62	0.05	15.40	9.38	3.48	0.39	97.26	amph	28.67
10-05	33 / 11 .	50.51	0.16	10.04	7.53	0.07	15.54	9.31	3.45	0.44	97.06	amph	31.86
10-05	33 / 12 .	50.72	0.16	8.61	7.34	0.09	15.66	9.59	3.44	0.43	96.03	amph	35.05
10-05	33 / 13 .	50.87	0.13	9.56	8.35	0.08	15.43	8.91	2.95	0.75	97.04	amph	38.23
10-05	33 / 14 .	50.82	0.14	10.08	7.14	0.04	15.70	9.09	3.50	0.45	96.95	amph	41.42
10-05	33 / 15 .	51.74	0.12	9.22	6.04	0.05	16.97	9.16	3.56	0.38	97.23	amph	44.6
10-05	33 / 16 .	52.88	0.10	8.89	5.27	0.06	17.24	9.00	3.52	0.31	97.26	amph	47.79
10-05	33 / 17 .	52.80	0.10	8.91	5.28	0.03	17.08	9.32	3.51	0.32	97.33	amph	50.97
10-05	33 / 18 .	52.50	0.09	8.74	5.30	0.05	17.17	9.26	3.52	0.31	96.94	amph	54.16
10-05	33 / 19 .	52.22	0.10	8.77	7.02	0.07	16.10	9.60	3.12	0.31	97.31	amph	57.35
10-05	33 / 20 .	52.54	0.09	8.94	5.97	0.04	16.69	9.25	3.36	0.33	97.19	amph	60.53
10-05	33 / 21 .	52.55	0.09	8.60	5.76	0.07	17.01	9.49	3.26	0.31	97.14	amph	63.72
10-05	33 / 22 .	52.50	0.10	8.72	6.45	0.08	16.57	9.50	3.15	0.35	97.43	amph	66.9
10-05	33 / 23 .	52.78	0.09	7.86	6.49	0.04	17.00	10.00	2.86	0.34	97.46	amph	70.09
10-05	33 / 24 .	52.20	0.09	8.34	6.83	0.07	16.46	9.96	2.80	0.37	97.12	amph	73.28
10-05	33 / 25 .	52.74	0.10	8.41	5.32	0.00	17.52	9.79	3.20	0.37	97.43	amph	76.46
10-05	33 / 26 .	52.94	0.09	8.62	4.99	0.00	17.64	9.67	3.17	0.35	97.47	amph	79.65
10-05	33 / 27 .	52.42	0.09	8.82	5.43	0.02	17.08	9.67	3.20	0.36	97.10	amph	82.83
10-05	33 / 28 .	52.23	0.08	8.78	6.34	0.03	16.44	9.66	3.20	0.37	97.15	amph	86.02
10-05	33 / 29 .	52.20	0.09	9.00	5.82	0.08	16.82	9.50	3.32	0.35	97.19	amph	89.21
10-05	33 / 30 .	52.26	0.10	8.80	5.81	0.05	16.93	9.50	3.31	0.34	97.10	amph	92.39
10-05	33 / 31 .	52.73	0.11	8.91	6.06	0.05	16.46	9.50	3.11	0.34	97.25	amph	95.58
10-05	33 / 32 .	52.08	0.10	8.68	7.78	0.08	15.55	9.21	3.04	0.34	96.86	amph	98.76
10-05	33 / 33 .	51.71	0.10	9.14	8.07	0.09	15.21	9.25	3.10	0.34	97.01	amph	101.95
10-05	33 / 34 .	51.18	0.13	9.89	8.53	0.06	14.56	9.07	3.23	0.41	97.06	amph	105.14
10-05	33 / 35 .	50.59	0.12	10.34	8.84	0.09	14.23	8.96	3.30	0.41	96.88	amph	108.32
10-05	33 / 36 .	50.00	0.15	9.94	8.89	0.07	14.60	9.68	3.13	0.37	96.84	amph	111.51
10-05	33 / 37 .	50.68	0.14	10.01	8.74	0.08	14.75	9.32	3.26	0.38	97.36	amph	114.69
10-05	33 / 38 .	50.39	0.13	10.25	8.78	0.10	14.74	8.85	3.41	0.46	97.11	amph	117.88
10-05	33 / 39 .	50.51	0.14	10.44	8.42	0.08	14.69	8.88	3.43	0.45	97.04	amph	121.07
10-05	33 / 40 .	50.29	0.16	10.35	8.04	0.07	14.82	9.22	3.48	0.45	96.88	amph	124.25
10-05	33 / 41 .	50.49	0.15	10.26	7.54	0.04	15.22	9.12	3.60	0.46	96.88	amph	127.44
10-05	33 / 42 .	50.38	0.14	10.13	8.97	0.09	14.34	8.86	3.52	0.44	96.87	amph	130.62
10-05	33 / 43 .	50.19	0.15	9.91	9.57	0.12	13.83	9.13	3.30	0.42	96.61	amph	133.81
10-05	33 / 44 .	50.16	0.18	9.82	10.07	0.09	13.42	9.44	3.09	0.35	96.62	amph	137
10-05	33 / 45 .	50.71	0.21	9.16	9.90	0.10	14.01	9.21	2.87	0.25	96.42	amph	140.18
10-05	33 / 46 .	51.11	0.20	8.62	10.23	0.08	13.99	8.94	3.15	0.27	96.59	amph	143.37
10-05	33 / 47 .	50.80	0.22	9.65	10.23	0.07	13.71	8.39	3.55	0.33	96.95	amph	146.55
10-05	33 / 48 .	50.49	0.17	10.28	9.19	0.07	14.34	8.81	3.57	0.43	97.34	amph	149.74
10-05	33 / 49 .	50.15	0.18	10.19	8.69	0.09	14.64	9.16	3.47	0.42	96.99	amph	152.92
10-05	33 / 50 .	49.97	0.19	10.05	8.50	0.07	14.72	9.05	3.52	0.44	96.51	amph	156.11
10-05	33 / 51 .	51.40	0.18	8.59	9.22	0.08	14.72	8.57	3.45	0.37	96.58	amph	159.3

Eclogites

Sample	Spot	SiO2	TiO2	Al2O3	FeO	MnO	MgO	CaO	Na2O	K2O	Total	Min	distance
10-05	33 / 52 .	50.96	0.21	9.03	10.06	0.10	14.23	9.10	3.16	0.38	97.23	amph	162.48
10-05	33 / 53 .	50.16	0.22	10.05	10.71	0.10	12.96	8.45	3.47	0.39	96.51	amph	165.67
10-05	33 / 54 .	49.44	0.22	10.39	11.13	0.07	12.66	8.88	3.42	0.29	96.49	amph	168.85
10-05	33 / 55 .	49.28	0.22	11.05	11.49	0.08	12.00	8.62	3.64	0.28	96.67	amph	172.04
10-05	33 / 56 .	49.33	0.23	11.25	11.37	0.11	12.05	8.35	3.80	0.27	96.77	amph	175.23
10-05	33 / 57 .	50.10	0.21	10.43	10.71	0.12	12.61	8.75	3.62	0.25	96.80	amph	178.41
10-05	33 / 58 .	55.89	0.05	10.56	5.31	0.02	8.40	11.94	7.31	0.04	99.52	prx	181.6
10-05	33 / 59 .	56.27	0.04	10.81	4.90	0.00	7.51	12.16	8.04	0.01	99.73	prx	184.78
10-05	33 / 60 .	56.03	0.04	9.36	5.08	0.00	8.71	13.82	7.06	0.01	100.11	prx	187.97
10-05	34 / 1 .	53.28	0.08	4.28	8.43	0.11	17.23	12.11	1.40	0.13	97.04	amph	
10-05	35 / 1 .	52.64	0.15	4.65	8.35	0.12	17.60	12.22	1.41	0.17	97.31	amph	
10-05	36 / 1 .	~~63.11~~	~~0.01~~	~~16.11~~	~~1.02~~	~~0.03~~	~~3.47~~	~~5.53~~	~~7.61~~	~~0.09~~	~~96.98~~	prx+	
10-05	37 / 1 .	58.34	0.07	7.37	3.46	0.18	10.71	18.31	4.50	0.45	103.40	prx	
10-05	38 / 1 .	~~53.46~~	~~9.27~~	~~11.65~~	~~0.94~~	~~0.03~~	~~5.48~~	~~11.46~~	~~4.93~~	~~0.02~~	~~97.24~~	ttn?	
10-05	39 / 1 .	~~67.16~~	~~0.06~~	~~20.34~~	~~0.71~~	~~0.01~~	~~0.11~~	~~0.84~~	~~9.07~~	~~0.08~~	~~98.38~~	plag?	
10-05	40 / 1 .	51.71	0.34	29.24	1.88	0.00	3.89	0.03	0.41	8.28	95.79	phe	
10-05	41 / 1 .	52.08	0.31	29.67	1.55	0.00	4.16	0.01	0.37	8.14	96.28	phe	
10-05	42 / 1 .	50.54	0.28	28.90	1.43	0.03	4.47	0.04	0.39	8.95	95.02	phe	
10-05	43 / 1 .	45.93	0.24	13.12	11.76	0.10	11.64	8.25	3.72	0.93	95.68	amph	
10-05	44 / 1 .	30.23	37.64	1.87	0.28	0.01	0.00	30.18	0.04	0.07	100.24	ttn?	
10-05	45 / 1 .	52.95	0.27	28.34	1.54	0.00	4.67	0.07	0.22	8.15	96.20	phe	
10-05	46 / 1 .	61.57	0.04	12.02	2.86	0.02	8.78	7.83	5.63	0.03	98.78	prx	0
10-05	46 / 2 .	62.65	0.03	14.60	2.32	0.02	5.39	4.16	7.01	0.03	96.20	prx	3.06
10-05	46 / 3 .	56.47	0.07	10.69	5.08	0.01	7.63	12.98	7.77	0.00	100.70	prx	6.12
10-05	46 / 4 .	55.43	0.07	11.09	5.36	0.02	7.28	12.15	8.01	0.00	99.41	prx	9.19
10-05	46 / 5 .	55.26	0.09	10.27	5.62	0.01	7.67	13.07	7.85	0.00	99.85	prx	12.25
10-05	46 / 6 .	55.05	0.05	9.08	5.65	0.01	8.53	14.53	6.68	0.00	99.57	prx	15.31
10-05	46 / 7 .	54.94	0.05	9.02	5.99	0.02	8.58	14.34	6.78	0.00	99.72	prx	18.37
10-05	46 / 8 .	55.21	0.04	9.41	5.74	0.01	8.07	13.93	7.29	0.00	99.69	prx	21.43
10-05	46 / 9 .	55.29	0.06	9.60	5.58	0.04	8.15	13.74	7.34	0.00	99.80	prx	24.49
10-05	46 / 10 .	55.00	0.04	10.01	5.72	0.00	7.80	13.60	7.28	0.00	99.42	prx	27.56
10-05	46 / 11 .	55.93	0.04	10.65	4.92	0.01	7.95	13.46	7.77	0.00	100.71	prx	30.63
10-05	46 / 12 .	55.76	0.04	10.29	5.75	0.02	8.32	13.83	7.34	0.00	101.36	prx	33.69
10-05	46 / 13 .	55.87	0.05	11.03	3.30	0.02	8.26	13.56	7.50	0.01	99.61	prx	36.76
10-05	46 / 14 .	55.90	0.05	11.02	4.79	0.00	7.86	12.81	7.99	0.01	100.42	prx	39.82
10-05	46 / 15 .	55.56	0.05	11.43	4.20	0.01	7.62	12.62	7.88	0.00	99.35	prx	42.88
10-05	46 / 16 .	56.03	0.04	11.95	3.42	0.00	8.20	13.22	7.98	0.00	100.85	prx	45.94
10-05	46 / 17 .	55.64	0.04	11.09	3.80	0.05	8.50	14.41	7.16	0.00	100.70	prx	49
10-05	46 / 18 .	55.81	0.04	11.07	2.45	0.01	9.32	15.16	6.54	0.00	100.40	prx	52.06
10-05	46 / 19 .	56.26	0.04	12.38	2.20	0.00	8.42	13.43	7.62	0.00	100.36	prx	55.12
10-05	46 / 20 .	56.29	0.04	12.59	2.14	0.01	8.21	13.09	7.99	0.00	100.36	prx	58.18
10-05	46 / 21 .	56.13	0.04	11.09	2.26	0.01	9.37	15.15	6.46	0.00	100.51	prx	61.27
10-05	46 / 22 .	55.73	0.04	10.89	2.26	0.00	9.35	15.48	6.68	0.00	100.41	prx	64.33
10-05	46 / 23 .	55.87	0.05	11.13	2.21	0.01	9.35	15.35	6.68	0.01	100.67	prx	67.39
10-05	46 / 24 .	55.57	0.04	10.48	2.35	0.01	9.77	15.95	6.34	0.00	100.50	prx	70.45
10-05	46 / 25 .	55.76	0.05	10.61	2.34	0.03	9.67	15.77	6.34	0.01	100.58	prx	73.51
10-05	46 / 26 .	56.02	0.05	11.27	2.19	0.00	9.41	15.01	6.79	0.01	100.75	prx	76.57
10-05	46 / 27 .	56.23	0.04	11.88	2.50	0.00	8.53	13.65	7.59	0.00	100.42	prx	79.63
10-05	46 / 28 .	55.83	0.05	10.62	3.61	0.00	8.80	14.18	7.20	0.01	100.29	prx	82.69
10-05	46 / 29 .	56.17	0.05	10.91	3.57	0.04	8.65	13.81	7.54	0.00	100.75	prx	85.75
10-05	46 / 30 .	56.10	0.04	10.61	3.66	0.02	8.79	14.05	7.35	0.00	100.61	prx	88.81
10-05	46 / 31 .	56.03	0.03	10.79	3.47	0.00	8.79	13.77	7.35	0.01	100.23	prx	91.9
10-05	46 / 32 .	56.07	0.04	9.42	3.33	0.08	11.58	13.56	6.04	0.05	100.18	prx	94.96
10-05	46 / 33 .	55.45	0.04	9.06	2.28	0.00	10.70	17.23	5.54	0.00	100.30	prx	98.02
10-05	46 / 34 .	55.88	0.04	9.70	2.28	0.01	10.39	16.79	5.81	0.02	100.92	prx	101.08
10-05	46 / 35 .	55.70	0.04	9.28	2.31	0.01	10.69	16.88	5.69	0.02	100.62	prx	104.14
10-05	46 / 36 .	53.14	0.06	10.92	6.26	0.02	9.23	14.48	5.07	0.23	99.40	prx	107.2
10-05	46 / 37 .	56.41	0.05	11.45	2.35	0.02	9.08	14.44	7.22	0.00	101.00	prx	110.27
10-05	46 / 38 .	56.58	0.04	12.67	2.12	0.00	8.21	12.94	7.95	0.02	100.52	prx	113.33
10-05	46 / 39 .	56.49	0.04	12.62	2.10	0.01	8.31	13.04	7.89	0.00	100.51	prx	116.39
10-05	46 / 40 .	56.61	0.05	12.08	2.35	0.00	8.55	13.50	7.70	0.00	100.83	prx	119.45
10-05	46 / 41 .	56.44	0.04	11.42	2.48	0.00	9.02	13.99	7.33	0.00	100.72	prx	122.54
10-05	46 / 42 .	56.47	0.04	11.54	2.51	0.01	8.93	14.12	7.32	0.00	100.93	prx	125.6
10-05	46 / 43 .	56.52	0.04	12.07	2.16	0.01	8.63	13.66	7.54	0.01	100.64	prx	128.66
10-05	46 / 44 .	56.43	0.04	11.53	2.11	0.01	9.03	14.38	7.44	0.00	100.97	prx	131.72
10-05	46 / 45 .	56.31	0.04	12.11	2.20	0.02	8.45	13.50	7.63	0.01	100.28	prx	134.78
10-05	46 / 46 .	55.87	0.03	10.60	2.06	0.00	9.64	15.68	6.46	0.00	100.34	prx	137.84
10-05	46 / 47 .	55.89	0.04	10.35	2.26	0.00	9.87	15.79	6.31	0.00	100.52	prx	140.9
10-05	46 / 48 .	55.91	0.04	10.32	2.23	0.02	9.78	15.98	6.28	0.01	100.57	prx	143.96
10-05	46 / 49 .	56.40	0.04	11.04	2.24	0.03	9.42	14.91	7.00	0.00	101.08	prx	147.02
10-05	46 / 50 .	56.27	0.04	11.50	2.52	0.01	8.68	13.77	7.27	0.00	100.06	prx	150.08

Eclogites

Sample	Spot	SiO2	TiO2	Al2O3	FeO	MnO	MgO	CaO	Na2O	K2O	Total	Min	distance
10-05	46 / 51 .	56.48	0.03	11.32	2.83	0.00	8.74	13.70	7.38	0.02	100.48	prx	153.17
10-05	46 / 52 .	56.23	0.04	11.25	2.89	0.02	8.73	13.82	7.43	0.00	100.42	prx	156.23
10-05	46 / 53 .	56.21	0.04	11.72	2.87	0.01	8.39	13.40	7.53	0.00	100.15	prx	159.29
10-05	46 / 54 .	56.30	0.04	11.50	2.07	0.00	9.21	14.24	7.28	0.00	100.64	prx	162.35
10-05	46 / 55 .	56.80	0.04	12.59	2.00	0.01	8.14	13.00	7.90	0.00	100.47	prx	165.41
10-05	46 / 56 .	56.40	0.04	12.04	2.53	0.02	8.37	13.16	7.94	0.00	100.49	prx	168.47
10-05	46 / 57 .	55.47	0.06	9.69	5.02	0.00	8.45	14.27	7.05	0.01	100.00	prx	171.53
10-05	46 / 58 .	55.54	0.05	10.43	4.55	0.01	8.34	13.79	6.51	0.01	99.23	prx	174.59
10-05	46 / 59 .	55.27	0.06	7.94	6.13	0.01	8.95	15.57	6.43	0.01	100.36	prx	177.65
10-05	46 / 60 .	55.65	0.06	8.48	5.80	0.03	8.62	14.92	6.87	0.01	100.43	prx	180.71
10-05	46 / 61 .	56.17	0.05	10.48	3.79	0.00	8.36	13.58	7.36	0.00	99.78	prx	183.81
10-05	46 / 62 .	55.80	0.05	9.65	5.55	0.02	8.47	13.55	7.17	0.00	100.24	prx	186.87
10-05	46 / 63 .	55.75	0.05	10.01	5.46	0.03	8.24	13.61	7.24	0.01	100.40	prx	189.93
10-05	46 / 64 .	56.11	0.05	11.25	3.68	0.01	8.13	12.96	7.62	0.01	99.81	prx	192.99
10-05	46 / 65 .	56.07	0.03	11.16	4.10	0.00	7.89	12.81	7.83	0.00	99.89	prx	196.05
10-05	46 / 66 .	56.08	0.04	11.02	4.27	0.03	7.80	12.66	7.88	0.00	99.78	prx	199.11
10-05	46 / 67 .	56.18	0.05	10.74	4.86	0.01	7.80	12.79	7.78	0.01	100.20	prx	202.17
10-05	46 / 68 .	56.27	0.05	10.95	4.57	0.01	7.81	12.72	7.83	0.01	100.23	prx	205.23
10-05	46 / 69 .	56.14	0.05	10.52	4.69	0.00	8.09	13.11	7.64	0.00	100.23	prx	208.29
10-05	46 / 70 .	55.93	0.04	10.25	5.02	0.04	8.01	13.40	7.54	0.02	100.25	prx	211.35
10-05	46 / 71 .	55.95	0.04	9.94	5.24	0.01	8.01	13.37	7.25	0.00	99.80	prx	214.44
10-05	46 / 72 .	55.76	0.07	9.64	5.87	0.01	7.97	13.24	7.39	0.00	99.95	prx	217.5
10-05	46 / 73 .	55.60	0.04	9.25	5.98	0.01	8.07	14.03	7.02	0.00	100.01	prx	220.56
10-05	46 / 74 .	55.71	0.06	9.20	5.94	0.02	8.05	13.91	7.12	0.00	99.99	prx	223.62
10-05	46 / 75 .	55.53	0.07	9.36	6.07	0.01	8.23	13.73	7.09	0.01	100.10	prx	226.68
10-05	46 / 76 .	55.52	0.05	8.80	6.54	0.00	8.24	14.10	6.80	0.00	100.07	prx	229.74
10-05	46 / 77 .	55.40	0.06	8.78	6.59	0.01	8.22	14.07	6.74	0.00	99.87	prx	232.8
10-05	46 / 78 .	55.24	0.04	7.57	7.06	0.01	8.97	15.23	5.98	0.00	100.10	prx	235.86
10-05	46 / 79 .	55.22	0.05	7.52	6.37	0.00	9.06	15.57	6.25	0.00	100.03	prx	238.92
10-05	46 / 80 .	55.30	0.04	7.70	6.35	0.01	9.02	15.48	6.00	0.00	99.91	prx	241.98
10-05	46 / 81 .	55.82	0.04	8.45	5.55	0.02	9.09	14.65	6.33	0.01	99.97	prx	245.07
10-05	46 / 82 .	55.60	0.06	7.19	6.39	0.02	9.61	16.04	6.01	0.00	100.92	prx	248.13
10-05	46 / 83 .	55.85	0.06	8.80	5.63	0.00	8.59	14.44	6.83	0.00	100.18	prx	251.19
10-05	46 / 84 .	55.36	0.10	7.95	5.72	0.01	9.03	15.54	6.31	0.00	100.02	prx	254.25
10-05	46 / 85 .	55.39	0.06	8.47	6.41	0.01	8.44	14.43	6.36	0.00	99.56	prx	257.31
10-05	46 / 86 .	55.56	0.04	8.39	6.09	0.01	8.46	14.54	6.70	0.00	99.80	prx	260.37
10-05	46 / 87 .	56.15	0.05	9.98	5.47	0.00	8.08	13.72	7.05	0.00	100.51	prx	263.44
10-05	46 / 88 .	55.86	0.06	9.96	6.30	0.01	7.81	13.07	7.48	0.00	100.54	prx	266.5
10-05	46 / 89 .	56.20	0.04	10.81	5.20	0.03	7.64	12.69	7.76	0.01	100.36	prx	269.56
10-05	46 / 90 .	56.34	0.04	10.61	4.97	0.00	7.91	12.95	7.78	0.00	100.60	prx	272.62
10-05	46 / 91 .	56.40	0.05	10.34	4.95	0.00	8.30	13.07	7.58	0.00	100.66	prx	275.71
10-05	46 / 92 .	56.27	0.05	9.49	5.12	0.01	8.67	13.80	7.12	0.00	100.52	prx	278.77
10-05	46 / 93 .	55.92	0.03	9.58	5.12	0.02	8.96	14.28	6.96	0.02	100.90	prx	281.83
10-05	46 / 94 .	56.51	0.04	10.17	2.71	0.02	9.78	15.36	6.19	0.01	100.79	prx	284.89
10-05	46 / 95 .	58.37	0.04	16.87	4.37	0.00	4.35	7.16	6.22	0.04	97.43	prx	287.95
10-05	46 / 96 .	41.32	0.02	22.06	22.20	0.35	7.73	6.97	0.31	0.10	101.06	czo	291.01
10-05	46 / 97 .	38.86	0.01	21.59	25.01	0.46	6.88	5.89	0.00	0.00	98.70	czo	294.07
10-05	46 / 98 .	38.65	0.02	21.57	25.75	0.33	6.77	6.21	0.04	0.00	99.34	czo	297.13
10-05	46 / 99 .	38.38	0.04	21.43	27.44	0.32	5.75	6.31	0.03	0.00	99.70	czo	300.19
10-05	46 / 100 .	38.24	0.03	21.19	28.14	0.27	5.46	6.28	0.01	0.00	99.61	czo	303.28
10-05	47 / 1 .	~~60.08~~	~~0.04~~	~~7.03~~	~~5.29~~	~~0.10~~	~~13.01~~	~~10.90~~	~~4.30~~	~~0.09~~	100.85	amph?	0
10-05	47 / 2 .	49.50	0.24	12.40	12.19	0.14	10.95	9.19	3.41	0.35	98.36	amph	3.06
10-05	47 / 3 .	48.66	0.28	12.03	12.13	0.09	10.99	8.27	3.81	0.30	96.55	amph	6.12
10-05	47 / 4 .	47.86	0.32	12.78	11.93	0.13	10.97	8.06	3.88	0.34	96.28	amph	9.18
10-05	47 / 5 .	48.13	0.34	12.56	11.70	0.11	11.22	8.55	3.72	0.33	96.64	amph	12.24
10-05	47 / 6 .	48.98	0.30	10.93	10.96	0.08	12.46	8.13	3.82	0.34	96.00	amph	15.31
10-05	47 / 7 .	49.92	0.25	10.93	10.66	0.08	12.86	8.20	3.65	0.33	96.87	amph	18.37
10-05	47 / 8 .	~~48.18~~	~~0.24~~	~~11.20~~	~~11.18~~	~~0.10~~	~~10.96~~	~~6.17~~	~~3.32~~	~~0.62~~	91.96	amph	21.43
10-05	47 / 9 .	49.88	0.22	10.68	10.92	0.09	12.91	7.76	3.47	0.74	96.68	amph	24.49
10-05	47 / 10 .	50.59	0.22	10.60	10.39	0.06	12.95	7.86	3.91	0.35	96.94	amph	27.55
10-05	47 / 11 .	50.09	0.23	10.33	10.22	0.08	13.08	8.03	3.62	0.36	96.03	amph	30.61
10-05	47 / 12 .	50.32	0.24	10.19	10.26	0.07	13.37	8.42	3.53	0.39	96.79	amph	33.67
10-05	47 / 13 .	51.29	0.21	9.71	10.07	0.07	13.48	7.83	3.61	0.35	96.63	amph	36.73
10-05	47 / 14 .	51.36	0.20	9.20	9.82	0.08	13.83	8.14	3.60	0.36	96.59	amph	39.79
10-05	47 / 15 .	51.60	0.21	8.58	9.76	0.07	14.35	8.48	3.39	0.38	96.83	amph	42.85
10-05	47 / 16 .	51.86	0.19	8.07	9.49	0.10	14.72	8.69	3.28	0.40	96.81	amph	45.92
10-05	47 / 17 .	52.35	0.17	8.31	9.10	0.09	14.96	8.41	3.37	0.37	97.11	amph	48.98
10-05	47 / 18 .	51.13	0.17	9.26	8.16	0.04	15.28	8.89	3.42	0.42	96.76	amph	52.04
10-05	47 / 19 .	50.17	0.16	9.01	8.51	0.08	14.90	8.52	2.89	0.66	94.90	amph	55.1
10-05	47 / 20 .	52.25	0.14	8.65	7.36	0.08	15.99	8.72	3.41	0.40	97.00	amph	58.16
10-05	47 / 21 .	51.40	0.13	8.97	7.59	0.06	15.83	8.80	3.40	0.44	96.63	amph	61.22

Eclogites

Sample	Spot	SiO2	TiO2	Al2O3	FeO	MnO	MgO	CaO	Na2O	K2O	Total	Min	distance
10-05	47 / 22 .	50.95	0.14	9.42	7.83	0.05	15.88	8.85	3.48	0.48	97.06	amph	64.28
10-05	47 / 23 .	51.67	0.14	9.33	7.10	0.06	16.09	9.02	3.72	0.43	97.57	amph	67.34
10-05	47 / 24 .	51.44	0.14	9.35	6.81	0.08	16.10	9.10	3.63	0.45	97.10	amph	70.4
10-05	47 / 25 .	51.85	0.12	9.29	6.57	0.08	16.40	9.09	3.65	0.43	97.50	amph	73.47
10-05	47 / 26 .	51.37	0.13	8.82	6.67	0.05	14.92	8.47	3.76	0.49	94.67	amph	76.53
10-05	47 / 27 .	51.42	0.14	9.64	6.44	0.06	16.31	8.83	3.78	0.43	97.06	amph	79.59
10-05	47 / 28 .	51.62	0.13	9.65	6.32	0.08	16.24	9.00	3.84	0.42	97.28	amph	82.65
10-05	47 / 29 .	51.33	0.14	9.77	6.39	0.06	16.26	9.07	3.75	0.42	97.19	amph	85.71
10-05	47 / 30 .	51.49	0.14	9.88	6.28	0.05	16.17	9.08	3.83	0.42	97.34	amph	88.77
10-05	47 / 31 .	51.45	0.13	9.71	6.09	0.03	16.58	9.11	3.89	0.44	97.41	amph	91.83
10-05	47 / 32 .	52.57	0.11	8.81	5.50	0.03	16.71	8.97	3.71	0.32	96.74	amph	94.89
10-05	47 / 33 .	52.51	0.11	8.99	5.39	0.05	16.98	8.86	3.79	0.35	97.03	amph	97.95
10-05	47 / 34 .	52.52	0.10	8.87	5.26	0.02	17.11	9.25	3.69	0.32	97.15	amph	101.01
10-05	47 / 35 .	52.72	0.10	8.68	5.31	0.02	17.11	9.24	3.65	0.33	97.16	amph	104.08
10-05	47 / 36 .	52.69	0.11	8.97	5.18	0.03	17.25	9.23	3.67	0.33	97.45	amph	107.14
10-05	47 / 37 .	52.87	0.09	8.60	5.10	0.02	17.31	9.36	3.56	0.34	97.25	amph	110.2
10-05	47 / 38 .	52.68	0.09	8.55	5.25	0.03	17.33	9.22	3.60	0.34	97.10	amph	113.26
10-05	47 / 39 .	52.80	0.09	8.55	5.08	0.03	17.38	9.33	3.55	0.31	97.12	amph	116.32
10-05	47 / 40 .	52.74	0.09	8.47	5.16	0.01	17.38	9.34	3.53	0.35	97.07	amph	119.38
10-05	47 / 41 .	52.49	0.10	8.91	5.13	0.04	17.21	9.15	3.60	0.35	96.99	amph	122.44
10-05	47 / 42 .	52.31	0.09	9.22	5.14	0.01	17.07	9.10	3.80	0.35	97.09	amph	125.5
10-05	47 / 43 .	52.62	0.10	9.44	5.19	0.01	16.88	8.91	3.90	0.35	97.40	amph	128.56
10-05	47 / 44 .	52.41	0.11	9.36	5.21	0.01	16.85	8.92	3.92	0.37	97.15	amph	131.63
10-05	47 / 45 .	52.43	0.11	9.21	5.18	0.02	16.89	9.18	3.79	0.36	97.15	amph	134.69
10-05	47 / 46 .	52.46	0.10	9.14	5.25	0.04	16.92	9.04	3.73	0.34	97.03	amph	137.75
10-05	47 / 47 .	52.86	0.09	8.82	5.31	0.03	17.19	9.21	3.71	0.32	97.56	amph	140.81
10-05	47 / 48 .	50.94	0.12	9.67	6.27	0.06	16.41	9.12	3.61	0.39	96.60	amph	143.87
10-05	47 / 49 .	51.47	0.14	9.21	7.18	0.07	15.70	8.89	3.66	0.40	96.73	amph	146.93
10-05	47 / 50 .	51.55	0.16	8.90	8.51	0.10	14.60	8.47	3.52	0.40	96.22	amph	149.99
10-05	47 / 51 .	49.11	0.28	11.51	10.76	0.11	12.41	8.17	3.69	0.39	96.43	amph	153.05
10-05	47 / 52 .	48.76	0.29	11.71	10.96	0.11	12.31	8.54	3.75	0.39	96.83	amph	156.11
10-05	47 / 53 .	48.60	0.27	11.68	11.23	0.10	12.14	8.45	3.79	0.38	96.63	amph	159.17
10-05	47 / 54 .	48.45	0.29	11.62	11.50	0.12	11.81	8.64	3.82	0.36	96.62	amph	162.24
10-05	47 / 55 .	47.56	0.31	12.45	12.12	0.11	11.29	8.80	3.78	0.36	96.77	amph	165.3
10-05	47 / 56 .	48.15	0.32	12.13	12.23	0.09	11.22	8.73	3.75	0.31	96.93	amph	168.36
10-05	47 / 57 .	47.51	0.33	12.34	12.07	0.11	11.33	9.09	3.74	0.32	96.84	amph	171.42
10-05	47 / 58 .	46.93	0.26	12.68	11.85	0.12	11.76	9.75	3.61	0.37	97.33	amph	174.48
10-05	47 / 59 .	~~38.22~~	~~0.19~~	~~4.49~~	~~10.82~~	~~0.06~~	~~5.78~~	~~32.83~~	~~3.54~~	~~0.38~~	~~96.31~~	?	177.54
10-05	47 / 60 .	~~0.08~~	~~0.00~~	~~0.03~~	~~0.24~~	~~0.10~~	~~0.00~~	~~65.80~~	~~0.01~~	~~0.00~~	~~66.19~~		180.6
10-05	1 / 1 .	44.61	0.09	12.98	14.67	0.11	9.81	10.35	3.20	0.41	96.21	amph	0
10-05	1 / 2 .	44.31	0.09	13.12	14.81	0.10	9.78	10.30	3.15	0.46	96.11	amph	3.09
10-05	1 / 3 .	44.08	0.09	13.29	14.79	0.12	9.95	10.30	3.23	0.49	96.32	amph	6.18
10-05	1 / 4 .	~~30.34~~	~~0.04~~	~~6.81~~	~~13.88~~	~~0.04~~	~~4.02~~	~~3.12~~	~~0.82~~	~~1.48~~	~~60.55~~		9.27
10-05	1 / 5 .	41.54	0.05	16.66	15.56	0.13	7.93	10.81	3.43	0.65	96.75	amph	12.36
10-05	1 / 6 .	38.72	0.02	20.05	15.27	0.13	7.03	11.53	3.12	0.91	96.79	amph	15.45
10-05	1 / 7 .	37.21	0.03	17.76	19.81	0.11	6.52	10.45	1.91	0.57	94.37	amph	18.54
10-05	1 / 8 .	38.27	0.03	21.78	26.10	0.29	7.64	5.86	0.00	0.00	99.96	grt	21.63
10-05	1 / 9 .	37.95	0.03	21.52	25.77	0.83	6.41	6.47	0.02	0.01	99.00	grt	24.72
10-05	1 / 10 .	37.88	0.04	21.24	27.48	1.31	5.13	6.31	0.02	0.01	99.43	grt	27.81
10-05	1 / 11 .	38.05	0.05	21.56	26.52	0.50	7.13	5.89	0.01	0.00	99.71	grt	30.9
10-05	1 / 12 .	38.13	0.04	21.66	26.17	0.37	7.10	6.09	0.02	0.01	99.59	grt	33.99
10-05	1 / 13 .	37.75	0.03	21.54	27.82	0.32	5.88	6.49	0.00	0.00	99.82	grt	37.08
10-05	1 / 14 .	37.50	0.05	21.31	28.33	0.27	5.18	6.59	0.02	0.00	99.25	grt	40.17
10-05	1 / 15 .	37.33	0.05	21.16	29.19	0.27	4.84	6.47	0.02	0.00	99.33	grt	43.26
10-05	1 / 16 .	37.34	0.05	21.29	29.55	0.29	4.42	6.64	0.02	0.01	99.59	grt	46.35
10-05	1 / 17 .	37.15	0.05	21.10	30.08	0.32	4.06	6.56	0.01	0.01	99.33	grt	49.44
10-05	1 / 18 .	37.17	0.05	21.15	30.04	0.29	3.86	6.90	0.01	0.00	99.46	grt	52.53
10-05	1 / 19 .	36.90	0.05	20.92	29.93	0.32	3.71	6.97	0.01	0.00	98.81	grt	55.62
10-05	1 / 20 .	36.98	0.05	21.07	30.28	0.32	3.66	7.00	0.01	0.01	99.39	grt	58.71
10-05	1 / 21 .	36.78	0.06	21.01	30.63	0.34	3.53	7.00	0.01	0.03	99.37	grt	61.8
10-05	1 / 22 .	36.99	0.04	20.89	30.28	0.34	3.33	7.21	0.02	0.02	99.11	grt	64.89
10-05	1 / 23 .	36.80	0.07	20.34	30.33	0.31	3.19	7.12	0.02	0.00	98.14	grt	67.98
10-05	1 / 24 .	36.80	0.06	20.91	30.57	0.31	3.02	7.42	0.02	0.01	99.12	grt	71.07
10-05	1 / 25 .	36.76	0.06	20.95	30.61	0.30	2.97	7.60	0.00	0.01	99.25	grt	74.16
10-05	1 / 26 .	36.80	0.08	20.90	30.71	0.26	2.70	7.92	0.00	0.02	99.38	grt	77.25
10-05	1 / 27 .	36.81	0.07	20.83	30.66	0.26	2.61	7.90	0.01	0.01	99.17	grt	80.34
10-05	1 / 28 .	36.72	0.09	20.84	30.59	0.25	2.53	8.30	0.01	0.00	99.34	grt	83.43
10-05	1 / 29 .	36.67	0.08	20.95	30.97	0.28	2.41	8.13	0.01	0.00	99.50	grt	86.52
10-05	1 / 30 .	36.76	0.08	20.93	30.92	0.27	2.39	8.02	0.01	0.00	99.36	grt	89.61
10-05	1 / 31 .	36.67	0.08	20.87	30.67	0.29	2.34	8.33	0.02	0.01	99.28	grt	92.7
10-05	1 / 32 .	36.76	0.08	20.85	30.70	0.30	2.23	8.06	0.01	0.00	98.99	grt	95.79

Eclogites

Sample	Spot	SiO2	TiO2	Al2O3	FeO	MnO	MgO	CaO	Na2O	K2O	Total	Min	distance
10-05	1 / 33 .	36.86	0.08	20.89	30.67	0.34	2.20	8.51	0.02	0.00	99.58	grt	98.88
10-05	1 / 34 .	36.72	0.09	20.77	30.73	0.35	2.13	8.71	0.00	0.00	99.50	grt	101.97
10-05	1 / 35 .	36.69	0.08	20.88	30.52	0.38	2.12	8.77	0.01	0.01	99.47	grt	105.06
10-05	1 / 36 .	36.71	0.08	20.75	30.47	0.40	2.09	8.69	0.02	0.01	99.21	grt	108.15
10-05	1 / 37 .	36.50	0.09	20.86	29.84	0.42	1.99	9.34	0.02	0.01	99.06	grt	111.24
10-05	1 / 38 .	36.82	0.10	20.75	29.77	0.53	1.91	9.44	0.01	0.00	99.32	grt	114.33
10-05	1 / 39 .	36.82	0.10	20.85	29.97	0.56	1.85	9.58	0.01	0.00	99.72	grt	117.42
10-05	1 / 40 .	36.77	0.09	20.82	30.11	0.56	1.93	9.17	0.00	0.00	99.44	grt	120.51
10-05	1 / 41 .	36.71	0.08	20.51	30.02	0.56	1.86	9.42	0.01	0.01	99.17	grt	123.6
10-05	1 / 42 .	36.70	0.04	20.68	30.63	0.62	1.80	9.11	0.02	0.01	99.62	grt	126.69
10-05	1 / 43 .	36.83	0.03	20.67	30.60	0.64	1.73	9.11	0.00	0.00	99.59	grt	129.78
10-05	1 / 44 .	36.80	0.06	20.66	30.30	0.65	1.61	9.50	0.02	0.00	99.58	grt	132.87
10-05	1 / 45 .	36.69	0.09	20.59	29.88	0.63	1.60	9.91	0.00	0.00	99.39	grt	135.96
10-05	1 / 46 .	36.70	0.14	20.66	29.61	0.62	1.56	10.34	0.00	0.00	99.63	grt	139.05
10-05	1 / 47 .	36.79	0.11	20.62	29.67	0.60	1.56	10.00	0.00	0.00	99.33	grt	142.14
10-05	1 / 48 .	36.73	0.14	20.54	29.11	0.58	1.44	10.81	0.02	0.00	99.35	grt	145.23
10-05	1 / 49 .	36.65	0.13	20.60	29.33	0.58	1.46	10.79	0.00	0.00	99.54	grt	148.32
10-05	1 / 50 .	36.90	0.13	20.59	29.80	0.60	1.69	9.80	0.00	0.00	99.51	grt	151.41
10-05	1 / 51 .	36.80	0.08	20.57	30.34	0.59	1.74	9.61	0.00	0.02	99.75	grt	154.5
10-05	1 / 52 .	37.45	0.11	20.95	29.60	0.60	1.63	9.85	0.02	0.00	100.21	grt	157.59
10-05	1 / 53 .	36.72	0.14	20.59	29.37	0.61	1.58	10.19	0.00	0.00	99.20	grt	160.68
10-05	1 / 54 .	36.62	0.09	20.65	29.70	0.57	1.70	10.10	0.01	0.00	99.45	grt	163.77
10-05	1 / 55 .	36.68	0.18	20.52	28.96	0.54	1.72	10.80	0.02	0.01	99.41	grt	166.86
10-05	1 / 56 .	36.83	0.16	20.60	28.70	0.57	1.90	10.83	0.01	0.00	99.59	grt	169.95
10-05	1 / 57 .	36.89	0.20	20.73	27.36	0.58	2.59	11.10	0.01	0.00	99.45	grt	173.04
10-05	1 / 58 .	37.14	0.18	20.78	27.86	0.55	2.64	10.84	0.01	0.01	100.03	grt	176.13
10-05	1 / 59 .	37.24	0.15	20.83	27.34	0.60	2.74	11.15	0.01	0.00	100.05	grt	179.23
10-05	1 / 60 .	36.79	0.16	20.75	28.54	0.61	1.91	10.79	0.00	0.00	99.54	grt	182.32
10-05	1 / 61 .	36.80	0.17	20.56	29.00	0.65	1.35	11.44	0.03	0.00	100.00	grt	185.4
10-05	1 / 62 .	36.67	0.20	20.47	28.35	0.65	1.37	11.79	0.02	0.00	99.51	grt	188.5
10-05	1 / 63 .	36.71	0.20	20.45	28.24	0.60	1.42	11.62	0.03	0.00	99.27	grt	191.59
10-05	1 / 64 .	36.84	0.17	20.63	28.43	0.63	1.80	11.06	0.02	0.00	99.57	grt	194.68
10-05	1 / 65 .	36.42	1.52	16.87	27.80	0.47	1.56	14.90	0.05	0.01	99.59	grt	197.77
10-05	1 / 66 .	36.59	0.19	20.48	28.92	0.65	1.29	11.70	0.02	0.01	99.83	grt	200.86
10-05	1 / 67 .	36.49	0.17	20.51	28.47	0.64	1.22	11.72	0.02	0.01	99.25	grt	203.95
10-05	~~1 / 68 .~~	~~17.49~~	~~0.44~~	~~29.29~~	~~16.16~~	~~0.36~~	~~1.52~~	~~6.14~~	~~0.19~~	~~1.92~~	73.52	czo	207.04
10-05	1 / 69 .	39.56	0.23	21.37	26.92	0.48	3.00	8.40	0.02	1.98	101.95	grt	210.13
10-05	1 / 70 .	36.69	0.20	20.44	28.38	0.67	1.08	11.94	0.02	0.01	99.45	grt	213.22
10-05	2 / 1 .	49.84	0.27	10.43	11.09	0.10	12.56	8.19	3.73	0.41	96.62	amph	0
10-05	2 / 2 .	52.68	0.16	6.77	9.74	0.11	15.49	9.31	2.63	0.31	97.21	amph	3.01
10-05	2 / 3 .	51.21	0.18	7.53	10.24	0.09	14.86	9.30	3.08	0.37	96.85	amph	6.02
10-05	2 / 4 .	51.03	0.20	8.17	10.20	0.08	14.46	9.15	3.29	0.40	96.97	amph	9.02
10-05	2 / 5 .	50.59	0.21	8.88	10.55	0.15	13.88	8.94	3.32	0.38	96.90	amph	12.03
10-05	2 / 6 .	49.85	0.24	10.02	10.83	0.09	12.98	8.65	3.52	0.46	96.63	amph	15.04
10-05	2 / 7 .	49.47	0.26	11.01	11.38	0.09	12.40	8.39	3.69	0.47	97.17	amph	18.05
10-05	2 / 8 .	48.55	0.28	11.79	11.78	0.09	11.77	8.06	3.80	0.44	96.56	amph	21.06
10-05	2 / 9 .	46.07	0.25	14.18	12.57	0.09	10.30	8.46	4.05	0.48	96.45	amph	24.06
10-05	2 / 10 .	42.46	0.10	17.19	13.90	0.12	8.57	9.39	3.98	0.60	96.30	amph	27.07
10-05	2 / 11 .	40.94	0.05	18.46	14.15	0.10	8.24	9.86	3.83	0.78	96.40	amph	30.08
10-05	2 / 12 .	39.10	0.03	19.84	15.03	0.09	7.36	10.66	3.67	0.60	96.38	amph	33.09
10-05	2 / 13 .	38.93	0.03	20.61	18.15	0.11	7.24	8.48	3.70	0.26	97.51	amph	36.1
10-05	2 / 14 .	~~37.72~~	~~0.02~~	~~19.27~~	~~18.34~~	~~0.19~~	~~5.29~~	~~9.55~~	~~2.20~~	~~0.23~~	~~92.81~~	amph	39.1
10-05	2 / 15 .	38.02	0.02	20.95	26.95	0.30	5.85	6.35	0.07	0.02	98.53	Grt	42.11
10-05	2 / 16 .	38.21	0.04	21.09	28.24	0.30	5.19	6.19	0.00	0.01	99.27	Grt	45.12
10-05	2 / 17 .	38.21	0.03	20.94	28.68	0.31	4.88	6.15	0.00	0.00	99.20	Grt	48.13
10-05	2 / 18 .	39.03	0.05	21.09	28.85	0.32	4.57	6.25	0.01	0.00	100.15	Grt	51.14
10-05	2 / 19 .	38.06	0.04	20.80	29.13	0.27	4.44	6.28	0.02	0.01	99.05	Grt	54.14
10-05	2 / 20 .	37.85	0.04	20.83	29.62	0.29	4.41	6.30	0.00	0.00	99.33	Grt	57.15
10-05	2 / 21 .	37.85	0.04	20.77	29.43	0.28	4.15	6.56	0.00	0.00	99.08	Grt	60.16
10-05	2 / 22 .	37.90	0.04	20.87	29.34	0.27	4.12	6.66	0.02	0.00	99.21	Grt	63.17
10-05	2 / 23 .	38.02	0.03	20.63	29.36	0.31	4.00	6.47	0.02	0.00	98.83	Grt	66.18
10-05	2 / 24 .	37.94	0.04	20.70	29.54	0.32	3.93	6.54	0.02	0.00	99.02	Grt	69.18
10-05	2 / 25 .	37.92	0.05	20.74	29.24	0.32	3.82	6.78	0.00	0.01	98.88	Grt	72.19
10-05	2 / 26 .	37.85	0.06	20.65	29.50	0.33	3.69	7.17	0.02	0.00	99.25	Grt	75.2
10-05	2 / 27 .	37.79	0.06	20.73	29.94	0.32	3.67	6.80	0.01	0.00	99.31	Grt	78.21
10-05	2 / 28 .	37.86	0.07	20.57	29.71	0.35	3.54	7.17	0.01	0.00	99.26	Grt	81.22
10-05	2 / 29 .	37.91	0.06	20.73	29.77	0.32	3.37	7.13	0.01	0.01	99.31	Grt	84.22
10-05	2 / 30 .	37.56	0.05	20.61	30.04	0.30	3.26	7.08	0.03	0.00	98.93	Grt	87.23
10-05	2 / 31 .	37.84	0.05	20.49	29.99	0.31	3.16	7.06	0.02	0.01	98.92	Grt	90.24
10-05	2 / 32 .	37.79	0.07	20.60	30.37	0.30	3.14	6.98	0.01	0.00	99.25	Grt	93.25
10-05	2 / 33 .	37.78	0.08	20.64	30.55	0.29	3.17	6.77	0.00	0.00	99.27	Grt	96.26

Eclogites

Sample	Spot	SiO2	TiO2	Al2O3	FeO	MnO	MgO	CaO	Na2O	K2O	Total	Min	distance
10-05	2 / 34 .	37.85	0.06	20.61	30.67	0.31	3.11	6.64	0.02	0.01	99.27	Grt	99.26
10-05	2 / 35 .	37.72	0.06	20.63	30.55	0.32	2.99	7.16	0.01	0.01	99.43	Grt	102.27
10-05	2 / 36 .	38.11	0.08	20.61	30.24	0.29	2.90	7.32	0.00	0.00	99.53	Grt	105.28
10-05	2 / 37 .	37.78	0.08	20.50	30.44	0.28	2.86	7.14	0.01	0.00	99.09	Grt	108.29
10-05	2 / 38 .	37.67	0.07	20.60	30.38	0.27	2.92	7.34	0.01	0.01	99.27	Grt	111.3
10-05	2 / 39 .	37.49	0.09	20.51	30.60	0.27	2.81	7.45	0.02	0.00	99.23	Grt	114.3
10-05	2 / 40 .	37.55	0.08	20.49	30.57	0.23	2.67	7.36	0.02	0.00	98.95	Grt	117.31
10-05	2 / 41 .	37.52	0.08	20.46	30.53	0.25	2.64	7.55	0.01	0.00	99.04	Grt	120.32
10-05	2 / 42 .	37.62	0.08	20.51	30.73	0.24	2.62	7.57	0.01	0.00	99.36	Grt	123.33
10-05	2 / 43 .	37.69	0.08	20.64	30.76	0.24	2.55	7.42	0.02	0.00	99.41	Grt	126.34
10-05	2 / 44 .	37.45	0.09	20.60	30.81	0.27	2.53	7.33	0.01	0.00	99.07	Grt	129.34
10-05	2 / 45 .	37.61	0.08	20.43	30.48	0.22	2.60	7.54	0.00	0.00	98.96	Grt	132.35
10-05	2 / 46 .	37.52	0.08	20.64	30.39	0.26	2.50	7.70	0.02	0.00	99.11	Grt	135.36
10-05	2 / 47 .	37.70	0.09	20.53	30.77	0.24	2.47	7.63	0.00	0.01	99.43	Grt	138.37
10-05	2 / 48 .	37.47	0.09	20.57	30.47	0.27	2.44	7.64	0.00	0.00	98.93	Grt	141.38
10-05	2 / 49 .	37.45	0.07	20.61	30.67	0.26	2.39	7.64	0.00	0.00	99.09	Grt	144.38
10-05	2 / 50 .	37.68	0.08	20.52	30.48	0.29	2.26	7.92	0.01	0.00	99.24	Grt	147.39
10-05	2 / 51 .	37.34	0.07	20.64	30.53	0.26	2.23	8.19	0.02	0.00	99.27	Grt	150.4
10-05	2 / 52 .	37.59	0.09	20.63	30.19	0.27	2.18	8.44	0.02	0.01	99.43	Grt	153.41
10-05	2 / 53 .	37.42	0.10	20.54	30.30	0.31	2.08	8.36	0.01	0.00	99.11	Grt	156.42
10-05	2 / 54 .	37.75	0.10	20.59	30.22	0.31	2.09	8.51	0.02	0.00	99.60	Grt	159.42
10-05	2 / 55 .	37.34	0.10	20.64	30.16	0.34	2.09	8.41	0.01	0.00	99.07	Grt	162.43
10-05	2 / 56 .	37.56	0.10	20.59	30.16	0.32	2.05	8.52	0.02	0.00	99.31	Grt	165.44
10-05	2 / 57 .	37.40	0.10	20.64	30.09	0.40	1.98	8.68	0.02	0.01	99.32	Grt	168.45
10-05	2 / 58 .	37.45	0.10	20.60	29.80	0.40	1.98	8.83	0.01	0.00	99.17	Grt	171.46
10-05	2 / 59 .	37.62	0.10	20.55	29.89	0.39	1.95	8.94	0.01	0.00	99.45	Grt	174.46
10-05	2 / 60 .	37.53	0.11	20.56	29.68	0.42	1.93	9.01	0.02	0.01	99.27	Grt	177.47
10-05	2 / 61 .	37.34	0.10	20.57	29.48	0.45	1.95	9.11	0.03	0.00	99.01	Grt	180.48
10-05	2 / 62 .	37.48	0.07	20.65	29.87	0.48	2.00	8.65	0.02	0.00	99.22	Grt	183.49
10-05	2 / 63 .	37.53	0.08	20.68	29.57	0.50	1.93	9.00	0.03	0.01	99.32	Grt	186.5
10-05	2 / 64 .	37.43	0.11	20.55	29.56	0.55	1.95	8.84	0.01	0.01	99.00	Grt	189.51
10-05	2 / 65 .	37.35	0.10	20.66	29.55	0.56	1.93	9.22	0.00	0.00	99.36	Grt	192.51
10-05	2 / 66 .	37.48	0.09	20.58	29.82	0.58	1.98	8.80	0.01	0.00	99.33	Grt	195.52
10-05	2 / 67 .	37.29	0.09	20.51	29.97	0.53	2.00	8.50	0.00	0.00	98.89	Grt	198.53
10-05	2 / 68 .	37.36	0.10	20.47	29.86	0.58	2.05	8.54	0.04	0.01	99.01	Grt	201.54
10-05	2 / 69 .	37.49	0.12	20.57	28.98	0.56	2.02	9.63	0.03	0.00	99.39	Grt	204.54
10-05	2 / 70 .	37.43	0.12	20.55	28.61	0.52	1.95	9.76	0.01	0.00	98.93	Grt	207.55
10-05	2 / 71 .	37.53	0.11	20.63	28.71	0.52	2.12	9.32	0.01	0.00	98.93	Grt	210.56
10-05	2 / 72 .	37.46	0.11	20.60	29.16	0.57	2.30	8.94	0.01	0.01	99.14	Grt	213.57
10-05	2 / 73 .	37.78	0.11	20.65	28.23	0.56	2.36	9.64	0.01	0.00	99.35	Grt	216.58
10-05	2 / 74 .	37.73	0.11	20.49	28.55	0.51	2.30	9.71	0.01	0.00	99.42	Grt	219.59
10-05	2 / 75 .	37.44	0.11	20.57	28.95	0.58	2.01	9.76	0.00	0.00	99.44	Grt	222.59
10-05	2 / 76 .	37.60	0.10	20.58	28.57	0.58	2.52	9.49	0.01	0.00	99.45	Grt	225.6
10-05	2 / 77 .	37.72	0.11	20.51	28.17	0.51	2.39	9.63	0.02	0.00	99.05	Grt	228.61
10-05	2 / 78 .	37.40	0.10	20.57	28.28	0.54	2.18	10.01	0.00	0.00	99.08	Grt	231.62
10-05	2 / 79 .	37.36	0.12	20.53	29.02	0.51	2.01	9.72	0.00	0.00	99.27	Grt	234.63
10-05	2 / 80 .	37.46	0.10	20.49	28.93	0.58	2.08	9.55	0.00	0.01	99.20	Grt	237.63
10-05	2 / 81 .	37.67	0.10	20.41	29.11	0.59	2.20	9.63	0.01	0.00	99.71	Grt	240.64
10-05	2 / 82 .	37.56	0.10	20.55	28.17	0.53	2.57	9.73	0.02	0.00	99.23	Grt	243.65
10-05	2 / 83 .	37.59	0.11	20.53	28.18	0.54	2.51	9.40	0.02	0.00	98.88	Grt	246.66
10-05	2 / 84 .	37.67	0.11	20.58	28.71	0.56	2.37	9.07	0.01	0.00	99.05	Grt	249.67
10-05	2 / 85 .	37.54	0.10	20.50	28.95	0.58	2.33	9.28	0.04	0.00	99.33	Grt	252.67
10-05	2 / 86 .	37.66	0.11	20.66	28.91	0.54	2.34	9.17	0.01	0.01	99.43	Grt	255.68
10-05	2 / 87 .	37.58	0.11	20.62	28.64	0.58	2.48	9.35	0.02	0.00	99.38	Grt	258.69
10-05	2 / 88 .	37.67	0.11	20.55	27.62	0.59	2.57	9.87	0.01	0.00	98.99	Grt	261.7
10-05	2 / 89 .	37.77	0.11	20.61	27.61	0.55	3.08	9.06	0.02	0.00	98.80	Grt	264.71
10-05	2 / 90 .	37.98	0.09	20.48	28.17	0.57	2.56	9.61	0.03	0.00	99.48	Grt	267.71
10-05	2 / 91 .	37.69	0.12	20.48	26.50	0.56	3.09	10.16	0.01	0.00	98.62	Grt	270.72
10-05	2 / 92 .	37.68	0.11	20.65	25.98	0.53	2.23	11.74	0.03	0.01	98.95	Grt	273.73
10-05	2 / 93 .	37.56	0.09	20.36	27.73	0.58	1.27	12.12	0.01	0.00	99.72	Grt	276.74
10-05	2 / 94 .	37.34	0.09	20.17	27.72	0.57	1.16	11.79	0.02	0.02	98.87	Grt	279.75
10-05	2 / 95 .	37.59	0.08	20.41	28.92	0.56	1.25	10.68	0.00	0.00	99.49	Grt	282.75
10-05	2 / 96 .	37.43	0.06	20.53	26.97	0.51	1.11	12.50	0.01	0.01	99.13	Grt	285.76
10-05	2 / 97 .	37.54	0.07	20.57	26.93	0.49	1.14	12.68	0.01	0.00	99.42	Grt	288.77
10-05	2 / 98 .	37.66	0.06	20.45	26.78	0.51	1.12	12.62	0.01	0.00	99.20	Grt	291.78
10-05	2 / 99 .	37.52	0.07	20.55	27.41	0.54	1.18	12.35	0.01	0.00	99.62	Grt	294.79
10-05	2 / 100 .	37.53	0.07	20.60	26.77	0.49	1.22	12.48	0.01	0.00	99.17	Grt	297.79
11-05	1 / 1 .	43.91	0.02	11.09	18.61	0.12	9.99	10.56	2.64	0.39	97.33	amph	
11-05	2 / 1 .	38.36	0.10	21.72	23.67	0.29	4.87	12.03	0.01	0.02	101.07	amph	
11-05	3 / 1 .	37.83	0.01	21.52	22.06	0.19	7.76	6.77	0.03	0.00	96.15	amph	

Eclogites

Sample	Spot	SiO2	TiO2	Al2O3	FeO	MnO	MgO	CaO	Na2O	K2O	Total	Min	distance
11-05	4 / 1 .	35.58	0.03	18.27	17.56	0.10	13.33	0.75	0.12	9.64	95.39	bt	
11-05	5 / 1 .	36.60	0.03	17.74	16.87	0.02	14.57	0.01	0.15	9.44	95.43	bt	
11-05	6 / 1 .	35.76	0.05	18.89	19.10	0.08	12.56	0.11	0.11	9.54	96.20	bt	
11-05	7 / 1 .	38.63	0.04	26.94	7.40	0.03	0.00	23.92	0.00	0.00	96.95	bt	
11-05	8 / 1 .	39.70	0.02	20.64	14.32	0.06	8.14	10.84	2.94	0.97	97.63	bt	
11-05	9 / 1 .	52.62	0.25	27.88	1.30	0.03	4.65	0.01	0.34	9.40	96.48	phe	
11-05	10 / 1 .	52.31	0.25	28.43	1.11	0.02	4.36	0.03	0.43	9.26	96.20	phe	
11-05	11 / 1 .	53.19	0.22	27.02	1.25	0.00	4.90	0.02	0.28	9.50	96.38	phe	
11-05	12 / 1 .	52.91	0.25	27.05	1.57	0.00	4.84	0.00	0.25	9.39	96.26	phe	
11-05	13 / 1 .	36.01	0.74	17.71	15.77	0.09	13.36	0.50	0.14	9.57	93.89	bt	
11-05	14 / 1 .	35.96	0.63	17.97	16.53	0.06	13.09	0.57	0.16	9.28	94.25	bt	
11-05	15 / 1 .	36.82	0.78	17.59	16.59	0.14	12.85	0.26	0.08	9.05	94.17	bt	
11-05	16 / 1 .	35.64	0.92	18.73	16.07	0.08	13.16	0.04	0.16	9.66	94.47	bt	
11-05	17 / 1 .	52.17	0.23	28.54	1.09	0.01	4.31	0.00	0.49	9.29	96.11	phe	
11-05	18 / 1 .	52.38	0.23	27.61	1.18	0.00	4.76	0.00	0.36	9.44	95.96	phe	
11-05	19 / 1 .	53.67	0.23	26.57	1.30	0.00	5.16	0.02	0.24	9.44	96.64	phe	
11-05	20 / 1 .	48.35	0.16	13.58	11.27	0.09	11.81	7.88	4.36	0.34	97.85	amph	
11-05	21 / 1 .	35.84	1.58	17.13	18.85	0.10	12.54	0.04	0.08	9.88	96.05	bt	
11-05	22 / 1 .	35.89	0.91	17.61	20.40	0.14	11.05	0.06	0.07	9.73	95.87	bt	
11-05	23 / 1 .	51.16	0.02	6.56	13.51	0.18	14.71	10.22	2.11	0.12	98.58	amph	
11-05	24 / 1 .	51.53	0.02	6.40	11.81	0.14	15.76	9.79	2.38	0.09	97.93	amph	
11-05	25 / 1 .	51.56	0.02	7.28	10.80	0.17	15.91	10.53	2.21	0.15	98.62	amph	
11-05	26 / 1 .	36.46	0.15	19.32	14.36	0.10	14.83	0.22	0.14	9.71	95.28	bt	
11-05	27 / 1 .	37.11	0.12	20.41	18.36	0.23	6.76	11.18	3.24	0.34	97.75	amph	
11-05	28 / 1 .	38.55	0.11	19.93	17.77	0.16	6.59	9.88	3.65	0.44	97.08	amph	
11-05	29 / 1 .	38.99	0.02	17.74	18.85	0.09	7.65	11.33	2.96	0.74	98.36	amph	
11-05	30 / 1 .	54.86	0.00	0.92	18.71	0.47	19.24	3.76	0.24	0.02	98.21	amph	
11-05	31 / 1 .	43.05	0.05	12.43	16.31	0.08	10.79	11.02	2.89	0.44	97.06	amph	
11-05	32 / 1 .	68.76	0.00	20.49	0.61	0.00	0.00	0.25	10.34	0.07	100.50	plag	
11-05	34 / 1 .	37.41	0.04	18.08	22.84	0.20	5.60	9.72	3.74	0.08	97.73	prx	
11-05	35 / 1 .	37.18	0.01	24.40	11.72	0.19	0.00	24.28	0.00	0.00	97.76	czo	
11-05	36 / 1 .	45.14	0.03	38.56	4.51	0.05	1.46	0.64	4.46	0.86	95.72	pa	
11-05	37 / 1 .	54.32	0.20	2.93	7.39	0.00	19.57	13.54	0.67	0.11	98.74	amph	
11-05	38 / 1 .	53.13	0.29	4.18	8.28	0.01	18.16	13.55	0.83	0.22	98.67	amph	
11-05	39 / 1 .	65.47	0.12	18.89	0.70	0.00	2.42	2.44	9.07	0.05	99.16	plag	
11-05	40 / 1 .	66.02	0.18	17.90	1.50	0.00	3.39	3.56	9.21	0.04	101.80	plag	
11-05	41 / 1 .	67.25	0.09	17.98	1.30	0.02	3.10	2.47	10.01	0.04	102.25	plag	
11-05	42 / 1 .	56.04	0.06	10.13	5.52	0.00	8.09	13.81	7.33	0.00	100.97	plag	
11-05	43 / 1 .	39.01	0.02	32.07	1.07	0.01	0.00	26.10	0.01	0.01	98.29	czo	
11-05	44 / 1 .	100.19	0.01	0.04	0.02	0.01	0.00	0.02	0.00	0.00	100.29	qtz	
11-05	45 / 1 .	100.65	0.00	0.01	0.01	0.00	0.00	0.00	0.00	0.00	100.66	qtz	
11-05	46 / 1 .	55.54	0.00	1.67	8.58	0.13	19.25	11.73	0.92	0.05	97.87	amph	
11-05	47 / 1 .	56.19	0.03	10.24	4.77	0.00	7.98	12.96	7.73	0.01	99.89	prx	
11-05	48 / 1 .	56.29	0.09	10.88	4.61	0.02	7.55	12.20	8.14	0.01	99.79	prx	
11-05	49 / 1 .	56.01	0.05	10.04	5.07	0.00	7.84	13.07	7.66	0.00	99.73	prx	
11-05	50 / 1 .	56.58	0.04	11.69	4.34	0.03	7.25	11.87	8.42	0.00	100.22	prx	
11-05	51 / 1 .	49.50	0.23	12.15	8.72	0.00	13.00	11.40	2.78	0.32	98.09	amph	
11-05	52 / 1 .	49.42	0.19	11.04	7.45	0.02	15.15	9.93	3.37	0.15	96.72	amph	
11-05	53 / 1 .	55.07	0.14	10.68	4.75	0.02	11.77	7.78	4.67	0.13	95.02	amph	
11-05	54 / 1 .	50.23	0.11	11.61	7.19	0.00	14.93	10.00	3.07	0.18	97.32	amph	
11-05	55 / 1 .	~~83.43~~	~~0.01~~	~~1.63~~	~~1.26~~	~~0.01~~	~~5.62~~	~~4.19~~	~~1.34~~	~~0.03~~	97.53	?	
11-05	56 / 1 .	~~67.67~~	~~0.03~~	~~20.98~~	~~0.22~~	~~0.00~~	~~0.13~~	~~1.41~~	~~10.04~~	~~0.17~~	100.65	plag?	
11-05	57 / 1 .	38.09	0.02	21.55	28.83	0.24	6.82	5.71	0.01	0.04	101.33	grt	0
11-05	57 / 2 .	38.11	0.03	22.10	27.57	0.22	6.78	4.95	0.04	0.98	100.78	grt	4.07
11-05	57 / 3 .	29.61	0.01	15.72	25.85	0.21	7.31	3.73	0.07	0.62	83.13	grt	8.14
11-05	57 / 4 .	38.41	0.03	21.59	29.30	0.24	5.98	5.98	0.00	0.00	101.51	grt	12.21
11-05	57 / 5 .	38.19	0.02	21.71	29.73	0.27	5.75	5.97	0.00	0.00	101.65	grt	16.29
11-05	57 / 6 .	38.10	0.03	21.50	29.79	0.22	5.49	6.07	0.01	0.00	101.22	grt	20.36
11-05	57 / 7 .	38.01	0.03	21.42	30.45	0.19	5.26	6.40	0.03	0.00	101.79	grt	24.43
11-05	57 / 8 .	38.12	0.02	21.41	30.52	0.20	5.23	6.01	0.01	0.01	101.52	grt	28.5
11-05	57 / 10 .	37.96	0.03	21.58	30.97	0.17	5.06	6.07	0.01	0.00	101.84	grt	36.64
11-05	57 / 11 .	38.08	0.02	21.41	31.10	0.17	4.93	6.31	0.01	0.02	102.06	grt	40.72
11-05	57 / 12 .	37.76	0.04	21.42	30.88	0.17	5.20	6.39	0.03	0.01	101.91	grt	44.79
11-05	57 / 13 .	37.79	0.04	21.52	30.81	0.17	4.85	6.29	0.01	0.00	101.46	grt	48.86
11-05	57 / 14 .	37.75	0.05	21.76	30.71	0.16	4.77	6.43	0.02	0.02	101.67	grt	52.93
11-05	57 / 15 .	37.92	0.04	21.49	31.02	0.21	4.75	6.30	0.00	0.00	101.73	grt	57
11-05	57 / 16 .	34.15	0.04	20.13	31.29	0.19	6.46	4.60	0.03	0.06	96.94	grt	61.07
11-05	57 / 17 .	37.83	0.03	21.48	30.16	0.24	4.32	7.51	0.02	0.03	101.61	grt	65.15
11-05	57 / 18 .	37.82	0.04	21.45	29.79	0.27	3.99	8.15	0.01	0.01	101.52	grt	69.22
11-05	57 / 19 .	37.80	0.03	21.40	29.89	0.33	3.36	9.13	0.03	0.00	101.97	grt	73.29
11-05	57 / 20 .	34.66	0.08	21.29	29.02	0.32	3.54	8.76	0.01	1.87	99.56	grt	77.36

Eclogites

Sample	Spot	SiO2	TiO2	Al2O3	FeO	MnO	MgO	CaO	Na2O	K2O	Total	Min	distance
11-05	57 / 21 .	37.77	0.08	21.14	29.30	0.27	3.07	10.09	0.01	0.01	101.73	grt	81.43
11-05	57 / 22 .	37.80	0.09	21.13	29.30	0.31	3.03	9.90	0.03	0.01	101.60	grt	85.5
11-05	57 / 23 .	37.63	0.06	21.22	29.38	0.28	2.96	10.18	0.02	0.01	101.74	grt	89.58
11-05	57 / 24 .	37.73	0.08	21.02	29.46	0.28	2.88	10.25	0.02	0.02	101.74	grt	93.65
11-05	57 / 25 .	37.70	0.10	21.23	29.06	0.29	2.91	10.22	0.02	0.03	101.56	grt	97.72
11-05	57 / 26 .	37.88	0.09	21.14	29.18	0.28	2.88	10.34	0.02	0.01	101.82	grt	101.79
11-05	57 / 27 .	37.71	0.10	21.25	29.20	0.32	2.84	10.33	0.02	0.01	101.77	grt	105.86
11-05	57 / 28 .	37.54	0.10	21.21	29.35	0.32	2.88	10.53	0.04	0.00	101.96	grt	109.93
11-05	57 / 29 .	37.64	0.10	21.12	28.79	0.34	2.80	10.94	0.02	0.00	101.76	grt	114.01
11-05	57 / 30 .	37.76	0.10	21.31	29.07	0.38	2.85	10.43	0.02	0.01	101.92	grt	118.08
11-05	57 / 31 .	37.53	0.08	21.10	29.01	0.32	2.88	10.48	0.03	0.01	101.44	grt	122.15
11-05	57 / 32 .	37.57	0.07	21.34	28.67	0.33	2.82	10.89	0.03	0.01	101.73	grt	126.22
11-05	57 / 33 .	37.83	0.08	21.35	28.60	0.37	2.80	10.87	0.03	0.00	101.94	grt	130.29
11-05	57 / 34 .	36.90	0.09	20.41	28.52	0.33	2.84	11.07	0.03	0.00	100.19	grt	134.36
11-05	57 / 35 .	37.61	0.08	21.18	28.39	0.34	2.82	10.97	0.04	0.01	101.45	grt	138.43
11-05	57 / 36 .	37.76	0.09	21.09	28.16	0.33	2.83	11.18	0.02	0.00	101.48	grt	142.51
11-05	57 / 37 .	37.71	0.10	21.18	28.16	0.33	2.74	11.04	0.03	0.02	101.31	grt	146.58
11-05	57 / 38 .	37.65	0.10	21.26	28.36	0.35	2.74	11.28	0.02	0.00	101.75	grt	150.65
11-05	57 / 39 .	37.69	0.09	21.08	28.06	0.36	2.75	11.18	0.03	0.00	101.23	grt	154.72
11-05	57 / 40 .	37.77	0.10	21.14	28.17	0.34	2.77	11.21	0.03	0.00	101.54	grt	158.79
11-05	57 / 41 .	37.78	0.10	21.15	28.01	0.32	2.74	11.30	0.01	0.00	101.42	grt	162.86
11-05	57 / 42 .	37.78	0.10	21.04	27.71	0.31	2.67	11.76	0.03	0.00	101.41	grt	166.94
11-05	57 / 43 .	37.77	0.09	21.18	27.66	0.32	2.64	12.05	0.02	0.00	101.73	grt	171.01
11-05	57 / 44 .	37.68	0.11	21.12	27.86	0.31	2.66	12.14	0.01	0.01	101.90	grt	175.08
11-05	57 / 45 .	37.77	0.11	21.28	27.16	0.32	2.58	12.22	0.04	0.00	101.47	grt	179.15
11-05	57 / 46 .	37.86	0.10	21.15	27.50	0.30	2.60	11.95	0.04	0.01	101.51	grt	183.22
11-05	57 / 47 .	37.68	0.10	21.18	27.75	0.31	2.64	11.87	0.01	0.00	101.53	grt	187.29
11-05	57 / 48 .	37.85	0.12	21.14	27.68	0.31	2.53	11.97	0.02	0.00	101.63	grt	191.37
11-05	57 / 49 .	37.71	0.10	21.19	27.84	0.29	2.57	12.41	0.02	0.00	102.13	grt	195.44
11-05	57 / 50 .	38.18	0.10	21.48	27.90	0.34	2.54	12.29	0.01	0.00	102.84	grt	199.51
11-05	57 / 51 .	37.71	0.09	21.27	27.61	0.35	2.42	12.16	0.01	0.00	101.63	grt	203.58
11-05	57 / 52 .	37.59	0.12	21.27	27.66	0.38	2.43	12.34	0.04	0.00	101.83	grt	207.65
11-05	57 / 53 .	37.88	0.11	21.27	27.70	0.35	2.37	12.17	0.01	0.00	101.85	grt	211.72
11-05	57 / 54 .	37.79	0.10	21.34	27.90	0.40	2.44	12.00	0.01	0.01	102.00	grt	215.8
11-05	57 / 55 .	37.81	0.13	21.18	27.65	0.35	2.37	12.14	0.02	0.00	101.64	grt	219.87
11-05	57 / 56 .	37.65	0.11	21.14	27.54	0.36	2.27	12.35	0.02	0.00	101.42	grt	223.94
11-05	57 / 57 .	37.78	0.11	21.15	27.47	0.40	2.27	12.46	0.00	0.02	101.65	grt	228.01
11-05	57 / 58 .	38.07	0.12	21.07	26.69	0.36	2.28	12.45	0.14	0.03	101.21	grt	232.08
11-05	57 / 59 .	37.47	0.12	21.13	26.74	0.52	2.16	13.01	0.05	0.03	101.24	grt	236.15
11-05	57 / 60 .	37.72	0.10	21.18	27.29	0.39	2.15	13.06	0.02	0.00	101.90	grt	240.23
11-05	57 / 61 .	37.77	0.13	21.20	26.63	0.45	2.08	13.61	0.00	0.00	101.85	grt	244.3
11-05	57 / 62 .	37.80	0.12	21.37	26.91	0.42	2.20	13.22	0.02	0.00	102.08	grt	248.37
11-05	57 / 63 .	37.84	0.05	21.39	27.37	0.44	2.32	12.72	0.01	0.00	102.14	grt	252.44
11-05	57 / 64 .	37.55	0.06	21.27	28.02	0.43	2.42	11.88	0.00	0.00	101.62	grt	256.51
11-05	57 / 65 .	37.71	0.08	21.10	27.95	0.48	2.39	11.65	0.01	0.00	101.38	grt	260.58
11-05	57 / 66 .	37.55	0.10	21.31	28.61	0.48	2.49	11.89	0.03	0.01	102.45	grt	264.66
11-05	57 / 67 .	37.61	0.10	21.15	28.43	0.42	2.46	11.35	0.01	0.00	101.54	grt	268.73
11-05	57 / 68 .	37.61	0.07	21.19	28.75	0.44	2.48	11.21	0.01	0.00	101.74	grt	272.8
11-05	57 / 69 .	37.60	0.09	21.04	28.79	0.44	2.48	10.88	0.04	0.01	101.37	grt	276.87
11-05	57 / 70 .	37.61	0.11	21.17	29.06	0.44	2.54	10.65	0.01	0.00	101.57	grt	280.94
11-05	57 / 71 .	37.57	0.12	21.13	29.33	0.39	2.51	10.54	0.01	0.00	101.59	grt	285.01
11-05	57 / 72 .	37.71	0.12	21.11	29.39	0.39	2.56	10.47	0.02	0.00	101.77	grt	289.08
11-05	57 / 73 .	37.47	0.08	21.19	29.53	0.41	2.53	10.32	0.02	0.01	101.56	grt	293.16
11-05	57 / 74 .	37.65	0.08	21.22	29.69	0.38	2.55	10.21	0.02	0.00	101.80	grt	297.23
11-05	57 / 75 .	37.64	0.09	21.15	29.50	0.40	2.61	10.41	0.02	0.00	101.80	grt	301.3
11-05	57 / 76 .	37.75	0.13	21.22	29.41	0.39	2.54	10.32	0.00	0.00	101.73	grt	305.37
11-05	57 / 77 .	37.59	0.11	21.12	29.43	0.39	2.53	10.53	0.04	0.00	101.72	grt	309.44
11-05	57 / 78 .	37.46	0.13	20.61	28.37	0.40	2.45	10.39	0.01	0.01	99.84	grt	313.51
11-05	57 / 79 .	37.74	0.13	21.20	29.32	0.39	2.55	10.87	0.00	0.00	102.20	grt	317.59
11-05	57 / 80 .	37.74	0.14	20.99	28.97	0.38	2.50	11.30	0.02	0.00	102.04	grt	321.66
11-05	57 / 81 .	37.73	0.15	21.17	28.23	0.38	2.44	11.71	0.02	0.01	101.83	grt	325.73
11-05	57 / 82 .	37.66	0.13	21.06	28.63	0.38	2.56	11.26	0.01	0.00	101.68	grt	329.8
11-05	57 / 83 .	37.73	0.14	21.10	28.89	0.41	2.63	11.24	0.04	0.00	102.17	grt	333.87
11-05	57 / 84 .	37.75	0.11	21.16	28.86	0.38	2.71	10.61	0.02	0.00	101.60	grt	337.94
11-05	57 / 85 .	37.68	0.11	21.24	28.86	0.40	2.71	10.35	0.00	0.00	101.36	grt	342.02
11-05	57 / 86 .	37.48	0.12	21.14	28.63	0.42	2.74	10.50	0.02	0.00	101.03	grt	346.09
11-05	57 / 87 .	37.38	0.10	21.18	28.96	0.47	2.86	10.38	0.02	0.01	101.37	grt	350.16
11-05	57 / 88 .	37.76	0.10	21.14	28.72	0.46	2.88	10.51	0.02	0.00	101.60	grt	354.23
11-05	57 / 89 .	37.88	0.13	21.19	28.61	0.40	2.94	10.76	0.08	0.00	101.98	grt	358.3
11-05	57 / 90 .	40.88	0.07	21.59	28.02	0.41	3.02	7.25	0.59	0.13	101.97	grt	362.37
11-05	57 / 92 .	100.17	0.00	0.09	0.80	0.02	0.01	0.07	0.00	0.00	101.16	qtz	370.52

Eclogites

Sample	Spot	SiO2	TiO2	Al2O3	FeO	MnO	MgO	CaO	Na2O	K2O	Total	Min	distance
11-05	57 / 93 .	100.35	0.00	0.09	0.79	0.02	0.01	0.06	0.01	0.01	101.34	qtz	374.59
11-05	57 / 94 .	100.29	0.01	0.11	0.85	0.02	0.01	0.07	0.00	0.00	101.35	qtz	378.66
11-05	57 / 95 .	~~86.12~~	~~0.01~~	~~7.46~~	~~9.88~~	~~0.16~~	~~0.99~~	~~3.24~~	~~0.00~~	~~0.00~~	107.87	?	382.73
11-05	57 / 96 .	37.75	0.12	21.05	28.33	0.45	2.72	11.04	0.01	0.00	101.47	grt	386.8
11-05	57 / 97 .	37.78	0.15	21.10	28.38	0.46	2.48	11.25	0.02	0.00	101.62	grt	390.88
11-05	57 / 98 .	37.62	0.15	21.15	28.61	0.46	2.40	11.28	0.03	0.01	101.70	grt	394.95
11-05	57 / 99 .	37.59	0.12	21.10	28.89	0.48	2.42	11.02	0.02	0.00	101.64	grt	399.02
11-05	57 / 100 .	37.81	0.12	21.17	28.90	0.46	2.43	10.75	0.01	0.01	101.68	grt	403.09
11-05	57 / 101 .	37.47	0.15	21.02	28.68	0.45	2.33	11.15	0.00	0.00	101.23	grt	407.16
11-05	57 / 102 .	37.77	0.13	21.17	29.11	0.55	2.37	10.47	0.01	0.01	101.59	grt	411.23
11-05	57 / 103 .	37.48	0.55	20.95	29.36	0.50	2.35	10.40	0.00	0.01	101.61	grt	415.31
11-05	57 / 104 .	37.47	0.11	21.04	28.97	0.49	2.35	10.67	0.00	0.00	101.09	grt	419.38
11-05	57 / 105 .	37.60	0.06	21.20	29.26	0.52	2.31	10.80	0.01	0.00	101.77	grt	423.45
11-05	57 / 106 .	37.55	0.08	21.22	29.33	0.54	2.35	10.62	0.02	0.00	101.69	grt	427.52
11-05	57 / 107 .	37.82	0.12	21.16	29.17	0.51	2.28	10.80	0.01	0.00	101.86	grt	431.59
11-05	57 / 108 .	37.61	0.13	21.15	29.11	0.51	2.30	10.93	0.02	0.00	101.74	grt	435.66
11-05	57 / 109 .	37.72	0.13	20.97	28.79	0.54	2.16	11.06	0.02	0.02	101.41	grt	439.73
11-05	57 / 110 .	37.66	0.13	21.01	28.72	0.54	2.13	11.43	0.03	0.03	101.67	grt	443.81
11-05	57 / 111 .	37.64	0.12	21.05	29.07	0.54	2.12	11.02	0.05	0.01	101.63	grt	447.88
11-05	57 / 112 .	37.63	0.09	21.02	29.49	0.56	2.10	10.75	0.01	0.01	101.66	grt	451.95
11-05	57 / 113 .	37.67	0.13	21.11	29.46	0.58	2.09	11.13	0.00	0.00	102.17	grt	456.02
11-05	57 / 114 .	37.42	0.22	20.85	29.09	0.58	2.04	11.18	0.04	0.00	101.43	grt	460.09
11-05	57 / 115 .	37.45	0.11	21.13	29.29	0.57	2.08	11.05	0.01	0.00	101.68	grt	464.16
11-05	57 / 116 .	~~42.55~~	~~0.31~~	~~21.73~~	~~20.47~~	~~0.45~~	~~1.61~~	~~9.68~~	~~0.03~~	~~0.00~~	96.83	grt+	468.24
11-05	57 / 117 .	37.70	0.12	20.96	28.80	0.60	2.08	11.30	0.01	0.00	101.56	grt	472.31
11-05	57 / 118 .	37.75	0.11	21.06	29.21	0.57	2.01	11.33	0.03	0.00	102.07	grt	476.38
11-05	57 / 119 .	37.88	0.09	21.09	29.08	0.56	2.01	11.07	0.03	0.01	101.82	grt	480.45
11-05	57 / 120 .	37.50	0.12	21.00	28.80	0.58	2.02	11.29	0.03	0.00	101.34	grt	484.52
11-05	57 / 121 .	37.64	0.13	20.97	28.73	0.59	1.96	11.55	0.03	0.00	101.58	grt	488.59
11-05	57 / 122 .	37.41	0.22	21.05	28.88	0.61	1.96	11.49	0.05	0.01	101.68	grt	492.67
11-05	57 / 123 .	37.57	0.14	21.17	29.17	0.60	1.95	11.63	0.02	0.00	102.24	grt	496.74
11-05	57 / 124 .	39.14	0.14	21.56	28.58	0.62	1.87	11.51	0.23	0.05	103.70	grt	500.81
11-05	57 / 125 .	37.79	0.12	21.12	28.81	0.56	1.85	11.58	0.00	0.00	101.82	grt	504.88
11-05	57 / 126 .	37.54	0.13	21.14	29.20	0.60	1.87	11.48	0.01	0.00	101.97	grt	508.95
11-05	57 / 127 .	37.57	0.10	21.21	28.96	0.59	1.90	11.47	0.02	0.00	101.82	grt	513.02
11-05	57 / 128 .	37.76	0.12	21.03	28.86	0.60	1.84	11.44	0.01	0.02	101.68	grt	517.1
11-05	57 / 129 .	37.76	0.13	20.91	28.79	0.53	1.81	11.41	0.04	0.01	101.38	grt	521.17
11-05	57 / 130 .	37.68	0.09	21.00	29.29	0.58	1.90	11.21	0.01	0.01	101.77	grt	525.24
11-05	57 / 131 .	37.54	0.09	21.13	28.88	0.62	1.84	11.52	0.02	0.01	101.66	grt	529.31
11-05	57 / 132 .	37.88	0.13	21.02	28.43	0.63	1.79	11.99	0.03	0.01	101.90	grt	533.38
11-05	57 / 134 .	98.77	0.00	0.30	0.87	0.01	0.03	0.16	0.00	0.01	100.15	qtz	541.53
11-05	57 / 135 .	100.46	0.00	0.05	0.74	0.02	0.01	0.05	0.00	0.00	101.33	qtz	545.6
11-05	57 / 136 .	100.29	0.01	0.06	0.74	0.01	0.00	0.08	0.00	0.01	101.19	qtz	549.67
11-05	57 / 137 .	100.23	0.00	0.07	0.79	0.02	0.01	0.08	0.00	0.01	101.21	qtz	553.74
11-05	57 / 138 .	97.47	0.00	1.14	1.60	0.03	0.10	0.62	0.00	0.01	100.97	qtz	557.81
11-05	57 / 139 .	~~81.17~~	~~0.01~~	~~9.65~~	~~11.87~~	~~0.28~~	~~0.67~~	~~4.95~~	~~0.00~~	~~0.00~~	108.58	?	561.88
11-05	57 / 140 .	37.59	0.06	21.00	29.24	0.70	1.81	11.26	0.00	0.00	101.64	grt	565.96
11-05	57 / 141 .	37.44	0.10	20.98	29.30	0.63	1.82	11.12	0.02	0.00	101.38	grt	570.03
11-05	57 / 142 .	37.61	0.09	21.01	29.62	0.67	1.79	10.95	0.00	0.00	101.73	grt	574.1
11-05	57 / 143 .	37.54	0.08	21.08	29.58	0.70	1.79	10.93	0.01	0.01	101.72	grt	578.17
11-05	57 / 144 .	37.44	0.12	20.60	29.22	0.73	2.24	10.91	0.00	0.02	101.27	grt	582.24
11-05	57 / 145 .	37.48	0.10	21.10	29.01	0.72	1.76	11.78	0.02	0.01	101.99	grt	586.31
11-05	57 / 146 .	37.54	0.12	21.10	29.25	0.72	1.73	11.49	0.02	0.01	101.99	grt	590.38
11-05	57 / 147 .	37.58	0.11	21.06	29.23	0.76	1.77	11.21	0.03	0.00	101.75	grt	594.46
11-05	57 / 148 .	37.63	0.13	21.04	29.07	0.76	1.66	11.63	0.02	0.00	101.94	grt	598.53
11-05	57 / 149 .	37.45	0.12	20.95	29.20	0.76	1.70	11.44	0.00	0.00	101.61	grt	602.6
11-05	57 / 150 .	37.51	0.11	20.99	29.10	0.79	1.67	11.53	0.00	0.00	101.70	grt	606.67
11-05	58 / 1 .	38.14	0.09	17.50	15.12	0.04	15.61	0.03	0.11	9.40	96.03	amph	
11-05	59 / 1 .	39.51	0.10	17.70	15.56	0.06	15.62	0.03	0.09	6.99	95.65	bt	
a03-16	1 / 1 .	55.92	0.03	10.05	5.33	0.01	8.36	13.84	7.15	0.01	100.70	prx	
a03-16	2 / 1 .	54.25	0.02	5.56	4.18	0.02	12.51	22.21	2.57	0.02	101.34	prx	
a03-16	3 / 1 .	56.18	0.05	9.29	2.30	0.02	11.04	17.30	5.34	0.01	101.52	prx	
a03-16	4 / 1 .	54.45	0.11	6.23	5.19	0.02	18.75	10.57	2.35	0.27	97.94	prx	
a03-16	5 / 1 .	54.96	0.22	24.95	1.19	0.03	5.73	0.04	0.13	8.96	96.20	mu	
a03-16	6 / 1 .	56.17	0.03	9.32	2.55	0.00	10.65	17.03	5.46	0.01	101.22	prx	
a03-16	7 / 1 .	54.91	0.21	25.18	1.13	0.02	5.74	0.03	0.13	9.13	96.48	mu	
a03-16	8 / 1 .	73.68	0.03	17.87	0.20	0.01	0.38	2.30	7.48	0.12	102.07	pl	
a03-16	9 / 1 .	60.32	0.04	3.94	2.53	0.02	10.41	17.46	2.10	0.01	96.83	amph	
a03-16	10 / 1 .	58.59	0.05	6.42	2.82	0.02	13.84	17.49	3.17	0.04	102.44	amph	
a03-16	11 / 1 .	96.33	0.00	0.21	0.38	0.00	2.22	3.48	0.03	0.00	102.66	qtz	

Eclogites

Sample	Spot	SiO2	TiO2	Al2O3	FeO	MnO	MgO	CaO	Na2O	K2O	Total	Min	distance
a03-16	12 / 1 .	100.41	0.00	0.01	0.00	0.00	0.00	0.01	0.00	0.01	100.44	qtz	
a03-16	13 / 1 .	55.40	0.05	7.18	7.67	0.03	9.26	15.80	5.87	0.00	101.27	amph	
a03-16	14 / 1 .	55.59	0.03	6.14	3.70	0.01	12.04	19.20	4.33	0.01	101.06	amph	
a03-16	15 / 1 .	56.23	0.06	9.37	2.49	0.03	10.35	16.82	5.59	0.01	100.93	amph	
a03-16	16 / 1 .	54.13	0.06	8.50	4.75	0.03	10.82	15.63	4.62	0.06	98.60	amph	
a03-16	17 / 1 .	55.44	0.02	7.43	3.32	0.01	11.73	20.16	3.27	0.00	101.38	amph	
a03-16	18 / 1 .	55.95	0.05	7.45	3.88	0.00	12.25	20.94	4.09	0.10	104.71	amph	
a03-16	19 / 1 .	38.61	0.03	21.93	24.68	0.30	9.44	5.84	0.02	0.02	100.88	grt	0
a03-16	19 / 2 .	37.28	0.04	21.29	29.89	1.12	5.33	5.72	0.01	0.04	100.72	grt	4.93
a03-16	19 / 3 .	35.64	0.10	17.16	17.11	0.05	14.03	0.50	0.27	6.69	91.55	grt	9.87
a03-16	19 / 4 .	36.52	0.11	15.24	16.46	0.03	15.82	0.55	0.22	5.30	90.24	grt	14.8
a03-16	19 / 5 .	36.38	0.12	15.53	16.36	0.09	15.63	0.55	0.20	5.53	90.38	grt	19.74
a03-16	19 / 6 .	36.60	0.13	16.20	16.74	0.08	15.50	0.59	0.25	5.79	91.89	grt	24.67
a03-16	19 / 7 .	36.77	0.16	15.58	16.81	0.03	15.30	0.53	0.26	6.05	91.49	grt	29.61
a03-16	19 / 8 .	35.87	0.14	17.40	17.38	0.02	14.70	0.38	0.45	7.31	93.65	grt	34.54
a03-16	19 / 9 .	35.25	0.14	17.95	17.52	0.04	14.48	0.22	0.55	7.98	94.12	grt	39.48
a03-16	19 / 10 .	30.72	0.10	17.98	16.46	0.23	0.66	1.01	0.00	5.56	72.71	grt	44.41
a03-16	19 / 11 .	35.22	0.13	20.61	25.24	0.79	6.65	8.70	0.04	0.12	97.49	grt	49.35
a03-16	19 / 12 .	37.64	0.09	21.30	27.21	0.90	5.03	9.36	0.03	0.03	101.58	grt	54.28
a03-16	19 / 13 .	37.63	0.09	21.35	27.84	0.97	4.63	9.46	0.02	0.01	102.00	grt	59.21
a03-16	19 / 14 .	37.73	0.08	21.34	27.92	1.00	4.41	9.37	0.02	0.01	101.89	grt	64.15
a03-16	19 / 15 .	37.81	0.11	21.20	27.98	0.93	4.51	9.34	0.03	0.01	101.92	grt	69.08
a03-16	19 / 16 .	37.84	0.09	21.31	27.85	0.89	4.70	9.24	0.01	0.00	101.92	grt	74.02
a03-16	19 / 17 .	37.85	0.06	21.37	27.64	0.96	4.90	9.10	0.03	0.00	101.92	grt	78.95
a03-16	19 / 18 .	38.20	0.09	21.61	26.76	0.80	5.71	8.67	0.00	0.00	101.83	grt	83.89
a03-16	19 / 19 .	38.01	0.06	21.45	26.90	0.92	5.75	8.76	0.00	0.01	101.86	grt	88.82
a03-16	19 / 20 .	37.93	0.04	21.59	27.15	0.83	5.54	8.74	0.02	0.00	101.85	grt	93.76
a03-16	19 / 21 .	38.36	0.09	21.61	25.83	0.71	6.22	9.01	0.01	0.00	101.83	grt	98.69
a03-16	19 / 22 .	38.40	0.12	21.47	24.58	0.49	7.09	9.14	0.03	0.00	101.33	grt	103.63
a03-16	19 / 23 .	38.32	0.06	21.60	25.87	0.58	6.53	8.90	0.03	0.00	101.88	grt	108.56
a03-16	19 / 24 .	38.07	0.04	21.40	26.04	0.68	5.80	9.56	0.01	0.02	101.63	grt	113.49
a03-16	19 / 25 .	37.47	0.06	21.01	29.44	0.87	3.56	9.77	0.00	0.01	102.19	grt	118.43
a03-16	19 / 26 .	37.27	0.10	20.80	29.90	0.84	2.88	9.88	0.01	0.00	101.67	grt	123.36
a03-16	19 / 27 .	37.30	0.08	20.84	30.53	0.87	2.62	9.88	0.01	0.00	102.13	grt	128.3
a03-16	19 / 28 .	37.14	0.11	20.49	30.54	0.91	2.40	10.01	0.00	0.01	101.61	grt	133.23
a03-16	19 / 29 .	36.85	0.12	20.64	30.53	0.81	2.34	10.24	0.02	0.00	101.55	grt	138.17
a03-16	19 / 30 .	37.04	0.09	20.79	30.41	0.88	2.42	10.19	0.02	0.00	101.84	grt	143.1
a03-16	19 / 31 .	37.24	0.12	20.78	29.58	0.88	2.53	10.54	0.00	0.00	101.67	grt	148.04
a03-16	19 / 32 .	37.43	0.12	20.85	29.09	0.77	3.04	10.61	0.00	0.01	101.93	grt	152.97
a03-16	19 / 33 .	37.87	0.07	21.33	26.75	0.69	4.98	10.01	0.00	0.00	101.70	grt	157.91
a03-16	19 / 34 .	38.69	0.04	21.89	25.42	0.40	8.46	6.62	0.00	0.01	101.54	grt	162.84
a03-16	19 / 35 .	38.51	0.03	22.03	24.63	0.46	8.09	8.07	0.03	0.01	101.87	grt	167.78
a03-16	19 / 36 .	35.52	0.90	20.76	11.11	0.02	15.64	3.60	1.52	0.64	89.71	grt	172.71
a03-16	19 / 37 .	39.63	0.47	17.82	14.99	0.06	10.41	11.00	3.61	0.10	98.10	grt	177.64
a03-16	19 / 38 .	38.73	0.50	18.23	14.75	0.07	10.64	10.76	3.73	0.11	97.50	grt	182.58
a03-16	19 / 39 .	37.80	0.09	20.89	25.72	0.84	5.34	10.26	0.23	0.06	101.23	grt	187.51
a03-16	19 / 40 .	37.27	0.12	20.86	27.14	0.83	3.38	11.13	0.01	0.00	100.73	grt	192.45
a03-16	19 / 41 .	37.47	0.15	21.07	27.70	0.77	3.16	11.56	0.02	0.00	101.89	grt	197.38
a03-16	19 / 42 .	37.49	0.17	20.89	27.63	0.82	3.13	11.81	0.02	0.02	101.97	grt	202.32
a03-16	19 / 43 .	37.56	0.17	21.10	27.43	0.82	3.14	11.78	0.02	0.00	102.02	grt	207.25
a03-16	19 / 44 .	37.42	0.20	20.82	27.74	0.83	3.22	11.69	0.03	0.02	101.97	grt	212.19
a03-16	19 / 45 .	37.14	0.15	20.87	27.30	1.01	3.05	11.25	0.00	0.00	100.77	grt	217.12
a03-16	19 / 46 .	37.45	0.16	21.09	27.36	0.88	3.26	11.54	0.02	0.00	101.76	grt	222.06
a03-16	19 / 47 .	37.41	0.17	20.90	27.45	0.84	3.19	11.50	0.02	0.00	101.48	grt	226.99
a03-16	19 / 48 .	37.62	0.17	21.02	27.30	0.90	3.51	11.42	0.00	0.00	101.94	grt	231.93
a03-16	19 / 49 .	37.81	0.18	21.25	26.30	0.81	4.07	11.79	0.02	0.00	102.24	grt	236.86
a03-16	19 / 50 .	38.06	0.19	21.41	24.45	0.69	5.36	11.72	0.03	0.01	101.90	grt	241.79
a03-16	19 / 51 .	38.40	0.06	21.95	24.32	0.56	7.82	9.00	0.02	0.00	102.12	grt	246.73
a03-16	19 / 52 .	38.62	0.04	21.94	24.35	0.43	8.55	7.73	0.02	0.00	101.67	grt	251.66
a03-16	19 / 53 .	38.32	0.04	21.93	24.25	0.50	8.33	7.99	0.02	0.00	101.38	grt	256.6
a03-16	19 / 54 .	38.60	0.03	21.88	24.53	0.51	8.33	7.74	0.02	0.00	101.63	grt	261.53
a03-16	19 / 55 .	38.38	0.14	21.39	23.07	0.65	6.93	10.79	0.04	0.00	101.39	grt	266.47
a03-16	19 / 56 .	38.12	0.22	21.27	23.41	0.86	5.53	12.30	0.02	0.00	101.74	grt	271.4
a03-16	19 / 57 .	38.09	0.18	21.30	23.67	0.93	5.47	11.90	0.01	0.00	101.56	grt	276.34
a03-16	19 / 58 .	38.12	0.19	21.31	23.81	0.95	5.51	11.72	0.01	0.00	101.61	grt	281.27
a03-16	19 / 59 .	38.27	0.15	21.43	23.86	1.03	5.85	11.49	0.01	0.00	102.10	grt	286.2
a03-16	19 / 60 .	38.19	0.15	21.57	23.80	1.06	6.12	10.98	0.02	0.00	101.90	grt	291.14
a03-16	19 / 61 .	38.32	0.17	21.52	23.45	1.11	6.19	10.82	0.01	0.00	101.58	grt	296.07
a03-16	19 / 62 .	38.20	0.16	21.59	23.27	1.16	6.05	11.13	0.02	0.01	101.58	grt	301.01
a03-16	19 / 63 .	38.32	0.19	21.40	23.73	1.24	6.12	10.90	0.02	0.00	101.90	grt	305.94
a03-16	19 / 64 .	38.10	0.18	21.38	23.49	1.36	6.15	10.82	0.02	0.00	101.51	grt	310.88

Eclogites

Sample	Spot	SiO2	TiO2	Al2O3	FeO	MnO	MgO	CaO	Na2O	K2O	Total	Min	distance
a03-16	19 / 65 .	38.09	0.21	21.40	23.38	1.46	6.08	10.97	0.02	0.02	101.62	grt	315.81
a03-16	19 / 66 .	38.17	0.16	21.54	23.16	1.54	6.37	10.62	0.01	0.00	101.57	grt	320.75
a03-16	19 / 67 .	38.27	0.16	21.56	23.16	1.61	6.40	10.52	0.01	0.00	101.67	grt	325.68
a03-16	19 / 68 .	38.31	0.10	21.63	23.27	1.51	7.10	9.73	0.03	0.00	101.66	grt	330.62
a03-16	19 / 69 .	38.50	0.19	21.61	22.21	1.34	7.26	10.50	0.05	0.01	101.66	grt	335.55
a03-16	19 / 70 .	38.45	0.15	21.61	22.92	1.09	7.38	9.85	0.04	0.00	101.49	grt	340.48
a03-16	19 / 71 .	38.55	0.06	21.82	23.44	1.40	7.85	8.75	0.02	0.00	101.90	grt	345.42
a03-16	19 / 72 .	38.44	0.14	21.68	22.48	1.76	7.28	9.80	0.03	0.01	101.61	grt	350.35
a03-16	19 / 73 .	38.42	0.13	21.61	22.34	2.03	6.97	9.86	0.03	0.00	101.38	grt	355.29
a03-16	19 / 74 .	38.43	0.21	21.53	22.06	1.89	6.88	10.51	0.04	0.00	101.56	grt	360.22
a03-16	19 / 75 .	38.37	0.20	21.48	22.03	2.24	6.71	10.54	0.01	0.00	101.58	grt	365.16
a03-16	19 / 76 .	38.28	0.20	21.47	21.78	2.48	6.70	10.57	0.00	0.00	101.49	grt	370.09
a03-16	19 / 77 .	38.42	0.15	21.67	21.89	2.27	7.02	10.16	0.02	0.00	101.60	grt	375.03
a03-16	19 / 78 .	38.54	0.18	21.66	21.75	2.04	7.29	10.39	0.03	0.00	101.87	grt	379.96
a03-16	19 / 79 .	38.42	0.16	21.79	21.73	1.70	7.69	9.91	0.03	0.00	101.43	grt	384.9
a03-16	19 / 80 .	38.69	0.18	21.87	22.11	1.51	7.83	9.46	0.03	0.00	101.69	grt	389.83
a03-16	19 / 81 .	38.76	0.18	21.72	21.34	1.67	7.73	10.37	0.04	0.00	101.80	grt	394.77
a03-16	19 / 82 .	38.61	0.12	21.79	22.34	1.38	8.07	9.48	0.04	0.00	101.84	grt	399.7
a03-16	19 / 83 .	38.61	0.15	21.80	22.08	1.23	7.81	9.82	0.03	0.00	101.51	grt	404.63
a03-16	19 / 84 .	38.70	0.13	21.67	22.42	1.25	7.79	9.85	0.02	0.01	101.83	grt	409.57
a03-16	19 / 85 .	38.76	0.15	21.77	22.76	1.03	7.66	9.54	0.04	0.00	101.72	grt	414.5
a03-16	19 / 86 .	41.76	0.13	19.61	20.35	0.82	7.57	10.98	1.23	0.00	102.45	grt	419.44
a03-16	19 / 87 .	39.32	0.12	21.36	22.68	0.87	7.91	9.67	0.48	0.01	102.42	grt	424.37
a03-16	19 / 88 .	~~51.59~~	~~0.05~~	~~10.86~~	~~6.09~~	~~0.13~~	~~9.01~~	~~14.80~~	~~6.06~~	~~0.00~~	98.60	grt+	429.31
a03-16	19 / 89 .	38.68	0.19	21.66	22.58	0.83	8.02	9.59	0.06	0.00	101.61	grt	434.24
a03-16	19 / 90 .	38.83	0.14	21.78	22.69	0.70	7.93	9.64	0.04	0.01	101.76	grt	439.18
a03-16	19 / 91 .	38.51	0.13	21.73	21.55	1.83	7.96	9.63	0.02	0.00	101.37	grt	444.11
a03-16	19 / 92 .	38.56	0.21	21.72	20.89	2.04	7.56	10.44	0.03	0.00	101.46	grt	449.05
a03-16	19 / 93 .	38.39	0.18	21.61	21.01	1.99	7.45	10.69	0.01	0.00	101.34	grt	453.98
a03-16	19 / 94 .	38.56	0.20	21.70	22.03	1.37	7.62	10.46	0.04	0.00	101.98	grt	458.91
a03-16	19 / 95 .	38.38	0.18	22.04	21.06	1.74	7.46	9.87	0.04	0.05	100.82	grt	463.85
a03-16	19 / 96 .	38.75	0.17	21.73	21.69	1.38	7.97	9.96	0.04	0.00	101.69	grt	468.78
a03-16	19 / 97 .	38.77	0.07	22.00	22.42	1.53	8.46	8.73	0.01	0.00	102.01	grt	473.72
a03-16	19 / 98 .	38.84	0.17	21.89	21.48	1.55	7.76	10.48	0.01	0.00	102.17	grt	478.65
a03-16	19 / 99 .	38.82	0.02	22.19	22.09	0.79	8.39	9.55	0.00	0.00	101.86	grt	483.59
a03-16	19 / 100 .	38.73	0.07	22.06	22.09	1.22	8.38	9.18	0.01	0.00	101.73	grt	488.52
a03-16	19 / 101 .	38.87	0.17	21.64	21.27	1.62	7.65	10.41	0.01	0.00	101.65	grt	493.46
a03-16	19 / 102 .	38.66	0.18	21.80	21.08	2.00	7.47	10.52	0.03	0.01	101.74	grt	498.39
a03-16	19 / 103 .	38.61	0.19	21.67	21.54	1.72	7.63	10.06	0.03	0.00	101.44	grt	503.33
a03-16	19 / 104 .	38.58	0.17	21.80	21.91	1.35	7.87	9.93	0.03	0.00	101.64	grt	508.26
a03-16	19 / 105 .	38.66	0.16	21.75	21.62	1.90	7.95	9.71	0.01	0.00	101.76	grt	513.19
a03-16	19 / 106 .	38.67	0.19	21.80	21.26	1.94	7.35	10.41	0.04	0.00	101.66	grt	518.13
a03-16	19 / 107 .	38.69	0.21	21.62	21.61	1.59	7.23	10.73	0.03	0.00	101.71	grt	523.06
a03-16	19 / 108 .	38.65	0.20	21.70	21.79	1.55	7.35	10.53	0.04	0.00	101.80	grt	528
a03-16	19 / 109 .	38.36	0.15	21.54	22.86	0.96	7.61	10.02	0.04	0.01	101.54	grt	532.93
a03-16	19 / 110 .	38.39	0.11	21.71	23.58	0.77	7.11	9.81	0.03	0.02	101.53	grt	537.87
a03-16	19 / 111 .	40.06	0.07	22.20	23.49	0.74	7.83	8.91	0.06	0.00	103.36	grt	542.8
a03-16	19 / 112 .	38.89	0.12	21.87	22.19	1.18	8.37	9.07	0.02	0.01	101.72	grt	547.74
a03-16	19 / 113 .	38.59	0.18	21.73	21.74	0.99	7.84	10.37	0.03	0.00	101.47	grt	552.67
a03-16	19 / 114 .	38.90	0.23	21.63	21.67	1.25	7.73	10.55	0.03	0.00	102.00	grt	557.61
a03-16	19 / 115 .	38.41	0.18	21.67	21.28	1.92	7.52	10.32	0.01	0.00	101.30	grt	562.54
a03-16	19 / 116 .	38.60	0.08	21.97	22.37	0.94	7.87	10.01	0.05	0.00	101.89	grt	567.48
a03-16	19 / 117 .	38.58	0.05	22.01	24.53	0.52	8.84	6.68	0.03	0.00	101.25	grt	572.41
a03-16	19 / 118 .	38.89	0.02	22.09	24.69	0.35	11.15	5.07	0.00	0.01	102.25	grt	577.34
a03-16	19 / 119 .	39.23	0.03	22.21	23.21	0.32	9.52	7.33	0.02	0.00	101.87	grt	582.28
a03-16	19 / 120 .	38.32	0.10	22.48	23.73	0.76	8.64	8.16	0.01	0.01	102.21	grt	587.21
a03-16	19 / 121 .	38.43	0.23	21.70	21.56	2.12	6.92	10.72	0.00	0.01	101.71	grt	592.15
a03-16	19 / 122 .	38.29	0.24	21.76	22.16	1.21	6.99	11.05	0.03	0.01	101.75	grt	597.08
a03-16	19 / 123 .	38.49	0.17	22.04	23.15	1.11	7.36	9.44	0.03	0.01	101.81	grt	602.02
a03-16	19 / 124 .	39.85	0.59	20.20	11.12	0.16	10.71	10.22	3.51	0.18	96.52	grt	606.95
a03-16	19 / 125 .	40.52	0.73	20.26	10.23	0.14	11.52	9.28	3.33	1.19	97.20	grt	611.89
a03-16	19 / 126 .	38.02	0.24	21.52	22.64	2.59	5.91	10.61	0.03	0.00	101.56	grt	616.82
a03-16	19 / 127 .	38.20	0.20	21.73	22.27	2.66	5.97	10.69	0.02	0.00	101.75	grt	621.76
a03-16	19 / 128 .	38.10	0.21	21.42	22.29	3.08	5.75	10.49	0.01	0.01	101.36	grt	626.69
a03-16	19 / 129 .	37.85	0.21	21.46	22.49	3.20	5.56	10.58	0.01	0.01	101.38	grt	631.62
a03-16	19 / 130 .	38.02	0.21	21.42	22.73	3.21	5.47	10.52	0.01	0.00	101.58	grt	636.56
a03-16	19 / 131 .	38.17	0.19	21.59	22.38	2.83	5.78	10.46	0.04	0.00	101.44	grt	641.49
a03-16	19 / 132 .	38.18	0.21	21.51	22.48	2.55	5.84	10.66	0.02	0.01	101.47	grt	646.43
a03-16	19 / 133 .	38.18	0.21	21.61	22.33	1.85	6.51	10.53	0.04	0.01	101.26	grt	651.36
a03-16	19 / 134 .	38.32	0.12	21.69	23.04	1.61	7.12	9.40	0.03	0.00	101.34	grt	656.3
a03-16	19 / 135 .	38.45	0.17	21.93	22.13	1.57	7.40	9.91	0.04	0.01	101.62	grt	661.23

Eclogites

Sample	Spot	SiO2	TiO2	Al2O3	FeO	MnO	MgO	CaO	Na2O	K2O	Total	Min	distance
a03-16	19 / 136 .	38.42	0.17	21.71	22.65	1.72	6.74	10.17	0.03	0.00	101.62	grt	666.17
a03-16	19 / 137 .	38.09	0.22	21.60	22.59	2.47	6.05	10.76	0.03	0.01	101.83	grt	671.1
a03-16	19 / 138 .	37.43	0.22	21.05	22.63	2.45	5.84	10.16	0.04	0.00	99.81	grt	676.04
a03-16	19 / 139 .	38.36	0.18	21.50	22.84	2.63	5.95	10.10	0.15	0.01	101.72	grt	680.97
a03-16	19 / 140 .	38.29	0.19	21.48	22.33	2.90	5.46	10.13	0.16	0.00	100.92	grt	685.9
a03-16	19 / 141 .	37.87	0.23	21.65	23.51	1.61	6.14	10.64	0.04	0.01	101.70	grt	690.84
a03-16	19 / 142 .	38.32	0.04	21.86	23.53	1.41	7.14	9.15	0.00	0.01	101.47	grt	695.77
a03-16	19 / 143 .	38.46	0.08	21.91	23.99	1.11	7.32	8.92	0.02	0.01	101.82	grt	700.71
a03-16	19 / 144 .	38.31	0.15	21.71	23.61	1.08	6.73	9.87	0.02	0.00	101.49	grt	705.64
a03-16	19 / 145 .	63.62	0.01	22.55	4.77	0.11	1.07	2.64	9.57	0.06	104.40	pl	710.58
a03-16	19 / 146 .	66.41	0.01	16.79	0.70	0.04	0.00	2.04	8.57	0.03	94.59	pl	715.51
a03-16	19 / 147 .	38.32	0.18	21.57	23.78	1.10	6.25	10.39	0.07	0.00	101.67	grt	720.45
a03-16	19 / 148 .	38.43	0.03	21.93	23.76	1.09	7.55	8.99	0.01	0.00	101.79	grt	725.38
a03-16	19 / 149 .	38.67	0.01	22.01	23.20	1.04	7.94	8.72	0.01	0.01	101.62	grt	730.32
a03-16	19 / 150 .	38.45	0.02	22.15	23.39	0.97	7.62	8.93	0.01	0.00	101.55	grt	735.25
05-04D	42 / 1 .	0.10	0.00	0.04	4.52	0.10	16.90	29.29	0.02	0.00	50.95	dolomite	
05-04D	44 / 1 .	0.01	0.00	0.00	9.80	0.10	42.07	0.53	0.01	0.00	52.52	magnesite	
05-04D	45 / 1 .	0.05	0.00	0.01	0.38	0.02	1.33	64.32	0.02	0.01	66.12	calcite	
05-04D	43 / 1 .	0.09	0.00	0.02	1.22	0.33	1.66	63.31	0.01	0.00	66.65	calcite	
05-04D	36 / 1 .	~~79.34~~	~~0.01~~	~~2.78~~	~~0.72~~	~~0.02~~	~~2.33~~	~~3.44~~	~~3.19~~	~~0.02~~	91.86	mix	
05-04D	47 / 1 .	~~61.96~~	~~0.01~~	~~0.83~~	~~3.09~~	~~0.00~~	~~27.15~~	~~0.02~~	~~0.11~~	~~0.00~~	93.19	talc	
05-04D	40 / 1 .	~~60.12~~	~~0.07~~	~~17.92~~	~~4.16~~	~~0.02~~	~~3.90~~	~~2.31~~	~~4.67~~	~~0.04~~	93.21	fsp	
05-04D	12 / 90 .	~~61.57~~	~~0.05~~	~~15.70~~	~~3.96~~	~~0.01~~	~~5.43~~	~~4.26~~	~~3.95~~	~~0.00~~	94.93	fsp	
05-04D	9 / 18 .	46.16	0.16	11.71	13.32	0.14	11.40	7.42	4.62	0.08	95.01	amph zone	60.87
05-04D	41 / 1 .	61.25	0.04	16.20	2.98	0.06	5.83	3.76	4.92	0.03	95.08	fsp	
05-04D	9 / 14 .	37.28	0.05	19.34	19.33	0.21	5.77	8.52	4.78	0.02	95.29	amph zone	46.55
05-04D	13 / 1 .	37.80	0.03	20.25	14.95	0.27	7.65	10.34	4.02	0.01	95.32	amph zone	
05-04D	9 / 6 .	38.29	0.04	18.93	20.47	0.21	4.93	8.12	4.40	0.02	95.40	amph	17.9
05-04D	12 / 69 .	61.29	0.01	14.81	2.33	0.01	3.57	7.66	5.79	0.02	95.49	fsp	
05-04D	9 / 15 .	37.67	0.05	18.80	19.61	0.21	5.50	9.13	4.48	0.03	95.49	amph zone	50.13
05-04D	12 / 92 .	~~64.39~~	~~0.01~~	~~18.46~~	~~1.77~~	~~0.00~~	~~1.92~~	~~2.67~~	~~6.09~~	~~0.23~~	95.53	fsp+	
05-04D	9 / 9 .	37.76	0.04	19.11	19.94	0.25	5.25	8.26	4.94	0.02	95.56	amph zone	28.65
05-04D	30 / 1 .	50.21	0.10	13.78	10.62	0.06	9.20	8.30	3.36	0.01	95.64	amph sym	
05-04D	8 / 1 .	38.49	0.03	20.70	13.63	0.10	8.31	10.52	4.01	0.02	95.81	amph grt r	
05-04D	17 / 1 .	39.39	0.12	18.78	14.62	0.14	8.25	10.29	4.19	0.04	95.82	amph zone	
05-04D	9 / 76 .	45.70	0.09	11.44	14.78	0.16	10.83	8.74	4.09	0.02	95.85	amph zone	268.56
05-04D	3 / 1 .	52.71	0.13	9.86	9.32	0.06	13.96	5.53	4.28	0.04	95.88	amph grt r	
05-04D	9 / 13 .	38.11	0.05	19.25	19.60	0.22	5.48	8.43	4.75	0.01	95.91	amph zone	42.97
05-04D	9 / 28 .	52.79	0.26	8.55	7.74	0.07	15.05	7.54	3.88	0.04	95.91	amph grt r	96.68
05-04D	25 / 1 .	~~60.25~~	~~0.00~~	~~17.73~~	~~1.08~~	~~0.00~~	~~3.21~~	~~6.67~~	~~6.94~~	~~0.02~~	95.91	fsp+	
05-04D	12 / 73 .	53.84	0.04	9.81	3.92	0.00	10.11	13.26	4.93	0.02	95.93	amph sym	
05-04D	9 / 75 .	44.23	0.10	12.93	15.44	0.16	10.04	8.93	4.15	0.04	96.02	amph zone	264.98
05-04D	9 / 38 .	50.38	0.18	10.27	12.29	0.13	11.23	7.81	3.76	0.06	96.12	amph zone	132.49
05-04D	9 / 78 .	45.02	0.06	12.27	15.38	0.16	10.15	9.02	4.02	0.06	96.14	amph zone	275.72
05-04D	9 / 17 .	39.16	0.06	18.94	16.10	0.15	7.55	9.88	4.32	0.04	96.19	amph zone	57.29
05-04D	1 / 1 .	49.77	0.14	12.27	11.20	0.08	13.81	4.39	4.52	0.04	96.21	amph grt r	
05-04D	9 / 88 .	38.35	0.05	19.09	18.02	0.18	6.63	9.52	4.35	0.02	96.22	amph zone	311.53
05-04D	9 / 37 .	51.12	0.28	8.49	10.71	0.13	13.68	8.11	3.63	0.07	96.23	amph zone	128.91
05-04D	9 / 64 .	47.39	0.17	10.03	12.73	0.11	12.67	9.61	3.53	0.01	96.25	amph zone	225.59
05-04D	9 / 74 .	49.39	0.10	9.18	13.17	0.14	12.27	8.10	3.85	0.04	96.25	amph zone	261.4
05-04D	9 / 57 .	52.03	0.26	8.79	8.91	0.15	14.33	7.87	3.87	0.07	96.26	amph zone	200.52
05-04D	9 / 16 .	38.61	0.07	19.46	16.53	0.18	7.27	9.69	4.42	0.04	96.26	amph zone	53.71
05-04D	9 / 63 .	49.91	0.14	9.65	12.14	0.16	12.43	7.59	4.20	0.05	96.27	amph zone	222.01
05-04D	9 / 79 .	42.84	0.07	14.39	16.20	0.15	8.97	9.32	4.27	0.05	96.27	amph zone	279.3
05-04D	12 / 7 .	45.95	0.12	11.61	11.75	0.10	12.54	10.67	3.55	0.00	96.28	amph sym	
05-04D	9 / 36 .	51.59	0.21	8.97	10.89	0.15	12.86	7.87	3.75	0.05	96.33	amph zone	125.33
05-04D	9 / 33 .	52.41	0.19	9.32	8.99	0.12	14.27	6.92	4.06	0.06	96.34	amph zone	114.58
05-04D	15 / 1 .	42.62	0.09	15.27	14.37	0.11	9.75	10.13	3.93	0.07	96.36	amph grt r	
05-04D	9 / 19 .	51.41	0.27	9.86	10.60	0.12	12.56	7.47	4.01	0.05	96.36	amph zone	64.45
05-04D	14 / 1 .	40.43	0.06	17.90	13.73	0.20	9.40	10.50	4.11	0.04	96.36	amph grt r	
05-04D	9 / 65 .	46.98	0.12	10.95	13.18	0.13	11.93	9.51	3.54	0.02	96.36	amph zone	229.17
05-04D	9 / 22 .	50.92	0.25	9.21	10.85	0.15	13.04	8.03	3.85	0.07	96.39	amph zone	75.2
05-04D	9 / 56 .	52.11	0.11	5.53	10.06	0.13	15.82	10.03	2.53	0.07	96.39	amph zone	196.94
05-04D	9 / 25 .	52.94	0.26	8.76	7.60	0.07	15.25	7.74	3.72	0.06	96.40	amph zone	85.94
05-04D	9 / 87 .	38.92	0.05	18.98	17.43	0.17	6.61	9.94	4.28	0.03	96.41	amph zone	307.95
05-04D	9 / 43 .	52.34	0.22	9.39	8.57	0.13	14.29	7.22	4.19	0.06	96.41	amph zone	150.39
05-04D	9 / 62 .	49.66	0.09	10.29	12.31	0.16	11.96	7.82	4.12	0.00	96.42	amph zone	218.43
05-04D	9 / 53 .	51.75	0.24	9.30	9.39	0.11	13.99	7.59	4.03	0.05	96.45	amph zone	186.2
05-04D	9 / 54 .	51.13	0.19	9.66	10.37	0.15	13.29	7.54	4.09	0.03	96.45	amph zone	189.78
05-04D	9 / 29 .	52.49	0.25	8.87	8.54	0.10	14.57	7.87	3.77	0.04	96.50	amph zone	100.26

Eclogites

Sample	Spot	SiO2	TiO2	Al2O3	FeO	MnO	MgO	CaO	Na2O	K2O	Total	Min	distance
05-04D	9 / 80 .	41.06	0.08	15.54	17.23	0.15	8.36	9.69	4.36	0.04	96.51	amph zone	282.88
05-04D	9 / 68 .	50.51	0.10	9.35	12.10	0.16	12.45	7.93	3.87	0.04	96.51	amph zone	239.91
05-04D	7 / 1 .	39.43	0.03	19.26	16.41	0.10	7.09	9.66	4.48	0.04	96.51	amph zone	
05-04D	9 / 66 .	47.11	0.12	11.59	13.19	0.13	11.62	8.98	3.77	0.01	96.53	amph zone	232.75
05-04D	9 / 42 .	52.73	0.27	9.36	7.71	0.14	15.02	7.16	4.09	0.06	96.54	amph zone	146.81
05-04D	9 / 82 .	47.13	0.06	11.88	14.40	0.15	10.60	8.23	4.03	0.06	96.54	amph zone	290.04
05-04D	9 / 59 .	51.71	0.18	9.51	10.37	0.12	13.05	7.29	4.27	0.06	96.56	amph zone	207.68
05-04D	18 / 1 .	46.83	0.26	11.21	12.31	0.11	12.45	9.77	3.60	0.02	96.56	amph zone	
05-04D	16 / 1 .	41.62	0.13	17.07	13.18	0.12	9.95	10.44	4.01	0.03	96.56	amph grt r	
05-04D	9 / 55 .	49.26	0.12	9.77	12.12	0.18	12.67	8.58	3.84	0.02	96.56	amph zone	193.36
05-04D	6 / 1 .	45.88	0.09	13.23	14.45	0.10	10.22	8.45	4.07	0.08	96.57	amph zone	
05-04D	9 / 20 .	50.90	0.26	9.97	11.45	0.13	12.36	7.28	4.18	0.05	96.57	amph zone	68.04
05-04D	9 / 73 .	50.38	0.13	8.80	12.60	0.16	12.67	8.18	3.64	0.04	96.58	amph zone	257.82
05-04D	9 / 60 .	51.89	0.16	9.65	10.16	0.12	12.97	7.55	4.04	0.05	96.59	amph zone	211.27
05-04D	9 / 34 .	51.86	0.22	9.31	8.71	0.16	14.53	7.68	4.08	0.06	96.60	amph zone	118.17
05-04D	9 / 26 .	53.13	0.25	8.65	7.54	0.08	15.40	7.65	3.84	0.06	96.60	amph zone	89.52
05-04D	2 / 1 .	55.87	0.06	11.87	7.47	0.03	12.63	2.66	6.04	0.01	96.64	amph grt r	
05-04D	9 / 31 .	52.60	0.26	8.57	7.82	0.08	15.42	8.06	3.79	0.04	96.64	amph zone	107.42
05-04D	9 / 84 .	41.37	0.07	16.83	16.33	0.15	7.73	9.89	4.22	0.04	96.64	amph zone	297.2
05-04D	9 / 85 .	40.60	0.06	17.46	17.00	0.15	7.26	9.76	4.30	0.04	96.65	amph zone	300.79
05-04D	9 / 70 .	51.42	0.15	8.86	11.39	0.14	12.99	7.95	3.71	0.06	96.67	amph zone	247.07
05-04D	9 / 69 .	48.15	0.15	10.58	13.04	0.14	12.16	8.55	3.87	0.03	96.67	amph zone	243.49
05-04D	9 / 77 .	42.89	0.09	14.03	16.52	0.18	9.12	9.70	4.13	0.01	96.67	amph zone	272.14
05-04D	9 / 71 .	50.82	0.18	8.64	11.90	0.12	13.01	8.19	3.76	0.07	96.68	amph zone	250.65
05-04D	9 / 47 .	52.03	0.22	9.51	8.39	0.13	14.56	7.73	4.08	0.03	96.68	amph zone	164.72
05-04D	9 / 48 .	51.71	0.24	9.51	8.66	0.13	14.58	7.80	4.04	0.08	96.76	amph zone	168.3
05-04D	9 / 21 .	51.53	0.28	9.44	9.76	0.13	13.91	7.80	3.88	0.06	96.78	amph zone	71.62
05-04D	12 / 13 .	~~65.03~~	~~0.01~~	~~17.43~~	~~1.09~~	~~0.00~~	~~2.14~~	~~3.72~~	~~7.36~~	~~0.02~~	96.78	fsp+	
05-04D	9 / 52 .	52.06	0.23	9.77	8.46	0.12	14.24	7.54	4.33	0.06	96.80	amph zone	182.62
05-04D	9 / 35 .	52.73	0.26	8.22	9.11	0.12	14.96	7.60	3.75	0.06	96.80	amph zone	121.75
05-04D	9 / 46 .	52.66	0.23	9.46	7.32	0.10	15.23	7.42	4.34	0.06	96.81	amph zone	161.13
05-04D	9 / 83 .	41.81	0.09	16.79	16.12	0.16	8.00	9.55	4.21	0.09	96.82	amph zone	293.62
05-04D	9 / 41 .	52.52	0.25	8.85	7.87	0.11	15.35	8.07	3.75	0.06	96.82	amph zone	143.23
05-04D	9 / 86 .	39.73	0.05	18.44	17.50	0.11	6.76	9.86	4.37	0.04	96.86	amph zone	304.37
05-04D	9 / 51 .	52.39	0.23	9.65	7.37	0.10	15.20	7.62	4.24	0.06	96.87	amph zone	179.04
05-04D	9 / 44 .	51.87	0.19	8.89	9.89	0.13	14.26	7.60	4.00	0.04	96.87	amph zone	153.97
05-04D	9 / 81 .	45.74	0.06	12.70	15.23	0.13	10.12	8.61	4.24	0.07	96.91	amph zone	286.46
05-04D	9 / 27 .	53.13	0.28	8.75	7.96	0.10	15.00	7.61	4.04	0.05	96.92	amph zone	93.1
05-04D	9 / 49 .	51.81	0.24	9.76	8.09	0.10	14.84	7.89	4.18	0.05	96.95	amph zone	171.88
05-04D	9 / 24 .	53.03	0.26	8.53	7.42	0.10	15.75	8.04	3.78	0.05	96.95	amph zone	82.36
05-04D	12 / 48 .	48.82	0.10	8.76	9.39	0.12	15.37	11.81	2.58	0.01	96.98	amph zone	
05-04D	9 / 45 .	52.30	0.26	9.66	7.91	0.11	14.93	7.39	4.40	0.05	97.00	amph zone	157.55
05-04D	9 / 72 .	50.24	0.14	9.04	12.45	0.15	12.73	8.62	3.57	0.06	97.00	amph zone	254.23
05-04D	9 / 58 .	52.11	0.16	8.88	11.01	0.13	13.24	7.23	4.20	0.05	97.02	amph zone	204.1
05-04D	9 / 32 .	52.43	0.28	8.77	7.77	0.10	15.48	8.20	3.95	0.05	97.02	amph zone	111
05-04D	9 / 40 .	52.00	0.12	5.99	10.43	0.13	15.94	9.61	2.75	0.05	97.02	amph zone	139.65
05-04D	9 / 89 .	38.70	0.04	18.49	18.33	0.14	7.13	9.44	4.73	0.03	97.03	amph zone	315.11
05-04D	38 / 1 .	53.74	0.08	3.39	7.29	0.08	18.48	12.61	1.35	0.02	97.05	amph zone	
05-04D	9 / 23 .	52.90	0.24	8.81	8.18	0.11	15.09	7.74	3.92	0.06	97.07	amph zone	78.78
05-04D	9 / 67 .	47.28	0.12	12.53	13.48	0.15	10.71	8.78	4.01	0.07	97.13	amph zone	236.33
05-04D	12 / 94 .	65.36	0.02	18.53	0.93	0.01	1.53	3.17	7.58	0.01	97.14	fsp	
05-04D	12 / 37 .	48.60	0.16	9.17	9.60	0.14	15.01	11.80	2.64	0.02	97.14	amph sym	
05-04D	9 / 12 .	38.30	0.05	19.87	19.52	0.24	6.48	8.12	4.56	0.04	97.17	amph zone	39.39
05-04D	9 / 50 .	52.53	0.25	9.66	7.50	0.09	15.12	7.89	4.09	0.05	97.17	amph zone	175.46
05-04D	12 / 58 .	48.80	0.11	9.30	9.46	0.10	14.76	11.87	2.78	0.01	97.19	amph zone	
05-04D	28 / 1 .	41.78	0.06	16.92	13.77	0.07	9.47	11.21	3.88	0.03	97.21	amph zone	
05-04D	19 / 1 .	51.53	0.12	5.84	9.09	0.07	16.48	12.13	1.96	0.00	97.23	amph zone	
05-04D	11 / 1 .	48.33	0.14	9.91	9.54	0.11	14.78	11.66	2.80	0.00	97.26	amph zone	
05-04D	9 / 30 .	52.15	0.22	9.01	9.16	0.08	14.79	7.79	4.02	0.06	97.28	amph zone	103.84
05-04D	12 / 47 .	51.34	0.13	9.13	7.49	0.10	14.31	12.10	2.73	0.00	97.32	amph zone	
05-04D	12 / 38 .	52.43	0.13	6.79	8.59	0.09	15.05	11.94	2.38	0.00	97.39	amph zone	
05-04D	12 / 30 .	64.79	0.00	19.67	0.40	0.00	0.40	2.58	9.57	0.00	97.41	fsp	
05-04D	9 / 61 .	47.94	0.14	12.15	12.85	0.16	11.55	8.41	4.20	0.03	97.43	amph zone	214.85
05-04D	9 / 90 .	39.99	0.03	19.58	18.10	0.18	5.97	9.30	4.25	0.05	97.46	amph zone	318.69
05-04D	12 / 95 .	70.12	0.00	20.18	0.36	0.02	0.14	0.55	6.09	0.00	97.46	fsp	
05-04D	12 / 40 .	65.82	0.01	19.68	0.28	0.00	0.33	1.55	9.80	0.00	97.47	fsp	
05-04D	9 / 39 .	48.47	0.12	11.60	14.46	0.15	10.57	8.37	3.83	0.04	97.62	amph zone	136.07
05-04D	12 / 91 .	64.86	0.01	18.94	0.91	0.00	1.39	2.11	9.52	0.01	97.75	fsp	
05-04D	12 / 49 .	58.51	0.02	10.38	3.11	0.04	7.73	13.47	4.53	0.01	97.80	amph sym	
05-04D	12 / 17 .	52.59	0.09	8.31	6.82	0.09	12.90	14.13	2.96	0.00	97.89	amph sym	
05-04D	12 / 33 .	63.35	0.01	19.72	0.47	0.00	1.20	3.86	9.32	0.01	97.93	fsp	

Eclogites

Sample	Spot	SiO2	TiO2	Al2O3	FeO	MnO	MgO	CaO	Na2O	K2O	Total	Min	distance
05-04D	12 / 88 .	56.09	0.04	9.88	4.71	0.06	8.87	13.88	4.56	0.01	98.12	amph sym	
05-04D	12 / 86 .	48.82	0.17	6.70	9.63	0.08	12.35	17.63	2.86	0.01	98.25	amph sym	
05-04D	22 / 1 .	~~62.79~~	~~0.06~~	~~16.41~~	~~3.44~~	~~0.03~~	~~5.72~~	~~5.02~~	~~4.79~~	~~0.02~~	98.28	fsp +	
05-04D	12 / 89 .	54.11	0.10	4.87	7.79	0.07	17.38	12.54	1.74	0.00	98.59	amph sym	
05-04D	12 / 6 .	53.58	0.03	4.22	4.93	0.09	12.78	20.63	2.40	0.01	98.66	pyr	
05-04D	12 / 99 .	51.06	0.15	8.63	9.19	0.11	14.59	12.28	2.72	0.01	98.73	amph sym	
05-04D	12 / 8 .	66.96	0.01	18.68	0.94	0.01	1.31	2.08	8.74	0.00	98.73	fsp	
05-04D	12 / 23 .	65.33	0.01	20.10	0.51	0.00	0.91	2.61	9.42	0.00	98.88	fsp	
05-04D	9 / 94 .	38.00	0.05	20.99	28.33	0.39	4.75	6.52	0.00	0.01	99.03	grt	333.01
05-04D	12 / 35 .	66.80	0.00	19.66	0.34	0.01	0.95	2.01	9.27	0.01	99.05	fsp	
05-04D	9 / 3 .	37.94	0.05	20.97	28.77	0.33	4.71	6.32	0.02	0.00	99.11	grt	7.16
05-04D	12 / 82 .	55.40	0.04	9.96	2.95	0.03	10.10	15.11	5.52	0.04	99.14	omph	
05-04D	9 / 5 .	37.50	0.05	21.09	28.64	0.42	5.59	5.58	0.29	0.01	99.15	grt	14.32
05-04D	9 / 4 .	37.86	0.05	21.10	28.54	0.34	4.90	6.36	0.02	0.01	99.17	grt	10.74
05-04D	9 / 93 .	38.14	0.05	20.93	28.38	0.33	4.87	6.49	0.01	0.01	99.20	grt	329.43
05-04D	9 / 98 .	38.04	0.06	20.81	28.94	0.40	4.20	6.77	0.02	0.00	99.24	grt	347.34
05-04D	9 / 2 .	38.07	0.05	20.96	28.48	0.34	4.72	6.58	0.03	0.01	99.24	grt	3.58
05-04D	12 / 78 .	53.61	0.05	6.26	4.73	0.08	11.44	19.50	3.57	0.01	99.25	pyr	
05-04D	12 / 45 .	53.95	0.05	5.23	4.79	0.08	12.50	19.73	2.92	0.01	99.26	pyr	
05-04D	12 / 27 .	54.48	0.03	6.97	4.77	0.03	11.38	18.77	2.84	0.00	99.27	pyr	
05-04D	9 / 92 .	38.33	0.06	20.98	28.08	0.41	4.91	6.52	0.02	0.00	99.29	grt	325.85
05-04D	9 / 1 .	37.79	0.05	20.97	28.98	0.30	4.50	6.66	0.04	0.01	99.30	grt	0
05-04D	9 / 95 .	38.27	0.04	21.04	28.53	0.37	4.58	6.48	0.01	0.00	99.34	grt	336.59
05-04D	9 / 91 .	38.25	0.05	21.18	28.06	0.40	4.88	6.50	0.01	0.01	99.34	grt	322.27
05-04D	12 / 39 .	67.56	0.00	18.61	0.21	0.01	0.83	1.99	10.14	0.01	99.35	fsp	
05-04D	9 / 97 .	38.12	0.05	20.93	28.93	0.42	4.37	6.51	0.02	0.00	99.35	grt	343.75
05-04D	9 / 99 .	37.95	0.07	20.95	29.24	0.42	4.18	6.56	0.02	0.00	99.40	grt	350.92
05-04D	9 / 100 .	37.87	0.05	20.97	29.44	0.41	4.20	6.46	0.00	0.00	99.40	grt	354.5
05-04D	4 / 1 .	56.27	0.04	10.31	3.90	0.02	8.25	13.58	7.03	0.01	99.40	omph	
05-04D	39 / 1 .	67.77	0.00	19.75	0.13	0.02	0.05	0.40	11.31	0.00	99.43	fsp	
05-04D	12 / 50 .	65.94	0.00	19.76	0.51	0.02	1.08	3.05	9.15	0.00	99.51	fsp	
05-04D	9 / 96 .	38.09	0.04	20.93	28.95	0.41	4.56	6.53	0.02	0.00	99.53	grt	340.17
05-04D	12 / 24 .	66.38	0.00	20.88	0.20	0.00	0.01	1.86	10.19	0.01	99.54	fsp	
05-04D	32 / 1 .	54.24	0.05	9.51	3.17	0.02	10.60	16.93	5.00	0.02	99.54	omph	
05-04D	9 / 11 .	40.42	0.04	20.20	20.16	0.24	5.13	8.91	4.39	0.07	99.56	amph	35.81
05-04D	12 / 25 .	67.30	0.00	20.71	0.16	0.01	0.02	1.48	9.88	0.00	99.56	fsp	
05-04D	12 / 72 .	55.95	0.04	10.55	2.86	0.00	9.65	14.92	5.57	0.02	99.56	omph	
05-04D	12 / 34 .	66.47	0.00	20.85	0.21	0.00	0.08	2.17	9.83	0.00	99.61	fsp	
05-04D	12 / 21 .	54.08	0.04	9.16	2.54	0.05	9.35	18.72	5.71	0.00	99.65	omph	
05-04D	12 / 63 .	55.95	0.04	10.14	2.98	0.02	9.62	14.75	6.28	0.00	99.79	omph	
05-04D	12 / 19 .	64.54	0.02	16.04	0.57	0.02	3.30	5.82	9.47	0.01	99.79	fsp	
05-04D	12 / 31 .	55.55	0.04	10.55	2.94	0.02	9.71	15.07	5.96	0.00	99.85	omph	
05-04D	12 / 75 .	55.30	0.06	9.90	3.31	0.06	10.94	14.65	5.66	0.01	99.88	omph	
05-04D	12 / 53 .	54.50	0.06	6.75	4.22	0.07	11.68	19.27	3.52	0.00	100.06	diop+Na	
05-04D	12 / 14 .	66.86	0.00	20.01	0.25	0.03	0.55	2.80	9.59	0.00	100.09	fsp	
05-04D	12 / 5 .	54.02	0.03	4.08	4.49	0.06	12.95	21.92	2.59	0.00	100.14	diop+Na	
05-04D	12 / 96 .	~~65.26~~	~~0.00~~	~~16.61~~	~~1.24~~	~~0.00~~	~~3.49~~	~~6.64~~	~~6.91~~	~~0.02~~	100.19	fsp+	
05-04D	12 / 67 .	54.83	0.03	5.84	4.66	0.07	11.58	19.71	3.38	0.10	100.19	diop+Na	
05-04D	37 / 1 .	55.44	0.05	10.36	2.93	0.01	9.45	15.87	6.10	0.00	100.20	omph	
05-04D	12 / 85 .	55.83	0.04	9.72	2.96	0.02	10.34	15.57	5.77	0.00	100.25	omph	
05-04D	31 / 1 .	56.03	0.04	12.08	2.44	0.01	8.43	13.85	7.40	0.00	100.26	omph	
05-04D	12 / 76 .	54.99	0.05	9.86	3.91	0.03	10.09	15.59	5.69	0.07	100.28	omph	
05-04D	12 / 10 .	54.10	0.04	4.49	3.89	0.05	13.11	21.97	2.67	0.00	100.33	diop+Na	
05-04D	5 / 1 .	56.93	0.04	11.90	2.29	0.05	8.43	13.51	7.18	0.01	100.33	omph	
05-04D	26 / 1 .	54.57	0.11	6.54	4.80	0.07	11.03	18.94	4.28	0.00	100.36	diop+Na	
05-04D	12 / 59 .	60.16	0.02	10.31	2.38	0.06	7.26	13.90	6.28	0.02	100.39	omph	
05-04D	29 / 1 .	67.66	0.00	20.55	0.27	0.03	0.01	1.12	10.76	0.03	100.42	fsp	
05-04D	12 / 44 .	54.38	0.07	4.97	4.53	0.09	12.50	20.72	3.17	0.00	100.43	diop+Na	
05-04D	12 / 87 .	54.33	0.06	5.05	5.01	0.06	12.10	20.87	3.04	0.00	100.52	diop+Na	
05-04D	46 / 1 .	57.09	0.04	12.12	2.68	0.03	8.05	12.69	7.84	0.02	100.56	omph	
05-04D	12 / 93 .	55.72	0.03	9.07	4.52	0.03	10.25	16.24	4.70	0.00	100.56	omph	
05-04D	12 / 11 .	54.07	0.03	2.35	5.30	0.09	13.39	23.04	2.29	0.02	100.56	diop+Na	
05-04D	12 / 41 .	56.06	0.04	9.06	2.80	0.01	10.31	16.50	5.77	0.00	100.57	omph	
05-04D	12 / 74 .	56.28	0.04	9.98	2.76	0.03	10.37	15.06	6.07	0.00	100.58	omph	
05-04D	12 / 71 .	56.34	0.04	10.09	2.67	0.04	9.77	15.57	6.07	0.00	100.59	omph	
05-04D	24 / 1 .	56.92	0.03	11.70	3.19	0.00	8.22	12.99	7.55	0.00	100.60	omph	
05-04D	12 / 83 .	56.72	0.05	10.46	2.73	0.00	9.42	15.16	6.07	0.00	100.62	omph	
05-04D	12 / 81 .	56.25	0.04	10.25	2.69	0.01	9.60	15.61	6.19	0.00	100.62	omph	
05-04D	12 / 9 .	54.34	0.05	4.13	4.12	0.08	12.83	21.82	3.27	0.00	100.64	diop+Na	
05-04D	12 / 56 .	54.63	0.05	5.37	4.56	0.08	12.18	20.85	2.94	0.00	100.66	diop+Na	
05-04D	12 / 3 .	54.28	0.03	4.16	3.80	0.04	13.26	22.58	2.51	0.00	100.67	diop+Na	

Eclogites

Sample	Spot	SiO2	TiO2	Al2O3	FeO	MnO	MgO	CaO	Na2O	K2O	Total	Min	distance
05-04D	12 / 32 .	54.17	0.04	4.06	4.25	0.09	13.29	22.37	2.43	0.00	100.71	diop+Na	
05-04D	12 / 84 .	56.31	0.04	9.99	2.83	0.03	9.76	15.60	6.16	0.00	100.72	omph	
05-04D	10 / 1 .	56.40	0.03	9.62	2.68	0.01	10.11	16.00	5.87	0.02	100.74	omph	
05-04D	12 / 18 .	54.82	0.04	6.06	3.94	0.05	11.95	20.46	3.43	0.00	100.75	diop+Na	
05-04D	12 / 97 .	54.48	0.05	5.46	4.79	0.08	11.81	20.34	3.75	0.00	100.76	diop+Na	
05-04D	9 / 8 .	41.65	0.03	21.20	19.95	0.24	4.72	8.50	4.47	0.00	100.76	amph	25.07
05-04D	21 / 1 .	66.42	0.01	17.77	0.59	0.00	2.40	5.06	8.48	0.02	100.76	fsp	
05-04D	12 / 64 .	54.92	0.06	9.70	3.92	0.03	11.14	15.11	5.92	0.01	100.81	omph	
05-04D	12 / 4 .	54.59	0.03	4.72	4.07	0.06	12.93	21.65	2.77	0.01	100.82	diop+Na	
05-04D	12 / 68 .	54.51	0.05	4.93	4.83	0.07	12.71	20.18	3.56	0.01	100.84	diop+Na	
05-04D	12 / 57 .	54.57	0.04	5.23	4.90	0.08	12.20	20.59	3.25	0.02	100.88	diop+Na	
05-04D	12 / 52 .	54.51	0.04	4.24	4.14	0.07	13.26	22.04	2.60	0.00	100.89	diop+Na	
05-04D	12 / 12 .	54.40	0.01	1.97	5.35	0.09	13.89	23.49	1.70	0.01	100.92	diop+Na	
05-04D	12 / 51 .	54.55	0.04	5.12	3.98	0.06	12.71	21.30	3.17	0.00	100.93	diop+Na	
05-04D	12 / 60 .	55.06	0.02	4.18	4.89	0.10	12.93	20.94	2.81	0.00	100.93	diop+Na	
05-04D	12 / 1 .	54.38	0.05	4.97	4.97	0.06	12.34	20.72	3.45	0.00	100.93	diop+Na	
05-04D	12 / 42 .	54.54	0.04	3.81	4.20	0.06	13.27	22.65	2.35	0.01	100.94	diop+Na	
05-04D	12 / 16 .	54.79	0.02	3.05	4.29	0.10	13.68	22.95	2.09	0.00	100.96	diop+Na	
05-04D	12 / 15 .	65.80	0.00	16.33	0.54	0.02	3.41	7.55	7.35	0.01	101.01	fsp	
05-04D	12 / 66 .	56.32	0.04	8.86	2.96	0.02	10.20	16.74	5.89	0.01	101.04	omph	
05-04D	12 / 79 .	54.40	0.01	2.47	5.65	0.09	13.64	22.98	1.84	0.00	101.08	diop+Na	
05-04D	33 / 1 .	53.80	0.02	3.42	3.68	0.01	14.02	23.72	2.42	0.02	101.10	diop+Na	
05-04D	12 / 65 .	53.53	0.04	3.64	4.83	0.07	13.69	22.65	2.66	0.00	101.10	diop+Na	
05-04D	12 / 36 .	54.88	0.02	2.74	4.40	0.08	14.02	23.18	1.80	0.00	101.12	diop+Na	
05-04D	12 / 46 .	54.69	0.05	4.54	4.63	0.06	12.58	21.47	3.11	0.00	101.12	diop+Na	
05-04D	12 / 29 .	54.59	0.04	5.60	4.96	0.09	11.76	20.30	3.81	0.01	101.18	diop+Na	
05-04D	12 / 2 .	54.84	0.06	5.32	5.12	0.05	12.48	20.62	2.73	0.01	101.23	diop+Na	
05-04D	12 / 70 .	55.00	0.03	3.83	5.05	0.11	12.89	21.27	3.11	0.00	101.27	diop+Na	
05-04D	12 / 55 .	54.51	0.02	2.84	4.38	0.09	14.05	23.34	2.08	0.00	101.32	diop+Na	
05-04D	12 / 22 .	54.46	0.03	4.39	4.70	0.08	12.56	21.39	3.70	0.02	101.33	diop+Na	
05-04D	12 / 43 .	55.23	0.05	5.51	4.22	0.06	12.15	20.61	3.51	0.01	101.35	diop+Na	
05-04D	12 / 28 .	54.66	0.04	7.35	4.82	0.07	11.66	18.09	4.71	0.00	101.40	omph/dio	
05-04D	20 / 1 .	69.08	0.00	20.78	0.23	0.02	0.03	0.46	10.79	0.02	101.41	fsp	
05-04D	12 / 62 .	55.08	0.05	5.33	3.91	0.06	12.61	20.78	3.61	0.02	101.44	diop+Na	
05-04D	12 / 80 .	62.47	0.01	12.43	1.83	0.04	6.65	11.70	6.48	0.01	101.64	fsp	
05-04D	12 / 54 .	56.01	0.05	8.30	3.10	0.05	10.57	17.32	6.29	0.00	101.69	omph	
05-04D	27 / 1 .	54.16	0.06	8.27	3.75	0.07	14.69	15.98	4.76	0.01	101.74	omph	
05-04D	35 / 1 .	55.53	0.05	6.48	3.56	0.06	12.85	19.48	3.76	0.00	101.76	diop+Na	
05-04D	12 / 98 .	55.37	0.05	6.44	4.76	0.07	11.47	19.83	3.80	0.01	101.79	diop+Na	
05-04D	12 / 26 .	52.78	0.12	11.24	8.87	0.10	13.65	11.32	3.93	0.01	102.03	omph	
05-04D	12 / 61 .	54.87	0.05	4.76	3.55	0.06	12.84	21.67	4.26	0.00	102.06	diop+Na	
05-04D	12 / 77 .	56.11	0.03	4.96	4.44	0.07	12.14	20.86	3.69	0.00	102.30	diop+Na	
05-04D	12 / 100 .	65.92	0.00	15.19	0.63	0.00	4.97	7.66	8.09	0.02	102.47	fsp	
05-04D	12 / 20 .	56.45	0.00	2.99	3.57	0.08	13.71	23.17	2.74	0.00	102.71	diop+Na	
05-04D	23 / 1 .	~~62.63~~	~~0.00~~	~~9.37~~	~~1.92~~	~~0.06~~	~~9.20~~	~~15.43~~	~~5.95~~	~~0.01~~	104.59	mix	
05-04D	1 / 1 .	56.10	0.12	11.93	6.81	0.04	12.61	2.88	5.99	0.00	96.49	pyr	
05-04D	2 / 1 .	62.87	0.00	23.23	0.69	0.01	0.00	4.98	8.69	0.00	100.48	fsp	
05-04D	3 / 1 .	48.21	0.07	39.71	0.59	0.03	0.22	0.37	4.99	0.27	94.45	pa	
05-04D	4 / 1 .	37.84	0.06	25.24	9.50	0.24	0.00	24.92	0.01	0.01	97.83	czo	
05-04D	5 / 1 .	45.05	0.40	11.03	19.96	0.14	7.65	8.38	3.87	0.05	96.52	pyr	
05-04D	6 / 1 .	38.12	1.10	20.72	27.09	1.34	3.32	8.84	0.04	0.08	100.65	grt	
05-04D	7 / 1 .	37.07	1.59	20.63	28.65	2.06	3.19	7.55	0.03	0.01	100.79	grt	
05-04D	8 / 1 .	54.58	0.00	0.31	21.94	0.37	18.25	0.82	0.11	0.00	96.38	ta	
05-04D	9 / 1 .	~~53.45~~	~~0.11~~	~~5.11~~	~~12.40~~	~~0.12~~	~~15.03~~	~~7.70~~	~~3.04~~	~~0.05~~	97.01	ta?	
05-04D	10 / 1 .	~~5.15~~	~~0.02~~	~~0.28~~	~~34.72~~	~~0.21~~	~~1.77~~	~~32.66~~	~~0.04~~	~~0.00~~	~~74.84~~	dolo	
05-04D	11 / 1 .	54.18	0.03	0.53	21.43	0.35	18.60	0.71	0.28	0.01	96.12	ta	
05-04D	12 / 1 .	44.56	0.54	12.70	15.53	0.04	10.05	8.96	4.17	0.04	96.58	pyr	
05-04D	13 / 1 .	55.76	0.04	10.57	5.02	0.02	7.75	13.16	7.49	0.01	99.83	pyr	
05-04D	14 / 1 .	53.22	0.01	0.24	24.06	0.52	16.90	0.87	0.05	0.00	95.88	ta	
05-04D	15 / 1 .	0.08	0.00	0.01	9.43	0.38	15.56	32.69	0.01	0.00	58.17	dolo	
05-04D	16 / 1 .	52.69	0.10	4.38	15.53	0.21	13.66	7.72	2.31	0.08	96.69	amph	
05-04D	17 / 1 .	58.06	0.00	12.57	1.68	0.65	3.35	8.24	8.75	0.00	93.31	pyr	
05-04D	18 / 1 .	38.85	0.71	17.19	20.74	0.07	5.47	9.16	4.62	0.04	96.86	amph	
05-04D	19 / 1 .	38.05	0.28	29.45	4.76	0.07	0.41	24.16	0.05	0.00	97.23	czo	
05-04D	20 / 1 .	45.74	0.19	38.02	3.22	0.00	0.41	0.86	4.37	0.07	92.88	pa	
05-04D	2 / 1 .	0.03	0.00	0.01	5.16	0.13	19.31	31.84	0.03	0.00	56.52	dolo	0
05-04D	2 / 2 .	0.11	0.00	0.11	4.91	0.13	17.22	31.33	0.03	0.00	53.83	dolo	9.99
05-04D	2 / 3 .	53.69	0.06	7.35	9.61	0.05	15.46	7.52	3.49	0.02	97.24	Amph	19.97
05-04D	2 / 4 .	52.14	0.06	9.05	10.33	0.08	14.23	6.71	3.96	0.03	96.59	Amph	29.96
05-04D	2 / 5 .	50.24	0.06	9.49	10.27	0.07	14.24	7.38	3.33	0.03	95.09	Amph	39.94
05-04D	2 / 6 .	35.41	0.02	24.32	10.25	0.03	14.51	1.80	5.90	0.01	92.26	Grt	49.93

Eclogites

Sample	Spot	SiO2	TiO2	Al2O3	FeO	MnO	MgO	CaO	Na2O	K2O	Total	Min	distance
05-04D	2 / 7 .	38.88	0.03	21.61	24.81	0.29	7.67	6.12	0.01	0.00	99.42	Grt	59.91
05-04D	2 / 8 .	38.64	0.03	21.66	25.84	0.21	7.25	5.88	0.00	0.00	99.52	Grt	69.9
05-04D	2 / 9 .	38.61	0.02	21.49	26.62	0.22	6.78	5.98	0.01	0.00	99.73	Grt	79.89
05-04D	2 / 10 .	38.65	0.02	21.50	26.54	0.20	6.82	6.03	0.01	0.00	99.78	Grt	89.87
05-04D	2 / 11 .	38.52	0.03	21.42	26.45	0.32	6.66	6.21	0.01	0.01	99.63	Grt	99.86
05-04D	2 / 12 .	38.62	0.03	21.40	26.89	0.27	6.40	6.15	0.00	0.00	99.76	Grt	109.84
05-04D	2 / 13 .	38.37	0.03	21.22	27.94	0.30	5.55	6.42	0.00	0.00	99.82	Grt	119.83
05-04D	2 / 14 .	37.98	0.03	21.30	28.31	0.31	5.09	6.29	0.02	0.00	99.33	Grt	129.81
05-04D	2 / 15 .	37.99	0.03	21.16	29.49	0.39	4.54	6.16	0.02	0.00	99.78	Grt	139.8
05-04D	2 / 16 .	38.06	0.05	21.11	29.42	0.46	4.29	6.34	0.00	0.00	99.73	Grt	149.79
05-04D	2 / 17 .	37.87	0.06	21.09	29.50	0.58	4.02	6.66	0.03	0.00	99.80	Grt	159.77
05-04D	2 / 18 .	37.63	0.05	20.93	29.60	0.60	3.94	6.62	0.02	0.00	99.40	Grt	169.76
05-04D	2 / 19 .	38.05	0.04	20.84	29.62	0.63	3.63	6.83	0.00	0.02	99.65	Grt	179.74
05-04D	2 / 20 .	37.71	0.03	20.96	30.21	0.62	3.49	6.21	0.02	0.00	99.24	Grt	189.73
05-04D	2 / 21 .	37.70	0.06	20.94	30.52	0.55	3.29	6.47	0.02	0.01	99.55	Grt	199.71
05-04D	2 / 22 .	37.56	0.09	20.65	30.51	0.50	3.20	6.73	0.01	0.00	99.26	Grt	209.7
05-04D	2 / 23 .	37.54	0.08	20.82	30.25	0.45	3.04	7.24	0.02	0.00	99.44	Grt	219.69
05-04D	2 / 24 .	37.56	0.08	20.57	30.61	0.41	2.95	7.22	0.00	0.00	99.42	Grt	229.67
05-04D	2 / 25 .	37.56	0.09	20.78	30.92	0.38	2.82	7.21	0.03	0.00	99.78	Grt	239.66
05-04D	2 / 26 .	37.53	0.11	20.72	30.57	0.36	2.65	7.44	0.02	0.00	99.42	Grt	249.64
05-04D	2 / 27 .	37.51	0.10	20.79	30.57	0.36	2.59	7.58	0.00	0.00	99.52	Grt	259.63
05-04D	2 / 28 .	37.31	0.11	20.67	30.86	0.37	2.55	7.51	0.01	0.00	99.40	Grt	269.61
05-04D	2 / 29 .	37.44	0.09	20.69	31.08	0.38	2.60	7.06	0.01	0.00	99.34	Grt	279.6
05-04D	2 / 30 .	37.54	0.09	20.65	31.20	0.40	2.54	7.18	0.01	0.00	99.62	Grt	289.58
05-04D	2 / 31 .	37.47	0.08	20.84	31.02	0.40	2.49	7.26	0.01	0.01	99.59	Grt	299.57
05-04D	2 / 32 .	37.44	0.04	20.92	31.67	0.43	2.66	6.47	0.01	0.00	99.63	Grt	309.56
05-04D	2 / 33 .	37.45	0.09	20.85	30.78	0.48	2.61	7.19	0.04	0.01	99.49	Grt	319.54
05-04D	2 / 34 .	37.54	0.17	20.73	30.53	0.43	2.59	7.80	0.02	0.00	99.82	Grt	329.53
05-04D	2 / 35 .	0.10	98.09	0.02	1.50	0.01	0.00	0.34	0.00	0.00	100.05	Rutile	339.51
05-04D	2 / 36 .	~~29.37~~	~~19.06~~	~~18.87~~	~~23.59~~	~~0.46~~	~~2.60~~	~~8.00~~	~~0.05~~	~~0.00~~	102.00	mix	349.5
05-04D	2 / 37 .	37.78	0.38	20.87	29.94	0.48	2.76	7.86	0.03	0.01	100.10	Grt	359.48
05-04D	2 / 38 .	37.61	0.75	20.51	29.50	0.49	2.81	8.08	0.04	0.00	99.79	Grt	369.47
05-04D	2 / 39 .	6.87	81.74	2.15	5.42	0.05	0.26	1.21	0.01	0.00	97.70	Grt	379.46
05-04D	2 / 40 .	37.71	0.59	20.74	29.20	0.53	2.87	8.00	0.05	0.00	99.69	Grt	389.44
05-04D	2 / 41 .	37.40	0.85	20.59	29.13	0.50	2.82	8.19	0.05	0.01	99.54	Grt	399.43
05-04D	2 / 42 .	0.09	98.20	0.03	1.22	0.01	0.00	0.35	0.03	0.01	99.93	Rutile	409.41
05-04D	2 / 43 .	37.43	0.34	20.83	29.16	0.59	2.49	8.82	0.02	0.00	99.67	Grt	419.4
05-04D	2 / 44 .	37.70	0.20	20.75	29.28	0.53	2.57	8.66	0.02	0.00	99.72	Grt	429.38
05-04D	2 / 45 .	37.88	0.09	21.01	29.90	0.57	3.10	7.41	0.03	0.00	99.98	Grt	439.37
05-04D	2 / 46 .	~~34.12~~	~~1.16~~	~~14.90~~	~~19.72~~	~~0.05~~	~~9.99~~	~~3.28~~	~~0.63~~	~~0.31~~	84.17		449.36
05-04D	2 / 47 .	35.59	2.68	15.27	21.65	0.04	9.80	0.91	1.32	2.80	90.06	Grt	459.34
05-04D	2 / 48 .	35.78	2.07	14.92	22.17	0.06	9.99	0.29	4.82	0.93	91.03	Grt	469.33
05-04D	2 / 49 .	37.82	0.10	20.79	29.42	0.60	2.71	8.43	0.01	0.01	99.90	Grt	479.31
05-04D	2 / 50 .	37.72	0.08	20.72	29.99	0.70	2.49	8.24	0.02	0.00	99.94	Grt	489.3
05-04D	2 / 51 .	37.61	0.08	20.68	29.83	0.67	2.24	8.41	0.01	0.00	99.52	Grt	499.28
05-04D	2 / 52 .	37.38	0.10	20.70	30.12	0.77	2.13	8.66	0.01	0.00	99.86	Grt	509.27
05-04D	2 / 53 .	37.81	0.09	20.68	30.09	0.82	2.05	8.66	0.02	0.00	100.21	Grt	519.25
05-04D	2 / 54 .	37.66	0.11	20.54	30.17	0.80	2.01	8.71	0.00	0.01	100.03	Grt	529.24
05-04D	2 / 55 .	37.57	0.13	20.58	29.46	0.71	2.00	9.14	0.00	0.00	99.59	Grt	539.23
05-04D	2 / 56 .	37.48	0.13	20.52	29.61	0.74	1.92	8.92	0.01	0.00	99.31	Grt	549.21
05-04D	2 / 57 .	37.61	0.12	20.60	29.47	0.84	1.94	9.01	0.02	0.00	99.61	Grt	559.2
05-04D	2 / 58 .	37.59	0.13	20.60	29.46	0.80	1.91	9.30	0.01	0.00	99.80	Grt	569.18
05-04D	2 / 59 .	37.54	0.15	20.48	29.10	0.82	2.07	9.41	0.01	0.00	99.57	Grt	579.17
05-04D	2 / 60 .	37.64	0.11	20.61	29.18	0.84	2.16	9.19	0.02	0.00	99.74	Grt	589.15
05-04D	2 / 61 .	37.66	0.12	20.69	29.03	0.86	2.37	9.19	0.02	0.00	99.94	Grt	599.14
05-04D	2 / 62 .	37.75	0.10	20.70	29.13	0.88	2.36	8.73	0.01	0.00	99.66	Grt	609.13
05-04D	2 / 63 .	37.75	0.12	20.65	29.22	0.88	2.28	8.84	0.03	0.00	99.76	Grt	619.11
05-04D	2 / 64 .	37.34	0.11	20.59	29.13	0.86	2.26	9.11	0.02	0.00	99.44	Grt	629.1
05-04D	2 / 65 .	37.39	0.12	20.43	29.14	0.87	2.21	9.19	0.01	0.00	99.38	Grt	639.08
05-04D	2 / 66 .	37.57	0.10	20.45	29.42	0.88	2.08	8.95	0.03	0.00	99.47	Grt	649.07
05-04D	2 / 67 .	37.43	0.13	20.31	29.10	0.89	2.04	9.31	0.03	0.00	99.25	Grt	659.05
05-04D	2 / 68 .	37.51	0.14	20.49	29.00	0.89	1.97	9.54	0.02	0.01	99.56	Grt	669.04
05-04D	2 / 69 .	37.38	0.14	20.44	29.23	0.90	1.98	9.32	0.01	0.00	99.39	Grt	679.03
05-04D	2 / 70 .	37.49	0.15	20.32	29.15	0.87	1.95	9.37	0.00	0.00	99.32	Grt	689.01
05-04D	1 / 1 .	57.04	0.04	11.79	3.40	0.02	8.10	12.71	7.55	0.00	100.63	Amph	0
05-04D	1 / 2 .	56.81	0.04	11.47	3.39	0.00	8.11	12.84	7.51	0.00	100.18	Amph	10.08
05-04D	1 / 3 .	56.74	0.04	11.76	3.23	0.01	7.98	12.41	7.65	0.01	99.83	Amph	20.15
05-04D	1 / 4 .	57.36	0.04	12.35	2.89	0.02	7.95	12.43	7.71	0.00	100.75	Amph	30.22
05-04D	1 / 5 .	56.68	0.05	12.03	3.38	0.01	8.04	12.06	7.49	0.01	99.73	Amph	40.3
05-04D	1 / 6 .	49.70	0.08	10.39	10.95	0.07	10.62	10.71	4.82	0.04	97.37	Amph	50.37
05-04D	1 / 7 .	40.15	0.06	17.11	16.05	0.08	8.28	9.55	4.33	0.07	95.66	amph	60.45

Eclogites

Sample	Spot	SiO2	TiO2	Al2O3	FeO	MnO	MgO	CaO	Na2O	K2O	Total	Min	distance
05-04D	1 / 8 .	39.17	0.05	19.04	16.44	0.11	7.44	9.61	4.32	0.09	96.26	amph	70.52
05-04D	1 / 9 .	38.32	0.03	19.42	17.40	0.08	6.71	9.61	4.27	0.06	95.89	Grt	80.6
05-04D	1 / 10 .	~~34.04~~	~~0.05~~	~~18.09~~	~~21.48~~	~~0.14~~	~~8.21~~	~~5.88~~	~~2.77~~	~~0.40~~	91.08		90.67
05-04D	1 / 11 .	38.43	0.03	21.23	27.18	0.22	5.96	6.10	0.02	0.00	99.17	Grt	100.75
05-04D	1 / 12 .	38.38	0.05	21.39	27.78	0.22	5.62	6.11	0.02	0.01	99.56	Grt	110.82
05-04D	1 / 13 .	38.29	0.04	21.14	27.86	0.24	5.41	6.37	0.01	0.00	99.37	Grt	120.9
05-04D	1 / 14 .	38.33	0.04	21.23	28.26	0.25	5.30	6.28	0.01	0.00	99.70	Grt	130.97
05-04D	1 / 15 .	38.03	0.05	21.16	28.55	0.29	5.11	6.13	0.01	0.00	99.34	Grt	141.05
05-04D	1 / 16 .	38.15	0.05	21.18	28.43	0.28	4.92	6.30	0.03	0.01	99.36	Grt	151.12
05-04D	1 / 17 .	38.05	0.04	21.31	28.91	0.27	4.87	6.12	0.02	0.00	99.57	Grt	161.2
05-04D	1 / 18 .	38.01	0.04	21.21	28.86	0.33	4.69	6.28	0.02	0.00	99.44	Grt	171.27
05-04D	1 / 19 .	37.89	0.04	21.14	29.28	0.34	4.57	5.94	0.01	0.00	99.21	Grt	181.35
05-04D	1 / 20 .	38.07	0.03	21.21	29.14	0.33	4.45	6.13	0.01	0.00	99.38	Grt	191.42
05-04D	1 / 21 .	38.05	0.05	21.15	29.40	0.38	4.33	6.07	0.03	0.00	99.46	Grt	201.5
05-04D	1 / 22 .	38.02	0.06	20.99	29.25	0.42	4.16	6.41	0.03	0.00	99.34	Grt	211.57
05-04D	1 / 23 .	37.98	0.05	21.06	29.74	0.38	4.01	6.20	0.02	0.00	99.45	Grt	221.65
05-04D	1 / 24 .	37.88	0.04	21.02	30.12	0.45	3.95	6.20	0.01	0.00	99.69	Grt	231.72
05-04D	1 / 25 .	37.76	0.06	21.00	30.06	0.44	3.69	6.36	0.01	0.00	99.38	Grt	241.8
05-04D	1 / 26 .	37.77	0.07	20.88	30.30	0.42	3.57	6.38	0.03	0.00	99.43	Grt	251.87
05-04D	1 / 27 .	37.81	0.08	20.92	30.42	0.49	3.47	6.43	0.03	0.00	99.65	Grt	261.95
05-04D	1 / 28 .	37.75	0.09	20.98	30.15	0.55	3.31	6.48	0.02	0.00	99.32	Grt	272.02
05-04D	1 / 29 .	37.69	0.10	20.85	30.31	0.55	3.21	6.73	0.01	0.00	99.45	Grt	282.1
05-04D	1 / 30 .	37.65	0.10	20.80	30.23	0.61	3.07	6.87	0.01	0.00	99.33	Grt	292.17
05-04D	1 / 31 .	37.77	0.09	20.80	30.49	0.65	3.00	6.73	0.02	0.00	99.56	Grt	302.25
05-04D	1 / 32 .	37.70	0.12	20.62	30.38	0.66	2.91	6.63	0.01	0.00	99.03	Grt	312.32
05-04D	1 / 33 .	37.61	0.13	20.74	30.60	0.63	2.95	6.54	0.02	0.00	99.20	Grt	322.4
05-04D	1 / 34 .	37.56	0.13	20.76	31.09	0.56	2.96	6.26	0.00	0.00	99.33	Grt	332.47
05-04D	1 / 35 .	37.58	0.15	20.82	30.88	0.51	2.94	6.66	0.01	0.00	99.55	Grt	342.55
05-04D	1 / 36 .	37.58	0.17	20.81	30.92	0.44	2.88	6.70	0.03	0.00	99.53	Grt	352.62
05-04D	1 / 37 .	37.58	0.20	20.59	30.69	0.39	2.82	6.67	0.02	0.00	98.97	Grt	362.7
05-04D	1 / 38 .	37.67	0.19	20.72	30.37	0.43	2.77	7.09	0.04	0.00	99.27	Grt	372.77
05-04D	1 / 39 .	37.42	0.17	20.57	30.50	0.43	2.68	7.19	0.05	0.01	99.03	Grt	382.84
05-04D	1 / 40 .	37.75	0.13	20.75	30.88	0.39	2.74	6.80	0.02	0.00	99.46	Grt	392.92
05-04D	1 / 41 .	37.57	0.23	20.70	31.01	0.40	2.55	7.01	0.03	0.00	99.51	Grt	402.99
05-04D	1 / 42 .	37.57	0.13	20.55	30.90	0.39	2.51	7.30	0.01	0.00	99.36	Grt	413.07
05-04D	1 / 43 .	37.60	0.12	20.61	30.86	0.38	2.43	7.31	0.00	0.00	99.30	Grt	423.14
05-04D	1 / 44 .	37.55	0.12	20.62	30.89	0.41	2.44	7.61	0.01	0.00	99.64	Grt	433.22
05-04D	1 / 45 .	37.45	0.12	20.71	30.57	0.41	2.36	7.43	0.01	0.00	99.07	Grt	443.29
05-04D	1 / 46 .	37.62	0.13	20.58	30.89	0.45	2.31	7.38	0.03	0.01	99.41	Grt	453.37
05-04D	1 / 47 .	37.72	0.12	20.60	31.02	0.44	2.31	7.48	0.01	0.01	99.70	Grt	463.44
05-04D	1 / 48 .	37.39	0.10	20.73	30.91	0.49	2.30	7.57	0.02	0.00	99.52	Grt	473.52
05-04D	1 / 49 .	37.57	0.09	20.63	30.77	0.49	2.26	7.61	0.02	0.00	99.44	Grt	483.59
05-04D	1 / 50 .	37.54	0.09	20.74	30.63	0.50	2.24	7.94	0.04	0.00	99.71	Grt	493.67
05-04D	1 / 51 .	37.60	0.11	20.67	30.21	0.55	2.20	7.93	0.02	0.01	99.31	Grt	503.74
05-04D	1 / 52 .	37.66	0.12	20.58	30.03	0.60	2.22	8.16	0.03	0.00	99.40	Grt	513.82
05-04D	1 / 53 .	37.54	0.09	20.80	30.14	0.56	2.29	8.18	0.02	0.00	99.62	Grt	523.89
05-04D	1 / 54 .	37.71	0.06	20.78	30.22	0.59	2.30	8.05	0.01	0.00	99.73	Grt	533.97
05-04D	1 / 55 .	37.78	0.05	20.65	30.39	0.71	2.42	7.66	0.03	0.00	99.69	Grt	544.04
05-04D	1 / 56 .	37.64	0.12	20.71	29.50	0.68	2.23	8.63	0.00	0.01	99.50	Grt	554.12
05-04D	1 / 57 .	37.68	0.09	20.62	29.64	0.66	2.22	8.47	0.01	0.00	99.38	Grt	564.19
05-04D	1 / 58 .	37.66	0.09	20.74	29.66	0.69	2.23	8.41	0.02	0.01	99.50	Grt	574.27
05-04D	1 / 59 .	37.74	0.09	20.58	29.50	0.71	2.28	8.57	0.03	0.01	99.49	Grt	584.34
05-04D	1 / 60 .	37.61	0.09	20.72	29.40	0.75	2.22	8.85	0.02	0.00	99.66	Grt	594.42
05-04D	1 / 61 .	37.54	0.10	21.11	28.29	0.95	3.45	6.95	0.17	0.38	98.94	Grt	604.49
05-04D	1 / 62 .	37.69	0.12	20.72	29.00	0.95	2.08	8.96	0.04	0.00	99.56	Grt	614.57
05-04D	1 / 63 .	37.58	0.12	20.57	29.11	0.78	2.42	8.75	0.04	0.00	99.37	Grt	624.64
05-04D	1 / 64 .	37.68	0.11	20.56	28.73	0.72	2.52	9.18	0.05	0.00	99.56	Grt	634.72
05-04D	1 / 65 .	38.72	0.05	20.89	29.55	0.74	2.47	7.95	0.05	0.01	100.43	Grt	644.79
05-04D	1 / 66 .	100.10	0.00	0.06	0.70	0.01	0.01	0.06	0.00	0.01	100.95	qtz	654.87
05-04D	1 / 67 .	46.57	0.01	11.72	26.21	0.26	2.15	7.84	3.88	0.02	98.67	amph?	664.94
05-04D	1 / 68 .	37.49	0.05	20.59	29.89	0.80	2.29	8.19	0.06	0.00	99.35	Grt	675.02
05-04D	1 / 69 .	37.77	0.07	20.78	29.60	0.88	2.08	8.69	0.01	0.01	99.88	Grt	685.09
05-04D	1 / 70 .	37.63	0.15	20.45	29.00	0.85	2.03	9.19	0.01	0.00	99.31	Grt	695.17
05-04D	1 / 71 .	37.52	0.05	20.59	30.03	0.98	2.05	8.13	0.01	0.00	99.37	Grt	705.24
05-04D	1 / 72 .	37.33	0.09	20.67	29.81	0.93	2.03	8.58	0.01	0.01	99.46	Grt	715.32
05-04D	1 / 73 .	37.37	0.08	20.52	29.75	0.98	2.05	8.25	0.04	0.00	99.02	Grt	725.39
05-04D	1 / 74 .	37.47	0.11	20.53	29.34	0.99	2.02	8.49	0.02	0.00	98.99	Grt	735.47
05-04D	1 / 75 .	37.60	0.11	20.63	29.32	0.97	2.10	8.85	0.02	0.02	99.62	Grt	745.54
05-04D	1 / 76 .	37.67	0.06	20.59	29.43	0.97	2.08	8.52	0.01	0.01	99.36	Grt	755.61
05-04D	1 / 77 .	37.56	0.12	20.55	29.10	0.99	2.22	8.72	0.04	0.01	99.30	Grt	765.69
05-04D	1 / 78 .	37.44	0.11	20.57	28.96	0.98	2.26	8.69	0.03	0.00	99.03	Grt	775.76

Eclogites

Sample	Spot	SiO2	TiO2	Al2O3	FeO	MnO	MgO	CaO	Na2O	K2O	Total	Min	distance
05-04D	1 / 79 .	37.36	0.10	20.56	28.77	1.03	2.27	8.89	0.03	0.00	99.01	Grt	785.84
05-04D	1 / 80 .	37.67	0.13	20.48	28.55	0.99	2.32	9.32	0.02	0.00	99.48	Grt	795.91
05-04D	1 / 81 .	38.05	0.08	20.87	29.11	1.05	2.42	8.51	0.07	0.10	100.25	Grt	805.99
05-04D	1 / 82 .	38.98	0.03	20.04	30.25	1.04	2.81	4.01	0.28	0.05	97.50	Grt	816.06
05-04D	1 / 83 .	37.71	0.02	20.74	29.73	1.09	2.46	7.88	0.03	0.01	99.68	Grt	826.14
05-04D	1 / 84 .	37.41	0.15	20.47	28.81	1.12	1.93	9.50	0.01	0.00	99.40	Grt	836.21
05-04D	1 / 85 .	37.54	0.18	20.31	28.25	1.10	1.92	9.99	0.03	0.00	99.32	Grt	846.29
05-04D	1 / 86 .	37.67	0.18	20.45	28.04	1.05	2.01	9.95	0.03	0.00	99.38	Grt	856.36
05-04D	1 / 87 .	37.53	0.15	20.51	28.74	1.12	2.10	9.13	0.05	0.00	99.33	Grt	866.44
05-04D	1 / 88 .	37.50	0.14	20.48	28.45	1.14	2.07	9.50	0.02	0.00	99.30	Grt	876.51
05-04D	1 / 89 .	37.59	0.13	20.50	28.93	1.18	2.14	8.87	0.02	0.00	99.35	Grt	886.59
05-04D	1 / 90 .	37.65	0.10	20.62	28.91	1.17	2.22	8.90	0.03	0.00	99.59	Grt	896.66
05-04D	1 / 91 .	~~39.82~~	~~0.27~~	~~27.83~~	~~26.65~~	~~1.01~~	~~1.47~~	~~8.03~~	~~0.08~~	~~0.16~~	105.33	?	906.74
05-04D	1 / 92 .	37.78	0.16	20.62	28.85	1.15	2.23	9.00	0.01	0.00	99.79	Grt	916.81
05-04D	1 / 93 .	37.66	0.12	20.52	28.41	1.16	2.21	9.10	0.04	0.00	99.22	Grt	926.89
05-04D	1 / 94 .	37.61	0.12	20.56	29.20	1.22	2.28	8.60	0.03	0.00	99.61	Grt	936.96
05-04D	1 / 95 .	37.54	0.12	20.76	28.92	1.26	2.32	8.62	0.02	0.00	99.56	Grt	947.04
05-04D	1 / 96 .	37.66	0.16	20.57	28.63	1.25	2.24	8.91	0.03	0.00	99.45	Grt	957.11
05-04D	1 / 97 .	37.87	0.18	20.52	28.03	1.20	2.31	9.47	0.04	0.00	99.62	Grt	967.19
05-04D	1 / 98 .	37.50	0.13	20.68	28.81	1.31	2.28	8.86	0.02	0.00	99.59	Grt	977.26
05-04D	1 / 99 .	37.47	0.14	20.50	28.41	1.32	2.11	9.17	0.01	0.00	99.14	Grt	987.34
05-04D	1 / 100 .	37.61	0.17	20.37	28.73	1.30	2.10	9.33	0.01	0.00	99.62	Grt	997.41
05-04D	1 / 101 .	37.48	0.17	20.30	28.39	1.30	1.71	10.24	0.01	0.00	99.62	Grt	1007.49
05-04D	1 / 102 .	37.55	0.17	20.58	28.81	1.36	1.65	10.00	0.03	0.00	100.14	Grt	1017.56
05-04D	1 / 103 .	37.56	0.13	20.64	28.62	1.46	1.76	9.34	0.03	0.00	99.53	Grt	1027.64
05-04D	1 / 104 .	37.47	0.18	20.59	27.98	1.36	2.11	9.67	0.03	0.00	99.39	Grt	1037.71
05-04D	1 / 105 .	37.64	0.11	20.47	28.40	1.35	2.04	9.26	0.01	0.00	99.29	Grt	1047.79
05-04D	1 / 106 .	99.72	0.00	0.02	0.60	0.02	0.00	0.04	0.00	0.00	100.40	Qtz	1057.86
05-04D	1 / 107 .	100.05	0.00	0.03	0.62	0.01	0.00	0.05	0.01	0.00	100.78	Qtz	1067.94
05-04D	1 / 108 .	37.60	0.18	20.55	28.81	1.42	2.07	9.18	0.03	0.00	99.84	Grt	1078.01
05-04D	1 / 109 .	37.54	0.19	20.49	27.59	1.43	2.01	10.16	0.02	0.01	99.44	Grt	1088.09
05-04D	1 / 110 .	37.40	0.20	20.35	27.98	1.48	1.72	10.13	0.01	0.00	99.29	Grt	1098.16
05-04D	1 / 111 .	37.54	0.21	20.43	28.28	1.52	1.72	9.95	0.03	0.00	99.67	Grt	1108.23
05-04D	1 / 112 .	37.40	0.18	20.39	28.53	1.50	1.63	9.81	0.00	0.02	99.46	Grt	1118.31
05-04D	1 / 113 .	37.38	0.17	20.39	29.05	1.54	1.59	9.18	0.02	0.00	99.31	Grt	1128.38
05-04D	1 / 114 .	37.00	0.17	20.38	29.07	1.49	1.52	9.42	0.04	0.00	99.10	Grt	1138.46
05-04D	1 / 115 .	37.39	0.19	20.29	28.80	1.57	1.52	9.76	0.03	0.01	99.55	Grt	1148.53
05-04D	1 / 116 .	36.98	0.17	19.91	29.13	1.46	1.71	8.92	0.02	0.14	98.45	Grt	1158.61
05-04D	1 / 117 .	37.58	0.14	20.55	29.20	1.64	1.55	9.03	0.02	0.01	99.70	Grt	1168.68
05-04D	1 / 118 .	37.25	0.17	20.45	28.87	1.55	1.51	9.16	0.01	0.01	98.99	Grt	1178.76

Appendix 6 - Isocon analysis

Appendix 6 - Isocon analysis

Isocon analysis was performed on whole rock XRF data in order to look at the mobility of elements within a suite of samples (05-01 to 05-06). These samples mark the transition from a macroscopically undeformed granite to an augen gneiss and a garnet-mica schist over a distance of ~20m. Isocon analysis using the method of Grant (1986) provides an effective means of quantitively evaluating the chemical mass transfer of a suite of samples. The equation by Gresens (1967) summarises the composition-volume relations during metasomatic alteration

$$C_i^A = \frac{M^O}{M^A}(C_i^O + \Delta C_i)$$

Where C_i is the concentration of species "i" in the original rock "O" and the altered rock "A". $M^O$and M^A are the equivalent masses before and after alteration.

For an immobile species where $\Delta C_i = 0$, $\frac{M^O}{M^A} = \frac{C_i^A}{C_i^O}$ = the slope of the immobile isocon, which yields the overall change in mass relative to M^O. This can be calculated by looking for clustering in the data, alternatively it can be plotted graphically where the immobile species define a straight line through the origin using a linear best fit method. Other methods of calculation are based on the assumptions that certain elements were immobile during alteration, that mass remained constant during alteration or that volume remained constant during alteration. Cail and Cline (2001) plotted pairs of species and looked for linear arrays passing through the origin, thus defining which elements were immobile. Baumngartner and Olsen (1995) suggested that elements are immobile if they lie within 1σ of an isocon defined by the largest number of species. However, this is based on the assumption that the majority of elements are immobile and does not allow any bias suggested by the geochemical characteristic of certain elements. It should therefore be used in conjunction with other geochemical arguments and petrographic observations (Baumgartner and Olsen, 1995, p1268). A fully x-y-weighted least squares procedure for the best fit of immobile elements is suggested when defining the isocon (Baumgartner and Olsen, 1995, p1268). It is important to note that scaling is irrelevant to the slope of an isocon if the isocon is based on the slope $\frac{C_i^A}{C_i^O}$ from the origin to each data point, as the scaling factor cancels during the slope calculations (Grant, 2004).

Clusters in the data were identified based on the more immobile elements TiO2, P2O5, Nb and Zr. The average slope of these clusters was used to define the immobile isocon through the origin ($\frac{M^O}{M^A}$). The values for the slopes of the immobile isocons are shown in Table 3. Species lying above the line were gained during alteration and species below the line were lost. The gain/loss of different elements is calculated by the equation

Appendix 6 - Isocon analysis

$$\frac{\Delta C_i}{C_i^O} = \frac{M^A}{M^O}\frac{C_i^A}{C_i^O} - 1$$

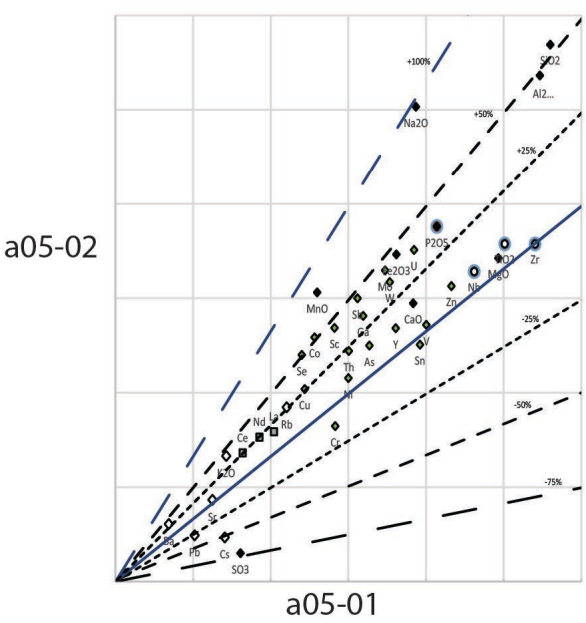
Where $\frac{C_i^A}{C_i^O}$ is the slope of the line from the origin to the data point, $\frac{M^A}{M^O}$ is the slope of the calculated immobile isocon. The data was then scaled in order to view the data to the best advantage. Data with larger uncertainties was scaled towards the origin of the diagram as in Baumgartner and Olsen (1995, p. 1264).

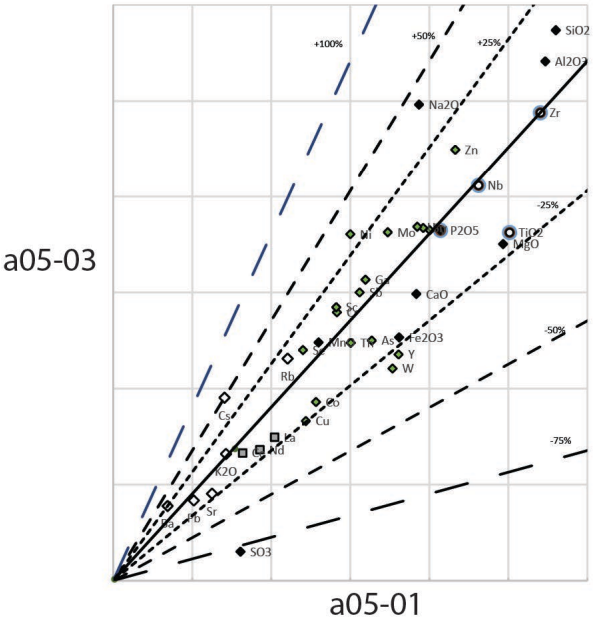
Sample	*a05-02*	*a05-03*	*a05-04*	*a05-05*	*a05-06*	*a05-07*
$\frac{M^O}{M^A}$	0.695	0.892	0.977	0.964	1.037	0.984

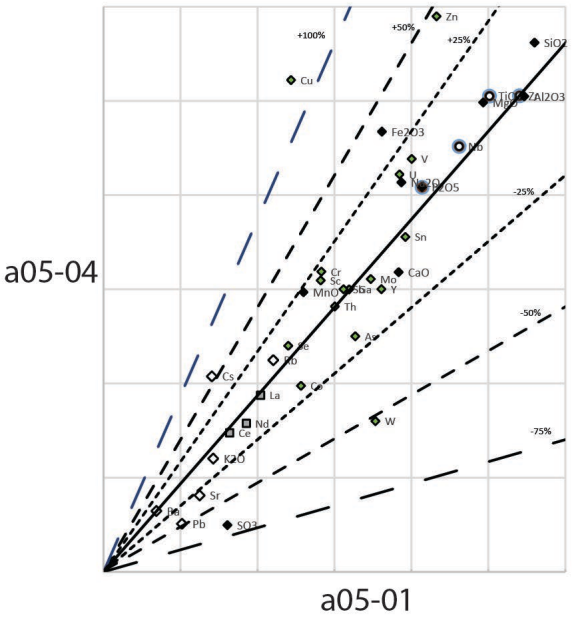
Table 1 average slope of from the origin through the elements TiO2, P2O5, Nb and Zr

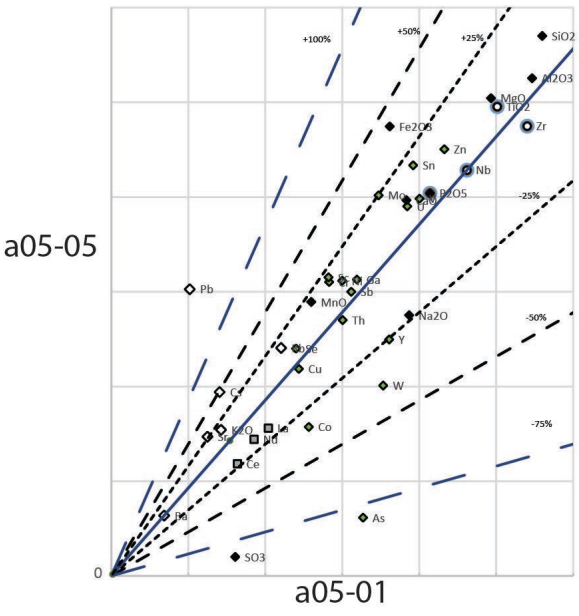
The largest source of uncertainty lies in the selection of the least altered protolith, where the original rock no longer exists. Sample a05-01 is selected to represent the 'original granite protolith', however it shows textures which indicate that it has been metamorphosed. The absence of a fabric is thought to limit the availability of fluid-access to the system and therefore limit the amount of metasomatism able to take place.

Appendix 6 - Isocon analysis









Appendix 6 - Isocon analysis

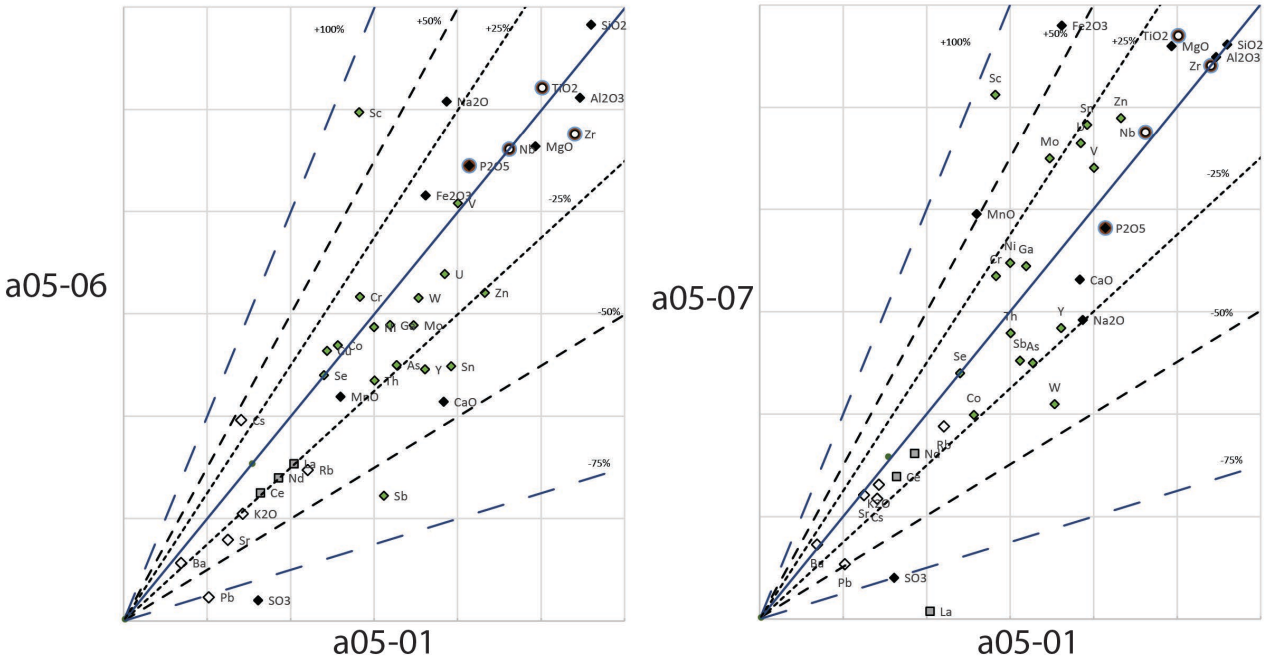


Figure 1 – Isocon analysis of the whole rock geochemistry of the transect from macroscopically undeformed granite (sample a05-02) to garnet-mica schist (sample a05-07) described in chapter 7. All samples plotted against least deformed sample a05-01.